STATE OF CALIFORNIA DEPARTMENT OF TRANSPORTATION

TECHNICAL REPORT DOCUMENTATION PAGE

TR0003 (REV. 10/98)

1. REPORT NUMBER	2. GOVERNMENT ASSOCIATION NUMBER	3. RECIPIENT'S CATALOG NUMBER
CA16-2423		

4. TITLE AND SUBTITLE	5. REPORT DATE
Seismic Performance of Bridge Column-Pile-Shaft Pin Connections for Application in Accelerated Bridge Construction	May 2016
	6. PERFORMING ORGANIZATION CODE UNR
7. AUTHOR(S) Mehrdad Mehraein, M. Saiid Saiidi	8. PERFORMING ORGANIZATION REPORT NO. UNR/CA16-2423 UNR/CCEER 16-01
9. PERFORMING ORGANIZATION NAME AND ADDRESS Department of Civil and Environmental Engineering, MS 258 University of Nevada, Reno 1664 N. Virginia Street Reno, NV 89557	10. WORK UNIT NUMBER 11. CONTRACT OR GRANT NUMBER 65A0466
12. SPONSORING AGENCY AND ADDRESS California Department of Transportation Engineering Service Center 1801 30th Street, MS 9-2/5i Sacramento CA 95816 California Department of Transportation Division of Research and Innovation, MS-83 1227 O Street Sacramento CA 95814	13. TYPE OF REPORT AND PERIOD COVERED Final Report 7/5/2012 – 11/30/2015 14. SPONSORING AGENCY CODE 913

15. SUPPLEMENTAL NOTES

Prepared in cooperation with the State of California Department of Transportation.

16. ABSTRACT

Bridges with integral superstructures are common in high-seismic regions. The superstructure and substructure are connected using rigid connections in these bridges. However, hinge or "pin" connections may be used to connect columns to pile-shafts to reduce the overall force demand in the integral bridges, leading to smaller and more economical foundations. Additionally, prefabrication of structural elements facilitates accelerated bridge construction (ABC), which could improve the quality and economy of project compared to cast-in-place (CIP).

The primary objectives of this research were to investigate the seismic performance of three types of bridge bent connections: (1) pipe-pin connections at column-pile shaft joints for CIP and precast constructions (2) rebar-pin connections at column-pile shaft joint for CIP and precast constructions, and (3) pocket connections to develop rigid joints between precast columns and precast pier caps. This research was comprised of experimental and analytical studies.

The experimental portion of the study was conducted on a shake table at the Earthquake Engineering Laboratory at the University of Nevada, Reno including two 1/3.75 scale, two-column bents subjected to seismic loadings. The cap beam in each bent was precast and connected to the columns using pocket details. The pin connections were used to connect the columns to pedestals, which simulated the pile-shafts. The column-pedestal joints were formed using pipe-pins in one bent and rebar-pin in the other bent. The available details of pin connections were modified for utilizing in the bents because the tensile force transfer mechanism and pile-shaft failure modes had not been accounted for in the current practices. A proposed ABC method for pin connections was investigated by constructing one column in each bent as a precast shell filled with self-consolidating concrete (SCC), whereas the other column was CIP. Furthermore, engineered cementitious composite (ECC) was incorporated in one column plastic hinge region of each bent to explore the effects of ECC on the seismic performance of the columns. The shake table experiments confirmed that the proposed design methods meet the safety and performance requirements of the codes under seismic loadings.

The analytical studies consisted of: (1) simple stick models for the pin connections that were developed for the bents as design tools, (2) nonlinear finite element (FE) models for the pin connections in OpenSEES that can be utilized for global analysis of bridges with pin connections, and (3) elaborate nonlinear FE models of the bent with pipe-pins using ABAQUS to investigate the microscopic performance and interactions of the components. The analytical models were evaluated based on their correlation with experimental data and were subsequently used in focused parametric studies to address the gaps in the experimental results and provide more insight into the pin behavior under various conditions. Lastly, design procedures and detailing recommendations for column-pile-shaft connections using pipe-pins and rebar-pins were developed and proposed based on the results of the experimental and analytical parametric studies.

17. KEY WORDS	18. DISTRIBUTION STATEMENT	
Seismic, Column-Pile-Shaft Connection, Pipe-Pin, Rebar-Pin, Column Key, Precast Cap Beam, Accelerated Bridge Construction, Precast Column	No restrictions. This document is available to the public through the National Technical Information Service, Springfield, VA 22161	
19. SECURITY CLASSIFICATION (of this report) Unclassified	20. NUMBER OF PAGES 748	21. PRICE

DISCLAIMER STATEMENT

This document is disseminated in the interest of information exchange. The contents of this report reflect the views of the authors who are responsible for the facts and accuracy of thedata presented herein. The contents do not necessarily reflect the official views or policies of the State of California or the Federal Highway Administration. This publication does not constitute a standard, specification or regulation. This report does not constitute an endorsement by the Department of any product described herein.

For individuals with sensory disabilities, this document is available in Braille, large print, audiocassette, or compact disk. To obtain a copy of this document in one of these alternateformats, please contact: the Division of Research and Innovation, MS-83, California Departmentof Transportation, P.O. Box 942873, Sacramento, CA 94273-0001.

Report No. CCEER 16-01

SEISMIC PERFORMANCE OF BRIDGE COLUMN-PILE-SHAFT PIN CONNECTIONS FOR APPLICATION IN ACCELERATED BRIDGE CONSTRUCTION

Mehrdad Mehraein
M. Saiid Saiidi

A report sponsored by the Civil and Environmental Engineering Department
Unversity of Nevada, Reno

Center for Civil Engineering Earthquake Research

University of Nevada, Reno
Department of Civil and Environmental Engineering, MS 258
1664 N. Virginia St.
Reno, NV 89557

May 2016

Abstract

Bridges with integral superstructures are common in high-seismic regions. The superstructure and substructure are connected using rigid connections in these bridges. However, hinge or "pin" connections may be used to connect columns to pile-shafts to reduce the overall force demand in the integral bridges, leading to smaller and more economical foundations. Additionally, prefabrication of structural elements facilitates accelerated bridge construction (ABC), which could improve the quality and economy of project compared to cast-in-place (CIP).

The primary objectives of this research were to investigate the seismic performance of three types of bridge bent connections: (1) pipe-pin connections at column-pile shaft joints for CIP and precast constructions (2) rebar-pin connections at column-pile shaft joint for CIP and precast constructions, and (3) pocket connections to develop rigid joints between precast columns and precast pier caps. This research was comprised of experimental and analytical studies.

The experimental portion of the study was conducted on a shake table at the Earthquake Engineering Laboratory at the University of Nevada, Reno including two 1/3.75 scale, two-column bents subjected to seismic loadings. The cap beam in each bent was precast and connected to the columns using pocket details. The pin connections were used to connect the columns to pedestals, which simulated the pile-shafts. The column-pedestal joints were formed using pipe-pins in one bent and rebar-pin in the other bent. The available details of pin connections were modified for utilizing in the bents because the tensile force transfer mechanism and pile-shaft failure modes had not been accounted for in the current practices. A proposed ABC method for pin connections was investigated by constructing one column in each bent as a precast shell filled with self-consolidating concrete (SCC), whereas the other column was CIP. Furthermore, engineered cementitious composite (ECC) was incorporated in one column plastic hinge region of each bent to explore the effects of ECC on the seismic performance of the columns. The shake table experiments confirmed that the proposed design methods meet the safety and performance requirements of the codes under seismic loadings.

The analytical studies consisted of: (1) simple stick models for the pin connections that were developed for the bents as design tools, (2) nonlinear finite element (FE) models for the pin connections in OpenSEES that can be utilized for global analysis of bridges with pin connections, and (3) elaborate nonlinear FE models of the bent with pipe-pins using ABAQUS to investigate the microscopic performance and interactions of the components. The analytical models were evaluated based on their correlation with experimental data and were subsequently used in focused parametric studies to address the gaps in the experimental results and provide more insight into the pin behavior under various conditions. Lastly, design procedures and detailing recommendations for column-pile-shaft connections using pipe-pins and rebar-pins were developed and proposed based on the results of the experimental and analytical parametric studies.

Acknowledgements

The research presented in this paper was funded by the California Department of Transportation (Caltrans) under grant No. 65A0466. However, the statements and findings presented in this document are those of the author and do not necessarily represent the views of Caltrans. The advice and support of Caltrans research program manager, Mr. Peter Lee, Caltrans Chief Earthquake Engineer, Dr. Mark Mahan, and senior Caltrans designers, Mr. Ron Bromenschenkel, and Dr. Amir Malek, are highly appreciated.

The support of Dr. Patrick Laplace, Mr. Mark Lattin, Mr. Chad Lyttle, and Mr. Todd Lyttle of the UNR Earthquake Engineering Laboratory is appreciated. Dr. Ali Mehrsoroush, Dr. Mostafa Tazarv, Ms. Hilda Lovasz, Messrs. Alireza Mohebi, Wheeler Musnicki, Osi Arias, and Farshad Meshkati are thanked for their dedicated assistance and support in the course of the study. Mr. Don Newman is particularly acknowledged for his careful construction of the test models.

This report is based on a Ph.D. dissertation by the first author supervised by the second author.

Executive Summary

1. Introduction

Standard bridges are designed for collapse prevention under extreme seismic events based on ductile design concepts. Bridges with integral superstructures are common in high seismic regions. The superstructure and substructure are connected using rigid connections in these bridges to enhance the integrity of the bridge under seismic loading. The substructure may be constructed on an enlarged pile-shaft foundation in cases that the use of spread footing is not feasible. In a properly designed bridge, plastic hinges are formed in the columns to dissipate energy during strong earthquakes. The plastic hinges act as a fuse to prevent damage in the superstructure and foundations. Therefore, at least one end of the columns should be connected to the foundation or cap beam rigidly to force formation of the plastic hinges in the column. A hinge or a "pin" connection may be used at one end of the column to reduce the overall force demand leading to smaller and more economical foundations.

The economy of bridge projects can also be improved by reducing the construction time. The bridge construction process may disrupt flow of transportation, require long detour, or require costly use of temporary structures. Cast-in-place (CIP) is the prevailing bridge construction method, which requires concrete to set and cure onsite leading to slow construction. In contrast, prefabricating bridge components can reduce the construction time by eliminating the need for on-site curing and making use of components that have been fabricated in parallel. Another important factor is that the quality of construction would be enhanced by offsite fabrication due to a better control over the material quality and construction. Prefabrication of the elements facilitates accelerated bridge construction (ABC), which is rapid bridge construction using innovative planning, design, materials, and efficient construction methods in a safe and cost-effective manner.

2. Research Objectives

The main objectives of this study were to investigate the seismic performance of three types of bridge bent connections through experimental testing and analytical modeling:

1- Pipe-pin connections to develop hinge support at column-pile shaft joints for CIP and precast constructions.

2- Rebar-pin connections to develop hinge supports at column-pile shaft joint for CIP and precast constructions.

3- Pocket connections to develop rigid connections between precast columns and precast pier caps in bridges with integral superstructure-pier connections.

An additional objective of the study was to improve the current design guidelines for each connection type based on the results of the experimental, analytical studies, and parametric studies. An objective of the study was also to investigate the performance of ECC in column plastic hinge zones to mitigate damage in CIP and precast columns.

The study consisted of shake table testing of two large-scale bent specimens and performing comprehensive analytical studies of connections to determine the adequacy of the concepts developed in this and other studies and the need for further refinements.

3. Experimental Studies

The experimental part of the project was testing of two, two-column bents on shake tables of the Earthquake Engineering Laboratory at the University of Nevada, Reno. The test specimens were 1/3.75 scale models that were based on some of the features of the approach spans bents of the San Francisco Oakland Bay Bridge. Pin connections were provided in column to shaft connections in the test models. Two test models were built, BPSA and BRSA. BPSA stands for bent with pipe-pin column-pile-shaft connection for accelerated bridge construction (ABC) and BRSA stands for bent with rebar-pin column-pile-shaft connection for ABC. Pipe-pin connections were used in BPSA model and rebar-pins in BRSA model.

Two methods of construction for columns were implemented. South column in each bent was cast-in-place (CIP) and the other was precast (PC) to study different construction methods. The components on the south side of the bent are referred to as CIP (cast in place) components such as CIP column hereafter. The components on the north side of the bent are referred to as PC (precast) components such as PC column, hereafter. The proposed precast construction method consisted of two parts. The column shells were cast first. The pin was inserted in a 3-inch [76-mm] thick precast concrete shell of the column. Then, the shell was filled with SCC at the same time with the joint. The columns were connected to the precast bent cap with pocket connections. The protruded bars at the top end of the columns were inserted into the pocket in the precast cap beam. Finally, self-consolidating concrete (SCC) was placed in the hollow section (Fig. 1).

Pedestals were built under each column to model column to Type II pile-shaft connections. The pedestals were sufficiently tall to represent the structural behavior of pile-shafts. The study of soil interaction with pile-shafts was beyond the scope of this research. Details of the experimental studies and results are presented in Chapter 2 and 3 of this document, respectively.

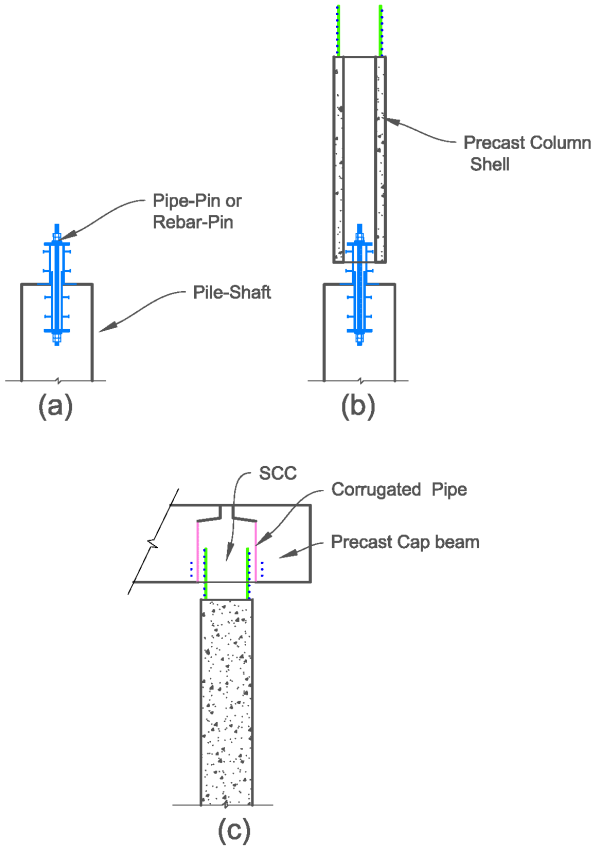

Fig. 1. Propose precast construction method

3.1. Bent with Pipe-Pin Column-Pile Shaft Connection (BPSA)

The connections of the columns to pedestals were pipe-pins in this model. The joints between column and precast cap beam were pocket connections. Figure 2 shows the elevation view of BPSA. ECC was used over the full height of the plastic hinge region of the CIP column. The model was designed according to the Caltrans ductile design guidelines (Seismic Design Criteria, 2010). The connections were designed as capacity protected members with plastic hinging allowed only in the columns. While the columns were expected to undergo plastic deformation, the rest of the structure including the pipe-pins were designed to remain undamaged. Figures 3 and 4 show the details of the pipe-pin and pocket connections respectively.

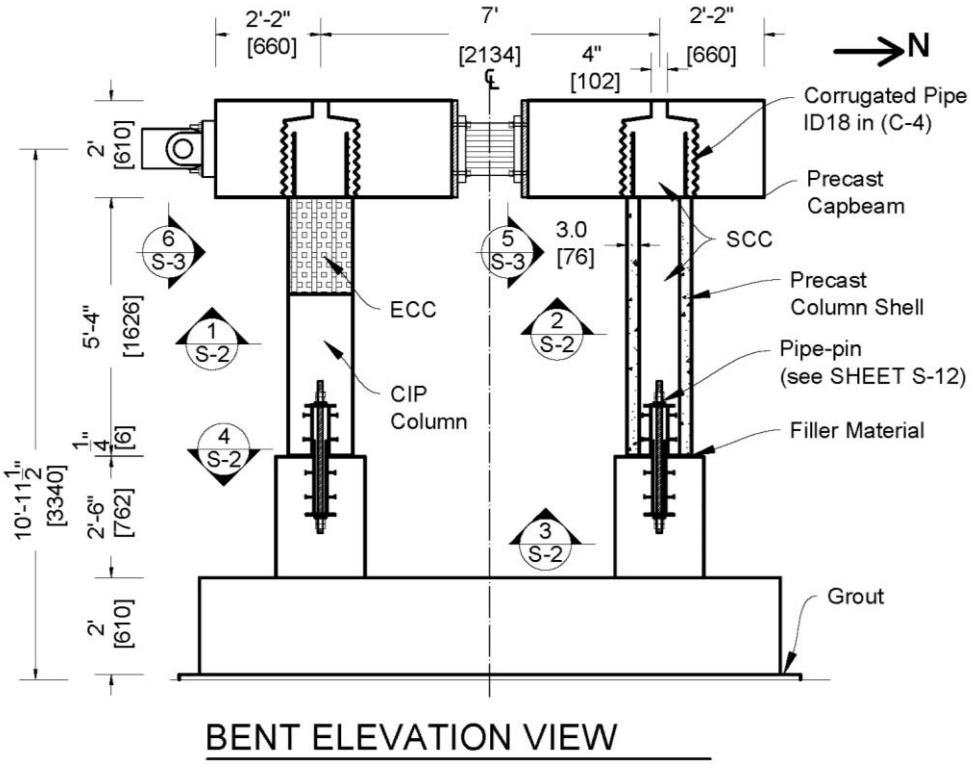

BENT ELEVATION VIEW

Fig. 2. BPSA elevation view

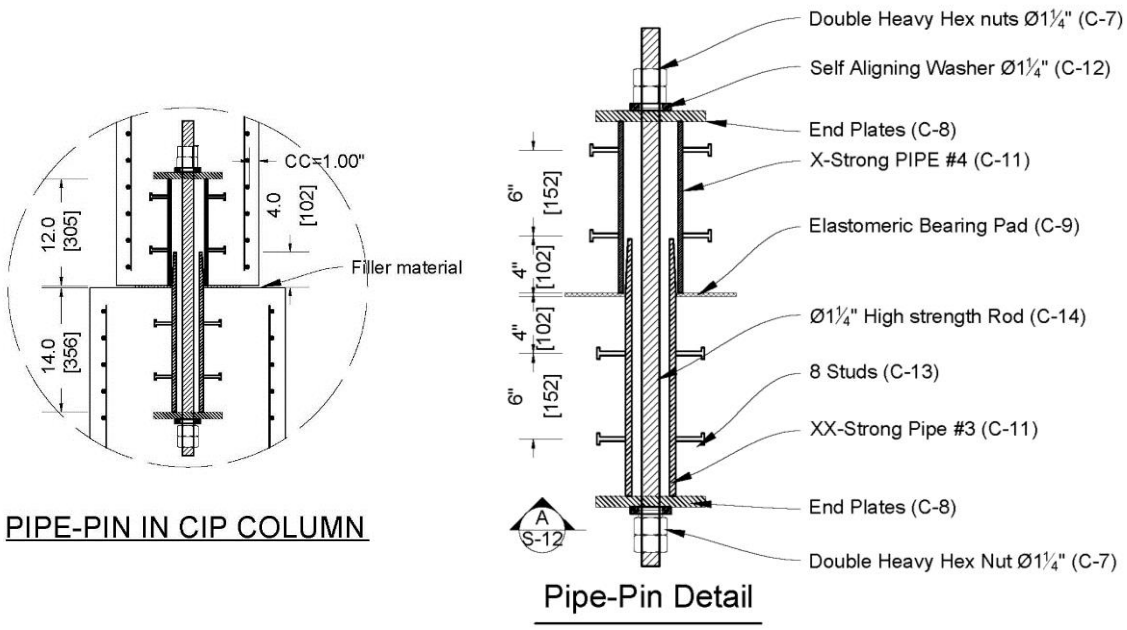

PIPE-PIN IN CIP COLUMN

Pipe-Pin Detail

(a) (b)

Fig. 3. Pipe-pin details

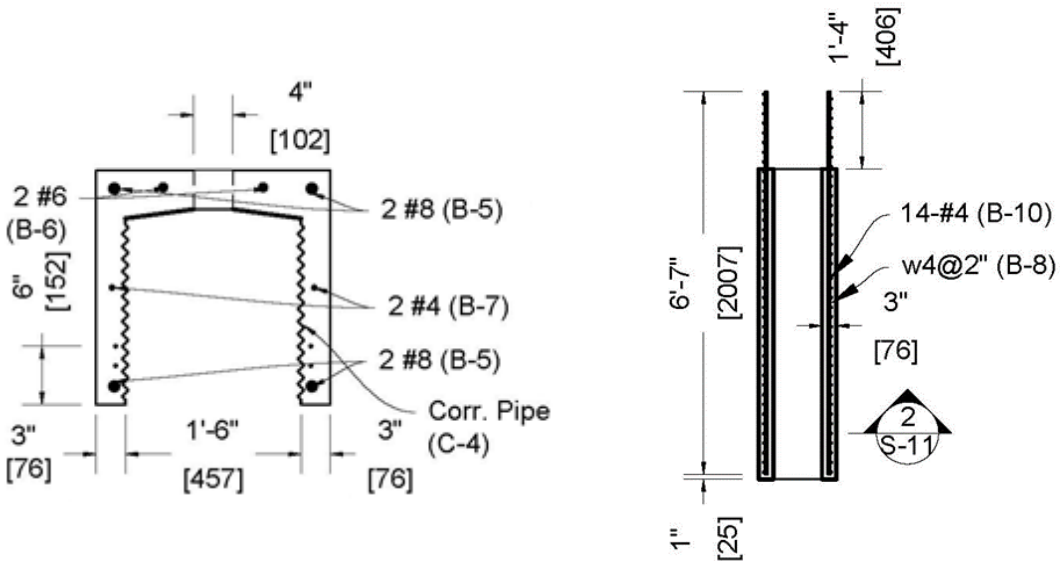

(a) (b)

Fig. 4. Precast elements details a) cap beam section b) columns

The input ground motion needed to be strong enough to generate sufficient demand. Yet its displacement, velocity, and acceleration needed to be within the shake table limits. It was also preferred to have symmetric response to investigate the performance under full reversed cycles. The 142-degree of Sylmar Converter Station of the 1994 Northridge earthquake was chosen for simulation in the shake table tests (Fig. 5). The acceleration was filtered to have a symmetric ground motion. Additionally, the time axis of the acceleration record had to be shortened to account for the scale of the test model. The time axis was scaled by the square root of the geometric scale factor to account for the shorter period of the model relative to the prototype (Harris, 1982). The specimen was subjected to series of excitations until it reached the ultimate capacity of the bent. BPSA was tested under 11 motions with peak ground motion accelerations (PGAs) of 0.09g, 0.27g, 0.45g, 0.54g, 0.54g, 0.54g, 0.63g, 0.81g, and 0.99g, respectively. A white noise motion also applied to the specimen before each run and after the last run to capture the dynamic characteristics of the bent.

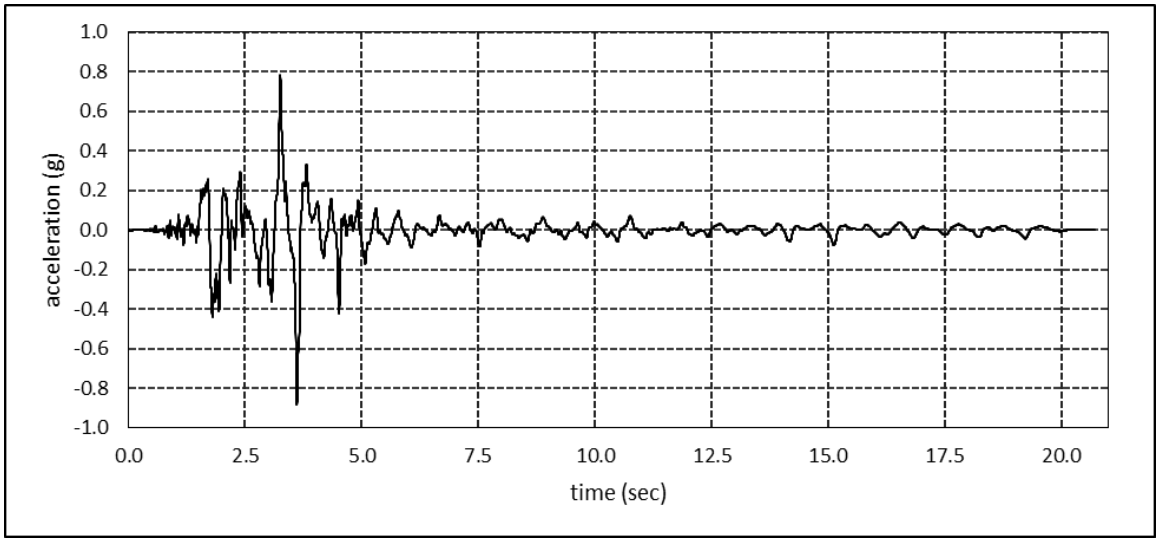

Fig. 5. Input ground motion acceleration

Detailed examination of the measured data indicated that the design of BPSA was satisfactory. Figure 6 shows the final condition of the specimen after the tests. Substantial plastic deformations were developed at the top of the columns (Fig. 7a and 7b). The lateral load capacity of the bent was reached due to plastic hinge failure in the CIP column, with no indication of damage in the pipe-pins. Minimal cracks were formed around the pipe-pin connection (Fig. 7c). The strain gages on the pipes also showed that the pipes remained elastic, as intended. Moments were developed at the bottom of the columns that were not considered in the design of the bent. The prefabricated column and pipe-pin performed as well as the cast-in-place elements. No difference was observed in the performance of the precast column and the cast in place column with pipe-pin connections. The pocket connections performed as designed to form the plastic hinge in the columns. Furthermore, the cap beam remained elastic. In addition, the column plastic hinge with ECC showed significantly less damage than that with conventional concrete (Fig. 7a and 7b).

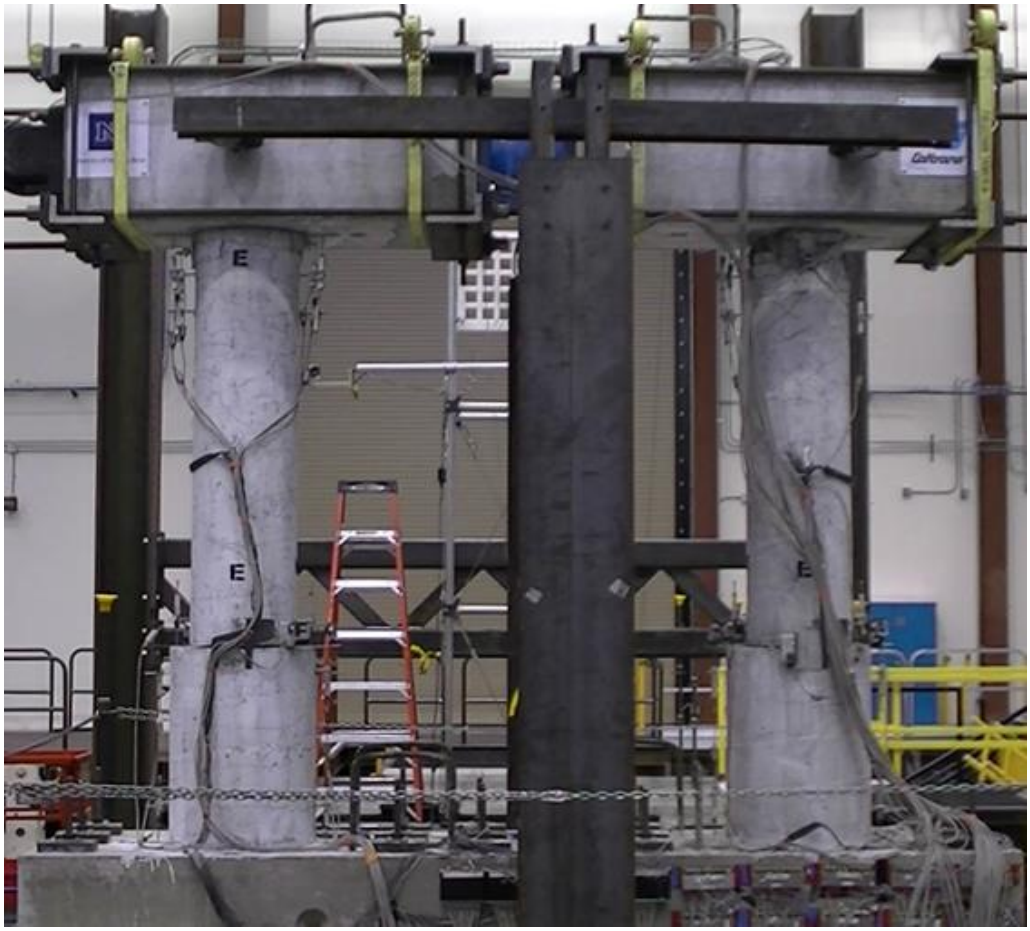

Fig. 6. BPSA final condition after the tests

(a) (b) (c)

Fig. 7. Final conditions of elements in BPSA a) CIP column with ECC b) PC column c) CIP pipe-pin

Figure 8 shows the measured force-displacement hysteretic curves for BPSA. The first yield occurred in longitudinal bars of the PC column at displacement of -0.65 in [17 mm]. The displacement ductility of the bent was 3.6 from the envelope of the tests. However, the formation of full column plastic hinges and the strain data in plastic hinges indicate substantially higher ductility. The measured initial stiffness was highly reduced because of the slippage of the load cell to cap beam connection in the early runs (section 3.2.4). The force-displacement hysteresis curves of the bent indicated a slight pinching effect near the origin. The pinching is attributed to slippage at the pipe pins due to the closure of the gaps between the two pipes at each pin. The fluctuating pattern also indicates that friction release was gradual and did not occur at a specific displacement of the pipe-pin.

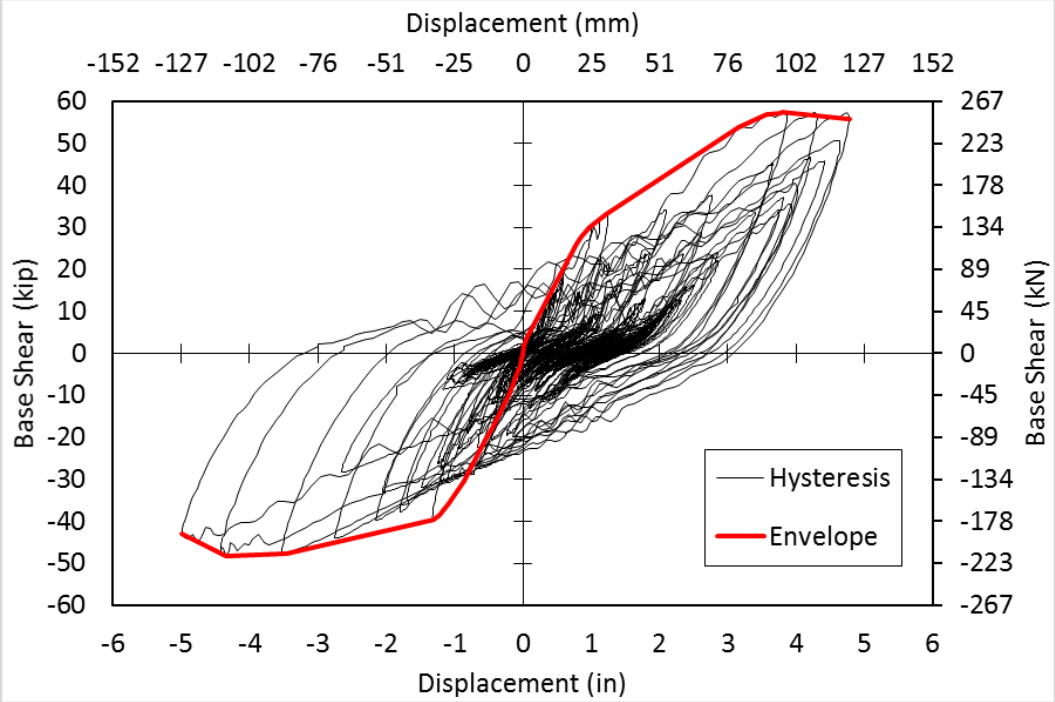

Fig. 8. BPSA force-displacement relationship

3.2. Bent with Rebar-Pin Column-Pile Shaft Connection (BRSA)

The connections of the columns to pedestals in this model were rebar-pins (Fig. 9). Similar to BPSA, the columns in BRSA were connected to the precast bent cap using pocket details. Additionally, ECC was used in the plastic hinge region of the precast concrete shell. The model was designed according to the Caltrans ductile design guidelines (Caltrans, 2010). The rebar-pins were designed based on previous research by Cheng et al. (2006). Figure 10 shows the detail of rebar-pins. They proposed a design method to provide sufficient ductility and shear capacity for the rebar-pins in a bent. While both rebar-pin and plastic hinge of the column undergo large plastic deformation, only the plastic hinge in the columns is expected to fail.

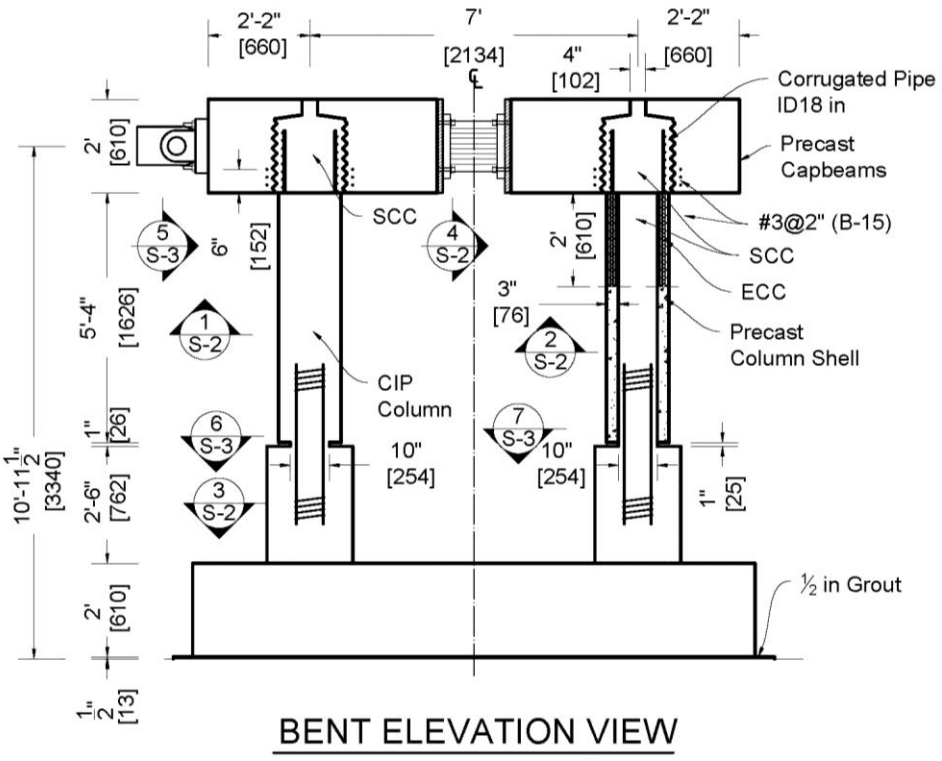

Fig. 9. BRSA elevation view

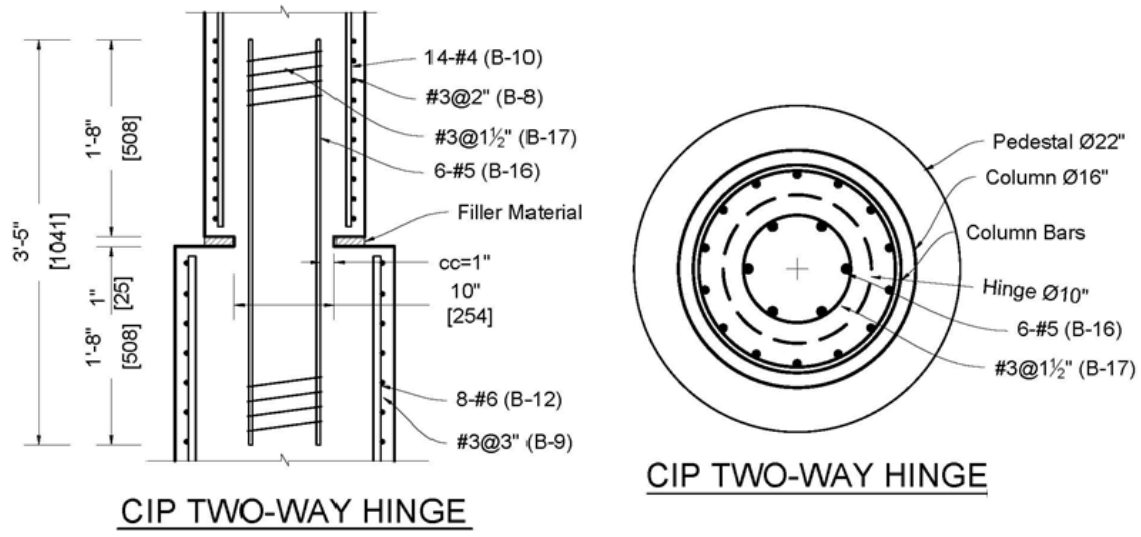

Fig. 10 rebar-pin detail

The criteria of ground motion selection were similar to BPSA ground motion selection. Therefore, same input motion as of that of BRSA was used for BRSA (Fig. 5). It was tested under

six motions with PGAs of 0.09g, 0.314g, 0.538g, 0.763g, 0.987g, and 1.211g, respectively. Before each run and after the last run a white noise motion applied to the bent. The white noise had frequency content of 0.7 to 40 Hz and amplitude of 0.05g similar to that in BPSA.

BRSA performed as it was designed. Figure 11 shows the final condition of BRSA after tests. Full plastic hinge capacity was reached at the top of the column while the rebar-pins did not fail. The rebar-pins underwent large plastic deformations under many cycles of earthquake loading without loss of capacity (Fig. 12a and 12b). The strains in the longitudinal reinforcement were safely under the ultimate strain. Despite the fact that the rebar-pin slipped horizontally, the shear friction was sufficient to resist the shear without gravitational axial load on the columns. The gap around the rebar-pin did not close in spite of the large rotations. The columns and pedestals did not yield near the rebar-pins but the rebar-pins and the surrounding concrete were damaged (Fig. 12c). The pocket connections of the columns to the cap beam performed as they were designed. The plastic hinges in the columns reached their rotation capacity while the reinforcement in the cap beam remained elastic. No damage was observed in the cap beam. Moreover, the PC column with ECC only in shell section showed significantly less damage than the CIP plastic hinge zone with conventional concrete (Fig. 12a and 12b).

Fig. 11. BRSA final condition after tests

(a) (b) (c)

Fig. 12. Final conditions of elements in BRSA a) CIP column b) PC column with ECC c) PC rebar-pin

4. Numerical Simulation of Experiments

Analytical studies of the test models were performed to validate the modeling assumptions based on the correlation between the analytical and experimental results. Three sets of analytical studies were conducted: pushover analysis using a simple stick model, pushover analysis using an elaborate model, and dynamic analysis of the shake-table tests. Details of the analytical studies and results are presented in Chapter 4 of this document.

4.1. Bent with Pipe-Pin Column-Pile Shaft Connection for ABC (BPSA)

4.1.1. Pushover Analysis Using Simple Stick Model

The forces and displacements of the bent were calculated using lumped plasticity. The simple stick model of BPSA consisted of two columns that were supported on pipe-pins and connected to a rigid cap beam at the top (Fig. 13a). The pipe-pins were modeled using the proposed pipe-pin springs. Linear rotational springs were used to model the moment-rotation relationship of the pipe-pins. The shear displacements of the pipe-pins were calculated assuming gap-rigid behavior. The calculated results are well correlated to the test data in terms of the stiffness, maximum base shear, and ultimate displacements with maximum error of 14% (Fig. 13b). The error was relatively small and acceptable considering the simple formulation of the analytical model.

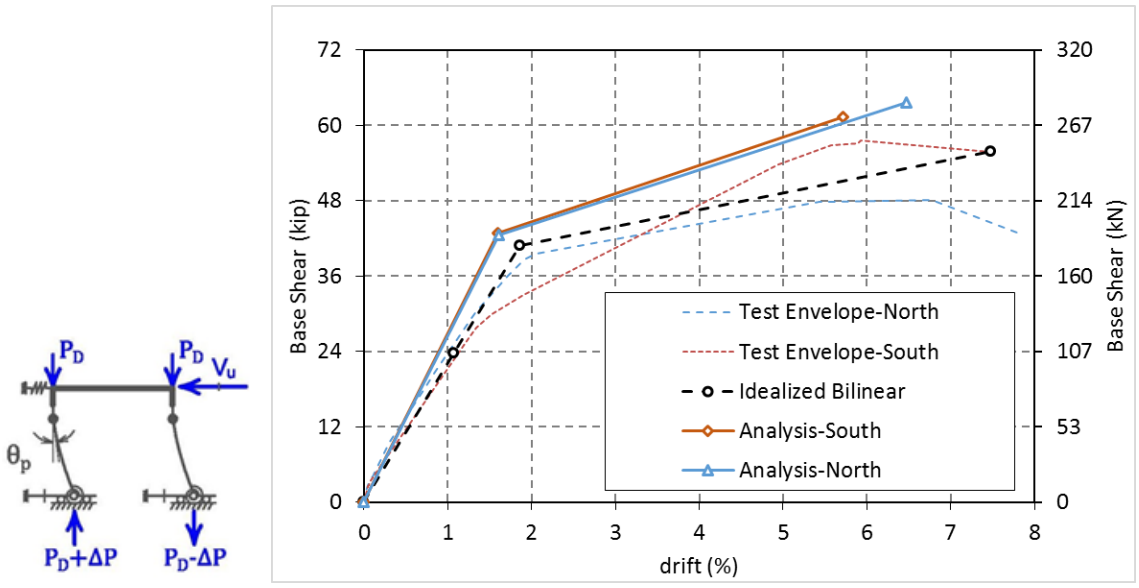

(a) (b)

Fig. 13. Pushover analysis of BPSA using simple stick model a) model b) calculated and measured force-displacement relationships

4.1.2. Dynamic Numerical Simulations Using Frame Elements

Dynamic analysis of BPSA was performed in OpenSEES using frame and zero-length elements. The columns and pedestals were modeled using force-based (FB) elements, which are distributed plasticity elements. The columns to the pedestals connections were modeled using the proposed pipe-pin springs. The mass of the mass rig was added to the cap beam. The weight of the cap beam was also distributed on its nodes.

BPSA was analyzed using different material models, section discretization, and numbers of integration points to investigate the effects of modeling techniques on the analytical results. The results showed that the effects of these parameters on the calculated base shear and displacement are less than 10%. The calculated responses correlated well with the test results in terms of peaks, history shapes, and amplitudes. The calculated base shear and displacement histories for Run-10 are compared with the measured history in Fig. 14. The averages of the calculated peaks were within 20% of the measured data.

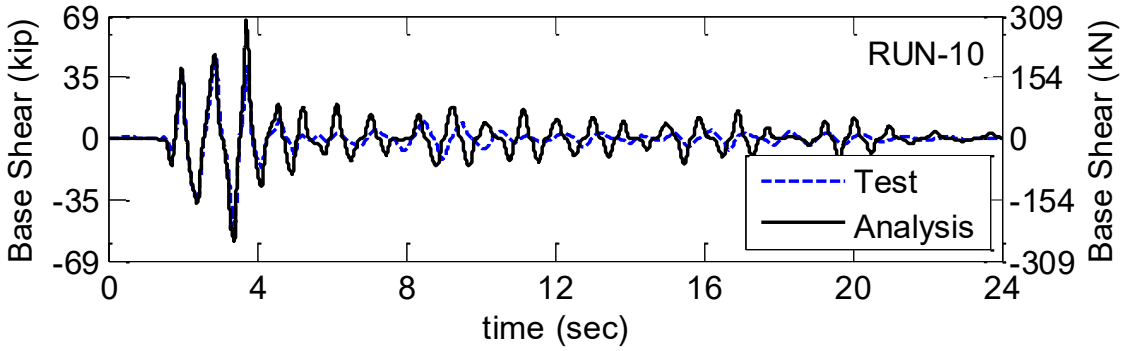

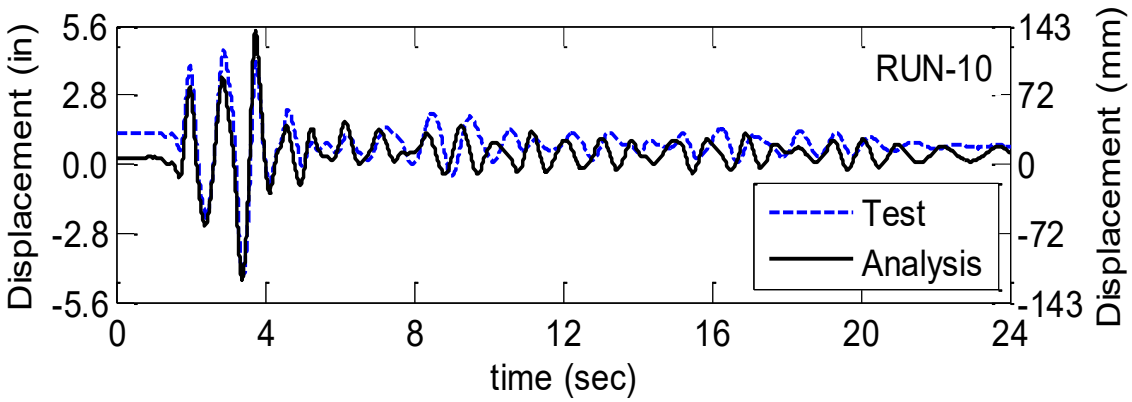

Fig. 14. BPSA calculated and measured force and displacement histories for Run-10

4.1.3. Quasi-Static Numerical Simulations Using Finite Element Modeling

Finite element (FE) models of BPSA were used for pushover analysis using ABAQUS/Explicit (V6.14-1) package. The purpose of the models was to investigate the complex interaction among different parts. Thus, the components of the pipe-pins were modeled with continuum elements to obtain more realistic force interaction through contact surfaces. A sketch of the finite element (FE) models is presented in Fig. 15. Those models were analyzed under quasi-static loading. The numerical simulations were verified by comparing the calculated and measured force-displacement envelopes.

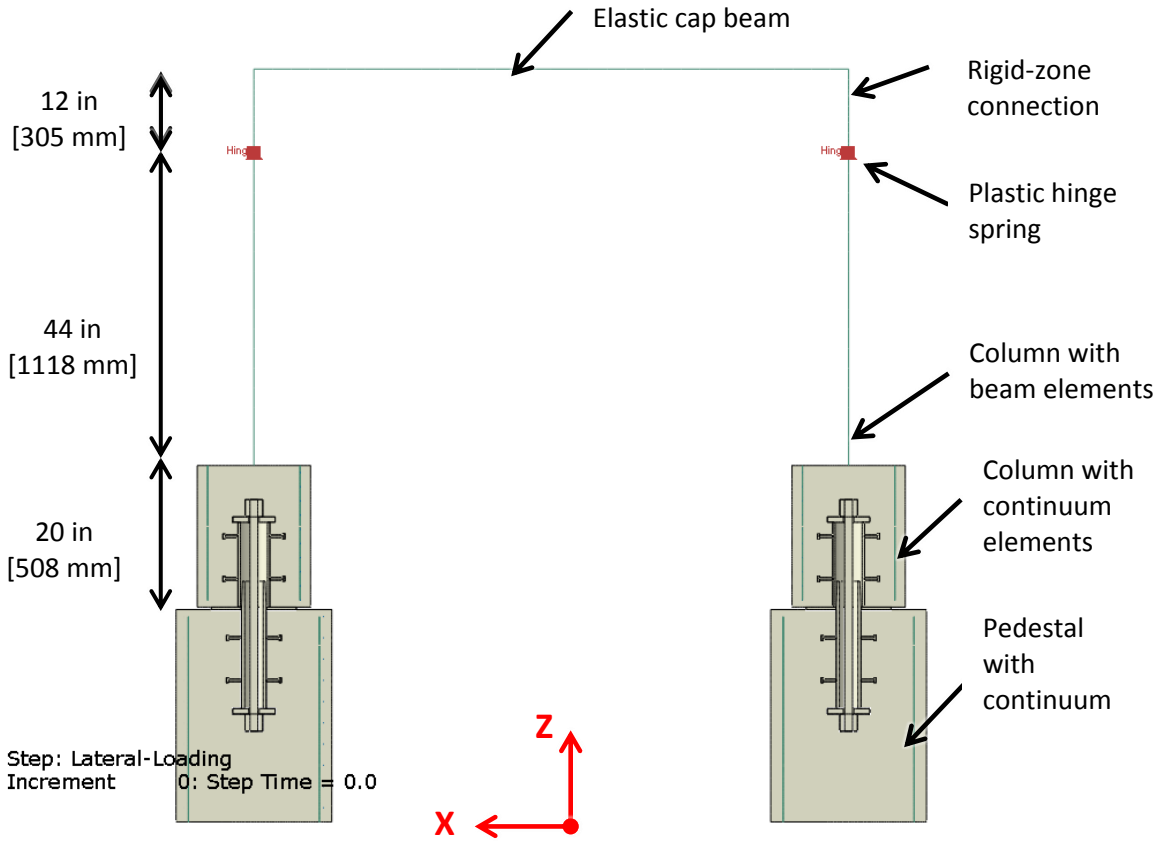

Fig. 15. Sketch of BPSA FE model

The calculated and measured results are well correlated in terms of the yield points, ultimate displacements, and base shear capacity (Fig. 16). The maximum error subsequent to the elastic part of the curve was 15%. The numerical model overestimated the initial stiffness because the actual initial stiffness of the model was relatively low due to the cap beam deformations. In addition to the global force-displacement responses, the cracking patterns, pipe forces, and pipe-pin rotations were well correlated with the measured data (section 4.8.6). This model was subsequently used in parametric studies described in the next section.

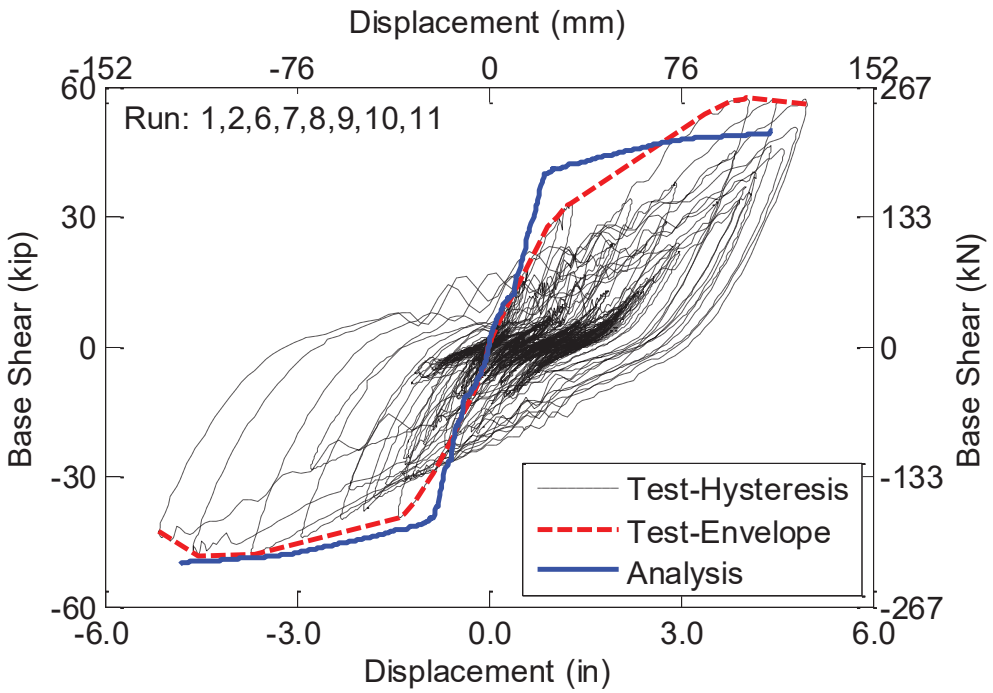

Fig. 16. Comparison of results of FE analysis with the tests envelopes

The forces in the rods versus the bent lateral displacements are shown in Fig. 17. The yielding fore of the rod is shown using a dotted line. The rod forces were tensile even when the columns were under compression because of the rotation of the pipe. The rotations of the pipe-pins generated uplift at the base of the columns. The uplift generated relatively large elongations of the rod to compensate for the compression of the elastomeric pads. While the axial force in the rod was well below the yielding force, the stress condition needed to be checked for the combination of the axial force and flexure. The Von Mises yield stress was 75.1 ksi [518 MPa]. As Fig. 18 shows, the Von Mises stresses in the rod reached the yielding criteria. The fixity of the rod at the end plates produced significant moments under the movements of the pipes and yielded the rod under flexure (dark regions on the rods in Fig. 18).

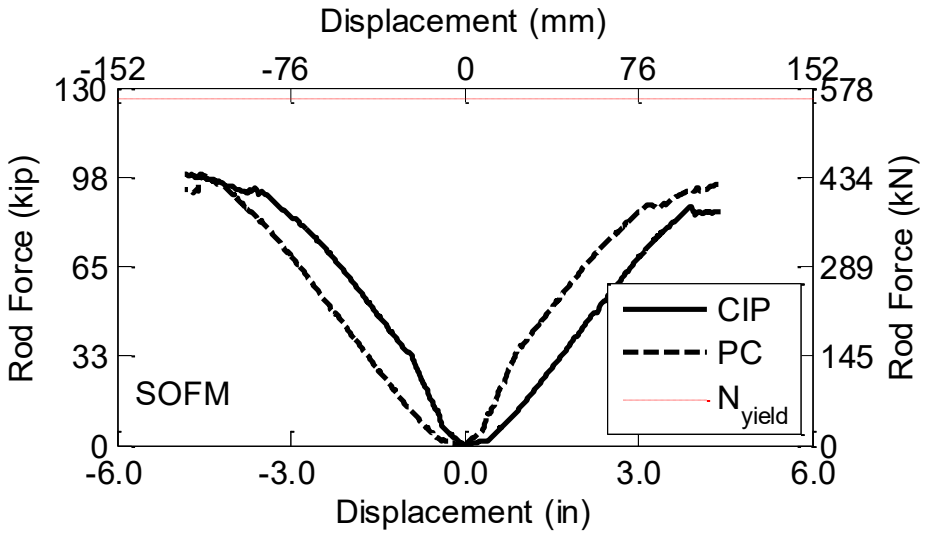

Fig. 17. BPSA threaded rods axial force

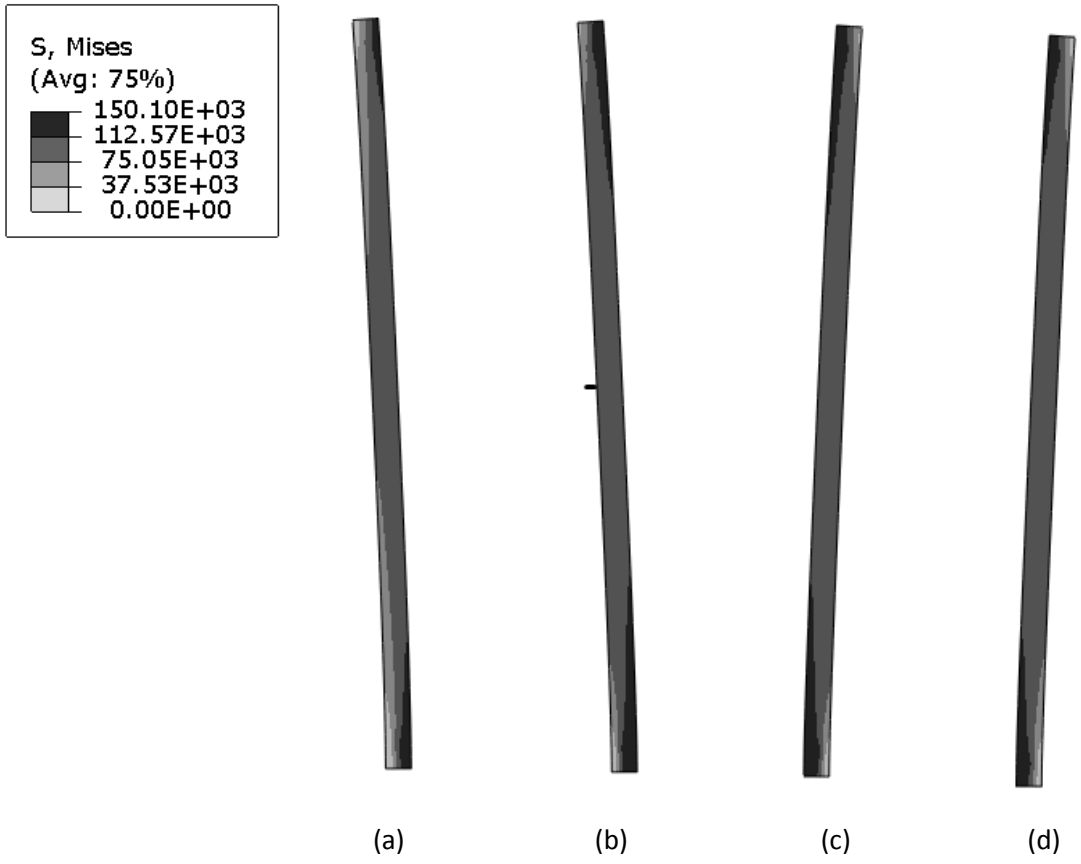

Fig. 18. Von Mises stress (psi) in the rods, South direction: (a) CIP (b) PC, North direction: (c) CIP (d) PC

4.2. Bent with Rebar-Pin Column-Shaft Connection for ABC (BRSA)

4.2.1. Static Numerical Simulations Using Simple Stick Model

A simple stick model of BRSA using the lumped plasticity springs was developed as a design tool. That model was composed of two elastic-plastic column elements supported on rebar-pins and connected to a rigid cap beam at top (Fig. 19a). The Paulay and Priestley (1992) plastic hinge model was used in the numerical simulation of the columns. Furthermore, the rotational behavior of the rebar-pins was modeled using bilinear rotational springs based on the Cheng et al. (2006) model. Moreover, the slippage of the rebar-pins was estimated from the average of the crack shear-slip models. Figure 19b compares the measured and calculated force-displacement relationships. The calculated displacement ductility was 7.4, which is 5% larger than the measured ductility. Despite the simplifying assumptions, the calculated and measured data were reasonably close.

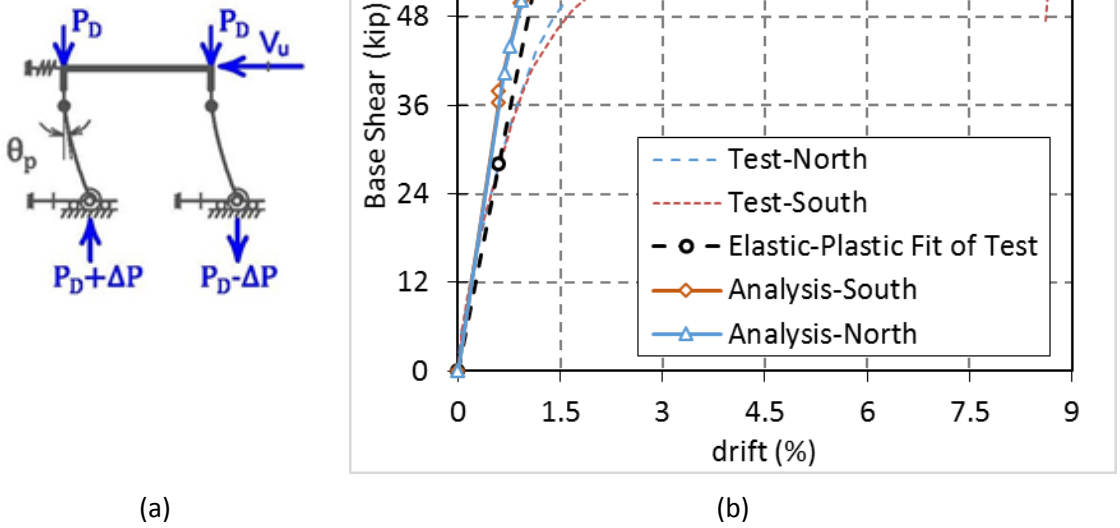

(a) (b)

Fig. 19. Pushover analysis of BRSA using simple stick model a) model b) calculated and measured force-displacement relationships

4.2.2. Static Numerical Simulations Using Frame Elements

Pushover analysis of BRSA was performed in OpenSEES using frame and spring elements. The pushover response was estimated twice, once using the lumped (springs) and again the distributed plasticity models of the rebar-pins (Fig. 20a and 21a). The spring properties of the rebar-pins were based on the Cheng et al. (2006) model. For the distributed model of rebar-pins, displacement-based (DB) and force-based (FB) elements were used. In both models, the columns and pedestals were modeled using the FB elements. The cap beam was modeled using an elastic element. The failure criteria in the analyses were the bent lateral displacement at

which either the core reached its ultimate strain capacity or reinforcing bars fractured. As Figs. 20b and 21b show, the correlation of the results from both models with the test results is acceptable in terms of initial stiffness, yield displacement, ultimate base shear, and ultimate displacement. The model with the springs for the rebar-pins was less sensitive to the displacement increments and number of integration points. The model with spring model of rebar-pins was subsequently used in parametric studies described in the next section.

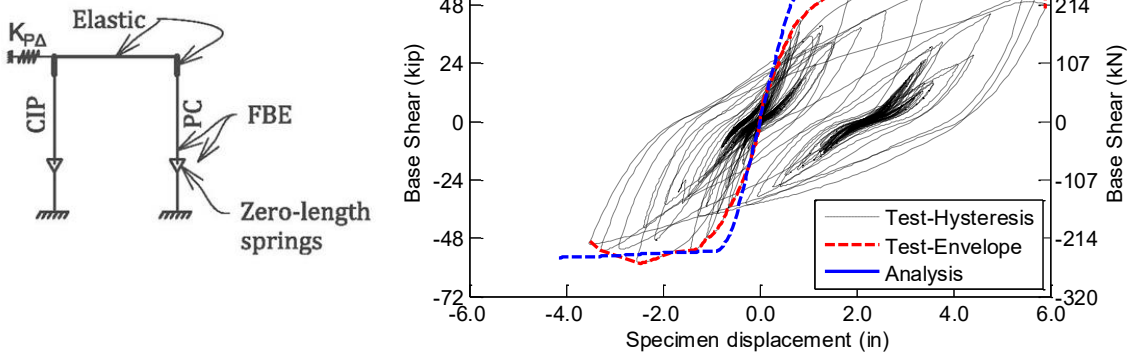

(a) (b)

Fig. 20. BRSA pushover analyses with lumped plasticity for rebar-pins a) bent model b) calculated and measured force-displacement relationships

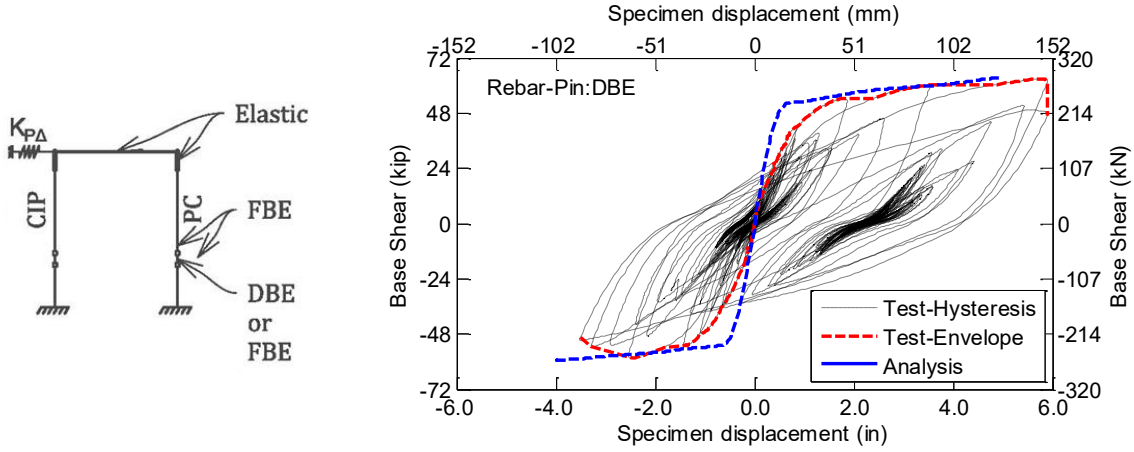

(a) (b)

Fig. 21. BRSA pushover analyses with distributed plasticity for rebar-pins a) bent model b) calculated and measured force-displacement relationships

4.2.3. Dynamic Response Simulation Using Frame Elements

Similar numerical models to the pushover analyses were adopted to analyze BRSA under dynamic loading to simulate the shake table tests (Figs. 20a and 21a). The calculated base shear and displacement using the spring model of the rebar-pins correlated well with the test results in terms of peaks, waveforms, and the base shear and displacement amplitudes. The calculated base shear and displacement histories for Run-4 are compared with the measured history in Fig. 22. Alternatively, the responses were calculated using the distributed plasticity model of the rebar-pins. Despite the good correlation in the base shear, the displacements were underestimated by as much as 26% using the distributed plasticity model of rebar-pins.

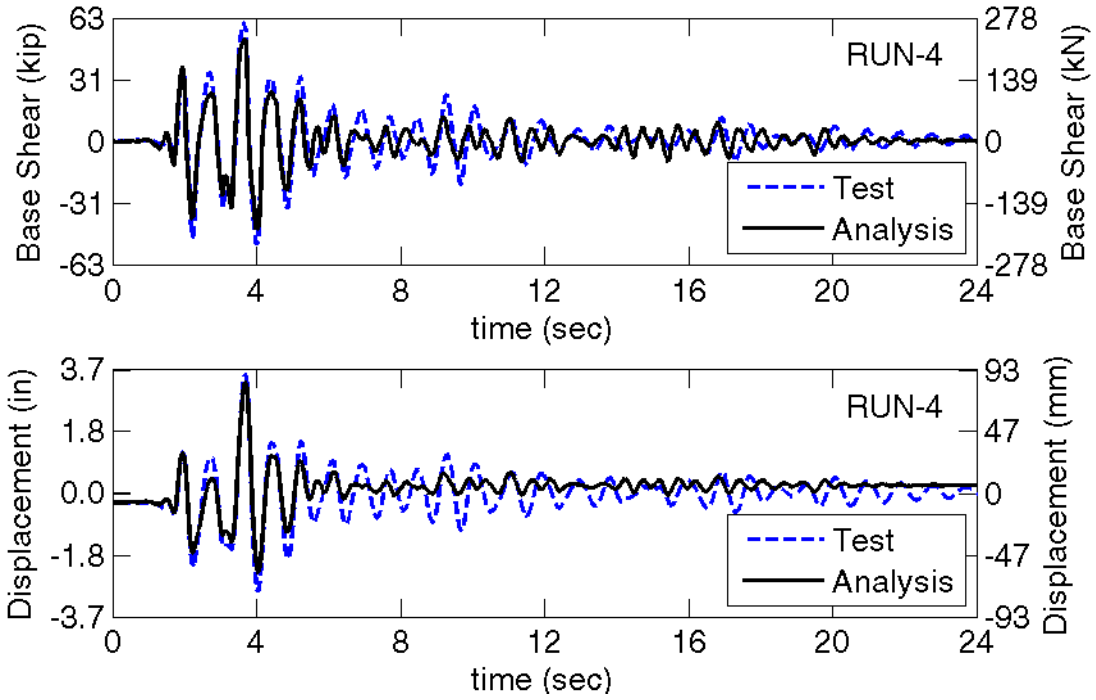

Fig. 22. BPSA calculated and measured force and displacement histories for Run-4

5. Parametric Studies

The effects of key parameters on the performance and capacity need to be investigated to develop a general design procedure for column-pile-shaft pin connections. For that reason, parametric studies were performed to fill in the knowledge gap that was not covered in the experimental and analytical studies. Details of the parametric analyses and results are presented in Chapter 5 of this document.

5.1. Pipe-Pin Connections of Column to Pile-Shaft

The influence of axial load index, lower pipe taper slope, strands instead of rods, and removing the tension member on the bent response and pipe-pin performance were studied. A summary of the general findings is listed below:

1- The pipe-pin moment significantly increased the base shear. Therefore, inclusion of the base moments is necessary for a safe design.
2- Increase of axial force increases the pipe-pin moments. Therefore, the axial load ratio should be included in the calculations of the pipe-pin moments to calculate the base shear.
3- The increase of axial force delays the development of the extension in the tension members and reduces the stress in those members. However, the rod remains in tension under large pipe-pin rotations.
4- The large column axial force produces compressive force in the rod. The development of this force should be prevented by isolating the nuts and rod from concrete.
5- The tapering of the lower pipe improves the behavior of the pipe-pin insignificantly. Therefore, a conical surface for the lower pipe is not necessary.
6- Using strands instead of rods reduces the base shear. The strands remain elastic under large rotations because they are not subjected to flexure. Therefore, it is suggested to use posttensioning strands as the tension members in pipe-pins.

5.2. Rebar-Pin Connections of Column to Pile-Shaft

The influence of the axial load index and core diameter on the bent response and pin performance were studied. A summary of the general findings is listed below:

1- The rebar-pin moment should be included in calculation of the base shear.
2- The axial force needs to be less than 20% of the rebar-pin ultimate compressive capacity to avoid strength loss.
3- An increase of axial force improves the safety factor against shear friction failure of the rebar-pins.
4- The increase of the axial load improves the flexural safety factor as long as the mode of failure of the rebar pin is not dominated by compressive failure of the concrete in the pin.
5- The reduction of the core diameter increases the ductility and reduces the pin moment. However, the core diameters smaller than 50% of the section cause softening in the force-displacement of the bent and are not desirable.

6. Design procedure

Pipe-pin and rebar-pin connections of column to pile-shaft are designed to transfer column shear and axial force while minimizing the moment transfer between the column and the pile-shaft. The findings of the present study were combined with those from previous studies and design codes to develop a practical design procedure. The details of the proposed design methods for “pinned” connections of column to pile-shaft are presented in Chapter 6 in this document.

6.1. Pipe-Pin Connection of Columns to Pile-Shafts

The pipes transfer column shear to the pile. A tension member within the pipes transfers the column uplift force. A pad at the interface of the column and pile-shaft provides rotational capacity and transfers the compressive column axial force. The experimental and analytical studies showed that the interaction of the forces in the column pile-shaft connection produced some moment at the connection.

6.1.1. Design Force and Moment Demand

Pipe-pins are designed as capacity-protected members to remain undamaged during large earthquakes. Therefore, pipe-pins are designed to resist the forces generated when the structure reaches its collapse limit state (CLS).

Pipe-Pin Moments: The pipe-pin moment, $M_{u,pin}$, is developed by the compressive force in the pad and the contact force between the pipes (Fig. 23). It was concluded based on analytical studies that the moment due to pipe contact was less than 10% of the total pipe-pin moment. Therefore, it was not included in the calculation of pin moment. A linear rotational spring was proposed to calculate the pipe-pin moments. The pipe-pin moment at the column base is estimated by the following equations.

$$M_{u,pin} = \frac{M_g}{\theta_g} \times \theta_{u,pin} \tag{1}$$

$$\theta_g = \frac{2\, t_{pad}}{D_{col}} \tag{2}$$

$$M_g = \frac{K_{c.pad}}{K_{c.pad} + K_{tm}} \left(\frac{OD_{pad}}{2} K_{tm} \theta_g + P \right) \times \frac{OD_{pad}}{2} \tag{3}$$

$$K_{tm} = \frac{E_{tm} \times A_{tm}}{L_{tm}} \tag{4}$$

$$K_{c,pad} = \frac{E_{pad} \times A_{pad}}{t_{pad}} \tag{5}$$

where,

A_{tm}: cross-sectional area of tension member (center rod or tendon), in^2 [mm^2]

A_{pad}: plan view area of the pad, in^2 [mm^2]

D_{col}: column diameter, in [mm]

E_{pad}: modulus of elasticity of the pad, ksi [MPa]

E_{tm}: modulus of elasticity of the tension member, ksi [MPa]

$K_{c.pad}$: compressive stiffness of the pad, kip/in [kN/mm]

K_{tm}: axial stiffness of the tension member, kip/in [kN/mm]

L_{tm}: effective length of the tension member, center-to-center of the nuts (Fig. 6-3), in [mm]

M_g: moment to close the gap

$M_{u,pin}$: base moment at the pipe-pin, kip.in [kN.m]

OD_{pad}: outer diameter of the pad, in [mm]

P: column axial force, positive sign for compression, kip [kN]

θ_g: rotation to close the gap, rad

$\theta_{u,pin}$: ultimate base rotation, estimated equal to the drift ratio, rad

t_{pad}: pad thickness, in [mm]

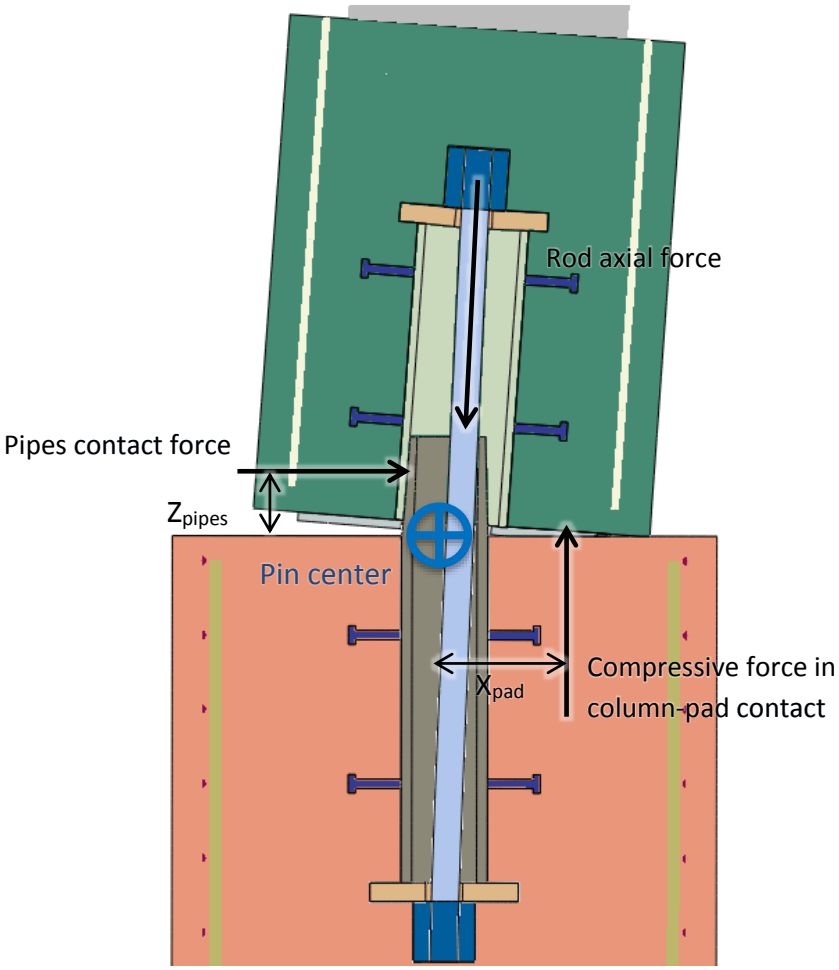

Fig. 23. Forces in pipe-pin

Column Shear: The shear demand on the column and adjacent members are associated with the overstrength column moment. Consequently, the overstrength base shear in the bent, $V_{u,bent}$, is the summation of the column shears as follows.

$$M_{o,col} = 1.2M_{p,col} \tag{6}$$

$$V_{u,col} = \frac{M_{o,col} + M_{u,pin}}{H_c} \tag{7}$$

$$V_{u,bent} = \sum V_{u,col} \tag{8}$$

where,

H_c: column clear height, in [mm]

$M_{o,col}$: column overstrength moment, kip.in [kN.m]

$M_{u,pin}$: pipe-pin base moment, kip.in [kN.m]

$V_{u,col}$ column shear demand, kip [kN]

Column Axial Force: The dead load generates equal axial forces, P_{dl}, in the columns of a symmetric bent. The overturning moment, OM, redistributes the axial force in the columns by increasing the axial force in one column and decreasing it in the other column. In the cases that the overturning moment is larger than the dead load moment, an uplift force is generated in the column.

$$OM = V_{u,bent} \times H - 2M_{u,pin} \tag{9}$$

$$T_{u,col} = P_{dl} - \frac{OM}{S} \tag{10}$$

$$P_{u,col} = P_{dl} + \frac{OM}{S} \tag{11}$$

Tension Member Force: The axial force in the pin tension member is calculated according to the following equation.

$$T_{u,tm} = \frac{K_{tm}}{K_{c.pad} + K_{tm}} \left(\frac{OD_{pad}}{2} K_{c.pad} \theta_{u,pin} - P\right) \tag{12}$$

Threaded Rod Moment Demand: As the upper pipe tends to move laterally and rotates, the partial fixity of the rod-end plate connection produces moment in the rod. The rod moment

demand is calculated according to the recommendations by Mehrsoroush and Saiidi (2014), assuming that the upper pipe rotates as a rigid body.

$$M_{u,rod} = \frac{3\ E_{rod}\ I_{rod}}{L_{rod}^2}\delta_{rod} \tag{13}$$

$$\delta_{rod} = \theta_{u,pin}\ H_{upper} \tag{14}$$

Impact Force between the Pipes: The upper pipe impacts the lower pipe subsequent to the friction release. The impact force is calculated from the following equation.

$$F_{impact} = 0.9 \times \sqrt{\frac{P_{dl}\ G_h\ EI_{cr,col}}{H_c^3}} \tag{15}$$

Lower Pipe and Upper Pipe Shear Demand: The shear demand in the pipes is the summation of the column shear and the impact force.

$$V_{u,pipes} = V_{u,col} + F_{impact} \tag{16}$$

6.1.2. Design Capacities

Lower Pipe: The lower pipe is designed to resist the column shear and the impact force according to the following equation based on the recommendations by Zaghi and Saiidi (2010).

$$V_{u,pipes} = V_u + F_{impact} \leq \phi\ V_{n,lower} \tag{17}$$

$$V_{n,lower} = \min\left(V_{n,lower}^{pipe}, V_{n,lower}^{pile}\right) \tag{18}$$

$$V_{n,lower}^{pipe} = \frac{F_{y,pipe}}{\sqrt{3}} A_{pipe} \tag{19}$$

$$L_1 = \sqrt{e^2 + \frac{2M_P}{OD_{lower} f_c^*}} - e \tag{20}$$

$$e = L_{protrude} \tag{21}$$

$$H_u = L_1 OD_{lower} f_c^* \tag{22}$$

$$V_{n,lower}^{noAxial} = \left(\sqrt{L_{protruded}^2 + \frac{2M_p}{OD_{lower} \times f_c'}} - L_{protruded}\right) \times OD_{lower} f_c' \tag{23}$$

$$P_{max,pile} = \begin{cases} 1A'_{c,lower}\ (ksi) \\ 0.007A'_{c,lower}\ (MPa) \end{cases} \tag{24}$$

For circular pile-shafts: $A'_{c,lower} = \frac{2\pi - 2\alpha_l + \sin(2\alpha_l)}{2}\left(\frac{D_{pile}}{2}\right)^2 - \frac{\pi OD_{lower}^2}{4}$ (25)

$$\alpha_l = arcos\left(\frac{D_{pad}}{D_{pile}}\right)(radians) \tag{26}$$

$$V'_{c,lower} = 0.8\ A'_{c,lower}\ f'_v \tan(54°) \tag{27}$$

$$f'_v = \begin{cases} 0.142\ \sqrt{f'_c}\ (ksi) \\ 0.374\ \sqrt{f'_c}\ (MPa) \end{cases} \tag{28}$$

$$V'_{p,lower} = \frac{M_p}{\frac{D_{pad} + D_{lower}}{2}\tan(54°)} = \frac{1.45M_p}{D_{pad} + OD_{lower}} \tag{29}$$

$$V'_{sp,lower} = \frac{0.34\ A_{sp}f_{ys}d_{pile}(\cos(\alpha_l)\sin(\alpha_l) + \pi - \alpha_l\ )}{s_{pile}}\ \text{(Zaghi and Saiidi, 2010)} \tag{30}$$

$$V_{n,lower}^{maxAxial} = V'_{c,lower} + V'_{p,lower} + V'_{sp,lower} \tag{31}$$

$$V_{n,lower}^{pile} = V_{n,lower}^{noAxial} + \left(\ V_{n,lower}^{maxAxial} - V_{n,lower}^{noAxial}\right)\left(\frac{P_u}{P_{max,pile}}\right)^{0.7} \tag{32}$$

where,

$V_{n,lower}$: nominal lower pipe shear strength, kip [kN]

ϕ: strength reduction factor, which is 0.75 according to Zaghi and Saiidi (2010) recommendation

$V_{n,lower}^{pipe}$: nominal lower pipe shear capacity, kip [kN]

$V_{n,lower}^{pile}$: nominal cracking shear capacity of pile-shaft, kip [kN]

$F_{y,pipe}$: pipe yield strength, ksi [MPa]

A_{pipe}: pipe gross section area, in^2 [mm^2]

L_1: depth of pipe plastic hinge from the pile surface

f_c^*: concrete bearing stress, ksi [MPa]

M_p: pipe plastic moment, in^2 [mm^2]

e: eccentricity of the pipes contact point from pile-shaft surface, in [mm]

OD_{lower}: lower pipe outer diameter, in [mm]

$l_{protrude}$: distance from the top of the lower pipe to the top of the pile-shaft, in [mm]

Z_{pipe}: plastic section modulus, in^3 [mm^3]

A'_c: horizontal projection of the cracking plane, in^2 [mm^2]

D_{pile}: pile-shaft diameter, in [mm]

D_{pad}: outer diameter of bearing pad, in [mm]

OD_{lower}: outer diameter of lower pipe, in [mm]

M_p: lower pipe plastic moment, kip.in [kN.m]

A_{sp}: spiral sectional area in pile-shaft, in^2 [mm^2]

d_{pile}: center-to-center diameter of pile-shaft spiral, in [mm]

f_{ys}: yield strength of spirals, ksi [MPa]

s_{pile}: pitch of spiral, in [mm]

Upper Pipe: The upper pipe is designed by the method proposed by Mehrsoroush and Saiidi (2014) in three steps:

$$V_{u,pipes} \leq \phi\, V_{n,upper} \tag{33}$$

$$V_{n,upper} = V_{n,upper}^{noAxial} + \left(V_{n,upper}^{maxAxial} - V_{n,upper}^{noAxial} \right) \left(\frac{P_u}{P_{max,col}} \right)^{0.7} \tag{34}$$

$$P_{max,col} = \begin{cases} 1A'_{c,upper}\ (ksi) \\ 0.007A'_{c,upper}\ (MPa) \end{cases} \tag{35}$$

$$V_{n,upper}^{noAxial} = V_c + V_{sp} = f_c^*\, OD_{upper} L_2 \tag{36}$$

$$L_2 = \sqrt{{e_2}^2 + \frac{2M_P}{OD_{upper} f_c^*}} + e_2 \tag{37}$$

$$e_2 = L_{protroded} - t_{pad} \tag{38}$$

$$M_p = Z_{pipe} F_{y,pipe} \tag{39}$$

$$V_c = 0.8 f_v A_c + f_t \left(D_{col} - OD_{upper} \right) L_2 \tag{40}$$

$$A_c = \frac{\pi (D_{col}^2 - OD_{upper})}{8} \tag{41}$$

$$f_v = \begin{cases} 0.095\sqrt{f_c'}\ (ksi) \\ 0.25\sqrt{f_c'}\ (MPa) \end{cases} \tag{42}$$

$$f_t = \begin{cases} 0.24\sqrt{f_c'}\ (ksi) \\ 0.62\sqrt{f_c'}\ (MPa) \end{cases} \tag{43}$$

$$V_{sp} = \frac{1}{4}\left(\frac{f_{ys}A_{sp}\pi d_{col}}{4s_{col}} + \frac{f_{ys}A_{sp}2L_2}{s_{col}}\right) \tag{44}$$

$$f_c^* = \frac{V_c + V_{sp}}{OD_{upper} \times L_2} \leq \begin{cases} \frac{\sqrt{f_c'}}{2.43}\left(2.95 - \frac{\sqrt[3]{OD_{upper}}}{3.35}\right) f_c' \\ \frac{\sqrt{f_c'}}{6.38}\left(2.95 - \frac{\sqrt[3]{OD_{upper}}}{9.85}\right) f_c' \end{cases} \tag{45}$$

$$V'_{c,upper} = 0.8\, A'_c\, f'_v \tan(54°) \tag{46}$$

$$f'_v = \begin{cases} 0.142\sqrt{f_c'}\ (ksi) \\ 0.374\sqrt{f_c'}\ (MPa) \end{cases} \tag{47}$$

$$A'_c = \frac{2\pi - 2\alpha_u + \sin(2\alpha_u)}{2}\left(\frac{D_{col}}{2}\right)^2 - \frac{\pi\, OD_{upper}^2}{4} \tag{48}$$

$$\alpha_u = arcos\left(\frac{D_{pad}}{D_{col}}\right)(radian) \tag{49}$$

$$V'_{p,upper} = \frac{1.45M_p}{D_{pad} - 1.45e_2} \tag{50}$$

$$V'_{sp,upper} = \frac{0.34\, A_{sp}f_{ys}d_{col}(\cos(\alpha_u)\sin(\alpha_u) + \pi - \alpha_u\ )}{s_{col}} \tag{51}$$

$$V_{n,upper}^{maxAxial} = V'_{c,upper} + V'_{p,upper} + V'_{sp,upper} \tag{52}$$

where,

L_2: depth of pipe plastic hinge in the column from the bottom of column

f_c^*: equivalent concrete bearing stress, ksi [MPa]

M_p: pipe plastic moment using, in^2 [mm^2]

e_2: eccentricity inside the pipe, in [mm]

$l_{protruded}$:the distance from the top of the lower pipe to the bottom of column, in [mm]

OD_{upper}: upper pipe outer diameter, in [mm]

A_c: horizontal projected area of cracked section, in^2

f_v : lower bound concrete shear strength, ksi [MPa]

f_t: lower bound concrete tensile strength, ksi [MPa]

D_{col}: column diameter, in [mm]

OD_{upper}: upper pipe outer diameter, in [mm]

A_{sp}: spiral sectional area in column, in^2 [mm^2]

d_{pile}: center-to-center diameter of column spiral, in [mm]

f_{ys}: yield strength of spirals, ksi [MPa]

s_{col}: pitch of spiral, in [mm]

L_2: The depth of plastic hinge, in [mm]

M_p: pipe plastic moment, kip.in [kN.m]

A_{sp}: spiral sectional area in pile-shaft, in^2 [mm^2]

d_{col}: center-to-center diameter of pile-shaft spiral, in [mm]

f_{ys}: yield strength of spirals, ksi [MPa]

s_{col}: pitch of spiral, in [mm]

$V_{n,upper}$: nominal lower pipe shear strength, kip [kN]

ϕ: strength reduction factor, which is 0.75 according to Zaghi and Saiidi (2010)

Threaded Rod: The threaded rod is designed for the combination of the tensile force and bending.

$$\text{if} \frac{T_{u,rod}}{T_{r,tm}} < 0.2 \text{ then, } \frac{T_{u,rod}}{2T_{r,rod}} + \frac{M_{u,rod}}{M_{r,rod}} \leq 1.0 \tag{53}$$

$$\text{if} \frac{T_{u,rod}}{T_{r,tm}} \geq 0.2 \text{ then, } \frac{T_{u,rod}}{T_{r,rod}} + \frac{8}{9}\frac{M_{u,rod}}{M_{r,rod}} \leq 1.0 \tag{54}$$

$$M_{r,rod} = \phi_f \, M_{n,rod} \tag{55}$$

$$M_{n,rod} = \min(M_{p,rod}, 1.6M_{y,rod}) \tag{56}$$

$$M_{p,rod} = F_{y,rod} \, Z_{rod} \tag{57}$$

$$M_{y,rod} = F_y \, S_{rod} \tag{58}$$

$$Z_{rod} = \frac{D_{rod}^3}{6} \tag{59}$$

$$S_{rod} = \frac{\pi D_{rod}^3}{32} \tag{60}$$

$$T_{r,tm} = \min(\phi_y F_{y,tm} A_{g,tm}, \phi_u F_{u,tm} A_{g,tm}) \tag{61}$$

where,

$T_{u,rod}$: factored tensile demand of threaded rod, kip [kN]

$T_{r,tm}$: factored tensile capacity of threaded rod, kip [kN]

$M_{u,rod}$: moment demand on threaded rod, kip.in [kN.mm]

$M_{r,rod}$: factored flexural capacity of threaded rod, kip.in [kN.mm]

$M_{n,rod}$: nominal flexural capacity of threaded rod, kip.in [kN.mm]

$M_{p,rod}$: plastic moment of threaded rod, kip.in [kN.mm]

$M_{y,rod}$: yield moment of threaded rod, kip.in [kN.mm]

Z_{rod}: plastic section modulus of threaded rod, in^3 [mm^3]

S_{rod}: elastic section modulus of threaded rod, in^3 [mm^3]

D_{rod}: threaded rod nominal diameter, in [mm]

ϕ_f: strength reduction factor for flexure, which is 1.0

ϕ_y: strength reduction factor for yielding of tension member, which is 0.95

ϕ_u: strength reduction factor for fracture of tension member, which is 0.80

Strands: Strands are designed only for tension using the following equations.

$$T_{u,tm} < T_{u,strand} \tag{62}$$

$$T_{r,tm} = \min(\phi_y F_{y,tm} A_{g,tm}, \phi_u F_{u,tm} A_{g,tm}) \tag{63}$$

where,

$T_{u,strand}$: factored tensile demand of strand, kip [kN]

Studs: The studs are designed to transfer the entire tensile capacity of the tension member to concrete through shear in the studs welded on the pipes.

$$V_{r,stud} = \phi_{v,studs}\, f_u\, A_v \leq \frac{T_{r,tm}}{n_{studs}} \quad (64)$$

where,

$V_{r,stud}$: shear capacity of one stud, kip [kN]

$\phi_{v,studs}$: strength reduction factor for shear of studs, which is 0.65

f_u: specified tensile strength of shear studs, ksi [MPa]

A_v: cross-sectional area of shear stud, in^2 [mm^2]

n_{studs}: number of studs on each pipe

$T_{r,rod}$: factored tensile capacity of threaded rod or strands, kip [kN]

6.1.3. Detailing Recommendations

Based on the results of the parametric studies and previous studies, a series of detailing recommendations for design of the pipe-pin connections of column to pile-shaft were presented in section 6.2.4 of this document.

6.1.4. Design Steps

In summary, the following steps are proposed to design pipe-pin connections between columns and pile-shafts:

Step 1. Determine the force and moment demands assuming base moment is zero.

Step 2. Determine the pad thickness based on the maximum expected pin rotation.

Step 3. Determine the dimension of the pipes.

Step 4. Determine the shear demand on the pipes.

Step 5. Check the lower pipe shear strength and adjust the dimension as necessary.

Step 6. Proportion the rubber pad based on the lower pipe dimensions.

Step 7. Design the tension member.

Step 8. Recalculate the force and moment demands including the pipe-pin moment.

Step 9. Repeat step 5 to 8 until the base moment converges.

Step 10. Design the upper pipe thickness based on the shear demand.

Step 11. Design the studs.

6.2. Rebar-Pin Connection of Columns to Pile-Shafts

Rebar-pins are designed to transfer shear and axial force while undergoing plastic deformations under strong earthquakes. The hinge longitudinal reinforcement is expected to yield and the cover concrete is expected to be damaged. The experimental and analytical studies of the present study showed that the Cheng et al. (2006) design provisions are generally adequate to design column to pile-shaft connections, and hence those provisions were adopted with necessary refinements to make them applicable to column-pile-shaft connections.

6.2.1. Design Force and Rotation Demand

The force demands on the rebar-pin connection are calculated using CLS, which is the global collapse mechanism with plastic hinges at the top of the columns and the rebar-pins.

Rebar-Pin Plastic Moment: The rebar-pin plastic moment, $M_{p,pin}$, is calculated based on the moment-curvature analysis of the hinge section assuming that the section was doubly confined, (1) provided by the transverse steel in the hinge, and (2) provided by the confined concrete in the column and pile-shaft immediately adjacent to the hinge (Cheng et al., 2006). The hinge cover concrete properties were modified using the average of confinement pressures generated by the column and pedestal transverse reinforcement. Those confinement pressures were added to the confinement pressures from the hinge transverse steel to determine the confinement pressure of the core concrete in the rebar-pins.

The plastic moment in the rebar pin is determined by bilinear or quadrilinear idealization of the moment-curvature relationship. It is proposed to idealize the moment-curvature relationship by a quadrilinear curve according to section 5.3.3 if the plastic moment using bilinear idealization is less than 90% of the maximum moment. Using either idealization methods, the rebar-pin plastic moment would be the maximum moment in the idealized moment-curvature relationship. Alternatively, the rebar-pin plastic moment is estimated conservatively as the maximum moment from the moment-curvature relationship prior to idealization.

Column and Rebar-Pin Shear: The column and rebar-pin shear demands are associated with the overstrength column and rebar-pin moment. The overstrength moments and shear demand, $V_{u,col}$, are calculated using the following relationships.

$$M_{o,col} = 1.2M_{p,col} \tag{65}$$

$$M_{o,pin} = 1.2M_{p,pin} \tag{66}$$

$$V_{u,col} = \frac{M_{o,col} + M_{o,pin}}{H_c} \tag{67}$$

$$V_{u,base} = \sum V_{u,col} \tag{68}$$

where,

H_c: column clear height, in [mm]

$M_{o,col}$: column overstrength moment, kip.in [kN.m]

$M_{o,pin}$: rebar-pin overstrength moment, kip.in [kN.m]

$V_{u,col}$: column and rebar-pin shear demand, kip [kN]

$V_{u,bent}$: overstrength base shear in bent, kip [kN]

6.2.2. Design Capacities

Rebar-Pin Shear Capacity: Based on the Cheng et al. (2006) study, the rebar-pin shear capacity is the same as the friction capacity of the hinge. The friction capacity is determined using a coefficient of friction of 0.45 and a clamping force that is the total compressive force in the section obtained from moment-curvature analysis. The friction coefficient accounts for loss of friction due to the cyclic action of earthquake forces in the hinge.

$$\phi\, V_{n,pin} > V_{u,col} \tag{69}$$

$$V_{n,pin} = \mu\, C \tag{70}$$

$$C = C_C + C_S = P + T_s \tag{71}$$

$$\mu = 0.45$$

where

$V_{u,col}$: column and rebar-pin shear demand, kip [kN]

$V_{n,pin}$: rebar-pin shear capacity, kip [kN]

C: total compressive force in the hinge section from moment-curvature analysis, kip [kN]

C_C: compressive force in concrete from moment-curvature analysis of hinge section, kip [kN]

C_S: compressive force in steel from moment-curvature analysis of hinge section, kip [kN]

P: column axial force, with compressive force being positive, kip [kN]

T_S: tensile force in steel from moment-curvature analysis of hinge section, kip [kN]

μ: coefficient of friction, which is 0.45

ϕ: strength reduction factor, which is 0.85

Rebar-Pin Rotation Capacity: Based on the Cheng et al. (2006) model, the rebar-pin ultimate rotation capacity is calculated by assuming that the plastic deformations occur over an equivalent plastic hinge length at the rebar-pin. The gap thickness should be sufficiently large to accommodate the rotation capacity of the rebar-pin.

$$\theta_{n,pin} < \theta_{close} \tag{72}$$

$$\theta_{close} = \arcsin(\frac{g}{0.5D_{col}}) \tag{73}$$

$$\theta_{n,pin} = \theta_p + \theta_e \tag{74}$$

$$\theta_e = g \times \phi_{y,pin} \tag{75}$$

$$\theta_p = \phi_{p,pin} \times L_{p,pin} \tag{76}$$

$$\phi_{p,pin} = \phi_{u,pin} - \phi_{y,pin} \tag{77}$$

$$\begin{aligned} L_{P,pin} &= g + 0.15 \times f_y \times d_b(in, ksi) \\ &= g + 0.022 \times f_y \times d_b(mm, MPa) \end{aligned} \tag{78}$$

where,

θ_n: rebar-pin rotation capacity, rad

θ_e: rebar-pin elastic rotation, rad

θ_p: rebar-pin plastic rotation, rad

$\phi_{p,pin}$: rebar-pin plastic curvature, in^{-1} [mm^{-1}]

$\phi_{u,pin}$: ultimate curvature of rebar-pin from moment-curvature analysis, in^{-1} [mm^{-1}]

$L_{p,pin}$: equivalent plastic hinge length of rebar-pin, in [mm]

f_y: rebar-pin longitudinal bar yield strength, ksi [MPa]

d_b: diameter of longitudinal bars in rebar-pin, in [mm]

g: gap thickness, in [mm]

6.2.3. Detailing Recommendations

Based on the results of the parametric studies and previous studies, a series of detailing recommendations for design of the rebar-pin connections of column to pile-shaft were presented in section 6.3.4.4 of this document.

6.2.4. Design Steps

Step 1. Determine the rebar-pin dimension, core diameter, and the required longitudinal steel.

Step 2. Calculate confined concrete properties for the hinge cover concrete. The cover concrete is confined by the average of column and pile-shaft confinement pressure.

Step 3. Determine the hinge transverse reinforcement for target curvature ductility of 10 using Mortensen and Saiidi (2002) performance based design method. The hinge

core concrete properties are calculated based on the double confinement from the hinge transverse steel and confinement steel in the column and the pile-shaft adjacent to the rebar-pin.

Step 4. Determine moment-curvature relationship for the rebar-pin and column.

Step 5. Determine demand forces and rotation.

Step 6. Check rebar-pin friction capacity. If the capacity is not sufficient, adjust the reinforcement or size of the hinge, and repeat steps 4 to 7.

Step 8. Check hinge gap closure and determine hinge gap thickness to prevent gap closure.

Step 9. Determine the reinforcement detailing for the rebar-pin.

7. Observations

Noteworthy observations made in the course of the experimental and analytical studies presented in this document were:

1- In both specimens, full plastic hinge capacity was reached at the top of the column while the pins did not fail.
2- Moments were developed at both pin types leading to an increase in the base shear by approximately 30%. Even the pipe-pins without any tension members and the rebar-pins with very small core diameters generated significant moments at the column base.
3- The damage in the pipe-pin connections was minimal because the strains in the pipes and longitudinal bars were well below the yield, and cracks in the column and pedestal were thin and few.
4- In the cases that strands were used instead of the rod for the tension member, no yielding was observed in the strands. While the axial force was well below the yield force in the rod, the Von Mises stress passed the yield criteria due to the combination of flexure and tension.
5- The moment-rotation relationship of rebar-pins was stable even when the pins underwent large plastic deformations under many cycles of earthquake loading. The concrete near the hinge throat was damaged but the column and pedestal reinforcement did not yield near the rebar-pins.
6- Softening behavior was observed in the rebar-pins with axial load level more than 20% of the maximum axial force capacity of the hinge.
7- The reduction of the rebar-pin core diameter increased the displacement ductility of the bent and reduced the pin moment. However, stiffness and strength of the hinge degraded when the core diameters was reduced below 50% of the section diameter.
8- Similar performance was observed in the cast-in-place and the precast columns, which were built using a precast shell and filled with self-consolidating concrete (SCC).
9- The pocket connection using corrugated steel pipe and longitudinal bars extended for approximately 1.2 times the column diameter performed well in forming the plastic hinge in the column. No damage was observed in the pocket connections.
10- The column plastic hinges with ECC showed significantly less damage compared to the counterpart plastic hinges with conventional concrete even when the ECC was used in the column shell.

8. Conclusions

The following conclusions were drawn from the results of the experimental and analytical studies presented in this document:

1- The design and detailing methods developed and used in this study for both the rebar-pins and pipe-pins as well as the pocket connections and the precast cap beams were effective in leading to a ductile bridge bent even under extreme earthquakes.
2- The two-way hinge moments must be taken into account to avoid column shear failure and damage to capacity-protected members such as pile-shafts.
3- Pipe-pins can be designed to remain entirely elastic when a strand is used for the tension member and may be treated as capacity-protected connections, whereas rebar pins are expected to yield.
4- Tension members should be used in pipe-pins to maintain global stability of the bent under larger lateral displacements, even in cases that the dead load is sufficiently large to prevent uplift.
5- Because rebar-pins undergo large plastic deformations, they should be designed as ductile elements with ample confinement for the concrete and sufficient development length for the reinforcement in the hinge.
6- In rebar-pins, slippage occurs even under small shear once a horizontal crack is formed across the entire section. The friction capacity increase with pin rotation and yielding of the reinforcement. This behavior is dominant in the pins with small axial force.
7- The proposed detailing for pocket connections was efficient and safe. In this detailing, a pocket with 1.2 times the column diameter is formed using a corrugated pipe, the spirals are provided around the corrugated pipe over the lower one-third of the pocket height, the column reinforcement is extended into the pocket, and the pocket is filled with self-consolidated concrete (SCC).

Table of Contents

List of Tables

List of Figures

1 Introduction

1.1 Introduction

Standard bridges are designed for collapse prevention under extreme seismic events based on ductile design concepts. Bridges with integral superstructures are common in high seismic regions. The superstructure and substructure are connected using rigid connections in these bridges to better maintain the integrity of the bridge under seismic loading. The substructure may be constructed on an enlarged pile-shaft foundation in cases that the use of spread footing is not feasible. In a properly designed bridge, plastic hinges are formed in the columns to dissipate energy during strong earthquakes. The plastic hinges act as a fuse to prevent damage in the superstructure and foundations. Therefore, at least one end of the columns should be connected to the foundation or cap beam rigidly to force formation of the plastic hinges in the column. A hinge or a "pin" connection may be used at one end of the column to reduce the overall force demand leading to smaller and more economical foundations.

The economy of bridge projects can also be improved by reducing the construction time. The bridge construction process may disrupt flow of transportation, require long detour, or require costly use of temporary structures. Cast-in-place (CIP) is the prevailing bridge construction method, which requires concrete to set and cure onsite leading to slow construction. In contrast, prefabricating bridge components can reduce the construction time by eliminating the need for on-site curing and making use of components that have been fabricated in parallel. Another important factor is that the quality of construction would be enhanced by offsite fabrication due to a better control over the material quality and construction. Prefabrication of the elements facilitates accelerated bridge construction (ABC), which is rapid bridge construction using innovative planning, design, materials, and efficient construction methods in a safe and cost-effective manner.

This study focused on three types of novel column connections for seismic regions that can be used in prefabricated bridge construction: pipe-pin and rebar-pin connections of column to pile-shafts to reduce the demand on the foundation, and pocket connections of column to cap beam to provide structural continuity.

Considering the concepts that were used in the present study, the past relevant studies are discussed in two sections: concrete hinge connections and pocket connections.

1.2 Literature Review

1.2.1 Concrete Hinge Connections

Hinge (or "pin") connections are used in reinforced concrete to transfer shear and axial forces and eliminate moment transfer. Relatively small rotational stiffness of the hinges reduces the moment and increases the rotation. The lower moment reduces the shear demand and may lead to smaller foundations. Concrete hinges using reinforcing bars are categorized as one-way or two-way hinges. One-way hinges reduce the moment transfer in the week direction but act as rigid joints in the perpendicular direction. Two-way hinges reduce the moment transfer in all directions.

The use of hinges in the reinforced concrete structures started in 1880 as reported by Kopcke (Schacht and Marx, 2015). The early hinges were made out of stone in a saddle-shape contact region, which had to be smooth and flat to provide rotation (Fig. 1-1). In early twentieth century, the bearing regions were made of concrete, steel, and lead sheets (Fig. 1-2) (Schacht and Marx, 2015; Mehrsoroosh and Saiidi, 2014). In 1907, Mesneger proposed a design method to cluster reinforcing bars in the middle assuming that the reinforcing bars transmitted the entire force of the hinge (Fig. 1-3) (Schacht and Marx, 2015). Freyssinet proved that the reinforcing bars are not necessary to transfer the force and plain concrete is sufficient to transmit the force due to the confinement. Based on assumed elastoplastic behavior of concrete, a design method was proposed to ensure that the hinge throat remains uncracked (Schacht and Marx, 2015). Some of the bridges built using these hinges are still in use such as the bridge over the Marne River in Luzancy (Fig. 1-5).

Another approach to decrease moment transfer at hinges is to reduce the cross sectional area and cluster the reinforcement close to the center of the hinge (Fig. 1-6). In this approach, the column longitudinal bars are bent toward the column centerline of the hinge (Fig. 1-6a). Alternatively, the column reinforcement is terminated near the top of the column and a smaller amount of longitudinal reinforcement is provided at the hinge (Fig. 1-6b). Steel pipes can be used instead of hinge longitudinal bars to transfer the shear.

1.2.1.1 Hinges with Reinforcing Bars

Hinges with reinforcing bars are relatively short element connecting columns to cap beams or footings. The plastic moment of hinge section is reduced by using a smaller cross-sectional area compared to the column section. Sufficient ductility is provided in the hinge to maintain stability while undergoing large rotations. Slippage is expected in the hinges subsequent to the flexural yielding of the hinge. To avoid collection of debris in the gap, a layer of compressible material is placed around the hinge.

Lim et al. tested 1/20 and 1/5 scale columns with two-way hinges at the base by applying lateral cyclic loads at the top. The specimens were designed using two different hinge details: a detail with only horizontal gap and a detail with horizontal and vertical gaps. Flexure dominated the failure mode in the specimens. It was concluded that the moment-deflection hysteresis curves of both details were stable and absorbed energy even under high displacement ductilities in the column. The failure mechanisms of the column with two-way hinges were found to be flexural or shear failure of the hinges (Henley and McLean, 1990).

Haroun et al. (1993) tested six 0.4 scale, two-way hinge columns under reverse cyclic lateral loads. The columns were scaled version of standard details that were used by the California Department of Transportation (Caltrans). The test parameters were hinge details with or without shear keys, ductility level, and axial load level. The failure mechanism was flexure associated with high ductility levels in all specimens. The load was moved to the bottom of the columns following these tests to fail the hinges in shear. It was concluded that 1) shear keys influence the lateral resistance only slightly 2) the ultimate strength of column with two-way hinges was governed by the strength of the column 3) the shear failure mechanism was diagonal tension failure of the entire column 4) the strength of the hinge section may be underestimated by using the beam shear design theory (Haroun et al., 1993).

The research on pinned connections started at the University of Nevada, Reno (UNR) in 1988. Saiidi et al. (1988) tested four 1/8 scale, one-way hinge specimens representing the Rose Creek Bridge hinges in the strong direction. The objectives of the project were to investigate the uniaxial moment transfer in the strong direction of the one-way hinges. All the specimens failed in flexure, and the capacity was not controlled by the shear friction theory, contrary to the common design assumption. It was found that the shear friction method overestimated the shear capacity. The shear resisting mechanism prior to dowel action took place was the aggregate interlock within the compression zone of the hinge.

The studies on the behavior of hinged columns in the strong directions continued with testing four 1/6 scaled hinge specimens in strong direction (Saiidi and Straw, 1993). Two test variables were investigated, cyclic vs. monotonic loading type and shear span-to-depth ratio. It was concluded that the shear friction method overestimated the lateral hinge strength, the energy dissipation decreased with the lower aspect ratio, the dowel action of the hinge did not occur until large displacement achieved, and the load-displacement curves showed pinching, which indicates the energy absorption capacity in the hinge was relatively small.

The third project that looked at the behavior of one-way hinges in the strong direction was followed up by Saiidi et al. (1993). The influence of many variable on the performance of hinges was investigated experimentally. The variables included aspect ratio, monotonic vs. cyclic loading, arrangement of steel in the hinge, and hinge throat thickness. It was concluded that the current method to estimate the shear capacity of the hinges based on the shear friction theory underestimate the capacity. A preliminary method was proposed for lateral load design of one-way hinges. Additionally, a repair method was developed to restore the strength and ductility of a damaged hinge with inadequate reinforcement development length (Saiidi and Straw, 1993; Jiang and Saiidi, 1995).

Sgambelluri et al. (1999) investigated the behavior and capacity of one-way hinges in the weak direction. Three identical 5/16 scale specimens representing the Rose Creek Bridge hinges were tested under cyclic lateral loading. The only test variable was the number of cycles applied to the specimens. The first specimen was tested monotonically. Then, cycles of pure shear were applied to the same specimen. The second specimen was tested by applying a limited number of cycles in pure shear, while the last specimen was tested by applying many cycles in pure shear. The conclusions were 1) the energy absorption capacity in the weak direction is small because of the heavy pinching in the hysteresis curves 2) the failure mechanism for one-way hinges in the weak direction did not resemble the shear friction mechanism, and 3) the resistance of column concrete cover near the hinge influences the behavior of the one-way hinge in the weak direction because of the bearing of column on the footing. An analysis method based on the wedge model was proposed to estimate the one-way hinge shear capacity (Sgambelluri et al., 1999).

The most recent research on columns with two-way hinges at UNR was by Saiidi et al. (2009). Based on this study, the rebar-pin connections of the present study were designed. Five one-third scale columns were tested in double curvature under increasing amplitudes of the Sylmar record simulated on a shake table. The specimens were designed to study the influence of the hinge size, column longitudinal steel ratio, hinge steel ratio, column aspect ratio, and the axial load level. Moment-rotation and shear-slippage models for two-way hinges were proposed. The followings were the findings from the study (Cheng et al., 2006; Saiidi et al., 2009):

1- The two-way hinge hysteresis response was stable and ductile.
2- Subsequent to the formation of the crack over the entire hinge section, significant shear slippage takes place in the hinge thus reducing the energy absorption capacity of the member.
3- The initial shear force in the hinges is resisted by the friction only in the compression zone. Dowel action of the hinge longitudinal bars provides shear resistance under large deformations.
4- The friction capacity is determined using a coefficient of friction of 0.45, and clamping force equal to the total compressive force in the section obtained from moment-curvature analysis. The friction coefficient is lower than the value specified by design codes because of the loss of friction due to the cyclic action of earthquake forces in the hinge.
5- The hinge concrete is capable of sustaining large strains because of confinements due to the hinge spirals and the adjacent column and footing.
6- The dowel action of the hinge longitudinal bars prevents total failure of hinge. However, the dowel action is only activated after large slippages. Therefore, it should not be used to determine the hinge shear capacity.

Even though the study by Saiidi et al. (2009) provided guidance on possible details for column-to-footing pin connections, the results could not be directly used for rebar-pin connections between columns and pile-shafts because mode of failure within the pile-shaft is different from that in footings. Furthermore, no literature was available on the seismic performance of the concrete hinges with reinforcing bars under tensile axial force.

1.2.1.2 Pipe-Pins

Steel pipes were first used as seat extenders in seismic retrofit of bridge in-span hinges with narrow seats. Steel pipe shear keys have been also studied in concrete wall rehabilitation to transfer shear between precast panels and existing building frames (Frosch, 1999). Based on testing of four specimens under cyclic shear loading, the mode of failure was interface sliding and yielding of the steel pipe. Nonuniform bearing stress distribution along the pipe length led to localized bearing failure of the wall adjacent to the pipe. It was concluded that the embedment of the pipe should be sufficient to eliminate the possibility of failure at the panel interface and induce shear yielding in the pipes instead of flexural yielding (Frosch, 1999).

Pipes shear keys were used in the San Francisco Bay Area Rapid Transit (BART) in vertical and horizontal pins. Restrepo and Panagiotou (2005) conducted four proof tests as a part of the BART earthquake safety program, two tests for each horizontal and vertical shear keys using round and square steel pipes. They concluded that the shear keys should be designed for the local bearing failure of concrete against the pipes and flexural strength of pipes (Restrepo and Panagiotou, 2005).

The first pipe-pin designs were used to connect cast-in-place columns to beams as a moment-free hinge. The pipe-pins consisted of a steel pipes that were embedded in concrete and extended into a larger pipe inside the cap beam (Fig. 1-7). The connection was designed to transfer axial compressive force by bearing of cap beam on the column and transfer shear by contact between the pipes. No tension members were included. The rod in Fig. 1-7 was a nominal rod of small diameter intended to keep the can in place during construction. One pipe was slightly larger to enable the extended segment to rotate freely inside the upper pipe, which was referred to as a can because it was made of a relatively thin metal (Zaghi and Saiidi, 2010).

Research on seismic response of pipe-pin connections started at the University of Nevada, Reno (UNR) in 2008. Doyle and Saiidi (2008) tested a 0.3-scale shear specimen and a 0.3-scale column specimen under cyclic loads. The shear specimen was loaded under pure shear and the column specimen was loaded under combined shear and flexure to represent an actual bridge column loading. Significant flexural yielding was observed in both specimens before the ultimate capacity was reached. The lateral load capacity and stiffness were reduced when bending and axial force were combined. A simple design method to estimate the ultimate capacity of pipe-pins for column-cap-beam connections was proposed (Doyle and Saiidi, 2008).

Zaghi and Saiidi (2010) conducted a comprehensive investigation to fill the research gaps in pipe-pin literature and develop seismic design methods for pipe-pins at column bent cap connections. Six 1/3.5 scale push-off specimens were tested under push and pull loading to evaluate the bearing strength of concrete against the steel pipes. The tests showed that confining effect of surrounding concrete increased the local bearing strength of concrete to twice the uniaxial compressive strength. The failure mode of pipes embedded in large body of concrete was the bearing failure of concrete against the pipe (Zaghi and Saiidi, 2010).

In addition, six concrete-filled pipes were tested under pure shear to determine the shear capacity of in-filled steel pipes. Based on the results, two design equations were developed for yield and ultimate capacity of pipes under pure shear. Zaghi and Saiidi (2010) also proposed a design method to determine the lateral load capacity of the pipe-pins in column to cap beam connections. To validate the method, a one-fifth scale, two-column bent with top pipe-pins was constructed and subjected to seismic loading on a shake table. The analytical and experimental results validated the proposed design guideline. The pipe-pin connection transferred shear and axial force and remained essentially elastic while acting as a moment-free connection (Zaghi and Saiidi, 2010).

Several other studies were carried out at the University of Nevada, Reno to explore the application of the pipe-pins design proposed by Zaghi and Saiidi (2010) in accelerated bridge construction. Motaref et al. (2011) used pipe-pins in a 0.3 scale, precast two-column bent subjected to shake-table tests and concluded that pipe-pins can be effectively used in accelerated bridge construction because of their ease of construction (Motaref et al., 2011; Motaref et al., 2013). Kavianpour and Saiidi (2013) conducted shake table tests of a one-quarter scale, four-span bridge. They showed that pipe-pins could be used to connect columns to superstructure to facilitate the bridge construction and prevent the transfer of moments from piers to the superstructure. Valera and Saiidi (2014) conducted shake table tests on a one-quarter scale precast modular two-span bridge with pipe-pins. One objective of this study was to develop and evaluate the concept of Design for Deconstruction (DFD), in which bridge components could be disassemble and reused or recycled at the end of the lifetime of the bridge. It was shown that pipe-pins could be used to connect the columns to the bent cap connection for DFD effectively.

The pipe-pins in all of the aforementioned studies were at top of the columns and were not subjected to tension under lateral loading of the bent. In contrast, pipe-pins at column bases could undergo tensile forces due to overturning moments caused by lateral loads. Mehrsoroush and Saiidi (2014) studied pipe-pins at column bases of a one-third scale, two-column bent to connect columns to the footing. The pipe-pin details were modified to carry tensile forces. The specimen consisted of precast and cast-in-place segments. The findings from that study were (Mehrsoroush and Saiidi, 2014; Mehrsoroush and Saiidi, 2016):

1- Column base pipe-pins can be designed to remain elastic even under high drift ratios.
2- Use of pipe-pins reduces the base shear significantly but some moments in the base are inevitable and should be included in the calculation of the base shear.
3- Base pipe-pins can be used in ABC effectively.

A design method for the pipe-pins at the base was proposed, in which high-strength rods or posttensioning strands were used to transfer the tensile force (Mehrsoroosh and Saiidi, 2014). Even though the study provided guidance on possible details for connecting column bases to footings, its results could not be directly used for pipe-pin connections between columns and pile-shafts because mode of failure within the pile-shaft is different than that in footings.

1.2.2 Pocket Connections

Precast cap beams have been used in more than sixty projects worldwide, mostly in regions of low seismicity (Restrepo et al., 2011). A comprehensive investigation is ongoing at the University of Nevada, Reno to develop earthquake-resistant precast pier systems for ABC (Mehrsoroush et al., 2015). One of the methods to connect precast elements of bridge piers is pocket connection, which is intended to perform similarly to CIP monolithic connections (Fig. 1-8 and Fig. 1-9). Pocket connections are constructed by making a pocket inside the cap beam or footing. Two general details may be used:

1- A fully precast column is extended into the pocket and the gap between the pocket and the column is grouted (Fig. 1-8).
2- The column is partially precast with extruded longitudinal bars that are extended into the pocket and the pocket is filled with concrete (Fig. 1-9).

A key parameter to develop the full moment transfer between the column and the cap beam is the embedment length of the column in the pocket.

Matsumoto et al. (2001) tested three full-scale, column-bent cap connection components with grout-pocket, grout-duct, and bolted connection details and two bent models. The results showed that strength and ductility capacity of the precast elements were similar to those of the CIP models.

Restrepo et al. (2011) tested two 0.42-scale, beam-column pocket connections under cyclic loading. One model was designed to provide high ductility and the other limited ductility. The connection with limited ductility underwent considerably more damage due to shear cracking and deformation. It was concluded that corrugated steel pipes could provide joint shear resistance (Restrepo et al., 2011).

Motaref et al. (2011) conducted shake table tests of a 0.3 scale, two-column bent up to failure of the bent. The bent consisted of a precast footing, two precast columns, and a precast cap beam. One column was constructed using conventional concrete incorporating engineered cementitious composite (ECC) in the plastic hinge area. The other was a concrete-filled glass fiber reinforced polymer (GFRP) tube. The embedment length in both columns was 1.5 times the column diameter. Because no damage was observed in the connection, it was concluded that the embedment length was adequate to develop the full moment capacity of the column (Motaref et al., 2011; Motaref et al., 2013).

Kavianpour and Saiidi (2013) conducted shake table tests of a one-quarter scale, four-span bridge specimen. One of the bents consisted of a precast footing and prefabricated concrete-filled GFRP columns. The columns were embedded into the pockets of the footing for a length equal to 1.5 times the column diameter and the gap was filled with high-strength grout. It was observed that the surface concrete in the footing around the columns was spalled while the GFRP tubes remained intact (Kavianpour and Saiidi, 2013). Pocket connections were also studied in connections between precast columns to pile-shafts subjected to seismic loading (Tran and Stanton, 2012; Larosche et al., 2014).

The seismic performance of pocket connections of fully precast columns and precast cap beam was first studied by Mehrsoroush and Saiidi (2014). A one-third scale, two-column bent model was tested under quasi-static cyclic loading at the University of Nevada, Reno. One column was CIP and the other was precast. The entire column cross-section was extended into the pocket connection for an embedment length of 1.2 times the column diameter (Fig. 1-10). The pockets were formed in the precast cap beam using corrugated steel pipes, which also enhanced the shear resistance of the joint. A confining spiral was also provided around the full height of each pocket to increase the splitting resistance of concrete due to the bearing of the column against the pocket edge. There were no cap beam bottom bars passing through the pocket because the precast column was fully prefabricated. The specimen was designed to generate relatively large tensile forces in the columns by not superimposing any dead load that would otherwise account for the superstructure weight. A threaded rod was embedded at the top of the column and anchored on the top of the cap beam to help transfer the column tensile forces. A reinforcing mesh was provided in the slab on top of the pocket to increase the punching shear resistance of the upper part of the cap beam covering the pocket under axial forces of the column. To form the integral connection, the space between the column and the pocket was filled with high-strength, non-shrinkage grout (Mehrsoroosh and Saiidi, 2014).

Engineered cementitious composite (ECC) was used in the plastic hinge of one of the columns. The test results showed that the cap beam remained elastic and intact. The plastic hinge with conventional concrete reached its full capacity. In the column with ECC, the plastic hinge reached its moment capacity but strength degradation and extensive pinching were observed in the hysteresis loops under larger drifts. After 4% drift, the column longitudinal bars slipped out of the ECC within the pocket connection due to low bond strength of ECC under cyclic loading. The following conclusions were drawn based on the study (Mehrsoroosh and Saiidi, 2014).

1- The embedment length of 1.2 column diameter was adequate.
2- The threaded rod in the upper part of the column was unnecessary because the column tensile force was transferred to the cap beam essentially through the corrugated steel pipes.
3- The spiral around the corrugated pipe is necessary only in the lower part of the pocket connections.
4- The reinforcing mesh placed at the top zone of the pocket connection may be eliminated.

1.3 Objective and Scope

The main objectives of this study were to investigate the seismic performance of three types of bridge bent connections through experimental testing and analytical modeling:

1- Pipe-pin connections to develop hinge support at column-pile shaft joints for CIP and precast constructions.

2- Rebar-pin connections to develop hinge supports at column-pile shaft joint for CIP and precast constructions.

3- Pocket connections to develop rigid connections between precast columns and precast pier caps in bridges with integral superstructure-pier connections.

An additional objective of the study was to improve the current design guidelines for each connection type based on the results of the experimental, analytical studies, and parametric studies. The study consisted of shake table testing of two large-scale bent specimens and performing comprehensive analytical studies of connections to determine the adequacy of the concepts developed in this and other studies and the need for further refinements.

Two 1/3.75 scale, two-column bents were constructed using the proposed accelerated bridge construction methods. The bents were tested on one of the shake tables of the Earthquake Engineering Laboratory at the University of Nevada, Reno subjected to the 1994 Northridge earthquake recorded at Sylmar Converter Station. The specific objectives of the experimental studies were

1- Study the overall seismic performance of two-column bents and the individual columns incorporating the proposed connections.
2- Develop a detail for hinge connections of precast column to pile-shaft and compare the performance with hinge connections of CIP columns.
3- Develop and study the behavior of the pocket connections with extended reinforcement and concrete in the pocket in bridges with integral superstructure-pier connections. Drop cap beam connections were not included in the study.
4- Investigate the performance of ECC in column plastic hinge zones to mitigate damage.

Analytical studies were also performed to meet the following specific objectives:

1- Develop relatively simple analytical models for the bents as design tools.
2- Develop efficient nonlinear finite element models for pipe-pin and rebar-pin to be used in global analysis of bridges with hinge connections.
3- Develop elaborate nonlinear finite element models of bent with pipe-pin connections to investigate the microscopic performance and interactions of components.
4- Use the numerical models for a focused parametric study that addressed the gaps in the experimental results and utilize the results of the parametric studies in developing seismic design guidelines for pipe-pins and rebar-pins.

A guideline for each hinge connection was prepared based on the parametric and experimental studies. Lastly, the guidelines were illustrated through numerical examples.

1.4 Document Layout

Chapter 1 describes a literature review on pipe-pin hinges, rebar-pin hinges, and pocket connections. This chapter includes the significance, main objectives, and scopes of the present study.

Chapter 2 presents the preliminary design, construction detail, material properties, instrumentation, test setup, and the loading protocol of the experimental studies.

Chapter 3 explains the observations and measured data from the shake table tests. This chapter includes the dynamic characteristics, general observations, measured load-displacement relationships, column curvatures, hinge rotations, internal forces, strain data, and other recordings from the instruments.

Chapter 4 is focused on the details and results of analytical studies. The analytical procedures are explained first. Then, the numerical models are validated by comparing the analytical results with the experimental data.

Chapter 5 presents the results of parametric studies on pipe-pin and rebar-pin connections. Sensitivity of the results to various parameters is presented in this chapter.

Chapter 6 explains the design procedures for pipe-pins and rebar-pins that were developed based on the experimental and analytical studies.

Chapter 7 provides a summary of the study and lists observations and important conclusions.

Five appendices, A, B, C, D, and E, are included in the document. Appendix A describes the procedure to determine the dynamic properties of the specimen from the shake-table tests. Appendix B and C present analysis procedures using the simple methods that were explained in Chapter 4. Appendix D and E contain the OpenSEES codes for the numerical models that were described in Chapter 4.

2 Experimental Studies

2.1 Introduction

The experimental part of the project was testing of two, two-column bents on shake tables of the Earthquake Engineering Laboratory at the University of Nevada, Reno. Details of the experimental study are explained in this chapter. First, the use of two-column bent models vs. a single column to test pin connections is justified. Second, the design criteria for the bents are discussed. Next, construction procedure, instrumentation design, and input ground motions for each model are described. In the subsequent two sections, the test setup of the specimens on the shake table was explained. Finally, the properties of the materials that were used in the models were presented.

2.2 Test Model Configuration

The goal of this research was to investigate performance of column to pile-shaft connections. The advantages of two-column bents specimen over single column models are as follows.

- Single pin connections are torsionally unstable when they pass a certain threshold. Special test setup is required if the pins are used in single column specimens. In contrast, two-column bents are torsionally stable.
- Since the top of the column is connected to an integral cap beam, a rigid boundary condition is required at the top if a single column model is used. Therefore, two parallel links are needed to connect the column to the mass rig to prevent rotation at the top of the column. This would complicate the test setup.
- Column base pins are used in multi-column bents. The axial load in the pins is variable because of the overturning moment effects during earthquakes. Varying the axial load in a single column specimen is complicated. Conversely, in a two-column bent the axial load varies to satisfy the equilibrium automatically.
- Two column bents provide the opportunity to study column to cap beam connections in addition to the study of pins.

The disadvantageous of two-column bent over a single column specimen are

- Because the model is indeterminate, lateral forces are redistributed between the columns.
- Testing should be stopped when one column fails. This could prevent evaluation of both columns.
- A load cell in the middle is needed to measure the load in each column. Hence, the accuracy of the loads is reliable on load cell accuracy.

The test specimens were 1/3.75 scale models that were based on some of the features of the approach spans bents of the San Francisco Oakland Bay Bridge. The columns of the prototype were square but the reinforcements were circular. Hence, circular sections in the models were used. The models were sufficiently large to use regular concrete rather than micro concrete. Furthermore, the lateral load capacity of the bents was within the force capacity of the actuator driving the shake table.

Pin connections were provided in column to shaft connections in the test models. Two test models were built, BPSA and BRSA. BPSA stands for bent with pipe-pin column-pile-shaft connection for accelerated bridge construction (ABC) and BRSA stands for bent with rebar-pin column-pile-shaft connection for ABC Pipe-pin connections were used in BPSA model and rebar-pins in BRSA model. To study different construction methods, one column in each bent was cast-in-place (CIP) and the other was precast (PC). This allowed for generating data on pin connection behavior for both conventional and accelerated bridge construction (ABC). To model column to Type II pile-shaft connections, pedestals were built under each column. The pedestals were sufficiently tall to represent the structural behavior of pile-shafts. The study of soil interaction with pile-shafts was beyond the scope of this research.
The construction consisted of two parts. The column shells were cast first. Subsequent to curing, the columns were secured on the pedestals. The precast cap beam with the pocket connections placed on top. Finally, self-consolidating concrete (SCC) was placed in the hollow section (Fig. 2-1). The engineered cementitious composite (ECC) was used in the plastic hinge zone of one column in each bent. Details of the specimen are described in subsequent sections.

The Earthquake Engineering Laboratory at University of Nevada, Reno has four shake tables, three biaxial tables and one six degrees of freedom table. The tests were conducted on the biaxial shake table number 2. The specifications of the shake table are presented in Table 2-1 (NEES at University of Nevada, Reno, 2014)

2.3 Bent with Pipe-Pin Column-Pile Shaft Connection (BPSA)

The connections of the columns to pedestals were pipe-pins in this model. The model was labeled as BPSA for bent with pipe-pin column-pile shaft connection for ABC. The columns were connected to the precast bent cap with pocket connections. The protruded bars at the top end of the columns were inserted into the pocket in the cap beam. Then the pockets were filled with self-consolidating concrete (SCC) to form an integral joint. Two methods of construction for columns were implemented. The north column was prefabricated, and is referred to as PC hereafter. The pipe-pin was inserted in a 3-inch [76-mm] thick precast concrete shell of the column. Then, the shell was filled with SCC at the same time with the joint. The south column was cast in place. ECC was used over the full height of the plastic hinge region of this column. The column is referred to as CIP hereafter (Fig. 2-2).

2.3.1 BPSA Design

The model was designed according to the Caltrans ductile design guidelines (*Seismic Design Criteria*, 2010). The connections were designed as capacity protected members with plastic hinging allowed only in the columns. While the columns were expected to undergo plastic deformation, the rest of the structure including the pipe-pins were designed to remain undamaged. The construction plans for BPSA are illustrated in Fig. 2-2 through Fig. 2-15.

It is known that the pipe-pin connections are not generally “perfect” pins. Previous research by Zaghi and Saiidi suggests the moments developed in top pins are negligible (Zaghi and Saiidi, 2010). However, relatively large moments can be developed in column base pipe-pins due to interaction of axial load and shear (Mehrsouroosh and Saiidi, 2014). For design purposes, the columns in BPSA were assumed to deform in single curvature meaning no moments would be developed at the bottom of columns.

The pipe-pin connections were designed in shear and tension independently. Shear and tensile demand forces were determined from equilibrium of the bent with plastic hinges formed at the top of the columns. Based on the column plastic moment and assuming no moment at the bottom, the column shear was estimated. Pipe-pins were designed for the forces caused from overestimated moment capacity at the plastic hinges. The overestimated moment capacity was 1.2 times the ultimate moment capacity estimated from moment-curvature analysis of the column sections. The moment-curvature analysis was performed on a section with expected material properties per Caltrans SDC. This complied with Caltrans SDC ductile design to ensure the pipe-pins were capacity protected (Caltrans, 2010). The assumption of no the moment at the pipe-pin underestimated the column shears. However, a high factor of safety was used for shear design of the columns. The columns were designed for nominal rather than expected material properties and strength reduction factor of 0.9 for shear.

2.3.1.1 Tensile Design of Pipe-Pins

Overturning moments lead to tensile forces in the pipe-pin connections. The tensile force was assumed to transfer from column bars to the pipe by the studs. Then, this force was transferred to the rod by bearing on the end plate. A similar load transfer mechanism existed in the pile-shaft. Five failure modes are possible under tensile forces:

1- Concrete section break out failure under tensile force around the pipe, Fig. 2-16a
2- Pullout of pipe-pin from concrete, Fig. 2-16b
3- Studs shearing off, Fig. 2-16c
4- Bearing plate failure, Fig. 2-16d
5- Failure of the center rod, Fig. 2-16e

For failure mode-1, the failure plane has a 35-degree angle with the horizontal plane. Based on ACI 318-Appendix D provisions, the tensile capacity of concrete was added to reinforcing bar capacity to estimate the break out capacity (ACI Committee 318, 2011). For failure mode-2, a cylindrical failure surface was assumed around the ends of the studs. The vertical shear capacity of the cylinder surface was added to the tensile capacity of the cylinder base to estimate the capacity for failure mode-2. Capacity of failure mode-3 is equal to the shear capacity of group of studs based on ACI-appendix D. To avoid failure mode-4, the end plate was designed to stay elastic under maximum tensile force from the rod. For failure mode-5, a high-strength rod was designed for combined tension and bending moment. The tensile force was the uplift force in the bent while plastic hinge forms in the columns. The bending moment was the elastic moment that develops at each end of the rod due to the relative displacement of the rod ends (Fig. 2-16e).

2.3.1.2 Shear Design of the Pipe-Pin

The shear force was assumed to transfer from column to the pipe by bearing on the upper pipe. Then, the force was transferred to the lower pipe through bearing of the pipes. Finally, the lower pipe delivered the shear to the pedestal.

Three failure modes are possible under shear:

1- Shear failure of concrete around pipes, Fig. 2-17a.
2- Failure of pipes under shear and bending, Fig. 2-17b.
3- Concrete compressive failure, Fig. 2-17c.

At the time of design, the only guideline to design the pipe-pins was that by Zaghi and Saiidi. The study discussed shear capacity of the pipe-pin connection under compression forces (Zaghi and Saiidi, 2010). Based on that study, the expected shear failure pattern for concrete was vertical plane up to the pipe plastic hinge then a diagonal shear failure plane at a 35-degree angle (Fig. 2-17a). The distance to the plastic hinge in the pipe was determined from equilibrium of bearing force on the pipe face and its plastic moment capacity.

2.3.1.3 BPSA Modification

As will be described later, the connection of the load cell to cap beam failed during the fourth shake table run. The connection was repaired and each segment of the cap beam was post-tensioned with details shown in Fig. 2-19. The post-tension system was designed to secure the load cell in the middle of the cap beam. Four horizontal Dywdag bars were post-tensioned to 100 kip [448 kN] each. Therefore, the post-tension stress on the cap beam was 694 psi [4.79 MPa].

2.3.2 BPSA Construction

The specimen was constructed in three phases. First, the footings, pedestals, and precast shell were cast. Second, CIP and precast cap beam were cast. Finally, all the precast parts were assembled and filled with self-consolidating concrete (SCC).

In the first phase, the reinforcement cages for footings and pedestals were built, instrumented, and placed. The pipe-pins were fabricated, instrumented, and assembled in this phase. The lower parts of the pipe-pins were assembled and held in place plumbed (Fig. 2-19). The pipes were held stationary by welded steel rods. At the end of this phase, concrete was placed in the forms for the footing, pedestals, and column shell (Fig. 2-20 and 2-21).

In the second phase, after placing bearing pads and the upper pipes, the nuts were snug tightened. The bearing pads were glued to the pedestal surface to prevent warping (Fig. 2-22). The south column rebar cage (CIP) was placed on a piece of Styrofoam that formed the gap around the pin-connections. Then, formworks held the columns forms plumb in place (Fig. 2-23). The load cell and corrugated pipes were placed inside the cap beam forms (Fig. 2-24). Next, the reinforcement cages were placed in cap beam forms. At the end of this phase, concrete was cast in CIP and the cap beam. Two hours after concrete cast, ECC was cast on the top of CIP.

The third phase was done four weeks after the last casting. Two braced frames were built to shore the cap beam while SCC was cast. A boom truck placed cap beam on the bracing form (Fig. 2-25). The cap beam to column connection was sealed to prevent leakage. Two days later, SCC was cast from the openings at the top of the cap beam into the precast column shell and the joint above the precast column (PC) as well as the joint above CIP. The specimen was kept under cover and heated with an electrical heater for a week to prevent freezing of concrete.

2.3.3 BPSA Instrumentation

More than 200 channels of various transducers recorded data to capture performance of the specimen. The instruments collected loads, displacements, acceleration, and strains data during the tests. The load cell in the mass rig link recorded the lateral load applied to the bent from the mass blocks. The load cell in the cap beam recorded forces and moments between the two segments of the cap beam. Accelerations were recorded at the footing, cap beam, and mass rig

using accelerometers. Wire transducers recorded displacements at the pedestals and the cap beam (Fig. 2-26). In addition, shake table internal instruments recorded the table displacements and accelerations. Position transducers are another type of instruments to record displacement. They were used to measure local displacements at the plastic hinge zones so they could be converted to curvatures. Position transducers were also used to monitor slip and rotation in the column to pedestal connections (Fig. 2-27).

Strain gages recorded strains in steel bars and elements. The general layout of strain gages is shown in Fig. 2-28. The strain gages at the upper part of the column and the pedestal help determine the plasticity level in the plastic hinge zone of the column and in the pedestal. The location of these gages is shown in Fig. 2-29 to 2-32. The strain gages on the pipes consist of horizontal, vertical and rosette gages. The rosette strain gages were used to measure shear strain on the pipe (Fig. 2-23 and 2-24).

2.3.4 Input Ground Motion and Loading Protocol in BPSA

The input ground motion needed to be strong enough to generate sufficient demand. Yet its displacement, velocity, and acceleration needed to be within the shake table limits. It was also preferred to have symmetric response to investigate the performance under full reversed cycles. The 142-degree of Sylmar Converter Station of the 1994 Northridge earthquake was chosen for simulation in the shake table tests. The ground motion properties for this record from the PEER ground motion database is presented in Table 2-3. The maximum acceleration, velocity, and displacement were 0.897-g, 40.2-in/s [102-cm/s] and 17.8-in [45.2-cm], respectively ('Peer Groung Motion Database,' 2011).

The record was modified before it was simulated on the shake table. The acceleration was filtered to have a symmetric ground motion by Butterworth bandpass 4^{th} order for frequencies exceeding 25 and below 0.2 Hz. This filtering smoothed some of the peaks in the acceleration record (Fig. 2-35). The negative and positive amplitudes were comparable in the filtered record but were significantly different in the unfiltered record. Moreover, the frequency content of the filtered record was in the range of the operating frequency of shake table. In addition, the time axis of the acceleration record had to be shortened to account for the scale of the test model. The time axis was scaled by the square root of the geometric scale factor to account for the shorter period of the model relative to the prototype (Harris, 1982). In this study, the scale factor is 1/3.75; hence, the time step of acceleration record was multiplied by $\sqrt{(1/3.75)}=0.5164$.

The specimen was subjected to series of excitations until it reached the ultimate capacity of the bent. Because the load cell connection in the cap beam had to be repaired twice, run-4 was repeated after each repair step. BPSA was tested under 11 motions. The amplification factors for the improved earthquake record were 0.10, 0.30, 0.50, 0.60, 0.60, 0.60, 0.70, 0.90 and 1.10, 1.30, 1.40. The corresponding peak ground motion accelerations (PGAs) were 0.09g, 0.27g, 0.45g, 0.54g, 0.54g, 0.54g, 0.63g, 0.81g, and 0.99g, respectively.

A white noise motion applied to the specimen before each run and after the last run to capture the dynamic characteristics of the bent. The white noise had frequency content of 0.75 to 40 Hz and PGA of 0.05 g.

2.4 Bent with Rebar-Pin Column-Pile Shaft Connection (BRSA)

The connections of the columns to pedestals in this model were rebar-pins. The model was labeled as BRSA for bent with rebar-pin column-pile shaft connection for ABC. Similar to BPSA, the columns in BRSA were connected to the precast bent cap using pocket details with protruded bars at the top end of the columns inserted into the pocket in the cap beam. Then the pockets were cast with self-consolidating concrete (SCC) to form an integral joint. Two methods of construction were implemented. The north column was prefabricated, and is referred to as PC hereafter. The rebar-pin was inserted in a 3-inch [76-mm] thick precast concrete shell in PC. Additionally, ECC was used in the plastic hinge region of the precast concrete shell. Then, the shell was filled with SCC at the same time with the joint. The south column was cast in place, referred to CIP hereafter (Fig. 2-37).

2.4.1 BRSA Design

The model was designed according to the Caltrans ductile design guidelines (Caltrans, 2010). Connections were designed as capacity protected members, with plastic deformation allowed in the columns and rebar-pins. The columns were expected to reach the plastic hinge capacity at the top. The rebar-pins were also expected to undergo large plastic deformation. Unlike pipe-pins, rebar-pins typically yield under moderate and strong earthquakes.

The rebar-pins were designed based on previous research by Cheng et al. (2006). They proposed a design method to provide sufficient ductility and shear capacity for the rebar-pins in a bent. While both rebar-pin and plastic hinge of the column undergo large plastic deformation, only the plastic hinge in the columns is expected to fail. The rest of the structure was designed for the lateral load caused by overestimated moments at the ends of columns. The overestimated moment is 1.2 times the ultimate moment capacity.

The ultimate moment capacity of the rebar-pin was estimated using a moment-curvature analysis of the reduced section. Based on research by Cheng et al., the section modeled using doubly confined concrete rather than unconfined cover and confined core. The cover concrete in the hinge was confined by column and pedestal transverse bars. The core concrete was confined by hinge spirals in addition to the column and pedestal transverse bars.

The overestimated capacity of the column and hinge led to the following shear demand in the column.

$$V_o = 1.2 \cdot \frac{M_p^{col} + M_p^{hinge}}{h_{col}} \tag{1.1}$$

where,

M_p^{col}: Plastic moment capacity in the column

M_p^{hinge}: Plastic moment capacity in the hinge

h_{col}: height of the column

The research by Cheng et al. concluded that the Coulomb friction model should be used to estimate the shear capacity of the hinge with a recommended friction coefficient of 0.45. The

clamping force is the total compressive force in the section when plastic moments have been developed. A moment-curvature analysis of doubly confined section is required to estimate the clamping force.

Cheng et al. suggested sufficiently large gap around the rebar-pin to prevent the edge of column to bear against the footing under large rotations. The ultimate rotation capacity was determined from modified plastic hinge length for rebar-pins proposed by Cheng et al. The construction plans of the BRSA are shown in Fig. 2-37 to 2-48.

2.4.2 BRSA Construction

BRSA was built in three phases similar to BPSA construction. First, the footing and pedestals were cast while the reinforcement cages for the pin were held in place by welded steel rods as shown in Fig. 2-49 and 2-50. The precast shell was also cast in this phase. ECC was cast two hours after concrete was placed. In the second phase, CIP and the cap beam were cast in place. In the third phase, all the precast parts were assembled after four weeks. Then, SCC was cast in the PC and joint above the PC as well as the joint above the CIP. The specimen was kept under cover and heated with an electrical heater for a week to prevent concrete from freezing.

2.4.3 BRSA Instrumentation

BRSA was instrumented to collect loads, displacement, acceleration, and strain gage data. Acceleration was recorded for the table and the cap beam. Displacements were recorded for the shake table, pedestals, and the cap beam (Fig. 2-51). Position transducers recorded local displacements at the plastic hinge zone to be converted to curvature. Position transducers were also used to monitor slip and rotation in the column to pedestal connections (Fig. 2-52). Strain gages were installed on the pedestal and column reinforcement bars as well as rebar-pin reinforcement to measure strain. The measured strain could help to determine the level of plasticity in the reinforcement bars. Strain gage instrumentation plans are presented in Fig. 2-53 to 2-59.

2.4.4 BRSA Input Ground Motion and Load Protocol

The criteria of ground motion selection were similar to BPSA ground motion selection. Since geometric scale factor for both specimens were the same, same input motion was used in both tests (Fig. 2-36). BRSA was tested for six load factors of 0.10, 0.35, 0.60, 0.85, 1.10, and 1.35. The corresponding PGAs were 0.09g, 0.314g, 0.538g, 0.763g, 0.987g, and 1.211g, respectively. Before each run and after the last run a white noise motion applied to the bent. The white noise had frequency content of 0.7 to 40 Hz and amplitude of 0.05g similar to that in BPSA.

2.5 Test setup

The sequence of specimen setup on the shake table were (Fig. 2-60)

1- The model was aligned on the table with spacers underneath the footing
2- The high strength rods were hand tightened
3- High-strength grout was placed under the footing
4- After the grout cured, the footing was clamped to the table by torqueing the rods to 250 lbf.ft [339 N.m]
5- The swivel head link was attached the mass rig and the cap beam.
6- The cap beam was post-tensioned

Four blocks placed on the mass rig provided translational mass equivalent to 100-kip [448 kN] weight for the bent. Because of the pin connections, the bent were unstable in the out of plane direction. Hence, safety frames were designed to provide lateral support (Fig. 2-61). During the first four runs of the BPSA, there was an inch gap between casters and side of the cap beam. The frame was moved to hold the cap beam aligned for the rest of the motions of BPSA and all the motions of the BRSA. The new setup prevented the structure from collapse. Additionally, it restrained torsional and out of plane movements.

The post-tensioning setup was the same for BPSA and BRSA, shown in Fig. 2-18. The post-tensioning force was 100 kip [448kN] and 80 kip [356 kN] for each Dywdag bar for BPSA and BRSA, respectively. Consequently, the post-tension stress was approximately 670 psi [4.62 MPa] and 530 psi [3.67 MPa] in BPSA and BRSA, respectively. BPSA was post-tensioned after the load cell connection failed, but BRSA was post-tensioned prior to testing. Smaller post-tensioning force was required to hold the load cell in BRSA because the connection was not damaged.

2.6 Material properties

Samples of the materials that were used in the test models were tested to assure they were representatives of the prototype and conformed to design. Since both specimens were constructed at the same time, the same materials were used in both. There are three main material that were used in the specimens: Concrete including conventional and self-consolidating (SCC), steel, and engineered cementitious composite (ECC).

2.6.1 Concrete

Two batches of conventional concrete and one batch of SCC were cast in the models. Slump tests were conducted according ASTM C143 for both conventional concrete casts. The results of the slump test are presented in Table 2-4 and Table 2-5. Slump flow test was conducted on SCC batch according to ASTM C1611. The test results were t50=1.75s, $R_{flow\ test}$=20 in and VSI=0. Additionally, cylinders of 6X12in [150X300 mm] were made in field according to ASTM C31. These cylinders were tested for compressive strength at 7-day, 28-day, and test day according to ASTM C39. The results of tests are presented for BPSA in Table 2-4 and for BRSA in Table 2-5.

2.6.2 Engineered Cementitious Composite (ECC)

Engineering cementitious composites (ECC) are fiber reinforced concrete. Cylinders of 4X8in [100X200 mm] were made on test day according to ASTM C31. These cylinders were tested on 28-day, 56-day, and test day for compressive strength according ASTM C39. The results of the tests are presented for BPSA in Table 2-4 and for BRSA in Table 2-5.

2.6.3 Steel

Reinforcing bars and wire were sampled and tested at University of Nevada, Reno according to ASTM A370. A summary of reinforcing bars properties are presented in Table 2-6. For the other steel parts, including the plates, pipes, and studs, material testing reports (MTR) by manufacturer were used. The results are presented in Table 2-7.

2.6.4 Rubber Pad

Elastomers can undergo large deformations and recover completely due to their molecular structure. The stress-strain relationship of the elastomers can be modeled with sufficient accuracy as linear-elastic for strains smaller than 25%. That relationship was used in the macro

model of the pipe-pins in described in the section 4.8.3. For strains exceeding 25%, strain energy potential function is required to relate strain and stress (Gent , 1992). In the FE model, the pads were modeled using the energy potential function that was determined from compression tests performed in the current study according to ASTM D575-91 (ASTM, 1991).

The purpose of the rubber pad versus steel rings at the hinge throat was to reduce the stiffness of the connections. The pads were cloth-inserted rubber with durometer of 75 shore A. Mechanical properties of the rubbers are affected by various parameters including chemical compound, cloth reinforcement, load history, and loading rate. To obtain accurate material properties, samples of that material were tested under uniaxial compression. The constituent models were calibrated and used in the analytical studies.

The compression tests were conducted on bonded samples using sand papers between the rubber surfaces and the platens of the loading machine to resist the slippage of the rubber at the contact surface. The dimensions of the samples are presented in 0 2-8. The tests were performed under a displacement rate of 0.5 in/min [13 mm/min] and were stopped when the force reached the capacity of the testing machine. The nominal stress-strain curves are presented in Fig. 2-62.

3 Experimental Results and Observations

3.1 Introduction

The key recorded data and important observations from the experimental studies of the two bent models for different earthquake runs are presented in this chapter. In the first two sections, the significance of the parameters is explained first. Next, the methods to calculate the performance indicators from measurements are described. Finally, the performance of the bents is discussed based on the indicators. This chapter was concluded with the comparison of the performance of the two models.

3.2 Bent with Pipe-Pin Column-Pile Shaft Connection for ABC (BPSA)

The columns were connected to the pile-shafts using pipe-pins in this model. As explained in Chapter 2, the model was designed to develop plastic hinges at the top end zones of the columns while the pipe- pins remained undamaged. Detailed examination of the measured data indicated that the design of the model was satisfactory. Substantial plastic deformations were developed at the top of the columns. The lateral load capacity of the bent was reached due to plastic hinge failure in the CIP column, with no indication of damage in the pipe-pins.

3.2.1 Dynamic Characteristics

The fundamental period of the model changed after each of the runs because of the progression of plastic deformations caused by yielding of the reinforcing bars as well as cracking and spalling of concrete. The concrete cracks and spalling decreased the stiffness of the bent. Additionally, the cracks became wider as the plastic strains in the longitudinal reinforcement increased. The opening and closing of the cracks and yielding of steel were the primary source of hysteretic damping in the bents. The fundamental period prior to each of the runs was estimated as the peak of Transfer Function (TF) under a white noise motion (WN). TFs correlated the recorded accelerations of the shake table to the accelerations of the cap beam recorded by ACC-6 (Fig. 2-26). The concept to find the natural periods of structures using transfer function is explained in Appendix A.

The fundamental periods before each run are presented in Fig. 3-1 and Table 3-1. Fundamental periods increased from 0.54 seconds for the intact structure to 1.32 seconds after the last run except for the WN prior Run-5. The periods were normalized to the period of the intact structure. The displacement in all of the runs was less than 0.20 in [5 mm] under the WN excitations. Moreover, the displacement of the model at the cap beam was approximately equal to the slippage of the pipe-pins in those tests.

The damping ratio was calculated from Fast Fourier Transform (FFT) curves of the accelerations at the cap beam from accelerometer ACC-6 (Chopra, 2007). Damping ratios for each of the runs are presented in Fig. 3-2. The damping ratio increased from eight percent for the intact structure to 12% at the end of the tests.

The out-of-plane movements of the bent were monitored to ensure that they were minimal and testing was indeed in the in-plane direction. Note that the bent was unstable in the out of plane direction because of the pin connections. As a result, two steel frames were installed to prevent out of plane collapse of the bent. There was a one-inch [25-mm] gap between the safety frames

and the cap beam for the runs before Run-4. There was no gap after Run-4 because the steel frames were moved to come in contact with the sides of the cap beam. The maximum out of plane accelerations were 0.045g, 0.634g, and 0.118g for all the white noise motions, Sylmar motions prior repair, and Sylmar motions after repair, respectively. The maximum out of plane displacement was 0.18 in [5 mm] in the course of testing.

The transfer functions were calculated based on the difference between the out of plane accelerations at both ends and the shake table acceleration. Accelerometers on the cap beam at the top of the columns, ACC-2X and ACC-3X as shown in Fig. 2-26, measure the out- of-plane accelerations. The data did not indicate torsional movements (about a vertical axis) for the runs prior to Run-4. However, there was a peak at 12-Hz for the runs after Run-4. This was the natural frequency of the safety frame because the safety frame moved to constrain the bent after Run-4, as explained in test setup. It was concluded that the torsion of the bent and the movement in the out of plane direction were negligible.

3.2.2 Target and Achieved Shake Table Motions

The actual motion of the shake table was different from the target motion because the specimen interacts with the shake table. The shake table drives a modified motion to reach to the target motion. However, the algorithms to modify the motion are not completely effective for all frequency ranges. The frequency content and magnitude of the achieved motions must be similar to that of the target motions to represent the earthquake loading. The spectral acceleration responses of the motions were selected to compare the effect of the achieved and target motions.

The correlation between the spectral acceleration response (Sa) of the target and achieved motions can be seen in Fig. 3-3 to 3-12. The measured fundamental periods of the bent before each run is depicted with the dashed line to identify the frequencies that were of concern. In the range of fundamental period plus/minus 0.5 seconds, the shape of spectral accelerations of the achieved and target motions were similar.

The spectral accelerations at the measured fundamental periods for the target and achieved motions are compared in Fig. 3-13. It can be seen that, at the fundamental periods of the bent, the spectral accelerations in the achieved motions were close to those from the target motions with the achieved accelerations being within 6.4% of the target values. Table 3-1 summarizes the peak ground acceleration (PGA), velocity (PGV), and displacement (PGD) of the achieved motions.

3.2.3 General Observation

The specimen was checked for cracks, spalling of cover concrete, failure of core concrete, and reinforcing bar rupture after each run. Moreover, the test videos were inspected for gap closure at the pipe-pins. The gaps did not close in any runs. Figure 3-14 shows the condition of BPSA after the final run.

As explained in Chapter-2, the north column was prefabricated (the right column in Fig. 3-14). The components on the north side of the bent are referred to as PC (precast) components such as PC pedestal, PC pipe-pin, PC column, etc. hereafter. The south column was cast in place (the left column in Fig. 3-14). The components on the south side of the bent are referred to as CIP (cast in place) components such as CIP pedestal, CIP rebar-pin, CIP column, etc. hereafter.

Moreover, the different sides of each component were labeled as N, S, W, and E indicating north, south, west, and east side.

3.2.3.1 CIP Components

The damage progression photos of the CIP column, its pipe-pin, and the supporting pedestal are presented in Fig. 3-15 to 3-29. Some minor surface cracks due to shrinkage existed on the ECC segment in the plastic hinge zone of the column prior to testing. The shrinkage cracks became wider after Run-1 (Fig. 3-16). Moreover, some minor flexural cracks were observed in the pedestal after Run-1. Flexural cracks were seen in the concrete segment of the column after Run-2 (Fig. 3-17). During Run-3, shear cracking was initiated in the mid part of the column. Additionally, a large crack was formed behind the plate of the load cell to the cap beam connection in Run-3 (Fig. 3-30).

The connection of the load cell to the cap beam failed during Run-4 (Fig. 3-31). Some flexural and shear cracks were seen in the column after Run-4. The specimen was repaired prior to continuation of the test. Run-5 was simulated with similar amplitude as that of Run-4 subsequent to post-tensioning of the cap beam. A few cracks were observed in the column and pedestal after Run-5 (Fig. 3-19). The load cell connection to the cap beam slid significantly during Run-5. Subsequent inspection of the videos revealed load cell slippage occurred also in Run-2 to Run-4. The sliding issue was fixed by placing steel shims between the load cell sides and the steel angles (Fig. 2-18).

Run-6 was applied with similar amplitude as that of Run-4. Minimal cracks were seen in the column after Run-6 (Fig. 3-20). The load cell to cap beam connection performed well starting with this run. One of the flexural cracks in the column plastic hinge zone opened significantly wider than the rest of the cracks after Run-7 (Fig. 3-21). This crack is referred to as principal crack, hereafter. Additionally, shear cracks were formed at the bottom of the column around the pipe-pin in Run-7. The principal crack became wider while the pipe-pin damage remained the same during Run-8 (Fig. 3-23 and 3-24).

The damage was concentrated at the principal crack in Run-9 and in the subsequent runs. In addition to the flexural deformation, the plastic hinge zone deformed in shear through sliding along the principal crack in Run-9 and afterward. This was observed in the video clips. Even though the cover concrete failed in compression, the ECC cover did not spall throughout the tests. The loose ECC pieces were removed by hand to expose the reinforcement after the last run as shown in Fig. 3-28. The longitudinal bars had buckled. The spiral reinforcement was ruptured. However, the core ECC was not damaged. No damage was observed in the pipe-pin after all the runs. Some minimal shear cracks were formed on the surface of the column above the pipe-pin (Fig. 3-29).

3.2.3.2 PC Components

The damage progression photos of the PC column, its pipe-pin, and the supporting pedestal are presented in Fig. 3-32 to 3-44. Some minor shrinkage cracks existed in the pedestal prior to testing. Minimal flexural cracks were observed on the column and pedestal after Run-1 (Fig. 3-33). After Run-2, few cracks were formed on the surface of the column and the pedestal above the pipe-pin (Fig. 3-34). Shear cracking in the plastic hinge zone of the column was initiated during Run-3 (Fig. 3-35). No significant cracks were formed in the column or pedestal in Run-4.

Run-5 was continued subsequent to the post-tensioning of the cap beam with similar amplitude as that of Run-4. Few shear cracks were extended to the lower part of the column after Run-5 (Fig. 3-36). Run-6 was simulated subsequent to installing the steel shims with the similar amplitude as that of Run-4. A few shear cracks were formed while flexural cracks widened during Run-6 and Run-7 (Fig. 3-38). The first cover concrete spalling occurred during Run-8 (Fig. 3-40). The last few cracks were formed in Run-9 with an X-shape pattern as flexural cracks extended into the shear cracks (Fig. 3-41).

The reinforcing bars were exposed due to extensive spalling of concrete during Run-10 (Fig. 3-42). Additionally, the longitudinal bars were buckled as well as the core concrete failed in compression. The damage state after Run-10 indicated that the plastic hinge reached its ultimate capacity during Run-10. Nevertheless, the test was continued with higher amplitude in Run-11 to investigate the performance of the CIP side. After Run-11, the core concrete was damaged further and the spiral ruptured (Fig. 3-43). The pipe-pin was carefully inspected after each run. No damage was observed in the pipe-pin connection (Fig. 3-44).

3.2.4 Measured Load and Displacements

Displacements of the points on the model were measured using displacement transducers shown in Fig. 2-26. Absolute displacement of center of the cap beam in the PC side at the extreme north was calculated by adding the readings of wire transducers SP-3, SP-4, and SP-5 with their corresponding weights. Assuming there was no rotation about the vertical axis of the section, the displacement of the center of the cap beam was calculated from

$$Y_{CB} = 0.25 \times (SP3 + SP4) + 0.50 \times SP5 \quad (3\text{-}1)$$

where,

Y_{CB}: absolute displacement of the center of the cap beam

SP3, SP4, and SP5: displacement readings from SP3, SP4, and SP5, respectively

Elongation of the load cell connection in the cap beam was monitored by readings from displacement transducer SP6. Table 3-2 shows the maximum reading of SP6 in each run. The resolution of SP6 was 0.04 in [1 mm]. The readings smaller than the resolution were not reliable but they were sufficiently small to conclude that elongation of the cap beam was negligible. The small elongation of the load cell connection was observed in all the runs subsequent to the repair of the cap beam. Additionally, the relatively large slippage at the load cell to cap beam connection during Run-5 rendered the results from Run-3 to Run-5 unreliable. Hence, only the results from Run-1, Run-2, and Run-6 to Run-11 are presented in this document.

The cap beam was repaired prior to Run-6. The permanent horizontal displacement of the cap beam was 0.14 in [4 mm] toward north after the repair. The columns were checked and were found to be plumb. Therefore, the permanent displacement of the model was due to the repair rather than the plastic deformation of the columns. Hence, the initial displacement of the bent and the data from the load cells were reset before applying Run-6.

The base shear of the specimen was calculated by adding the inertia force of the mass rig to the inertia force of the cap beam. The inertia force of the mass rig was measured by the load cell installed in the connection of the cap beam to the mass rig. This force was added to the inertia force of the cap beam calculated by multiplying the acceleration of the cap beam, recorded by

ACC2 and ACC3 in Fig. 2-26, and the mass of the cap beam, post-tensioning hardware, and one-half of the columns.

3.2.4.1 Lateral Force-Displacement of the Bent

The relative displacement of the center of the cap beam to the shake table consisted of pedestals deformation, pipe-pins slippage, and columns deformation. This is referred to as 'specimen' displacement, hereafter. The average of pedestals displacement was subtracted from the specimen displacement to investigate the performance of the two-column bent on pipe-pins. The aforementioned relative displacement of the center of the cap beam to the top of the pedestals (including the pipe-pin throat) is referred to as 'bent' displacement, hereafter.

The comparison between specimen and pedestal displacements showed that the contribution of the pedestal displacement to the overall displacement was less than 7% as presented in Table 3-3. The distance from the top of the pedestals to the soffit of the cap beam, the column clear height, was used to calculate the drift ratio. The following equations show the calculation of the displacements:

$$D_{specimen} = Y_{CB} - Y_{shake\ table} \tag{3-2}$$

$$D_{pedestal} = SP1 + 0.5 \times \frac{SP2W - SP2E}{2} \tag{3-3}$$

$$D_{bent} = D_{specimen} - D_{pedestal} \tag{3-4}$$

$$drift = \frac{D_{bent}}{h_c} \times 100 \tag{3-5}$$

where,

$Y_{shake\ table}$: absolute displacement of the shake table, in [mm]

$SP1, SP2W, SP2E$: displacement readings from SP1, SP2W, and SP2E in Fig. 2-26, respectively, in [mm]

$D_{specimen}$: specimen displacement, in [mm]

$D_{pedestal}$: average of pedestals displacement, in [mm]

D_{bent}: bent displacement, in [mm]

$drift$: bent drift, percent

h_c: the clear height of the columns

Table 3-4 presents the maximum and minimum bent displacement and corresponding base shear for the considered runs. Figures 3-45 and 3-46 show the measured force-displacement hysteretic curves for the bent with their envelopes in Fig. 3-47. The envelopes were discontinuous because the results of Run-3 to Run-5 were not included. To reconstruct the missing segment of the envelope, the average of the envelopes in the positive and negative displacement ranges were first determined. Then, a third degree polynomial was passed through the discontinuous segment while passing through the average of envelopes at 2% and 5% drift ratios.

Figure 3-47 shows the idealized bilinear curve for the bent determined based on the average of the envelopes following the procedure in Caltrans SDC (Caltrans, 2010). The initial stiffness of idealized curve is equal to the secant tangent of the envelope at initial yielding. The first yield occurred in longitudinal bars of the PC column at displacement of -0.65 in [17 mm]. The effective yield point was estimated assuming the plastic part has zero stiffness. The yield force in the idealized curve was determined by preserving energy.

The displacement ductility of the bent was 3.6 from the envelope of the tests. However, the formation of full column plastic hinges and the strain data in plastic hinges indicate substantially higher ductility. The measured initial stiffness was highly reduced because of the slippage of the load cell to cap beam connection in the early runs. The analytical simulation of the model presented in Chapter 4 shows that the ductility of the bent would have been 6.5, if the cap beam performed as an elastic beam without slippage at the load cells.

The force-displacement hysteresis curves of the bent indicated a slight pinching effect near the origin (Fig. 3-45 and 3-46). The pinching is attributed to slippage at the pipe pins due to the closure of the gaps between the two pipes at each pin. The fluctuating pattern also indicates that friction release was gradual and did not occur at a specific displacement of the pipe-pin.

3.2.4.2 Lateral Force-Displacement Relationship for Individual Columns

The slippage of the pipe-pin was subtracted from the bent displacements to calculate deformations of the CIP and the PC column. The slippages of the pipe-pins were estimated using the procedure explained in section 3.2.11.1. Moreover, the shear force in each of the column was estimated based on equilibrium using the axial load measurement from the load cell in the cap beam.

Table 3-4 presents the maximum and minimum displacements for the columns and the corresponding shear force for each of the runs. The idealized bilinear curves were determined using the same procedure that was explained in previous sections for the bent. Figure 3-48 and 3-49 show the hysteretic curves and the envelopes of the curves for the CIP and the PC column, respectively. The displacement ductility was 3.9 and 4.2 for the CIP and the PC column, respectively. The reason for the apparent low ductility is the underestimated initial stiffness that was caused by the slippage of the load cell at mid span of the cap beam.

The columns did not exhibit symmetric response in the positive and negative lateral displacement despite the near symmetric behavior of the bent. Due to the overturning moment, the CIP side was under axial compressive forces when displacement was positive. Likewise, the PC side was under compressive forces when displacement was negative. Both columns showed larger strength and wider hysteretic loops under compressive loads. However, because the maximum column compressive forces occurred at different times, stiffness and strength degradation of one column affected the load distribution to the other column. This issue was less pronounced in the overall bent because the bent lateral force was the summation of column lateral forces.

3.2.5 Axial Load Variation

The weight of the cap beam and overturning moments produced axial loads in the columns. The overturning moment was sufficiently large to produce tensile forces during the tests. Table 3-5 presents the maximum of tensile and compressive force in the columns. The weight was added

to the shear data from the load cell in the cap beam to calculate the axial load in the columns. This is because the readings from the load cells had been reset prior to the tests. The columns underwent a maximum of 48.2 kip [214 kN] and 39.2 kip [174 kN] in compression and tension, respectively. Note that in a real bent, the tensile axial forces would be lower because of the gravity forces. Gravity forces from the super structure in this bent were not simulated to ensure that the pins are subjected to the maximum possible tensile forces.

3.2.6 Dissipated Energy

The dissipated energy was calculated by integrating the area enclosed by the force-displacement curves. This energy was determined separately for the two columns, the two pipe-pins, and the bent. The accumulated dissipated energies for the columns, the pipe-pins, and the overall bent are compared in Fig. 3-50. The dissipated energy in the pipe-pins due to friction accounted for approximately ten percent of the total dissipated energy. The plastic deformation of the columns dissipated most of the energy in the bent.

3.2.7 Measured Strains

Strains were measured on longitudinal and transverse reinforcement in the columns, the pedestals, and the cap beam. Additionally, longitudinal and shear strains on the pipes were monitored during the tests. Figures 2-28 to 2-34 show strain gage instrumentation configuration.

Strain gages are generally accurate up to 20% strain (200,000 με). The readings are sensitive to localized strains caused by concrete cracks, interaction of the ribs on the bars with the concrete, and effect of aggregates pressing on strain gages. Moreover, strain gages measure true strain on a small surface of the element. Whereas, engineering stress-strain curves are typically measured in reinforcing bar tensile tests. Therefore, comparison of the measured strain with the strain from material testing can be erroneous at large strains. Physical damages to instruments such as wire breakage also cause the instruments to malfunction. As a result, it was assumed in this study that the measured strains are reliable in the range of plus/minus 20% with resolution of 0.02% [200 με].

In this chapter, the reliable part of the data is shown in the graphs. Strains are presented in percentage with a positive sign indicating tension. Additionally, the strains larger than the measured yield strain are shown in bold in the Tables.

3.2.7.1 Column Longitudinal Reinforcement in Plastic Hinge Region

The northern- and southern-most longitudinal bars were instrumented at three levels in the plastic hinge zones of the columns. However, all the strain gages on the southern-most longitudinal bar of the PC column malfunctioned. Tables 3-6 and 3-7 present the maximum and minimum strains in the longitudinal bars in the CIP and PC column, respectively. Figures 3-51 and 3-52 show the strain profile of the longitudinal bars in tension. The measured yield strain of 0.23% was reached first in the CIP column then 0.277 seconds later in the PC column during Run-2, recorded in CSG-39 and CSG-A36, respectively. The maximum strain was 8.01% in tension for the CIP column, which is approximately 34 times the yield strain. Additionally, the maximum strain in the PC column was 3.23%, which is approximately 14 times the yield strain. The actual maximum strains were larger for both columns because the strain gages at the upper-most section malfunctioned during the last run.

Large tensile residual strains were noted after Run-6 especially in the PC column. These bars remained extended in the subsequent runs. The tensile strains were intensified by crack opening in the plastic hinges because of the relatively small gravitational axial load. The strain profiles show that spread of plasticity in the CIP column was less extensive than that of the PC column. Cracks were distributed over a longer potion of the PC column as opposed to the single principal crack that was formed on ECC in the CIP column. Therefore, a longer length of the longitudinal bars yielded in the PC column.

3.2.7.2 Columns Transverse Reinforcement in Plastic Hinge Region

Strain gage locations on transverse bars in plastic hinge region of the columns were presented in Figs. 2-31 and 2-32. Recall that positive strains indicate tension. Tables 3-8 and 3-9 summarize the maximum tensile and compressive strains in the transverse bars in plastic hinge region. Figure 3-53 depicts the profile of average of maximum tensile strain of both strain gages for both columns. The data indicate that none of the spirals yielded. The maximum tensile strain was 0.055%, which is 27% of the yield strain.

As mentioned before, the spirals in both columns ruptured in Run-11. The fracture was caused by the buckling of the southern- and northern-most longitudinal bars. It is logical to conclude that the spiral yielded prior to fracture, even though the measured data did not indicate high strains nor yielding. It is believed that the large local deformation of the longitudinal bars and damage to concrete led to damage to the gages and wires, thus terminating collection of data.

3.2.7.3 Pipes in Pipe-pin Connections

Steel pipes in the pipe-pin connections were instrumented according to Fig. 2-33 and 2-34. The vertical strain gages at the north and south sides were used to calculate axial force and bending moment in each section of the pipes. Furthermore, the data from the rosette strain gages on the east side were used to determine shear strains and stresses in the pipes.

Tables 3-10 to 3-13 present the maximum and minimum vertical strain on the pipes. All the measured strains were smaller than the yield strain of 0.20% and 0.17% for the lower and upper pipes, respectively, indicated in the material testing report (MTR). Figures 3-54 and 3-55 depict the profile of vertical strain on the pipes. The horizontal axis indicates the column-pedestal interface in each figure. The maximum tensile strains were 0.180 and 0.137%, respectively in the lower pipes of CIP and PC pipe-pin, which are 92% and 70% of the yield strains occurred at the north faces in Run-8. The maximum tensile strains were 0.128% and 0.114%, respectively, in the upper pipes of the CIP and PC pipe-pin, which are 77% and 68% of the yield strains and occurred at the north faces in Run-8.

Figure 3-56 shows the vertical strains during Run-8 on the lower pipe of the PC pipe-pin at 1 in [25 mm] below the pedestal surface (Section-3 in Fig. 2-34). The strain gages P(V)-A71 and P(V)-A73 were on the south and north sides of the lower pipe, respectively. The strain history indicates no forces were present in that section until the pipes were activated. This strain pattern was observed in all the strain gages on the pipes including the rosette strain gages.

The force transfer mechanism is different during small motions from large motions. Tensile and shear forces were transferred from the column to the pedestal through the pipes under large drifts as explained in Chapter 2. Under small drifts, the forces in the pipes were negligible because the pipes were not engaged in the load transfer mechanism. The shear forces in the

pipes were minimal prior to the contact of the upper pipe and the lower pipe because the forces were transferred to the pedestal through friction of the column on the pad. The axial forces were also minimal under small drifts. The relatively small tensile forces of the rod were transferred to the surrounding concrete body through the embedded end plates. The mechanism that led to forces in the pipes was investigated and is described in Chapter 4 in conjunction with numerical simulation.

The maximum shear strain is a measure of distortion energy for ductile material in complex stress condition based on Von Mises criteria. The maximum shear strain was calculated using the strains measured with three strain gages in the rectangular rosette arrangements on the east sides of the pipes as described below.

$$\gamma_{max} = \sqrt{2 \times [(\varepsilon_H - \varepsilon_{45})^2 + (\varepsilon_V - \varepsilon_{45})^2]} \quad (3\text{-}6)$$

γ_{max}: maximum shear strain

$\varepsilon_{45}, \varepsilon_V, \varepsilon_H$: diagonal strain at 45 degrees, vertical, and horizontal directions, respectively (Fig. 3-57)

Tables 3-14 and 3-15 present the maximum shear strain in the CIP and PC pipe-pins, respectively. Figure 3-58 shows the maximum shear strain profile in the pipes. The maximum shear strains were only 46% of the yield shear strain. The yield shear strains calculated from Eq. 3-7 were 0.29% and 0.25% for the lower and upper pipes, respectively.

$$\gamma_y = \frac{\tau_y}{G} \quad (3\text{-}7)$$

$$\tau_y = \frac{f_y}{\sqrt{3}} \quad (3\text{-}8)$$

γ_y: yield shear strain

τ_y: yield shear strength, ksi [MPa]

G: elastic shear modulus, ksi [MPa]

f_y: tensile yield strength, ksi [MPa]

3.2.7.4 Columns and Pedestals Longitudinal Reinforcement at Pipe-Pin

The pipe-pins were designed to transfer the forces to pedestal without damage. Tables 3-16 and 3-17 show the maximum and minimum strains in the longitudinal bars of the columns and pedestals near the pipe-pins. Figures 3-59 and 3-60 depict the profile of the maximum and minimum strains in the longitudinal bars. The maximum strain was 0.151% near the pipe-pin connections, which is 66% of the yield strain.

3.2.7.5 Columns and Pedestals Transverse Bars at Pipe-Pin

Tables 3-18 and 3-19 show the maximum transverse reinforcement strains in the columns and pedestals at the pipe-pin. Figures 3-61 and 3-62 present the profile of the maximum strain in the transverse reinforcement at pipe-pin. The maximum strain was 0.1325% recorded in CSG-A7 and was 59% of the yield strain. That indicates sufficient shear strength of the sections at the pipe-pins.

3.2.7.6 Cap Beam Reinforcement Strain

Table 3-20 shows the maximum and minimum strains in the cap beam reinforcement. The strain gages on the reinforcement of the cap beam were reset to zero after post-tensioning of the cap beam. The post-tensioning forces produced an average stress of 694 psi [4.79 MPa] on the cap beam cross section and reduced the tensile strains. This is evident by comparing the maximum longitudinal bar tensile strains in Run-2 versus Run-6 in the table. The maximum strain was 0.098% occurred in Run-2, which was 39% of the yield strain indicating that the cap beam was indeed capacity protected with no yielding, as intended.

3.2.8 Internal Forces in the Pipes

The sectional forces of the pipes were determined using the strains on the three sides of the section and assuming the Euler-Bernoulli beam principal. The bending moment and axial force were estimated using two vertical strains at the north and south sides of the sections. In addition, the rosette strain gages were used to determine the shear strains on the east side of the pipes.

In previous section, it was discussed that strains did not pass the yield strain. Therefore, linear-elastic behavior was assumed for materials to calculate stress from the strain data. However, the strain gages showed small permanent strains during some of the runs. The residual strains are believed to be due to small permanent deformations at the pipe-pin connections due to permanent displacement of the overall bent. The residual strains in the pipes do not indicate inelastic deformation.

3.2.8.1 Axial Force in Pipes

Three strain gages at the north, south, and east recorded the vertical strain of the pipe in each section. The axial force at each section was calculated from following equation.

$$P = \frac{0.5\ (\varepsilon_S + \varepsilon_N) + \varepsilon_V}{2} E\ A_P \tag{3-9}$$

P: internal axial force in the pipe, kip [kN]

$\varepsilon_S, \varepsilon_N, \varepsilon_V$: strain of the pipe on the south side, north side, and the vertical component of the rosette, respectively

E: modulus elasticity, ksi [MPa]

A_P: gross area of the pipe, in^2 [mm^2]

Figures 3-63 and 3-64 show the profile of axial load in the pipes. The compressive force in the pipe-pin is shown with a positive sign. The profile of axial load was determined at the maximum drift ratios in both directions. The CIP column was under compression at the positive drifts and under tension at the negative drifts. The PC pipe-pin was under compression at the negative drifts and under tension at the positive drifts. Regardless of the sign of the axial force in the columns, the axial forces were compressive at the embedded ends of the pipes and changed to tension at the free ends.

The load path in pipe-pins was explained in Chapter 2. The tensile force of the rod was transferred to the pipes by bearing on the end plates. Due to the rotation in the pipe-pin, the rod was under tension regardless of the axial force in the column. The axial force in the upper-

most section of the pipe-pin, Section-6 in Fig. 2-34 and 2-35, was a lower bound estimate of the rod axial force. The axial force in the upper-most section of the upper pipe was equal to the tensile force of the rod minus the friction force of the end plate and the pipe with concrete as illustrated in Fig. 3-65. The maximum axial force was 57.8 [257] and 35.2 [157 kN] in the upper-most sections of the CIP and PC pipe-pins, respectively.

3.2.8.2 Shear Forces in Pipes

The shear strains in the pipes were estimated using the rosette strain gages on the east sides of the pipes. Torsion was assumed negligible because of the symmetry of the pipes about the vertical central plane of the bent. The shear in each of the sections of the pipes was calculated using following equations:

$$\gamma_{12} = 2 \times \varepsilon_{45} - (\varepsilon_V + \varepsilon_H) \tag{3-10}$$

$$\tau_{12} = G\,\gamma_{12} \tag{3-11}$$

$$V_p = \tau_{12} \times A_v \tag{3-12}$$

$$A_v = \frac{A_P}{2 + \frac{t}{r}} \tag{3-13}$$

γ_{12}: shear strain on the horizontal plane

G: shear modulus, ksi [MPa]

τ_{12}: shear stress on the horizontal plane, ksi [MPa]

V_p: pipe internal shear force, kip [kN]

A_v: effective shear area, in^2 [mm^2] (P.C.J. and Spaan, 2005)

A_p: pipe gross area, in^2 [mm^2]

r: pipe outer radius, in [mm]

t: pipe thickness, in [mm]

Figures 3-66 and 3-67 show the profile of shear on the pipes at the maximum drift in both directions. The CIP column was in compression under positive drifts and in tension under negative drifts. The PC pipe-pin was in compression under negative drifts and in tension under positive drifts. The maximum shear in the pipes were 14.8 [65.8] and 10.3 kip [45.8 kN] in the CIP and PC pipe-pin, respectively. Those are smaller than the columns shear because a portion of the shear was transferred to the pedestal through friction. Moreover, strain gages in sections with the largest shear were installed 1 in [25 mm] below the surface of pedestal inside the concrete (Fig. 2-23 and 2-24). Therefore, a part of the force was carried through bearing of the pipe on concrete before it was registered by the gages.

Previous research has shown that some shear is transferred through contact between the top of the lower pipe and the inner wall of the upper pipe (Mehrsouroosh and Saiidi, 2014). With this assumption, the contact point would be at 4-in [101.6-mm] above the top of the pedestal. Consequently, the shear force profile should change sign at this point. This trend was not observed in the result for the tests in the present study because the inner pipes in this test were

tapered. As a result, the upper and lower pipes came in contact over the tapered zone of the inner pipes rather than a single point at the top of the pipe.

3.2.8.3 Bending in Pipes

The internal bending moments in the pipes were calculated from following equation.

$$M = \frac{(\varepsilon_S - \varepsilon_N)}{2\,r} EI \tag{3-14}$$

In Eq. 3.14, variables are similar to those defined in the previous section with positive moment producing compressive stress on the south side of the pipe. Figures 3-68 and 3-69 depict the profile of bending moment in pipes in both directions. The CIP column was under compression at the positive drift and under tension at the negative drift. The PC pipe-pin was under compression at the negative drift and under tension at the positive drift. The yield moments of the lower and upper pipes were 113 [12.8] and 207 kip-in [23.4 kN.m], respectively. The maximum moments were 106 [12.0] and 75 kip.in [8.48 kN.m], which were 94% and 36% of the yield moments of the lower and upper pipes, respectively. Note that the combination of moment and axial force in the pipe was critical as discussed in section 3.2.7.3.

3.2.9 Strain Rate

The strain rate is highly variable during shake table tests. Material testing is typically conducted under very slow loading rate. The relatively high strain rate during shake table testing could affect the concrete and steel properties and make them different from those obtained from slow testing. In the next chapter, proper models are used to modify the properties of concrete and steel based on the average strain rate to reflect the strain rate effects in the shake table testing.

It is suggested to amplify yield and ultimate stress of the reinforcing bars as a function of the rate of loading (Kulkarni and Shah, 1998). Models to modify properties of the reinforcement steel were based on the strain rate for tensile tests in the range of one-half of the yield strain to the yield strain (Zadeh and Saiidi, 2007). Therefore, the average of the strain rates was calculated while strains were in that range prior to yielding. Figure 3-70 shows the average strain rate and average strain in the strain gages in the plastic hinges of the columns. The average strain rate for the bars was 10200 $\mu\varepsilon.s^{-1}$.

The strain rate for concrete was measured for the strains in the range around the unconfined concrete failure strain prior to yielding of the longitudinal bars that were under compression. Implied in this method was that longitudinal bars had perfect bond with concrete. The assumption of the perfect bond between concrete and bars is proper prior to yielding. However, the sample size to satisfy both conditions was not sufficiently large. Consequently, the average strain rate for the compressive strains in the range of 0.15 to 0.25% was calculated considering the points beyond yielding. The average strain rate from strain gages are shown in Fig. 3-71. The average strain rate for concrete in the plastic hinge zone was 10500 $\mu\varepsilon.s^{-1}$.

3.2.10 Measured Curvature in Column Plastic Hinges

Two displacement potentiometers (NTs) measured vertical displacements on opposite sides of the columns at three levels in the plastic hinge region as shown in Fig. 2-27. The difference of the displacements was divided by the horizontal distance of the NTs to calculate the rotation of

the sections. Then the rotation at each section relative to the adjacent section determined. Each relative rotation was the summation of curvature over the gage length for the NTs. Therefore, the relative rotations were divided by the vertical distance of the sections to calculate the average curvature over the gage length. Extensive damage and wide cracks during stronger motions caused a few of the potentiometers to malfunction. Table 3-21 lists the runs during which the curvature data were unreliable.

Figure 3-72 shows profile of the maximum and minimum rotations at the top of the columns. The profiles of the average curvature are shown in Fig. 3-73. The positive rotations and curvatures in these figures correspond to positive displacement of the bent. Because of the difference in the crack patterns, plasticity was more localized in the top 7-in [178-mm] portion the CIP column than the PC column. Consequently, larger rotations and curvatures were observed in the PC column than the CIP column below 7-in [178-mm]. In addition to a crack at the column-cap beam joint, only one crack became wider with the test progression in the ECC segment of the CIP column, which was labeled principal crack in Fig. 3-21. Therefore, the higher tensile strength of ECC reduced the extent of plasticity in the column but the top portion of the column underwent larger deformation.

3.2.11 Pipe-Pin Force-Displacement

The slippage, uplift, and rotation of the pipe-pins were determined using six displacement potentiometers. Because it was not feasible to instrument the column-pedestal interfaces, the transducers were installed four inches [ten millimeters] above the interface (Fig. 2-27). In each column, two displacement potentiometers at the east and west sides were used to measure the horizontal movement of the column relative to the pedestal. Additionally, two displacement potentiometers measured the vertical movement of the north and south faces of the bottom of each column relative to the reference plates that were attached to the pedestal on each side. Two vertical transducers were used to measure the movements between the reference plates and the pedestal.

The column deformations were assumed negligible in the part below the instrumented section. The slippage, uplift, and rotation of the pipe-pins were determined using the following equations that are based on the rigid body displacements shown in Fig. 3-74.

$$s_B = \frac{NT7 + NT8}{2} \tag{3-15}$$

$$\theta_B = \frac{(NT6 + NT4) - (NT5 + NT3)}{D + 2 \times a_h} \tag{3-16}$$

$$z_B = \frac{NT6 + NT4 + NT5 + NT3}{2} \tag{3-17}$$

$$s_{pin} = s_B \cdot \cos(\theta_B) - a_v \cdot \theta_B \tag{3-18}$$

$$\theta_{pin} = \theta_B \tag{3-19}$$

$$z_{pin} = z_B \cdot \cos(\theta_B) - s_{pin} \cdot \sin(\theta_B) \tag{3-20}$$

where,

$s_B \; and \; z_B$: slip and uplift of instrumented section, in [mm]

θ_B: rotation of instrumented section, rad

D: diameter of the column, in [mm]

a_h: horizontal distance of transducers to the column surface equal to 4 in [11 mm]

$s_{pin} and\ z_{pin}$: slip and uplift of pipe-pin, in [mm]

θ_{pin}: rotation of the pipe-pin, rad

a_v: measured vertical distance of instrumented section and bottom of column, in [mm]

3.2.11.1 Pipe-Pin Shear-Slip

Figure 3-75 shows the hysteresis curve of the column shear versus slip in the pipe-pins in each run. The maximum and minimum shear force and slip for the runs are shown in Table 3-22. The shear-slip relationships and inspections of the close up videos showed that the columns slipped on prior to impact between the pipes accompanied with a rocking motion. The maximum slip was 0.39 in [10 mm] and 0.44 in [11 mm] in the CIP and PC pipe-pin, respectively. This data also confirms that the inner and outer pipes came in contact over the lower part of the upper pipe and not at the top of the inner pipe. The gap between the two pipes was 0.37 in [9 mm] at the column pedestal interface but was increased to 0.70 in [18 mm] at the top end of the tapered zone of the inner pipe. The maximum slips are close to the gap at the interface indicating that the contact occurred at the interface.

Slippage of the PC pipe-pin could not be measured after Run-10 because the horizontal transducers were damaged by falling pieces of concrete.

3.2.11.2 Pipe-pin Moment-Rotation

Three independent internal forces are required to calculate the moment at the pipe-pins. The shear and axial force readings of the load cell in the cap beam was used to estimate the axial and shear forces in the columns with sufficient accuracy. However, inspection of the moment from the load cell indicated the readings were suspicious. The FFT of all the measurements including force and displacement had a peak around the natural frequency of the structure. The moment from the load cell in the cap beam did not indicate a peak in the FFT. Furthermore, the measured pipe-pin moments indicated a negative stiffness in the pipe-pins. Therefore, the measured moments from the load cells were dismissed and the pipe-pin moments were estimated based on equilibrium using the base shear and axial forces of the columns.

Based on the estimated data, the summation of the two pin moments could be calculated with sufficient accuracy. The summation of the moments is useful because it is an upper bound estimate of the moment in the pipe-pins assuming the two pipe-pin moments are in the same direction in each instance. Additionally, one-half of the summation of the moments is the average pipe-pin moment, which is an approximate estimate of the pipe-pin moments. Moreover, the shapes of the hysteresis curves of the average pipe-pin moment show no moments were developed in the pipe-pins under small rotations (Fig. 3-76).

Figure 3-76 shows the average pipe-pin moments at the bottom of the columns versus bent drift for each run. Table 3-23 presents the maximum and minimum rotation in the pipe-pins and the average pipe-pin moments. The positive rotations and positive moments correspond to positive displacements in the bent. The fluctuation of moment around zero drift shows friction-slip

behavior of the pipe-pin prior to the contact of the pipes. The hysteresis curves show moment in the pipe-pins were mobilized at 3% drift. Comparison of the maximum and minimum rotations of the pipe-pins indicated the rotations of both pipe-pins were similar under the large drifts but not under small drifts. The maximum average pipe-pin moment were 383 [43.2] and 364 kip.in [41.1 kN.m] in positive and negative drift direction, respectively.

3.2.11.3 Pipe-Pin Vertical Force-Uplift

Figure 3-77 shows the column axial force and the pipe-pin uplift hysteresis curves for each of the runs. Table 3-24 presents the uplifts at the instance of the maximum and minimum pipe-pin rotations. The column compression force and the uplift are positive in this figure. The figure shows comparable uplifts in the pipe-pins cause by the rotation of the pipe-pin regardless of the direction of axial force.

The distance of instantaneous center of rotation relative to the center of the pipe-pin was calculated at instance of the maximum and minimum rotations in each run by dividing the uplift by the rotation (Fig. 3-78). That is an estimation of the distance of the compressive force in the pad relative to the threaded rod in the center. That compression force couples with the tension in the rod to produce the pipe-pin moment due to the rotation. The average distance is presented in Table 3-24 for different cases.

3.2.12 Evaluation of the Bent with Pipe-Pin

BPSA performed as it was designed. Full plastic hinge capacities were developed at the top of the columns while the pipe-pins remained undamaged. Minimal cracks were formed around the pipe-pin connection. The strain gages on the pipes also showed that the pipes remained elastic, as intended. Moments were developed at the bottom of the columns that were not considered in the design of the bent. However, the shear capacity of the columns were sufficiently larger than the extra shear due to the pipe-pin moments.

The prefabricated column and pipe-pin performed as well as the cast-in-place elements. No difference was observed in the performance of the precast column and the cast in place column with pipe-pin connections. The pocket connections performed as designed. One longitudinal bar of the columns ruptured in tension without any observable damage in the connection while other bars reached very close to their capacities. In addition, the column plastic hinge with ECC showed significantly less damage than that with conventional concrete.

3.3 Bent with Rebar-Pin Column-Pile Shaft Connection (BRSA)

The connections of the columns to the pedestals in this model were rebar-pins. As explained in Chapter 2, the model was designed to develop plastic deformations in the columns and the rebar-pins. However, the columns were expected to reach the plastic hinge capacity only at the top. The columns and the rebar-pins underwent large plastic deformations. Eventually, the model failed due to rupture of a reinforcing bar at the top of the column. In the rebar-pin, the cover concrete spalled as well as the longitudinal bars yielded extensively, but there was no fracture or strength degradation.

3.3.1 Dynamic Characteristics

The fundamental period and the damping ratio of the specimen changed after each of the runs because of the progression of the plastic action. The source of the plastic action is explained in

section 3.2.1. The dynamic characteristics were estimated using the methods explained in Appendix A. Figures 3-79 and 3-80 show the changes of the fundamental period and the damping ratio before each run. The fundamental periods were normalized relative to the initial period of the bent. Table 3-25 presents the fundamental period of the model for all the runs. The fundamental periods and the damping ratios of the bent increased after each run because of the increased damage in the column plastic hinges and rebar-pins.

The bent was sufficiently stable in the out of plane direction as opposed to BPSA. Despite that, two steel frames were installed to prevent the out of plane movements of the bent. The out-of-plane displacements of the bent were monitored to ensure that the bent was subjected to in-plane loading and the response was two-dimensional. The maximum out of plane displacement was 0.45 in [12 mm]. Additionally, the transfer functions were calculated based on the differences between the out- of-plane displacements at ends of the cap beam and the shake table acceleration. The data did not indicate torsional movements about the vertical axis for any of the runs. Therefore, the torsion of the bent and the movements in the out-of-plane direction were negligible.

3.3.2 Target and Achieved Shake Table Motions

The actual motions were different from the target motions as explained in section 3.2.2. Figures 3-81 to 3-86 show the spectral acceleration response for the target and the achieved motions. The measured fundamental period before each run is depicted with a dashed line to identify the frequencies that were of concerned. The similarity in the shape and amplitude of the spectra indicated that the frequency contents were sufficiently close in the range of the fundamental period plus/minus 0.5 seconds.

The spectral accelerations at the fundamental period of each run are depicted in Fig. 3-87. This Figure shows that the spectral accelerations in the achieved motions were close to those from the target motions with the achieved accelerations being within 16% of the target values. However, the spectral acceleration of Run-1 at the measured fundamental period was 50% more than that of the target motion. It is typically difficult for the shake-table drive system to replicate initial runs because the intact structure is relatively stiff and affects the shake table motions significantly. Nevertheless, the differences for Run-1 were acceptable because the motions were of low amplitude. Table 3-25 summarizes the peak ground acceleration (PGA), velocity (PGV), and displacement (PGD) of the achieved motions.

3.3.3 General Observation

The specimen was checked for cracks, spalling of concrete, failure of core concrete, sliding of the rebar-pin, and reinforcing bar rupture after each run. Moreover, the close-up test videos were reviewed to determine any gap closure at the rebar-pins. The gaps did not close in any of the runs. Loud sounds of two bar ruptures were heard during Run-6, but the fracture location was not evident in the exposed section of the bars. The condition of the model after the test is presented in Fig. 3-88.

As explained in Chapter 2, the north column was prefabricated (the right column in Fig. 3-88). The components on the north side of the bent are referred to as PC (precast) components such as PC pedestal, PC rebar-pin, and PC column, etc. hereafter. The south column was cast in place (the left column in Fig. 3-88). The components on the south side of the bent are referred to as CIP (cast in place) components such as CIP pedestal, CIP rebar-pin, CIP column, etc. hereafter.

Different sides of each component were labeled as N, S, W, and E indicating north, south, west, and east side to document and describe the damage more clearly.

3.3.3.1 CIP Components

The damage progression photos of the CIP column, its rebar-pin, and the supporting pedestal are presented in Fig. 3-89 to 3-99. The column remained essentially elastic in Run-1 with no observable cracks (Fig. 3-89). Flexural cracks were observed in the plastic hinge region of the column as well as at the rebar-pin and column connection after Run-2 (Fig. 3-90 and 3-91). Few flexural cracks were also seen on the pedestal after Run-2 (Fig. 3-92). The cracks propagated out of the plastic hinge region of the column in Run-3 (Fig. 3-93). During Run-4, the cover concrete failed at the north side of the plastic hinge of the column as shown in Fig. 3-94. Furthermore, the flexural cracks turned into the X-shape shear cracks in the plastic hinge region. A shear crack was also observed in the rebar-pin after Run-4 (Fig. 3-95).

The cover concrete at the top of the column spalled during Run-5 causing the spiral to be exposed (Fig. 3-96). The cover concrete of the rebar-pin also started to fail in compression during Run-5 but the spiral was not exposed in that location. Finally, the core concrete failed in compression at the top of the column during Run-6 as shown in Fig. 3-98. The loose concrete was removed by hand from the model to inspect the reinforcing bars. The longitudinal bars buckled but did not rupture. The spiral was exposed in the reduced section of the rebar-pin after Run-6 (Fig. 3-99). Moreover, the top surface of the pedestal spalled during the last run.

3.3.3.2 PC Components

The damage progression photos of the PC column, its rebar-pin, and the supporting pedestal are presented in Fig. 3-100 to 3-111. Some minor construction and shrinkage cracks existed prior to testing. Those cracks became wider during Run-1 (Fig. 3-100). After Run-2, flexural cracking was observed in the plastic hinge zone of the column (Fig. 3-101). The cracks extended below the intersection of ECC in Run-3, as is shown in Fig. 3-102. A crack was extended around the entire perimeter of the column at the interface of the ECC segment with the conventional concrete (Fig. 3-103). Flexural cracks were also formed at the top of the pedestal in Run-3.

Some cracks were formed on the lower part of the column in Run-4 while the flexural cracks at the top of the column turned into shear cracks (Fig. 3-104). Shear cracks were also observed on the reduced section of the rebar-pin after Run-4 (Fig. 3-105 and 3-106). Few cracks were formed on the top surface of the pedestal in Run-4. Nothing new was observed but the existing cracks became wider during Run-5 (Fig. 3-107). One of the shear cracks in the rebar-pin was extended to the column surface (Fig. 3-108). Furthermore, the flexural crack in the rebar-pin became significantly wider.

The shear cracking expanded to the lower part of the column during Run-6. The damage state in the rebar-pin remained the same. A block of concrete spalled in the mid-height of the pedestal during the last run due to the lack of sufficient concrete cover (Fig. 3-112).

3.3.3.3 Precast Cap Beam

As explained in Chapter 2, the cap beam was post-tensioned from the beginning of the test. Therefore, there was minimal cracking in the cap beam. A vertical crack on each side of the cap beam was observed after Run-4. They were extended from the bottom to about 1/5 of the cap

beam height similar to the corrugated duct height (Fig. 3-113). The bars were sufficiently anchored in the cap beam to reach to the full capacity of the plastic hinge.

3.3.4 Measured Loads and Displacements

The lateral forces were estimated similar to BPSA by adding the inertia forces of the mass rig to that of the cap beam. Absolute displacement of the center of the cap beam in the PC side at the extreme north was calculated by averaging the readings of two wire transducers, SP3 and SP4, shown in Fig. 2-51. The displacement of the cap beam was estimated from SP3, SP4, and SP6 readings (Fig. 2-51)

$$Y_{CB} = 0.5 \times (SP3 + SP4) + SP6 \quad (3\text{-}21)$$

where,

Y_{CB}: absolute displacement of the center of the cap beam

SP3, SP4, and SP6: displacement readings from SP3, SP4, and SP6, respectively (Fig. 2-51)

The maximum difference between the displacements measured at the top and bottom of the cap beam was 0.17 in [4 mm]. This corresponded to less than 1.5-degree rotation of the section. The maximum elongation of the cap beam was 0.02 in [0.6 mm] measured by SP-6. Hence, the rotation and the elongation were negligible.

3.3.4.1 Lateral Force-Displacement of the Bent

The relative displacement of the center of the cap beam to the shake table was due to the deformation of the pedestals, rebar-pins slippage, and column deformations. This is referred to as 'specimen' displacement, hereafter. The average of the pedestal displacements was subtracted from the specimen displacement to determine the combined displacement of the columns and pins and to investigate the performance of the part of the bent above the pedestal. The aforementioned relative displacement of the center of the cap beam to the top of the pedestals (including the rebar-pin throat) is referred to as 'bent' displacement, hereafter. Equations 3-2 to 3-5 were used to calculate the aforementioned displacements. The comparison between the specimen and the average pedestal displacements in Table 3-26 shows that the contribution of the pedestals to the overall performance was less than 10% after the bent yielded.

Table 3-27 presents the maximum and minimum bent displacements and the corresponding base shears. The measured force-displacement hysteresis curves for the bent during each run are depicted in Fig. 3-114. The hysteresis loops indicate relatively high ductility and good energy dissipation. The envelope of the force-displacement of the entire test is shown in Fig. 3-115. The primary movement of the bent was in the positive displacement direction (south). The idealized bilinear curve for the bent was determined based on the maximum of the envelopes following the procedure explained for BPSA in section 3.2.4. The first yield occurred in the longitudinal bars of the CIP column at the displacement of 0.60-in [15-mm]. The displacement ductility of the bent was 7.0 based on the elastoplastic idealization of the envelope.

3.3.4.2 Lateral Force-Displacements Relationship for Individual Columns

The slippage of the rebar-pin was subtracted from the bent displacement to calculate displacement of the columns. The slippages of the rebar-pins were estimated using the

procedure explained in section 3.3.10.1. Moreover, the shear force in the columns was estimated based on equilibrium using the axial load measurement from the load cell in the cap beam.

The force-displacement hysteresis curves and the envelopes of the CIP column are presented in Fig. 3-116. The plastic hinge reached full capacity in the CIP column based on the strain data. The longitudinal bar of the CIP column in strain gage CSG 81 in Fig. 2-58 passed the measured ultimate strain during Run-6. Additionally, the core concrete failed in compression in Run-6. Using the procedure explained in previous section, the displacement ductility of the CIP column was 7.0 from the envelope of the hysteresis curves.

The force-displacement hysteresis curves and envelopes for the PC column are presented in Fig. 3-117. The plastic hinge in the PC column did not reach its ultimate capacity. The maximum measured strain in the plastic hinge was 5.80%. This strain was only 41% of the measured ultimate strain. Furthermore, the core concrete in the plastic hinge region did not fail. Therefore, the maximum displacement of the PC column was less than the ultimate capacity of the column. The achieved displacement ductility of the PC column was 6.3 from the envelope of the tests, but this was not the ductility capacity.

3.3.5 Axial Load Variation in the Columns

The overturning moments were sufficiently large to produced tensile forces in the columns. The weight of the cap beam was added to the shear data from the load cell in the cap beam to calculate the axial load in the columns. Table 3-28 summarizes the maximum tensile and compressive axial forces in the columns for each run. The columns underwent a maximum compression of 46.9 kip [209 kN] and tension of 37.9 kip [169 kN]. Note that, in a real bent the tensile axial forces would be lower because of the gravity forces that were not simulated.

3.3.6 Dissipated Energy

The dissipated energy was calculated by integrating the area enclosed by the force-displacement curves. Figure 3-118 shows the accumulated dissipated energy and the energy dissipated during each run. The major mechanisms of the dissipating energy included the plastic hinging at the top of the columns, the plastic hinging of the rebar-pins, and the shear-slippage of the rebar pins. The plastic deformations in the columns and rebar-pins dissipated most of the energy. The slippage of the rebar-pins accounted for approximately three percent of the total dissipated energy.

3.3.7 Measured Strains

Strains were measured on the longitudinal and transverse bars in the columns, the pedestals, the rebar-pins, and the cap beam. As explained in section 3.2.7, it was assumed in this study that the measured strains are reliable in the range of plus/minus 20% with the resolution of 0.02%. Figures 2-53 to 2-59 show strain gage instrumentation configuration. The reliable part of the data is shown in the strain profiles (Figs. 3-119 to 3-129). Strains are presented in percentage with a positive sign indicating tension. Additionally, the strains larger than the measured yield strain are shown in bold in the Tables.

3.3.7.1 Column Longitudinal Reinforcement in Plastic Hinge Region

The northern- and southern-most longitudinal bars were instrumented at three levels in the plastic hinge zones of the columns. The reinforcing bars underwent strains substantially larger than the measured yield strain. This verifies the full formation of the plastic hinges at the top of the columns.

3.3.7.1.1 CIP Column

Table 3-29 presents the maximum and minimum strains in the longitudinal bars in the plastic hinge of the CIP column, and Fig. 3-119 shows the strain profile of the longitudinal bars. The measured yield strain of 0.23% was reached first at the north side during Run-2 recorded in CSG-81 and CSG-82 within 0.01 second. All the instrumented bars underwent strains greater than 40 times the measured yield strain during Run-6. The maximum tensile strain was 10.83% and was registered in the southern-most longitudinal bar recorded in CSG-79. That was 48 times the measured yield strain and 77% of the measured ultimate strain of 14%.

Large compressive strains were noted in the longitudinal bars at the north side in Run-4 to Run-6. The cover concrete started spalling during Run-4. The compressive force of the section was carried by core concrete and reinforcing bars. The large compressive force and the lack of concrete support led to buckling of the longitudinal bars during the last run.

3.3.7.1.2 PC Column

Table 3-30 presents the maximum and minimum strains in the longitudinal bars in the plastic hinge region of the PC column. Figure 3-120 shows the strain profile of the longitudinal bars. The measured yield strain of 0.23% was reached first at the north side in Run-2 recorded in CSG-A81 and CSG-A82. The maximum strain was 5.80% occurred in the southern-most bar recorded in CSG-A73 in Run-5. This strain was 25 times the measured yield strain and 48% of the measured ultimate strain of 12%. As opposed to the CIP column, the compressive strains in the longitudinal bars were small because ECC cover did not spall.

3.3.7.2 Column Transverse Reinforcement in Plastic Hinge Region

The transverse bars in the plastic hinges of the columns were instrumented at the east and west sides as shown in Figs. 2-58 and 2-59. Tables 3-31 and 3-32 present the maximum and minimum strains in the spirals in the plastic hinges of the CIP and PC column, respectively. Figure 3-121 shows the profile of average tensile strain in the spirals. The data indicates that none of the spirals reached the measured yield strain of 0.23%. The maximum tensile strain of 0.07% was reached in CSG-77 in Run-6 for the CIP column, which is 31% of the measured yield strain. In the PC column, the maximum strain of 0.03% was reached in CSG-A77 in Run-5, which is 13% of the measured yield strain.

The strains in the transverse bars of the CIP column were larger compared to the PC column spiral strains despite the almost similar shear in the columns. Because the ECC segment of the PC column did not spalled, the spiral carried a smaller portion of the shear in the PC column compared to the CIP column.

3.3.7.3 Rebar-Pin Longitudinal Reinforcement

Yielding of the longitudinal bars in the rebar-pin connections was necessary to accommodate the rotation at the bottom of the columns. To avoid failure at the hinges, the strains in the

longitudinal bars were required to remain safely less than the ultimate strain. The longitudinal bars in the rebar-pins were instrumented according to Figs. 2-56 and 2-57. Tables 3-33 and 3-34 present the maximum and minimum strains of the longitudinal bars in the CIP and PC rebar-pins, respectively. Figures 3-122 to 3-125 show the strain profile in the longitudinal bars. The horizontal axis indicates the column-pedestal interface in each figure.

The measured yield strain of 0.23% was reached first in the southern-most bar of the CIP rebar-pin recorded in PSG-27 in Run-2. That followed by the yield of the northern-most bar recorded in PSG-A29 in the PC column also in Run-2. The maximum tensile strains were respectively 5.676% and 6.568% in the CIP and the PC rebar-pins, which are 25 and 28 times the measured yield strain. The maximum strains were 52% and 60% of the measured ultimate strain of 11% in the CIP and PC rebar-pin, respectively.

After yielding initiated, the longitudinal bars strains did not increase significantly in the two deeper sections that were 7 in [178 mm] inside the columns and the pedestals. Meanwhile, the strains closer to the intersection increased in successive tests. This showed that the longitudinal bars were sufficiently anchored and there was no de-bonding.

3.3.7.4 Column and Pedestal Longitudinal Reinforcement at Rebar-Pin

The longitudinal bars of the columns and pedestals were instrumented near the rebar-pins to investigate the force transfer mechanism from the reinforcement of the rebar-pins to the reinforcement of the columns and the pedestals. Tables 3-35 and 3-36 present the maximum and minimum strains in the longitudinal bars of the columns and pedestals near the rebar-pins. Figures 3-126 and 3-127 show the strain profile in the longitudinal bars. The strains in the reinforcement were well below the measured yield strain of 0.23% in the columns and pedestals. The maximum tensile strains were respectively 0.093% and 0.132% in the CIP and PC side, which are 40% and 57% of the measured yield strains.

The strain profiles show strains increased in the columns away from the rebar-pins (Figs. 3-126 and 3-127). However, the column moments were largest at the intersections based on the equilibrium. This suggests that struts were formed in the lower part of the columns to transfer tensile forces from the rebar-pin bars to the column reinforcement.

3.3.7.5 Rebar-Pins Transverse Reinforcement

The spirals in the rebar-pins, columns, and pedestals were instrumented near the column-pedestal intersections according to Figs. 2-55 to 2-59. Tables 3-37 to 3-38 present the maximum and minimum strains in the rebar-pin spirals. Recall that positive strains indicate tension. The strains in the spirals in the rebar-pins were insignificant with maximum tensile strain of 0.01 and 0.05% in the CIP and PC rebar-pin, respectively, which are 4 and 22% of the measured yield strain. The strain profile is not presented because most of data were smaller than the resolution.

The strains were small in spirals because no cracks were extended to the instrumented sections in the cores. Strains could be larger in the hinge throats in which flexural and shear cracks were observed. However, no data was obtained for that section because the spirals were not instrumented in the section.

3.3.7.6 Columns and Pedestals Transverse Reinforcement near Rebar-Pins

Tables 3-39 and 3-40 present the maximum and minimum strains in the spirals of the columns and the pedestals near the column-pedestal intersections. Figure 3-128 and 3-129 show the profile of the average maximum strains. The maximum strains in the transvers bars were 0.15% and 0.11% in the CIP and PC rebar-pin, which are 67% and 49% of the measured yield strain, respectively.

3.3.7.7 Cap Beam Reinforcement Strains

The maximum and minimum strains in the reinforcement of the cap beam are presented in Table 3-41. The strain data were well below the yield strain of 0.25%. The maximum of strain was 0.03% in the longitudinal bars, which is 12% of the yield strain indicating that the cap beam was indeed capacity protected with no yielding as intended. The post-tensioning forces produced an average stress of 530 psi [3.86 MPa] on the cap beam cross section and reduced the steel tensile strains by approximately 0.012%.

3.3.8 Strain Rate

The significance of strain rate was explained in section 3.2.9. Strain rate was determined for the longitudinal bars in the plastic hinge regions, the longitudinal bars in the rebar-pins, and the concrete in the plastic hinge regions of the columns. Similar to BPSA, average of strain rates were calculated for the strains in the range of one-half of the yield strain to yield strain in tension prior to yielding. Figures 3-130 and 3-131 show the average strain rate versus the average strain in the plastic hinge region and the rebar-pin, respectively. The mean average strain rates in each region was selected to modify the properties of the reinforcement steels, which were 1.33 $\%.s^{-1}$ and 1.31 $\%.s^{-1}$ for the longitudinal bars in the plastic hinge zones and the rebar-pins, respectively.

The strain rate of concrete in the plastic hinge zones was calculated around the failure strain of the unconfined concrete prior to yielding of compressive steel for the compressive strains in the range of 0.15 to 0.25%. However, the sample size was not sufficiently large to satisfy both conditions. Therefore, the rate was estimated considering also the points beyond yielding. The strain rates of concrete in the plastic hinge regions of the columns are presented in Fig. 3-132. The average strain rate for concrete in the plastic hinge was 1.23 $\%.s^{-1}$.

3.3.9 Measured Curvatures in Column Plastic Hinges

The rotations and curvatures of the column in the plastic hinge region were estimated using a method similar to that for BPSA as explained in section 3.2.10. Figure 3-133 shows the profile of the maximum and minimum rotation at the top of the columns. The profiles of the average curvature are shown in Fig. 3-134. The positive rotation and curvature in these figures correspond to positive displacements of the bent. The data were unreliable in the CIP column after Run-4 because the connection of displacement potentiometers was damaged during Run-4.

3.3.10 Rebar-Pin Force-Displacement Relationship

The displacements of the rebar-pin were measured using four displacement potentiometer as illustrated in Fig. 2-52. The slippage, rotation, and uplift were calculated using Eq. 3-15 to 3-20. The rotation of the CIP rebar-pin was not available after Run-5 because the instrumentations were damaged by the pieces of concrete that dropped from the top plastic hinge during Run-5.

Therefore, the rotations and uplifts were not measured. Equation 3-22 was used Instead of Eq. 3-18 to estimate the slippage subsequent to Run-4.

$$s_{pin} = s_B \tag{3-22}$$

3.3.10.1 Rebar-Pin Shear-Slip

Figures 3-135 and 3-136 show the hysteresis curves of the shear and slippage in the rebar-pins for each run. Table 3-42 presents the maximum and minimum shear and slippage in the rebar-pins. The shear behavior of the rebar-pin was linear elastic until Run-2. The section started to slide once the rebar-pin longitudinal bars yielded. The cyclic load reduced the aggregate interlock in the section due to the failure of the matrix and widening of the cracks. The hinging action caused the horizontal cracks become wider in successive runs, thus further softening of the rebar-pin. In each cycle, the section slipped until the moment was sufficiently large in the reduced section to close the cracks and produce sufficient friction to resist further slippage. The rebar-pin shear resistance did not deteriorate significantly even after undergoing a considerable number of the large cyclic deformations.

3.3.10.2 Rebar-Pin Moment-Rotation

The moments at the bottom of the columns were calculated using equilibrium and data from the load cell in the cap beam. Figures 3-137 and 3-138 show the hysteresis curves of the moment versus rotation in the rebar-pins. Table 3-43 shows the maximum and minimum moments and rotations. The moments under large rotations are not accurate because the moments measured in the cap beam load cell were saturated. The moment capacity of the rebar-pins did not deteriorate throughout the tests.

3.3.10.3 Rebar-Pin Vertical Force-Uplift

Table 3-43 shows the maximum and minimum uplift in the rebar-pins. The maximum uplift was 0.3 in [8 mm] in the PC rebar-pin during Run-4. Comparison of the column axial force and uplift in the rebar-pin showed there were negligible deformations in the section due to the column axial forces. However, comparing rotations of the rebar-pin to the uplift showed uplift increased with the increase of the rotation (Fig. 3-139). Larger rotations caused the horizontal crack to open wider. Consequently, the slippage of the section increased due to the wider crack.

3.3.11 Evaluation of the Bent with Rebar-Pin

BRSA performed as it was designed. Full plastic hinge capacity was reached at the top of the column while the rebar-pins did not fail. The rebar-pins underwent large plastic deformations under many cycles of earthquake loading without loss of capacity. The strains in the longitudinal reinforcement were safely under the ultimate strain. Despite the fact that the rebar-pin slipped horizontally, the shear friction was sufficient to resist the shear without gravitational axial load on the columns. The gap around the rebar-pin did not close in spite of the large rotations. The columns and pedestals did not yield near the rebar-pins but the rebar-pins and the surrounding concrete were damaged.

The pocket connections of the columns to the cap beam performed as they were designed. The plastic hinges in the columns reached their rotation capacity while the reinforcement in the cap beam remained elastic. No damage was observed in the cap beam. Moreover, the PC column with ECC showed significantly less damage than the CIP plastic hinge zone with conventional concrete.

3.4 Comparison of BPSA and BRSA

The main purpose of using pins at the bottom of the columns is to reduce the size of the pile-shafts by reducing the moment transferred from the bent. The bent is designed to fail in the plastic hinge in the columns rather than the pins. The two models were similar in dimensions and reinforcement except the transverse reinforcement of the columns and the type of column to pile-shaft connection. As explained in Chapter 2, it was assumed that pipe-pins produce negligible moments while rebar-pins produce up to 50 percent of the column moment capacity. Therefore, larger transverse reinforcement ratio was required in the columns of BRSA than those of BPSA. In this section, the performance of the two bent are compared.

3.4.1 Force-Displacement of the Bents

The force-displacements of the bents were a function of the plastic hinge action at the top of the columns and the pin action at the bottom of the columns. The two actions are discussed separately in the next sections. Figure 3-140 compares the force-displacement envelopes of the two bents. As explained in section 3.2.4, the initial stiffness of BPSA was reduced unrealistically because of the slippage of the load cell within the cap beam. Therefore, the performance is compared for drift ratios larger than 2%.

The maximum base shear in the bents were 52.3 [233] and 58.2 kip [259 kN] in BPSA and BRSA, respectively. The maximum bent drift ratios were 7.48% and 8.63% in BPSA and BRSA, respectively. As a result, the base shear and bent displacements of BRSA were respectively 11% and 15% larger than BPSA.

It cannot be concluded that the pipe-pin produce smaller moments than the rebar-pin because the pipe-pins underwent smaller rotations than the rebar-pins. The BPSA force envelopes show significant hardening under drift ratios exceeding 3%. As mentioned in section 3.2.11.2, pipe-pin moments were mobilized at that drift and higher. To compare the pin moments for similar bent displacement, the rising part of the envelope was extrapolated, which is depicted in Fig. 3-140 with a dashed line. That shows that, if the bent underwent similar drifts, the base shear would have been the same under larger drifts. Therefore, both pins can produce almost comparable moments under large drifts while pipe-pins produce significantly smaller moment under smaller drifts.

3.4.2 Plasticity of Columns

The longitudinal bars in the plastic hinges of both models were identical. In both bents, the plastic hinge in one column was cast with ECC while the other with conventional concrete. The average measured concrete strengths in the CIP column and the precast shell of the PC column were close (8030 [55.4] and 7640 psi [52.7 MPa] for BPSA and BRSA, respectively). The confining stresses based on Mander's model were respectively 245 [1.69] and 528 psi [3.64 MPa] in the columns of BPSA and BRSA. The column design shear in BPSA was smaller because

the pipe-pin moments were assumed negligible. Conversely, BRSA was designed for a large moment at the rebar-pins.

The plastic hinges in BPSA reached their capacities due to failure of the core concrete in compression with no longitudinal bar fracture. The longitudinal bars buckled and spirals ruptured in the last run. The maximum tensile strain was at least 34 times the measured yield strain. Recall the strain data in the upper-most sections was unavailable. The plastic hinges in BRSA reached their capacities due to failure of the concrete core and longitudinal bar rupture. The maximum tensile strain was 48 times the measured yield strain. The differences between the failure modes of the bents were due to transverse reinforcement. The test results indicated the larger moments in the rebar-pin increased the overall base shear in BRSA compared to BPSA but did not affect the plastic hinging of the columns.

The ECC plastic hinges did not show extensive damages in either bent. The damage was concentrated at two cracks in the plastic hinges. In addition to a crack at the column-cap beam joints, the principal crack in the plastic hinge zone became wider as the plastic hinge underwent larger rotations. Because of the crack concentration, the strain and curvature were larger in the upper portion of the columns with ECC than that with conventional concrete. The length of the ECC segment in the columns was sufficiently large to prevent shifting of damage to concrete segment below ECC.

3.4.3 Performance of the Pins

The rebar-pins and pipe-pins successfully transferred the forces to the pile-shafts. However, the damage was more intense in the rebar-pin than the pipe-pins. The cracks in the pipe-pins and the adjacent components were less extensive. No yielding was observed in the pipes or the reinforcement in the columns and pedestals near the pipe-pins. The pipe moments reached close to the yield moment while the shear strains were well below the yield shear. Conversely, the rebar-pins underwent extensive damage, but the load carrying capacity did not drop. Cracks were formed on the rebar-pins and the components near the rebar-pins. The longitudinal bars in the rebar-pins started yielding under relatively small drifts. The maximum strains were 28 times the measured yield strain. This led to large residual rotations and slippage at the end of the tests. The reinforcement did not yield in the columns and pedestals near the rebar-pins.

3.4.4 Performance of the Cap Beam Pocket Connections

The pocket connections performed as they were designed. Plastic hinges reached their full capacities without any damages in the pocket connection. The strains in the cap beam reinforcement were small because of the post-tensioning forces. The maximum strain prior to the post-tensioning was 0.098% in the longitudinal bars of BPSA. Subsequent to the repair and post-tensioning, the maximum strain was 0.058%. The maximum strain in BRSA was 0.03% despite the smaller post-tensioning force in the section and the larger base shear. Because the cap beam was intact in BRSA, the loss of the post-tensioning force was smaller in BRSA than BPSA. The test results did not indicate any influence of the type of the column base pin on the cap beam and pocket connections response.

4 Numerical Simulations of Experiments

4.1 Introduction

Analytical studies of the test models were performed to validate the modeling assumptions based on the correlation between the analytical and experimental results. Three sets of analytical studies were conducted: pushover analysis using a simple-stick model, pushover analysis using a distributed plasticity model, and dynamic analysis of the shake-table tests. OpenSEES (version 2.4.3) was used to perform moment-curvature, dynamic, and pushover analyses. OpenSEES, Open System for Earthquake Engineering Simulation, is a software framework for simulating the seismic response of structural and geotechnical systems. This software utilizes advanced capabilities for modeling and analyzing the nonlinear response of systems using a wide range of material models, elements, and solution algorithms. Additionally, the pushover analysis of BPSA was simulated in ABAQUS/Explicit (version 6.14-1). ABAQUS/Explicit is a special-purpose analysis product that uses an explicit dynamic finite element formulation. It employs explicit integration schemes to solve highly nonlinear systems with many complex contacts. In this chapter, the analytical modeling methods and results are presented. Finally, the validity of the analytical results is discussed based on their correlation with the measured data.

4.2 Definitions

The naming convention in this chapter is similar to that of the previous chapters. The north column in each bent was prefabricated (the right columns in Fig. 3-14 and 3-88). The components on the north side of the bent are referred to as PC (precast) components such as PC pedestal, PC pipe-pin, PC column, etc. hereafter. The south column of each bent was cast-in-place (CIP) (the left columns in Fig. 3-14 and 3-88). The components on the south side of the bent are referred to as CIP components such as CIP pedestal, CIP rebar-pin, CIP column, etc. hereafter.

The global coordinate system is defined in the plane of the bent. The X-axis is the horizontal axis with southward positive direction. The Y-axis is vertical with upward positive direction. Consequently, the positive rotation is defined by the right-hand rule, which is clockwise in the figures.

To validate the numerical methods, the difference between the analytical and the experimental results were monitored. That difference, which is also called error, was determined using the following equation.

$$Err = \frac{calculated - measured}{measured} \tag{4-1}$$

where

Err: error or difference of calculated variable, ratio or percent

$calculated$: calculated value from numerical modeling

$measured$: measured value from experimental studies

4.3 Mass Rig Effects on Structural Model

The elevation view of the test setup is illustrated in Fig. 4-1. The bent was fixed to the shake table. The mass rig provided the inertia force. Restraining cables are installed in the mass rig to prevent the collapse of the specimen. In case the model loses significant lateral stiffness, the restraining cables provide lateral resistance to enhance safety. The structural model of the test with the mass rig is shown in Fig. 4-2a. The numerical model was consolidated to a bent based on the Laplace et al. (1999) model, as shown in Fig. 4-2b. Because the stiffness and damping of the mass rig were negligible, the geometry of the mass rig was not required to simulate the tests accurately.

Due to the large stiffness of the link, the absolute horizontal displacement of the mass rig was equal to that of the cap beam. Therefore, the effective mass of the mass rig was added to the mass of the cap beam and one-half of the column masses to calculate the inertia forces. The effective mass of the mass rig was 0.259 kip.s^2/in [45359 kg], which corresponds to an effective weight of 100 kip [113 kN] (Laplace, et al., 1999).

In addition to the inertia force, the effective weight of the mass rig creates overturning moments at the base due to its displacement (Fig. 4-3). These moments produce "second-order" displacements in the bent, which is known as the P-Delta effect. The lateral force caused by the P-Delta effect is calculated using following equations based on static equilibrium.

$$\text{Mass rig free-body diagram: } W\ D_{cap\ beam} + V_{p\Delta}\ H_{mass} = 0 \tag{4-2}$$

$$V_{P\Delta} = -\frac{W}{H_{mass}} D_{cap\ beam} \tag{4-3}$$

Assuming,

$$D_{cap\ beam} \cong d_{specimen} \tag{4-4}$$

$$V_{P\Delta} = -\frac{W}{H_{mass}}\ d_{specimen} \tag{4-5}$$

$$K_{\mathrm{P}\Delta} = -\frac{W}{H_{mass}} \tag{4-6}$$

where,

$D_{cap\ beam}$: absolute displacement of the cap beam, in [mm]

H_{mass}: height of the link from the mass rig base, 183 in [4648 mm]

W: mass rig effective weight, 100 kip [113 kN]

$V_{P\Delta}$: additional lateral force caused by P-Delta effect, kip [kN]

$d_{specimen}$: relative displacement of the cap beam to the shake table, in [mm]

$K_{P\Delta}$: equivalent P-Delta spring stiffness, kip/in [kN/mm]

Thus, a spring with stiffness of –0.546 kip/in [-95.7E-3 kN/mm] was added to the CIP column node to account for the P-Delta effect. To simplify the analytical studies, it was desirable to assume that the absolute and relative displacements of the cap beam are the same. The P-Delta effect was related to the cap beam displacement relative to the shake table. Therefore, the P-

Delta force was included in the numerical models without modeling the geometry of the mass rig. However, this assumption had to be checked. Using the measured absolute and relative displacements, the errors in the estimation of the P-Delta effect were determined from the following relation.

$$Er_{P\Delta} = \frac{V_{P\Delta} - (V_{P\Delta})_{estimate}}{Vb_{max}} = \frac{D_{cap\ beam} \times K_{P\Delta} - d_{specimen} \times K_{P\Delta}}{Vb_{max}} \quad (4\text{-}7)$$

where,

$Er_{P\Delta}$: error ratio in P-Delta force estimation

$V_{P\Delta}$: lateral force using Eq. (4-3), kip [kN]

$(V_{P\Delta})_{estimate}$: estimated lateral force using Eq. (4-5), kip [kN]

Vb_{max}: maximum measured lateral force, kip [kN]

For BRSA, those errors are shown versus the displacement in Fig. 4-4. The maximum force error was respectively 1.92 kip [8.54 kN] and 2.53 [11.3 kN] in BPSA and BRSA, which are 5% and 3% of the maximum base shears. Considering the approximations in the nonlinear finite element modeling, the error was acceptable.

4.4 Plasticity Models for Column Plastic Hinges

As explained in Chapter 3, the columns underwent large plastic deformations during the tests due to yielding of reinforcement, spalling of concrete, strain penetration, and shear deformation. The plastic deformations were limited to the upper parts of the columns because of the pin connections at the bottom. Lumped and distributed plasticity modeling techniques were used to simulate the plastic deformations in the columns. A simple lumped plasticity model was utilized to simulate the plastic hinge responses of the columns. Because of its simplicity, the model was suitable for the analyses of the simple stick models implementing in a spreadsheet or “hand” calculation. The lumped plasticity model was also used in the FE analysis of BPSA using ABAQUS to reduce the size of the problem. Distributed plasticity models were used in the response history dynamic nonlinear analyses utilizing OpenSEES. The material and element constitutive relationships that were used in the distributed plasticity model are capable of modeling the hysteretic response of the plastic hinge with more details than the lumped plasticity model.

4.4.1 Lumped Plasticity Models of Columns

The lumped plasticity models were used in the pushover analyses to simulate the force-displacement relationship of the test models. A rotational spring added to the top of the column accounted for deformations due to the bond-slip and yielding of the reinforcement. The columns were modeled as elastic elements with cracked stiffness of the sections. The properties of the rotational springs were determined using the yield and ultimate points in a bilinear spring from the moment-curvature data. The columns were sufficiently slender to neglect their shear deformation.

The yield displacement of the model was composed of flexural and bond-slip displacements (Fig. 4-5). The flexural displacement was calculated assuming the Euler-Bernoulli beam theory using the cracked sectional stiffness (AASHTO, 2010). Additionally, the bond-slip displacement was

calculated based on the Wehbe (1999) model, which is explained in section 4.6.1. Therefore, the yield displacement was calculated from the following relations.

$$\Delta_{y.column} = \Delta_{y.flex} + \theta_{y.bond} \times h_c \quad (4\text{-}8)$$

$$\Delta_{y.flex} = \frac{1}{3}\, \phi_y\, h_c^2 \quad (4\text{-}9)$$

where,

$\Delta_{y.column}$: column displacement at yield, in [mm]

$\Delta_{y.flex}$: displacement due to elastic deformation, in [mm]

ϕ_y: yield curvature from moment-curvature analysis, in^{-1} [mm^{-1}]

h_c: column clear height, in [mm]

$\theta_{y.bond}$: bond-slip rotation at yield (section 4.6.1), rad

The ultimate displacement was calculated assuming that plastic curvature occurs over an empirical plastic hinge length. The bond-slip and shear deformations were included over that length. The plastic displacement was added to the flexural yield displacement to calculate the ultimate displacement (Fig. 4-5c).

$$\Delta_u = \Delta_{y.flex} + \Delta_p \quad (4\text{-}10)$$

$$\Delta_p = \theta_p \times (h_c - \frac{L_p}{2}) \quad (4\text{-}11)$$

$$\theta_p = \left(\phi_u - \phi_y\right) L_p \quad (4\text{-}12)$$

where,

Δ_u: ultimate displacement, in [mm]

Δ_p: displacement due to plastic deformation, in [mm]

θ_p: plastic rotation of the column, rad

ϕ_u: ultimate displacement from moment-curvature analysis, in^{-1} [mm^{-1}]

L_p: empirical plastic hinge length, in [mm]

The plastic hinge length was estimated using the Paulay and Priestly (1992) method:

$$\begin{aligned} L_P &= 0.08l + 0.15 d_b\, f_y\ (ksi) \\ &= 0.08l + 0.022\ (MPa) \end{aligned} \quad (4\text{-}13)$$

where,

l: height of the column, in [mm]

f_y: longitudinal bars yield strength, ksi [MPa]

d_b: diameter of longitudinal bars, in [mm]

4.4.2 Distributed Plasticity Models of Columns

The columns were modeled with distributed plasticity elements in the dynamic and pushover analyses using OpenSEES. Two formulations of beam-column elements were suitable for modeling the columns: force-based (FB) and displacement-based (DB) elements. An FB beam-column element was used to model the columns and pedestals. The FB elements use force interpolation functions for the bending moment variation in the flexibility-based formulation (Neuenhofer and Filippou, 1996; Neuenhofer and Filippou, 1998). Curvature distribution along the FB elements is a polynomial curve passing through the integration points while it is linear in the DB elements. Therefore, fewer FB elements are needed to achieve comparable accuracy to that from DB elements.

The formulation of FB elements is based on the principle of virtual force. As shown in Fig. 4-6, the moment distribution is assumed linear along the length of the element. The moment is known from static equilibrium at each integration point along the length. At each point, the curvature is estimated based on the sectional properties. Using numerical methods, the curvatures are integrated twice to calculate the displacement. Those displacements need to be in equilibrium with the external displacements, which is achieved by the Newton iterative method (Neuenhofer and Filippou, 1997; 1998).

Three methods were selected to add the effect of strain-penetration to the distributed plasticity models: Wehbe (1999), Zhao (2007), and Tazarv (2014). The Wehbe (1999) and Zhao (2007) methods require adding a zero-length element (rotational spring) at the joint (Wehbe, et al., 1999; Zhao and Sritharan, 2007). Whereas, the Tazarv (2014) method uses a modified steel stress-strain relationship in the FB element to account for the bond-slip effect (Tazarv and Saiidi, 2014). The models with Tazarv and Saiidi bond-slip method performed faster and was more stable while requiring fewer elements. Therefore, Tazarv (2014) method was used to model the bond-slip behavior in the distributed plasticity model.

4.5 Moment-Curvature Analysis

Moment-curvature analysis, also referred to as section analysis, was required to obtain the properties of the lumped plasticity models. The moment-curvature analysis was performed using an OpenSEES code. The code was modified from an example of the program manual (Mazzoni, et al., 2009). A zero-length element with a fiber section was analyzed under constant axial load while curvature was increased linearly up to a predefined value. The program calculates the moment corresponding to the curvature assuming a linear strain distribution in the section based on the Euler-Bernoulli beam theory. The moments, curvatures, strains, and stresses were recorded in each analytical step.

The general sources of the nonlinearity are stress-strain relations of the materials. Those relations were determined based on the material test data. The fibers of the longitudinal reinforcement were modeled with “steel02”, which is the Giuffre-Menegotto-Pinto steel model (Fig. 4-7a) (Mazzoni, et al., 2009). Furthermore, the core and cover concrete fibers were modeled with “concrete04” based on their respective compressive strengths (Fig. 4-7b). Additionally, the properties of the concrete were modified to reflect the confinement effects based on the Mander (1988) confinement model (Mander, et al., 1988). This model was used for concrete, ECC, and SCC.

From the analysis result, the moment-curvature behavior was idealized by a bilinear curve with four parameters: yield curvature, yield moment, ultimate curvature, and ultimate moment. The ultimate point was determined by the curvature at which the strain of the core concrete reached the confined concrete failure or the steel bars reached the ultimate strain. The initial stiffness of the bilinear curve was equal to the secant tangent at initial yielding, which is the curvature in which the outermost bar reached yield strain. Then, the yield point was determined by preserving energy in both curves.

Because of the overturning moment, the axial forces of columns change with lateral displacements. The moment-curvature analyses were performed under the axial forces corresponding to the ultimate base shear. Therefore, the ultimate base shear and axial force had to be determined iteratively. For the initial trial, the moment-curvature analysis was performed with the dead load on the column sections. Assuming the ultimate moments occur simultaneously at the plastic hinges, the base shear was estimated. Next, the axial forces were updated based on the new base shear using static equilibrium. This iteration was continued until the updated base shear was within 5% of the previously determined base shear. The convergence was achieved only with a few iterations.

4.6 Bond-Slip Models

Deformations of the longitudinal bars in the joints cause additional rotation at the beam-column intersection as shown in the rotation profiles in Fig. 3-72 and 3-133. That is known as strain penetration effect and the rotation is called bond-slip rotation. As an example, Fig. 4-8 shows the bond-slip rotation of the plastic hinge in the southern column of BRSA at the instance at which the largest displacement occurred during Run-5. While concrete deforms minimally in the joint, the reinforcing bars deform in tension. Because the tensile forces transfer through a development length, the bars elongate in the joints (Fig. 4-9). The elongations of the bars widen the crack at the intersection generating a rotation in the connection. In this document, two methods were used to account for the bond-slip rotation: the Wehbe (1999) and Tazarv (2014) model.

4.6.1 Wehbe (1999) Bond-Slip Model

Wehbe et al. developed a model to estimate joint rotation of beam-columns with fully anchored bars (Wehbe, et al., 1999). The bond-slip behavior was modeled using a rotational spring at the interface assuming that the bond-slip rotation, θ_{bond}, occurs about the neutral axis of the column section (Fig. 4-9).

$$\theta_{bond} = \frac{\delta l}{d - C_{N.A}} \tag{4-14}$$

where,

θ_{bond}: bond-slip rotation, rad

δl: bar extension at the outermost bar from Eq.(4-15), in [mm]

$C_{N.A}$: neutral axis depth at yield point, in [mm]

d: distance of the extreme bar in tension to the extreme compressive bar, in [mm]

The bar extension was calculated by integrating the theoretical strain profile along the embedded bar length inside the joint. Assuming that the bond strength was uniform along the development length, the bar extension at the outermost bar is calculated from the following relation.

$$\delta l = \frac{d_b}{8u}\left(\varepsilon_s \times f_s - \varepsilon_s \times f_y + \varepsilon_y \times f_s\right) \tag{4-15}$$

where,

d_b: longitudinal bar diameter, in [mm]

ε_s: strain in the reinforcing bar, in/in

f_s: stress in the reinforcing bar, ksi [MPa]

f_y: reinforcing bar yield stress, ksi [MPa]

u: bond strength, ksi [MPa]

The bar stress, strain, and neutral axis depth were determined from the moment-curvature analysis of the section. The basic bond strength for bars smaller than No. 11 [ϕ 35-mm] was calculated from the following equation.

$$u = 9.5\frac{\sqrt{f_c'}}{d_b} \leq 800\ psi\ (\text{US customary}) \tag{4-16}$$
$$= \quad 20\frac{\sqrt{f_c'}}{d_b} \leq\ 5.5\ MPa\ (\text{SI})$$

where,

f_c': measured concrete strength of the joint, psi [MPa]

4.6.2 Tazarv (2014) Bond-Slip Model

The Tazarv (2014) bond-slip model is a simple method to account for bond slip in the distributed plasticity model by assigning a modified stress-strain relationship to the reinforcing bars (Tazarv and Saiidi, 2014). The effective strain of the bar at the joint intersection is estimated by adding the bar strain and bond deformations, as follows.

$$\varepsilon_s' = \varepsilon_s + \frac{F}{k_b\, L} \tag{4-17}$$

$$k_b = 78.5\, d_b\, L_{emd}\, u \tag{4-18}$$

where,

ε_s': modified bar strain, in/in

ε_s: bar strain, in/in

F: bar force, kip [kN]

k_b: bond force-slip stiffness, kip/in [kN/mm]

L: effective development length, in [mm]

d_b: bar diameter, in [mm]

L_{emd}: embedment length of the bar in the joint, in [mm]

u: bond strength from Eq. (4-16)

The effective development length, L, is the length along which the force of the bar is transferred to the concrete and is calculated from the following.

$$L = \frac{F}{\pi\, d_b\, u} = \frac{f_s\, d_b}{4u} \leq L_{emd} \tag{4-19}$$

where,

f_s: stress in bar, ksi [MPa]

The modified stress-strain relationship of the reinforcing bars is softer than the original to account for the bond-slip effect. The softer material properties were used in the reinforcing bars of the sections that were assigned to the integration point at the end of the column.

4.7 Strain-Rate Effect

The strain rates of the reinforcing bars were determined in Chapter 3. The Zadeh and Saiidi (2007) model for strain-rate effect was used to amplify the yield and ultimate stresses of the reinforcing bars. Table 4-1 presents the amplification factors for the reinforcing bars. The properties of the longitudinal bars of the columns were modified to reflect the strain rate effect. In addition, the properties of the longitudinal reinforcement of the rebar-pins in BRSA were modified. The measured stress-strain relations were used for other reinforcement.

As explained in the previous chapter, concrete strain and strain rate were estimated assuming that longitudinal bars had perfect bond with concrete. The assumption of perfect bond between concrete and bars is proper prior to yielding. However, the sample sizes were not sufficiently large for both specimens to estimate strain rate satisfying that condition. Therefore, the stress-strain relationships of the concrete were not modified.

4.8 Bent with Pipe-Pin Column-Pile Shaft Connection for ABC (BPSA)

4.8.1 Introduction

The connections of the columns to the pedestals in this model were pipe-pins. As explained in Chapter 3, plastic hinging was observed in the columns while the pipe-pins remained elastic. Eventually, the plastic hinge in the CIP column reached its capacity and failed. This mode of failure is expected for the bents with pipe-pins connections that were designed based on the

recommendations of this document. Therefore, the numerical model included inelastic deformations in the columns while treating pipe-pins as elastic components.

First, the properties of the elastic spring models of the connections were determined based on the geometry and mechanical properties of the pipe-pins. In section 4.8.4, the force-displacement relationship of the bent was determined using the pipe-pin springs and the lumped plastic hinges in the columns. That model was sufficiently simple to be implemented in a spreadsheet and is referred to as the simple stick model. The pipe-pin spring model was utilized to simulate the dynamic response of the tests in section 4.8.5. In section 4.8.6, the force-displacement relationship was calculated using ABAQUS/Explicit. The quality and purpose of the numerical models are compared in section 4.8.7.

The analytical results were compared with the test data to validate the numerical models. As explained in Chapter 3, Run-3 to Run-5 were dismissed because of the malfunction of the connection of the load cell to the cap beam. Therefore, the measured force-displacement envelopes were determined using test data for Run-1, Run-2, and Run-6 to Run-11. The calculated force and displacements using the simple stick and FE models were compared with the measured envelopes. The numerical model of BPSA was analyzed subjected to the measured shake table accelerations for the runs subsequent to the repair, which are Run-6 to Run-11. The forces and displacements calculated from the dynamic analyses were compared to the test data to evaluate the numerical models.

4.8.2 Constituents Models of Elastomeric Pad

Stress-strain relationship of the elastomeric pad was assumed linear elastic in calculating the pipe-pin spring model properties. The apparent measured modulus of elasticity was adjusted to reflect that both surfaces of the samples were restrained because the sand papers resisted the slippage. The Lindley (1981) equations were used to calculate the unbonded modulus of elasticity of the elastomer from the apparent modulus of elasticity (Lindley, 1981):

$$\text{For circular sections: } E_{apparent} = 3G + \frac{6GS^2}{1 + \frac{6GS^2}{B}} \tag{4-20}$$

$$S = \frac{\text{loaded area}}{\text{force-free area}} = \frac{4D}{t} \tag{4-21}$$

where,

$E_{apparent}$: apparent compressive modulus for the bonded samples, ksi [MPa]

G: shear modulus, ksi [MPa]

B: bulk modulus, ksi [MPa]

S: shape factor

D: diameter of samples, in [mm]

The elastomers were assumed incompressible with a large bulk modulus. Thus, Eq. (4-20) reduces to the following equation.

$$E_{apparent} = 3G(1 + 2S^2) \tag{4-22}$$

$$G = \frac{E_{apparent}}{3\,(1 + 2S^2)} \tag{4-23}$$

$$E = 3G \tag{4-24}$$

E: Young's modulus of the pad, ksi [MPa]

A line was fitted to the nominal stress-strain from zero to 20% strain for each sample, and the slope of that line was used as the apparent stiffness. The data for Sample-2 was dismissed because the measured data was not comparable with the rest of the tests. The average shear modulus was 670 psi [4.62 MPa] with standard deviation of 27 psi [0.68 MPa]. Note that the effect of the cloth reinforcement in the rubber was implicitly included in the compression modulus. Under large deformations, strain-stress relations are defined using strain energy potential. This method was used in modeling of the pad in the FE analyses, which is explained in section 4.8.6.4.1.

4.8.3 Proposed Springs Model for Pipe-Pin

Based on the mechanics of solids principles, a model was developed to estimate the effects of the pipe-pins on the overall performance of the bent. The model comprises three zero-length springs, one for each degree of freedom, associated with the axial force, shear, and rotation. The major assumptions to determine the properties of those springs are:

- All the components remain elastic.
- The friction between the pad and the column is insignificant.
- The rods move freely between the pipes and did not bear against the side of the lower pipe.
- Time-dependent and rate-dependent behaviors of the rubber pad as well as the rest of the components are negligible.
- The gap between the column and pedestal does not close.

In well-designed pipe-pin connections, those criteria are satisfied by design.

The calculated forces and displacements using the proposed spring model showed close correlation to the measured data, as presented in sections 4.8.4 and 4.8.5. Note that some force transfer mechanisms were not included in determination of the properties of the springs such as moments from contact of the pipes, effects of axial load on the shear and moment, etc. Those mechanisms are simulated in the more sophisticated finite element model presented in section 4.8.6.

4.8.3.1 Pipe-Pin Axial Spring

The load transfer mechanism of the tensile forces is different from the compressive forces in pipe-pins. The tensile force is transferred to the pedestal through the rod. The compressive force is transferred by bearing of the column on the pad. Therefore, the axial stiffness in each direction was calculated based on the mechanics of solids principles, as follows.

$$\text{Tension: } K_{rod} = \frac{E_{rod} \times A_t}{L_{rod}} \tag{4-25}$$

$$\text{Compression: } K_{c,pad} = \frac{E_{pad} \times A_{pad}}{t_{pad}} \quad (4\text{-}26)$$

where,

K_{rod}: axial stiffness of the pipe-pin in tension, kip/in [kN/mm]

E_{rod}: modulus elasticity of the high-strength rod, ksi [MPa]

A_t: tensile area of the rod, in^2 [mm^2]

L_{rod}: effective length of the rod from center to center of the nuts, in [mm]

$K_{c,pad}$: axial stiffness of the pipe-pin in compression, kip/in [kN/mm]

E_{pad}: module of elasticity of rubber, ksi [MPa]

A_{pad}: area of the plan view section of the pad, in^2 [mm^2]

t_{pad}: thickness of rubber pad, in [mm]

The lateral movement of the pads was not restrained. Therefore, the unconfined modulus of elasticity of the pads was used in calculation of the compressive stiffness. The tensile and compressive stiffness of the pipe-pins were 899 [157] and 689 kip/in [121 kN/mm], respectively.

4.8.3.2 Pipe-pin Shear Spring

The shear behavior of the pipe-pins was determined under two limits with respect to the contact of the pipes. Prior to the contact of the pipes, the movements were a combinations of the slippages of the column on the pad and shear deformation of the rubber pad. Because of the small friction between the pad and concrete, the shear deformation of the pad was not significant. Thus, the shear stiffness of the pipe-pin prior to the contact of the pipes was assumed to be negligible.

Subsequent to the contact, the shear force was transferred to the pedestal through the pipes. The stiffness of the pipes was estimated assuming the protruded part of the lower pipe acting as a cantilever with the force at the top of the pipe. Therefore, the shear stiffness after the contact is:

$$K_{s,pipe} = \frac{3\, E_{pipe} \times I_{pipe}}{l_{protruded}} \quad (4\text{-}27)$$

where,

$K_{s,pipe}$: shear stiffness of the pipe-pin subsequent to the contact of pipes, kip/in [kN/mm]

E_{pipe}: module of elasticity of the lower pipe, ksi [MPa]

I_{pipe}: moment of inertia of the lower pipe, in^4 [mm^4]

$l_{protruded}$: protruded length of the lower pipe, in [mm]

The shear stiffness was 6850 kip/in [1200 kN/mm]. The relatively large stiffness indicates the shear displacement after contact was negligible. Recall that the maximum measured lateral force of the entire bent was 55.8 kip [280 kN].

The test data showed that the contact slippages were asymmetric (Fig. 3-75). However, the differences between slippage in the two directions were small. Therefore, it was assumed that the pipes were concentric. The slippage gap, s_{gap}, was estimated as one-half of the clearance between the pipes, as follows.

$$s_{gap} = \frac{OD_{lower\ pipe} - ID_{upper\ pipe}}{2} \tag{4-28}$$

where,

s_{gap}: slippage at initiation of contact of pipes, in [mm]

$OD_{lower\ pipe}$ measured outer diameters of the lower pipes, in [mm]

$ID_{upper\ pipe}$ measured inner diameters of the upper pipes, in [mm]

The slippage gaps were 0.25 in [6 mm] based on the average measured dimensions of the pipes. This shear-slippage relationship is referred to as "gap-rigid", hereafter.

4.8.3.3 Pipe-Pin Rotational Springs

Two forces produced moments in each pipe-pin: the contact force between the pipes and the column-pile shaft contact due to hinge gap closure. The former was due to the shear force in the columns. To simplify the proposed pipe-pin model, it was assumed that the shear deformation and rotation were uncoupled. More sophisticated FE analyses showed the moment due to the contact force between the pipes was a small portion of the pipe-pin moment (section 4.8.6).

The free-body diagram of a pipe-pin connection is shown in Fig. 4-10. The summation of the tensile force in the rod and the axial force in the column is equal to the compressive force on the pad. The pipe-pin moment is equal to the force couple of the tensile force in the rod and compressive force in the pad, as follows.

$$T + P = C \tag{4-29}$$

$$M = (T + P) \times a = C \times a \tag{4-30}$$

where,

T: tensile force of the rod, kip [kN]

C: contact force in the pad, kip [kN]

P: column axial force with compression being positive, kip [kN]

M: pipe-pin moment, kip.in [kN.m]

a: moment arm, in [mm]

The variables in Eq. (4-29) and (4-30) are functions of the pipe-pin rotation and contact area between the pad and column. The compatibility relationship was used to determine the forces. The extension of the rod, δ_{rod}, is the uplift due to the rotation minus the average compression of the pad.

$$\delta_{rod} = \frac{OD_{pad}}{2} \times \theta - \delta_c \quad (4\text{-}31)$$

where,

δ_{rod}: extension in the rod, in [mm]

θ: pipe-pin rotation (Fig. 4-10b), rad

OD_{pad}: outer diameter of the pad, in [mm]

δ_c: displacement of the pad at the center due to the axial deformation of the pad , in [mm]

The tensile force in the rod, T, was determined based on its stiffness.

$$\delta_{rod} = \frac{T}{K_{rod}} \quad (4\text{-}32)$$

where,

K_{rod}: tensile stiffness of the rod from Eq. (4-25), kip/in [kN/mm]

δ_{rod}: extension of the rod, in [mm]

Based on the free-body diagram of the pad and Eq. (4-29), the axial deformation of the pad was calculated from the following equation (Fig. 4-10b).

$$\delta_c = \frac{C}{K_{c.pad}} = \frac{P}{K_{c.pad}} + \frac{T}{K_{c.pad}} \quad (4\text{-}33)$$

where,

$K_{c,pad}$: compressive stiffness of the pad from Eq. (4-26), kip/in [kN/mm]

Substituting Eq. (4-32) and (4-33) in (4-31),

$$\frac{T}{K_{rod}} = \frac{OD_{pad}}{2}\theta - \frac{P}{K_{c.pad}} - \frac{T}{K_{c.pad}} \quad (4\text{-}34)$$

After rearranging the terms and substituting in Eq. (4-29), the tensile force in the rod and the compressive force in the pad were as follows.

$$T = \frac{K_{rod}}{K_{c.pad} + K_{rod}}\left(\frac{OD_{pad}}{2}K_{c.pad}\theta - P\right) \quad (4\text{-}35)$$

$$C = \frac{K_{c.pad}}{K_{c.pad} + K_{rod}}\left(\frac{OD_{pad}}{2}K_{rod}\theta + P\right) \quad (4\text{-}36)$$

Accordingly, the equation to relate the pipe-pin moment to the rotation is determined by substituting Eq. (4-35) in (4-30).

$$M = \frac{K_{c.pad}}{K_{c.pad} + K_{rod}}\left(\frac{OD_{pad}}{2}K_{rod}\theta + P\right) \times a(\theta) \quad (4\text{-}37)$$

The axial force in the rod is a linear function of the pipe-pin rotation. Consequently, the relation between moment and rotation is nonlinear because the moment arm (a in Eq. (4-37)) varies with rotation. As explained in the previous chapter, the measured hysteresis curves show that the moment in the pipe-pins was mobilized at 3% drift (section 3.2.11). The development of moment was gradual, contrarily to the abrupt translation under shear (Fig. 3-75 and 3-76). The gradual development of the moment was because of the increase of the moment arm with the rotation.

Two simplifying assumptions were made to determine the properties of the rotational springs. The first assumption was the moment arm (a in Eq. (4-37)) was equal to the outer radius of the pad at the rotation corresponding to the gap closure. The rotation at which the hinge gap closes was calculated from the following equation based on the geometry.

$$\theta_g = \frac{2\,g}{D_{col}} \tag{4-38}$$

where,

θ_g: hinge closure rotation, rad

g: vertical gap between the column and pedestal, equal to the pad thickness, in [mm]

D_{col}: diameter of the column, in [mm]

The second assumption was that the moment-rotation relationship was linear. Thus, the rotational spring was defined as a linear elastic element with stiffness equal to the secant stiffness at the hinge closure.

$$K_\theta = \frac{M_g}{\theta_g} \tag{4-39}$$

$$M_g = \frac{K_{c.pad}}{K_{c.pad} + K_{rod}} \left(\frac{OD_{pad}}{2} K_{rod} \theta_g + P \right) \times \frac{OD_{pad}}{2} \tag{4-40}$$

The rotation at the closure of the gap, θ_g, was 0.0375 radian based on the measured dimensions. The stiffness of the rotational spring was 14,445 kip.in.rad^{-1} [1632 kN.m.rad^{-1}]

4.8.4 Static Numerical Simulations Using Simple Stick Model

4.8.4.1 Description of Simple Stick Model

The forces and displacements of the bent were calculated using lumped plasticity. It was discussed in section 3.2.4 that the pedestals remained elastic with insignificant effect on the deformations of the bent. Therefore, the pedestals were not simulated in that model. The simple stick model of BPSA consisted of two columns that were supported on pipe-pins and connected to a rigid cap beam at the top (Fig. 4-11).

The Paulay and Priestley (1992) plastic hinge model, which was explained in section 4.4.1, was used in the numerical simulation of the columns. The pipe-pins were modeled using the proposed pipe-pin springs. Linear rotational springs were used to model the moment-rotation relationship of the pipe-pins. The shear displacements of the pipe-pins were calculated assuming the gap-rigid behavior. The post-contact shear displacements of pipe-pins were

negligible because of the large stiffness of the pipes. Finally, the P-Delta effect was accounted for using the translational spring with the negative stiffness, which was derived based on static equilibrium in section 4.3.

The analysis procedure is presented in Appendix B. First, the column axial forces due to overturning moments were determined iteratively (section 4.4.1). The elastoplastic moment-curvature relationships of the columns were determined using the axial forces due to the weight of the cap beam. The ultimate displacement of each column was calculated assuming they were cantilever elements that were fixed against rotation at the top. Then, the rotations of the pipe-pins were assumed to be the same as the drift ratios of the columns. Based on the rotations, the ultimate pipe-pin moments were estimated using the following equation.

$$\mathrm{M}_{pin} = K_\theta \times \delta \tag{4-41}$$

where,

M_{pin}: pipe-pin moment, kip.in [kN.m]

$K_{\theta:}$ pipe-pin rotational stiffness from Eq. (4-39), kip.in.rad^{-1} [kN.m.rad^{-1}]

δ: drift ratio

The ultimate base shear was determined based on the static equilibrium of the ultimate moments at the top and the pipe-pin moments at the bottom. The corresponding overturning moment was compared with the axial forces of the columns from the last iteration and analysis was repeated until the latest results were within 10% of the previous iteration.

The slippage gap, S_{gap} in Eq. 4-28, was added to the ultimate displacement of the columns to calculate the ultimate displacement of the bent. Based on the ultimate displacement, the shear due to the P-Delta effect was subtracted from the ultimate base shear.

$$\mathrm{V}_{b.u} = \frac{M_{u.col1} + M_{u.pin1}}{h_c} + \frac{M_{u.col2} + M_{u.pin2}}{h_c} + K_{P\Delta} \times \Delta_u \tag{4-42}$$

where,

$\mathrm{V}_{b.u}$: ultimate base shear, kip [kN]

$M_{u.col1}$: CIP columns ultimate moments from moment-curvature analysis, kip.in [kN.mm]

$M_{u.col2}$: PC columns ultimate moments from moment-curvature analysis, kip.in [kN.mm]

$M_{u.pin1}$: CIP pipe-pins ultimate moments from Eq. (4-41), kip.in [kN.mm]

$M_{u.pin2:}$ PC pipe-pins ultimate moments from Eq. (4-41), kip.in [kN.mm]

$K_{P\Delta}$: equivalent P-Delta spring with negative stiffness from Eq. (4-6), kip/in [kN/mm]

Δ_u: ultimate displacement of the bent, in [mm]

h_c: columns clear height, in [mm]

The yield displacement was calculated by adding the displacements of the columns and slippages of the pipe-pins, as follows.

$$\Delta_y = \Delta_{y.column} + S_{gap} \tag{4-43}$$

where,

Δ_y: bent yield displacement at yield, in [mm]

$\Delta_{y.column}$: column displacement at yield from Eq. (4-8) , in [mm]

S_{gap}: slippage of pipe-pin from Eq. (4-28), in [mm]

The pipe-pin moments under the yield displacements were calculated using the drift ratios. Finally, the yield base shear was calculated based on the static equilibrium, as follows.

$$V_{b.y} = \frac{M_{y.col1} + M_{y.pin1}}{h_c} + \frac{M_{y.col2} + M_{y.pin2}}{h_c} + K_{P\Delta} \times \Delta_y \tag{4-44}$$

where,

$M_{y.col1}$: CIP columns yielding moments from moment-curvature analysis, kip.in [kN.mm]

$M_{y.col2}$: PC columns yielding moments from moment-curvature analysis, kip.in [kN.mm]

$M_{y.pin1}$: CIP pipe-pins yielding moments from Eq. (4-41), kip.in [kN.mm]

$M_{y.pin2:}$ PC pipe-pins yielding moments from Eq. (4-41), kip.in [kN.mm]

$K_{P\Delta}$: equivalent P-Delta spring with negative stiffness from Eq. (4-6), kip/in [kN/mm]

As explained in the previous chapter, the measured force-displacement relationship was determined from the envelope of the measured hysteresis curves from Run-1, Run-2, and Run-6 to Run-11 (section 3.2.5). The connection of the load cell to the cap beam was damaged in Run-4, but was repaired prior to Run-6. While negligible displacements were observed subsequent to Run-6, relatively large displacements were observed at the connection in Run-1 and Run-2. The effect of rotation and slippage at the middle of the cap beam on the bent displacement is shown schematically in Fig. 4-12. The rotational stiffness of the load cell to cap beam connection was calculated from the bolt group stiffness, as follows.

$$K_{\theta.CB} = \frac{1}{2} \times \sum_{1=1}^{4} k_{bolt}\, c_{yi}^2 \tag{4-45}$$

where,

$K_{\theta.CB}$: rotational stiffness of load cell to cap beam connection, kip.in^2 [kN.mm^2]

K_{bolt}: tensile stiffness of bolt connection, kip/in [kN/mm]

c_{yi}: vertical distance of the bolt to center of cap beam, 6 in [152.4 mm]

The bent displacements due to rotations at the connections were calculated assuming small displacements, which leads to the following equation.

$$\Delta_{CB.rot} = \frac{M_{y.col1} - M_{y.col2}}{2\, K_{\theta.CB}} \times h \tag{4-46}$$

where,

$\Delta_{CB.rot}$: bent displacement due to rotation in the cap beam, in [mm]

h: center-to-center height of the column, in [mm]

The bent displacement due to the rotation was 0.06 in [2 mm]. The slippages in the connection, δ_{slide} in the figure, were assumed one-half of the clearances between the bolts and the holes in the plates of the load cell, which was 0.13 in [3 mm]. The additional horizontal bent displacement due to the load-cell cap beam connection slippage was 0.28 in [7 mm].

4.8.4.2 Results of Simple Stick Model Analysis

The calculated and measured force-displacement relationships are shown in Fig. 4-13. The idealized bilinear envelope based on the average measured forces-displacements envelopes is shown in thicker dashed lines in the figure. The calculated results are well correlated to the test data in terms of the stiffness, maximum base shear, and ultimate displacements. The average calculated and measured forces and displacements at the yield and ultimate points as well as the corresponding errors are listed in Table 4-2. It can be seen that the error was relatively small and acceptable considering the simple formulation of the analytical model.

The displacement ductility of the bent was 3.6 from the envelope of the tests. The ductility of the bent was relatively low despite the formation of full column plastic hinges in plastic hinges. The reason for the apparent "low" ductility is that the measured initial stiffness was low because of the slippage of the load cell to cap beam connection in the early runs led to a relatively large effective yield displacement. As a result, the measured ductility was not a reliable indicator of the bent behavior. The force-displacement envelops were recalculated excluding deformation of the cap beam (Fig. 4-14) leading to an average displacement ductility of 4.7.

As Table 4-2 presents, the model underestimated the ultimate displacements in both directions because of the strain limits in the moment curvature analyses. The ultimate curvatures were determined as the curvature in which either the steel or the core concrete strain reached their corresponding failure strains. In the simple stick models, the core concrete strains reached failure strain, which was the confined concrete failure strain calculated using the Mander (1988) confined concrete model. It was observed in previous studies that confined concrete strain could reach strains greater than that failure limit in the plastic hinges (Paulay and Priestley, 1992; Johnson, et al., 2008).

4.8.5 Dynamic Numerical Simulations Using Frame Elements

4.8.5.1 Description of Model Using Frame Elements

Dynamic analysis of BPSA was performed in OpenSEES using frame and zero-length elements. The sketch of the models for the dynamic analysis is presented in Fig. 4-15. Furthermore, the OpenSEES scripts for the dynamic analysis are presented in Appendix D. The columns and pedestals were modeled using FB elements, which are distributed plasticity elements (section 4.4.2). The cap beam was modeled using an elastic element with gross section properties because of the post-tensioning force in the cap beam. The rigid zones of the column-cap beam connections were modeled using elastic elements with a large stiffness.

The columns to the pedestals connections were modeled using the proposed pipe-pin springs, which were explained in section 4.8.3. The mass of the mass rig was added to the cap beam, as explained in section 4.3. The weight of the cap beam was also distributed on its nodes.

Furthermore, damping was assigned to the element using “Rayleigh” command. The damping ratio was 0.02 of the committed stiffness matrix (Mazzoni, et al., 2009; Chopra, 2007). The measured shake-table accelerations in Run-6 to Ran-11 were used as the ground motion excitations. Additionally, zero-amplitude excitations were added after each run to assure that the model was stationary prior to the start of the next runs.

4.8.5.2 Sensitivity Analysis of Dynamic Simulations with Frame Elements

BPSA was analyzed using different material models, section discretization, and numbers of integration points to investigate the effects of modeling techniques on the analytical results. The errors in the calculated base shear and bent displacement were compared to determine the most efficient model. The results show that the effects of these parameters on the calculated base shear and displacement are less than 10%. The more important results of the dynamic analyses using different options are presented here.

Three concrete stress-strain models were compared: “Concrete04”, “Concrete01withSTIC”, and ”Concrete02” (Mazzoni, et al., 2009). The Concrete04 material is based on the Popovic (1973) stress-strain relationship (Mander, et al., 1988), which was used in the model (labeled BPSA-1). The two latter material models are based on the Kent-Scot-Park stress-strain envelope. The Concrete01withSTIC material was intended to improve the residual displacement, which was used in the model (labeled BPSA-2) (Lee and Billington, 2010). The Concrete02 material generally encounters less convergence issues than the other two. The model using Concrete02 was labeled BPSA-3. Two models for the steel bars were compared: “Steel02” and “ReinforcingSteel”. The stress strain relations for those models are shown in Fig. 4-16 superimposed on the measured stress-strain relationship of the column longitudinal bars. The Steel02 material is a bilinear hardening steel model and was used in BPSA-1, BPSA-2, and BPSA-3. The ReinforcingSteel model consists of linear-elastic, yield plateau, strain hardening, and strain softening segments. The ReinforcingSteel material was used in a model that was labeled as BPSA-4. Both steel models use Menegotto-Pinto curve to connect the elastic segment to the inelastic segments.

The difference in the calculated displacements and base shears is presented in Table 4-3. The differences larger than 20% are shown in bold in the Table. The measured base shear and displacement histories are compared with the analytical results of BPSA-1, BPSA-2, BPSA-3, and BPSA-4 in Fig. 4-17 to 4-20. The effect of the concrete materials on the base shear and displacement was insignificant as the results of BRSA-1, BRSA-2, and BRSA-3 were similar. For all the models, the properties of core concrete were defined using the Mander (1988) confined concrete model. Therefore, the peak and ultimate points of the concrete stress-strain relationship were identical among all the models leading to similar stress-strain envelopes. Thus, the different hysteresis behavior of concrete was the only variable in these three analyses, which affected the global response minimally.

The calculated base shear and displacement using the Steel02 material (BPSA-1) and ReinforcingSteel material (BPSA-4) also correlated closely to the measured data. The hysteresis loops of the model with Steel02 were better correlated with those of the measured curves (Fig. 4-21 to 4-23). While the ReinforcingSteel model showed a better match for the direct tensile test of the reinforcing bars, the cyclic behaviors of both steel models were similar. In a reinforcing bar under plastic strain reversal, strain hardening is initiated at a lower strain for monotonic loading, which is known as the diminishing yield plateau effect (Chang and Mander,

1994). Therefore, the results from the model with Steel02 were in closer agreement with the test results. In summary, the results from BPSA-1 (the model with Concrete 04 and Steel02) exhibited the best correlation with the test data.

4.8.5.3 Results of Dynamic Analysis using Frame Elements

The calculated base shear and displacement histories for BPSA using the proposed pipe-pin model are compared with the measured history in Fig. 4-24 to 4-27. The calculated responses correlated well with the test results in terms of peaks, history shapes, and amplitudes. The errors at the peak response are presented in Table 4-3 (BPSA-1). The averages of the calculated peaks were within 20% of the measured data. The numerical model overestimated the base shear because of the assumptions in developing rotational model of the pipe-pin. It was assumed that the contact point was at the edge of the pad, while more detailed analytical studies showed that the force acts at 85% of the radius. The measured and calculated force-displacement hysteresis curves are shown in Fig. 4-28 and 4-29. The measured envelope of the entire tests is shown with a solid thick line in the figures. The hysteretic behavior also well correlated with that of the tests. However, the residual displacements were not close to the test results, seen in Fig. 4-30, which shows the combined histories of the calculated and measured base shears and displacements.

4.8.6 Quasi-Static Numerical Simulations Using Finite Element Modeling

Finite element models of BPSA were used for pushover analysis using ABAQUS/Explicit (V6.14-1) package. The purpose of the models was to investigate the complex interaction among different parts. Thus, the components of the pipe-pins were modeled with continuum elements. Those models were analyzed under quasi-static loading. The numerical simulations were verified by comparing the calculated and measured force-displacement envelopes.

4.8.6.1 Description of Finite Element Model

A sketch of the FE models is presented in Fig. 4-31. The components of the pipe-pins were modeled with continuum elements to obtain more realistic force interaction through contact surfaces. From bottom to top, continuum elements were used to model the pedestal concrete, the components of the pipe-pins, and the lower 20-inch [508-mm] portion of the columns. The reinforcement was modeled using beam elements. The rest of the columns was modeled using elastic beam elements with cracked properties. The plastic hinges were modeled using bilinear rotational springs, connecting the top node of the column to the bottom node of the rigid zone element. The rigid zone elements were also modeled as elastic beam elements with the stiffness ten times larger than the columns stiffness. The cap beam was also simulated as an elastic beam.

The bent was symmetric about its vertical XZ plane (Fig. 4-31). Therefore, only one-half of the bent was modeled to reduce the number of elements. The beam elements and the plastic hinge springs were defined with one-half of their full properties.

4.8.6.2 ABAQUS/Explicit Solver

Two numerical solvers are available in ABAQUS to solve the dynamic equilibrium through time: explicit solver and implicit solver. The dynamic equilibrium is determined as follows.

$$M\,\ddot{u} = P - I \tag{4-47}$$

where,

M: mass matrix

$\ddot{u}$: nodal accelerations

P: external forces

I: internal forces

Both procedures solve for nodal accelerations. At the beginning of each time step, the velocity and displacement of the nodes are known. The explicit procedure solves that equilibrium explicitly, as follows:

$$\ddot{u}(t) = M^{-1}\,(P(t) - I(t)) \tag{4-48}$$

The velocity and displacement of the next step are calculated using the central difference integration method. Because ABAQUS/explicit uses lumped mass at the nodes, Eq. (4-48) is direct. The acceleration matrix, $\ddot{u}$, is calculated directly because variables in the right-hand side of the equation are known at each time increment. Because no iterations are required, the solution advances efficiently in models with a large number of elements, contact conditions, and extremely discontinuous events. The internal forces are changed significantly in the extremely discontinuous events such as contacts, impacts, and buckling. The most salient feature of the explicit solver is the absence of a global tangent stiffness matrix.

Conversely, in the implicit method a set of linear equations are solved.

$$\widehat{K}_j C_j = P_j - I_j - M_j \ddot{u}_j \tag{4-49}$$

where,

$\widehat{K}_j$: effective stiffness matrix

C_j: correction in the Newton iterations method

Because the process is iterative, the computational cost of the implicit method is high compared to the cost of the explicit method. The solution may not converge in the problems with large discontinuities such as concrete cracks, contact conditions, and slippage. As a result, the explicit solver was used in the FE analyses.

4.8.6.3 Stability and Mass Scaling

The explicit solver integrates through time using the central difference integration method. The time increments larger than the stability limit cause the solution to be unbound or result in inaccurate solutions. The stability limit is often approximated conservatively with the smallest transit time of a dilatational wave to cross each element of the mesh, as shown in the equation.

$$\Delta t_{stable} \leq \frac{L_{min}}{C_d} \tag{4-50}$$

where,

L_{min}: smallest element dimension in the mesh

C_d: current effective, dilatational wave speed of the material

The dilatational wave speed is a property of the material. For instance, the wave speed for a linear elastic material with a Poisson's ratio of zero can be calculated from the following relation.

$$\mathrm{C_d} = \sqrt{\frac{E}{\rho}} \tag{4-51}$$

where,

E: Young's modulus of elasticity

ρ: mass density

The program automatically sets the time increments just below this limit.

The effect of the mass on the solutions is not significant in the quasi-static problem with small accelerations. Using the mass-scaling feature of ABAQUS/Explicit, the mass densities of the elements were increased. Consequently, the stable time increments were increased, leading to efficient solutions.

In BPSA, the initial unscaled stable time increment was 1.152E-7 second. A target stable time increment of 2.E-5 second was used. The mass of the elements with stable time increments smaller than the target were amplified. The initial mass-scaling factors of the elements in the lower part of the column are shown in Fig. 4-32. The largest mass-scaling factors were used for the elements of the studs because of their small sizes and relatively high modulus of elasticity. The mass of the model was increased 83.06 times to reach to that target stable time increment.

In the case of dynamic analyses, real mass need to be assigned to the nodes to simulate the inertial forces correctly. Accordingly, the mass scaling may not be used in dynamic simulations, and an extremely small time increment is necessary to simulate the dynamic tests accurately. Thus, the quasi-static pushover analysis rather than dynamic analysis was performed using ABAQUS/Explicit in this study.

4.8.6.4 Material Models

The measured material properties were used in FE simulations. Based on the conventions in ABAQUS/Explicit, the stress measure is Caughy or "true" stress, which is the force per updated area. The strain measure is logarithmic or "true" strain. However, engineering stresses and strains are usually reported. The measured stresses and strains were converted to true stresses and strains using the following equations.

$$\epsilon_{true} = \ln(1 + \epsilon_{eng}) \tag{4-52}$$

$$\sigma_{true} = \sigma_{eng}(1 + \epsilon_{eng}) \tag{4-53}$$

$$\epsilon_{eng} = \frac{\Delta L}{L_0} \tag{4-54}$$

$$\sigma_{eng} = \frac{F}{A_0} \tag{4-55}$$

where,

ϵ_{true},ϵ_{eng}: true and engineering strain

σ_{true},σ_{eng}: true and engineering stress, ksi [MPa]

L_0,A_0: initial length and area of the element, in [mm] and in^2 [mm^2]

F: force on the element, kip [kN]

The elastic materials were used in the upper 44-in [1118-mm] of the columns, end zone elements, cap beam, and the nuts in the pipe-pin (Fig. 4-31). Those materials were defined as linear elastic by their Young's modulus, E, and Poisson's ratio, v. Additionally, the rubber pads were modeled using "hyperelastic" material properties. The materials in the other elements were modeled using combinations of elasticity and plasticity constitutive models. Linear elastic and plastic material properties were used for the steel materials in the pipes, end plates, rods, and reinforcements. The concrete in the pedestals and lower portions of the columns was modeled using the concrete damage plasticity (CDP) model.

4.8.6.4.1 Rubber Material Model

The stress-strain relation of the rubber is nonlinear elastic because rubber recovers nearly its entire deformation. For small strains, the stress-strain relation can be assumed linear. However, the elements underwent large deformations in the FE model. Hence, the stress-strain relation needed to be defined in terms of "strain energy potential". The strain energy potential is the strain energy stored in the material per unit volume of material. The stress-strain relations are obtained from the strain-energy function based on virtual work methods (Gent , 1992).

Several strain energy functions are available in ABAQUS. For the compressive test samples (Chapter 2), the best correlation between the calculated and measured displacements and forces was achieved using Neo-Hookean form of strain energy. That strain energy function is a reduced polynomial of first strain deviator invariant (Yeoh, 1993; SIMULIA, 2015).

$$U = C_{10}(I_1 - 3) + \frac{1}{D_1}\left(J^{el} - 1\right)^2 \tag{4-56}$$

$$I_1 = \lambda_1^2 + \lambda_2^2 + \lambda_3^2 \tag{4-57}$$

where

I_1 first deviatoric strain invariant

J^{el}: elastic volume ratio

λ_1^2 deviatoric stretches

C_{10}, D_1: material parameters

The second term on the right-hand side of Eq. (4-56) includes volume change because ABAQUS/Explicit has no mechanism to impose perfect incompressibility in the elements (SIMULIA, 2015). While Poisson's ratio for the incompressible materials is 0.5, it was necessary to use a smaller Poisson's ratio to provide compressibility in the elements for the explicit solver to function. The material parameters were determined by the internal subroutine in

ABAQUS/Explicit based on the average measured stress-strain curve assuming Poisson's ratio of 0.495. The bulk modulus was 100 times the shear modulus with Poisson's ratio of 0.495, which is sufficiently large to obtain accurate results. The material parameters were 357 and 2.79E-5 for C_{10} and D_1 respectively in pound and inch unit system.

4.8.6.4.2 Steel Material Model

The stress-strain relations were defined linear elastic up to the yielding strain with measured true Young's module and Poisson's ratio of 0.3. The measured strains beyond the yield point were converted to true plastic strains. Those plastic strains were added to the elasticity model.

4.8.6.4.3 Concrete Material Model

The stress-strain relationship of concrete is linear elastic up to a yield surface. Subsequently, the strains are plastic, meaning that the strains are unrecoverable and cause stiffness degradation upon unloading. Two concrete nonlinear materials are available in ABAQUS/Explicit: "Brittle cracking" and "Concrete Damage plasticity". The Brittle cracking material is a plastic smeared crack model to simulate the brittle tensile behavior of concrete. Because the compressive behavior is initially linear elastic, that model is suitable when behavior is dominated by tensile cracking. Alternatively, the concrete damaged plasticity (CDP) model utilizes the plastic behavior for compressive and tension. The CDP model is multi-hardening plasticity and scalar damaged elasticity. The continuum concrete elements in the lower part of the columns and pedestals were modeled using the CDP model.

Two failure mechanisms of CDP are tensile cracking and compressive failure of concrete material (Fig. 4-33). The failure mechanisms are controlled by plasticity-based yield surfaces. The stress-strain response is linear elastic up to the failure stress. The failure stress under uniaxial tension corresponds to the onset of micro cracking, σ_{t0}. Under uniaxial compression, the response is linear until the initial yield, σ_{c0}. In the plastic regime, the response is characterized by strain hardening followed by strain softening beyond the ultimate stress, σ_{cu}.

The concrete properties were defined based on the measured compressive cylinder strength on the test day. The elastic behavior of the concrete was defined by Poisson's ratio of 0.2 and Young's modulus determined based on ACI-318, as follows (ACI Committee 318, 2011).

$$E_c = 1803\sqrt{f_c'}\ (\text{ksi}) \tag{4-58}$$

where,

f_c': compressive strength of concrete, ksi

The tensile failure (or yield) stress was determined from the mean splitting strength of normal-weight concrete (Wight and McGregor, 2009).

$$\begin{aligned}\sigma_{t0} &= 0.206\sqrt{f_c'}\ (\text{ksi}) \\ &= 0.531\sqrt{f_c'}\ (\text{MPa})\end{aligned} \tag{4-59}$$

Beyond the tensile failure strain, the tension stiffening behavior of the crack was defined by stress-displacement relation based on the fracture energy cracking criterion. The fracture energy concept proposed by Hillerborg et al. (1976) was used in determining the crack widening in the continuum. The energy required to open a unit area of crack is defined as a material

parameter, using brittle fracture concept. The bilinear softening relation that was used for the stress-displacement response of concrete is shown in Fig. 4-34. The parameters of the curve were calculated from the empirical equations proposed by Roesler et al. and Bazant et al.

$$w_1 = \frac{2G_f}{f_t'} \text{ (Roesler, et al., 2007)} \tag{4-60}$$

$$w_f = \frac{2}{\psi f_t'}\left[G_F - (1-\psi)G_f\right] \text{ (Roesler, et al., 2007)} \tag{4-61}$$

$$G_F = 2.5G_f \text{ (Bazant and Becq} - \text{Giraudon, 2002)} \tag{4-62}$$

$$G_f = \alpha_0 \left(\frac{f_c'}{0.051}\right)^{0.46} \left[1 + \frac{d_a}{11.27}\right]^{0.22} \left(\frac{w}{c}\right)^{-0.3} \times 10^{-3} \text{ (N/mm) (Bazant and Becq} - \text{Giraudon, 2002)} \tag{4-63}$$

where,

w_1: crack opening at the kink point, mm

f_t': tensile strength of concrete, MPa

G_f: initial fracture energy, N/mm

G_F: total fracture energy, N/mm

ψ: ratio of cohesive stress, which was assumed 0.25 (Roesler, et al., 2007)

w_f: ultimate crack opening, mm

α_0: assumed 1.14 (Bazant and Becq-Giraudon,2002)

d_a: maximum aggregate size, mm

w/c: water-cement ratio

f_c': compressive strength of concrete, MPa

The compressive stress-strain relation was determined based on the Popovic (1973) model using the measured compressive strength. The initial "yield" stress in the compression was assumed 30% of the measured compressive strength based on the reported observations (Chen, 1982). Beyond the yield stress, the plastic strains and stresses were input to the program to define the uniaxial stress-strain relationship. Based on the uniaxial relationship and the CDP failure criteria, the program defines the yield surface to relate stresses and strains in the triaxially loaded elements. .

The yield surface is defined by the Drucker-Prager failure criterion in the CDP materials. This model incorporates hydrostatic pressure in the shear capacity of the material such as the following relation.

$$f = \sqrt{J_2} + \alpha I_1 = k \tag{4-64}$$

$$I_1 = tr(\boldsymbol{\sigma}) \tag{4-65}$$

$$J_2 = \frac{1}{2}\boldsymbol{s}:\boldsymbol{s} \tag{4-66}$$

where,

I_1: first invariant of stress tensor

J_2: second invariant of stress deviator tensor

α, k: positive material constants

$\boldsymbol{\sigma}$: stress tensor

$\boldsymbol{s}$: deviatoric stress tensor

The Drucker-Prager surface is a smooth generalization of the Mohr-Coulomb failure criterion. That surface in the principal stress space is "a right-circular cone with its axis equally inclined to the coordinate axes and its apex in the tension octant", which is shown in Fig. 4-35 (Chen, 1982). This yield function shows increase in volume while deforms plastically, which is known as dilatancy.

CDP uses the Barcelona model to represent the difference between tensile region and compressive region. The yield function for that model with damage parameter, κ, is shown in the following (Lee and Billington, 1998).

$$F = \frac{1}{1-\alpha}\left(\alpha I_1 + \sqrt{3J_2} + \beta\langle\hat{\sigma}_{max}\rangle\right) = c_c(\boldsymbol{\kappa}) \tag{4-67}$$

$$\alpha = \frac{f_{b0} - f_{c0}}{2f_{b0} - f_{c0}}, \qquad 0 \le \alpha < 0.5 \tag{4-68}$$

$$\beta = \frac{c_c(\boldsymbol{\kappa})}{c_t(\boldsymbol{\kappa})}(\alpha - 1) - (1 + \alpha) \tag{4-69}$$

where,

$c(\boldsymbol{\kappa})$: damage cohesion in compression or tension

f_{b0}: initial equibiaxial compressive yield stress

f_{c0}: initial uniaxial compressive yield stress

$\hat{\sigma}_{max}$: algebraically maximum principal stress

The damage was not included in this study. For initially undamaged material, i.e. κ=0

$$c_c(0) = f_{c0} \tag{4-70}$$

$$c_t(0) = f_{t0} \tag{4-71}$$

A plane stress curve of the initial undamaged yield surface is shown in Fig. 4-36. The ratio of the initial equibiaxial compressive yield stress to the initial uniaxial compressive yield stress was 1.16 in BPSA, based on the default value of ABAQUS/Explicit. Additionally, the ratio of the second stress invariant on the tensile meridian to that on the compressive meridian at initial yield needs to be defined. The default value of 2/3 was used.

Beyond the yield surface, the rate of the plastic strain is defined with an associative flow rule.

$$d\varepsilon_{ij}^{p} = d\lambda \frac{\partial g}{\partial \sigma_{ij}} \ , \qquad d\lambda \geq 0 \tag{4-72}$$

$$g(\sigma_{ij}) = constant$$

where,

$d\lambda$: factor of proportionality and is non-zero when plastic deformation occurs

$g(\sigma_{ij})$: plastic potential function

The plastic potential function defines the surface of the plastic potential in a nine-dimensional stress space based on the nine components of the stress tensor (σ_{ij}). For CDP, that function is a Drucker-Prager hyperbolic function type, as follows.

$$G = \sqrt{(\epsilon \sigma_{t0} \tan\psi)^2 + \bar{q}^2} - \bar{p} \tan\psi \tag{4-73}$$

$$\bar{p} = -\frac{1}{3} trace(\bar{\boldsymbol{\sigma}}) \tag{4-74}$$

$$\bar{q} = \sqrt{\frac{3}{2}(\bar{\boldsymbol{S}} : \bar{\boldsymbol{S}})} \tag{4-75}$$

$$\bar{\boldsymbol{S}} = \bar{\boldsymbol{\sigma}} + \bar{p}\boldsymbol{I} \tag{4-76}$$

where,

ψ: dilation angle in the ***p*-*q*** plane at high confining pressure

σ_{t0}: uniaxial tensile stress at failure

ϵ: eccentricity

$\bar{p}$: hydrostatic pressure stress

$\bar{q}$: Mises equivalent effective stress

$\bar{\boldsymbol{S}}$: effective stress deviator

The dilation angle was assumed 37 degrees based on the suggestions of the program manual. The uniaxial tensile stress at failure was taken from the user-defined tension stiffening data. The eccentricity is the rate at which the function approaches the asymptote. The default flow potential eccentricity of 0.1 was used, which implies that the material has almost the same dilation angle over a wide range of the flow potential. This indicates that the dilation angle increases more rapidly as the confining pressure decreases.

Summarizing, the elastic properties of concrete were defined using the modulus of elasticity and Poisson's ratio. The parameters of the CDP plastic surface was defined as presented in Table 4-4. The compressive yield stress was assumed $0.3f_c'$. Beyond that stress, the behavior was defined based on the plasticity model with the aforementioned properties. In tension, the yield stress was taken the same as the cracking stress from Eq. (4-59). Beyond cracking, the relation of the stress crack opening (displacement) was defined based on Eqs. (4-60) to (4-63).

4.8.6.5 Elements and Meshing

The three-node quadratic beam element was utilized to model the cap beam, upper parts of the columns, rigid zone elements, and longitudinal reinforcing bars. That beam element is referred to as "B32" in ABAQUS/Explicit. The two-node linear displacement truss element was used to model the spirals of the columns and pedestals. Those truss elements are referred to as "T3D2" in ABAQUS/Explicit. The other parts that were modeled with continuum elements were modeled using eight-node linear brick (hexahedral) with the reduced integration and hourglass control. That continuum element is referred to as "C3D8R" in ABAQUS/Explicit. The reduced integration formulation increases the speed of analysis by using only one integration point. Therefore, the strain distribution is uniform within those elements.

The reduced integration elements may distort in such a way that the strains calculated at the integration point are all zero because the elements have only one integration point. That effect is called "hourglassing" and leads to uncontrolled distortions of the mesh. To prevent this, hourglass control algorithms are included in the formulations of the reduced-integration elements. Additionally, those elements had to be used in reasonably refined meshes to produce accurate results.

The meshing of the parts was performed by the internal subroutines of ABAQUS/Explicit based on the user-defined seeds on the edges. The edges on the perimeter were seeded to obtain 36 elements. The seeds on the radial edges were for 21 elements in the columns. The mesh was finer around the studs and the contact surfaces. The FE meshes for the columns, pedestals, lower pipe, and studs are shown in Fig. 4-37. The number of elements and nodes were respectively 306,288 and 359,801. The total number of variables in the problem was 1,078,322 including degrees of freedoms and Lagrange multipliers.

4.8.6.6 Interaction among Elements

4.8.6.6.1 Constraints

The interaction of the reinforcement with the continuum elements was modeled using the embedded element technique, in which the translational degrees of freedom (DOFs) of the reinforcement are constrained to those of the host elements. The host elements were the continuum concrete elements. ABAQUS/Explicit default values were used to define the embedded element constraints. Those constraints along with the tension stiffening of the concrete material simulate load transfer across the cracks.

The connection of the studs to the pipes was modeled using the surface-to-surface mesh tie constraints. The mesh tie constraint enforces the DOFs of each node on the slave surface to be equal to those of the closest node on the master surface. In each constraint definition, the stud end surface and outer pipe surface were respectively the slave and master surfaces.

The nodes on the edges of the end surfaces of the studs were part of the tie constraints as well as the kinematic contacts between the studs and concrete. Because the tie and contact constraints are kinematic constraints, the nodes on the edges of the end surfaces of the studs were over-constrained. The kinematic contact constraints override the kinematic constraints in ABAQUS/Explicit. Because the pipe surfaces were also part of the contact constraints with the concrete and the geometry, the override of the contacts on the tie constraints did not introduce any inaccuracy.

The end nodes of the cap beam and the rigid zone elements were constrained using beam-type multi-point constraints (MPC). The beam-type MPC forces the DOFs of the slave nodes to be equal to those of a control point assuming they are connected with a rigid beam. The end nodes of the cap beam and top nodes of the rigid zones elements were respectively the control and slave nodes.

The top surface nodes of the columns were constrained to the bottom nodes of the column with beam element utilizing coupling constraints. The kinematic coupling constraints restrain a large number of nodes ("coupling" nodes) to the rigid body motion of a single node ("control" node) similar to the beam-type MPC. The coupling nodes were the nodes on the top surface of the part of the column that was modeled with continuum elements (Fig. 4-31). The control node was the bottom node of the elastic beam element of the column.

4.8.6.6.2 Contacts

Surface-based contacts were used to simulate the interaction between the elements that were initially in contact or might come in contact under loads. Contact properties were defined "Hard" and "Penalty" respectively in the normal and tangential directions, except for the bottom surface of the rubber pad. The pad-pedestal contacts were defined as "Hard" and "Rough" respectively in the normal and tangential directions. The Hard contact relationship minimizes the penetration of the slave surface into the master surface. Furthermore, it does not allow the transfer of tensile stress across the interface. The Penalty contact relationship uses the basic form of the Coulomb friction model to relate the maximum allowable frictional stress across an interface to the contact pressure between the contacting bodies. Two contacting surfaces can carry shear stresses up to a certain magnitude across their interface prior to their sliding. The critical shear stress that triggers sliding is determined from the coefficient of friction and contact pressure, as follows.

$$\tau_{cr} = \mu\, p \tag{4-77}$$

where,

μ: coefficient of friction

p: contact pressure

The coefficients of the friction that were used in the numerical simulations are presented in Table 4-5.

As explained in Chapter 2, the bearing pads were glued to the pedestal surface to prevent warping. The contact properties between the bottom surface of the pads and pedestal were defined as "Rough". That option prevents all relative sliding motion between the contacting surfaces.

ABAQUS/Explicit uses two different methods to enforce contact constraints: penalty and kinematic. The kinematic contact algorithm uses a kinematic predictor/corrector algorithm to enforce contact constraints strictly. For example, no penetrations are allowed in the Hard contact pairs. The penalty contact algorithm has a weaker enforcement of contact constraints but allows for modeling of a more general type of contact. The kinematic contact algorithm was used in all of the contact pairs in the model, which is also the default algorithm for ABAQUS/Explicit.

Because the kinematic contact algorithm is a predictor/corrector algorithm, it has no influence on the stable time increment. Over each time increment, ABAQUS/Explicit first advances the kinematic state of the model into a predicted configuration without considering the contact conditions. Then, the slave nodes that penetrate the master surface are determined. The resisting forces and corresponding acceleration that are required to oppose the penetration are calculated. Those forces and accelerations are distributed on the master surface to correct the predicted configuration.

All the contact pairs except those with rubber material were defined balanced master-slave contact pairs. Using this method, two sets of correction forces and accelerations are made, each considering each surface as the master surface at a time. Then, the averages of the two forces and accelerations are applied to the surfaces. Because the mass of the rubber elements was significantly smaller than the mass of the steel and concrete elements, the surfaces of the rubber elements were defined as the slave surface in those contact pairs to prevent tensile contact forces.

4.8.6.7 Plastic Hinge Springs

The plastic hinges were modeled by bilinear rotational springs connecting the top of the column to the rigid zone beam element. A concept similar to the lumped plasticity model that was presented in section 4.4.1 was utilized to model the springs. The elastic deformations of the columns were simulated by the beam and continuum elements of the columns. Therefore, the plastic hinge springs were defined to account for only the post-yield rotations.

Moment-curvature analyses were performed using the column axial forces including the axial force due to the overturning moments. The properties of the plastic hinges were determined under the maximum measured column axial loads. The axial forces were calculated iteratively based on the base shear. The iteration was continued until the updated base shear was within 10% of the previously calculated base shear. This procedure does not account for the effects of the variations of the axial forces on the moment-curvature analysis. Because the axial load variation is not significant beyond the yield point, the effect of the axial force variation does not add significant error to the analysis.

The yielding and ultimate moments of the plastic hinge springs were one-half of those of the calculated elastoplastic moment-curvature relationships because one-half of the pier was analyzed due to its symmetry. The yielding rotation was determined from Eq. (4-14) for the bond-slip rotations. The ultimate rotation was calculated from the plastic rotation using the plastic hinge length. The plastic rotation in Eq. (4-12) was derived assuming the hinge was in the middle of the plastic hinge length. The equivalent maximum plastic rotations for the spring at the top of the column were determined as follows.

$$\theta_{p.spring} = \theta_p \left(1 - \frac{0.5L_p}{h_c}\right) \tag{4-78}$$

where,

$\theta_{p.spring}$: equivalent maximum plastic rotation of the spring at the top of the column, rad

θ_p: maximum plastic rotation of the spring at the middle of the plastic hinge length from Eq. (4-12), rad

L_p: plastic hinge length from Eq. (4-13), in [mm]

h_c: clear height of the column, in [mm]

The properties of the springs are presented in Table 4-6. Failure was assumed to occur when the rotations of the plastic hinge springs reached the corresponding maximum plastic rotation capacity.

4.8.6.8 Boundary Conditions

Supports were assigned to the bent by restraining the DOFs of the nodes on the bottom surfaces of the pedestals. As explained in section 4.8.6.1, due to the symmetry of the bent, material, and loadings, only one-half of the bents were simulated. Three DOFs of the nodes on the plane of symmetry were constrained: translation in the Y-direction, rotation about X-axis, and rotation about Z-axis (Fig. 4-31). These boundary conditions are referred to as "YSYMM Type" in ABAQUS/Explicit.

4.8.6.9 Loadings

The models were subjected to quasi-static lateral loadings for the pushover analyses after the application of gravity loads. For the most efficient solution, the loads should be applied in the shortest possible time during which the solutions remain nearly "true" static solutions and the inertia forces remain insignificant. Any sudden application of the loads or displacements introduces a level of momentum to the model, which can cause inaccurate results due to dynamic effects. Therefore, loading was applied slowly in a smooth manner using the built-in smooth step amplitude curve. In that curve, the path between the initial and target displacements or loads is a curve with smooth first and second derivatives as well as zero slopes at the data points. The amplitude, *a*, between two consecutive data points (t_i, A_i) and (t_{i+1}, A_{i+1}) is calculated from the following relationship (SIMULIA, 2015).

$$a = A_i + (A_{i+1} - A_i)\xi^3(10 - 15\xi + 6\xi^2) \text{ for } t_i \le t \le t_{i+1} \quad (4\text{-}79)$$

$$\xi = \frac{t - t_i}{t_{i+1} - t_i}$$

Additionally, the ratio of the kinetic to internal energy was kept below 10% throughout the analyses.

First, the gravity forces were applied on the cap beam nodes in 0.10 seconds (Fig. 4-38). Then, the 5-in [127 mm] target displacement was applied to the center of the cap beam over 4.40 seconds. The P-Delta effect due to the displacement of the mass rig was included using the spring with negative stiffness, which was determined in section 4.3. Because negative stiffness is not allowed in the explicit solver, the force was applied directly. The bent displacement is known at each time because the analysis is displacement-controlled. Consequently, the P-Delta force is known. Therefore, the lateral P-Delta forces were applied to the cap beam to include the P-Delta effect (Fig. 4-38).

4.8.6.10 Sensitivity Analysis

The effects of two parameters on the force-displacement curve were investigated: the material parameters of the elastomeric pad in the strain energy functions and the friction between the column and pedestals. While the material properties were from testing of virgin rubber pad

samples, the properties could change with time, loading, etc. in construction or testing. For example, the rubber and rubber-like materials tend to soften under cyclic loading (Gent , 1992). Therefore, the results of the analyses with different stiffnesses were compared to investigate the effect of the pad stiffness on the results. Furthermore, because a large range of the coefficient of the friction between rubber and concrete is reported in engineering guidelines, the effect of the pad friction coefficient on the global response of the bent was also studied.

Two models with material stiffness factors, C_{10}, equal to 359 and 171 psi [MPa] were used. The former was obtained from the best fit to the compressive test on the samples of the pad. The latter stiffness was selected based on the following equations, which relate the durometer stiffness to the modulus of elasticity and C_{10} factor.

$$E = \frac{15.75+2.15H_A}{100-H_A}\ (MPa)\ \ (\text{Gent}, 1992\ \text{p.}\ 310) \tag{4-80}$$

$$C_{10} = \frac{G}{2}\ (\text{Yeoh}, 1993) \tag{4-81}$$

where,

H_A: Shore A durometer of rubber

The specified durometer of the pad by manufacturer was 75±5 shore-A. Using H_A=75, C_{10} is 171 psi.

The comparison of the force displacement envelopes of two materials are shown in Fig. 4-39. The differences between those models were insignificant. The redistribution of force in the contact between the column and pad caused the moment at the bottom remain essentially constant. Additionally, it was noticed that the pipe-pin remained elastic while the column underwent large inelastic deformations. Therefore, the bent response was controlled by the plastic hinging at the top of the columns rather than the pipe-pin. The C_{10} parameter was selected 359 psi [2.48 MPa].

Models with the friction coefficients of 0.85 and 0.0 (frictionless) in the pad-column contact were compared. The former value was the selected parameter based on the suggestion in the engineering guides (Oberg, et al., 2012). However, the coefficient of friction may decrease by the rate of loading or surface wear under cyclic loading. The effect of friction coefficient on the force displacement relationship of the bent is shown in Fig. 4-40. The force-displacement relationships were almost identical for displacements larger than 0.5 in [13 mm], in which the pipes came into contact. The friction force transfer between the column and the pad was negligible subsequent to the contact of pipes. Prior to the contacts, the force-displacement relationship was better correlated to the measured force-displacement envelope with μ=0.85 than no friction.

4.8.6.11 Finite Element Analysis Results

The calculated and measured force-displacement relationships are compared in Fig. 4-41. The calculated and measured results are well correlated in terms of the yield points, ultimate displacements, and base shear capacity. The maximum error subsequent to the elastic part of the curve was 15%. The ultimate displacements were calculated 4.43 [113] and 4.82 in [122 mm] respectively in the south and north directions, which are 13 and 7% below the measured

data. The numerical model overestimated the initial stiffness because the actual initial stiffness of the model was relatively low due to the cap beam deformations.

The shear force distribution between the columns is shown in Fig. 4-42. Similar to the observations made in the experimental study, the shear forces were larger in the CIP than PC side in the positive displacement, push to the south, and larger in the PC side in the north direction. Due to the overturning moment, the CIP side was under axial compressive forces when the displacement was positive (south). Likewise, the PC side was under compressive forces when the displacement was negative (north). Because the column and pipe-pin stiffness was larger under compression force, the shear distribution was not uniform.

The deformed shape of the bent at the ultimate lateral displacement is shown in Fig. 4-43. The progression of the deformation in a pipe-pin under compression is shown in Figs. 4-44 to 4-46. Initially, the upper pipe slipped until it bore on the lower pipe (Fig. 4-44). The column shear was transferred to the pedestal through the pad prior to the contact between the pipes. Under small rotations, the contact point was at the lower part of the protruded section but the contact area increased at higher rotations (Fig. 4-45). Furthermore, the bearing area of the column on the pad shifted further away from the center of the pipes (right side in the figures). The pad was fully compressed when the edge of the column bore on the pedestal at 6.9% drift. The column forces were transferred to the pedestal through contact forces, which are shown in Fig. 4-47.

The contact between the pipes is the main mechanism to transfer shear from the columns to the pedestals. The horizontal components of the contact forces versus bent displacement is shown in Fig. 4-48a. The average bent displacement prior to the contact between the pipes was 0.32 in [8 mm]. Subsequent to the contact of the pipes, the contact forces were almost equal in both columns. Nearly, the entire shear in the column that was under tension was transferred through pipes. The remaining shear was transferred through the pad. Using the measured strain gage data in the lower pipe, the contact force in the pipes was estimated (section 3.2.11). The calculated shear forces are almost twice those measured using strain gages data because the instrumented sections were 1-in [25-mm] below the column-pedestal interface. As Fig. 4-49 Fig. 4-49 shows, the stress in the pipes diminishes with the embedded length. At 1 in [25 mm] below the interface, the calculated Von Mises stress is 49% lower than the interface stress.

The elevations of the point of contact, Z_{pipes} in Fig. 4-47, are presented in Fig. 4-48b for different displacements. The contact points were initially at the lower part of the protruded sections, but moved to the mid-height under larger displacements. Recall, the protruded length of the lower pipe was 4 in [102 mm]. In previous studies, the contact points were at the top of the lower pipes (Mehrsoroush and Saiidi, 2014) because, unlike the present study, the pipes were not tapered.

The forces in the rods versus the bent lateral displacements are shown in Fig. 4-50. The yielding fore of the rod is shown using a dotted line. As explained in Chapter 3, the rod forces were tensile even when the columns were under compression because of the rotation of the pipe. The rotations of the pipe-pins generated uplift at the base of the columns. The uplift generated relatively large elongations of the rod to compensate for the compression of the elastomeric pads. The axial forces of the rods were always well below the yield force of the rods, which was 126.1 kip [560.7 kN]. While the axial force in the rod was well below the yielding force, the stress condition needed to be checked for the combination of the axial force and flexure. The Von Mises yield stress was 75.1 ksi [518 MPa]. As Fig. 4-51 shows, the Von Mises stresses in the

rod reached the yielding criteria. The fixity of the rod at the end plates produced significant moments under the movements of the pipes and yielded the rod under flexure.

The components of the forces and points of contact between the column and the pad are shown in Fig. 4-52. Because of the relatively small rotations, the vertical and horizontal components of the contact force were respectively normal and tangential force in the column-pad contact pair. The tangential force was the friction force between the column and the pad. The normal force increased with the lateral bent displacements until the hinge gap closed. Subsequent to the bearing of the column on the pedestal, the normal forces dropped. Based on static equilibrium, the normal force was the summation of the column axial force and the rod force. Because the rod was always under tension due to the hinge rotation, the normal force under compression was considerably larger than the tensile side. For instance at the bent displacement of +3.89 in [99 mm], the axial forces in the CIP and PC columns were respectively 39.9 [177] in compression and 33.4 kip [149 kN] in tension. The rod forces were respectively 86.7 [386] and 92.8 kip [413 kN] in tension. The total normal force on the compression side (CIP) was 128.6 kip [572 kN], which was the summation of the column axial force and rod force. The normal force on the tension side (PC) was 59.4 [264 kN], which was equal to the rod force minus the column axial force.

The friction forces in the compression side were approximately one-third of the column shears while the friction forces were insignificant in the columns under tension. With increase of the rotation, the distance of the contact point from the center of the pipes increased to 5 in [127 mm], which is 85% of the exterior radius of the pad (a in Fig. 4-52c).

The analytical results show the column bore on the pedestal under compression under large displacements. The bearing forces of the column-pedestal interface are shown in Fig. 4-53. The hinge gap closes under 4.40 [112] and 4.43 in [113 kN] lateral bent displacement respectively in the south and north directions. The maximum vertical force was 10.7 [47.6] and 2.3 kip [10.2 kN] respectively under the positive and negative displacements, which are less than 10% of the corresponding contact forces between the columns and the pads. The contact points were 8 in [203 mm] from the center of the pipes, which is equal to the radius of the column.

The pipe-pin moments were calculated from the plastic hinge shear and moment based on static equilibrium (shown in Fig. 4-54 with the thick lines). The pipe-pin moment were compared with the moment due to the major force mechanisms that was shown in Fig. 4-47 to investigate the significance of each contact pair. The three aforementioned force transfer mechanisms generate a moment in the pipe-pin as it rotates: the vertical forces at the column-pad interface, the bearing forces between the column and the pedestal, and the horizontal forces due to the contact between the pipes. These forces were multiplied by the corresponding moment arm take to the center of the pipe-pin to obtain the corresponding moments. The moment due to the normal force in the column-pad contact pair generated more than 90% of the entire pipe-pin moment (shown with thinner lines in Fig. 4-54). The pipe-pin moments are linearly proportional to the lateral displacements of the bent. The slope of the lines fitted to the moment-displacement data are 168 [747] and 99 kip [440 kN] under compression and tension force, respectively.

The calculated crack pattern is shown in Fig. 4-55 and 4-56, which represent the equivalent plastic strain (PEEQT) in the concrete. The equivalent plastic strain is defined as $\int \dot{\epsilon}_t^{pl} dt$, which is a measure of the crack width. As explained in section 4.8.6.4.3, the concrete with CDP model

accounts for the crack as a scalar. Therefore, the directions of the cracks are not determined. The equivalent plastic strain also depends on the element size. Similar to the experimental observations, the numerical simulation did not show major crack formations on the surface concrete (Fig. 4-55). The numerical model calculated the horizontal cracks at the pedestal, which are shown with a solid arrow in those figures. The model also calculated the shear cracks on the columns, which are shown with a dashed arrow in Fig. 4-55.

The cracks were wider around the studs because of stress concentration. The analytical model showed some cracks on the surface of column at the tensile side, which are shown with dashed arrows in Fig. 4-56. The cracks were not observed in the tests perhaps because they were thin. The calculated PEEQT strain was 0.01096 at the PC column. The average length of the element is 0.39 in [9.9 mm], which leads to the crack width of 0.004 in [0.11 mm].

4.8.7 Concluding Remarks on Analysis of BPSA

The force-displacement relationship of BPSA was calculated using numerical simulations utilizing three analysis techniques. The calculated forces and displacements were compared with the measured data to determine the accuracy of those methods. All the models led to peak base shears and displacements with less than 20% error.

First, a lumped elastic model was proposed for modeling pipe-pins behavior using three springs. The force-displacement envelops were estimated by simple-stick model pushover analyses in both directions using this model. The procedure was quick and suited for preliminary design purposes.

Next, dynamic analyses of the bent were performed using frame elements in OpenSEES. The columns and pedestals were modeled with distributed plasticity while the proposed elastic springs were used to simulate the pipe-pins. The results showed the proposed model led to calculated dynamic responses of the bent accurately.

In the third model, a sophisticated FE model of BPSA with solid elements and contact interactions was analyzed using ABAQUS to determine the pushover response. The purpose of the model was to calculate the force, stress, and contact forces among the structural components. In addition to the global force-displacement responses, the cracking patterns, pipe forces, and pipe-pin rotations were well correlated with the measured data. That model was subsequently used in parametric studies described in the next chapter.

4.9 Bent with Rebar-Pin Column-Shaft Connection for ABC (BRSA)

4.9.1 Introduction

The connections of the columns to the pedestals in this model were rebar-pins. As explained in Chapter 3, plastic hinging was observed in the columns and rebar-pins. Eventually, the plastic hinge in the upper part of the CIP column reached its capacity. The failure of the plastic hinges of the columns is expected for the bents with rebar-pins at the base under lateral loading that were designed based on the recommendations of this document. Numerical models were developed that included the plastic deformations of the plastic hinges and rebar-pins in static and dynamic analyses.

In this section, numerical modeling techniques of the rebar-pins are explained first. Shear models are proposed based on crack shear-slip models. Additionally, two modeling techniques for the rotation of the rebar-pins are proposed. In section 4.9.3, the calculation of the force-displacement relationship of the bent using the simple stick models with lumped plasticity in the columns and rebar-pins is explained. The pushover analysis of the bent is explained in section 4.9.4. The response histories obtained from the dynamic analyses are presented in section 4.9.5. The analytical results were compared with the test data to validate the numerical models. Lastly, the overall comparison of the numerical models is discussed.

4.9.2 Rebar-Pin Models

The modeling techniques that were used in the numerical simulations of the tests are explained in this section.

4.9.2.1 Rebar-Pin Axial and Rotational Models

The rotational behavior of the rebar-pins was assumed independent from the shear behavior. The rotation of the rebar-pins is composed of two bond-slip rotations, one at the connection to the column and the other at the anchorage in the pedestal, in addition to the flexural deformation of the rebar-pin along the gap length. The lumped plasticity and distributed plasticity models were used to relate the rotation to the moment of the hinges. Those models were evaluated in the pushover and dynamic analyses by comparing the calculated forces and displacements to the measured data.

4.9.2.1.1 Lumped Plasticity for Rotation of Rebar-Pins

Based on the Cheng et al. (2006) model, bilinear zero-length rotational springs were used to model the rotational behavior of the rebar-pins. The properties of thee springs were derived from the moment-curvature analyses of the hinge throat assuming the section was doubly confined because rebar-pins are confined by the column and pedestal in addition to the spirals within the hinge. The hinge throat cover concrete properties were modified using the averages of confinement pressures generated by the column and pedestal transverse reinforcement. Those confinement pressures were added to the confinement pressures due to the hinge spirals to determine the confinement pressure of the core concrete in the rebar-pins. The Mander (1988) model was used to calculate stress-strain relationships of the confined concrete (Mander, et al., 1988).

The properties of the lumped plasticity springs were determined for two points: yield and ultimate points. Using the bilinear moment-curvature data, the rotations that correspond to the yield and ultimate moments were calculated based on the Cheng et al. (2006) model. The rotations of the rebar-pins consist of flexural and two bond-slip rotations. As an example, Fig. 4-57 shows the deformed state of the northern rebar-pin at the instance when the largest displacement occurred in Run-5. The yield rotation was calculated using the following equation.

$$\theta_{y.R} = \theta_{y.flex} + 2 \times \theta_{y.bond} \tag{4-82}$$

where,

$\theta_{y.R}$: rebar-pin rotation at yield, rad

$\theta_{y.flex}$: flexural rotation of the rebar-pin at yield, rad

$\theta_{y.bond}$: bond rotation at yield from Wehbe (1999) model, rad

The flexural rotation was calculated assuming constant curvature along the gap. Thus, flexural rotation at the yield point is given by the following equation.

$$\theta_{y.flex} = \phi_y \times g \tag{4-83}$$

ϕ_y: yield curvature from moment-curvature analysis, in^{-1} [mm^{-1}]

g: rebar-pin gap length, in [mm]

Based on the Cheng et al. (2006) model, the ultimate rotations were calculated assuming that the plastic deformations occur over an equivalent plastic hinge length. Therefore, the ultimate rotation was determined as follows.

$$\theta_u = \theta_p + \theta_e \tag{4-84}$$

$$\theta_e = g \times \phi_y \tag{4-85}$$

$$\theta_p = \phi_p \times L_p \tag{4-86}$$

$$\phi_p = \phi_u - \phi_y \tag{4-87}$$

where,

θ_e: elastic rotation, rad

θ_p: plastic rotation, rad

ϕ_p: plastic curvature, in^{-1} [mm^{-1}]

ϕ_u: ultimate curvature, in^{-1} [mm^{-1}]

L_p: equivalent plastic hinge length, in [mm]

The equivalent plastic hinge length is an empirical length that accounts for strain penetration in addition to flexural deformation at the ultimate point.

$$\begin{aligned} L_P &= g + 0.15 \times f_y(ksi) \times d_b(in) \\ &= g + 0.022 \times f_y(MPa) \times d_b(mm) \end{aligned} \tag{4-88}$$

where

f_y: longitudinal bars yield strength, ksi [MPa]

d_b: diameter of longitudinal bars, in [mm]

g: gap length, in [mm]

The plastic hinge lengths of the rebar-pins were 7.7 in [196 mm] including the amplification of the yield strength of the reinforcing bars to reflect the strain rate effect.

The rotational behavior was modeled using “Hysteretic” materials that were assigned to zero-length elements in OpenSEES. The Hysteretic material is a uniaxial bilinear material with the ability to model the pinching of the force-deformation relationship, damage, and degraded unloading stiffness. No damage or degrading stiffness was modeled because the test data did not exhibit either of them. However, the pinching effects were observed in the rotational

behavior of the rebar-pins (Fig. 3-137). In a well-designed hinge, degradation or damage are not expected but a slight pinching behavior is likely. The pinching is caused by opening and closing of the cracks and small horizontal slippage of the hinge. The cracks open wider with the progression of yielding in the reinforcing bars. It was assumed in the analytical model that the moment at the pinching point is 60% the yield moment. This arbitrary factor is the same as the ratio of the initial yielding moment to the effective yield moment of the hinge section. Additional sensitivity analyses that ignored the pinching effect showed that the effect of pinching of the rebar-pins on the overall response was not significant (as described in section 4.9.5.2.3). The hysteresis behavior of the rotational springs that were used to model the rebar-pins is shown in Fig. 4-58. The moment-rotation curves were determined for the cyclic loading shown in Fig. 4-58a.

4.9.2.1.2 Distributed Plasticity for Rotation of Rebar-Pins

Each rebar-pin was modeled using a beam-column element in which the bond-slip effects were included in the stress-strain relations of the fibers using Tazarv and Saiidi method (2014). The hinges were modeled with two types of elements, displacement-based (DB) and force-based (FB) beam-column elements. The accuracy of both models was nearly the same. However, the model with FB elements can become unstable depending on the number of integration points, while the model with the DB elements does not require stability at the element level.

One DB element is sufficient to model each rebar-pin. The curvature along the length of the DB elements is linear, whereas the curvature is polynomial in the FB elements. Therefore, as explained in section 4.4.2, FB elements are more efficient than DB elements in simulating the deformation of nonlinear beam-column elements. In reality, the distribution of the curvature is constant along the length of the rebar-pins (Cheng, et al., 2006). Thus, one DB element is sufficient to accurately model the rebar-pin rotational behavior. Furthermore, the convergence issue that exists in the internal iteration of the FB elements is not a concern with DB elements.

The Tazarv and Saiidi (2014) method, which is explained in section 4.6.2, was used to add bond-slip to the rebar-pin elements. The softened stress-strain relation was assigned to the reinforcing bars of the DB elements. To account for the bond-slip effects on both sides of the hinges, the strain increase due to bond slip was doubled. Therefore, Eq. (4-89) was used in lieu of Eq. (4-17).

$$\varepsilon_s' = \varepsilon_s + 2 \times \frac{F}{k_b\, L} \tag{4-89}$$

The variables are the same as those of Eq. (4-17).

4.9.2.2 Rebar-Pin Shear Model

The Cheng et al. (2006) model is the most-recent shear model for the rebar-pins. A curve was proposed in that study to model the shear-slip relation in rebar-pins (Fig. 4-59). The envelope consisted of four segments. The first segment models the behavior prior to friction release. In that segment, the slope is determined using the truss analogy method for cracked beams. Subsequent to the friction release, there is a plateau up to 0.6-in [15-mm] slip (Δ in Fig. 4-59). The shear force drops linearly due to the loss of friction in the third segment until the dowel action of hinge longitudinal bars starts. The fourth segment is linear up to the ultimate stress of the longitudinal bars, which defines the ultimate shear resistance of the rebar-pin. The friction

capacity was determined using a coefficient of friction of 0.45 and clamping force equal to the total compressive force in the section from moment-curvature analysis. The stiffness prior to the reaching friction capacity was estimated from the truss analogy method in cracked reinforced concrete members (Fig. 4-60). In the truss analogy method, the diagonal cords were concrete struts that were formed between cracks. The reinforcement was assumed to act as tension cords. Then, the stiffness was estimated assuming that the cracks were formed at a 45-degree angle. Figure 4-61 shows the calculated and measured shear-slip relationship of a rebar-pin with no axial force from the Cheng et al. (2006) study. While the maximum force was calculated closely, the initial stiffness and force plateau were underestimated.

The rebar-pins in BRSA should have remained in the first segment during the tests based on the Cheng model. The friction capacity was respectively 41.8 [189] and 62.0 kip [276 kN] under the maximum tensile and compressive axial loads. The maximum column shear force was only 32.5 kip [147 kN], which is 78% of the friction capacity. Based on the Cheng model, the maximum slippage is 0.001 in [0.026 mm]. However, the maximum measured slippage was 0.26 in [7 mm]. The measured displacements at the rebar-pins shows friction release, which is the start of the second segment in the Cheng model, at a shear force of approximately 25 kip [111 kN] (Fig. 3-136).

The calculated force-displacement relationship using the Cheng model was not close to the measured data because the axial load on the section was small. The video clips of the rebar-pins showed that the slippages occurred along the surfaces of the cracks, which were formed mainly due to the rotation of the connections. In the absence of compressive axial force, the flexural cracks opened wider with the progression of yielding in the bars compared to the hinges with compressive forces. Additionally, the stiffness was reduced because the aggregate interlocks were reduced due to the cyclic loads (Fig. 4-62). The crack shear-slip models were used in sections 4.9.2.1 and 4.9.2.2 to calculate the rebar-pin slippage including the effects of the crack

4.9.2.2.1 Crack Shear-Slip Models for Rebar-Pins

Two crack shear-slip models were used to simulate the sliding of the rebar-pins, the Walraven and Reinhardt (1981) and the Okamura-Maekawa (1991) models. In both models, the slippage of a cracked section is related to the crack width.

Walraven and Reindhardt showed that three mechanisms transmitted force across a crack: 1) aggregate interlock 2) axial restrained forces in the reinforcement 3) dowel action (Walraven and Reinhardt, 1981; Walraven, 1994). They proposed an empirical equation to relate four variables: shear stress, shear displacement, normal stress, and crack opening (Vecchio and Lai, 2004).

$$\delta_s = \frac{v_{ci} + v_{co}}{1.8w^{-0.8} + (0.234w^{-0.707} - 0.20) \times f_{cc}} \text{ (SI)} \tag{4-90}$$

$$v_{co} = \frac{f_{cc}}{30} \text{ (SI)} \tag{4-91}$$

where,

δ_s: tangential slip, mm

v_{ci}: shear stress on the crack surface, MPa

f_{cc}: concrete cube strength, MPa

w: width of the crack, mm

This equation shows the significant influence of the crack width. Based on the model, the crack becomes wider after each cycle, which leads to larger slippages (Fig. 4-62).

Another alternative crack shear-slip model, the Okamura-Maekawa (1991) model is derived using a fixed non-orthogonal crack model to formulate the following equations (Vecchio and Lai, 2004).

$$\delta_s = w \times \sqrt{\frac{\Psi}{1-\Psi}} \tag{4-92}$$

$$\Psi = \frac{v_{ci}}{v_{c,max}} \tag{4-103}$$

$$v_{c,max} = \frac{\sqrt{f_c'}}{0.31 + \frac{24w}{a+16}} (MPa) \tag{4-104}$$

where,

$v_{c,max}$: theoretical shear stress resisted by the crack, MPa

f_c': concrete 28-day cylinder strength, MPa

w: crack width, mm

a: maximum aggregate size, mm

4.9.2.2.2 Comparison of Results using Shear-Slip Models with Tests

The measured forces and displacements of the rebar-pins were presented in section 3.3.10. The slippages at the maximum measured shear of each run are compared to those calculated using the aforementioned crack shear-slip models.

As mentioned before, the crack width is a key variable in both models. Due to the variable rotation in the rebar-pins, the crack width is not constant in the section. The crack opening width, *w*, was estimated using the measured hinge uplifts assuming that the uplift is approximately the same as the maximum crack opening. The results from the crack shear-slip models are compared to the experimental data in Fig. 4-63. As shown in Appendix C, the slippages that were determined using the Cheng et al. (2006) model were almost zero. The crack shear-slip models overestimated the maximum slippage of the rebar-pins with maximum error of 35%, while the Cheng model underestimated the slip by 96%. Considering the general scatter in concrete response under shear, the correlation between the measured data and those from Walraven and Reindhart (1981) and Okamura-Maekawa (1991) models was reasonable in the initial portion of the shear-slip relationship. Subsequently, the measured uplifts were not an accurate representation of the crack width because of the permanent rotations at the rebar-pins. Another source of inaccuracy was that the planes of the cracks were not parallel because of the pin rotation. As a result, Eqs. (4-104) and (4-100) did not produce accurate results.

4.9.3 Static Numerical Simulations Using Simple Stick Model

4.9.3.1 Description of Simple Stick Model

A simple stick model using the lumped plasticity springs was developed as a design tool. It was discussed in section 3.3.4 that the pedestals remained elastic with insignificant effects on the performance of the bent. Therefore, the pedestals were not simulated in the model. The simple stick model of BRSA was composed of two elastic-plastic column elements supported on rebar-pins and connected to a rigid cap beam at top (Fig. 4-64).

The Paulay and Priestley (1992) plastic hinge model, explained in section 4.4.1, was used in the numerical simulation of the columns. Furthermore, the rotational behavior of the rebar-pins was modeled using bilinear rotational springs based on the Cheng, et al. (2006) model as explained in section 4.9.2.1.1. Moreover, the slippage of the rebar-pins was estimated from the average of the crack shear-slip models, explained in section 4.9.2.2.1. The columns were assumed to have equal lateral displacements at the top because of the large stiffness of the cap beam. Finally, the P-Delta effects were included using the negative stiffness translational spring (section 4.3).

The analysis procedure is presented in Appendix C. First, the column axial forces due to the overturning moments were determined iteratively (section 4.4.1). Using the corresponding moment-curvature data, the yield and ultimate points of the force-displacement envelopes were calculated.

The yield displacements were calculated by adding the displacements of the columns and rebar-pins, as follows.

$$\Delta_y = \Delta_{y.col} + \Delta_{y.pin} + \Delta_{slip} \tag{4-93}$$

$$\Delta_{y.rebarpin} = \theta_{\mathrm{y.R}} \times h_c \tag{4-94}$$

where,

Δ_y: bent yield displacement at yield, in [mm]

$\Delta_{y.col}$: column displacement at yield from Eq. (4-8) , in [mm]

$\Delta_{y.pin}$: displacement due to rebar-pin rotation, in [mm]

$\theta_{\mathrm{y.R}}$: rebar-pin rotation at yield from Eq. (4-82), rad

Δ_{slip}: rebar-pin slippage under yield base shear as explained in section 4.9.2.2.1, in [mm]

At the yield point, the moments at the top and bottom of each column were respectively equal to the yielding moment of the column and yielding moment of the rebar-pin. Therefore, the base shear was determined from Eq. (4-95) using static equilibrium.

$$\mathrm{V}_{b.y} = \frac{M_{y.col1} + M_{y.pin1}}{h_c} + \frac{M_{y.col2} + M_{y.pin2}}{h_c} + K_{P\Delta} \times \Delta_y \tag{4-95}$$

where,

$M_{y.col1}$: CIP columns yielding moments from moment-curvature analysis, kip.in [kN.mm]

$M_{y.col2}$: PC columns yielding moments from moment-curvature analysis, kip.in [kN.mm]

$M_{y.pin1}$: CIP rebar-pins yielding moments from moment-curvature analysis, kip.in [kN.mm]

$M_{y.pin2:}$ PC rebar-pins yielding moments from moment-curvature analysis, kip.in [kN.mm]

$K_{P\Delta}$: equivalent P-Delta spring with negative stiffness from Eq. (4-6), kip/in [kN/mm]

h_c: columns clear height, in [mm]

The ultimate displacement was calculated assuming fully formed plastic hinging at the top of the columns. The displacement of each column was determined using the kinematic relations of the plastic deformation, presented in Eqs. (4-10) to (4-12). The ultimate displacement of the bent was estimated as the smaller of the ultimate displacements of the two columns.

The ultimate base shear was calculated assuming the ultimate moments were developed in the columns and rebar-pins using static equilibrium of the bent as follows.

$$\mathrm{V}_{b.u} = \frac{M_{u.col1} + M_{u.pin1}}{h_c} + \frac{M_{u.col2} + M_{u.pin2}}{h_c} + K_{P\Delta} \times \Delta_u \quad (4\text{-}96)$$

where,

$\mathrm{V}_{b.u}$: ultimate base shear, kip [kN]

$M_{u.col1}$: CIP columns ultimate moments from moment-curvature analysis, kip.in [kN.mm]

$M_{u.col2}$: PC columns ultimate moments from moment-curvature analysis, kip.in [kN.mm]

$M_{u.pin1}$: CIP rebar-pins ultimate moments from moment-curvature analysis, kip.in [kN.mm]

$M_{u.pin2:}$ PC rebar-pins ultimate moments from moment-curvature analysis, kip.in [kN.mm]

$K_{P\Delta}$: equivalent P-Delta spring with negative stiffness from Eq. (4-6), kip/in [kN/mm]

Δ_u: ultimate displacement of the bent, in [mm]

h_c: columns clear height, in [mm]

4.9.3.2 Results from the Simple Stick Model Analysis

The calculated and measured force-displacements relationships are compared in Fig. 4-65. Table 4-7 presents the average calculated and measured forces and displacements at the yield and ultimate points. The calculated results were lower than the measured data by 21%. Moreover, the calculated displacement ductility was 7.4, which is 5% larger than the measured ductility. Despite the simplifying assumptions, the calculated and measured data were reasonably close.

4.9.4 Static Numerical Simulations Using Frame Elements

4.9.4.1 Description of Model using Frame Elements for Static Analysis

Pushover analysis of BRSA was performed in OpenSEES using frame and spring elements. The analytical models are shown in Fig. 4-66. The OpenSEES scripts of those models are presented in Appendix E. The pushover response was estimated twice, once using the lumped and again the distributed plasticity models of the rebar-pins. In both models, the columns and pedestals were

modeled using the FB elements, which are distributed plasticity elements (section 4.4.2). The cap beam was modeled using an elastic element. The gross section properties were used to model the cap beam because it was post-tensioned. The rigid zones of the column-cap beam connections were modeled using elastic elements with a relatively large stiffness. The failure criteria in the analyses were the bent lateral displacement at which either the core reached its ultimate strain capacity or reinforcing bars fractured.

4.9.4.2 Static Analysis Results for the Model with Frame Elements

The results from the pushover analysis of BRSA using the lumped plasticity model for the rebar-pins are compared with the tests data in Fig. 4-67. The calculated ultimate displacements were respectively 5.57 in [141 mm] and 2.24 in [57 mm] in the south and north directions. The core concrete failure occurred in the CIP and PC columns in the south and north directions analyses, respectively. The errors in the estimation of the ultimate displacements were 4 and 32% below the measured data in the south and north directions, respectively. The maximum error in the calculated base shear was 16% in the ascending part of the envelopes.

To investigate the effect of using a distributed plasticity model (section 4.9.2.1.2), the rebar-pins were also modeled with the DB elements. The calculated pushover curves are compared with the envelopes of the measured force–displacement hysteresis curves in Fig. 4-68. The calculated ultimate displacements were respectively 4.94 in [125 mm] and 3.29 in [84 mm] in the south and north directions. Similar to the previous model, the core concrete failure occurred in the CIP and PC columns with forces acting in the south and north directions, respectively. The errors in the estimation of the ultimate displacements were 15 and 20% respectively in the south and north direction. The error in the calculated maximum base shear was 16%.

The correlation of the results from both models with the test results is acceptable in terms of initial stiffness, yield displacement, ultimate base shear, and ultimate displacement. The model with the springs for the rebar-pins was less sensitive to the displacement increments and number of integration points.

4.9.5 Dynamic Response Simulation Using Frame Elements

4.9.5.1 Description of Model using Frame Element for Dynamic Analyses

Similar numerical models to those explained in the previous sections were adopted to analyze the bent under dynamic loading simulated using the shake table (Fig. 4-69). The OpenSEES scripts of those models were presented in Appendix D. The measured accelerations recorded by the shake-table instruments were spliced and used as the ground motion excitation in the simulations. Zero-amplitude excitations were inserted after each run to assure that the bent model became stationary prior to the start of the next runs.

The effective mass of the mass rig was added to the cap beam. That mass was modeled as the translational mass. The weight of the cap beam was distributed among its nodes. The damping was assigned to the elements using “Rayleigh” command with the damping equal to 0.02 of the committed stiffness matrix (Mazzoni, et al., 2009; Chopra, 2007).

4.9.5.2 Sensitivity Analysis of Model using Frame Element for Dynamic Analyses

BRSA were analyzed using different material stress-strain relations, hysteric models, and numbers of integration points to investigate the effects of modeling techniques on the analytical results. The results show that the effects of these parameters on the calculated base shear and displacements are less than 10%. The more important results of the dynamic analyses using different options are presented here.

4.9.5.2.1 Effect of Concrete Stress-Strain Relations on Analysis of BRSA

Three concrete stress-strain models were compared: "concrete01", "concrete01WithSITC", "concret04" (Mazzoni, et al., 2009). The two former material models are based on the Kent-Scot-Park stress-strain envelope. The latter is based on the Popovics (1973) stress-strain relation (Mander, et al., 1988). Table 4-8 presents the differences in the maximum displacements and base shears using each concrete model. Figures 4-70 to 4-75 show the measured and calculated base shear and bent displacement histories with different concrete materials. The calculated base shears and displacements were insensitive to the change of the material model. None of the concrete materials led to close estimates of the residual displacements. Residual displacements are secondary effects and are very sensitive to modeling assumptions with no clear trends (Saiidi and Ardekani, 2012)

The Motaref (2011) model for ECC suggests assuming the unconfined strain of ECC at the maximum stress equal to 0.025 (Motaref, et al., 2011). They also developed a stress-strain model for confined ECC based on the experimental results. The Motaref model for ECC was used in the analysis. The results are shown as BRSA-4 in the legends. The results did not show significant differences compared to the Mander (1988) confined model for concrete.

4.9.5.2.2 Effect of Steel Stress-Strain Relations on Analysis of BRSA

The results of the models with bilinear stress-strain relations of steel, "steel02", were compared with the model with "ReinforcingSteel" (Mazzoni, et al., 2009). The stress strain relations for those models are shown in Fig. 4-16. The ReinforcingSteel model consists of linear-elastic, yield plateau, strain hardening, and strain softening segments. Both models use Menegotto-Pinto curve to connect the elastic segment to the inelastic segments. Table 4-9 presents the differences in the maximum displacements and base shears using each concrete model. Figures 4-76 and 4-77 show the measured and calculated force-displacement hysteresis curves with two reinforcing material models. The results of the model with steel02 materials were in better agreement with the test data than the model with ReinforcingSteel material. While the ReinforcingSteel model shows a better match for the direct tensile test of the reinforcing bars, the cyclic behaviors of both steel models are similar because of the effect of diminishing yield plateau. The effect of diminishing yield plateau was explained in section 4.8.5.2.

4.9.5.2.3 Effect of Hysteretic Pinching of Rebar-Pin on Analytical Results for BRSA

The influence of rebar-pin pinching on the force-displacement response was studied. The rotational hysteresis behavior of models with and without pinching is presented in Fig. 4-58. The differences between the calculated base shear and bent displacement compared to the test data are presented in Table 4-10. Figures 4-78 and 4-79 show the effect of rebar-pin pinching on the calculated force-displacement curves. The measured force-displacement curves are shown with thin dashed lines in the figures. It can be seen that rebar-pin pinching did not affect the calculated force-displacement relationship. However, the model without pinching

underestimated the peak displacements in the last three runs. Those values are shown in bold in Table 4-10.

4.9.5.3 Dynamic Analysis Results using Frame Elements

The calculated base shears and displacements histories of BRSA using the spring model of the rebar-pins are compared with the measured histories in Fig. 4-80 to 4-83. Generally, the calculated responses correlated well with the test results in terms of peaks, waveforms, and the base shear and displacement amplitudes. The errors at the peak responses are presented in Table 4-11, with errors exceeding 20% shown in bold. The errors were below 20% in Run-3 to Run-6, which were the runs with strong motions. The hysteretic curves were also well correlated with those of the tests (Fig. 4-84 and 4-85). However, the calculated residual displacements were not close to the test results, as seen in Fig. 4-86. The model also overestimated the initial stiffness of the bent. Residual displacements are secondary effects and are sensitive to modeling assumptions with no clear trends (Saiidi and Ardakani, 2012).

Alternatively, the responses were calculated using the distributed plasticity model of the rebar-pins that was explained in section 4.9.2.1.2. As the base shear and displacement histories show in Fig. 4-87 to 4-90, the responses were in good agreement with the test data. The errors at the peak responses are presented in Table 4-11, with errors exceeding 20% are shown in bold. Despite the good correlation in the base shear, the displacements were underestimated by as much as 26%. The hysteretic curves were also generally well correlated with those of the tests (Fig. 4-91 to 4-92). The residual displacements deviated from the measured data for reasons explained previously (Fig. 4-93).

4.9.6 Concluding Remarks on Analysis of BRSA

The shake-table tests of BRSA were numerically simulated using five analysis techniques. The calculated forces and displacements were compared with those of the measured data to validate the accuracy of those methods. The pushover response was estimated by a simple-stick model in each direction and satisfactory results were obtained. The procedure is simple, efficient, and suited for design purpose. Embedded in the analytical model was a numerical model of the rebar-pins that was developed in this study. It was shown that the proposed method to calculate shear stiffness led to slippage results that were in good agreement with the measured data. Two modeling techniques were proposed for the rotational behavior of the rebar-pins. The measured base shear and displacement of the bent were compared with the calculated data using each model. The responses using the lumped plasticity model of the rebar-pins were closer to the test data.

Pushover analysis was performed using the distributed plasticity model in the columns. The rebar-pins were modeled using lumped in one analysis and distributed plasticity in another. The accuracy of both models was comparable. Using similar numerical models, the entire test histories were simulated in dynamic analyses. Similar to the pushover analyses, the results from two rebar-pin modeling were compared. The base shear histories were well correlated with those measured from both models. However, the distributed plasticity models of the rebar-pins underestimated the peak displacements considerably. Despite the good correlation of the displacement histories, the residual displacements were not well correlated in either analysis due to sensitivity of residual displacement to simplifying assumptions.

In summary, the lumped plasticity model of the rebar-pins showed better correlation with the test data. The numerical stability of the lumped plasticity model was also superior to that from the distributed plasticity models. Thus, the lumped plasticity model of rebar-pins was used in the parametric studies described in the next chapter.

4.10 Summary and Conclusions

The numerical simulation of the shake table tests was presented in this chapter. It was shown that modeling of the precast and cast-in-place members are similar. The numerical models of the pins were verified with the test results. Using those models, the responses of the tests were simulated with different levels of complexity.

It was shown that the lumped plasticity model of the pins is an effective tool to determine the seismic response of the test model and leads to good estimate of the pushover response. The major difference between the pipe-pin and rebar-pin was their plasticity. While pipe-pins remained elastic throughout the response, the rebar-pins yielded even under moderate earthquakes.

5 Parametric Studies

5.1 Introduction

The effects of key parameters on the performance and capacity need to be investigated to develop a general design procedure for column-pile-shaft pin connections. It is not feasible to study the role of all variables experimentally. Therefore, analytical studies are necessary. Numerical models were developed and verified with the experimental results obtained in the present study. The modeling details, calibration process, results, and the accuracy of the models were described in Chapter 4. Parametric studies that were conducted using finite element models to understand and quantify the effects of important parameters are described in the present chapter.

The variables and the range used for each are described first. Then, the analytical results are presented and the sensitivity of the results to each parameter is discussed. Similar naming and coordinate conventions to those of the previous chapters are used in this chapter. Similar coordinate conventions as section 4.2 were used in this chapter. The southward direction is shown with a positive sign and the northward direction is shown with a negative sign in the figures of this chapter.

5.2 Bent with Pipe-Pin Column-Pile Shaft Connection for ABC (BPSA)

5.2.1 Introduction

The finite element model for BPSA that was described in section 4.8.6 for pushover analyses was used to study the influence of different design parameters on the performance and capacity of pipe-pins. This model is referred to as the reference model hereafter. Table 5-1 lists the parameters and their ranges. The influence of axial load index, lower pipe taper slope, strands instead of rods, and removing the tension member on the bent response and pipe-pin performance were studied. The pushover analyses were performed in both directions. The parameters were changed one at a time. The tension member is not required if the column axial force is sufficiently large to prevent uplift and maintain stability. The effect of removal of the tension member was studied under 10% axial load index by comparing results from models P2, P7, and P8. Lastly, the performance of a model with “perfect pins” (P9) was compared with P2, P7, and P8 to investigate the significance of modeling the pipe-pin.

Results from past comprehensive parametric studies on the effects of other parameters that are applicable to the present study were utilized. Mehrsoroush and Saiidi (2014) conducted parametric studies from which the conclusions on the effects of upper pipe height and embedment length of the lower pipe were applied to the design procedure developed in the present study. From the parametric studies by Zaghi and Saiidi (2010), the conclusions on the effects of column spirals, inner spirals, embedment length of the pipes, protruded pipe length, horizontal gap between the pipes, pipe thickness, pipe diameter, and studs on the pipes were utilized in the present study.

5.2.2 Effect of Column Axial Load Index

A pin under large tensile forces requires larger rod to transfer the tension to the pile-shaft. Overturning moments could generate tensile forces in the columns. The column tensile force

transfers to the pedestal through the rod. Additional tension is caused by the rotation of pipe-pins (section 4.8.6.11). As explained in Chapter 2, the specimen was designed to generate relatively large tensile forces in the pipe-pins by not superimposing in the tests any dead load to account for the superstructure weight. Therefore, the only gravity loads on the columns of the reference model (P0) was the weight of the cap beam, which corresponds to 1% axial load index. The axial load index (ALI) is calculated from the following equation:

$$ALI = \frac{P}{f_c' \times A_g} \tag{5-1}$$

where,

P: axial load on the column prior to application of lateral load, kip [kN]

f_c': specified concrete strength, ksi [MPa]

A_g: gross cross-sectional area of column, in^2 [mm^2]

Three additional models with ALIs of 5%, 10%, and 15% were analyzed in the parametric studies to investigate the effects of the column axial loads on the global and local response. Table 5-1 presents the properties the models. The Caltrans Bridge Design Practice document suggests "to keep the dead load axial forces in columns to about 10% of their ultimate compressive capacity ($P_u = A_g \times f_c'$) to ensure that the column does not experience brittle compression failure and also to ensure that any potential P-Δ effects remain within acceptable limits" (Caltrans, 2015).

The FE models for pushover analysis using ABAQUS were adopted to perform the parametric studies. The properties of the plastic hinge springs were adjusted based on the axial forces in the columns. Figure 5-1 shows the effects of ALI on the moment-curvature relationship of the plastic hinges of the columns. The moment-curvature relationships were determined based on the axial load accounting for the overturning moment according to section 4.5. The maximum moment and initial stiffness were increased with the increase of ALI whereas the ultimate curvature decreased. Consequently, the ductility of the sections decreased under larger axial forces, which led to the lower ductility of the bent.

Figure 5-2 shows the effect of ALI on the force-displacement relationship of BPSA. The increase of ALI increased the maximum base shear and initial stiffness of the bent and reduced the bent ductility (Table 5-2). Figure 5-3 shows the column axial forces versus drift. Positive forces in these graphs indicate compression. The column in which the overturning moment produced compressive force is referred to as "compression" regardless of the dead load. Similarly, the column in which the overturning moment produced tensile force is referred to as "tension." This labeling convention was used throughout the figures in this chapter. Recall that the positive lateral load is applied on the bent cap from right to left causing tension in the right column and compression in the left column due to overturning, and vice versa. The overturning moments generated uplift only in the reference model (P0) (indicated by negative force in Fig. 5-3b). No uplifts were produced in the other models (P1, P2, and P3) and the column axial forces remained compressive.

The pushover curves were also calculated using the simple stick model (section 4.8.4). Table 5-3 presents the analytical results of the simple stick model and their difference from the FE model in ABAQUS. The analyses using the simple stick model overestimated the base shears and ultimate displacements respectively by 18% and 11% compared to the analytical results from

the FE model. As a result, the ductility was increased by 4%. The lumped springs representing the pipe-pins overestimated the column base moments by an average of 26% compared to the FE models (Table 5-3). The overestimation of the base moment led to the larger base shear. The first assumption in the proposed model described in section 4.8.3 is that the compressive force acts on the edge of the pad, which was at 6 in [152.4 mm] from the pin center. The sensitivity of eccentricity of the compressive force to the column axial load is shown in Fig. 5-4. The maximum eccentricity was 85% of the pad radius. Because of the larger assumed moment arm of full pad radius, the calculated pipe-pin moments would be overestimated. However, the difference was relatively small and the assumption was deemed acceptable considering the simple formulation of the analytical model.

The effect of ALI on the force transfer mechanisms in the pipe-pins was investigated using the sophisticated FE analyses. The increase of ALI increased the pipe-pin moment except for the initial segments, which are highlighted by an arrow in Fig. 5-5. The linear initial segments correspond to the pre-uplift condition. The column bottom surface was entirely in contact with the pad top surface under small rotations. The increase of the pin rotation increased the pin moments with a similar slope. The contact stress was decreased at the edge of the pad until the column lifted off the pad. The separation of the column from the pad caused the stiffness to decrease.

The contact forces at the column-pad interface and between the pipes increased with ALI as expected (Fig. 5-6 to Fig. 5-8). The column in which the overturning moment (OM) produced compression is labeled as “compression” regardless of the dead load and vice versa. The elevation of the point of contact between the pipes, Z_{pipes} in Fig. 4-47, was independent of ALI (Fig. 5-9). The contact point between the pipes was initially at the lower part of the protruded sections, but shifted to the mid-height under large displacements.

The increase of ALI reduced the axial forces in the rods significantly (Fig. 5-10). Compressive forces were developed in the rods at small drift ratios. However, almost all of the column compressive force was transferred to the pedestal by the bearing of the column on the pad. A small portion of the dead load was transferred to the pedestal through the rod. For example, the rod force was 7% of the column-pad normal force at zero drift in P3 with ALI of 15%. The curves also show that an increase in ALI delayed initiation of the tensile force in the rod to larger drift ratios. Consequently, the Von Mises stress in the rod was smaller with increase of ALI.

Tensile axial forces were developed in the rods due to the pipe-pin rotation. Figures 5-11 and 5-12 show the Von Mises stress in the rod respectively in the left and right columns for the lateral load toward the north. Recall that the lateral load toward north is applied on the bent cap from left to right causing tension on the left column and compression on the right column due to overturning. The Von Mises yield stress was 75.1 ksi [518 MPa]. The analytical results indicated that the increase of ALI reduced the Von Mises stress in the rod significantly. The rods in P3 and in the right column in P2 only yielded near the bottom nut, but yielding extended to other parts of the rod in other cases.

The cracking patterns for different ALIs are shown in Fig. 5-13 and 5-14 respectively in the left and right columns for the lateral load toward the north. The figures show the cracks were the longest in the pipe-pin of the reference model (P0) with ALI=1%. However, the cracks widths were generally small even in P0. The cracks diminished with the increase of ALI because the rod force decreased. The bearing force in column-pedestal interface was zero in P1, P2, and P3. The

gap between the column and the pile shaft closed only in P0 with small bearing force at the interface (section 4.8.6.11).

In conclusion, the results show that an increase in ALI increases the column flexural strengths, as expected. Therefore, larger force and moment demands were developed in the pipe-pins, which was also expected. High ALI reduced the rod forces but the pin rotation generated significant forces in the rod. Recall the overturning moment was sufficiently large only in the reference model (P0) to generate uplift.

5.2.3 Effect of Tapering Protruded Pipe

The top part of the lower pipes was tapered in a conical shape to increase the rotational capacity of the pipe-pins. The experimental and analytical results showed that the contact points between the pipes were at the mid-height of the protruded length for the reference model (P0) with 4% slope. The point of contact in the study by Mehrsoroush and Saiidi (2014) was at the top of the lower pipes because the pipes were not tapered. The effect of the conical shape of the pipes was investigated by comparing the responses of three models with different taper angles. Table 5-1 presents the properties of the models in the parametric study. In addition to the reference model (P0) with the taper slope of 4%, two bents with taper slopes of 0% (P4) and 8% (P5) were analyzed (Fig. 5-15). The taper slope was calculated from the following equation:

$$s = \frac{c}{L_{protruded}} \tag{5-2}$$

where,

c: reduction in radius at top of the pipe, in [mm]

$L_{protruded}$: protruded length, the distance from the top surface of pile to the top of pipe, in [mm]

The pushover curves of the bent for different taper slopes are shown in Fig. 5-16. The increase of the slopes from s=0% to 8% reduced the base shear by less than 5% (Table 5-4). The changes of the ultimate displacement and ductility were also insignificant. The response of the bent remained almost identical with change of the taper slope because the effect of the taper on the pipe-pin moment was small. The average pipe-pin moment decreased 13% with an increase of taper slope from s=0% to s=4% and no difference was observed when *s* was changed from 4% to 8% (Fig. 5-17).

Three force transfer mechanisms generate moments in the pipe-pins as they rotate: the vertical forces at the column-pad interface, the bearing forces between the column and the pedestal, and the horizontal forces due to the contact between the pipes. These forces were multiplied by the corresponding moment arm taken to the center of the pipe-pin to obtain the corresponding moments. The moment due to the contact between the pipes was less than 10% of the entire pipe-pin moment. The taper slope of the pipe affected the normal (vertical) component of the column-pad contact and the rod force insignificantly (Fig. 5-18 and 5-19). The increase of the taper slope reduced the contact forces between the pipes (Fig. 5-20) and shifted the contact application point to the mid-height of the protruded length (Fig. 5-21), which led to slight decrease of the pipe-pin moments. However, the moments within the pipe-pins

decreased slightly because the moment due to the contact between the pipes contributed to merely 10% of the total pipe-pin moments.

The friction force at the column-pad contact area was relatively small in all the models (Fig. 5-22) because most of the column shear was transferred to the pedestal through the pipes. A larger portion of the column shear was transferred through the pipes in the model without taper (P4) compared to the model with taper (P0 and P5). The friction force in the column-pad interface was 28% and 2% of the pipe contact force respectively in P0 (s=4%) and P4 (s=0%) at the ultimate drift. The Von Mises stress in the pipes changed less than 15%, without any specific trend (Fig. 5-23).

In summary, the conical shape of the lower pipes slightly reduced the pin moment while the taper slope exceeding 4% did not show any additional benefit. Therefore, tapering of the lower pipe is not necessary.

5.2.4 Effect of Type of Tension Member in the Pipe-Pin

Tensile forces were developed in the columns of the reference model (P0) because of the relatively small dead load and large overturning moment. Higher dead loads generate moments that counteract overturning moments and prevent uplift. When the dead load is sufficiently small, uplift forces are generated at the base of the columns. The uplift force in this study was transferred to the column by the tension member in the pipe-pin, which was a high-strength rod in the reference model (P0). The pipe-pin rotation produced additional tension in the rods. The analytical studies showed that the rods yielded under the combined axial load and flexure. The fixity of the rod at the end plates produced significant moments under the movements of the pipes and yielded the rod under flexure. However, the parametric studies of the effect of ALI on the pipe-pin response showed that the increase of ALI reduced the rod force because the resisting moments were sufficiently large to prevent uplift (section 5.2.2).

The effect of type of the tension members was investigated for two cases: (a) bent with uplift (b) bent without uplift. A tension member was required in the former to maintain stability. The same is not true in the latter because the dead load provides sufficient resisting moment to prevent uplift. For case (a), the response of the pipe-pins with strands and rods as the tension members were compared. For case (b), the effect of the tension members on the response of the bents was investigated by comparing the analytical results of the models with rods, strands, and no tension members (Fig. 5-24). Additionally, the results from these models were compared to those from a bent with “perfect pins” (P9) to investigate the significance of the pipe-pin.

Previous studies by Mehrsoroush and Saiidi (2014) investigated the effect of using strands instead of rod in a column-base pipe-pin connection with uplift. The use of strands instead of rod slightly reduced the pipe-pin moment, which led to slightly smaller column shear. Bearing of the rod on the inner pipe caused larger pin moment but the effect of bearing of the strand and lower pipe was insignificant. Moreover, the use of strands reduced the extent of damage to the pip-pin connection by reducing the hinge compressive force and the tension member remained elastic because strands were not subjected to bending.

5.2.4.1 Use of Strand instead of Rod in Bents with Uplift

Uplift forces are generated in the cases that overturning moments are larger than the resisting moments. The uplift force is transferred to the foundation through the tension member in the pipe-pins to maintain the stability of the structure. In this section, two options for the tension members are compared: 1) high-strength threaded rods 2) post-tensioning strands. The tension members are highlighted with the solid arrows in Fig. 5-24a and 5-24b. The model with the high-strength treaded rods was labeled P0, the reference model. The model with the posttensioning strands was labeled P6.

The posttensioning strands and the rods were designed with comparable yield strengths. The yield strength of the rod was 126.1 kip [560.7 kN]. It was found that using three 0.6-in [15.2-mm] diameter strands with Grade-270 and nominal cross-sectional area of 0.217 in^2 [140 mm^2] provides a yielding strength of 158 kip [703 kN], which was the closest value to the yield strength of the threaded rods. The yield and ultimate stress of the Grade-270 strands are respectively 243 [1675] and 270 ksi [1862 MPa]. The tendons were modeled in ABAQUS as tension-only, truss elements. To account for the possible contact between the strands and the inner edge of the lower pipe, the middle section of the tendon was modeled using continuum (brick) elements as a semi-cylinder, which is shown with a dashed arrow in Fig. 5-24b. The possible contact between the strand and the pipe was defined between the surface of the extruded part and the inner surface of the lower pipe. The Analytical results showed the tension member did not bear on the lower pipe in any of the models (P6, P0, and P8). The base of the semi-cylinder was equivalent to one-half of the total nominal area of the tendons.

Table 5-5 compares the maximum base shears, displacements, initial stiffness, pipe-pin moment, and displacement ductility of P0 and P6. The maximum base shear and displacement were decreased slightly (3%) by substitution of the rod with the strands because the pipe-pin moment decreased by 11% (Fig. 5-25 and 5-26). Figure 5-27 shows that the axial force in the strand was 14% smaller than that of the rod because the stiffness of the strands was almost one-half of the rod stiffness. The axial force in the strands and rods were well below the yielding force. Because of the stress condition for the combinations of the axial force and flexure in the rod, the Von Mises stress reached the yielding criteria in the rod (Fig. 5-11a and 5-12a). However, because of the negligible flexural stiffness of the strands, the tendons were not subjected to flexural stresses and remained elastic. The normal force in the column-pad interface was also smaller when strands were used because the axial force in the strand was smaller (Fig. 5-28). Furthermore, thinner cracks were formed in the model with the strand (P6) than those with the rod (P0) (Fig. 5-29 and 5-30). The friction force in the column-pad interface, the contact force between the pipes, and point of contact were similar in both models (Fig. 5-31 to 5-33).

In conclusion, the use of strands in pipe-pin rather than rods improved the behavior of the pipe-pins in the bents with uplift by reducing the pipe-pin moments and crack width. Additionally, all the pipe-pin elements remained elastic in the model with strands making the pipe-pin a capacity protected connection.

5.2.4.2 Effect of Tension Members in Bents without Uplift

The gravity load moments might be sufficiently large to prevent uplift (section 5.2.2). To investigate the effects of the tension member type on the performance of the bents without uplift, three bent models were analyzed (Fig. 5-24):

1. A bent with rods in pipe-pins (P2)
2. A bent with strands in pipe-pins (P8)
3. A bent without any tension member in pipe-pins (P7).

The model that was described in the previous section was used for the strands. P7 was similar to P2 except that the rods, end plates, and nuts were removed. The force-displacement relationships of the bents with the pipe-pins were compared to that of a bent with "perfect" pins for the column to pile-shaft connections (P9). P9 was included to show that a pipe pin with no tension member is not the same as a model with a perfect pin connection. It also showed that the effect of pipe-pins on the performance of the bent need to be modeled. The simple stick model (section 4.8.4) was used to calculate the pushover curve for P9 assuming the pin moment and the shear deformation were zero. The axial dead load on each column was 100 kip [444.8], which corresponds to ALI=10% (Table 5-1). The bent reactions were well above uplift threshold in all the models (P2, P7, P8, and P9), with the safety factor against uplift being 2.64 in P9.

Table 5-6 compares the maximum base shears, displacements, pipe-pin moments, and displacement ductilities of the models with different tension members. Using pipe-pins even without the tension members increased the maximum base shear approximately 20% compared to the bent on prefect pins (P9). Conversely, the ultimate displacements and initial stiffness in the models with the pipe-pins were respectively 8% and 30% smaller than that of the bent with perfect pins, which reduced the displacement ductility by 36% compared to P9. The lower stiffness of the models with pipe pins compared to that of the model with perfect pin is attributed to the pipe-pin slippages. The shear stiffness of the pipe-pins was decreased subsequent to the friction release, which is shown with an arrow in Fig. 5-34. The stiffness increased later when the pipes came in contact. P7 and P9 showed considerable softening behavior because of the large P-Delta effect. The axial force on each column was 100 kip [444.5 kN], which caused a negative stiffness of 1.89 kip/in [0.331 kN/mm] for the P-Delta effect (section 4.3).

The results clearly demonstrate that pipe-pins should be included in the analysis to avoid underestimating the base shear, which may lead to premature column failure and damage to the capacity-protected elements such as foundations and cap beams.

The change of the tension member type or eliminating it affected the maximum base shear by less than 5% (Fig. 5-34). The base shear at yielding was approximately the maximum base shear because the force-displacement hardening was small (Fig. 5-34). The ultimate base shears in P2 and P8 were 4% higher than the yield force, whereas the ultimate base shear in P9 decreased by 8% compared to the yield base shear. The plastic hinges were identical and reached the yield moment at 0.89%, 0.86%, and 1.03% drift respectively in P2, P7, and P8. The pipe-pin moments were initially similar regardless of the tension members because the rotations were too small to produce extension in the tension members (Fig. 5-35). The tensile force in the rods and strands were initiated at 0.96% and 1.08% drift respectively in P2 and P8 (Fig. 5-36). The pipe-pin rotation did not generate tensile force in the rods or strands under small drifts because the compressive axial force in the pipe-pins prevented uplift. The total pipe-pin moments increased with drift in the models with the tension members (Fig. 5-35) but decreased in the left column when the tension member was removed (Fig. 5-35b). The major source of the pipe-pin moments was the eccentricity of normal force in the column-pad interface. The normal component of the force was equal to the column axial force and the rod tensile force. An

increase in the pin rotation increased the force in the tension member, which led to the increase of the normal force in P2 and P8 (Fig. 5-37 and 5-38). In P7, however, there was no tension member and the normal force on the pad was only the column axial force. Another source of pipe-pin moment was the contact force between the two pipes. This force was increased by the increase of the pin rotation. The other contact points were not affected by type of the tension member (Fig. 5-39 and 5-40). Consequently, the ultimate pipe-pin moments were 36% smaller in P7 than P8 and P9, which led to the 11% smaller base shear in P7 than P8 and P9 (Fig. 5-34).

Minimal cracks were formed in all of the models (Fig. 5-41 and 5-42). Essentially no cracks were formed in the pipe-pins without a tension member. The strand and rod forces remained well below the yielding force. The Von Mises stress of the rod reached the yielding criteria under bending and axial combination while the strand did not undergo bending (Fig. 5-11 and 5-12). The friction force in the column-pad interface and the contact force between the pipes were similar in both models (Fig. 5-43 and 5-44).

To conclude, no significant differences were observed in the maximum base shear by changing the tension member in a bent without uplift. The removal of the tension member showed no benefits in the maximum base shear, displacement, and initial stiffness. The ultimate base shear was reduced by removing the tension members. Fewer cracks were formed in the pipe-pin without the tension member compared to the bents with the tension member. Removing the tension members slightly improved the performance of the pipe-pins but the bent was prone to instability. More research is required to address the stability issue. Thus, the removal of the tension members is not recommended.

5.2.5 Concluding Remarks on Parameters of Pipe-Pins

The following conclusions were drawn based on the results of the parametric studies:

1- The pipe-pin moment significantly increased the base shear. Therefore, inclusion of the base moments is necessary for a safe design.
2- Increase of axial force increases the pipe-pin moments. Therefore, the axial load ratio should be included in the calculations of the pipe-pin moments to calculate the base shear.
3- The increase of axial force delays the development of the extension in the tension members and reduces the stress in those members. However, the rod remains in tension under large pipe-pin rotations.
4- The large column axial force produces compressive force in the rod. The development of this force should be prevented by isolating the nuts and rod from concrete.
5- The tapering of the lower pipe improves the behavior of the pipe-pin insignificantly. Therefore, a conical surface for the lower pipe is not necessary.
6- Using strands instead of rods reduces the base shear. The strands remain elastic under large rotations because they are not subjected to flexure. Therefore, it is suggested to use posttensioning strands as the tension members in pipe-pins.

5.3 Bent with Rebar-Pin Column-Shaft Connection for ABC (BRSA)

5.3.1 Introduction

The numerical model that was described in section 4.9.4 for pushover analyses was used to study the influence of different parameters on the performance and capacity of pipe-pins. That

model is referred to as the reference model hereafter. The columns and pedestals were force-based elements (FBEs). The cap beam was elastic. The rebar-pins were modeled using the lumped plasticity model with zero length springs (section 4.9.2.1.1). Table 5-7 lists the parameters and their ranges. The influence of the axial load index and core diameter on the bent response and pin performance were studied. The parameters were changed one at a time.

Previous studies conducted comprehensive parametric studies on the effects of other parameters that are relevant to the present study and were utilized herein. Cheng et al. (2006) conducted parametric studies on the effects of axial load level, column longitudinal steel ratio, and hinge size, the results of which are applied to the design procedure developed in this study.

5.3.2 Effects of Column Axial Force

The axial load influences the capacity and performance of the plastic hinges and rebar-pins. The column axial load index (column ALI) (Eq. 5-1) was used to quantify the axial load level in the bents. Note that the corresponding rebar-pins ALIs were 2.6 times the column ALIs because the rebar-pin diameter was 63% of the column diameter. ALI was 1% in the reference model (R0). Analytical results using four additional models were compared to quantify the effects of the ALI on the performance of the bent. ALIs were 5%, 10%, 15%, and 20% in the models, which were labeled respectively R1, R2, R3, and R4 (Table 5-8). The properties of the springs for the rebar-pins were modified to account for the change of the axial force in the pins. The columns were simulated by FBEs with fiber sections, which automatically accounted for the axial loads in the columns.

The moment-curvature relationships of the rebar-pins are shown in Fig. 5-45. The increase of ALI increased the maximum moments of the rebar-pins, as expected (Table 5-8). The failure modes changed from steel fracture to core concrete failure under ALIs of 15% and higher, which corresponds to 25% or more in rebar-pins. The reinforced concrete sections are designed to be under-reinforced to be ductile. In under-reinforced sections, steel fracture is the mode of failure (Wight and MacGregor, 2009). Figure 5-45 also shows that there is a significant reduction in the moment capacity under moderate curvatures when column ALIs exceeds 10%. To minimize such reduction, it is suggested to keep rebar-pin ALI smaller than 20%. Cheng et al. (2006) also made a similar suggestion based on experimental studies.

The properties of the rebar-pin springs were determined based on the idealized moment-curvature relationships (Fig. 5-47). The stiffness of the rebar-pins did not change significantly by the increase of ALI from 1% to 20%, but the rotation ductility of the pins decreased by 40% from R0 to R4 (Fig. 5-47).

The pushover curves for the bents with different ALIs are shown in Fig. 5-48. The failure mode in all models was compressive failure of the core concrete in the upper column plastic hinges. The rebar-pin rotations were well below their rotational capacity in the pushover analyses. Table 5-8 presents the maximum shear, initial stiffness, and displacement ductility of the bents. Figure 5-49 shows the base shear linearly increased by 40% with the increase of column ALI from 1% to 20%. The initial stiffness was changed less than 20% (Fig. 5-50). The maximum initial stiffness was at ALI=13% based on a second-degree polynomial fit to the data (Fig. 5-50).

The larger ALIs increased the friction capacity of the pins (Fig. 5-49). The friction capacity was determined using a coefficient of friction of 0.45 and clamping force being the total compressive

force in the section obtained from moment-curvature analysis (Cheng, et al., 2006). The slope of the friction capacity versus ALI was steeper than the slope of the base shear versus ALI. The safety factor against friction resistance release was defined as the ratio of the friction capacity of the two pins to the total base shear (Fig. 5-51). It can be seen that the increase of ALI enhanced the safety factor against overcoming the friction capacity.

An increase in ALI reduced the ultimate displacement, which led to the lower column base rotations (Table 5-8). The safety factor against rebar-pin flexural failure was defined as the ratio of the ultimate rebar-pin spring rotation to the maximum column base rotation (Fig. 5-51). It is clear in the figure that the safety factor against flexural failure generally increased with an increase in ALI up to 15%. However, the safety factor was reduced once the mode of rebar-pin failure mode was dominated by compression.

In summary, the increase of ALI increased the forces in the bent and reduced the ultimate displacement and ductility. The present numerical model is able to capture all of these parameters. The safety factor against shear and flexure failure of the rebar-pins increased with the increase of ALI as long as compression did not dominate the failure mode.

5.3.3 Effects of Core Diameter of Rebar-Pin

Figure 5-52 shows the free-body diagram of a rebar-pin. The force couples of T and C generate the rebar-pin moment at the base of the column. T is the tensile force in the reinforcement and C is the compressive force in the concrete. The gross area of the rebar-pin is determined based on the axial dead load in the section (Cheng, et al., 2006). Therefore, the hinge diameter, D_{pin}, is determined from the dead load. To minimize the rebar-pin moment, the arm of the force couple (a in Fig. 5-52) can be reduced by placing the reinforcement close to the center of the rebar-pin. The core diameter is defined as the center-to-center diameter of the longitudinal reinforcement in the rebar-pin sections (Fig. 5-52). The core diameter in the reference model (R0) was 7.25 in [184 mm], which correspond to $\frac{D_{core}}{D_{pin}} = 0.73$. Three additional models with $\frac{D_{core}}{D_{pin}}$ of 0.9, 0.5, and 0.3 with D_{pin} equal to 10 in [254 mm] were selected to study the effects of bundling reinforcement (Table 5-9). The transverse steel was the same in the parametric study. The transverse reinforcement was according to the design provisions in all cases based on the pushover analysis. The pushover results showed that the column base rotation was smaller than the rotation capacity of the rebar-pin springs. The core concrete material properties were modified to account for the change of confining stress due to the change of the core diameter.

The moment-curvature relationships for the models with different core diameters are shown in Fig. 5-53. It can be seen that the decrease of the core diameter caused considerable loss in the moment capacity. The increase in the core diameter increased the maximum moment but reduced the ductility of the rebar-pins (Fig. 5-54 and 5-55). The ultimate moments were 68% and 43% smaller than the maximum moments in R6 and R7, respectively. To account for the strength loss, a quadrilinear idealization of the moment-curvature relationships was developed to determine the properties of the rebar-pin springs. As illustrated in Fig. 5-56 for R7, the moment-curvature behavior was idealized using four parameters: 1) effective yield moment and curvature, 2) the maximum strength, 3) degraded strength, and 4) ultimate curvature.

The ultimate curvature was defined as the smaller of the curvature at failure of the core concrete or curvature at fracture of steel bars. The maximum point was the peak of the

moment-curvature relationship. The initial stiffness of the quadrilinear curve was equal to the secant tangent at initial yielding, which is the curvature at which the outermost bar yielded. Then, the yield point was determined by preserving energy in both curves between the origin and maximum point. Finally, the degraded strength was determined by preserving energy in both curves between the maximum and ultimate point assuming that the degraded and ultimate moments were the same.

Cheng, et al. (2006) model was adopted to calculate the rebar-pin rotations of R6 and R7 using the quadrilinear idealization to model the rotational behavior (section 4.9.2). The rotations corresponding to the first three points were calculated by adding flexural and two bond-slip rotations (Eq. 4-82). The flexural rotation was calculated assuming constant curvature along the hinge gap. The bond rotation was calculated based on the Wehbe (1999) model. The ultimate rotations were calculated assuming that the plastic deformations occur over an equivalent plastic hinge length (Eq. 4-84). The properties of the rebar-pin springs in R0 and R5 were calculated based on the bilinear idealization similar to that in section 4.9.3.

The moment-rotation relationships of the rebar-pin springs for different core diameters are shown in Fig. 5-57. Using the springs for the rebar-pins and FBEs for the columns, the pushover analysis of the bent was conducted in both directions (Fig. 5-58). The average initial stiffnesses, ductilities, base shears, and the ultimate displacements for different core diameters are presented in Table 5-9. The force-displacement relationship of the bent with rebar-pins at base were also compared with that of a bent with “perfect” pins (R8) to develop a better understanding of the effect of the rebar pins. Compared to R8, the use of rebar-pins at the base of the columns increased the base shear, initial stiffness, and ultimate displacement respectively by 41%, 13%, and 4%. However, the rebar-pins reduced the displacement ductility by at least 17% compared to the bent with perfect pins. Even when the pin bars were clustered near the center (core diameter to the pin diameter ratio of 0.3), use of the rebar-pins increased the base shear by 30%. Thus, the influence of the rebar-pin connections at the base of the column is significant and should be included in the calculation of the plastic column shear.

An increase in the core diameter increased the maximum moment of the rebar-pins, which led to larger base shears (Fig. 5-60). However, the base shear was within 8% of the average base shears of R5, R0, R6, and R7. With change of the core diameter, the initial stiffness, ultimate displacement, and displacement ductility remained within the 5% of their average. A decrease in the core diameter adversely influenced the friction capacity, which led to the decrease of safety factor against shear failure (Fig. 5-60). In contrast, concentrating the reinforcement close to the pin center increased the rebar-pin rotational ductility, which led to increase of safety factor against flexural failure (Fig. 5-55 and 5-60). Another downfall of the reduction of the core diameter was the significant softening in force-displacement relationships of R7 because of the loss of flexural strength in the rebar-pins (Fig. 5-57).

To conclude, the effect of the rebar-pin moment on the base shear should be included even when the core diameter is relatively small giving the perception that the pin section is close to being a perfect pin. This is because the presence of concrete in the hinge throat still leads to a compressive normal force that combines with the tensile force of the rebar pin to produce a moment. The decrease of the core diameter reduces the base shear by less than 10% but increases the risk of the shear failure in the rebar-pins. The core diameters in the range of 50-70% of the pin diameters showed the optimum safety factor and insignificant loss of strength.

5.3.4 Concluding Remarks on Parameters of rebar-Pins

The following conclusions were drawn based on the results of the parametric studies:

1- The rebar-pin moment should be included in calculation of the base shear.
2- The axial force needs to be less than 20% of the rebar-pin ultimate compressive capacity to avoid strength loss.
3- An increase of axial force improves the safety factor against shear friction failure of the rebar-pins.
4- The increase of the axial load improves the flexural safety factor as long as the mode of failure of the rebar pin is not dominated by compressive failure of the concrete in the pin.
5- The reduction of the core diameter increases the ductility and reduces the pin moment. However, the core diameters smaller than 50% of the section cause softening in the force-displacement of the bent and are not desirable.

5.4 Concluding Remarks on Parametric Studies

The parametric studies presented in this chapter showed that the pin performance influences the base shear significantly. The results showed that the pipe-pin and rebar-pin moments respectively increase the base shear at least 20% and 30%. The Caltrans SDC does not include any moments at the pinned footings to account for the increase in the column plastic shear. The pin moment needs to be taken into account to avoid column shear failure and damage to capacity-protected members.

The results from the parametric studies presented in this chapter were used in addition to the experimental and analytical results described in previous chapters to develop design methods for pins. The design method and illustrative examples are presented in the next chapter.

6 Proposed Design Methods for Pin Connections

6.1 Introduction

The details of the proposed design methods for "pinned" connections of column to pile-shaft are presented in this chapter based on the experimental and analytical studies presented in previous chapters. The effect of different variables on the behavior of the pipe-pins and rebar-pins was discussed in Chapter 5. The findings of the present study were combined with those from previous studies and design codes to develop a practical design procedure.

For each pin type, methods to calculate the force and moment demand of the pin elements are discussed first followed by a step-by-step design procedure and detailing for each element. Illustrative design examples for pipe-pin and rebar-pin connections are also presented in this chapter to clarify the application of the proposed methods.

6.2 Pipe-Pin Connection of Columns to Pile-Shafts

6.2.1 Introduction

Pipe-pin connection of column to pile-shaft is designed to transfer column shear and axial force while minimizing the moment transfer between the column and the pile-shaft. The pipes transfer column shear to the pile. A tension member within the pipes transfers the column uplift force. A pad at the interface of the column and pile-shaft provides rotational capacity and transfers the compressive column axial force. The experimental and analytical studies showed that the interaction of the forces in the column pile-shaft connection produced some moment at the connection. A simple spring model was proposed in Chapter 4 to determine the pipe-pin moment and tension-member force based on the mechanics of solids principles.

Zaghi and Saiidi (2010) proposed a method to design pipe-pin connections between column and cap beam for shear. Based on that study, the failure mode of a pipe embedded in a small body of concrete (e.g. a column) is shear cracking of the column. However, the failure mode of a pipe that is surrounded by a large body of concrete (e.g. the cap beam) is the bearing failure of concrete against the pipe or pure shear failure of the pipe. The Zaghi and Saiidi (2010) provisions for the pipe that is embedded in column are adopted for the design requirements of the lower pipe in the pipe-pin connection of columns to pile-shafts.

Mehrsoroush and Saiidi (2014) proposed a method to design pipe-pin connections at the column base. They proposed a method to design the upper pipe of the pipe-pin based on the Zaghi and Saiidi (2010) provisions for a pipe embedded in concrete. In the method proposed in the present study, the upper pipe of the pipe-pins in column to pile-shaft connections is designed according to the Mehrsoroush and Saiidi (2014) method.

6.2.2 Design Force and Moment Demand

Pipe-pins are designed as capacity-protected members to remain undamaged during large earthquakes. Therefore, pipe-pins are designed to resist the forces generated when the structure reaches its collapse limit state. The global mechanism associated with plastic hinging at the top of columns is defined as the collapse limit state. The force and moment demands on pipe-pin connections are calculated based on static equilibrium in this mechanism. The force

and moment demands are formulated in this document for a two-column bent, but a similar procedure applies to bents with multiple columns.

6.2.2.1 Column Plastic Moment

The moment-curvature relationship of the column section is calculated using the expected material properties. Subsequently, the moment-curvature relationship is idealized by an elastoplastic curve by preserving energy in both curves as shown in Fig. 6-1 (Caltrans, 2010). The maximum moment in the idealized curve is the plastic moment, $M_{p,col}$.

6.2.2.2 Pipe-Pin Moment

The pipe-pin moment,$M_{u,pin}$, is developed by the compressive force in the pad and the contact force between the pipes (Fig. 6-2). It was explained in chapter 4 and 5 that the moment due to pipe contact was less than 10% of the total pipe-pin moment. Therefore, it was not included in the calculation of pin moment. A linear rotational spring was proposed in section 4.8.3 to calculate the pipe-pin moments. The pipe-pin moment at the column base is estimated by the following equations.

$$M_{u,pin} = \frac{M_g}{\theta_g} \times \theta_{u,pin} \tag{6-1}$$

$$\theta_g = \frac{2\, t_{pad}}{D_{col}} \tag{6-2}$$

$$M_g = \frac{K_{c.pad}}{K_{c.pad} + K_{tm}} \left(\frac{OD_{pad}}{2} K_{tm} \theta_g + P \right) \times \frac{OD_{pad}}{2} \tag{6-3}$$

$$K_{tm} = \frac{E_{tm} \times A_{tm}}{L_{tm}} \tag{6-4}$$

$$K_{c,pad} = \frac{E_{pad} \times A_{pad}}{t_{pad}} \tag{6-5}$$

where,

A_{tm}: cross-sectional area of tension member (center rod or tendon), in^2 [mm^2]

A_{pad}: plan view area of the pad, in^2 [mm^2]

D_{col}: column diameter, in [mm]

E_{pad}: modulus of elasticity of the pad, ksi [MPa]

E_{tm}: modulus of elasticity of the tension member, ksi [MPa]

$K_{c.pad}$: compressive stiffness of the pad, kip/in [kN/mm]

K_{tm}: axial stiffness of the tension member, kip/in [kN/mm]

L_{tm}: effective length of the tension member, center-to-center of the nuts (Fig. 6-3), in [mm]

M_g: moment to close the gap

$M_{u,pin}$: base moment at the pipe-pin, kip.in [kN.m]

OD_{pad}: outer diameter of the pad, in [mm]

P: column axial force, positive sign for compression, kip [kN]

θ_g: rotation to close the gap, rad

$\theta_{u,pin}$: ultimate base rotation, estimated equal to the drift ratio, rad

t_{pad}: pad thickness, in [mm]

6.2.2.3 Column Shear

The shear demand on the column and adjacent members are associated with the overstrength column moment. The column moment capacity is magnified to account for material strength variation and a column moment capacity that could exceed the idealized plastic moment capacity (Caltrans, 2010). Based on the parametric studies described in the previous chapter, the proposed pipe-pin spring properties led to an overestimation of the pipe-pin moment by 26% compared to the FE model, which led to 18% overestimation of the base shear. Therefore, magnification of the pipe-pin moment is not recommended in calculating the column base shear in design. The overstrength column moment, $M_{o,col}$, and shear demand, $V_{u,col}$, are calculated using the following relationships.

$$M_{o,col} = 1.2M_{p,col} \tag{6-6}$$

$$V_{u,col} = \frac{M_{o,col} + M_{u,pin}}{H_c} \tag{6-7}$$

where,

H_c: column clear height, in [mm]

$M_{o,col}$: column overstrength moment, kip.in [kN.m]

$M_{u,pin}$: pipe-pin base moment, kip.in [kN.m]

$V_{u,col}$ column shear demand, kip [kN]

Consequently, the overstrength base shear in the bent, $V_{u,bent}$, is the summation of the column shears as follows.

$$V_{u,bent} = \sum V_{u,col} \tag{6-8}$$

where

$V_{u,bent}$: overstrength base shear in bent, kip [kN]

6.2.2.4 Column Axial Force

The dead load generates equal axial forces in the columns of a symmetric bent. The overturning moment, OM, redistributes the axial force in the columns by increasing the axial force in one column and decreasing it in the other column. In the cases that the overturning moment is larger than the dead load moment, an uplift force is generated in the column. Based on static equilibrium, the uplift and compressive column forces are calculated using the following equations.

$$OM = V_{u,bent} \times H - 2M_{u,pin} \tag{6-9}$$

$$T_{u,col} = P_{dl} - \frac{OM}{S} \quad (6\text{-}10)$$

$$P_{u,col} = P_{dl} + \frac{OM}{S} \quad (6\text{-}11)$$

where,

H : bent height from top of pile-shaft to the center of the deck, in [mm]

OM : overturning moment, kip.in [kN.m]

S: center-to-center distance between columns, in [mm]

P_{dl}: column axial force due to the dead load, kip [kN]

$T_{u,col}$: column uplift force, which is positive for compressive forces, kip [kN]

$P_{u,col}$ column compressive force, which is positive for compressive forces, kip [kN]

6.2.2.5 Tension Member Force

The axial force in the pin tension member is calculated according to the following equation, which was derived in section 4.8.3 based on the mechanics of solids principles.

$$T_{u,tm} = \frac{K_{tm}}{K_{c.pad} + K_{tm}} \left(\frac{OD_{pad}}{2} K_{c.pad} \theta_{u,pin} - P\right) \quad (6\text{-}12)$$

where,

$K_{c.pad}$: compressive stiffness of the pad from Eq. 6.5, kip/in [kN/mm]

K_{rod}: axial stiffness of the tension member from Eq. 6.4, kip/in [kN/mm]

P: column axial force, kip [kN]

6.2.2.6 Threaded Rod Moment Demand

The column uplift force and pipe-pin rotation generate the tensile force in the rod. As the upper pipe tends to move laterally and rotates, the partial fixity of the rod-end plate connection produces moment in the rod. The rod moment demand is calculated according to the recommendations by Mehrsoroush and Saiidi (2014), assuming that the upper pipe rotates as a rigid body.

$$M_{u,rod} = \frac{3\, E_{rod}\, I_{rod}}{L_{rod}^2} \delta_{rod} \quad (6\text{-}13)$$

$$\delta_{rod} = \theta_{u,pin}\, H_{upper} \quad (6\text{-}14)$$

where,

δ_{rod}: displacement of the top nut of rod relative to the pile-shaft surface, in [mm]

E_{rod}: modulus of elasticity of the rod, ksi [MPa]

L_{rod}: effective length of the rod center-to-center of nuts, in [mm]

H_{upeer}: the distance of top nut from the top of the pile-shaft, in [mm]

I_{rod}: moment inertia of rod section, in^4 [mm^4]

6.2.2.7 Impact Force between the Pipes

The upper pipe impacts the lower pipe subsequent to the friction release. The impact increases with the increase in the gap and stiffness of the column. Zaghi and Saiidi derived the following equation to calculate the impact force assuming that the column behaves as a cantilever column subsequent to the friction release. They also assumed that the impact duration is one-quarter of the natural period of the column (Zaghi and Saiidi, 2010). The impact force is calculated from the following equation.

$$F_{impact} = 0.9 \times \sqrt{\frac{P_{dl}\, G_h\, EI_{cr,col}}{H_c^3}} \tag{6-15}$$

where,

G_h: gap between lower and upper pipes, in [mm]

E : modulus elasticity of the column concrete, ksi [MPa]

$I_{cr,col}$: cracked moment of inertia of the column, in^4 [mm^4]

H_c: clear height of the column, in [mm]

6.2.2.8 Lower Pipe and Upper Pipe Shear Demand

The shear demand in the pipes is the summation of the column shear and the impact force. Analytical studies showed that a portion of the column shear is transferred through friction in the column-pad interface of the column under compression. This friction was negligible on the tension side of the bent. Conservatively, the shear demands on the lower and upper pipes are calculated ignoring friction in column-pad interface.

$$V_{u,pipes} = V_{u,col} + F_{impact} \tag{6-16}$$

6.2.3 Design Capacities

6.2.3.1 Lower Pipe

The lower pipe is designed to resist the column shear and the impact force according to the following equation.

$$V_{u,pipes} = V_u + F_{impact} \leq \phi\, V_{n,lower} \tag{6-17}$$

where,

$V_{n,lower}$: nominal lower pipe shear strength, kip [kN]

ϕ: strength reduction factor, which is 0.75 according to Zaghi and Saiidi (2010) recommendation

Base on the Zaghi and Saiidi studies, two modes of failure were found for the pipe in the pile-shaft:

1- Pipe shear failure, $V_{n,lower}^{pipe}$.

2- Shear cracking of concrete, $V_{n,lower}^{pile}$.

Thus, the nominal shear capacity of the lower pipe is as follows.

$$V_{n,lower} = \min\left(V_{n,lower}^{pipe}, V_{n,lower}^{pile} \right) \tag{6-18}$$

where,

$V_{n,lower}^{pipe}$: nominal lower pipe shear capacity, kip [kN]

$V_{n,lower}^{pile}$: nominal cracking shear capacity of pile-shaft, kip [kN]

Base on the AISC Steel Manual, the pipe shear capacity is as follows.

$$V_{n,lower}^{pipe} = \frac{F_{y,pipe}}{\sqrt{3}} A_{pipe} \tag{6-19}$$

where,

$F_{y,pipe}$: pipe yield strength, ksi [MPa]

A_{pipe}: pipe gross section area, in^2 [mm^2]

The shear cracking failure modes respectively for a pile-shaft under zero axial force and its maximum effective axial force are shown in Fig. 6-4a and Fig. 6-5a. The shear cracking capacity is calculated by nonlinear interpolation between the two lateral load capacities using the following steps:

Step-1: Determine the lower bound shear capacity corresponding to zero axial load on the pile-shaft. The lower bound shear capacity is calculated based on the simplified procedure by Zaghi and Saiidi (2010). The free-body diagram of the lower pipe is shown in Fig. 6-6. The depth of the pipe plastic hinge, L_1, is calculated using the following equation assuming uniform bearing stress distribution, f_c^*.

$$L_1 = \sqrt{e^2 + \frac{2M_P}{OD_{lower} f_c^*}} - e \tag{6-20}$$

where,

L_1: depth of pipe plastic hinge from the pile surface

f_c^*: concrete bearing stress, ksi [MPa]

M_p: pipe plastic moment, in^2 [mm^2]

e: eccentricity of the pipes contact point from pile-shaft surface, in [mm]

OD_{lower}: lower pipe outer diameter, in [mm]

The experimental studies by Zaghi and Saiidi (2010) showed that the bearing stress against the pipe can be taken as f_c'. Based on the parametric studies conducted in the current project, the contact point is at the top of the pipe when the pipe is not tapered. The point of contact is at

the middle of the protruded segment when the pipe is tapered with a slope of 4% or more. The current parametric studies also showed that tapering of the lower pipe was not advantageous; therefore, tapering of the pipe is not recommended. The eccentricity of pipe contact point is equal to the protruded length in the lower pipe when the taper is zero.

$$e = L_{protrude} \tag{6-21}$$

where,

$l_{protrude}$: distance from the top of the lower pipe to the top of the pile-shaft, in [mm]

Base on static equilibrium, the lateral of force is determined using the following equation.

$$H_u = L_1 OD_{lower} f_c^* \tag{6-22}$$

Substituting the parameters in Eq. (6-22), the lower-bound shear capacity corresponding to zero axial force on the pile is calculated from following equation.

$$V_{n,lower}^{noAxial} = \left(\sqrt{L_{protruded}^2 + \frac{2M_p}{OD_{lower} \times f_c'}} - L_{protruded} \right) \times OD_{lower} f_c' \tag{6-23}$$

where,

$$M_p = Z_{pipe} F_{y,pipe} \tag{6-24}$$

Z_{pipe}: plastic section modulus, in^3 [mm^3]

Zaghi and Saiidi also proposed a more complex set of formulations to calculate the lower bound shear cracking strength by accounting for each resisting force separately. The resisting forces are shear and tensile resistance of concrete, column spiral, inner spiral, and any jacket (Fig. 6-4b-d).

Step-2: Determine the upper bound shear capacity corresponding to the maximum effective axial load. The upper bound shear strength, $V_{n,lower}^{maxAxial}$, is associated with the maximum effective axial load defined as the axial load beyond which no increase in the shear resisting is observed. The failure mechanism is shown in Fig. 6-5a. Zaghi and Saiidi (2010) suggested the maximum axial load capacity to be determined based on Eq. 3.21 of Seismic Design Criteria (Caltrans, 2010).

$$P_{max,pile} = \begin{cases} 1A_{c,lower}' \ (ksi) \\ 0.007A_{c,lower}' \ (MPa) \end{cases} \tag{6-25}$$

where,

A_c': horizontal projection of the cracking plane Eq. (6-26) , in^2 [mm^2]

Assuming the cracking plane starts from the edge of the bearing pad (Fig. 6-5a), the horizontal projection of the cracking plane, $A_{c,lower}'$, is calculated from the following equation.

For circular pile-shafts: $A'_{c,lower} = \frac{2\pi - 2\alpha_l + \sin(2\alpha_l)}{2}\left(\frac{D_{pile}}{2}\right)^2 - \frac{\pi OD_{lower}^2}{4}$ (6-26)

where,

$$\alpha_l = arcos\left(\frac{D_{pad}}{D_{pile}}\right)(radians) \quad (6\text{-}27)$$

D_{pile}: pile-shaft diameter, in [mm]

D_{pad}: outer diameter of bearing pad, in [mm]

OD_{lower}: outer diameter of lower pipe, in [mm]

Figure 6-5 shows the three components of the resisting force in the upper bound failure mechanism:

1- Concrete shear strength (Fig. 6-5b), $V'_{c,lower}$.

2- Dowel action of the steel pipes (Fig. 6-5b), $V'_{p,lower}$.

3- Column spiral effect (Fig. 6-5c and 6-5d), $V'_{sp,lower}$.

The parametric studies by Zaghi and Saiidi showed that the angle of cracking plane was 54 degree. The upper limit of concrete shear strength suggested by Caltrans was used to calculate the concrete capacity (Zaghi and Saiidi, 2010 and Caltrans, 2010)

$$V'_{c,lower} = 0.8\, A'_{c,lower}\, f'_v \tan(54°) \quad (6\text{-}28)$$

where,

$$f'_v = \begin{cases} 0.142\sqrt{f'_c}\ (ksi) \\ 0.374\sqrt{f'_c}\ (MPa) \end{cases} \quad (6\text{-}29)$$

The dowel action of the steel pipe is calculated based on the lateral load resisted by the bending of the cantilever pipe from the following equation.

$$V'_{p,lower} = \frac{M_p}{\frac{D_{pad} + D_{lower}}{2}\tan(54°)} = \frac{1.45M_p}{D_{pad} + OD_{lower}} \quad (6\text{-}30)$$

where,

M_p: lower pipe plastic moment Eq. (6-24), kip.in [kN.m]

The shear resistance of the spirals is calculated assuming that one-half of the spirals have reached the yield strength simultaneously.

$$V'_{sp,lower} = \frac{0.34\, A_{sp} f_{ys} d_{pile}(\cos(\alpha_l)\sin(\alpha_l) + \pi - \alpha_l)}{s_{pile}} \text{ (Zaghi and Saiidi, 2010)} \quad (6\text{-}31)$$

where,

A_{sp}: spiral sectional area in pile-shaft, in^2 [mm^2]

d_{pile}: center-to-center diameter of pile-shaft spiral, in [mm]

f_{ys}: yield strength of spirals, ksi [MPa]

α_l: from equation Eq. (6-27)

s_{pile}: pitch of spiral, in [mm]

Therefore, the upper bound shear cracking strength is:

$$V_{n,lower}^{maxAxial} = V'_{c,lower} + V'_{p,lower} + V'_{sp,lower} \tag{6-32}$$

Step-3: Interpolate between the two based on the column maximum axial load. The lateral load capacity of the pipe-pin, $V_{n,lower}$, is calculated by interpolating between the lower bound and upper bound shear cracking strength using the following equation.

$$V_{n,lower}^{pile} = V_{n,lower}^{noAxial} + \left(V_{n,lower}^{maxAxial} - V_{n,lower}^{noAxial} \right) \left(\frac{P_u}{P_{max,pile}} \right)^{0.7} \tag{6-33}$$

In summary, the procedure to calculate the lower pipe shear capacity is to

1- Determine the pipe shear capacity by Eq. (6-19)
2- Determine the pile shear cracking capacity for zero axial force by Eq. (6-23)
3- Determine the pile shear cracking capacity for the maximum axial force by Eqs. (6-26) to (6-32).
4- Determine the maximum effective axial force using Eq. (6-25).
4- Determine the pile shear cracking capacity for the ultimate axial force by interpolation using Eq. (6-33).
5- Determine the nominal shear capacity of the lower pipe using Eq. (6-18)
6- Determine the allowable shear capacity of the lower pipe by using a strength reduction factor of 0.75.

6.2.3.2 Upper Pipe

The upper pipe is designed by the method proposed by Mehrsoroush and Saiidi (2014) in three steps:

Step 1: Calculate the lower bound shear resistance associated with no axial force. The failure mode associated with no axial force in the column is shown in Fig. 6-7a. The lower bound shear resistance of this failure mode is calculated using the following iterative procedure:

Step 1-A) Estimate the flexural capacity of the upper pipe, M_p, using the following equation.

$$M_p = Z_{pipe} F_{y,pipe} \tag{6-34}$$

Z_{pipe}: plastic section modulus, in^3 [mm^3]

Step 1-B) Determine the location of the plastic hinge, L_2. Assuming that the bearing stress of concrete against the upper pipe, f_c^* in Fig. 6-7a, is uniform and the contact point of the pipes is

at the top of the lower pipe, the plastic hinge depth of the upper pipe in the column is calculated using the following equations.

$$L_2 = \sqrt{{e_2}^2 + \frac{2M_P}{OD_{upper} f_c^*}} + e_2 \tag{6-35}$$

$$e_2 = L_{protroded} - t_{pad} \tag{6-36}$$

where,

L_2: depth of pipe plastic hinge in the column from the bottom of column

f_c^*: equivalent concrete bearing stress, ksi [MPa]

M_p: pipe plastic moment using, in^2 [mm^2]

e_2: eccentricity inside the pipe, in [mm]

$l_{protruded}$: the distance from the top of the lower pipe to the bottom of column, in [mm]

OD_{upper}: upper pipe outer diameter, in [mm]

In the first iteration, the bearing strength may be assumed f_c'.

Step 1-C) Calculate the equivalent bearing stress of concrete against the upper pipe. Two components contribute to the shear resistance of the pipe in the column: tensile and shear strength of concrete (Fig. 6-7b) and tensile strength of the column spirals (Fig. 6-7c). The resistance provided by concrete is calculated based on the minimum limits for the shear and tensile capacity of concrete suggested by Caltrans Seismic Design Criteria using following equations.

$$V_c = 0.8 f_v A_c + f_t \left(D_{col} - OD_{upper}\right) L_2 \tag{6-37}$$

$$A_c = \frac{\pi (D_{col}^2 - OD_{upper})}{8} \tag{6-38}$$

$$f_v = \begin{cases} 0.095\sqrt{f_c'}\ (ksi) \\ 0.25\sqrt{f_c'}\ (MPa) \end{cases} \tag{6-39}$$

$$f_t = \begin{cases} 0.24\sqrt{f_c'}\ (ksi) \\ 0.62\sqrt{f_c'}\ (MPa) \end{cases} \tag{6-40}$$

where,

A_c: horizontal projected area of cracked section, in^2

f_v : lower bound concrete shear strength, ksi [MPa]

f_t: lower bound concrete tensile strength, ksi [MPa]

D_{col}: column diameter, in [mm]

OD_{upper}: upper pipe outer diameter, in [mm]

The resistance provided by the column spiral is calculated using the following equation (Mehrsoroush and Saiidi, 2014).

$$V_{sp} = \frac{1}{4}\left(\frac{f_{ys}A_{sp}\pi d_{col}}{4s_{col}} + \frac{f_{ys}A_{sp}2L_2}{s_{col}}\right) \quad (6\text{-}41)$$

where,

A_{sp}: spiral sectional area in column, in^2 [mm^2]

d_{pile}: center-to-center diameter of column spiral, in [mm]

f_{ys}: yield strength of spirals, ksi [MPa]

α_1: Eq. (6-27)

s_{col}: pitch of spiral, in [mm]

L_2: The depth of plastic hinge using Eq. (6-35), in [mm]

Therefore, the equivalent bearing stress of the upper pipe is calculated using the following relationships. The upper limit in this equation is the bearing strength of concrete against the upper pipe in the presence of the inner spiral.

$$f_c^* = \frac{V_c + V_{sp}}{OD_{upper} \times L_2} \leq \begin{cases} \frac{\sqrt{f_c'}}{2.43}\left(2.95 - \frac{\sqrt[3]{OD_{upper}}}{3.35}\right) f_c' \\ \frac{\sqrt{f_c'}}{6.38}\left(2.95 - \frac{\sqrt[3]{OD_{upper}}}{9.85}\right) f_c' \end{cases} \quad (6\text{-}42)$$

The updated f_c^* is inserted in Eq. (6-35) to calculate the plastic hinge depth, L_2. Iterations are required if the calculated $L_2$is not sufficiently close to the assumed value.

Step 1D) Calculate the lateral load capacity corresponding to zero axial force, which is equal to the summation of the resisting forces.

$$V_{n,upper}^{noAxial} = V_c + V_{sp} = f_c^*\, OD_{upper} L_2 \quad (6\text{-}43)$$

Step 2: Calculate the upper bound shear resistance associated with the maximum effective axial force. The upper bound shear cracking resistance associated with the maximum effective axial force is the lateral force capacity of the upper pipe corresponding to the failure mode as shown in Fig. 6-8. Similar to the lower pipe, three components provide the lateral force capacity:

1. Concrete shear strength (Fig. 6-8b), $V'_{c,upper}$.
2. Dowel action of the steel pipes (Fig. 6-8c), $V'_{p,upper}$.
3. Column spiral effect (Fig. 6-8d), $V'_{sp,upper}$.

Assuming the angle of cracked plane is 54 degree and using the upper limit of concrete shear strength specified by Caltrans, the concrete capacity is calculated using the following equation (Mehrsoroush and Saiidi, 2014 and Caltrans, 2010).

$$V'_{c,upper} = 0.8\, A'_c\, f'_v \tan(54°) \tag{6-44}$$

where,

$$f'_v = \begin{cases} 0.142\sqrt{f'_c}\ (ksi) \\ 0.374\sqrt{f'_c}\ (MPa) \end{cases} \tag{6-45}$$

$$A'_c = \frac{2\pi - 2\alpha_u + \sin(2\alpha_u)}{2}\left(\frac{D_{col}}{2}\right)^2 - \frac{\pi\, OD^2_{upper}}{4} \tag{6-46}$$

$$\alpha_u = arcos\left(\frac{D_{pad}}{D_{col}}\right)(radian) \tag{6-47}$$

The dowel strength of the upper pipe is calculated based on the lateral load resisted by the bending of the cantilever pipe from the following equation.

$$V'_{p,upper} = \frac{1.45M_p}{D_{pad} - 1.45e_2} \tag{6-48}$$

where,

M_p: pipe plastic moment Eq. (6-24), kip.in [kN.m]

The shear resistance by the spirals is calculated assuming one-half of the spirals have yielded.

$$V'_{sp,upper} = \frac{0.34\, A_{sp} f_{ys} d_{col}(\cos(\alpha_u)\sin(\alpha_u) + \pi - \alpha_u\,)}{s_{col}} \tag{6-49}$$

where,

A_{sp}: spiral sectional area in pile-shaft, in^2 [mm^2]

d_{col}: center-to-center diameter of pile-shaft spiral, in [mm]

f_{ys}: yield strength of spirals, ksi [MPa]

α_u: using Eq. (6-47), rad

s_{col}: pitch of spiral, in [mm]

Therefore, the total upper bound lateral resistance is:

$$V^{maxAxial}_{n,upper} = V'_{c,upper} + V'_{p,upper} + V'_{sp,upper} \tag{6-50}$$

Step-3: Interpolate between the lower and upper bounds of shear resistance for the column axial force. The lateral load capacity of the pipe-pin, $V_{n,upper}$, is calculated by interpolating between the lower and upper bound lateral resistance using the following equation.

$$V_{n,upper} = V^{noAxial}_{n,upper} + \left(V^{maxAxial}_{n,upper} - V^{noAxial}_{n,upper}\right)\left(\frac{P_u}{P_{max,col}}\right)^{0.7} \tag{6-51}$$

$$P_{max,col} = \begin{cases} 1A'_{c,upper}\ (ksi) \\ 0.007A'_{c,upper}\ (MPa) \end{cases} \quad (6\text{-}52)$$

Finally, the available lateral resistance of the upper pipe is determined from the following equation.

$$V_{u,pipes} \leq \phi\ V_{n,upper} \quad (6\text{-}53)$$

where,

$V_{n,upper}$: nominal lower pipe shear strength, kip [kN]

ϕ: strength reduction factor, which is 0.75 according to Zaghi and Saiidi (2010)

6.2.3.3 Tension Members

6.2.3.3.1 Threaded Rod

The threaded rod is designed for the combination of the tensile force and bending. The column uplift force and pipe-pin rotation generate the tensile force in the rod (section 6.2.2.5). When the upper pipe rotates, the rod is bent at the top plate producing a bending moment (section 6.2.2.6). The interaction of tension and flexure should be satisfied according to AASHTO LRFD Bridge Design Specification as follows (Mehrsoroush and Saiidi, 2014 and AASHTO, 2012).

$$\text{if}\frac{T_{u,rod}}{T_{r,tm}} < 0.2\ \text{ then, } \frac{T_{u,rod}}{2T_{r,rod}} + \frac{M_{u,rod}}{M_{r,rod}} \leq 1.0 \quad (6\text{-}54)$$

$$\text{if}\frac{T_{u,rod}}{T_{r,tm}} \geq 0.2\ \text{ then, } \frac{T_{u,rod}}{T_{r,rod}} + \frac{8}{9}\frac{M_{u,rod}}{M_{r,rod}} \leq 1.0 \quad (6\text{-}55)$$

$$M_{r,rod} = \phi_f\ M_{n,rod} \quad (6\text{-}56)$$

$$M_{n,rod} = \min(M_{p,rod}, 1.6M_{y,rod}) \quad (6\text{-}57)$$

$$M_{p,rod} = F_{y,rod}\ Z_{rod} \quad (6\text{-}58)$$

$$M_{y,rod} = F_y\ S_{rod} \quad (6\text{-}59)$$

$$Z_{rod} = \frac{D_{rod}^3}{6} \quad (6\text{-}60)$$

$$S_{rod} = \frac{\pi D_{rod}^3}{32} \quad (6\text{-}61)$$

$$T_{r,tm} = \min(\phi_y F_{y,tm} A_{g,tm}, \phi_u F_{u,tm} A_{g,tm}) \quad (6\text{-}62)$$

where,

$T_{u,rod}$: factored tensile demand of threaded rod, kip [kN]

$T_{r,tm}$: factored tensile capacity of threaded rod, kip [kN]

$M_{u,rod}$: moment demand on threaded rod, kip.in [kN.mm]

$M_{r,rod}$: factored flexural capacity of threaded rod, kip.in [kN.mm]

$M_{n,rod}$: nominal flexural capacity of threaded rod, kip.in [kN.mm]

$M_{p,rod}$: plastic moment of threaded rod, kip.in [kN.mm]

$M_{y,rod}$: yield moment of threaded rod, kip.in [kN.mm]

Z_{rod}: plastic section modulus of threaded rod, in^3 [mm^3]

S_{rod}: elastic section modulus of threaded rod, in^3 [mm^3]

D_{rod}: threaded rod nominal diameter, in [mm]

ϕ_f: strength reduction factor for flexure, which is 1.0

ϕ_y: strength reduction factor for yielding of tension member, which is 0.95

ϕ_u: strength reduction factor for fracture of tension member, which is 0.80

6.2.3.3.2 Strands

Strands are designed only for tension using the following equations.

$$T_{u,tm} < T_{u,strand}$$

$$T_{r,tm} = \min(\phi_y F_{y,tm} A_{g,tm}, \phi_u F_{u,tm} A_{g,tm}) \quad (6\text{-}63)$$

where,

$T_{u,strand}$: factored tensile demand of strand, kip [kN]

6.2.3.3.3 Studs

The studs are designed to transfer the entire tensile capacity of the tension member to concrete through shear in the studs welded on the pipes. The shear capacity of one stud embedded in concrete, $V_{r,stud}$, is calculated according to ACI-318 in the absence of an equation in AASHTO LRFD (AASHTO, 2010).

$$V_{r,stud} = \phi_{v,studs}\, f_u\, A_v \leq \frac{T_{r,tm}}{n_{studs}} \quad (6\text{-}64)$$

where,

$V_{r,stud}$: shear capacity of one stud, kip [kN]

$\phi_{v,studs}$: strength reduction factor for shear of studs, which is 0.65

f_u: specified tensile strength of shear studs, ksi [MPa]

A_v: cross-sectional area of shear stud, in^2 [mm^2]

n_{studs}: number of studs on each pipe

$T_{r,rod}$: factored tensile capacity of threaded rod from Eq. (6-62), kip [kN]

6.2.4 Detailing Recommendations

6.2.4.1 Upper Pipe Height

Shorter pipes tend to postpone the contact between the rod and the lower pipe but increase the possibility of diagonal concrete cracking in the column near the pipe. To anchor the upper pipe in the column, the spacing of the studs should be sufficiently large to allow development of the stud ultimate capacity. Based on the Mehrsoroush and Saiidi (2014) suggestions, the height of the upper pipe is recommended to be $0.2H_c \leq H_{upper} \leq 0.25H_c$, with H_c being the column clear height.

6.2.4.2 Lower Pipe Height

Short embedment of the lower pipe might lead to loss of bond between concrete and the pipe and rigid body rotation of the pipe in the pile-shaft. To prevent this mode of failure, Zaghi and Saiidi (2010) suggested a minimum pipe embedment length of $4.5OD_{lower}$. In addition, the lower pipe needs to be anchored in the pile-shaft to carry the tensile force of the rod or strand. Therefore, the minimum limit for the anchorage of the upper pipe is also applicable to the lower pipe. The lower pipe embedment length should be the larger of the followings.

$$\mathrm{L}_{embed,lower} \geq \begin{cases} 0.2H_c \\ 4.5OD_{lower} \end{cases} \tag{6-65}$$

where,

$L_{embed,lower}$: embedment length of the lower pipe, in [mm]

OD_{lower}: outer diameter of the lower pipe, in [mm]

H_c: clear height of the upper pipe, in [mm]

6.2.4.3 Lower Pipe Protruded Length

Excessive protruded length may cause double-curvature bending of the inner pipe inside the upper pipe resulting in a higher base shear. A length of $1.2OD_{lower}$ is recommended to prevent double curvature bending up to 12% drift of the bent (Mehrsoroush and Saiidi, 2014 and Zaghi and Saiidi, 2010).

6.2.4.4 Lower Pipe Diameter

The inner diameter of the lower pipe should be sufficiently large to prevent bearing of the rod on the inner edge of the lower pipe. Previous studies have shown that bearing of the rod on the inner edge of the lower pipe significantly increases the stress on rods but does not affect the demand on the strands (Mehrsoroush and Saiidi, 2014). Based on the linear interpolation of the rod displacement, the following relationships should be satisfied to prevent bearing of the rod on the edge of the inner pipe.

$$ID_{lower} \geq 2\delta_{rod}\frac{L_{rod@pipe}}{L_{rod}} + D_{rod} \tag{6-66}$$

$$L_{rod@pipe} = L_{embed,lower} + l_{protruded} \tag{6-67}$$

where,

δ_{rod}: displacement of the top nut of rod relative to the pile-shaft surface, Eq. (6-14), in [mm]

t_{pad}: pad thickness , in [mm]

6.2.4.5 Pipes Thickness

Local buckling of the lower pipe under shear and impact force should be prevented by using sufficiently thick pipe. The width-to-thickness ratio for the compact section according to AISC Steel specification is suggested for the lower pipe. Additionally, a practical minimum thickness of 0.5 in [13mm] is suggested.

$$\frac{OD_{lower}}{t_{lower}} \leq \frac{0.07E}{F_{y,pipe}} \tag{6-68}$$

where,

t_{lower}: lower pipe thickness, in [mm]

6.2.4.6 Studs

Closely spaced and unsymmetrical arrangement of shear studs may lead to diagonal cracking of concrete. Sufficient clearance should be provided around the studs to allow the development of the ultimate capacity of the studs. One-quarter of the pipe length ($0.25L_{embed,lower}$ or $0.25H_{upper}$) is recommended for the spacing of the stud layers. The studs should be uniformly distributed around the pipe and in each layer (Mehrsoroush and Saiidi, 2014).

6.2.4.7 Gap between Lower and Upper Pipe

The gap between the pipes needs to be sufficiently large to facilitate construction and allow for some rotation prior to gap closure. However, a large gap is detrimental because of the resulting horizontal slippage. A gap of $\frac{OD_{lower}}{16}$ between the lower and outer pipes provides sufficient rotational capacity for the pipes to rotate in the protruded part (Zaghi and Saiidi, 2010).

6.2.4.8 Tension Member Posttensioning

Creep of the rubber pad and dead load might compress the column, leading to a gap between the nuts and the end plates in the upper rod-plate connection. Such a gap postpones the activation of the tension member. Therefore, a minimal posttensioning of the strands and rods is recommended to ensure tight tension members.

6.2.4.9 Rubber Pad Thickness

The rubber pad thickness should be sufficiently large to prevent the closure of the gap between the column and the pile shaft. The pad thickness can be determined by the following equation to prevent the gap closure.

$$\frac{2t_{pad}}{D_{col}} \geq \theta_{\mathrm{u,pin}} \tag{6-69}$$

where,

$\theta_{u,pin}$: ultimate base rotation, which can be estimated as the target drift ratio, rad

t_{pad}: pad thickness , in [mm]

D_{col}: column diameter, in [mm]

6.2.4.10 Rubber Pad Diameters

Decreasing the diameter of the rubber pad decreases the pipe-pin moment, which leads to lower force and moment demands in the pipe-pin elements and columns. However, the pad needs to be sufficiently large to transfer the column axial load to the pile-shaft. Based on the Mehrsoroush and Saiidi (2014) recommendations, a pad outer diameter of $0.6D_{col}$ is suggested.

6.2.5 Design Steps

In summary, the following steps are proposed to design pipe-pin connections between columns and pile-shafts:

Step 1. Determine the force and moment demands assuming base moment is zero.

Step 2. Determine the pad thickness based on the maximum expected pin rotation.

Step 3. Determine the dimension of the pipes.

Step 4. Determine the shear demand on the pipes.

Step 5. Check the lower pipe shear strength and adjust the dimension as necessary.

Step 6. Proportion the rubber pad based on the lower pipe dimensions.

Step 7. Design the tension member.

Step 8. Recalculate the force and moment demands including the pipe-pin moment.

Step 9. Repeat step 5 to 8 until the base moment converges.

Step 10. Design the upper pipe thickness based on the shear demand.

Step 11. Design the studs.

6.3 Rebar-Pin Connection of Column to Pile-Shaft

6.3.1 Introduction

Rebar-pins are designed to transfer shear and axial force while undergoing plastic deformations under strong earthquakes. The hinge longitudinal reinforcement is expected to yield and the cover concrete is expected to be damaged. Cheng et al. (2006) proposed a design method for column-footing connections and column-cap-beam connections using “two-way hinges”, which are called rebar-pins in this document. The experimental and analytical studies of the present study showed that those design provisions are generally adequate to design column to pile-shaft connections, and hence those provisions were adopted with necessary refinements to make them applicable to column-pile-shaft connections.

6.3.2 Design Force and Rotation Demand

Rebar-pins are designed for the axial and shear forces associated with the collapse limit state (CLS), which is the global collapse mechanism with plastic hinges at the top of the columns and the rebar-pins. The force demands on the rebar-pin connection are calculated using CLS.

6.3.2.1 Column Plastic Moment

Similar to section 6.2.2, the column plastic moment, $M_{p,col}$ is calculated from the moment-curvature relationship using an elastoplastic idealization (Fig. 6-1) (Caltrans, 2010).

6.3.2.2 Rebar-Pin Plastic Moment

The rebar-pin plastic moment, $M_{p,pin}$, is calculated based on the moment-curvature analysis of the hinge section assuming that the section was doubly confined, (1) provided by the transverse steel in the hinge, and (2) provided by the confined concrete in the column and pile-shaft immediately adjacent to the hinge (Cheng, et al., 2006). The hinge cover concrete properties were modified using the average of confinement pressures generated by the column and pedestal transverse reinforcement. Those confinement pressures were added to the confinement pressures from the hinge transverse steel to determine the confinement pressure of the core concrete in the rebar-pins.

The plastic moment in the rebar pin is determined by bilinear or quadrilinear idealization of the moment-curvature relationship. In the parametric studies presented in section 5.3.3, strength degradation was observed in the moment-curvature relationships of the rebar-pins with core diameters smaller than 70% of the total hinge diameter. It is proposed to idealize the moment-curvature relationship by a quadrilinear curve according to section 5.3.3 if the plastic moment using bilinear idealization is less than 90% of the maximum moment. Using either idealization methods, the rebar-pin plastic moment would be the maximum moment in the idealized moment-curvature relationship. Alternatively, the rebar-pin plastic moment is estimated conservatively as the maximum moment from the moment-curvature relationship prior to idealization.

6.3.2.3 Column and Rebar-Pin Shear

The column and rebar-pin shear demands are associated with the overstrength column and rebar-pin moment. The overstrength moments and shear demand, $V_{u,col}$, are calculated using the following relationships.

$$M_{o,col} = 1.2M_{p,col} \tag{6-70}$$

$$M_{o,pin} = 1.2M_{p,pin} \tag{6-71}$$

$$V_{u,col} = \frac{M_{o,col} + M_{o,pin}}{H_c} \tag{6-72}$$

where,

H_c: column clear height, in [mm]

$M_{o,col}$: column overstrength moment, kip.in [kN.m]

$M_{o,pin}$: rebar-pin overstrength moment, kip.in [kN.m]

$V_{u,col}$: column and rebar-pin shear demand, kip [kN]

Thus, the overstrength base shear in the bent, $V_{u,bent}$, is the summation of the column shear forces as follows.

$$V_{u,base} = \sum V_{u,col} \tag{6-73}$$

where,

$V_{u,bent}$: overstrength base shear in bent, kip [kN]

6.3.3 Design Capacities

6.3.3.1 Rebar-Pin Shear Capacity

Based on the Cheng et al. (2006) study, the rebar-pin shear capacity is the same as the friction capacity of the hinge. The friction capacity is determined using a coefficient of friction of 0.45 and a clamping force that is the total compressive force in the section obtained from moment-curvature analysis. The friction coefficient accounts for loss of friction due to the cyclic action of earthquake forces in the hinge. The shear capacity is determined using the following equations.

$$\phi\, V_{n,pin} > V_{u,col} \tag{6-74}$$

$$V_{n,pin} = \mu\, C \tag{6-75}$$

$$C = C_C + C_S = P + T_s \tag{6-76}$$

$$\mu = 0.45 \tag{6-77}$$

where

$V_{u,col}$: column and rebar-pin shear demand, kip [kN]

$V_{n,pin}$: rebar-pin shear capacity, kip [kN]

C: total compressive force in the hinge section from moment-curvature analysis, kip [kN]

C_C: compressive force in concrete from moment-curvature analysis of hinge section, kip [kN]

C_S: compressive force in steel from moment-curvature analysis of hinge section, kip [kN]

P: column axial force, with compressive force being positive, kip [kN]

T_S: tensile force in steel from moment-curvature analysis of hinge section, kip [kN]

μ: coefficient of friction, which is 0.45

ϕ: strength reduction factor, which is 0.85

6.3.3.2 Rebar-Pin Rotation Capacity

Based on the Cheng et al. (2006) model, the rebar-pin ultimate rotation capacity is calculated by assuming that the plastic deformations occur over an equivalent plastic hinge length at the rebar-pin. The equivalent plastic hinge length is an empirical length that accounts for strain penetration in the adjoining members in addition to ultimate flexural deformation of the pin. The rebar-pin rotation capacity is the sum of elastic and plastic rotations based on the idealized moment-curvature relationship of the section as follows.

$$\theta_{n,pin} = \theta_p + \theta_e \tag{6-78}$$

$$\theta_e = g \times \phi_{y,pin} \tag{6-79}$$

$$\theta_p = \phi_{p,pin} \times L_{p,pin} \tag{6-80}$$

$$\phi_{p,pin} = \phi_{u,pin} - \phi_{y,pin} \tag{6-81}$$

$$\begin{aligned} L_{P,pin} &= g + 0.15 \times f_y \times d_b(in, ksi) \\ &= g + 0.022 \times f_y \times d_b(mm, MPa) \end{aligned} \tag{6-82}$$

where,

θ_n: rebar-pin rotation capacity, rad

θ_e: rebar-pin elastic rotation, rad

θ_p: rebar-pin plastic rotation, rad

$\phi_{p,pin}$: rebar-pin plastic curvature, in^{-1} [mm^{-1}]

$\phi_{u,pin}$: ultimate curvature of rebar-pin from moment-curvature analysis, in^{-1} [mm^{-1}]

$L_{p,pin}$: equivalent plastic hinge length of rebar-pin, in [mm]

f_y: rebar-pin longitudinal bar yield strength, ksi [MPa]

d_b: diameter of longitudinal bars in rebar-pin, in [mm]

g: gap thickness, in [mm]

The gap thickness should be sufficiently large to accommodate the rotation capacity of the rebar-pin. The rotation corresponding to the gap closure is calculated using the following equation with the assumption that the rotation axis of the hinge passes through the center of the section. The maximum rotation demand of the rebar-pin should be less than the rotation at gap closure, otherwise the gap thickness has to increase to avoid gap closure and development of large moments.

$$\theta_{n,pin} < \theta_{close} \tag{6-83}$$

$$\theta_{close} = \arcsin\left(\frac{g}{0.5D_{col}}\right) \tag{6-84}$$

where,

D_{col}: column diameter, in [mm]

6.3.4 Detailing Recommendations

6.3.4.1 Rebar-Pin Cross Section

Large axial load index in the rebar-pin decreases the ductility and strength of the section. Based on the parametric studies and recommendations by Cheng et al. (2006), the axial load index of the rebar-pin should be smaller than 20%. The rebar-pin area is determined based on the column axial force excluding the overturning effect to simplify the analysis.

$$A_g \geq \frac{P_u}{0.2 f_c'} \tag{6-85}$$

where,

P_u: design axial force, kip [kN]

f_c': concrete compressive strength, ksi [MPa]

A_g: gross area of rebar-pin section, in^2 [mm^2]

6.3.4.2 Core Diameter

The reduction of the core diameter increases the ductility and reduces the pin moment. However, when the core diameter is less than 50% of the hinge diameter, there is significant strength degradation, which is not desirable. The core diameter is suggested to be 50-70% of the hinge diameter.

6.3.4.3 Minimum Rebar-Pin Longitudinal Reinforcement

The minimum longitudinal reinforcement ratio of 1%, which is permitted by AASHTO provision, is suggested for the rebar-pin reinforcement.

$$A_s \geq 0.01 A_g \tag{6-86}$$

where,

A_s: rebar-pin longitudinal steel area, in^2 [mm^2]

6.3.4.4 Development Length of Rebar-Pin Longitudinal Bars

Based on Caltrans SDC (2010), the hinge longitudinal reinforcement should be extended for 1.3 times the tension development length (L_d) in the column and pile-shaft. The study by Cheng et al. (2010) found that 1.25L_d is sufficient. The transverse reinforcement should extend into the column and pile-shaft along the entire development length.

6.3.5 Design Steps

Step 1. Determine the rebar-pin dimension, core diameter, and the required longitudinal steel.

Step 2. Calculate confined concrete properties for the hinge cover concrete. The cover concrete is confined by the average of column and pile-shaft confinement pressure.

Step 3. Determine the hinge transverse reinforcement for target curvature ductility of 10 using Mortensen and Saiidi (2002) performance based design method. The hinge core concrete properties are calculated based on the double confinement from the hinge transverse steel and confinement steel in the column and the pile-shaft adjacent to the rebar-pin.

Step 4. Determine moment-curvature relationship for the rebar-pin and column.

Step 5. Determine demand forces and rotation.

Step 6. Check rebar-pin friction capacity. If the capacity is not sufficient, adjust the reinforcement or size of the hinge, and repeat steps 4 to 7.

Step 8. Check hinge gap closure and determine hinge gap thickness to prevent gap closure.

Step 9. Determine the reinforcement detailing for the rebar-pin.

6.4 Illustrative Design Examples

The column-pile-shaft connections of a prototype two-column bent, which is shown in Fig. 6-10, are designed based on the proposed design procedures presented in this chapter. The connections were designed using three alternatives: pipe-pins with high-strength rods, pipe-pins with strands, and rebar pins. The procedures presented in section 6.4.1 and 6.4.2 were used for pipe-pins, and section 4.6.3 was used for rebar-pins.

The dead load on each column is 1306 kip [5827 kN], based on the weight of the superstructure. The specified concrete strength, f_c', is 4.0ksi [27.6MPa] in the columns and pile-shafts. The reinforcement is A706 reinforcing steel according with $f_y = 60ksi$ $[420MPa]$ and $f_u = 80\ ksi$ $[550MPa]$ (Caltrans, 2010). The pipes are according ASTM A519 Gr. 4140/Norm requirements with $f_y = 90ksi$ $[621MPa]$ and $f_u = 120\ ksi$ $[827MPa]$. The rod is according to ASTM A354, Gr. BD requirements with $f_y = 130\ ksi$ $[896MPa]$ and $f_u = 150ksi$ $[1034\ MPa]$. The rubber pad is Hardness Shore-A 70 with $G = 300psi$ $[2.1MPa]$. The minimum required area for the rubber pad under dead and live loads is 18 ft^2 [1.672m^2].

6.4.1 Pipe-Pin connection with Rod as Tension Member

Step 1. Determine the force and moment demands assuming perfect pins at the column-pile-shaft connection.

Based on the expected material properties, the plastic moment was calculated under only the dead load in the first iteration (Table 6-1). In the second iteration, the axial forces were updated including the overturning moment. Then, the plastic moments were recalculated under updated axial force. The updated overturning moment was within 1% of the overturning moment from the first iteration. Therefore, the convergence was achieved. Based on the plastic moments in the second iteration, the demand forces and moments at the compressive and tensile sides are as follow.

Compressive side	Tensile side
$M_p = 12{,}192\ kip.ft\ [16532kN.m]$	$M_p = 10{,}531\ kip.ft\ [14280kN.m]$
$M_{u.col} = 1.2 \times 12192$ $= 14630\ kip.ft\ [19838kN.m]$	$M_{u.col} = 1.2 \times 10531$ $= 12637kip.ft\ [17136kN.m]$
$V_{u,col}^{comp} = \frac{14630 + 0}{51 \times 12} = 287\ kip\ [1277kN]$	$V_{u.col}^{tensile} = \frac{12637 + 0}{51 \times 12} = 247.8\ kip\ [1102kN]$

The overestimated bent shear is calculated using Eq. (6-8).

$$V_{u.bent} = 287 + 248 = 535\ kip\ [2380kN]$$
$$OM = 535 \times \frac{(55 \times 12 + 4)}{12} = 29495kip.ft\ [39990kN.m]$$

$$P_{u.col} = 1306 + \frac{29495}{36.67} = 2110\ kip\ [9396kN]$$

$$T_{u,col} = 1306 - \frac{29495}{36.67} = 502\ kip\ [2233kN]$$

Step 2. Determine the pad thickness based on the maximum pin rotation.

Based on the plastic analysis of the bent with pin, the ultimate bent displacement is 4.479ft [1.366m], which corresponds to an 8.8% drift ratio.

$$\theta_u^{pin} = \frac{8.8}{100} = 0.088\ rad$$
$$\text{required: } t_{pad} = 0.088 \times \frac{5.5 \times 12}{2} = 2.9\ in\ [74\ mm]$$
$$\text{select: } t_{pad} = 3\ in\ [76\ mm]$$

Step 3. Determine the pipe dimensions based on the detailing recommendations of sections 6.2.4.

$$0.25H_c = 153\ in\ [3886mm]$$
$$0.2H_c = 122.4\ in\ [3109mm]$$
$$\text{select: } H_{upper} = 10' - 4"\ [3150mm]$$

For the first iteration, a pipe with OD_{lower}=18in [457mm] and t_{lower}=1.0in [25mm] is selected to prevent bearing of the rod on the inner surface of the lower pipe. This pipe also satisfies the compactness criterion.

$$\frac{0.07 \times 29000}{90} = 22.6 > \frac{OD_{lower}}{t_{lower}} = 18 \quad OK$$

Based on the detailing recommendations, the protruded length is

$$\text{recommendation: } L_{protruded} = 1.2D_{lower} = 21.6in[549mm]$$
$$\text{select: } L_{protruded} = 22in[559mm]$$

The lower pipe embedment length is

$$\text{recommendation: } \min\begin{cases} 0.2 \times 51 \times 12 = 1224in\ [3111mm] \\ 4.5 \times 18 = 81in[2057mm] \end{cases}$$
$$\text{select: } L_{embed,lower} = 10ft[3048mm]$$

The inner diameter of the lower pipe is checked to control the bearing of the rod on the inner edge assuming the rod diameter is 3 in [76mm].

$$\delta_{rod} = \theta_{u,pin} \times H_{upper} = 10.9in\ [277mm]$$
$$L_{rod} = L_{embed,lower} + t_{pad} + H_{upper} = 20.58\ ft\ [6273mm]$$

$$L_{rod@pipe} = L_{emb,lower} + l_{protruded} = 11.83\ ft\ [3606mm]$$
$$2\left(\frac{12.42}{20.58}\right)10.9 + 3 = 15.521\ in\ [164mm] < 16in\ [406mm]\ OK$$

The recommended gap between the pipes is

$$\text{recommended: } G_h = \frac{OD_{lower}}{16} = 1.125in[29mm]$$
$$\text{select: } G_h = 1.25in\ [32mm]$$
$$ID_{upper} = 20.5in\ [521mm]$$

Step 4. Determine the shear demand on the pipes.

The shear demand is calculated in the column with the largest shear, which is in the column under compression due to the overturning moment. The stiffness is calculated based on the effective yield point in the moment-curvature relationship.

$$V_{u,col} = 287kip\ [1277\ kN]$$
$$EI_{cr} = \frac{M_{ye}}{\phi_{ye}} = 10721211\ kip.ft^2\ [4430576\ kN.m^2]$$
$$F_{impact} = 0.9 \times \sqrt{\frac{1306 \times 1.25 \times 10721211}{12 \times\ 51^3}} = 94.4\ kip\ [420kN]$$
$$F_{impact} \leq 0.5 \times 1306 = 653\ [2905kN]\ OK$$
$$V_{u,pipes} = 287 + 94 = 381kip\ [1695kN]$$

Step 5. Check the lower pipe shear strength and adjust the dimension as necessary.

The pipe yield strength is 90ksi [620MPa].

$$\tau_y = \frac{f_{y,pipe}}{\sqrt{3}} = 52ksi\ [359MPa]$$
$$A_g = 53.07in^2\ [34460mm^2]$$
$$V_{n,lower}^{pipe} = \tau_y\ A_g = 2775kip\ [12343kN]$$
$$Z_{pipe} = \frac{1}{6}(18^3 - 16^3) = 289.3in^3[4.741 \times 10^6 mm^3]$$
$$M_p = 289.3 \times 90 = 26040kip.in\ [2942kN.m]$$
$$V_{n,lower}^{noAxial} = (4)(18)\left(\sqrt{22^2 + 2\frac{26040}{4 \times 18}} - 22\right) = 918\ kip\ [4083kN]$$

The lower limit of the shear capacity is larger than the shear demand. Therefore, no interpolation is required.

$$\frac{381}{0.75 \times 918} = 0.554 < 1\ \ OK$$

Step 6. Proportion the rubber pad based on the lower pipe dimension.

$$ID_{pad} = OD_{lower} = 18in\ [457mm]$$

$$\left(OD_{pad}\right)_{required} = \sqrt{\frac{4A_{req}}{\pi} - ID_{pad}^2} = 4.54ft\ [1384mm]$$

$OD_{pad} = 5ft\ [1524m]$

recommended: $0.6D_{col} = 3.3ft = 3ft4in\ [84mm]$

Step 7. Design the tension member.

$$K_{c,pad} = \frac{0.90 \times 2573}{3} = 772\frac{kip}{in}\left[135.2\frac{kN}{mm}\right]$$

Because the rod force depends on the rod stiffness, iterations are required to achieve the diameter of the rod. Table 6-2 shows the iterative process. The final design is a 3.5-in [89-mm] diameter rod.

Step 8. Determine the force and moment demands including the pipe-pin moment.

$$\theta_g = \frac{3 \times 2}{5.5 \times 12} = 0.091\ rad$$

$$M_g = \frac{772}{772 + 1130}\left((\frac{60}{2})(1130)(0.091) + 1306\right)\frac{60}{2} = 4452\ kip.ft\ [6036\ kN.m]$$

$$M_{pin} = (\frac{0.088}{0.091})(4452) = 4301\ kip.ft\ [5831\ kN.m]$$

Compressive side	Tensile side
$M_p = 12{,}192\ kip.ft\ [16532kN.m]$	$M_p = 10{,}531\ kip.ft\ [14280kN.m]$
$M_{u.col} = 1.2 \times 12192$ $= 14630\ kip.ft\ [19838kN.m]$	$M_{u.col} = 1.2 \times 10531$ $= 12637kip.ft\ [17136kN.m]$
$V_{u,col}^{comp} = \frac{14630 + 4301}{51}$ $= 371\ kip\ [1651kN]$	$V_{u.col}^{tensile} = \frac{12637 + 4301}{51}$ $= 332\ kip\ [1477kN]$

$$V_{u.bent} = 371 + 332 = 703\ kip\ [2380kN]$$

$$OM = 703 \times \frac{(55 \times 12 + 4)}{12} - 2 \times 4301 = 30198kip.ft\ [39990kN.m]$$

$$P_{u.col} = 1306 + \frac{30198}{36.67} = 2130\ kip\ [9472kN] \quad T_{u,col} = 1306 - \frac{30198}{36.67} = 482kip\ [2146kN]$$

The updated base shear in the bent is 703 kip [3127kN], an increase of 31% compared to the shear for the bent with perfect pins. The updated overturning moment in the bent is within 2% of the previous trial. The design process is repeated from Step 4 to check the capacity of the lower pipes under the updated shear demand.

Step 9. Check the design from step 5 using updated forces.

The impact force is the same as before but the column shear is larger.

$V_{u,pipe} = V_{u,col} + F_{impact} = 465\ kip\ [2068kN]$

The shear demand to capacity ratio of the lower pipe is as follows.

$$\frac{465}{0.75 \times 918} = 0.68 < 1.0\ OK$$

The rod design was checked using the updated column axial force listed in Table 6-2 in the third iteration.

Step 10. Design the upper pipe thickness based on the shear demand.

A pipe with OD_{upper}=21.5in [546mm] and minimum practical thickness of t_{upper}=0.5in [13mm] was used for the upper pipe. The sectional properties are:

$A_{pipe} = 32.99\ in^2\ [21280mm^2]$
$Z_{pipe} = 220.5\ in^3\ [3.614 \times 10^6 mm^3]$
$M_p = 220.5 \times 90 = 19845 kip.ft\ [2243kN.m]$
$A_c = \frac{\pi\left(D_{col}^2 - OD_{upper}^2\right)}{8} = 1529in^2[0.987m^2]$
$e_2 = 22 - 3 = 19in\ [483mm]$ (Eq. 6-36)

$e_2$is the eccentricity inside the upper pipe.

The bearing strength of the upper pipe against the concrete in the column is calculated iteratively. In the first iteration, the bearing strength was assumed the same as the compressive strength of concrete. The nominal lower bound shear capacity associated with no axial load, $V_{n,upper}^{noAxial}$, exceeded the required strength. Therefore, no interpolation is required. The shear demand to capacity ratio for the upper pipe is as follows.

$$\frac{465}{0.75 \times 1729} = 0.36$$

Step 11. Design the studs.

The studs should be able to transfer the pipe force to concrete. The number of studs is determined assuming 1-in [25 mm] diameter and 6 ¼-in [156-mm] long studs with material properties according to AWS A.1 Type B.

required: $n = \frac{T_{r,rod}}{\phi_{v,studs}\ f_u\ A_v} = \frac{1155}{(0.65)(65)(0.785)} = 34.8$
spacing: $\frac{H_{upper}}{4} = 62in\ [1575]$
select: 3 layers of 12 studs with vertical spacing of 60in[1524mm]

Figure 6-11a shows the final design of the pipe-pin with rod for this example.

6.4.2 Pipe-Pin Connection with Strands as Tension Members

The design procedure of a pipe-pin with strands is identical to that of a pipe-pin with rod from step 1 to step 7, which are explained in section 6.4.1.

Step 7. Design the tension member.

Six 0.6-in [15-mm] diameter posttensioning strands with mechanical properties conforming to ASTM A416, Grade 270 satisfy the requirements.

$$A_{strand} = 0.217in^2\ [140mm^2]$$
$$A_{g,tm} = 6(0.217) = 1.3in^2[840mm^2]$$
$$K_{strand} = \frac{28500 \times 1.302}{247} = 150\frac{kip}{in}\ \left[26.31\frac{kN}{mm}\right]$$
$$T_{u,strand} = \frac{150}{150+772}\left(\frac{60}{2}(772)(0.088) - 341\right) = 276\ kip\ [1228kN]$$
$$T_{r,strand} = \min\begin{cases}0.95 \times 243 \times 1.302 = 301\ kip\\ 0.80 \times 270 \times 1.302 = 281\ kip\end{cases} = 281kip\ [1250kN]$$
$$\frac{T_{u,strand}}{T_{r,strand}} = \frac{276}{281} = 0.98 < 1.0\ OK$$

Step 8. Determine the force and moment demand including the pipe-pin moment

$$\theta_g = \frac{3 \times 2}{5.5 \times 12} = 0.091\ rad$$
$$M_g = \frac{772}{772+150}\left((\frac{60}{2})(150)(0.091) + 1306\right)\frac{60}{2} = 3590\ kip.ft\ [4868\ kN.m]$$
$$M_{pin} = (\frac{0.088}{0.091})(3590) = 3468\ kip.ft\ [4703\ kN.m]$$

Compressive side

$$M_p = 12{,}192\ kip.ft\ [16532kN.m]$$
$$M_{u.col} = 1.2 \times 12192 = 14630\ kip.ft\ [kN.m]$$
$$V_{u,col}^{comp} = \frac{14630 + 3468}{51} = 355\ kip\ [1651kN]$$

Tensile side

$$M_p = 10{,}531\ kip.ft\ [14280kN.m]$$
$$M_{u.col} = 1.2 \times 10531 = 12637kip.ft\ [kN.m]$$
$$V_{u.col}^{tensile} = \frac{12637 + 3468}{51} = 318\ kip\ [1477kN]$$

$$V_{u.bent} = 355 + 316 = 671\ kip\ [2994kN]$$
$$OM = 671 \times \frac{(55 \times 12 + 4)}{12} - 2 \times 3468 = 30193kip.ft\ [40758kN.m]$$

$$P_{u.col} = 1306 + \frac{30193}{36.67} = 2129\ kip\ [9471kN]$$
$$T_{u,col} = 1306 - \frac{30193}{36.67} = 482kip\ [2144kN]$$

The updated base shear in the bent is 671 kip [2985kN], an increase of 25% compared to the shear for the bent with perfect pins. The design process is repeated from step 4 to check the capacity of the pipes under the updated shear demand.

Step 9. Check the design from step 5 using updated forces.

The impact force is the same as the force in a pipe-pin with rod (section 6.4.1), but the column shear is different.

$$V_{u,pipe} = V_{u,col} + F_{impact} = 355 + 94 = 449\ kip\ [1997kN]$$

The shear demand to capacity ratio for the lower pipe is:

$$\frac{449}{0.75 \times 918} = 0.65 < 1.0\ OK$$

Step 10. Design the upper pipe thickness based on the shear demand.

A pipe with OD_{upper}=21.5in [546mm] and minimum practical thickness of t_{upper}=0.5in [13mm] was used for the upper pipe. The cross section properties are:

$$A_{pipe} = 32.99\ in^2\ [21280mm^2]$$
$$Z_{pipe} = 220.5\ in^3\ [3.614 \times 10^6 mm^3]$$
$$M_p = 220.5 \times 90 = 19845 kip.ft\ [2243kN.m]$$
$$A_c = \frac{\pi\left(D_{col}^2 - OD_{upper}^2\right)}{8} = 1529in^2[0.987m^2]$$
$$e_2 = 22 - 3 = 19in\ [483mm]$$

Bearing strength of the upper pipe against concrete in the column is calculated iteratively. For the first iteration, the bearing strength was assumed the same as the compressive strength of concrete. The nominal lower bound shear capacity associated with no axial load, $V_{n,upper}^{noAxial}$, exceeded the required strength. Therefore, no interpolation is required.

$$\frac{465}{0.75 \times 1729} = 0.36$$

Step 11. Design the studs.

The studs should be able to transfer the pipe force to concrete. The number of studs is determined assuming 1-in [25-mm] diameter and 6 ¼-in [156-mm] long studs with material properties according to AWS A.1 Type B.

$$\text{required: } n = \frac{T_{r,strand}}{\phi_{v,studs}\ f_u\ A_v} = \frac{1227}{(0.65)(65)(0.785)} = 37$$
$$\text{spacing: } \frac{H_{upper}}{4} = 62in\ [1575]$$
$$\text{select: 3 layers of 13 studs with vertical spacing 60in[1524mm]}$$

Figure 6-11b shows the final design of the pipe-pin with strands for this example.

6.4.3 Rebar-Pin Connection

Step 1. Determine the hinge section dimensions, core diameter, and the required longitudinal steel.

$$P_{dl} = 1306kip\ [5809kN]$$
$$\text{required: } \left(A_g\right)_{req'd} = \frac{P_{dl}}{0.2f_c'} = \frac{1306}{0.2 \times 4 \times 12^2} = 11.34ft^2\ [1.054m^2]$$

$\Rightarrow D_{req'd} = 43in[1092mm]$
select:$D_{hinge} = 48in\ [1219mm]$
$A_g = \frac{\pi}{4}(48^2) = 12.566ft^2\ [1.167m^2]\ \ OK$

Minimum longitudinal reinforcement is used in the first trial.

required:$(A_s)_{min} = (0.01)(12.566 \times 12^2) = 18.10in^2\ [11678mm^2]$
select 12-#11: $A_s = 12 \times 1.56 = 18.72in^2\ [12078mm^2]$

The diameter of confined concrete, measured inside the spirals is selected as 32 in [813 mm].

$D_{core} = 32 - 1.41 = 30.59in\ [777\ mm]$
$\frac{D_{core}}{D_{hinge}} = \frac{30.59}{48} = 0.64$ GOOD: in the recommended range.

Step 2. Calculate confined concrete properties for the hinge cover concrete.

The bottom section of the column (section B-B):

$D_{col} = 5.5ft[1.678m]$
$cc = 2in\ [51mm]$
#7@8in: $d_{sp} = 0.875in\ [22mm], A_{sp} = 0.60in^2\ [387mm^2]\ and\ s = 8in\ [203mm]$
$d' = 5.5 \times 12 - 2 \times 2 - 1.0 = 61.125in\ [1553\ mm]$
$\rho_{s,col} = \frac{4\ A_{sp}}{d' \times s} = \frac{4(0.60)}{(61.125)(8)} = 0.00491$
$f_{l,col} = \frac{2\ A_{sp}\ f_{yh}}{d'\ s} = \frac{2(0.60)(68)}{(61.125)(8)} = 0.334ksi\ [2.303\ MPa]$

The top section of the pile-shaft (section C-C):

$D_{pile} = 7.5ft\ [2.288m]$
$cc = 6in\ [152mm]$
#8@6-1/4" in: $d_{sp} = 1.0in\ [25mm], A_{sp} = 0.79in^2\ [510mm^2], and\ s = 6.25in\ [159mm]$
$d' = 7.5 \times 12 - 2 \times 6 - 1.0 = 77in\ [1956\ mm]$
$\rho_{s,pile} = \frac{4\ A_{sp}}{d' \times s} = \frac{4(0.79)}{(77)(6.25)} = 0.00657$
$f_{l,pile} = \frac{2\ A_{sp}\ f_{yh}}{d'\ s} = \frac{2(0.79)(68)}{(77)(6.25)} = 0.223ksi\ [1.538\ MPa]$

The average confinement steel ratio and pressure of the column and pile-shaft is as follows.

$\rho_{s,cover} = \frac{\rho_{s,col} + \rho_{s,pile}}{2} = \frac{0.00491 + 0.00657}{2} = 0.00574$
$f_{l,cover} = \frac{f_{l,col} + f_{l,pile}}{2} = \frac{0.334 + 0.223}{2} = 0.195ksi\ [1.345MPa]$

Based on the Mander (1987) concrete model, the confined concrete properties of the hinge cover concrete are as follows.

$f_c = 5.2ksi\ [35.9MPa]$
$f_{cc} = 6.442ksi\ [44.4MPa]$
$\epsilon_{cc} = 0.00439$
$\epsilon_{cu} = 0.01417$
$E_c = 4110ksi\ [28339MPa]$

Step 3. Determine the hinge transverse reinforcement for a target curvature ductility of 10 using the Mortensen and Saiidi (2002) performance based design method. Using this method, the neutral axis depth, c, and yield curvature, ϕ_y, are determined from the moment-curvature analysis of the hinge using cover concrete properties for the entire section. The axial force on the section was 1514kip [kN], which is the unfactored dead load.

$c = 18.3in\ [465mm]$
$\phi_y = 0.128 \times 10^{-3} in^{-1} [0.0050m^{-1}]$
$\phi_u = \mu\phi_y = 10 \times 0.128 \times 10^{-3} = 12.8 \times 10^{-3}\ in^{-1} [0.0504m^{-1}]$
$\epsilon_{cu} = c\ \phi_u = 18.3 \times 1.28 \times 10^{-3} = 0.0234$

$$\left(\rho_{s,hinge}\right)_{req'd} = (\epsilon_{cu} - 0.004)\left(\frac{f_c}{f_{yh}\ \epsilon_{sm}}\right) = (0.0234 - 0.004)\left(\frac{5.2}{(68)(0.12)}\right) = 0.0124$$

select #6@4in: $d_{sp} = 0.750in\ [19mm], A_{sp} = 0.44in^2\ [284mm^2], s = 4in\ [102mm]$
$d' = 32 + 0.625 = 32.625in\ [829mm]$

$$\rho_{s,hinge} = \frac{4(0.44)}{32.75 \times 4} = 0.0134$$

$$f_{l,hinge} = \frac{2(0.44)(68)}{(32.75)(4)} = 0.457ksi\ [3.15MPa]$$

Based on the Mander (1987) concrete model, the confined concrete properties of the hinge core concrete are as follows.

$\rho_{s,core} = \rho_{s,hinge} + \rho_{s,cover} = 0.0134 + 0.00574 = 0.0192$
$f_{l,core} = f_{l,hinge} + f_{l,cover} = 0.457 + 0.195 = 0.625ksi\ [4.31MPa]$
$f_{cc} = 8.732ksi\ [60.2MPa]$
$\epsilon_{cc} = 0.088$
$\epsilon_{cu} = 0.02908$
$E_c = 4110ksi\ [28339MPa]$

Step 4. Determine moment-curvature relationship of the rebar-pins and columns.

The moment-curvature analysis results are presented in Table 6-4.

Step 5. Determine demand forces and rotation.

The column shear was calculated in both column and presented in Table 6-4.

Step 6. Check rebar-pin friction capacity.

The friction capacity in the pin at the base of the column with the smaller axial force is:

$P_{pin} = 798\ kip\ [kN]$
$V_{u,col} = 322kip\ [kN]$
$C = C_S + C_C = 1655kip\ [kN]$

$$V_n = \mu\, C = (0.45)(1655) = 745kip\ [kN]$$
$$\frac{V_{u,col}}{\phi\, V_n} = \frac{322}{(0.85)(745)} = 0.51 < 1.0\ OK$$

The friction capacity in the pin at the base of the column with the larger axial force is:

$$P_{pin} = 2178\ kip\ [kN]$$
$$V_{u,col} = 387kip\ [kN]$$
$$C = C_S + C_C = 3309kip\ [kN]$$
$$V_n = \mu\, C = (0.45)(3309) = 1489kip\ [kN]$$
$$\frac{V_{u,col}}{\phi\, V_n} = \frac{387}{(0.85)(1489)} = 0.31 < 1.0\ OK$$

Step 8. Check hinge gap closure and determine hinge gap thickness.

The moment-curvature relationship of the pin at the base of the column with the smaller axial force is shown in Fig. 6-12.

Assume g=3in [76mm],

$$L_p = g + 0.15 \times f_y \times d_b = 3 + (0.15)(68)(1.41) = 14.69in[373mm]$$
$$\phi_y = 1.253 \times 10^{-4}\ in^{-1}\ [0.0493m^{-1}]$$
$$\phi_u = 3.858 \times 10^{-3} in^{-1}\ [0.1519m^{-1}]$$
$$\theta_e = g \times \phi_y = 3 \times 1.253 \times 10^{-4} = 3.759 \times 10^{-4} rad$$
$$\theta_p = L_p\left(\phi_u - \phi_y\right) = 14.69\ (3.858 \times 10^{-3} - 1.253 \times 10^{-4}) = 0.0548\ rad$$
$$\theta_n = \theta_e + \theta_p = 3.759 \times 10^{-4} + 0.0548 = 0.0552\ rad$$
$$\theta_{close} = \arcsin\left(\frac{g}{0.5D_{col}}\right) = \arcsin\left(\frac{3}{0.5 \times 5.5 \times 12}\right) = 0.091\ rad$$
$$\frac{\theta_n}{\theta_g} = 0.61 < 1.0\ \ OK$$

Step 9. Determine the reinforcement detailing.

Based on AASHTO LRFD article 4.8.6.11, the development length of hinge bars under tension is

$$\#11:\ \ l_{db} = \frac{1.25\ A_b\ f_y}{\sqrt{f_c'}} = \frac{1.25\ (1.56)(68)}{\sqrt{5.2}} = 58in\ [1473mm]$$
$$1.3l_{db} = 1.3 \times 58 = 76in\ [1930mm]$$
Extend the bars for 7ft on each side.

Figure 6-13 shows the final design of the rebar-pins for this example.

7 Summary and Conclusions

7.1 Summary

Economy and safety of bridge projects improve by reducing size of structural elements and facilitating construction. Two-way hinges, also known to as "pins," have been used in reinforced concrete bridge columns to reduce the force demand on the structural elements. Hinges allow for relative rotation between structural elements and reduce moment transfer through the connection. As a result, smaller structural elements are needed compared to structures with rigid connections. The use of hinge connections in combination with prefabricated structural elements reduces the construction time and facilitates construction by using smaller and lighter components. Two types of modern two-way hinges are used in bridge structures: rebar-pins, which are made with reinforcing bars, and pipe-pins, which are made with steel pipes. The former is by far the more common type, but the latter is beginning to find application in some bridges because of its ease of construction and potentially superior performance. Through previous research at the University of Nevada, Reno, details were developed and the seismic performance of both hinges for column-superstructure and column-footing connections were studied, and design methods were developed. The adequacy of those hinge details, any necessary refinement, and the seismic performance of the details in column-pile-shaft joints was unknown.

The primary objectives of this study were: (1) to investigate through large-scale testing and analysis the seismic performance of available hinge connections of column to pile-shaft, and propose necessary modifications, (2) to develop reliable analytical methods for pipe-pin and rebar-pin hinges that reflect their actual behavior, (3) to develop a reliable design methods for use of hinges in column to pile-shaft connection, and (4) to study the performance of the hinge and pocket connections in precast bridge construction for eventual use in accelerated bridge construction (ABC).

To meet these objectives, two 1/3.75 scale two-column bent specimens were designed, constructed, and subjected to seismic loadings. In each bent, one column was constructed with precast members for ABC, whereas the other column was conventional cast-in-place (CIP). Engineered cementitious composite (ECC) was used in the plastic hinge zone of one column in each bents to investigate novel material use to mitigate post-earthquake damage in structures. Pocket connections were used for column to cap beam joints in both bents. Based on findings of previous studies, the pocket connection detailing was simplified to facilitate construction. The specimens were subjected to several earthquake records of increasing amplitude based on the acceleration record from the 1994 Northridge earthquake simulated on one of the shake tables of the Earthquake Engineering Laboratory at the University of Nevada, Reno.

The experimental studies were followed by numerical simulations of the tests. Numerical models for the hinges with different levels of sophistication were developed and validated with the test results. New models representing the constitutive relationships of pipe-pins and rebar-pins were developed and implemented in an existing computer program, OpenSEES. The numerical models are useful in global finite element analyses of bridges with base hinges. Additionally, a numerical finite element model of pipe-pin with continuum elements was developed using ABAQUS/Explicit to investigate the interaction and stresses in different parts at

a microscopic level. The results from the numerical models correlated reasonably well with the test results. The numerical models were utilized to conduct parametric studies. Important parameters that might affect the seismic performance of the hinges were investigated using the numerical models. The parameters were included axial load level, taper slope on the pipes, and tension member type for the pipe-pins as well as axial load level and core diameter for the rebar-pins. Design procedures and detailing for connections of column to pile-shaft using pipe-pins and rebar-pins were developed based on the experimental observations and parametric studies.

7.2 Observations

Noteworthy observations made in the course of the experimental and analytical studies presented in this document were:

1- In both specimens, full plastic hinge capacity was reached at the top of the column while the pins did not fail.
2- Moments were developed at both pin types leading to an increase in the base shear by approximately 30%. Even the pipe-pins without any tension members and the rebar-pins with very small core diameters generated significant moments at the column base.
3- The damage in the pipe-pin connections was minimal because the strains in the pipes and longitudinal bars were well below the yield, and cracks in the column and pedestal were thin and few.
4- The uplift force was successfully transferred to the pile-shaft through the high-strength rod in the pipe-pin connections. While the axial force was well below the yield force in the rod, the Von Mises stress passed the yield criteria due to the combination of flexure and tension.
5- In the cases that strands were used instead of the rod for the tension member, no yielding was observed in the strands based on the analytical studies. The use of strands slightly reduced the pipe-pin moment, which led to smaller column shear.
6- The increase in dead load postponed the development of tensile forces in the rods and tendons and reduced the stress. However, some tension was developed in the rods and tendons due to pipe-pin rotation even when the dead load was relatively large.
7- The initial lateral stiffness of a bent with pipe-pin connections was smaller than that of a bent with perfect pins because of the gap between the pipes that allowed for small lateral movement before the engagement of the pipes.
8- The tapering of the lower pipe did not improve the behavior of the pipe-pin significantly.
9- The moment-rotation relationship of rebar-pins was stable even when the pins underwent large plastic deformations under many cycles of earthquake loading. The concrete near the hinge throat was damaged but the column and pedestal reinforcement did not yield near the rebar-pins.
10- Despite the fact that the rebar-pin slipped under shear, the friction capacity was sufficient to resist the shear forces even though the axial load in the column was relatively small and did not contribute to the pin friction capacity.
11- An increase in axial force improved the safety factor against shear friction and flexural failure of the rebar-pins.
12- Softening behavior was observed in the rebar-pins with axial load level more than 20% of the maximum axial force capacity of the hinge.

13- The reduction of the rebar-pin core diameter increased the displacement ductility of the bent and reduced the pin moment. However, stiffness and strength of the hinge degraded when the core diameters was reduced below 50% of the section diameter.
14- Similar performance was observed in the cast-in-place and the precast columns, which were built using a precast shell and filled with self-consolidating concrete (SCC).
15- The precast cap beam remained elastic with no damage. The posttensioning force was helpful in reducing the damage.
16- The pocket connection using corrugated steel pipe and longitudinal bars extended for approximately 1.2 times the column diameter performed well in forming the plastic hinge in the column. No damage was observed in the pocket connections.
17- The column plastic hinges with ECC showed significantly less damage compared to the counterpart plastic hinges with conventional concrete even when the ECC was used in the column shell.
18- Under strong earthquakes, the ECC plastic hinges were damaged by forming a few concentrated cracks in the plastic hinges and at the column-cap beam joints. This led to higher local strains and curvatures compared to those in the conventional concrete plastic hinges.
19- Use of ECC in the column for a length equal to 1.5 times column diameter effectively prevented shifting of damage to concrete segment below ECC.

7.3 Conclusions

The following conclusions were drawn from the results of the experimental and analytical studies presented in this document:

1- The design and detailing methods developed and used in this study for both the rebar-pins and pipe-pins as well as the pocket connections and the precast cap beams were effective in leading to a ductile bridge bent even under extreme earthquakes.
2- The two-way hinge moments must be taken into account to avoid column shear failure and damage to capacity-protected members such as pile-shafts.
3- For the design of the pipe-pin connections, the lower pipe and upper pipe should be designed for shear and tension separately. The shear demand in the pipes is the column shear and the impact force. The tension demand in the pipes is due to the force in the tension member (rod or strands) and is present even in the columns that are not subjected to uplift forces under overturning moments on the bent.
4- In the design of the pipe-pin connections, rods should be designed for combined tension force and flexure. However, strands should be designed for only tension force.
5- Pipe-pins can be designed to remain entirely elastic when a strand is used for the tension member and may be treated as capacity-protected connections, whereas rebar pins are expected to yield.
6- Tension members should be used in pipe-pins to maintain global stability of the bent under larger lateral displacements, even in cases that the dead load is sufficiently large to prevent uplift.
7- The calculated displacement ductility is smaller in a bent with pipe-pins compared to ductility in a bent with perfect pins at column to pile-shaft connections. This is because the gap between the pipes leads to slight slippage that reduces the effective initial stiffness.

8- Because rebar-pins undergo large plastic deformations, they should be designed as ductile elements with ample confinement for the concrete and sufficient development length for the reinforcement in the hinge.
9- In rebar-pins, slippage occurs even under small shear once a horizontal crack is formed across the entire section. The friction capacity increase with pin rotation and yielding of the reinforcement. This behavior is dominant in the pins with small axial force.
10- The proposed detailing for pocket connections was efficient and safe. In this detailing, a pocket with 1.2 times the column diameter is formed using a corrugated pipe, the spirals are provided around the corrugated pipe over the lower one-third of the pocket height, the column reinforcement is extended into the pocket, and the pocket is filled with self-consolidated concrete (SCC).
11- Use of ECC in the plastic hinge regions for a length equal to 1.5 times column diameter significantly reduces the plastic hinge damage.

References

AASHTO. (2010). *AASHTO LRFD Bridge Design Specifications.* Washington, DC: AASHTO.

ACI Committee 318. (2011). Building code requirements for Structural concrete (ACI 318-11). American Concrete Institude.

ASTM. (1991). Standard test methods for rubber properties in compression. ASTM International.

Bažant, Z. P., & Becq-Giraudon, E. (2002). Statistical prediction of fracture parameters of concrete and implications for choice of testing standard. *Cement and Concrete Research*, *32*(4), 529-556.

Caltrans, S. D. C. (2010). Caltrans seismic design criteria version 1.6. *California Department of Transportation, Sacramento*.

Caltrans. (2015). *Bridge Design Practice, 4th Ed.* State of California Department of Transportation. Retrieved from http://www.dot.ca.gov/hq/esc/techpubs/manual/bridgemanuals/bridge-design-practice/pdf/bdp_21.pdf

Chang, G., & Mander, J. (1994). *Seismic energy based fatigue damage analysis of bridge columns: Part 1-Evaluation of seismic capacity.* National Center for Earthquake Engineering Research.

Chen, W. F. (1982). *Plasticity in reinforced concrete*. McGraw-Hill.

Cheng, Z., Saiidi, M., & Sanders, D. H. (2006). *Development of a seismic Design Method for Reinforced Concrete Two-way Bridge Column Hinges.* University of Nevada, Reno, Department of Civil Engineering. Reno: Center for Civil Engineering Earthquake Research.

Chopra, A. K. (2007). *Dynamics of structure - Theory and Application to Earthquake Engineering.* Upper Saddle River, New Jersey: Pearson Prentice Hall.

Doyle, K. A., & Saiidi, M. S. (2008). *Seismic response of telescopic pipe pin connection.* University of Nevada, Rerno, Department of civil engineering . Reno, NV: Center for Civil Engineering Earthquake Research.

Frosch, R. J. (1999). Shear transfer between concrete elements using steel pipe connection. *ACI Structural Journal, 96*(6), 1003-1008.

Gent , A. N. (1992). *Engineering with Rubber: How to design rubber components.* Hanser.

Haroun, M., Pardoen, G., & Shepherd, R. (1993). Shear strength of pinned columns. *Proceedings of the 2nd Annual Seismic Research Workshop.*

Harris, H. G.; American Concrete Institude Commiitte 444 . (1982). dynamic modeling of concrete structures. *SP-73.* Detroit: American Concrete Institude.

Henley, E., & McLean, D. I. (1990). *Moment-reducing hinge details for the bases of bridge columns.* Washington, DC: Transportation Research Board.

Hillerborg, A., Modéer, M., & Petersson, P. E. (1976). Analysis of crack formation and crack growth in concrete by means of fracture mechanics and finite elements. *Cement and concrete research*, *6*(6), 773-781.

Jiang, Y., & Saiidi, M. (1995). Response and design of R/C one-way pier hinges in strong direction. *ASCE Journal of Structural Engineering, 121*(8).

Johnson, N., Ranf, T., Saiidi M., & Sanders, D. (2008, March-April). Seismic testing of a two-span reinforced concrete bridge. *Journal of bridge Engineering, 13*(2), 173-182.

Kavianpour, F., & Saiidi, M. (2013). *Experimental and Analytical Seismic Studies of a Four-Span Bridge System with Composite Piers.* University of Nevada, Reno, Department of Civil and Environmental Engineering. Center for Civil Engineering Earthquake Research.

Kulkarni, S. M., & Shah, S. P. (1998). Response of Reinforced Concrete Beams at High Strain Rate. *ACI STRUCTURAL JOURNAL, 95*(6).

Laplace, P., Sanders, D., Saiidi, S., & Douglas, B. (1999). *Shake Table Testing of Flexure Dominated Reinforced Concrete Bridge Columns.* University of Nevada, Reno, Department of Civil Engineering. Reno: Center for Earthquake Engineering Research.

Larosche, A., Cukrov, M., Sanders, D., & Ziehl, P. (2014). Prestressed Piles to Bent Cap Connections: Seismic Performance of a Full-Scale Three-Pile Specimen. *Journal of Bridge Engineeing, 19*(3), 04013012.

Lee, W., & Billington, S. (2010). Modeling Residual Displacements of Concrete Bridge Columns under Earthquake Loads Using Fiber Elements. *Journal of Bridge Engineering, 15*(3), 240-249.

Lee, W., & Billington, S. (2010). Modeling Residual Displacements of Concrete Bridge Columns under Eqrthquake Loads Using Fiber Elements. *Journal of Bridge Engineering, 15*(3), 240-249.

Lindley, P. B. (1981). Natural Rubber Structural Bearings. *ACI Special Publication, 70*, 353-373.

Maddaloni, G., Ryu, K. P., & Reihorn, A. M. (2011). Simulation of floor response spectra in shake table experiments. *Earthquake Engineering and Structural Dynamics*(40).

Mander, J. B., Priestley, M. J., & Park, R. (1988). Theoretical stress-strain model for confined concrete. *Journal of Structural Engineering, 114*(8), 1804-1826.

Matsumoto, E., Waggoner, M., Sumen, G., Kreger, M., Wood, S., & Breen, J. (2001). *Development of a precast bent cap system.* Center for Transportation Research.

Mazzoni, S., McKenna, F., Scott, M., & Fenves, G. (2009). *Open System for Earthquake Engineering Simulation User Command-Language Manual*. (Pacific Earthquake Engineering Research Center) Retrieved 2014, from

http://opensees.berkeley.edu/OpenSees/manuals/usermanual/HTMLUserManualOpeningPage.htm

Mehrsoroush, A., & Saiidi, S. (2014). *Experimental and Analytical Seismic Studies of Bridge Piers with Innovative Pipe Pin Column-Footing Connections and Precast Cap Beams.* University of Nevada, Reno.

Mehrsoroush, A., & Saiidi, M. S. (2014). An Earthquake-Resistant Column Base Pipe Pin Connection for ABC. *Proceedings of National Accelerated Bridge Construction Conference*, Miami, Florida, 650-658.

Mehrsoroush, A. and Saiidi, M. S. (2014). Seismic Performance of Two-Column Bridge Piers with Innovative Precast Members and Pipe Pin Connections. *Bridge Maintenance, Safety, Management and Life Extension [Proceedings of 7th International Conference on Bridge Maintenance, Safety, and Management* (*IABMAS*)*]*, Shanghai, China, 1472-1479.

Mehrsoroush, A., & Saiidi, M. S. (2016). Cyclic Response of Precast Bridge Piers with Novel Column-Base Pipe Pins and Pocket Cap Beam Connections. *Journal of Bridge Engineering*, 04015080.

Mehrsoroush, S., Saiidi, M., & Ryan, K. (2015). *Development of earthquake-resistant precast pier system for acceleration bridge costruction in Nevada.* University of Nevada, Reno. Retrieved from http://wolfweb.unr.edu/homepage/saiidi/NDOT/Pier/PDFs/ABCProject-CompiledTask1-7-16-2015.pdf

Morell, B. (1935, March). Articulations for concrete structures-the Mesnager hinge. In *Journal Proceedings* (Vol. 31, No. 3, pp. 368-381).

Motaref, S., Saiidi, M., & Sanders, D. (2011). *Seismic Response of Precast Bridge Columns with Energy Dissipating Joints.* Center for Civil Engineering Earthquake Research.

Motaref, S., Saiidi, M. S., & Sanders, D. (2013). Shake table studies of energy-dissipating segmental bridge columns. *Journal of Bridge Engineering*, *19*(2), 186-199.

NEES at University of Nevada, Reno. (2014). *NEES@Nevada*. Retrieved from University of Nevada, Reno Web site: http://nees.unr.edu/facilities-and-equipment/equipment/shake-tables/biaxial-specifications

Neuenhofer, A., & Filippou, F. (1996, July). Evaluation of Nonlinear Frame Finite-Element Models. *Journal of Structural Engineering, 123*(7), 958-966.

Neuenhofer, A., & Filippou, F. (1997, July). Evaluation of Nonlinear Frame Finite-Element Models. *journal of Structural Engineering, 123*(7).

Neuenhofer, A., & Filippou, F. C. (1998). Geometrically Nonlinear Flexibility-Based Frame Finite Element. *Journal of Structural Engineering, 124*(6), 704-711.

Oberg, E., Jones, F. D., Horton, H. L., & Ryffel, H. H. (2012). *Machinery's handbook: A reference book for the mechanical engineer, designer, manufacturing engineer, draftsman, toolmaker, and machinist* (29th ed.). New York: Industrial Press.

P.C.J., H., & Spaan, R. (2005). Shear Stiffness and Maximum Shear Stress of Tubular Members. *International Offshore and Polar Engineering Conference* (pp. 316-319). Seoul, Korea: International Society of Offshore and Polar Engineers.

Pacific Earthquake Engineering Research Center. (2011, November 8). *Peer Groung Motion Database*. (University of California, Berkeley) Retrieved December 16, 2013, from PEER: http://peer.berkeley.edu/peer_ground_motion_database/site

Paulay, T., & Priestley, M. (1992). *Seismic design of Reinforced Concrete and Masonry Buildings.* John Wiley & Sons, Inc.

Restrepo, j. I., & Panagiotou, M. (2005). *BART Aerial guideway shear key tests.* University of California San Diego, Department of Structural Engineering, La Jolla, CA.

Restrepo, J., Tobolsky, M. J., & Matsumoto, E. E. (2011). *Development of a precast bent cap system for seismic regions.*

Roesler, J., Paulino, G. H., Park, K., & Gaedicke, C. (2007). Concrete fracture prediction using bilinear softening. *Cement and Concrete Composites*, *29*(4), 300-312.

Saiidi, M., & Ardekani, S. (2012). An analytical study of residual displacements in RC bridge columns subjected to near-fault earthquakes. *Journal of Bridge Structures, 8*, 35-45.

Saiidi, M., & Straw, D. (1993). Monotonic and cyclic response of one-way R/C. *ACI Structural Journal, 90*(5), 568-573.

Saiidi, M. S., Cheng, Z. Y., & Sanders, D. (2009). Experimental Study of Two-Way Reinforced Concrete Column Hinges under Seismic Loads. *ACI Structural Journal*, *106*(3), 340.

Schacht, G., & Marx, S. (2015). Concrete hinges in bridge engineering. *Engineering History and Heritage, 168*(EH2), pp. 64-74. Retrieved from http://dx.doi.org/10.1680/ehah.14.00020.

Sgambelluri, M., Sanders, D. H., & Saiidi, M. S. (1999). *Behavior of One-Way Reinforced Concrete Bridge Column Hinges in the Weak Direction.* University of Nevada, Reno, Department of civil engineering. Reno, NV: Center for Civil Engineering Earthquake Research .

Tazarv, M., & Saiidi, S. (2014). *Innovative material of bridge columns for accelerated bridge construction in high seismic zones.* University of Nevada, Reno, Civil and Environmental Engineering Department. ProQuest LLC.

Tran, H., & Stanton, J. (2012). *Drilled Shaft Socket Connections for Precast Column in Seismic Regions.* M.S. Thesis, University of Washington, Seattle.

Vecchio, F. J., & Lai, D. (2004). Crack Shear-Slip in Reinforced Concrete Elements. *Journal of Advanced Concrete Technology, 2*(3), 289-300.

Walraven, J. (1994). Rough Cracks Subjected to Earthquake Loading. *J. Struct. Eng.*, 1510-1524.

Walraven, J. C., & Reinhardt, H. W. (1981). *Theory and Experiments on the Mechanical behavior of Cracks in Plain and Reinforced Concrete Subjected to Shear Loading.* Delf: HERON.

Wehbe, N. I., Saiidi, M. S., & Sanders, D. H. (1999, March-April). Seismic Performance of Rectangular Bridge Columns with Moderate Confinement. *ACI Structural Journal, 96*(2), 248-258.

Wight, J., & MacGregor, J. (2009). *Reinforced Concrete: Mechanics and Design* (6th ed.). Pearson.

Yeoh, O. H. (1993, November). Some Forms of the Strain Energy Function for Rubber. *Rubber Chemistry and Technology, 66*(5), 754-771. doi: http://dx.doi.org/10.5254/1.3538343.

Zadeh, M., & Saiidi, M. (2007). *Effect of Strain Rates on Stress-Strain Properties and Yield Propagation in Steel Reinforcing Bars.* University of Nevada, Reno. Reno: Center of Civil Engineering Earthquake Research.

Zaghi, A. E., & Saiidi, M. S. (2010). Seismic performance of pipe-pin two-way hinges in concrete bridge columns. *Journal of Earthquake Engineering*,*14*(8), 1253-1302.

Zaghi, A. E., Saiid, S. M., & El-Azazy, S. (2010). Shake table studies of a concrete bridge pier utilizing pipe-pin two-way hinges. *Journal of Bridge Engineering*, *16*(5), 587-596.

Zaghi, A. E., & Saiidi, M. S. (2010). Bearing and shear failure of pipe-pin hinges subjected to earthquakes. Journal of Bridge Engineering, 16(3), 340-350.

Zaghi, A. E., & Saiidi, M. ". (2010). *Seismiv Design of Pipe-Pin Connection Concrete Bridges.* University of Nevada, Reno, Department of Civil Engineering. Reno: Center for Civil Engineering Earthquake research.

Zhao, J., & Sritharan, S. (2007, March-April). Modeling of Strain Penetration Effects in Fiber-Based Analysis of reinforced concrete Structures. *ACI Structural Journal, 104*(2), 133-141.

Tables

Table 2-1. Biaxial shake table specifications at University of Nevada, Reno

Table size	14ftX14.6ft [4.3mX4.5m]
Allowable specimen Mass	50 ton [445 kN]
Allowable Pitch moment	1000 kip-ft [1356 kN-m]
Allowable yaw moment	400 kip-ft [542 kN-m]
Allowable roll moment	400 kip-ft [542 kN-m]
Force capacity of actuators (x and y axis)	165 kip [734 kN]
Dynamic displacements (x and y axis)	± 12 in [±0.30 m]
Static displacements (x and y axis)	±14 in [±0.36 m]
Peak velocity (x and y axis with bare table)	±50 in/sec [1.27 m/sec]
Peak acceleration (x and y axis with 50-ton payload)	± 1 g
Operating Frequency	0-50 Hz

Table 2-2. Specification of the specimens

Model	**BPSA**	**BRSA**
Scale factor	1/3.75	
Column diameter	16 in [406 mm]	
Column longitudinal rebar	14-#4	
Column steel ratio	1.37%	
Column spirals	W4@2”	#3@2”
Column spiral yield strength	51 ksi [352 MPa]	68 ksi [468 MPa]
Column spirals ratio	0.7%	1.62%
Pedestal diameter	22 in [559 mm]	
Pedestal longitudinal rebar	8-#6	
Pedestal longitudinal steel ratio	0.93%	
Pedestal spirals	#3@3”	
Pedestal spiral ratio	0.75%	

Table 2-3. Ground motion characteristic

NGA#	1084
Tp (s)	3.5 --
D5-95 (s)	13.5 11.9
Event	Northridge-01
Year	1994
Station	Sylmar – Converter Station
Magnitude	6.69
Mechanism	reverse
Rjb (km)	0.0
Rrup (km)	5.3
Vs30 (m/s)	251.2
Lowest usable frequency (Hz)	0.41

Table 2-4. Concrete and ECC material test results for BPSA

Location	slump in [mm]	7 days ksi [MPa]	28 days ksi [MPa]	56 days ksi [MPa]	test day ksi [MPa]	test day age day
Footing, Pedestal, column shells	5.50 [140]	2.68 [18.5]	3.99 [27.5]	-- --	6.91 [47.7]	368
CIP Column, Cap beam	3.17 [80]	2.45 [16.9]	3.73 [25.7]	-- --	6.31 [43.5]	350
Filling SCC	0	4.80 [33.1]	5.24 [36.1]	-- --	9.87 [68.1]	346
ECC (second phase)	0	--	4.02 [27.7]	4.25 [29.3]	9.15 [63.1]	350

Table 2-5. Concrete and ECC material test results for BRSA

Location	slump in [mm]	7 days ksi [MPa]	28 days ksi [MPa]	56 days ksi [MPa]	test day ksi [MPa]	test day age day
Footing, Pedestal, column shells	5.50 [140]	2.68 [18.5]	3.99 [27.5]	-- --	7.45 [51.4]	406
CIP Column, cap beam	3.17 [80]	2.45 [16.9]	3.73 [25.7]	--	6.26 [43.2]	388
Filling SCC	-- --	4.80 [33.1]	5.24 [36.1]	-- --	10.40 [71.7]	353
ECC (first phase)	--	-- --	4.50 [31.0]	4.80 [33.1]	9.02 [62.2]	406

Table 2-6. Reinforcing bars material test results

	Fy	**Fu**	**E_{sh}**	**ε_{sh}**	**ε_u**
	ksi [MPa]	ksi [MPa]	ksi [Mpa]	in/in [mm/mm]	in/in [mm/mm]
W4-wire	56.83 [391.9]	79.021 [545.0]	--	--	0.151
#3	65.19 [449.6]	100.52 [693.2]	1200 [8275.9]	0.0095	0.15
#4	68.00 [469.0]	92.91 [640.8]	800 [5517.2]	0.0140	0.14
#5	67.09 [462.7]	99.50 [686.2]	1200 [8275.9]	0.0040	0.11
#6	66.30 [457.2]	93.50 [644.8]	900 [6206.9]	0.009	0.18
#8	72.00 [496.6]	99.00 [682.8]			

Table 2-7. Manufacturer material testing report for steel parts

	Fy	**Fu**	**elongation**
	ksi [MPa]	**Ksi [MPa]**	**%**
Upper pipe	48.4 [334]	81.5 [562]	50
Lower pipe	39.1 [270]	80.4 [554]	66.5
Mass rig link plate	48.8 [337]	71.1 [491]	44
Pipe-pin End plates (3/4")	45.0 [310]	65.8 [454]	24
Load cell plate	39.6 [273]	61.5 [424]	32
Studs	62.5 [431]	75.5 [521]	24
High strength rod	130 [896]	150 [1034]	14

Table 2-8. Elastomers compressive tests samples dimensions

Sample		1	2	3	4	5	6	7	8
Diameter	in	1.86	1.86	1.85	1.87	1.87	0.91	0.91	0.92
	[mm]	[47]	[47]	[47]	[47]	[47]	[23]	[23]	[23]
Thickness	in	0.34							
	[mm]	[9]							

Table 3-1. BPSA Fundamental periods, target and achieved motion properties

		Target		Achieved			
	Fundamental Period sec	PGA g	Sa g	PGA g	PGV in/s [mm/s]	PGD in [mm]	Sa g
RUN-1	0.54	0.09	0.16	0.12	2.44 [62]	0.19 [5]	0.17
RUN-2	0.65	0.27	0.49	0.20	6.82 [173]	0.57 [15]	0.46
RUN-3	0.80	0.44	0.82	0.57	11.25 [286]	1.02 [26]	0.83
RUN-4	0.85	0.53	0.99	0.78	15.92 [404]	1.19 [30]	1.07
RUN-5	0.74	0.53	0.99	0.35	11.58 [294]	1.15 [29]	0.92
RUN-6	0.87	0.53	0.99	0.30	11.90 [302]	1.18 [30]	0.92
RUN-7	0.90	0.62	1.15	0.42	14.37 [365]	1.32 [34]	1.10
RUN-8	0.92	0.80	1.48	0.60	19.43 [493]	1.63 [41]	1.46
RUN-9	1.08	0.97	1.81	0.77	24.44 [621]	1.94 [49]	1.83
RUN-10	1.09	1.15	2.14	0.97	29.11 [739]	2.29 [58]	2.18
RUN-11	1.10	1.24	2.30	1.14	32.06 [814]	2.49 [63]	2.40

Table 3-2. BPSA maximum cap beam elongation

RUN		1	2	3	4	5	6	7	8	9	10	11
$SP6_{max}$	in [mm]	0.01 [0.1]	0.07 [1.8]	0.42 [10.6]	2.88 [73.1]	0.04 [1.0]	0.05 [1.1]	0.04 [1.1]	0.04 [1.0]	0.03 [0.8]	0.02 [0.6]	0.02 [0.5]

Table 3-3. BPSA specimen and pedestal displacements

	Specimen Displacement in [mm]			Pedestal Displacement in [mm]			$\left(\frac{D_{pedestal}}{D_{specimen}}\right)_{max}$
	Maximum		Residual	Maximum		Residual	
	South(+)	North(-)		South(+)	North(-)		
RUN-1	0.44 [11.3]	-0.42 [-10.7]	0.02 [0.4]	0.03 [0.8]	-0.03 [-0.6]	0.00 [0.0]	0.071
RUN-2	1.31 [33.4]	-1.42 [-35.9]	0.05 [1.2]	0.10 [2.5]	-0.09 [-2.2]	0.00 [0.1]	0.070
RUN-6	4.07 [103.5]	-1.96 [-49.8]	0.43 [11.0]	0.22 [5.7]	-0.15 [-3.9]	0.009 [0.2]	0.055
RUN-7	4.51 [114.46]	-2.32 [-58.83]	0.98 [24.91]	0.26 [6.49]	-0.20 [-5.03]	0.014 [0.35]	0.057
RUN-8	4.99 [126.7]	-2.93 [-74.5]	1.48 [37.6]	0.26 [6.7]	-0.18 [-4.6]	0.022 [0.6]	0.053
RUN-9	4.83 [122.6]	-3.72 [-94.4]	1.27 [32.4]	0.29 [7.3]	-0.20 [-5.1]	0.021 [0.5]	0.059
RUN-10	4.62 [117.4]	-4.61 [-117.2]	0.73 [18.5]	0.31 [7.8]	-0.30 [-7.7]	0.021 [0.5]	0.066
RUN-11	4.10 [104.2]	-5.16 [-131.1]	-0.30 [-7.6]	0.29 [7.4]	-0.23 [-5.8]	0.008 [0.2]	0.057

Table 3-4. BPSA maximum displacements and forces for bent and columns

	Bent				CIP				PC			
	Displacement		Base Shear		Displacement		Shear		Displacement		Shear	
	in [mm]		kip [kN]		in [mm]		kip [kN]		in [mm]		kip [kN]	
	South(+)	North(-)	South(+)	North(-)	South(+)	North(-)	South(+)	North(-)	South(+)	North(-)	South(+)	North(-)
RUN-1	0.43 [11]	-0.40 [-10]	12.9 [57.2]	-14.3 [-63.7]	0.23 [6]	-0.32 [-8]	5.2 [23.1]	-6.2 [-27.4]	0.32 [8]	-0.25 [-6]	7.6 [33.6]	-8.2 [-36.3]
RUN-2	1.25 [32]	-1.32 [-34]	32.8 [146]	-39.0 [-174]	0.96 [24]	-1.19 [-30]	14.3 [64]	-15.3 [-68]	1.04 [26]	-1.08 [-27]	18.5 [82]	-23.7 [-105]
RUN-6	3.87 [98]	-1.80 [-46]	56.8 [252.4]	-37.4 [-166.3]	3.50 [89]	-1.67 [-42]	26.9 [119.6]	-13.8 [-61.5]	3.56 [90]	-1.55 [-39]	29.9 [132.9]	-23.6 [-104.9]
RUN-7	4.32 [110]	-2.15 [-55]	56.3 [250.6]	-39.6 [-176.0]	3.94 [100]	-2.01 [-51]	26.4 [117.4]	-14.1 [-62.5]	4.01 [102]	-1.87 [-48]	29.9 [133.2]	-25.5 [-113.5]
RUN-8	4.79 [122]	-2.76 [-70]	55.8 [248.4]	-43.7 [-194.5]	4.41 [112]	-2.62 [-67]	26.1 [116.3]	-15.6 [-69.3]	4.49 [114]	-2.45 [-62]	29.7 [132.1]	-28.2 [-125.2]
RUN-9	4.65 [118]	-3.53 [-90]	50.3 [223.8]	-47.3 [-210.4]	4.27 [109]	-3.38 [-86]	23.0 [102.1]	-17.4 [-77.5]	4.36 [111]	-3.17 [-81]	27.4 [121.7]	-29.9 [-132.8]
RUN-10	4.42 [112]	-4.42 [-112]	45.7 [203.2]	-46.7 [-207.7]	4.05 [103]	-4.25 [-108]	20.4 [90.8]	-19.3 [-85.8]	4.14 [105]	-4.00 [-102]	25.3 [112.4]	-27.4 [-121.9]
RUN-11	3.94 [100]	-4.99 [-127]	35.1 [156.0]	-42.9 [-191.0]	3.59 [91]	-4.80 [-122]	14.3 [63.5]	-20.1 [-89.4]	3.93 [100]	-5.02 [-127]	20.8 [92.6]	-22.8 [-101.6]
Ductility	**3.6**				**3.8**				**4.1**			

Table 3-5. BPSA maximum column axial loads

	CIP		PC	
	comp.	ten.	comp.	ten.
	kip [kN]	kip [kN]	kip [kN]	kip [kN]
RUN-1	15.0 [67]	-6.8 [-30]	15.8 [70]	-6.0 [-27]
RUN-2	30.5 [136]	-25.7 [-114]	34.7 [154]	-21.5 [-95]
RUN-6	48.2 [214]	-26.1 [-116]	35.1 [156]	-39.2 [-174]
RUN-7	47.5 [211]	-27.1 [-120]	36.1 [160]	-38.5 [-171]
RUN-8	46.8 [208]	-29.6 [-132]	38.6 [172]	-37.8 [-168]
RUN-9	43.0 [191]	-31.7 [-141]	40.7 [181]	-34.0 [-151]
RUN-10	39.7 [177]	-29.8 [-132]	38.8 [172]	-30.7 [-137]
RUN-11	32.7 [145]	-26.2 [-116]	35.2 [157]	-23.7 [-105]

Table 3-6. BPSA maximum and minimum strains in longitudinal bars of CIP plastic hinge region in percent

	South Long. Bar						**North Long. Bar**					
	maximum			**minimum**			**maximum**			**minimum**		
section	**L8**	**L7**	**L6**	**L8**	**L7**	**L6**	**L8**	**L7**	**L6**	**L8**	**L7**	**L6**
Elev. from soffit	***-1***	***-7***	***-13***	***-1***	***-7***	***-13***	***-1***	***-7***	***-13***	***-1***	***-7***	***-13***
RUN-1	0.124	0.109	0.080	-0.073	-0.103	-0.080	0.095	0.137	0.093	-0.048	-0.074	-0.052
RUN-2	**0.339**	**0.281**	**0.244**	-0.187	**-0.291**	-0.191	**0.826**	**0.646**	**0.260**	-0.101	-0.170	-0.152
RUN-6	**6.657**	**5.101**	**0.896**	-0.188	-0.047	**-0.235**	**1.943**	**0.878**	**0.278**	0.046	**-0.680**	**-0.491**
RUN-7	**8.014**	**5.919**	**0.944**	**-0.650**	**0.558**	-0.191		**1.077**	**0.312**		**-0.755**	**-0.595**
RUN-8		**6.681**	**0.936**		**1.201**	-0.184		**1.782**	**0.344**		**-0.908**	**-0.622**
RUN-9			**0.837**			-0.202		**2.841**	**0.386**		**-0.695**	**-0.582**
RUN-10			**0.749**			-0.046		**3.731**	**0.411**		-0.151	**-0.539**
RUN-11			**0.563**			0.096		**3.834**	**0.408**		**2.195**	-0.234

Table 3-7. BPSA maximum and minimum strains in longitudinal bars of PC plastic hinge region in percent

	Extreme North Long. Bar			
	maximum		minimum	
section	R7	R6	R7	R6
Elev. from soffit	*-7*	*-13*	*-7*	*-13*
RUN-1	0.111	0.111	-0.060	-0.046
RUN-2	**0.366**	**0.318**	-0.137	-0.107
RUN-6	**1.484**	**0.845**	-0.102	0.143
RUN-7	**1.791**	**1.319**	-0.039	0.222
RUN-8	**2.412**	**1.729**	0.057	**0.284**
RUN-9	**3.090**	**1.957**	0.197	**0.373**
RUN-10	**3.233**	**2.011**	**0.495**	**0.465**
RUN-11	**1.712**	**1.460**	**1.234**	**1.301**

Table 3-8. BPSA maximum and minimum strains in transverse bars of CIP plastic hinge region in percent

	West side spiral				East side spiral			
	maximum		minimum		maximum		minimum	
section	L7	L6	L7	L6	L7	L6	L7	L6
Elev. from soffit	*-7*	*-13*	*-7*	*-13*	*-7*	*-13*	*-7*	*-13*
RUN-1	0.004	0.004	-0.002	-0.003	0.004	0.000	-0.003	0.000
RUN-2	0.009	0.006	-0.002	-0.001	0.004	0.000	-0.003	0.000
RUN-6	0.009	0.001	-0.007	-0.005	0.015	0.000	-0.016	0.000
RUN-7	0.010	0.002	-0.006	-0.004	-0.006	0.000	-0.026	0.000
RUN-8	0.009	0.003	-0.004	-0.004	-0.015	0.000	-0.038	0.000
RUN-9	0.007	0.002	-0.007	-0.004	-0.024	0.000	-0.054	0.000
RUN-10	0.005	0.003	-0.011	-0.005	-0.033	0.000	-0.074	0.000
RUN-11	0.003	0.003	-0.015	-0.004	-0.046	0.000	-0.096	0.000

Table 3-9. BPSA maximum and minimum strains in transverse bars of PC plastic hinge region in percent

	West side spiral				East side spiral					
	maximum		minimum		maximum			minimum		
section	R7	R6	R7	R6	R8	R7	R6	R8	R7	R6
Elev. from soffit	*-7*	*-13*	*-7*	*-13*	*-1*	*-7*	*-13*	*-1*	*-7*	*-13*
RUN-1	0.004	0.009	-0.003	-0.003	0.005	0.006	0.004	-0.003	-0.003	-0.003
RUN-2	0.004	0.011	-0.023	-0.012	0.007	0.025	0.005	-0.001	0.002	-0.014
RUN-6	-0.047	-0.052	-0.104	-0.083	0.007	0.021	-0.010	-0.011	-0.042	-0.064
RUN-7	-0.057	-0.037	-0.119	-0.080	0.011	0.000	0.004	-0.005	-0.056	-0.066
RUN-8	-0.075	-0.033	-0.140	-0.077	0.007	0.005	-0.003	-0.007	-0.055	-0.069
RUN-9	-0.092	-0.028	-0.163	-0.081	0.007	0.019	-0.003	-0.010	-0.047	-0.071
RUN-10	-0.107	-0.030	-0.166	-0.095	0.008	0.029	0.006	-0.018	-0.033	-0.074
RUN-11	-0.119	-0.039	-0.178	-0.102	0.007	0.055	0.008	-0.054	-0.035	-0.084

Table 3-10. BPSA maximum and minimum vertical strains on pipes at south side of CIP pipe-pin in percent

	maximum						minimum					
	P(V) 51	**P(V) 61**	**P(V) 71**	**P(V) 81**	**P(V) 91**	**P(V) 101**	**P(V) 51**	**P(V) 61**	**P(V) 71**	**P(V) 81**	**P(V) 91**	**P(V) 101**
Elev. from top of pedestal	***-12***	***-7***	***-2***	***2***	***6***	***11***	***-12***	***-7***	***-2***	***2***	***6***	***11***
RUN-1	0.004	0.010	0.016	0.007	0.004	0.003	-0.003	-0.003	-0.003	-0.002	-0.003	-0.003
RUN-2	0.008	0.028	0.043	0.010	0.005	0.004	-0.005	-0.015	-0.013	-0.014	-0.014	-0.015
RUN-6	0.014	0.040	0.049	0.005	0.004	0.003	-0.028	-0.069	-0.062	-0.029	-0.026	-0.026
RUN-7	0.016	0.044	0.055	0.005	0.006	0.003	-0.032	-0.074	-0.067	-0.033	-0.027	-0.027
RUN-8	0.017	0.050	0.063	0.005	0.007	0.000	-0.037	-0.081	-0.077	-0.036	-0.034	-0.037
RUN-9	0.019	0.058	0.073	0.005	0.007	0.002	-0.036	-0.073	-0.062	-0.045	-0.041	-0.047
RUN-10	0.019	0.062	0.082	0.002	0.007	-0.001	-0.032	-0.062	-0.047	-0.058	-0.045	-0.058
RUN-11	0.019	0.062	0.088	-0.004	0.007	0.000	-0.023	-0.046	-0.024	-0.065	-0.046	-0.062

Table 3-11. BPSA maximum and minimum vertical strains on pipes at north side of CIP pipe-pin in percent

	maximum						minimum					
	P(V) 53	**P(V) 63**	**P(V) 73**	**P(V) 83**	**P(V) 93**	**P(V) 103**	**P(V) 53**	**P(V) 63**	**P(V) 73**	**P(V) 83**	**P(V) 93**	**P(V) 103**
Elev. from top of pedestal	***-12***	***-7***	***-2***	***2***	***6***	***11***	***-12***	***-7***	***-2***	***2***	***6***	***11***
RUN-1	0.004	0.004	0.004	0.014	0.004	0.003	-0.002	-0.004	-0.005	-0.004	-0.004	-0.004
RUN-2	0.009	0.024	0.037	0.018	0.005	0.004	-0.004	-0.010	-0.010	0.003	-0.015	-0.010
RUN-6	0.016	0.073	0.157	0.112	0.003	0.004	-0.022	-0.039	-0.024	-0.028	-0.040	-0.031
RUN-7	0.019	0.078	0.168	0.117	0.004	0.003	-0.024	-0.043	-0.012	-0.020	-0.039	-0.033
RUN-8	0.022	0.084	0.180	0.128	0.003	0.003	-0.031	-0.054	-0.012	-0.018	-0.042	-0.036
RUN-9	0.019	0.073	0.148	0.106	0.002	0.002	-0.037	-0.063	-0.011	-0.019	-0.041	-0.032
RUN-10	0.017	0.060	0.122	0.087	0.002	0.002	-0.042	-0.071	-0.019	-0.021	-0.035	-0.025
RUN-11	0.014	0.045	0.080	0.012	0.003	0.002	-0.040	-0.069	-0.021	-0.017	-0.027	-0.030

Table 3-12. BPSA maximum and minimum vertical strains on pipes at south side of PC pipe-pin in percent

	maximum						minimum					
	P(V) A51	**P(V) A61**	**P(V) A71**	**P(V) A81**	**P(V) A91**	**P(V) A101**	**P(V) A51**	**P(V) A61**	**P(V) A71**	**P(V) A81**	**P(V) A91**	**P(V) A101**
Elev. from top of pedestal	***-12***	***-7***	***-2***	***2***	***6***	***11***	***-12***	***-7***	***-2***	***2***	***6***	***11***
RUN-1	0.004	0.004	0.003	0.004	0.003	0.003	-0.002	-0.003	-0.006	-0.003	-0.004	-0.010
RUN-2	0.009	0.025	0.033	0.004	0.004	-0.002	-0.003	-0.009	-0.015	-0.009	-0.009	-0.021
RUN-6	0.009	0.030	0.043	0.004	0.003	0.006	-0.025	-0.056	-0.053	-0.021	-0.013	-0.009
RUN-7	0.010	0.034	0.050	0.005	0.003	0.008	-0.026	-0.058	-0.056	-0.021	-0.015	-0.009
RUN-8	0.011	0.040	0.059	0.004	0.001	0.009	-0.029	-0.060	-0.062	-0.026	-0.020	-0.016
RUN-9	0.012	0.045	0.068	0.002	0.000	0.005	-0.027	-0.057	-0.055	-0.033	-0.028	-0.025
RUN-10	0.012	0.044	0.067	0.001	-0.001	0.004	-0.025	-0.051	-0.044	-0.038	-0.035	-0.034
RUN-11	0.011	0.040	0.061	0.001	0.001	0.005	-0.020	-0.040	-0.029	-0.039	-0.034	-0.037

Table 3-13. BPSA maximum and minimum vertical strains on pipes at north side of PC pipe-pin in percent

	maximum						minimum					
	P(V) A53	**P(V) A63**	**P(V) A73**	**P(V) A83**	**P(V) A93**	**P(V) A103**	**P(V) A53**	**P(V) A63**	**P(V) A73**	**P(V) A83**	**P(V) A93**	**P(V) A103**
Elev. from top of pedestal	***-12***	***-7***	***-2***	***2***	***6***	***11***	***-12***	***-7***	***-2***	***2***	***6***	***11***
RUN-1	0.004	0.008	0.013	0.008	0.003	0.003	-0.004	-0.003	-0.002	-0.003	-0.007	-0.003
RUN-2	0.008	0.026	0.045	0.008	0.006	0.004	-0.006	-0.014	-0.014	-0.018	-0.009	-0.010
RUN-6	0.005	0.053	0.125	0.097	0.003	0.003	-0.015	-0.030	-0.021	-0.029	-0.029	-0.047
RUN-7	0.007	0.057	0.133	0.108	0.003	0.002	-0.016	-0.035	-0.016	-0.034	-0.029	-0.051
RUN-8	0.008	0.059	0.137	0.114	0.000	0.002	-0.023	-0.044	-0.018	-0.028	-0.032	-0.052
RUN-9	0.011	0.057	0.125	0.100	-0.001	0.003	-0.028	-0.051	-0.021	-0.028	-0.031	-0.044
RUN-10	0.011	0.052	0.113	0.089	-0.002	0.002	-0.032	-0.057	-0.027	-0.031	-0.031	-0.037
RUN-11	0.011	0.043	0.088	0.046	-0.001	0.003	-0.033	-0.054	-0.024	-0.034	-0.028	-0.028

Table 3-14. BPSA maximum shear strains on pipes of CIP pipe-pin in percent

	lower pipe			**upper pipe**		
Section	**1**	**2**	**3**	**4**	**5**	**6**
elevation from top of pedestal	***-12***	***-7***	***-2***	***2***	***6***	***11***
RUN-1	0.007	0.009		0.024	0.013	0.008
RUN-2	0.012	0.016		0.068	0.022	0.015
RUN-6	0.028	0.058		0.090	0.058	0.018
RUN-7	0.032	0.040		0.092	0.057	0.024
RUN-8	0.035	0.053		0.103	0.057	0.032
RUN-9	0.038	0.074		0.113	0.054	0.025
RUN-10	0.043			0.116	0.054	0.039
RUN-11	0.045			0.112	0.055	0.052

Table 3-15. BPSA maximum shear strains on pipes of PC pipe-pin in percent

	lower pipe			**upper pipe**		
Section	**1**	**2**	**3**	**4**	**5**	**6**
elevation from top of pedestal	***-12***	***-7***	***-2***	***2***	***6***	***11***
RUN-1	0.007	0.009	0.009	0.011	0.011	0.008
RUN-2	0.012	0.022	0.024	0.035	0.019	0.016
RUN-6	0.021	0.047	0.044	0.061	0.033	0.018
RUN-7	0.025	0.050	0.044	0.070	0.035	
RUN-8	0.026	0.050	0.054	0.086	0.039	
RUN-9		0.044	0.062	0.099	0.042	
RUN-10		0.040	0.059	0.097	0.043	
RUN-11		0.032	0.051	0.088	0.040	

Table 3-16. BPSA column and pedestal longitudinal reinforcement strains at CIP pipe-pin in percent

	South long. bar										North long. bar							
	maximum					minimum					maximum				minimum			
	pedestal			column		pedestal			column		pedestal		column		pedestal		column	
section	L1	L2	L3	L4	L5	L1	L2	L3	L4	L5	L2	L3	L4	L5	L2	L3	L4	L5
Elev. from top of pedestal	*-25*	*-10*	*-5*	*5*	*10*	*-25*	*-10*	*-5*	*5*	*10*	*-10*	*-5*	*5*	*10*	*-10*	*-5*	*5*	*10*
RUN-1	0.019	0.008	0.003	0.004	0.005	-0.010	-0.009	-0.003	-0.007	-0.013	0.005	0.002	0.004	0.013	-0.007	-0.002	-0.003	-0.019
RUN-2	0.119	0.062	0.033	0.010	0.007	-0.045	-0.030	-0.009	-0.030	-0.026	0.020	0.007	0.034	0.086	-0.025	-0.008	-0.008	-0.046
RUN-6	0.121	0.064	0.037	0.008	0.010	-0.126	-0.075	-0.014	-0.078	-0.071	0.067	0.056	0.074	0.109	-0.014	-0.012	-0.023	-0.064
RUN-7	0.130	0.067	0.039	0.008	0.014	-0.131	-0.072	-0.013	-0.082	-0.071	0.082	0.059	0.076	0.105	-0.007	-0.011	-0.020	-0.061
RUN-8	0.145	0.074	0.047	0.010	0.017	-0.135	-0.068	-0.015	-0.086	-0.076	0.084	0.057	0.074	0.108	-0.010	-0.016	-0.018	-0.062
RUN-9	0.163	0.112	0.067	0.012	0.025	-0.118	-0.054	-0.015	-0.075	-0.066	0.068	0.049	0.075	0.108	-0.022	-0.028	-0.023	-0.063
RUN-10	0.174	0.146	0.070	0.014	0.030	-0.109	-0.044	-0.013	-0.067	-0.058	0.059	0.042	0.074	0.102	-0.029	-0.031	-0.028	-0.068
RUN-11	0.173	0.151	0.058	0.018	0.040	-0.082	-0.021	-0.009	-0.048	-0.041	0.045		0.061	0.067	-0.030		-0.027	-0.059

Table 3-17. BPSA column and pedestal longitudinal reinforcement strains at PC pipe-pin in percent

	South long. bar								North long. bar									
	maximum				minimum				maximum					minimum				
	pedestal			column	pedestal			column	pedestal			column		pedestal			column	
section	R1	R2	R3	R4	R1	R2	R3	R4	R1	R2	R3	R4	R5	R1	R2	R3	R4	R5
Elev. from top of pedestal	*-25*	*-10*	*-5*	*5*	*-25*	*-10*	*-5*	*5*	*-25*	*-10*	*-5*	*5*	*10*	*-25*	*-10*	*-5*	*5*	*10*
RUN-1	0.021	0.006	0.003	0.010	-0.010	-0.004	-0.003	-0.003	0.015	0.007	0.003	0.004	0.006	-0.017	-0.010	-0.003	-0.005	-0.010
RUN-2	0.115	0.032	0.020	0.033	-0.044	-0.013	-0.006	-0.005	0.086	0.036	0.020	0.012	0.017	-0.065	-0.041	-0.013	-0.041	-0.018
RUN-6	0.114	0.036	0.026	0.029	-0.079	-0.037	-0.017	-0.015	0.160	0.117	0.050	0.018	0.041	-0.059	-0.033	-0.011	-0.042	-0.018
RUN-7	0.121	0.040	0.027	0.025	-0.081	-0.036	-0.017	-0.016	0.160	0.118	0.050	0.021	0.048	-0.059	-0.025	-0.007	-0.049	-0.018
RUN-8	0.132	0.043	0.028	0.023	-0.083	-0.037	-0.018	-0.019	0.158	0.115	0.054	0.021	0.050	-0.065	-0.023	-0.003	-0.061	-0.025
RUN-9	0.143	0.049	0.032	0.029	-0.075	-0.030	-0.016	-0.016	0.141	0.101	0.051	0.023	0.046	-0.071	-0.023	0.000	-0.069	-0.038
RUN-10	0.146	0.054	0.032	0.026	-0.069	-0.027	-0.015	-0.015	0.130	0.090	0.048	0.027	0.043	-0.072	-0.023	0.000	-0.083	-0.040
RUN-11	0.145	0.058	0.034	0.021	-0.055	-0.017	-0.010	-0.008	0.106	0.075	0.043	0.025	0.027	-0.070	-0.022	0.000	-0.093	-0.047

Table 3-18. BPSA column and pedestal transverse reinforcement maximum strains at CIP pipe-pin in percent

	SOUTH				NORTH				EAST				WEST			
section	**L2**	**L3**	**L4**	**L5**	**L2**	**L3**	**L4**	**L5**	**L2**	**L3**	**L4**	**L5**	**L2**	**L3**	**L4**	**L5**
Elev. from top of pedestal	***-10***	***-5***	***5***	***10***	***-10***	***-5***	***5***	***10***	***-10***	***-5***	***5***	***10***	***-10***	***-5***	***5***	***10***
RUN-1	0.005	0.005	0.005	0.005	0.005	0.005	0.005	0.007	0.004	0.006	0.0065	0.007	0.005	0.004	0.007	0.006
RUN-2	0.014	0.011	0.031	0.011	0.005	0.009	0.024	0.019	0.006	0.012	0.0124	0.008	0.006	0.010	0.018	0.013
RUN-6	0.038	0.027	0.089	0.002	0.051	0.034	0.060	0.004	0.030	0.032	0.0026	-0.003	0.009	0.037	0.029	0.039
RUN-7	0.043	0.031	0.107	0.015	0.075	0.045	0.060	0.005	0.034	0.033	-0.003	-0.005	0.026	0.042	0.032	0.045
RUN-8	0.048	0.032	0.128	0.022	0.095	0.048	0.058	0.008	0.035	0.034	-0.002	-0.011	0.040	0.046	0.035	0.048
RUN-9	0.047	0.027	0.123	0.022	0.090	0.042	0.054	0.014	0.035	0.041	-0.007	-0.022	0.042	0.042	0.039	0.042
RUN-10	0.054	0.021	0.115	0.018	0.083	0.038	0.046	0.020	0.039	0.050	-0.01	-0.023	0.044	0.038	0.046	0.039
RUN-11	0.067	0.016	0.106	0.014	0.074	0.043	0.042	0.024	0.044	0.057	-0.012	-0.023	0.063	0.035	0.050	0.045

Table 3-19. BPSA column and pedestal transverse reinforcement maximum strains at PC pipe-pin in percent

	SOUTH				NORTH				EAST				WEST			
section	**L2**	**L3**	**L4**	**L5**	**L2**	**L3**	**L4**	**L5**	**L2**	**L3**	**L4**	**L5**	**L2**	**L3**	**L4**	**L5**
Elev. from top of pedestal	***-10***	***-5***	***5***	***10***	***-10***	***-5***	***5***	***10***	***-10***	***-5***	***5***	***10***	***-10***	***-5***	***5***	***10***
RUN-1	0.005	0.004	0.005		0.005	0.005	0.005	0.007	0.004	0.005	0.00654	0.007	0.005	0.004	0.010	0.005
RUN-2	0.006	0.008	0.011		0.010	0.010	0.012	0.012	0.006	0.007	0.00915	0.010	0.006	0.010	0.011	0.010
RUN-6	0.012	0.020	0.009		0.094	0.063	0.028	0.035	0.012	0.028	0.01308		0.026	0.028	-0.003	
RUN-7	0.016	0.021	0.012		0.115	0.092	0.031	0.042	0.014	0.030	0.01308		0.030	0.034	-0.002	
RUN-8	0.020	0.023	0.014		0.133	0.106	0.032	0.045	0.013	0.029	0.01308		0.033	0.038		
RUN-9	0.021	0.019	0.016		0.130	0.104	0.035	0.034	0.012	0.027	0.01438		0.032	0.035		
RUN-10	0.021	0.017	0.014		0.124	0.097	0.046	0.043	0.011	0.026	0.01569		0.030	0.032		
RUN-11	0.020	0.016	0.012		0.112	0.083	0.055	0.064	0.011	0.025	0.01177		0.028	0.026		

Table 3-20. BPSA maximum and minimum strains in cap beam reinforcement in percent

	maximum						minimum					
	Longitudinal bars				Trans. Bars		Longitudinal bars				Trans. Bars	
	CSG 41	CSG 42	CSG A41	CSG A42	CSG 43	CSG A43	CSG 41	CSG 42	CSG A41	CSG A42	CSG 43	CSG A43
RUN-1	0.009	0.018	0.006	0.012	0.003	0.004	-0.008	-0.006	-0.007	-0.006	-0.003	-0.003
RUN-2	0.066	0.076	0.049	0.098	0.004	0.005	-0.011	-0.006	-0.015	-0.007	-0.003	-0.007
RUN-6	0.019	0.017	0.036	0.058	0.003	0.002	-0.013	-0.007	-0.001	-0.008	-0.004	-0.004
RUN-7	0.019	0.017	0.036	0.056	0.003	0.002	-0.014	-0.006	-0.002	-0.009	-0.004	-0.003
RUN-8	0.017	0.020	0.038	0.055	0.001	0.002	-0.015	-0.007	-0.009	-0.010	-0.005	-0.004
RUN-9	0.015	0.021	0.038	0.050	0.001	0.002	-0.015	-0.008	-0.005	-0.009	-0.006	-0.003
RUN-10	0.013	0.021	0.040	0.044	0.001	0.002	-0.016	-0.009	-0.002	-0.012	-0.006	-0.005
RUN-11	0.010	0.019	0.039	0.033	0.001	0.004	-0.013	-0.008	-0.002	-0.009	-0.004	-0.004

Table 3-21. BPSA unreliable displacement potentiometer instruments at top of the columns

Column	Section	Broken instrument	in run
PC	Top	NT A14	RUN-10
	middle	NT A11	RUN-10
		NT A12	RUN-9
	Bottom	NT A9	RUN-10
		NT A10	RUN-10

Table 3-22. BPSA maximum and minimum shear and slippage in pipe-pins

	CIP Pipe-Pin					PC Pipe-Pin				
	Slip			Shear		Slip			Shear	
	Max	Min	Residual	Max	Min	Max	Min	Residual	Max	Min
	in [mm]	in [mm]	in [mm]	kip.in [kN.m]	kip.in [kN.m]	in [mm]	in [mm]	in [mm]	kip.in [kN.m]	kip.in [kN.m]
RUN-1	0.20 [5.1]	-0.08 [-2.1]	0.01 [0.3]	5.1 [0.58]	-5.8 [-0.65]	0.11 [2.8]	-0.15 [-3.8]	0.01 [0.1]	7.3 [0.83]	-7.9 [-0.89]
RUN-2	0.29 [7.4]	-0.12 [-3.2]	0.03 [0.8]	14.4 [1.63]	-14.4 [-1.63]	0.14 [3.4]	-0.29 [-7.3]	-0.03 [-0.8]	18.7 [2.12]	-23.0 [-2.60]
RUN-6	0.37 [9.5]	-0.12 [-3.0]	0.04 [1.0]	26.5 [2.99]	-12.4 [-1.40]	0.27 [6.9]	-0.27 [-6.7]	0.08 [2.1]	30.0 [3.39]	-21.4 [-2.41]
RUN-7	0.37 [9.5]	-0.12 [-3.1]	0.10 [2.5]	26.7 [3.02]	-13.7 [-1.55]	0.27 [6.8]	-0.29 [-7.3]	0.13 [3.4]	29.9 [3.38]	-24.9 [-2.81]
RUN-8	0.37 [9.5]	-0.13 [-3.2]	0.11 [2.9]	26.6 [3.00]	-14.9 [-1.68]	0.27 [6.8]	-0.32 [-8.1]	0.13 [3.4]	28.2 [3.18]	-27.7 [-3.13]
RUN-9	0.37 [9.5]	-0.13 [-3.4]	0.05 [1.2]	23.2 [2.62]	-17.0 [-1.92]	0.27 [6.8]	-0.39 [-9.8]	0.04 [1.0]	23.6 [2.66]	-29.6 [-3.34]
RUN-10	0.37 [9.4]	-0.14 [-3.6]	-0.02 [-0.4]	20.4 [2.31]	-19.1 [-2.16]	0.26 [6.5]	-0.45 [-11.4]	0.00 [0.0]	24.9 [2.81]	-27.5 [-3.11]
RUN-11	0.36 [9.2]	-0.14 [-3.6]	-0.05 [-1.2]	14.4 [1.63]	-20.3 [-2.30]				1.3 [0.14]	1.3 [0.14]

Table 3-23. BPSA maximum and minimum pipe-pins rotations

	CIP			PC			$\frac{M_{CIP}^{pin} + M_{PC}^{pin}}{2}$	
	Max rad	Min rad	residual rad	Max rad	Min rad	residual rad	Max kip.in [kN.m]	Min kip.in [kN.m]
RUN-1	0.0036	-0.0052	-0.0001	0.0049	-0.0038	0.0001	62 [7.0]	-78 [-8.8]
RUN-2	0.0129	-0.0171	-0.0002	0.0138	-0.0133	0.0005	177 [20.0]	-227 [-25.6]
RUN-6	0.0430	-0.0232	0.0048	0.0430	-0.0200	0.0043	348 [39.4]	-311 [-16.6]
RUN-7	0.0475	-0.0270	0.0106	0.0483	-0.0238	0.0107	365 [41.2]	-186 [-21.0]
RUN-8	0.0523	-0.0338	0.0157	0.0541	-0.0306	0.0164	383 [43.2]	-235 [-26.5]
RUN-9	0.0496	-0.0418	0.0146	0.0515	-0.0392	0.0159	319 [36.0]	-285 [-32.2]
RUN-10	0.0459	-0.0511	0.0076	0.0481	-0.0496	0.0103	256 [28.9]	-325 [-36.7]
RUN-11	0.0378	-0.0565	-0.0051	0.0416	-0.0560	-0.0003	167 [18.9]	-364 [-41.1]

Table 3-24. BPSA pipe-pin uplift at maximum and minimum rotations

	CIP		PC	
	@max in [mm]	@min in [mm]	@max in [mm]	@min in [mm]
RUN-1	0.00 [0]	0.02 [0]	0.02 [0]	0.00 [-0]
RUN-2	0.03 [1]	0.07 [2]	0.06 [2]	0.02 [1]
RUN-6	0.13 [3]	0.09 [2]	0.19 [5]	0.05 [1]
RUN-7	0.14 [4]	0.11 [3]	0.21 [5]	0.07 [2]
RUN-8	0.16 [4]	0.13 [3]	0.23 [6]	0.09 [2]
RUN-9	0.15 [4]	0.17 [4]	0.23 [6]	0.13 [3]
RUN-10	0.14 [3]	0.20 [5]	0.22 [6]	0.17 [4]
RUN-11	0.11 [3]	0.21 [5]	0.21 [5]	0.24 [6]
average distance of center of rotation	3.00 [76]	3.90 [99]	4.41 [112]	3.19 [81]

Table 3-25. BRSA Fundamental periods, target and achieved motion properties

		Target		Achieved			
	Fundamental period sec	PGA g	Sa g	PGA g	PGV in/s [mm/s]	PGD in [mm]	Sa g
RUN-1	0.38	0.09	0.14	0.17	2.87 [73]	0.23 [6]	0.21
RUN-2	0.39	0.31	0.48	0.32	9.18 [233]	0.72 [18]	0.44
RUN-3	0.58	0.53	0.81	0.44	12.33 [313]	1.12 [29]	0.71
RUN-4	0.75	0.75	1.15	0.57	16.73 [425]	1.63 [41]	1.12
RUN-5	0.85	0.97	1.49	0.63	20.85 [530]	2.02 [51]	1.26
RUN-6	0.99	1.20	1.83	1.17	27.86 [708]	2.34 [59]	1.73
end of tests	1.09						

Table 3-26. BRSA specimen and pedestal displacement

	Specimen Displacement in [mm]			Pedestal Displacement in [mm]			$\left(\frac{D_{pedestal}}{D_{specimen}}\right)_{max}$
	Maximum		Residual	Maximum		Residual	
	South(+)	North(-)		South(+)	North(-)		
RUN-1	0.18 [5]	-0.20 [-5]	0.00 [0]	0.04 [1]	-0.03 [-1]	0.01 [0]	0.185
RUN-2	0.84 [21]	-1.09 [-28]	-0.05 [-1]	0.12 [3]	-0.16 [-4]	-0.01 [-0]	0.147
RUN-3	1.87 [47]	-2.54 [-64]	-0.33 [-8]	0.21 [5]	-0.25 [-6]	-0.01 [-0]	0.098
RUN-4	3.53 [90]	-2.91 [-74]	0.03 [1]	0.27 [7]	-0.25 [-6]	0.00 [-0]	0.076
RUN-5	5.90 [150]	-3.29 [-84]	2.45 [62]	0.35 [9]	-0.35 [-9]	0.08 [2]	0.060
RUN-6	5.91 [150]	-3.53 [-90]	2.31 [59]	0.48 [12]	-0.34 [-9]	0.08 [2]	0.082

Table 3-27. BRSA maximum displacement and force for bent and columns

	Bent				CIP column				PC column			
	Displacement		Base Shear		Displacement		Column Shear		Displacement		Column Shear	
	in [mm]		kip [kN]		in [mm]		kip [kN]		in [mm]		kip [kN]	
	South(+)	North(-)	South(+)	North(-)	South(+)	North(-)	South(+)	North(-)	South(+)	North(-)	South(+)	North(-)
RUN-1	0.15 [4]	-0.17 [-4]	13.01 [58.0]	-14.17 [-63.1]	0.15 [4]	-0.17 [-4]	7.02 [31.3]	-7.09 [-31.6]	0.15 [4]	-0.17 [-4]	6.65 [29.6]	-7.19 [-32.0]
RUN-2	0.76 [19]	-0.94 [-24]	41.89 [186.6]	-47.99 [-213.7]	0.74 [19]	-0.92 [-23]	21.26 [94.7]	-23.16 [-103.2]	0.74 [19]	-0.93 [-24]	20.63 [91.9]	-24.39 [-108.6]
RUN-3	1.66 [42]	-2.29 [-58]	53.38 [237.8]	-58.02 [-258.4]	1.63 [41]	-2.27 [-58]	26.16 [116.5]	-28.67 [-127.7]	1.61 [41]	-2.27 [-58]	27.24 [121.3]	-28.71 [-127.9]
RUN-4	3.27 [83]	-2.66 [-68]	59.74 [266.1]	-52.19 [-232.5]	3.21 [82]	-2.59 [-66]	28.77 [128.2]	-25.71 [-114.5]	3.16 [80]	-2.61 [-66]	30.98 [138.0]	-26.16 [-116.5]
RUN-5	5.59 [142]	-2.94 [-75]	61.86 [275.5]	-53.36 [-237.7]	5.54 [141]	-2.84 [-72]	29.34 [130.7]	-26.30 [-117.2]	5.41 [138]	-2.89 [-73]	32.52 [144.8]	-26.83 [-119.5]
RUN-6	5.52 [140]	-3.24 [-82]	47.45 [211.3]	-49.84 [-222.0]	5.59 [142]	-2.94 [-75]	23.32 [103.9]	-24.54 [-109.3]	5.26 [134]	-3.10 [-79]	24.04 [107.1]	-25.76 [-114.7]
Ductility	**7.0**				**7.0**				**6.3**			

Table 3-28. BRSA maximum and minimum column axial load

	CIP		PC	
	comp. kip [kN]	ten. kip [kN]	comp. kip [kN]	ten. kip [kN]
RUN-1	13.5 [60.0]	-5.6 [-24.8]	14.6 [64.8]	-4.5 [-20.0]
RUN-2	31.8 [141.2]	-29.3 [-130.3]	38.3 [170.3]	-22.8 [-101.2]
RUN-3	40.8 [181.6]	-37.9 [-168.5]	46.9 [208.5]	-31.8 [-141.5]
RUN-4	45.1 [200.5]	-34.3 [-152.7]	43.3 [192.7]	-36.1 [-160.5]
RUN-5	46.9 [208.8]	-35.7 [-158.6]	44.7 [198.7]	-37.9 [-168.8]
RUN-6	39.7 [176.7]	-33.7 [-149.7]	42.7 [189.7]	-30.7 [-136.6]

Table 3-29. BRSA maximum and minimum strains in longitudinal bars of CIP column in the plastic hinge region in percent

	Extreme North-Long Bar						**Extreme South-Long Bar**					
	maximum			**minimum**			**maximum**			**minimum**		
	L8	**L7**	**L6**	**L8**	**L7**	**L6**	**L8**	**L7**	**L6**	**L8**	**L7**	**L6**
Elev. from soffit:	***-1***	***-7***	***-13***	***-1***	***-7***	***-13***	***-1***	***-7***	***-13***	***-1***	***-7***	***-13***
RUN-1	0.139	0.146	0.120	-0.072	-0.035	-0.025	0.121	0.119	0.065	-0.034	-0.040	-0.015
RUN-2	**0.930**	**0.633**	**0.457**	-0.189	-0.161	-0.152	**0.454**	**0.334**	**0.256**	-0.183	-0.161	-0.091
RUN-3	**2.906**	**2.337**	**1.383**	**-0.778**	**-0.264**	-0.196	**2.054**	**1.447**	**0.344**	**-0.304**	-0.187	-0.135
RUN-4	**3.827**	**2.983**	**1.849**	**-2.163**	**-0.266**	-0.206	**4.383**	**3.219**	**1.614**	-0.046	-0.054	-0.120
RUN-5	**4.499**	**3.207**	**2.054**	**-5.605**	-0.046	-0.109	**9.019**	**5.241**	**2.465**	**0.716**	**0.638**	0.124
RUN-6		**3.733**	**2.430**		0.132	0.036	**10.831**	**4.816**	**2.212**	**7.207**	**2.990**	**0.545**
	Second Extreme North-Long Bar						**Second Extreme South-Long Bar**					
	maximum			**minimum**			**maximum**			**minimum**		
	L8	**L7**	**L6**	**L8**	**L7**	**L6**	**L8**	**L7**	**L6**	**L8**	**L7**	**L6**
Elev. from soffit:	***-1***	***-7***	***-13***	***-1***	***-7***	***-13***	***-1***	***-7***	***-13***	***-1***	***-7***	***-13***
RUN-1	0.122	0.127	0.107	-0.062	-0.030	-0.020	0.089	0.109	0.063	-0.017	-0.027	-0.012
RUN-2	**0.917**	**0.346**	**0.332**	-0.139	-0.168	-0.132	**0.362**	**0.325**	**0.274**	-0.122	-0.113	-0.062
RUN-3	**2.523**	**2.259**	**1.207**	**-0.419**	**-0.401**	-0.120	**2.246**	**1.534**	**0.393**	-0.146	-0.118	-0.125
RUN-4	**3.440**	**3.023**	**1.540**	**-1.017**	**-0.342**	-0.114	**4.338**	**3.163**	**1.780**	**0.371**	0.091	-0.109
RUN-5	**3.977**	**3.303**	**1.685**	**-2.845**	-0.228	-0.077	**5.745**	**4.963**	**2.704**	**1.258**	**0.616**	0.130
RUN-6	**10.180**	**4.151**	**1.861**	**-1.973**	0.049	0.030	**3.979**	**4.645**	**2.436**	**3.380**	**2.405**	**0.629**

Table 3-30. BRSA maximum and minimum strains in longitudinal bars of PC column in the plastic hinge region in percent

	Extreme North-Long Bar						Extreme South-Long Bar					
	maximum			minimum			maximum			minimum		
	R8	R7	R6	R8	R7	R6	R8	R7	R6	R8	R7	R6
Elev. from soffit:	***-1***	***-7***	***-13***	***-1***	***-7***	***-13***	***-1***	***-7***	***-13***	***-1***	***-7***	***-13***
RUN-1	0.084	0.071	0.047	-0.044	-0.043	-0.020		0.098	0.054		-0.052	-0.043
RUN-2	**0.365**	**0.323**	**0.284**	-0.163	-0.135	-0.140		**0.323**	**0.272**		**-0.238**	-0.182
RUN-3	**2.338**	**1.091**	**0.347**	**-0.292**	**-0.258**	-0.123		**0.933**	**0.329**		**-0.635**	**-0.262**
RUN-4	**2.878**	**1.460**	**0.348**	**-0.502**	**-0.338**	-0.153		**3.775**	**0.402**		**-0.500**	**-0.253**
RUN-5	**3.190**	**1.986**	**0.355**	**-0.757**	**-0.401**	-0.176		**5.796**	**2.663**		-0.156	**-0.262**
RUN-6	**4.423**	**2.651**	**0.364**	**-0.346**	**-0.288**	-0.151		**5.322**	**2.372**		0.340	0.126

	Second Extreme North-Long Bar						Second Extreme South-Long Bar					
	maximum			minimum			maximum			minimum		
	R8	R7	R6	R8	R7	R6	R8	R7	R6	R8	R7	R6
Elev. from soffit:	***-1***	***-7***	***-13***	***-1***	***-7***	***-13***	***-1***	***-7***	***-13***	***-1***	***-7***	***-13***
RUN-1	0.083	0.054	0.055	-0.030	-0.031	-0.025		0.083	0.052		-0.043	-0.037
RUN-2	**0.541**	**0.293**	**0.275**	-0.054	-0.086	-0.080		**0.280**	**0.257**		-0.187	-0.147
RUN-3	**2.699**	**0.857**	**0.375**	-0.007	-0.139	-0.118		**1.528**	**0.314**		**-0.419**	-0.209
RUN-4	**3.463**	**1.168**	**0.397**	0.382	**-0.279**	-0.150			**0.338**			-0.226
RUN-5	**3.927**	**1.445**	**0.427**	0.947	**-0.352**	-0.174			**2.528**			**-0.238**
RUN-6	**5.298**	**1.944**	**0.441**	1.169	**-0.287**	-0.148			**2.188**			0.151

Table 3-31. BRSA maximum and minimum strains in transvers bars of CIP column in the plastic hinge region in percent

	West side spiral						East side spiral					
	maximum			minimum			maximum			minimum		
	L8	L7	L6	L8	L7	L6	L8	L7	L6	L8	L7	L6
Elev. from soffit	*-1*	*-7*	*-13*	*-1*	*-7*	*-13*	*-1*	*-7*	*-13*	*-1*	*-7*	*-13*
RUN-1	0.007	0.017	0.007	-0.005	-0.003	-0.003	0.006	0.012	0.004	-0.003	-0.003	-0.002
RUN-2	0.009	0.028	0.031	-0.009	0.009	0.002	0.023	0.021	0.018	0.002	-0.006	-0.001
RUN-3		0.030	0.040	-0.029	0.013	0.011				0.000		0.009
RUN-4		0.035	0.042	-0.040	0.004					-0.017		0.008
RUN-5		0.043		-0.032	-0.013					-0.045		0.002
RUN-6		**0.070**		-0.046	-0.004					-0.057		0.002

Table 3-32. BRSA maximum and minimum strains in transvers bars of PC column in the plastic hinge region in percent

	West side spiral						East side spiral					
	maximum			minimum			maximum			minimum		
	R8	R7	R6	R8	R7	R6	R8	R7	R6	R8	R7	R6
Elev. from soffit	*-1*	*-7*	*-13*	*-1*	*-7*	*-13*	*-1*	*-7*	*-13*	*-1*	*-7*	*-13*
RUN-1	0.001	0.003	0.006	-0.001	-0.001	-0.001		0.003	0.003		-0.001	-0.001
RUN-2	0.007	0.020	0.029	0.000	0.001	0.003		0.015	0.016		0.001	0.001
RUN-3	0.012	0.033	0.033	-0.009	0.007	0.010		0.025	0.023		0.006	0.010
RUN-4	0.002	0.030	0.028	-0.024	0.007	0.011		0.019	0.022		-0.002	0.009
RUN-5	0.016	0.034	0.026	-0.035	0.002	0.011		0.016	0.021		-0.010	0.008
RUN-6	0.023	0.030	0.024	-0.034	-0.016	0.009		0.023	0.018		-0.010	0.003

Table 3-33. BRSA maximum and minimum strains in longitudinal bars of CIP rebar-pin in percent

	Southern-most								**Northern-most**							
	maximum				**minimum**				**maximum**				**minimum**			
	L2	**L3**	**L4**	**L5**	**L2**	**L3**	**L4**	**L5**	**L2**	**L3**	**L4**	**L5**	**L2**	**L3**	**L4**	**L5**
Elev. from top of pedestal	***-9***	***-3***	***3***	***9***	***-9***	***-3***	***3***	***9***	***-9***	***-3***	***3***	***9***	***-9***	***-3***	***3***	***9***
RUN-1	0.02	0.07	0.09	0.04	-0.01	-0.04	-0.06	-0.02	0.02	0.04	0.05	0.02	-0.01	-0.03	-0.04	-0.01
RUN-2	0.21	**0.33**	**0.26**	0.17	-0.07	-0.16	-0.20	-0.07	0.16	0.22	**0.25**	0.12	0.00	-0.05	-0.10	-0.02
RUN-3	**0.30**	**1.76**		0.20	-0.12	-0.21		-0.11	0.22		**1.71**	0.16	-0.03		-0.12	-0.06
RUN-4	**0.31**	**1.99**		0.20	-0.15	-0.14		-0.14	**0.26**		**3.17**	0.19	-0.06		**0.53**	-0.07
RUN-5	**0.31**	**2.37**		0.21	-0.20	**-0.29**		-0.15	**0.29**		**5.68**	0.21	-0.07		**1.22**	-0.09
RUN-6				0.22				-0.13	**0.29**		**5.65**	0.22	-0.08		**3.68**	-0.10
	Second southern-most								**Second northern-most**							
RUN-1	0.01	0.04	0.06	0.02	-0.01	-0.02	-0.04	-0.01	0.01	0.04	0.03	0.00	0.00	-0.01	-0.01	0.00
RUN-2	0.18	**0.25**	**0.25**	0.12	0.00	-0.06	-0.07	-0.04	0.11	0.22	0.18	0.07	0.00	-0.01	0.00	0.00
RUN-3	**0.26**	**0.99**	**1.76**	0.17	-0.06	-0.10	-0.06	-0.10	0.19	**0.32**	**0.31**	0.13	0.01	-0.06	-0.03	-0.01
RUN-4	**0.28**	**1.59**	**2.17**	0.18	-0.08	0.10	**0.80**	-0.11	**0.24**	**2.21**	**2.20**	0.17	0.00	-0.01	0.02	-0.03
RUN-5	**0.29**	**1.80**	**2.34**	0.19	-0.11	**0.56**	**1.25**	-0.14	**0.27**	**3.74**		0.21	-0.02	**1.06**		-0.04
RUN-6		**3.01**	**2.87**	0.20		**0.79**	**1.41**	-0.15				0.21				-0.05

Table 3-34. BRSA maximum and minimum strains in longitudinal bars of PC rebar-pin in percent

	Southern-most								**Northern-most**							
	maximum				**minimum**				**maximum**				**minimum**			
	R2	**R3**	**R4**	**R5**	**R2**	**R3**	**R4**	**R5**	**R2**	**R3**	**R4**	**R5**	**R2**	**R3**	**R4**	**R5**
Elev. from top of pedestal	**-9**	***-3***	***3***	***9***	**-9**	***-3***	***3***	***9***	**-9**	***-3***	***3***	***9***	**-9**	***-3***	***3***	***9***
RUN-1	**0.007**	**0.049**	**0.069**	**0.016**	-0.004	-0.025	-0.041	-0.007	**0.019**	**0.084**	**0.055**	**0.018**	-0.013	-0.061	-0.036	-0.011
RUN-2	**0.158**	**0.250**	**0.231**	**0.111**	-0.004	-0.111	-0.130	-0.016	**0.173**	**0.307**	**0.270**	**0.102**	-0.079	-0.185	-0.124	-0.045
RUN-3	**0.205**	**1.734**	**1.876**	**0.134**	-0.037	-0.161	-0.163	-0.028	**0.234**	**2.099**	**0.383**	**0.137**	-0.138	-0.213	**-0.251**	-0.059
RUN-4	**0.211**	**2.056**	**2.269**	**0.138**	-0.052	**0.438**	**0.609**	-0.044	**0.276**	**3.801**	**3.868**	**0.174**	-0.173	**0.411**	-0.231	-0.068
RUN-5	**0.215**		**2.538**	**0.141**	-0.068		**1.074**	-0.055	**0.311**	**6.523**	**6.567**	**0.200**	-0.197	**0.740**	**0.517**	-0.071
RUN-6	**0.224**		**3.016**	**0.147**	-0.075		**1.044**	-0.053	**0.322**	**6.348**	**5.745**	**0.195**	-0.218	**1.215**	**1.231**	-0.082
	Second southern-most								**Second northern-most**							
RUN-1	**0.005**	**0.031**	**0.025**	**0.009**	-0.003	-0.004	-0.002	-0.003	**0.010**	**0.041**	**0.028**	**0.009**	-0.007	-0.016	-0.011	-0.005
RUN-2	**0.118**	**0.221**	**0.191**	**0.080**	**0.001**	0.000	**0.004**	**0.001**	**0.106**	**0.269**	**0.243**	**0.064**	-0.008	-0.015	-0.008	-0.011
RUN-3	**0.197**	**1.658**	**0.269**	**0.106**	-0.007	-0.054	-0.058	-0.031	**0.190**	**0.844**	**0.334**	**0.096**	-0.048	-0.069	-0.021	-0.007
RUN-4	**0.213**	**2.015**	**1.342**	**0.117**	-0.008	**1.116**	-0.040	-0.036	**0.248**	**2.283**	**1.824**	**0.135**	-0.064	**0.240**	**0.022**	-0.011
RUN-5	**0.217**	**2.417**	**1.538**	**0.114**	**0.001**	**1.391**	**0.975**	-0.036	**0.282**	**3.766**	**2.876**	**0.164**	-0.076	**0.772**	**0.484**	-0.012
RUN-6	**0.232**	**3.218**	**2.067**	**0.131**	**0.002**	**1.881**	**1.167**	-0.040	**0.267**	**3.676**	**2.223**	**0.156**	-0.084	**1.417**	**0.519**	-0.014

Table 3-35. BRSA maximum and minimum strains in longitudinal bars of CIP column and pedestal at rebar-pin in percent

	Southern-most										**Northern-most**									
	maximum					**minimum**					**maximum**					**minimum**				
	L1	**L2**	**L3**	**L4**	**L5**	**L1**	**L2**	**L3**	**L4**	**L5**	**L1**	**L2**	**L3**	**L4**	**L5**	**L1**	**L2**	**L3**	**L4**	**L5**
Elev. from top of pedestal	***-25.5***	***-9***	***-3***	***3***	***9***	***-25.5***	***-9***	***-3***	***3***	***9***	***-25.5***	***-9***	***-3***	***3***	***9***	***-25.5***	***-9***	***-3***	***3***	***9***
RUN-1	0.02	0.02	0.00	0.01	0.01	-0.01	-0.01	0.00	-0.01	-0.01	0.03	0.01	0.01	0.01	0.01	-0.02	-0.01	0.00	0.00	-0.01
RUN-2	0.15	0.06	0.02	0.05	0.04	-0.06	-0.03	0.00	-0.03	-0.05	0.20	0.06	0.03	0.01	0.03	-0.10	-0.03	0.00	-0.01	-0.02
RUN-3	0.18	0.07	0.05	0.07	0.05	-0.08	-0.04	0.00	-0.03	-0.06	**0.24**	0.08	0.04	0.02	0.03	-0.12	-0.02	0.01	-0.01	-0.01
RUN-4	0.16	0.04	0.05	0.07	0.04	-0.09	-0.03	0.00	-0.03	-0.06	**0.25**	0.09	0.04	0.03	0.04	-0.11	-0.01	0.01	0.00	-0.01
RUN-5	0.16	0.04	0.05	0.07	0.05	-0.09	-0.02	0.00	-0.02	-0.06	**0.24**	0.09	0.03	0.03	0.05	-0.11	0.00	0.00	0.00	-0.01
RUN-6	0.15	0.04	0.05	0.06	0.04	-0.07	0.00	0.01	0.00	-0.03	0.19	0.08	0.02	0.03	0.05	-0.11	0.01	0.00	0.01	-0.01
	Second Southern-most										**Second Northern-most**									
RUN-1	0.02	0.01	0.00	0.01	0.01	-0.01	-0.01	0.00	0.00	-0.01	0.03	0.01	0.00	0.01	0.01	-0.01	0.00	0.00	0.00	0.00
RUN-2	0.14	0.05	0.01	0.04	0.04	-0.04	-0.04	0.00	-0.02	-0.05	0.16	0.06	0.02	0.01	0.02	-0.03	-0.01	0.00	-0.01	-0.01
RUN-3	0.18	0.09	0.02	0.06	0.05	-0.05	-0.04	0.00	-0.03	-0.07	0.20	0.07	0.02	0.02	0.03	-0.03	-0.01	0.01	0.00	0.00
RUN-4	0.17	0.08	0.03	0.05	0.04	-0.05	-0.03	-0.01	-0.04	-0.08	0.21	0.08	0.03	0.03	0.04	-0.04	0.00	0.01	0.00	0.00
RUN-5	0.18	0.09	0.04	0.06	0.04	-0.04	-0.02	-0.01	-0.04	-0.07	0.21	0.09	0.03	0.03	0.05	-0.02	0.00	0.02	0.00	0.00
RUN-6	0.18	0.09	0.04	0.05	0.03	-0.03	-0.01	-0.02	-0.01	-0.04	**0.92**	0.08	0.04	0.03	0.06	-0.07	0.00	0.02	0.00	0.00

Table 3-36. BRSA maximum and minimum strains in long. bars of PC column and pedestal at rebar-pin in percent

	Southern-most										**Northern-most**									
	maximum					**minimum**					**maximum**					**minimum**				
	R1	**R2**	**R3**	**R4**	**R5**	**R1**	**R2**	**R3**	**R4**	**R5**	**R1**	**R2**	**R3**	**R4**	**R5**	**R1**	**R2**	**R3**	**R4**	**R5**
Elev. from top of pedestal	***-25.5***	***-9***	***-3***	***3***	***9***	***-25.5***	***-9***	***-3***	***3***	***9***	***-25.5***	***-9***	***-3***	***3***	***9***	***-25.5***	***-9***	***-3***	***3***	***9***
RUN-1	0.02	0.02	0.00	0.00	0.01	-0.01	-0.01	0.00	0.00	-0.01	0.04	0.02	0.00	0.01	0.02	-0.03	-0.01	0.00	-0.01	-0.02
RUN-2	0.14	0.09	0.02	0.01	0.04	-0.03	-0.02	0.00	-0.01	-0.01	0.17	0.06	0.01	0.04	0.07	-0.13	-0.05	-0.01	-0.04	-0.06
RUN-3	0.18	0.13	0.02	0.02	0.05	-0.05	-0.02	0.00	0.00	0.00	0.20	0.08	0.02	0.05	0.07	-0.16	-0.04	-0.02	-0.04	-0.06
RUN-4	0.16	0.11	0.02	0.02	0.04	-0.06	-0.02	-0.01	0.00	0.00	0.20	0.08	0.04	0.05	0.07	-0.14	-0.02	-0.02	-0.02	-0.04
RUN-5	0.16	0.10	0.03	0.02	0.03	-0.07	-0.03	-0.01	0.00	-0.01	0.19	0.08		0.04	0.07	-0.13	-0.02	-0.01	-0.01	-0.03
RUN-6	0.15	0.10	0.03	0.02	0.04	-0.07	-0.02	0.00	0.00	-0.01	0.15	0.06		0.04	0.06	-0.10	-0.01	-0.01	0.00	-0.02
	Second southern-most										**Second northern-most**									
RUN-1	0.03	0.01	0.00	0.01	0.01	-0.01	0.00	0.00	0.00	0.00	0.03	0.01	0.01	0.01	0.02	-0.02	-0.01	0.00	-0.01	-0.02
RUN-2	0.13	0.08	0.02	0.02	0.03	-0.01	0.00	0.00	0.00	-0.01	0.14	0.05	0.01	0.03	0.08	-0.08	-0.05	-0.01	-0.04	-0.06
RUN-3	0.20	0.12	0.03	0.02	0.03	-0.02	0.01	0.01	0.00	0.00	0.19	0.07	0.01	0.04	0.09	-0.09	-0.04	-0.01	-0.04	-0.05
RUN-4	0.19	0.11	0.03	0.02	0.02	-0.02	0.00	0.01	0.00	-0.01	0.21	0.10	0.01	0.05	0.09	-0.07	-0.04	-0.01	-0.02	-0.04
RUN-5	0.19	0.12	0.03	0.02	0.02	-0.02	0.00	0.01	0.00	-0.02	0.22	0.13	0.04	0.04	0.09	-0.07	-0.04	-0.01	0.00	-0.03
RUN-6	0.20	0.12	0.03	0.02	0.03	0.00	0.01	0.01	0.00	-0.03	0.18	0.10	0.09	0.05	0.08	-0.05	-0.03	0.00	0.02	-0.01

Table 3-37. BRSA maximum and minimum strains in trans. bars of CIP rebar-pin in percent

	East								West						North				South			
	maximum				minimum				maximum			minimum			maximum		minimum		maximum		minimum	
	L2	L3	L4	L5	L2	L3	L4	L5	L2	L3	L5	L2	L3	L5	L3	L4	L3	L4	L3	L4	L3	L4
Elev. from top of pedestal	-9	-3	3	9	-9	-3	3	9	-9	-3	9	-9	-3	9	-3	3	-3	3	-3	3	-3	3
RUN-1	0.00	0.00	0.00	0.00	0.00	0.00	0.00	0.00	0.00	0.00	0.00	0.00	0.00	0.00	0.00	0.00	0.00	0.00	0.00	0.00	0.00	0.00
RUN-2	0.01	0.00	0.00	0.00	0.00	-0.01	-0.02	0.00	0.01	0.01	0.00	0.00	-0.02	-0.01	0.00	0.00	-0.01	-0.02	0.01	0.00	0.00	-0.02
RUN-3	0.01	0.00	0.00	0.00	-0.03	-0.02	-0.02	0.00	0.01	0.00	0.00	0.00	-0.03	-0.01	0.00	0.00	-0.01	-0.03	0.01	0.01	0.00	-0.03
RUN-4	0.00	0.00	0.00	0.00	-0.03	-0.02	-0.04	-0.01	0.01	0.00	-0.01	-0.01	-0.04	-0.02	0.00	-0.01	-0.01	-0.04	0.01		0.00	-0.02
RUN-5	0.00	0.00	0.00	0.00	-0.03	-0.03	-0.07	-0.02	0.01	0.00	-0.01	-0.01	-0.03	-0.02	0.00	-0.01	-0.02	-0.04	0.01		-0.01	-0.02
RUN-6	0.00			0.00	-0.03			-0.02		0.00	-0.01		-0.03	-0.02	0.00		-0.02					-0.02

Table 3-38. BRSA maximum and minimum strains in trans. bars of PC rebar-pin in percent

	East								West								North				South			
	maximum				minimum				maximum				minimum				maximum		minimum		maximum		minimum	
	R2	R3	R4	R5	R2	R3	R4	R5	R2	R3	R4	R5	R2	R3	R4	R5	R3	R4	R3	R4	R3	R4	R3	R4
Elev. from top of pedestal	-9	-3	3	9	-9	-3	3	9	-9	-3	3	9	-9	-3	3	9	-3	3	-3	3	-3	3	-3	3
RUN-1	0.00	0.00	0.00	0.00	0.00	-0.01	0.00	0.00	0.00	0.00	0.00	0.00	0.00	0.00	0.00	0.00	0.00	0.00	0.00	0.00	0.00	0.00	0.00	-0.01
RUN-2	0.00	0.00	0.00	0.00	-0.01	-0.06	-0.02	-0.01	0.00	0.00	0.01	0.00	0.00	-0.05	0.00	0.00	0.01	0.00	0.00	-0.01	0.00	0.00	-0.01	-0.02
RUN-3	0.00	-0.01	-0.01	0.00	-0.03	-0.07	-0.05	-0.02	0.00	-0.01	0.01	0.01	-0.03	-0.05	-0.01	0.00	0.01	0.00	0.00	-0.02	0.01	0.01	-0.01	-0.02
RUN-4	-0.01	-0.01	-0.02	-0.01	-0.04	-0.06	-0.08	-0.03	0.00	-0.01	0.00	0.01	-0.03	-0.05	-0.03	0.00	0.01	0.00	0.00	-0.03	0.02	0.02	-0.01	-0.03
RUN-5	-0.01	0.00	-0.03	-0.01	-0.04	-0.05	-0.08	-0.03	0.00	-0.01	0.00	0.01	-0.03	-0.05	-0.04	0.00	0.02	0.01	0.00	-0.03	0.03	0.05	0.00	-0.04
RUN-6	-0.01	0.01	-0.03	-0.01	-0.03	-0.05	-0.10	-0.04	0.00	-0.01	0.00	0.01	-0.02	-0.04	-0.04	0.00	0.02	0.02	0.00	-0.03	0.03	0.05	-0.01	-0.09

Table 3-39. BRSA maximum and minimum strains in trans. bars of the CIP column and pedestal near rebar-pin in percent

	South								**North**							
	maximum				**minimum**				**maximum**				**minimum**			
	L2	**L3**	**L4**	**L5**	**L2**	**L3**	**L4**	**L5**	**L2**	**L3**	**L4**	**L5**	**L2**	**L3**	**L4**	**L5**
Elev. from top of pedestal	***-9***	***-3***	***3***	***9***	***-9***	***-3***	***3***	***9***	***-9***	***-3***	***3***	***9***	***-9***	***-3***	***3***	***9***
RUN-1	0.006	0.006	0.006	0.006	0.001	0.000	0.000	0.001	0.005	0.006	0.004	0.005	-0.001	-0.001	-0.002	-0.001
RUN-2	0.034	0.025	0.017	0.012	0.002	0.001	0.001	0.001	0.023	0.019	0.008	0.010	0.000	0.001	-0.001	-0.001
RUN-3	0.090	0.046	0.026	0.019	0.017	0.001	0.006	0.007	0.052	0.038	0.013	0.016	0.013	0.007	0.003	0.005
RUN-4	0.125	0.070	0.027	0.017	0.037	-0.001	0.006	0.007	0.056	0.044	0.014	0.018	0.021	0.007	0.004	0.005
RUN-5	0.140	0.070	0.035	0.019	0.034	-0.002	0.008	0.008	0.061	0.044	0.018	0.020	0.026	0.013	0.006	0.007
RUN-6	0.149	0.044	0.034	0.021	0.034	-0.002	0.015	0.010	0.064	0.055	0.019	0.022	0.028	0.017	0.009	0.009
	West								**East**							
RUN-1	0.005	0.005	0.005	0.006	0.000	-0.001	0.000	0.000	0.003	0.007	0.008	0.005	-0.001	0.001	0.002	-0.001
RUN-2	0.013	0.019	0.011	0.019	0.001	0.001	0.001	0.001	0.006	0.009		0.010	-0.001	-0.002	0.003	-0.001
RUN-3	0.044	0.052	0.014	0.029	0.009	0.008	0.006	0.008	0.019	0.017		0.015	0.002	-0.006	-0.103	0.005
RUN-4	0.054	0.058	0.012	0.027	0.020	0.016	0.004	0.008	0.026	0.048		0.015	0.007	-0.002	-0.310	0.006
RUN-5	0.062	0.064	0.011	0.026	0.019	0.018	0.002	0.011	0.032	0.056		0.017	0.015	0.000	0.005	0.007
RUN-6	0.069	0.071	0.012	0.026	0.019	0.023	0.003	0.016	0.036	0.063		0.020	0.019	0.006		0.010

Table 3-40. BRSA maximum and minimum strains in trans. bars of the PC column and pedestal near rebar-pin in percent

	South								**North**							
	maximum				**minimum**				**maximum**				**minimum**			
	R2	**R3**	**R4**	**R5**	**R2**	**R3**	**R4**	**R5**	**R2**	**R3**	**R4**	**R5**	**R2**	**R3**	**R4**	**R5**
Elev. from top of pedestal	***-9***	***-3***	***3***	***9***	***-9***	***-3***	***3***	***9***	***-9***	***-3***	***3***	***9***	***-9***	***-3***	***3***	***9***
RUN-1	0.005	0.006	0.005	0.005	-0.001	0.000	-0.001	-0.001	0.003	0.007	0.008	0.007	-0.003	0.000	0.001	0.001
RUN-2	0.035	0.050	0.008	0.006	0.000	0.001	-0.001	0.000	0.029	0.035	0.028	0.012	-0.001	0.001	0.003	0.001
RUN-3	0.051	0.073	0.010	0.008	0.020	0.027	0.001	0.001	0.075	0.086	0.041	0.021	0.011	0.012	0.015	0.008
RUN-4	0.064	0.087	0.008	0.005	0.025	0.036	-0.001	-0.001	0.086	0.092	0.055	0.019	0.014	0.020	0.018	0.008
RUN-5	0.082	0.104	0.010	0.007	0.024	0.035	-0.001	0.000	0.098	0.105	0.067	0.020	0.012	0.010	0.020	0.008
RUN-6	0.072	0.085	0.012	0.008	0.029	0.034	0.001	0.001	0.095	0.076	0.063	0.022	0.011	0.007	0.025	0.012
	West								**East**							
RUN-1	0.003	0.005	0.006	0.005	-0.002	-0.001	-0.001	0.000	0.003	0.006	0.007	0.005	-0.003	-0.002	0.001	-0.002
RUN-2	0.012	0.021	0.008	0.006	-0.002	-0.001	0.001	0.001	0.009	0.064	0.013	0.006	-0.003	0.000	0.002	-0.001
RUN-3	0.023	0.033	0.008	0.007	0.008	0.008	0.001	0.002	0.029	0.077	0.019	0.008	0.003	0.014	0.008	0.001
RUN-4	0.024	0.050	0.008	0.006	0.008	0.010	0.000	0.000	0.040	0.059	0.019	0.010	0.014	-0.005	0.010	0.001
RUN-5	0.031	0.074	0.009	0.007	0.002	0.012	0.001	0.000	0.060	0.058	0.018	0.014	0.014	-0.037	0.009	0.003
RUN-6	0.037	0.060	0.012	0.008	0.002	0.016	0.003	0.003	0.096	0.034		0.016	0.019	-0.037		0.007

Table 3-41. BRSA maximum and minimum strains in the cap beam in percent

	maximum						minimum					
	Longitudinal bars				Trans. Bars		Longitudinal bars				Trans. Bars	
	CSG 85	CSG 87	CSG A85	CSG A87	CSG 86	CSG A86	CSG 85	CSG 87	CSG A85	CSG A87	CSG 86	CSG A86
RUN-1	0.006	0.003	0.005	0.004	0.002	0.003	-0.004	-0.004	-0.004	-0.005	-0.003	-0.003
RUN-2	0.021	0.014	0.017	0.015	0.003	0.003	-0.014	-0.010	-0.009	-0.013	-0.003	-0.003
RUN-3	0.029	0.021	0.023	0.023	0.003	0.003	-0.017	-0.012	-0.013	-0.015	-0.005	-0.006
RUN-4	0.030	0.019	0.021	0.026	0.000	0.000	-0.017	-0.013	-0.016	-0.016	-0.008	-0.008
RUN-5	0.030	0.021	0.022	0.030	-0.001	0.000	-0.017	-0.012	-0.018	-0.016	-0.008	-0.009
RUN-6	0.027	0.024	0.022	0.025	0.001	0.002	-0.017	-0.010	-0.016	-0.014	-0.007	-0.006

Table 3-42. BRSA maximum and minimum shear and slippage at rebar-pins

	CIP					PC				
	Displacement in [mm]			Shear kip [kN]		Displacement in [mm]			Shear kip [kN]	
	max	min	residual	max	min	max	min	residual	max	min
Run-1	0.00 [0]	0.00 [-0]	0.00 [-0]	5.0 [22.3]	-5.3 [-23.5]	0.00 [0]	0.00 [-0]	0.00 [-0]	4.2 [18.5]	-6.3 [-28.0]
Run-2	0.01 [0]	-0.01 [-0]	0.00 [0]	17.5 [78.0]	-22.3 [-99.1]	0.01 [0]	-0.01 [-0]	0.00 [-0]	18.8 [83.8]	-23.3 [-103.7]
Run-3	0.04 [1]	-0.03 [-1]	0.00 [0]	19.1 [85.0]	-13.0 [-57.8]	0.05 [1]	-0.04 [-1]	0.01 [0]	17.1 [76.0]	-27.1 [-120.6]
Run-4	0.08 [2]	-0.07 [-2]	0.02 [0]	17.1 [75.9]	-13.6 [-60.4]	0.09 [2]	-0.07 [-2]	0.03 [1]	14.1 [62.7]	-24.7 [-109.8]
Run-5	0.14 [4]	-0.13 [-3]	0.03 [1]	21.3 [94.6]	-14.6 [-64.9]	0.19 [5]	-0.09 [-2]	0.10 [3]	31.1 [138.4]	-17.6 [-78.4]
Run-6	0.15 [4]	-0.24 [-6]	-0.01 [-0]	9.3 [41.4]	-16.8 [-74.9]	0.26 [7]	-0.15 [-4]	0.06 [2]	24.4 [108.3]	-24.0 [-106.7]

Table 3-43. BRSA maximum and minimum rotations, uplift and moments at rebar-pins

	CIP								PC							
	Rotation rad			Uplift in [mm]			Moment kip.in [kN.m]		Rotation rad			Uplift in [mm]			Moment kip.in [kN.m]	
	max	min	residual	max	min	residual	max	min	max	min	residual	max	min	residual	max	min
Run-1	0.002	-0.002	0.000	0.00 [0]	0.00 [0]	0.00 [0]	-198 [-22.3]	27 [3.0]	0.002	-0.002	0.000	0.00 [0]	0.00 [0]	0.00 [0]	-111 [-12.5]	260 [29.3]
Run-2	0.008	-0.011	-0.001	0.02 [0]	0.04 [1]	0.01 [0]	-634 [-71.6]	232 [26.2]	0.009	-0.010	0.000	0.03 [1]	0.03 [1]	0.01 [0]	-311 [-35.1]	610 [68.9]
Run-3	0.021	-0.031	-0.005	0.07 [2]	0.13 [3]	0.06 [1]	-651 [-73.6]	317 [35.9]	0.022	-0.029	-0.005	0.08 [2]	0.11 [3]	0.09 [2]	-451 [-50.9]	599 [67.7]
Run-4	0.046	-0.036	0.000	0.16 [4]	0.19 [5]	0.13 [3]	-670 [-75.7]	235 [26.6]	0.043	-0.034	-0.001	0.30 [8]	0.13 [3]	0.14 [4]	-538 [-60.8]	547 [61.8]
Run-5	0.081	-0.039	0.035	0.27 [7]	0.21 [5]	0.21 [5]	-647 [-73.1]	197 [22.3]	0.072	-0.042	0.026	0.27 [7]	0.12 [3]	0.14 [4]	-630 [-71.2]	524 [59.2]
Run-6									0.061	-0.045	0.026	0.24 [6]	0.17 [4]	0.18 [5]	-399 [-45.1]	527 [59.6]

Table 4-1. Strain-rate effect modification factor

Model	Location	Strain rate	$\frac{F_{y.Dynamic}}{F_{y.Static}}$	$\frac{F_{u.Dynamic}}{F_{u.Static}}$
		με/sec		
BPSA	Columns longitudinal bars	10201	1.063	1.042
BRSA	Columns longitudinal bars	11372	1.064	1.042
BRSA	Rebar-pins longitudinal bars	13078	1.070	1.046

Table 4-2. BPSA simple stick model calculated force-displacement vs. measured

	Measured		Calculated		Error	
	drift	Base Shear	drift	Base Shear	drift	Base Shear
	%	kip [KN]	%	kip [KN]	%	%
Yield	1.86	40.9 [182]	1.61	42.7 [190]	-13%	4%
Ultimate	7.48	55.8 [248]	6.47	62.5 [278]	-14%	12%
ductility	4.0		4.0		0%	

Table 4-3. Effect of material models on the response of BPSA, in percent

Name	Model	Type	RUN	Base shear		Displacement		
				South	North	South	North	Res
BPSA-1	concrete	Concrete04	6	-11.0	**28.2**	**-38.8**	**37.1**	**-149.2**
			7	-8.2	0.9	**-20.7**	4.0	**-104.5**
			8	2.9	7.7	-8.7	3.8	**-98.0**
	steel	Steel02	9	**20.7**	12.5	10.1	5.0	**-82.6**
			10	**46.1**	**22.0**	17.5	2.6	**-35.4**
			11	**65.7**	**27.1**	**35.0**	-6.6	**-248.2**
			Average	17.9		3.4		-119.6
BPSA-2	concrete	Concrete01withSITC	6	-13.9	**28.0**	**-43.5**	**28.9**	**-144.1**
			7	-4.0	**22.7**	**-22.5**	**25.1**	**-110.9**
			8	12.8	5.0	-1.2	-4.8	**-94.7**
	steel	Steel02	9	**36.4**	16.7	**24.8**	1.3	**-45.2**
			10	**45.0**	**26.3**	**31.9**	-0.6	16.6
			11	**80.2**	**35.2**	**46.8**	-7.0	**-400.3**
			Average	24.2		6.6		-129.8
BPSA-3	concrete	Concrete04	6	-13.0	**34.1**	**-41.9**	**39.5**	**-135.0**
			7	-7.2	-0.7	**-21.9**	1.0	**-103.9**
			8	4.6	9.0	-8.7	4.5	**-98.7**
	steel	Steel02	9	**23.4**	16.0	11.7	4.9	**-78.5**
			10	**39.2**	**24.4**	**21.5**	1.7	**-20.7**
			11	**65.4**	**46.4**	**30.1**	-8.3	**-270.2**
			Average	20.1		2.8		-117.8
BPSA-4	concrete	Concrete04	6	-5.4	**37.1**	**-41.9**	17.7	**-105.6**
			7	-3.9	**27.7**	**-40.6**	3.5	**-107.7**
			8	12.2	**24.1**	**-26.7**	-3.2	**-110.6**
	steel	ReinforcingSteel	9	**37.6**	4.3	1.5	**-27.5**	**-90.3**
			10	**55.1**	-1.3	**38.0**	**-56.8**	**46.5**
			11	**112.6**	0.6	**95.3**	**-70.7**	**-984.6**
			Average	25.1		-9.3		-225.4

Table 4-4. Parameters of CDP model

Dialation angle	Eccentricity	fb0/fc0	K	Viscosity Parameter
37	0.1	1.16	0.666	0

Table 4-5. Coefficients of friction

material pair	coefficient of friction, μ	reference(s)
concrete/concrete	0.45	(Cheng, et al., 2006; Mehrsoroush and Saiidi, 2014)
steel/concrete	0.45	(Mehrsoroush and Saiidi, 2014)
steel/steel	0.3	(Mehrsoroush and Saiidi, 2014)
steel/rubber	0.6	(Oberg, et al., 2012)
concrete/rubber	0.85	(Oberg, et al., 2012)

Table 4-6. Properties of plastic hinge springs in ABAQUS

	CIP		**PC**	
	moment kip.in [kN.m]	rotation rad	moment kip.in [kN.m]	rotation rad
	South Direction			
yield	690.5 [78.03]	0.0021	491.3 [55.52]	0.0018
ultimate	720.8 [81.5]	0.0558	549.1 [62.05]	0.088
	North Direction			
yield	518.5 [58.59]	0.0018	663.2 [74.94]	0.0021
ultimate	574.9 [64.96]	0.0843	684 [77.29]	0.0622

Table 4-7. BRSA simple stick model calculated force-displacement vs. measured

	Measured		Calculated		Error	
	drift	Base Shear	drift	Base Shear	drift	Base Shear
	%	kip [KN]	%	kip [KN]	%	%
Yield	1.23	56.7 [252]	0.97	51.7 [230]	-21%	-9%
Ultimate	8.63	56.7 [252]	7.21	56.9 [253]	-16%	0%

Table 4-8. Effect of concrete model on the response of BRSA, in percent

			Base shear		Displacement		
Name	Description	RUN	Vs	Vn	South	North	Residual
BRSA-1	concrete04, Mander, Steel02	1	**82.8**	**40.1**	**77.5**	**39.6**	**-94.9**
		2	**25.4**	-13.0	6.6	**-45.1**	**-278.0**
		3	-5.4	-10.6	**-26.4**	-10.4	-1.0
		4	-13.8	-14.2	-5.1	-15.1	**1615.7**
		5	-15.9	-14.2	-16.8	-20.0	**-63.5**
		6	2.3	-5.3	-15.0	-12.4	**-68.9**
		average	4.9		-3.5		-101.3
BRSA-2	concrete02, Mander, Steel02	1	**70.2**	**25.1**	**63.4**	**20.5**	**-92.5**
		2	**24.2**	-14.6	3.3	**-47.1**	**-269.4**
		3	-5.4	-10.4	**-22.9**	-10.8	-17.8
		4	-13.7	-17.7	-2.4	-16.9	**1793.2**
		5	-15.5	-15.1	-16.4	**-20.4**	**-64.1**
		6	1.7	-5.7	-15.1	-10.1	**-69.5**
		average	1.9		-6.2		-102.6
BRSA-3	concrete01withSITC, Mander, Steel02	1	**70.5**	**25.2**	**63.6**	**20.6**	**-91.0**
		2	**24.4**	-14.3	4.8	**-46.5**	**-280.7**
		3	-5.8	-11.9	**-24.4**	**-21.0**	**-56.8**
		4	-13.5	-10.8	-5.5	-9.2	**907.0**
		5	-13.7	-11.9	-10.2	-10.2	**-62.4**
		6	-3.8	-4.2	-13.1	5.4	**-70.7**
		average	2.5		-3.8		-112.3
BRSA-4	concrete02, Motaref, Steel02	1	**76.8**	**32.7**	**70.8**	**30.2**	**-95.7**
		2	**25.0**	-13.8	4.8	**-46.1**	**-275.0**
		3	-3.9	-12.4	**-25.0**	-11.4	-9.3
		4	-14.2	-17.4	-4.1	-15.5	**1709.7**
		5	-17.2	-16.4	-18.4	-19.7	**-70.8**
		6	0.1	-7.4	-16.8	-11.2	**-70.0**
		average	2.6		-5.2		-104.2

Table 4-9. Effect of reinforcement model on the response of BRSA, in percent

Name	Description	RUN	Base shear Vs	Base shear Vn	Displacement South	Displacement North	Displacement Residual
BRSA-1	concrete04, Mander, Steel02	1	**82.8**	**40.1**	**77.5**	**39.6**	**-94.9**
		2	**25.4**	-13.0	6.6	**-45.1**	**-278.0**
		3	-5.4	-10.6	**-26.4**	-10.4	-1.0
		4	-13.8	-14.2	-5.1	-15.1	**1615.7**
		5	-15.9	-14.2	-16.8	-20.0	**-63.5**
		6	2.3	-5.3	-15.0	-12.4	**-68.9**
		average	4.9		-3.5		-101.3
ReinfSteel	concrete02, Mander, ReinfSteel	1	**82.1**	**39.3**	**76.8**	**38.5**	**-95.0**
		2	**24.8**	-12.8	5.8	**-45.3**	**-323.5**
		3	-1.5	-5.2	**-24.2**	-18.1	-17.7
		4	-3.9	0.2	-18.4	-17.3	**-2604.2**
		5	-3.9	**-27.8**	**-20.4**	**-52.9**	**-56.5**
		6	19.3	**-27.1**	**21.8**	**-78.6**	**61.1**
		average	7.0		-11.0		-86.3

Table 4-10. Effect of rebar-pin pinching on response of BRSA, in percent

			Base shear		Displacement		
Name	Description	RUN	Vs	Vn	South	North	Residual
BRSA-1	60% Pinch	1	**82.8**	**40.1**	**77.5**	**39.6**	**-94.9**
		2	**25.4**	-13.0	6.6	**-45.1**	**-278.0**
		3	-5.4	-10.6	**-26.4**	-10.4	-1.0
		4	-13.8	-14.2	-5.1	-15.1	**1615.7**
		5	-15.9	-14.2	-16.8	-20.0	**-63.5**
		6	2.3	-5.3	-15.0	-12.4	**-68.9**
		average	4.9		-3.5		-101.3
No pinch	No pinch	1	**82.8**	**40.1**	**77.5**	**39.6**	**-94.9**
		2	**25.3**	-13.0	6.4	**-45.1**	**-278.0**
		3	-5.6	-10.9	**-23.4**	-13.6	-18.1
		4	-14.0	-14.3	-5.9	-19.4	**1627.1**
		5	-13.9	-19.8	-13.7	**-31.5**	**-55.0**
		6	3.8	-11.6	-8.3	**-23.4**	**-53.3**
		average	4.1		-5.1		-99.8

Table 4-11. BRSA difference between calculated and measured response peaks, in percent

Rebar-pin model	RUN	Base shear		Displacement		
		Vs	Vn	South	North	Residual
Lumped plasticity	1	**82.8**	**40.1**	**77.5**	**39.6**	**-94.9**
	2	**25.3**	-13.0	6.4	**-45.1**	**-278.0**
	3	-5.6	-10.9	**-23.4**	-13.6	-18.1
	4	-14.0	-14.3	-5.9	-19.4	**1627.1**
	5	-13.9	-19.8	-13.7	**-31.5**	**-55.0**
	6	3.8	-11.6	-8.3	**-23.4**	**-53.3**
	average	4.1		-5.1		-99.8
DB element	1	-5.0	19.8	**-51.0**	**-37.3**	**-98.7**
	2	19.1	10.5	**-46.2**	**-46.9**	**-47.6**
	3	-1.6	-10.4	**-40.8**	**-30.5**	**-43.5**
	4	-8.7	-5.2	-6.6	-19.7	**561.0**
	5	-11.1	-19.2	**-20.2**	**-38.1**	**-86.7**
	6	11.0	-0.3	-7.6	-19.1	**-80.6**
	average	-0.1		-30.3		-71.4

Table 5-1. BPSA parametric study matrix

Model	Column axial force	ALI	Taper slope	Tension member
	kip [kN]	%	%	
P0	4.5 [20.0]	1	4	high strength rod
P1	51 [222.4]	5		
P2	100 [444.8]	10		
P3	150 [667.2]	15		
P4	4.5 [20.0]	1	0	
P5			8	
P6			4	strand
P7	100 [444.8]	10		none
P8				strand
P9			‘perfect’ Pinned	

Table 5-2. Effect of ALI on response of BPSA

Model		P00		P01		P02		P03	
Loading direction		South	North	South	North	South	North	South	North
Column axial load	kip	4.5		50.3		100.6		150.8	
	[kN]	[20]		[224]		[447]		[671]	
Axial load Index		1%		5%		10%		15%	
Base shear	kip	50.0	50.3	57.6	56.5	62.1	61.6	68.3	67.5
	[kN]	[222]	[224]	[256]	[251]	[276]	[274]	[304]	[300]
Ultimate displacement	in	4.43	4.82	3.64	4.56	3.18	3.09	2.9	3.12
	[mm]	[113]	[122]	[92]	[116]	[81]	[78]	[74]	[79]
Displacement ductility		4.3	4.8	3.9	4	3.4	3.3	3.1	3.3
Initial stiffness	kip/in	44.3	45.7	57.6	56.5	66.4	65	72.9	72.1
	[kN/mm]	[7.8]	[8.0]	[10.1]	[9.9]	[11.6]	[11.4]	[12.8]	[12.6]
Average pipe-pin moment	kip.in	487.6		596.3		674		765.2	
	[kN.m]	[55.1]		[67.4]		[76.2]		[86.5]	

Table 5-3. Calculated responses with simple-stick model and comparison with FE model

Model		P00		P01		P02		P03	
Loading direction		South	North	South	North	South	North	South	North
Base shear	kip	57.0	59.4	66.2	66.5	73.6	75.1	80.1	82.5
	[kN]	[254]	[264]	[294]	[296]	[327]	[334]	[356]	[367]
	Diff	14%	18%	15%	18%	19%	22%	17%	22%
Ultimate displacement	in	3.66	4.14	3.35	3.45	2.9	3.15	2.61	2.84
	[mm]	[93]	[105]	[85]	[88]	[74]	[80]	[66]	[72]
	Diff	-17%	-14%	-8%	-24%	-9%	2%	-10%	-9%
Displacement ductility		4.2	4.7	4.1	4.2	3.5	3.8	3.2	3.4
	Diff	-2%	-2%	5%	5%	4%	16%	3%	4%
Average maximum pipe-pin moment	kip.in	693		758		817		865	
	[kN.m]	[78]		[86]		[92]		[98]	
	Diff	42%		27%		21%		13%	

Table 5-4. Effect of pipe taper slope on maximum base shear and displacement

Model		**P04**		**P00**		**P05**	
Loading direction		South	North	South	North	South	North
Tapering slope (s)		0%		4%		8%	
Base shear	kip	51.5	51.6	50.1	50.3	49.1	49.4
	[kN]	[229]	[230]	[223]	[224]	[218]	[220]
Ultimate displacement	in	4.26	4.66	4.43	4.82	4.56	4.83
	[mm]	[108]	[118]	[113]	[122]	[116]	[123]
Displacement ductility		4.5	4.8	4.3	4.8	4.3	4.6
Average maximum	kip.in	499	524	461	515	429	474
pipe-pin moment	[kN.m]	[56.4]	[59.2]	[52.1]	[58.2]	[48.5]	[53.6]

Table 5-5. Effect of tension member in bents with uplift

Model		**P0**		**P6**	
Loading direction		South	North	South	North
Tension member		HS-Rod		Strand	
Base shear	kip	50.0	50.3	48.4	49.0
	[kN]	[222]	[224]	[215]	[218]
Ultimate displacement	in	4.43	4.82	4.36	4.78
	[mm]	[113]	[122]	[111]	[121]
Displacement ductility		4.3	4.8	4.4	4.7
Initial stiffness	kip/in	44.3	45.7	44	43.7
	[kN/mm]	[7.8]	[8.0]	[7.7]	[7.7]
Average maximum	kip.in	487.6		344	
pipe-pin moment	[kN.m]	[55.1]		[38.9]	

Table 5-6. Effect of tension member in bent without uplift

Model		**P2**	**P8**	**P7**	**P9**
Loading direction		North	North	North	North
Column axial load	kip	100			
	[kN]	[445]			
Axial load Index		10%			
Tension member		HS-Rod	Strand	No member	Pinned
Base shear	kip	61.6	60.2	58.9	49.7
	[kN]	[274]	[268]	[262]	[221]
Ultimate displacement	in	3.09	3.25	3.09	2.9
	[mm]	[78]	[83]	[78]	[74]
Displacement ductility		3.3	3.0	3.4	5.1
Initial stiffness	kip/in	65	55.8	62.5	87.2
	[kN/mm]	[11.4]	[9.8]	[10.9]	[15.3]
Average maximum	kip.in	671.3	630.9	436.6	0
pipe-pin moment	[kN.m]	[75.9]	[71.3]	[49.3]	[0.0]

Table 5-7. BRSA parametric study matrix

Model	Column axial force	ALI	Core diameter	$\frac{D_{core}}{D_{hinge}}$
	kip [kN]	%	in [mm]	
R0	4.5 [20]	1	7.3 [185]	0.73
R1	50 [222]	5		
R2	100 [445]	10		
R3	150 [667]	15		
R4	201 [894]	20		
R5	4.5 [20]	1	9 [229]	0.9
R6			5 [127]	0.5
R7			3 [76]	0.3
R8			Pinned	

Table 5-8. Effect of ALI on performance of rebar-pins and bent

		Rebar-pins				Bent			
	ALI	**Curvature ductility**	**Rotational ductility**	**Ultimate rotation**	**Friction capacity**	**Initial stiffness**	**Displacement ductility**	**Base shear**	**Ultimate displacement**
	%			rad	kip [kN]	kip/in [kN/mm]		kip [kN]	in [mm]
R0	1	23	18.7	0.153	63.4 [282]	77.6 [13.6]	6.2	61.2 [272]	4.67 [118]
R1	5	25	18.1	0.161	71.4 [318]	87.3 [15.3]	6.1	66.1 [294]	4.48 [114]
R2	10	25	16.5	0.165	89.9 [400]	92.5 [16.2]	5.3	74.4 [331]	4.04 [102]
R3	15	26	15.6	0.174	112.4 [500]	91.4 [16.0]	4.5	81.1 [361]	3.76 [95]
R4	20	22	11.3	0.147	134.1 [596]	88.9 [15.6]	3.7	85.7 [381]	3.41 [87]

Table 5-9. Effect of core diameter on performance of rebar-pins and bent

		Rebar-pins				Bent			
	$\frac{D_{core}}{D_{pin}}$	**Maximum moment**	**Rotational ductility**	**Ultimate rotation**	**Friction capacity**	**Initial stiffness**	**Ductility**	**Base shear**	**Ultimate displacement**
				rad	kip [kN]	kip/in [kN/mm]		kip [kN]	in [mm]
R5	0.9	760.6 [85.9]	16.1	0.129	67.8 [302]	77.6 [13.6]	6.1	63.5 [282]	4.73 [120]
R0	0.73	673.9 [76.2]	18.7	0.153	63.4 [282]	78.5 [13.7]	6.2	61.3 [273]	4.67 [119]
R6	0.5	558.7 [63.1]	28.8	0.237	44.9 [200]	73.4 [12.9]	6.2	58.93 [262]	4.64 [118]
R7	0.3	506.2 [57.2]	49.1	0.413	34.6 [154]	72.1 [12.6]	6.3	55.2 [246]	4.67 [119]
R8	NA	0 [0.0]	NA	NA	NA	66.5 [11.6]	7.5	55.2 [246]	4.67 [119]

Table 6-1. Plastic moment calculation in bent on pin

iteration		1	2	
$(OM)_{try}$		0	29565 [40090]	
M_{pin}	kip.ft [kN.m]	0 [0]	0 [0]	0 [0]
P_{col}	kip [kN]	1306 [5809]	2110 [9396]	502 [2233]
$M_{p,col}$	kip.ft [kN.m]	11389 [15441]	12190 [16530]	10530 [14280]
$V_{u,col}$	kip.ft [kN]	268 [1192]	287 [1277]	248 [1103]
$V_{u,bent}$	kip [kN]	536 [2384]	535 [2380]	
$(OM)_{achieved}$	kip.ft [kN.m]	29565 [40090]	29495 [39990]	
$\frac{(OM)_{achieved}}{(OM)_{try}}$		--	0.998 (OK)	

Table 6-2. Rod design for bent with pipe-pin

Iteration		1	2		3
ϕ_{rod}	in [mm]	3 [76]	3.5 [89]		3.5 [89]
K_{rod}	kip/in [kN/m]	830 [145.3]	1130 [197.8]		1130 [197.8]
$T_{u,rod}$	kip [kN]	877 [3902]	1006 [4473]		921.5 [4099]
$M_{u,rod}$	kip.in [kN.m]	6.976 [62.29]	114.4 [12.92]		114.4 [12.92]
$T_{r,rod}$	kip [kN]	848.2 [3773]	1155 [5136]		1155 [5136]
$M_{r.rod}$	kip.in [kN.m]	551.4 [62.3]	875.5 [98.92]		875.5 [98.21]
$\frac{T_{u.rod}}{T_{r,rod}} + \frac{8}{9}\frac{M_{u,rod}}{M_{r,rod}}$		1.13	0.99 (OK)		0.914 (OK)

Table 6-3. Upper pipe strength iterations

iteration		1	2
$(f_c^*)_{try}$	ksi [MPa]	f'$_c$=4 [27.6]	1.378 [9.5]
L_2	in [mm]	47.68 [1211]	60.25 [1530]
V_c	kip [kN]	1251 [5564]	1519 [6757]
V_{sp}	kip [kN]	161.3 [717]	190 [845]
$(f_c^*)_{achived}$	ksi [MPa]	1.378 [9.50]	1.319
$\frac{(f_c^*)_{achived}}{(f_c^*)_{try}}$		0.34	0.96
$V_n^{noAxial}$	kip [kN]	NG	1729 [7691]

Table 6-4. Moment-curvature analysis results for design example with rebar-pins

		1	2	
$(OM)_{try}$		0 [0]	31860.81 [15461]	
P_{col}	kip [kN]	1306 [5809]	616 [2740]	1996 [8878]
$M_{p,col}$	kip.ft [kN.m]	11402 [15461.1]	10528 [14276.0]	12222 [16573.0]
$\phi_{u,col}$	1/in [1/m]	1.49E-03 [0.0587]	1.69E-03 [0.0665]	1.34E-03 [0.0528]
$\phi_{y,col}$	1/in [1/m]	8.80E-05 [0.00346]	9.04E-05 [0.00356]	8.94E-05 [0.00352]
P_{pin}	kip [kN]	1514.1 [6735]	798 [3550]	2178 [9688]
$M_{y,pin}$	kip.ft [kN.m]	3173 [4302.6]	2622 [3555.4]	3583 [4858.5]
$\phi_{y,pin}$	1/in [1/m]	1.28E-04 [0.00504]	1.25E-04 [0.00492]	1.33E-04 [0.00524]
$M_{m,pin}$	kip.ft [kN.m]	3788 [5136.5]	3162 [4287.7]	4242 [5752.2]
$\phi_{m,pin}$	1/in [1/m]	1.24E-03 [0.04882]	1.63E-03 [0.06409]	1.04E-03 [0.04110]
$M_{degraded,pin} = M_{u,pin}$	kip.ft [kN.m]	2750 [3729.0]	2420 [3281.5]	3011 [4082.9]
$\phi_{degraded,pin}$	1/in [1/m]	1.89E-03 [0.07445]	2.82E-03 [0.11094]	1.52E-03 [0.05965]
$\phi_{ultimate}$	1/in [1/m]	3.25E-03 [0.12787]	3.86E-03 [0.15189]	2.92E-03 [0.11480]
$V_{u,col}$	kip [kN]	357.4 [1590]	322.1 [1433]	387.4 [1723]
$V_{u,bent}$	kip [kN]	714.8 [3180]	709.5 [3156]	
$(OM)_{achieved}$	kip.ft [kN.m]	31861 [43203]	31739 [43039]	

Figures

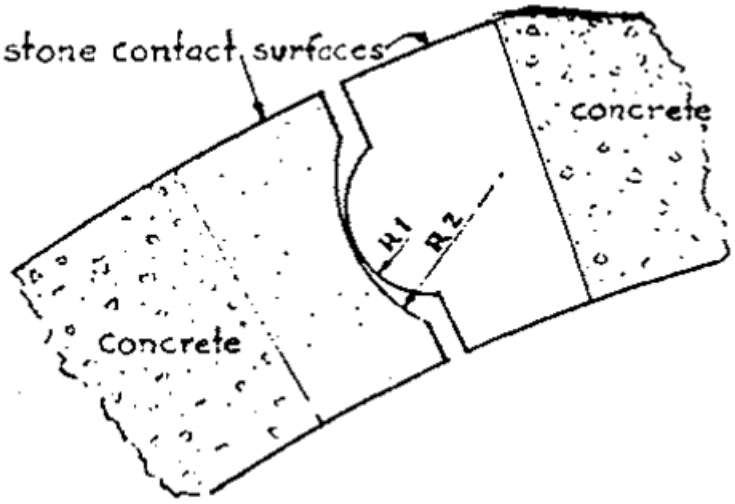

Fig. 1-1. Saddle shape concrete hinges (Morell, 1935)

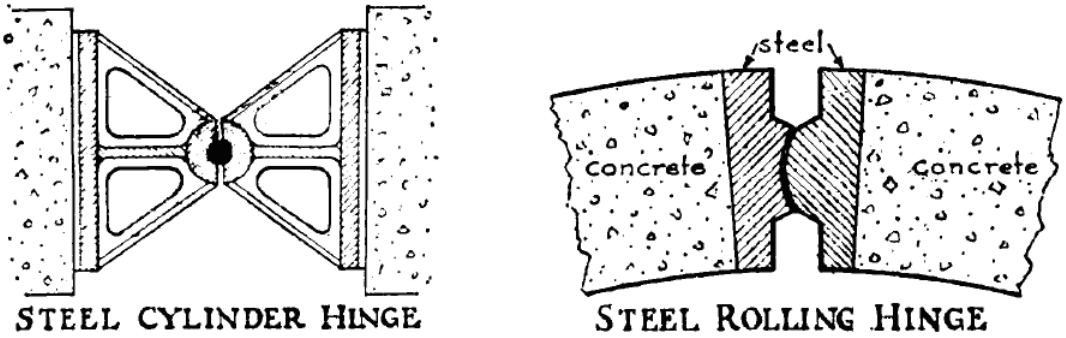

Fig. 1-2. Steel hinges in reinforce concrete structures (Morell, 1935)

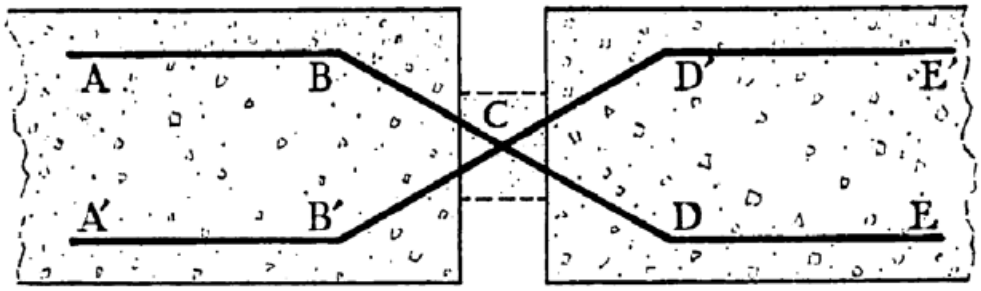

Fig. 1-3. Mesneger concrete hinge (Morell, 1935)

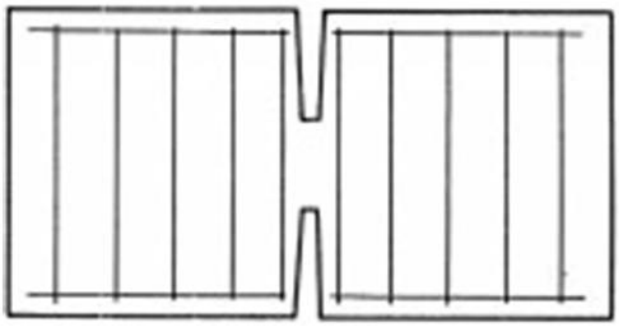

Fig. 1-4. Freyssinet concrete hinge (Schacht and Marx, 2015)

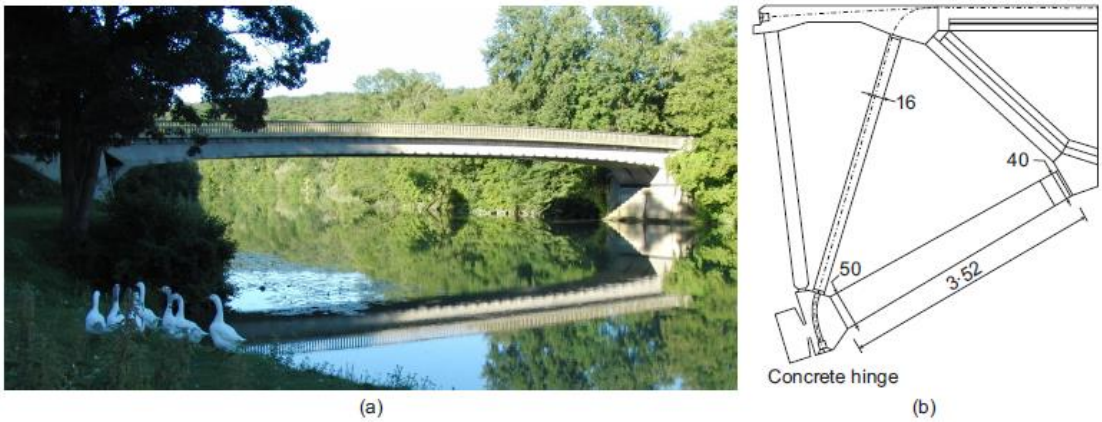

Fig. 1-5. Bridge over the Marne in Luzancy with Freyssinet concrete hinge at the abutment (a) bridge (b) detail of concrete hinge (in cm) (Schacht and Marx, 2015)

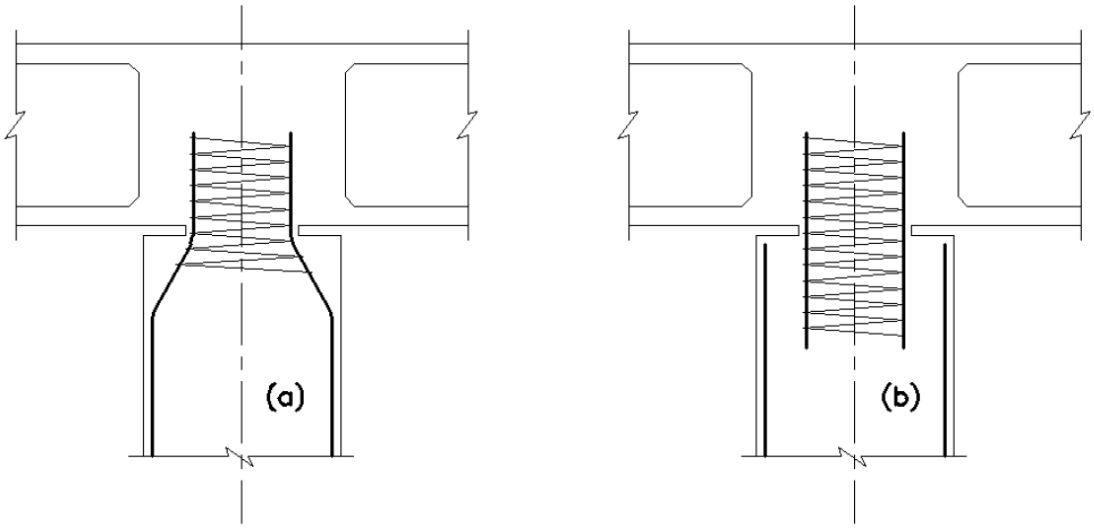

Fig. 1-6. Hinges with reinforcing bars a) Clustered bar hinges b) Distributed bar hinges (Zaghi and Saiidi, 2010)

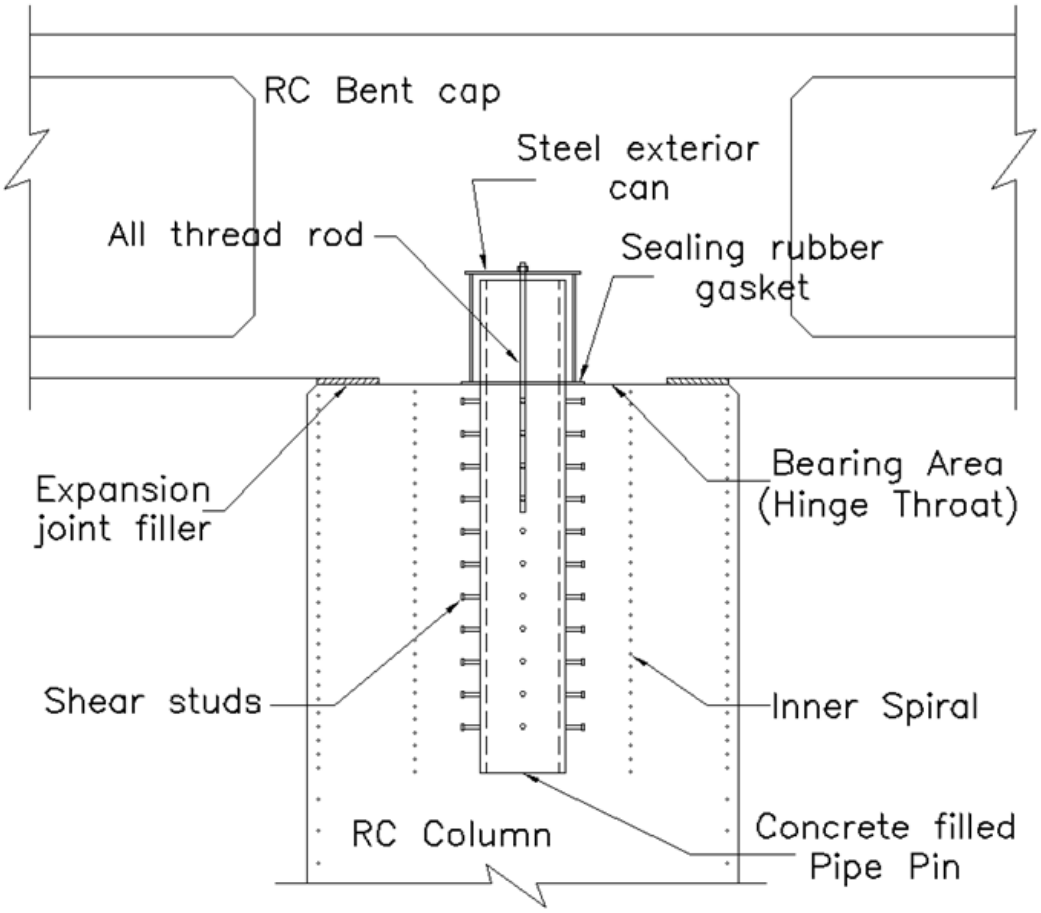

Fig. 1-7. Column-cap-beam pipe-pins connection (Zaghi and Saiidi, 2010)

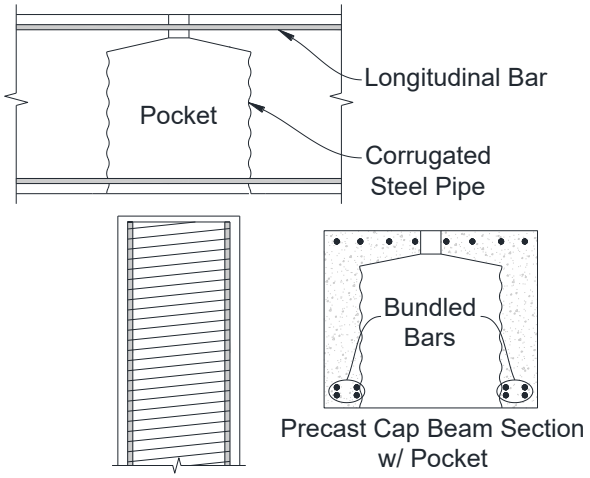

Fig. 1-8. Schematic of pocket connections with extended precast column (Mehrsoroush, et al., 2015)

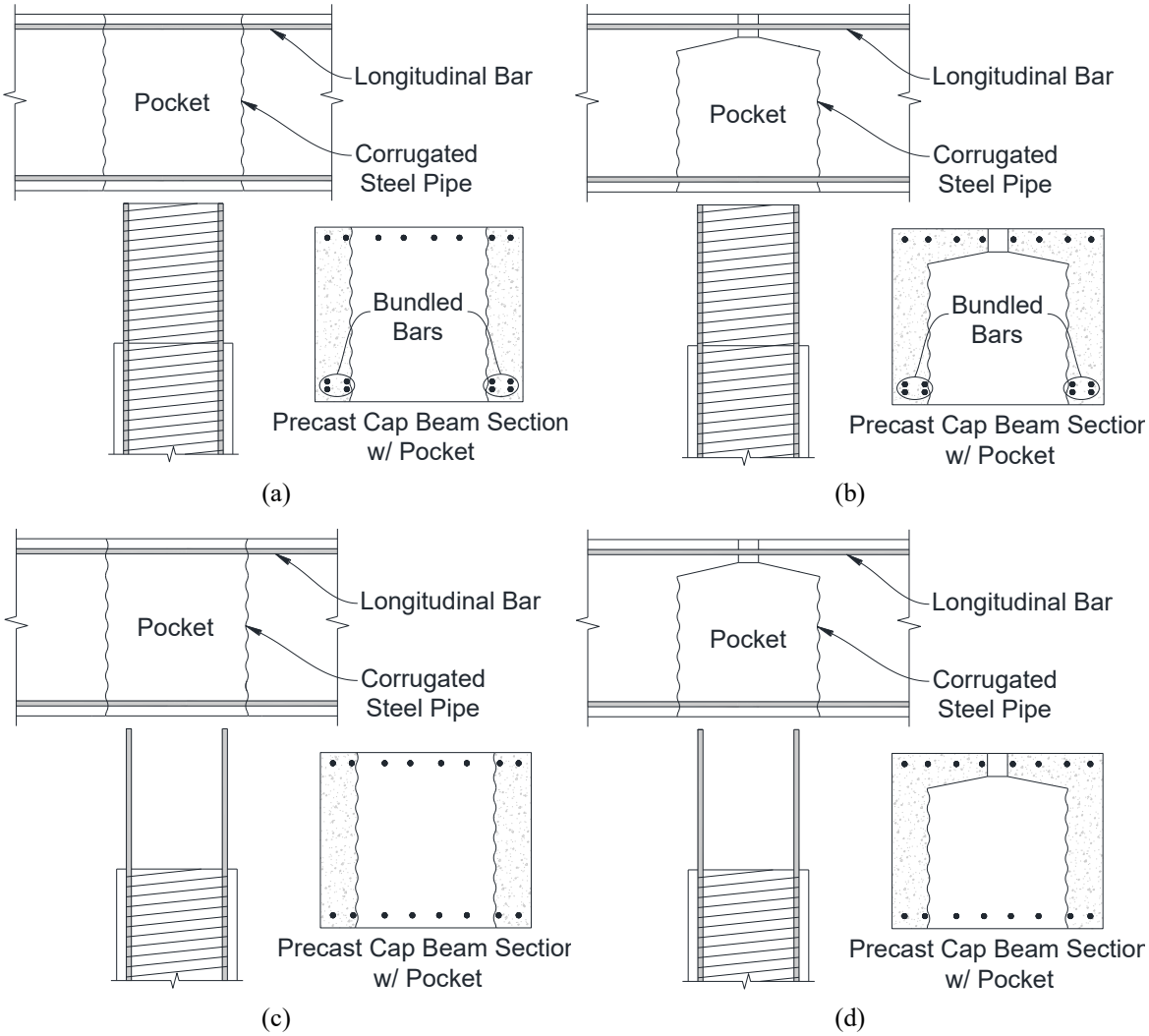

Fig. 1-9. Schematic of alternatives for pocket connections with extended longitudinal bars (Mehrsoroush, et al., 2015)

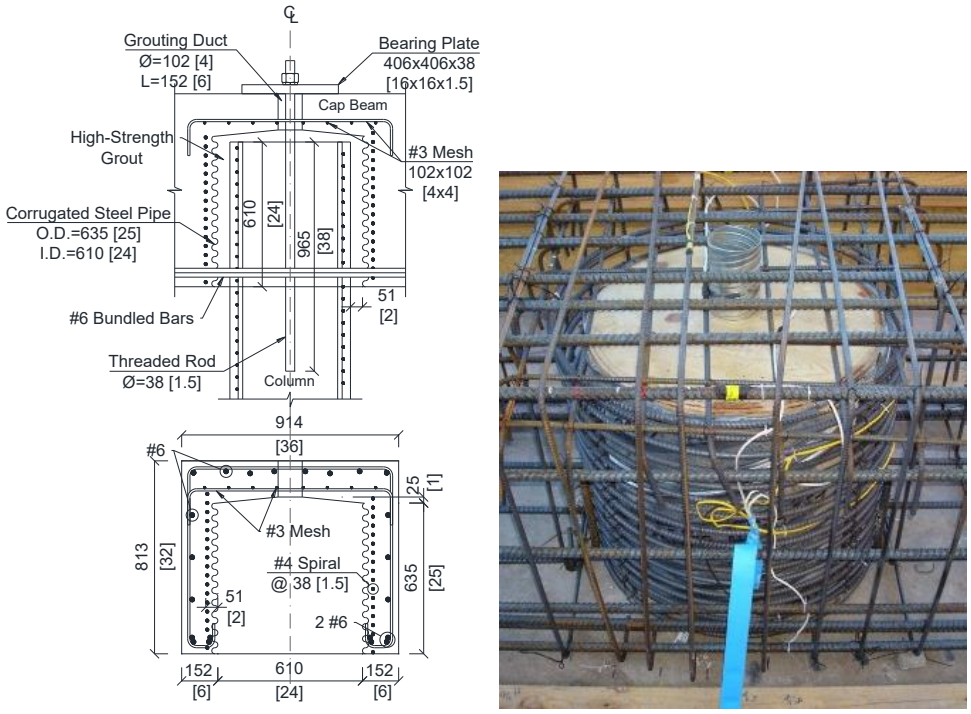

Fig. 1-10. Details of pocket connections in the Mehrsoroush and Saiidi (2014) model

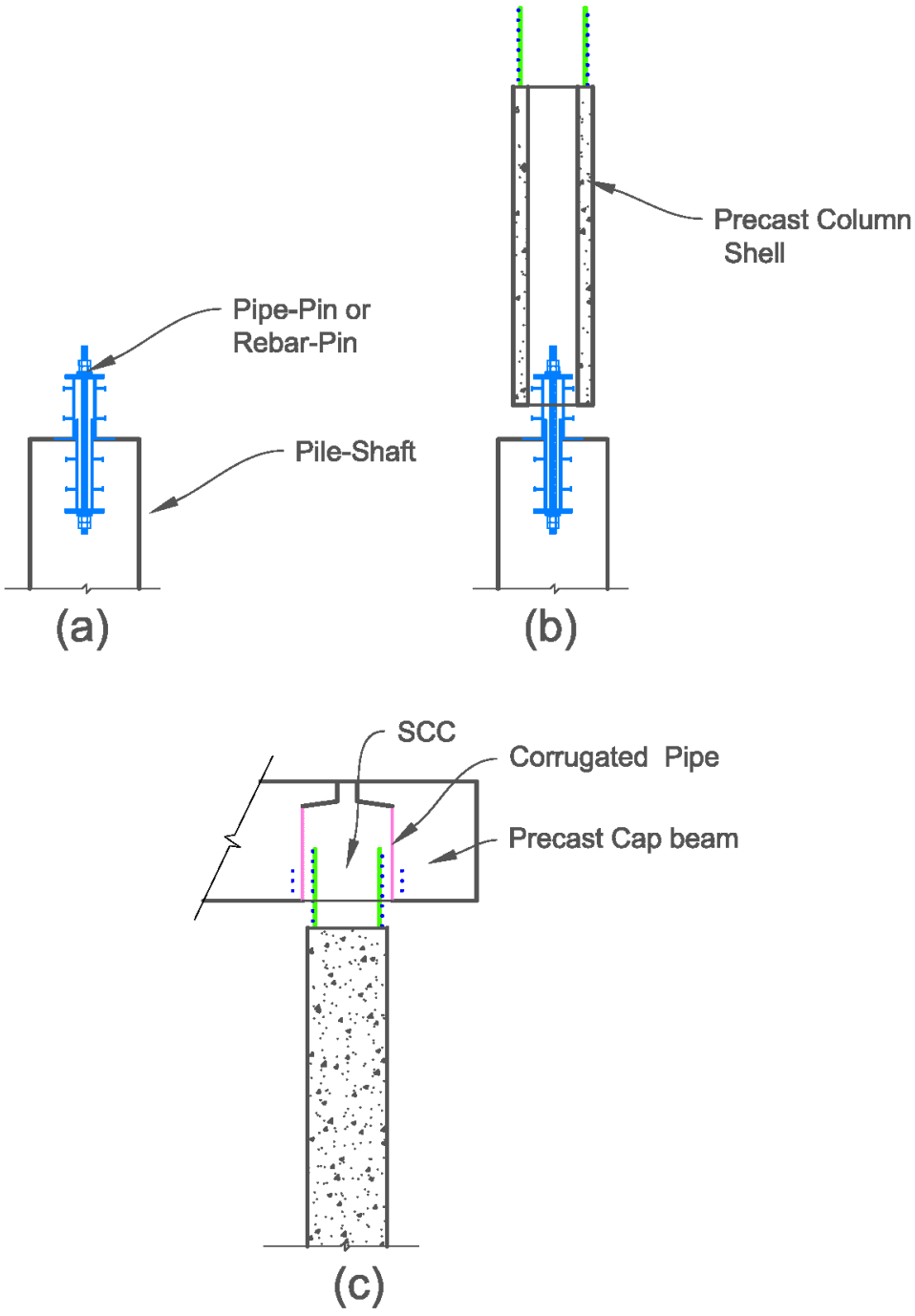

Fig. 2-1. Assembling the precast members

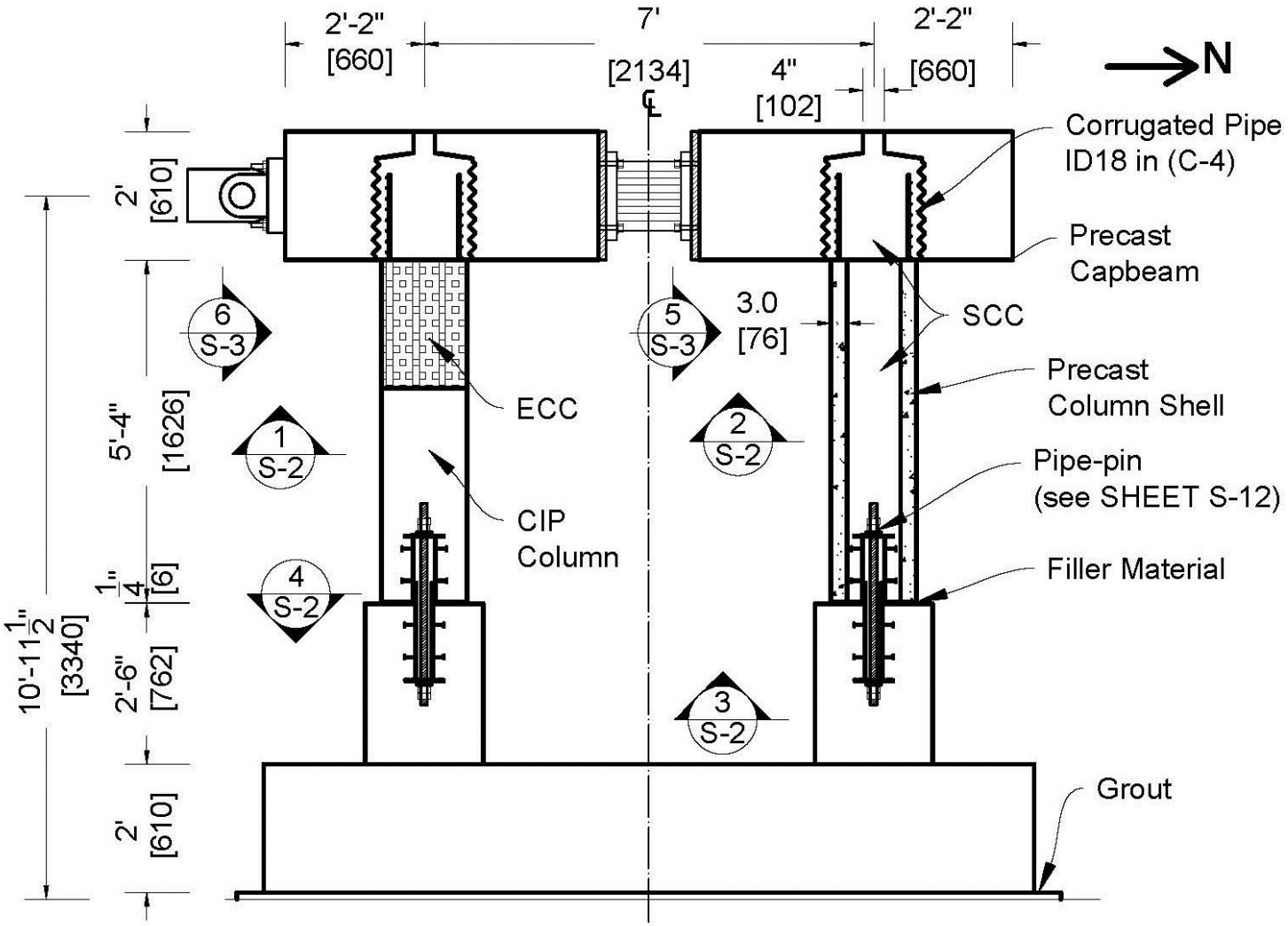

BENT ELEVATION VIEW

SCALE 3/8"=1'-0"

NOTES

1- SCC is self-consolidated concrete.

2- ECC is engineering cementitious compposite.

Fig. 2-2. BPSA elevation view

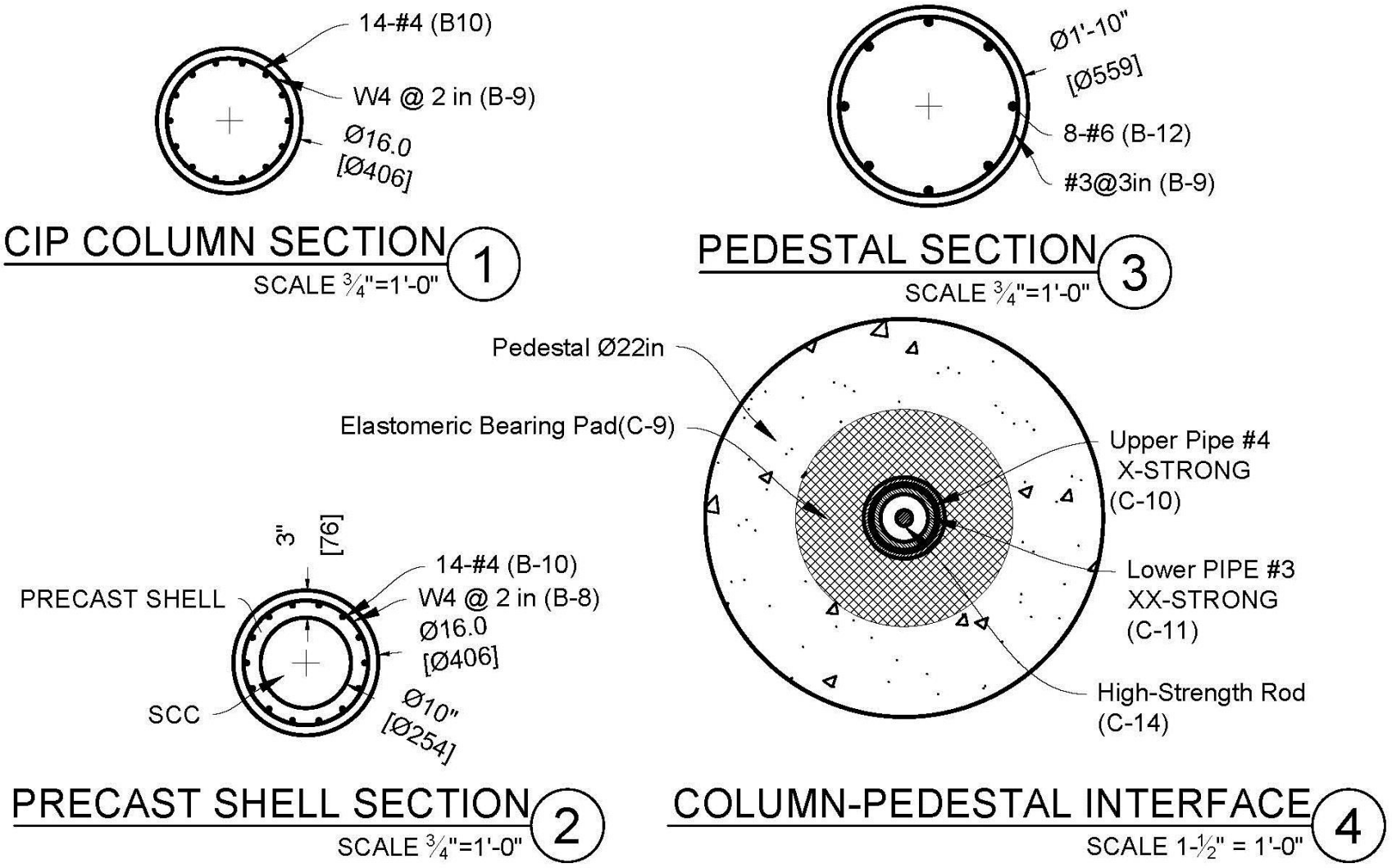

Fig. 2-3. BPSA sections

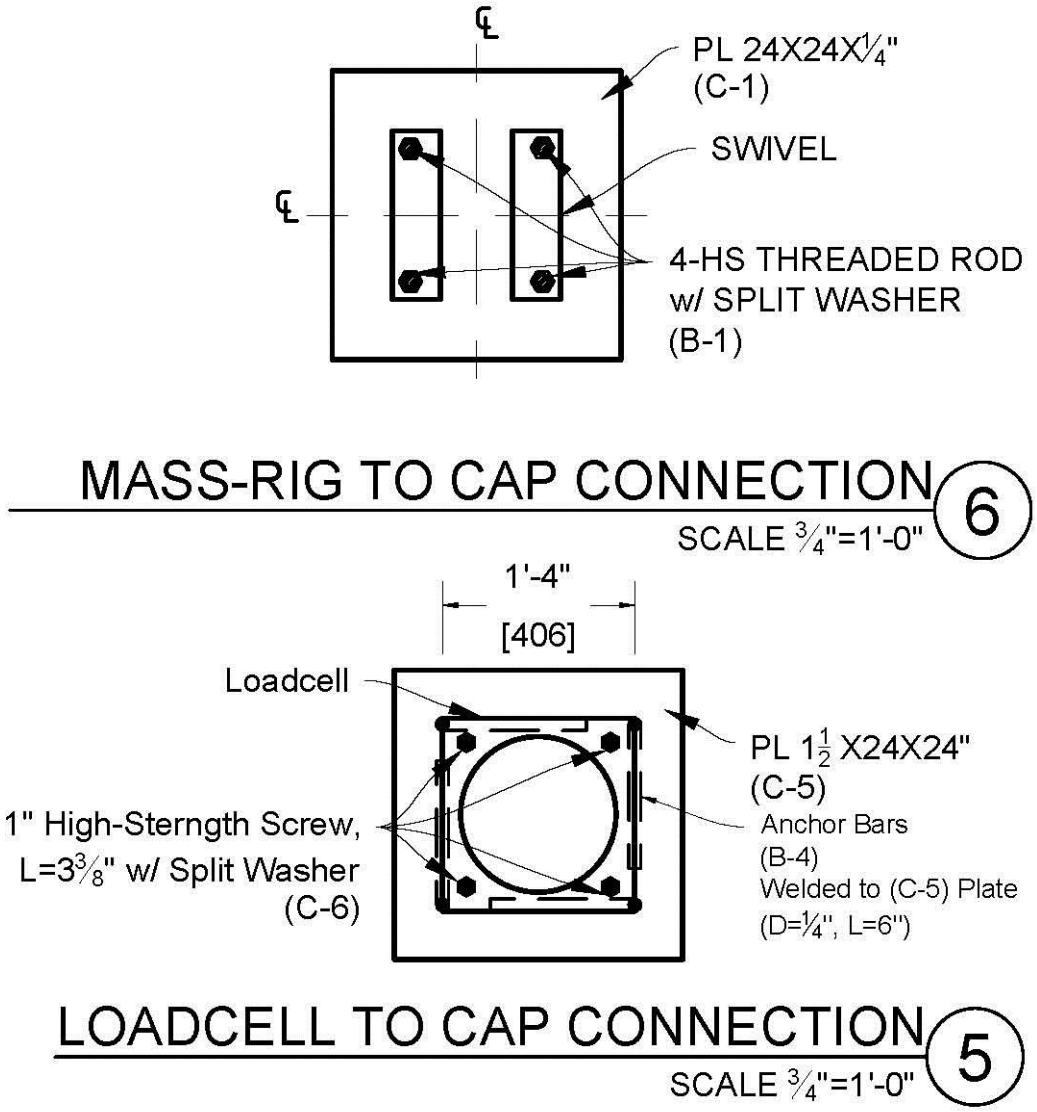

Fig. 2-4. BPSA sections (continued)

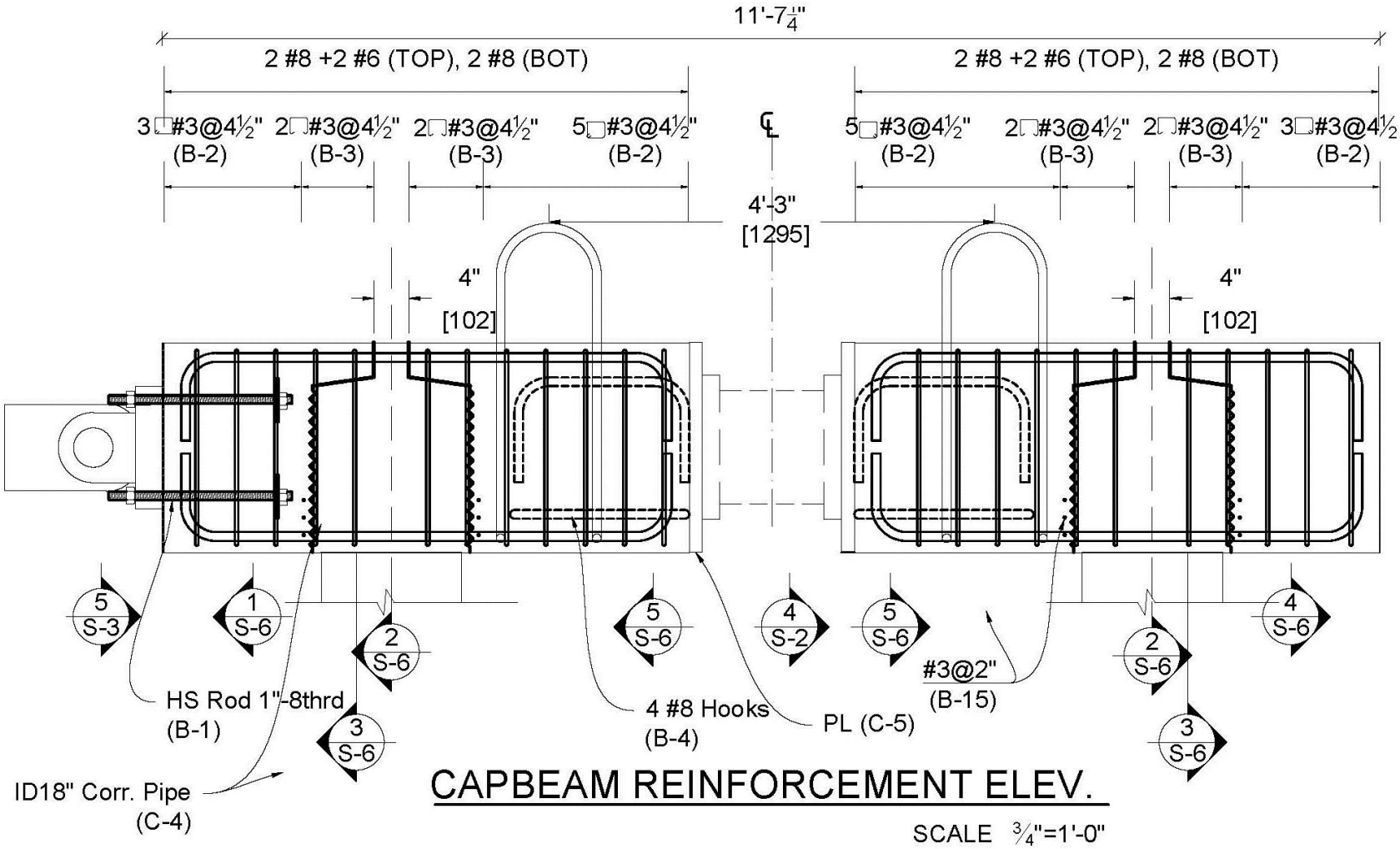

Fig. 2-5. BPSA cap beam reinforcements elevation view

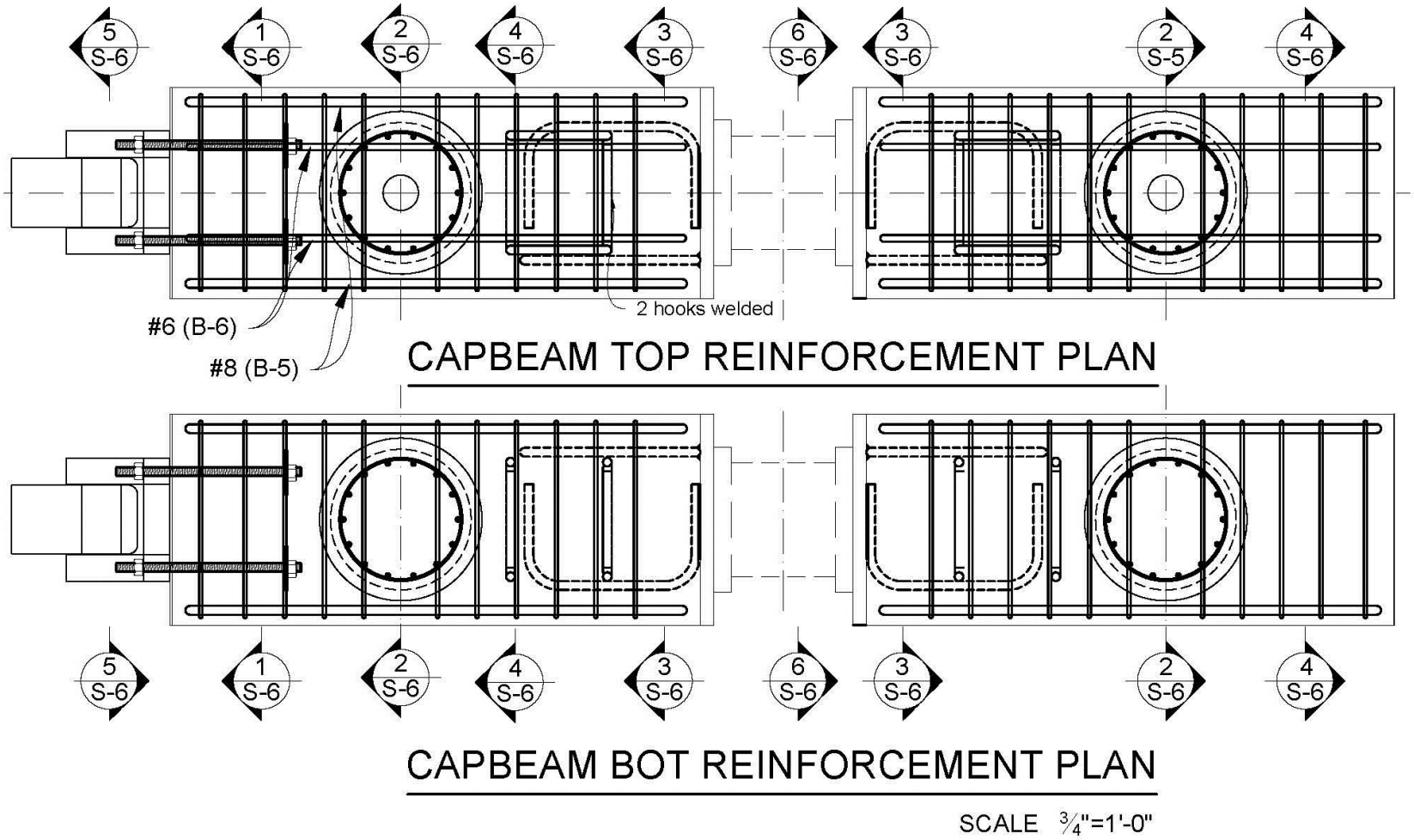

Fig. 2-6. BPSA cap beam reinforcements plan view

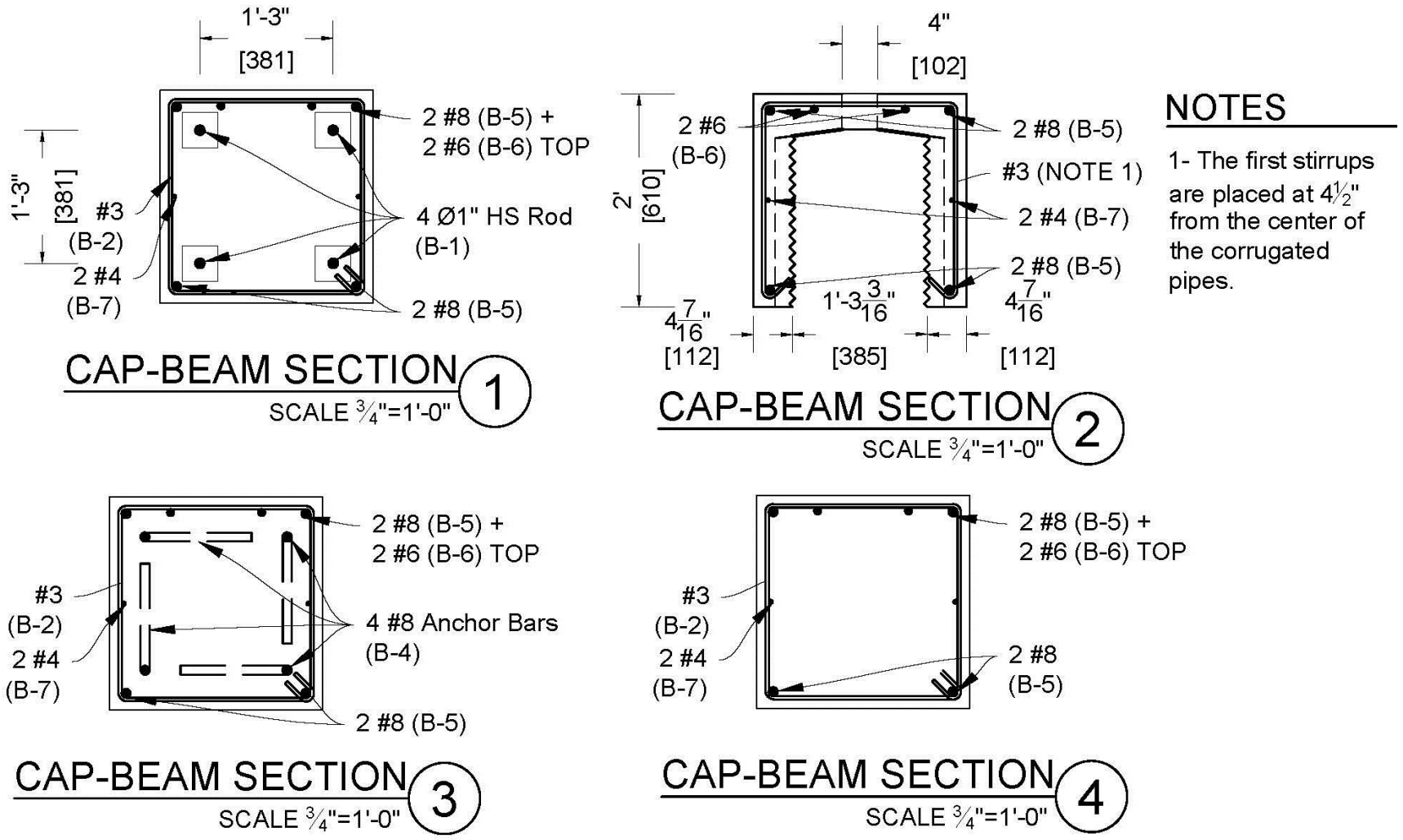

Fig. 2-7. BPSA cap beam sections

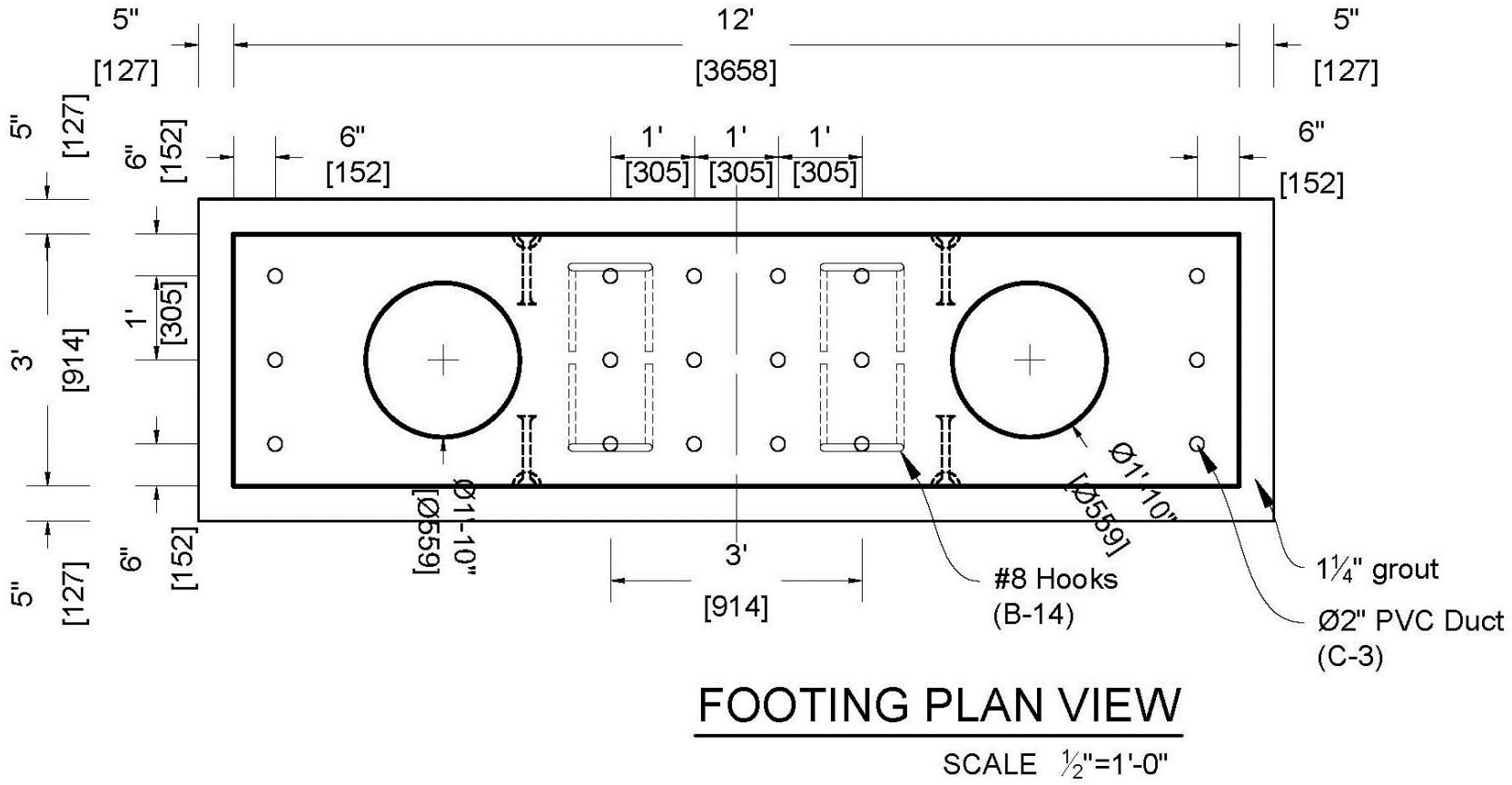

Fig. 2-8. BPSA footing plan view

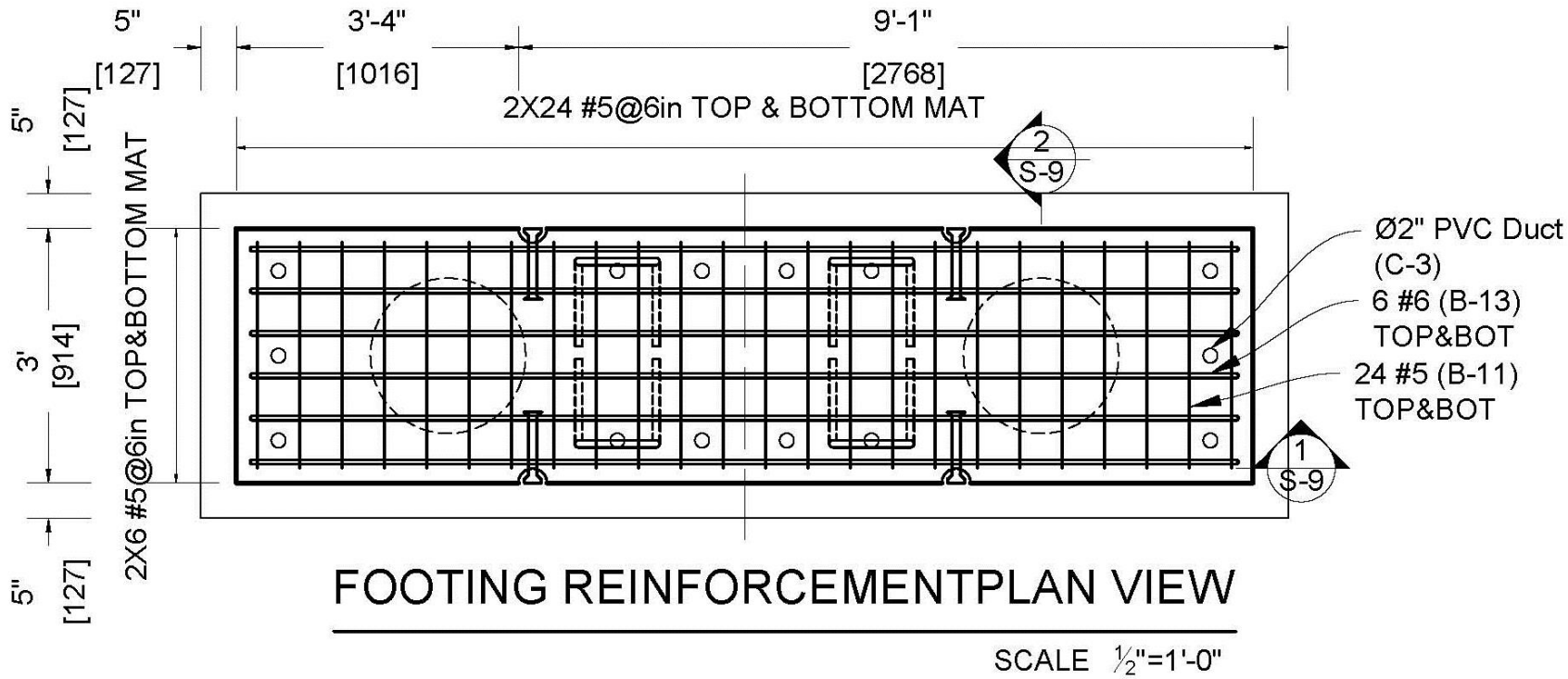

Fig. 2-9. BPSA footing reinforcements

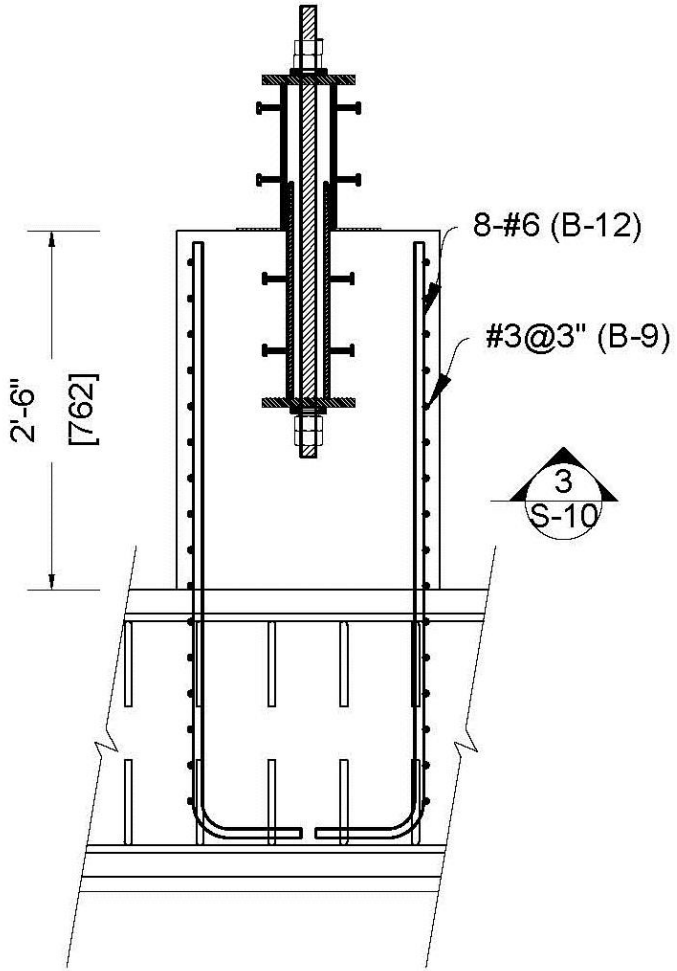

PEDESTAL REINFORCEMENT

SCALE ¾"=1'-0"

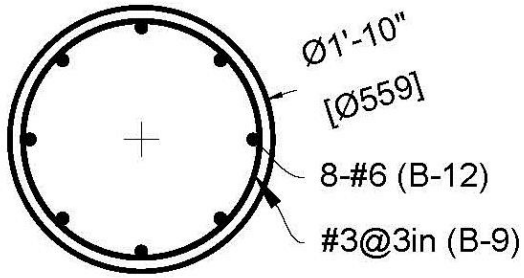

PEDESTAL SECTION 3

SCALE ¾"=1'-0"

Fig. 2-10. BPSA pedestal reinforcements

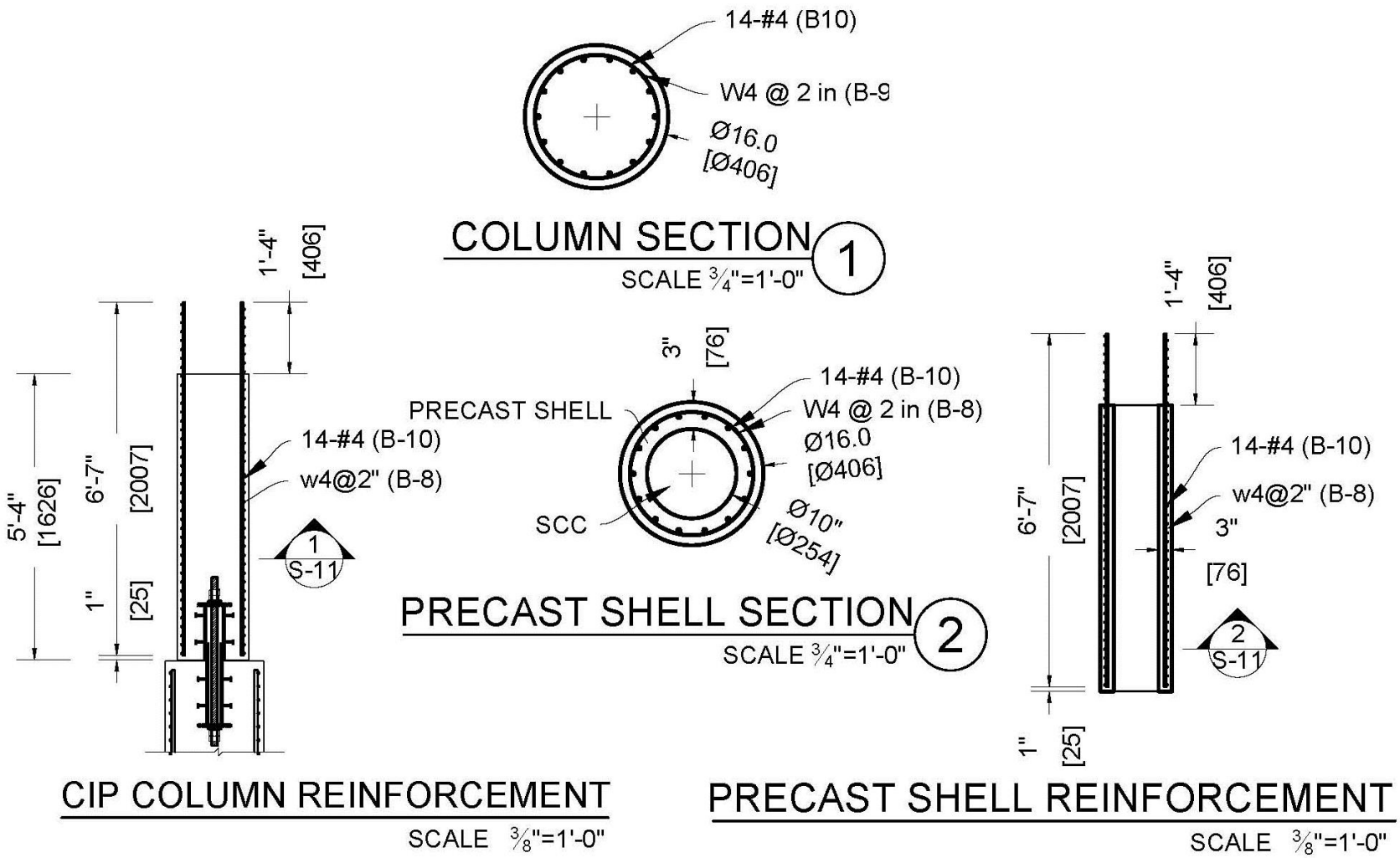

Fig. 2-11. BPSA column reinforcements

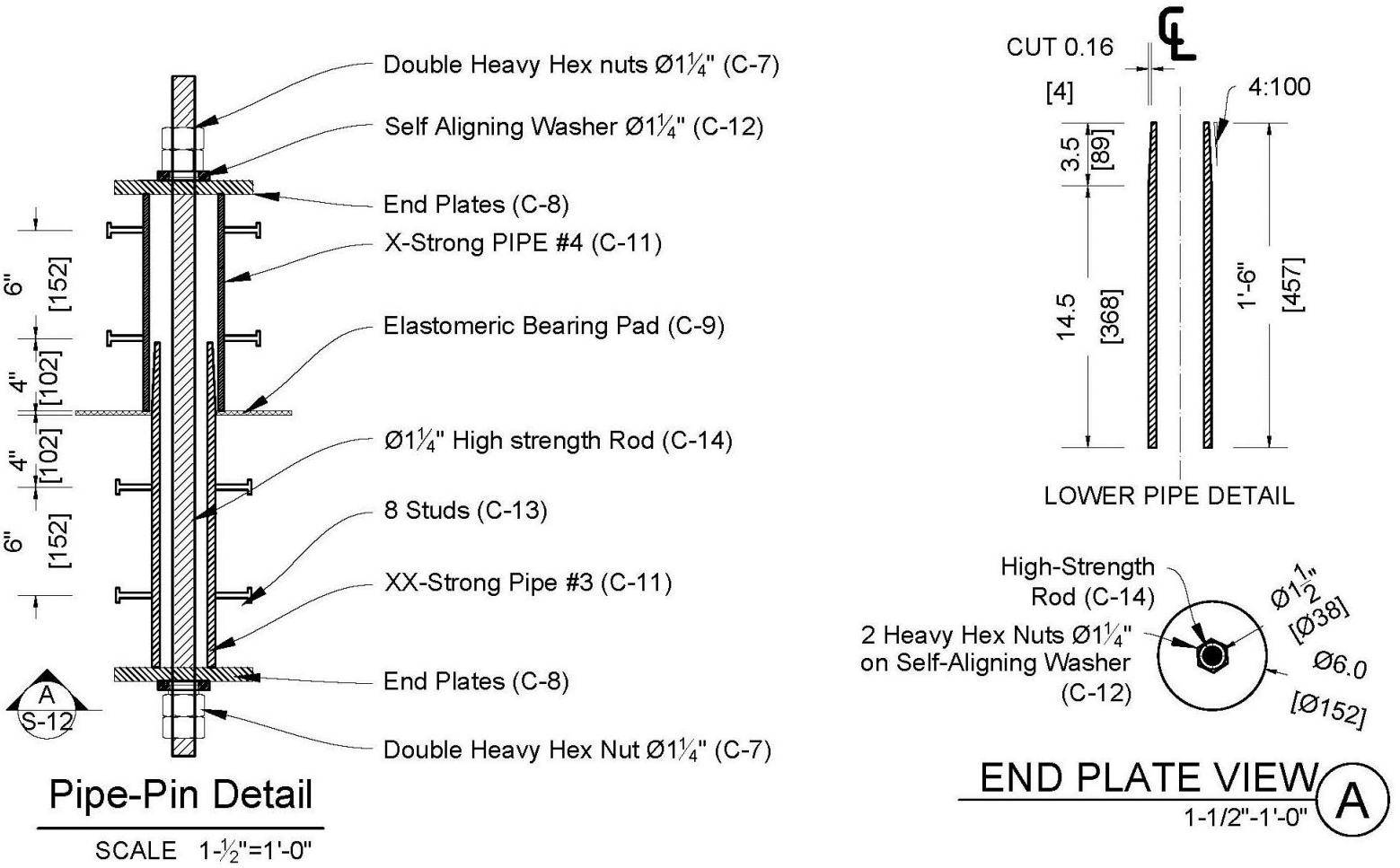

Fig. 2-12. BPSA pipe-pin detail

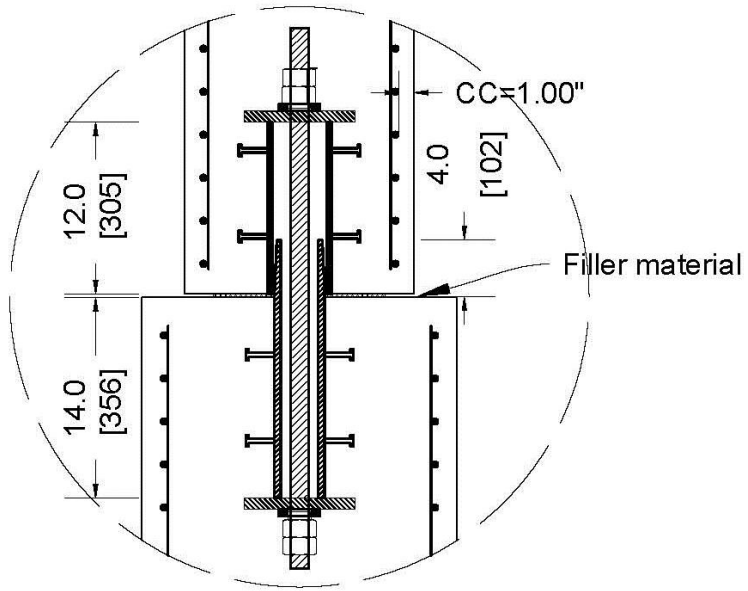

PIPE-PIN IN CIP COLUMN
SCALE 1"=1'-0"

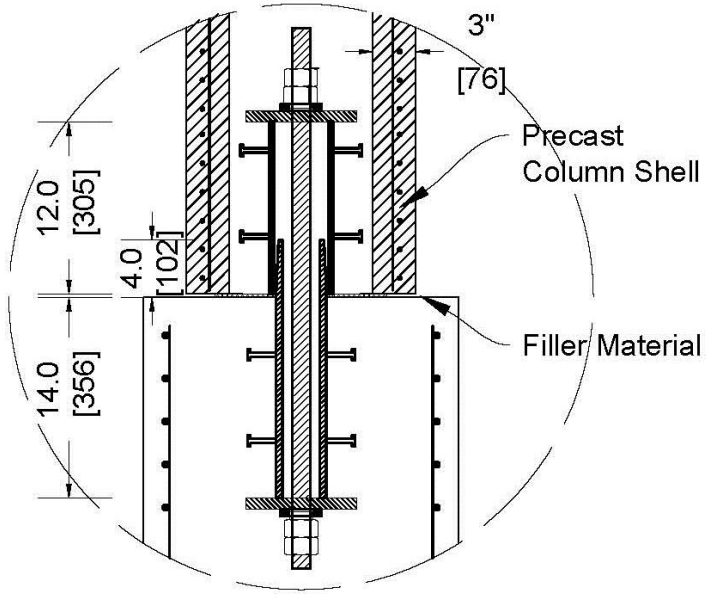

PIPE-PIN IN PRE-CAST COLUMN
SCALE 1"=1'-0"

Fig. 2-13. BPSA pipe-pin placement

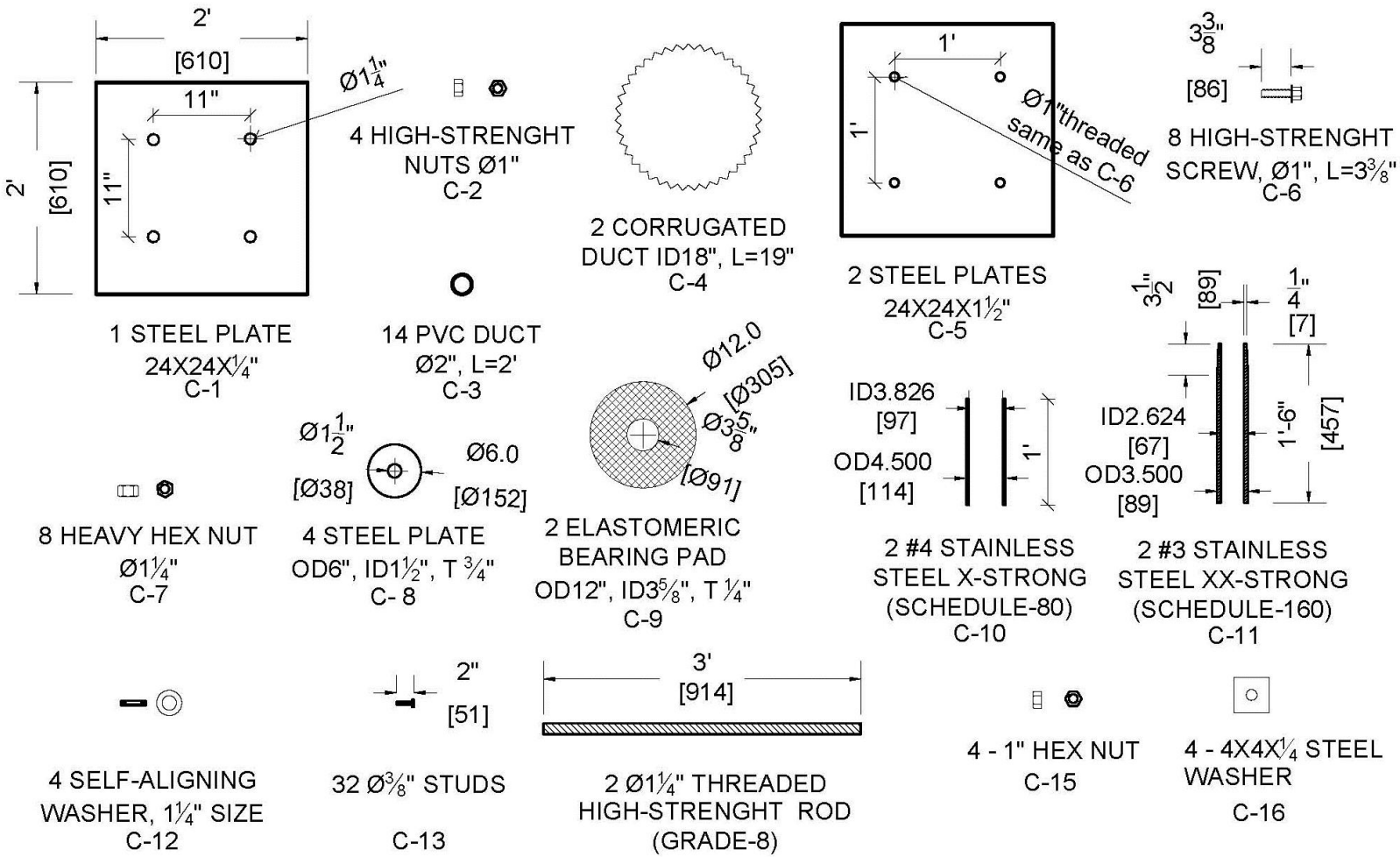

Fig. 2-14. BPSA steel detail

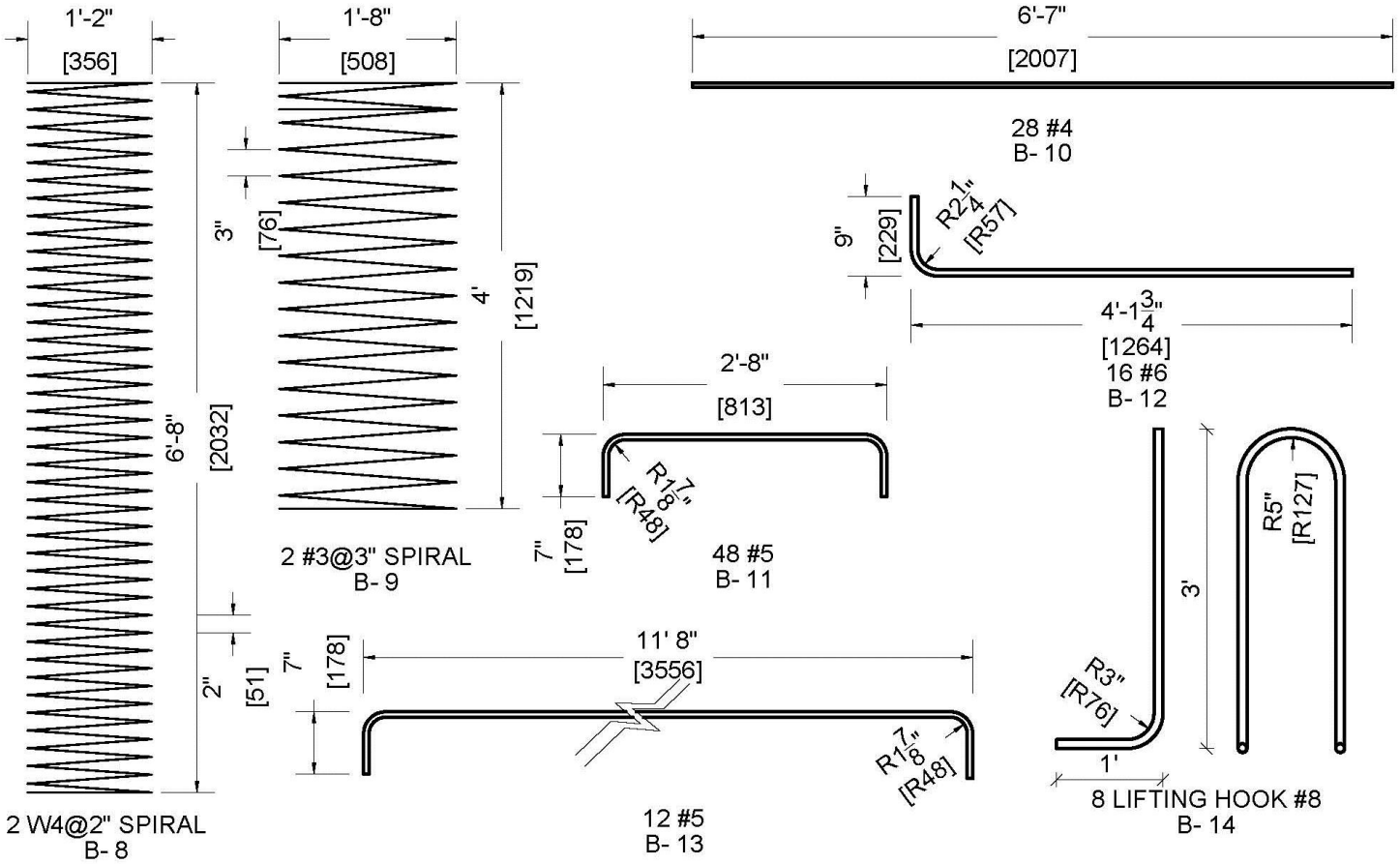

Fig. 2-15. BPSA rebar details

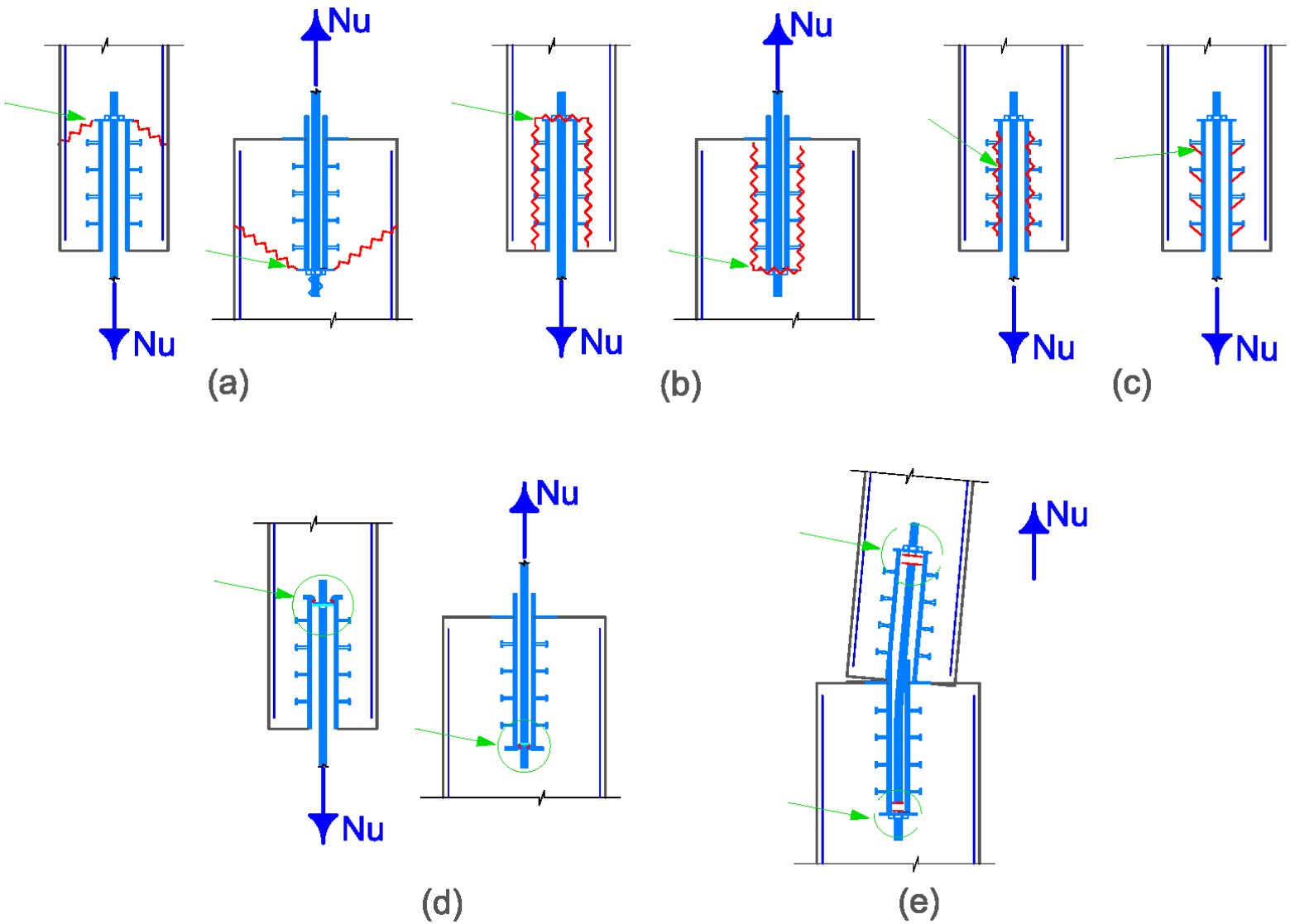

Fig. 2-16. Tensile failure modes of pipe-pin

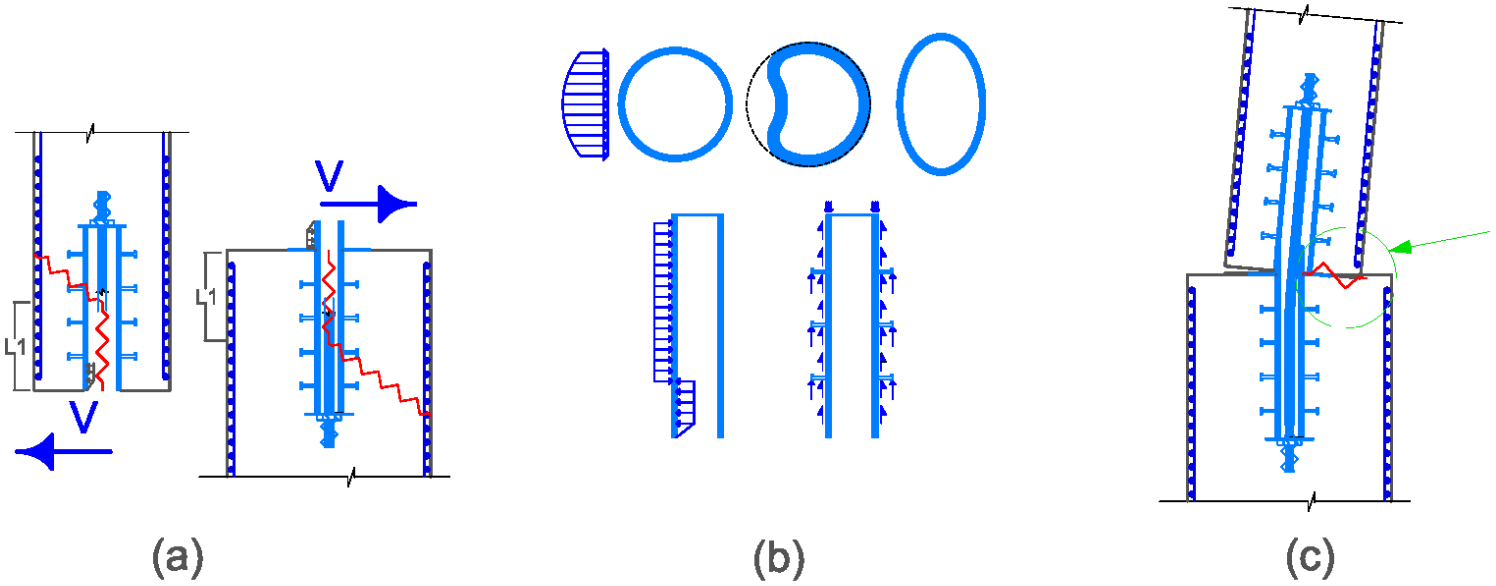

Fig. 2-17. Shear failure modes of pipe-pin

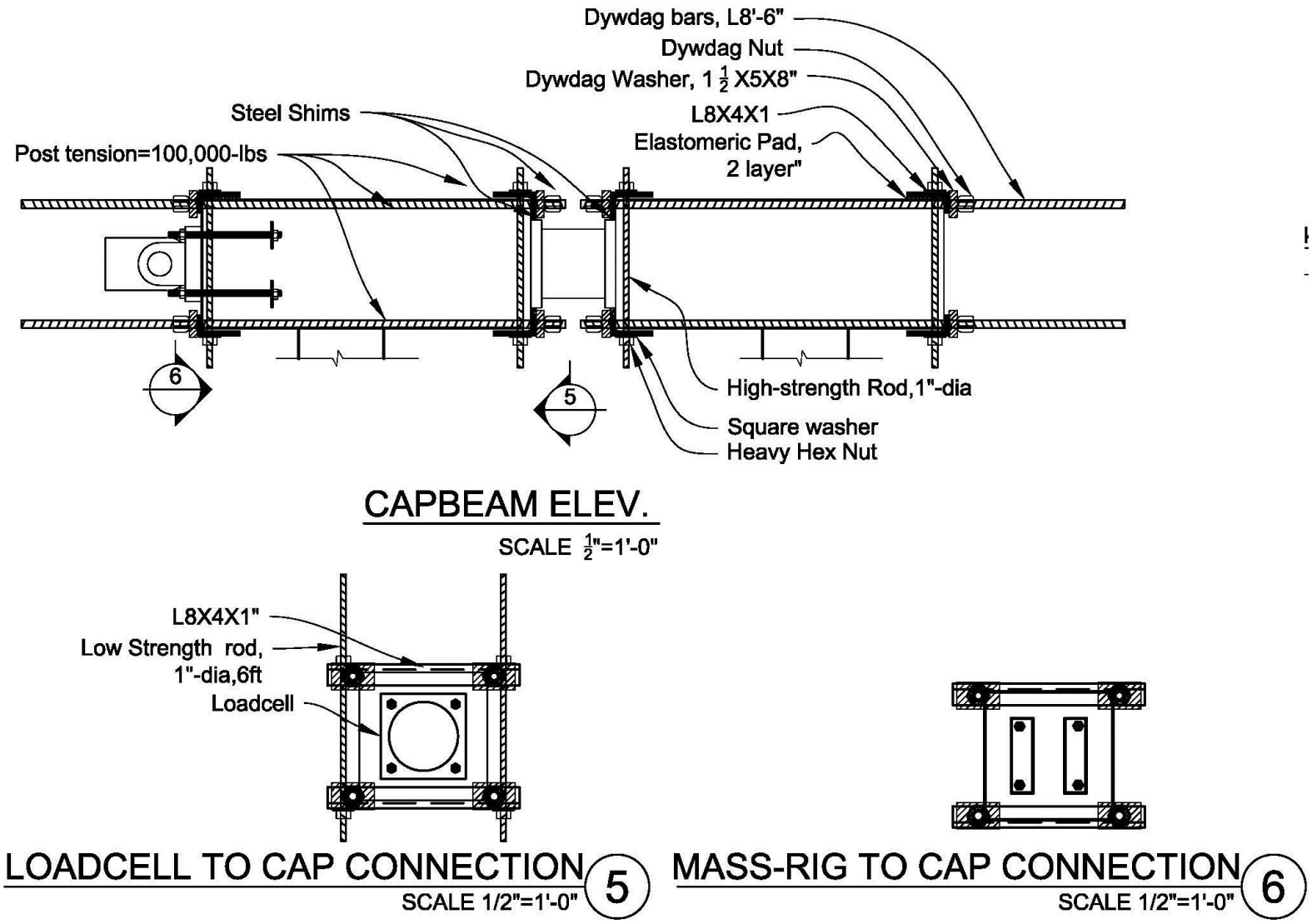

Fig. 2-18. Post-tensioning detail

Fig. 2-19. Assembling the lower part of pipe-pin which embed in pedestal

Fig. 2-20. Concrete cast for precast shells

Fig. 2-21. Phase one concrete cast for BPSA

Fig. 2-22. Pipe-pin after placing the bearing pad and top pipe

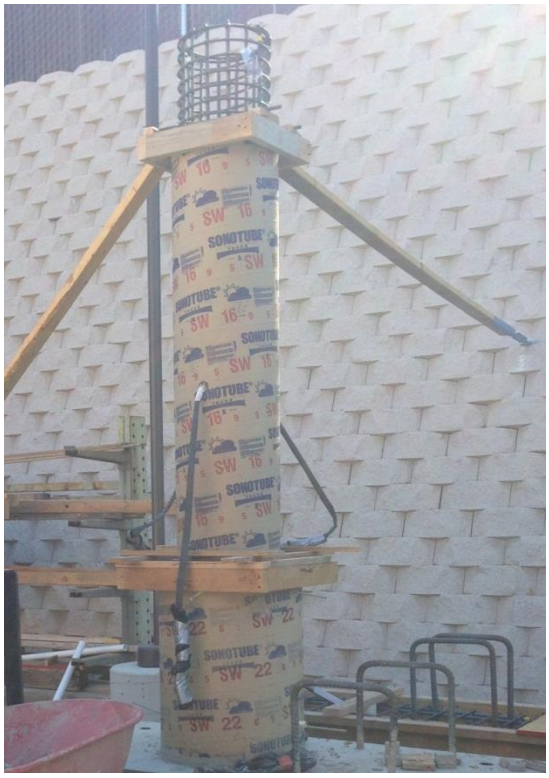

Fig. 2-23. Preparing the CIP columns

Fig. 2-24. Placing the load-cell, ducts and their spirals before placing the bar cage

Fig. 2-25. Placing beam cap on the columns

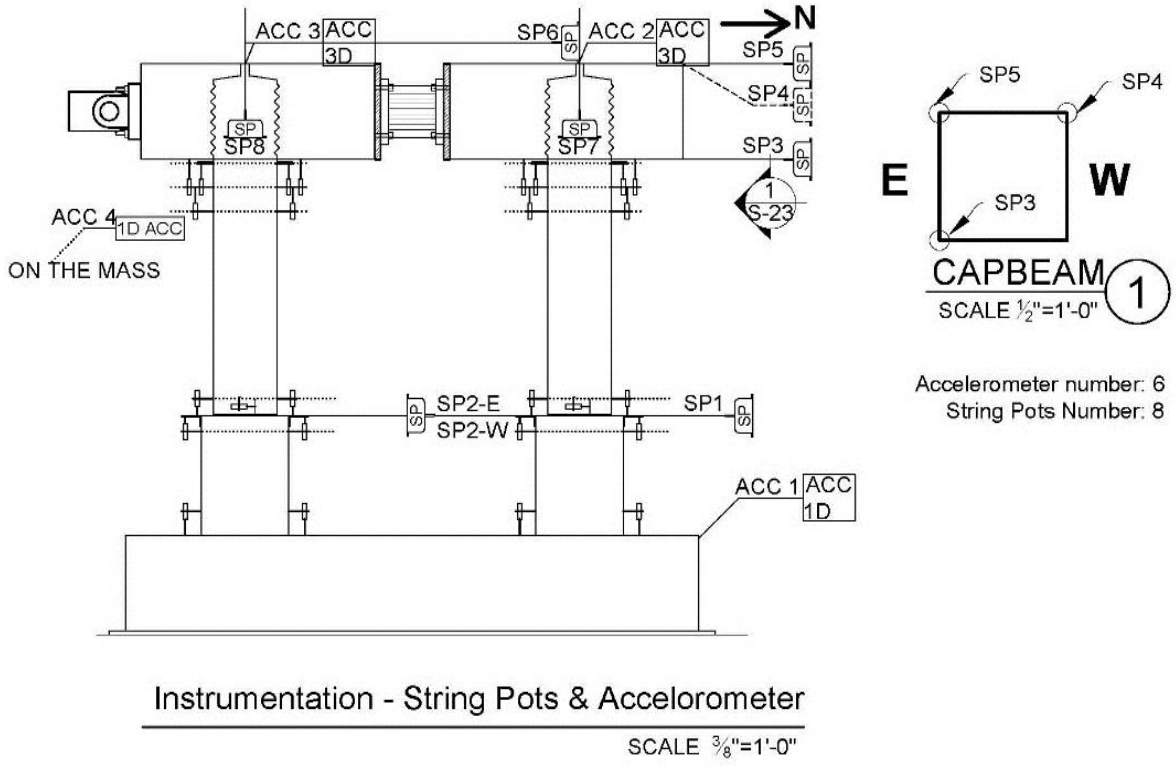

Fig. 2-26. BPSA displacements and acceleration instruments

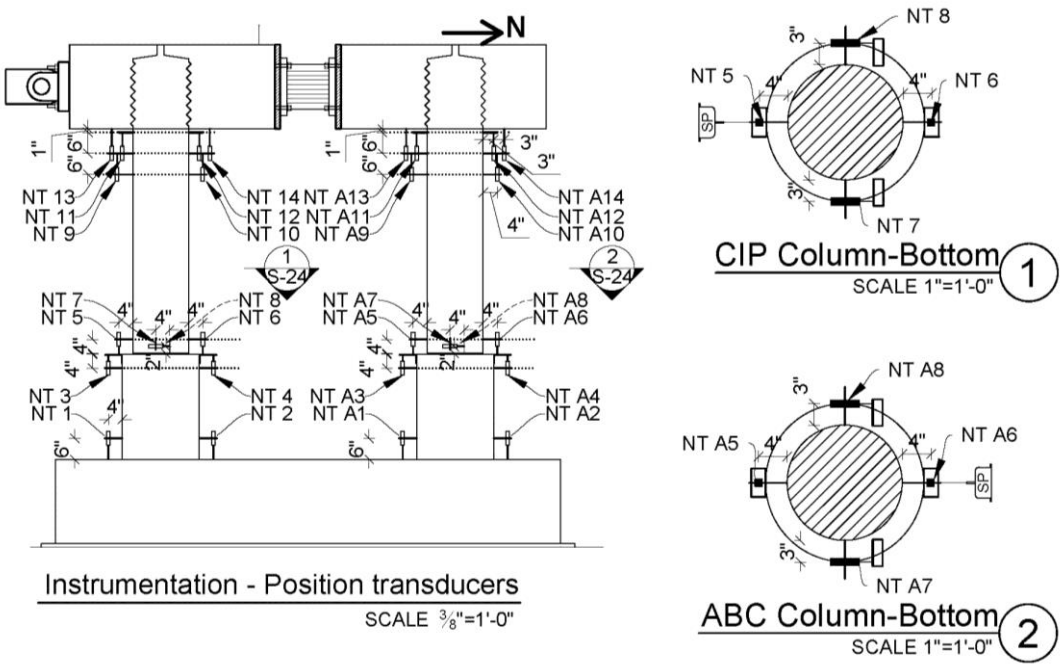

Novotechniks number: 28

Fig. 2-27. BPSA instrumentation position transducer plan

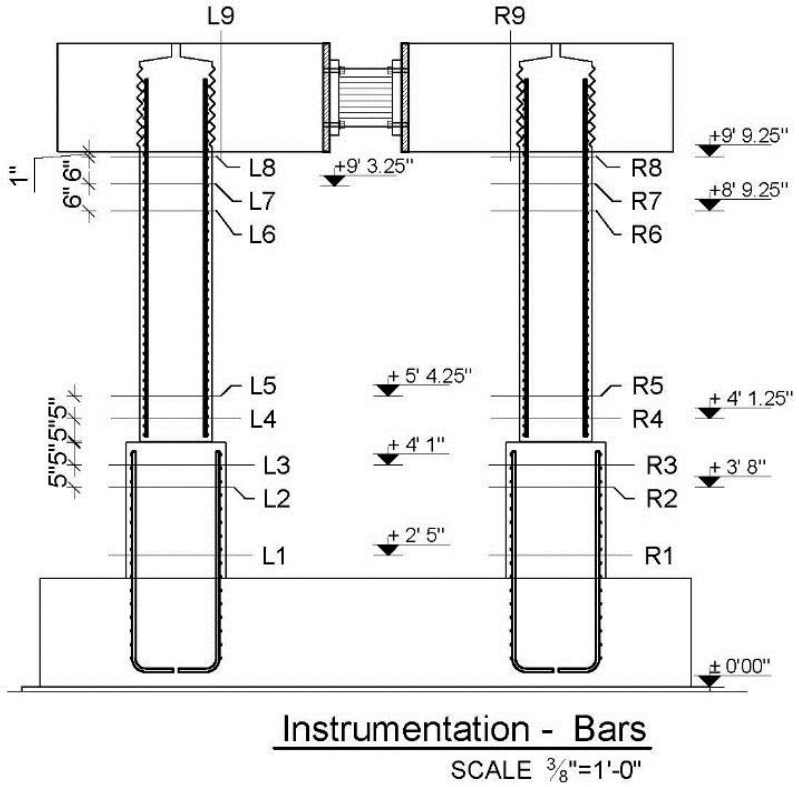

Fig. 2-28. BPSA strain gage sections layout

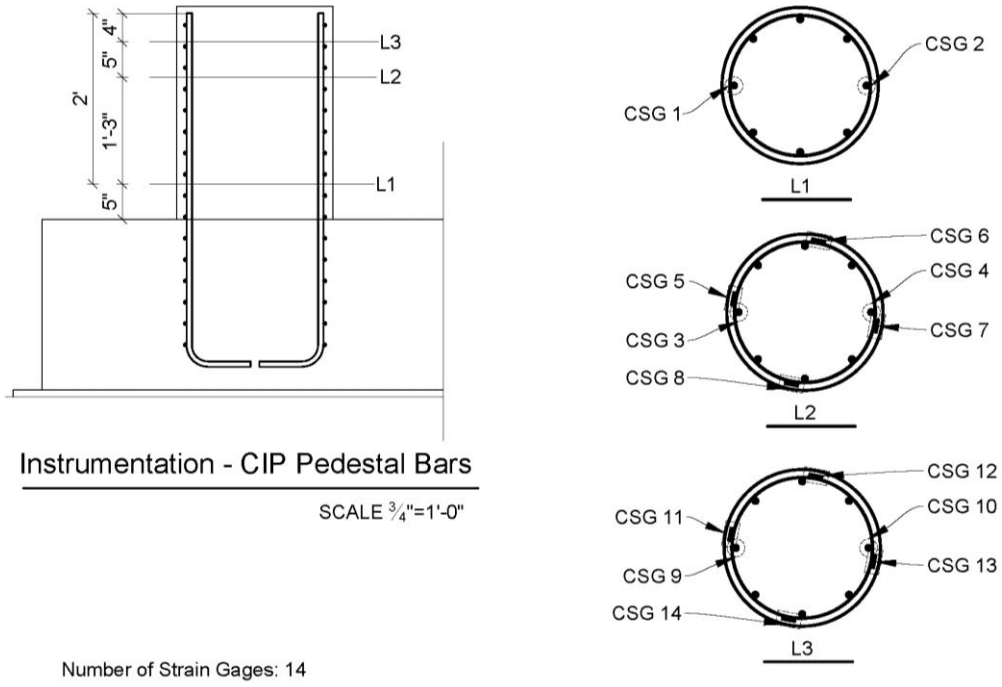

Fig. 2-29. BPSA pedestal strain gages under CIP

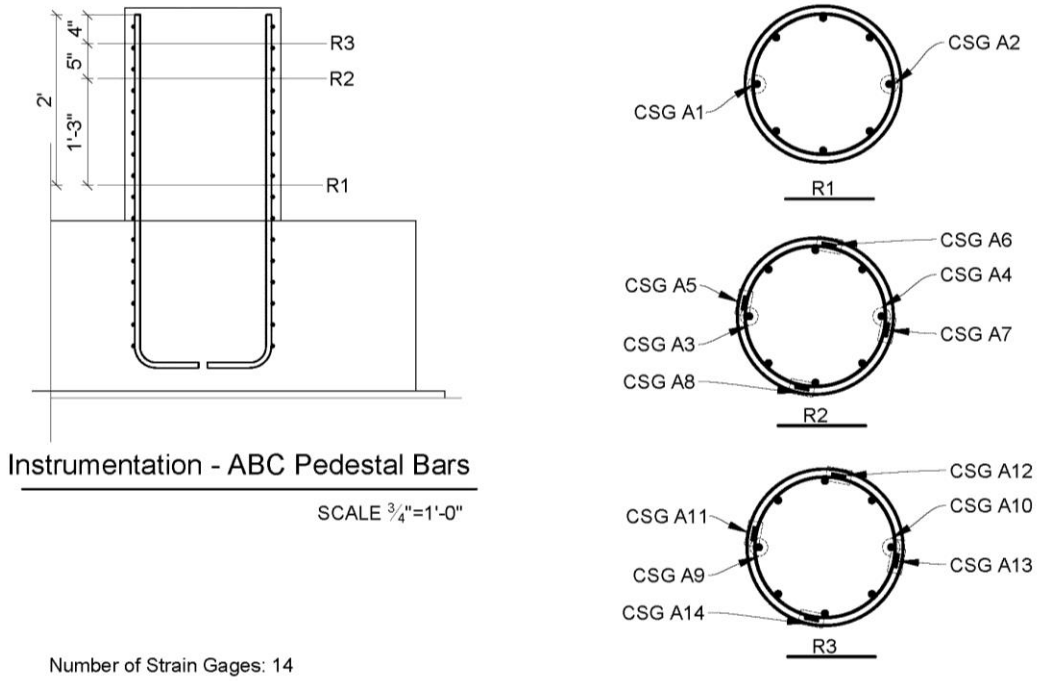

Fig. 2-30. BPSA pedestal strain gages under PC

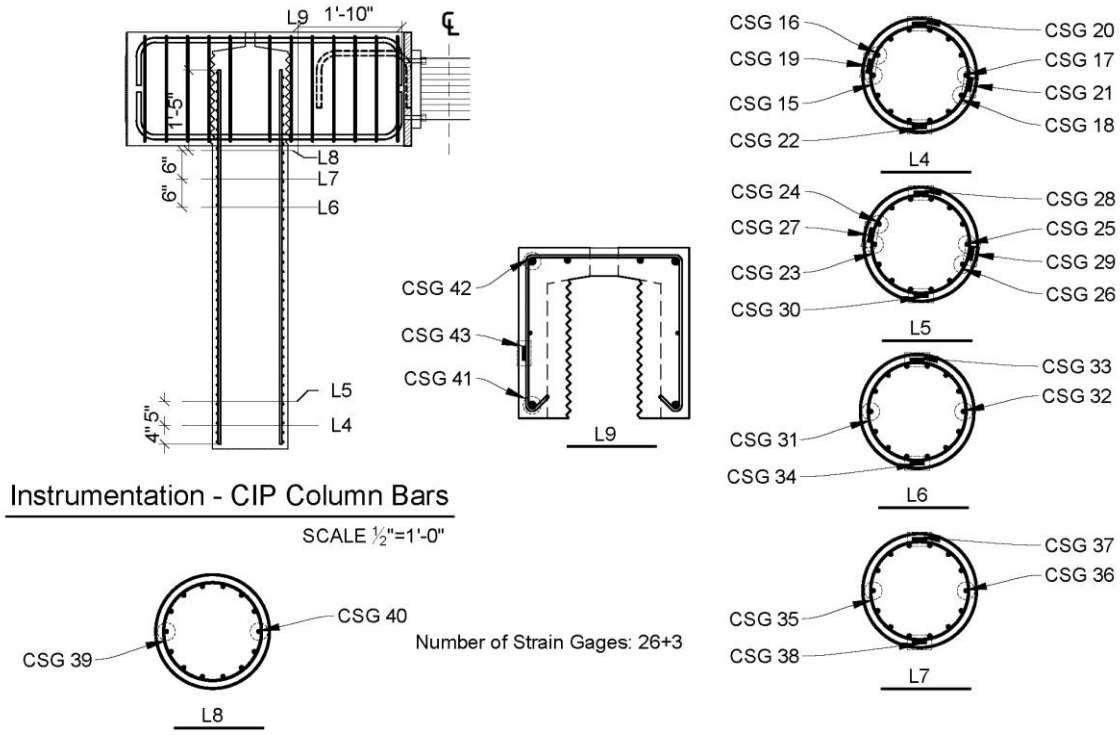

Fig. 2-31. BPSA CIP and cap beam strain gages

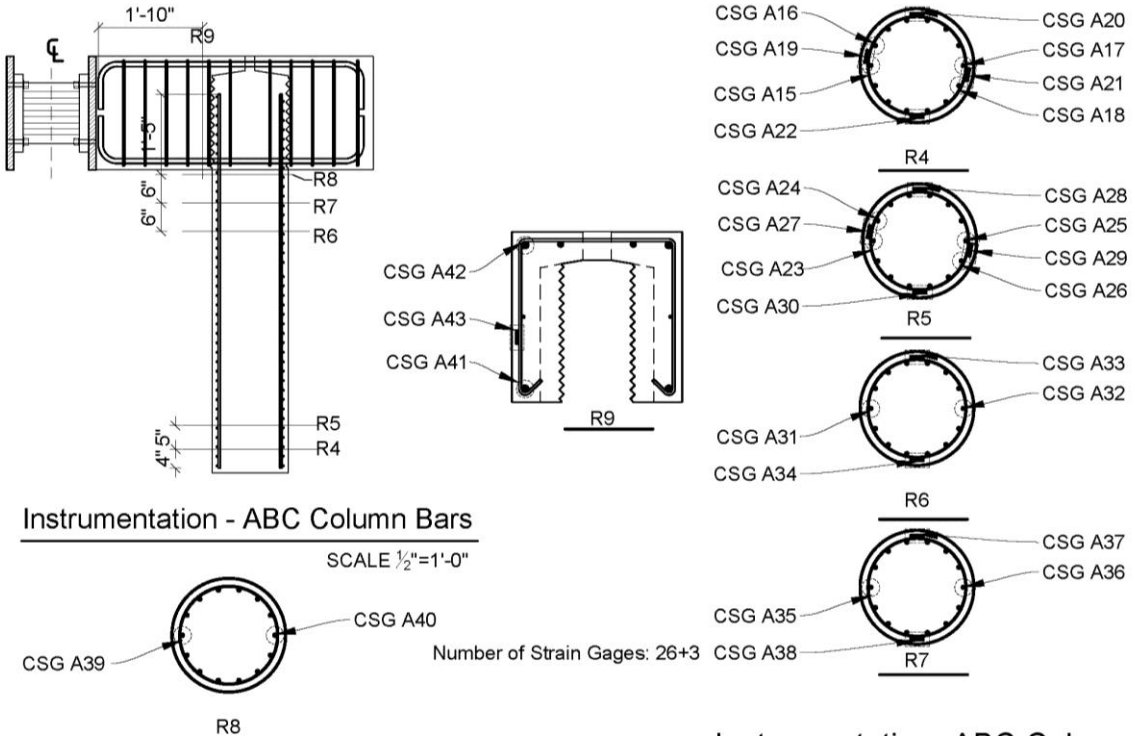

Fig. 2-32. BPSA PC and cap beam strain gages

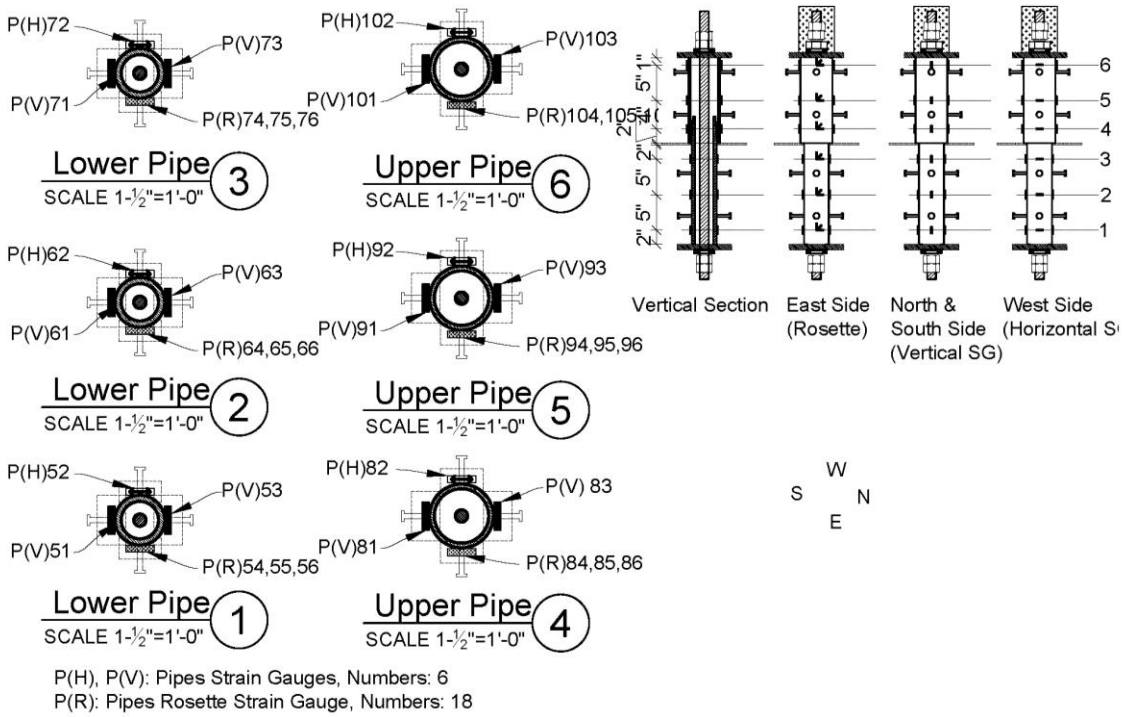

Fig. 2-33. BPSA pipes strain gages in CIP

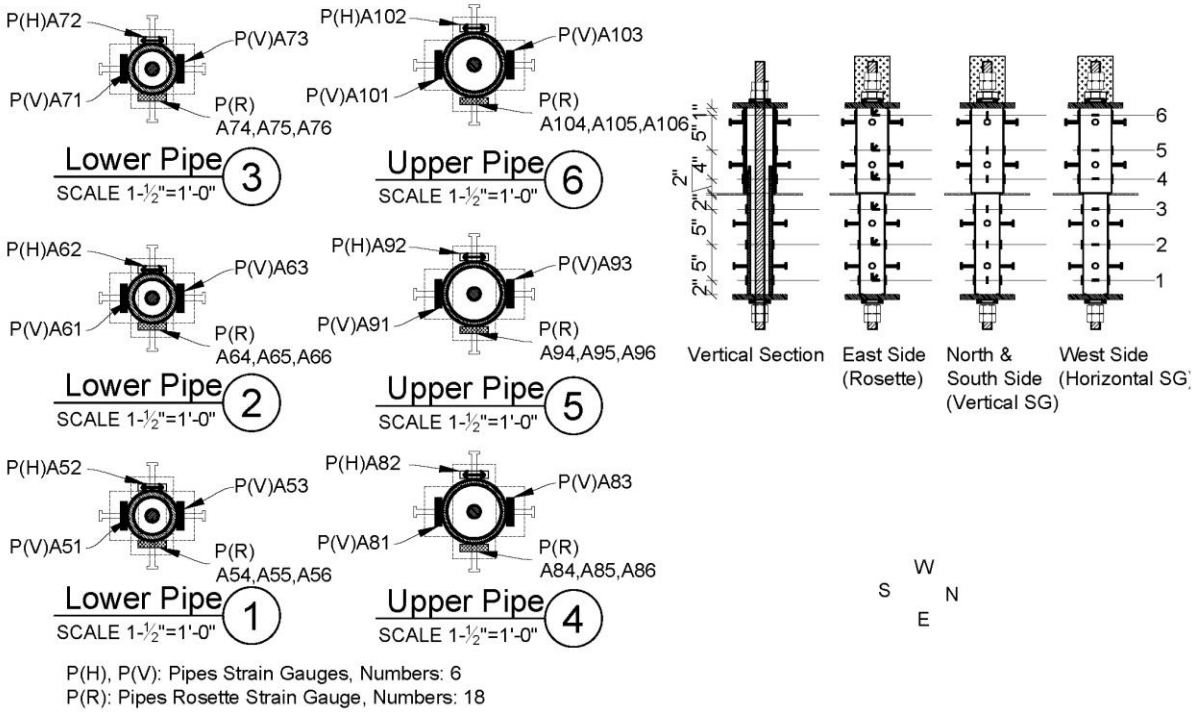

Fig. 2-34. BPSA pipes strain gages in PC

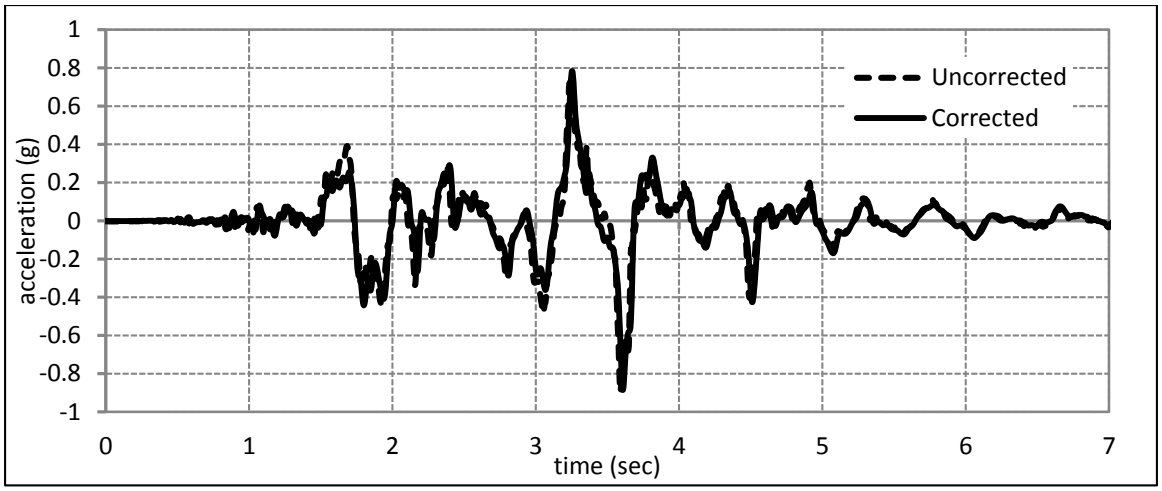

Fig. 2-35. Comparison between filtered and original record in first 7 seconds (scaled for time)

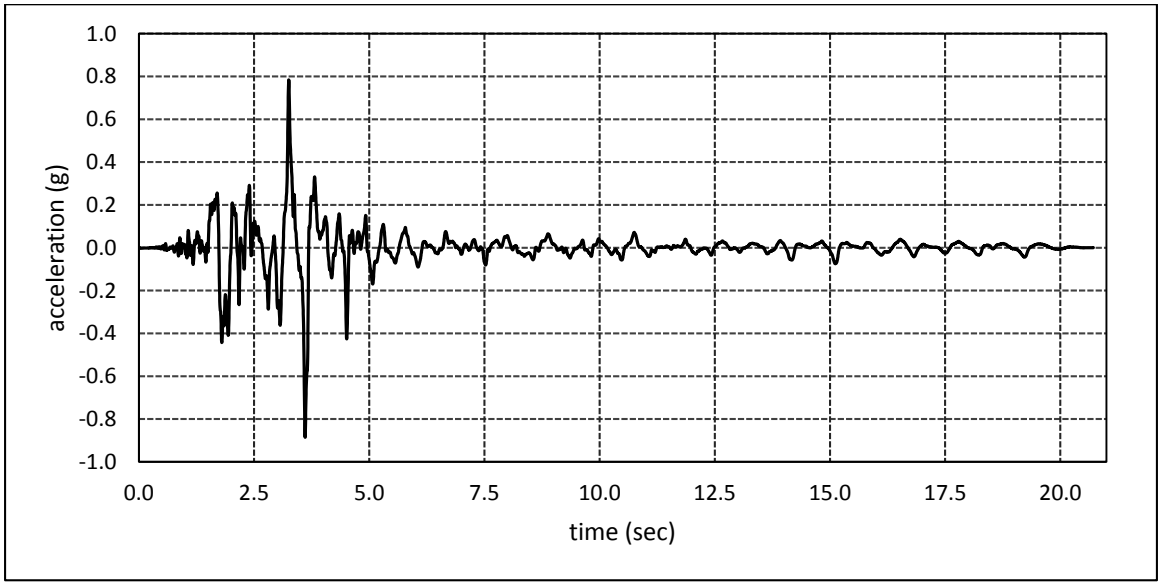

Fig. 2-36. Input ground motion acceleration

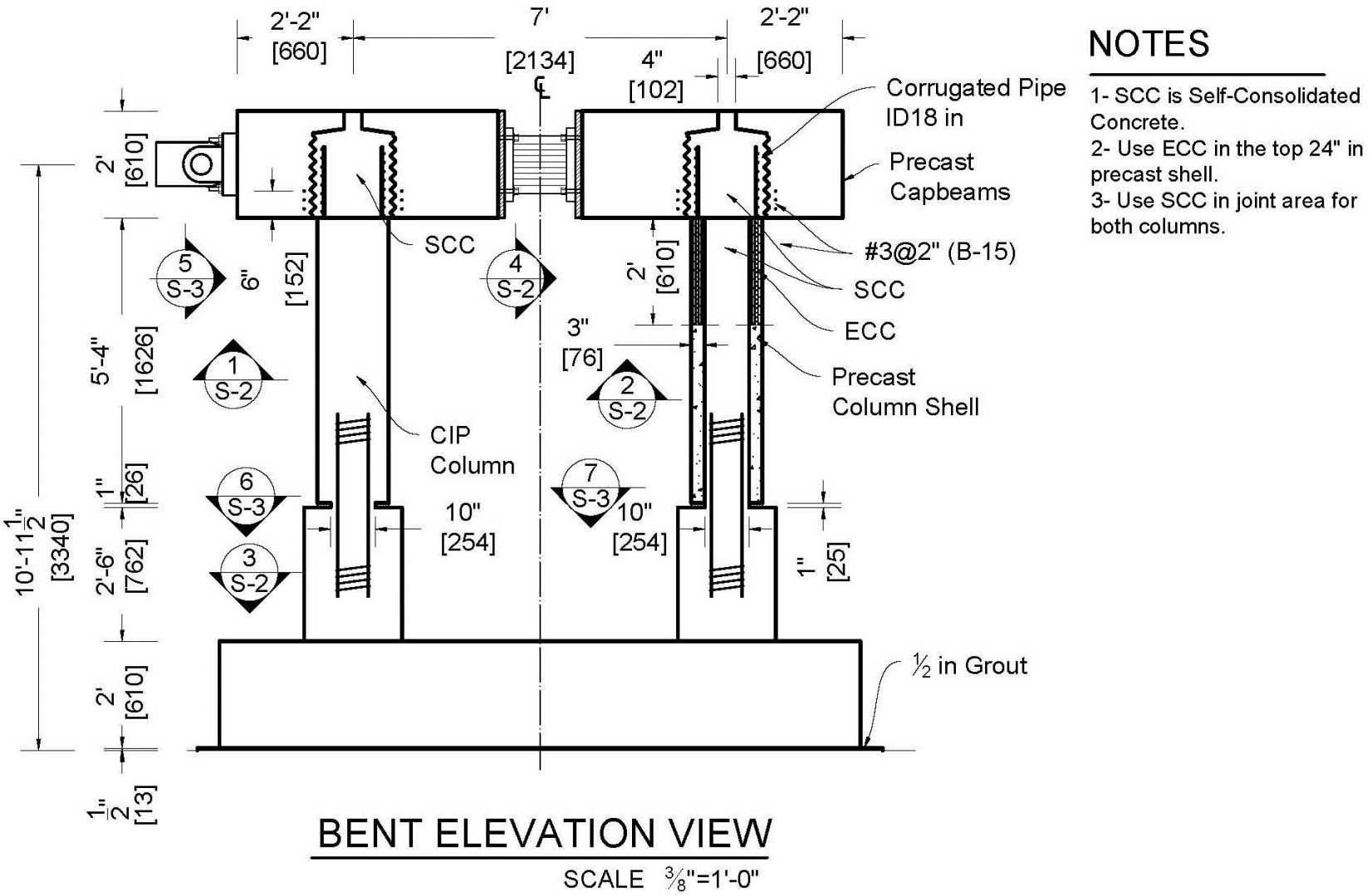

NOTES

1- SCC is Self-Consolidated Concrete.
2- Use ECC in the top 24" in precast shell.
3- Use SCC in joint area for both columns.

Fig. 2-37. BRSA elevation view

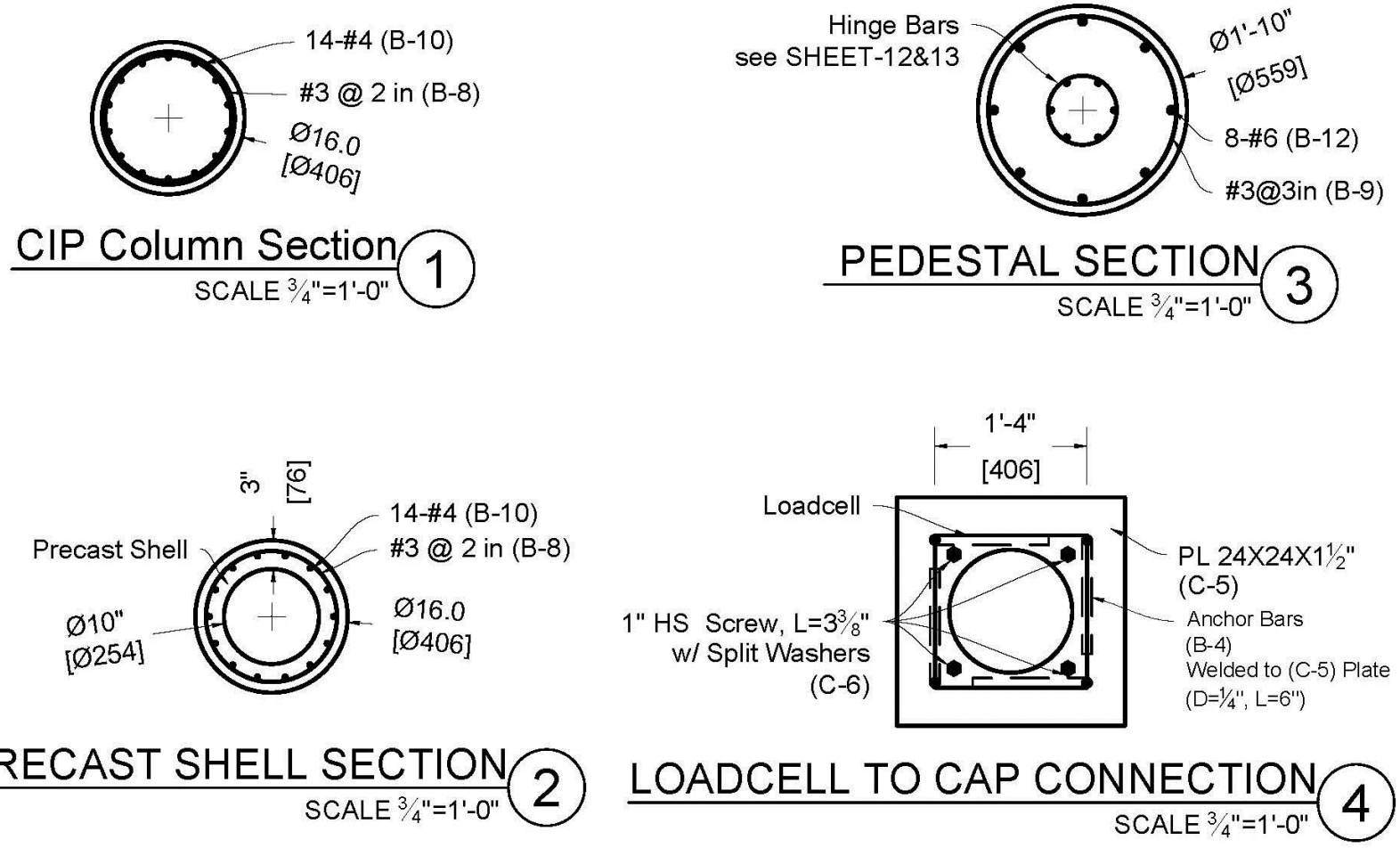

Fig. 2-38. BRSA sections

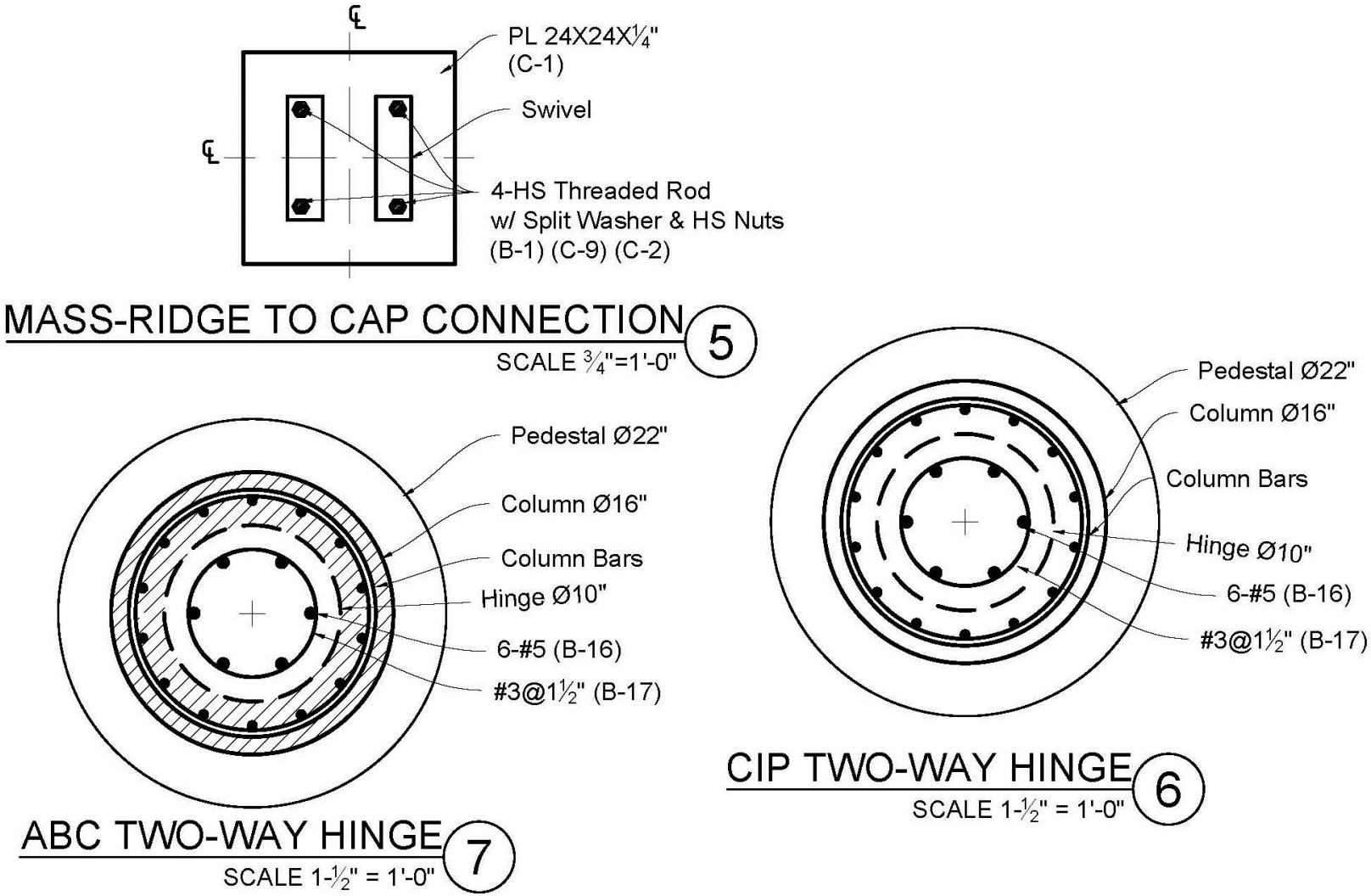

Fig. 2-39. BRSA sections (continued)

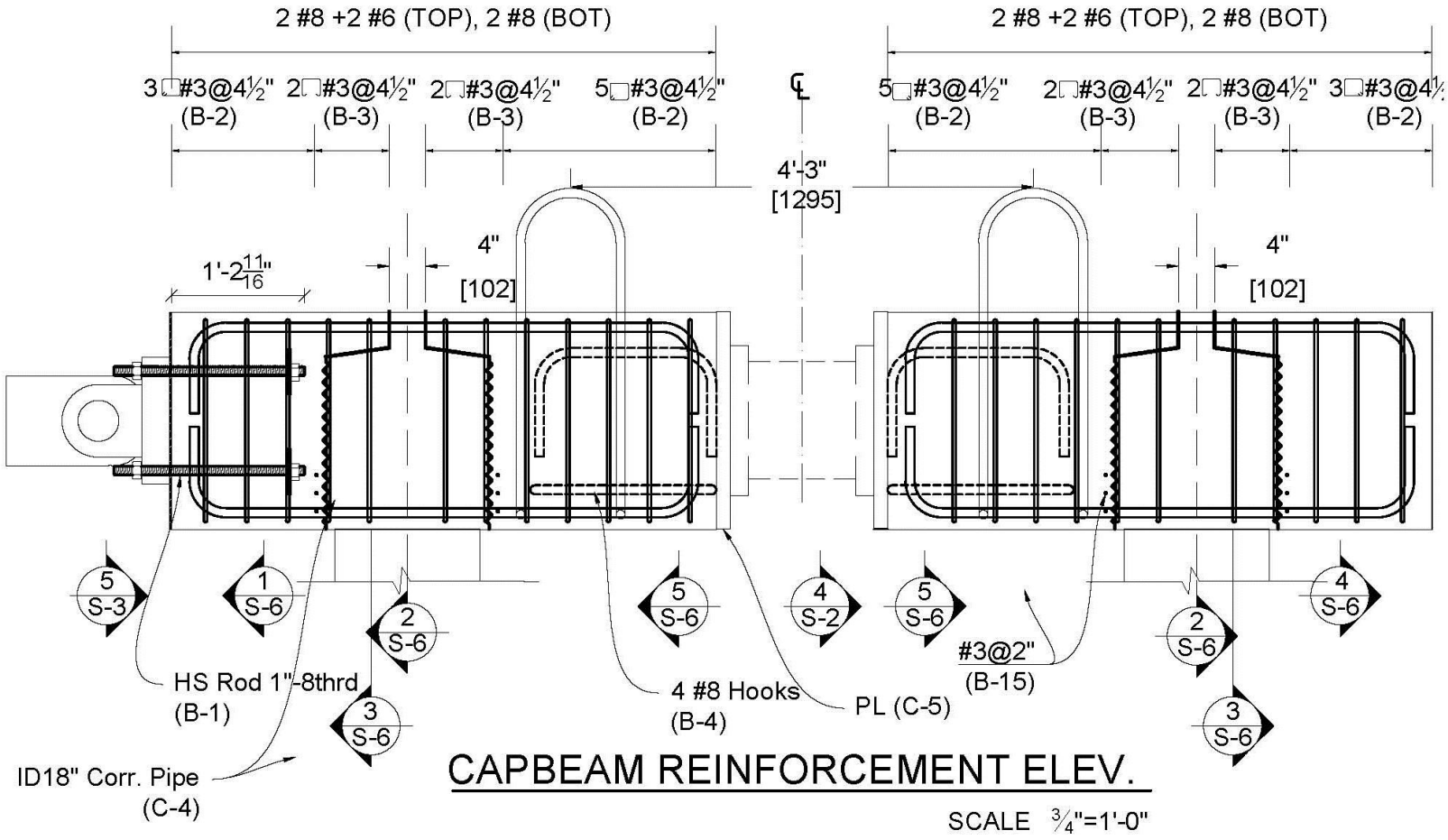

Fig. 2-40. BRSA cap beam reinforcement

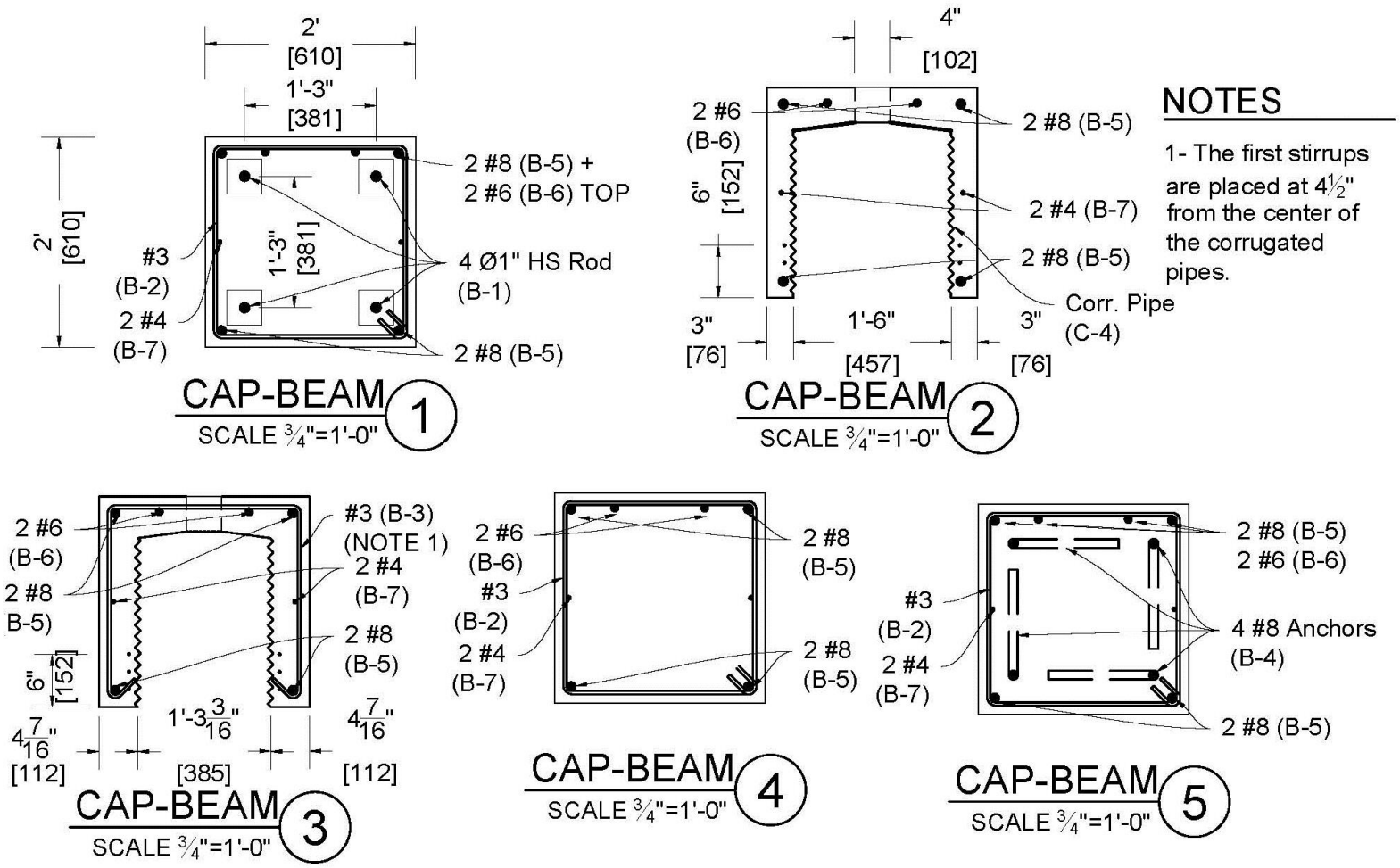

Fig. 2-41. BRSA cap beam section

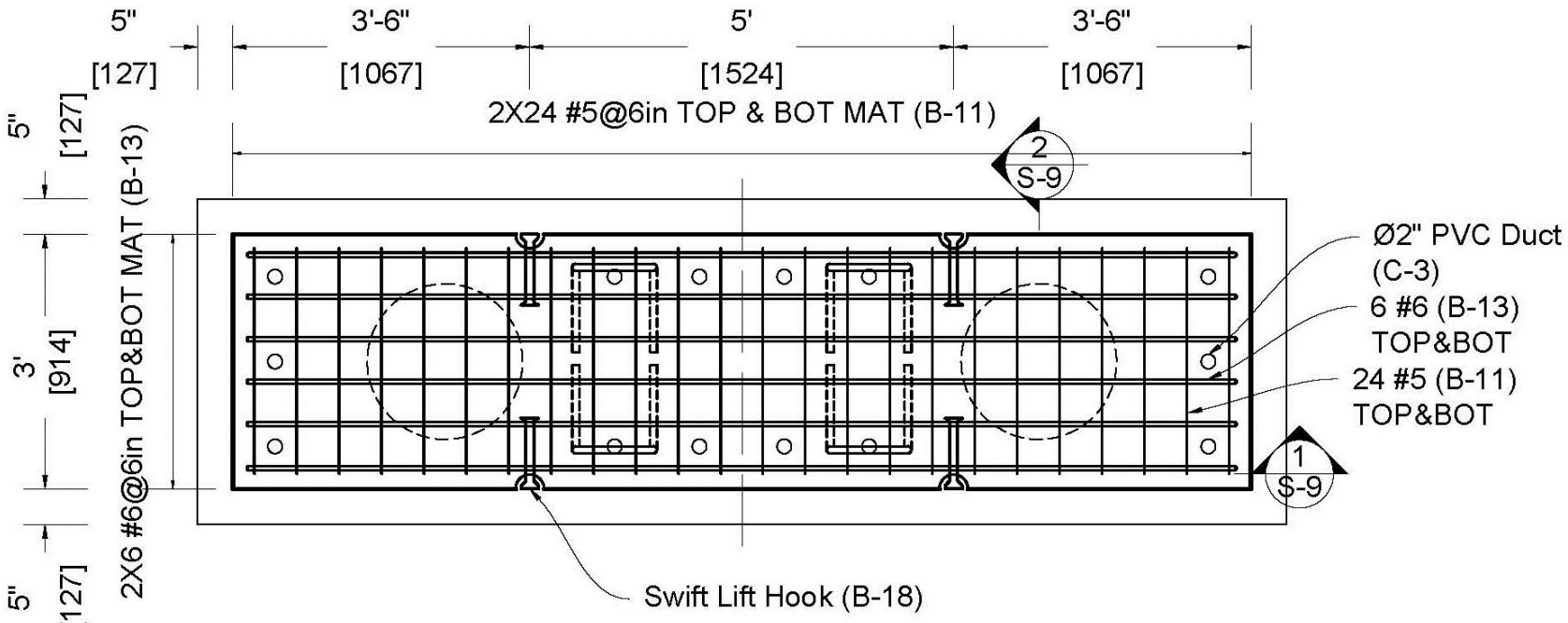

FOOTING REINFORCEMENTPLAN VIEW

SCALE ½"=1'-0"

Fig. 2-42. BRSA footing plan view

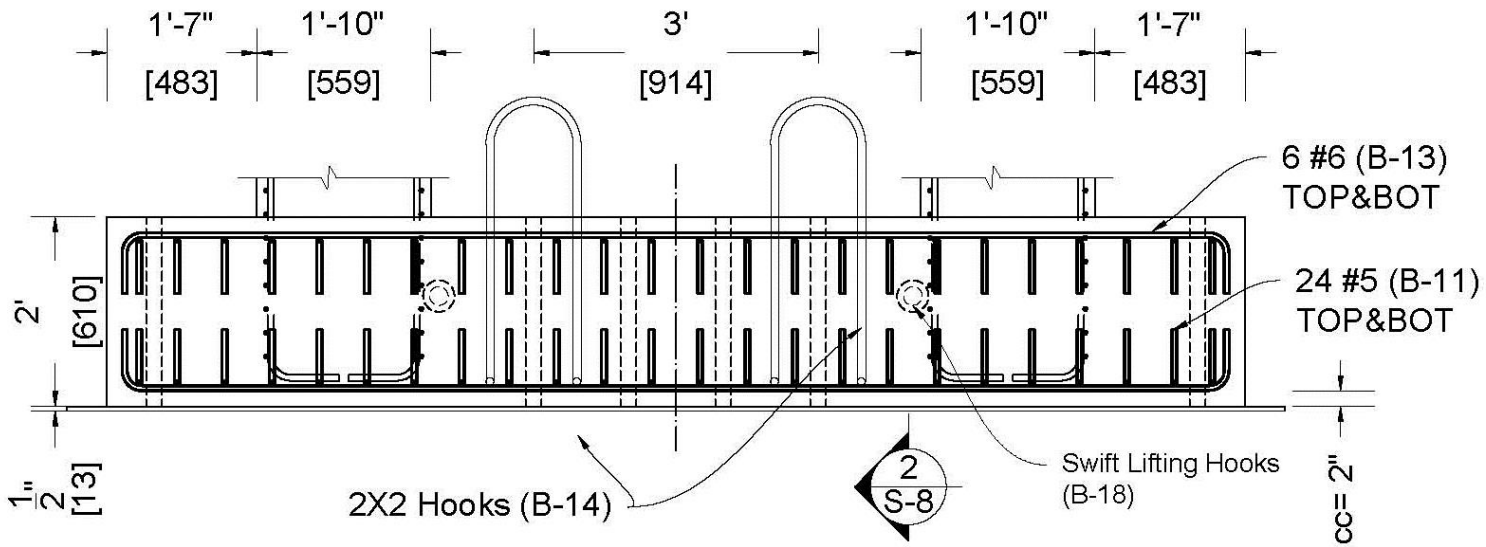

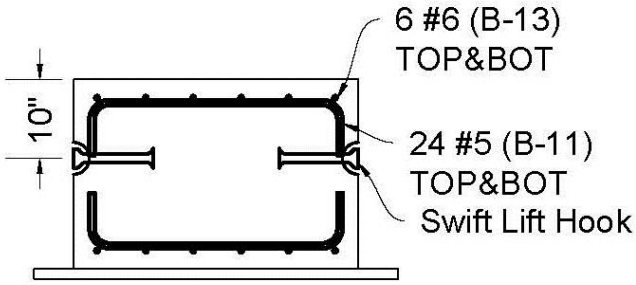

Fig. 2-43. BRSA footing Reinforcement

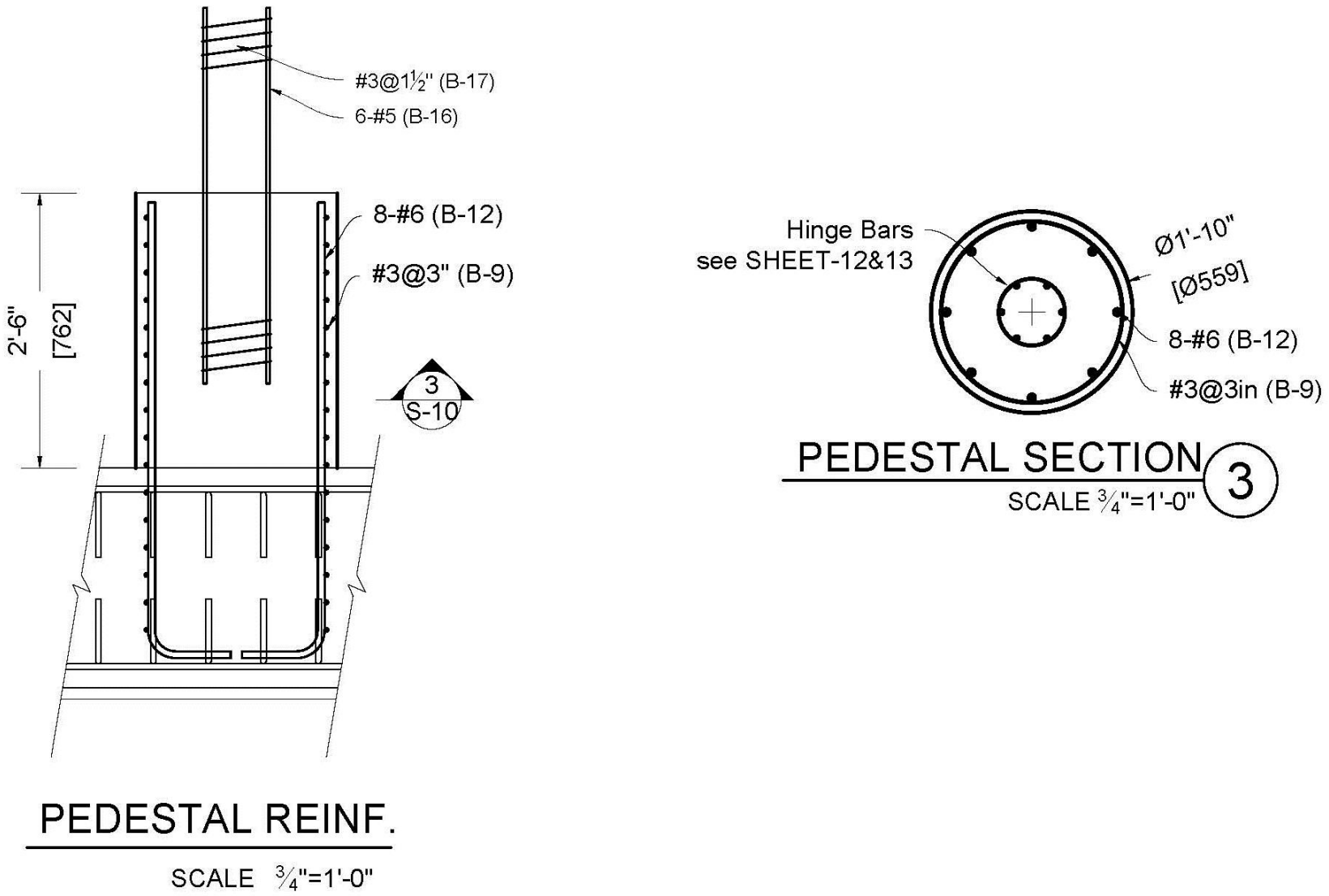

Fig. 2-44. BRSA pedestal reinforcement

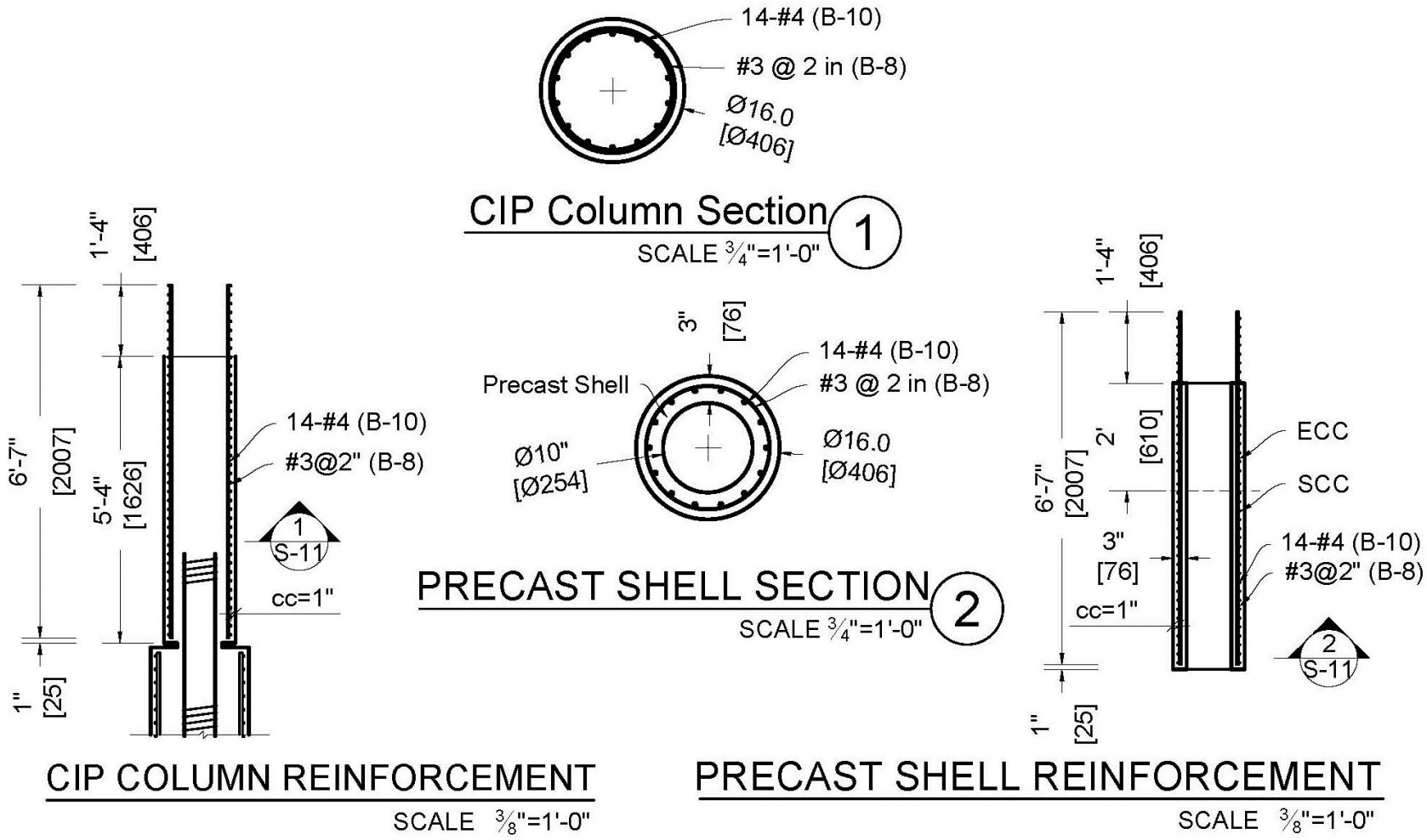

Fig. 2-45. BRSA column reinforcement

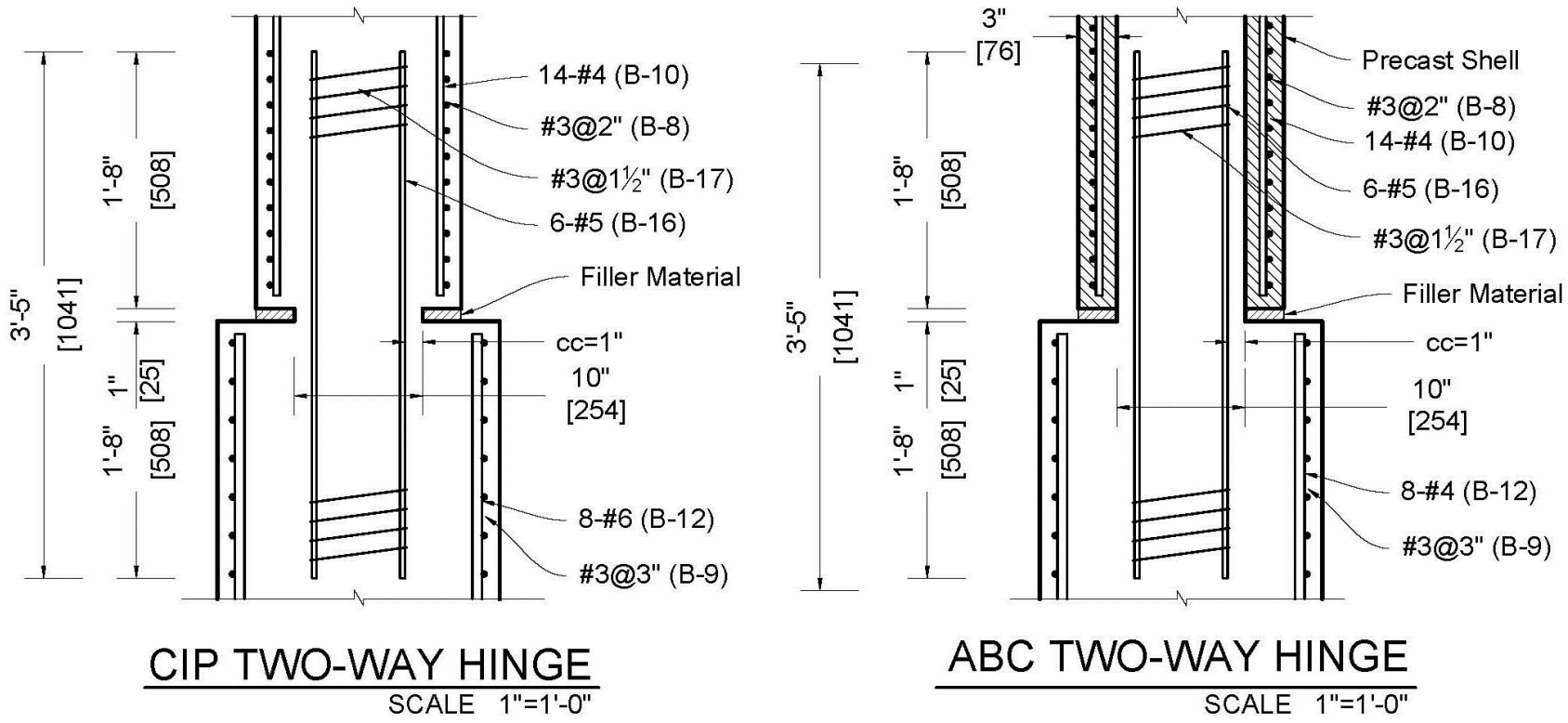

Fig. 2-46. BRSA rebar hinge detail

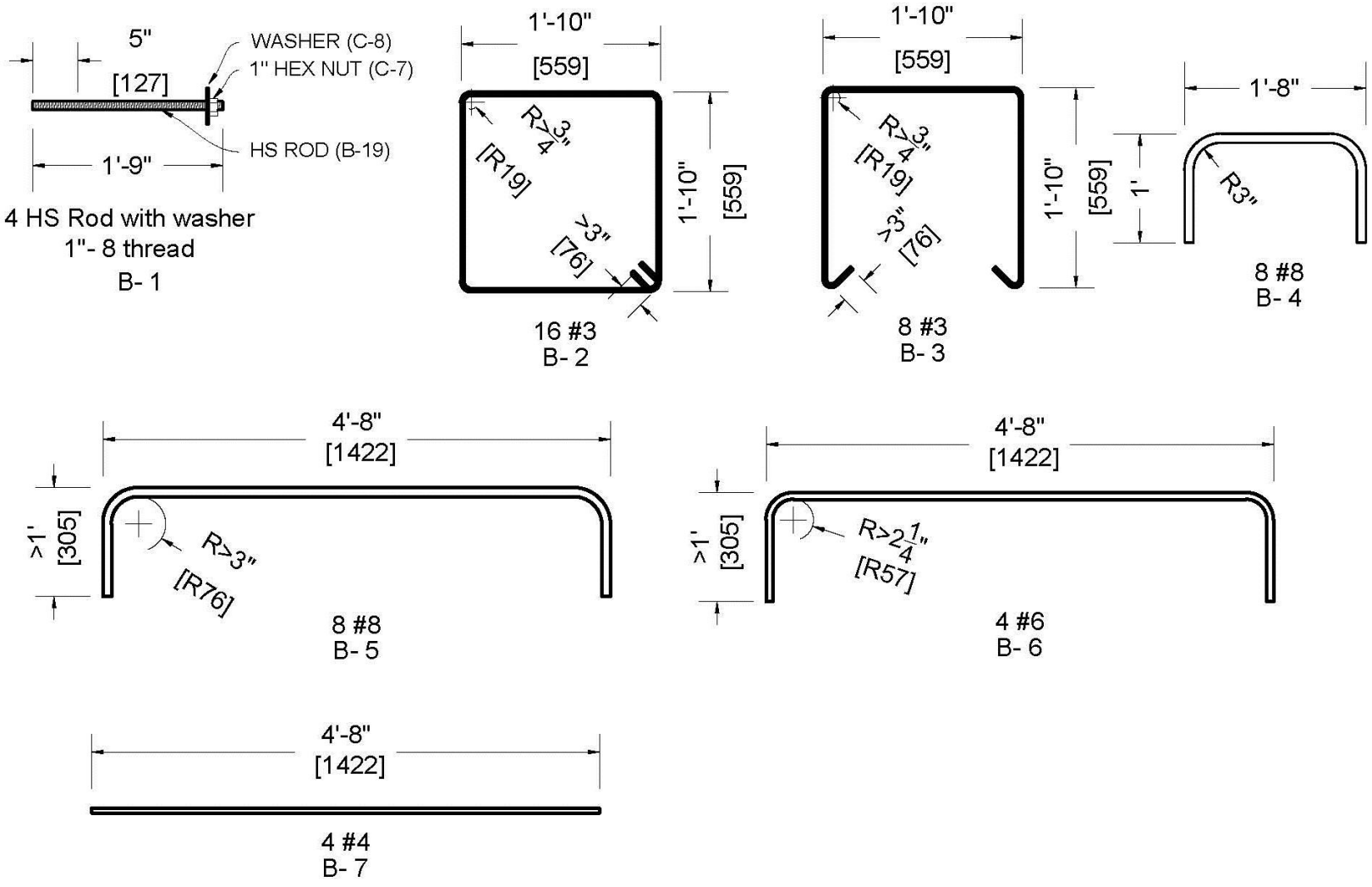

Fig. 2-47. BRSA steel detail

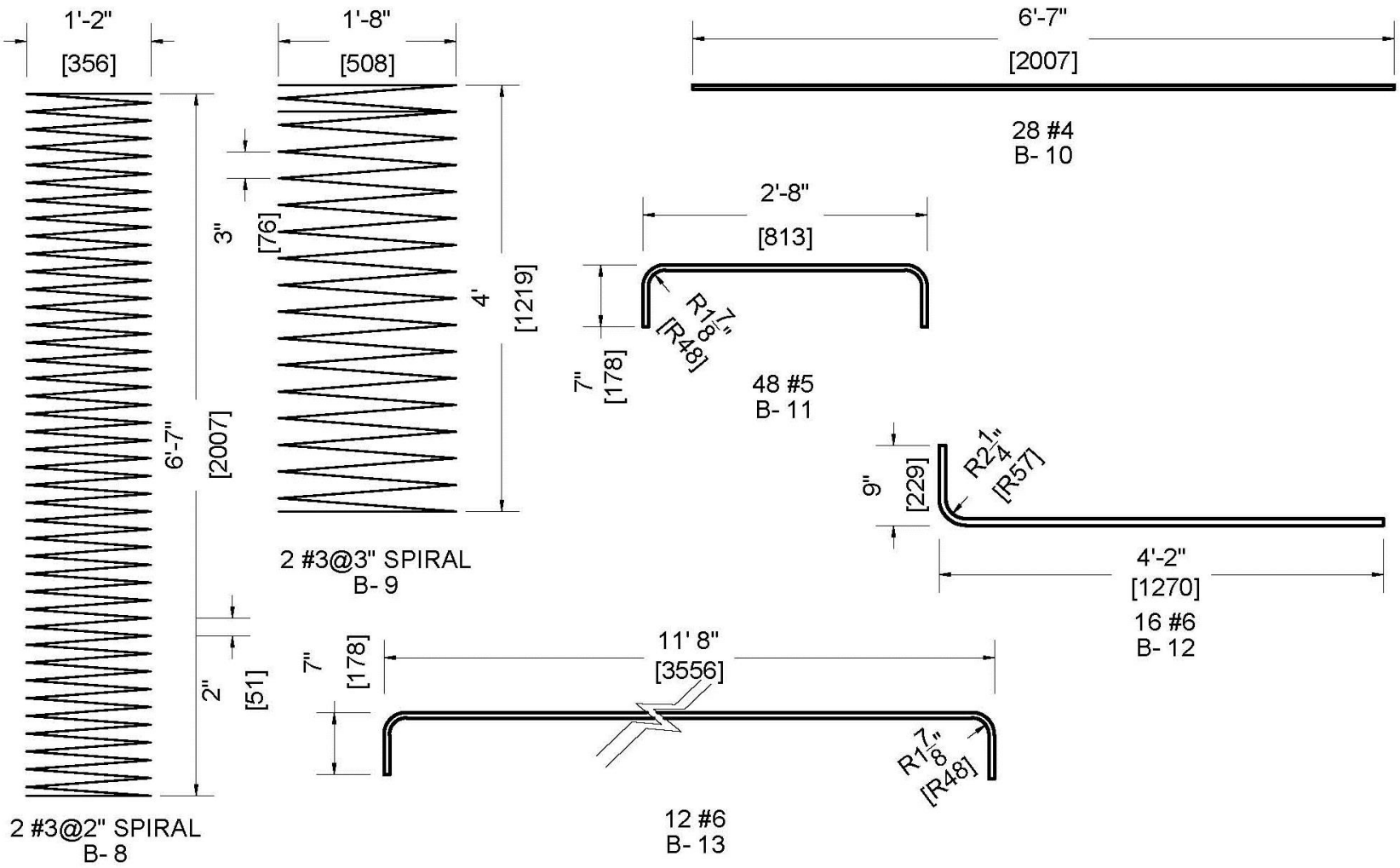

Fig. 2-48. BRSA steel detail-2

Fig. 2-49. Holding rebar-pin reinforcement cage stationary using welded rods

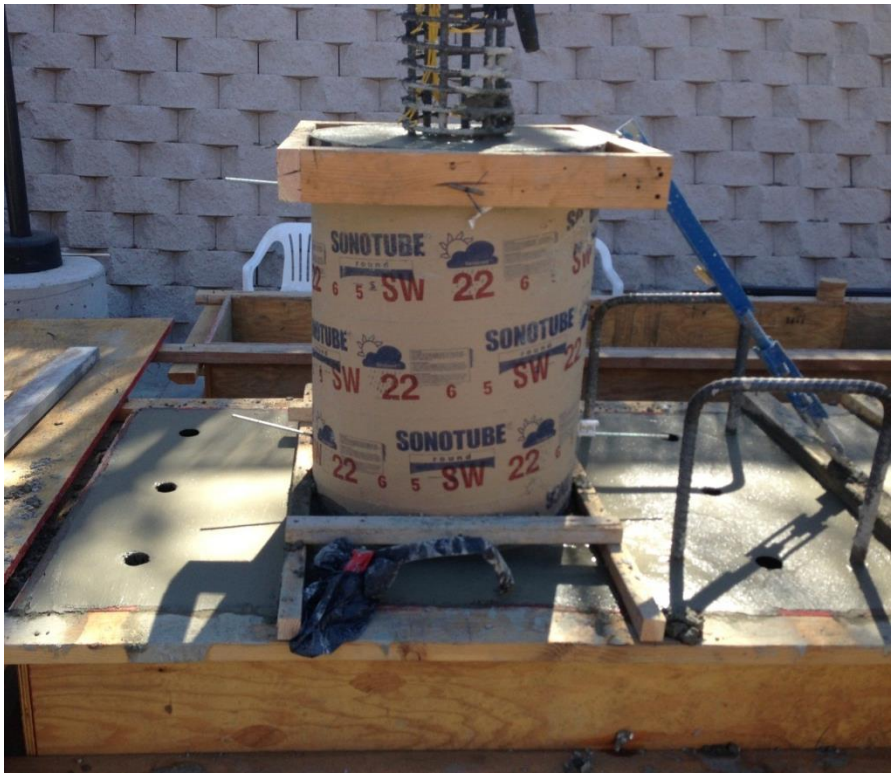

Fig. 2-50. BRSA concrete cast for Phase one

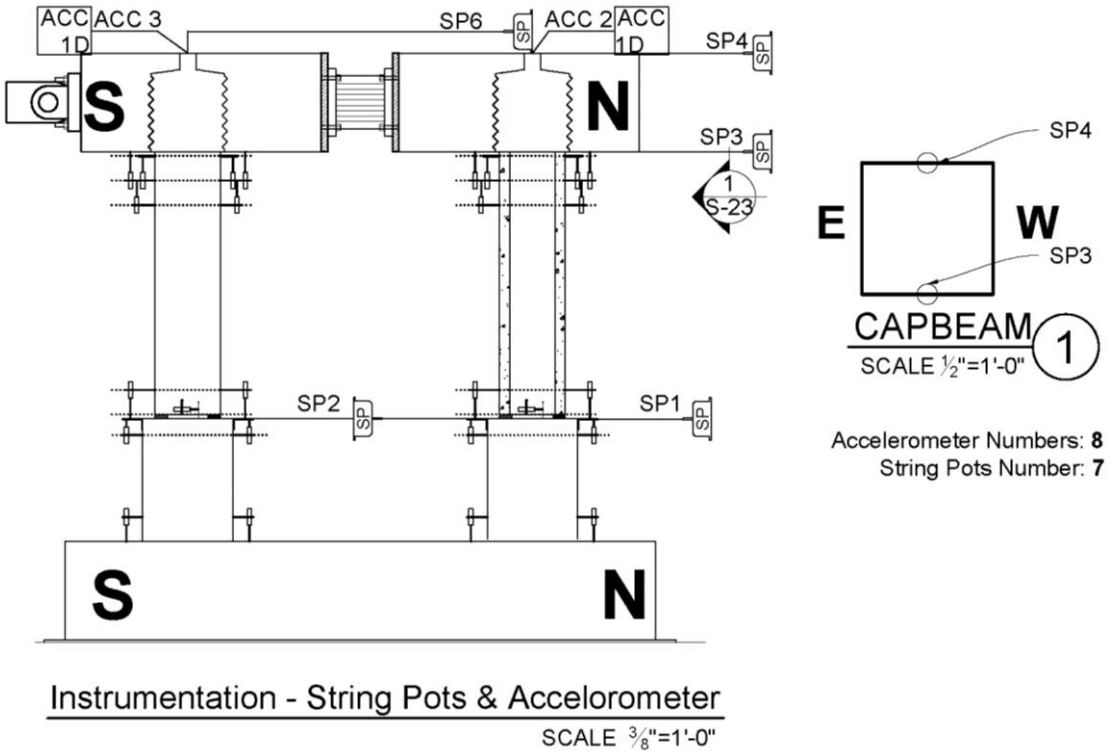

Fig. 2-51. BRSA displacements and acceleration instruments

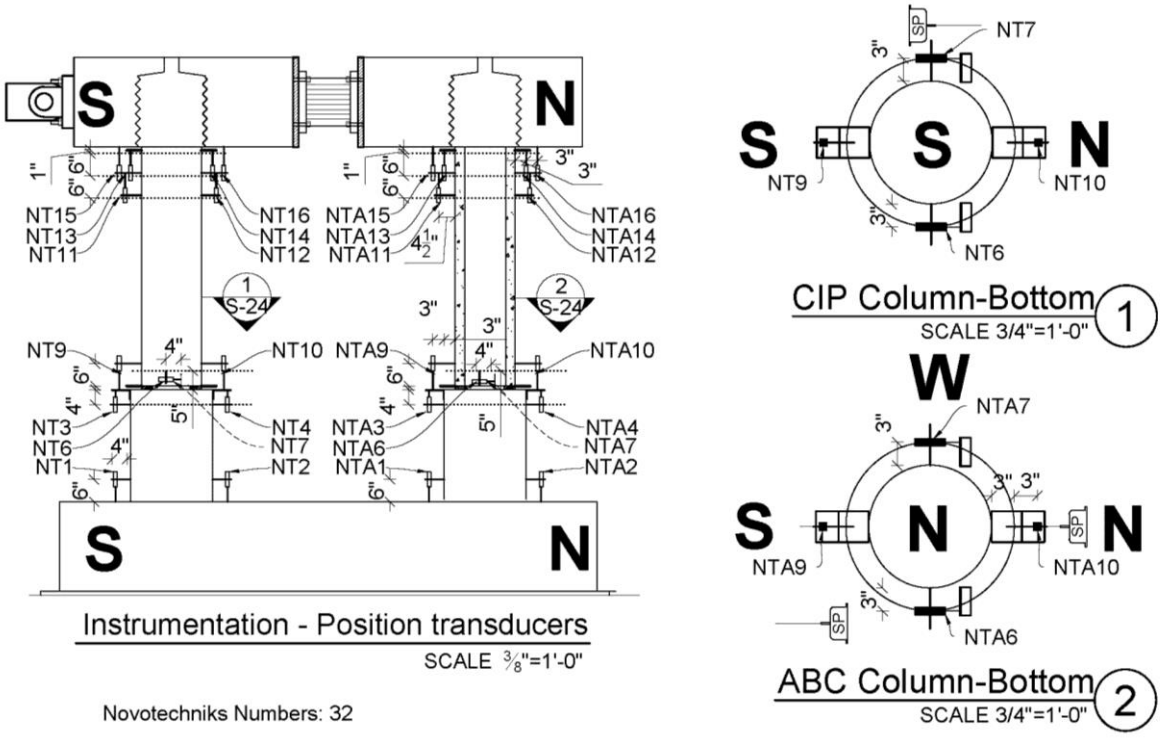

Fig. 2-52. BRSA potentiometers instrumentation

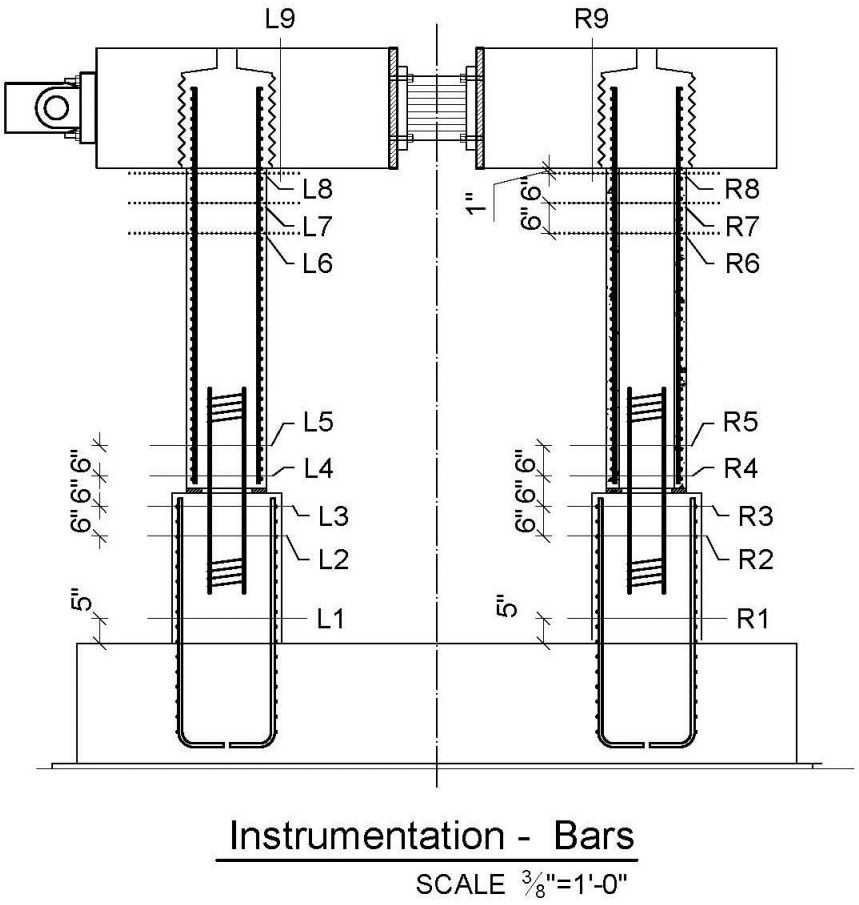

Fig. 2-53. BRSA strain gage sections layout

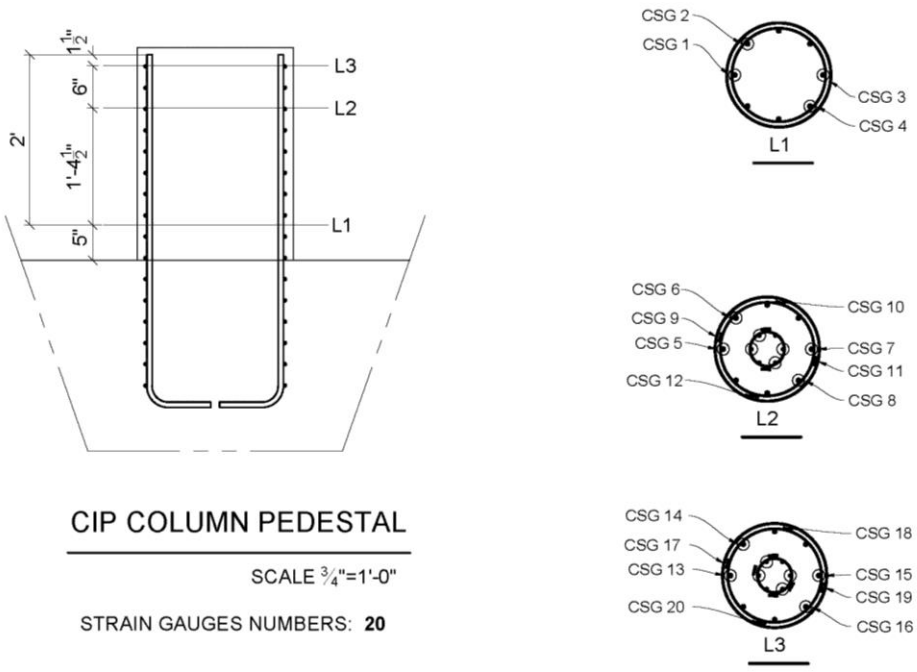

Fig. 2-54. BRSA pedestal strain gages under CIP pedestal

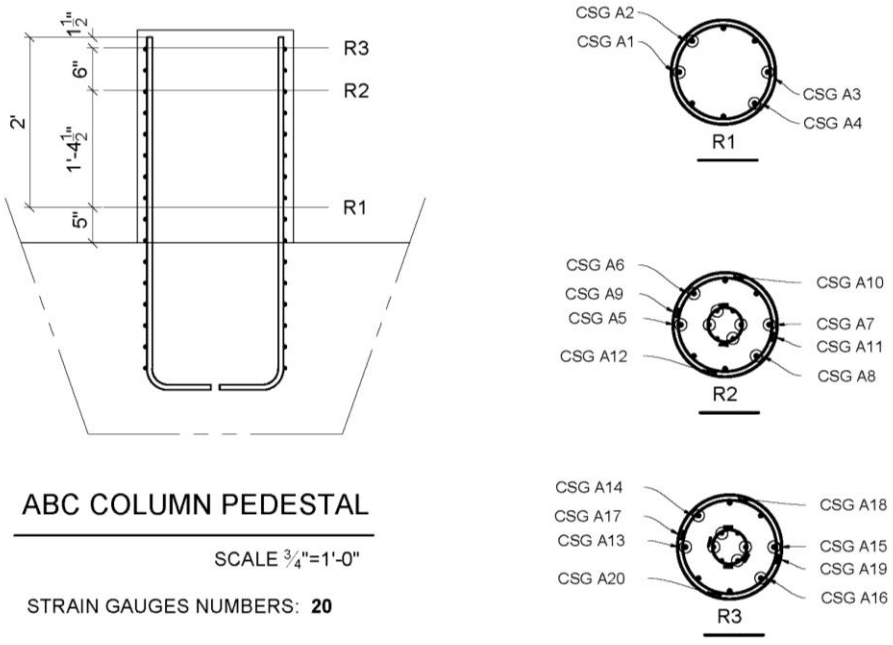

Fig. 2-55. BRSA pedestal strain gages under PC pedestal

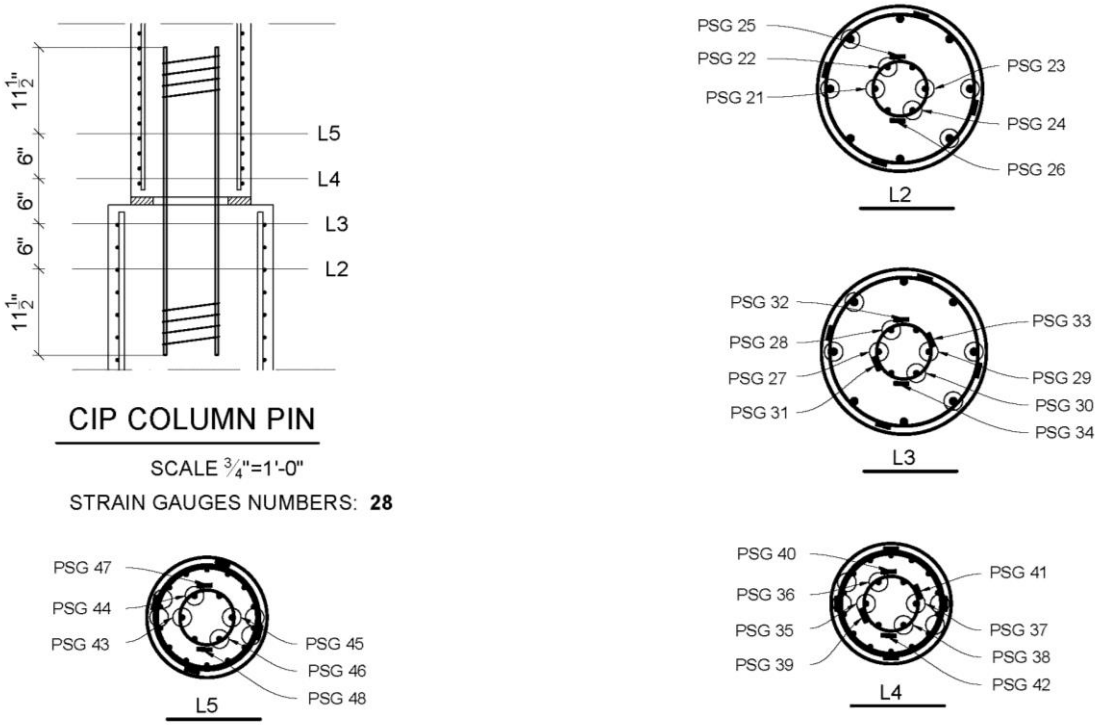

Fig. 2-56. BRSA hinge strain gages in CIP rebar-pin

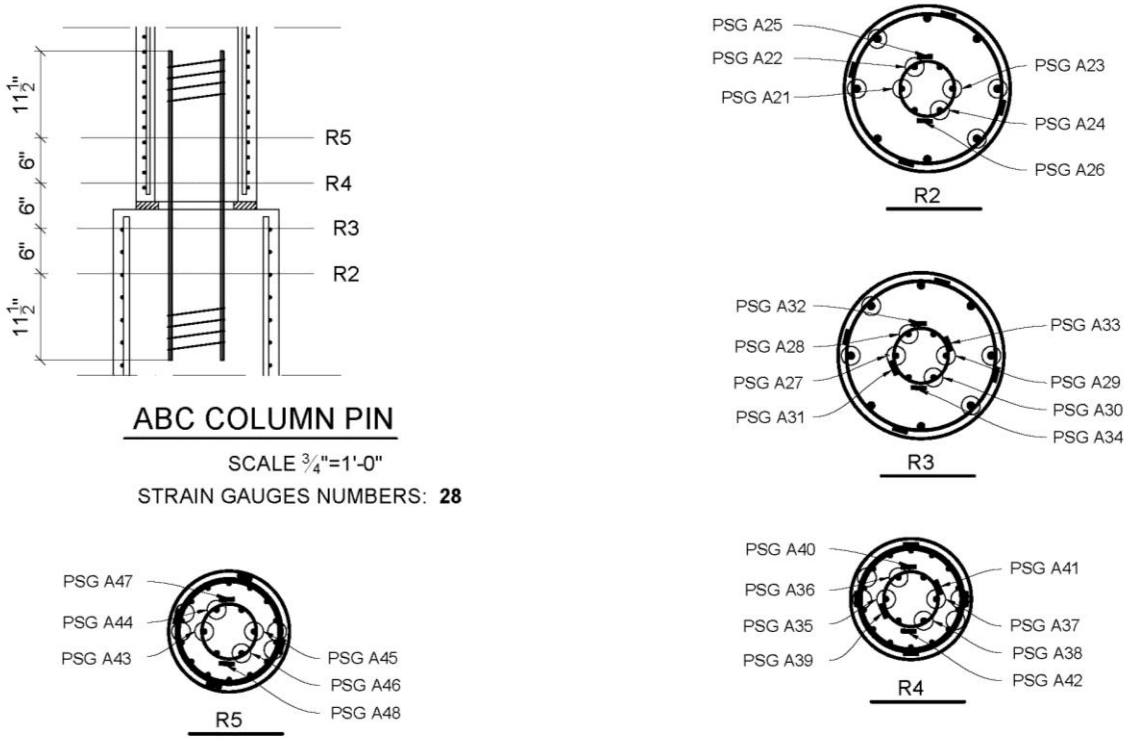

Fig. 2-57. BRSA strain gages for PC rebar-pin

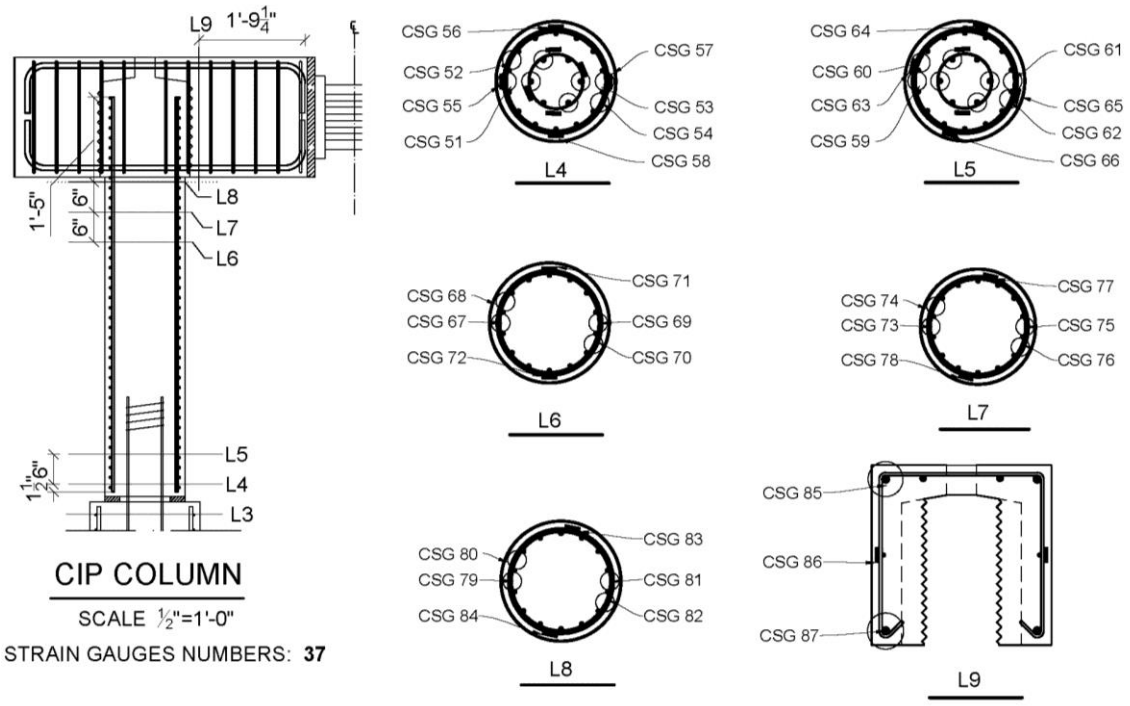

Fig. 2-58. BRSA CIP strain gages

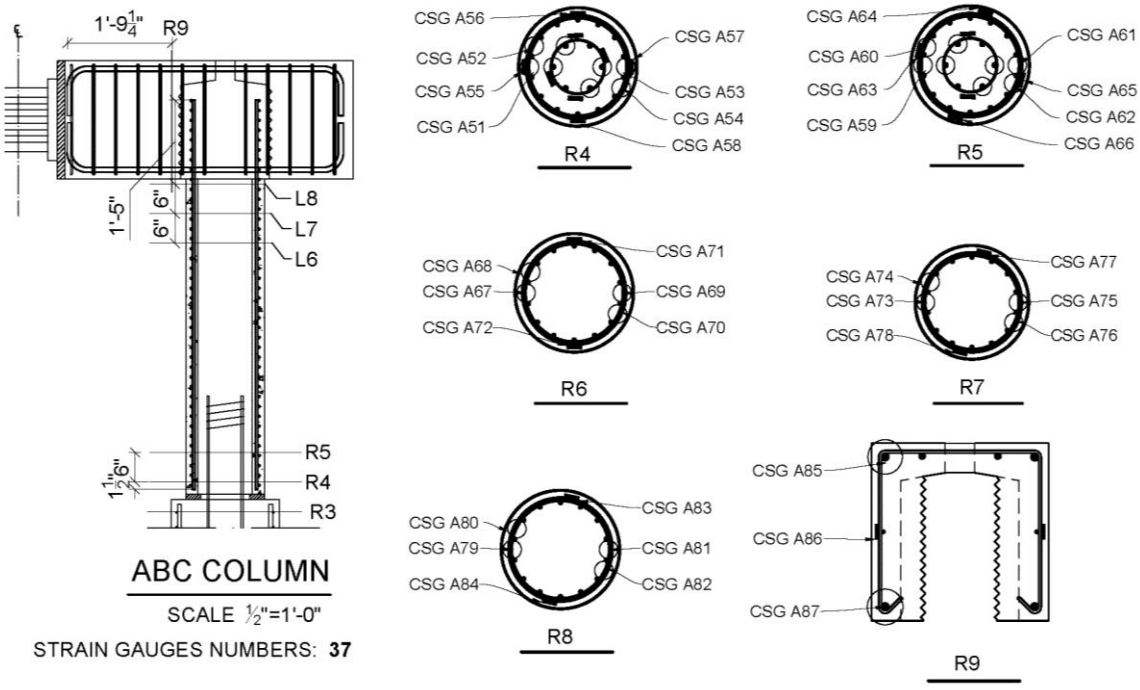

Fig. 2-59. BRSA PC strain gages

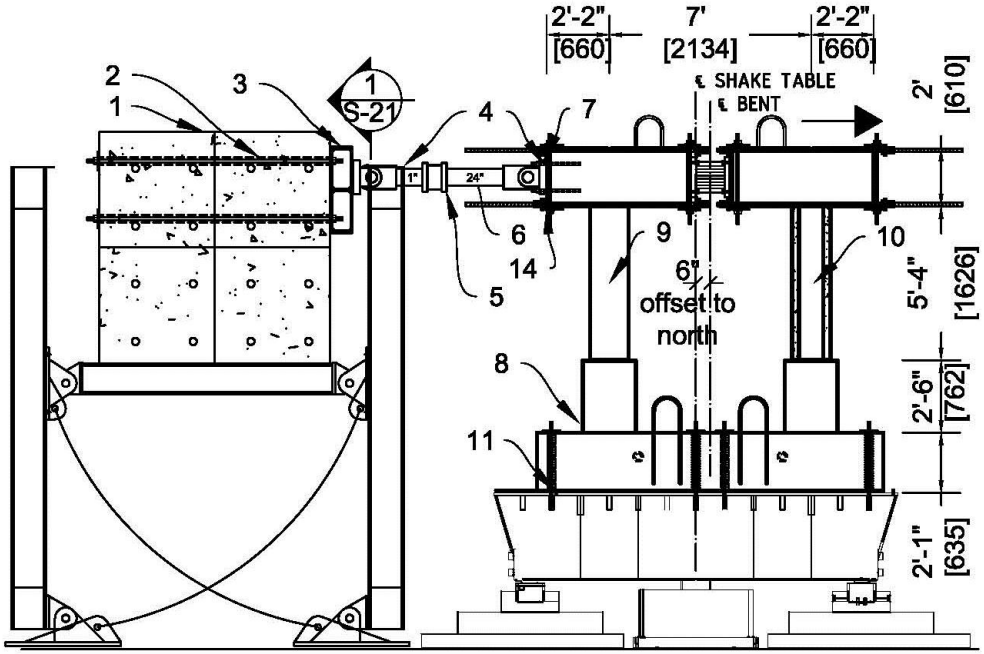

SHAKE TABLE SETUP ELEVATION VIEW

scale: $\frac{3}{16}$"=1'-0"

SHAKE TABLE SETUP			
ID	ELEMNT	QUANTITY	LENGTH
1	20 KIPS MASS BLOCKS	4	–
2	1 ½" HIGH-STRENGTH ROD	4	6'-6"
3	BLOCK-PLATE (DETAIL-1)	1	9 "
4	SWIVEL	2	18 "
5	LOAD CELL	1	10
6	LINK	1	23 $\frac{5}{8}$
7	1" THREADED BAR	12	
8	Ø1" HIGH STRENGTH THREADED ROD	12	
9	CIP COLUMN	1	–
10	ABC COLUMN	1	–
11	1 ½" GROUT	--	–

Fig. 2-60. Shake table setup

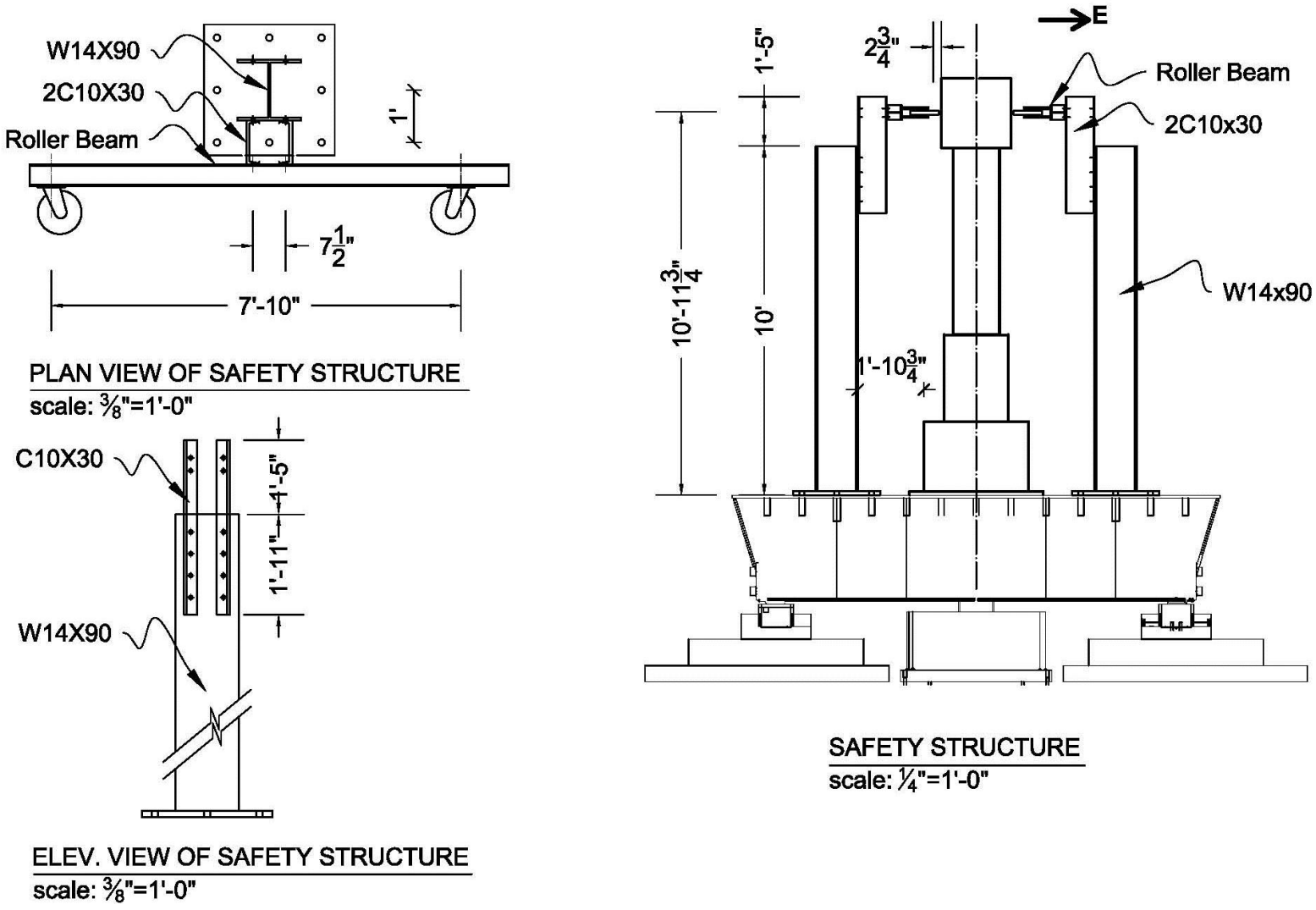

Fig. 2-61. Safety structure details

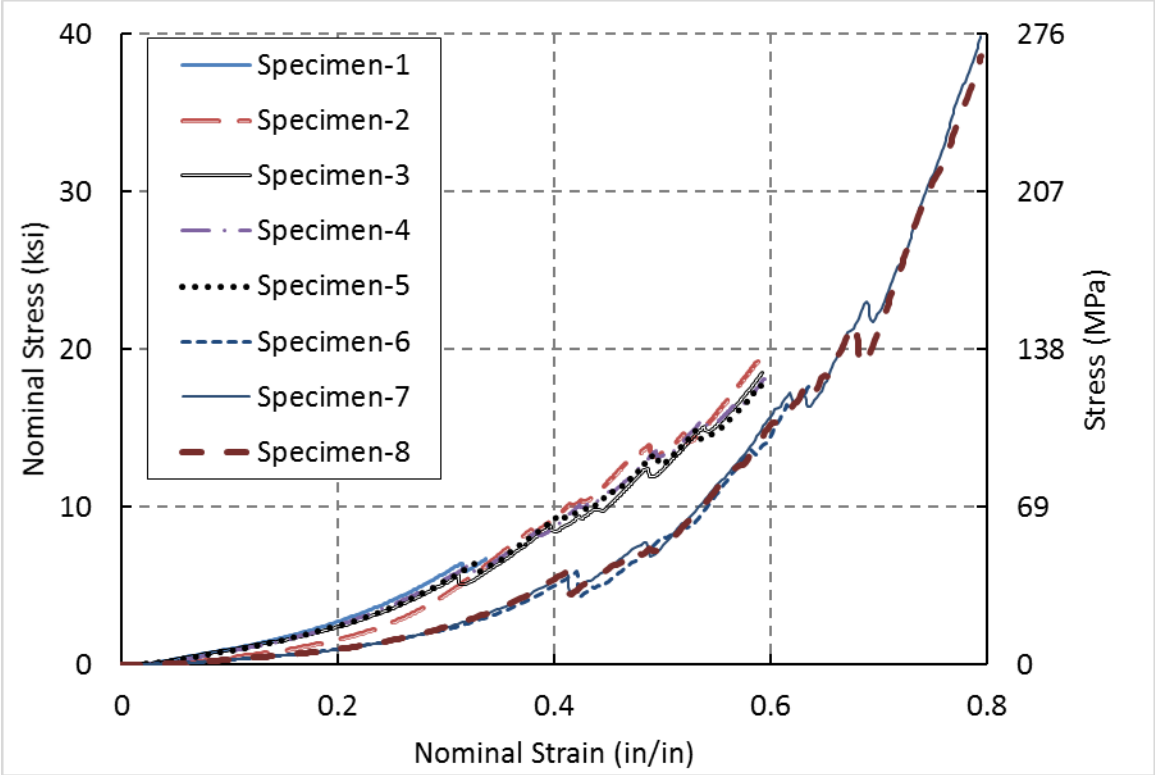

Fig. 2-62. Stress-strain curves of compressive test on elastomers

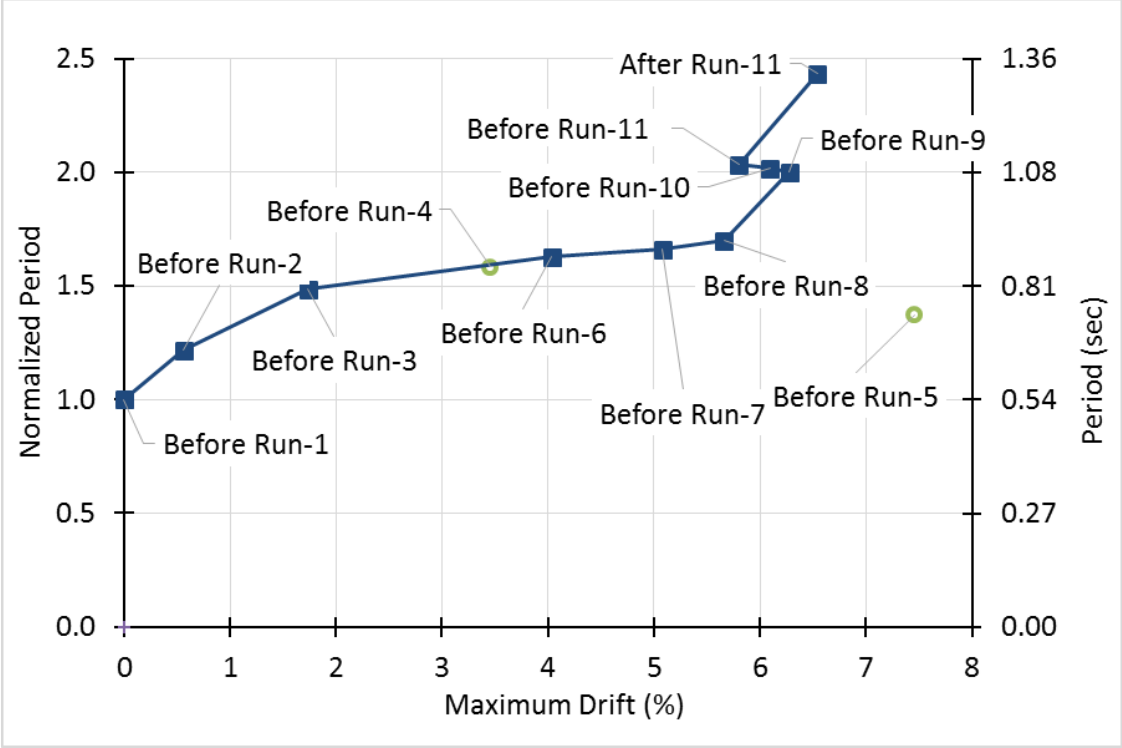

Fig. 3-1. BPSA fundamental periods

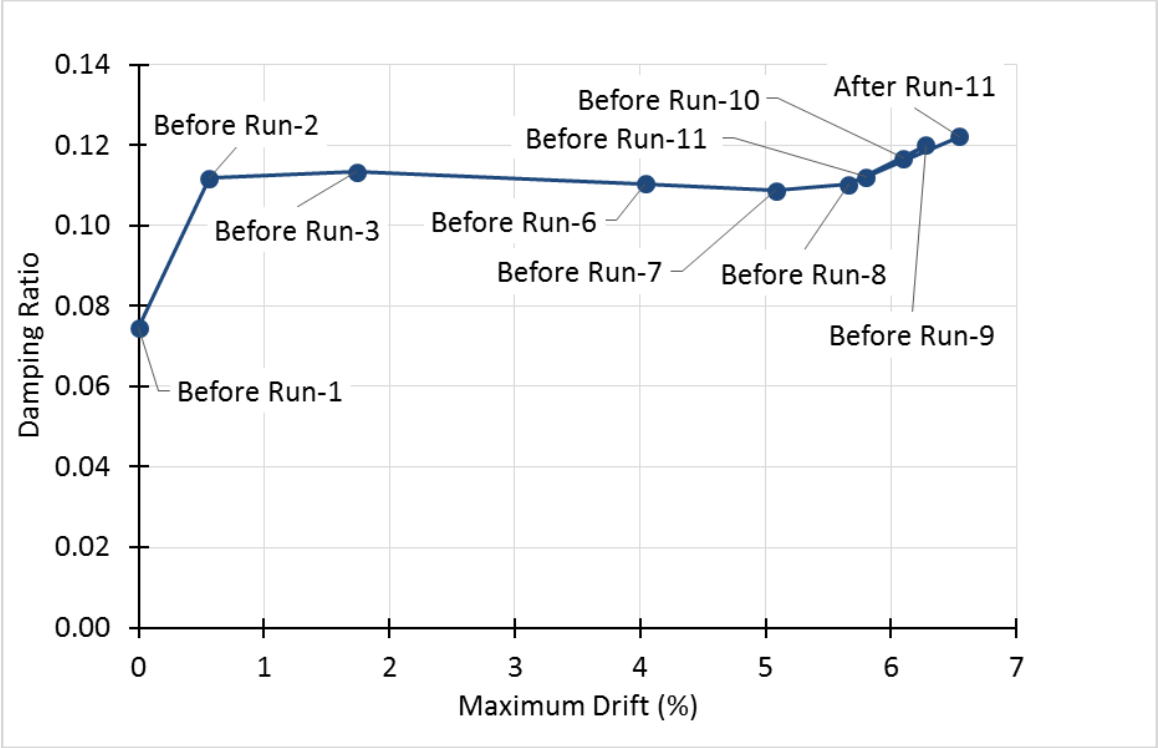

Fig. 3-2. BPSA damping ratios

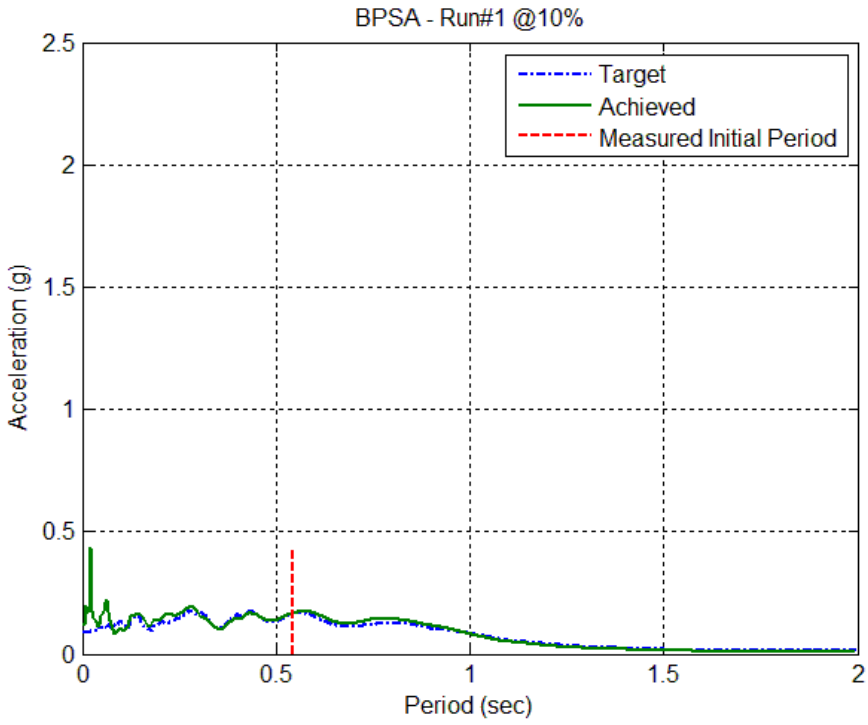

Fig. 3-3. BPSA target vs... achieved motion response spectra for Run-1

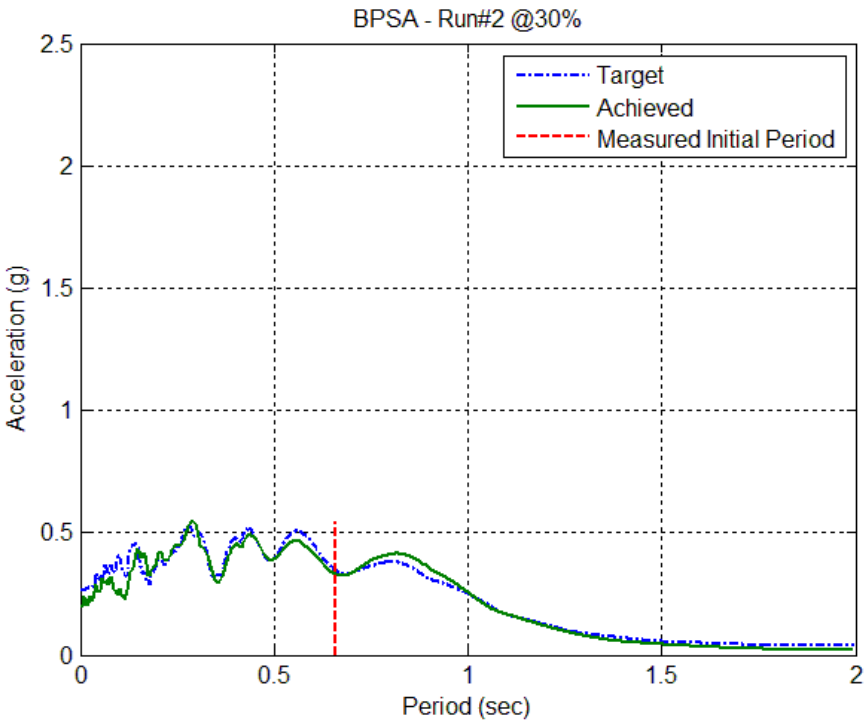

Fig. 3-4. BPSA target vs.. achieved motion response spectra for Run-2

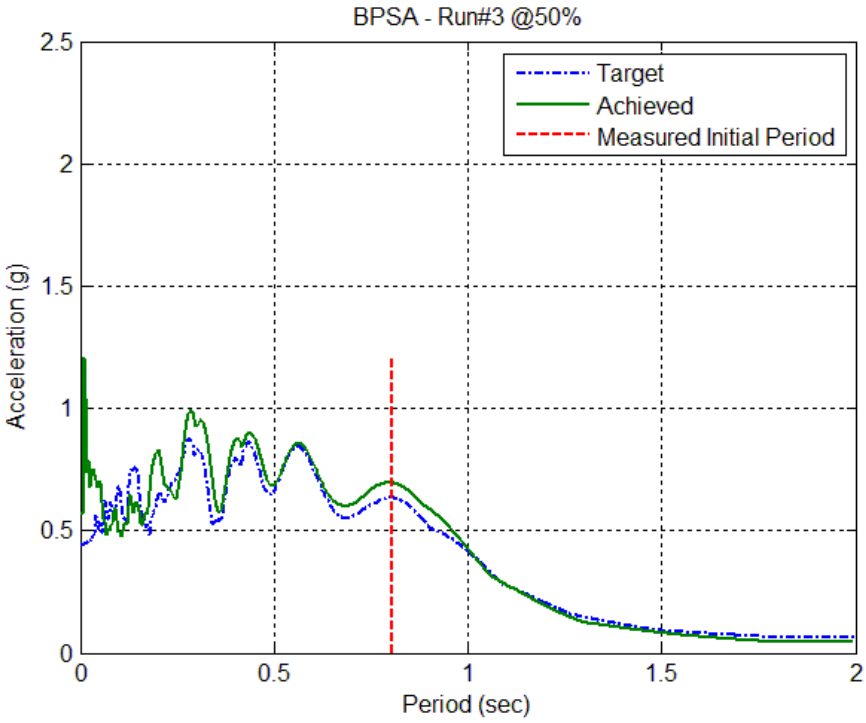

Fig. 3-5. BPSA target vs. achieved motion response spectra for Run-3

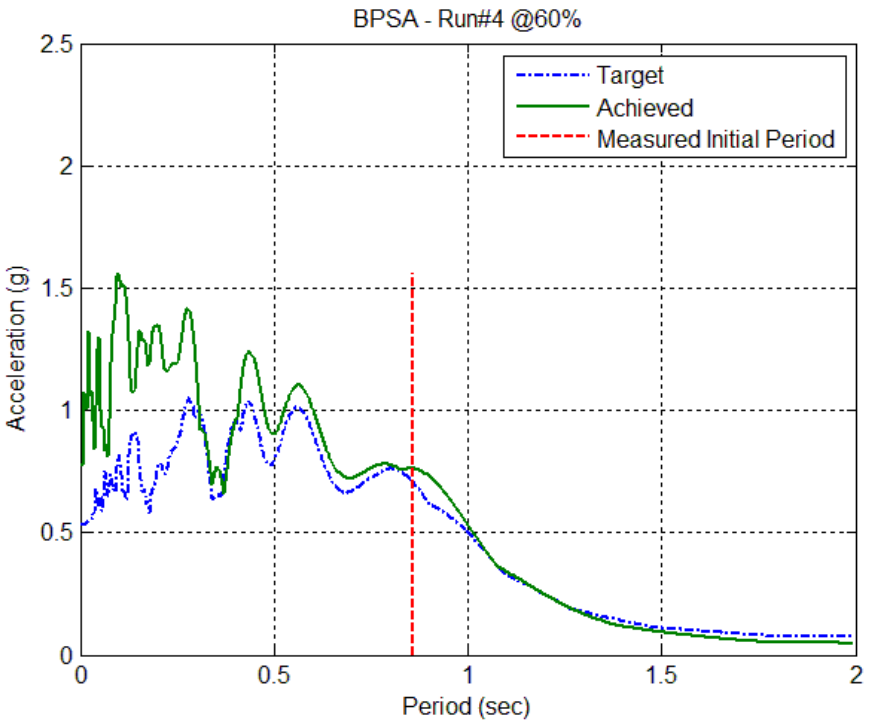

Fig. 3-6. BPSA target vs.. achieved motion response spectra for Run-4

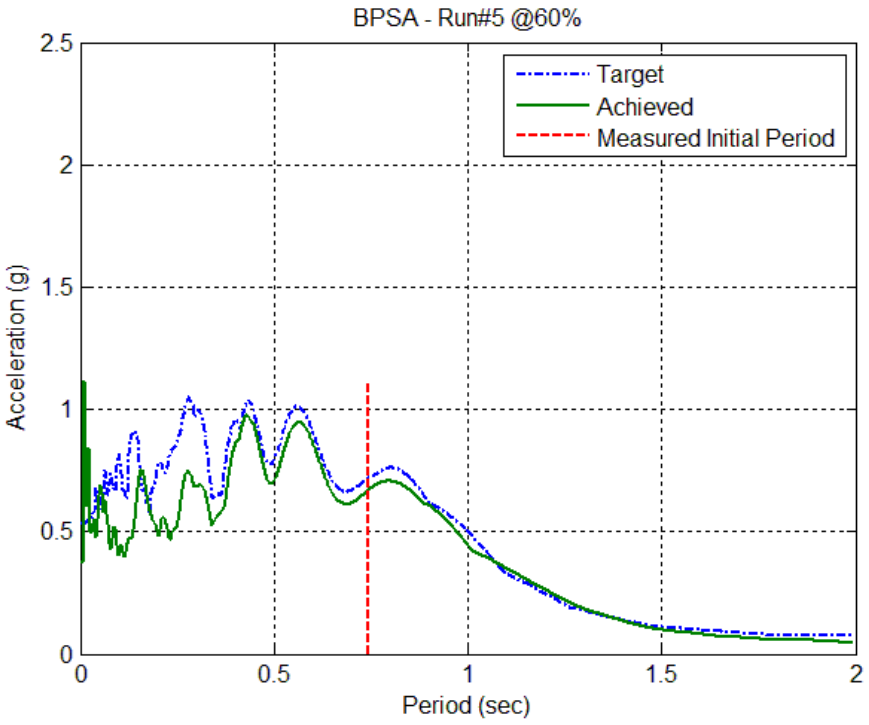

Fig. 3-7. BPSA target vs.. achieved motion response spectra for Run-5

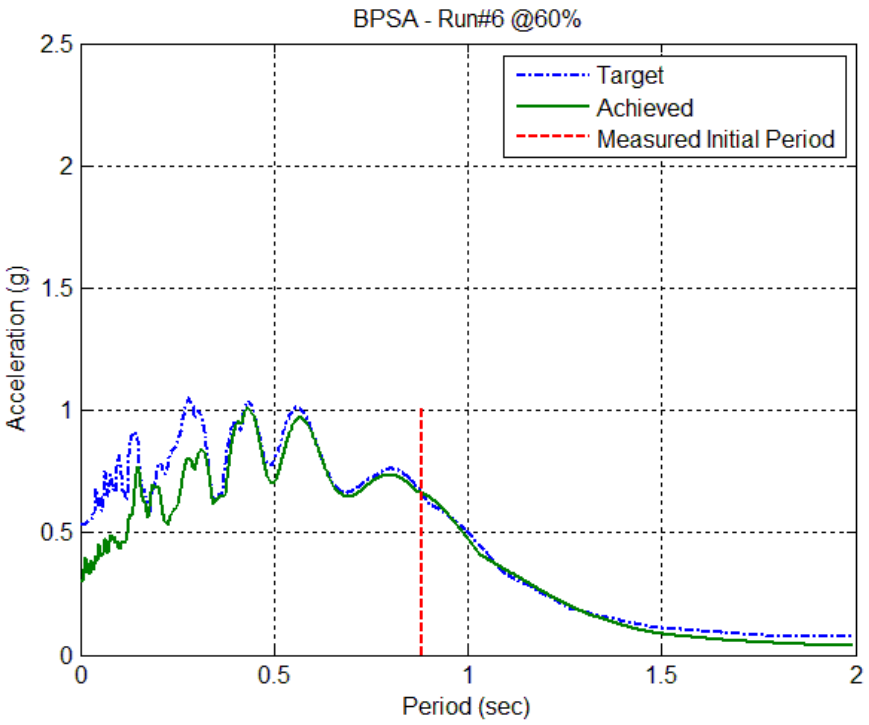

Fig. 3-8. BPSA target vs.. achieved motion response spectra for Run-6

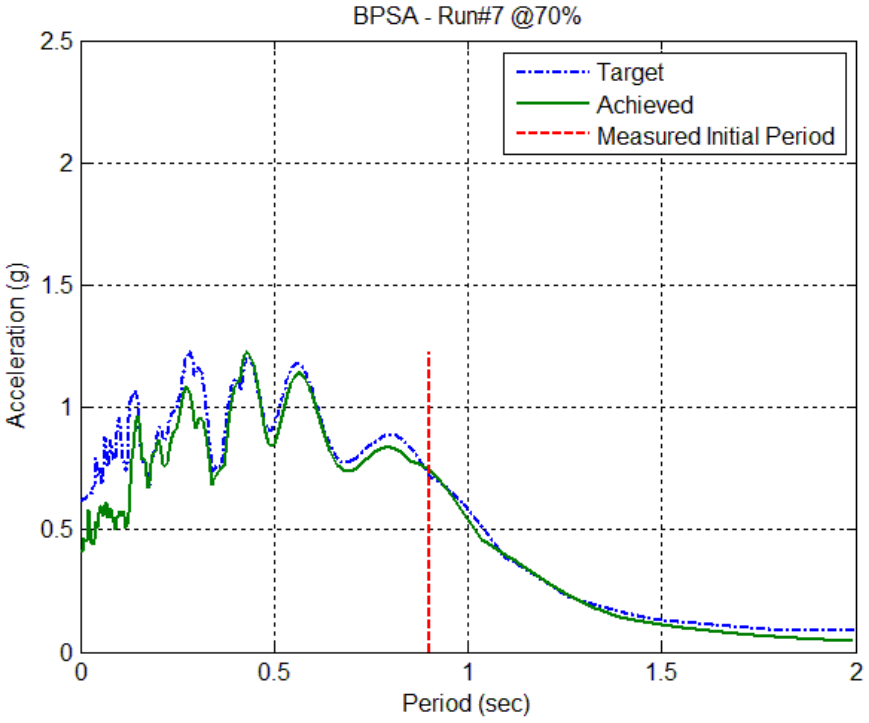

Fig. 3-9. BPSA target vs.. achieved motion response spectra for Run-7

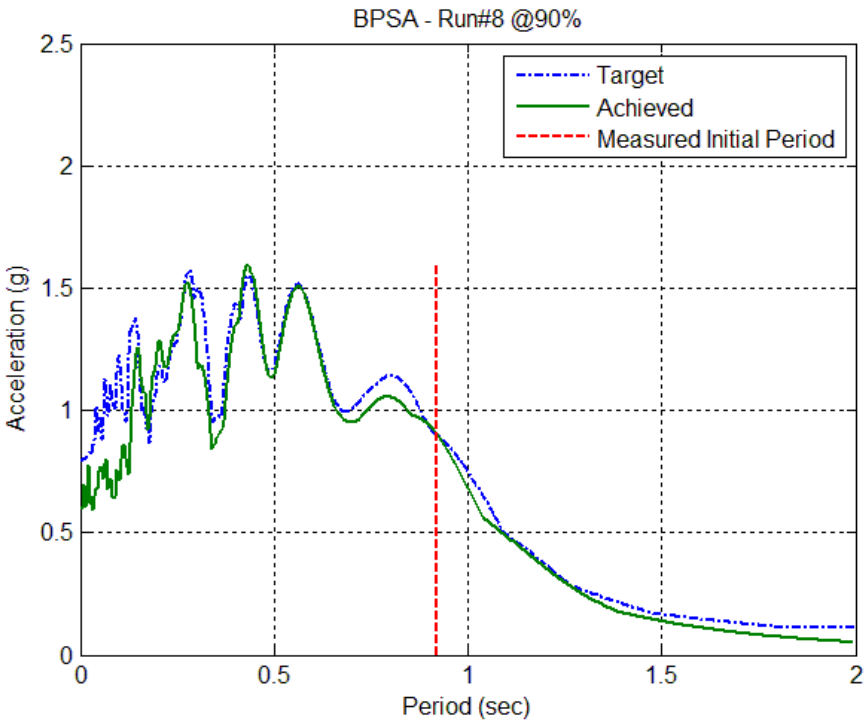

Fig. 3-10. BPSA target vs. achieved motion response spectra for Run-8

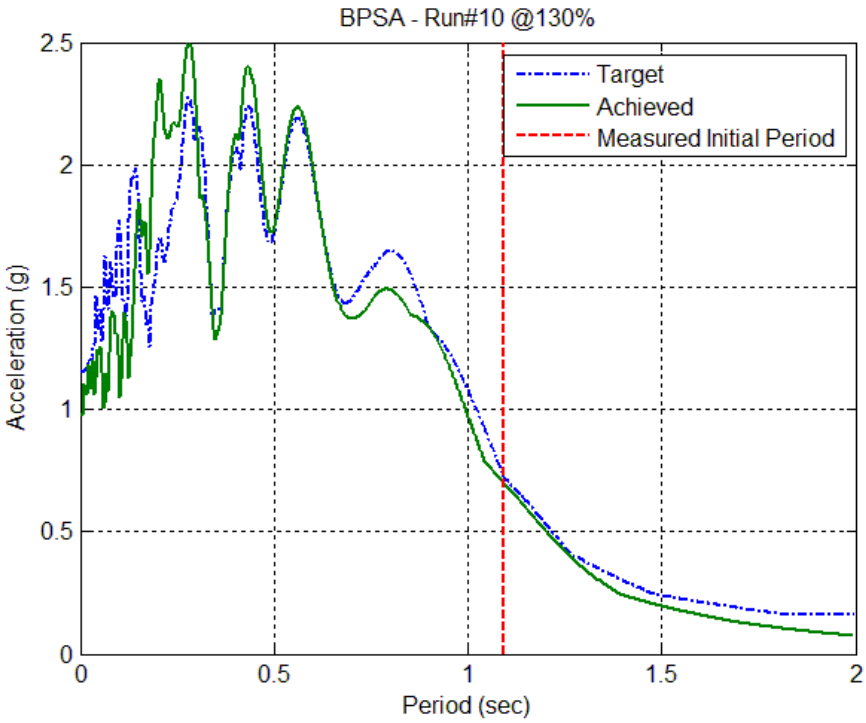

Fig. 3-11. BPSA target vs. achieved motion response spectra for Run-10

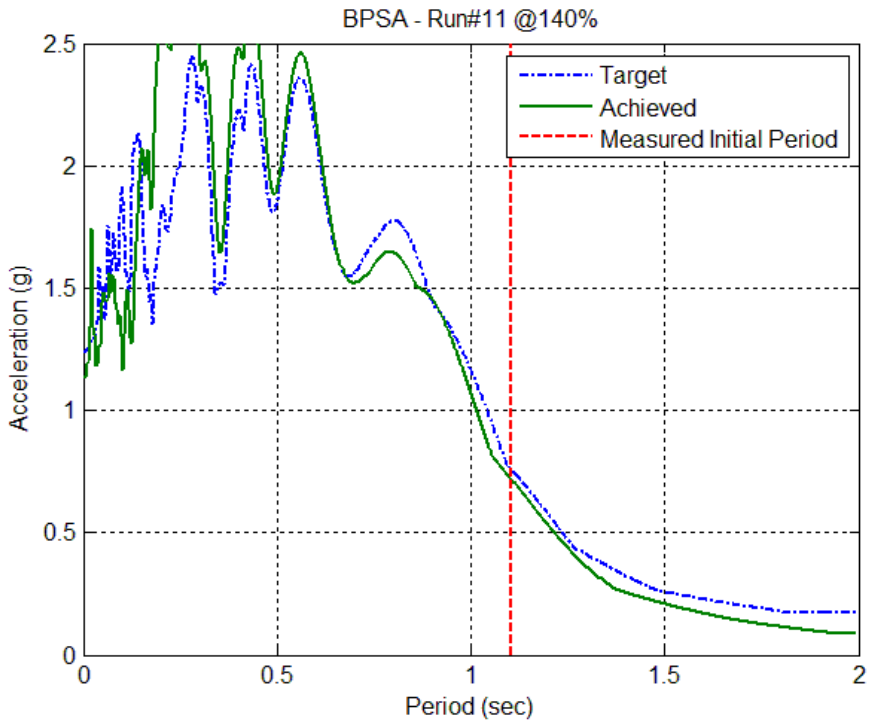

Fig. 3-12. BPSA target vs. achieved motion response spectra for Run-11

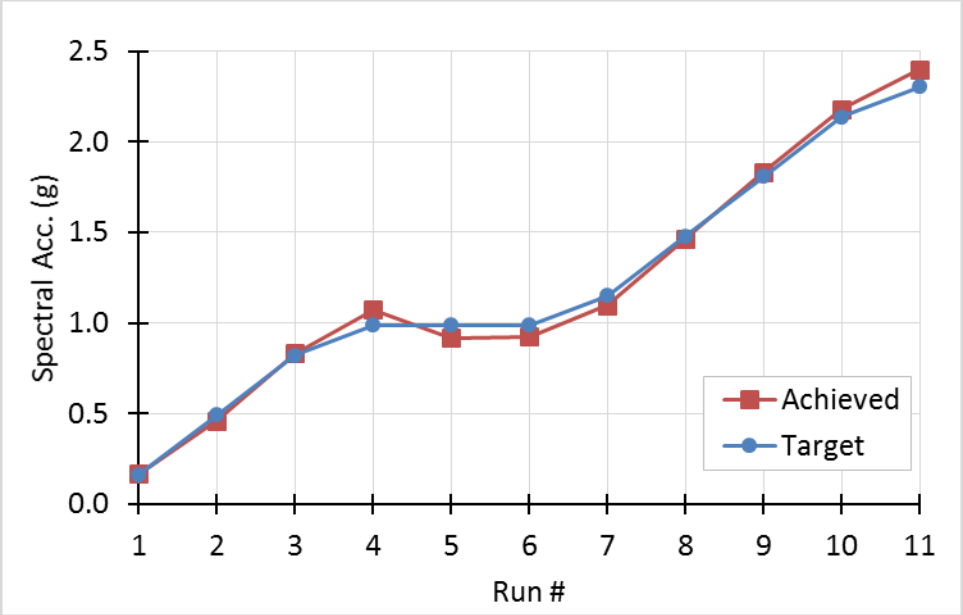

Fig. 3-13. BPSA achieved and target spectral acceleration response for fundamental period

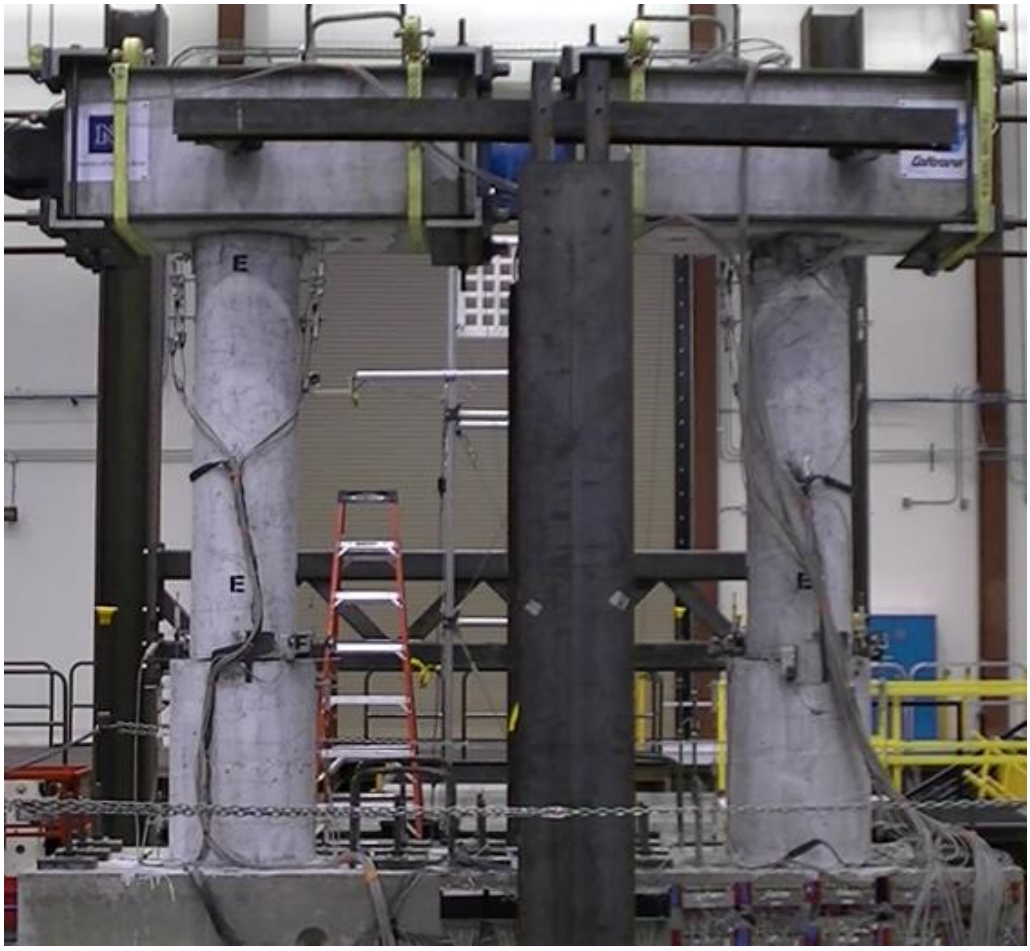

Fig. 3-14. BPSA final condition after the tests

Fig. 3-15. BPSA ECC shrinkage cracks in CIP column before test

a)

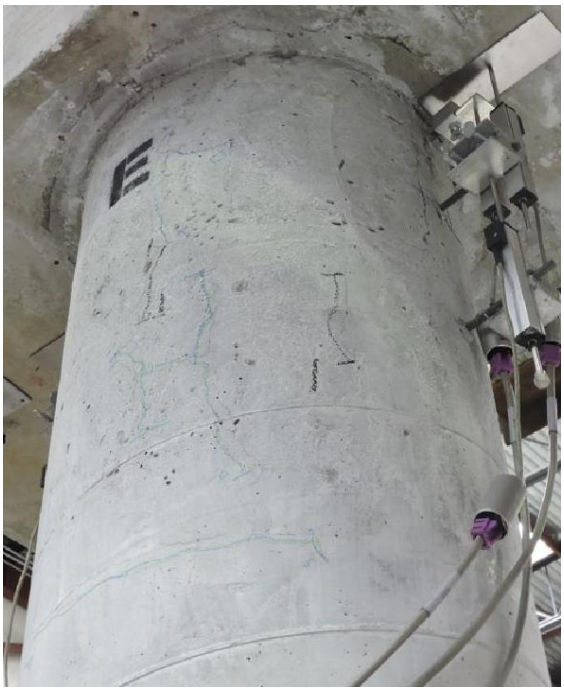

b)

Fig. 3-16. BPSA CIP side after Run-1 NE view a) column b) pedestal

a) b)

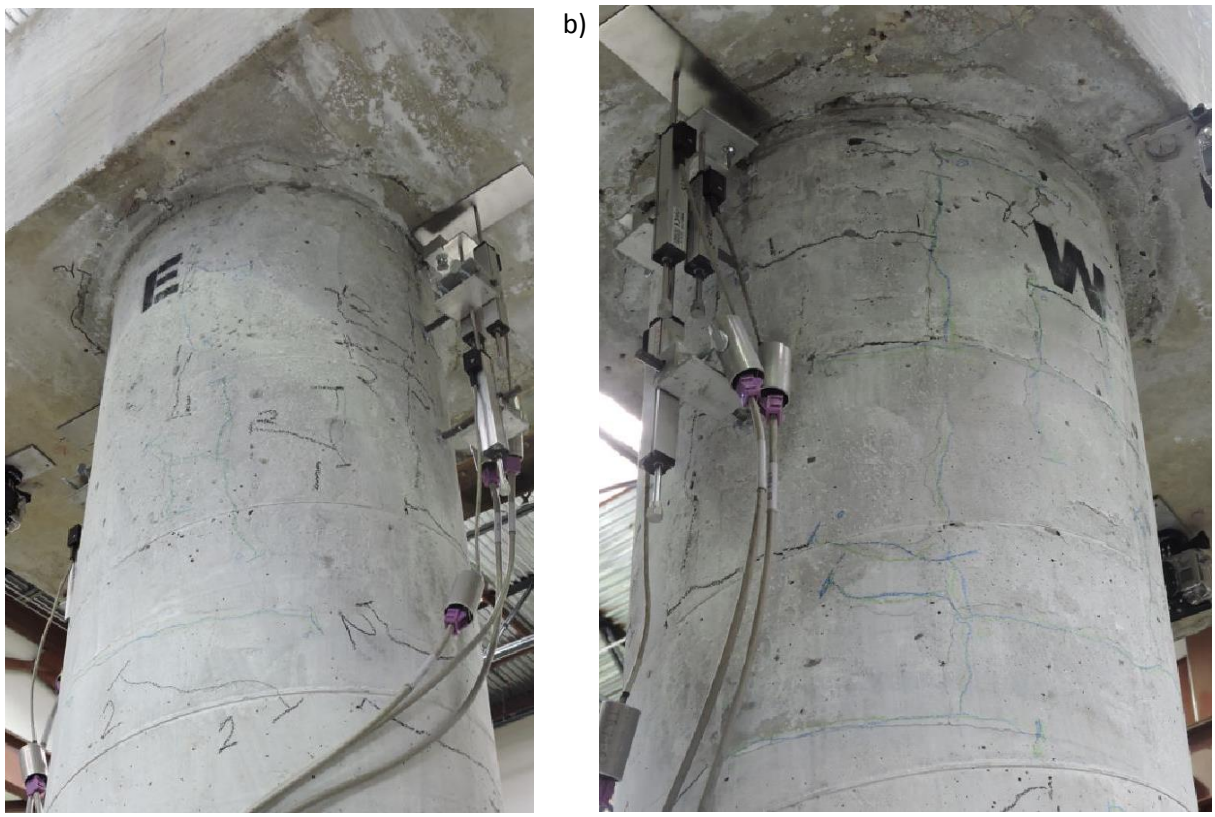

Fig. 3-17. BPSA CIP column after Run-2 a) NE view b) SW view

a) b)

Fig. 3-18. BPSA CIP column after Run-3 a) SW view b) NE view

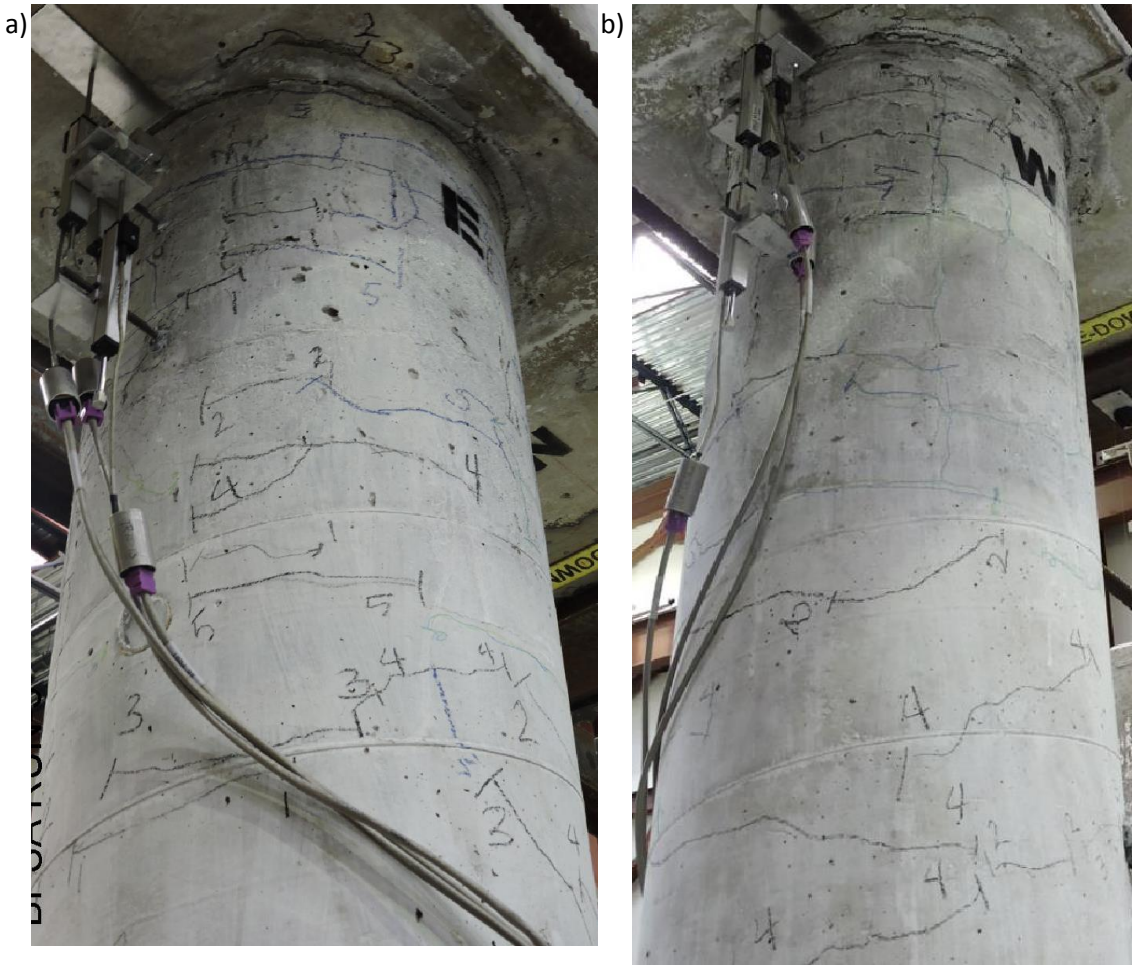

Fig. 3-19. BPSA CIP column after Run-5 a) SE view b) NW view

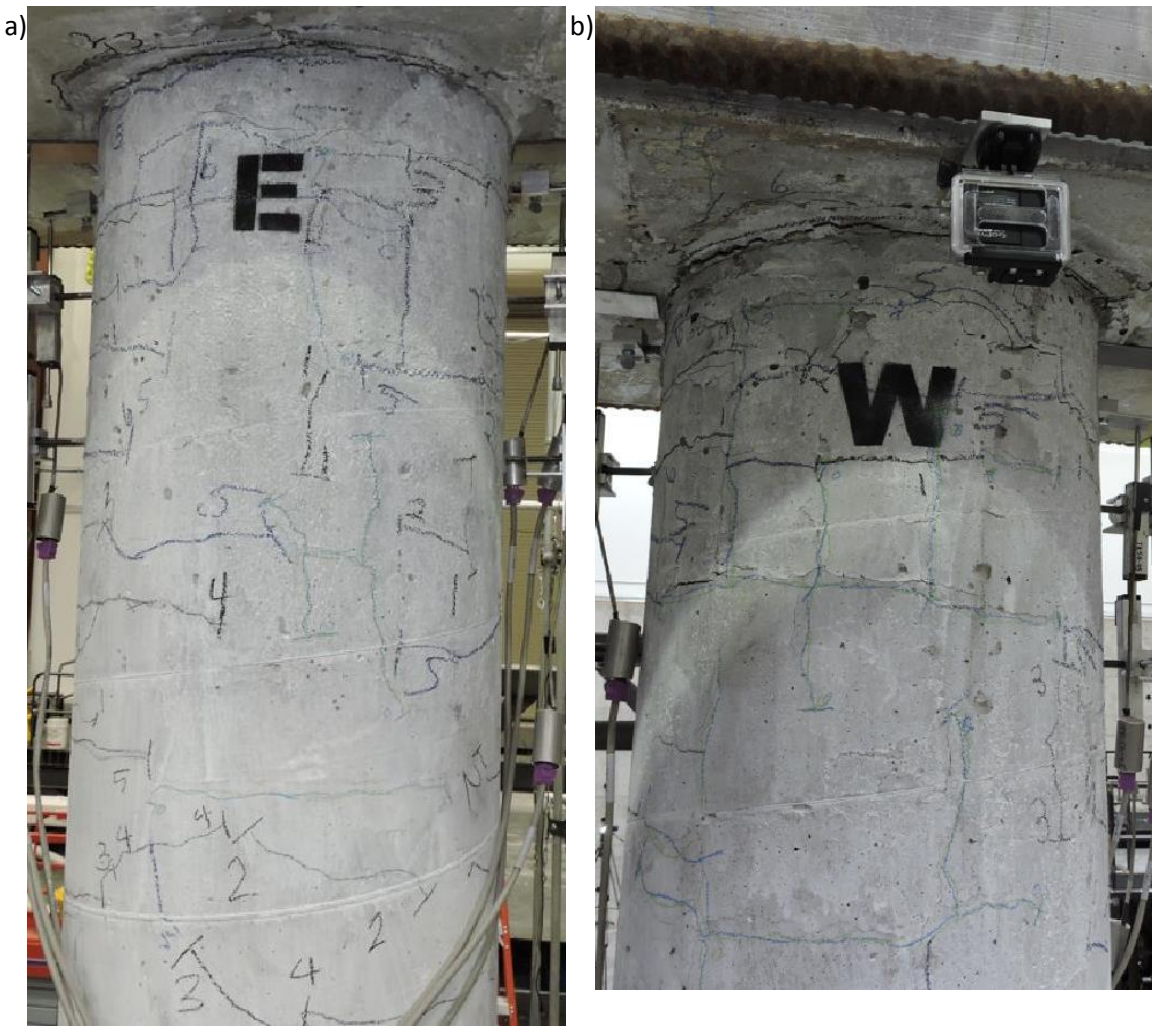

Fig. 3-20. BPSA CIP column after Run-6 a) East view b) West view

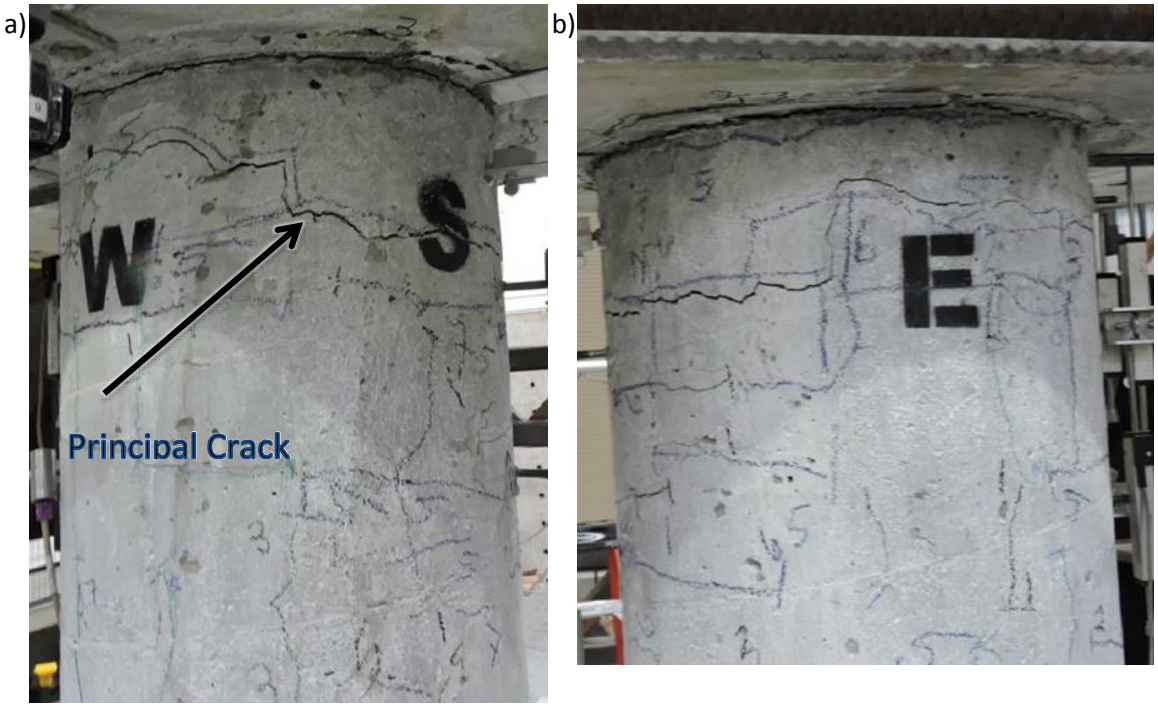

Fig. 3-21. BPSA CIP column after Run-7 a) SW view b) East view

Fig. 3-22. BPSA CIP pipe-pin after Run-7 a) SW view b) NE view

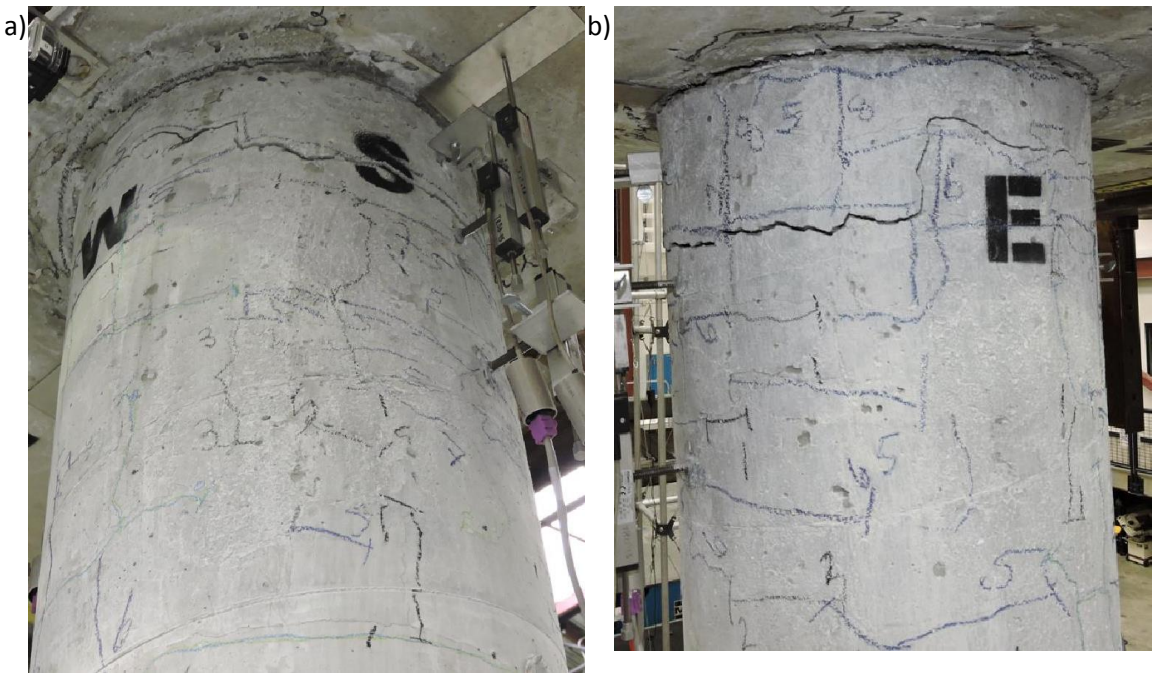

Fig. 3-23. BPSA CIP column after Run-8 a) SW view b) E view

Fig. 3-24. BPSA CIP pipe-pin after Run-8 a) SW view b) NE view

a)

b)

Fig. 3-25. BPSA CIP column after Run-9, a) W view b) SW view

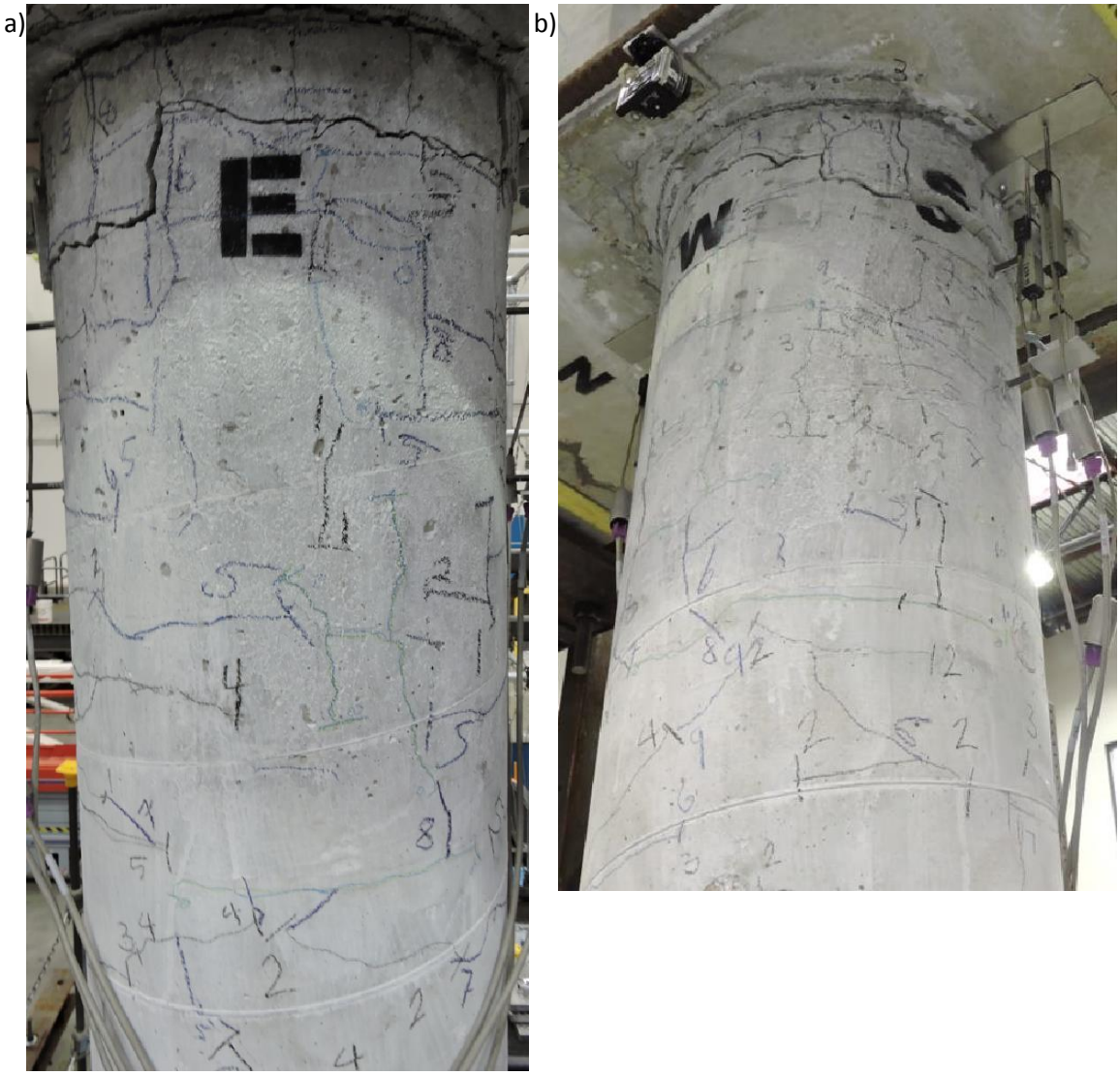

Fig. 3-26. BPSA CIP column after Run-10 a) E view b) SW view

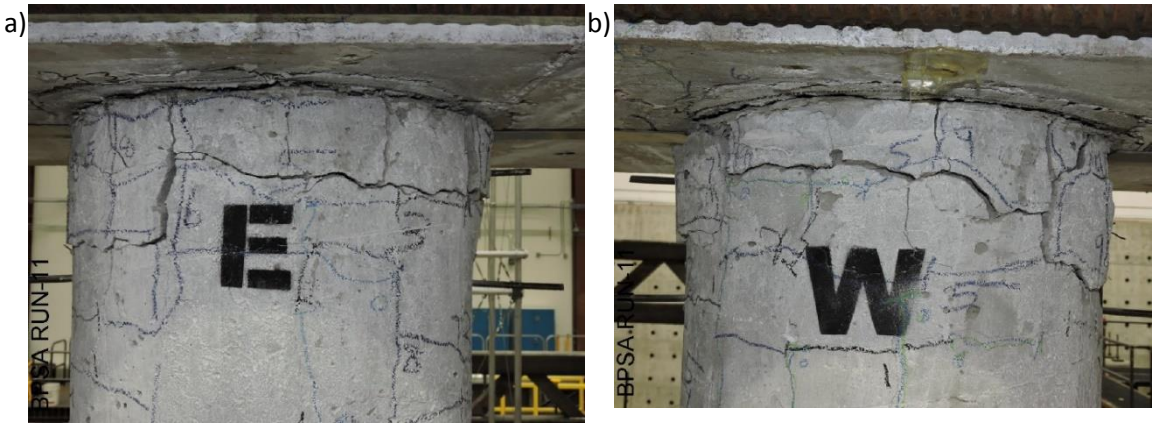

Fig. 3-27. BPSA CIP column after Run-11, a) E view b) W view

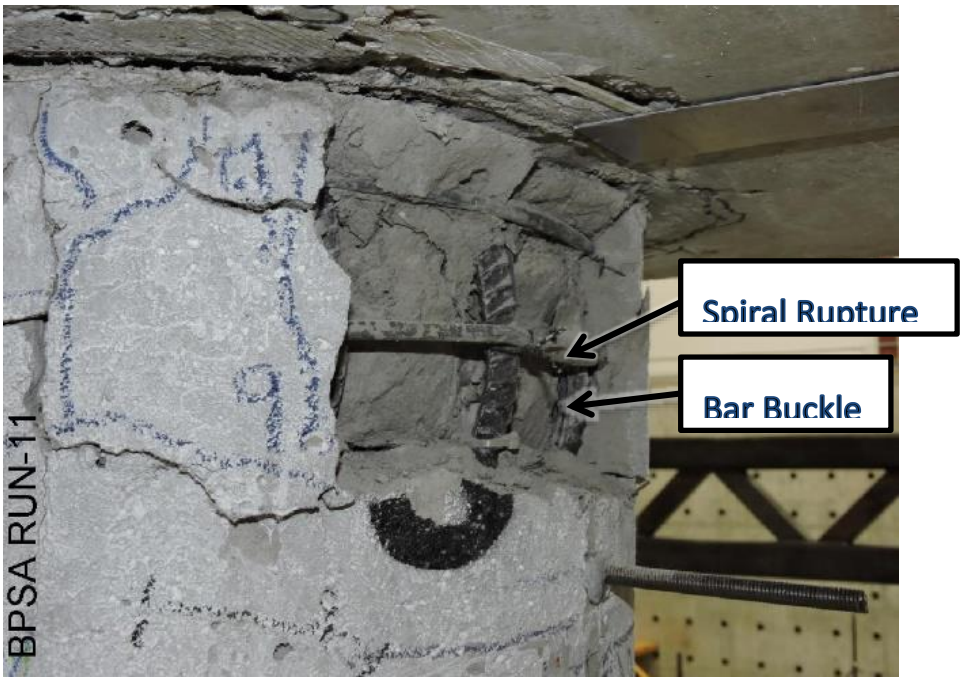

Fig. 3-28. BPSA CIP column end of the test condition after removing the spalled ECC

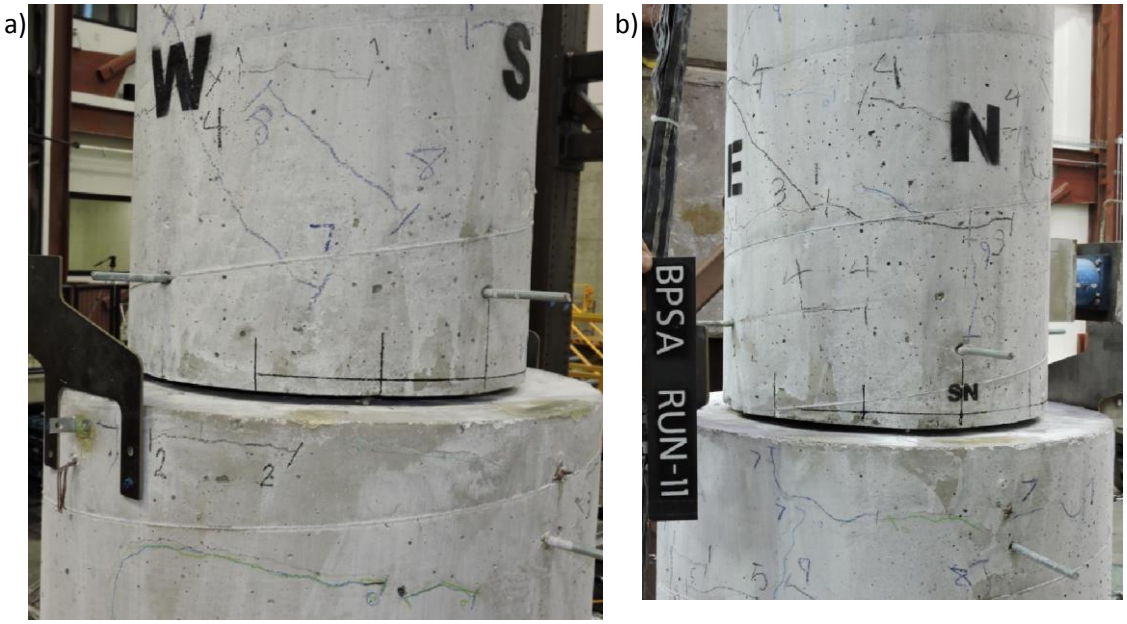

Fig. 3-29. BPSA CIP pipe-pin end of the test condition a) SW view b) NE view

Fig. 3-30. BPSA crack formation at load cell connection after Run-3

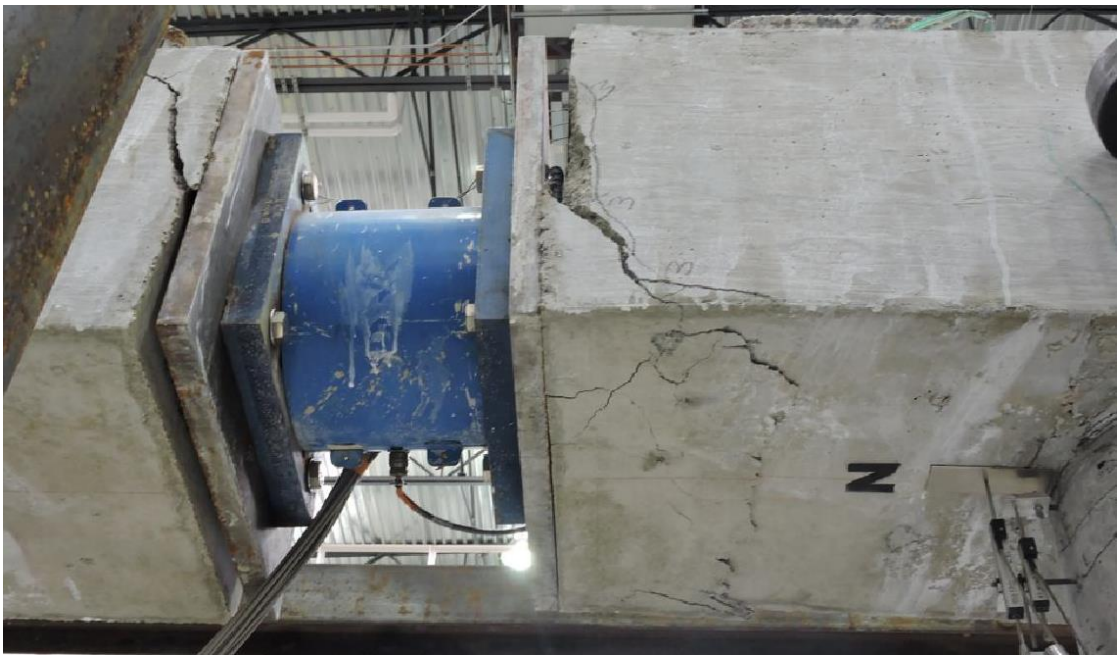

Fig. 3-31. BPSA cap beam condition after load cell failure end of Run-4

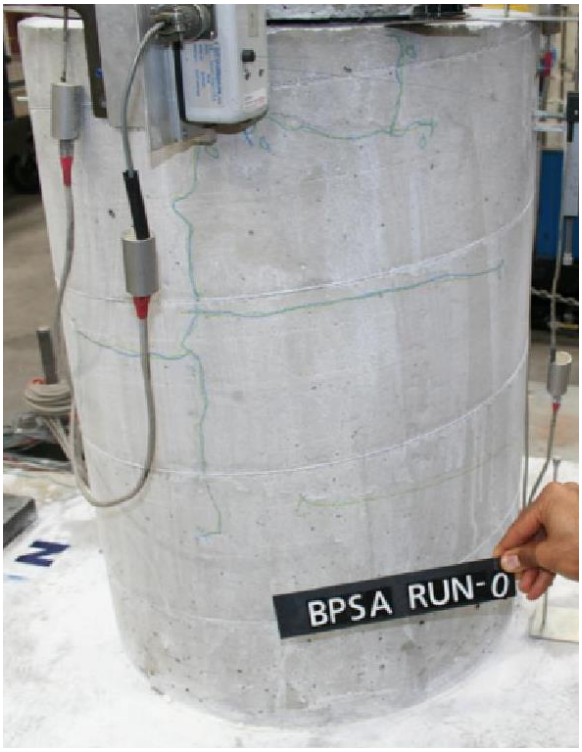

Fig. 3-32. BPSA shrinkage cracks on PC pedestal prior to tests

(a) (b)

Fig. 3-33. BPSA PC column after Run-1 a) NE view b) SW view

(a) (b)

Fig. 3-34. BPSA PC column after Run-2 a) SE view b) NW view

a) b)

Fig. 3-35. BPSA PC side after Run-3 a) W view b) E view

a) b)

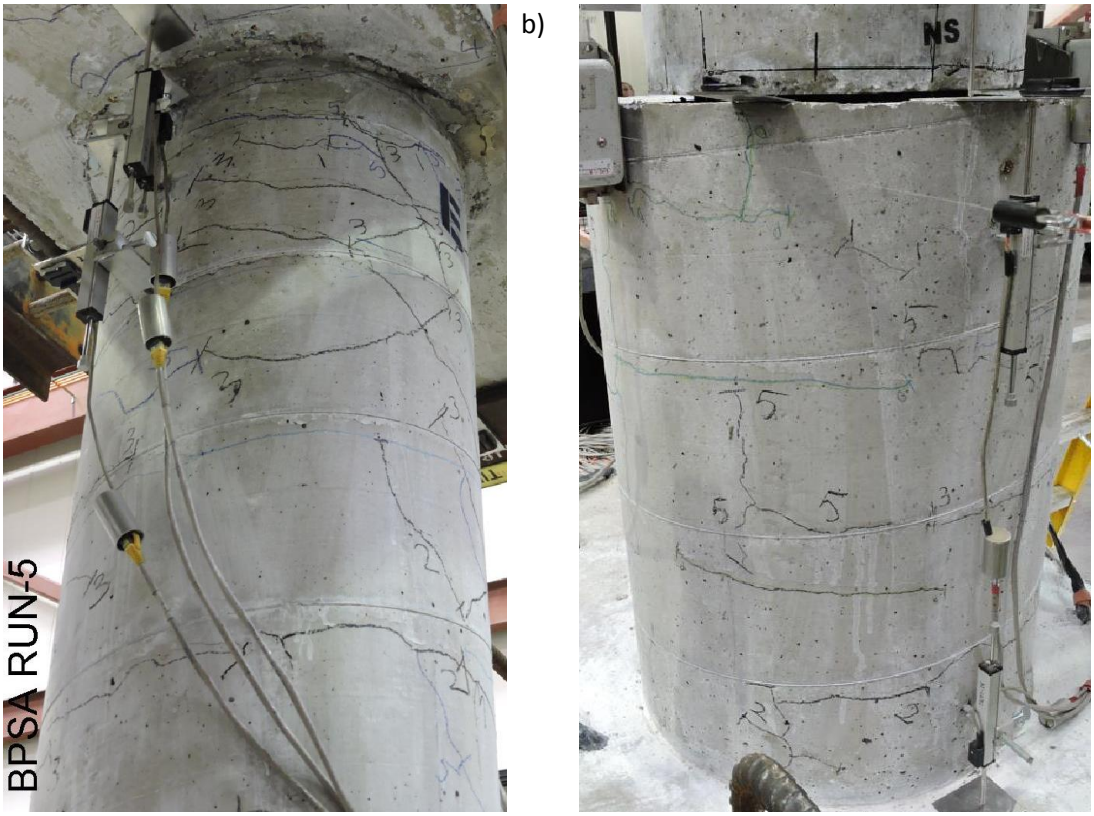

Fig. 3-36. BPSA PC side after Run-5 a) SE view of column b) SW view of pedestal

a) b)

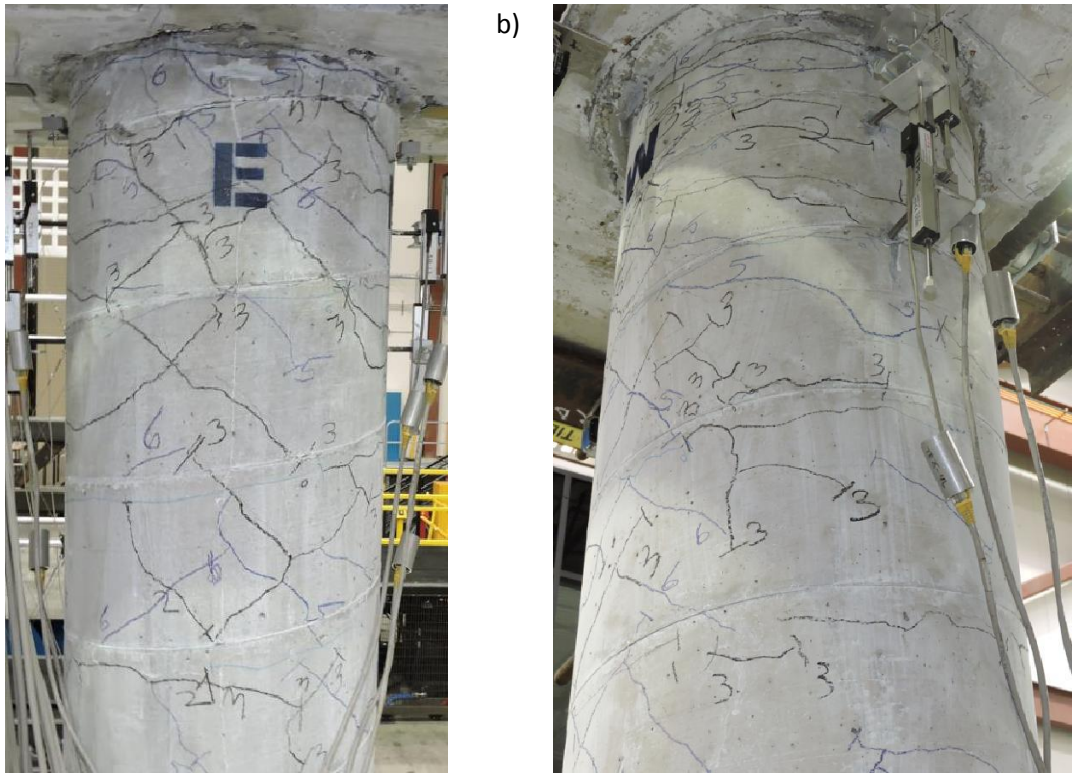

Fig. 3-37. BPSA PC after Run-6 a) East view b) SE view

a)

b)

Fig. 3-38. BPSA PC after Run-7 a) W view b) E view

a) b)

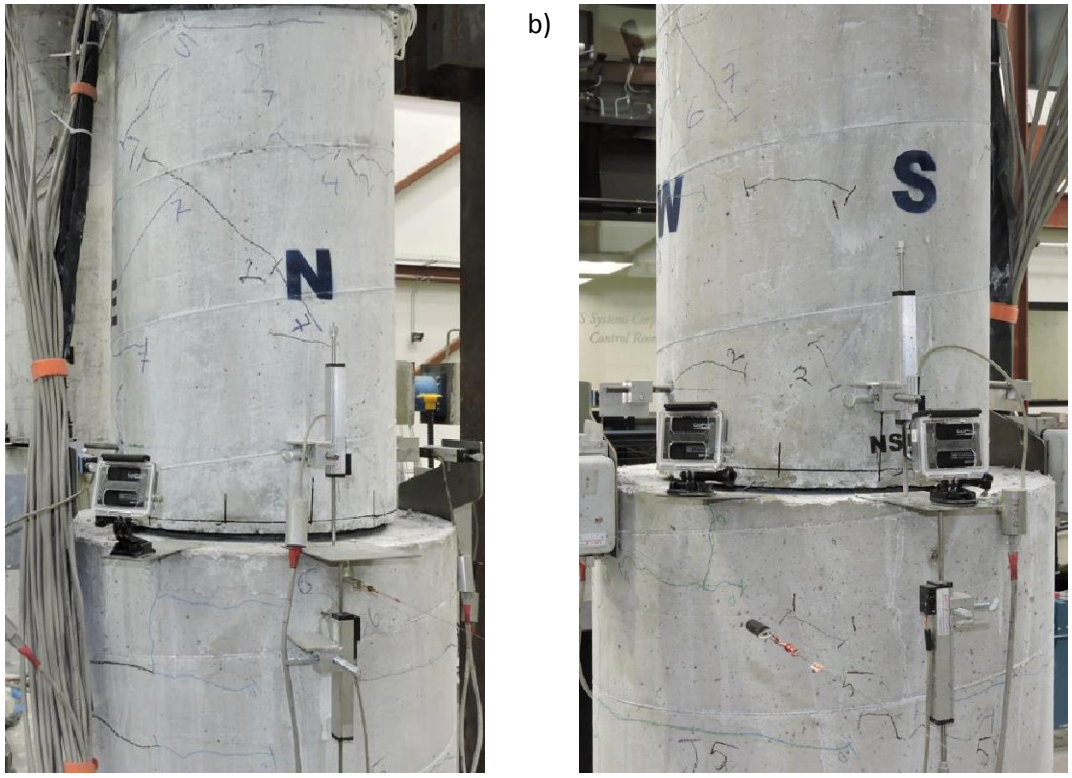

Fig. 3-39. BPSA PC pipe-pin after Run-7 a) North view b) SW view

(a) (b)

Fig. 3-40. BPSA PC column after Run-8 a) East view b) West view

Fig. 3-41. BPSA PC column after Run-9 a) NE view b) SW view c) NE top

a)

b)

c)

Fig. 3-42. BPSA PC column after Run-10 a) East view b) SE view c) W view

Fig. 3-43. BPSA PC column after Run-11 a) West view b) SE view c) W view

(a) (b)

Fig. 3-44. BPSA PC pipe-pin after final run a) SW view b) NE view

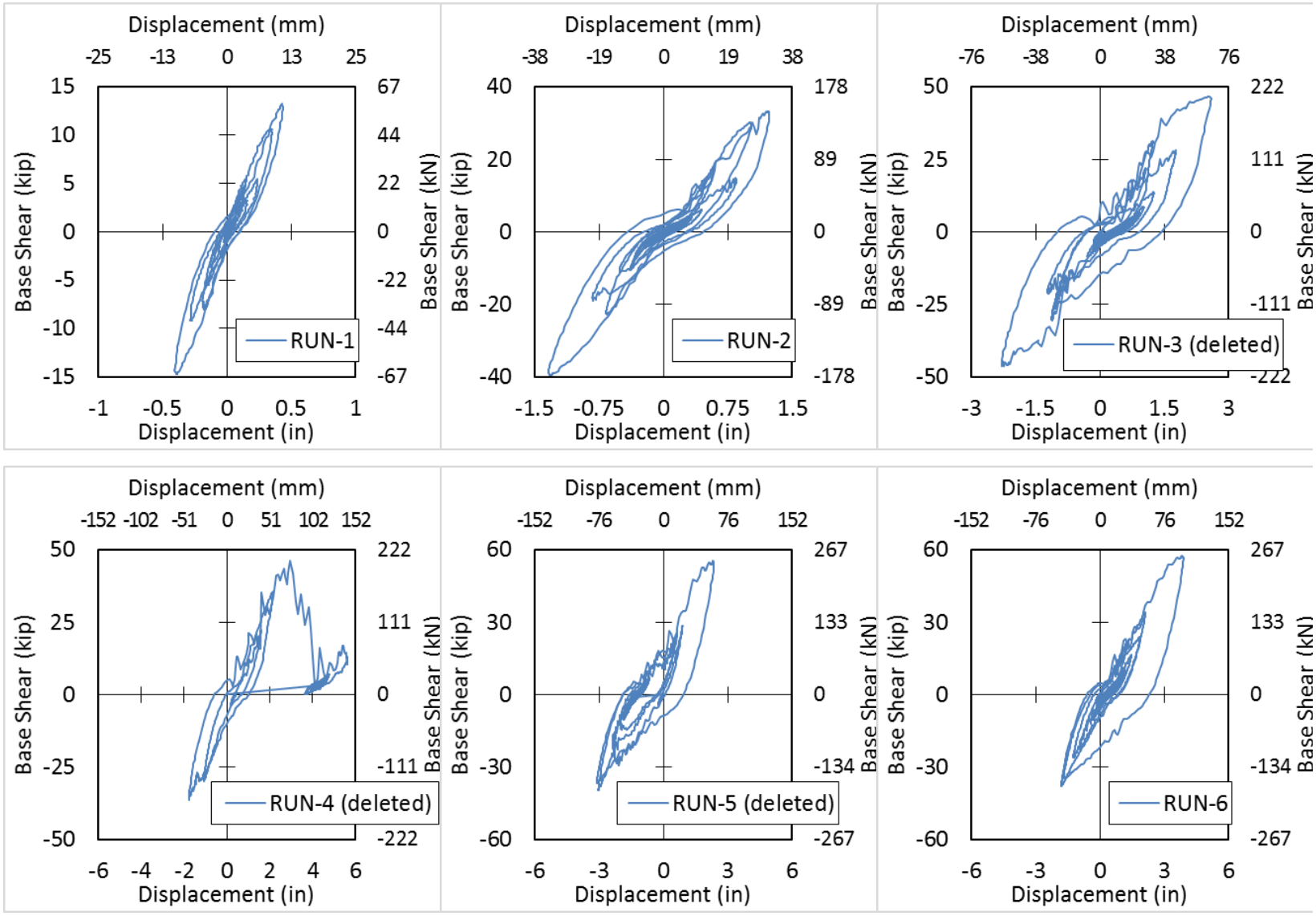

Fig. 3-45. BPSA bent displacement-base shear hysteresis curves for Runs-1 to Run-6

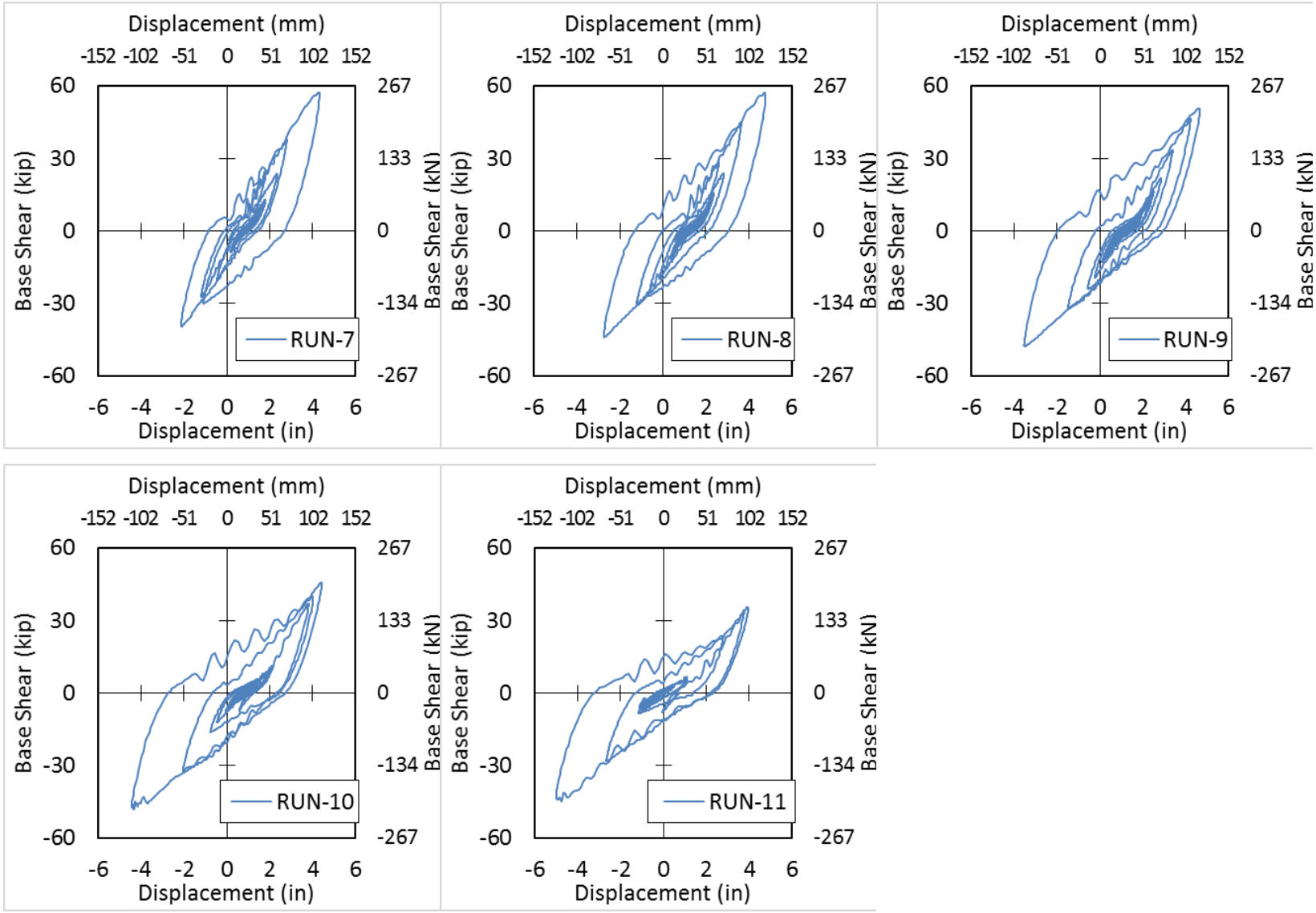

Fig. 3-46. BPSA bent displacement-base shear hysteresis curves for Run-7 to Run-11

a)

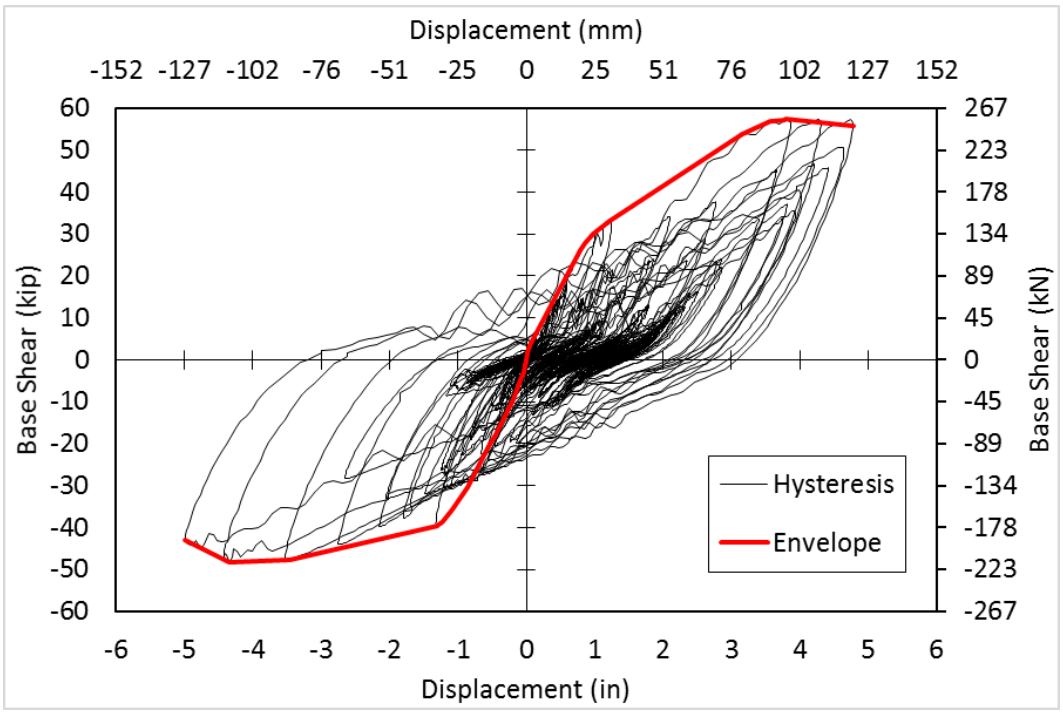

b)

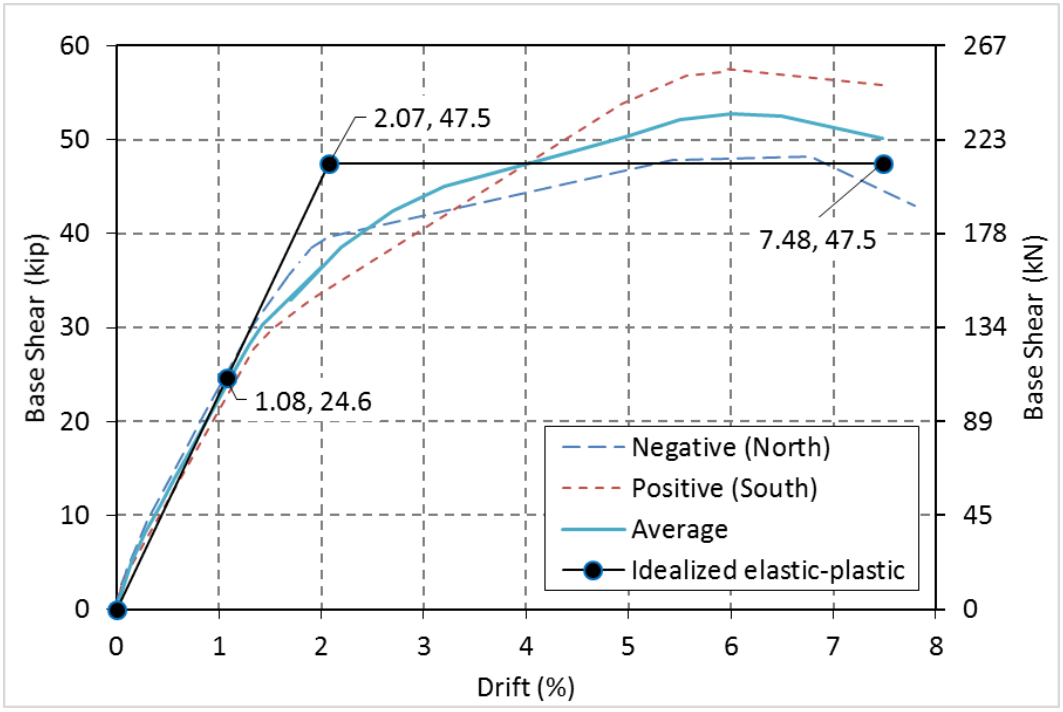

Fig. 3-47. BPSA bent force-displacement a) hysteresis curve b) idealized elastic-plastic

a)

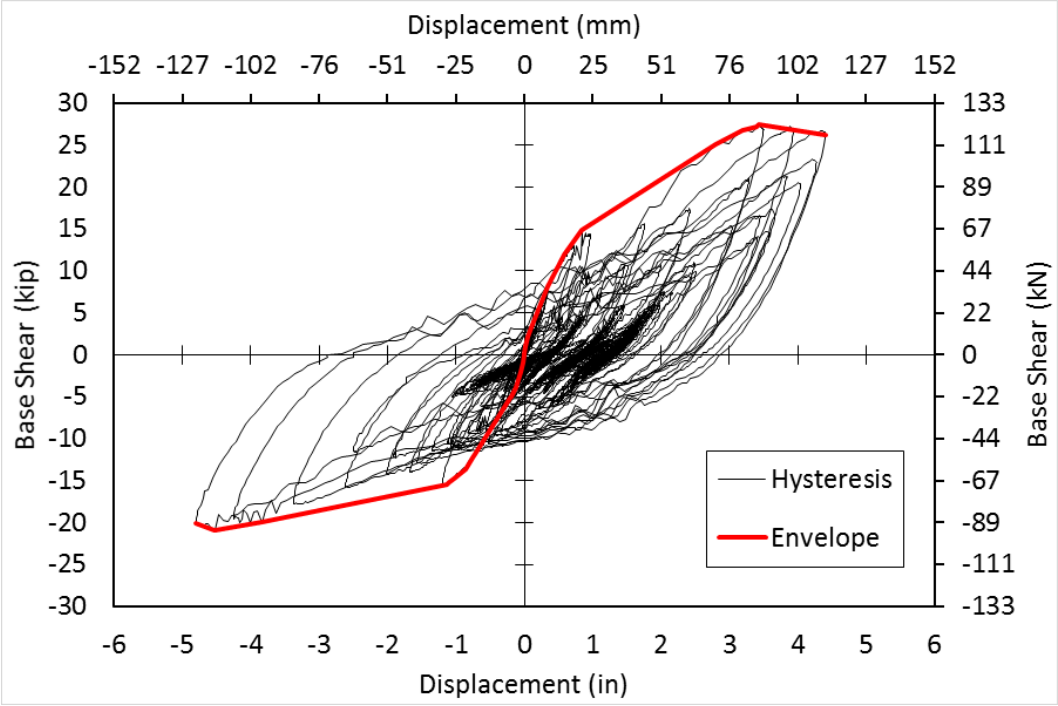

b)

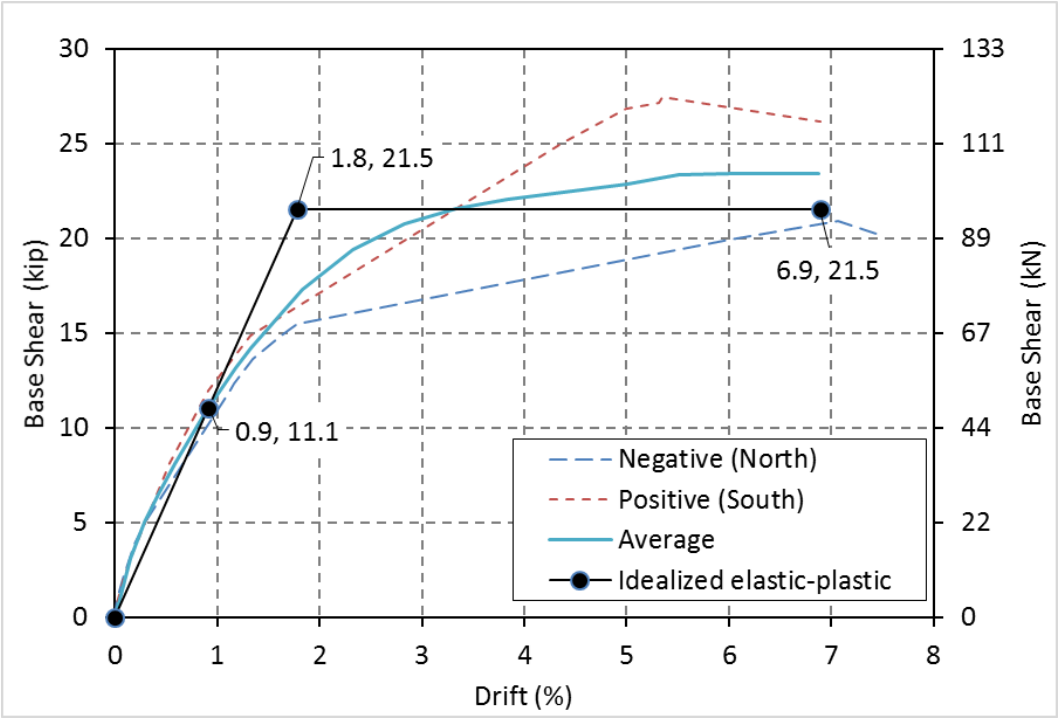

Fig. 3-48. BPSA CIP force-displacement a) hysteresis curve b) idealized elastic-plastic

a)

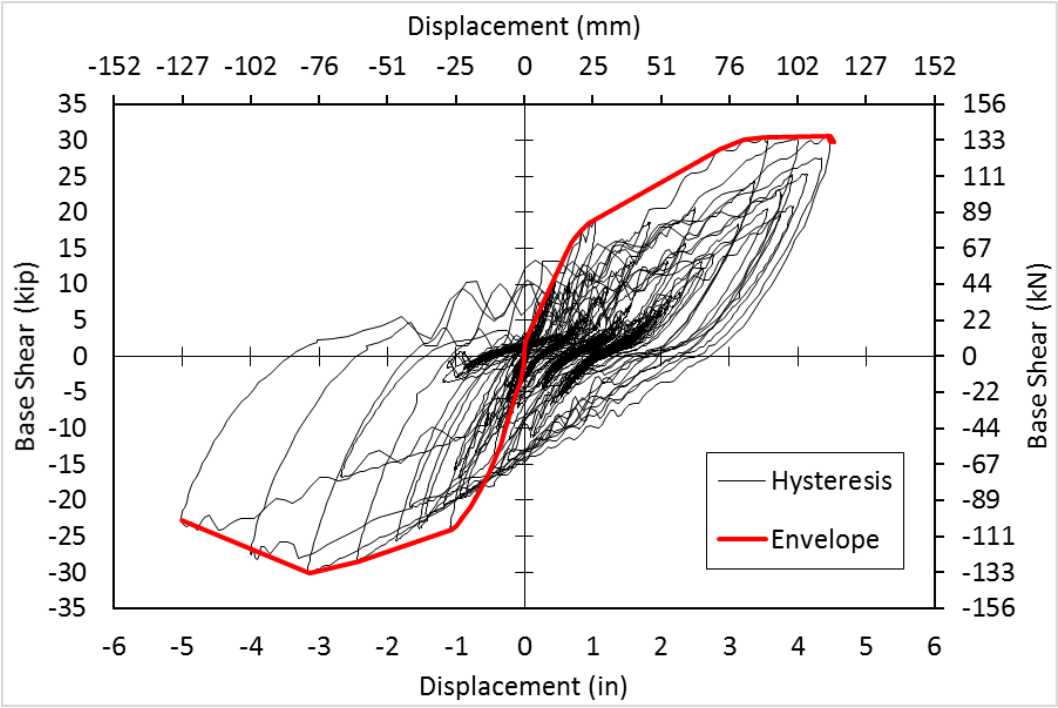

b)

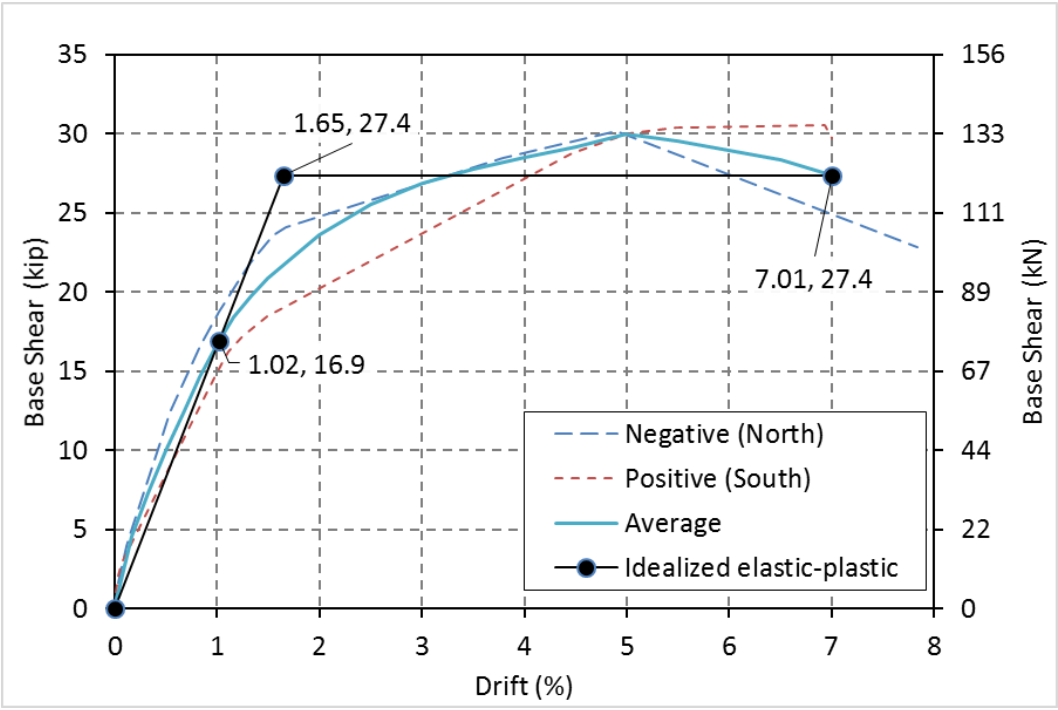

Fig. 3-49. BPSA PC force-displacement a) hysteresis curve b) idealized elastic-plastic

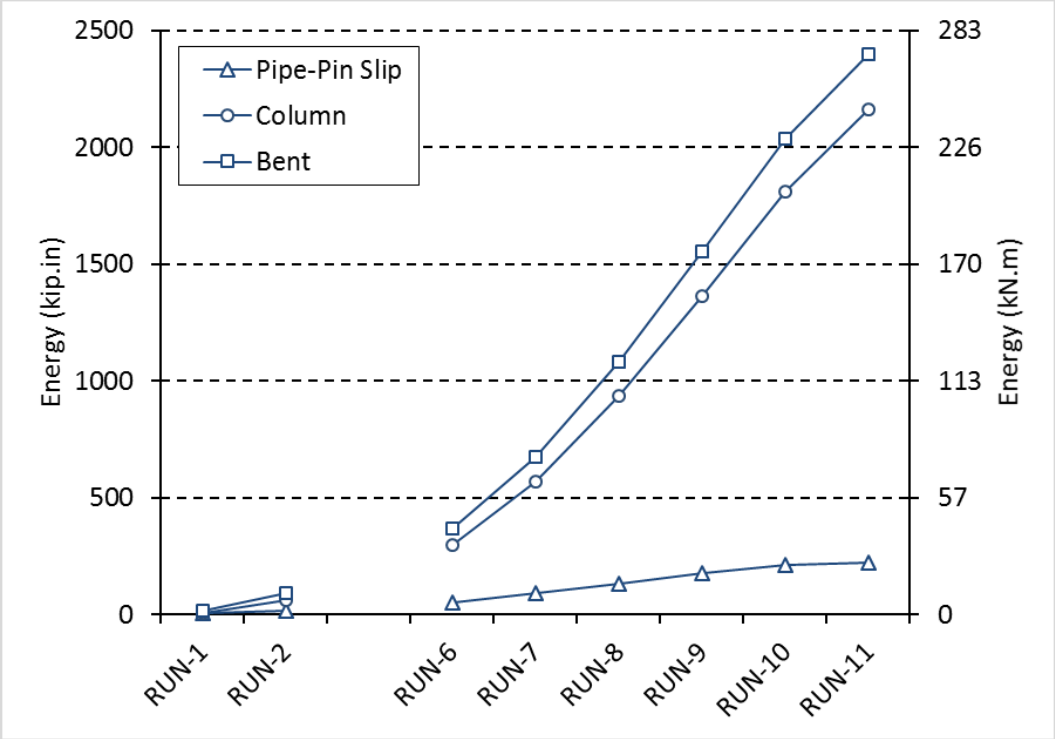

Fig. 3-50. BPSA accumulated energy dissipated for different actions

a)

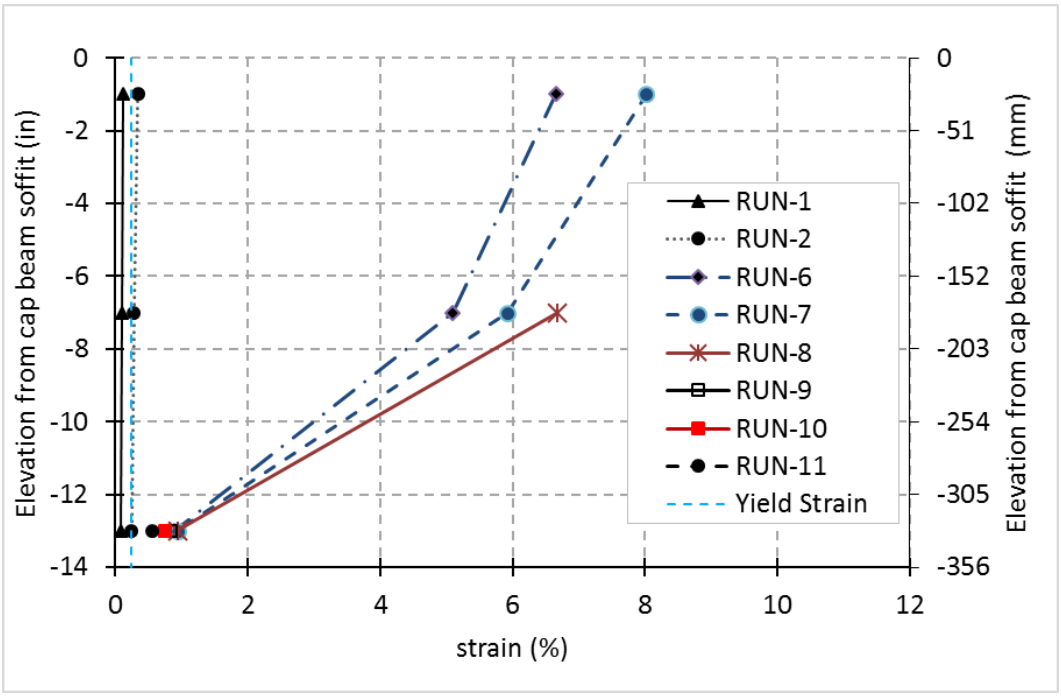

b)

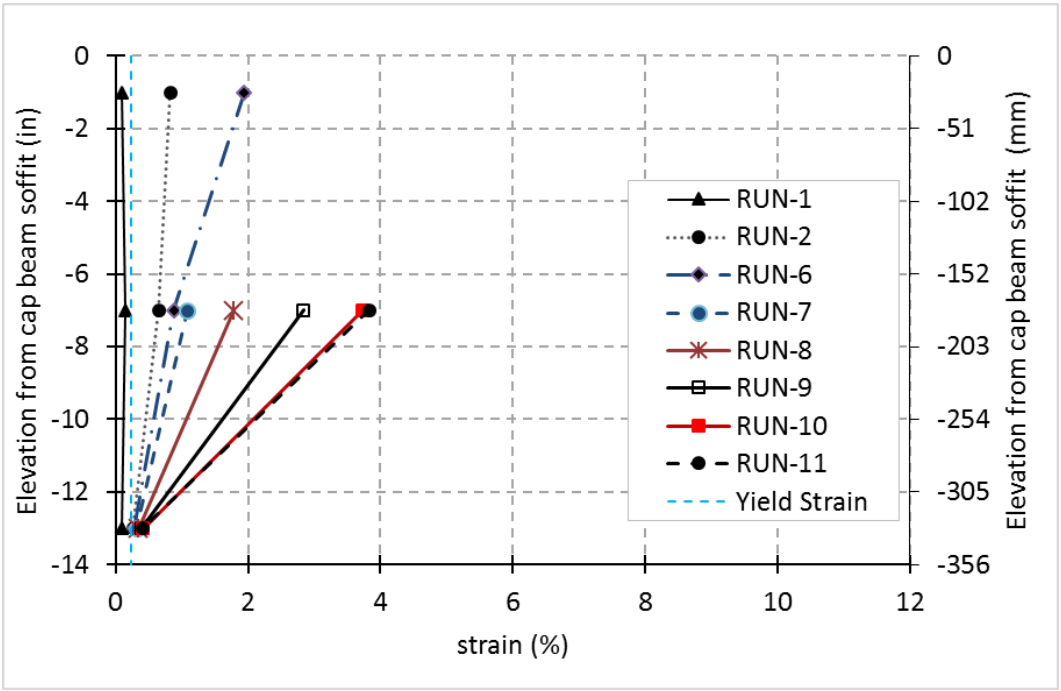

Fig. 3-51. BPSA tensile strain profile in long. bars in plastic hinge of CIP column a)south b)north

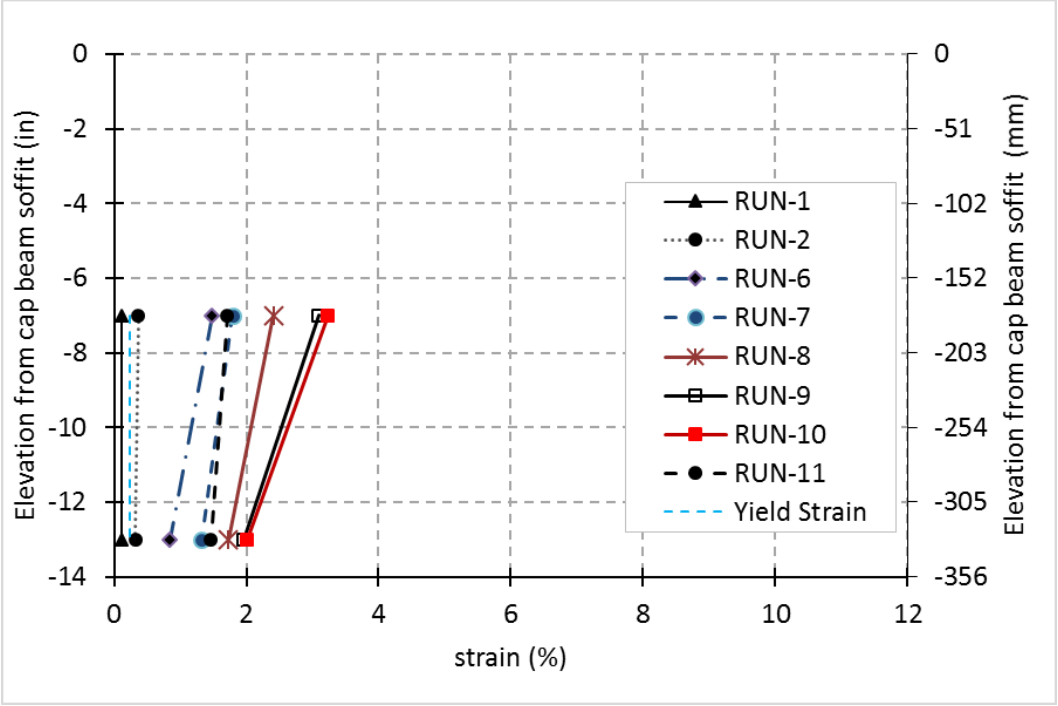

Fig. 3-52. BPSA tensile strain profile in long. bars in plastic hinge of PC column at north

a)

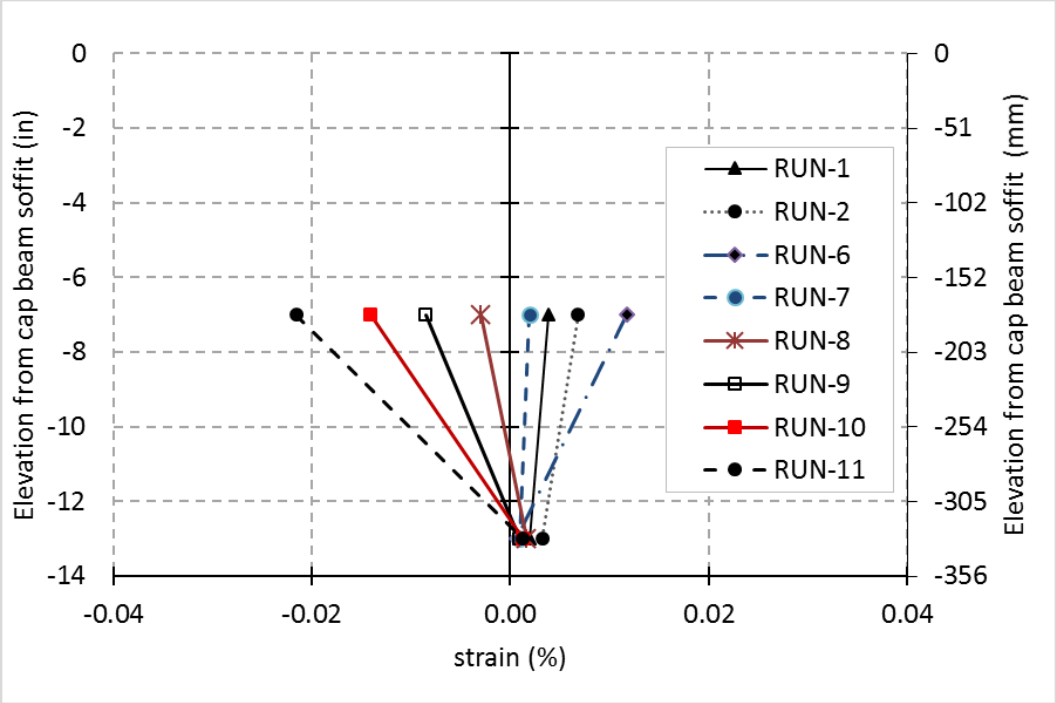

b)

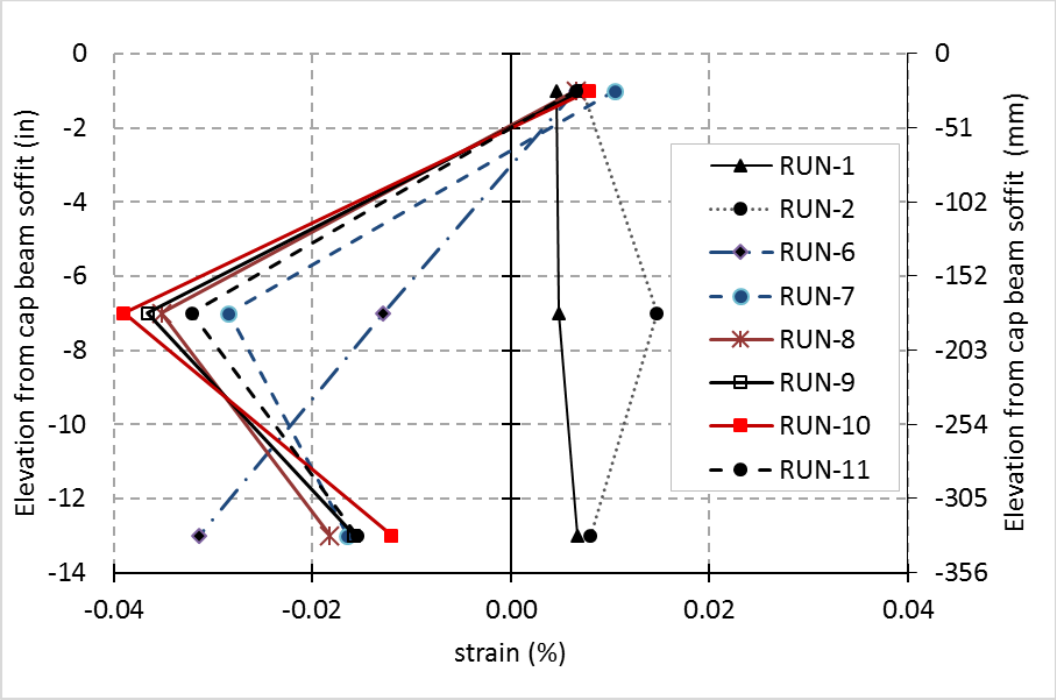

Fig. 3-53. BPSA average strain profile in trans. bars in plastic hinge a)CIP b) PC

a)

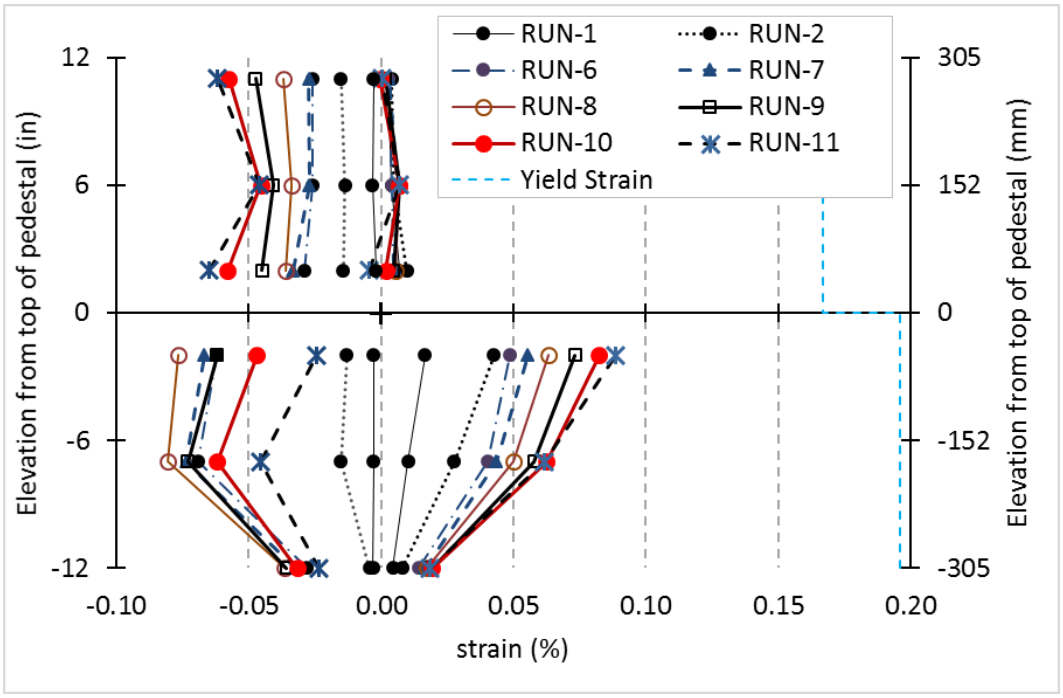

b)

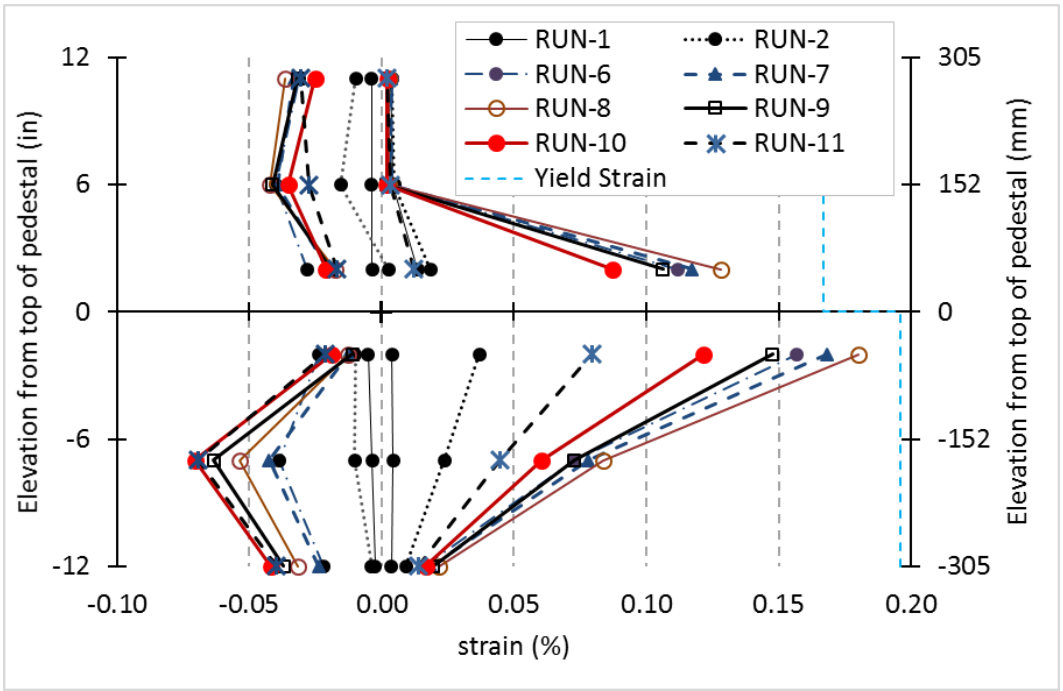

Fig. 3-54. BPSA max. and min. vertical strain profile in pipes of CIP a)south b)north

a)

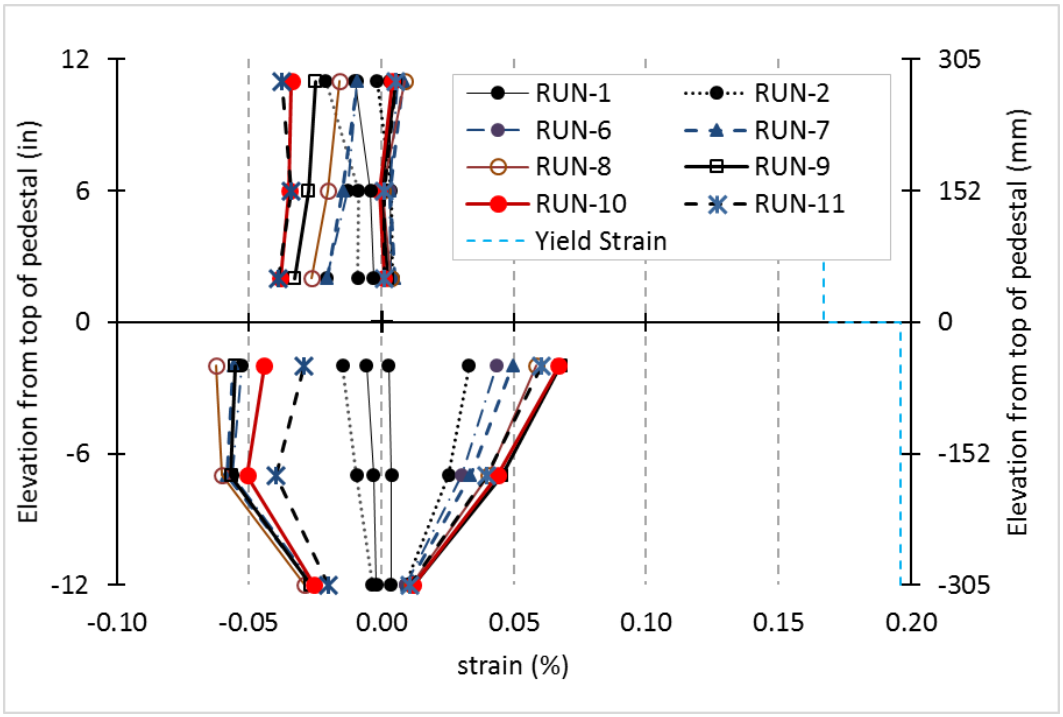

b)

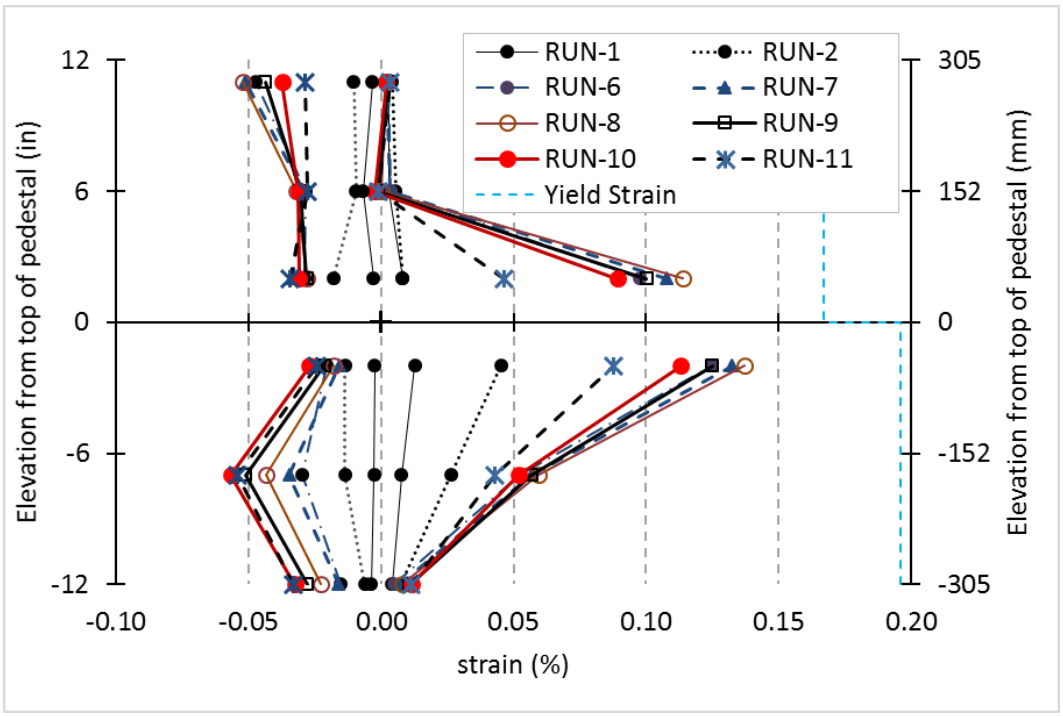

Fig. 3-55. BPSA max. and min. vertical strain profile in pipes of PC a)south b)north

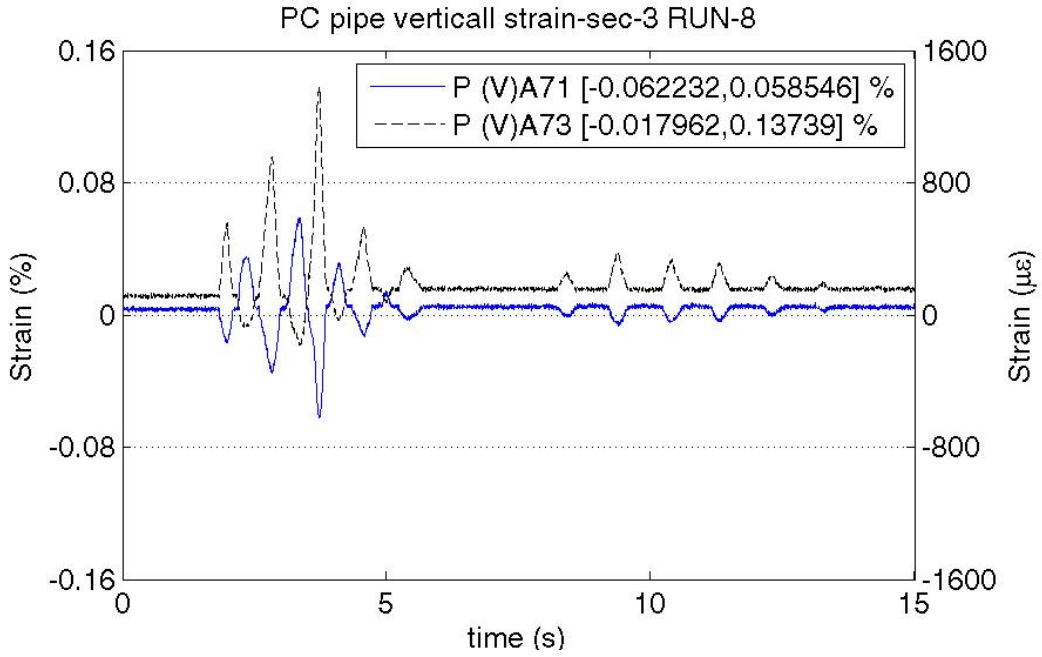

Fig. 3-56. BPSA PC pipe-pin vertical strain history for sec-3 and Run-8

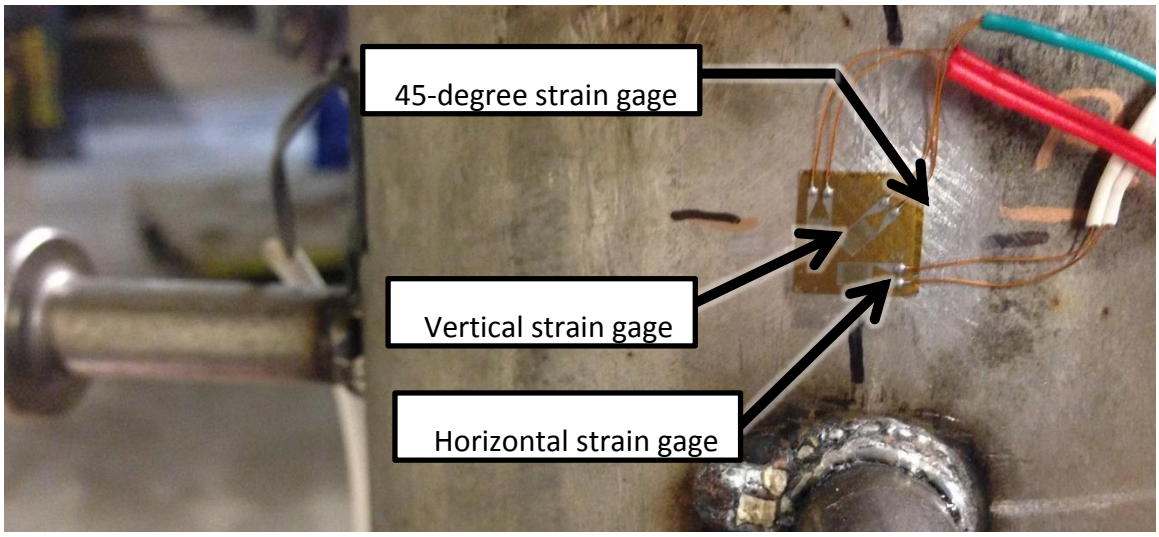

Fig. 3-57. BPSA orientation of rosette strain gage on pipes

a)

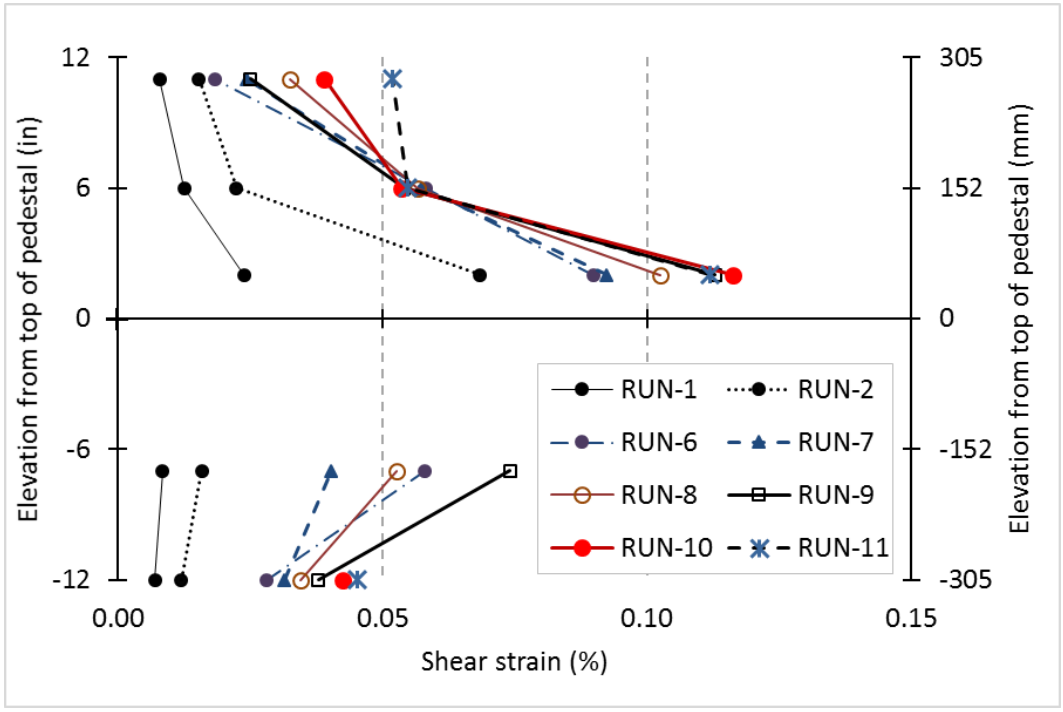

b)

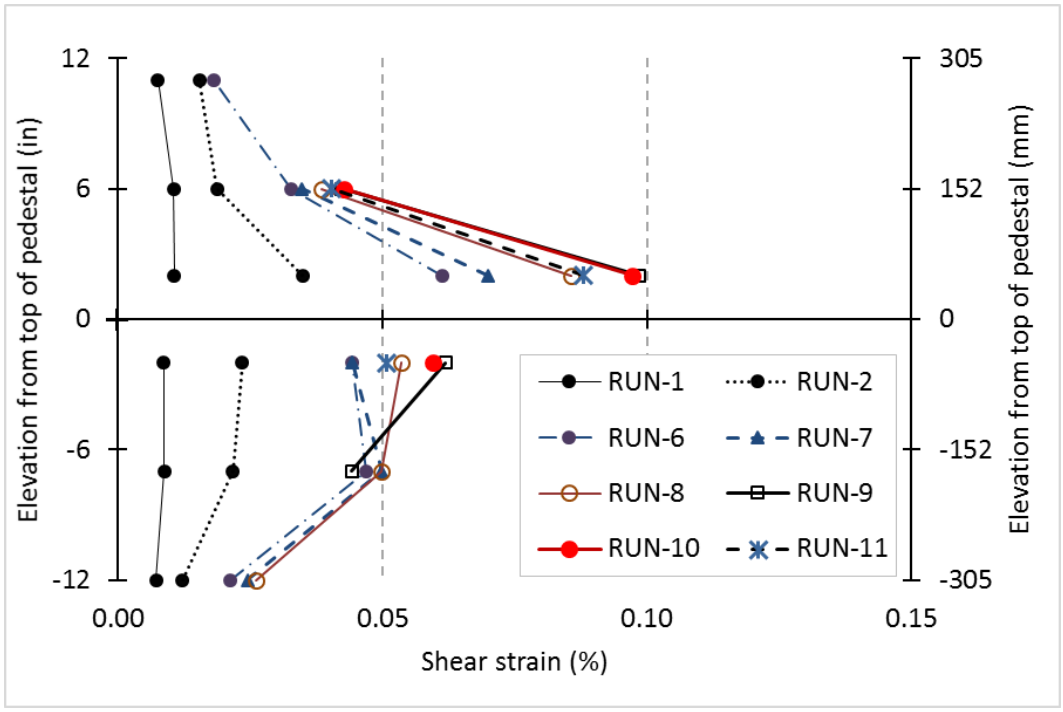

Fig. 3-58. BPSA maximum shear strain profile in pipes of a)CIP b)PC

a)

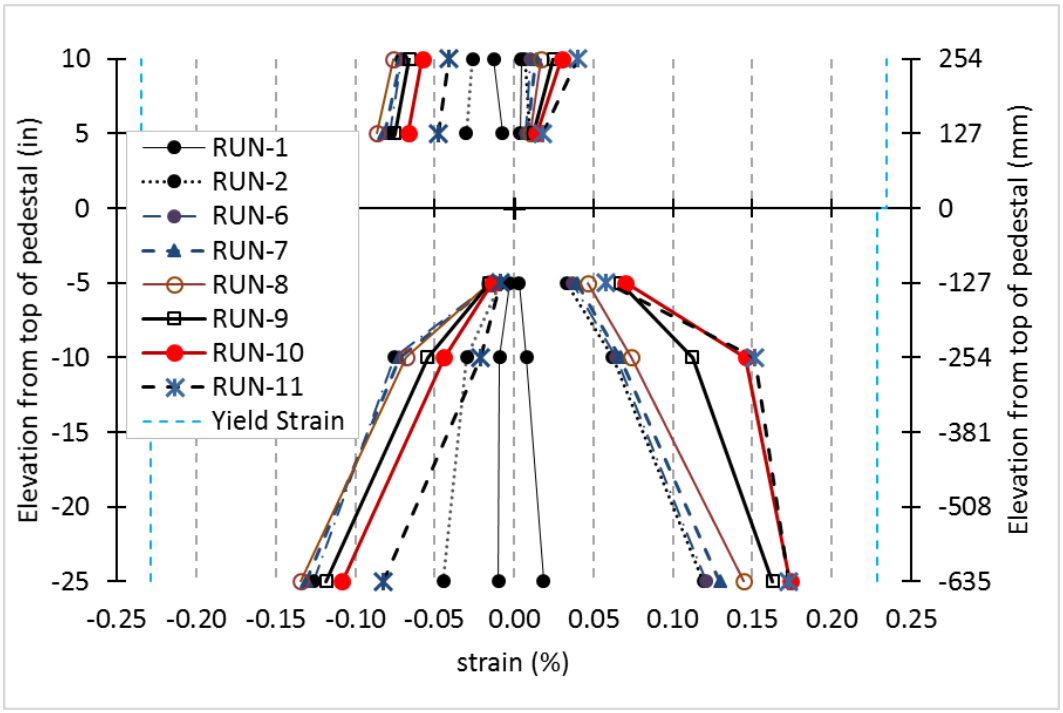

b)

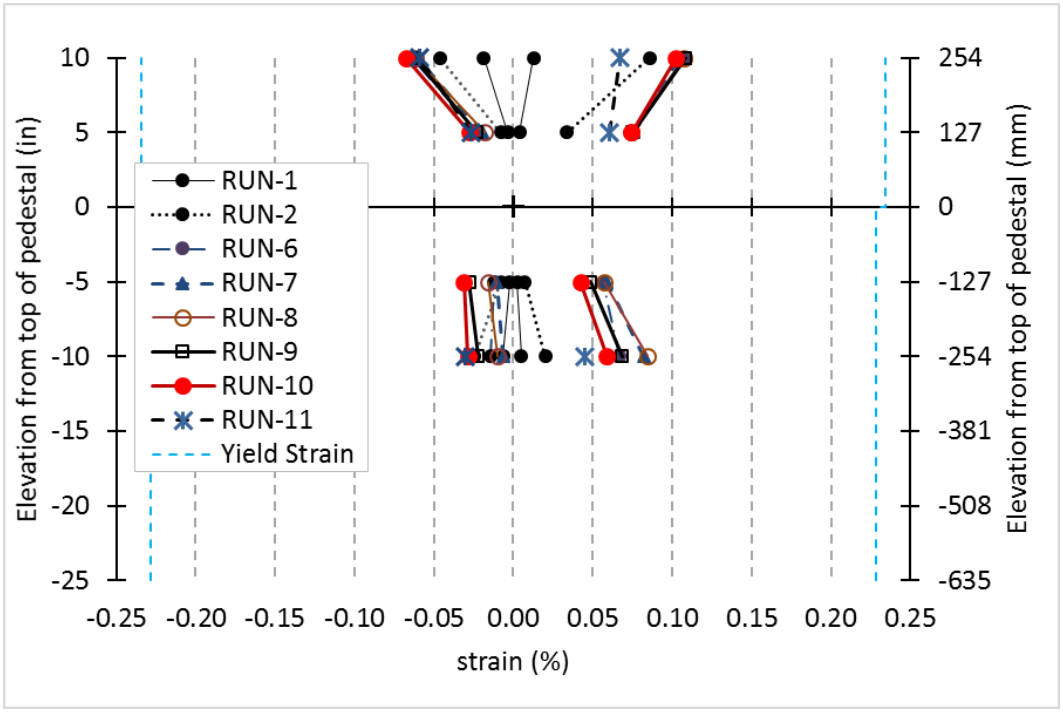

Fig. 3-59. BPSA strain profile for long. bars of column and pedestal near CIP pipe-pin a)south b)north

a)

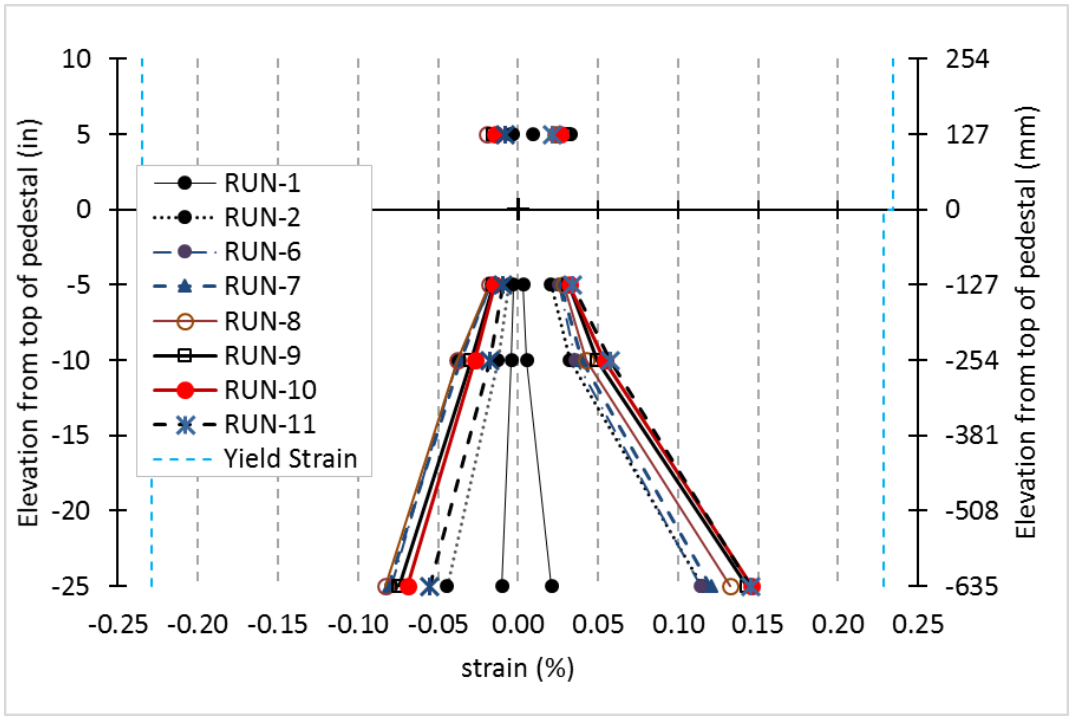

b)

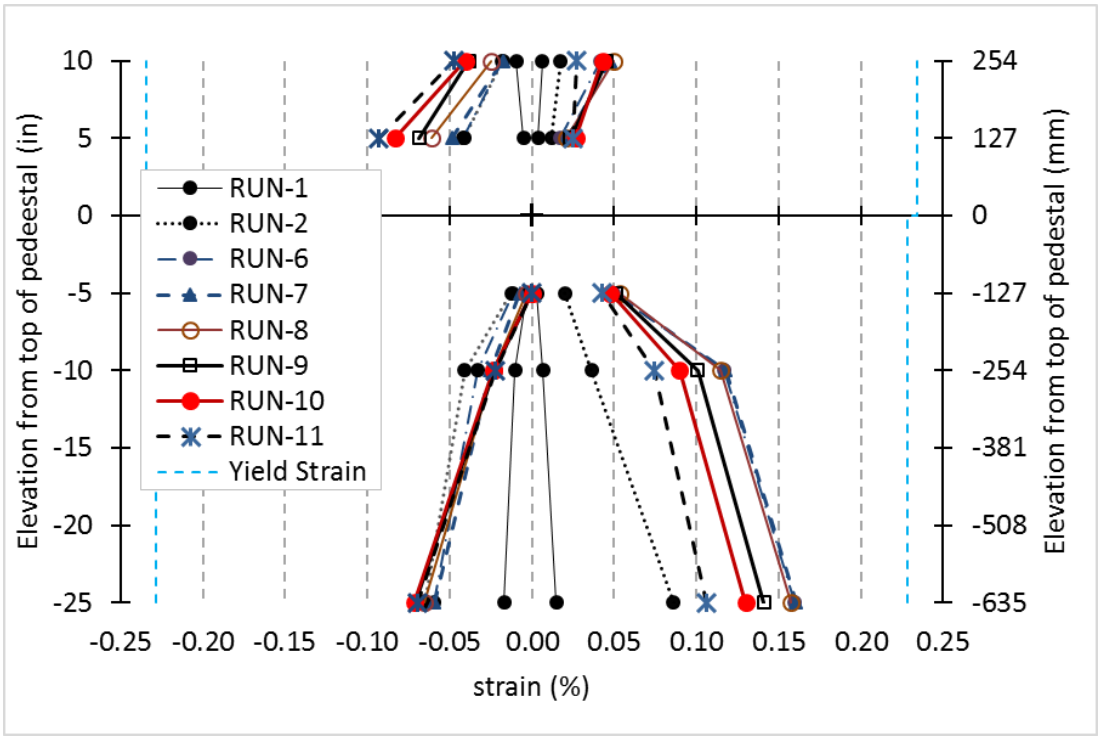

Fig. 3-60. BPSA strain profile for long. bars of column and pedestal near PC pipe-pin a)south b)north

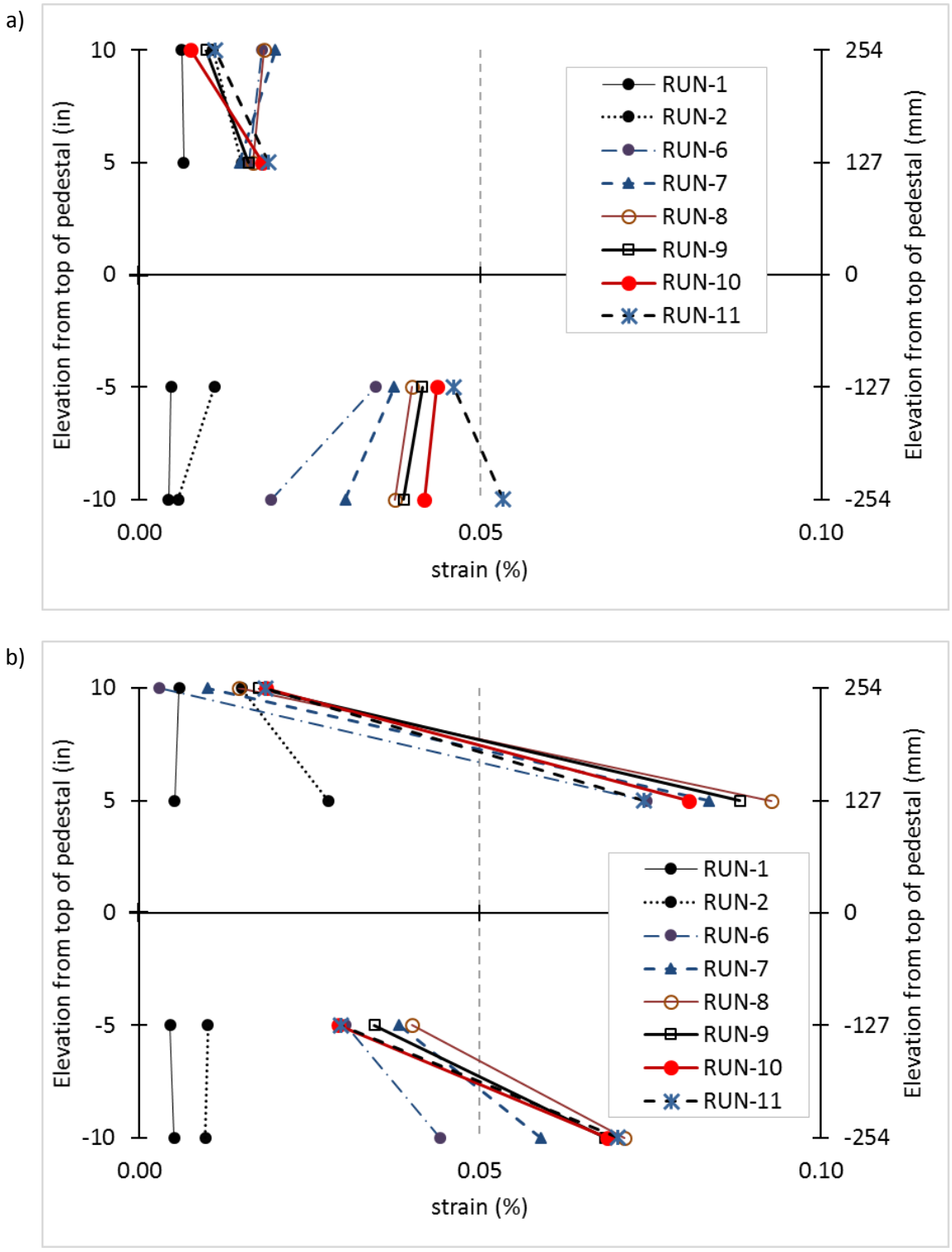

Fig. 3-61. BPSA strain profile for trans. bars of column and pedestal at CIP pipe-pin a) average of north and south b) average of east and west

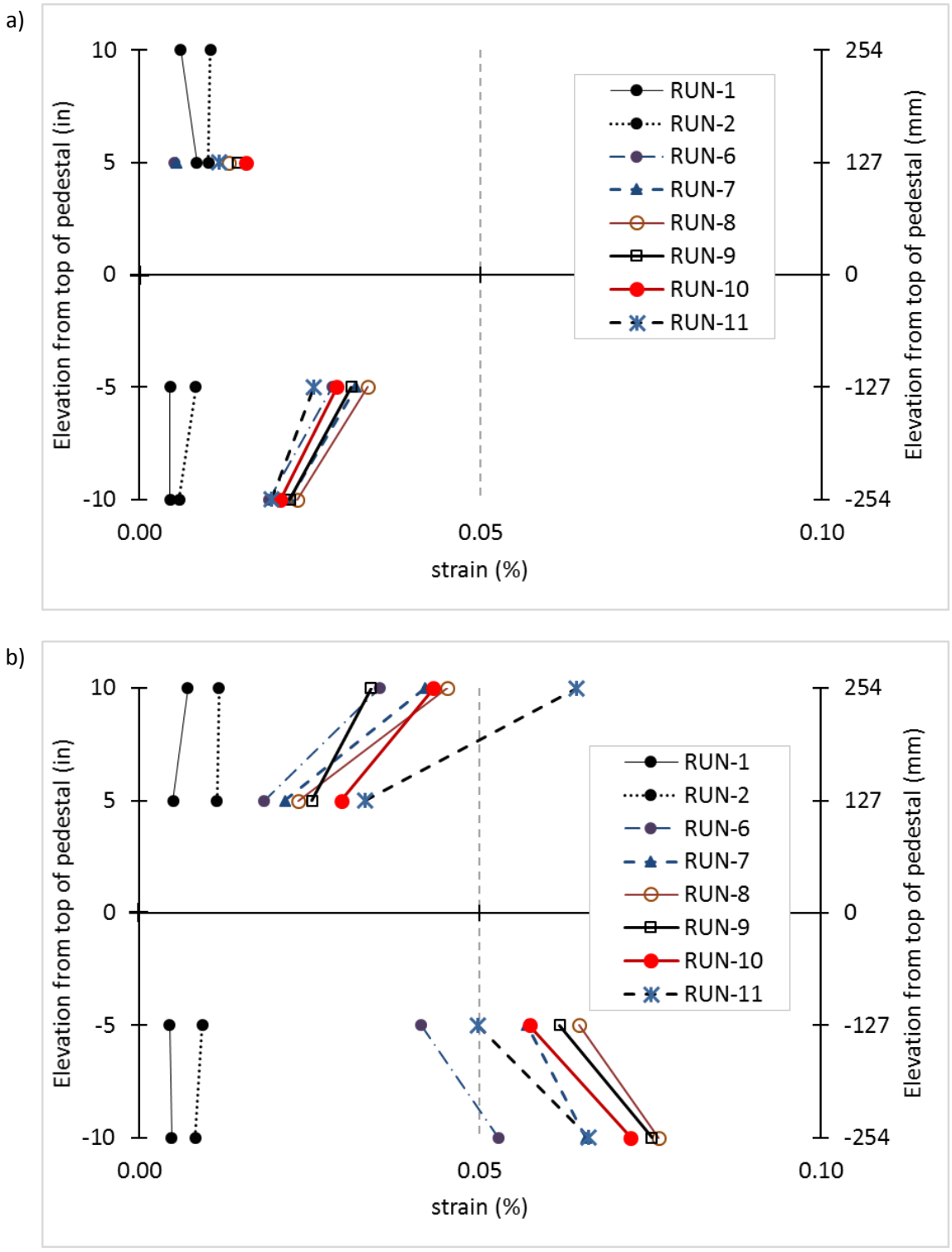

Fig. 3-62. BPSA strain profile for trans. bars of column and pedestal at PC pipe-pin a) average of north and south b) average of east and west

a)

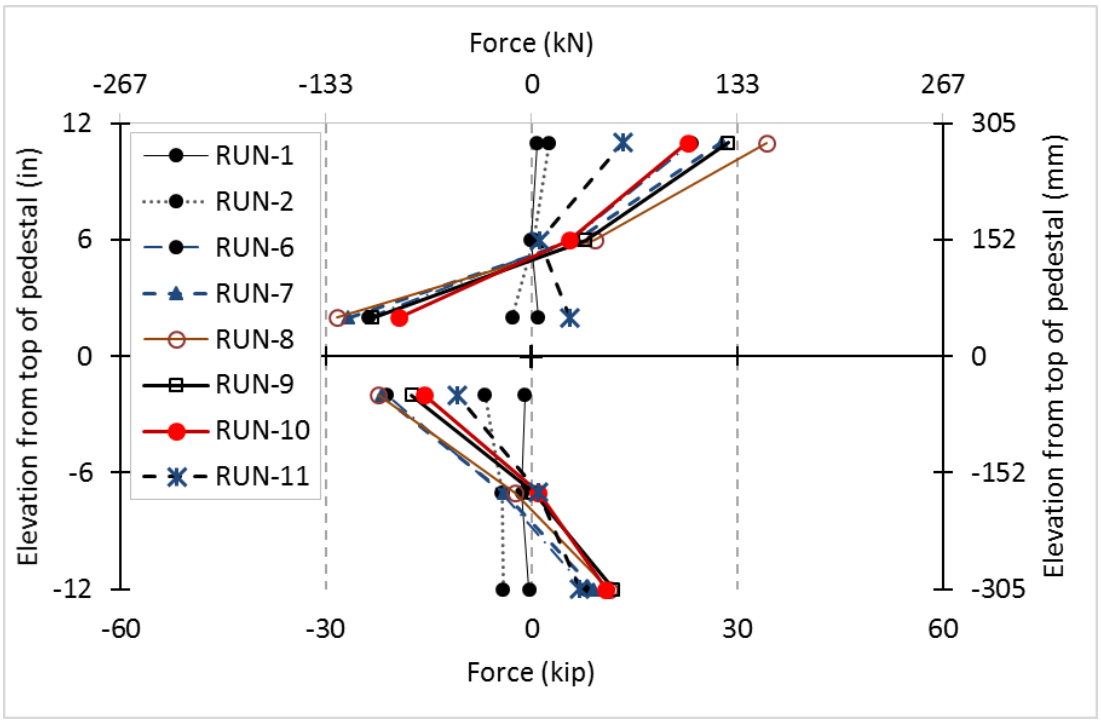

b)

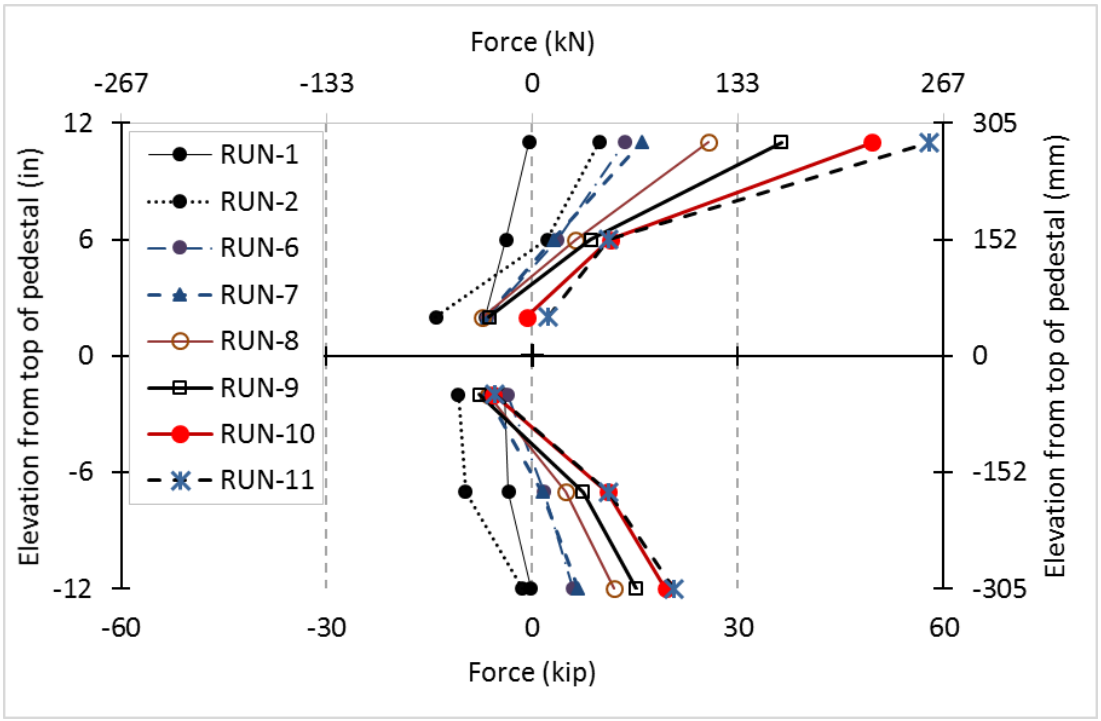

Fig. 3-63. Profile of axial force in CIP pipes when column is under a) compression b) tension

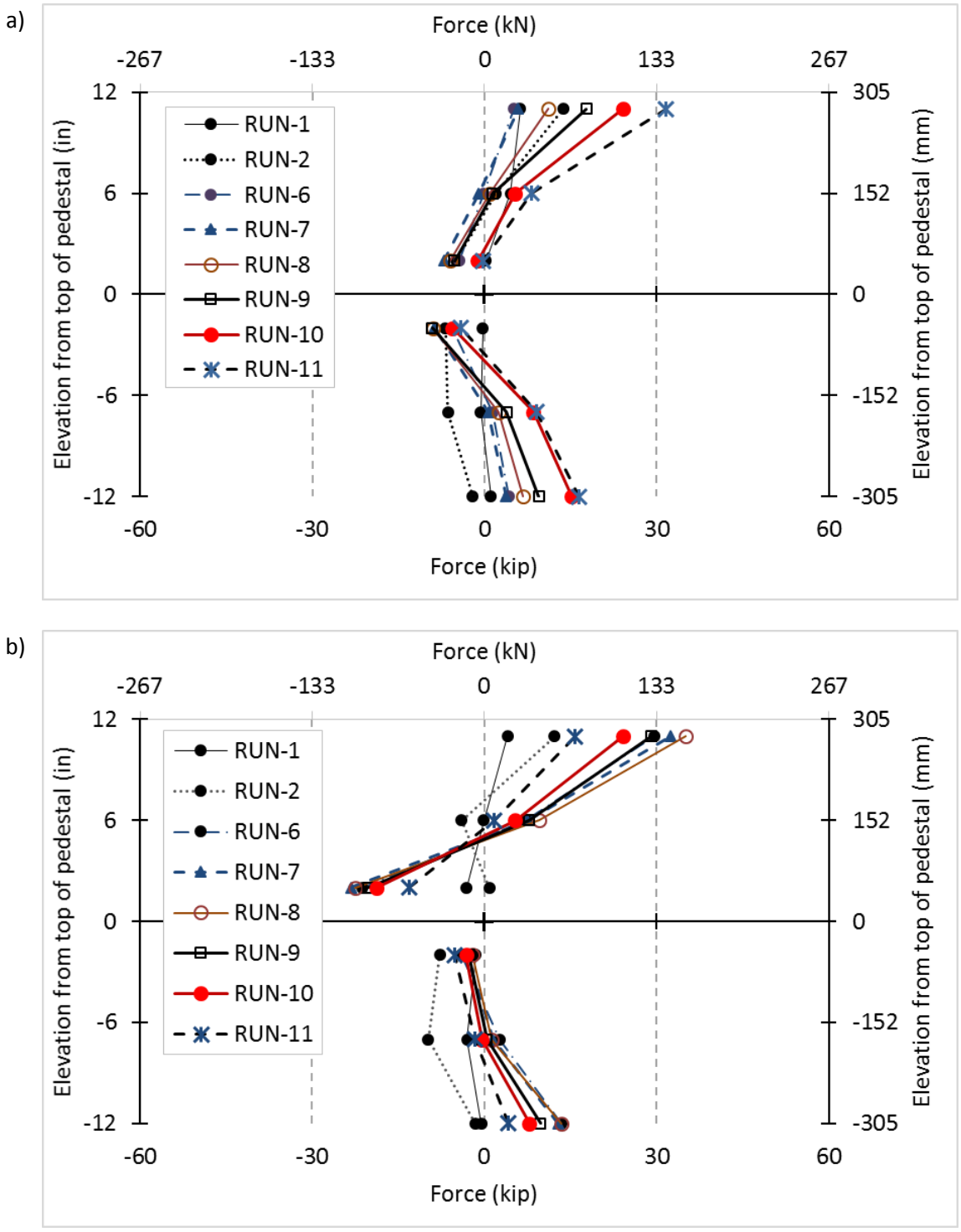

Fig. 3-64. Profile of axial force in PC pipes when column is under a) compression b) tension

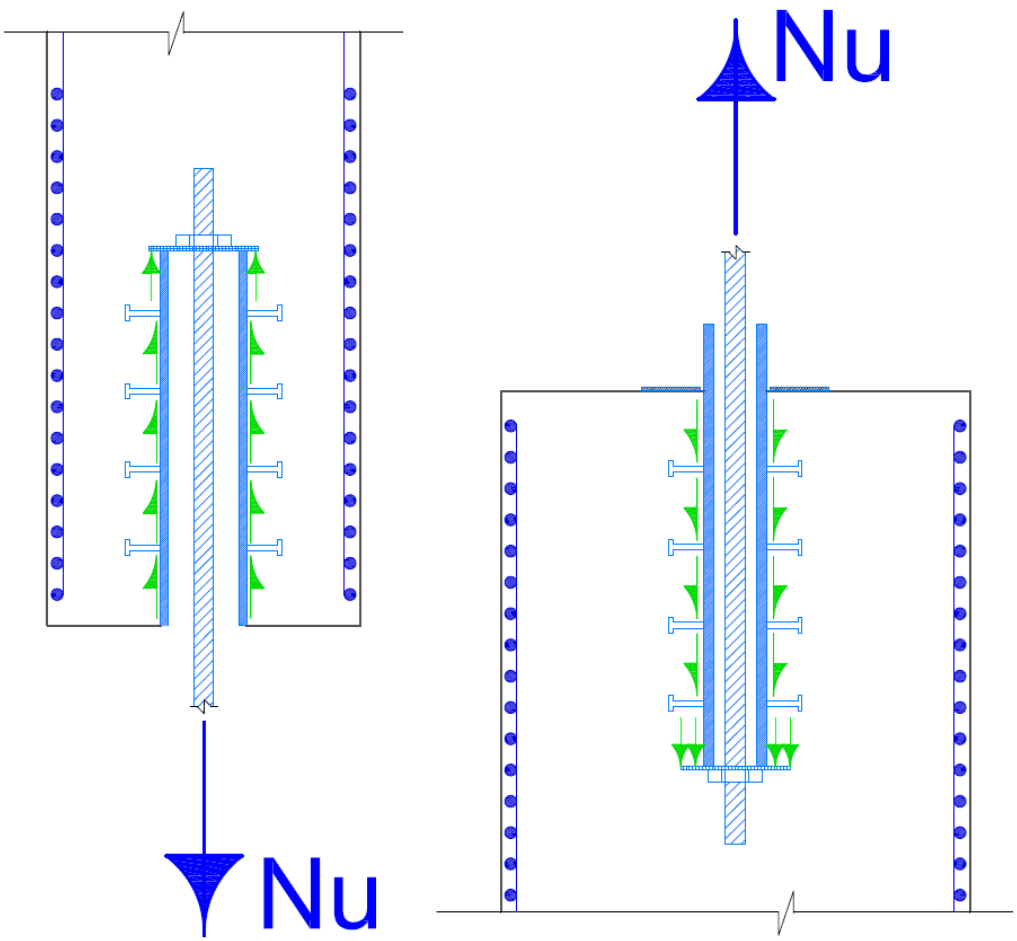

Fig. 3-65. Friction distribution on pipes

a)

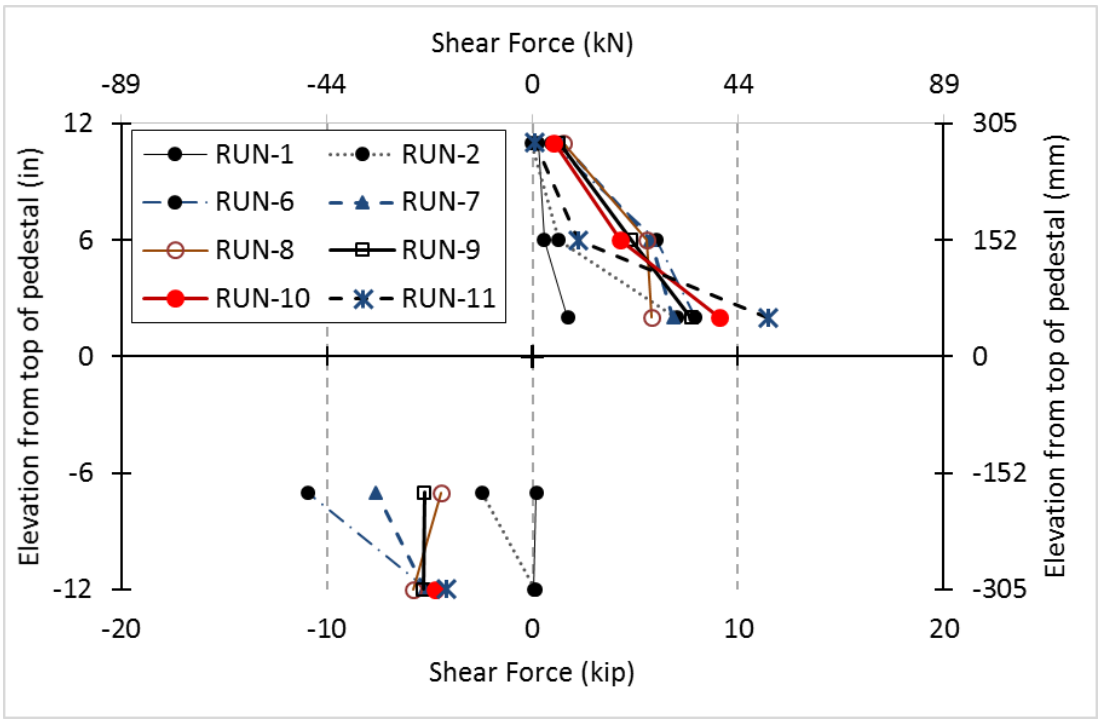

b)

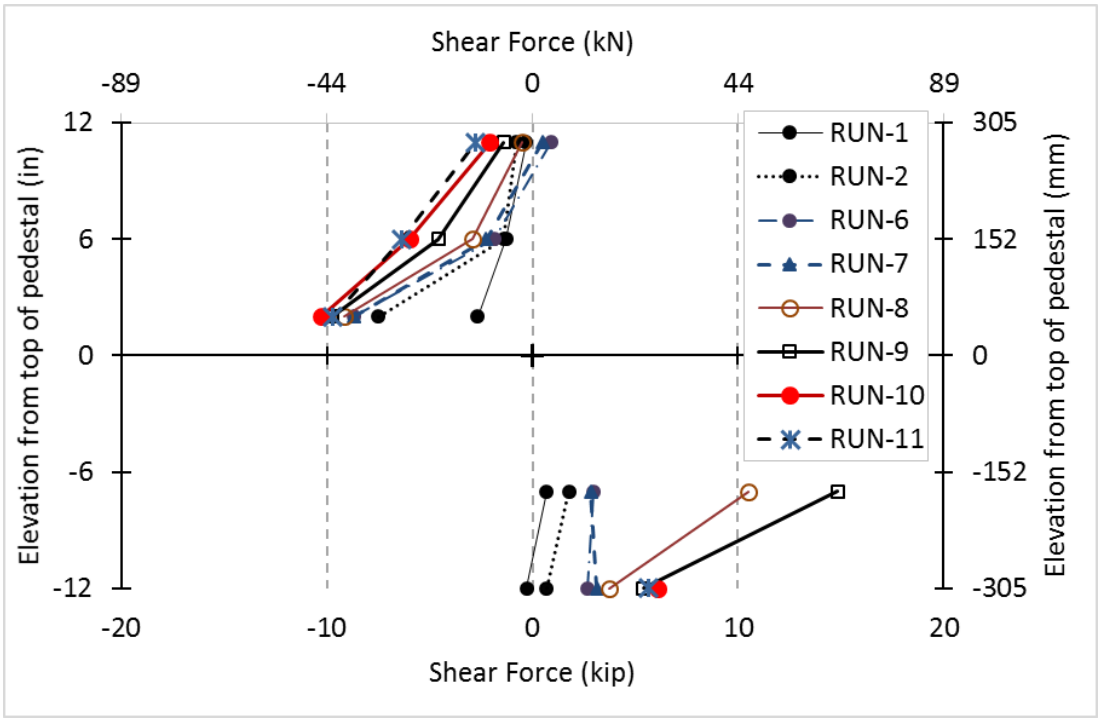

Fig. 3-66. Profile of shear force in CIP pipes when column is under a) compression b) tension

a)

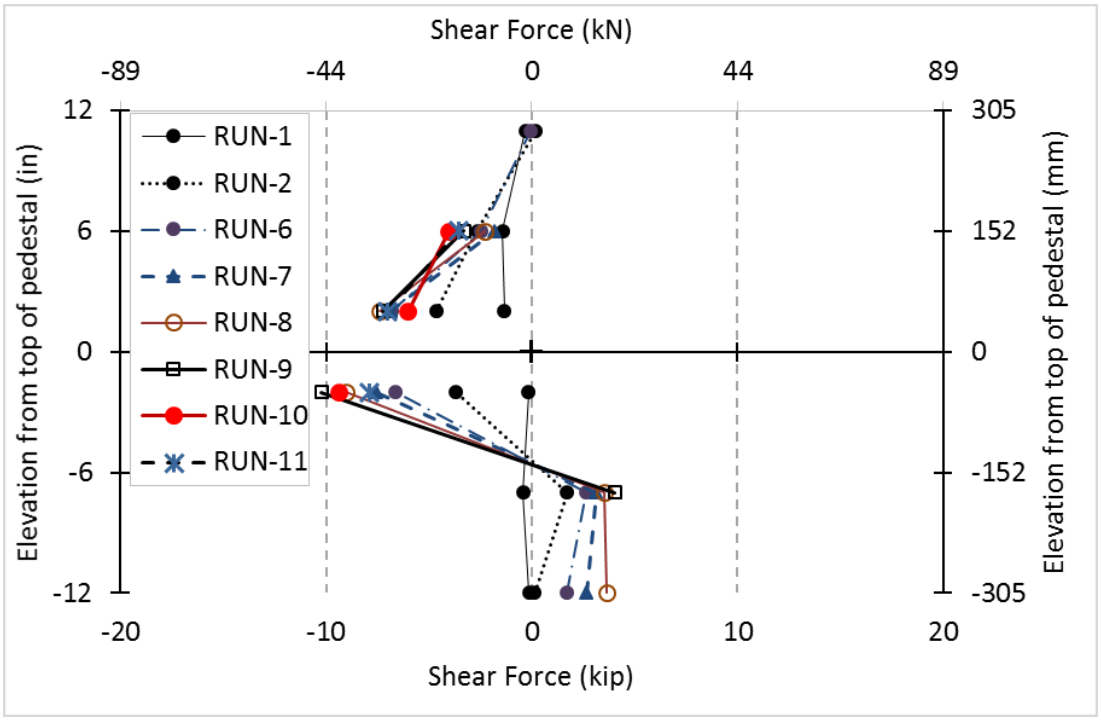

b)

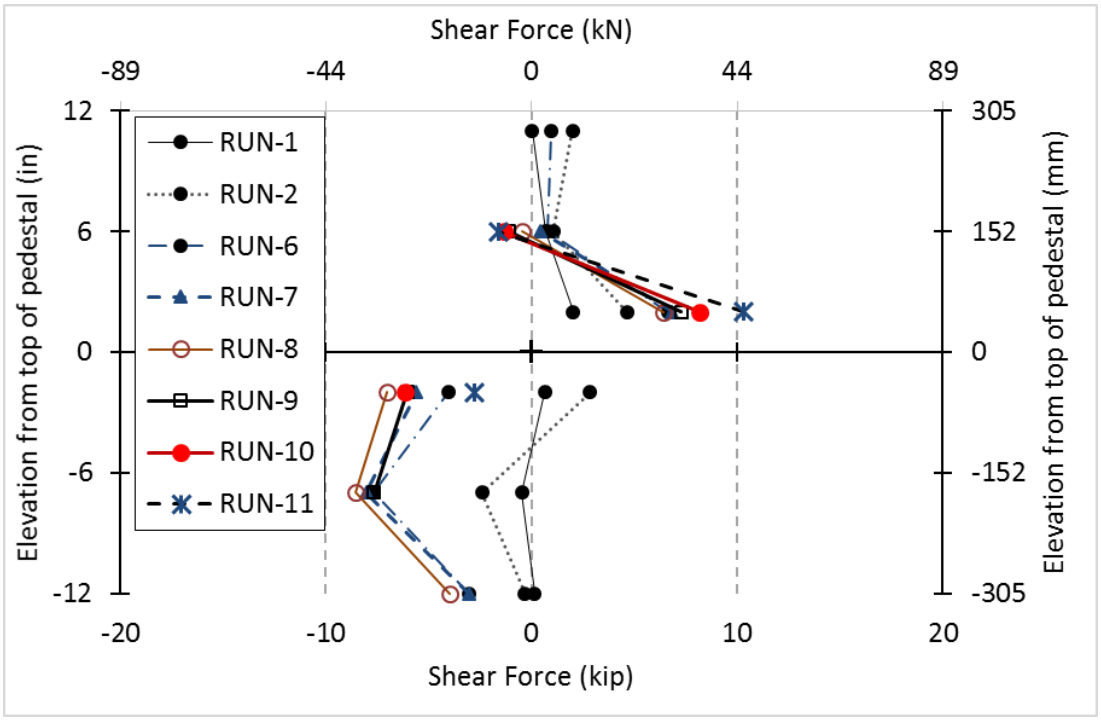

Fig. 3-67. Profile of shear force in PC pipes when column is under a)compression b)tension

a)

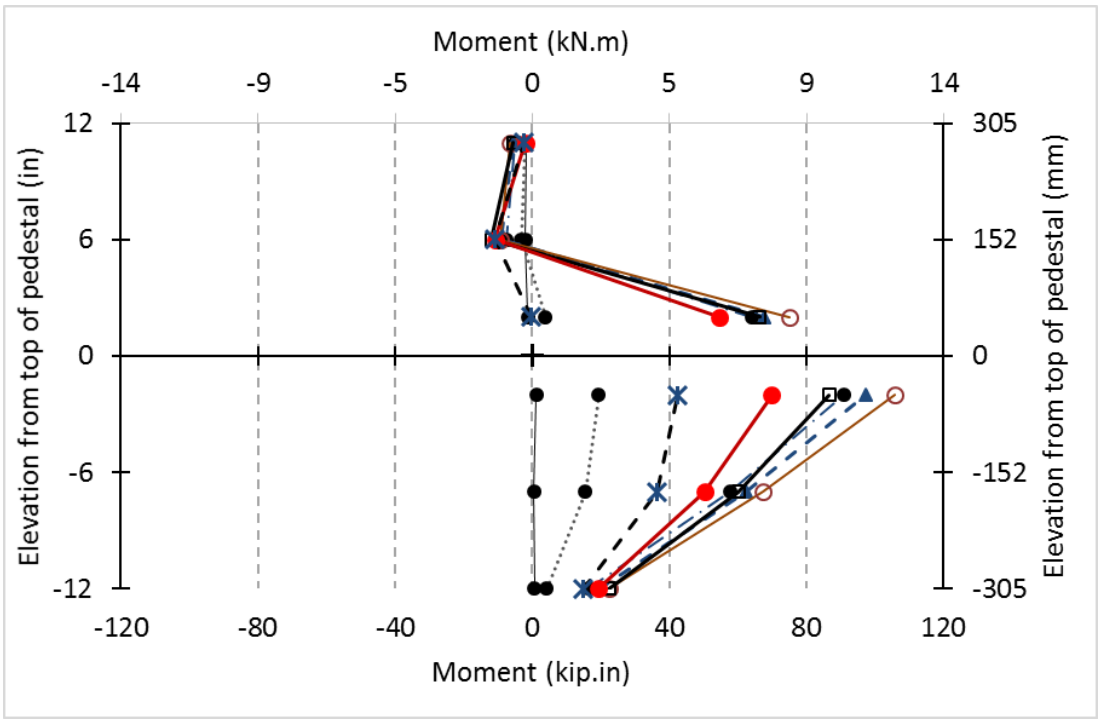

b)

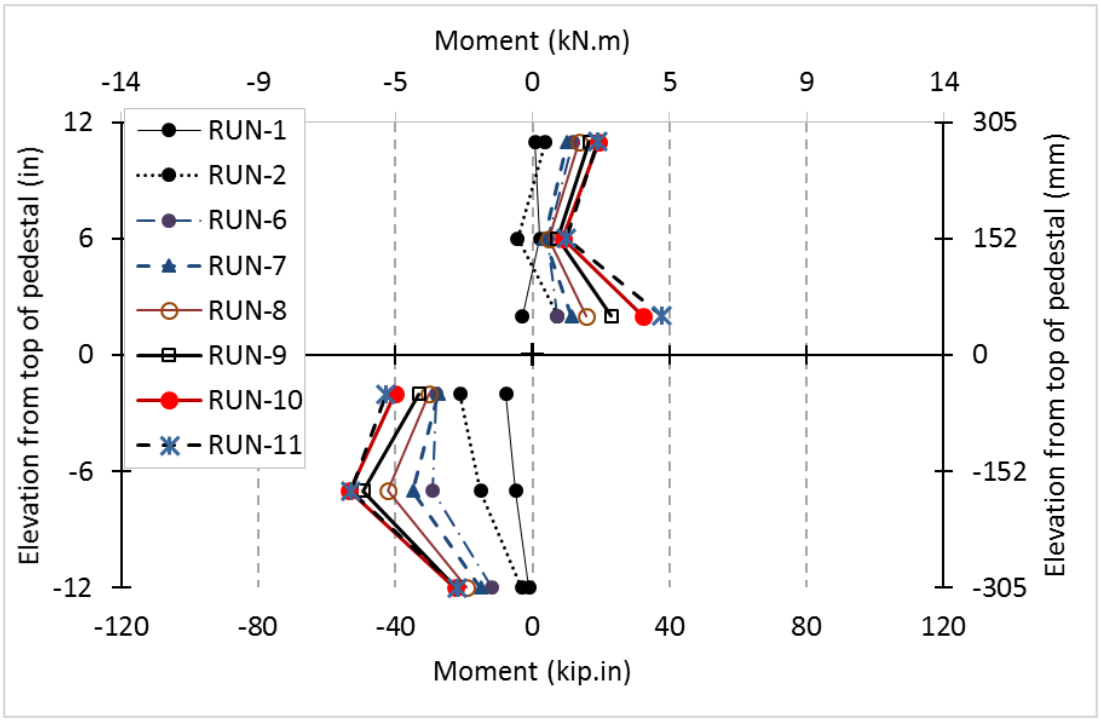

Fig. 3-68. Profile of bending in CIP pipes when column is under a) compression b) tension

a)

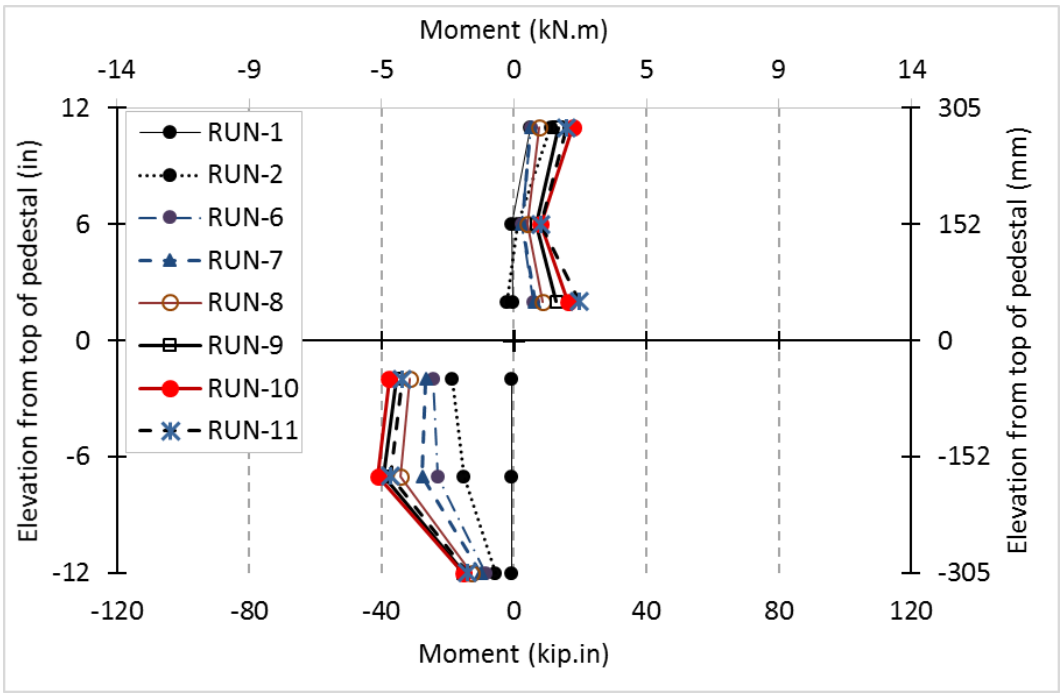

b)

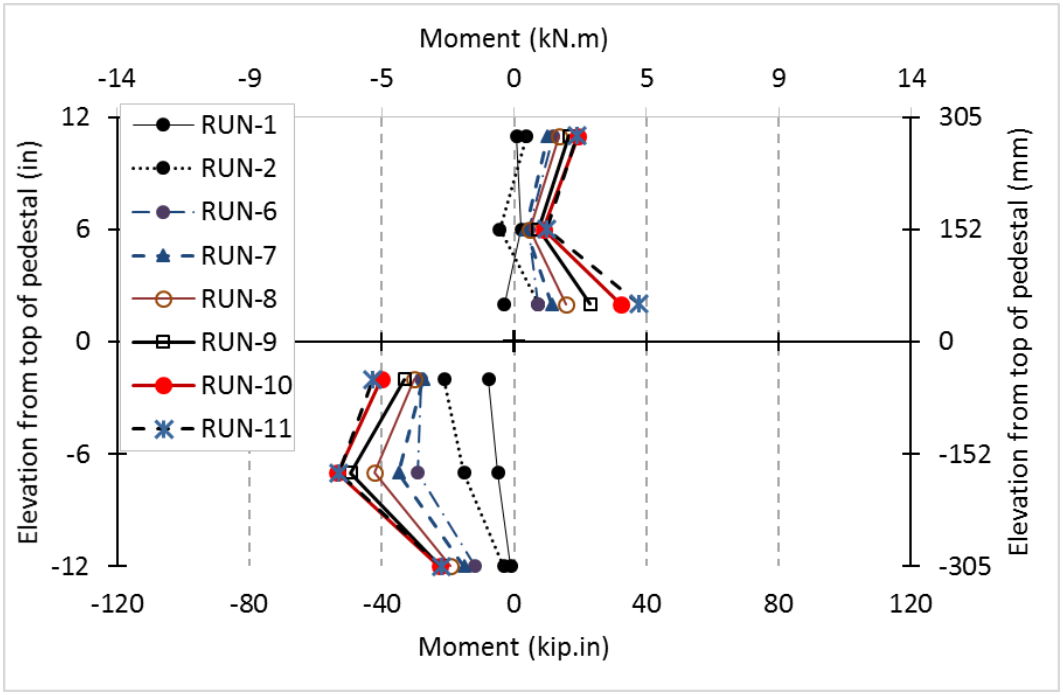

Fig. 3-69. Profile of bending in PC pipes when column is under a) compression b) tension

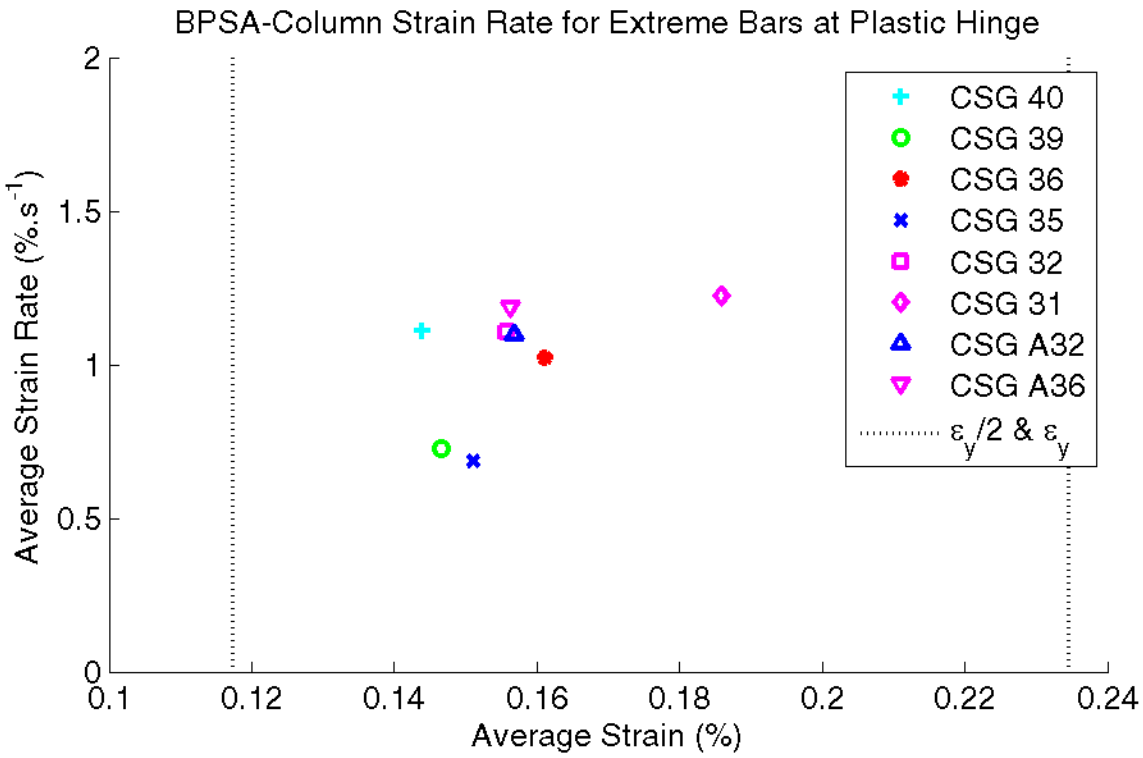

Fig. 3-70. BPSA average strain rate in longitudinal bars in plastic hinges zone of columns

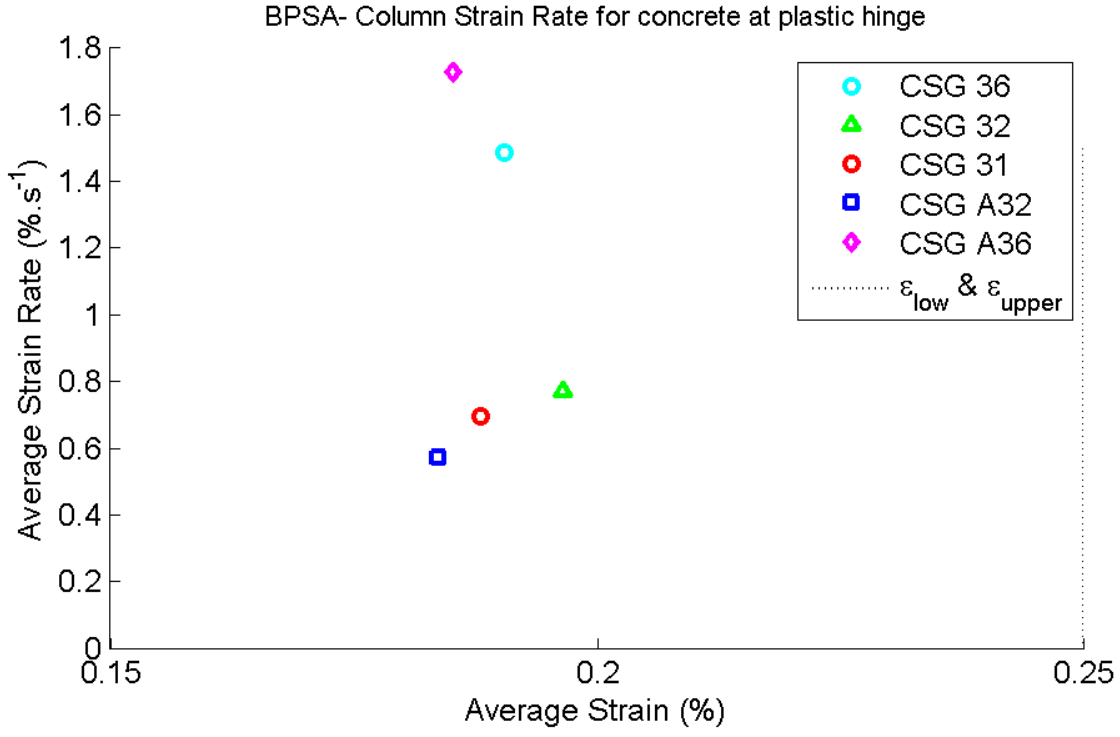

Fig. 3-71. BPSA average strain rate in concrete in plastic hinge zone of columns

a)

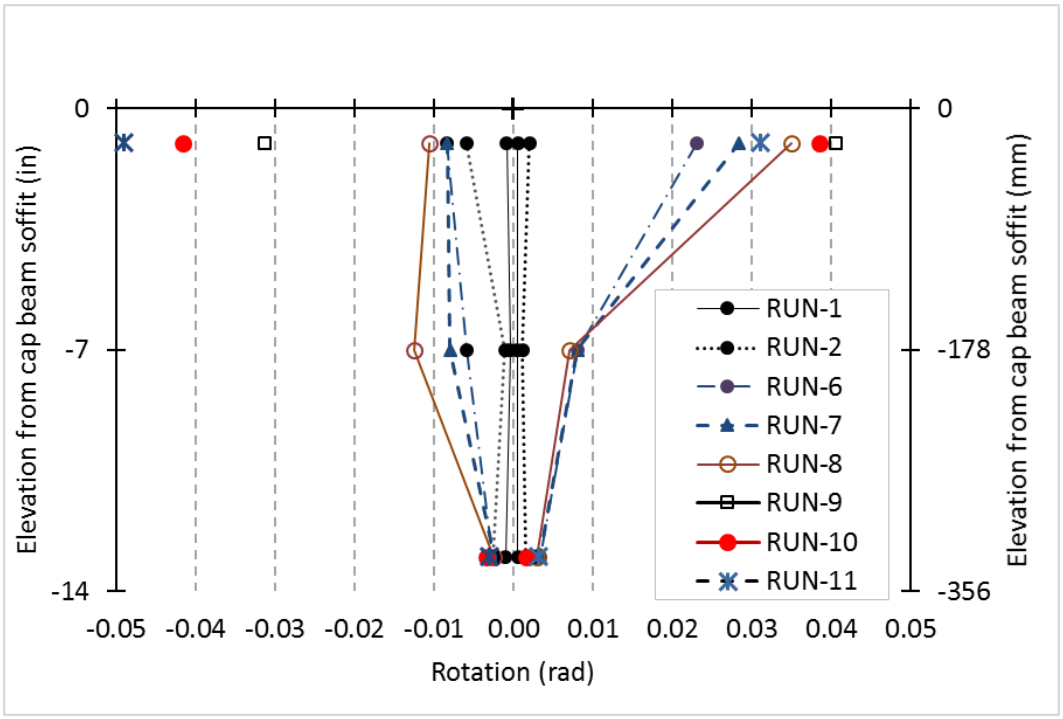

b)

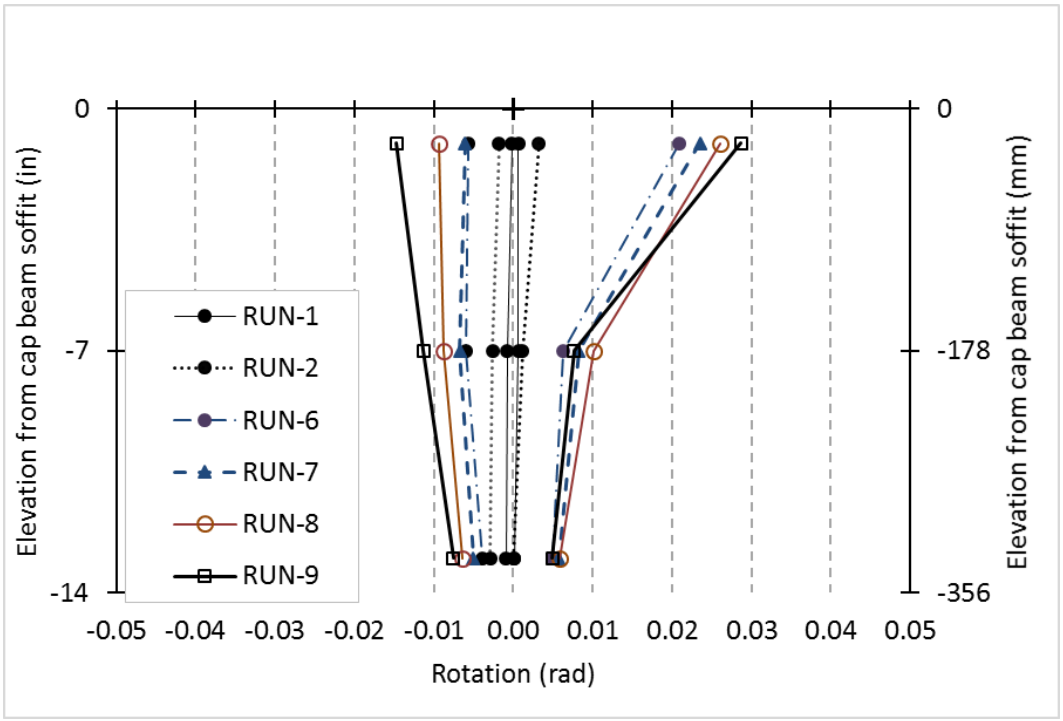

Fig. 3-72. BPSA Profile of maximum and minimum of rotation at top of a)CIP b) PC

a)

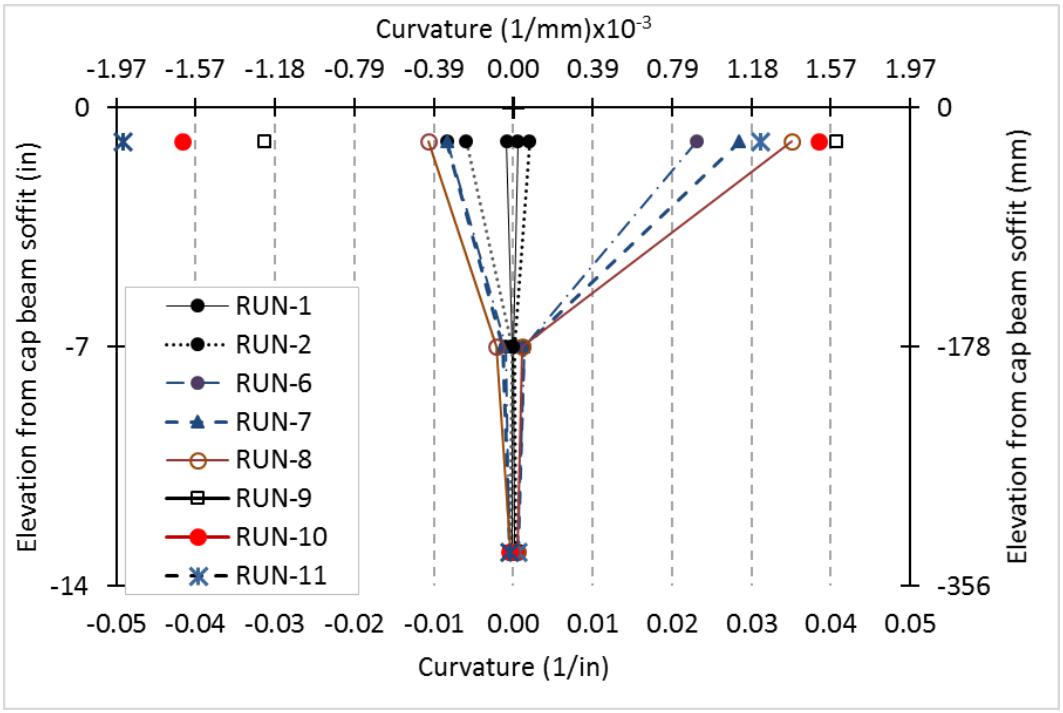

b)

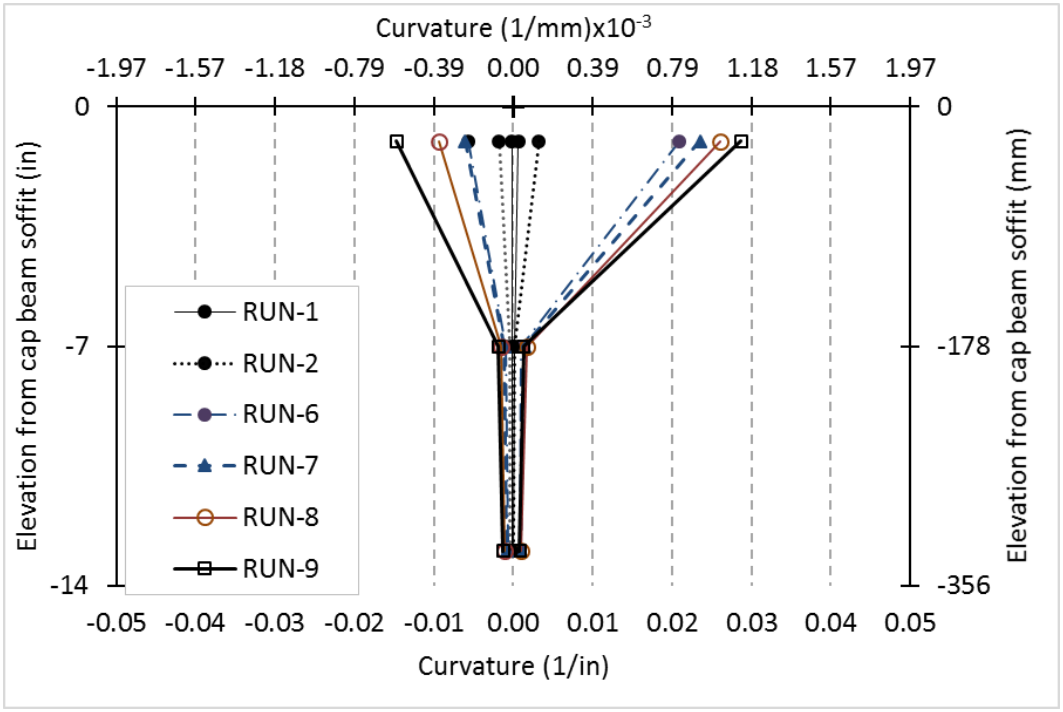

Fig. 3-73. BPSA Profile of maximum and minimum of curvature at top of a)CIP b) PC

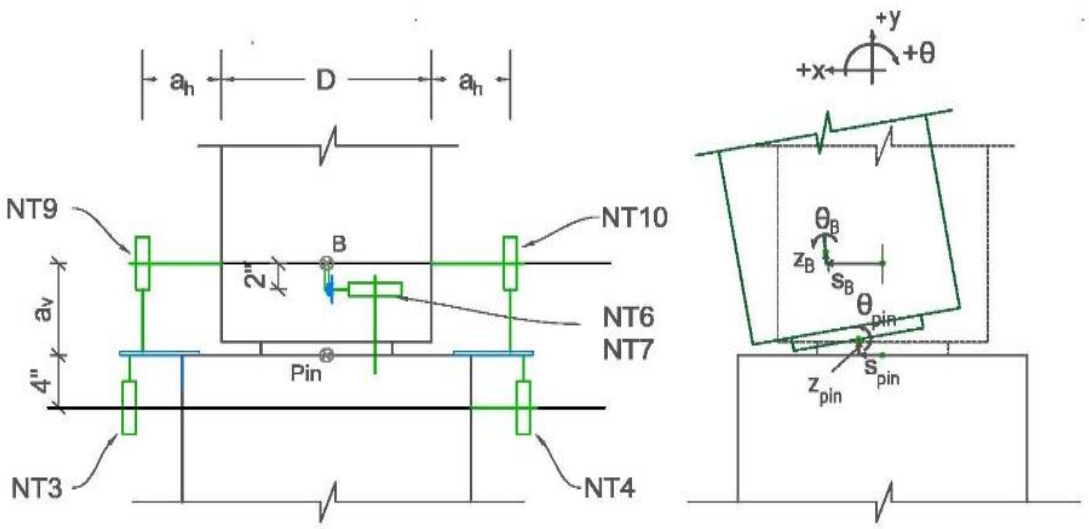

Fig. 3-74. Rigid body movements of the pins

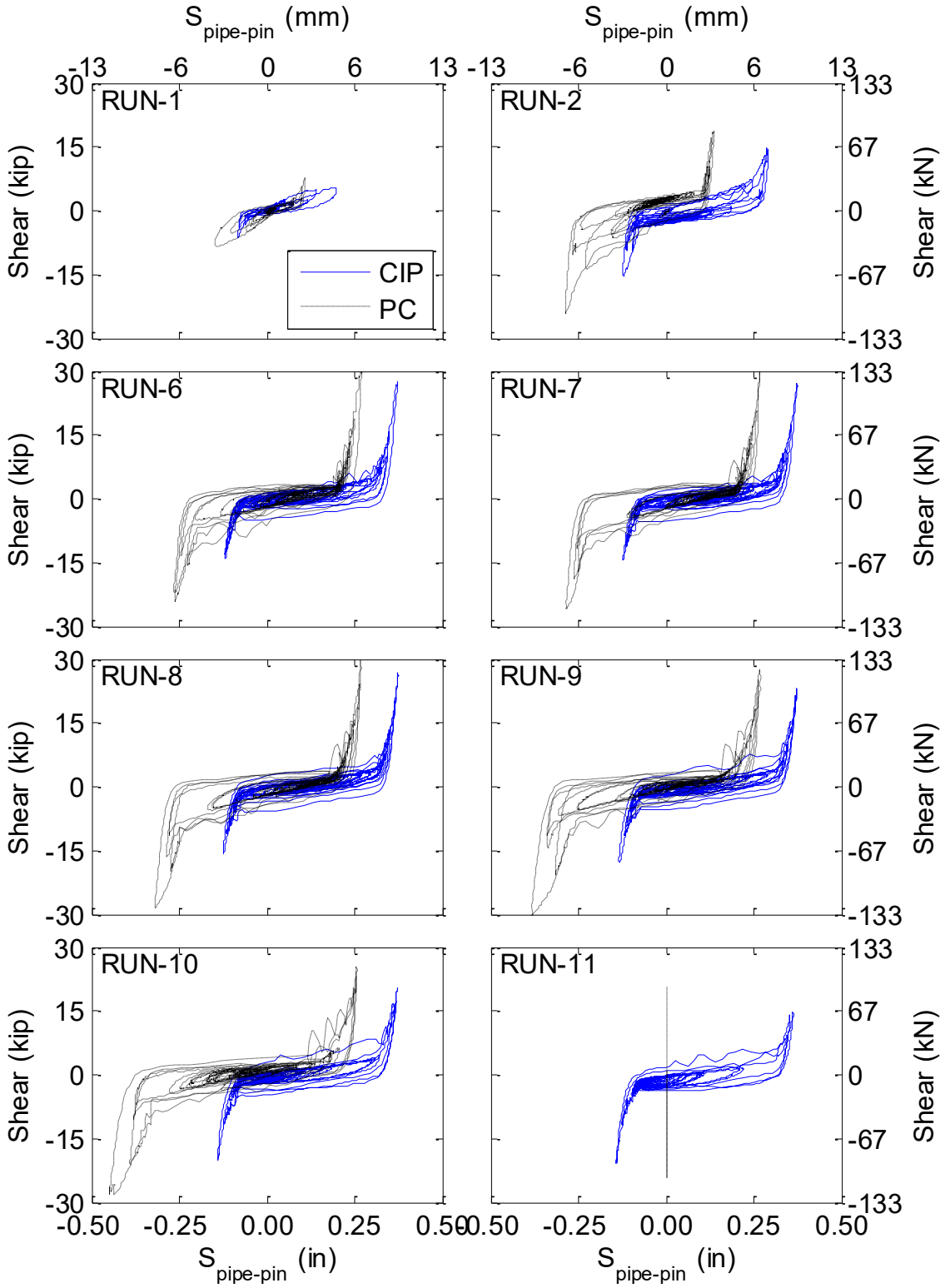

Fig. 3-75. BPSA pipe-pins shear-slip

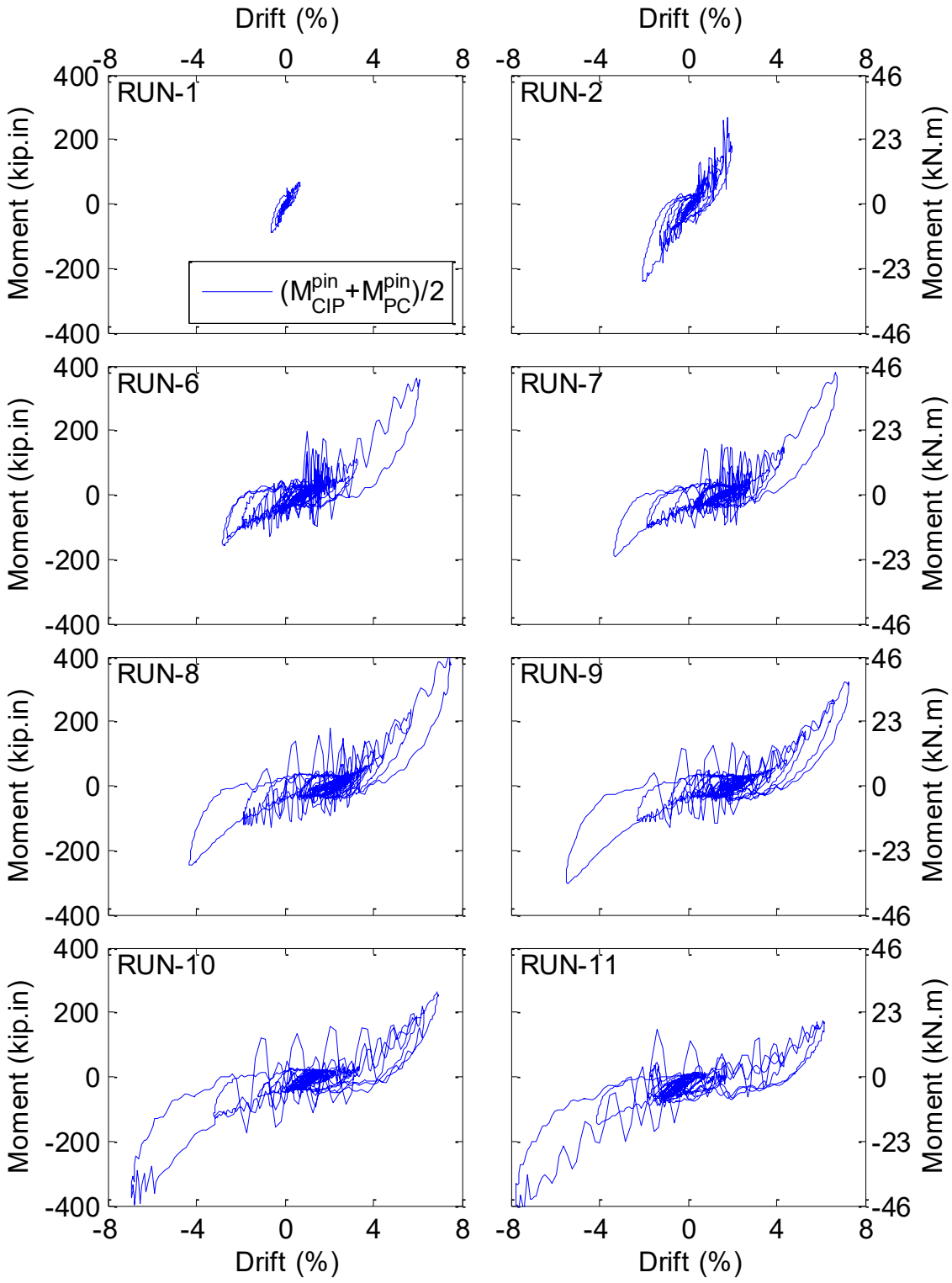

Fig. 3-76. BPSA average pipe-pin moments versus bent drift

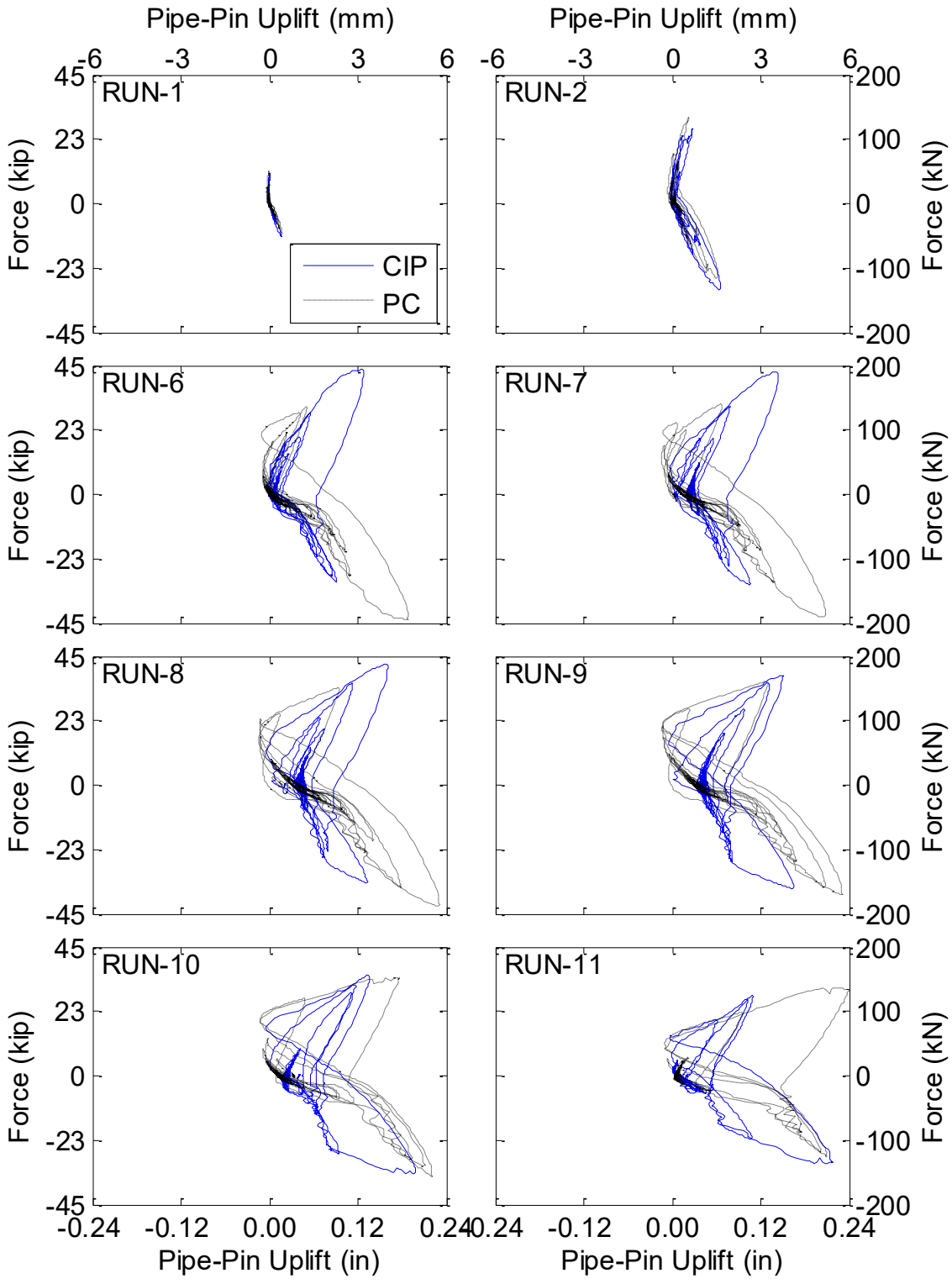

Fig. 3-77. BPSA pipe-pin axial force-uplift

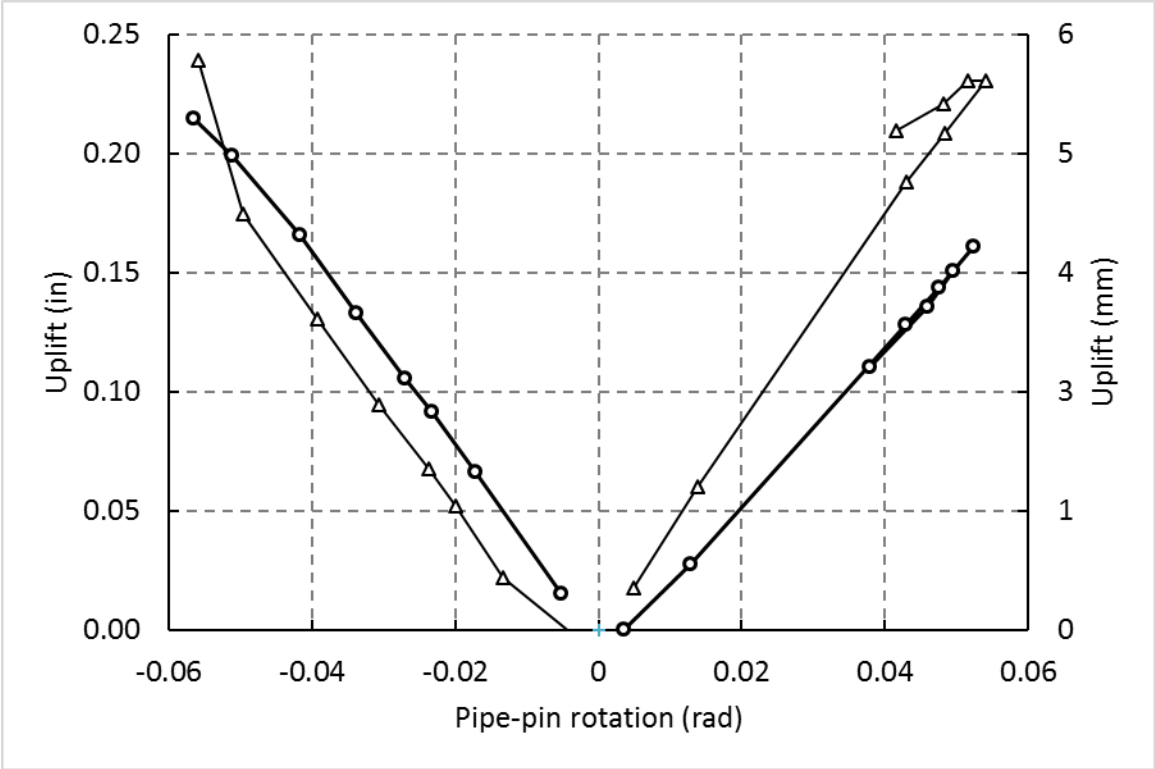

Fig. 3-78. BPSA instantaneous center of rotation for pipe-pin

Fig. 3-79. BRSA fundamental periods

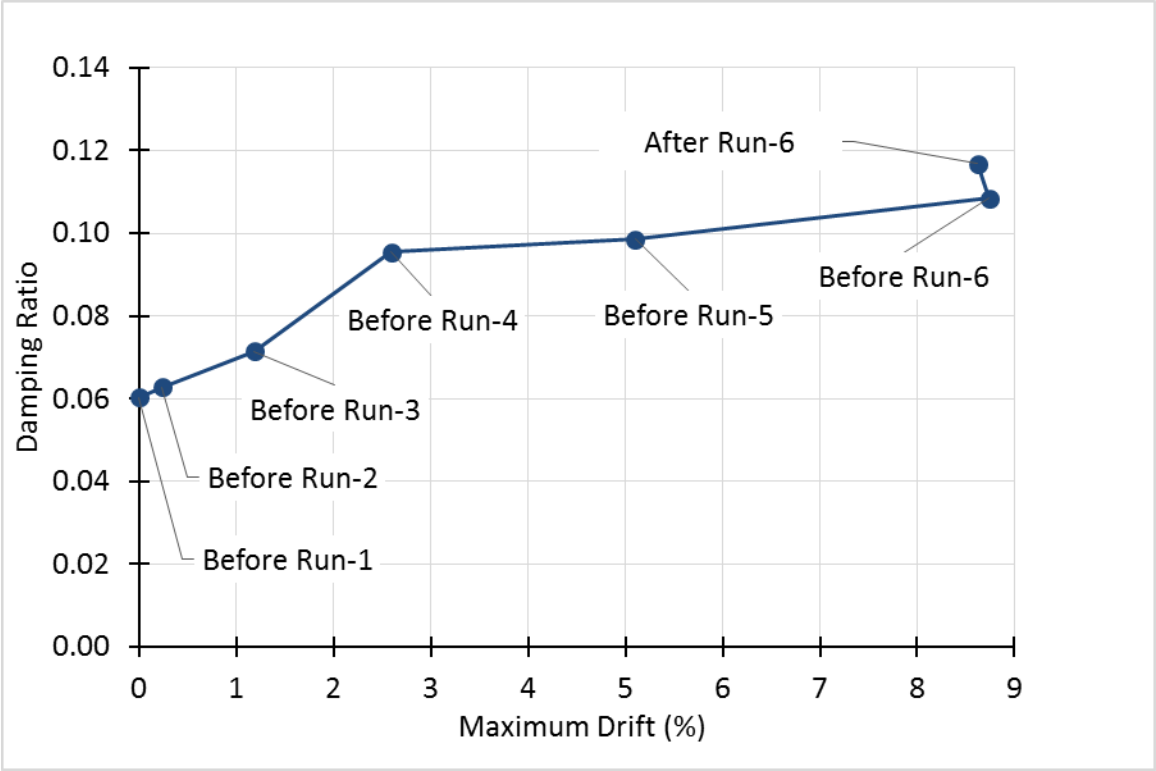

Fig. 3-80. BRSA Damping ratios

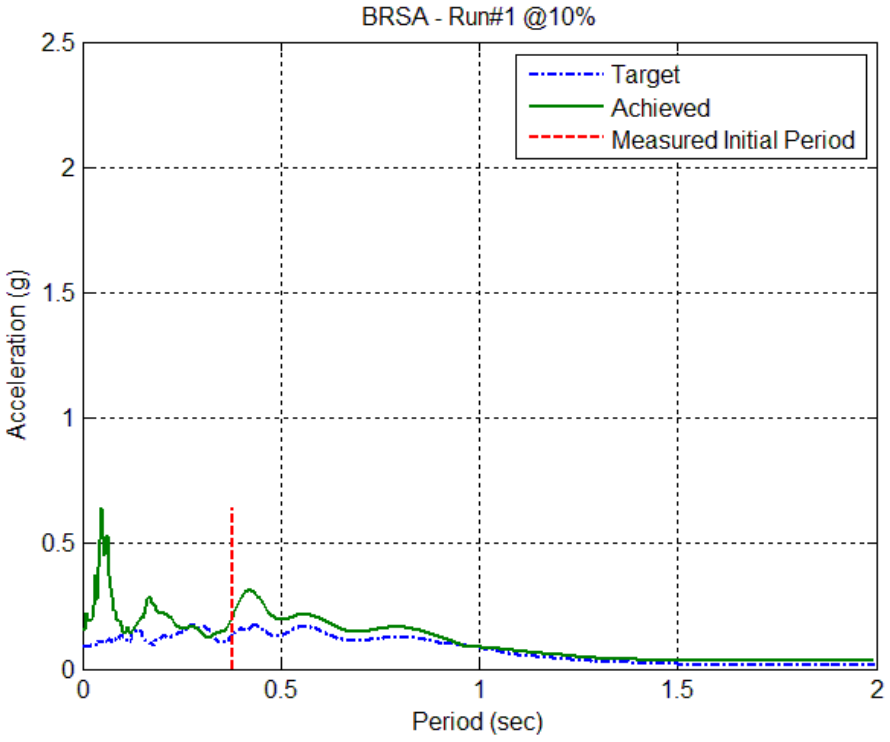

Fig. 3-81. BRSA target vs. achieved motion response spectra for Run-1

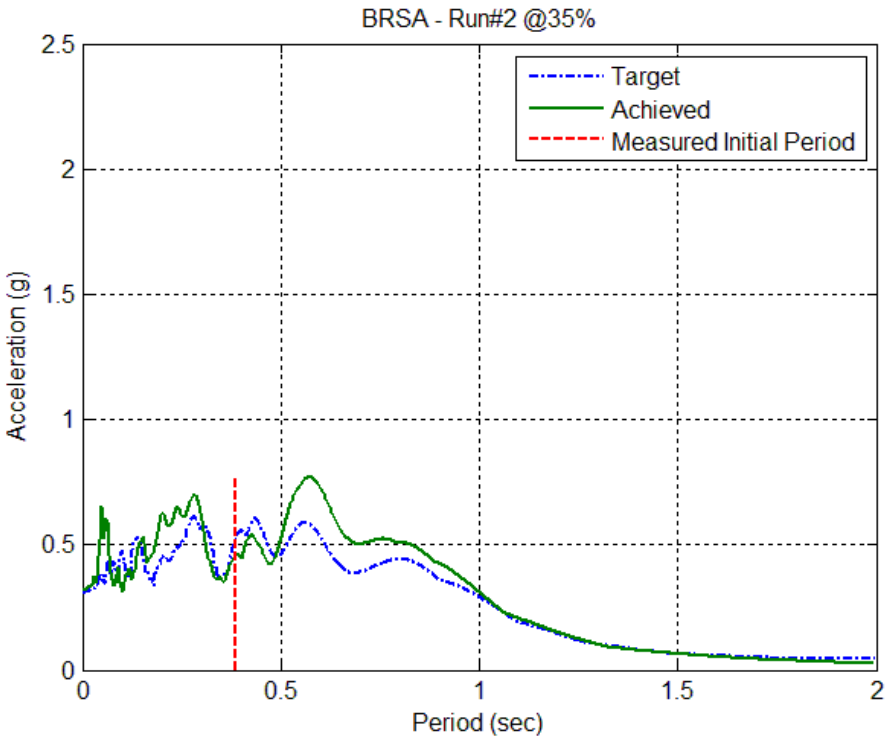

Fig. 3-82. BRSA target vs. achieved motion response spectra for Run-2

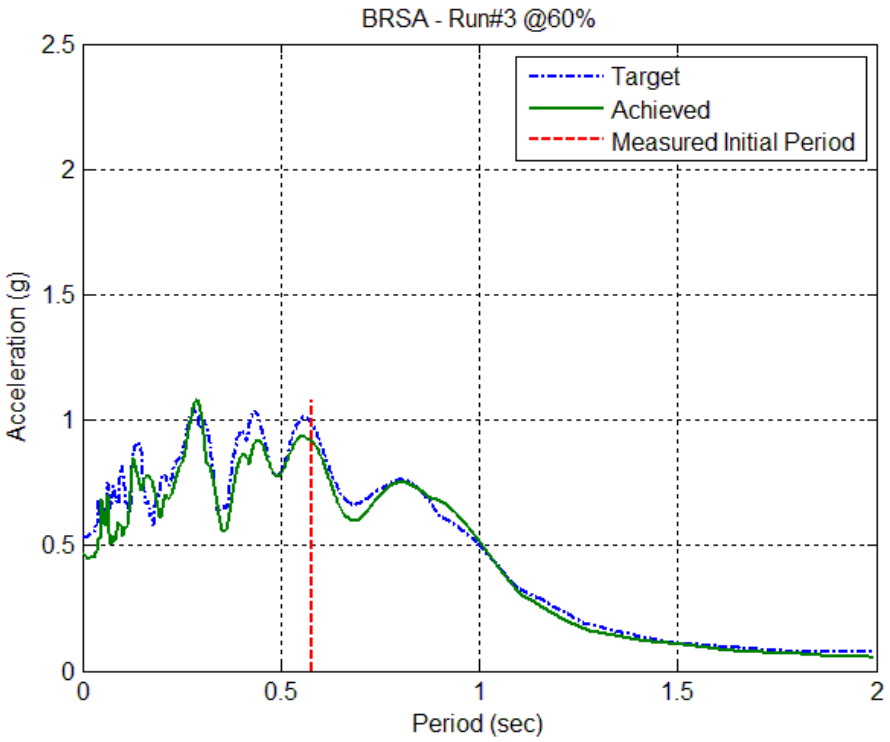

Fig. 3-83. BRSA target vs. achieved motion response spectra for Run-3

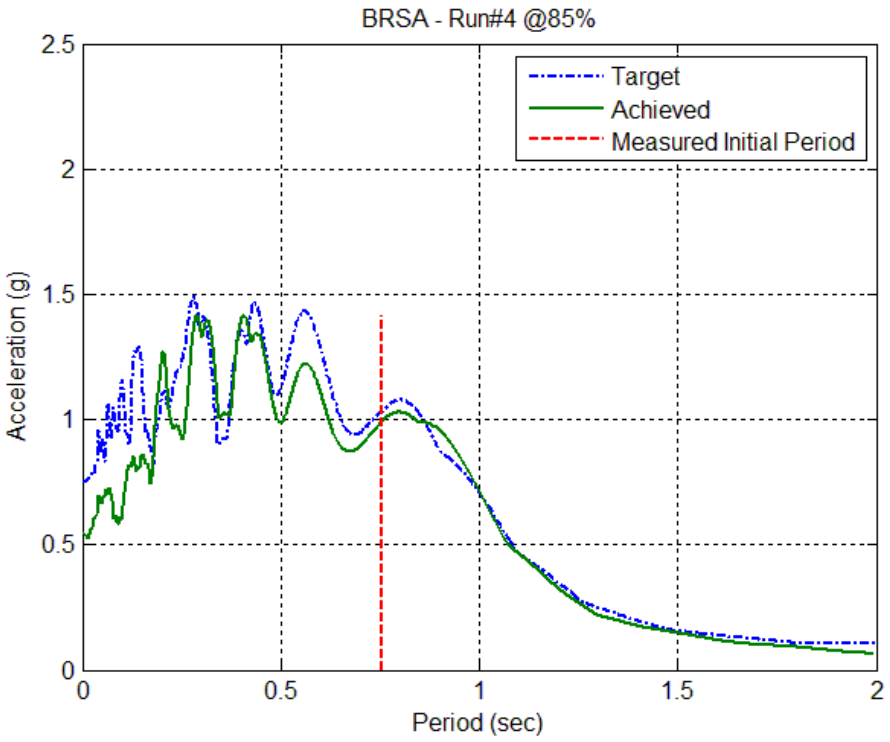

Fig. 3-84. BRSA target vs. achieved motion response spectra for Run-4

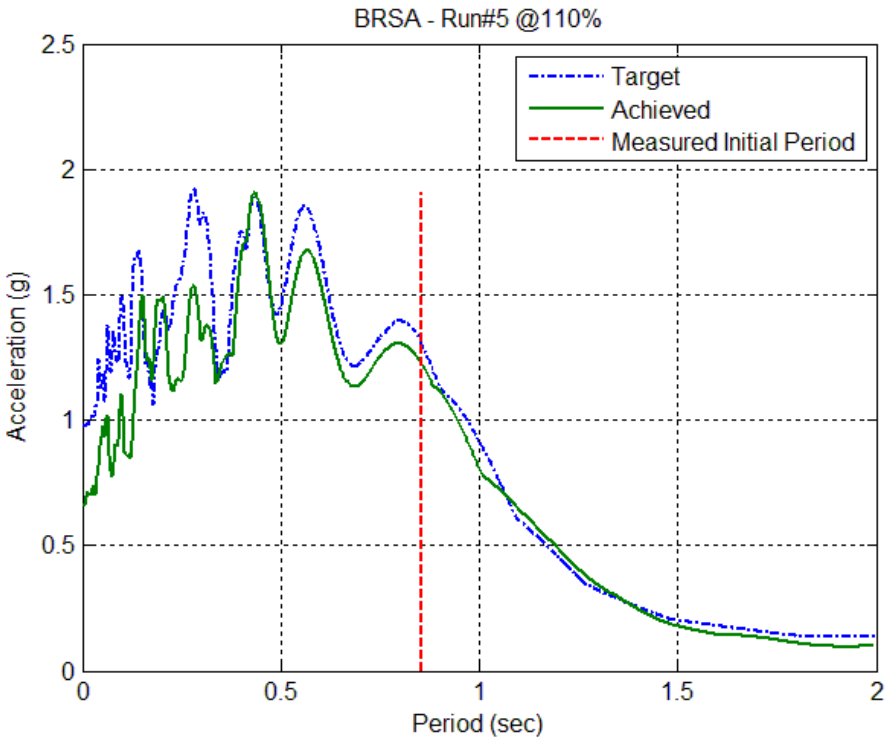

Fig. 3-85. BRSA target vs. achieved motion response spectra for Run-5

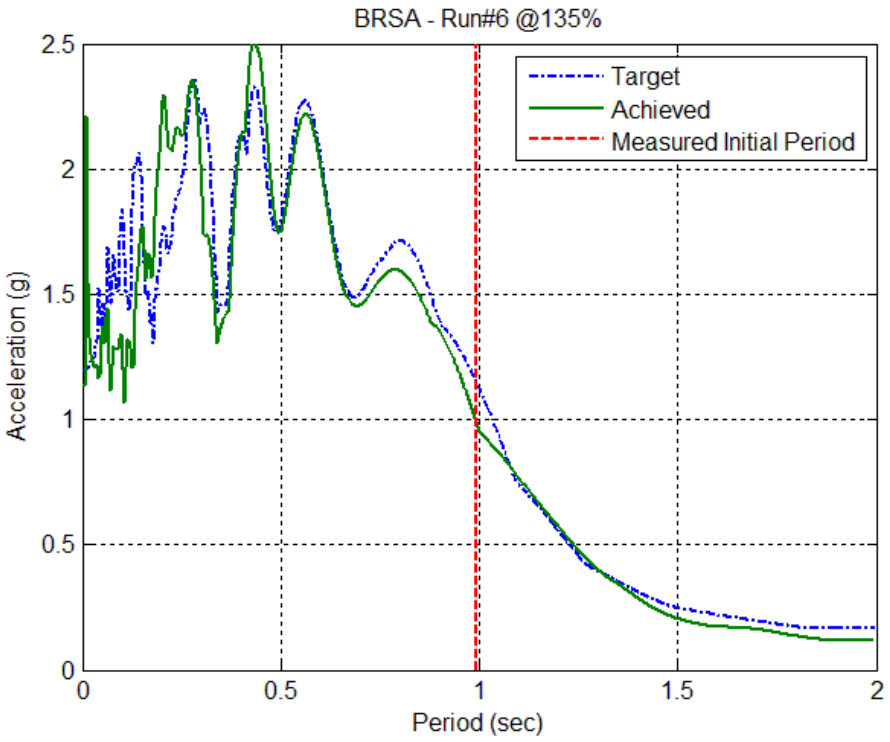

Fig. 3-86. BRSA target vs. achieved motion response spectra for Run-6

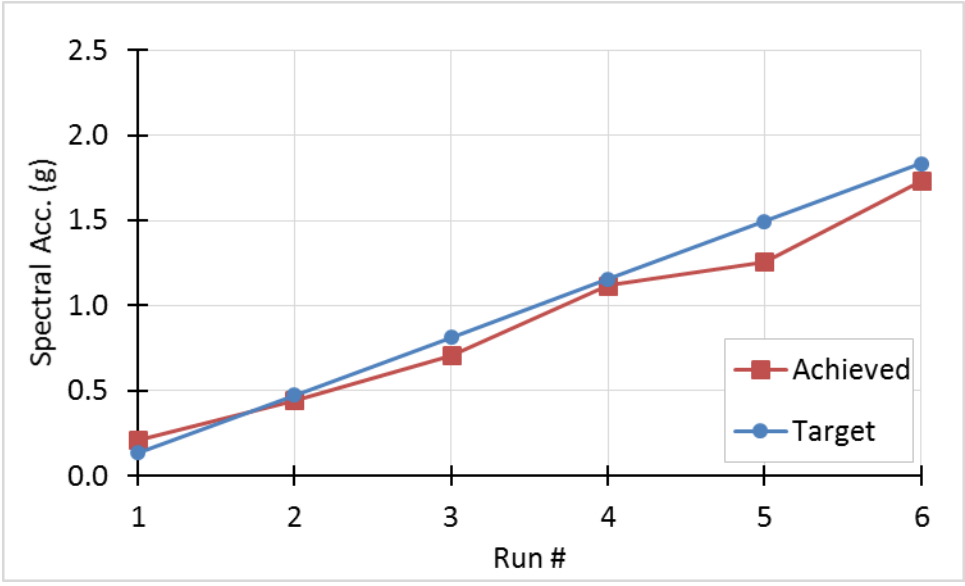

Fig. 3-87. BRSA achieved and targeted spectral acceleration for the fundamental period

Fig. 3-88. BRSA final condition after tests

a)

b)

Fig. 3-89. BRSA CIP condition after Run-1 a) column, NW view b) rebar-pin, SW view

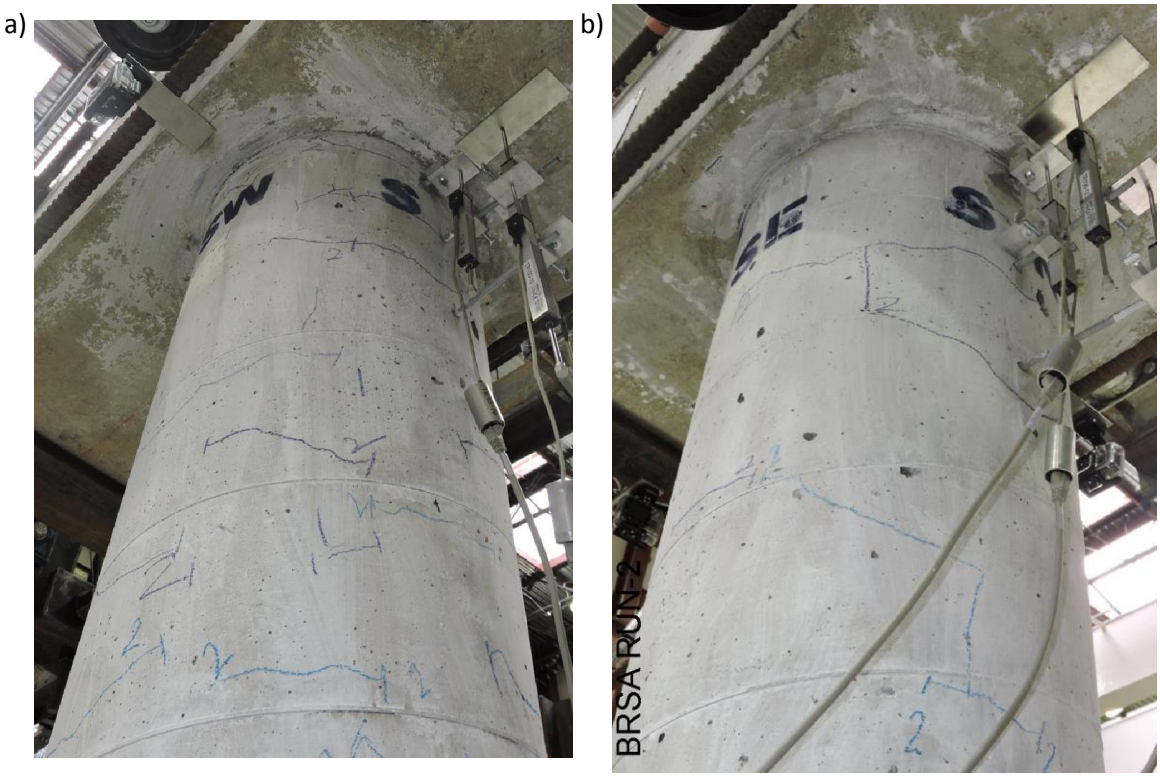

Fig. 3-90. BRSA CIP column after Run-2 a) SW view b)NE view

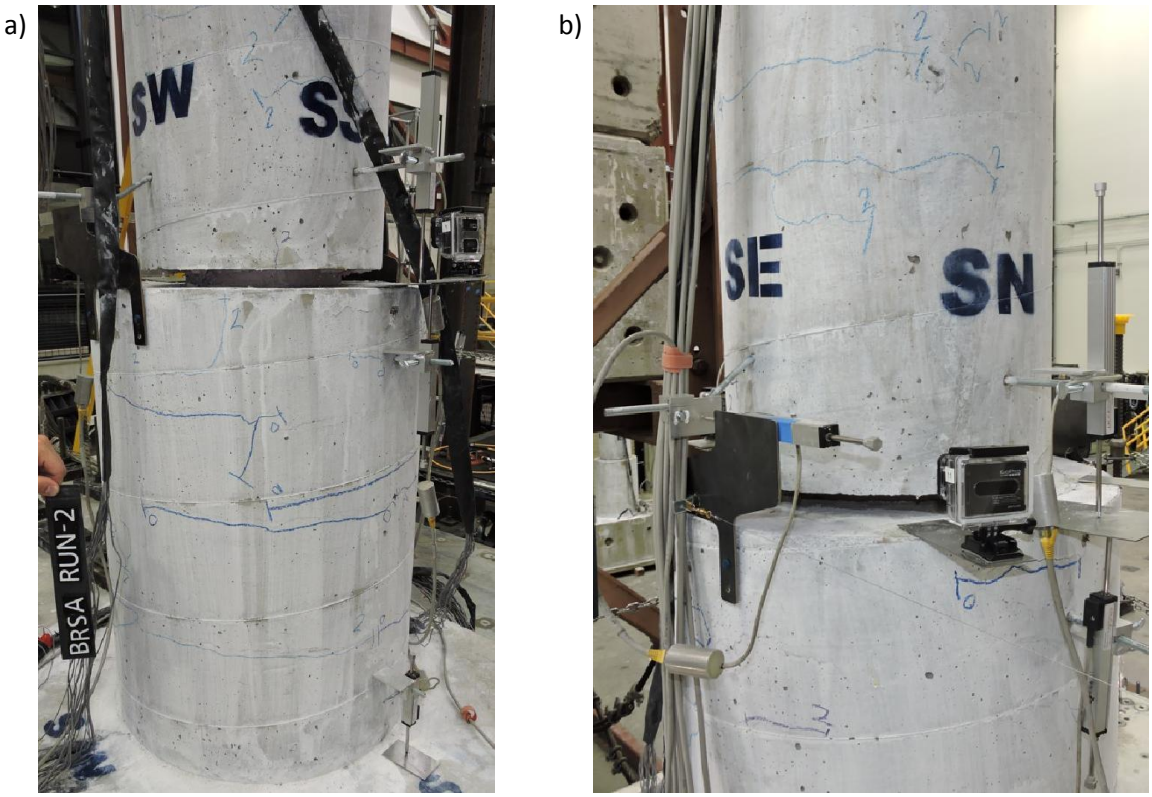

Fig. 3-91. BRSA CIP rebar-pin after Run-2 a) SW view b)NE view

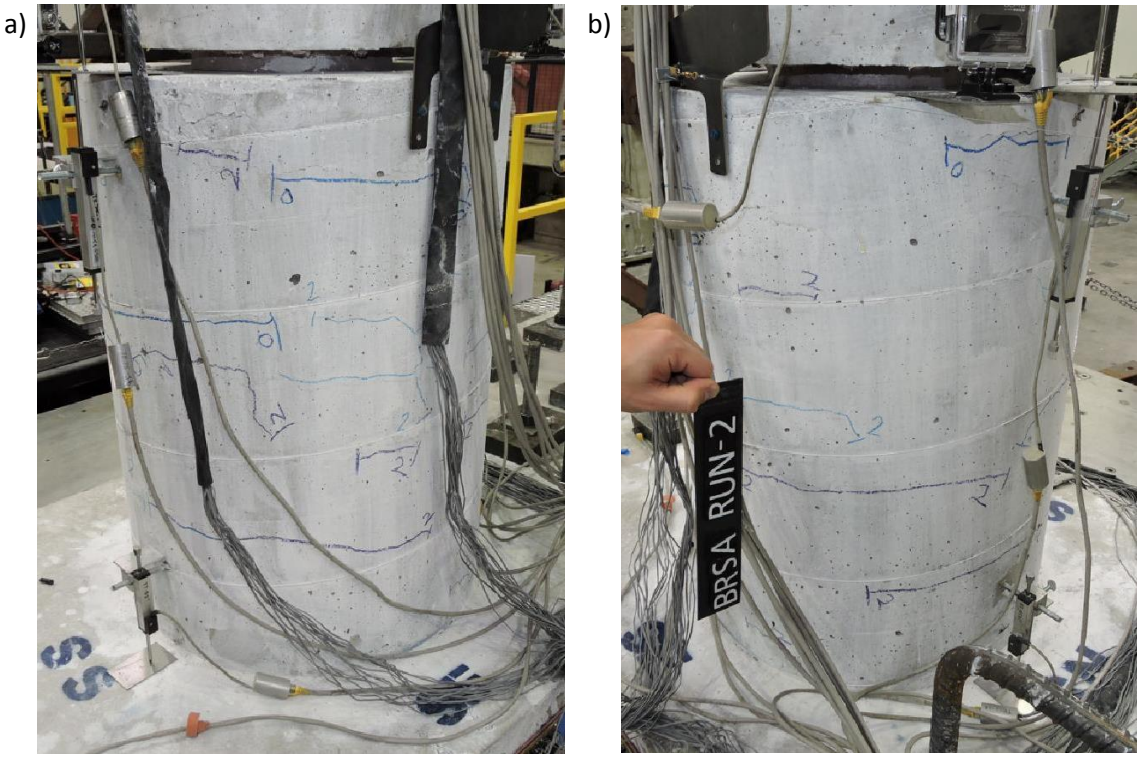

Fig. 3-92. BRSA CIP pedestal after Run-2 a) SE view b)NE view

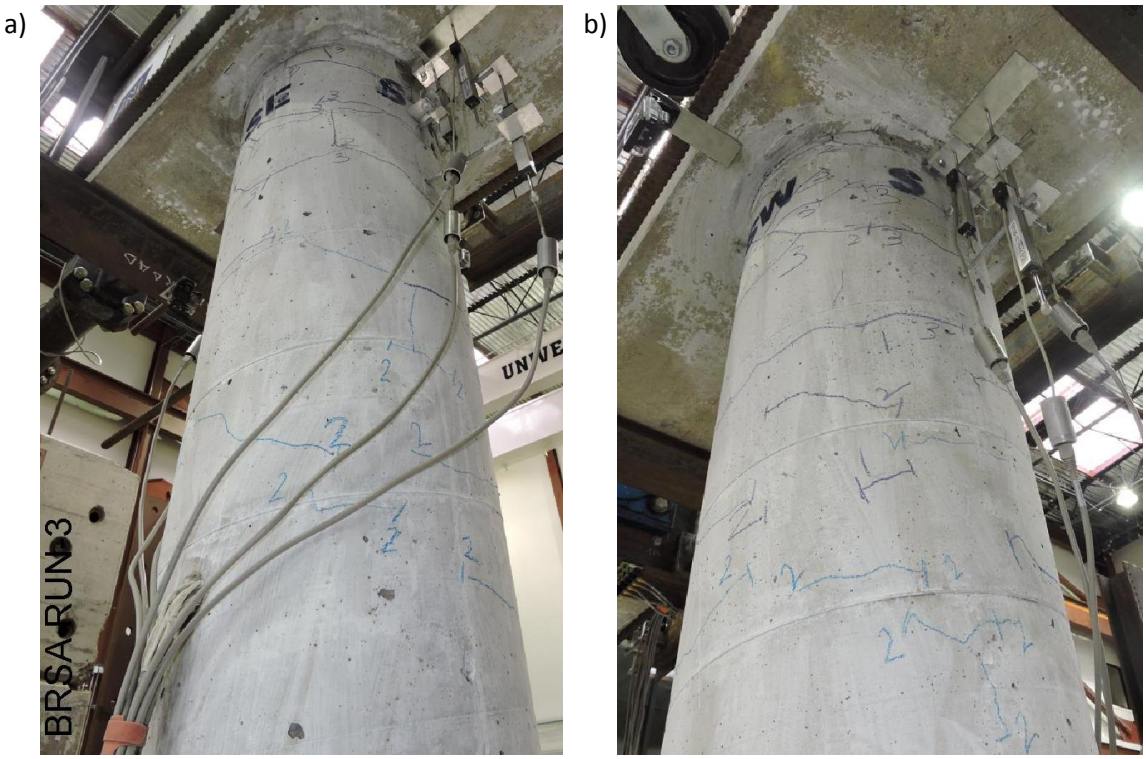

Fig. 3-93. BRSA CIP column after Run-3 a) NE view b)SW view

a) b)

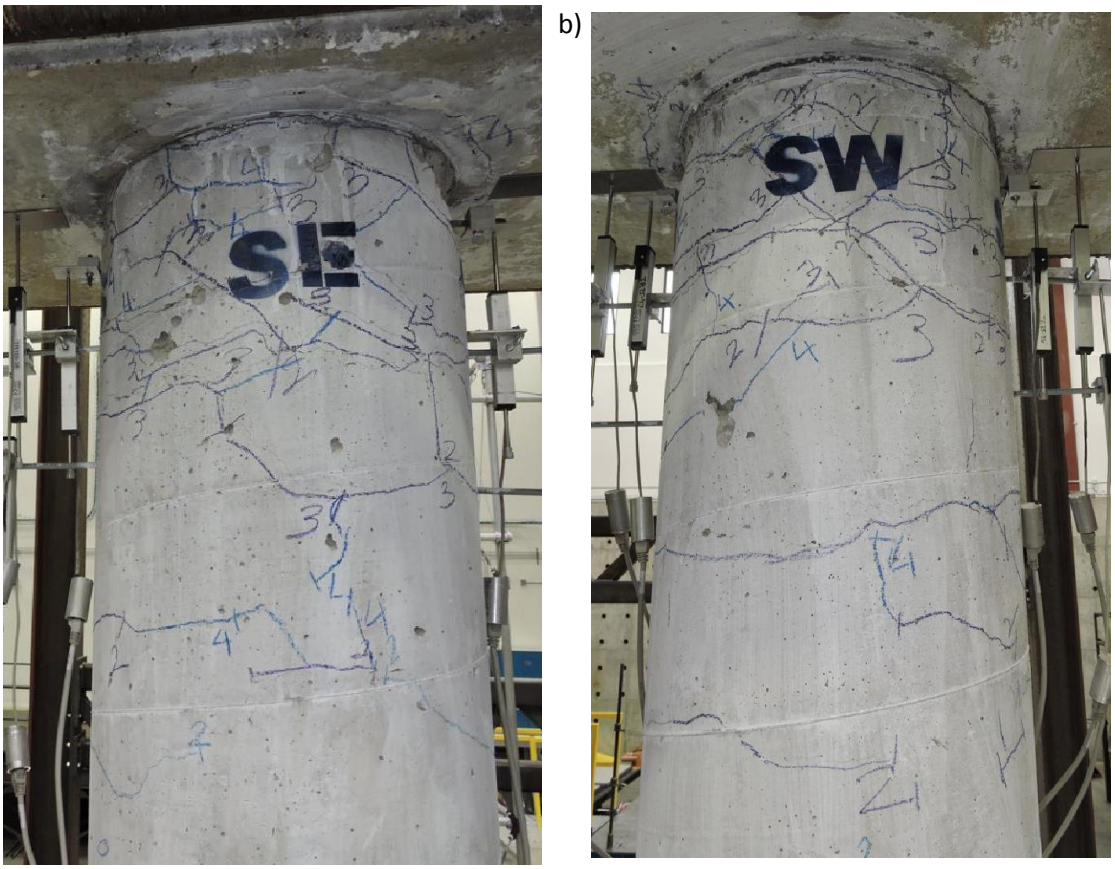

Fig. 3-94. BRSA CIP column after Run-4 a) E view b)W view

Fig. 3-95. BRSA CIP rebar-pin after Run-4 a) E view b)W view

(a) (b)

Fig. 3-96. BRSA CIP column condition after Run-5 a) NW view b)E view

Fig. 3-97. BRSA CIP rebar-pin after Run-5, NW view

(a) (b)

Fig. 3-98. BRSA CIP column after Run-6 a) NE view b)W view

Fig. 3-99. BRSA CIP rebar-pin after Run-6, NE view

a) b)

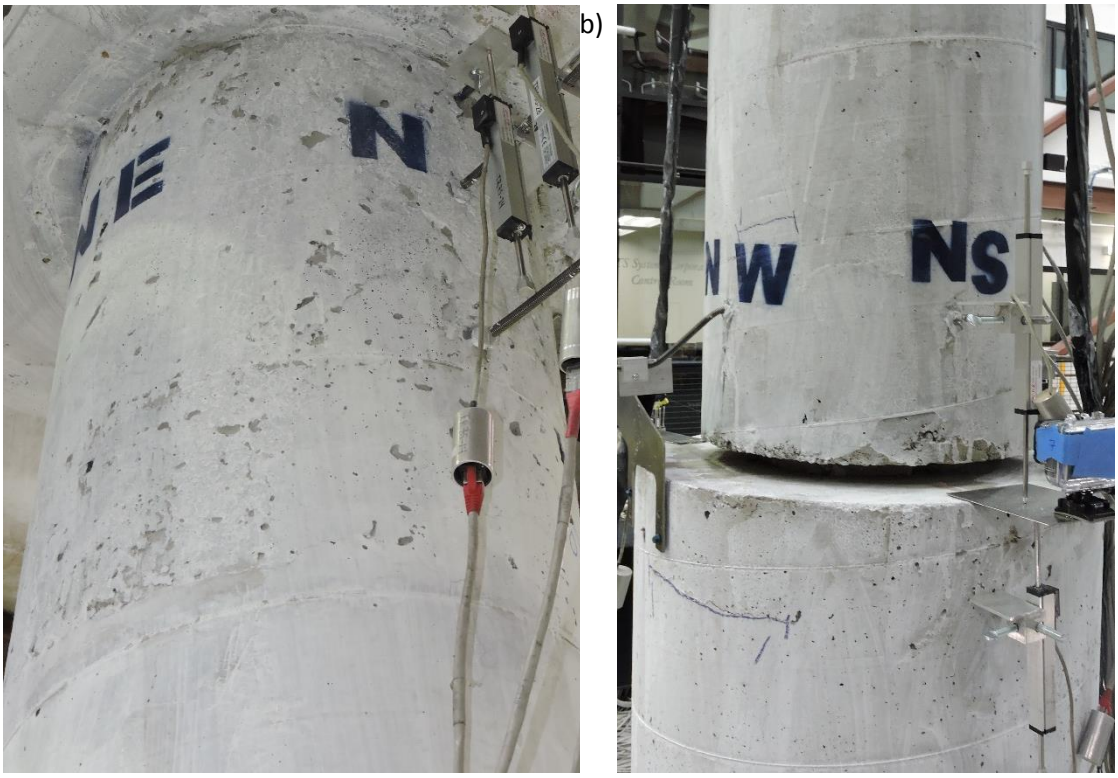

Fig. 3-100. BRSA PC side after Run-1 a) column, NE view b) pedestal, SW view

a) b)

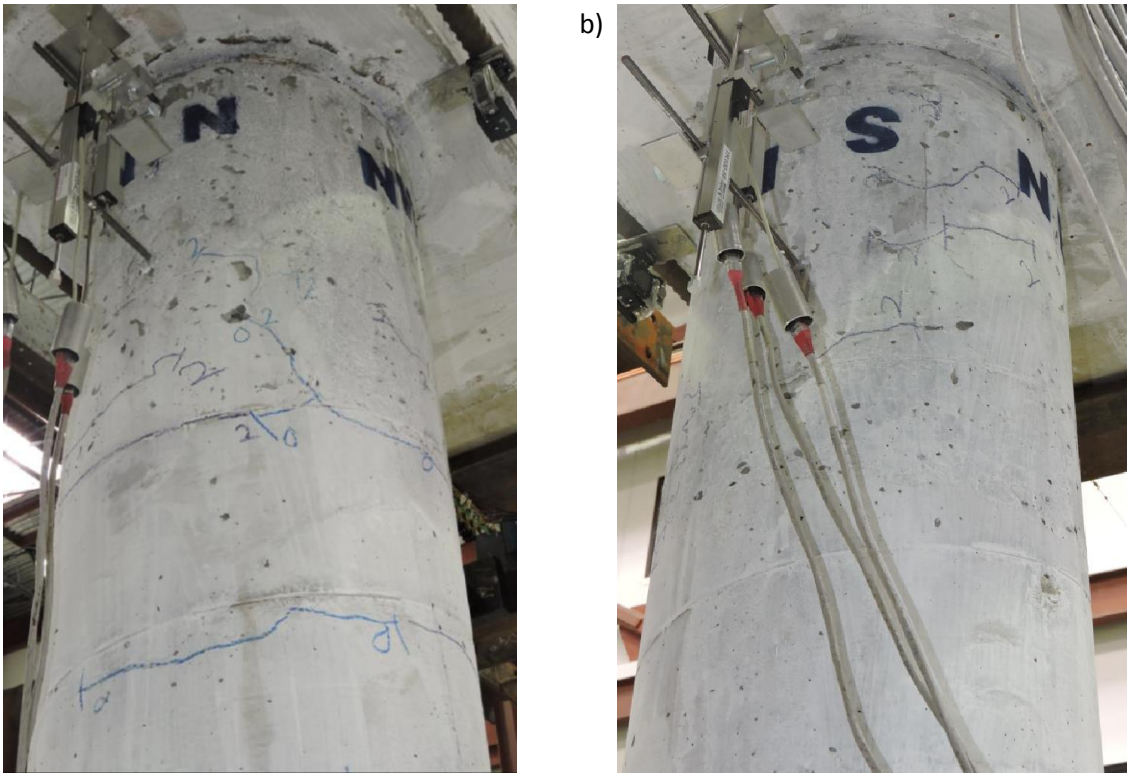

Fig. 3-101. BRSA PC column after Run-2 a) NW view b) SE view

a) b)

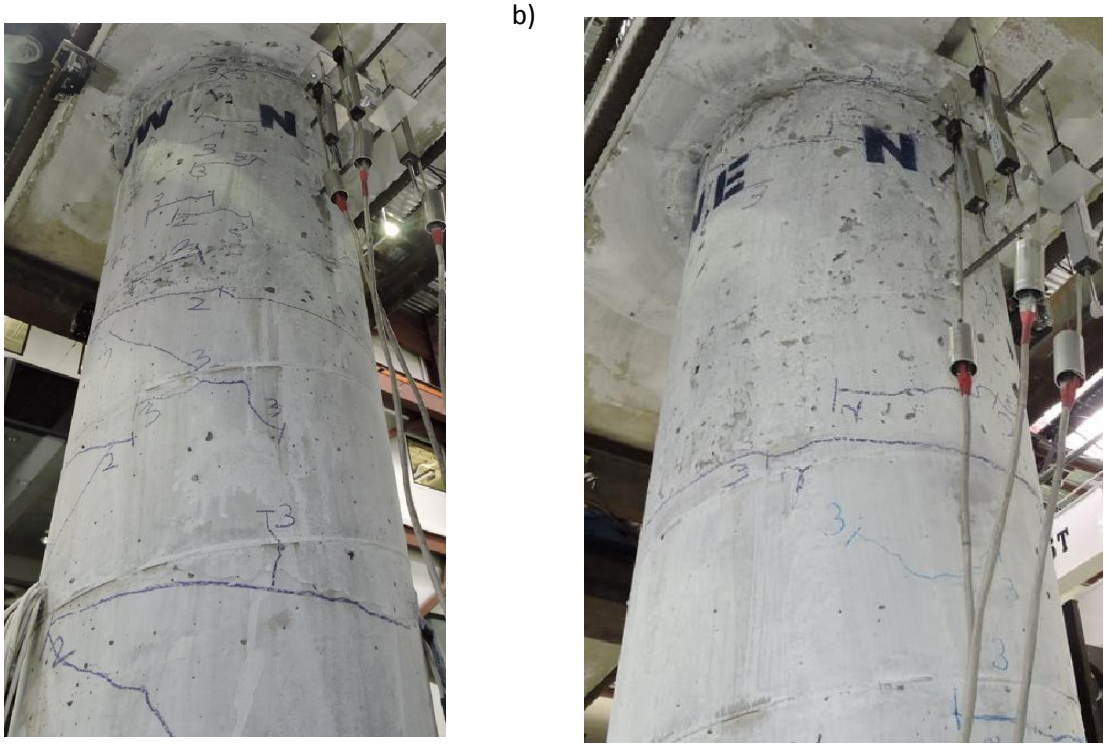

Fig. 3-102. BRSA PC column after Run-3 a) SW view b) NE view

a) b)

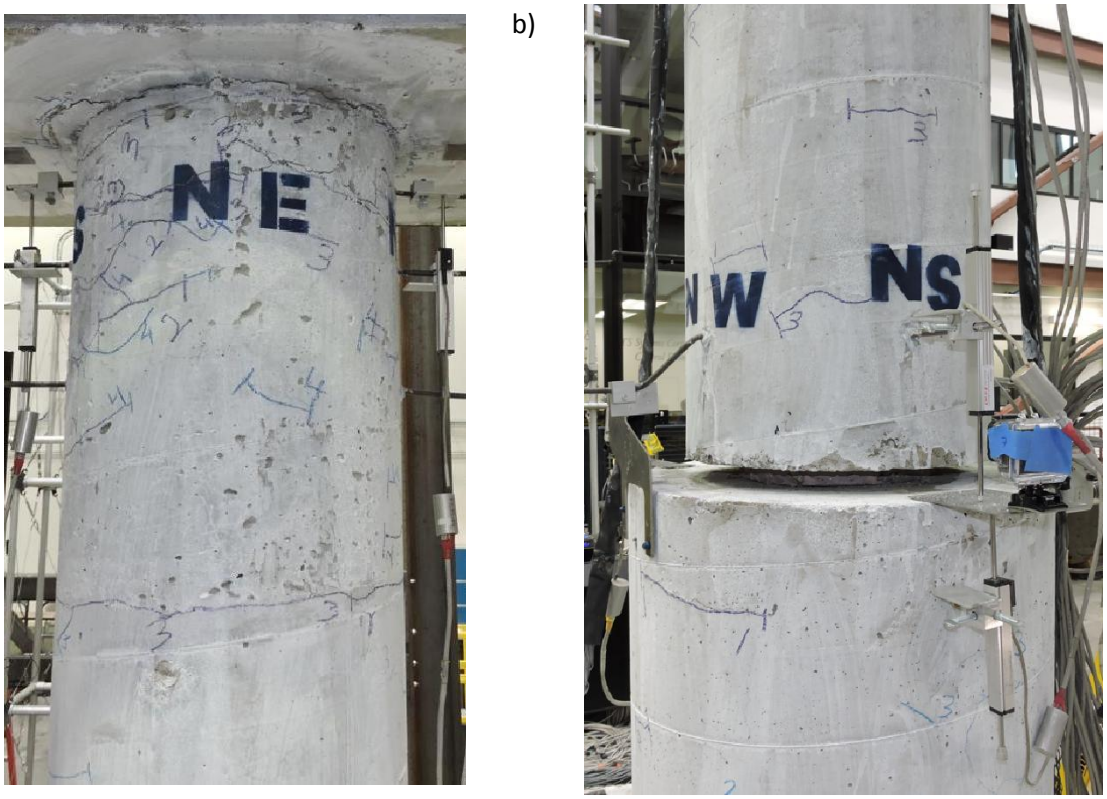

Fig. 3-103. BRSA PC side after Run-3 a) column, E view b) rebar-pin, NW view

a) b)

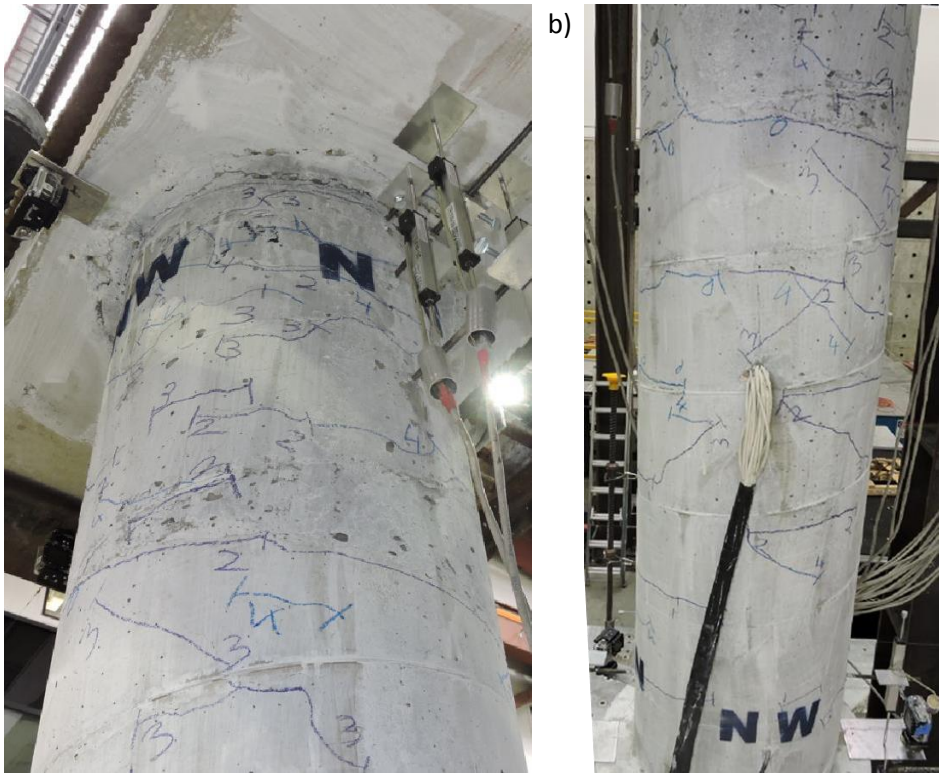

Fig. 3-104. BRSA PC column after Run-4 a) SW view b) W view

a) b)

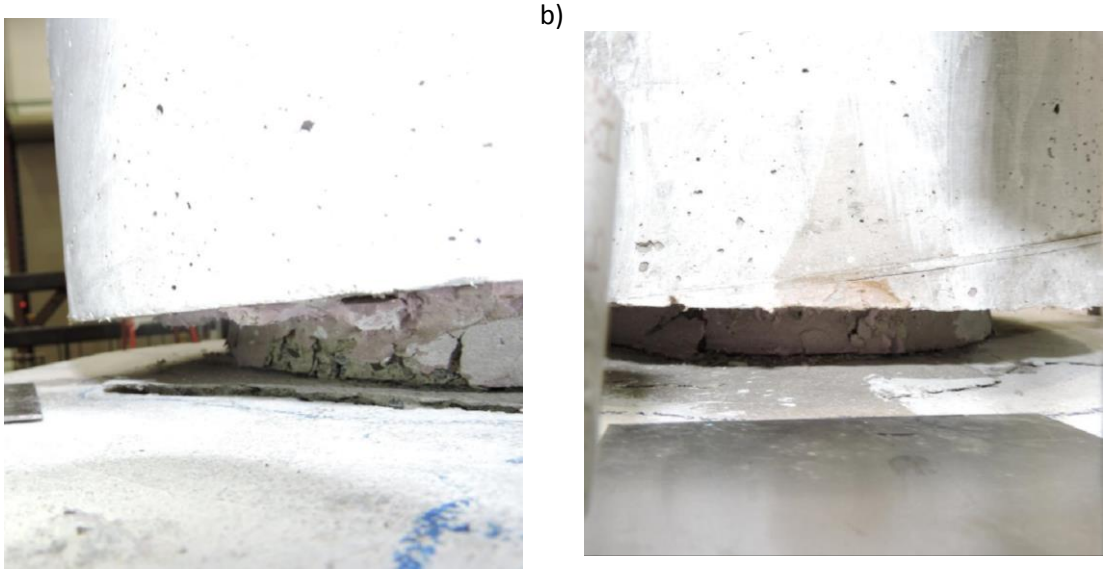

Fig. 3-105. BRSA PC rebar-pin after Run-4 a) W view b) NE view

Fig. 3-106. BRSA PC rebar-pin after Run-4, south view

a)

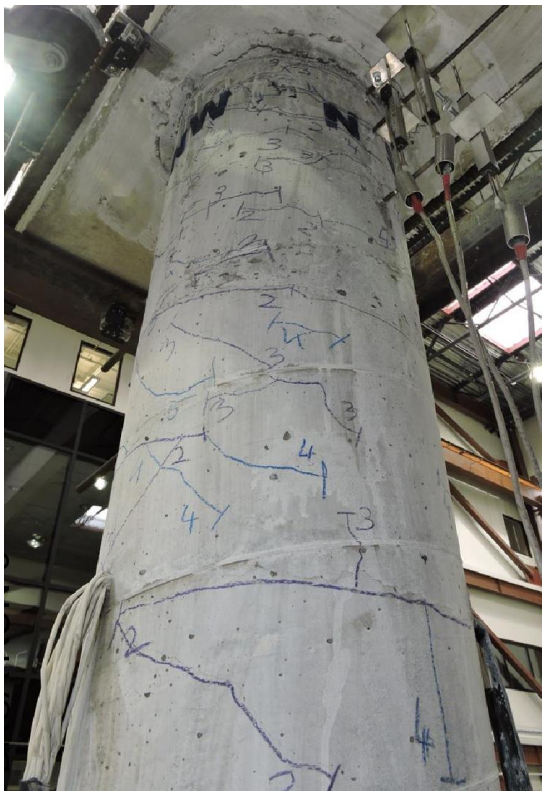

b)

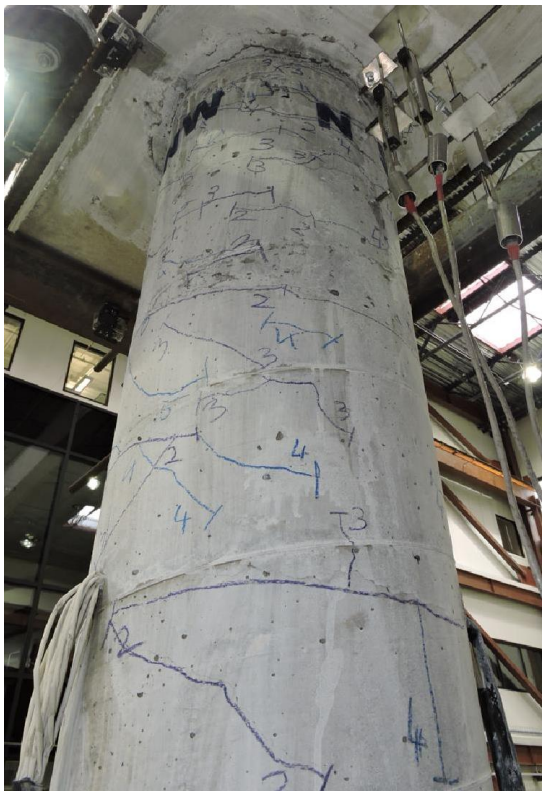

Fig. 3-107. BRSA PC column after Run-5 a) SW view b) NE view

a) b)

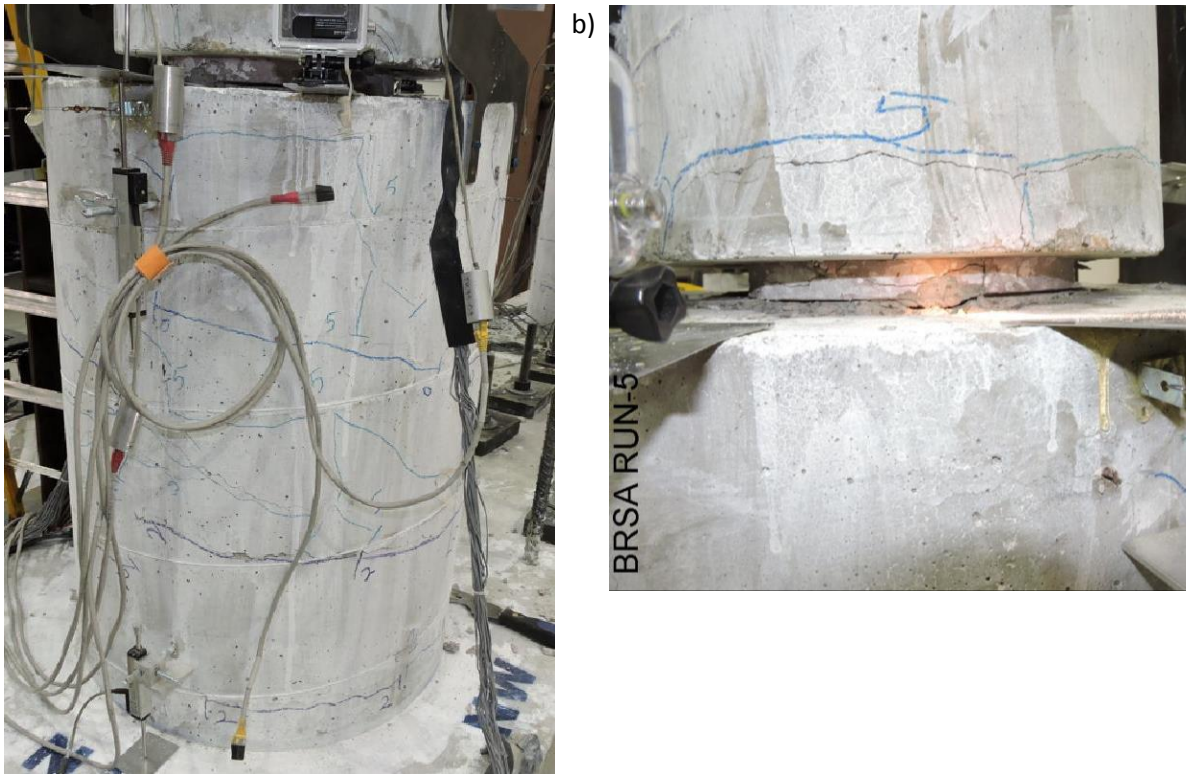

Fig. 3-108. BRSA PC after Run-5 a) pedestal, NW view b) rebar-pin, NE view

Fig. 3-109. BRSA PC rebar-pin after Run-5

a) b)

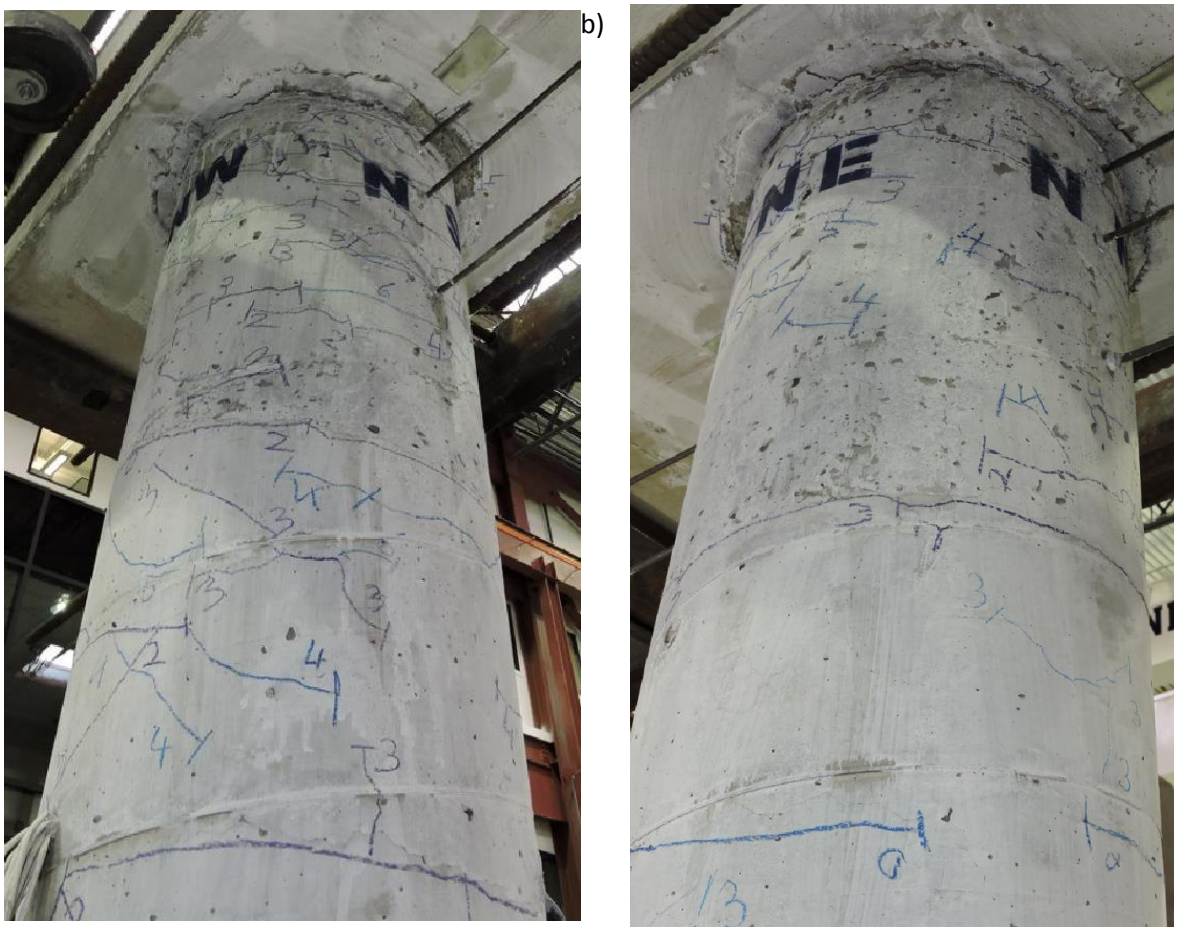

Fig. 3-110. BRSA PC column after Run-6 a) SW view b) NE view

a) b)

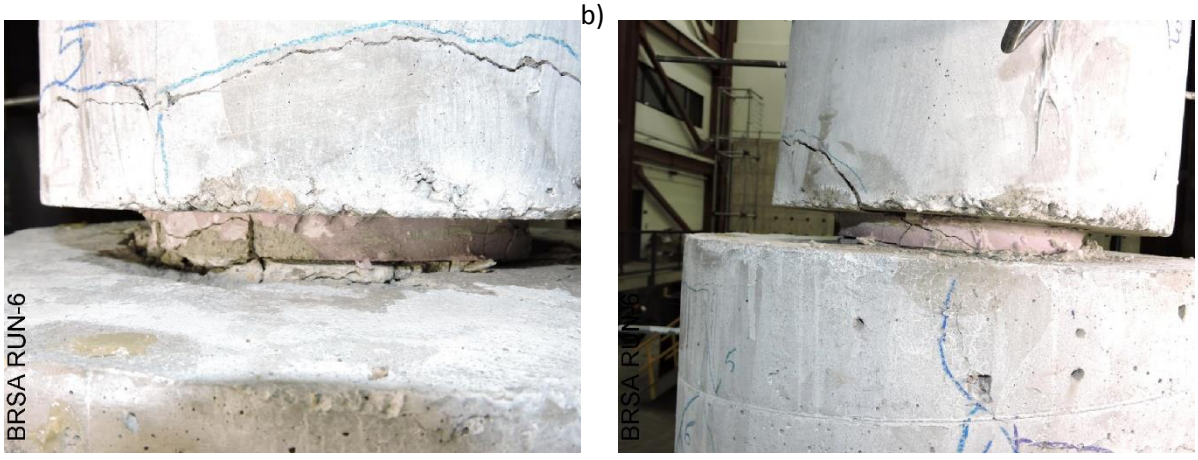

Fig. 3-111. BRSA PC rebar-pin after Run-6 a) NE view b) W view

Fig. 3-112. BRSA PC pedestal after run-6, N view

a)

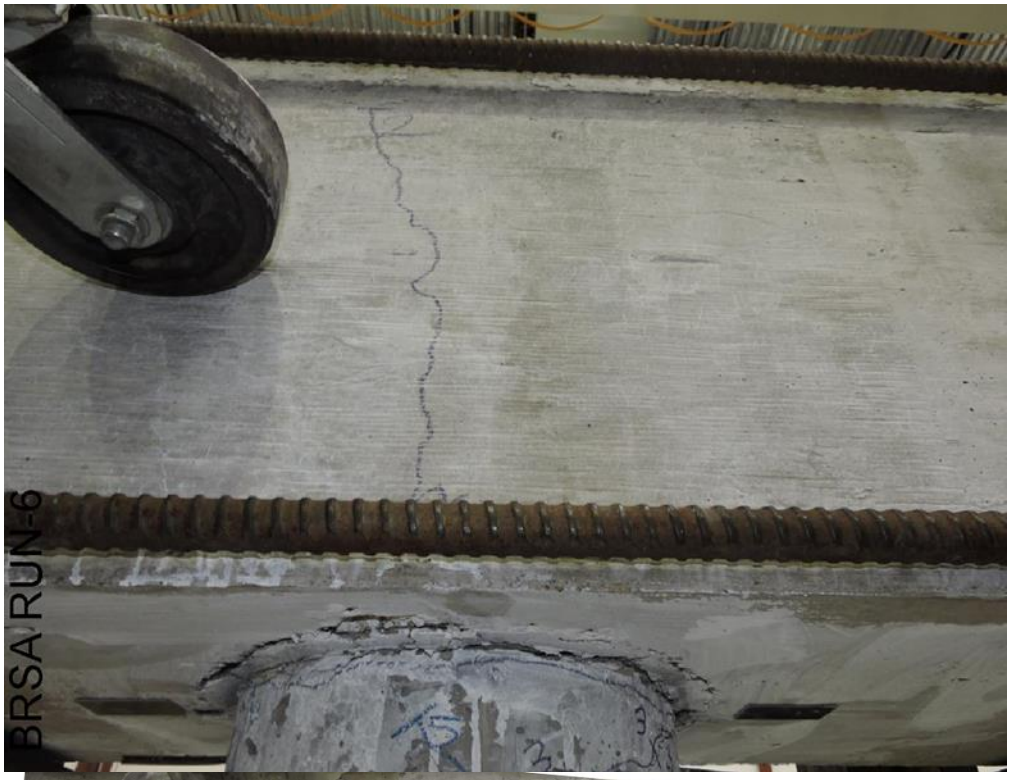

b)

Fig. 3-113. BRSA cap beam after Run-6 a)E view b) W view

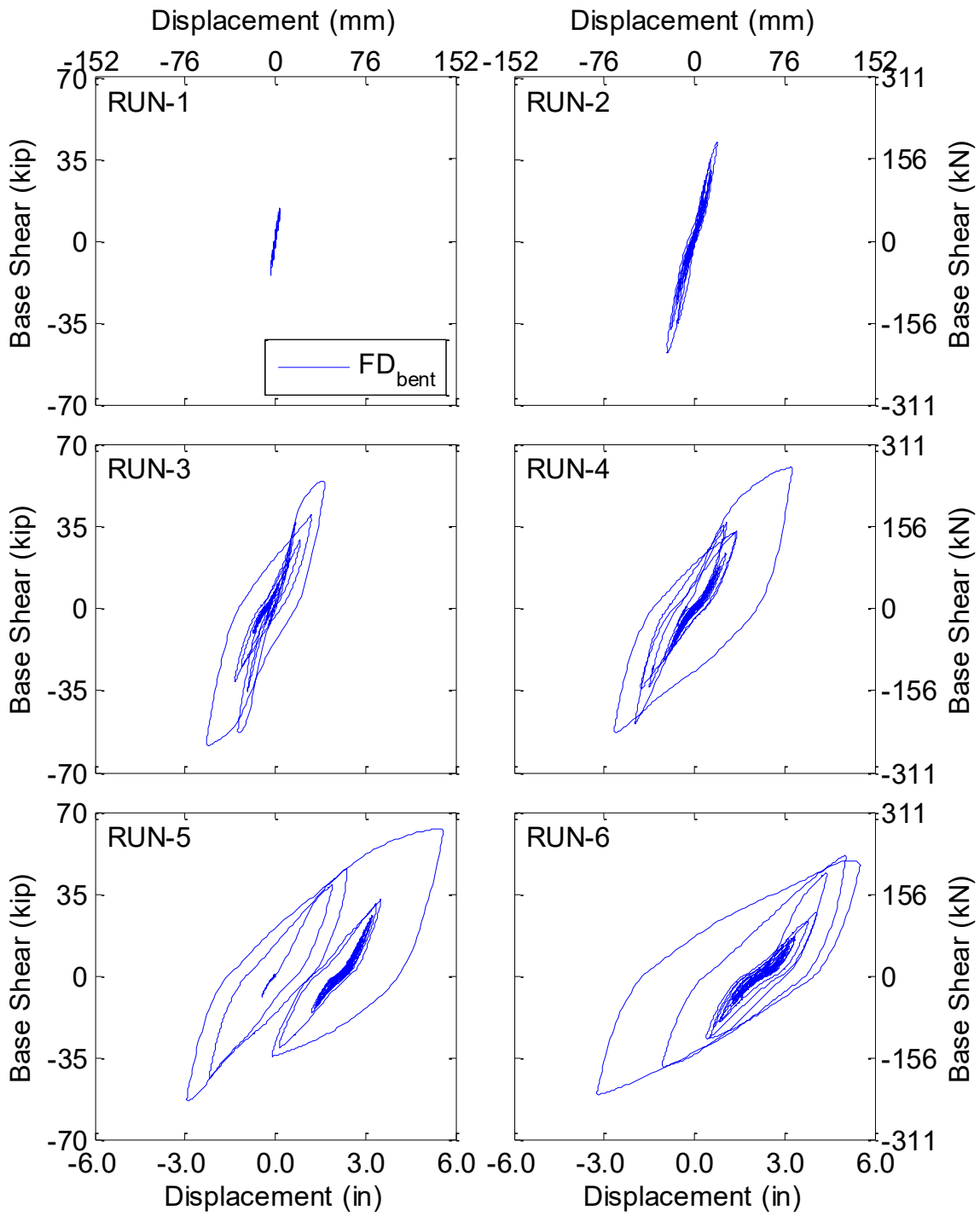

Fig. 3-114. BRSA bent displacement-base shear hysteresis curves for each run

a)

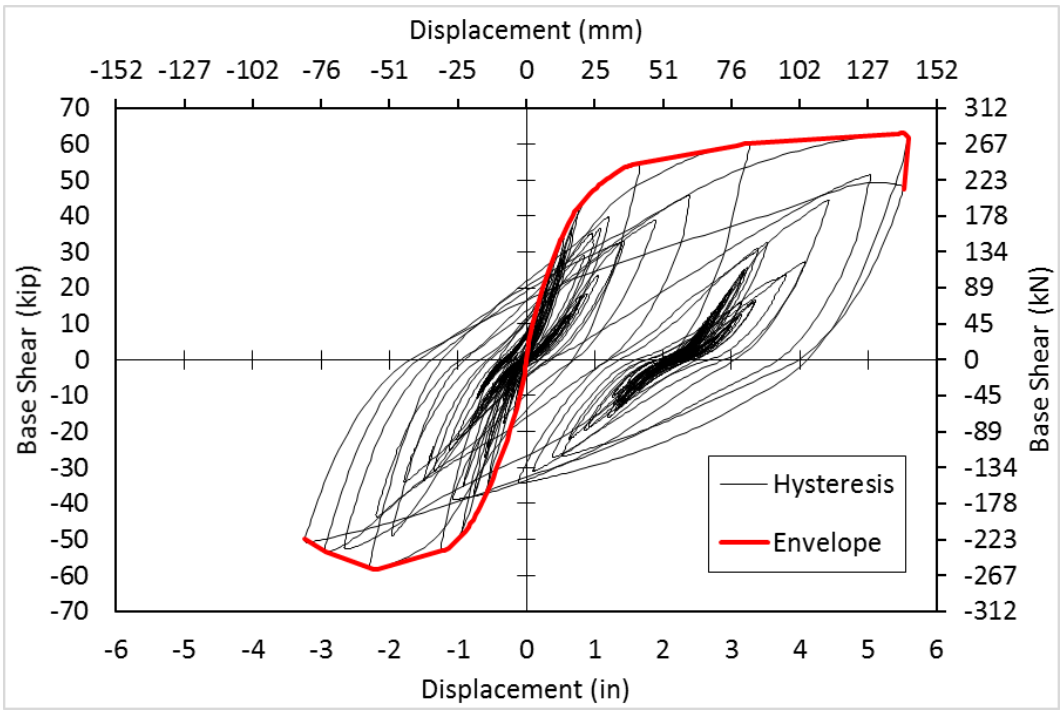

b)

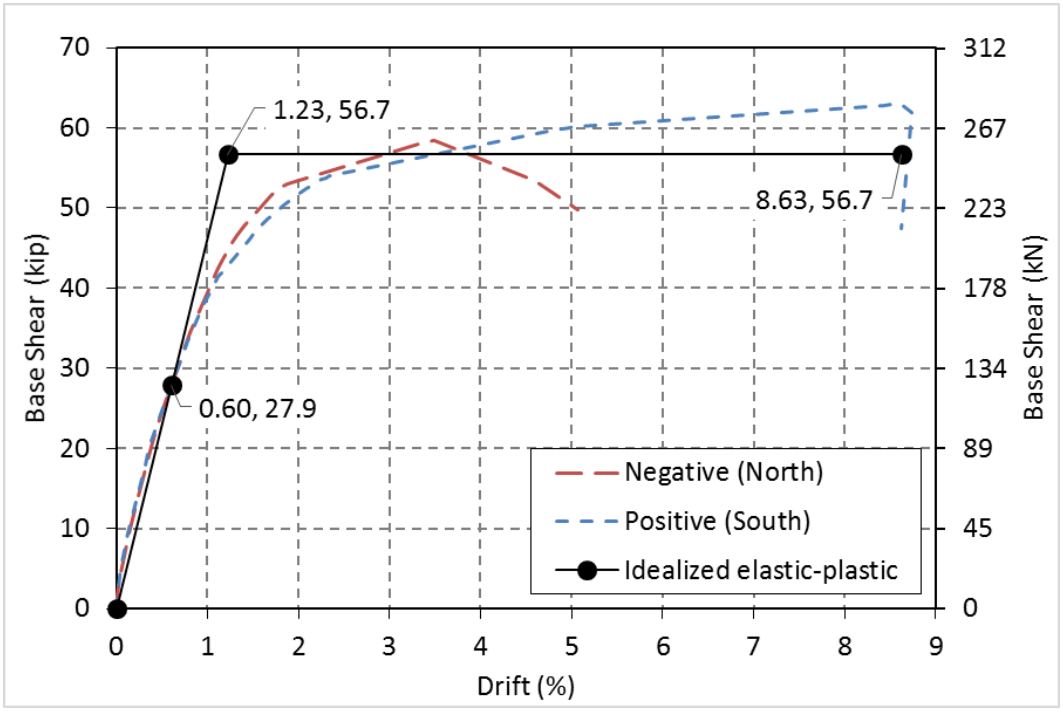

Fig. 3-115. BRSA bent force-displacement a) hysteresis curve b) idealized elastic-plastic

a)

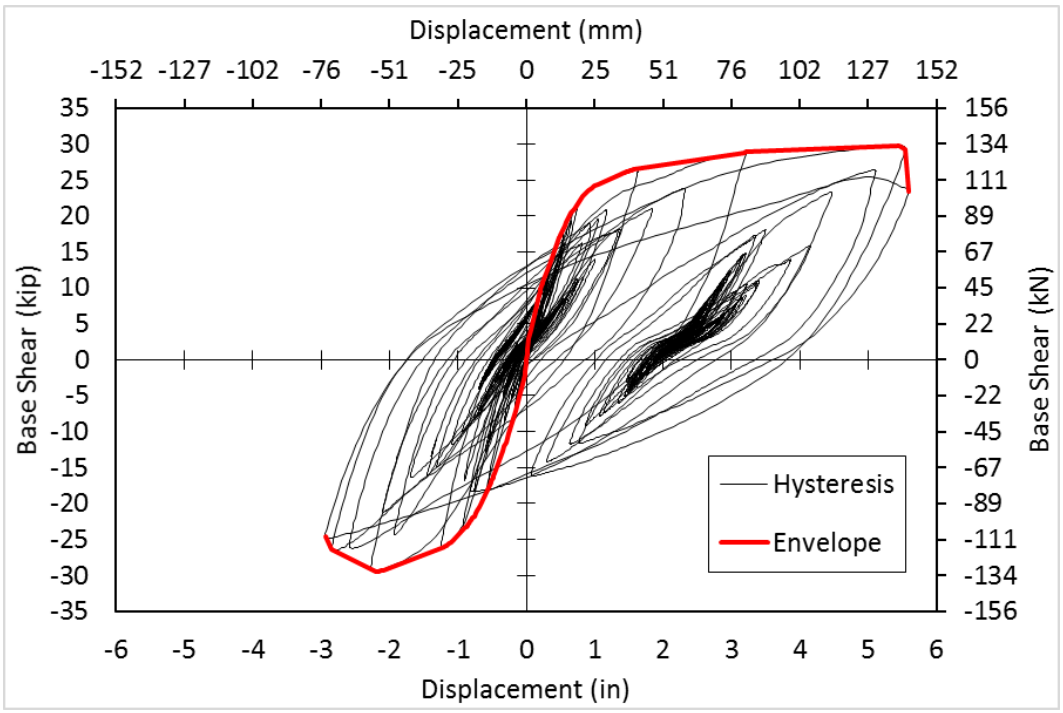

b)

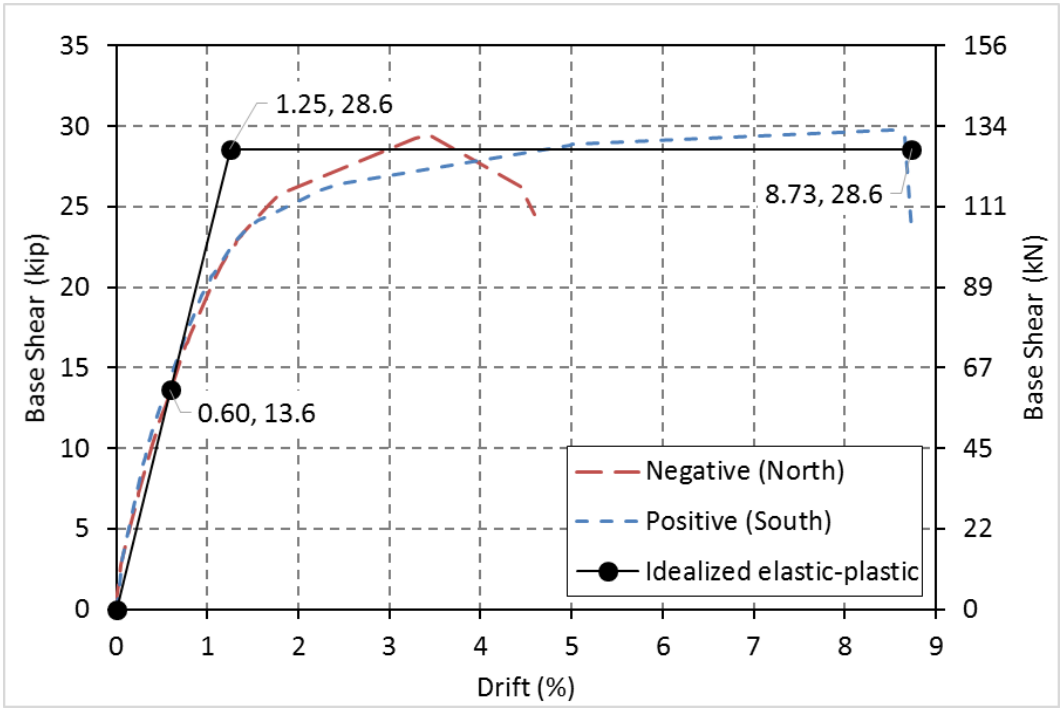

Fig. 3-116. BRSA CIP column force-displacement a) hysteresis curve b) idealized elastic-plastic

a)

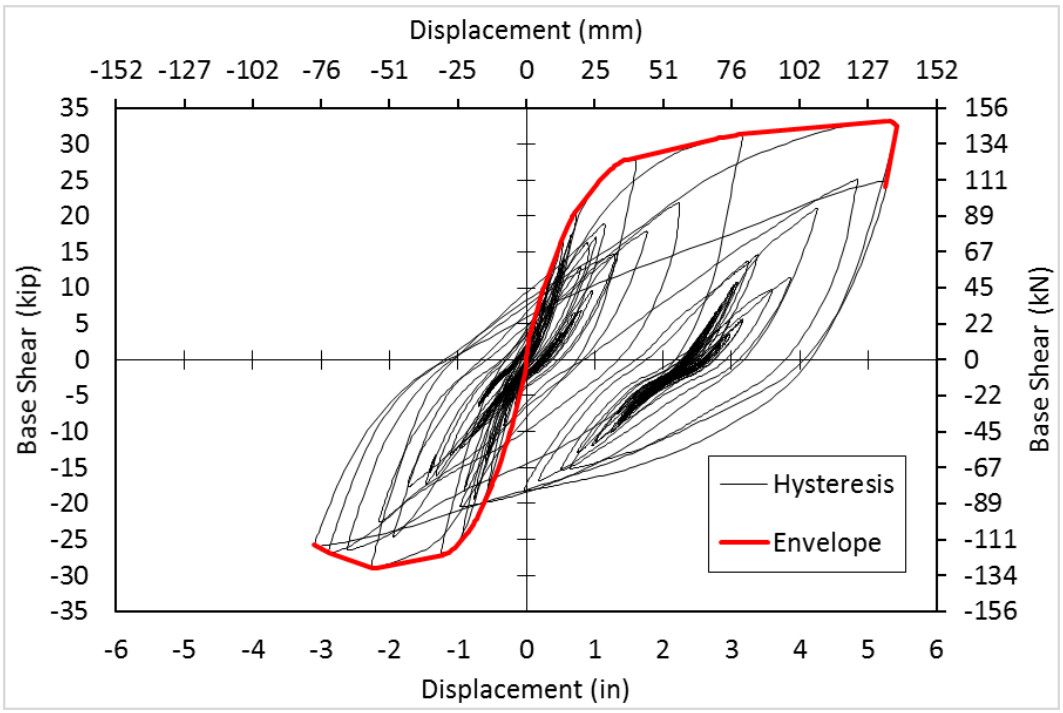

b)

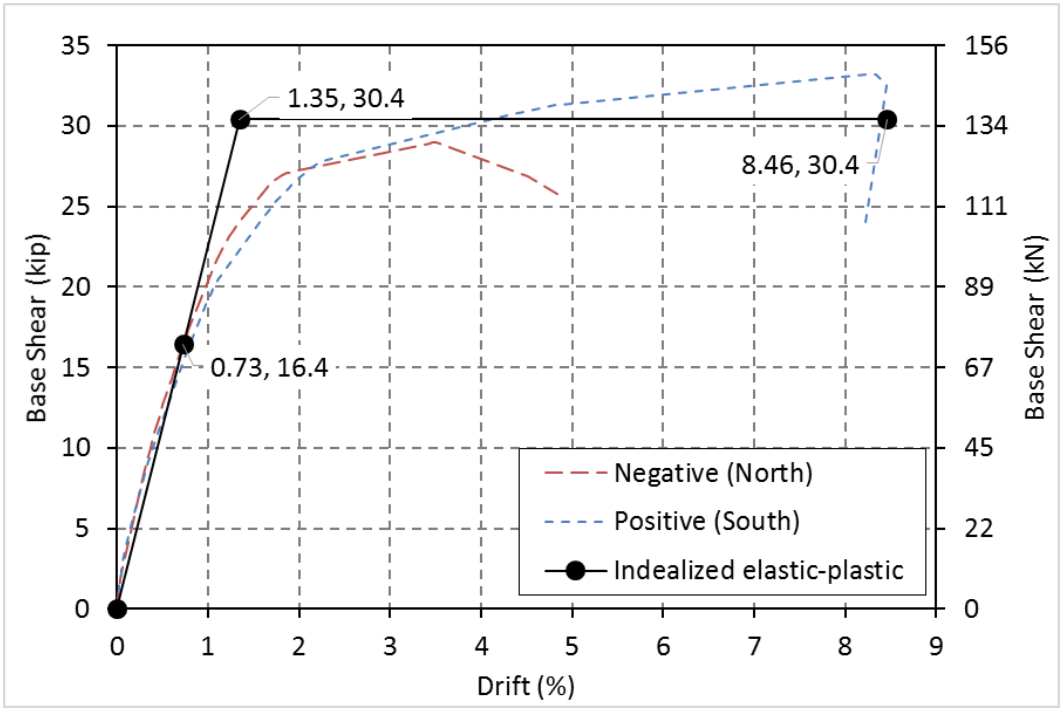

Fig. 3-117. BRSA PC column force-displacement a) hysteresis curve b) idealized elastic-plastic

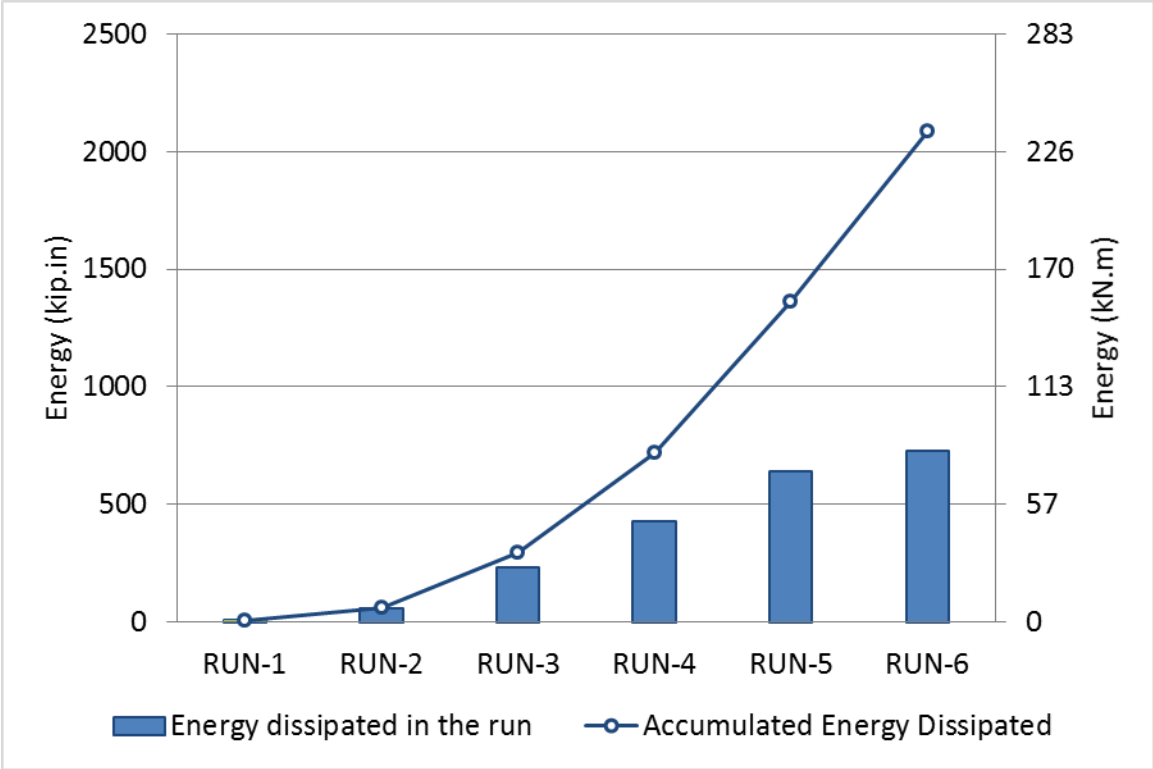

Fig. 3-118. BRSA energy dissipated in each run

a)

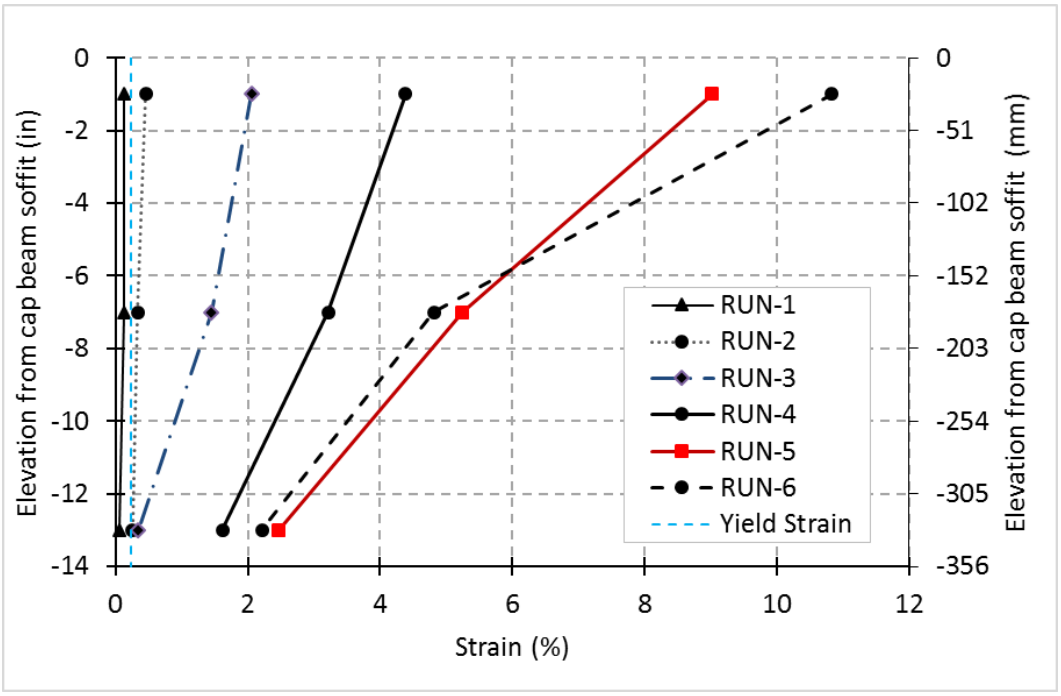

b)

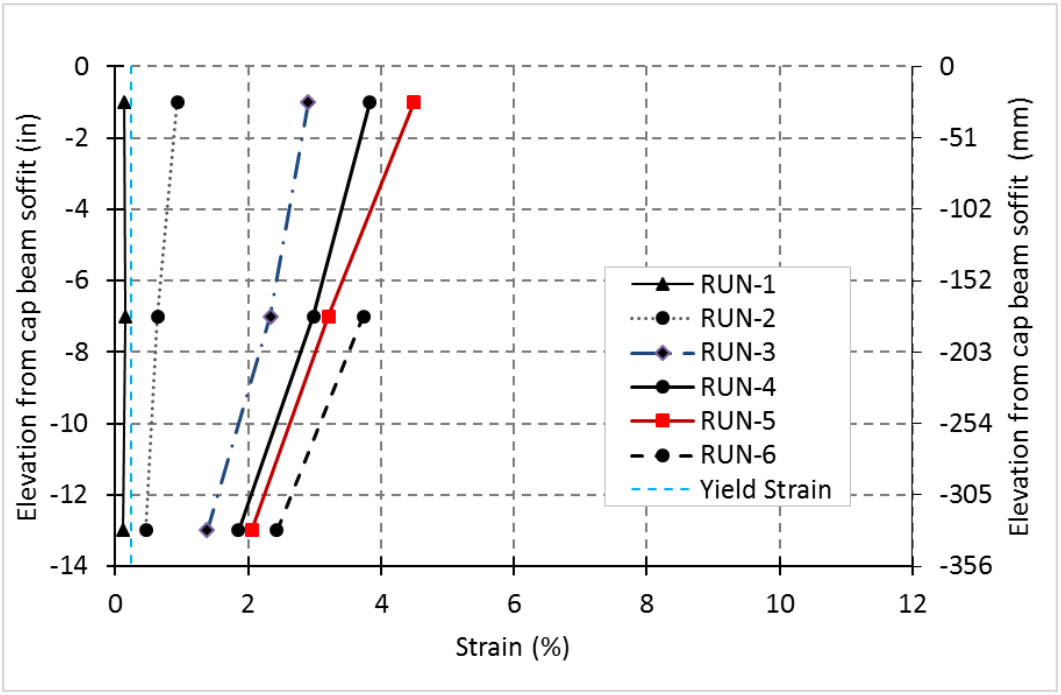

Fig. 3-119. BRSA strain profile in long. bars in plastic hinge of CIP column a)south b)north

a)

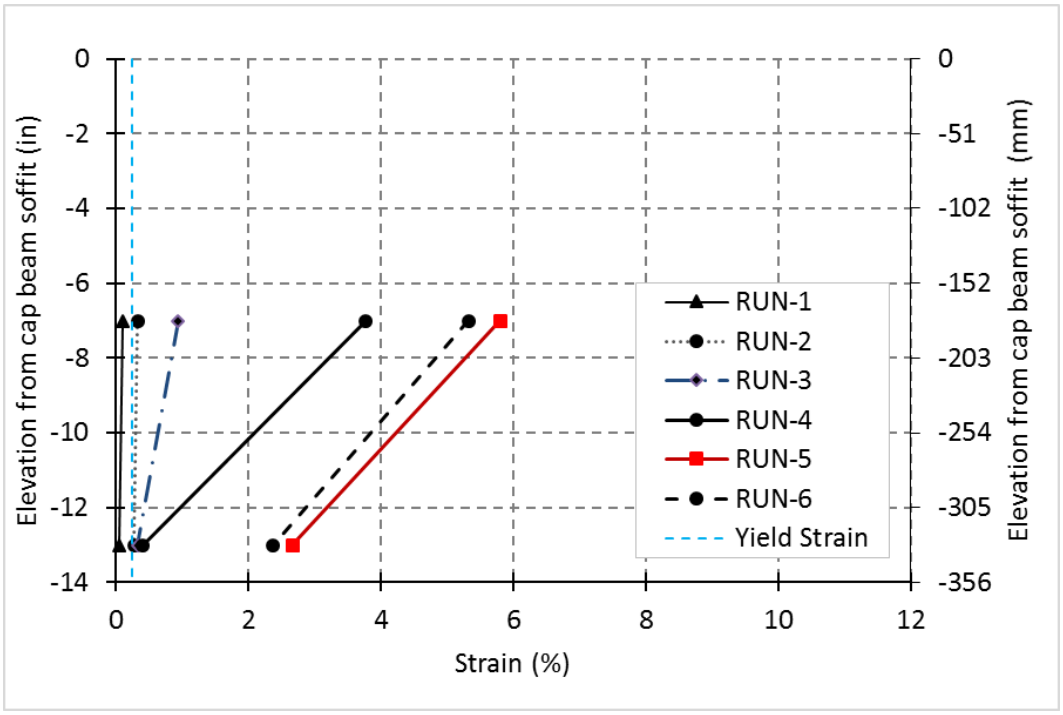

b)

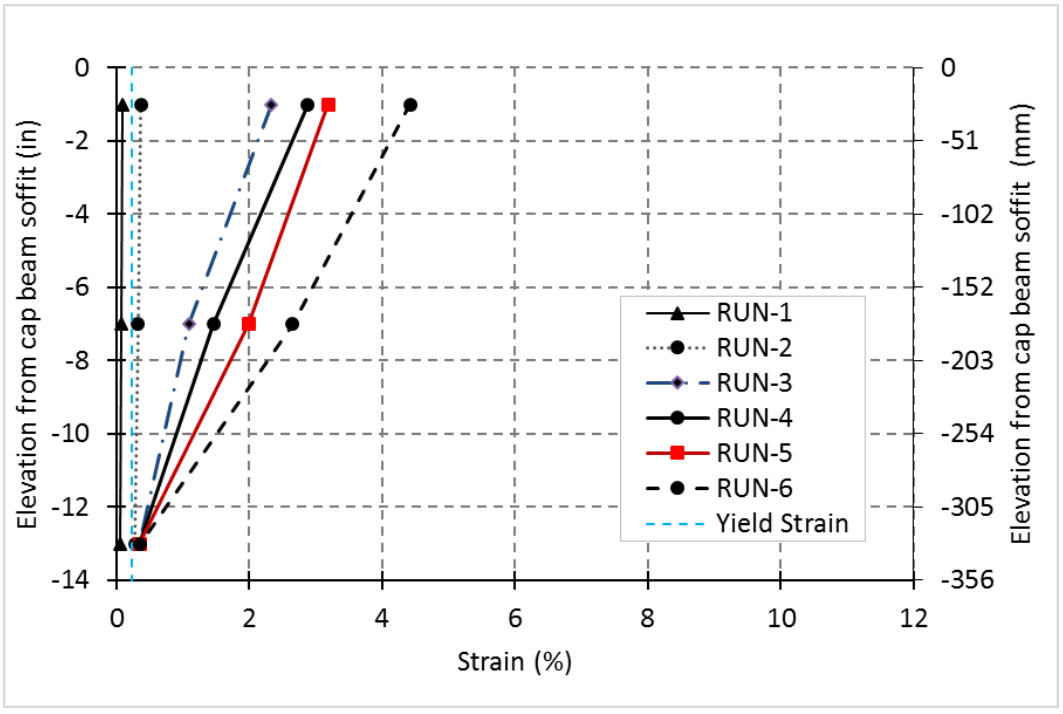

Fig. 3-120. BRSA strain profile in long. bars in plastic hinge of PC column a)south b)north

a)

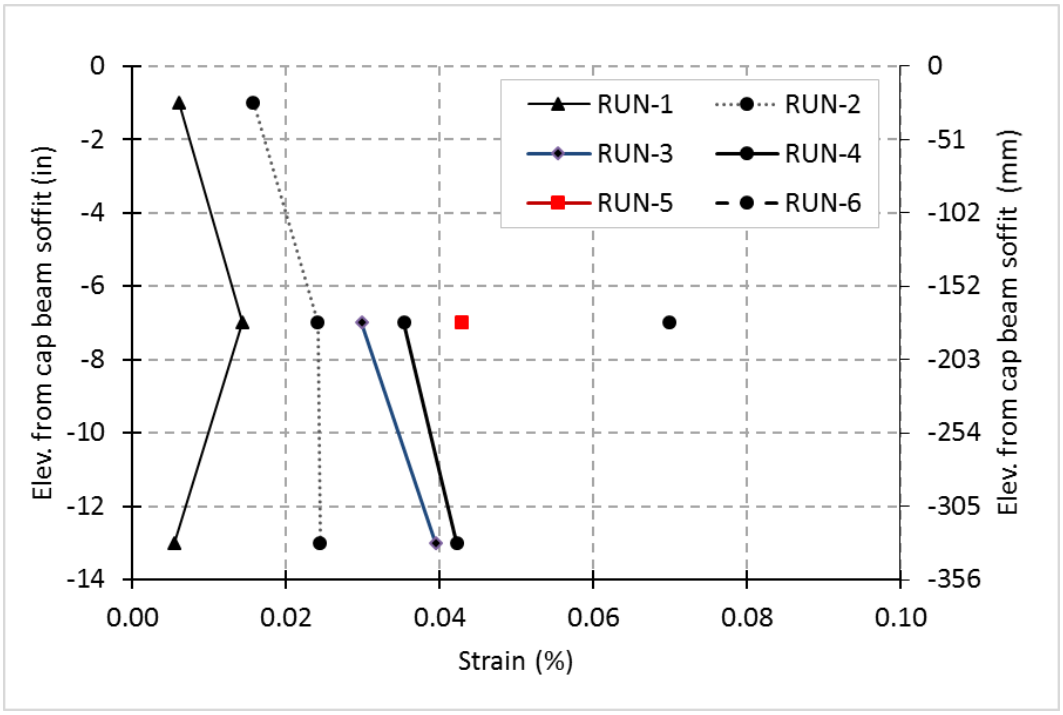

b)

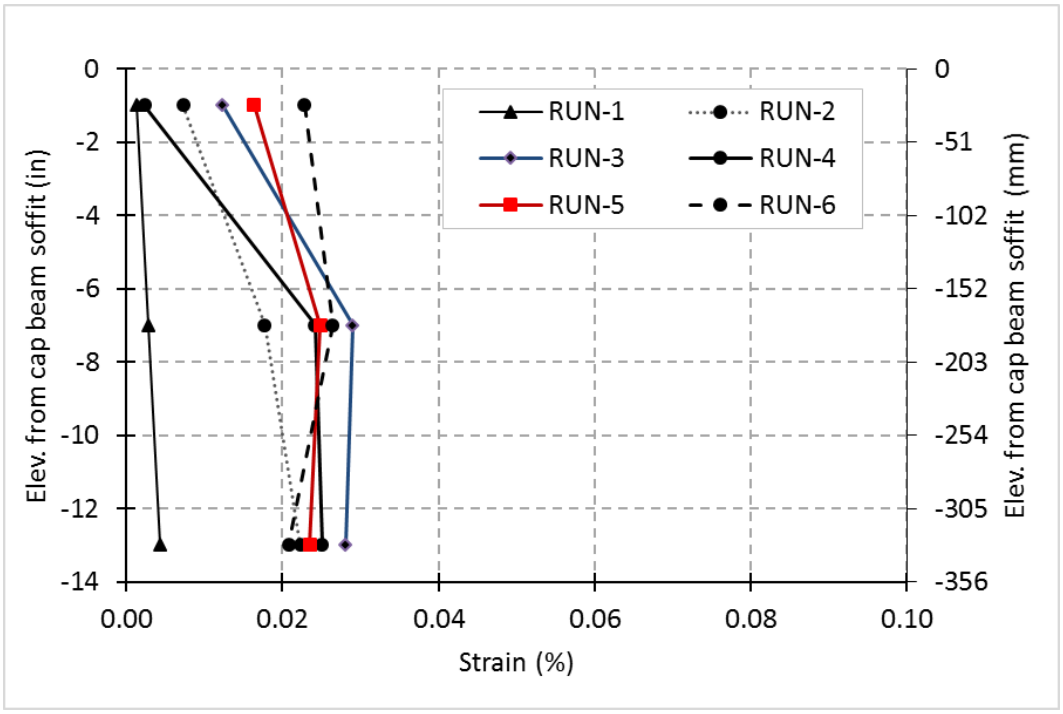

Fig. 3-121. BRSA average strain profile in trans. bars in plastic hinge of a) CIP column b) PC column

a)

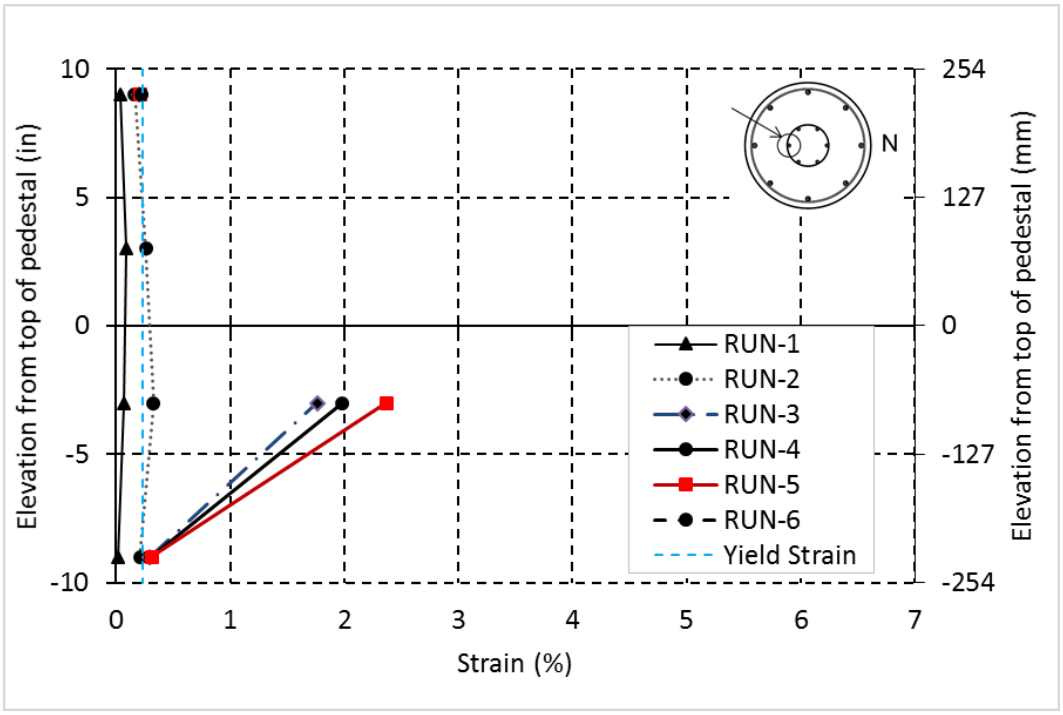

b)

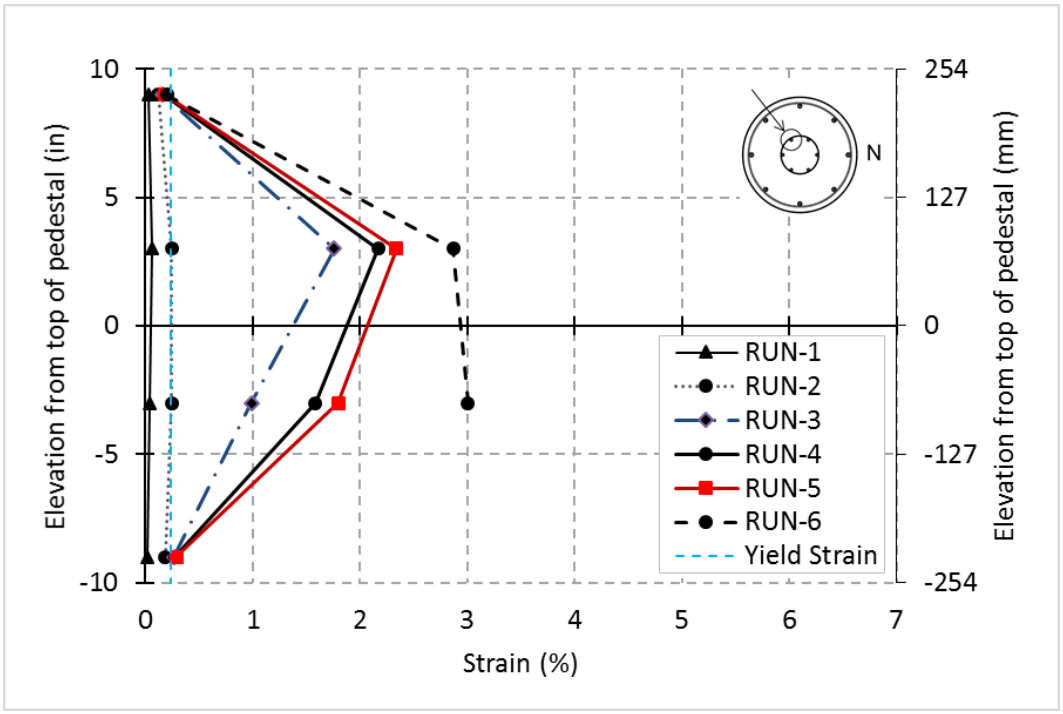

Fig. 3-122. BRSA strain profile of long. bars in CIP rebar-pin at a)S b)SW

a)

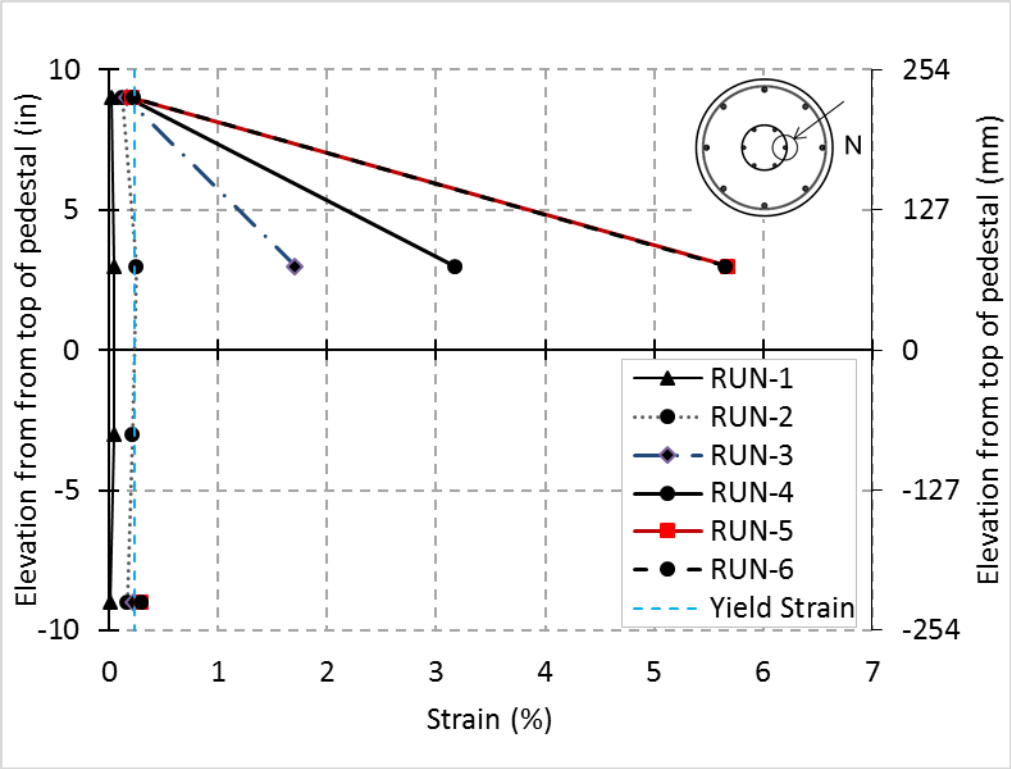

b)

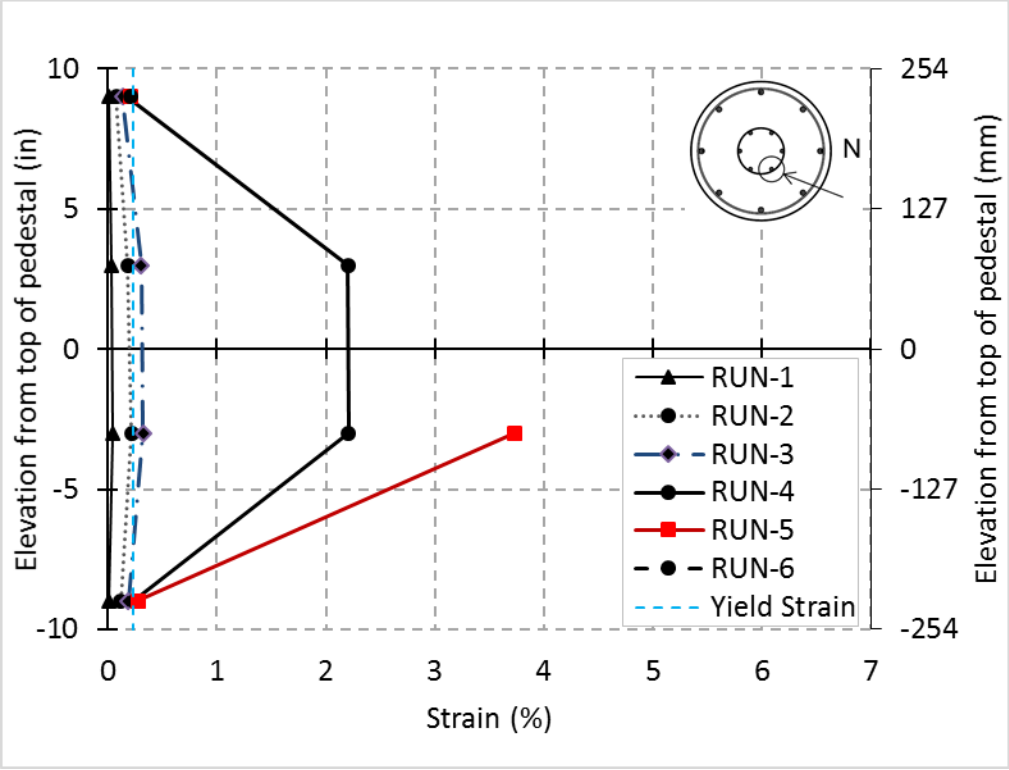

Fig. 3-123. BRSA strain profile of long. bars in CIP rebar-pin a)N b)NE

a)

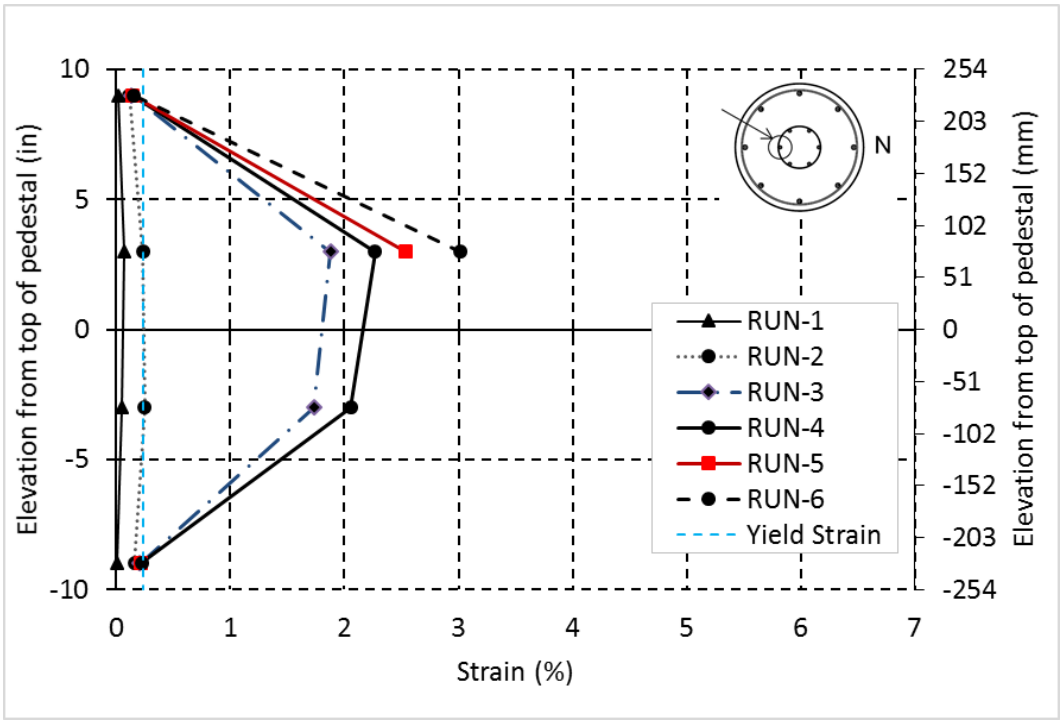

b)

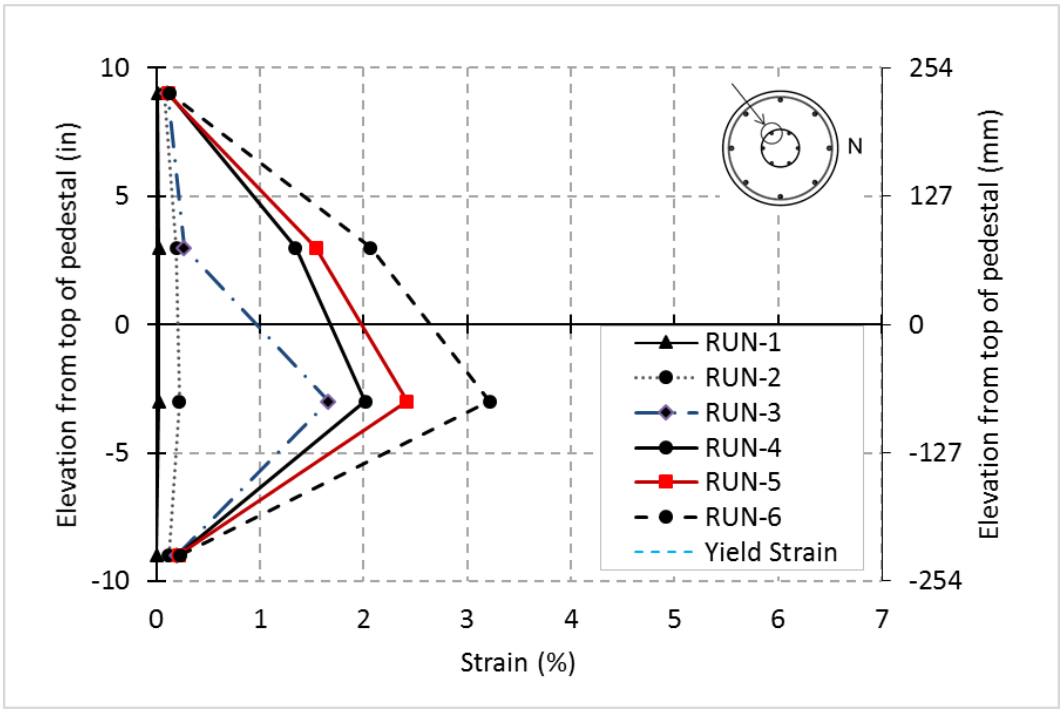

Fig. 3-124. BRSA strain profile of long. bars in PC rebar-pin a)S b)SW

a)

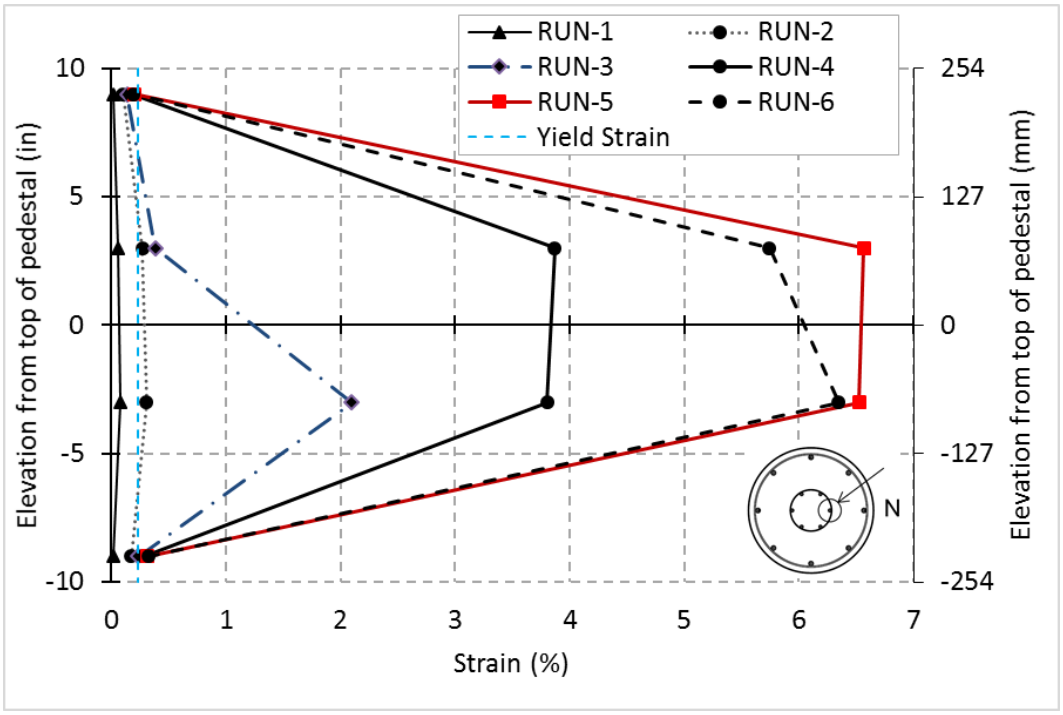

b)

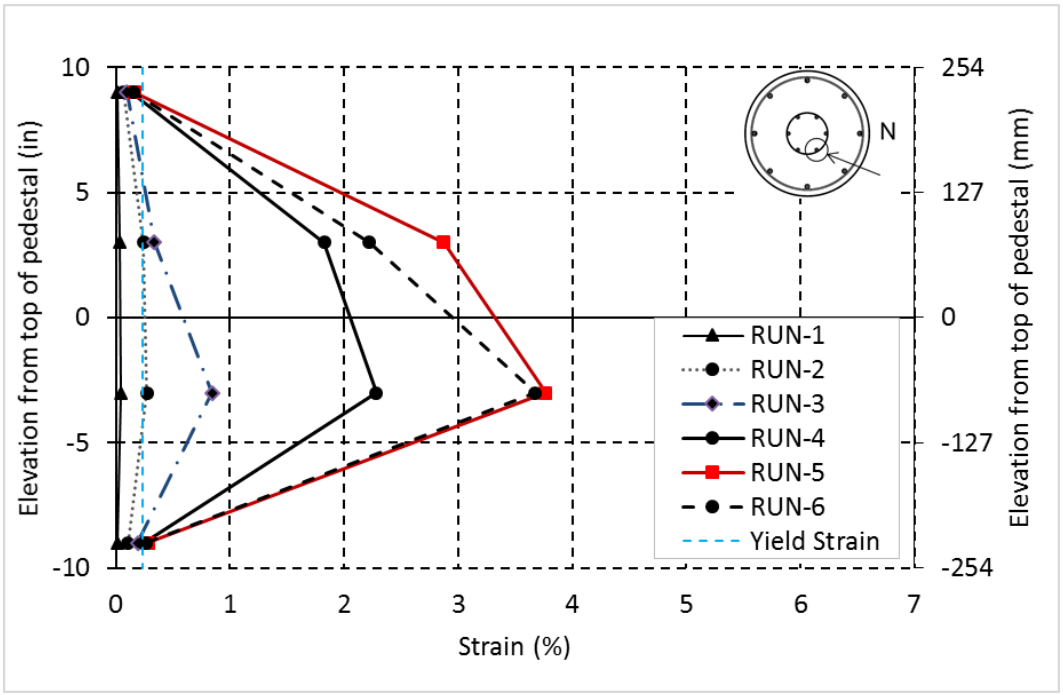

Fig. 3-125. BRSA strain profile of long. bars in PC rebar-pin a)N b)NE

a)

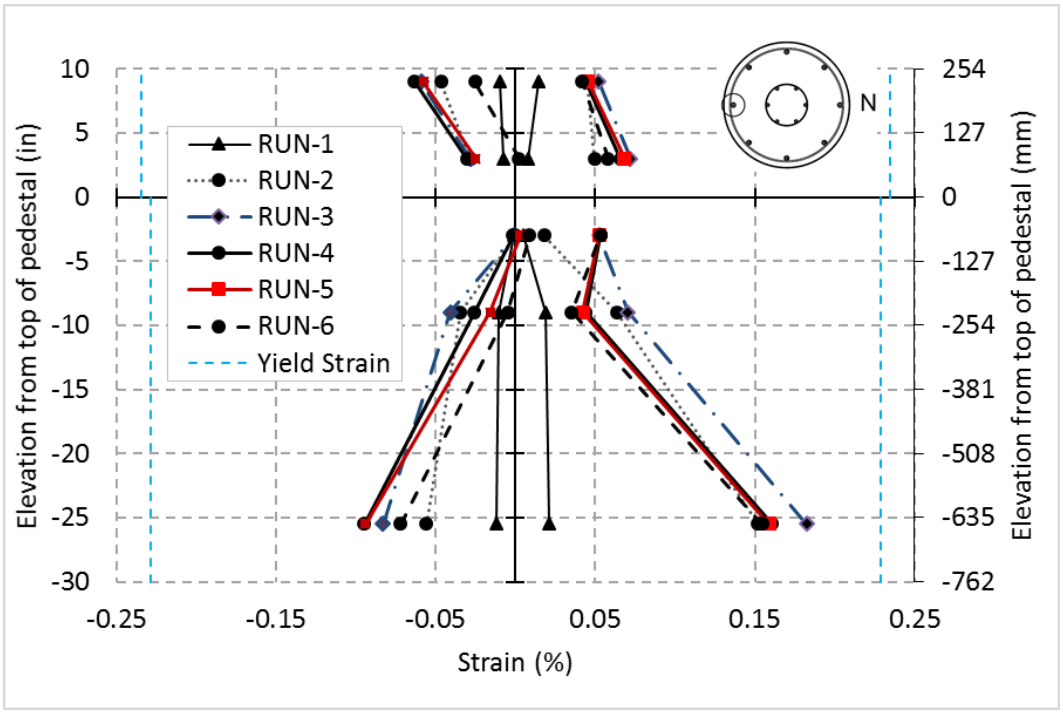

b)

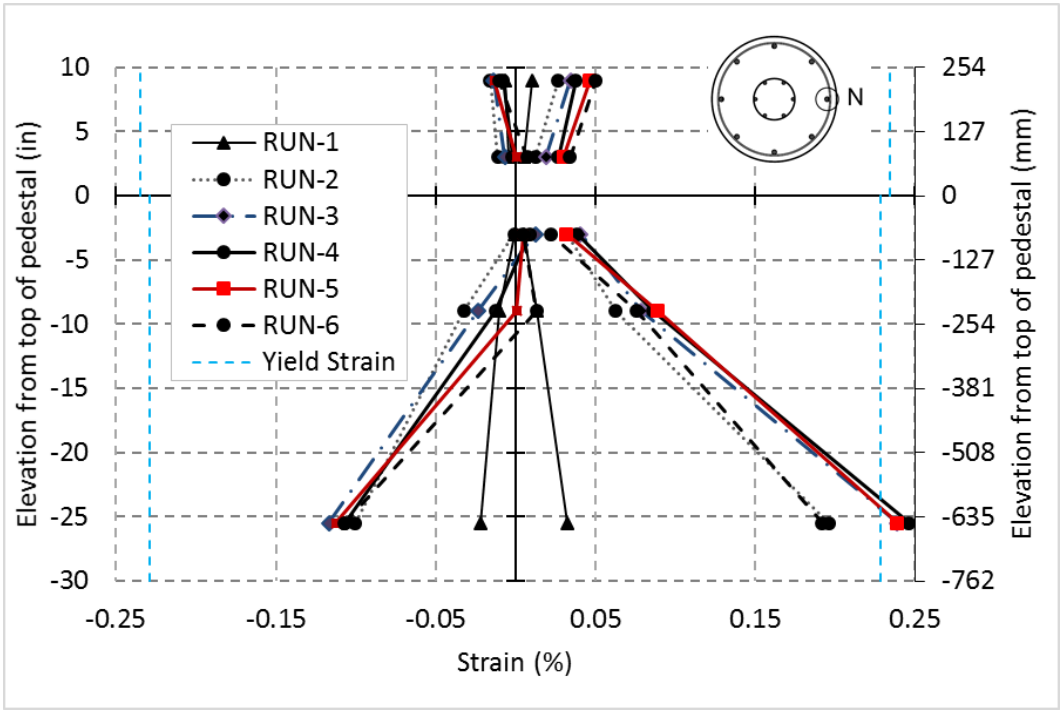

Fig. 3-126. BRSA profile of maximum and minimum strain in long. bars of CIP column and pedestal near rebar-pin at a)south b)north

a)

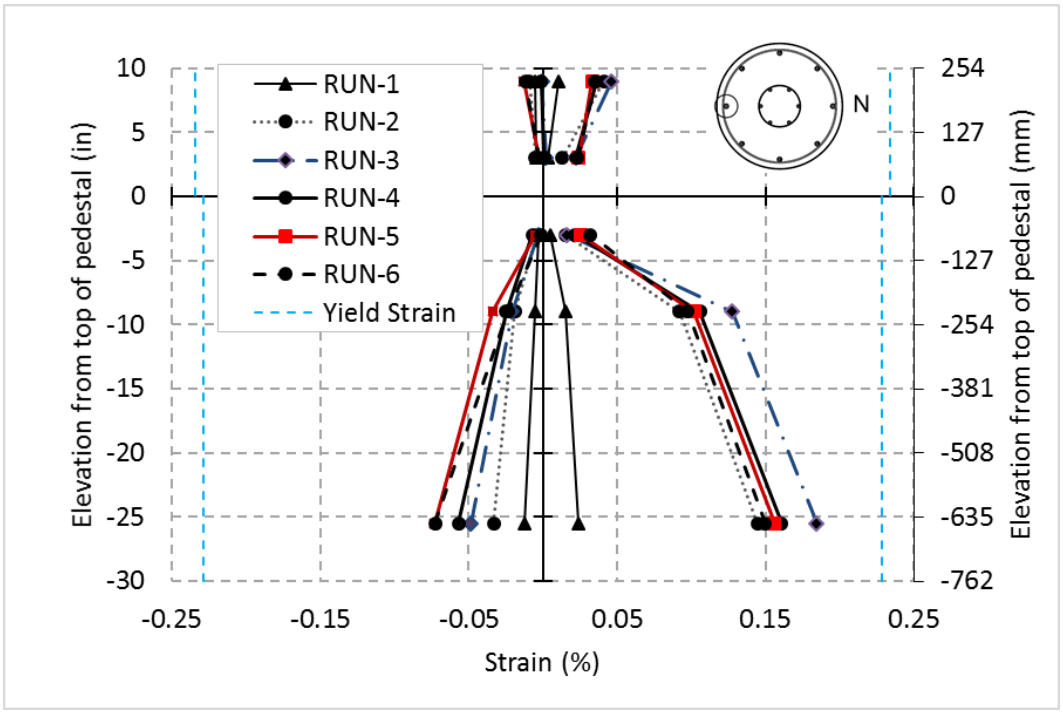

b)

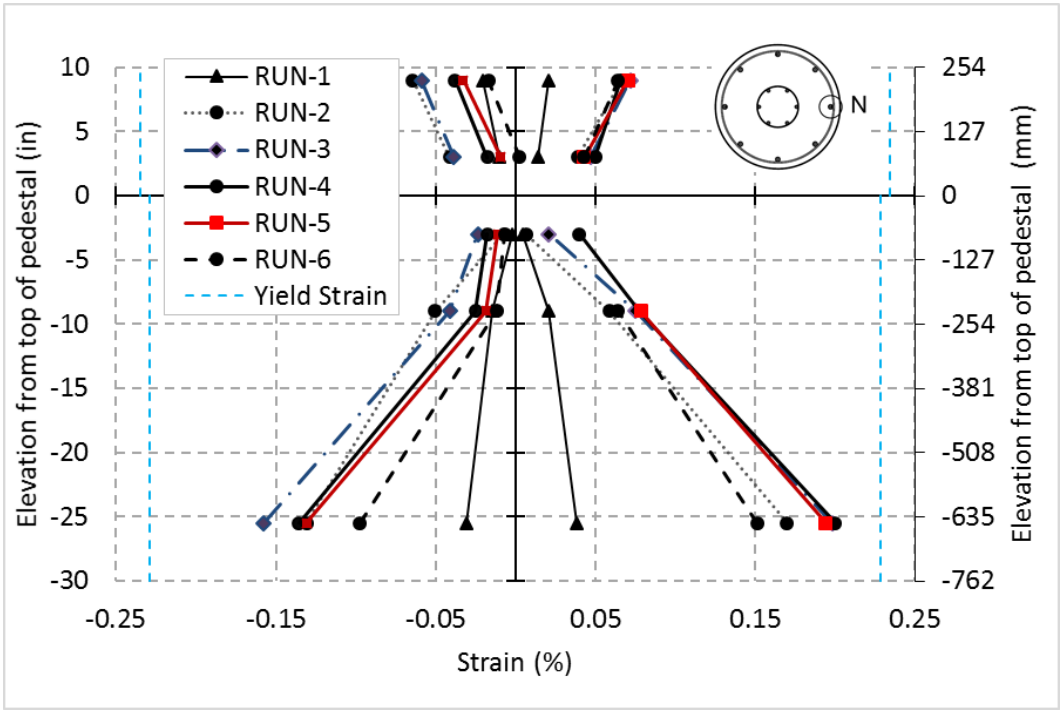

Fig. 3-127. BRSA profile of maximum and minimum strain in long. bars of PC column and pedestal near rebar-pin at a)south b)north

a)

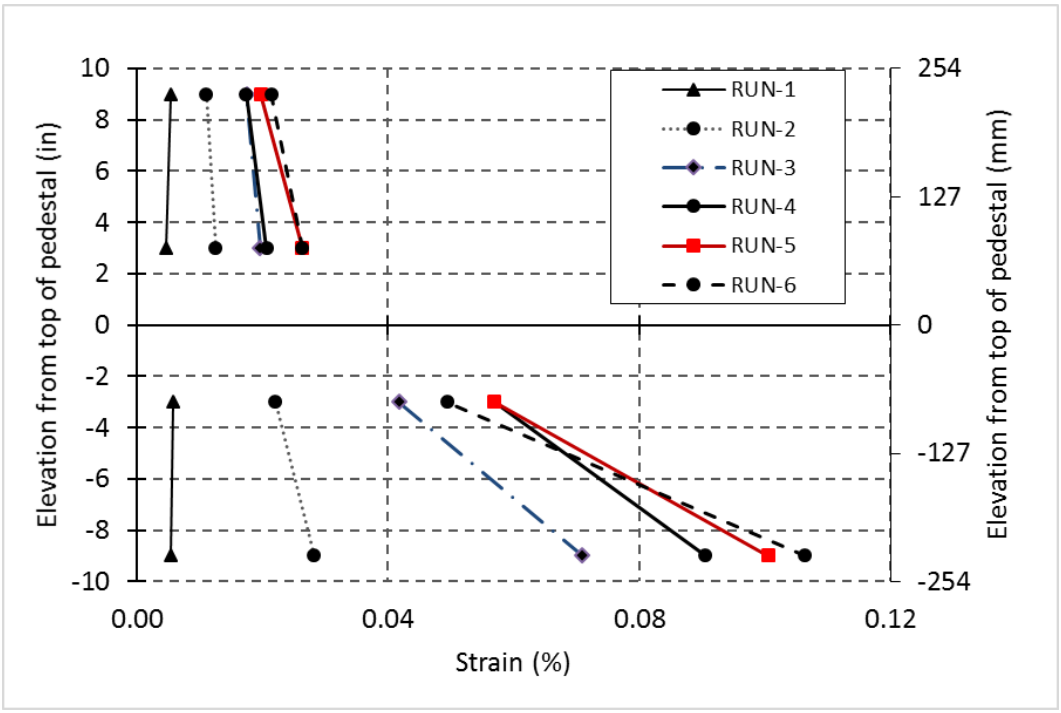

b)

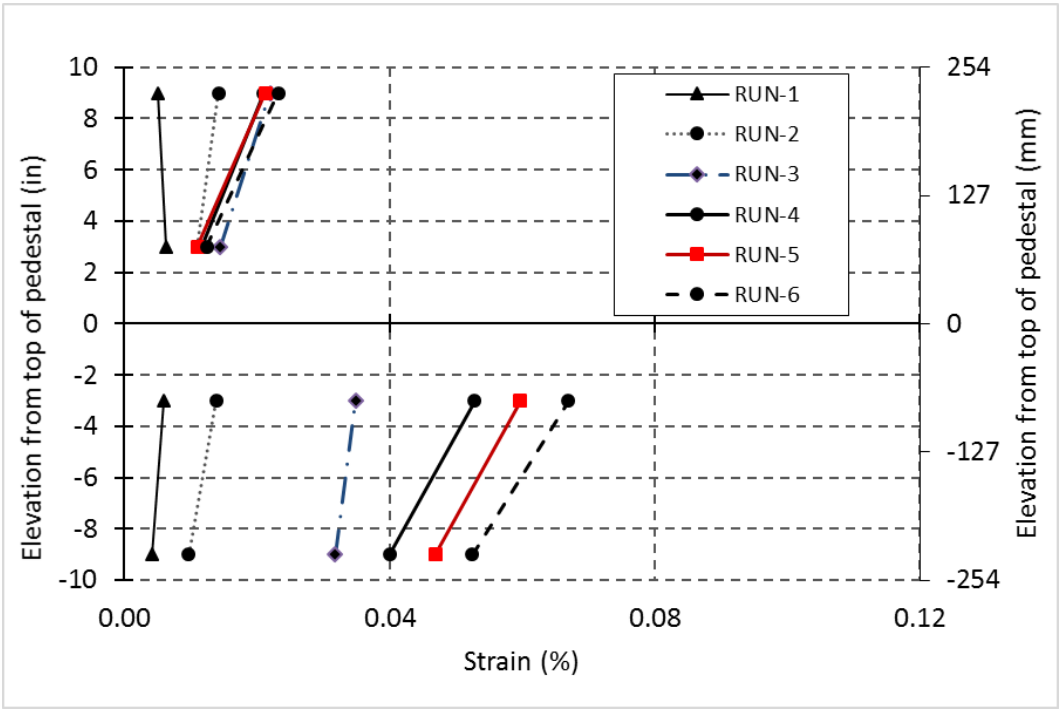

Fig. 3-128. BRSA strain profile of trans. bars in CIP column and pedestal near rebar-pin a) average of north and south b) average of east and west

a)

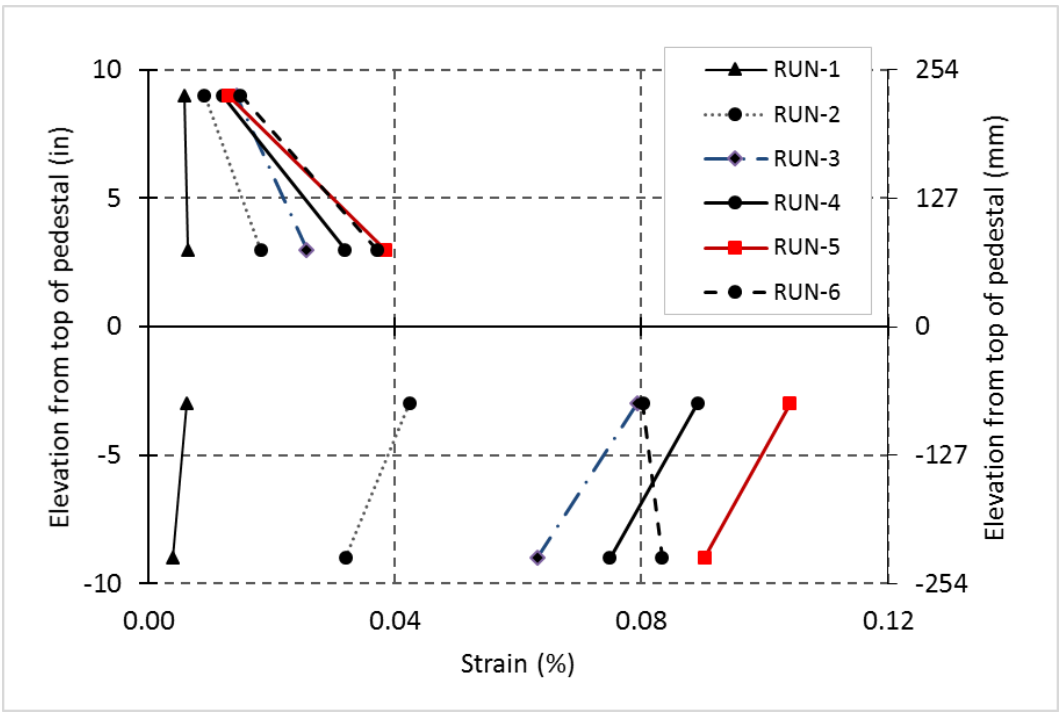

b)

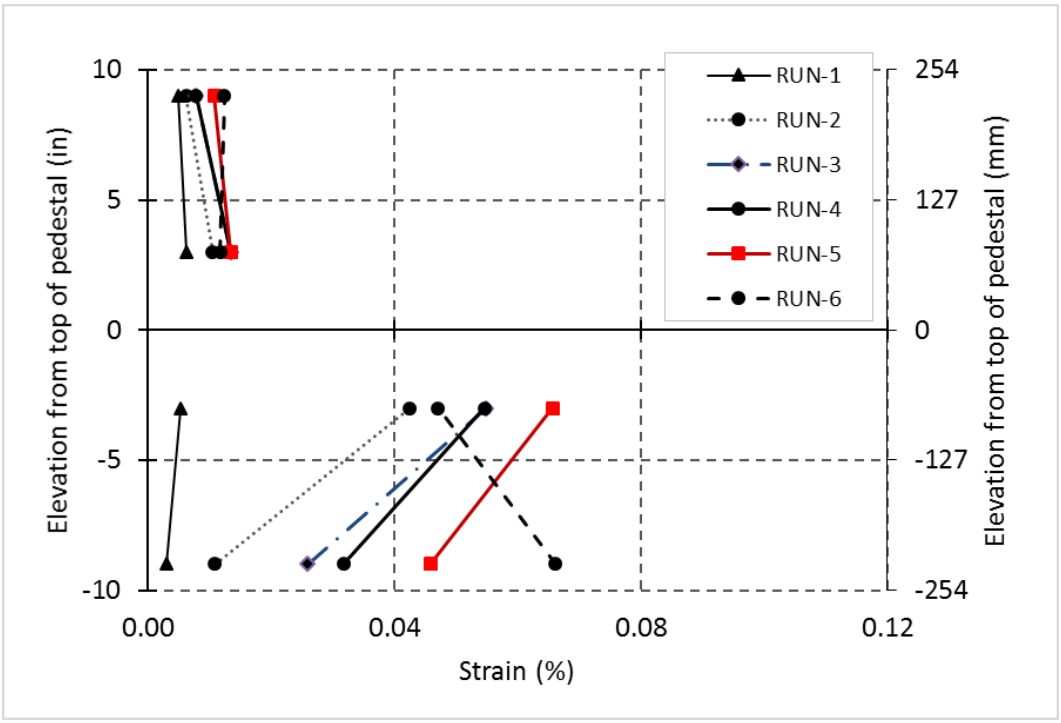

Fig. 3-129. BRSA strain profile of trans. bars of PC column and pedestal near rebar-pin a) average of north and south b) average of east and west

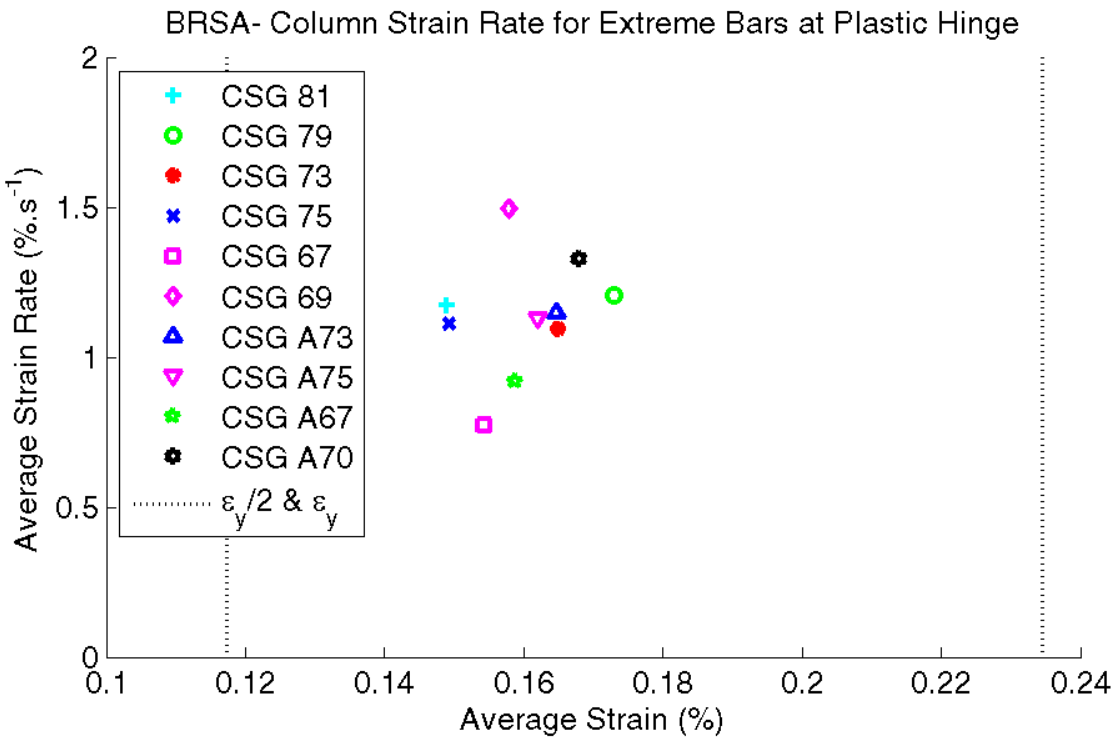

Fig. 3-130. BRSA strain rate in the longitudinal bars of the plastic hinge region

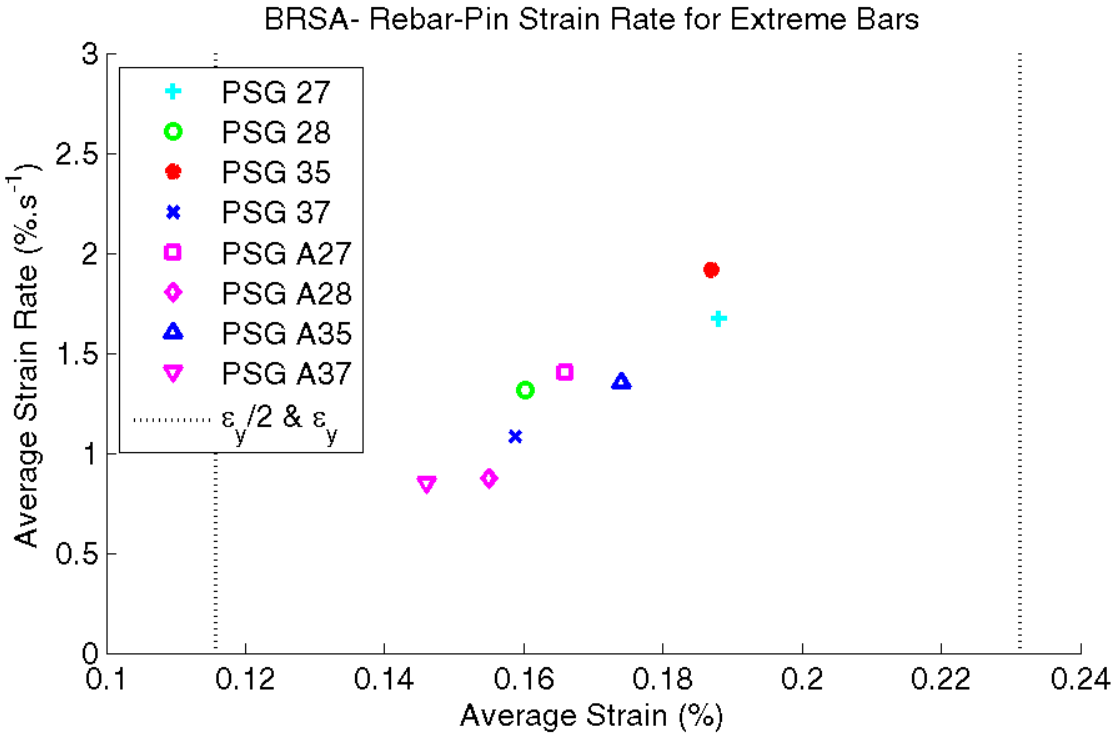

Fig. 3-131. BRSA strain rate in the longitudinal bars of the rebar-pin

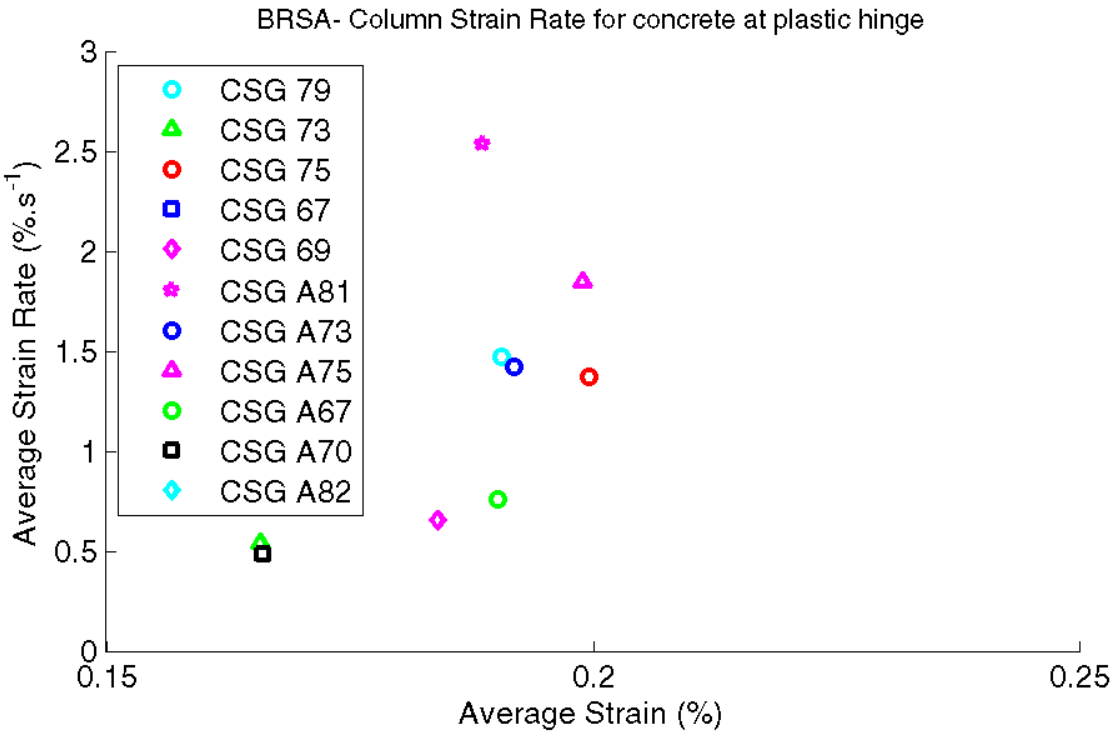

Fig. 3-132. BRSA strain rate of concrete in the plastic hinge region

a)

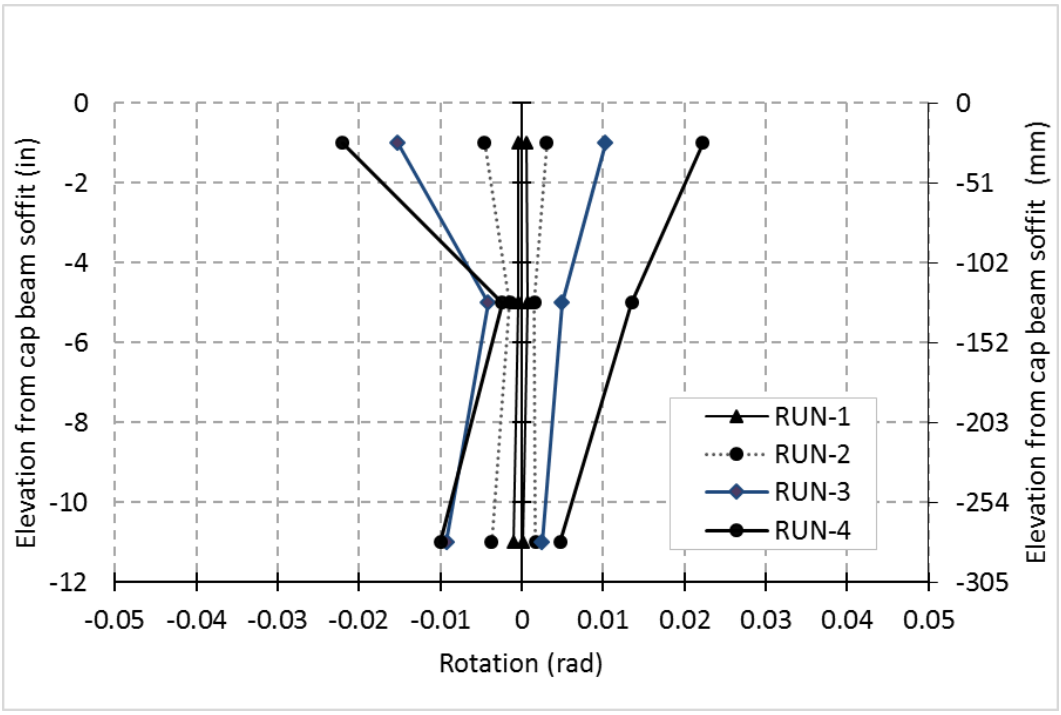

b)

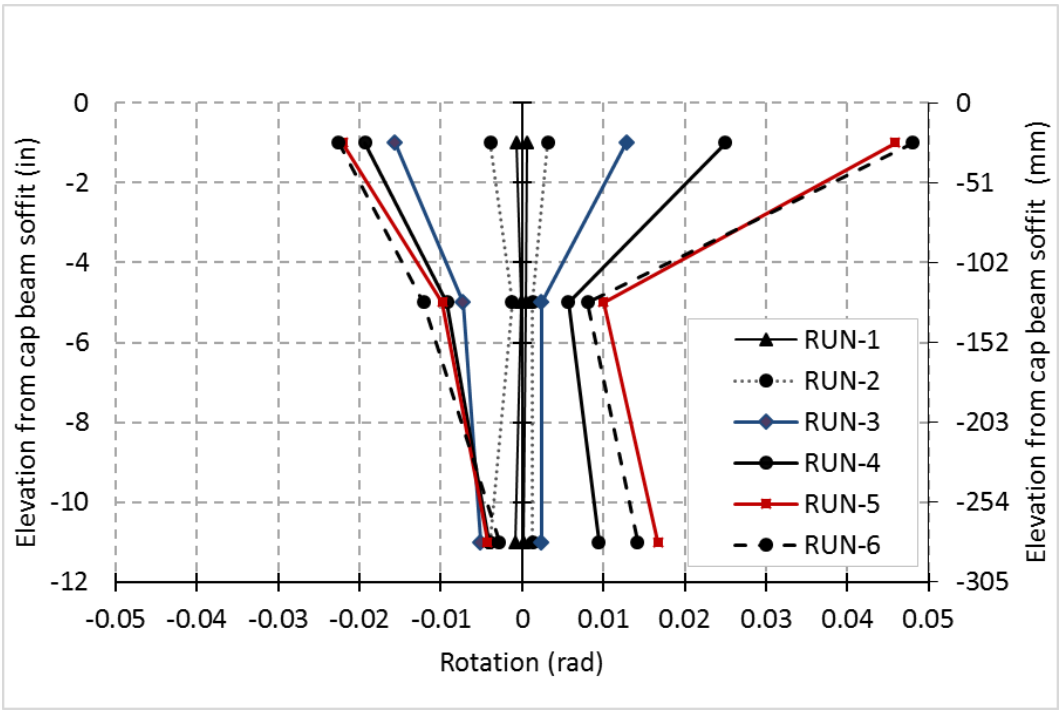

Fig. 3-133. BRSA profile of rotation for plastic hinge region of the columns a) CIP b) PC

a)

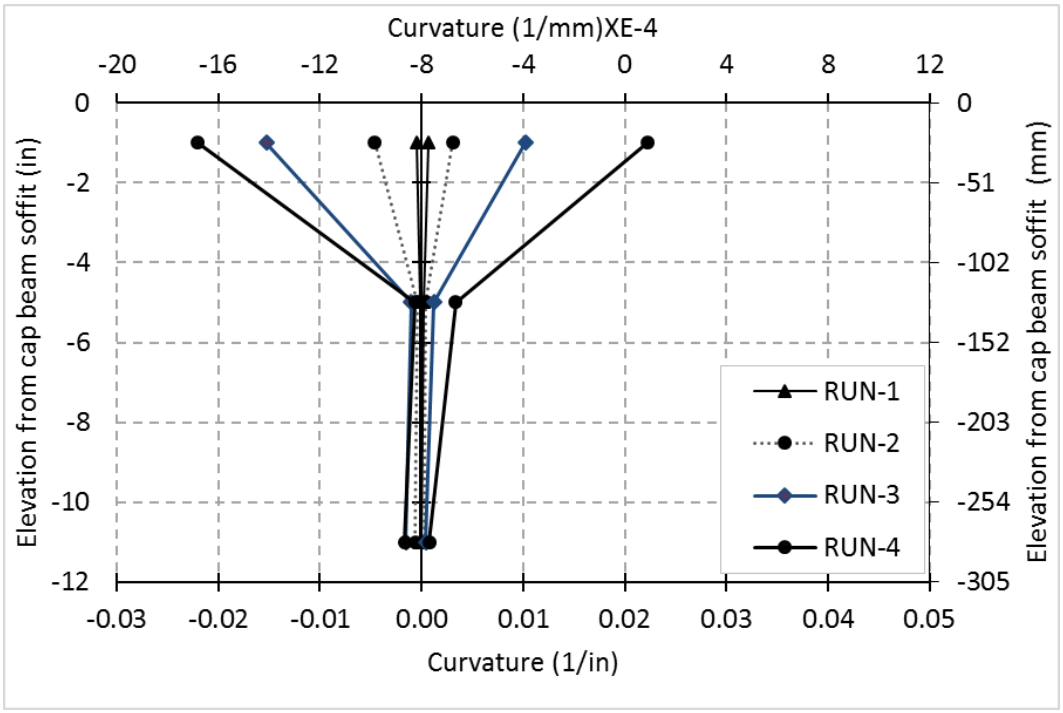

b)

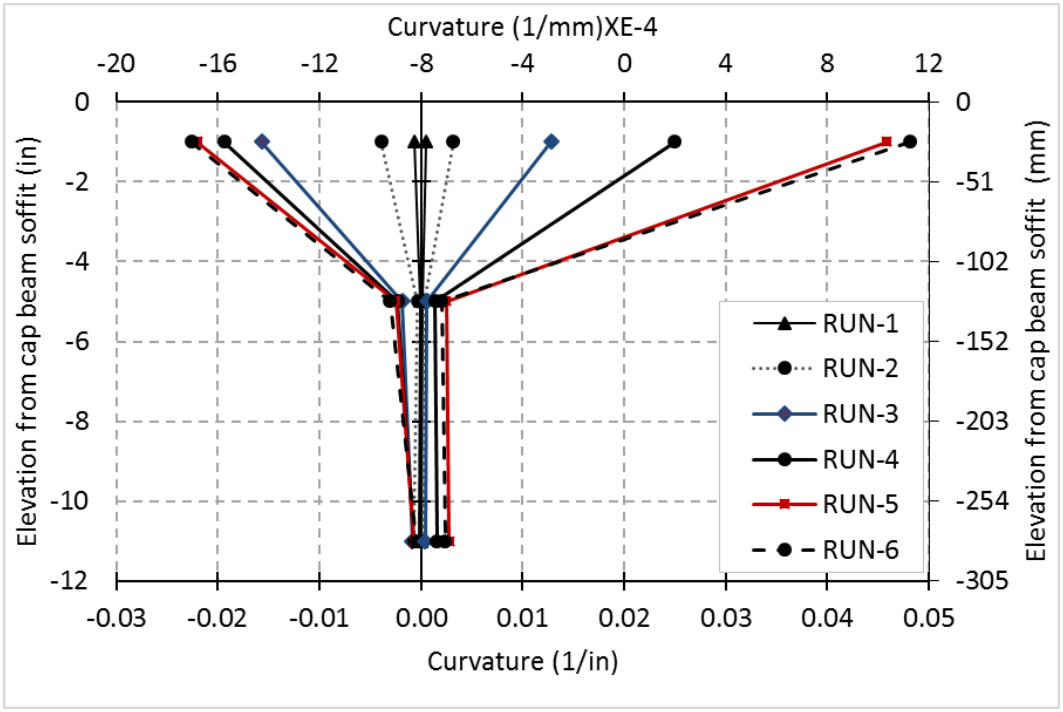

Fig. 3-134. BRSA profile of curvature for plastic hinge region of the columns a) CIP b) PC

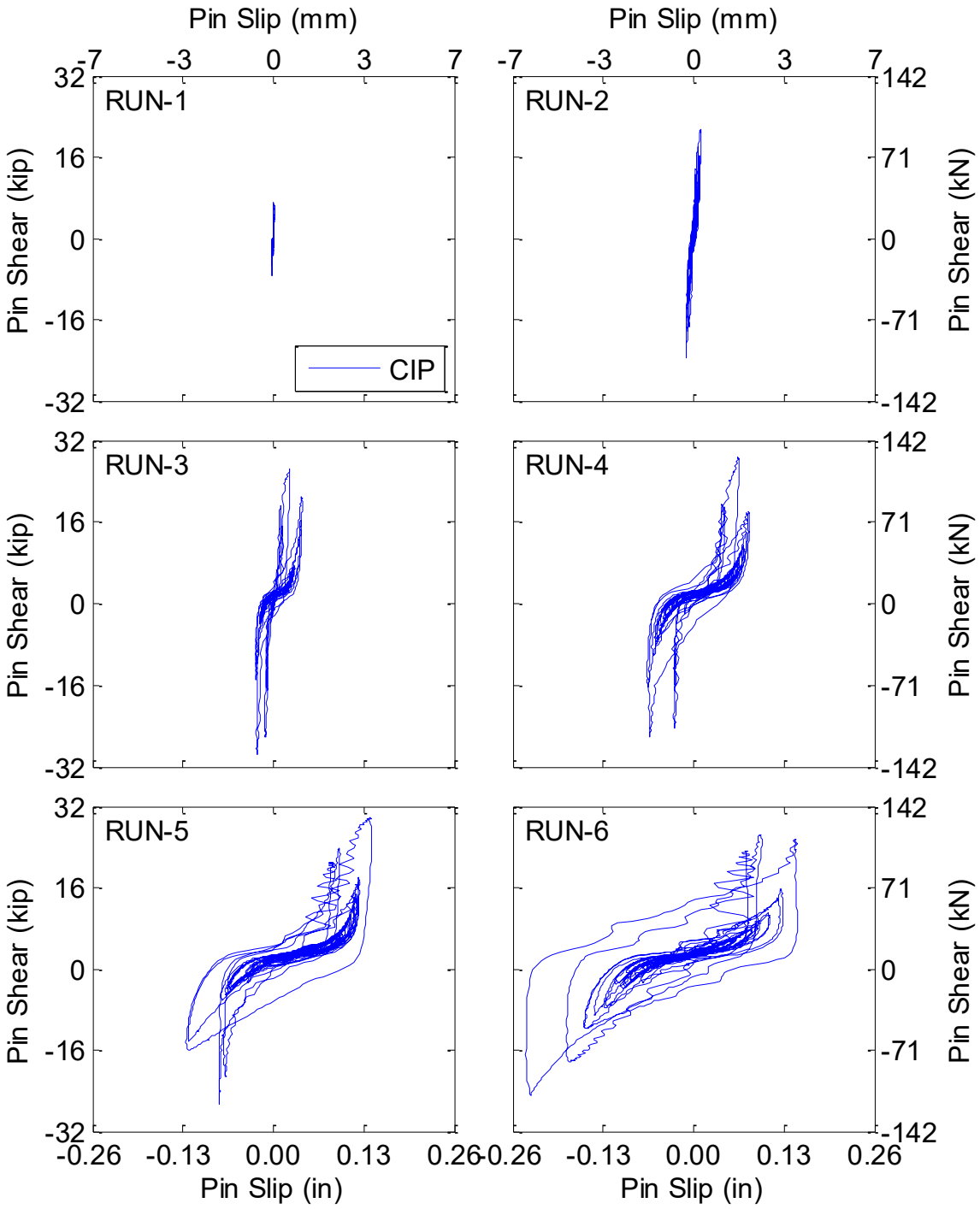

Fig. 3-135. BRSA shear-slip hysteresis for CIP rebar-pin

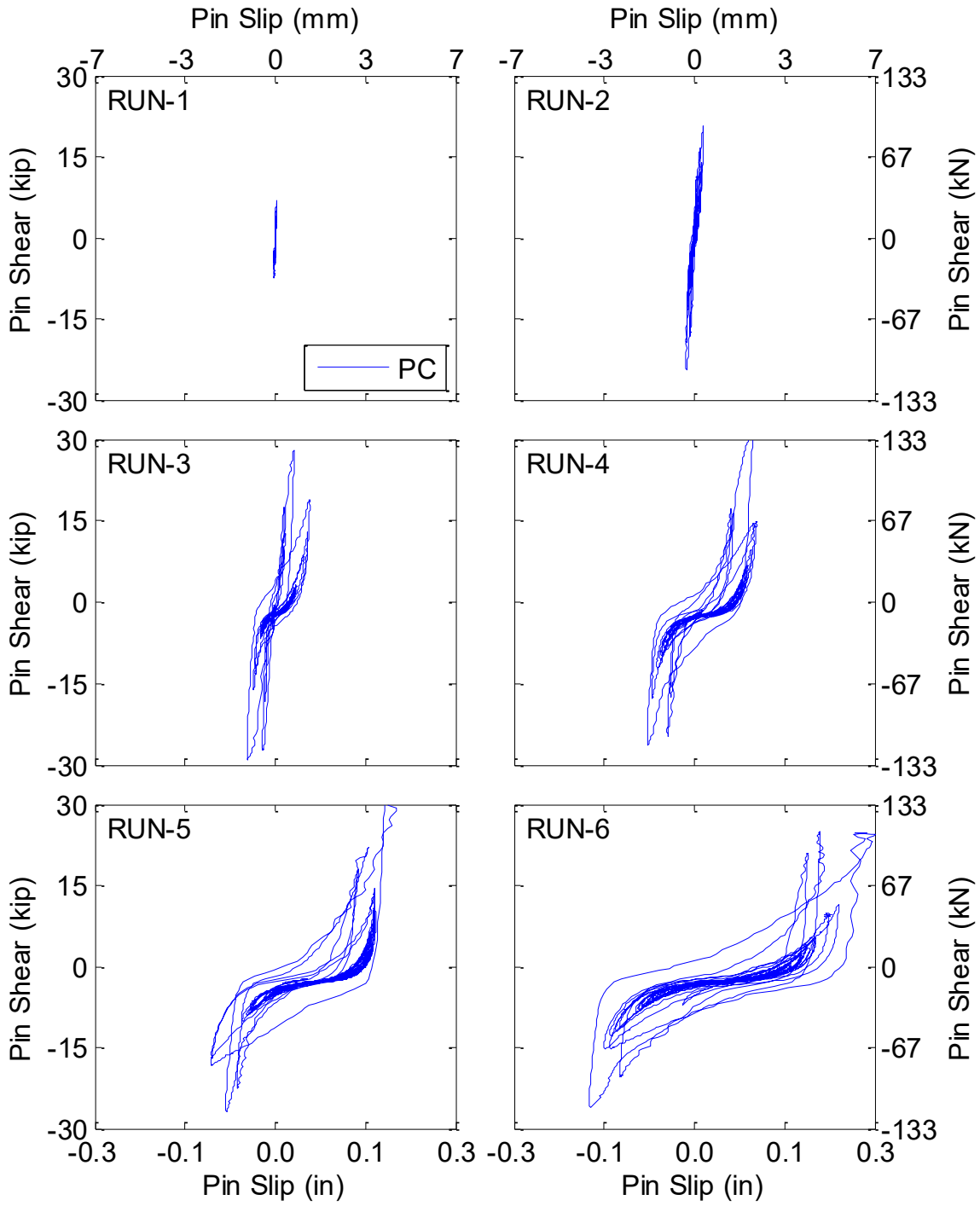

Fig. 3-136. BRSA shear-slip hysteresis for PC rebar-pin

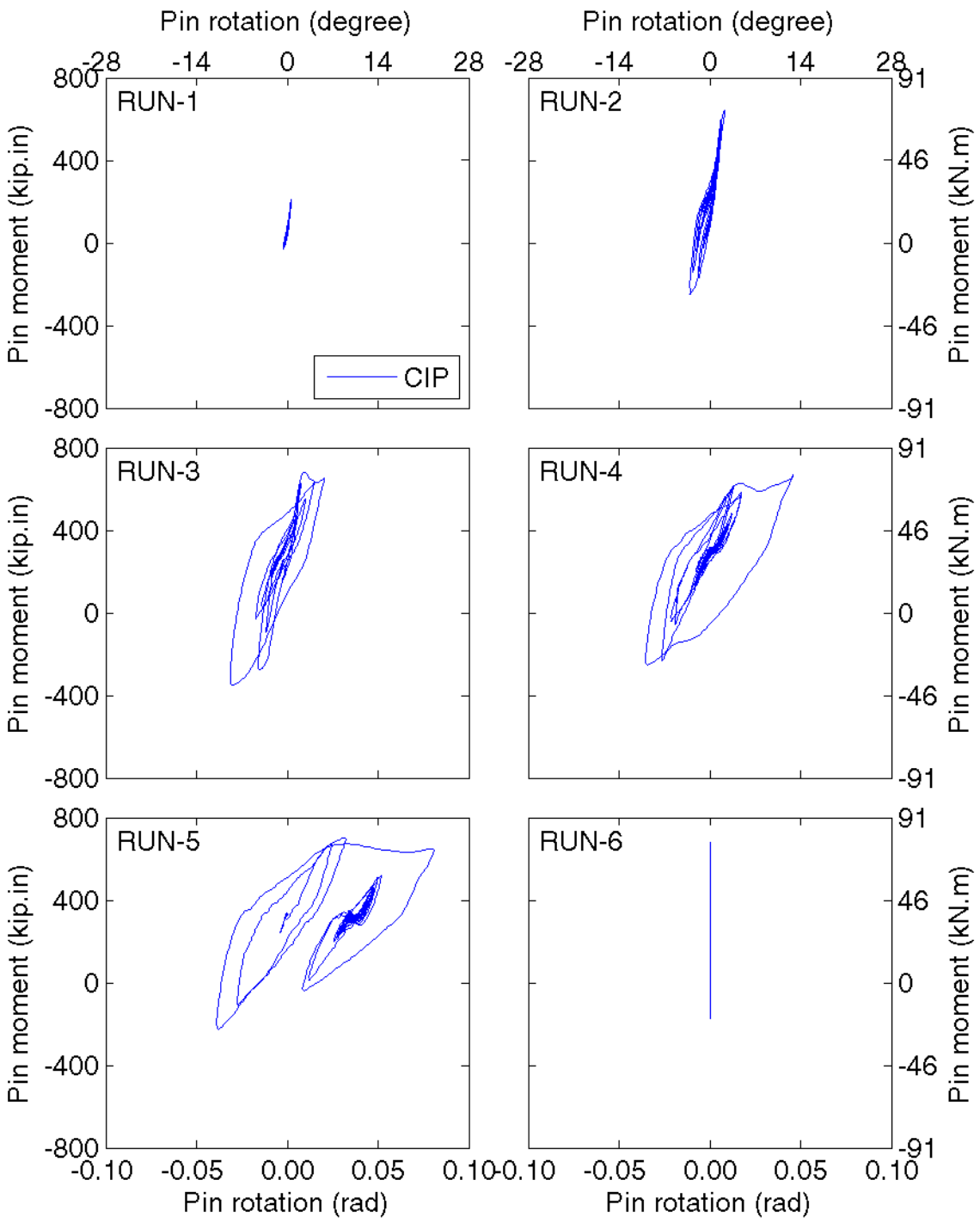

Fig. 3-137. BRSA moment-rotation hysteresis for CIP rebar-pin

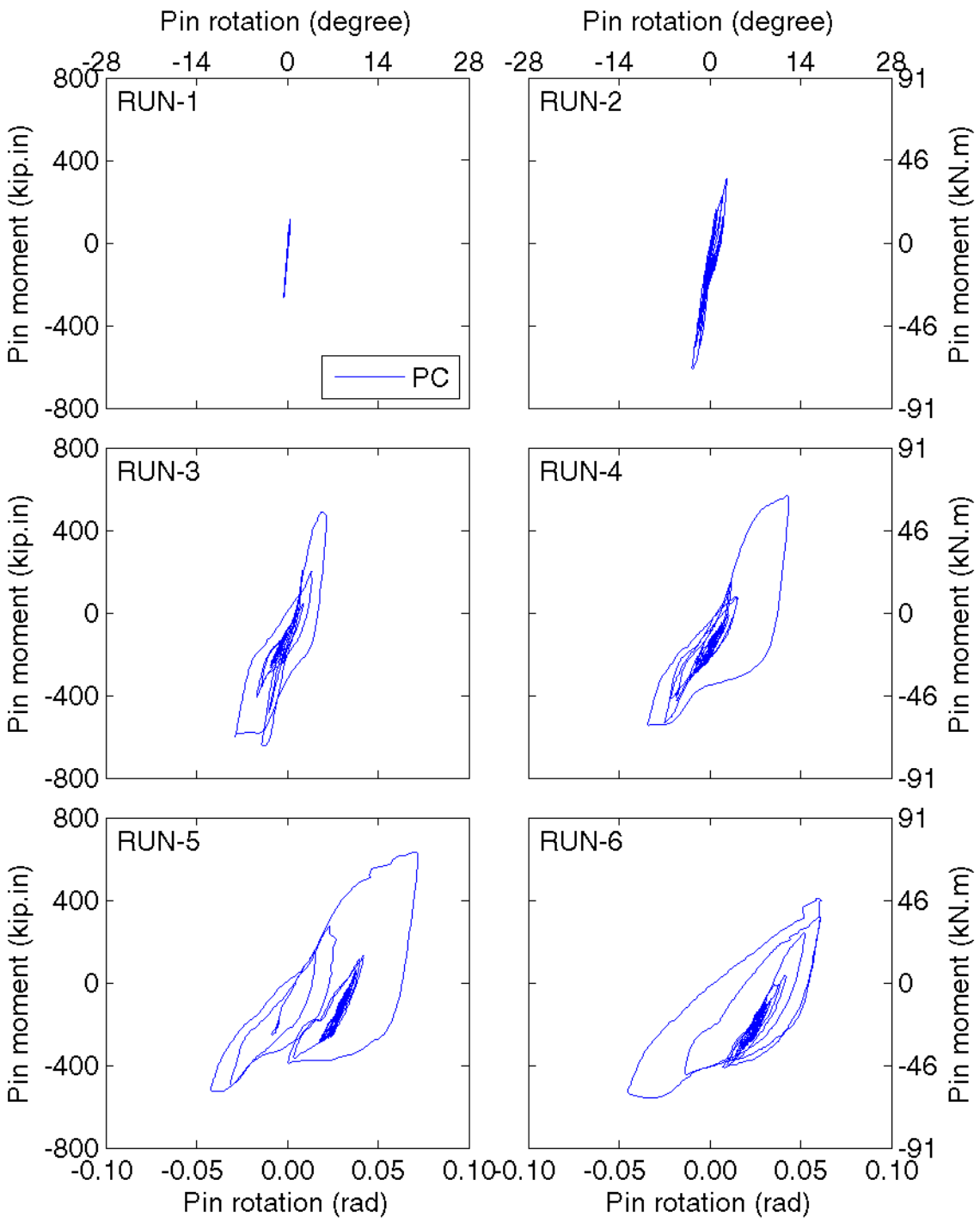

Fig. 3-138. BRSA moment-rotation hysteresis for PC rebar-pin

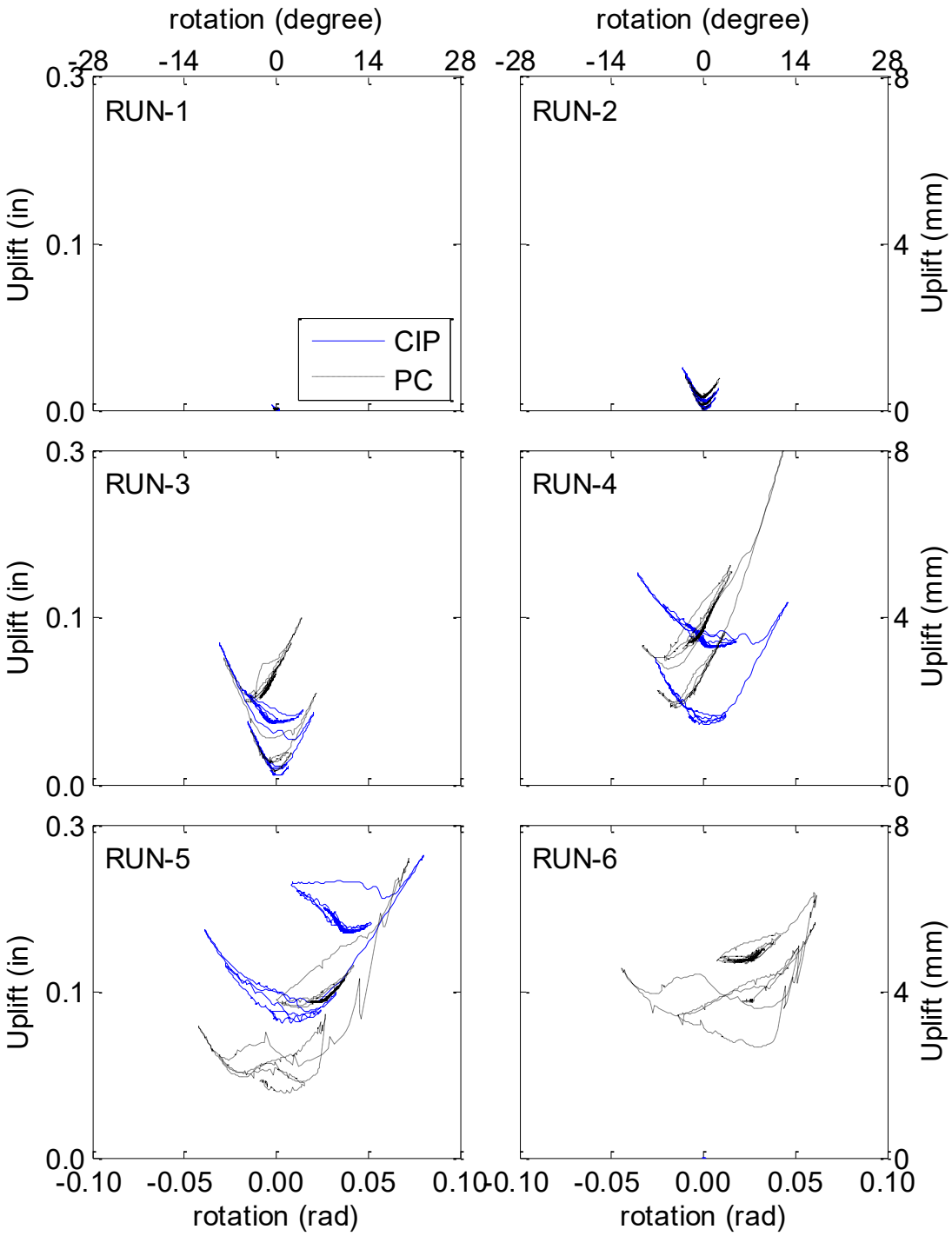

Fig. 3-139. BRSA rotation vs. uplift of rebar-pins

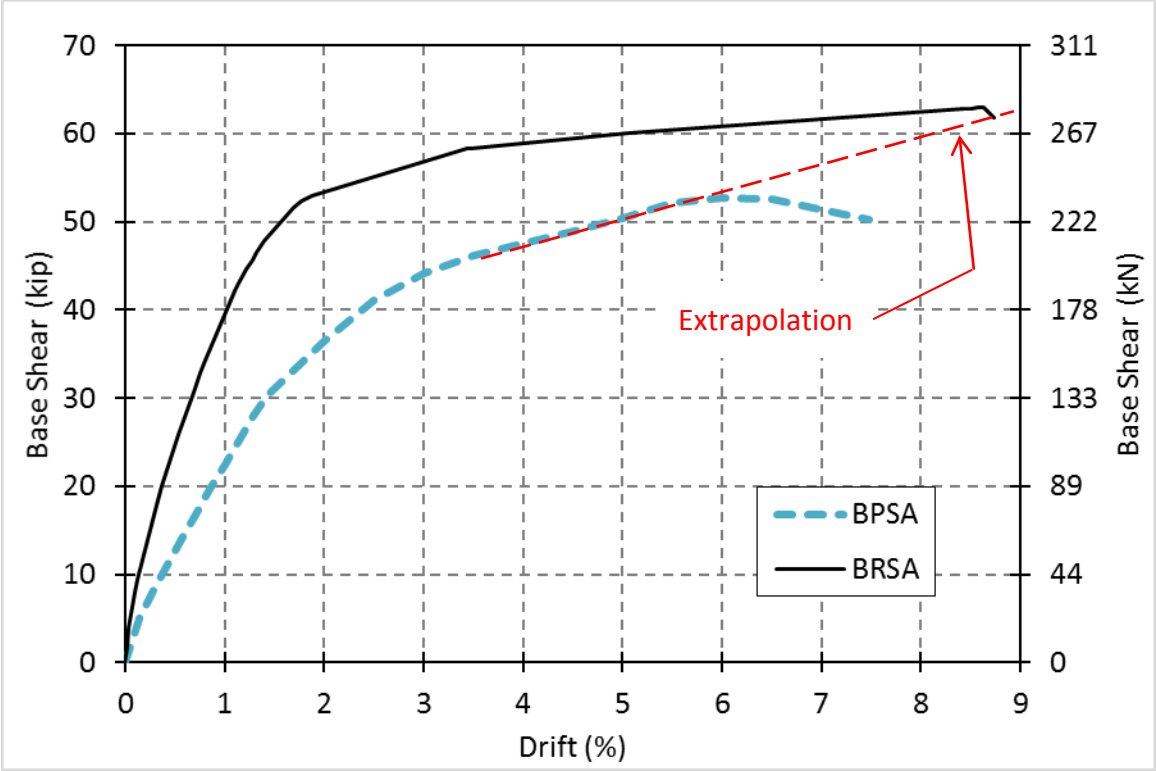

Fig. 3-140. Force-displacement envelope comparison of two bents

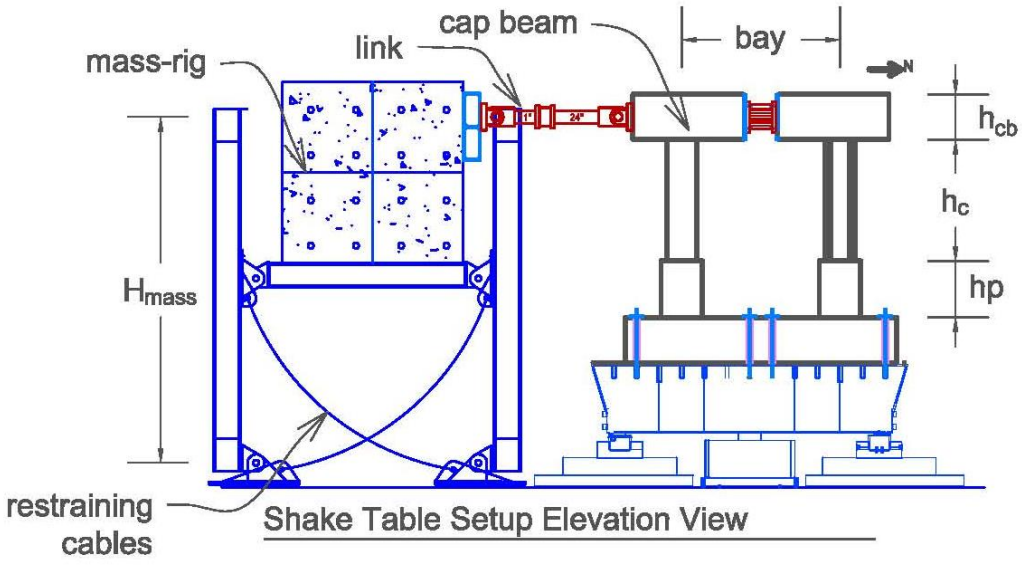

Fig. 4-1. Test setup – elevation view

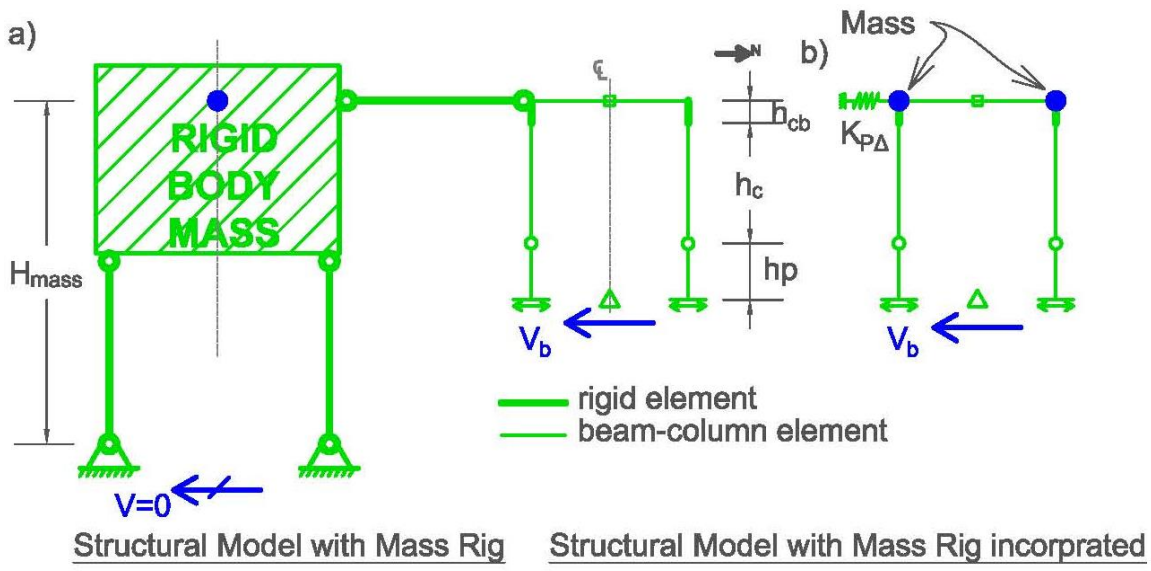

Fig. 4-2. Frame structural models

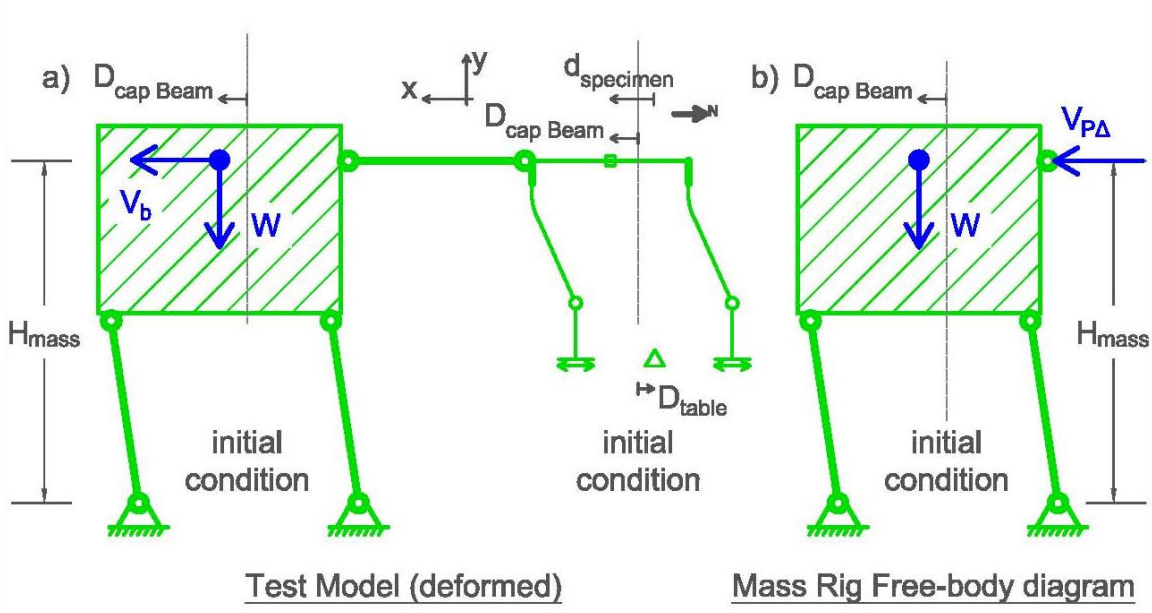

Fig. 4-3. P-Delta effect

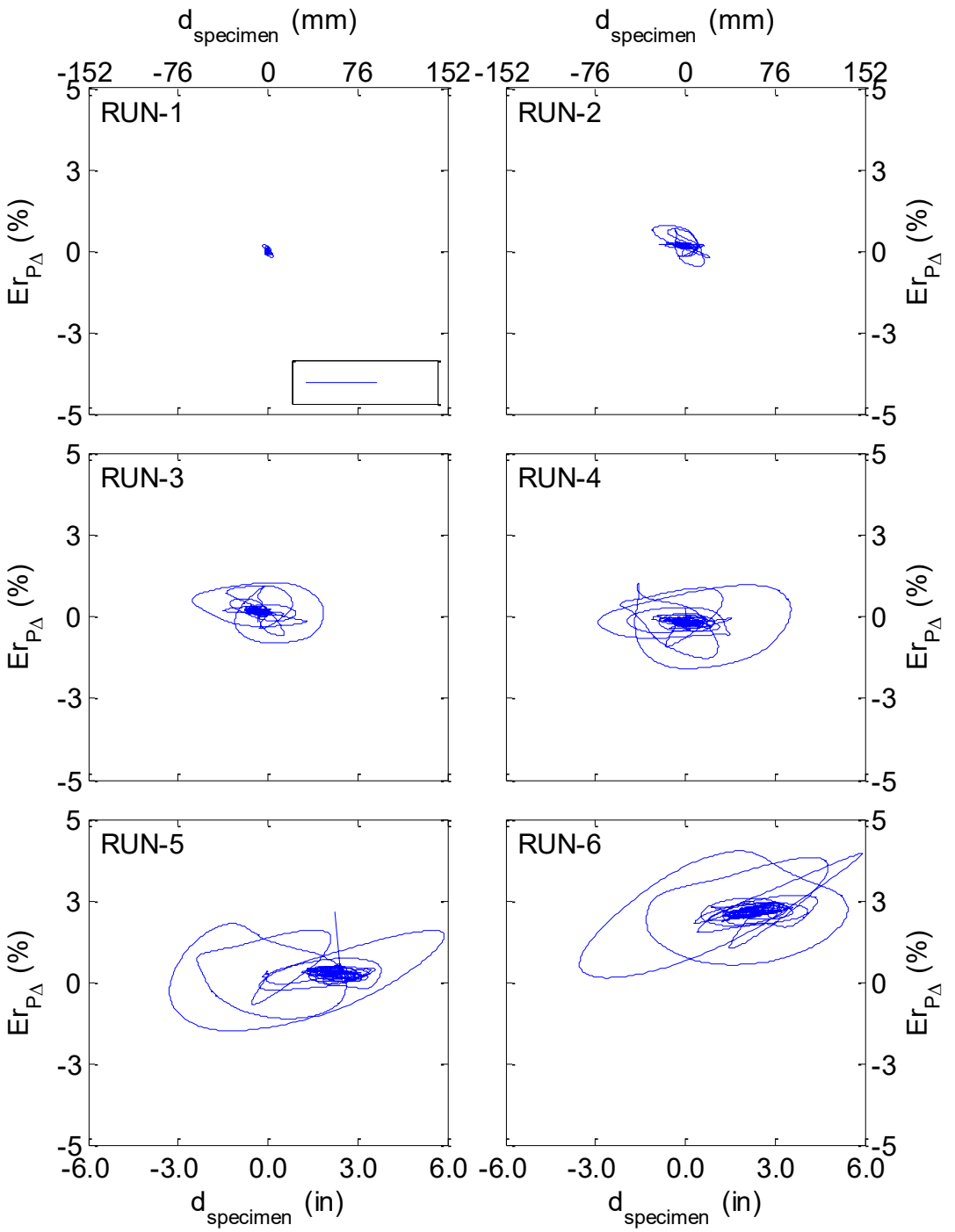

Fig. 4-4. Error of P-Delta estimation in BRSA

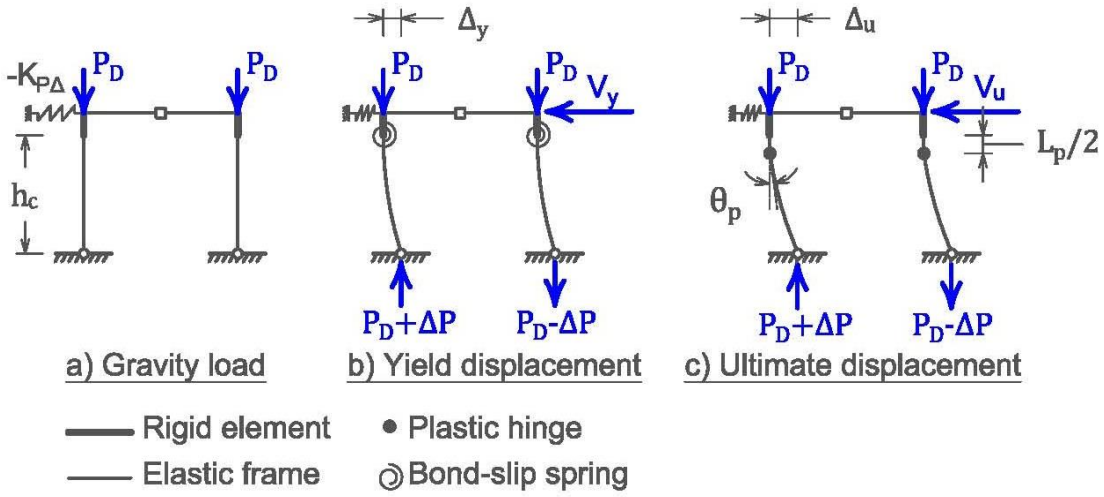

Fig. 4-5. Lumped plasticity model

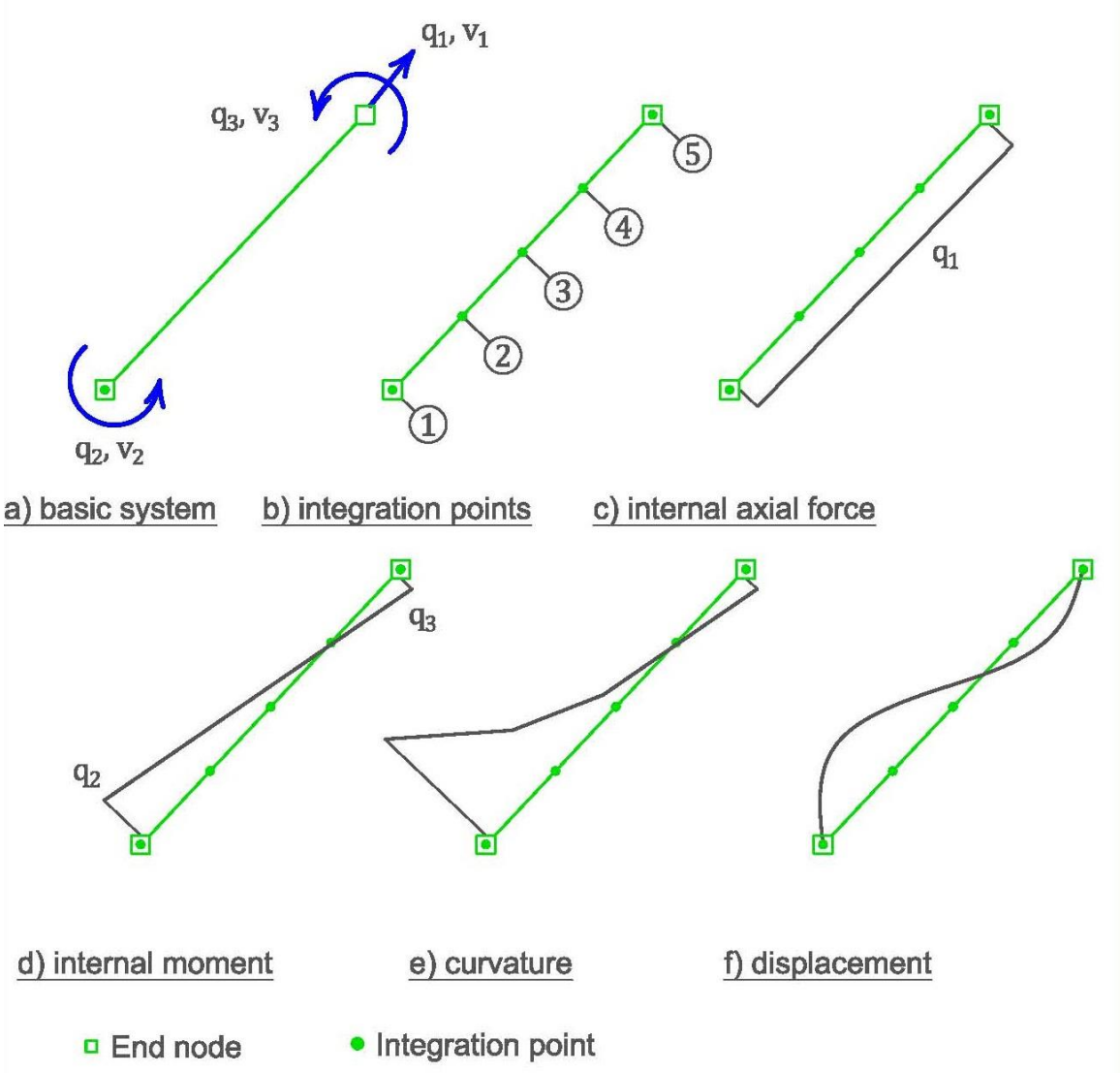

Fig. 4-6. Force-based displacement element formulation

(a)

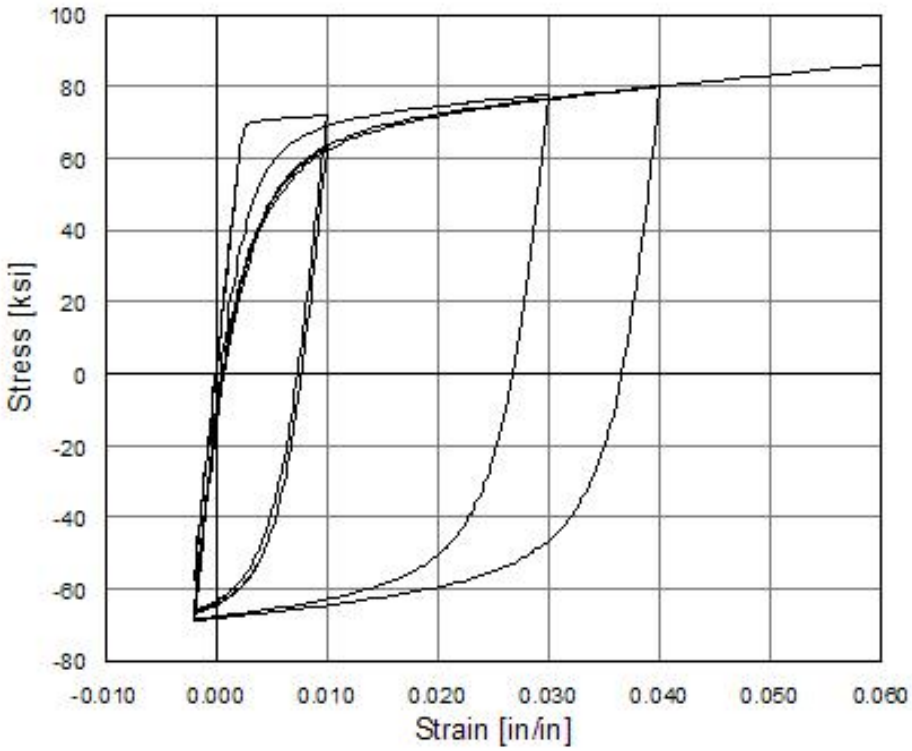

(b)

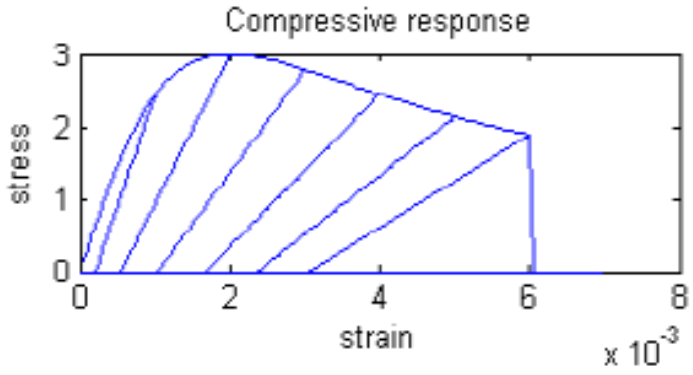

Fig. 4-7. OpenSEES stress-strain relations of a) steel02 b) concrete04

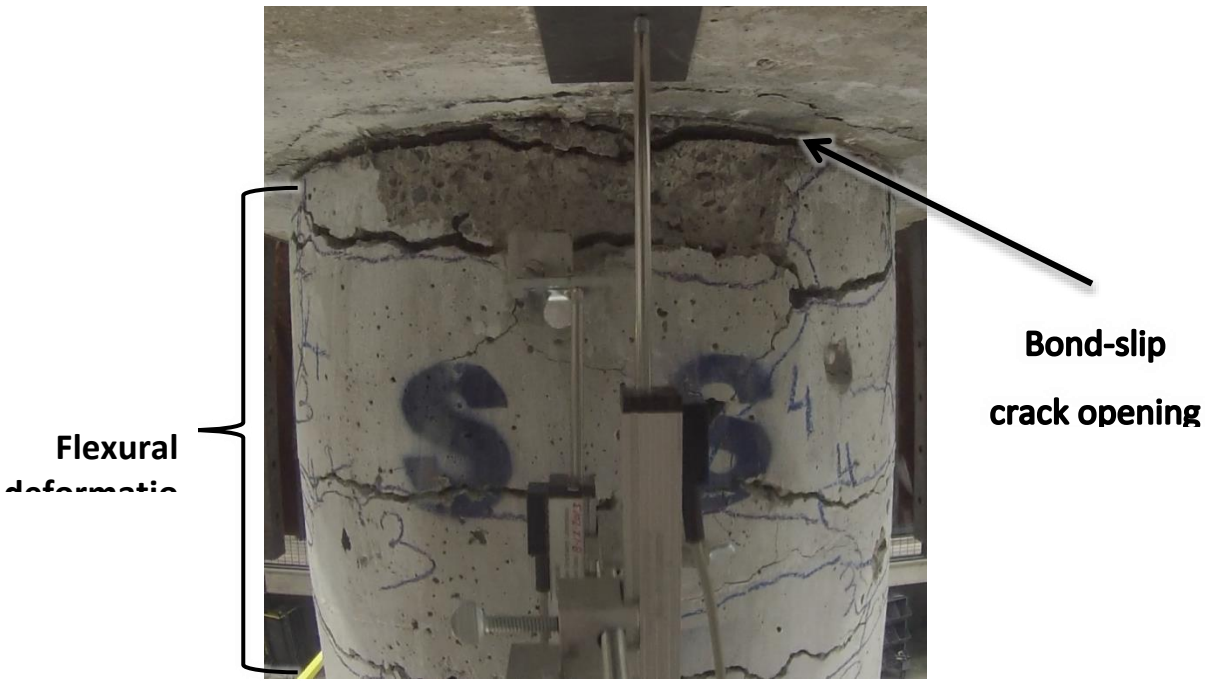

Fig. 4-8. Bond-slip rotation CIP column of BRSA during Run-5

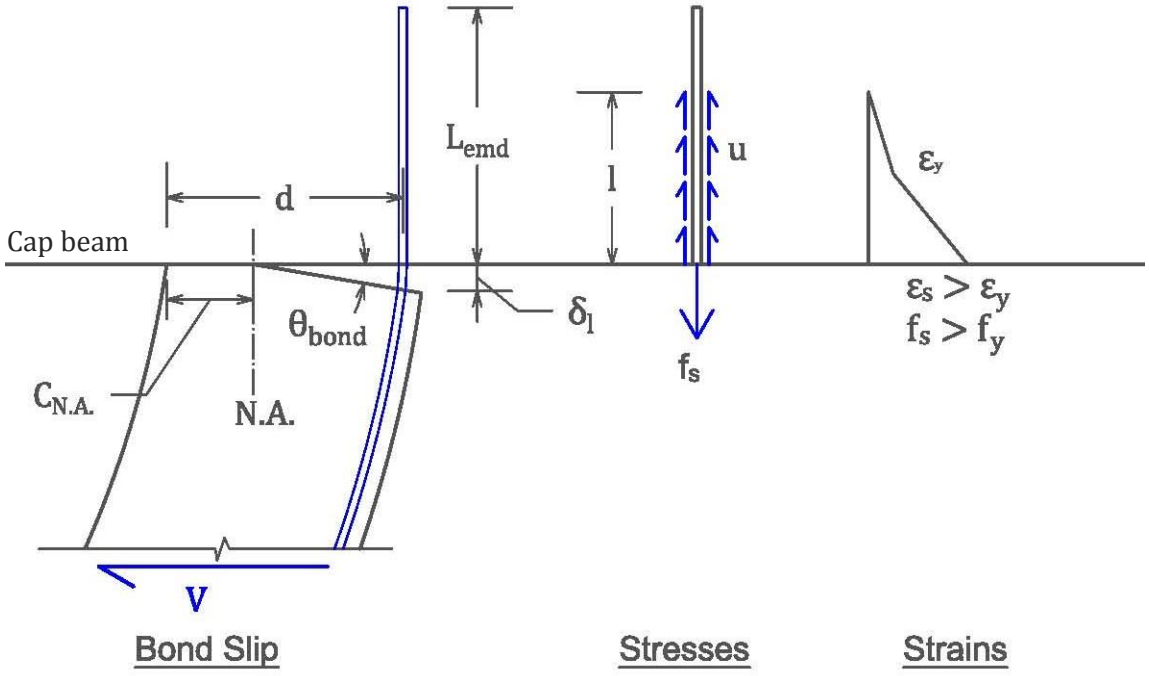

Fig. 4-9. The Wehbe(1999) bond-slip model

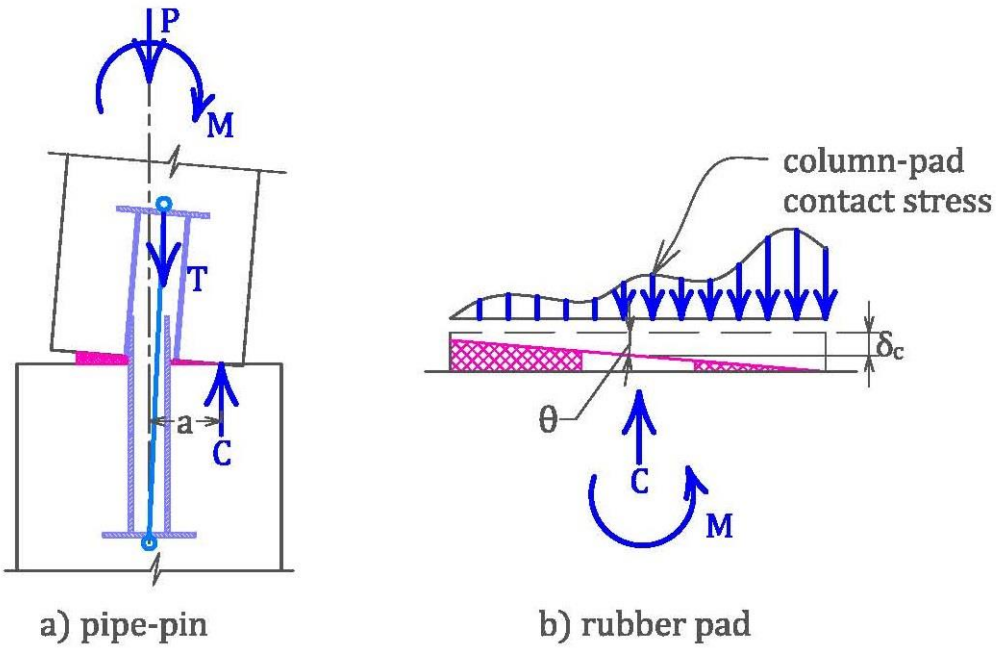

Fig. 4-10. Free-body diagrams of pipe-pin

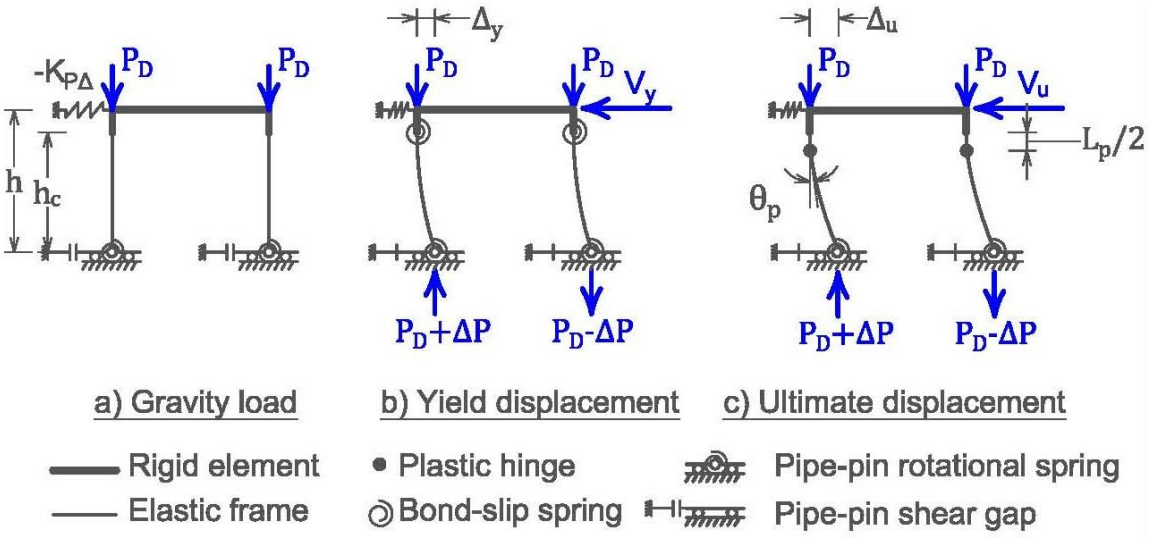

Fig. 4-11. BPSA simple stick model

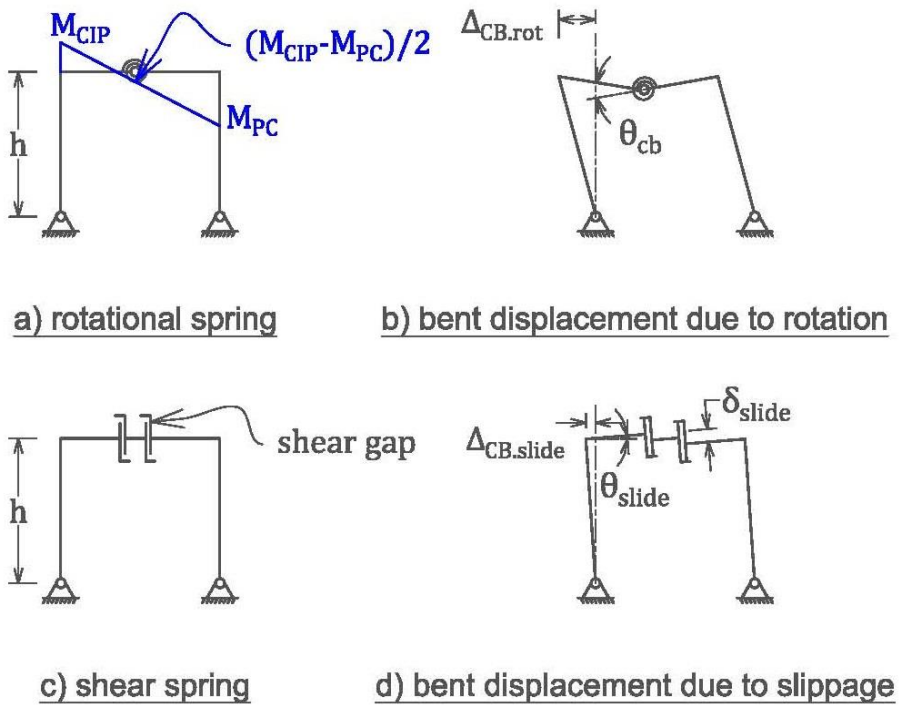

Fig. 4-12. Effect of cap beam deformation on bent displacement

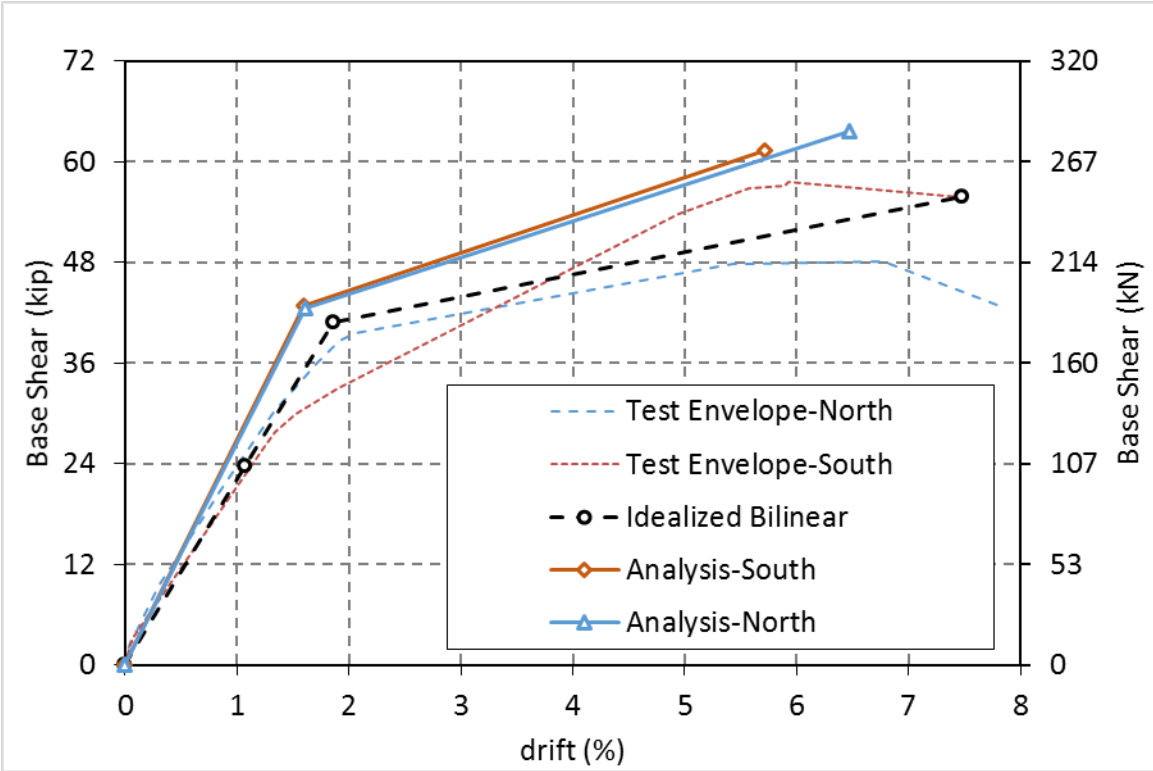

Fig. 4-13. BPSA force-displacement envelopes using simple stick model

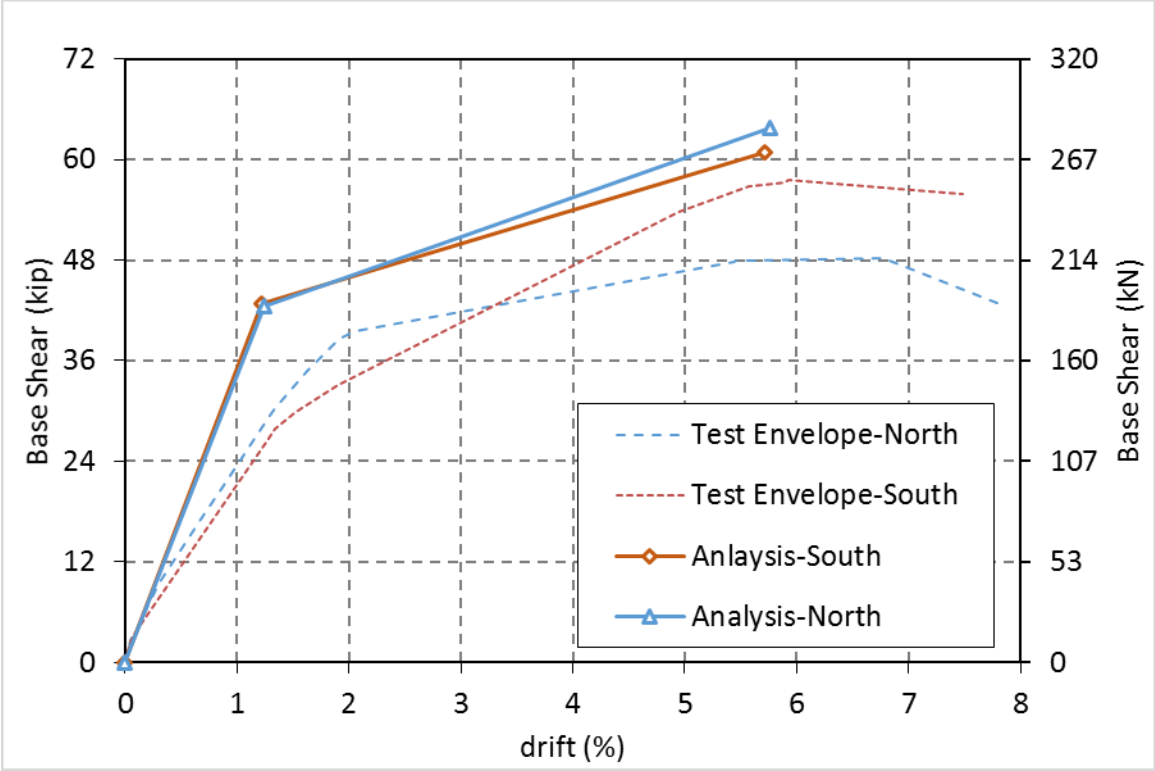

Fig. 4-14. BPSA force-displacement envelopes using simple stick model with rigid cap beam

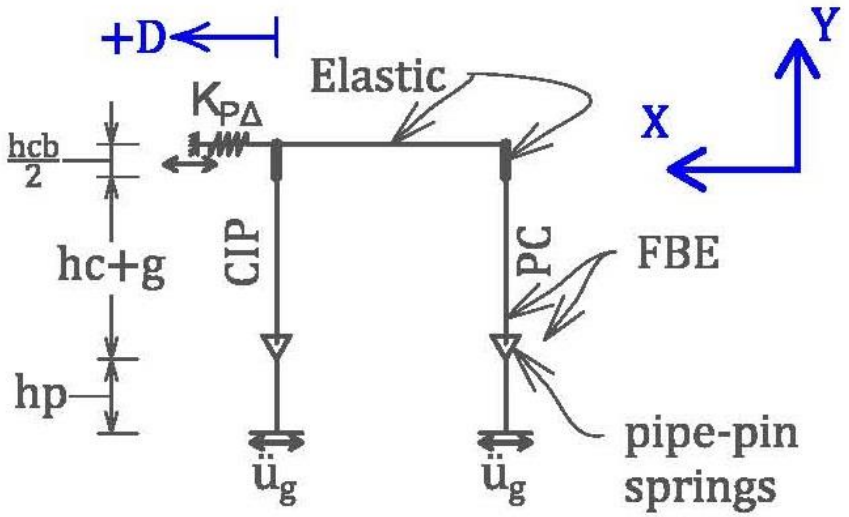

Fig. 4-15. BPSA models for dynamic analyses

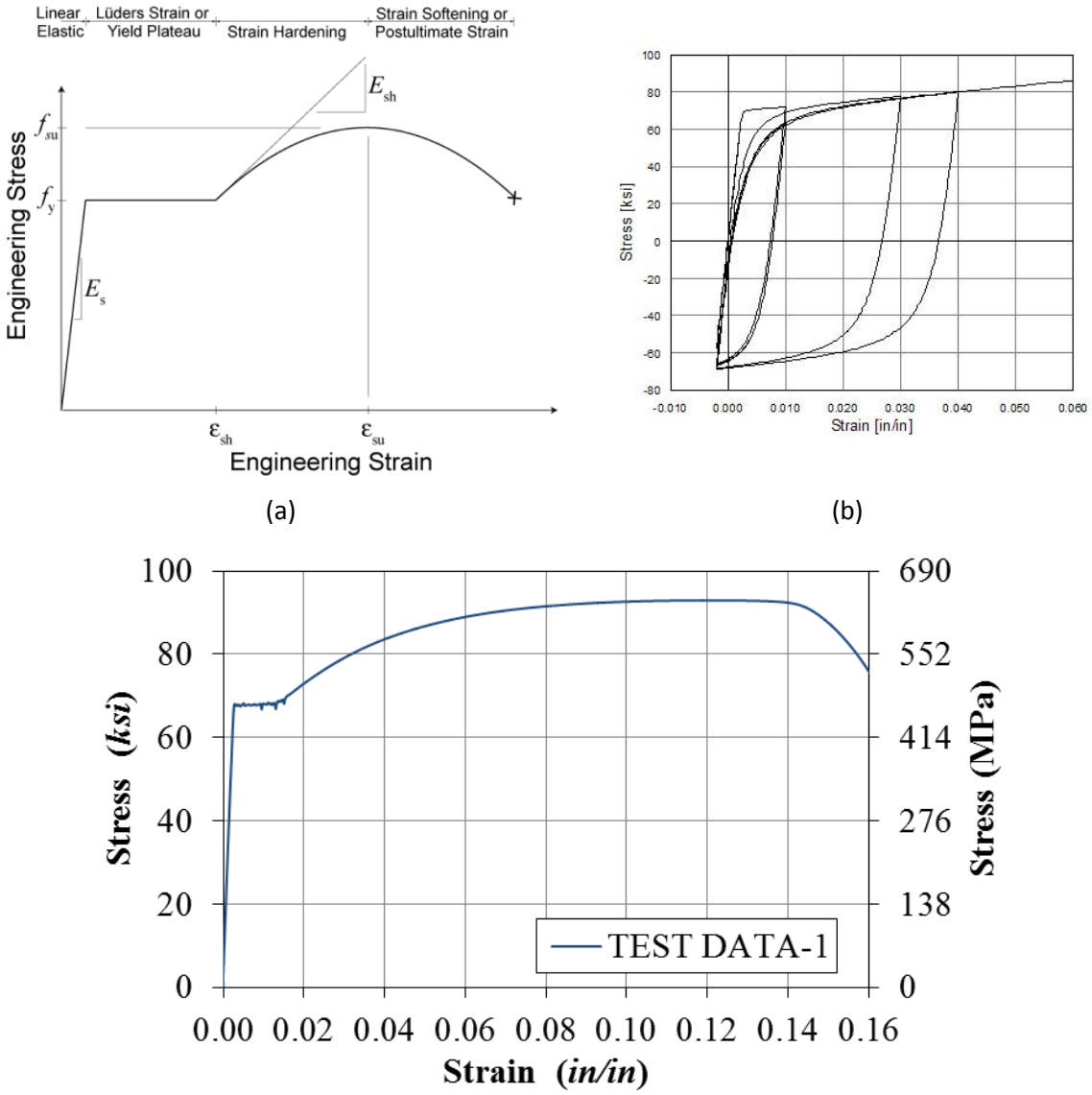

(a) (b)

(c)

Fig. 4-16. steel stress-strain relationship a) Steel02 b)ReinforcingSteel c) Tensile test results of #4 bars

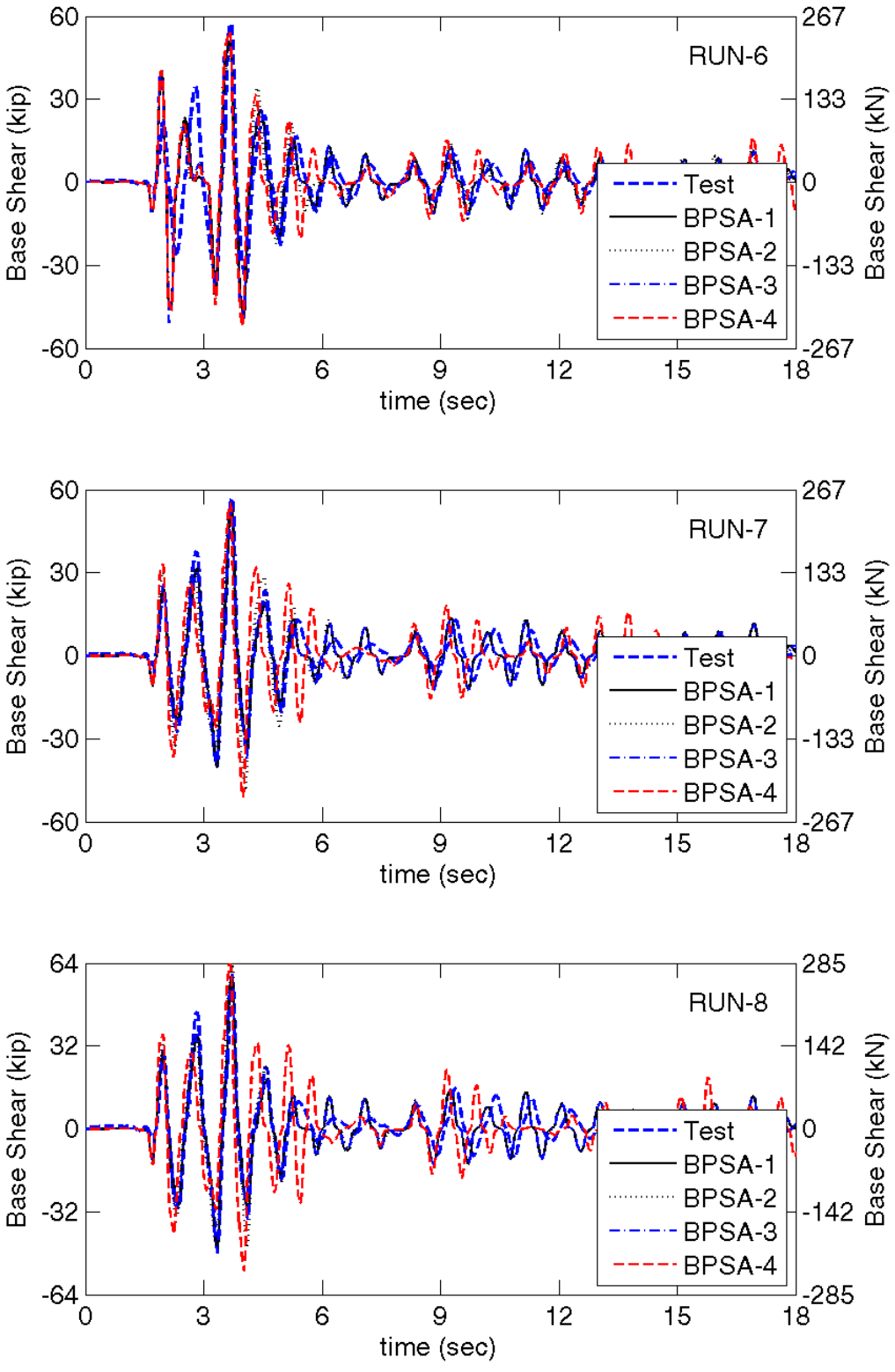

Fig. 4-17. Effect of material models on BPSA base shear, Run-6 to Run-8

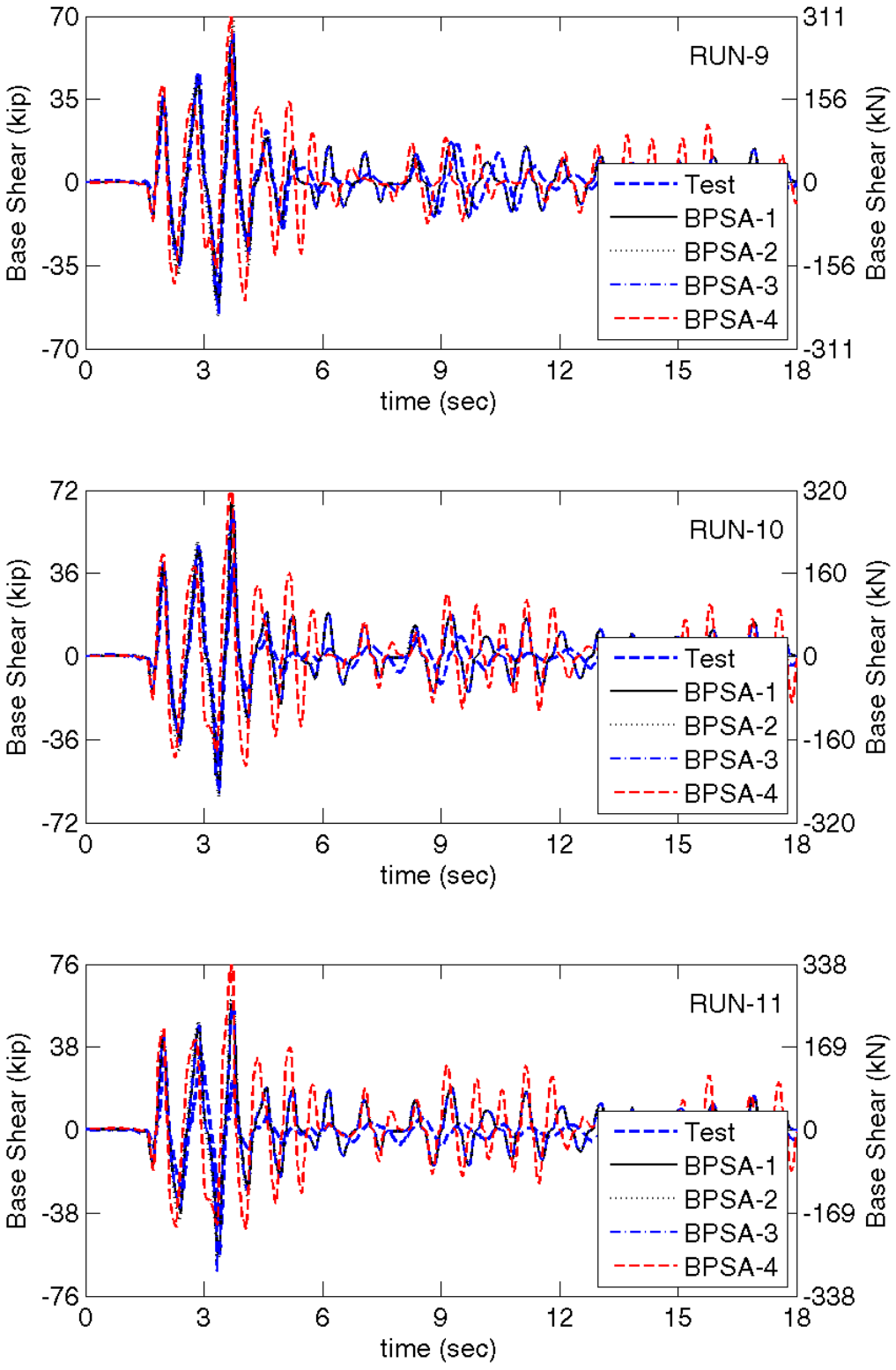

Fig. 4-18. Effect of material models on BPSA base shear, Run-9 to Run-11

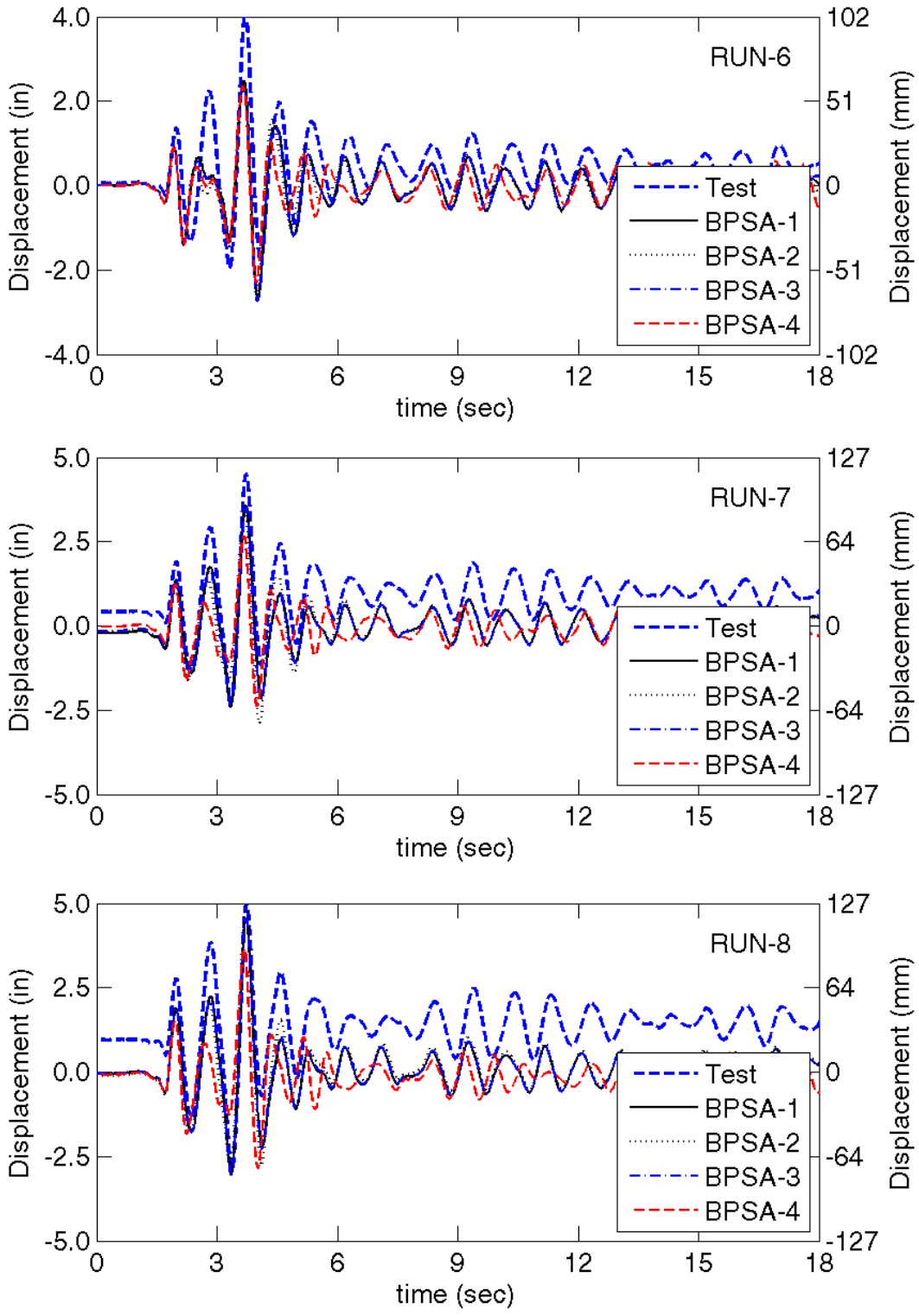

Fig. 4-19. Effect of material models on BPSA displacement, Run-6 to Run-8

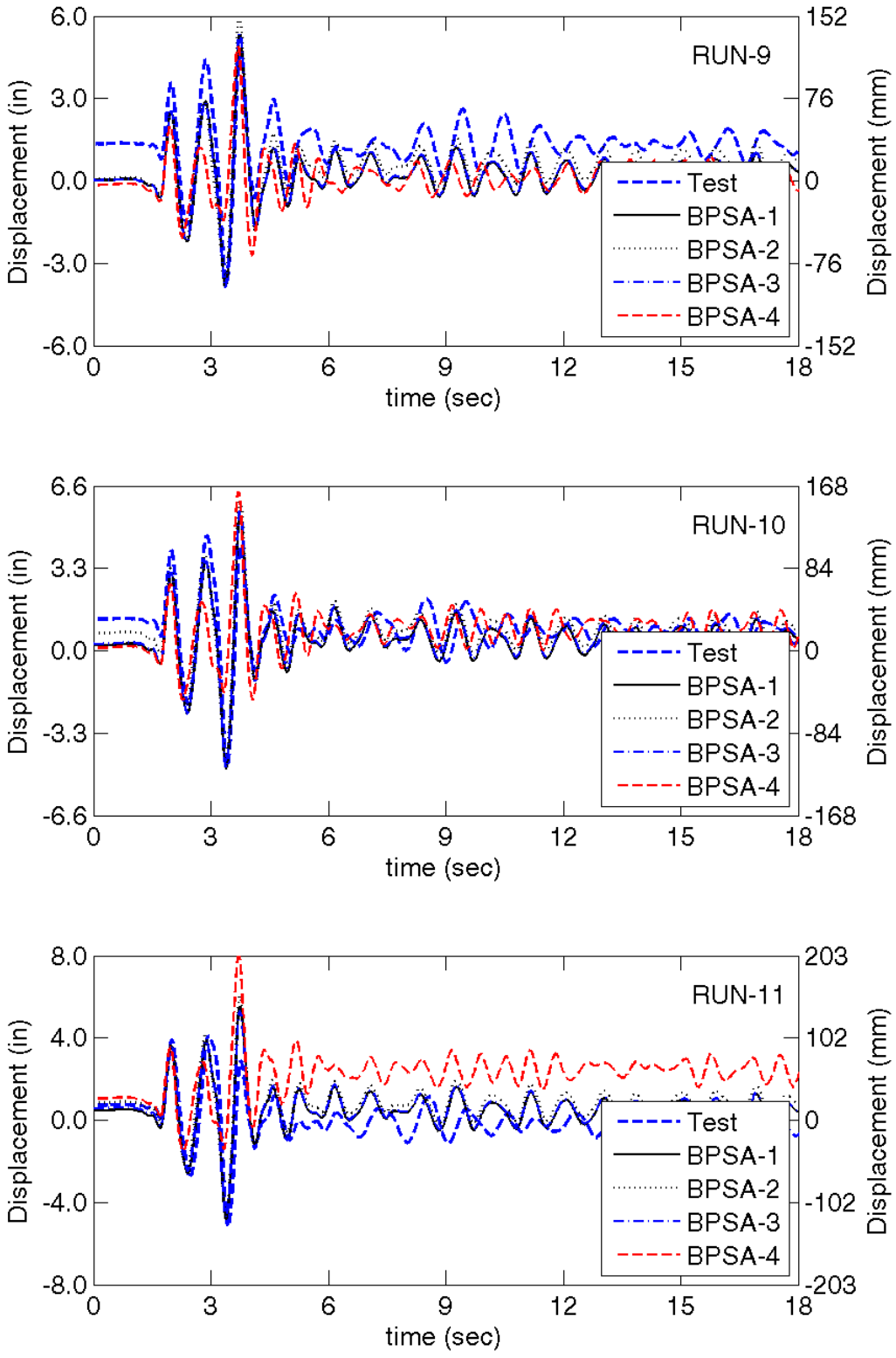

Fig. 4-20. Effect of material models on BPSA displacement, Run-9 to Run-11

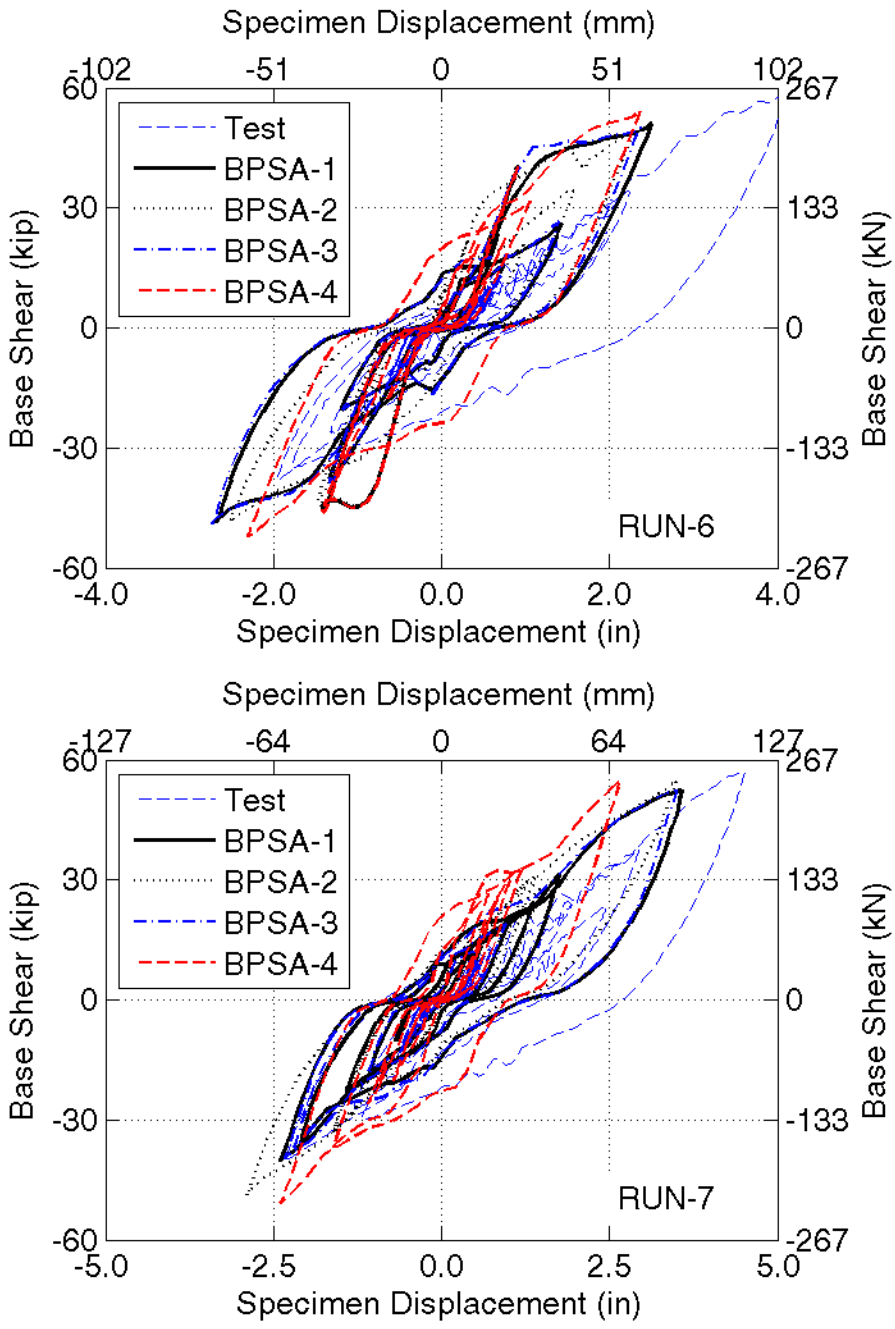

Fig. 4-21. Effect of material models on BPSA hysteresis, Run-6 to Run-7

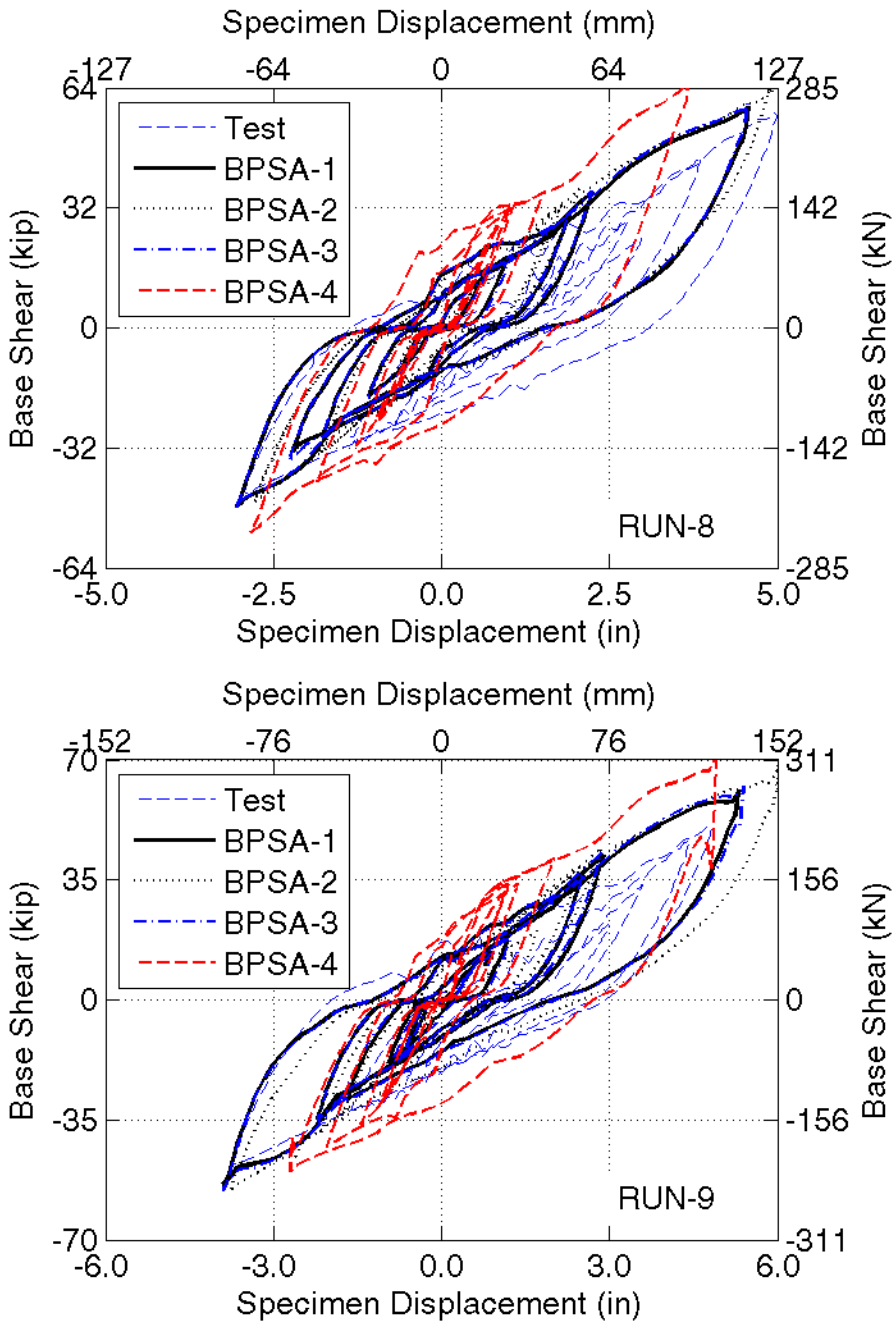

Fig. 4-22. Effect of material models on BPSA hysteresis, Run-8 to Run-9

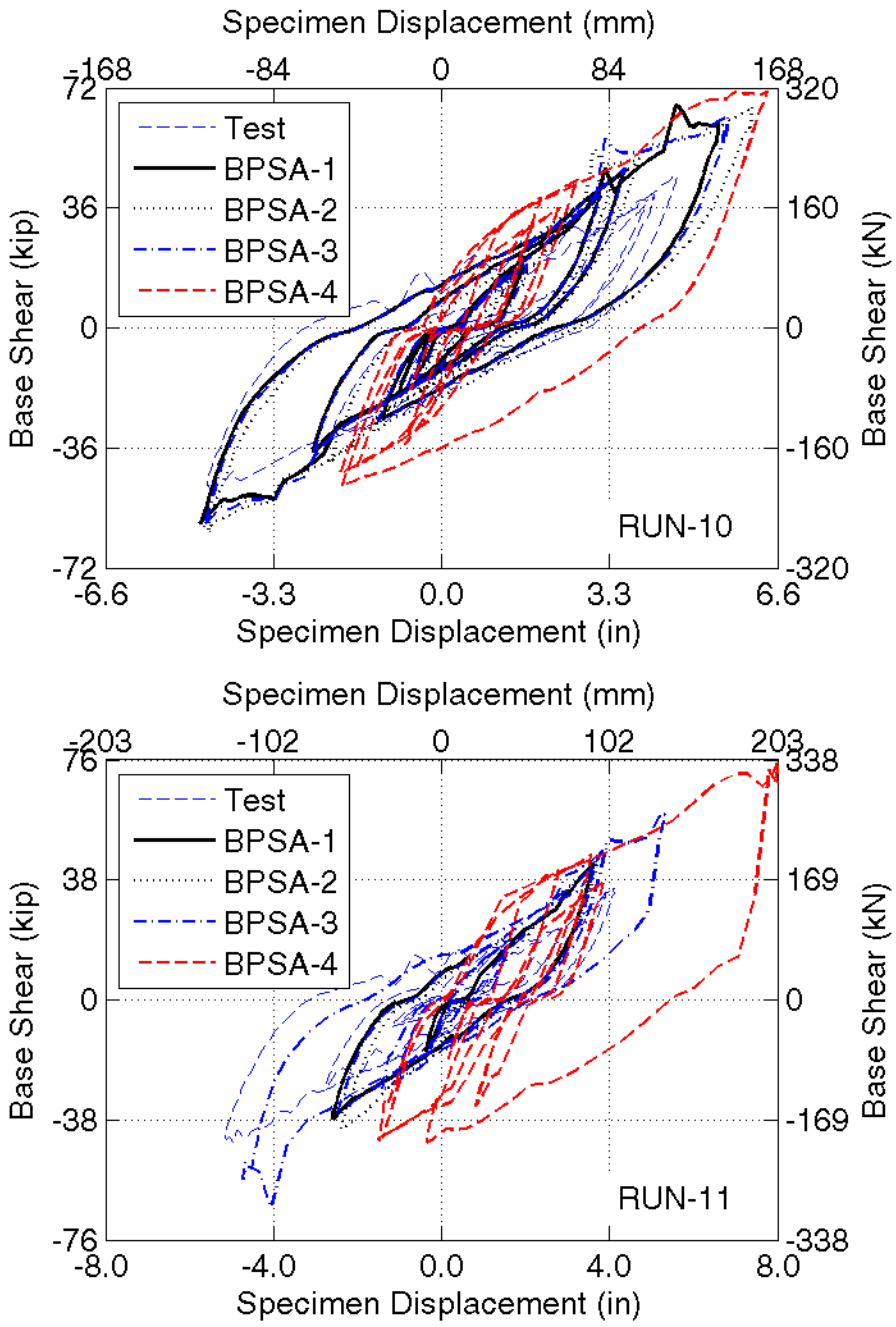

Fig. 4-23. Effect of material models on BPSA hysteresis, Run-10 to Run-11

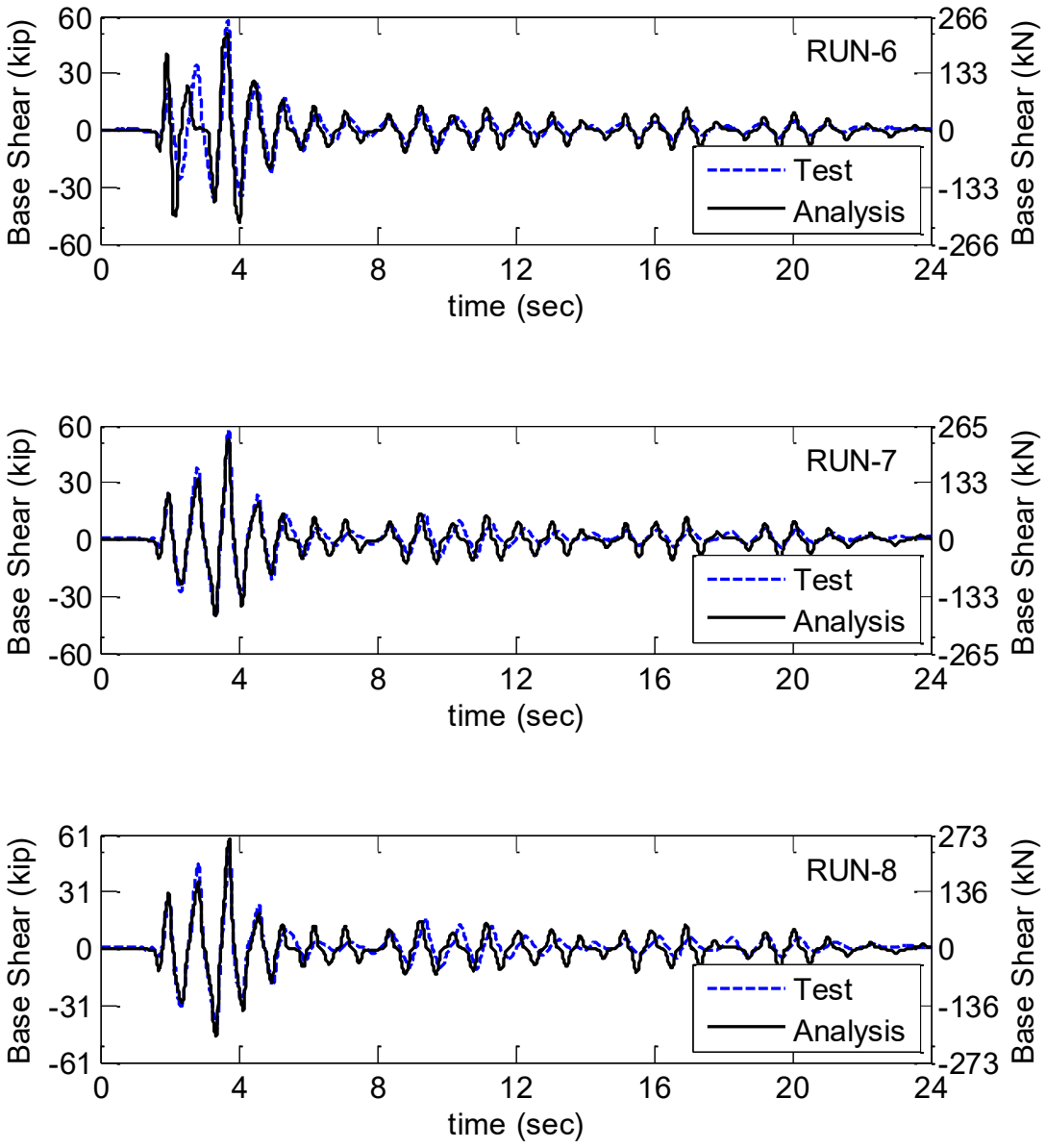

Fig. 4-24. Base shear history of BPSA, Run-6 to 8

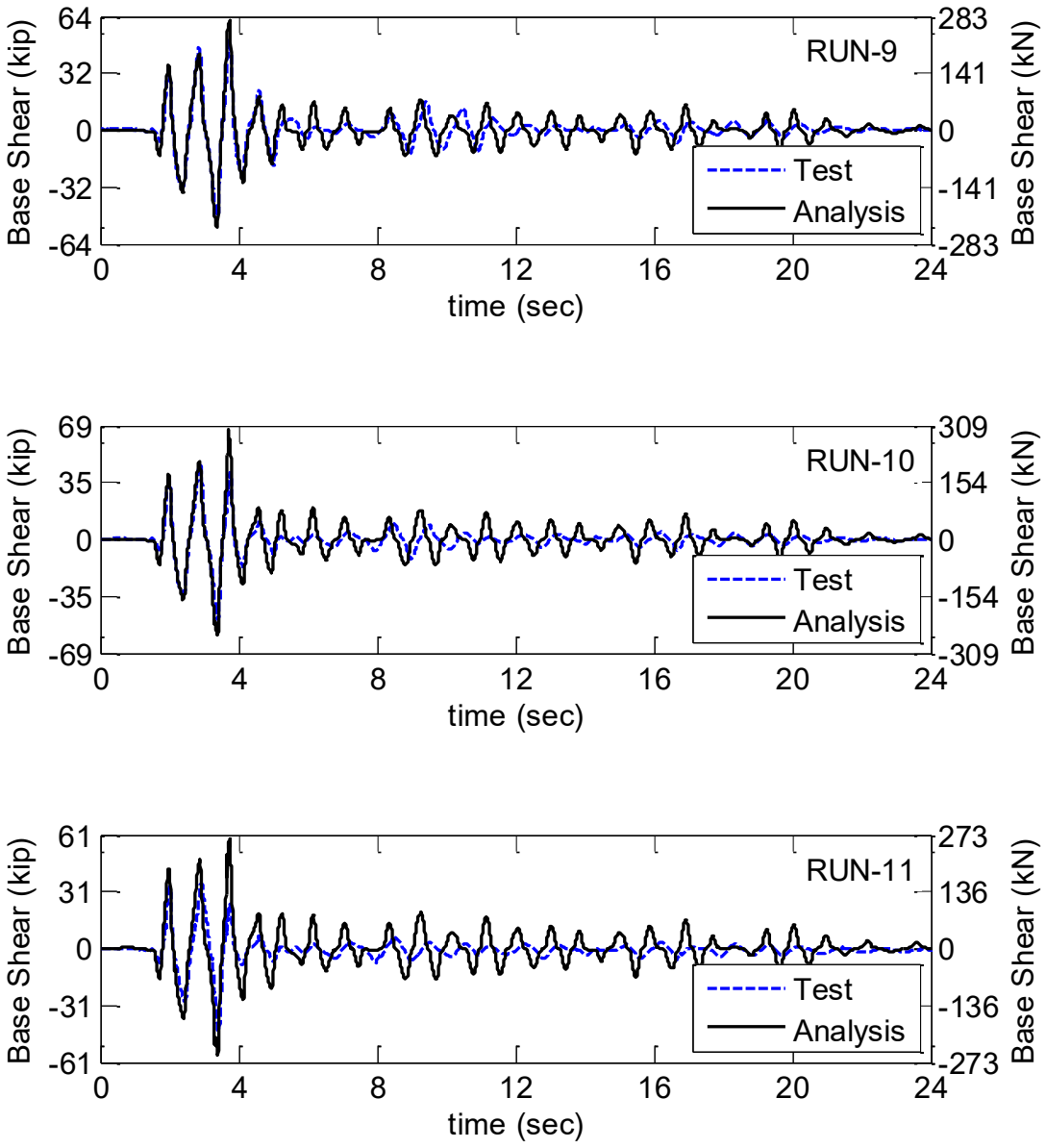

Fig. 4-25. Base shear history of BPSA, Run-9 to 11

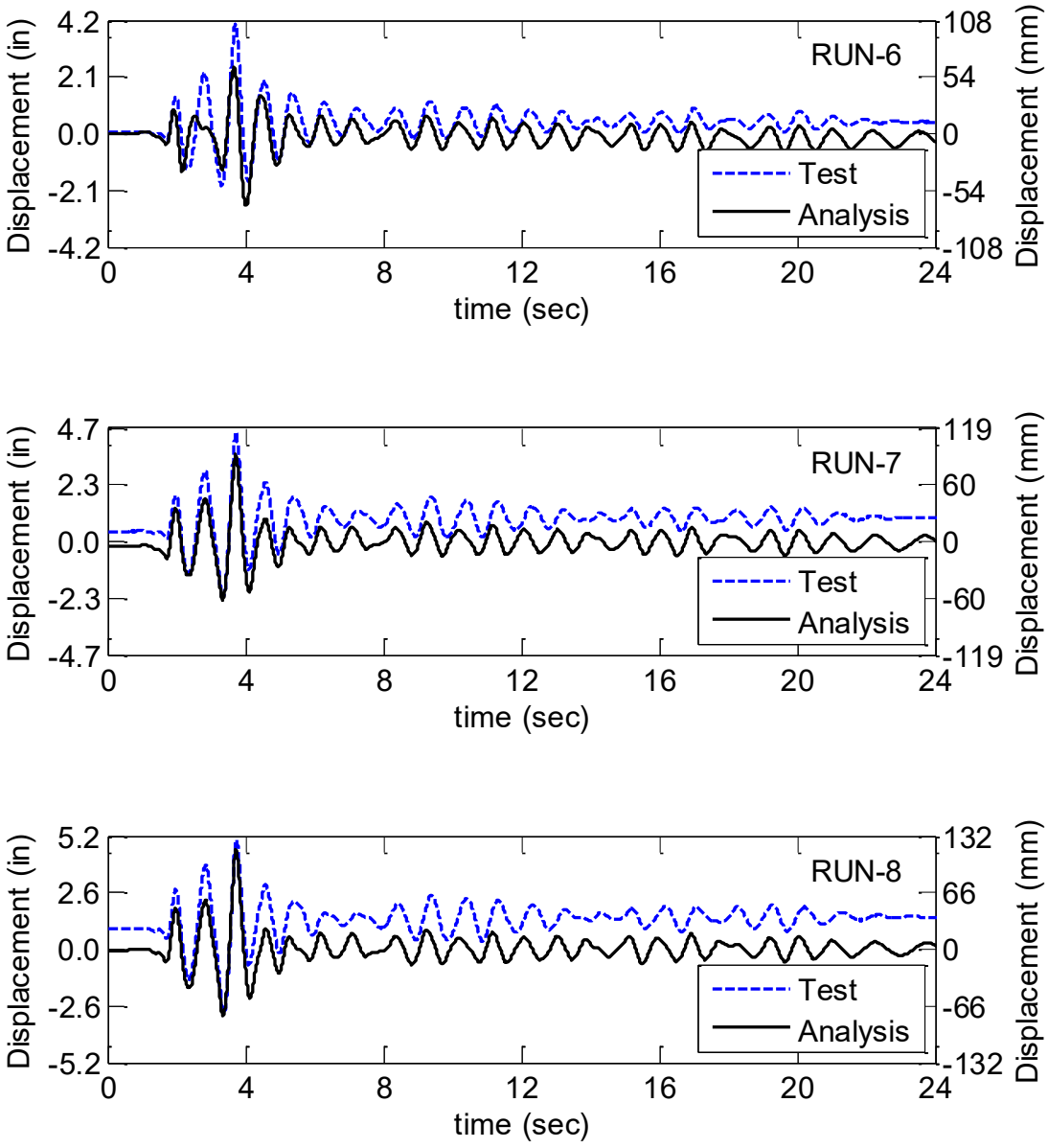

Fig. 4-26. Displacement history of BPSA, Run-6 to 8

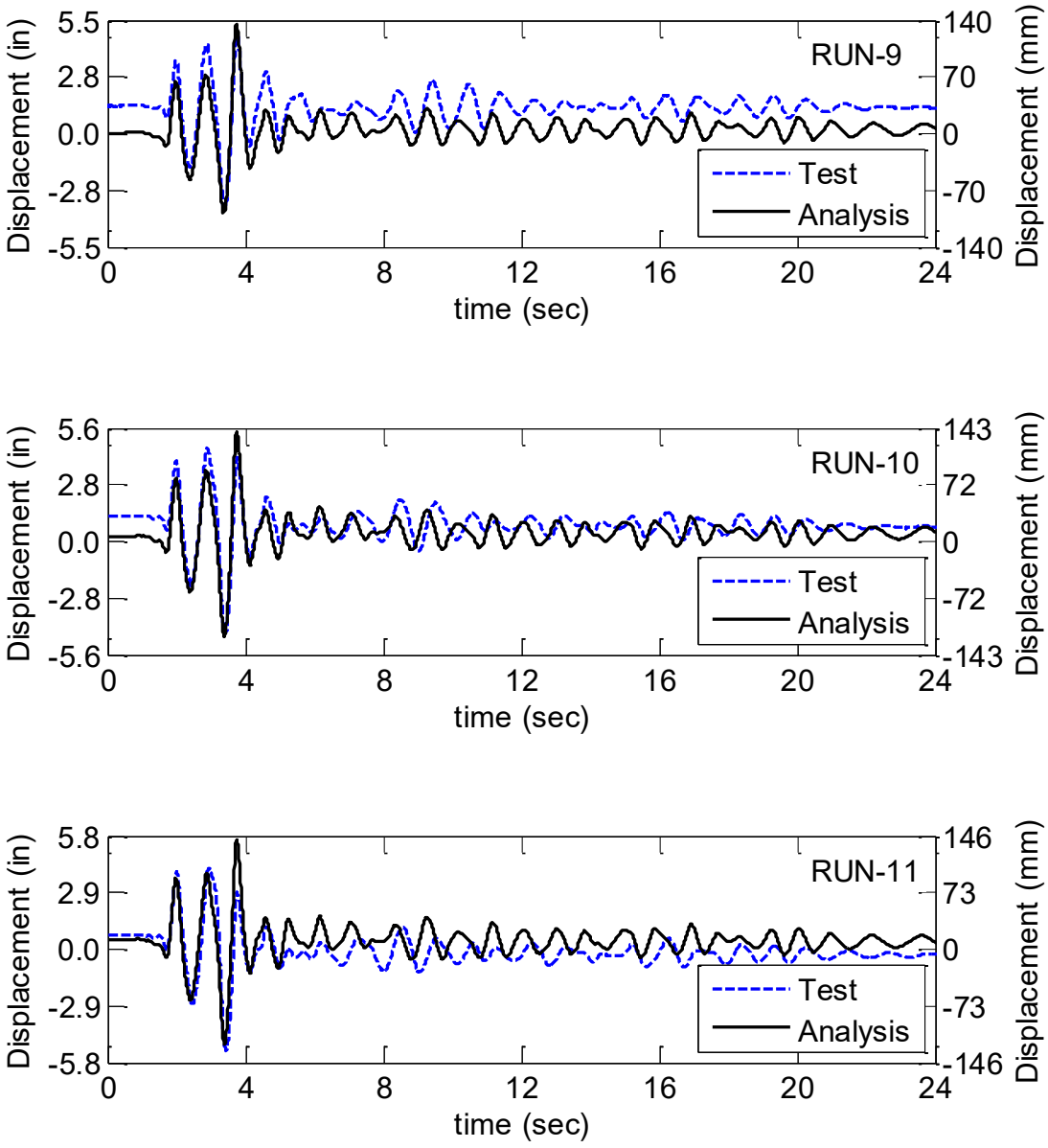

Fig. 4-27. Displacement history of BPSA, Run-9 to 11

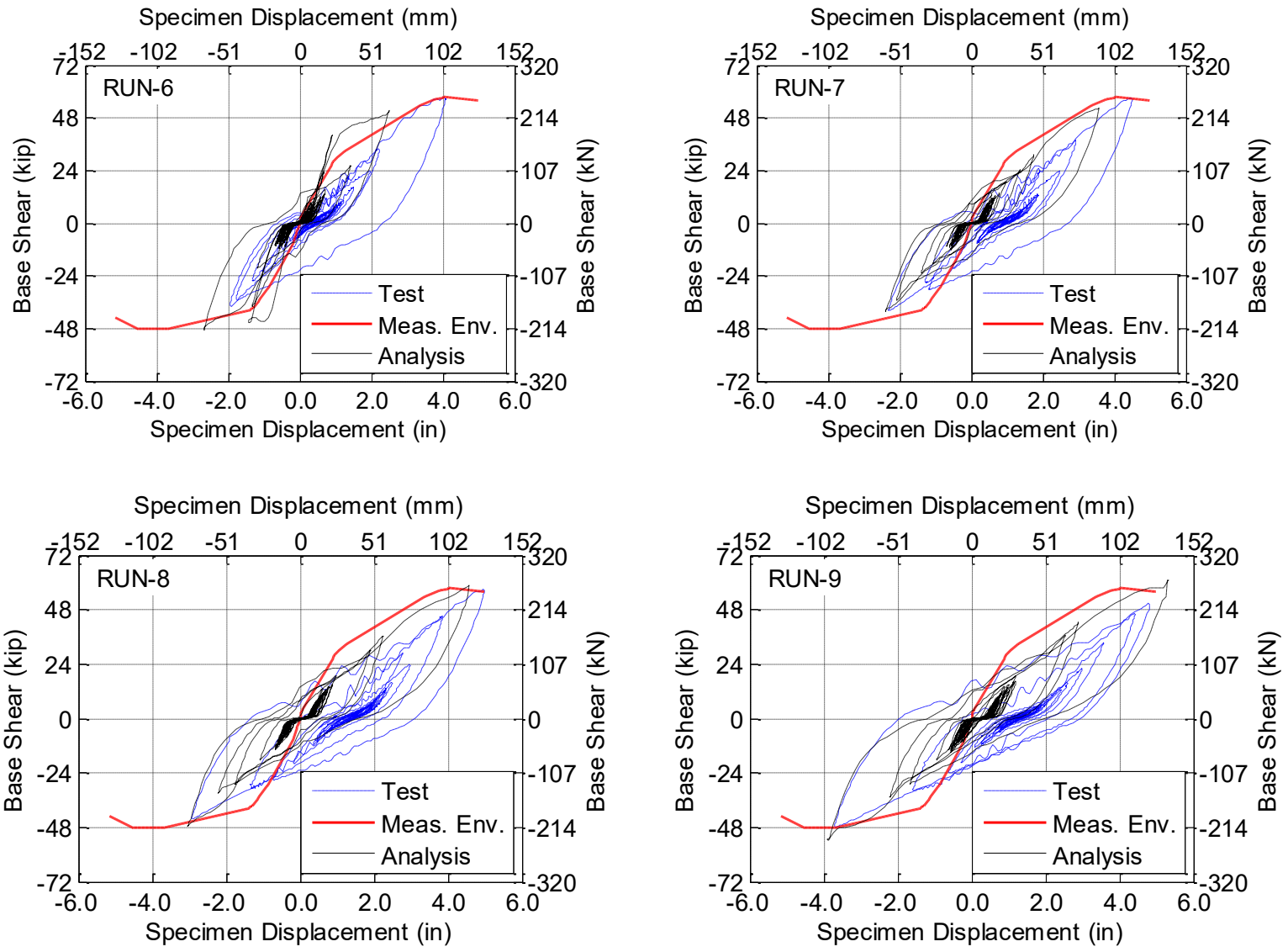

Fig. 4-28. Force-displacement curves of BPSA , Run-6 to 9

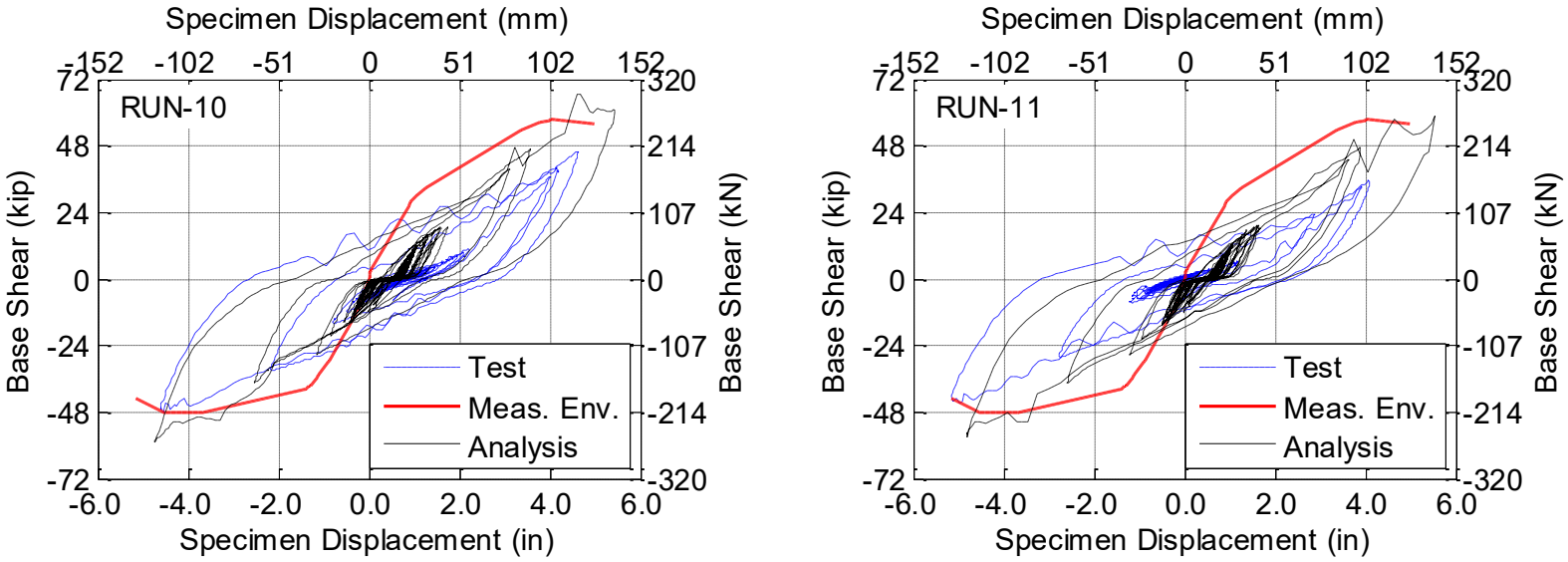

Fig. 4-29. Force-displacement curves of BPSA, Run-10 and 11

a)

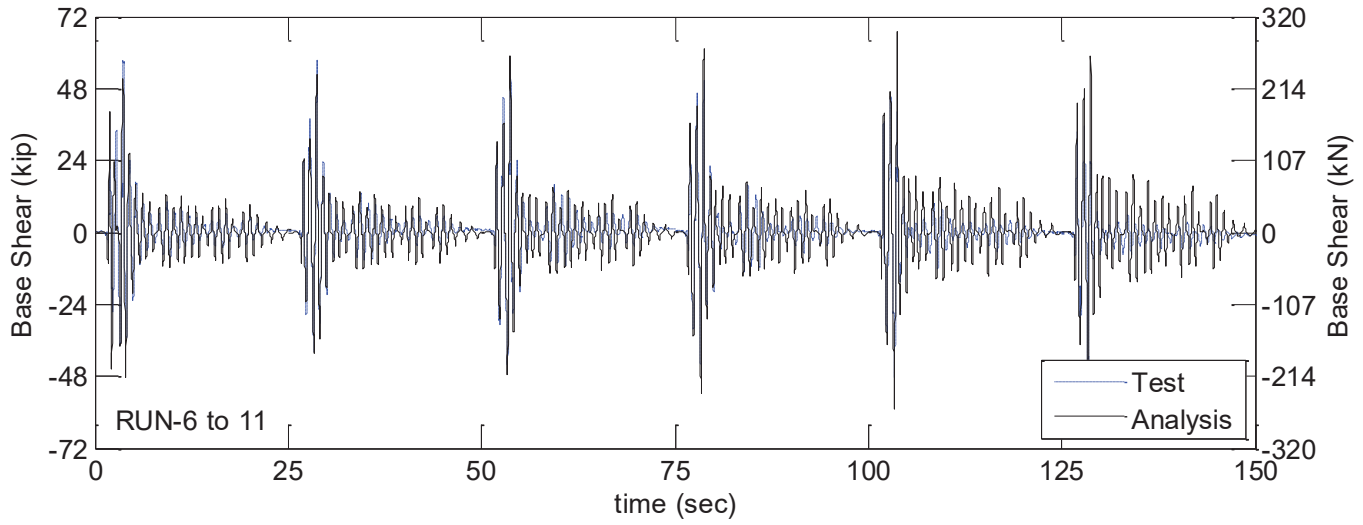

b)

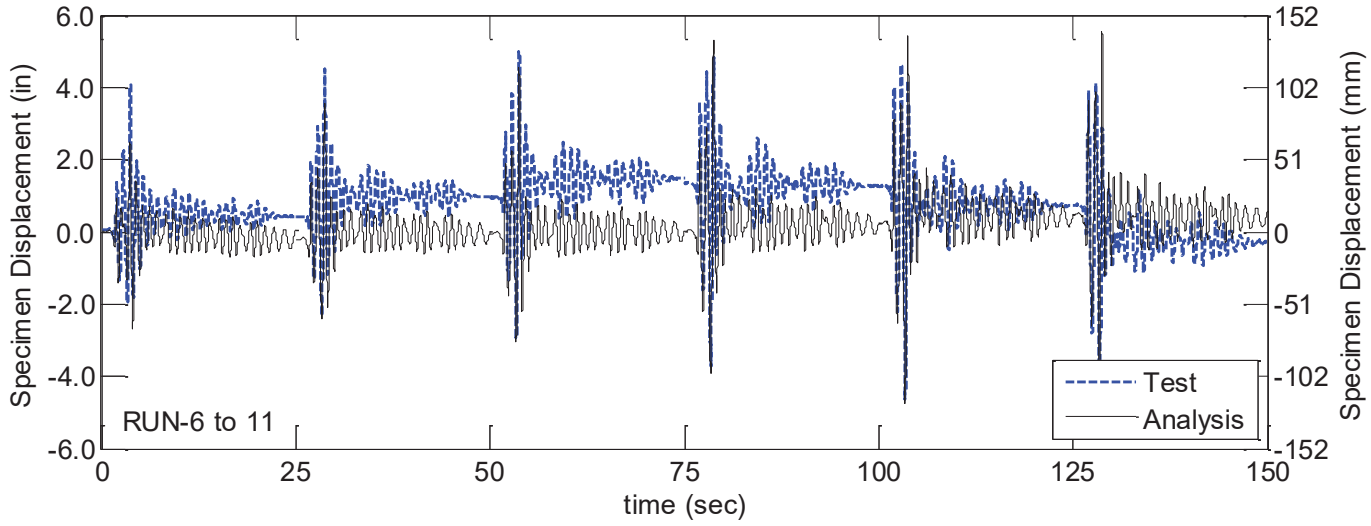

Fig. 4-30. Response history of entire test of BPSA with lumped plasticity a) base shear b) displacement

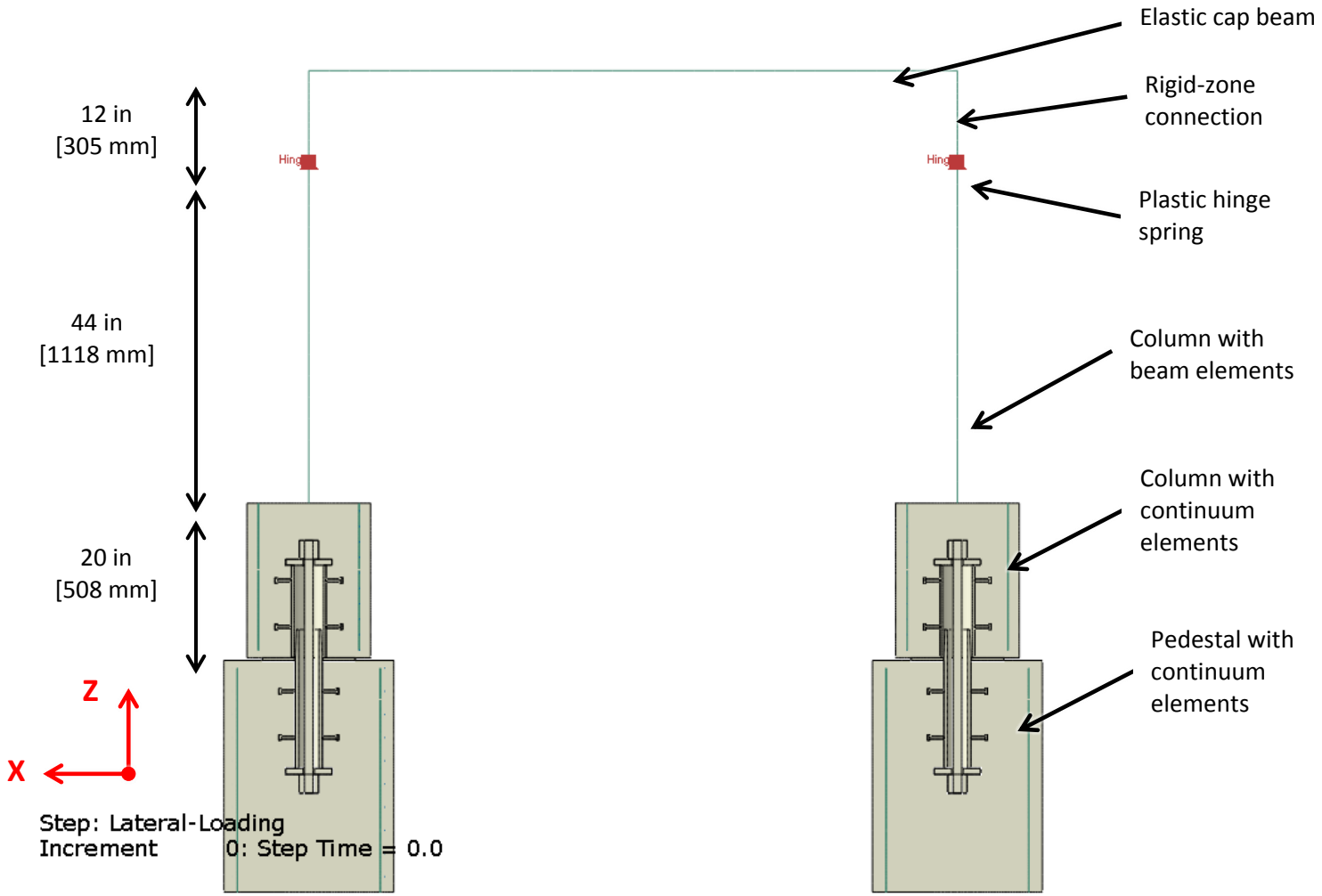

Fig. 4-31. Sketch of BPSA FE model

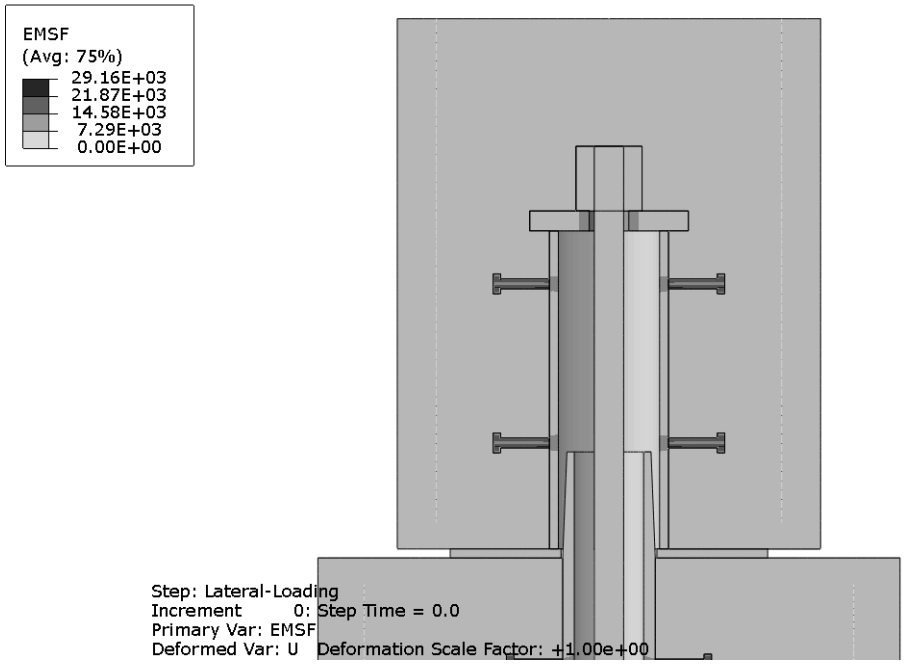

Fig. 4-32. Initial mass scaling factors in CIP column for the north direction analysis

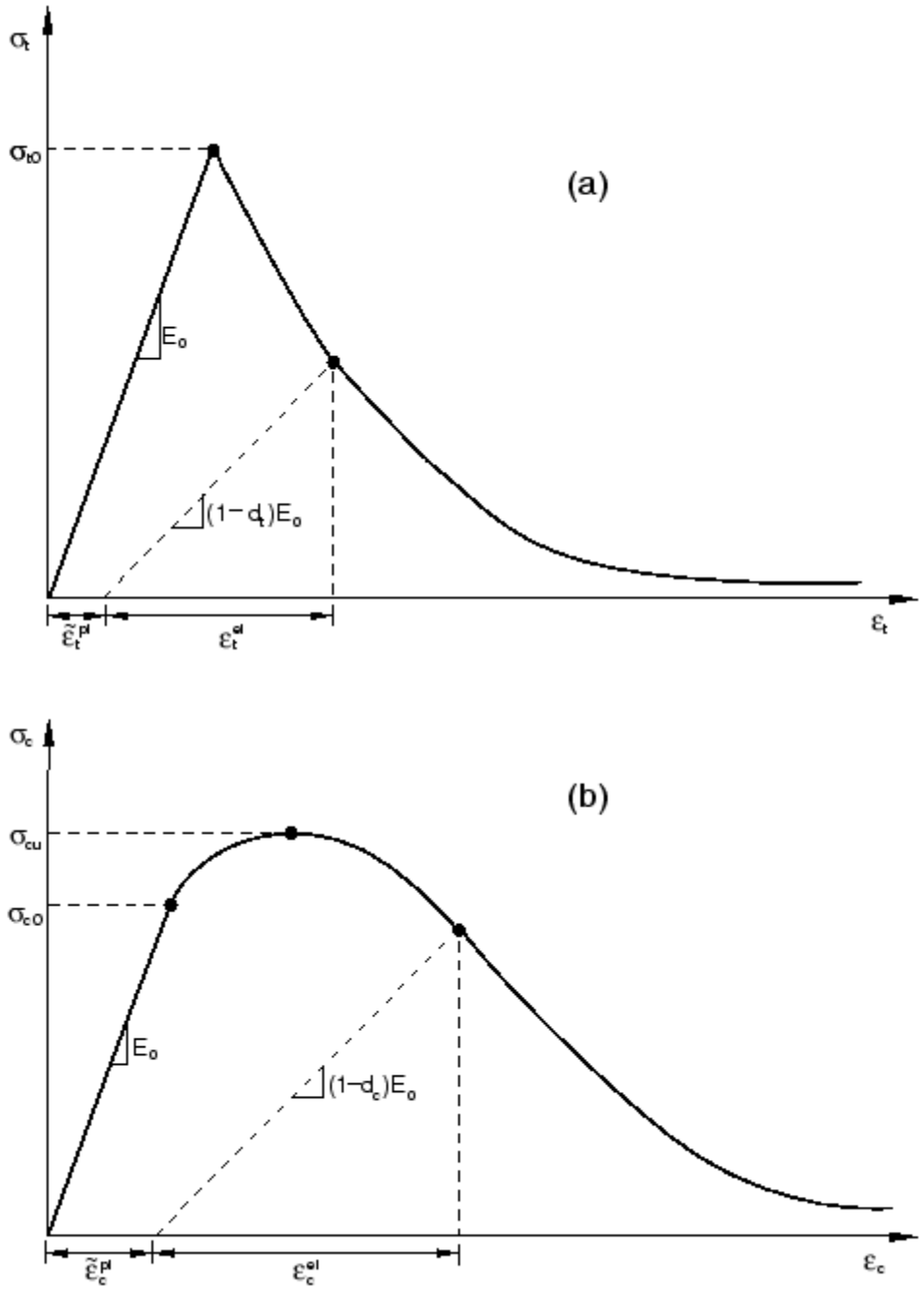

Fig. 4-33. Stress-strain response of CDP to uniaxial a) tension b) compression (SIMULIA, 2015)

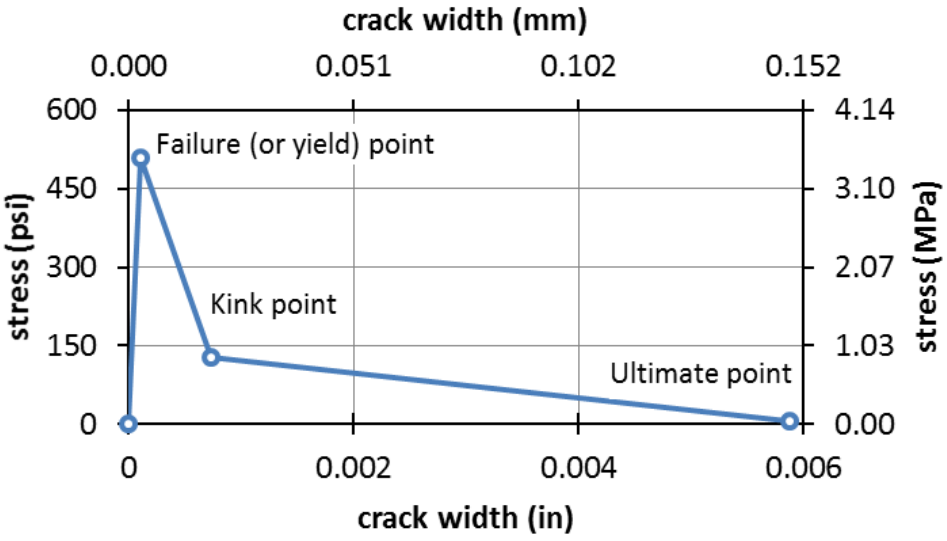

Fig. 4-34. Bilinear tensile stress-displacement response of column concrete

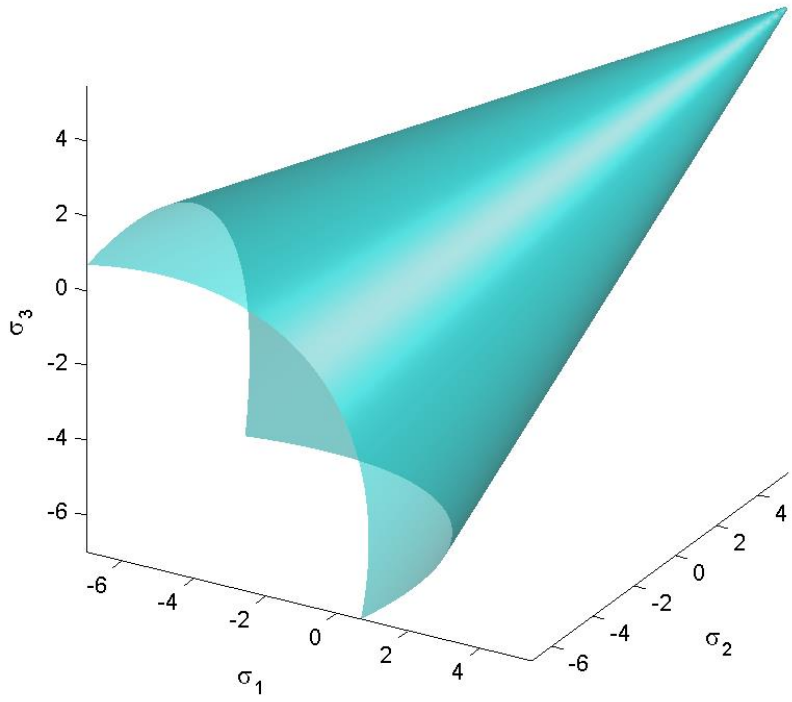

Fig. 4-35. Drucker-Prager yield surface in principal stress coordinate (Wikipedia)

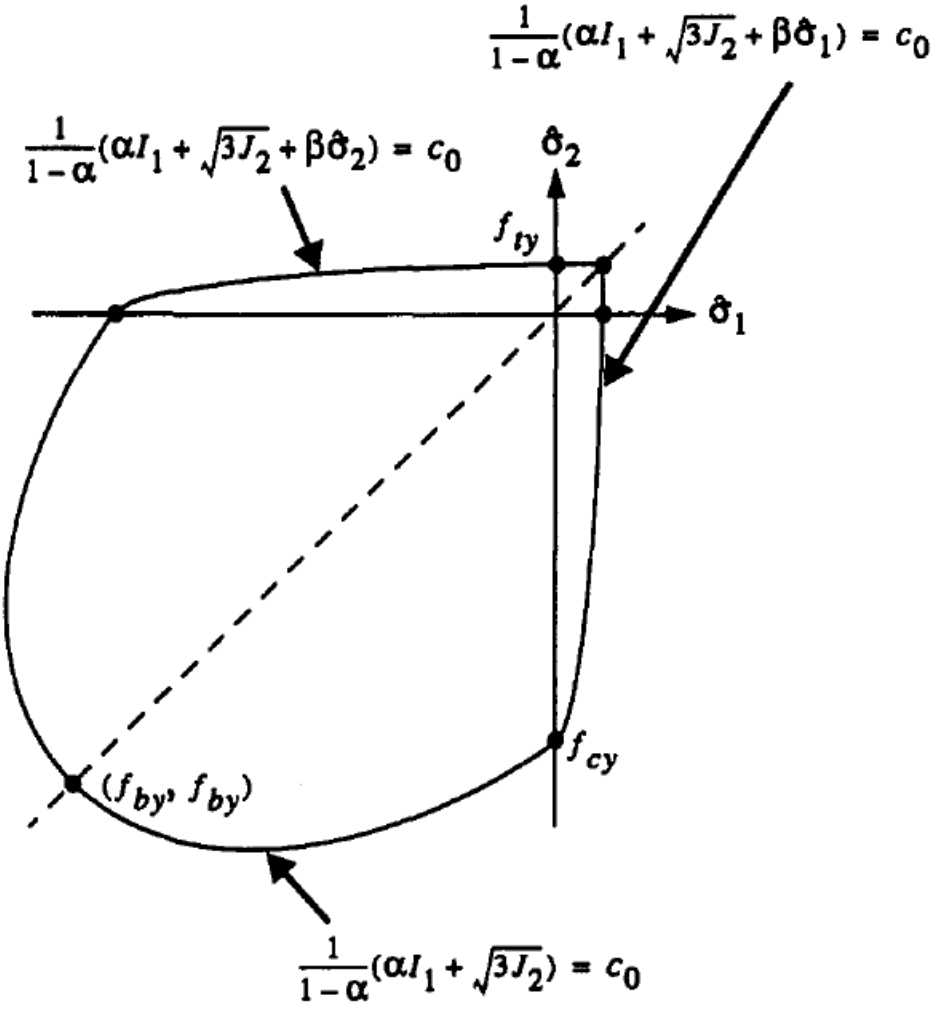

Fig. 4-36. CDP yield surface in plane stress condition (Lee, et al., 1998)

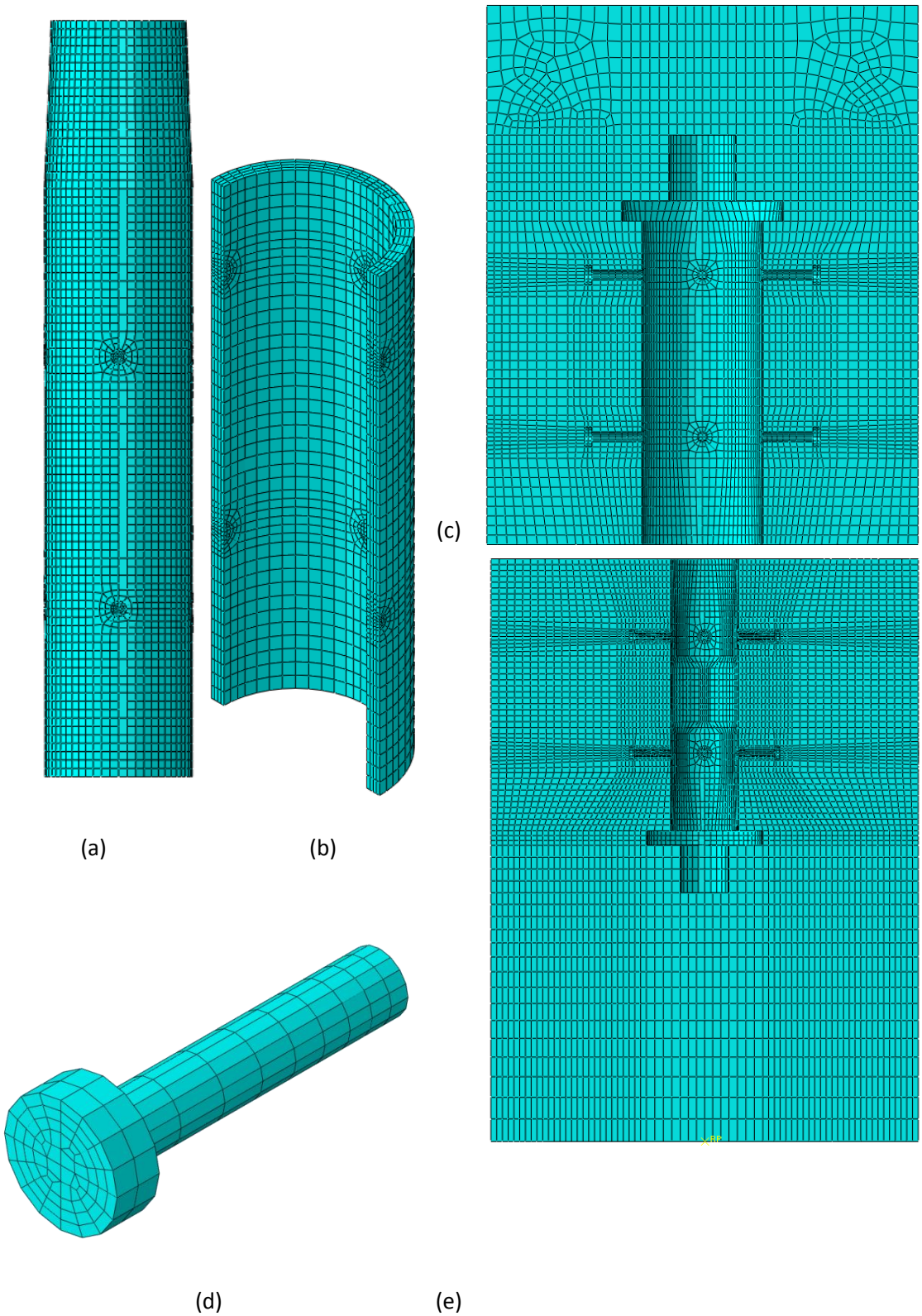

Fig. 4-37. Element discretization a) lower pipe b)upper pipe c) column d)stud e)pedestal

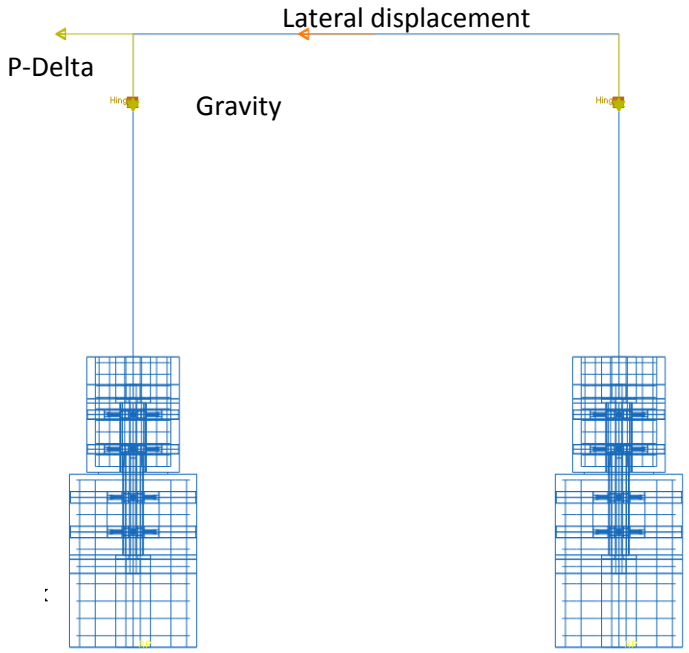

Fig. 4-38. BPSA loading in ABAQUS, positive direction

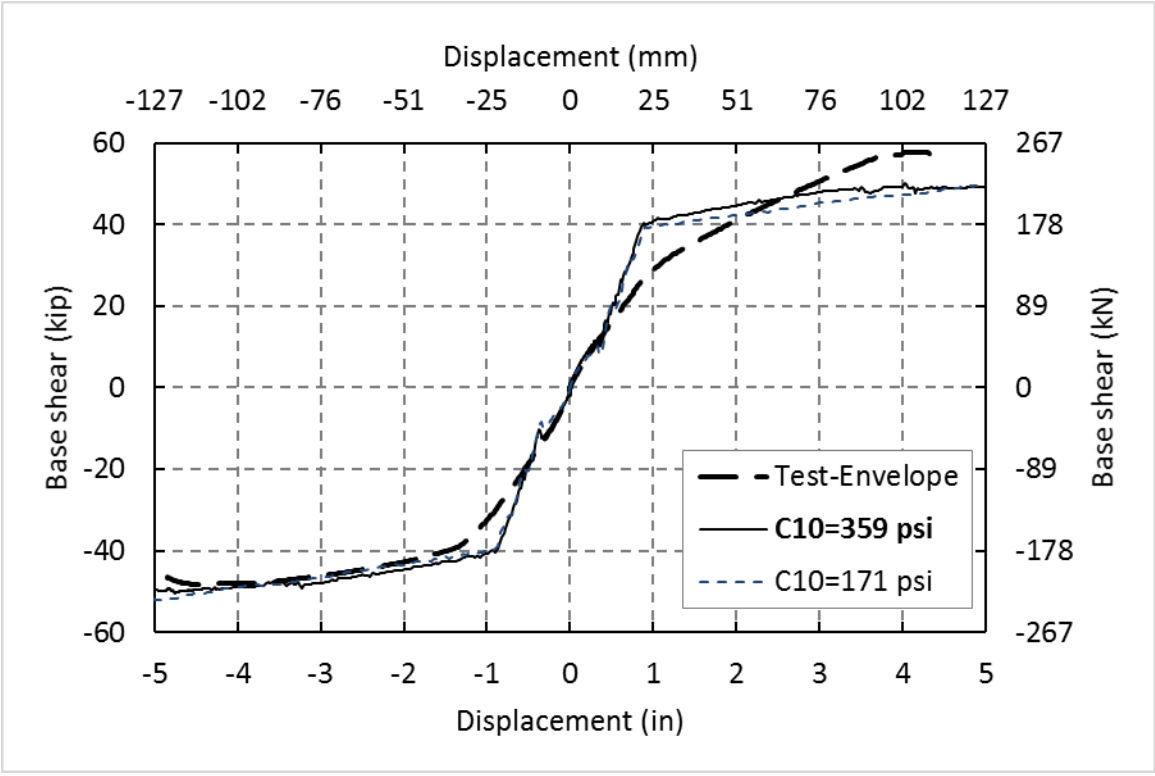

Fig. 4-39. Sensitivity of FE analysis to rubber stiffness

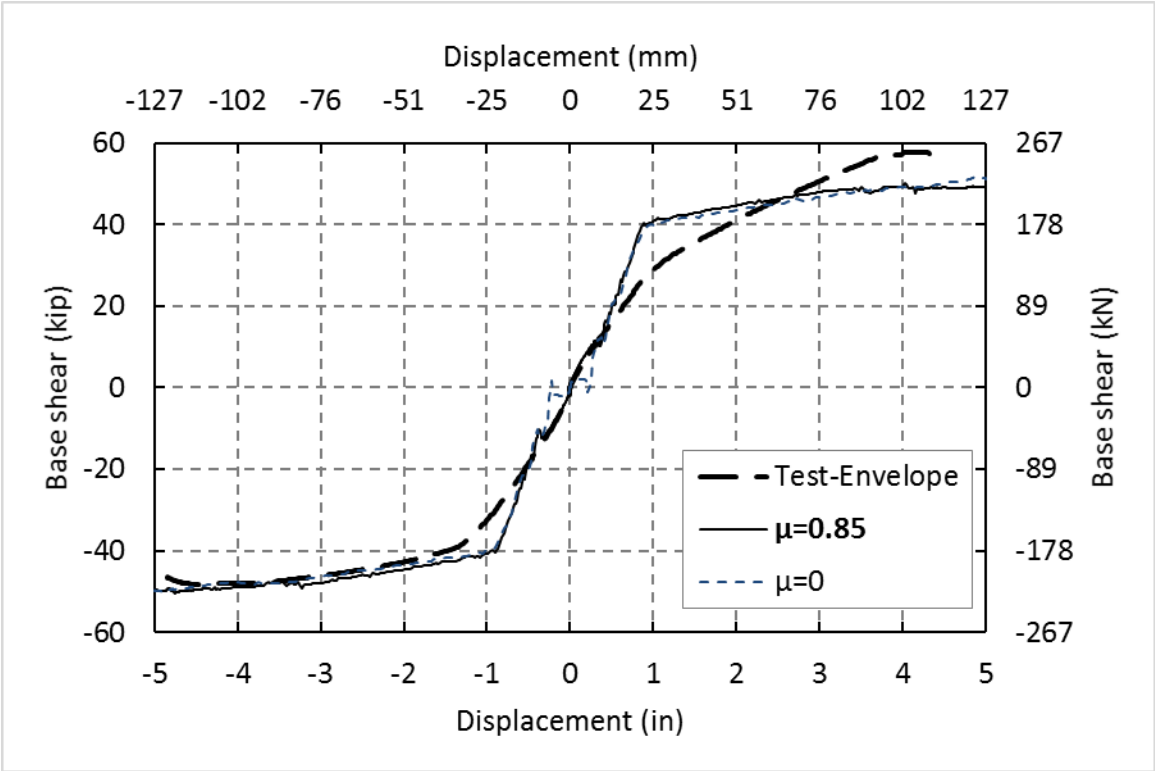

Fig. 4-40. Sensitivity of FE analysis to rubber boundary conditions

a)

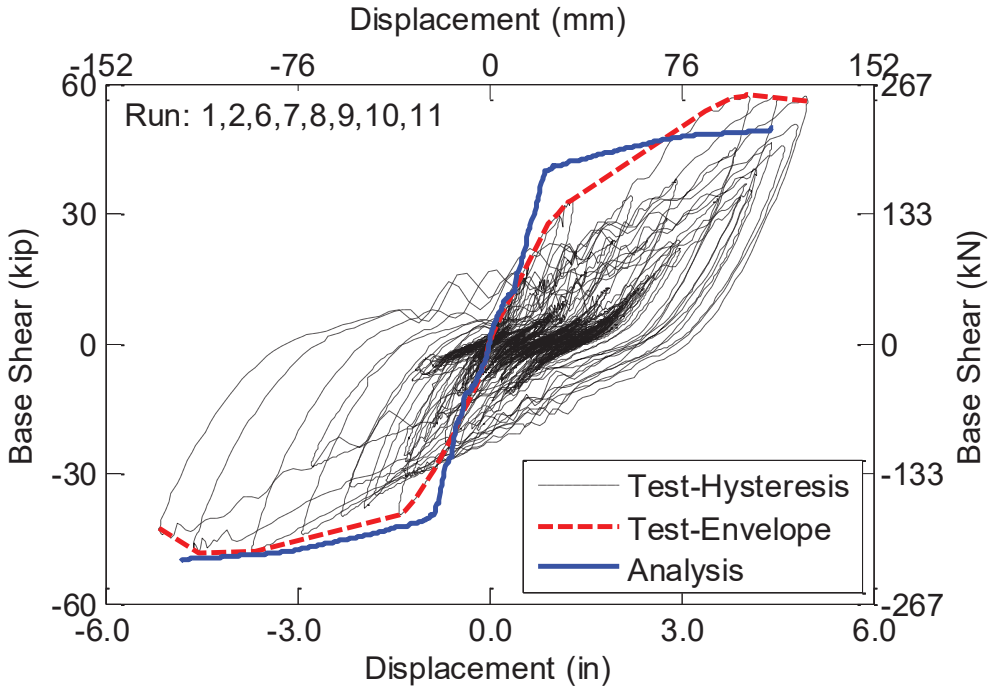

b)

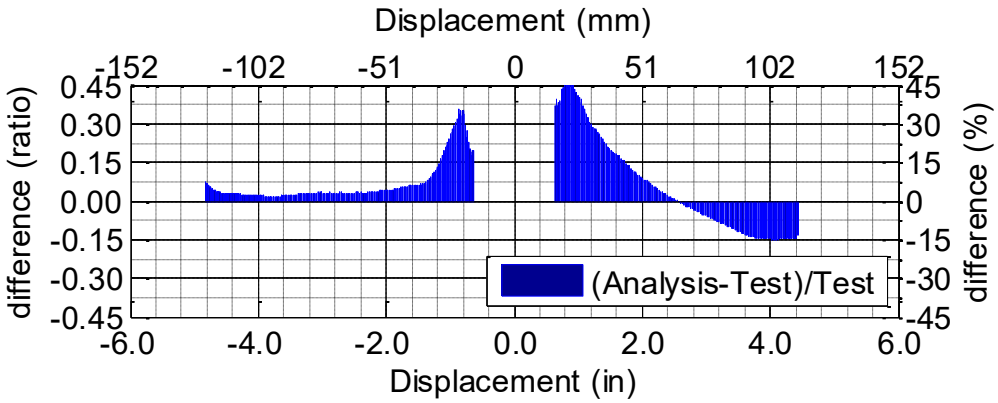

Fig. 4-41. Comparison of results of FE analysis with the tests envelopes

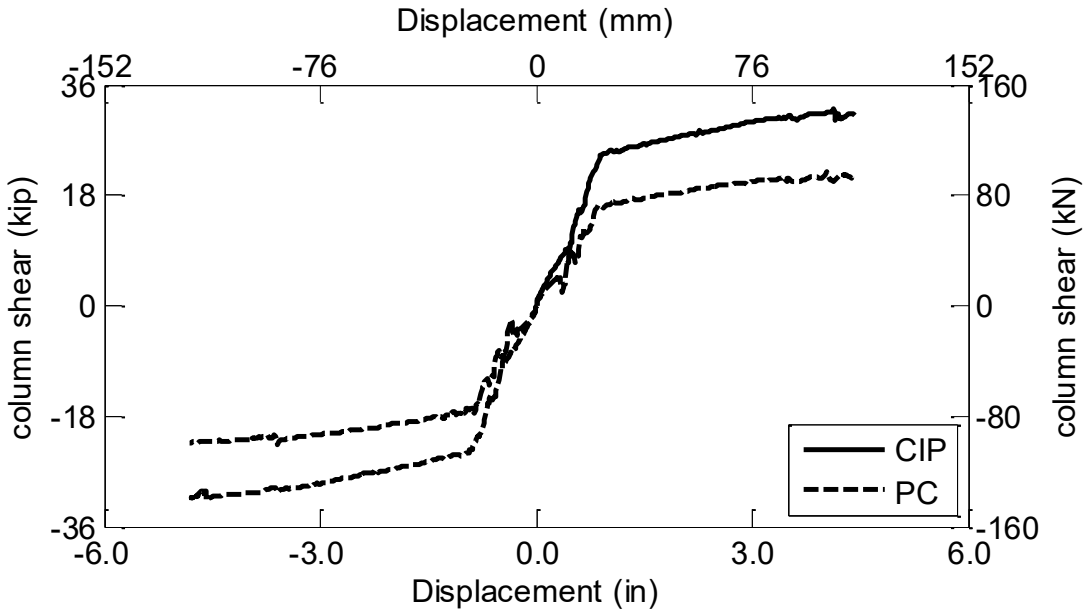

Fig. 4-42. Shear distribution between columns

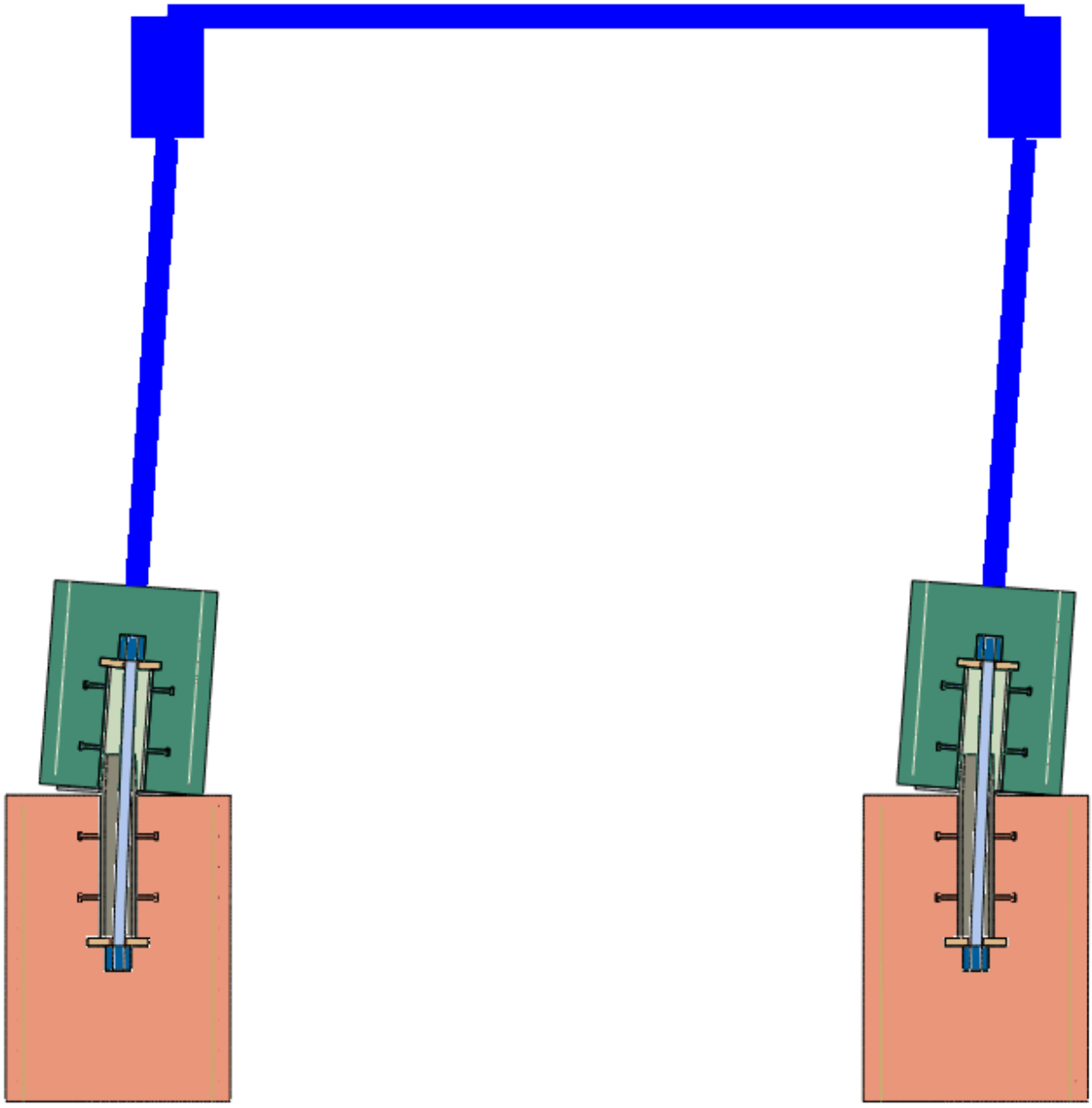

Fig. 4-43. BPSA FE model deformed shape at ultimate displacement

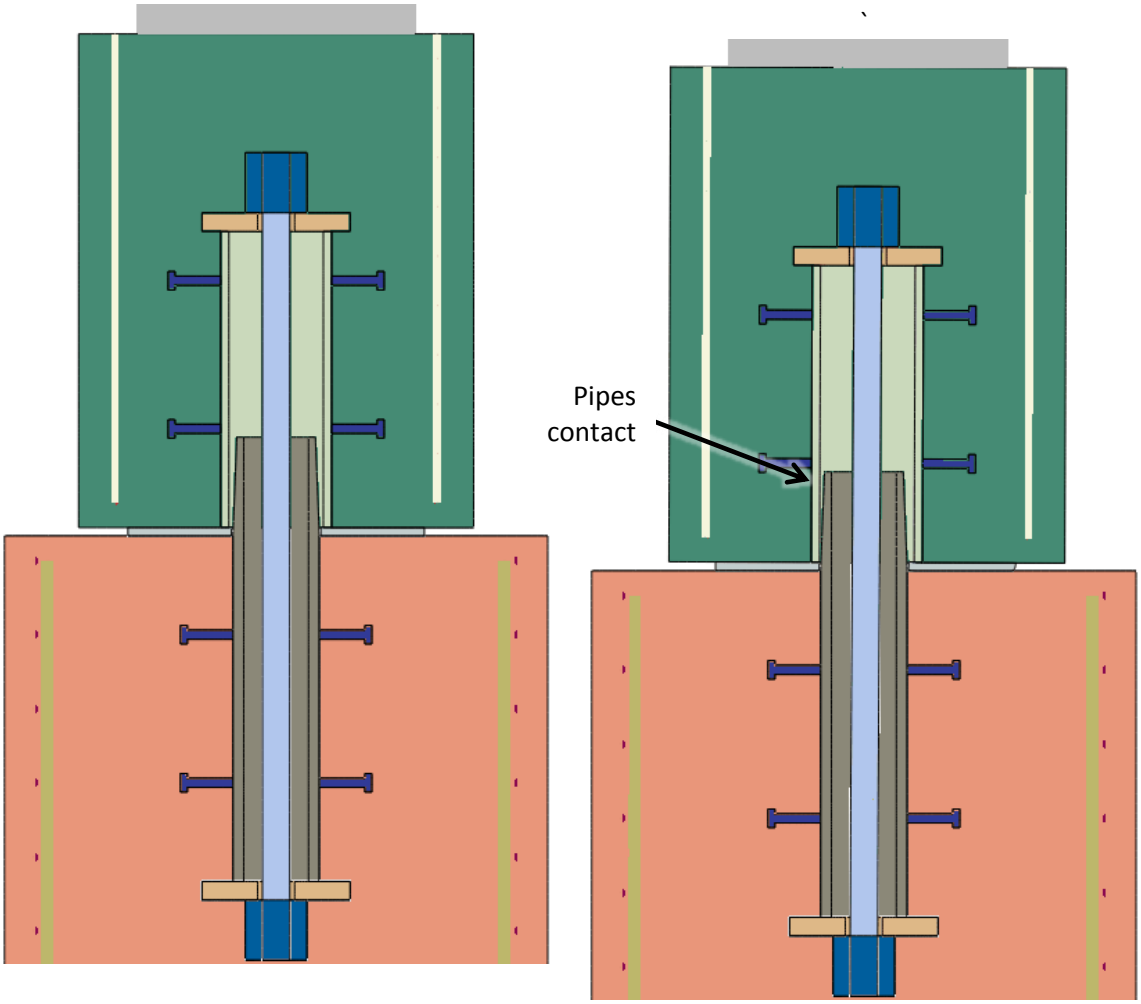

a) drift=0 b) drift=0.5%

Fig. 4-44. Deformed shape of pipe-pin at a) 0.0% drift b) 0.5% drift

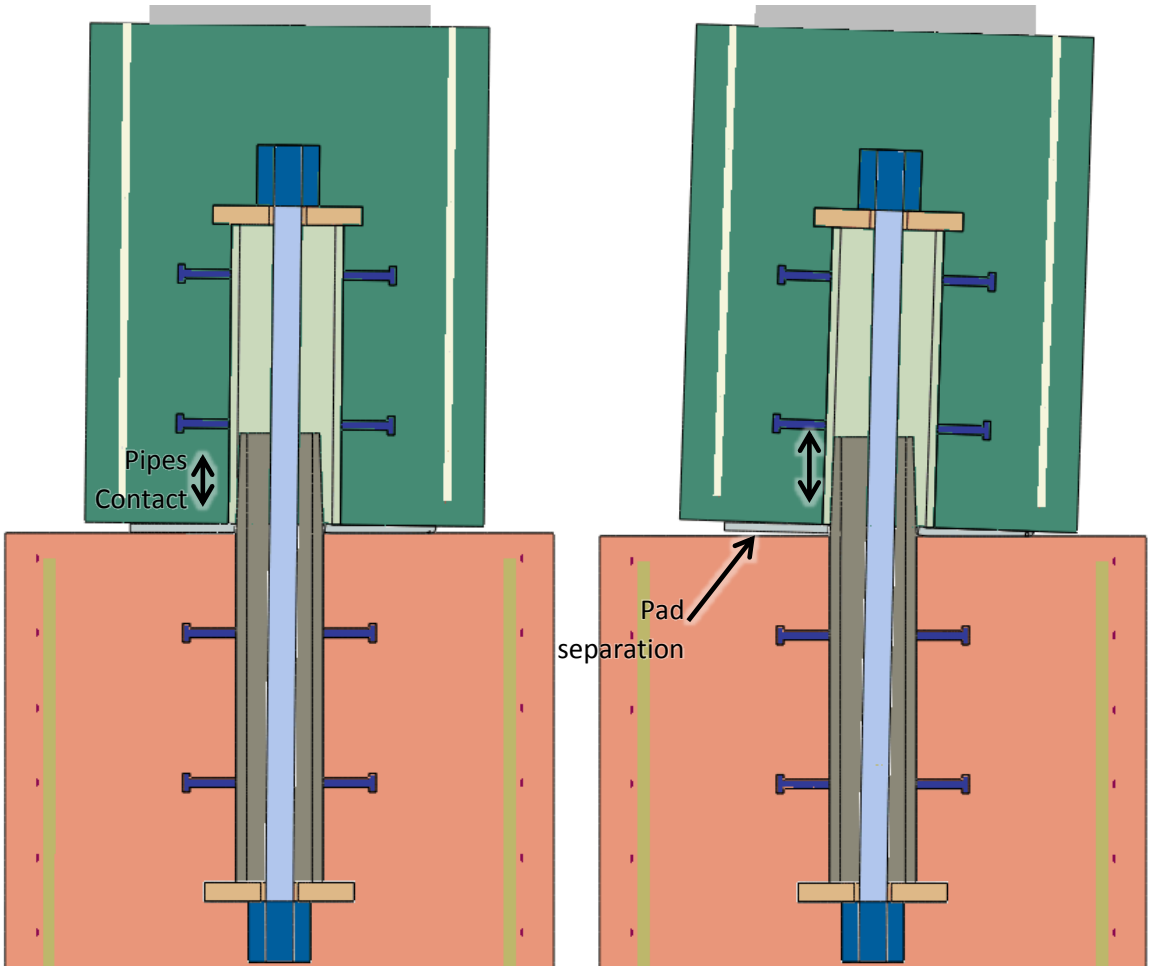

Fig. 4-45. Deformed shape of pipe-pin at a) 1.2% drift b) 4.5% drift

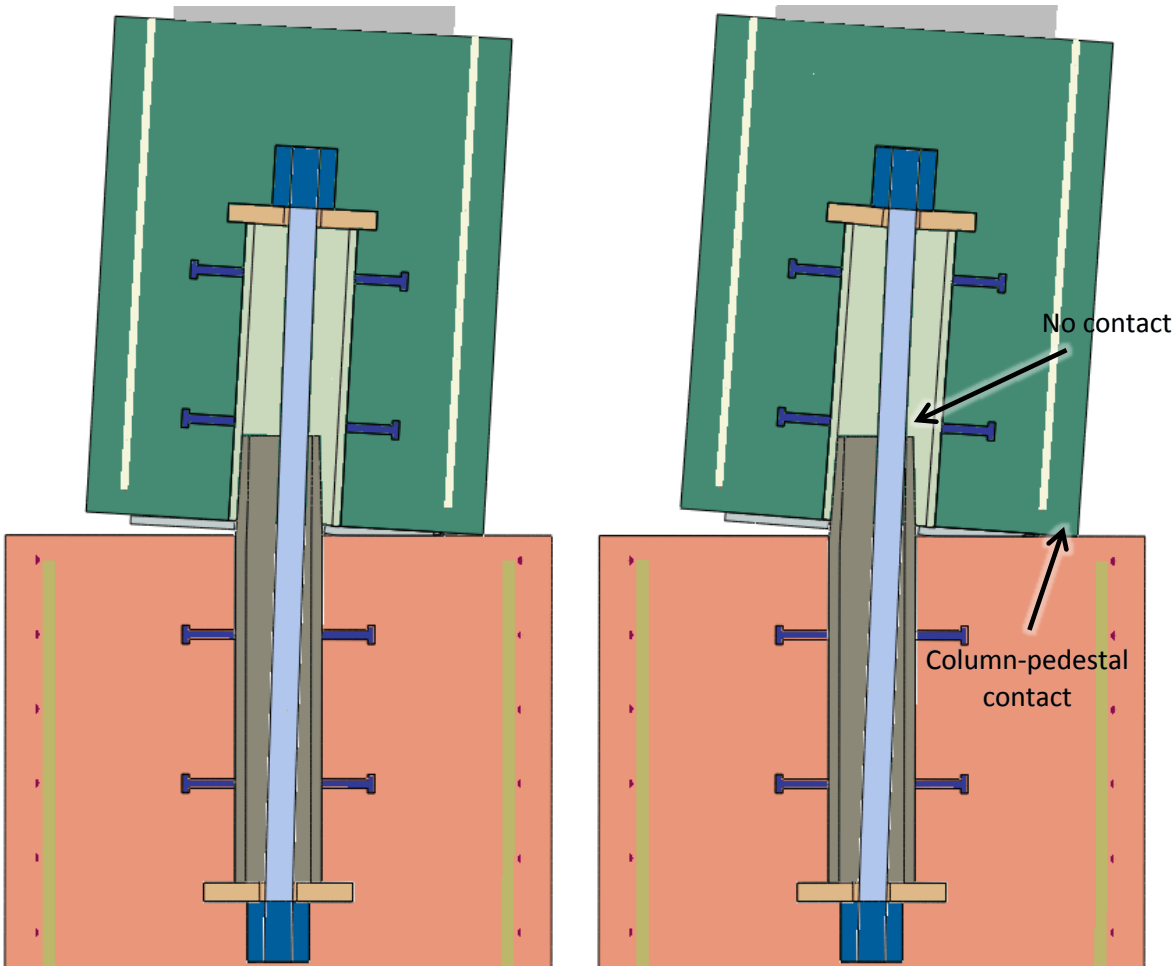

a) drift=6.1%

b) drift=7.5%

Fig. 4-46. Deformed shape of pipe-pin at a) 6.1% drift b) 7.5% drift

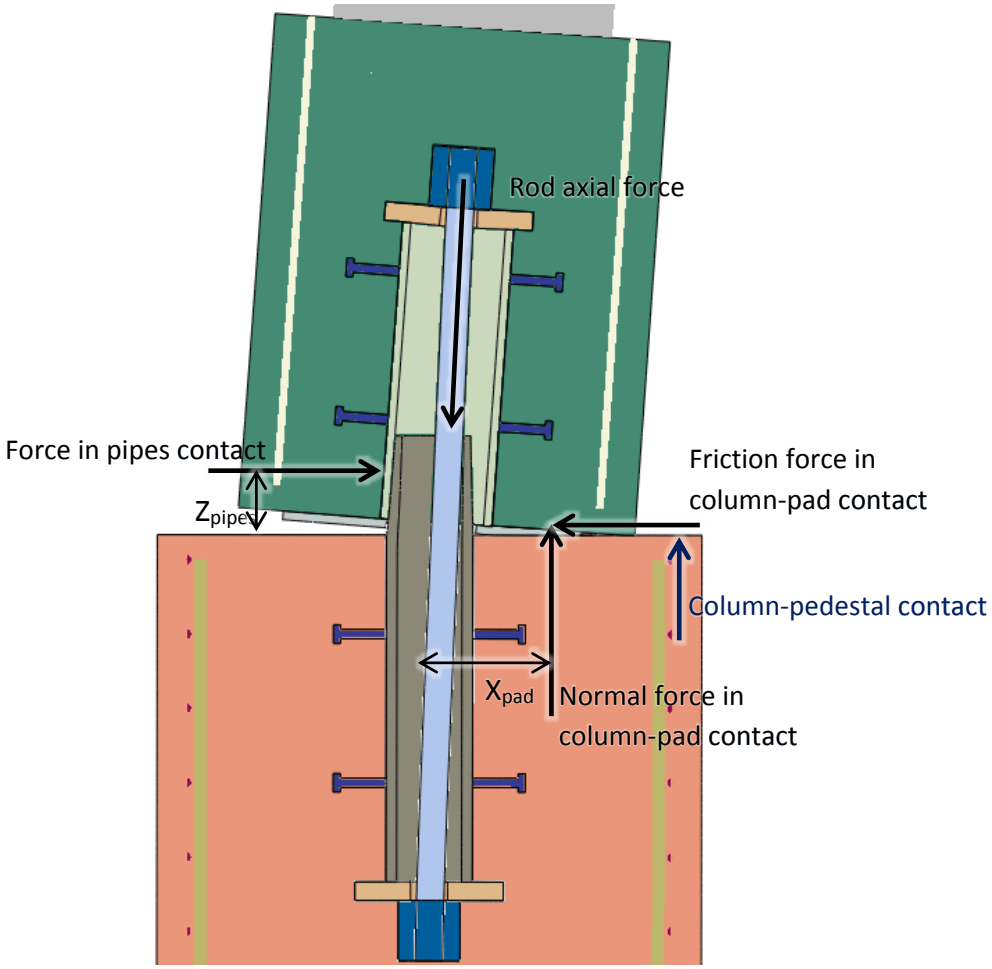

Fig. 4-47. Contact forces in the pipe-pin

a)

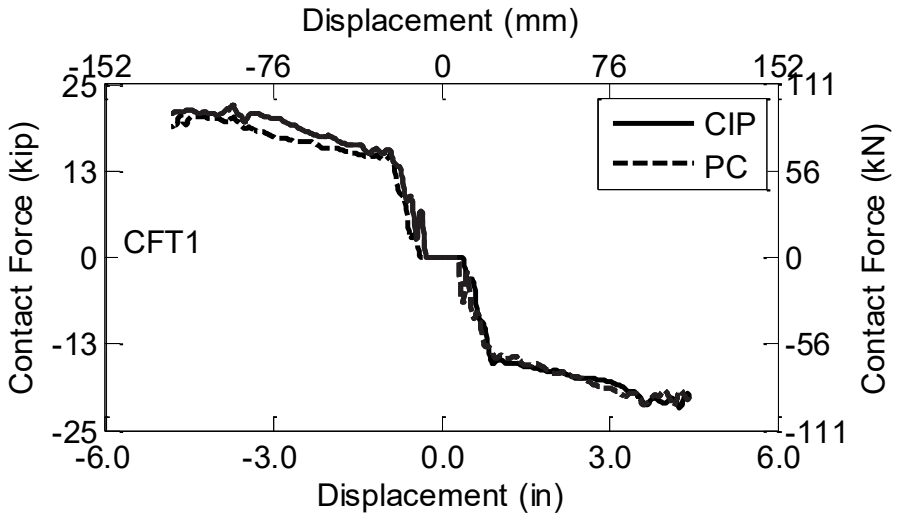

b)

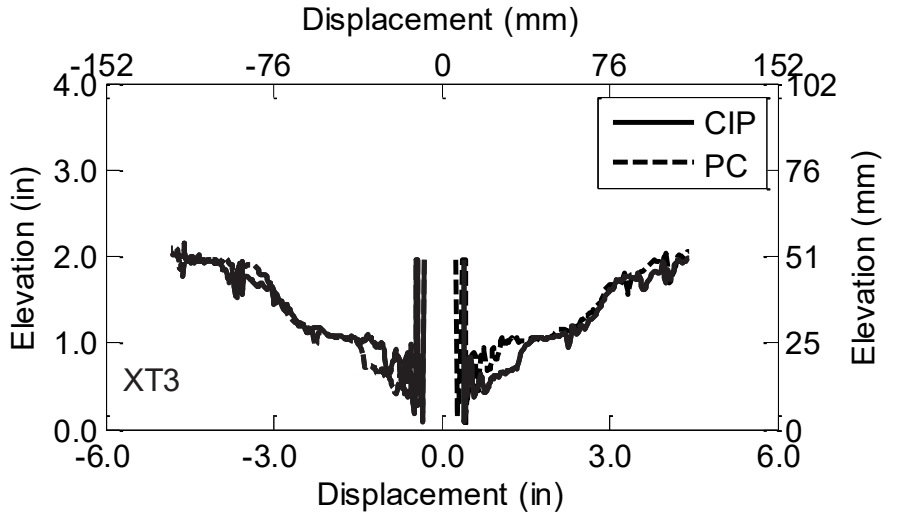

Fig. 4-48. BPSA results of contact of pipe a) force b) distance from intersection

a)

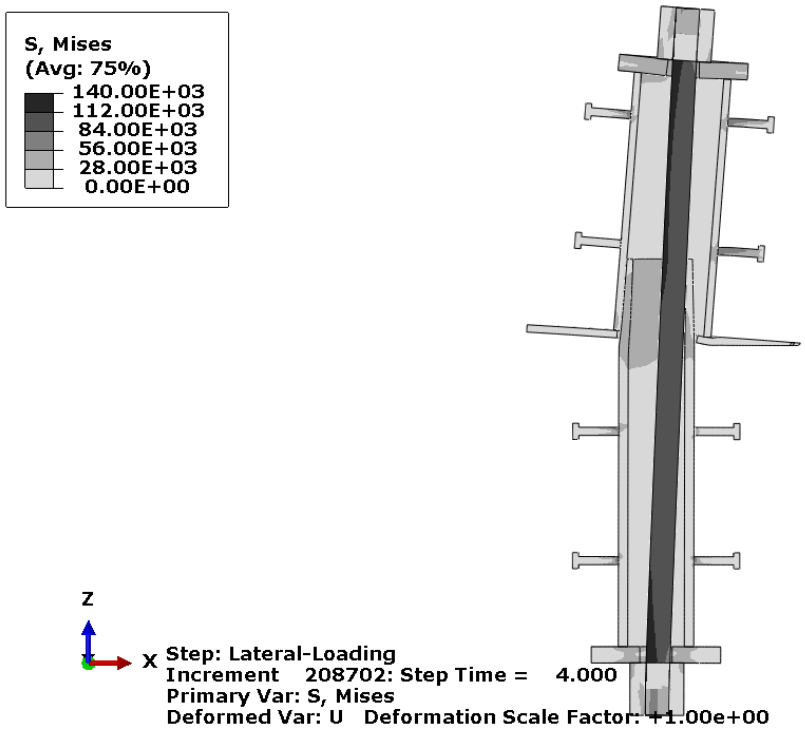

b)

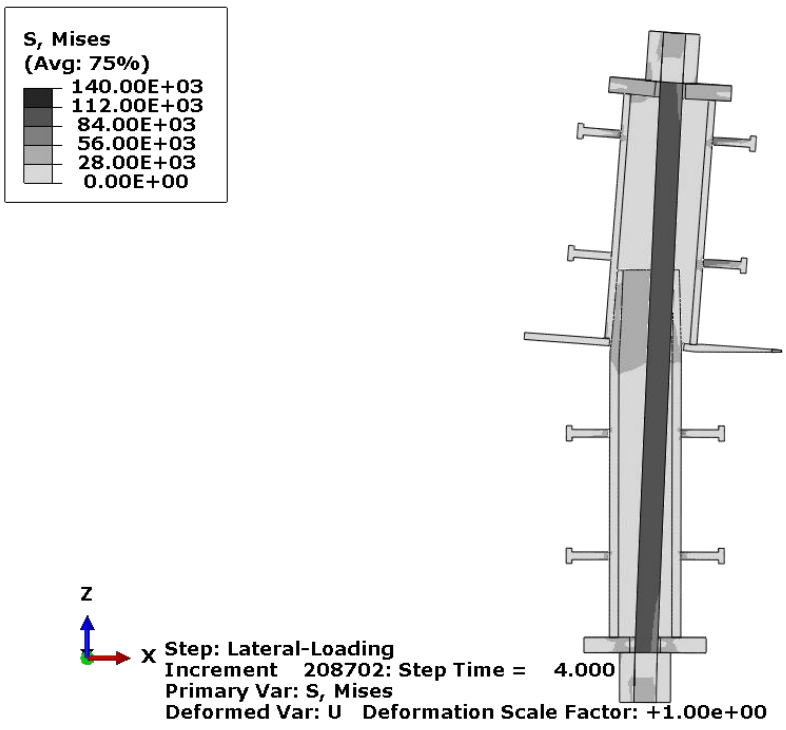

Fig. 4-49. BPSA Von Mises stress (psi) of steel parts, push to north direction a)CIP b)PC

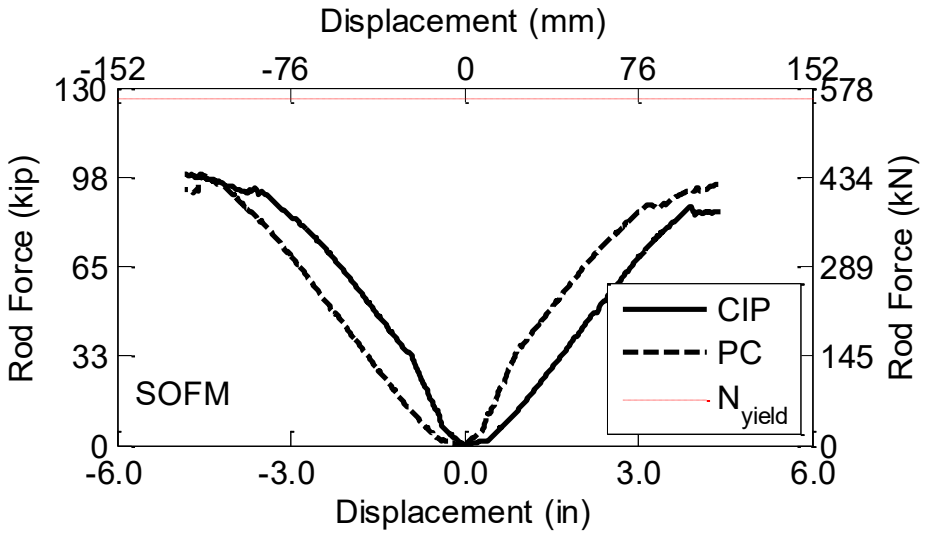

Fig. 4-50. BPSA threaded rods axial force

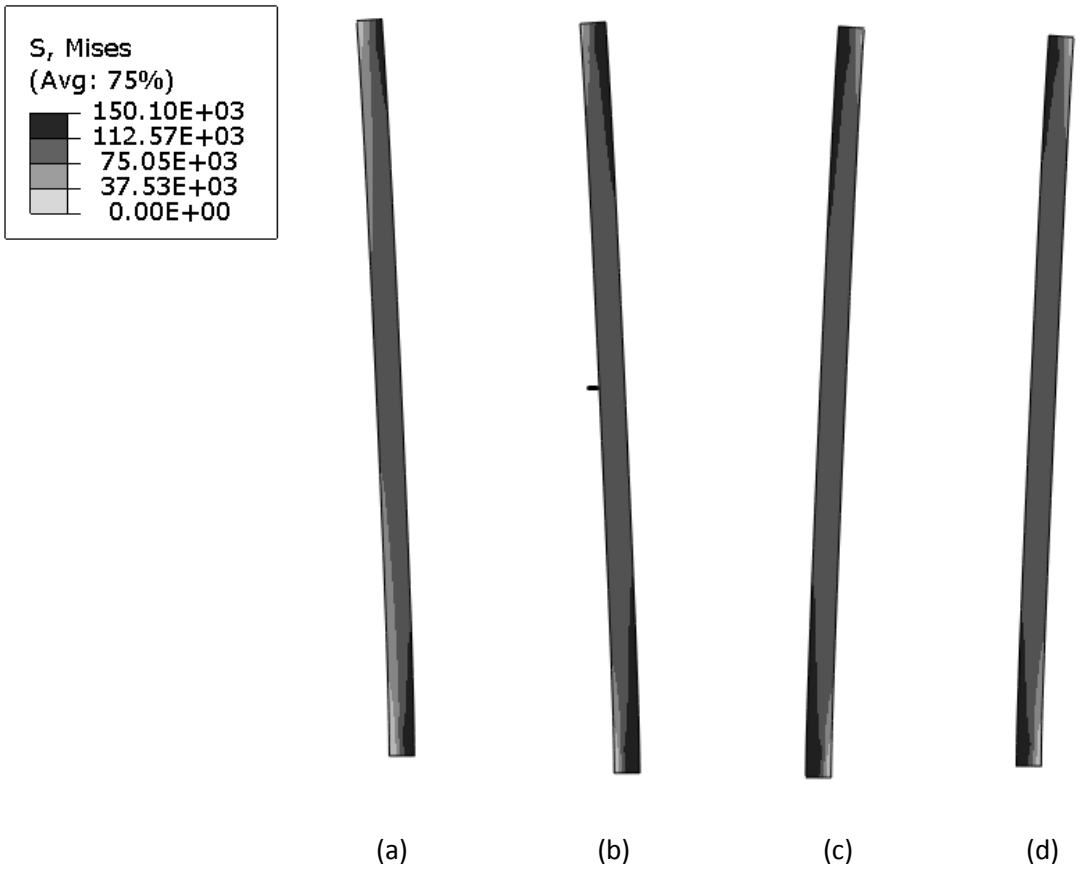

Fig. 4-51. Von Mises stress (psi) in the rods, South direction: (a) CIP (b) PC, North direction: (c) CIP (d) PC

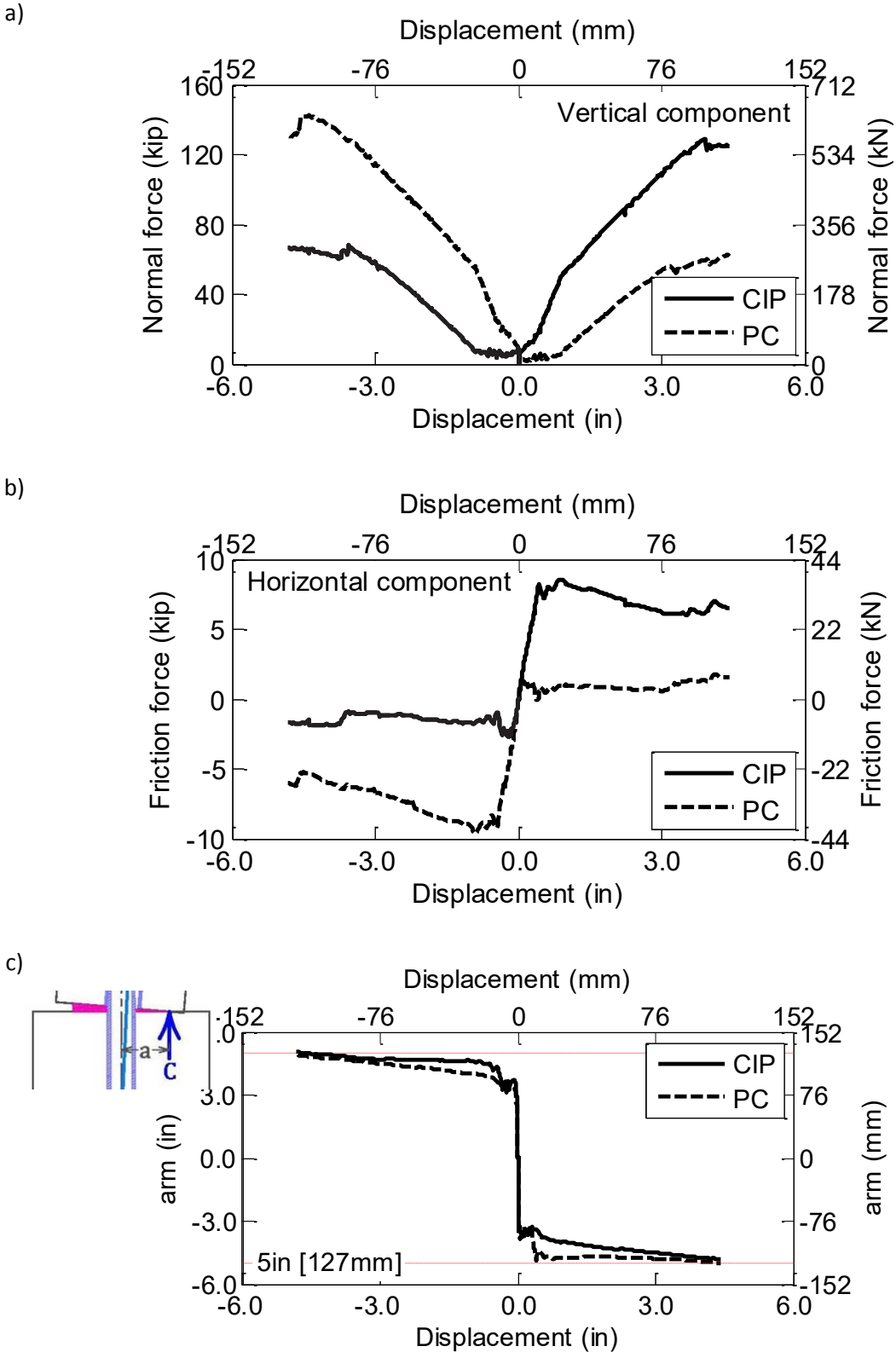

Fig. 4-52. Results of columns-pads contact a) normal component b) friction component c) moment arm

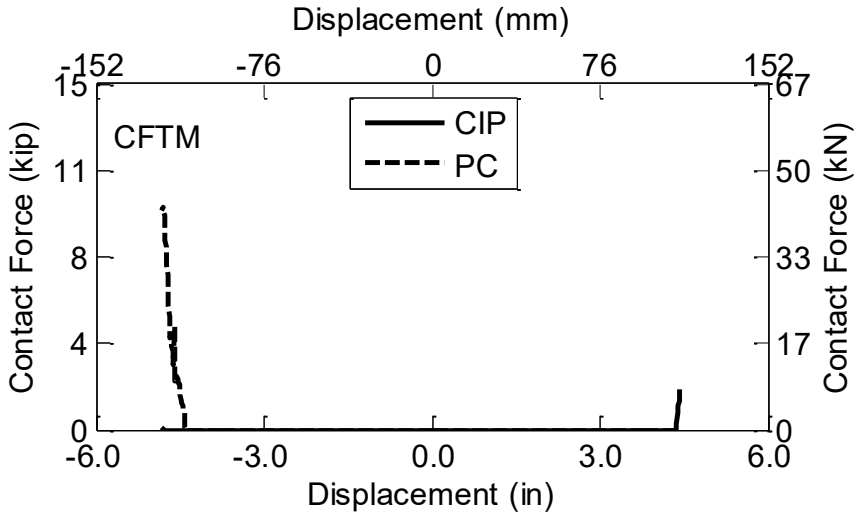

Fig. 4-53. Contact force between columns and pedestals

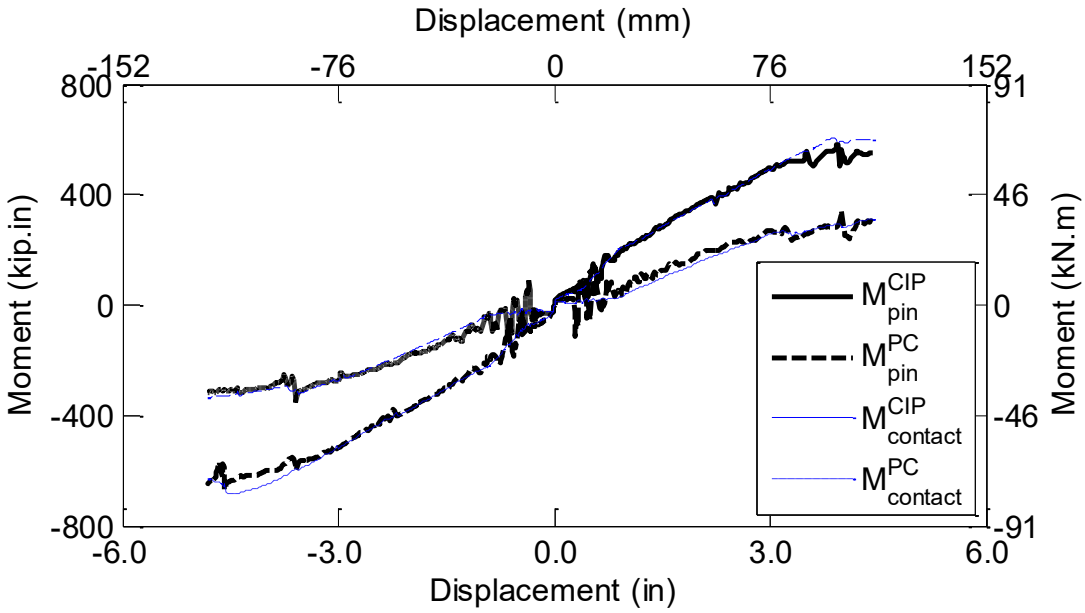

Fig. 4-54. BPSA pipe-pin moments

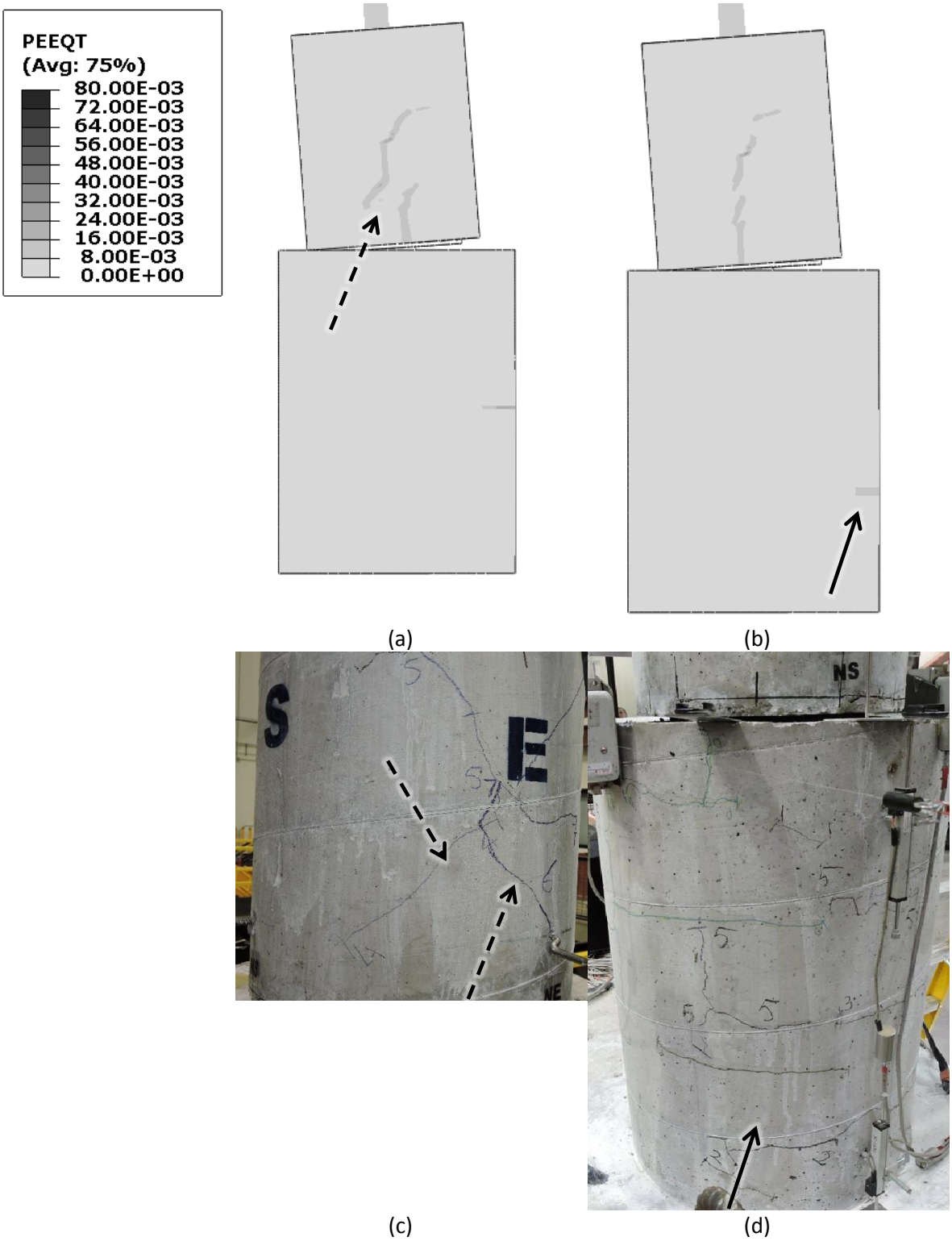

Fig. 4-55. Concrete cracking strain (PEEQT) on surface at ultimate displacement a) CIP b)PC c) CIP column d) PC

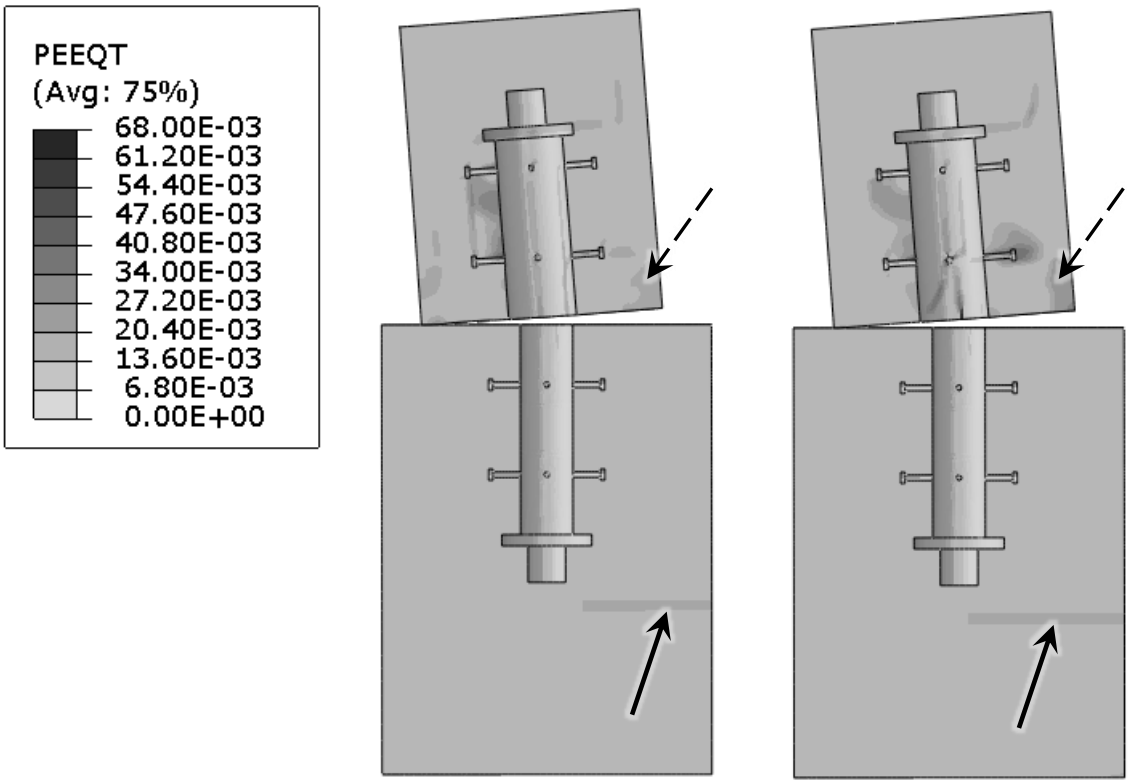

Fig. 4-56. Concrete cracking strain (PEEQT)on the cut at ultimate displacement a) CIP b)PC

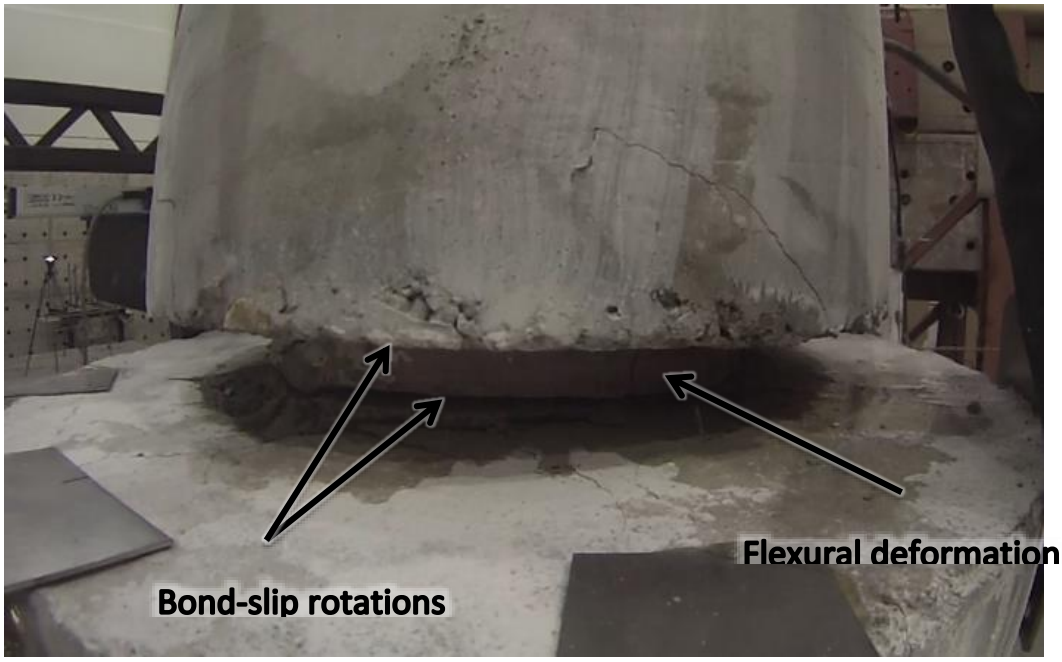

Fig. 4-57. Rebar-pin deformation during Run-5

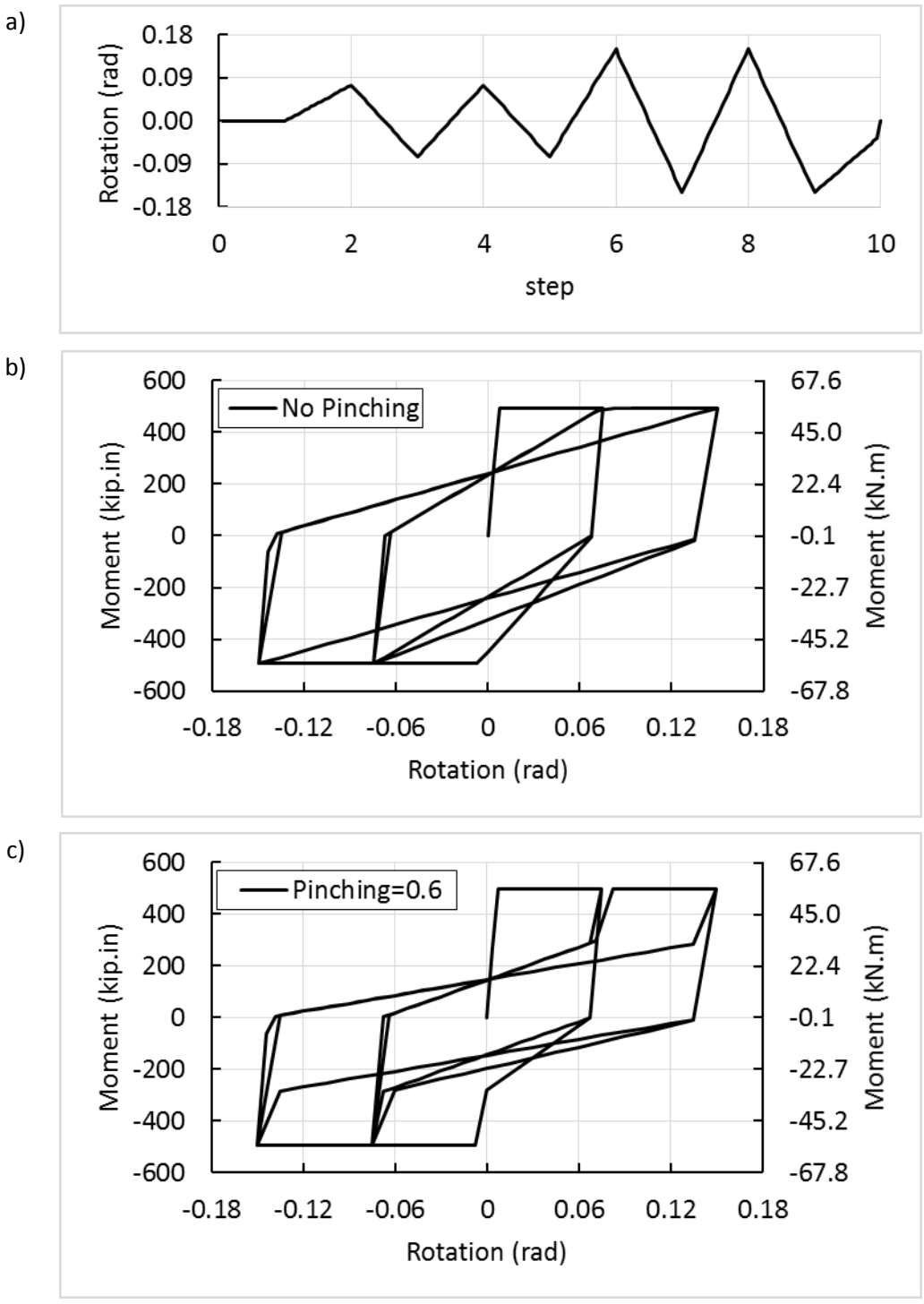

Fig. 4-58. Moment-rotation of Rebar-pin a) loading history b) no pinching c) with pinching

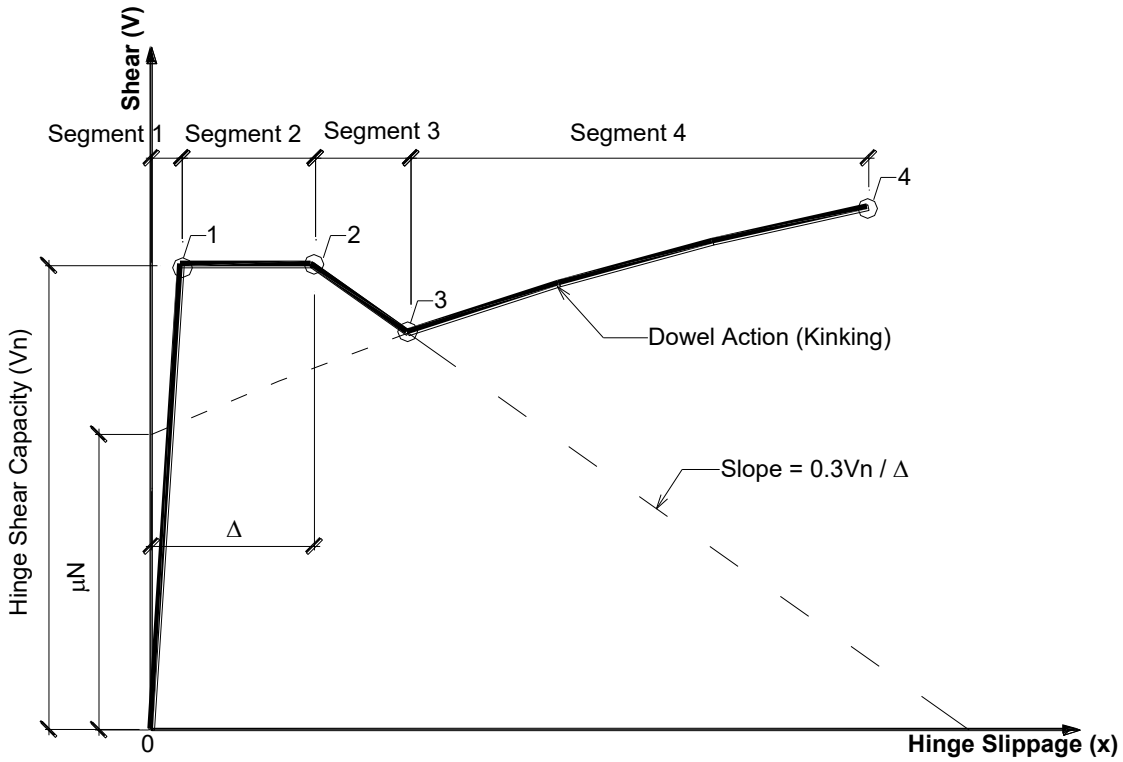

Fig. 4-59. Rebar-pin shear-slip model (Cheng et al. 2006)

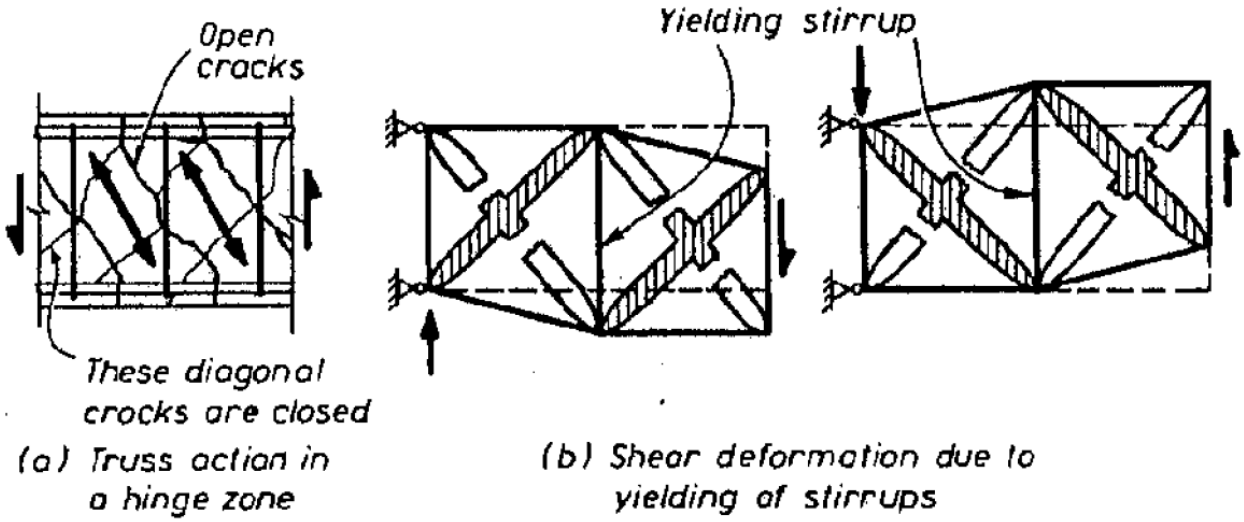

Fig. 4-60. Truss analogy models for shear transfer in plastic hinges (Paulay and Priestley, 1992)

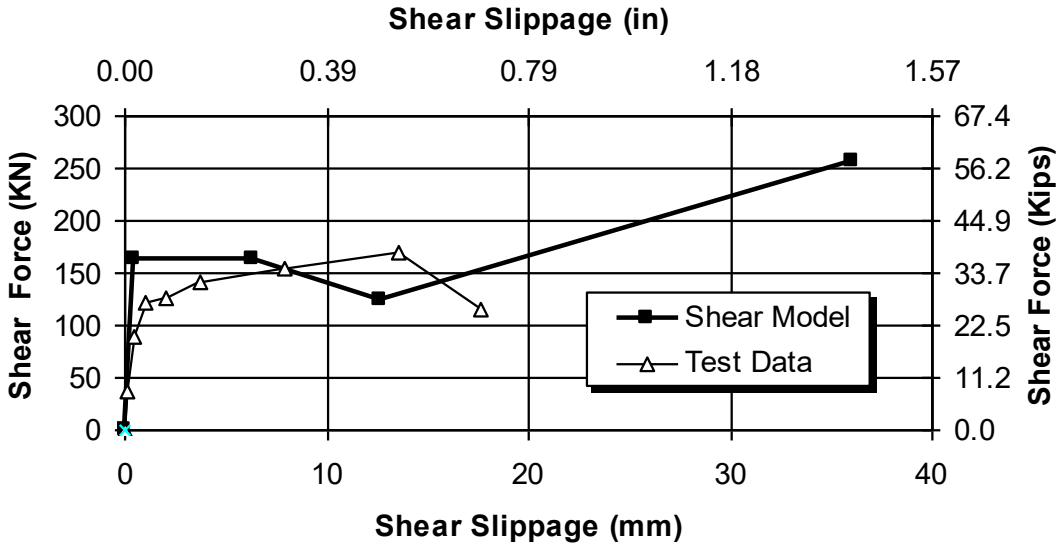

Fig. 4-61. Shear-slip relationship in two-way hinges at the top from Cheng et al. (2006)

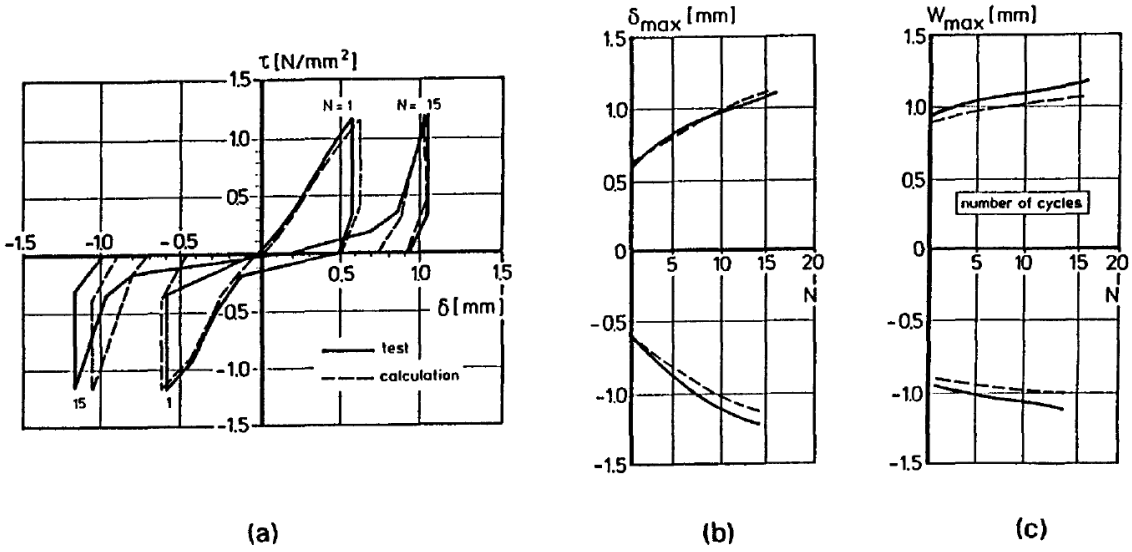

Fig. 4-62. Cracked reinforced concrete behavior under cyclic shear force (Walraven J. , 1994)

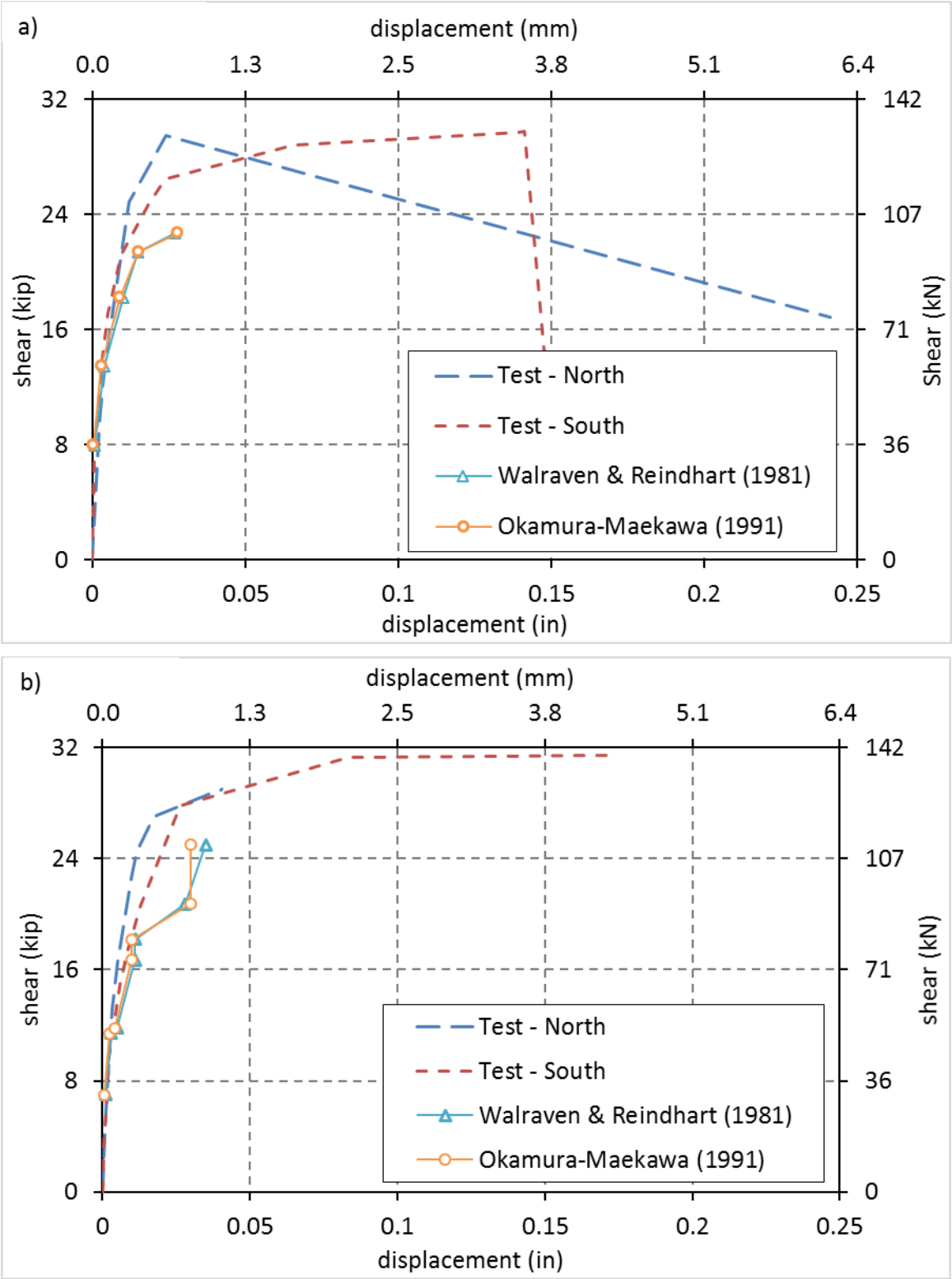

Fig. 4-63. Experimental results vs. numerical models of shear-slip in rebar-pins

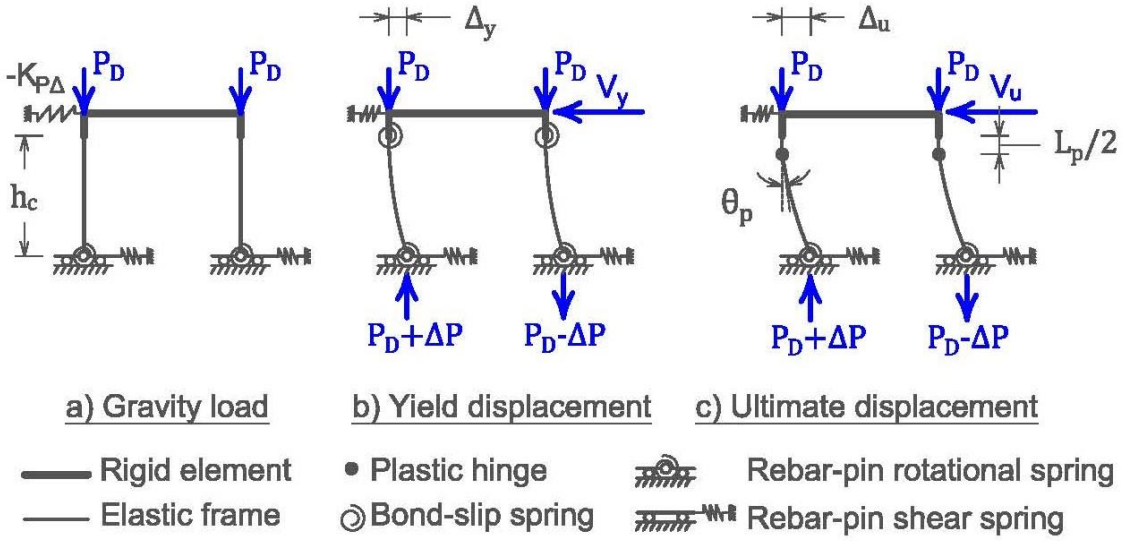

Fig. 4-64. BRSA simple stick model

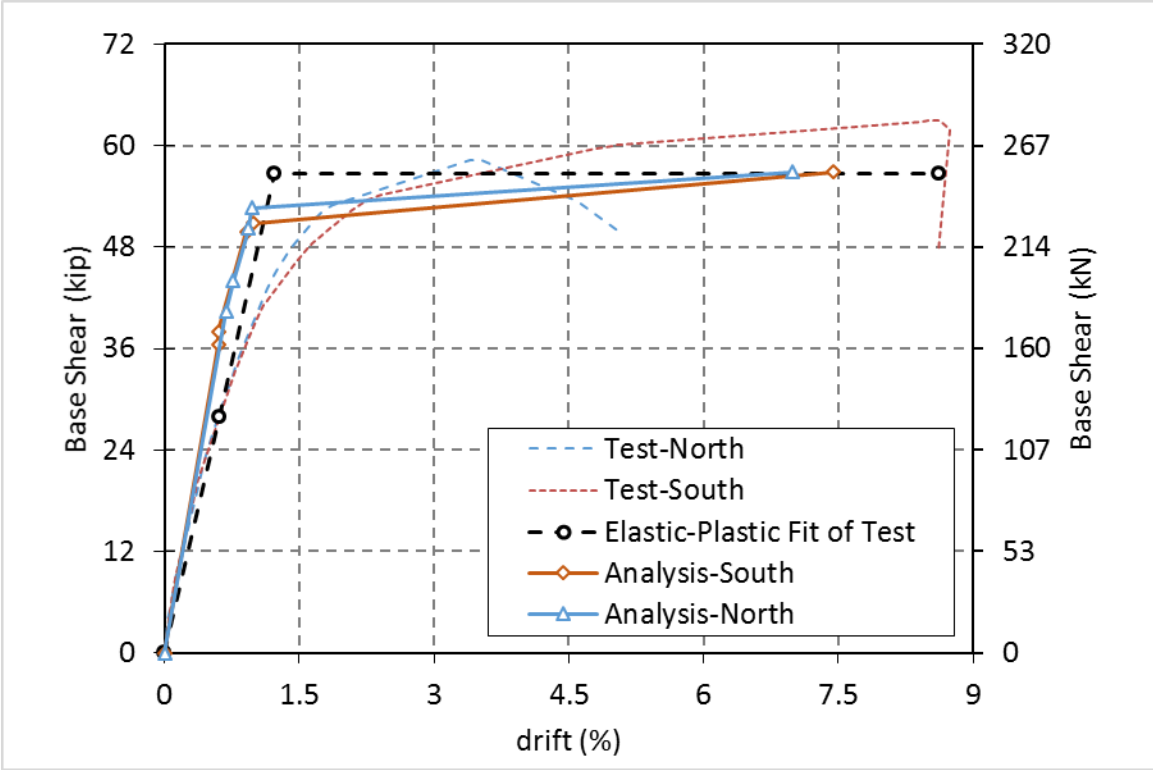

Fig. 4-65. BRSA force-displacement envelope using simple stick model

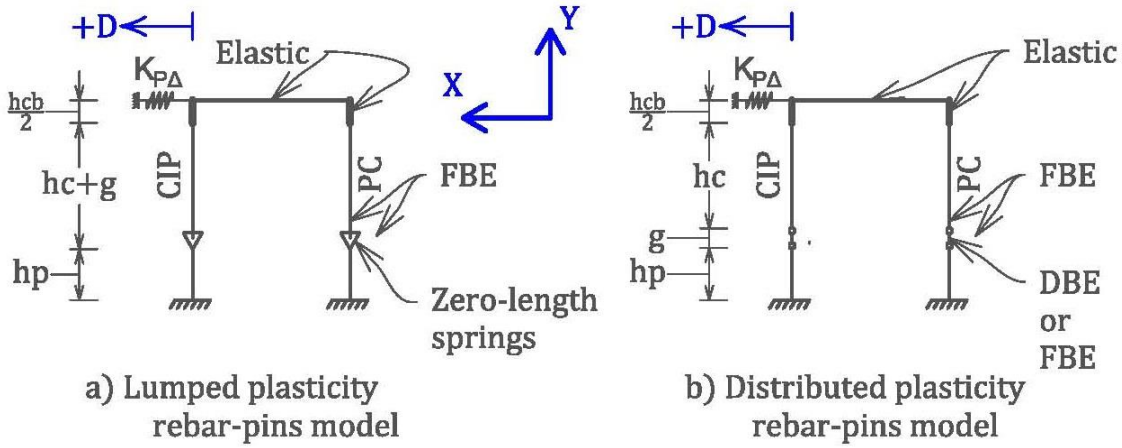

Fig. 4-66. BRSA models for pushover analyses

a)

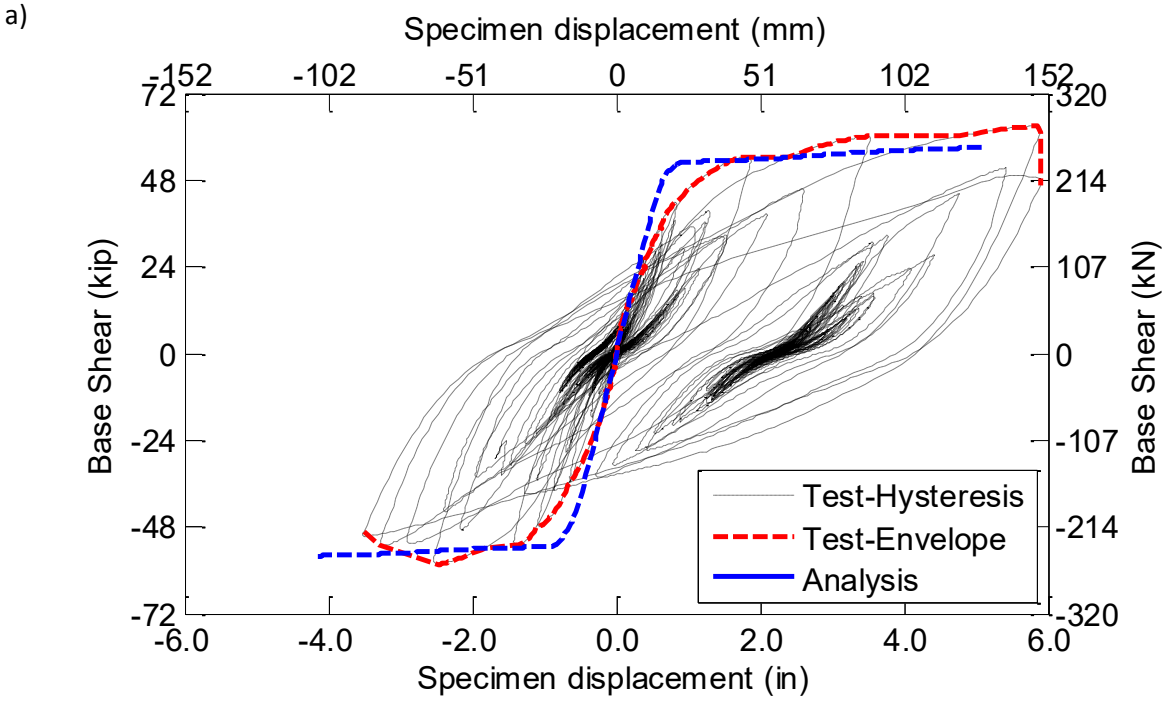

b)

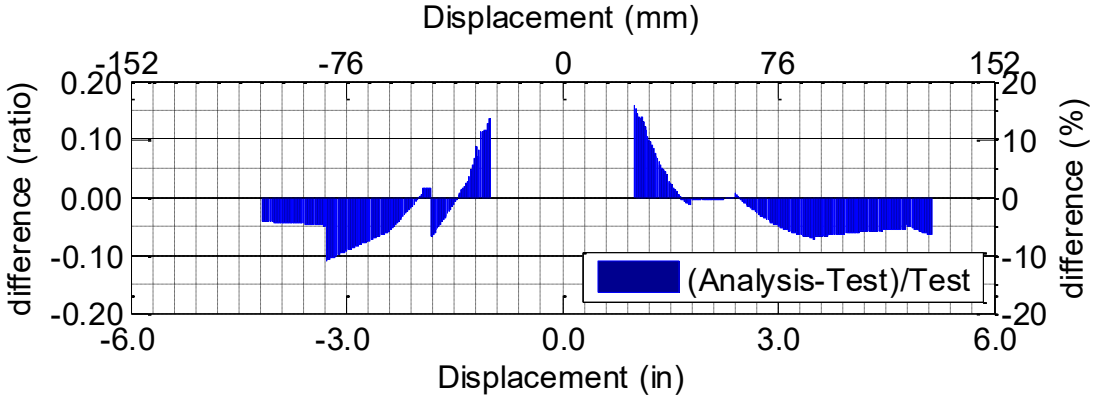

Fig. 4-67. BRSA pushover results of model with lumped plasticity for rebar-pins a) comparison b) error

a)

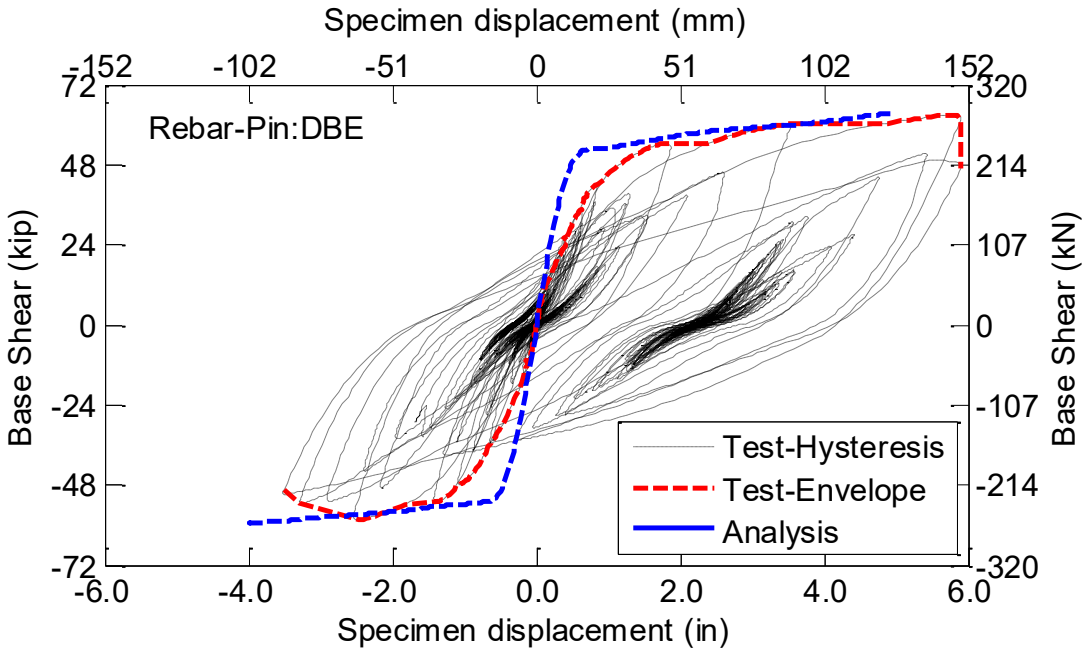

b)

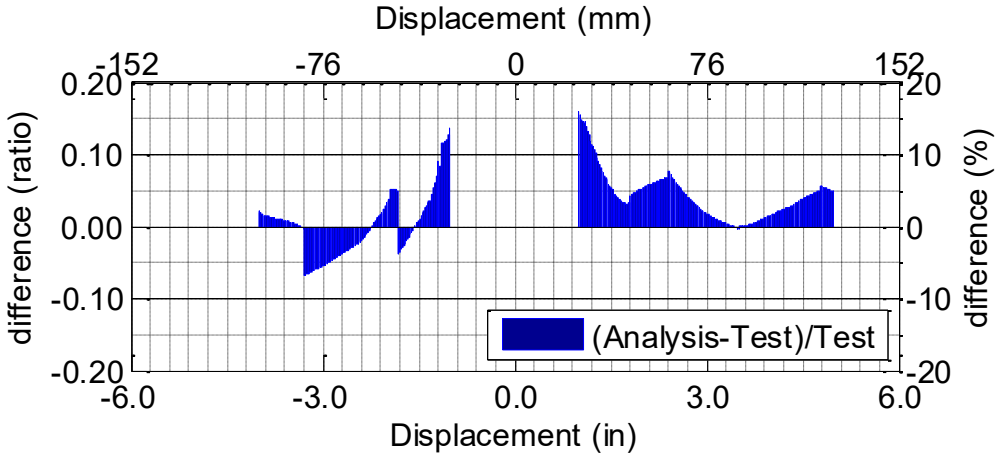

Fig. 4-68. BRSA pushover results of model with DB elements for rebar-pins a) comparison b) error

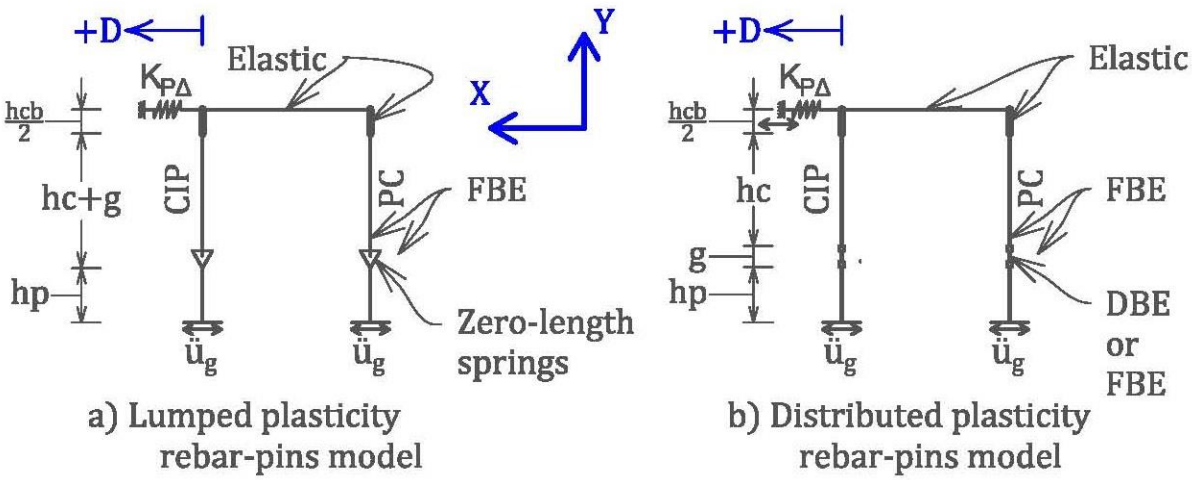

Fig. 4-69. BRSA Models for dynamic analysis

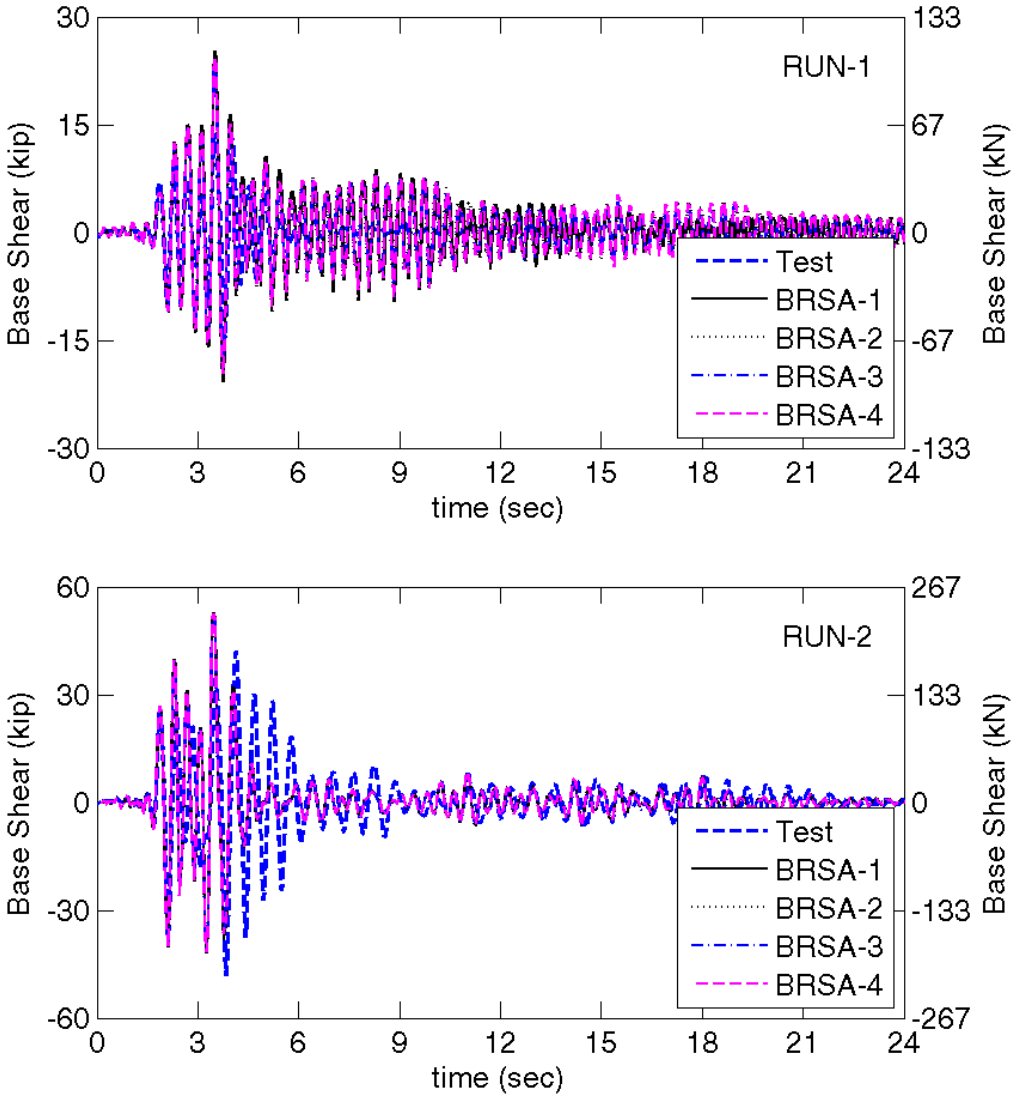

Fig. 4-70. BRSA base shear history for different concrete models , Run1 and 2

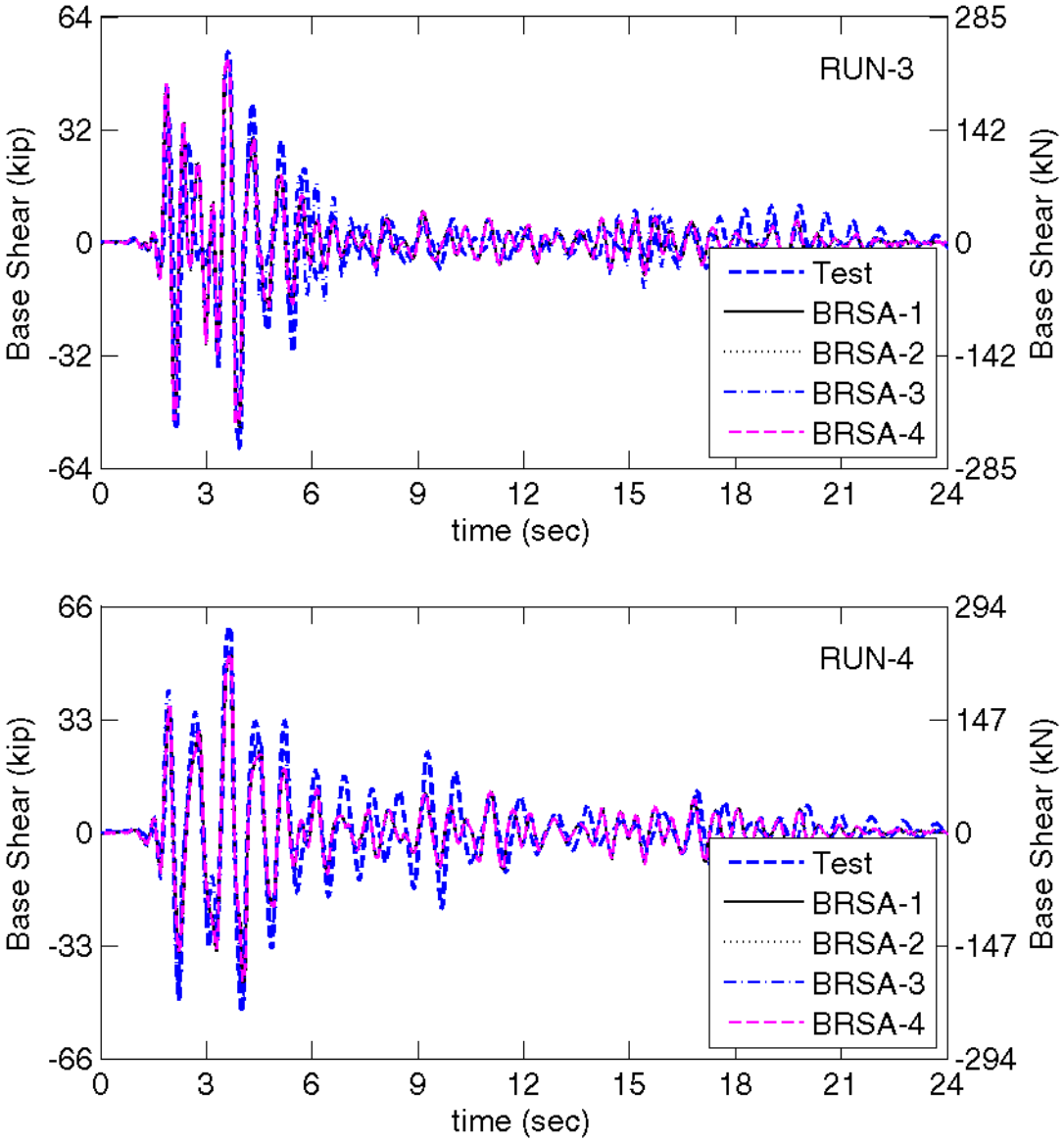

Fig. 4-71. BRSA base shear history for different concrete models , Run3 and 4

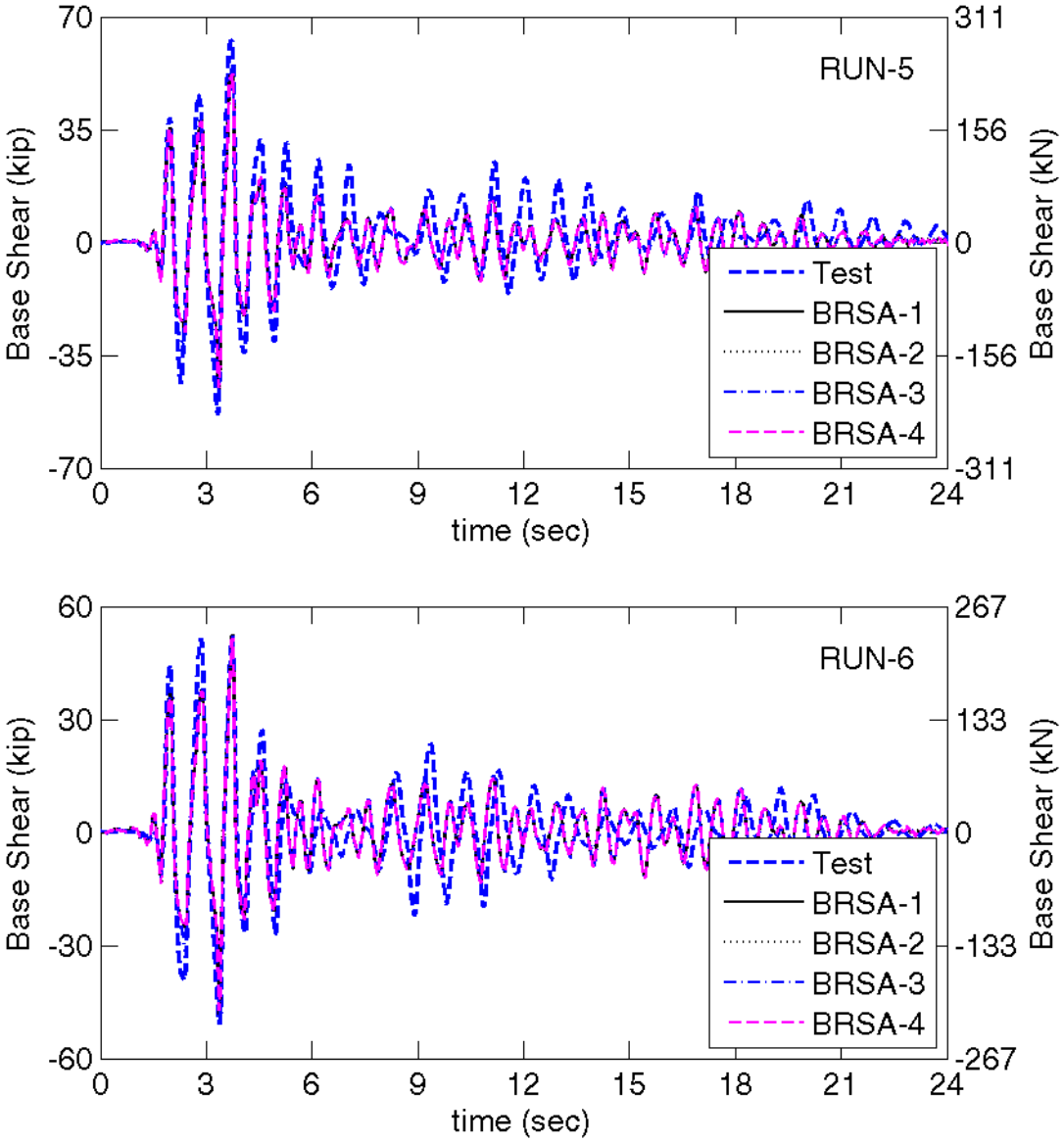

Fig. 4-72. BRSA base shear history for different concrete models , Run5 and 6

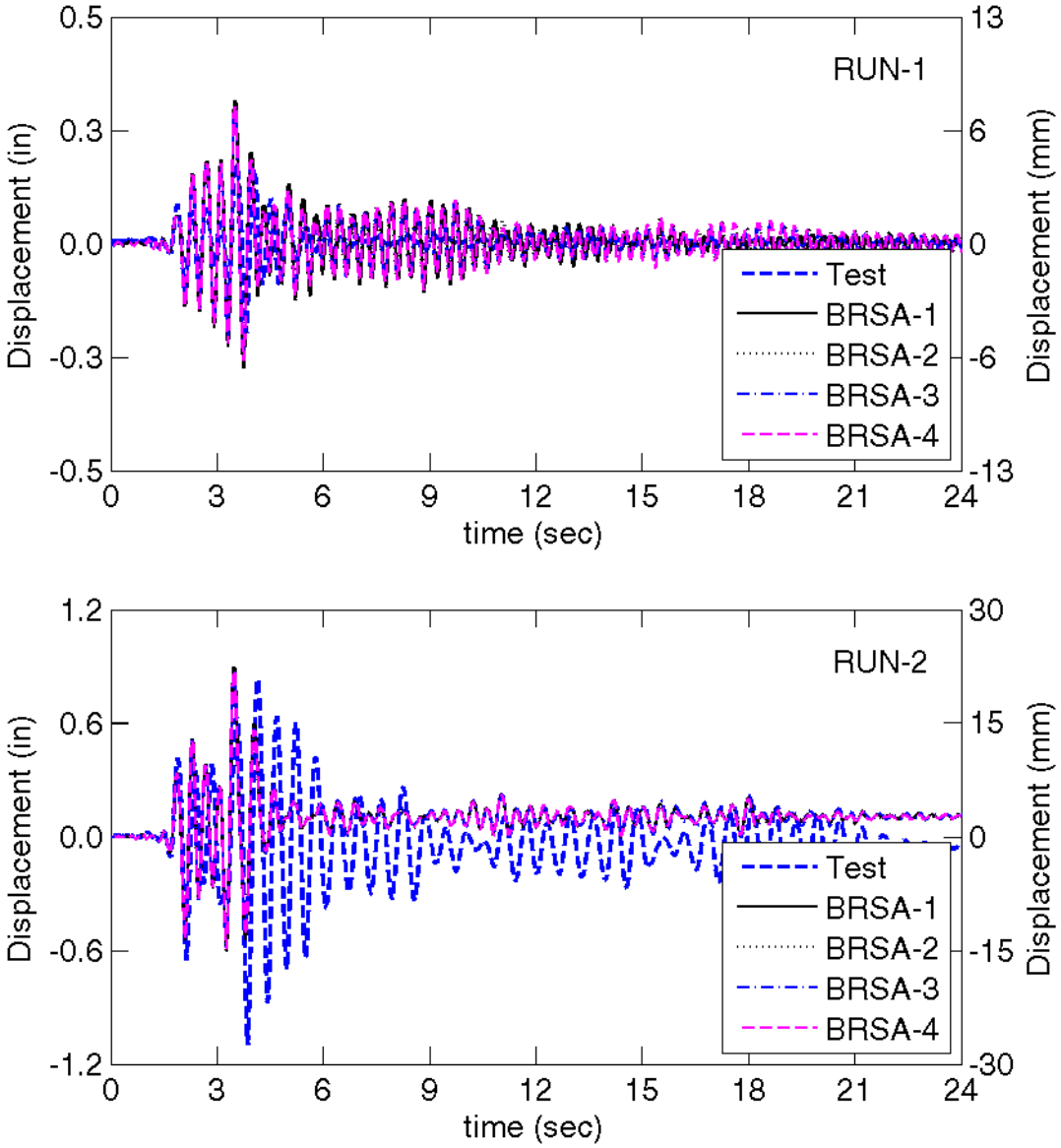

Fig. 4-73. BRSA displacement history for different concrete models , Run1 and 2

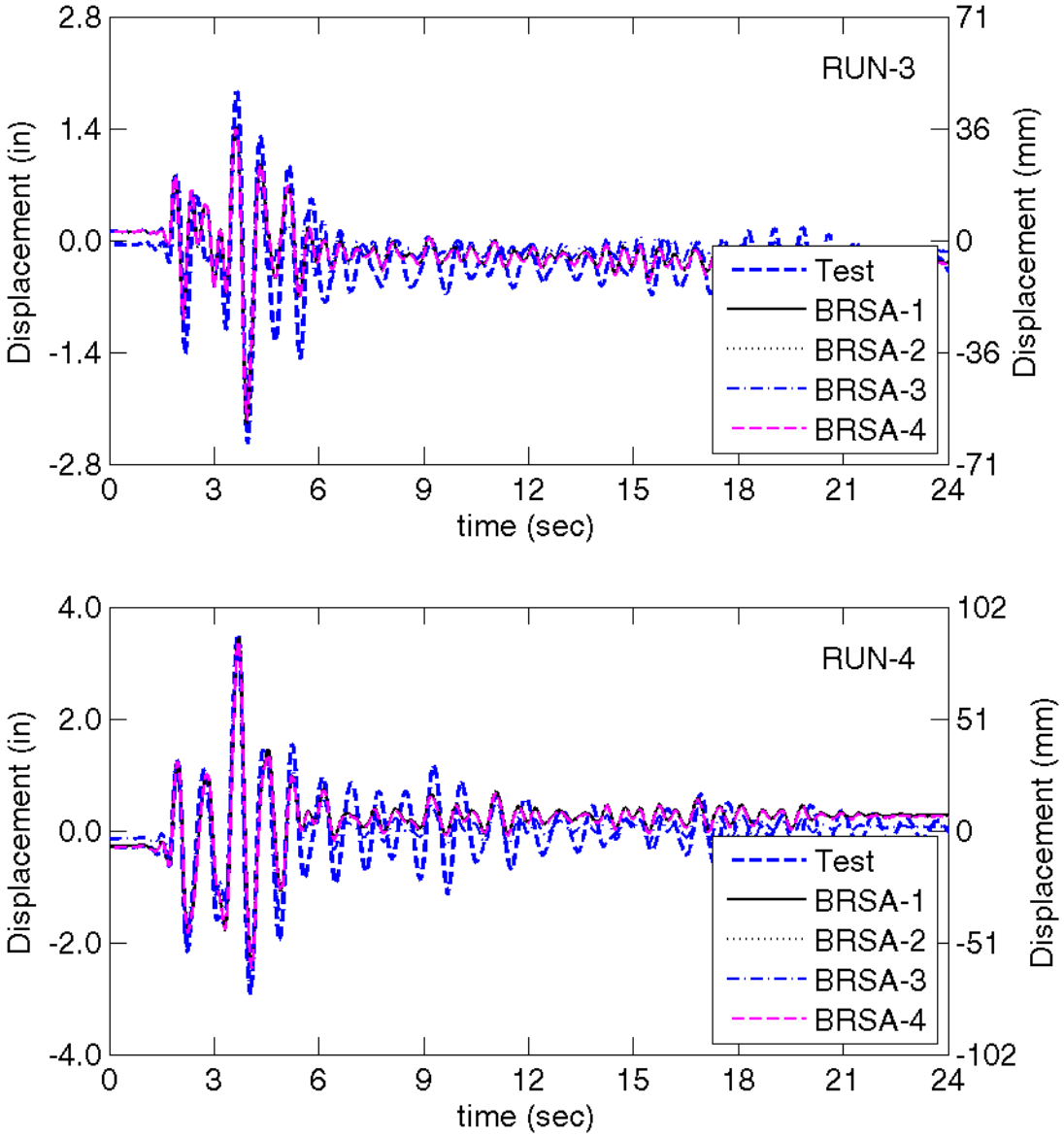

Fig. 4-74. BRSA displacement history for different concrete models, Run3 and 4

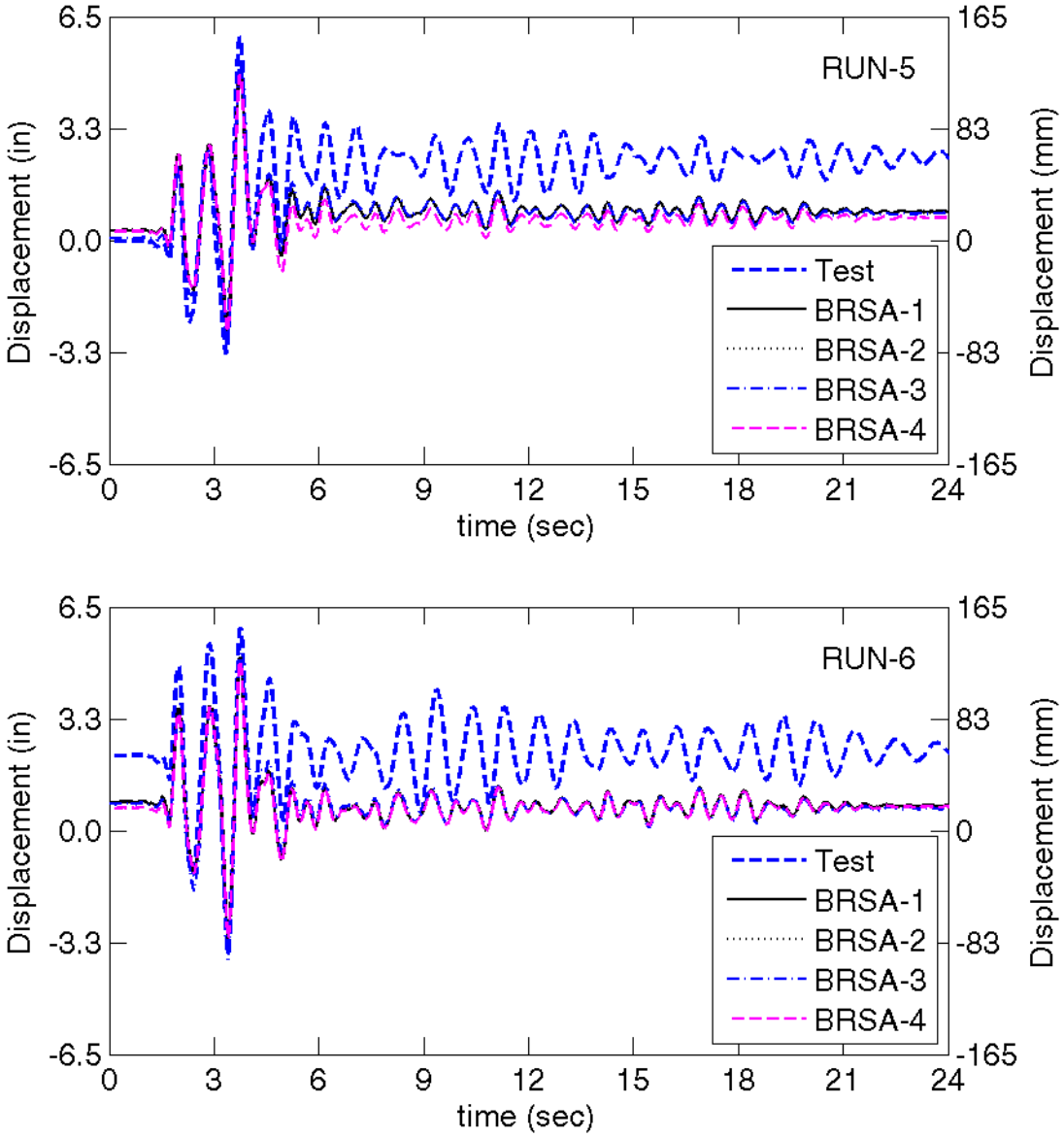

Fig. 4-75. BRSA displacement history for different concrete models, Run 5 and 6

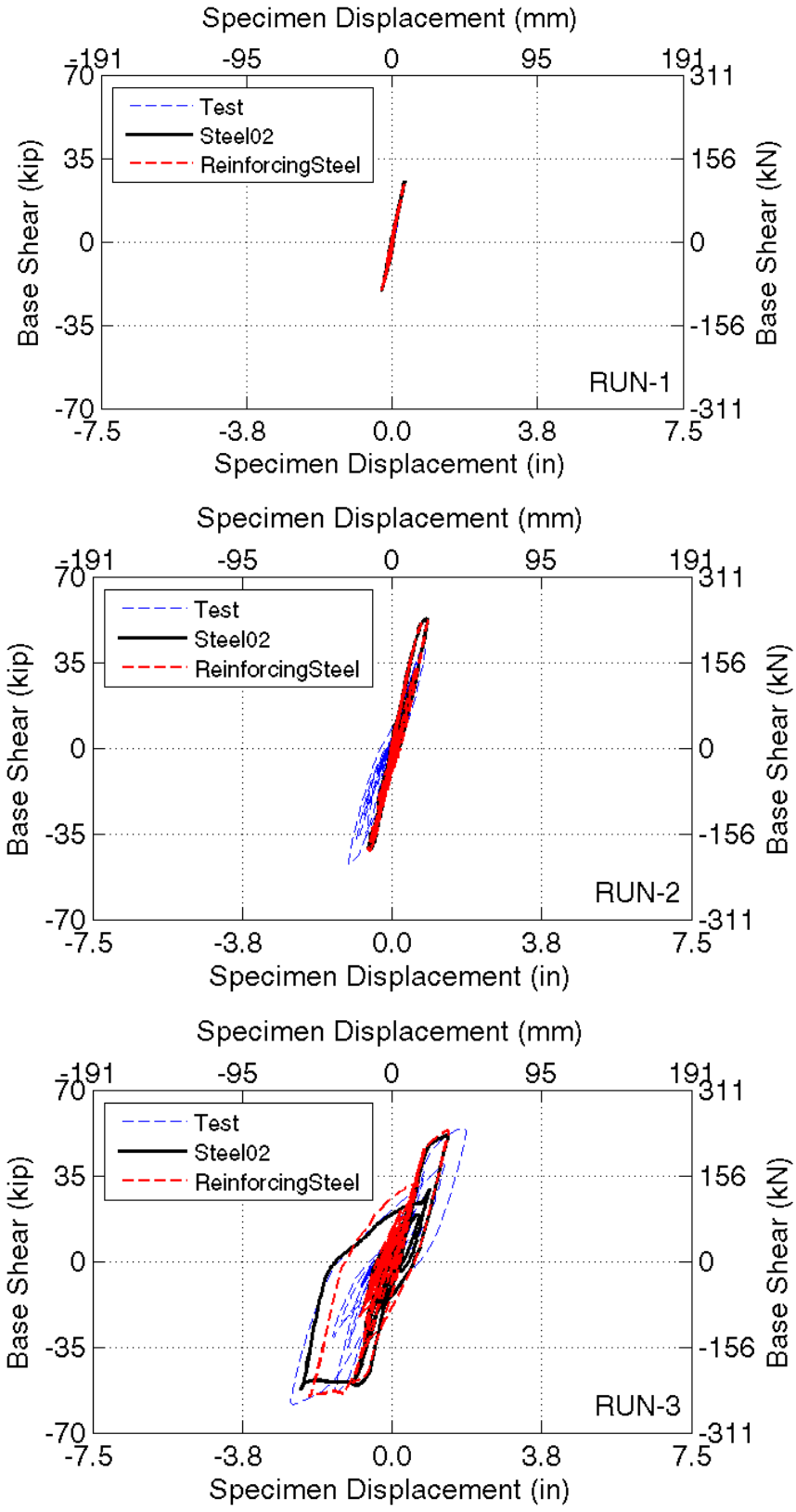

Fig. 4-76. BRSA force-displacements for different reinforcement, Run-1 to Run-3

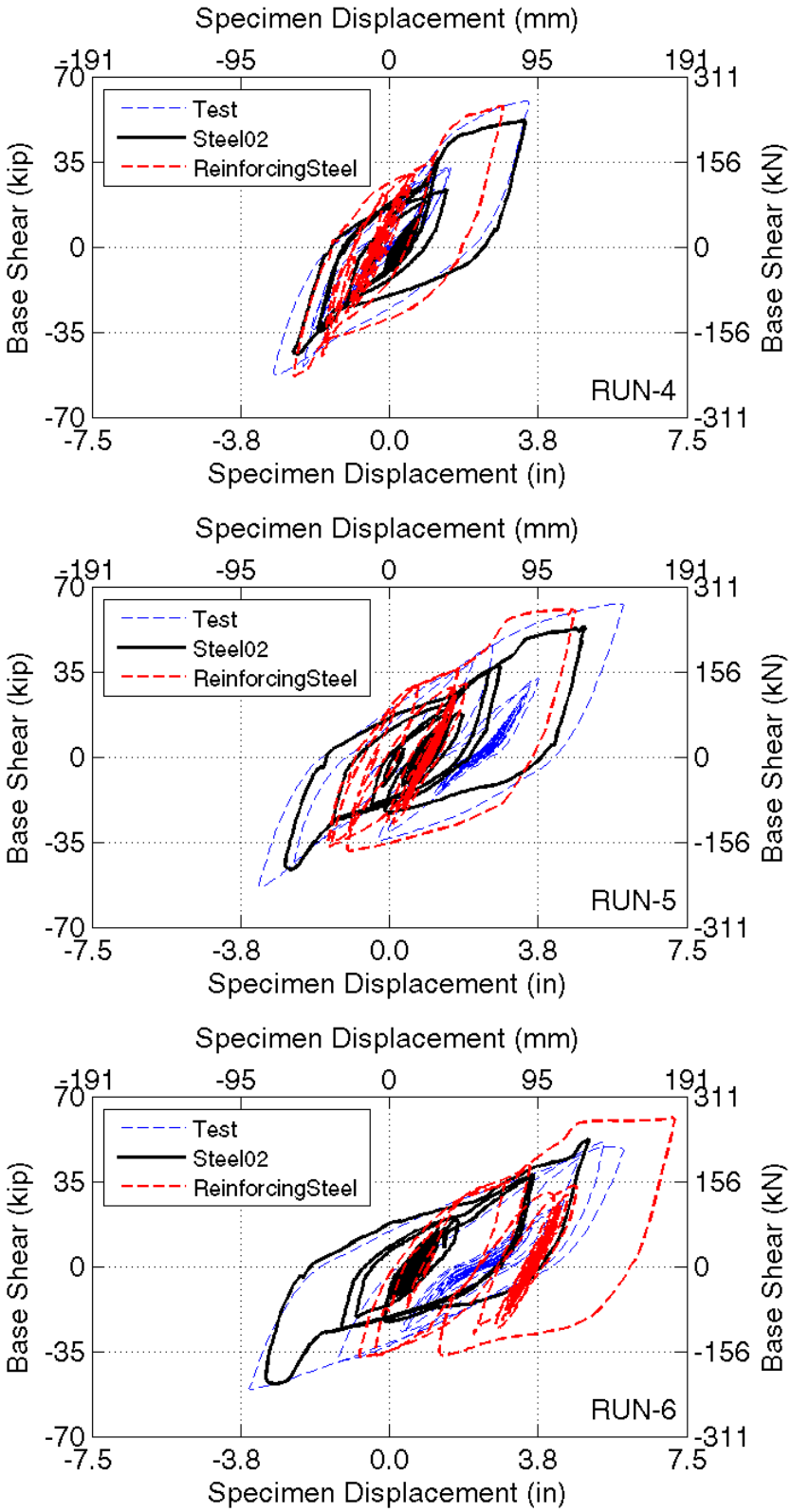

Fig. 4-77. BRSA force-displacements for different reinforcement, Run-4 to Run-6

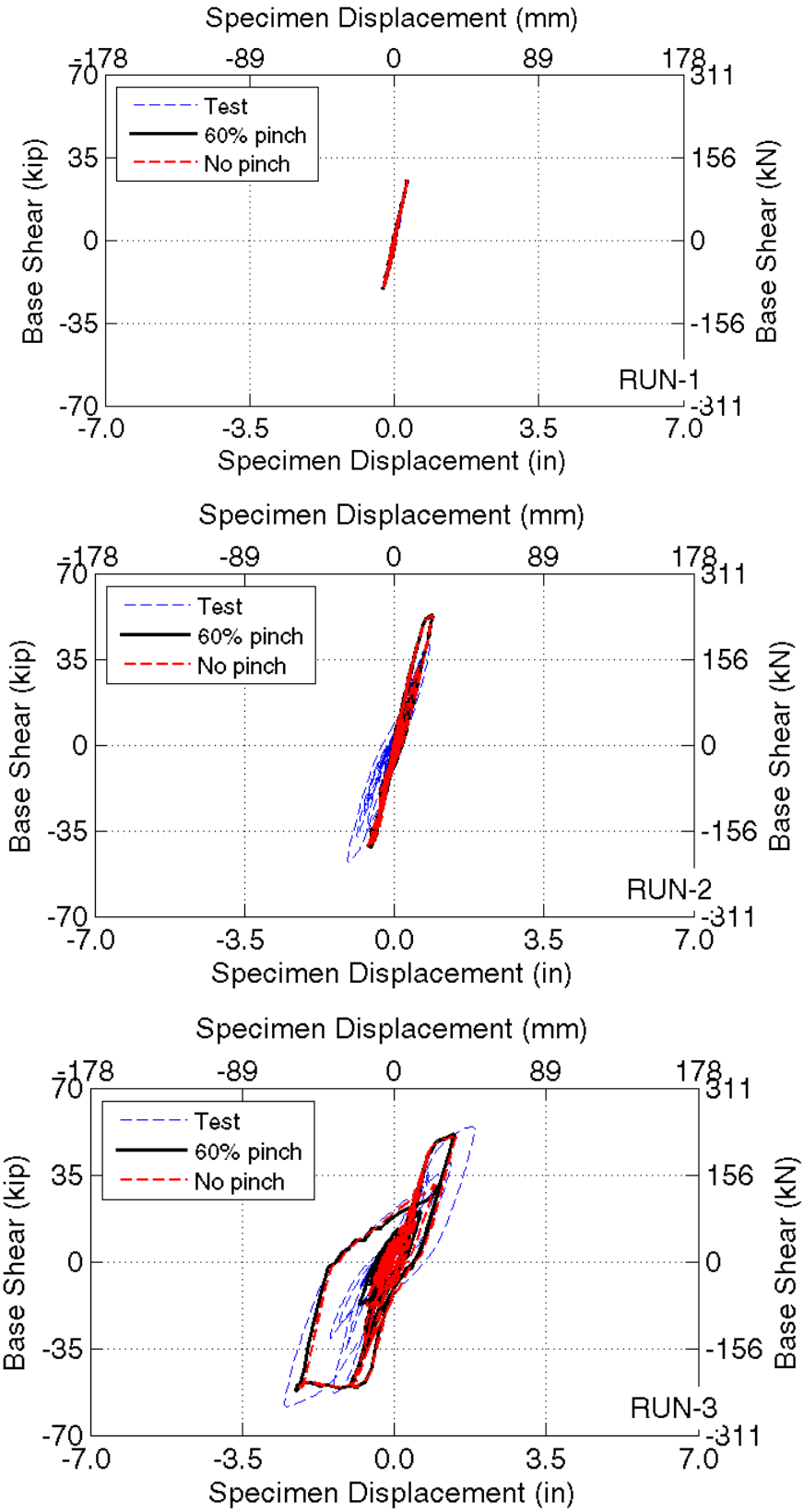

Fig. 4-78. Effect of pinching on the calculated response of the bent, Run-1 to Run-3

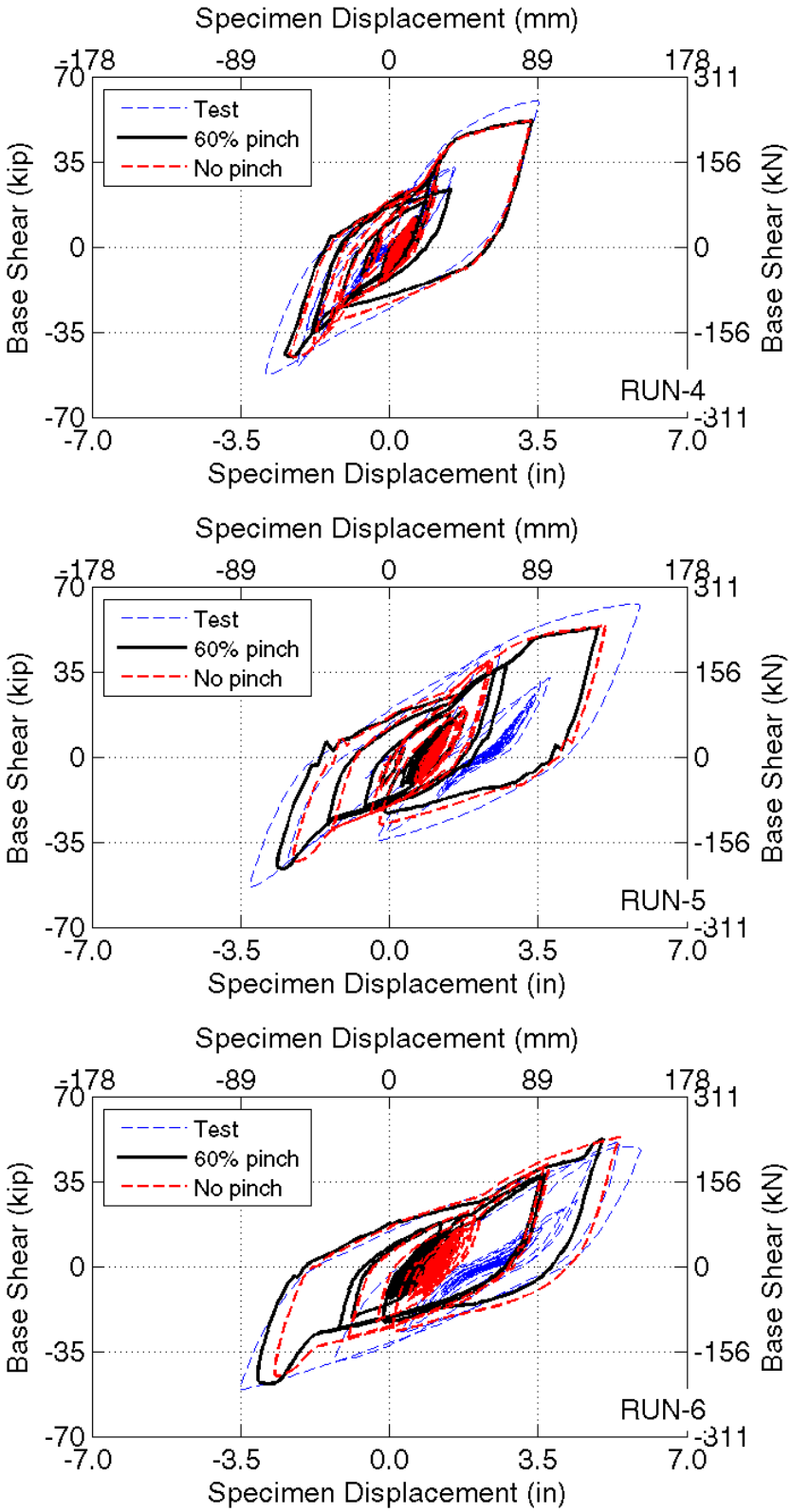

Fig. 4-79. Effect of pinching on the calculated response of the bent, Run-4 to Run-6

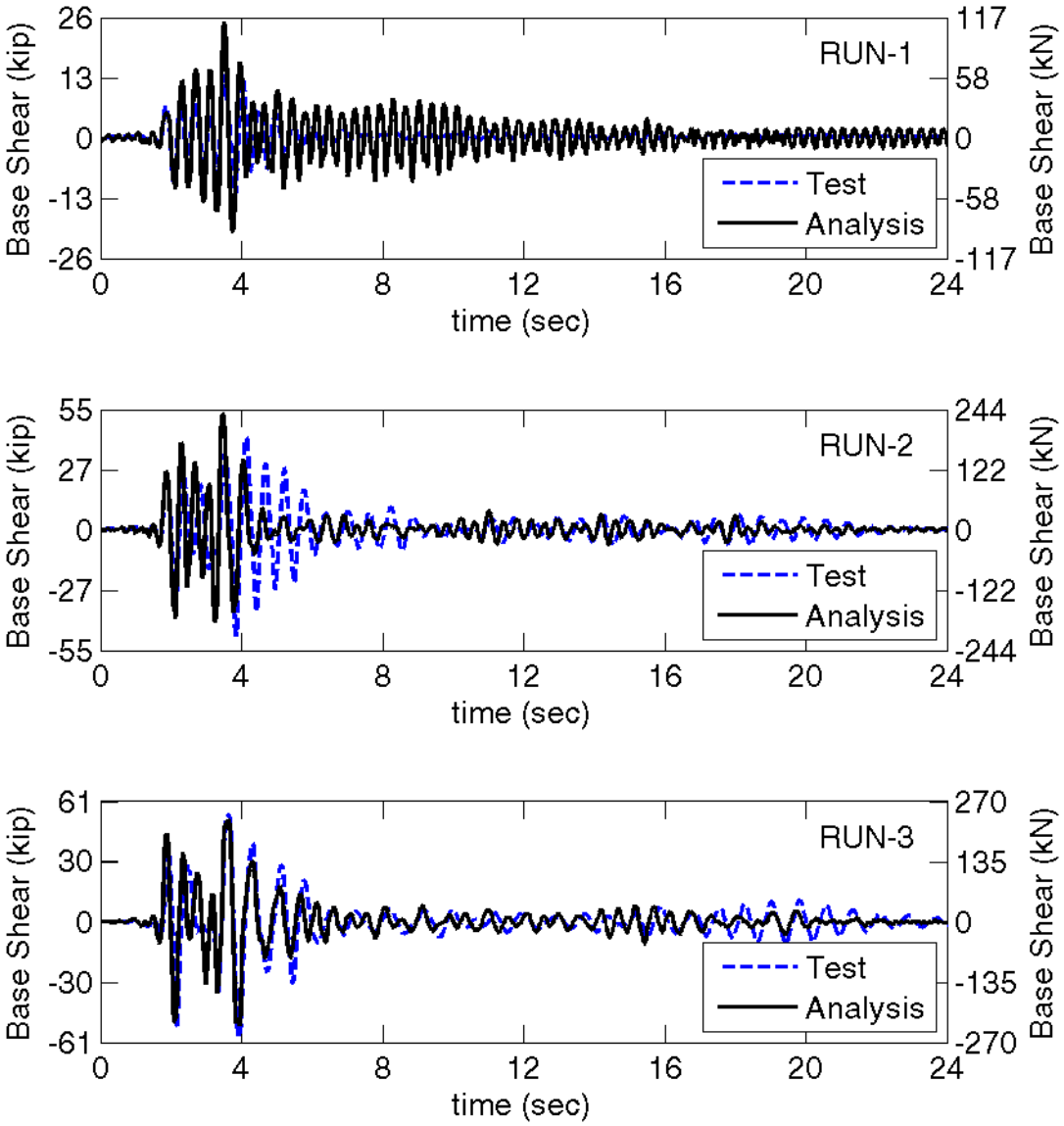

Fig. 4-80. Base shear history of BRSA with lumped plasticity model of rebar-pin, Run-1 to 3

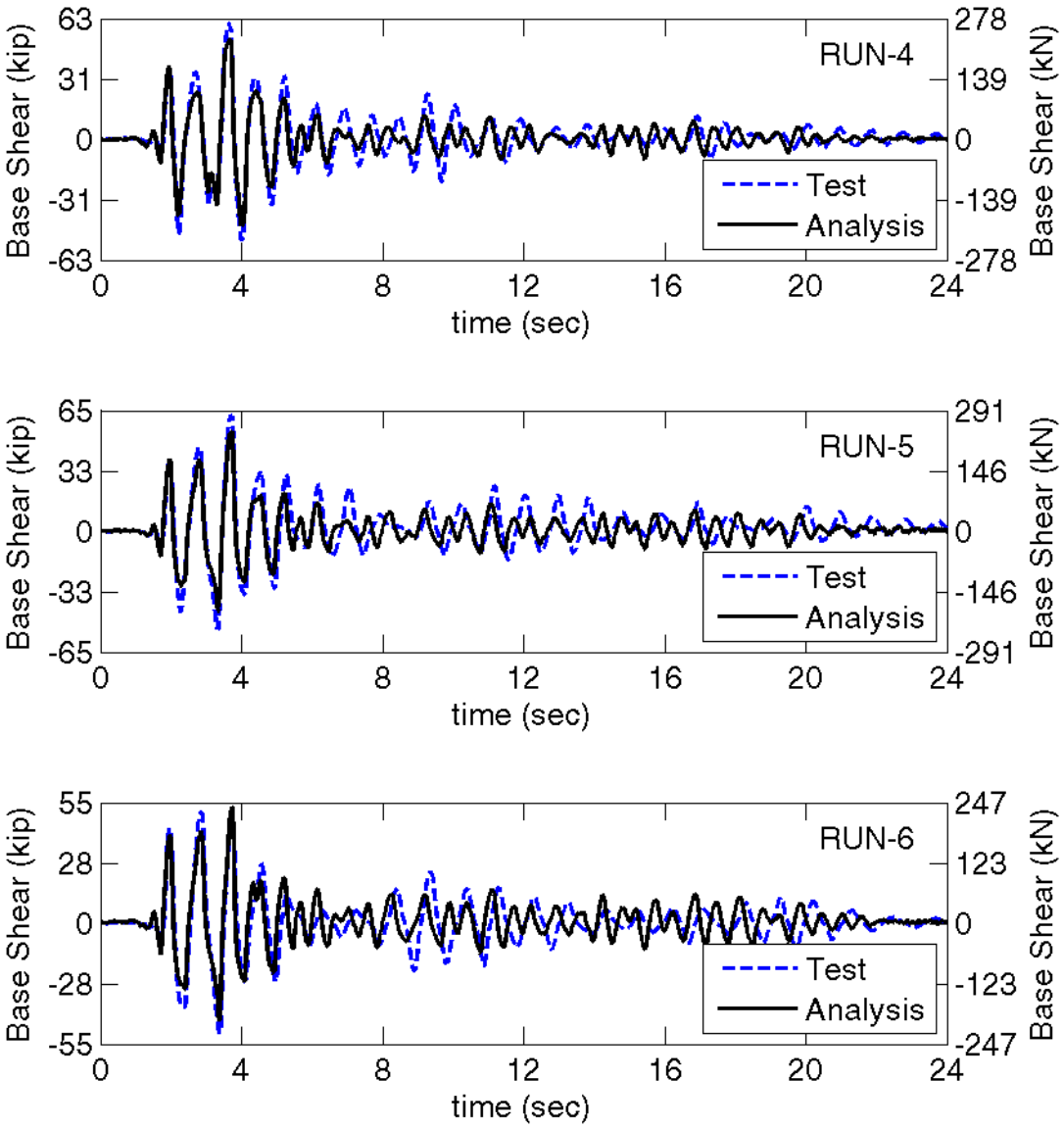

Fig. 4-81. Base shear history of BRSA with lumped plasticity model of rebar-pin, Run-3 to 6

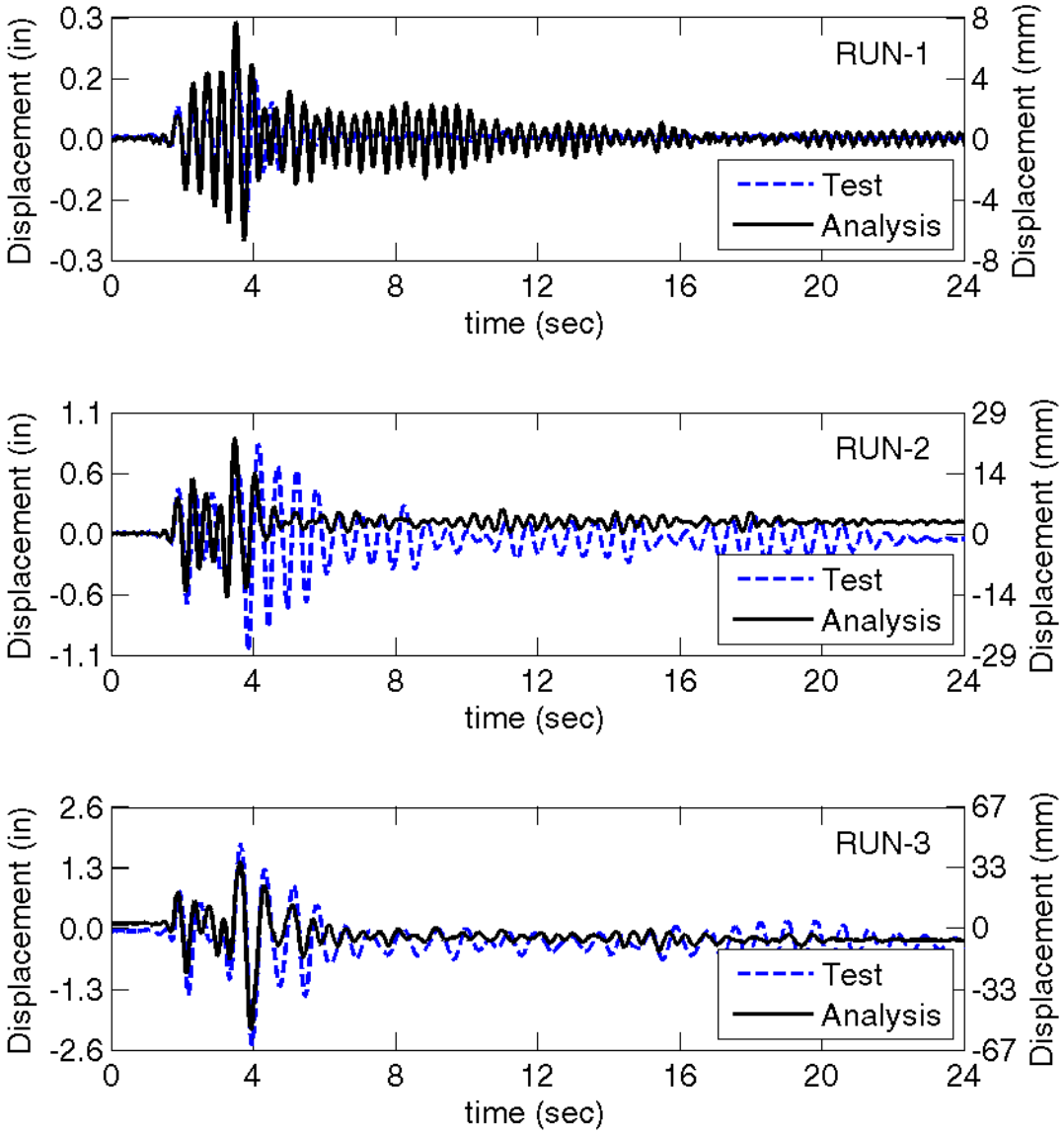

Fig. 4-82. Displacement history of BRSA with lumped plasticity model of rebar-pin, Run-1 to 3

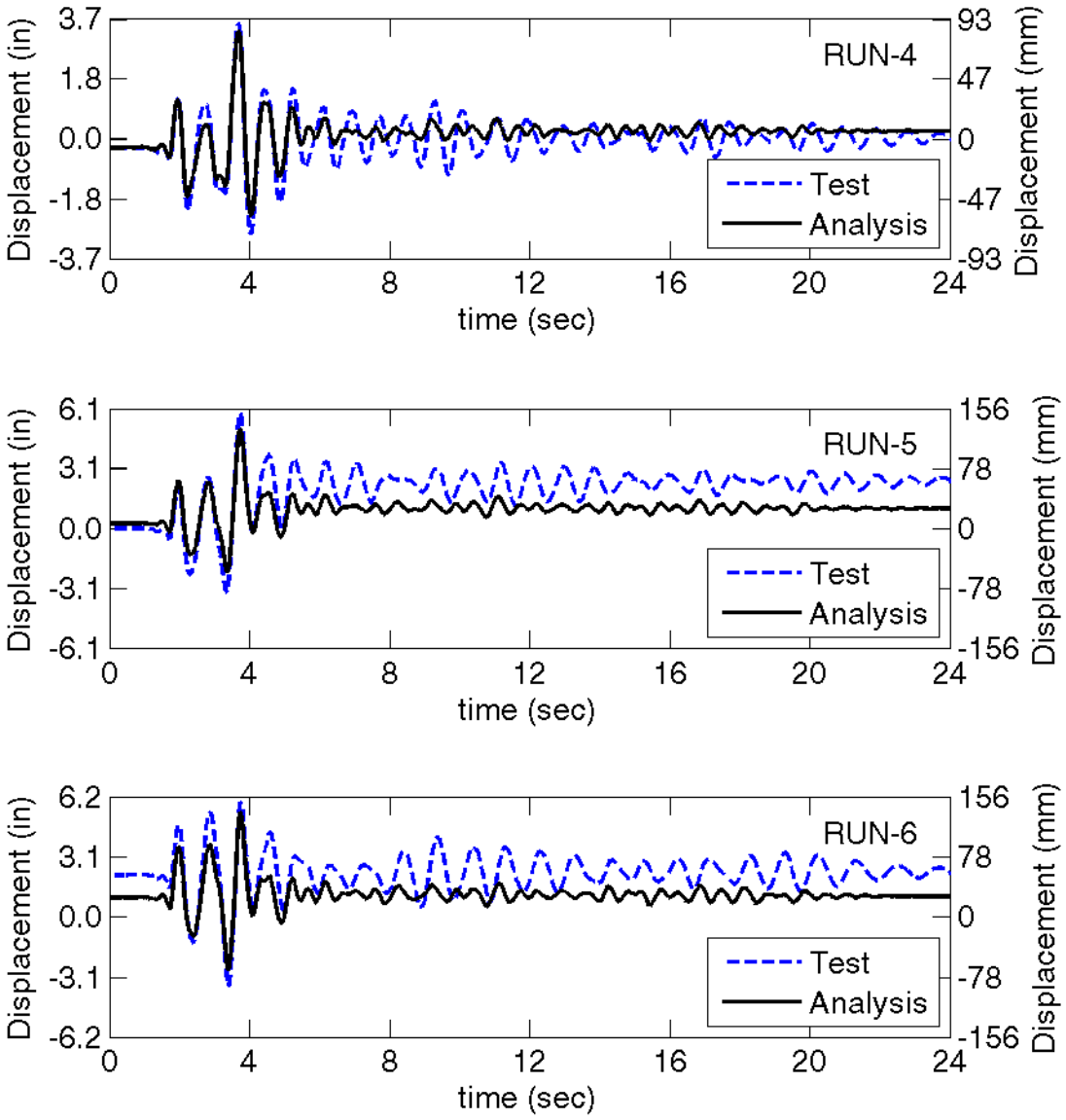

Fig. 4-83. Displacement history of BRSA with lumped plasticity model of rebar-pin, Run-4 to 6

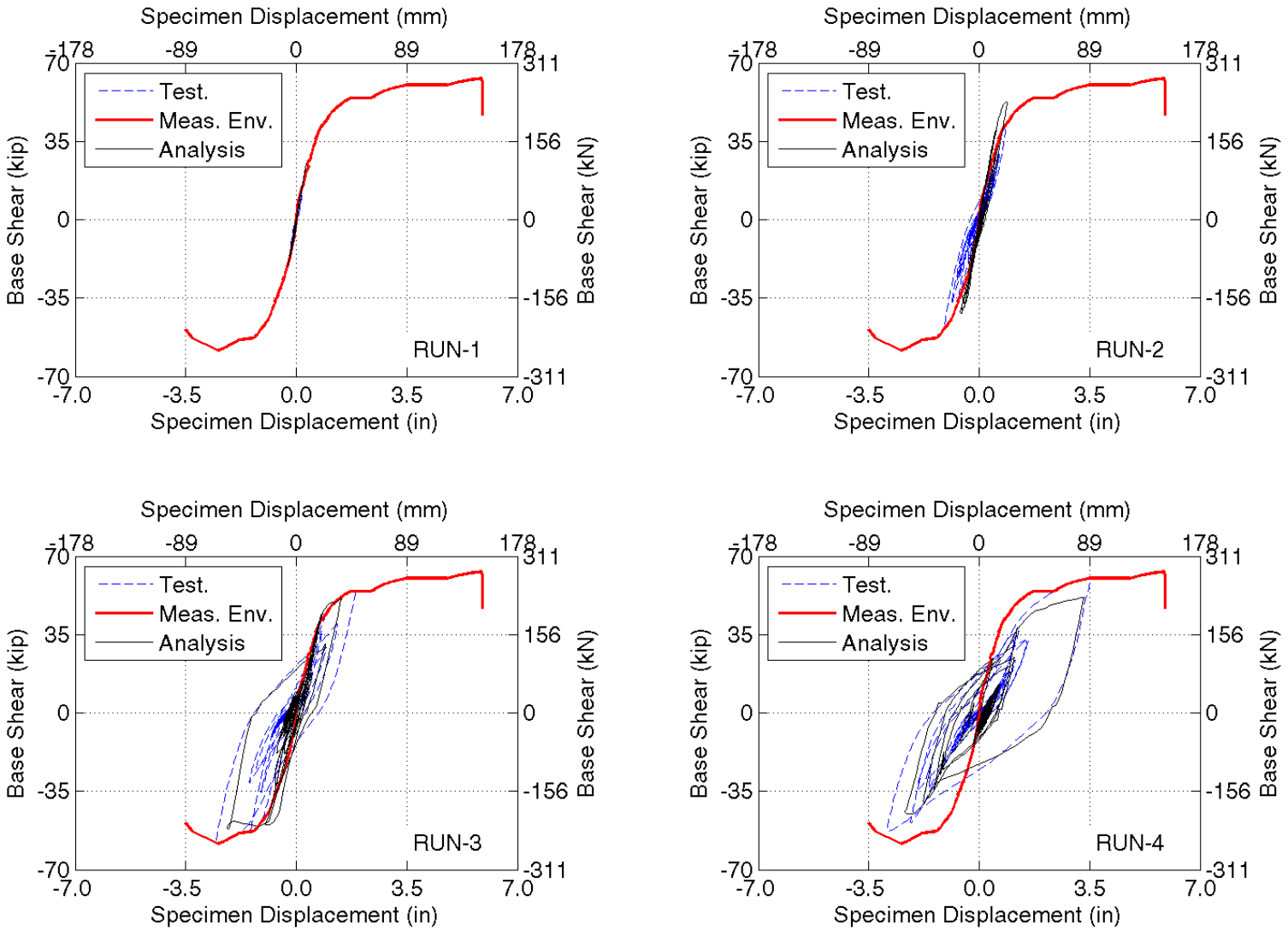

Fig. 4-84. Force-displacement curves of BRSA with lumped plasticity model of rebar-pins Run-1 to 4

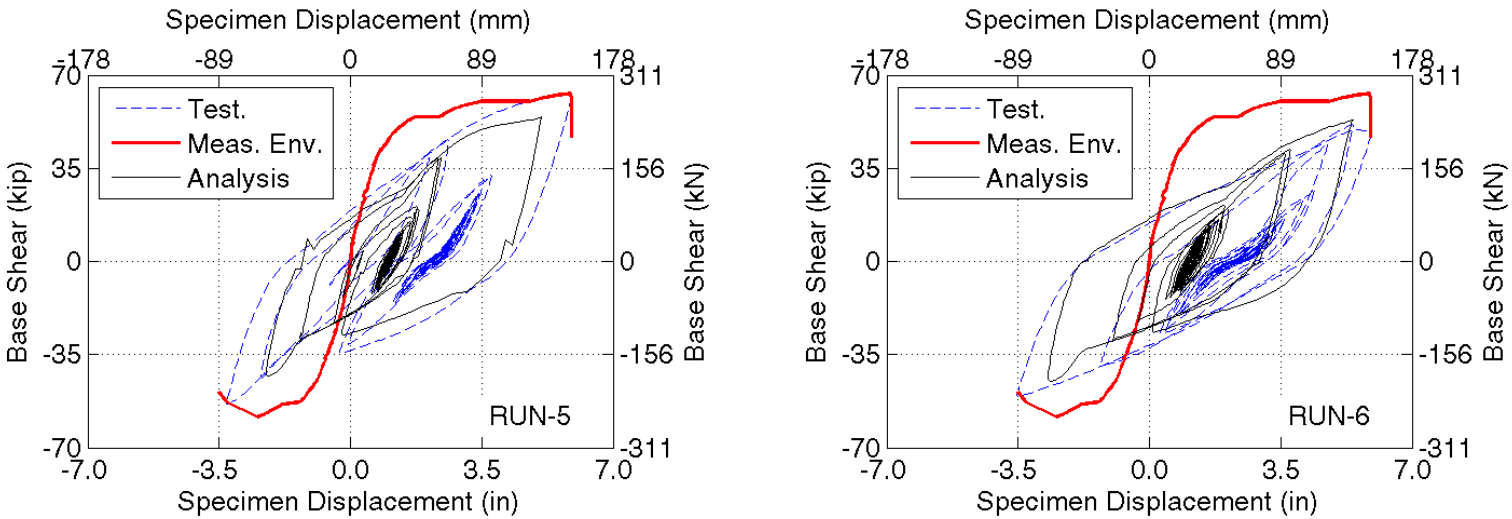

Fig. 4-85. Force-displacement curves of BRSA with lumped plasticity model of rebar-pins, Run-5 and 6

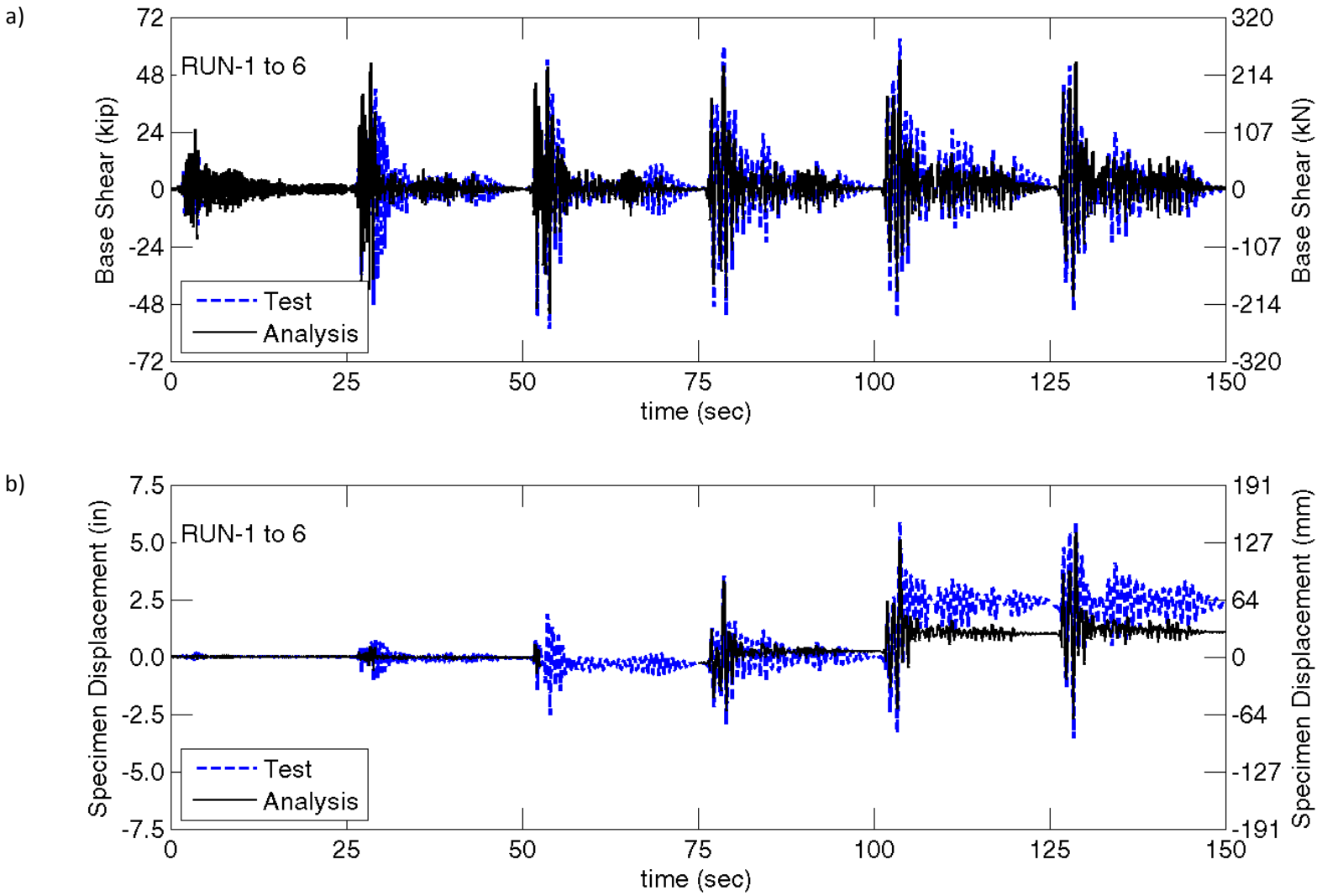

Fig. 4-86. Response history of entire test of BRSA with lumped plasticity a) base shear b) displacement

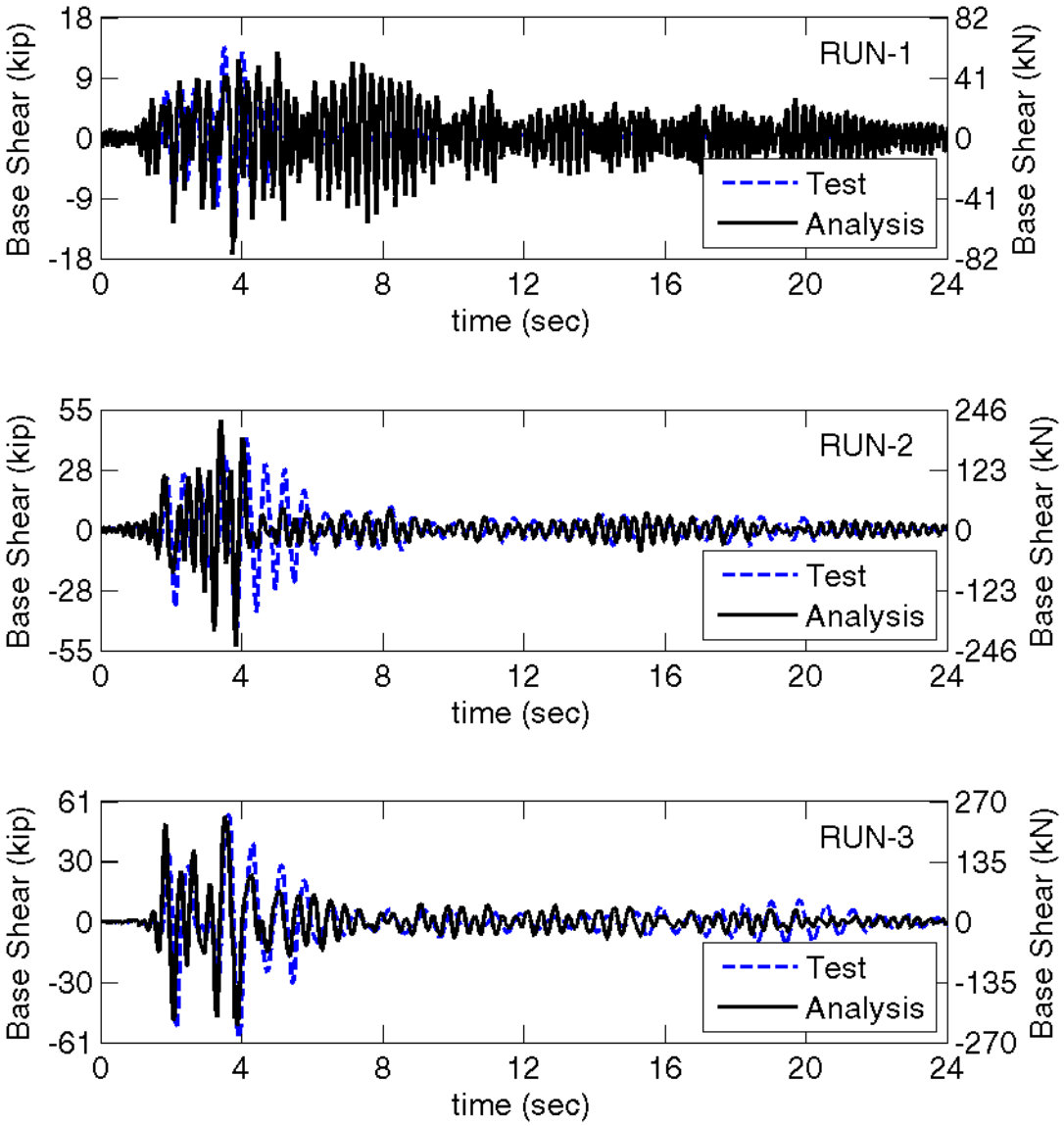

Fig. 4-87. Base shear history of BRSA with DB element for rebar-pin, Run-1 to 3

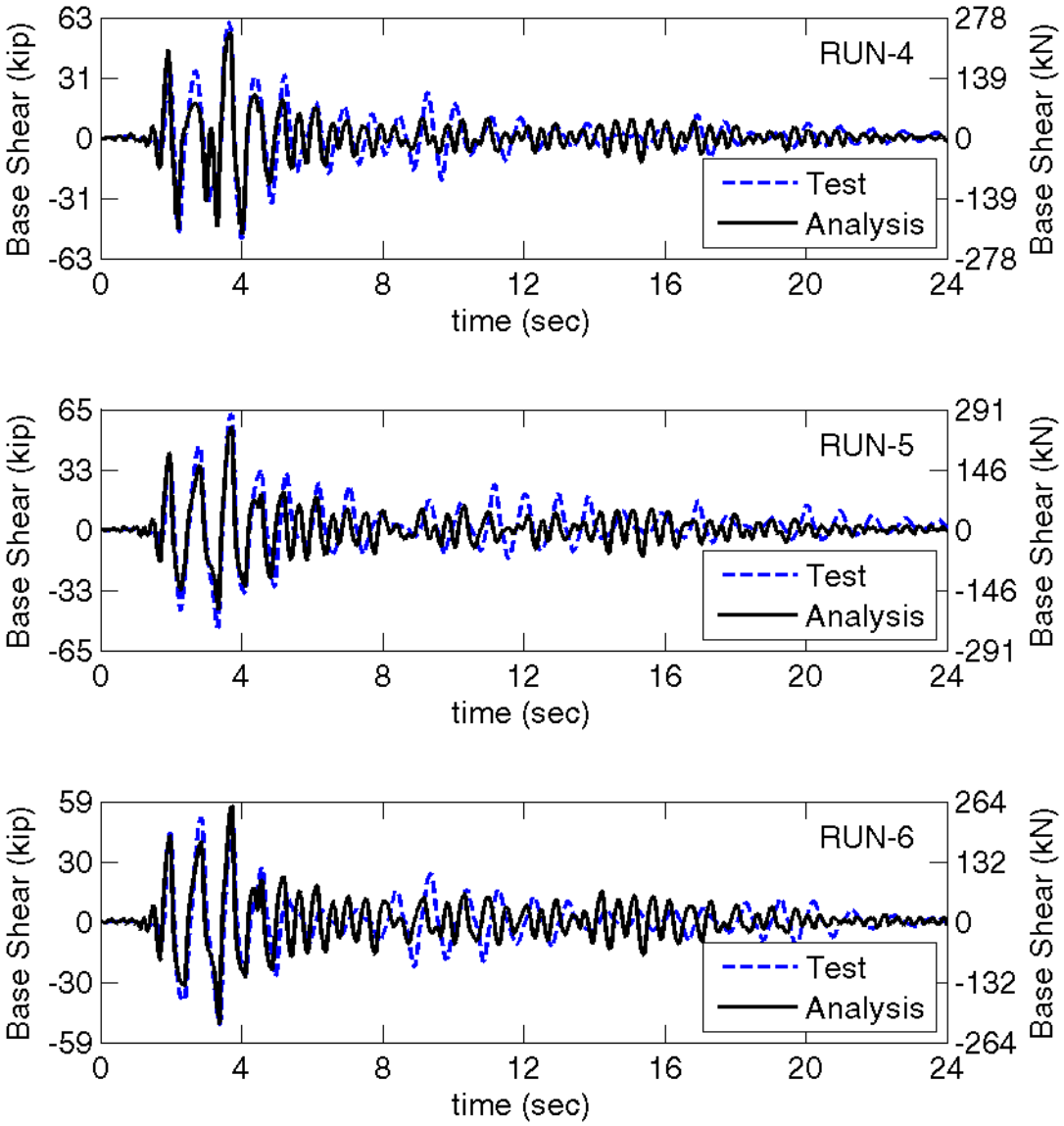

Fig. 4-88. Base shear history of BRSA with DB element for rebar-pin, Run-4 to 6

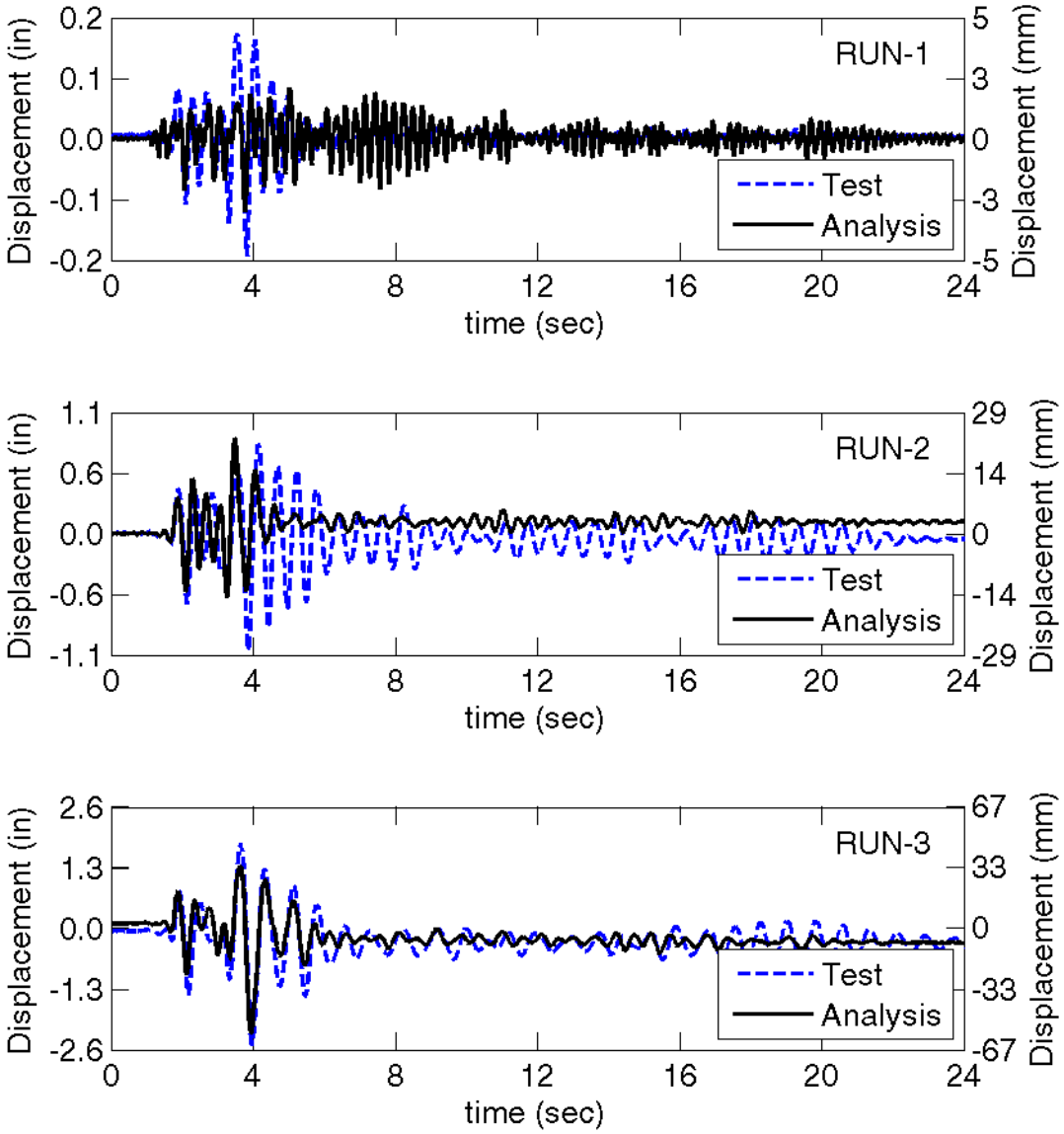

Fig. 4-89. Displacement history of BRSA with DB element for rebar-pin, Run-1 to 3

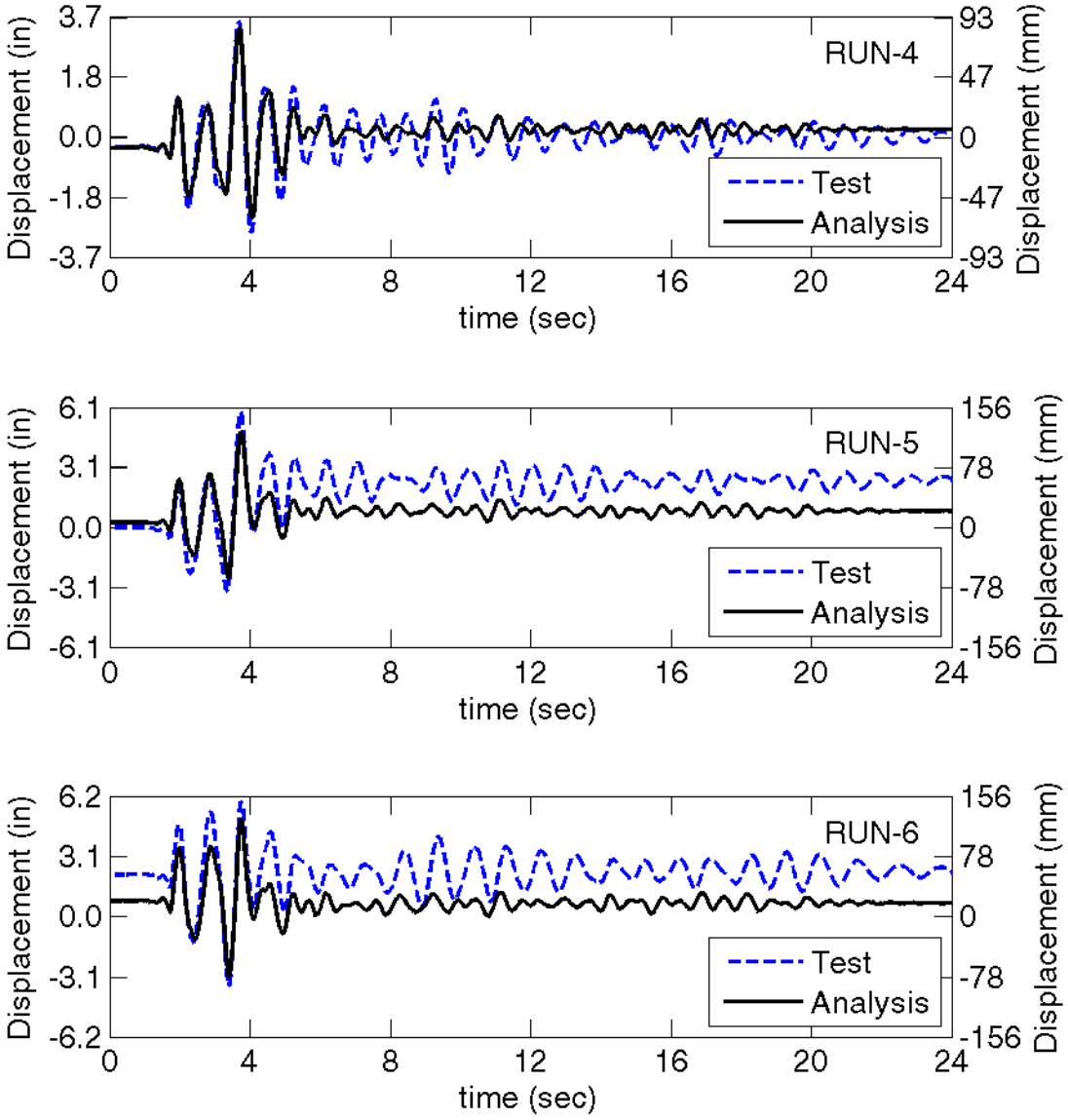

Fig. 4-90. Displacement history of BRSA with DB element for rebar-pin, Run-4 to 6

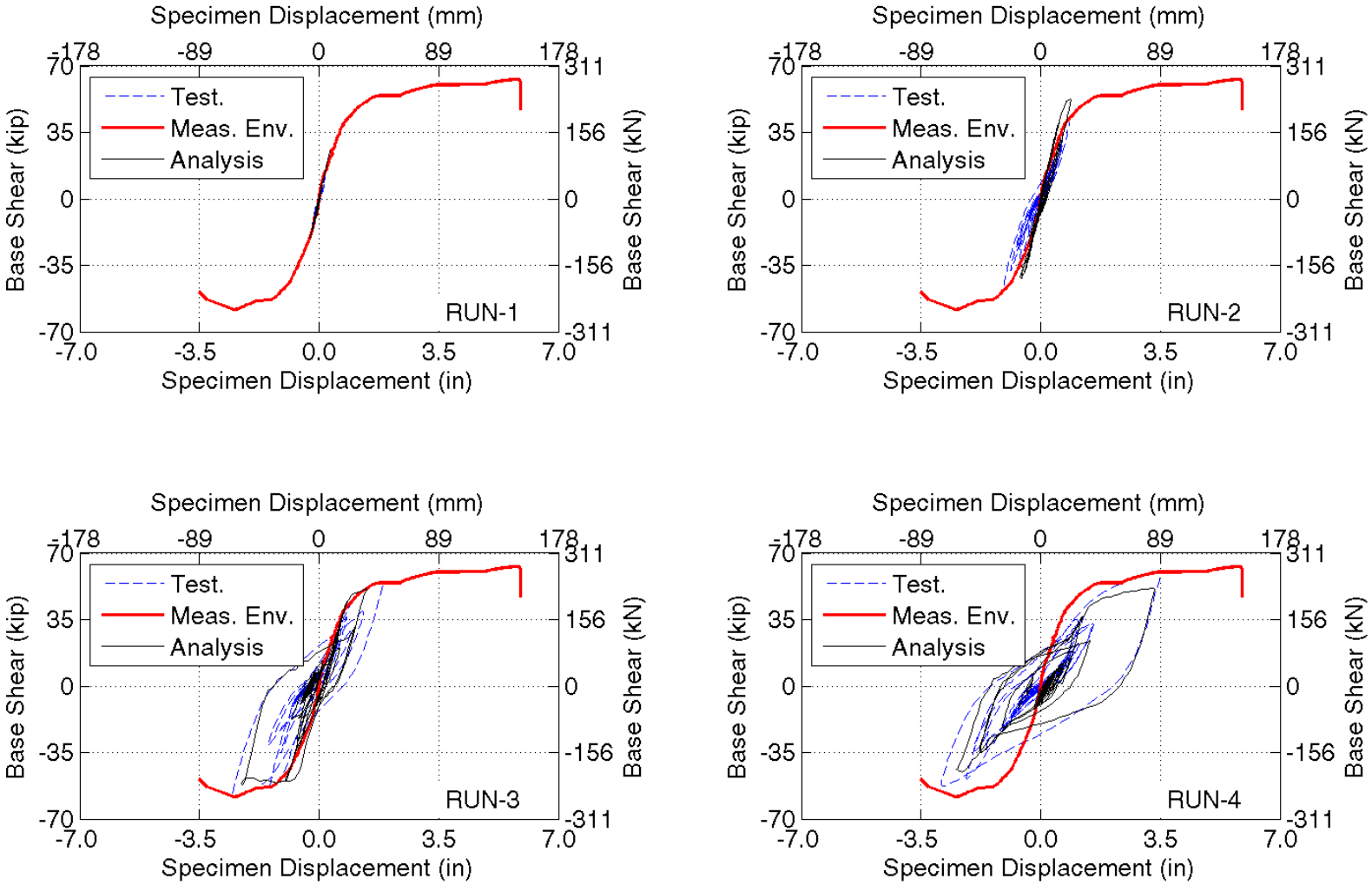

Fig. 4-91. Force-displacement curves of BRSA with DB element Run-1 to 4

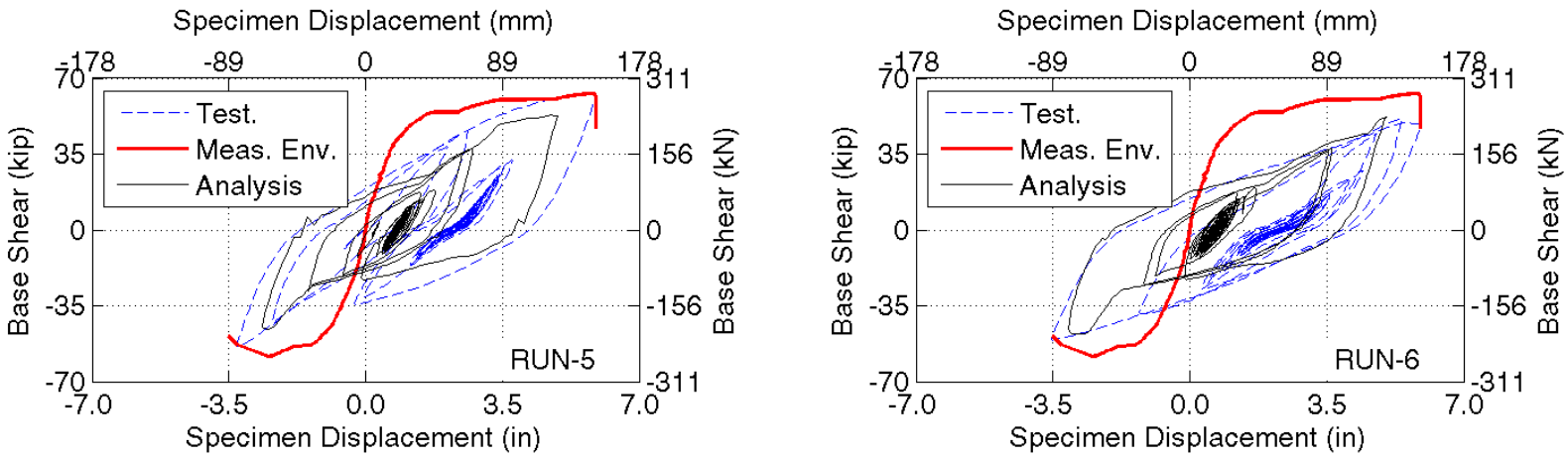

Fig. 4-92. Force-displacement curves of BRSA with DB element Run-5 and 6

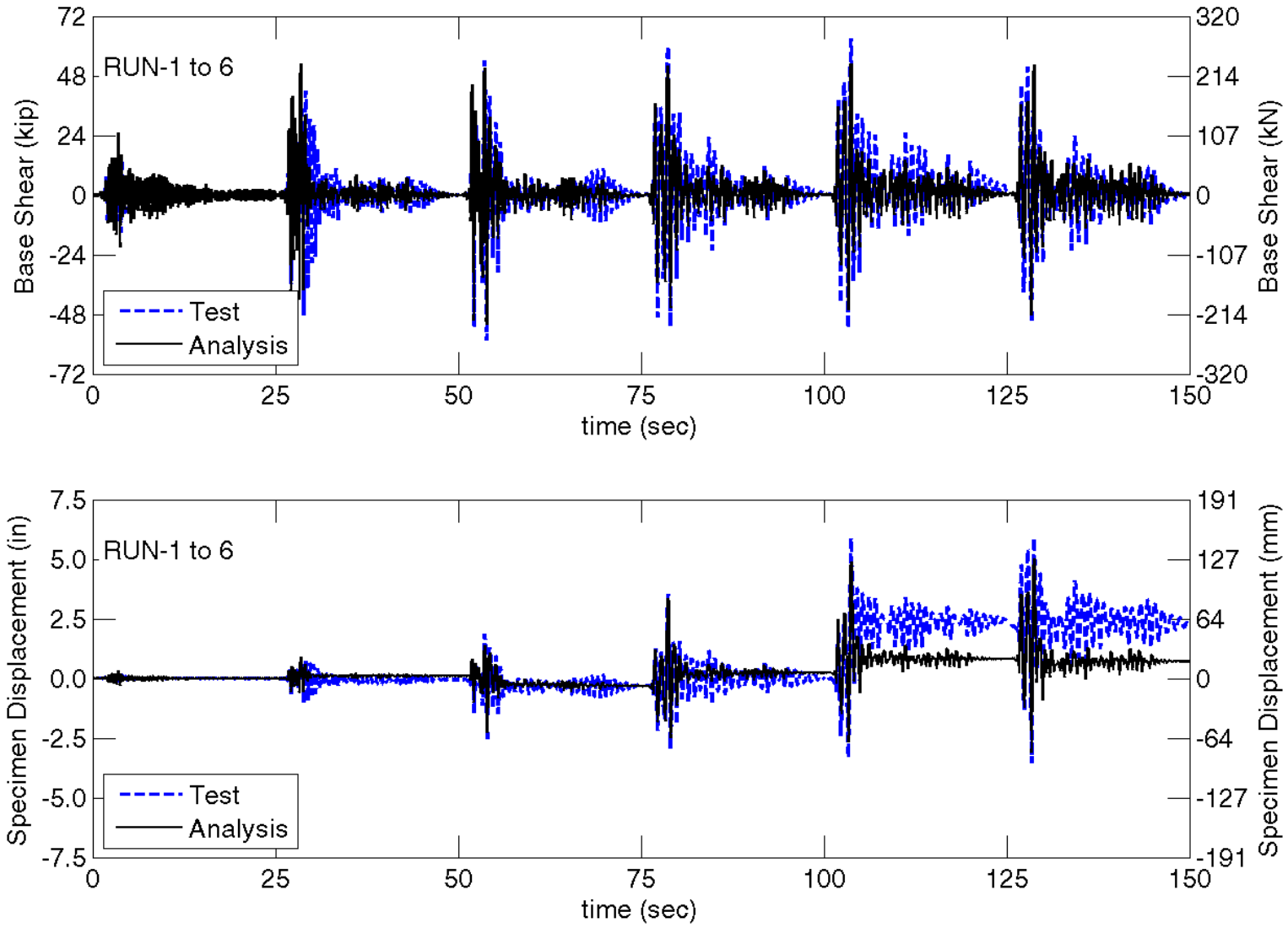

Fig. 4-93. Response history of entire test of BRSA with lumped plasticity a) base shear b) displacement

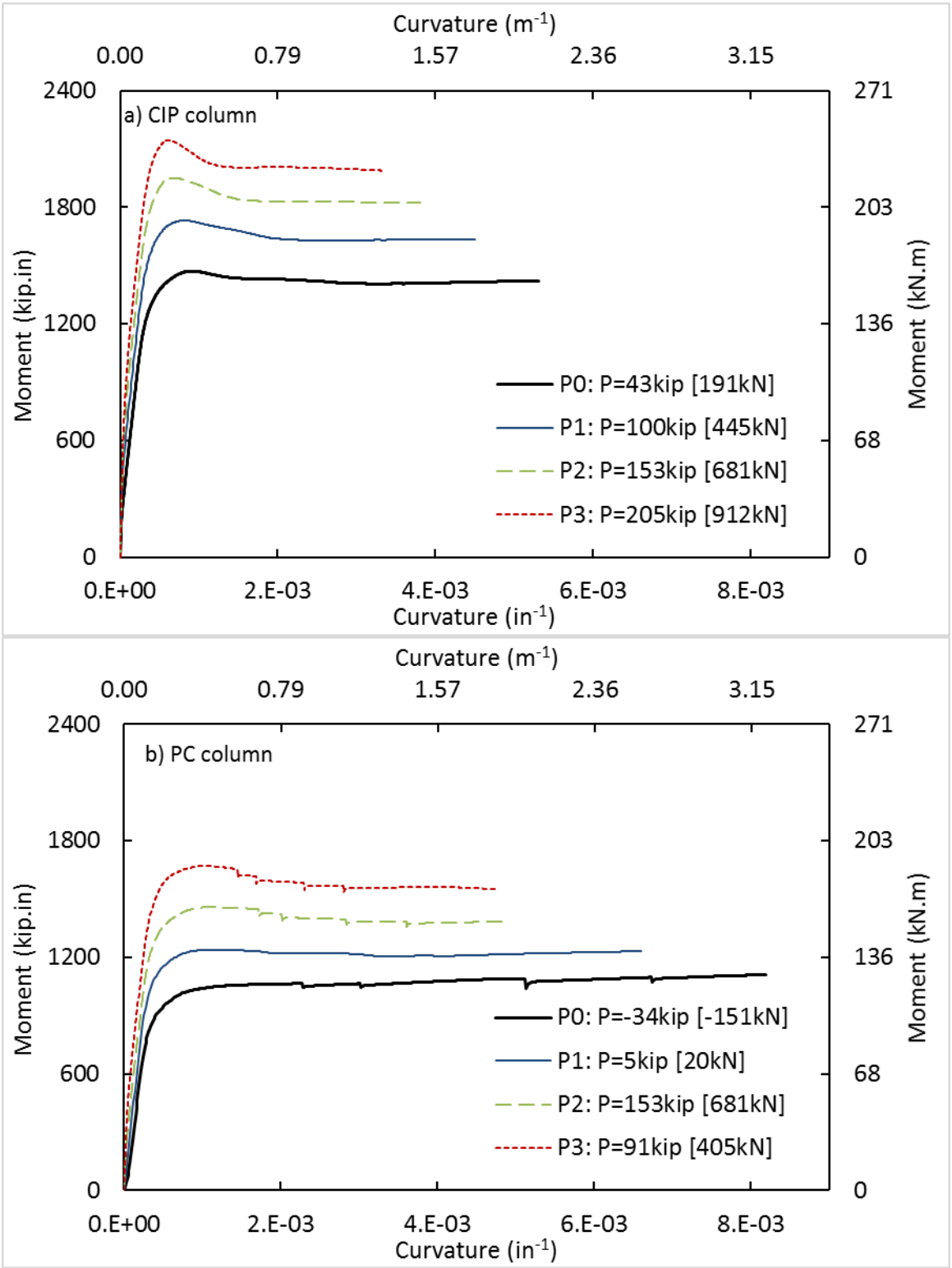

Fig. 5-1. Effect of ALI on moment-curvature curves of plastic hinge sections in BPSA

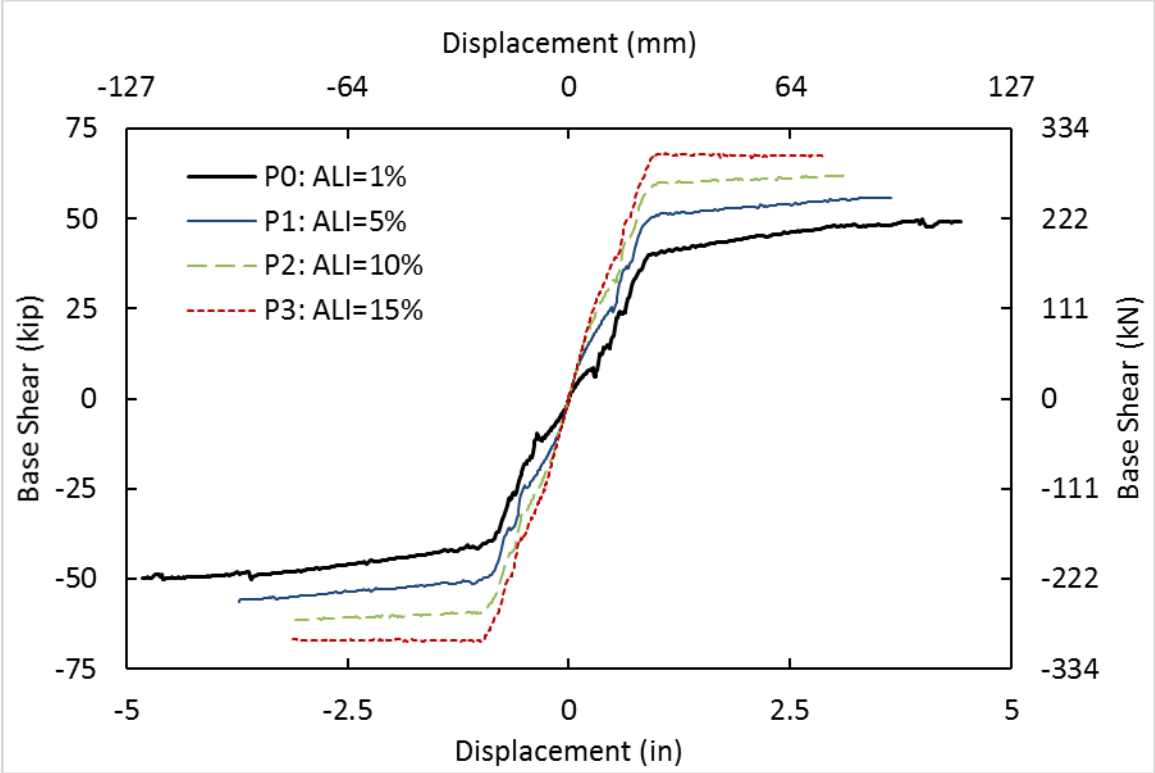

Fig. 5-2. Effect of ALI on pushover curves of the BPSA

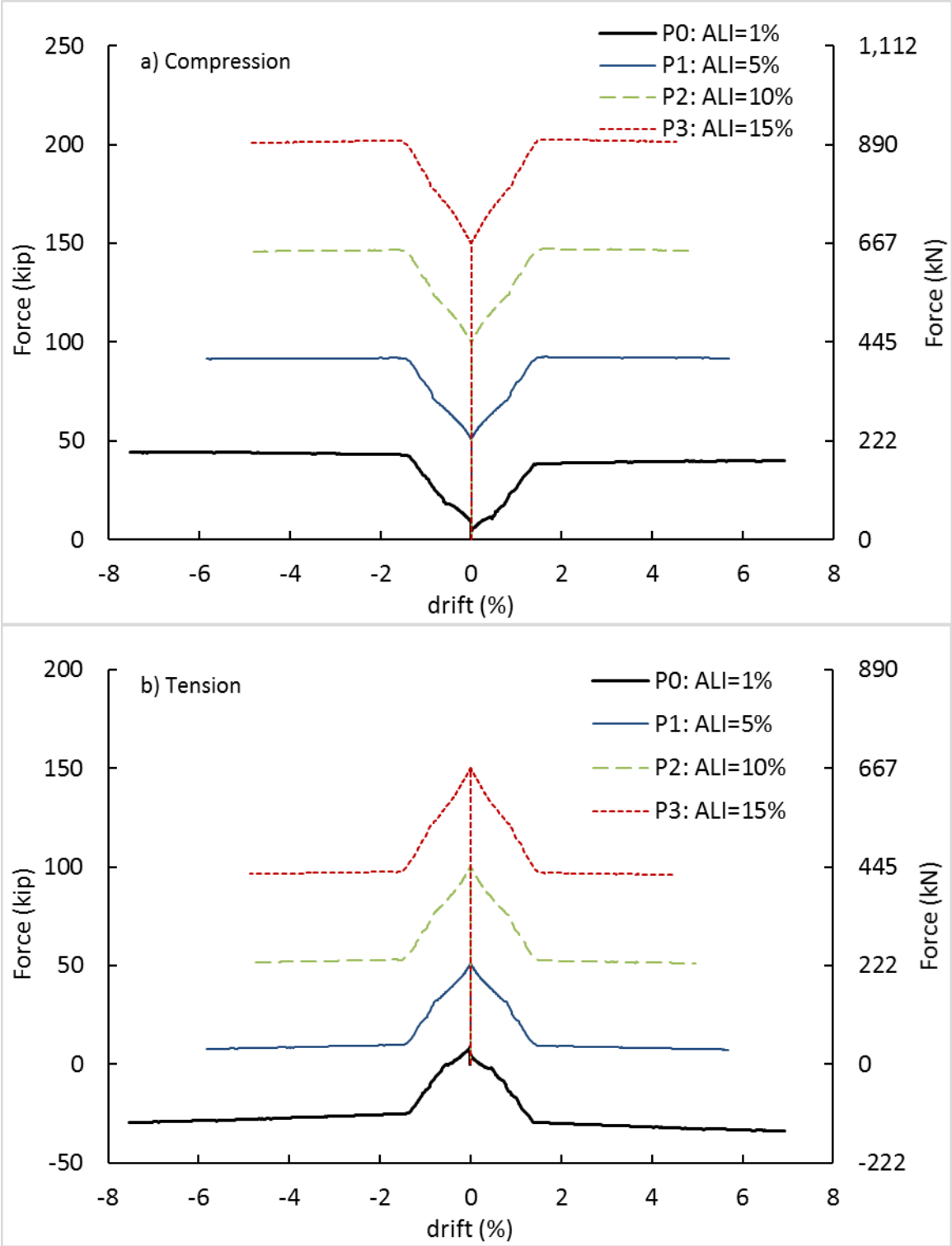

Fig. 5-3. Effect of ALI on column axial force a) compression side due to OM b) tension side due to OM

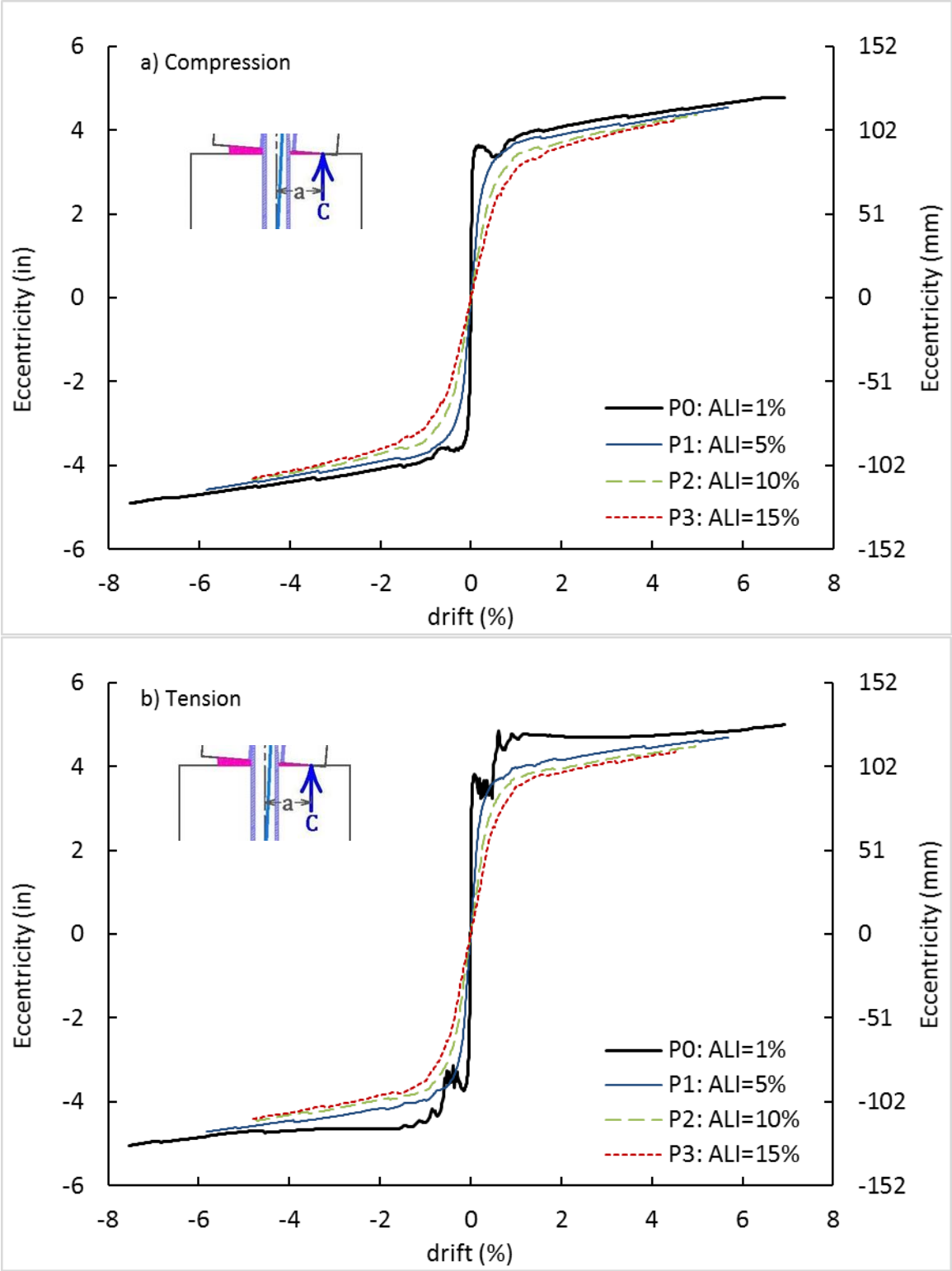

Fig. 5-4. Effect of ALI on eccentricity of column-pad contact in a) compression side due to OM b) tension side due to OM

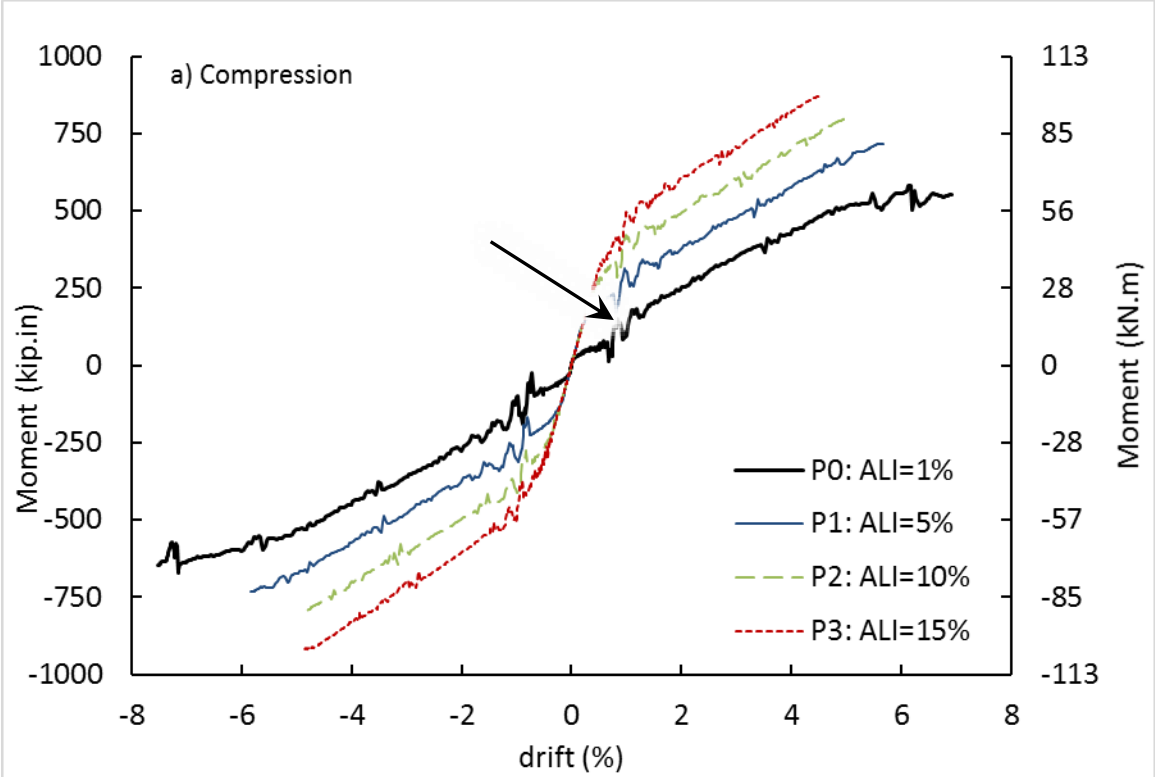

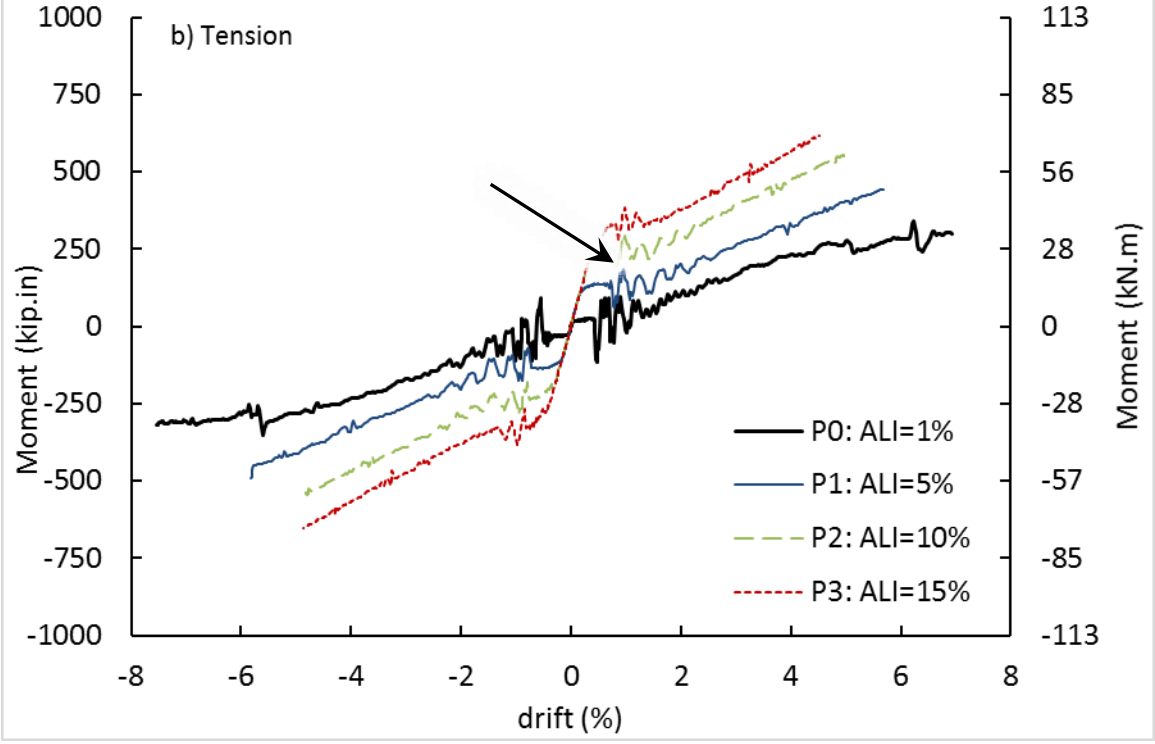

Fig. 5-5. Effect of ALI on pipe-pin moment in a) compression side due to OM b) tension side due to OM

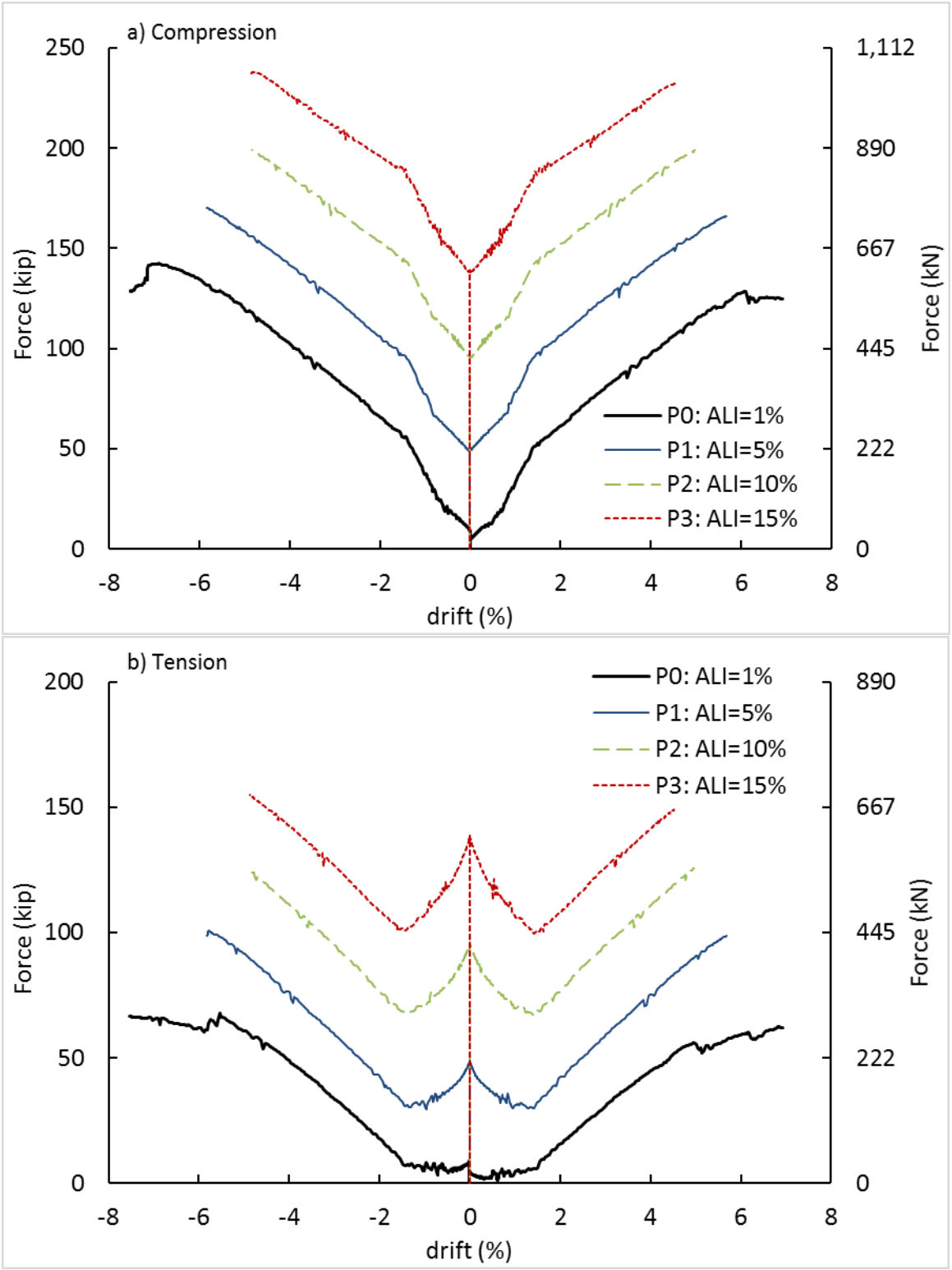

Fig. 5-6. Effect of ALI on normal force in column-pad interface a) compression side due to OM b) tension side due to OM

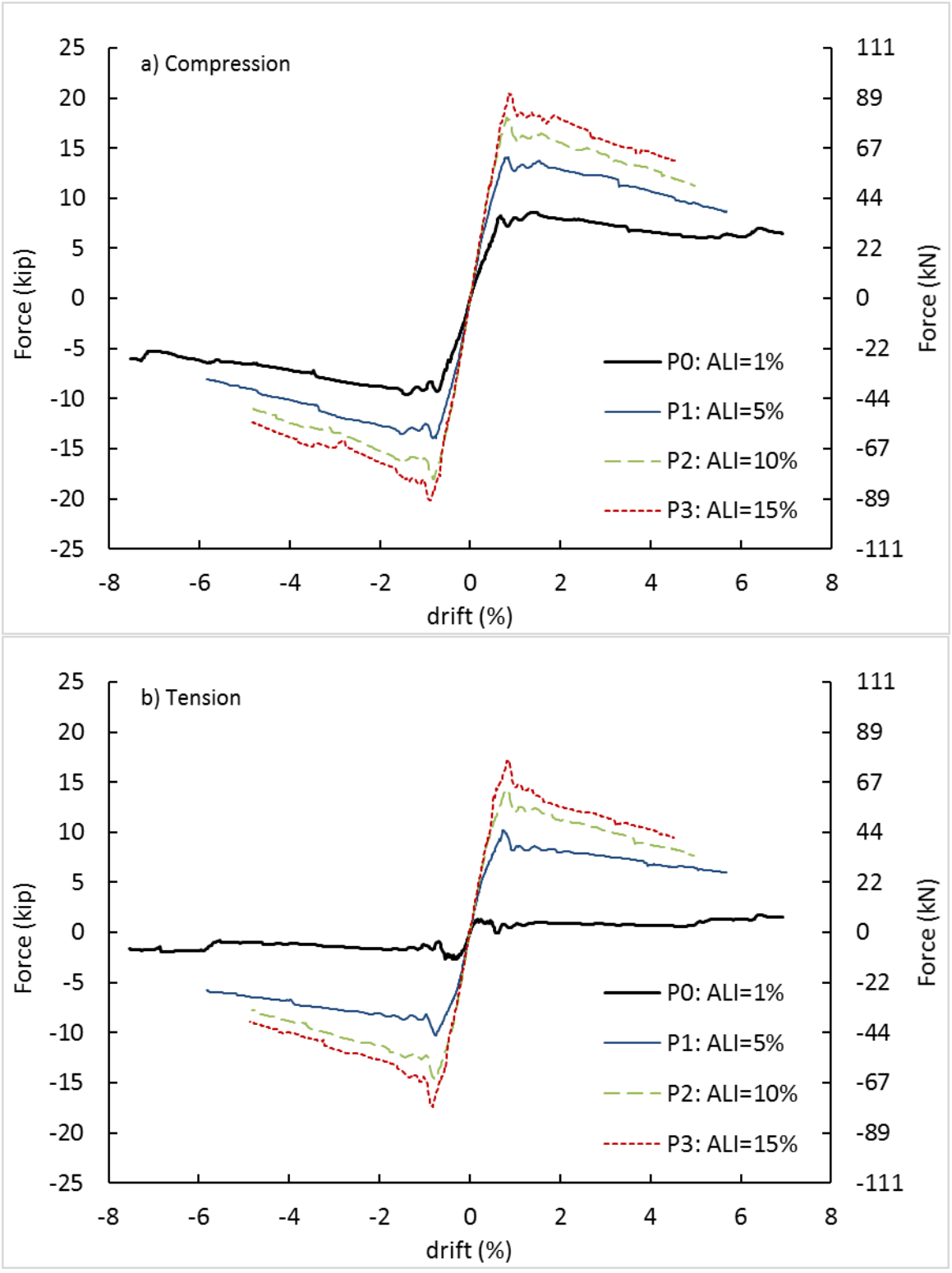

Fig. 5-7. Effect of ALI on friction in column-pad interface in a) compression side due to OM b) tension side due to OM

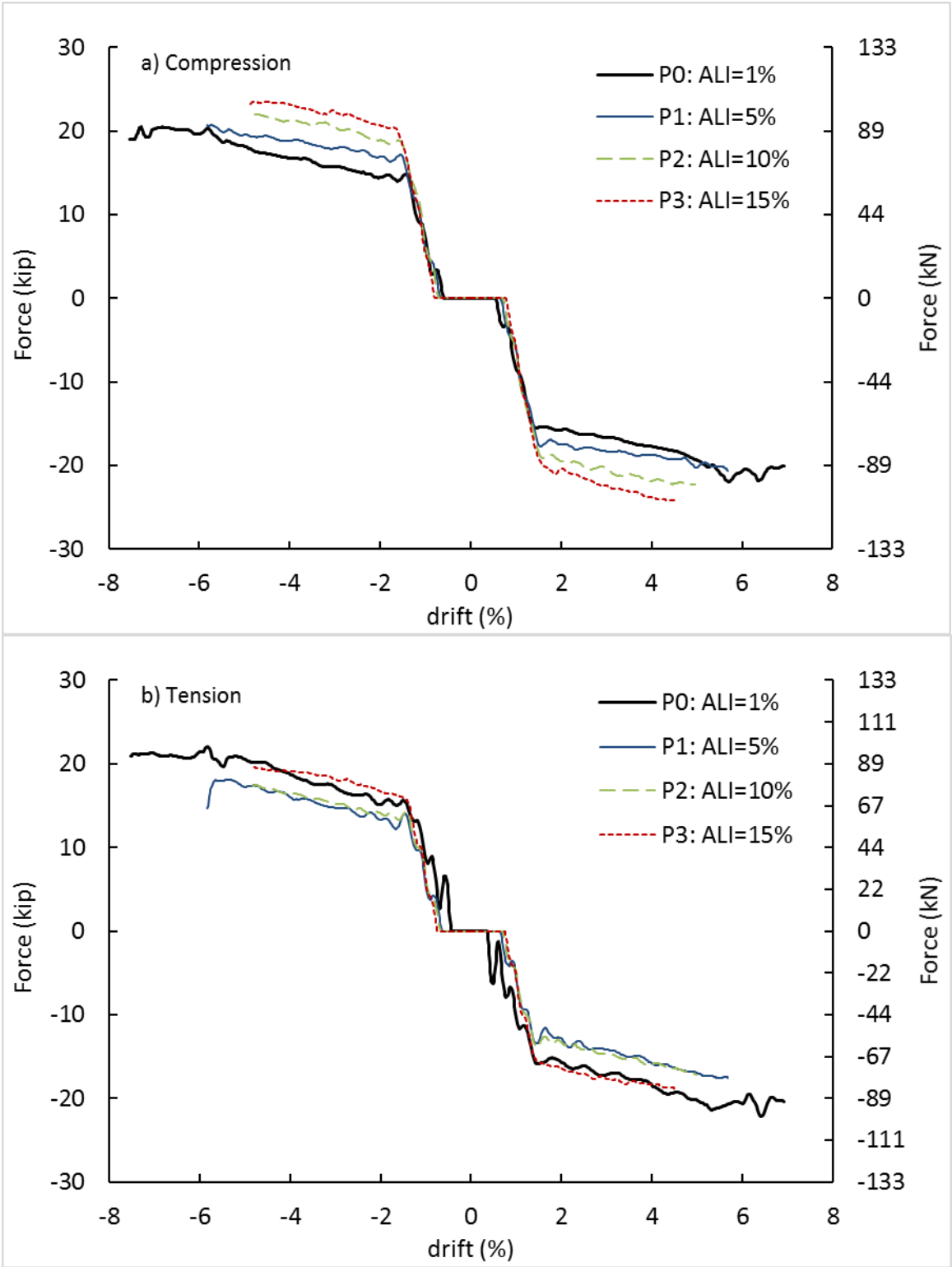

Fig. 5-8. Effect of ALI on contact force between the pipes in a) compression side due to OM b) tension side due to OM

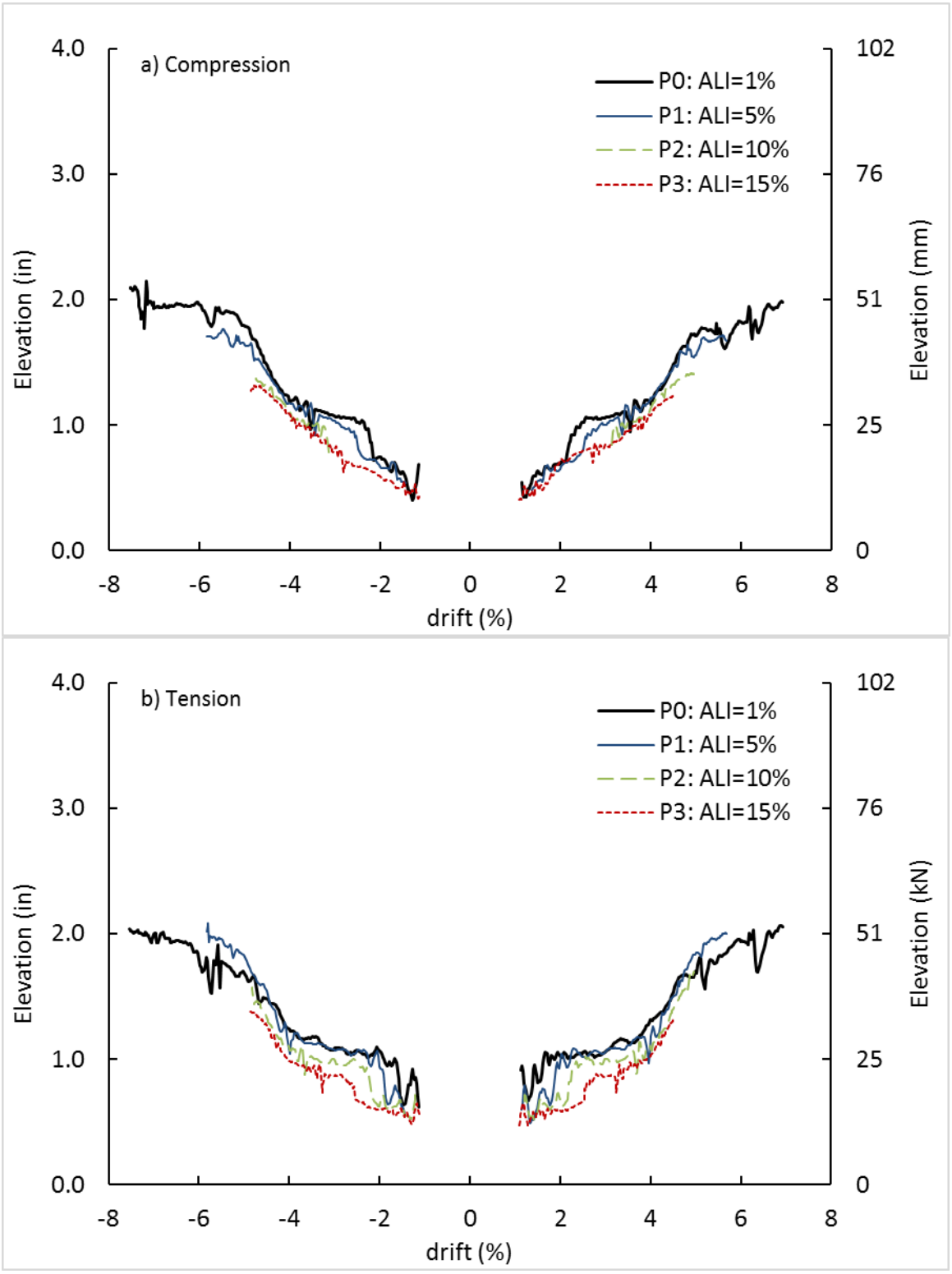

Fig. 5-9. Effect of ALI on point of contact between pipes a) compression side due to OM b) tension side due to OM

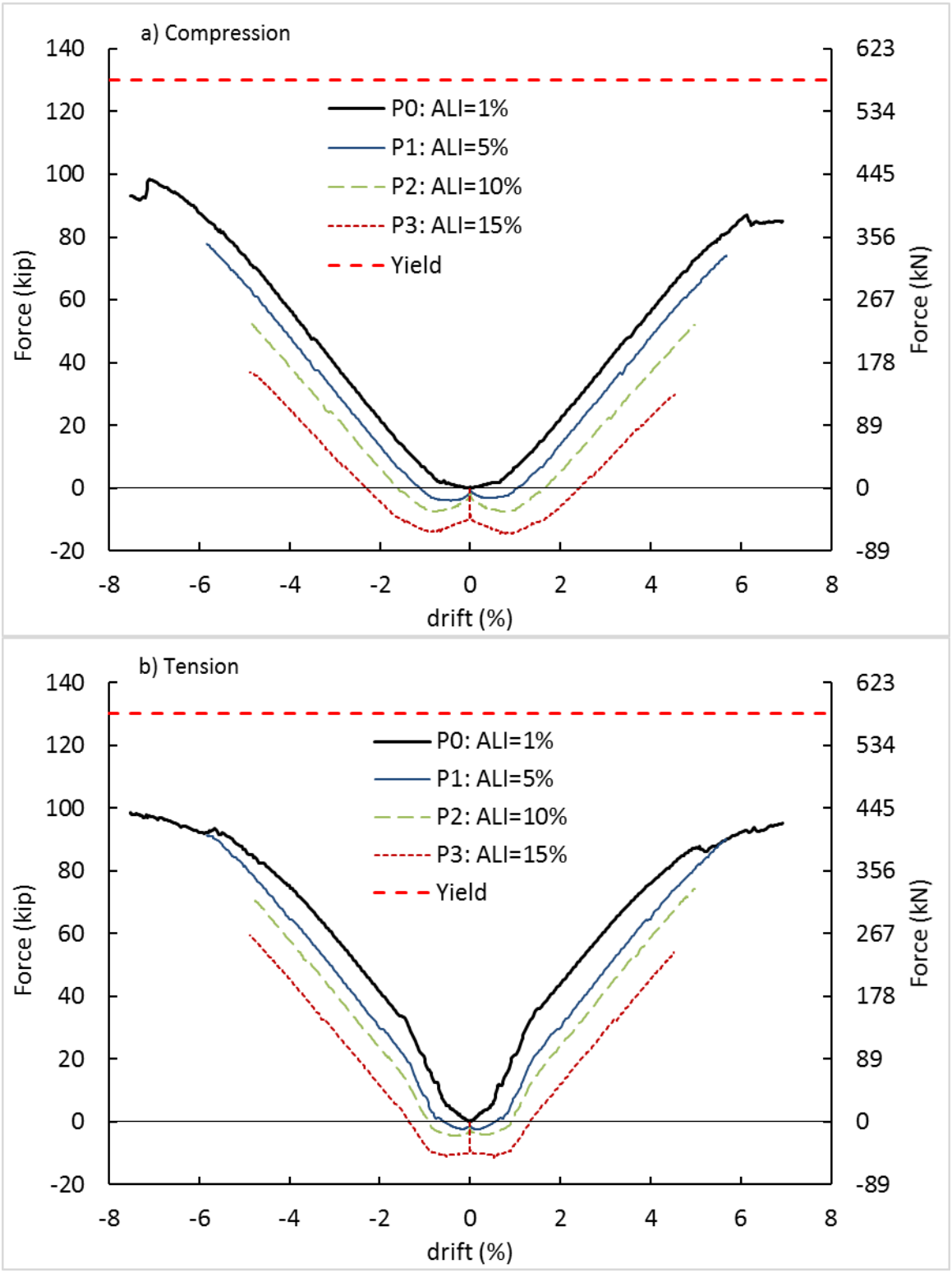

Fig. 5-10. Effect of ALI on the tensile force of the rod a) compression side due to OM b) tension side due to OM

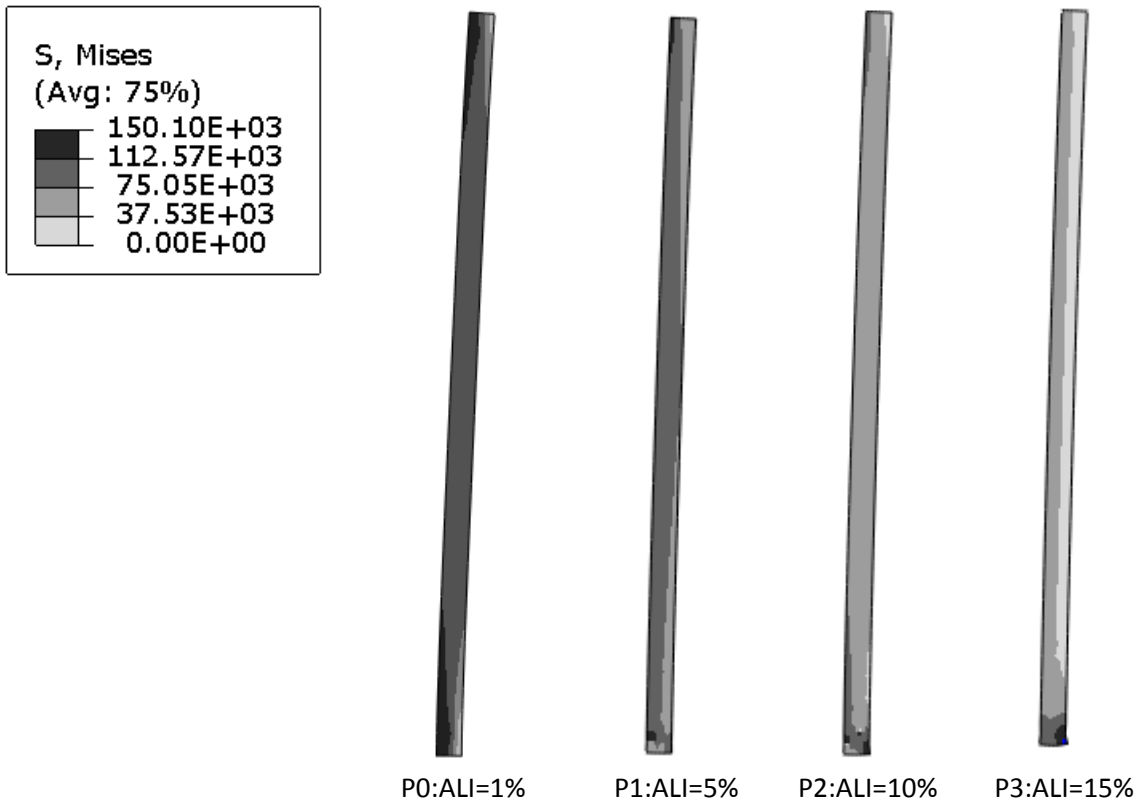

Fig. 5-11. Effect of ALI on the Von Mises stress in the rod in left column

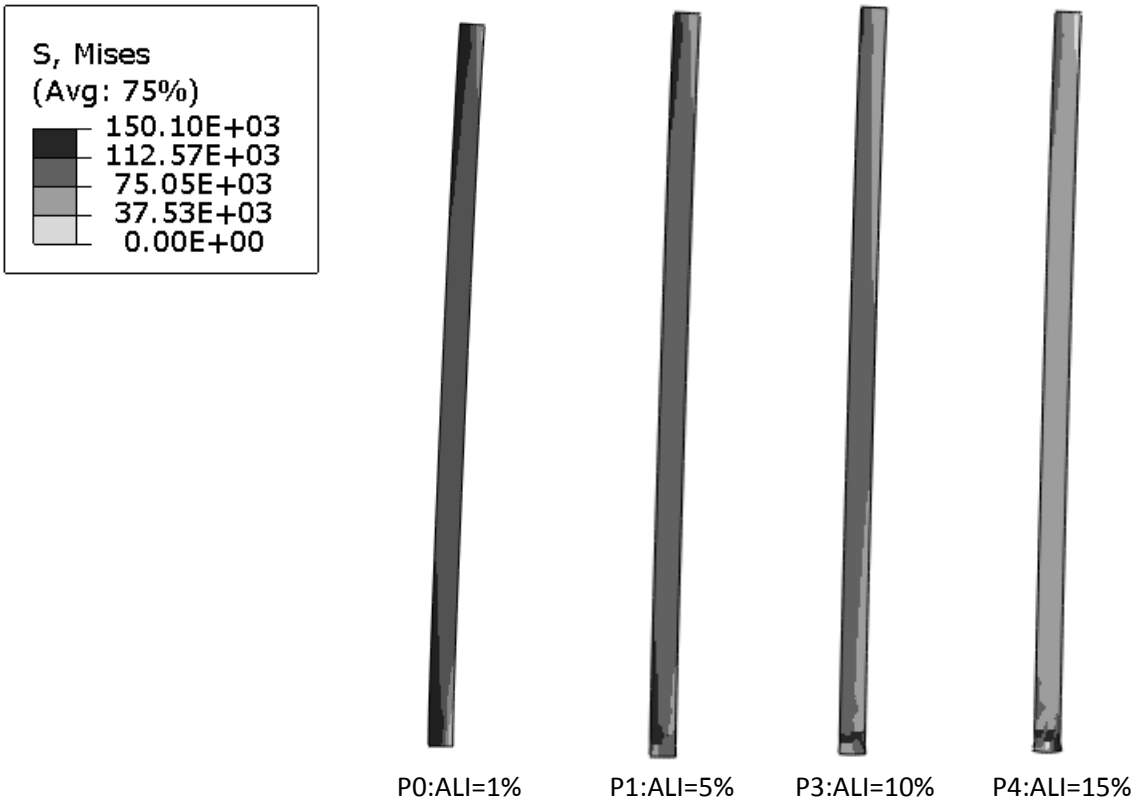

Fig. 5-12. Effect of ALI on the Von Mises stress in the rod in right column

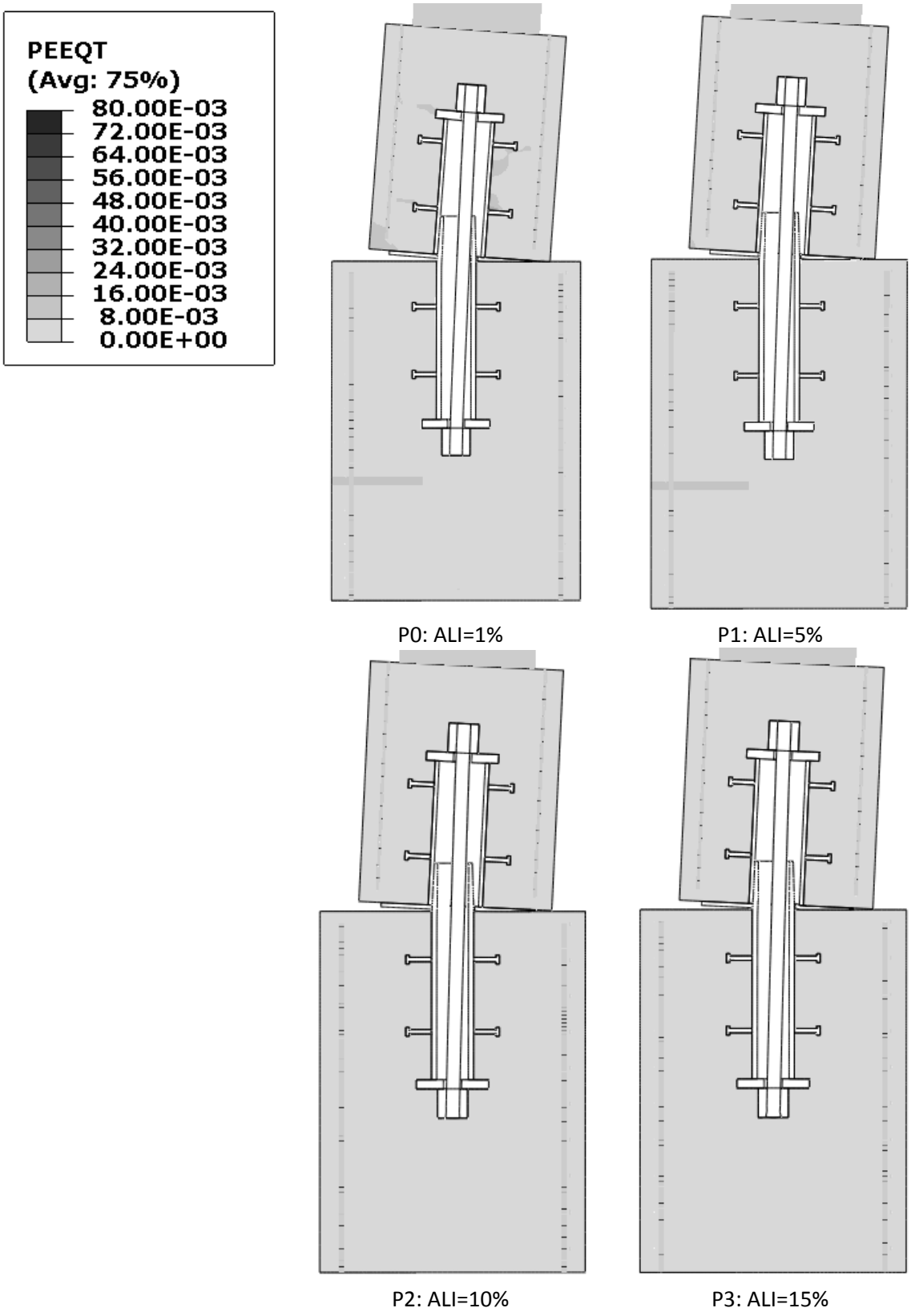

Fig. 5-13. Effect of ALI on cracking pattern in left column in BPSA

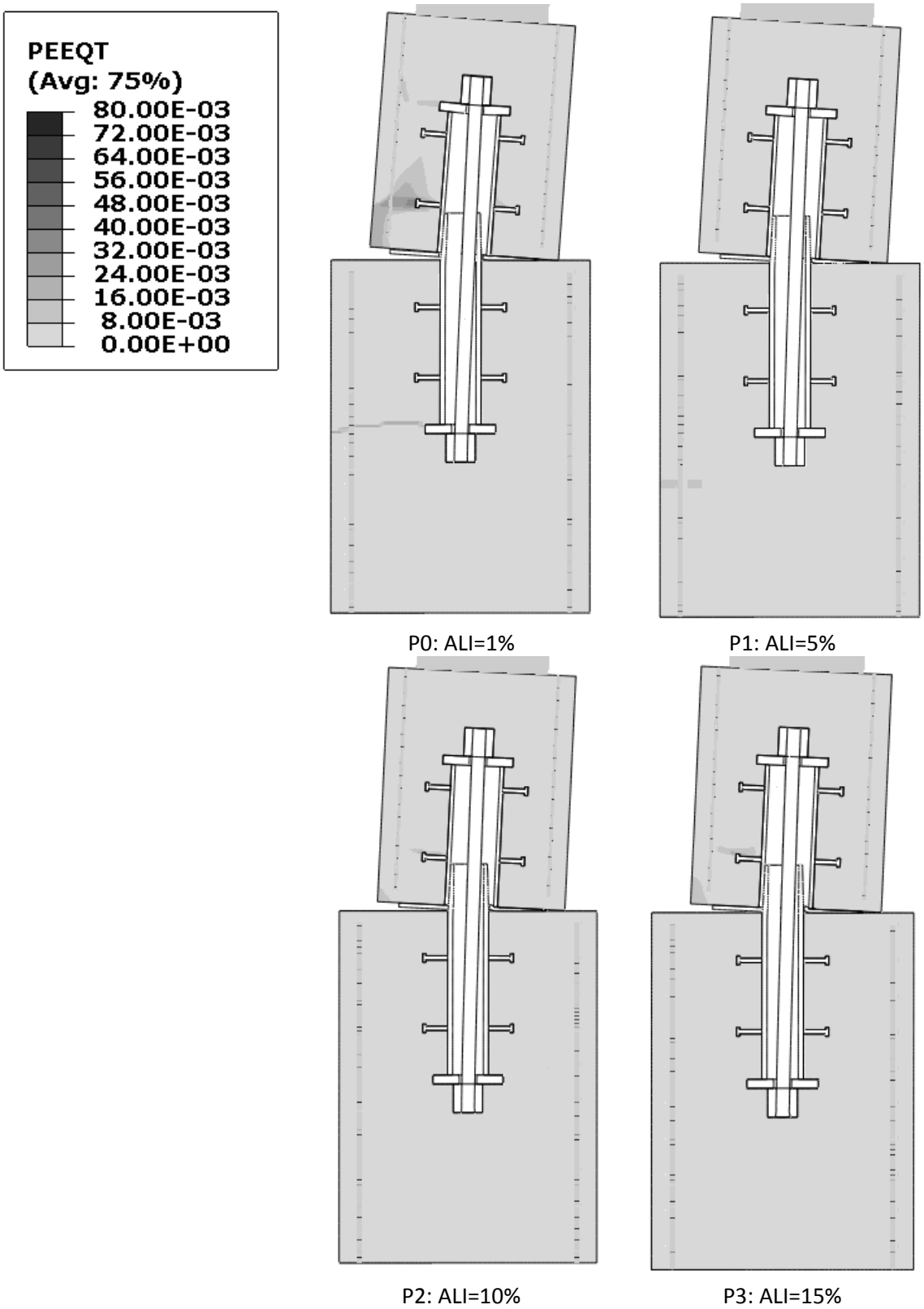

Fig. 5-14. Effect of ALI on cracking pattern in right column in BPSA

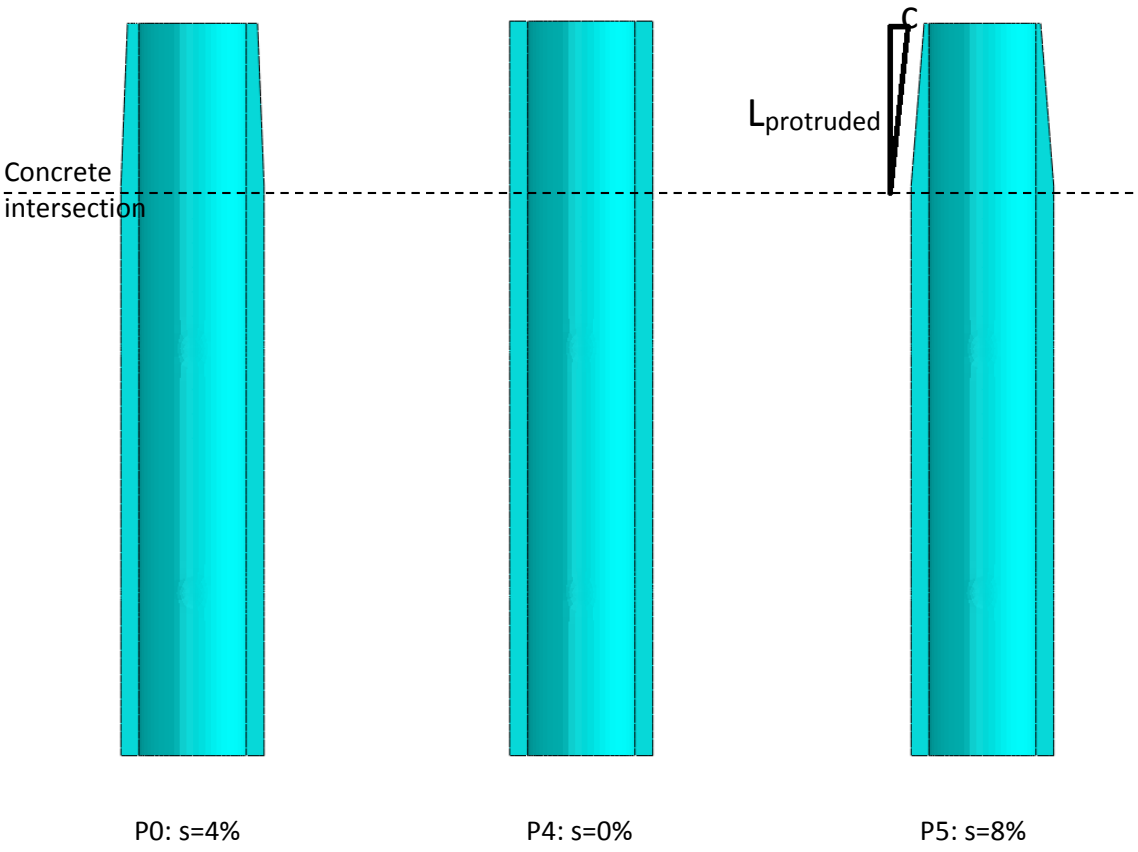

Fig. 5-15. Taper slope in the lower pipes

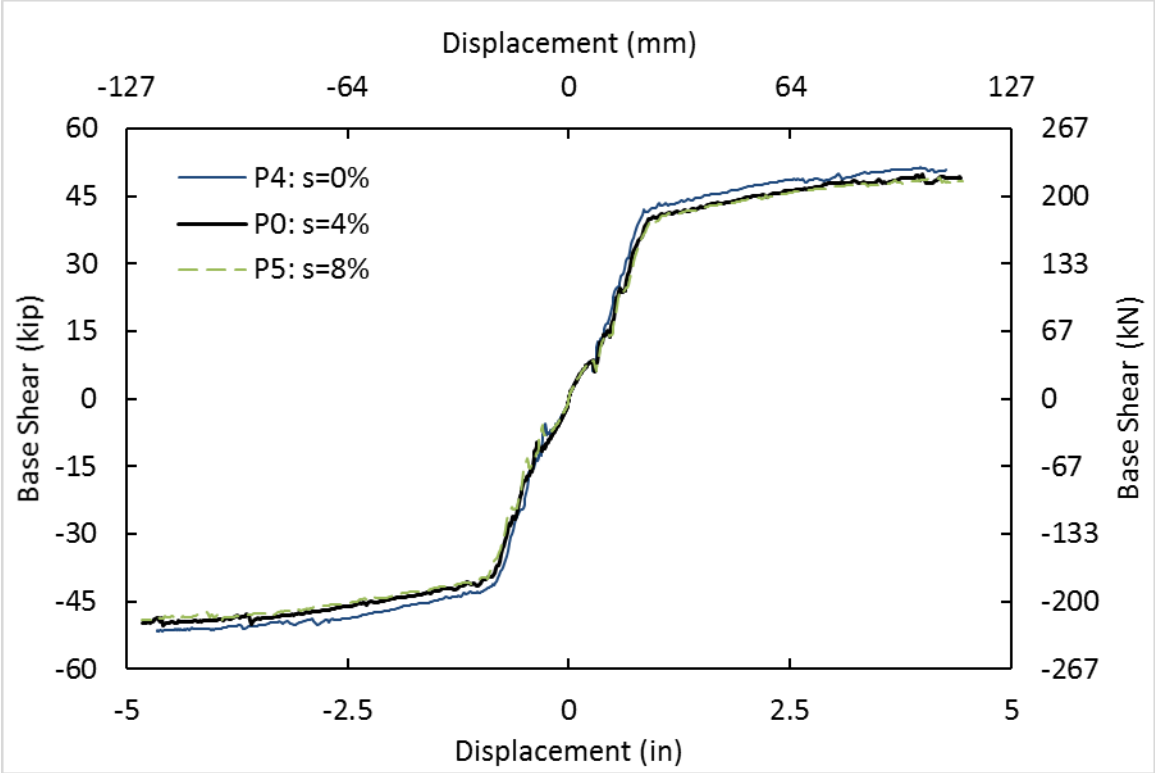

Fig. 5-16. Effect of taper slope on bent pushover curves

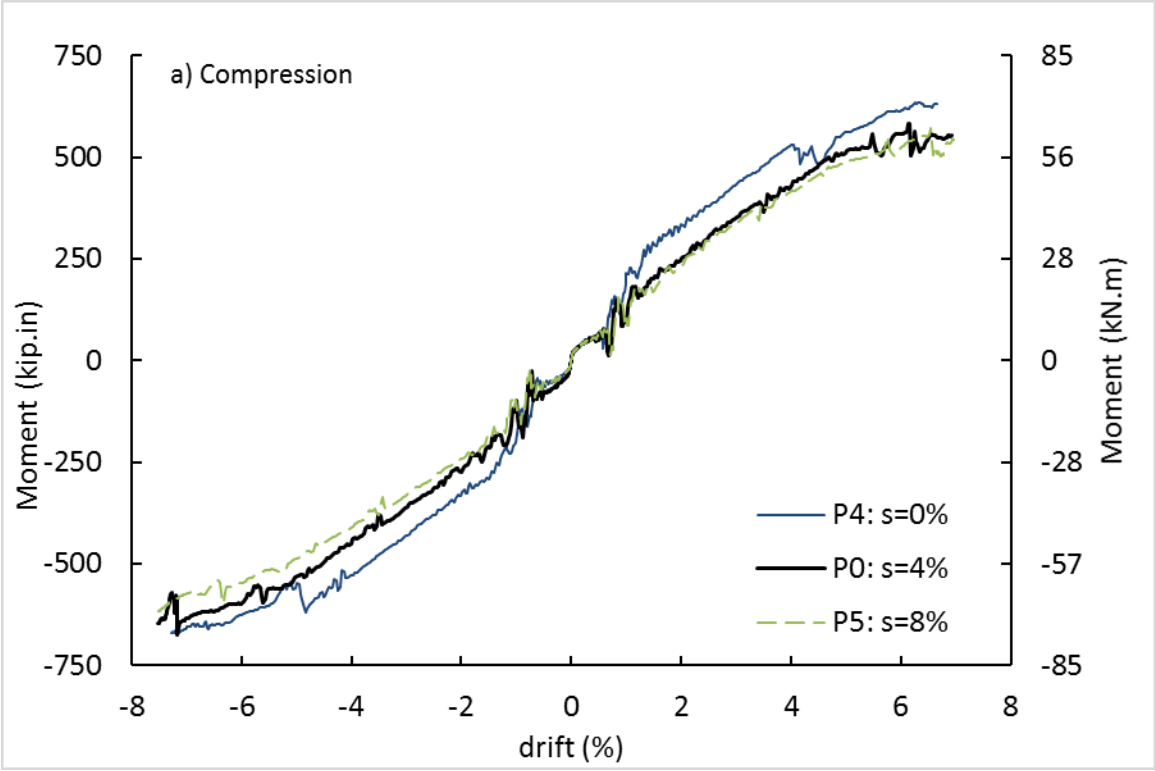

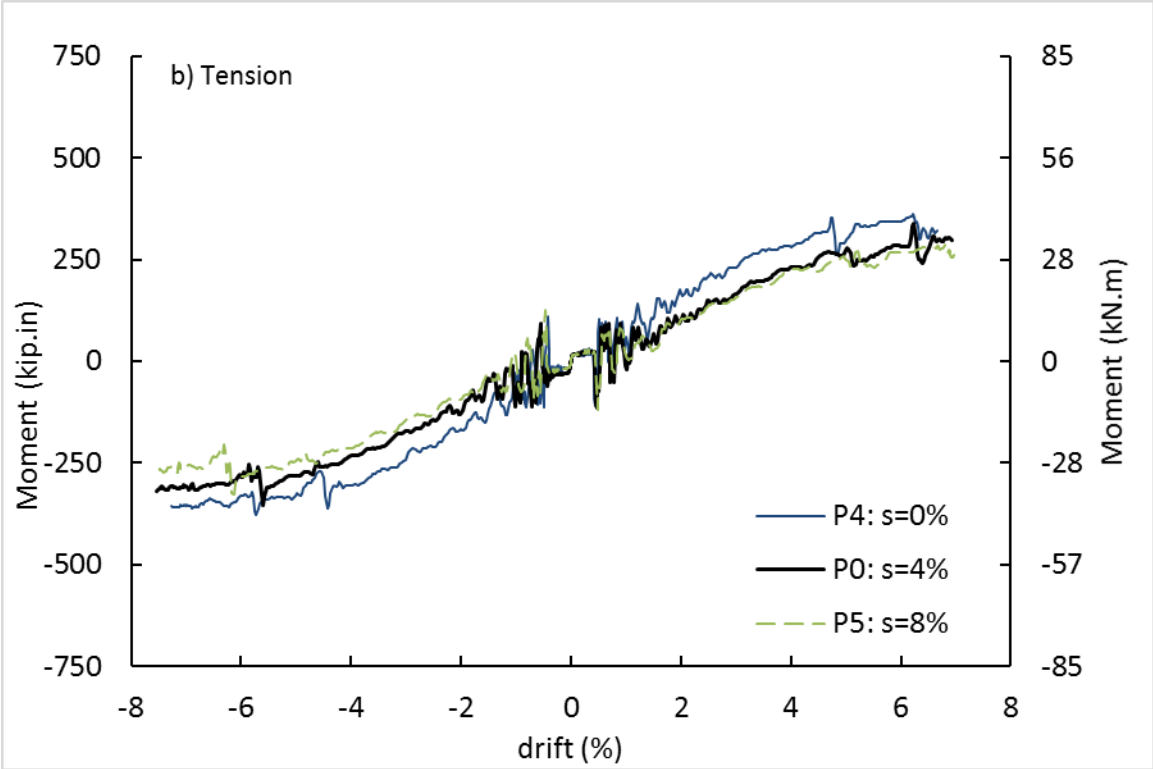

Fig. 5-17. Effect of taper slope on pipe-pin moment a) compression side due to OM b) tension side due to OM

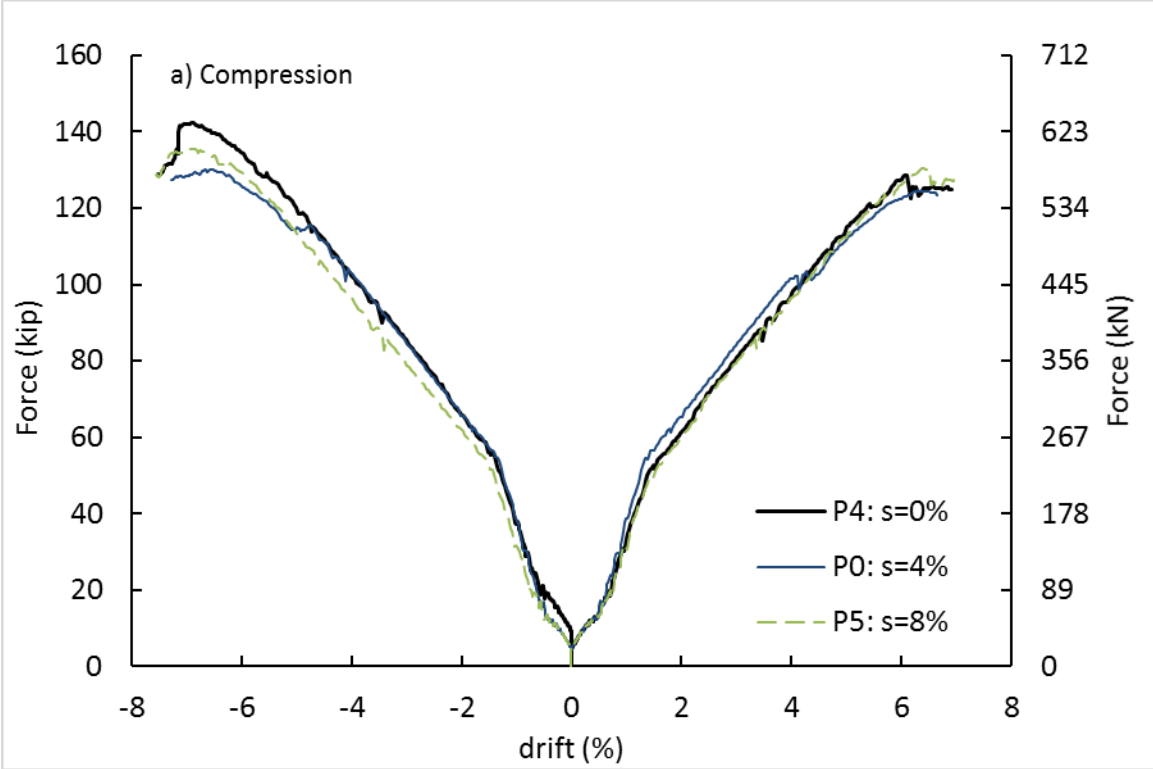

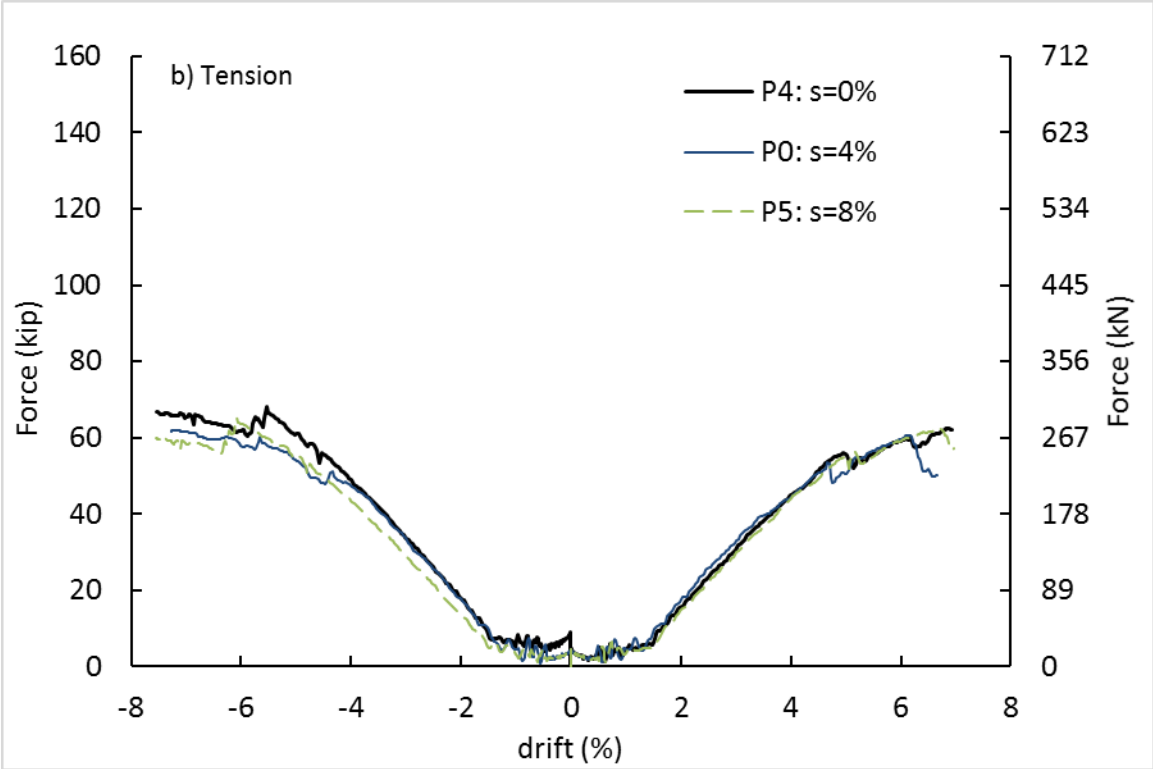

Fig. 5-18. Effect of taper slope on normal force in column-pad interface a) compression side due to OM b) tension side due to OM

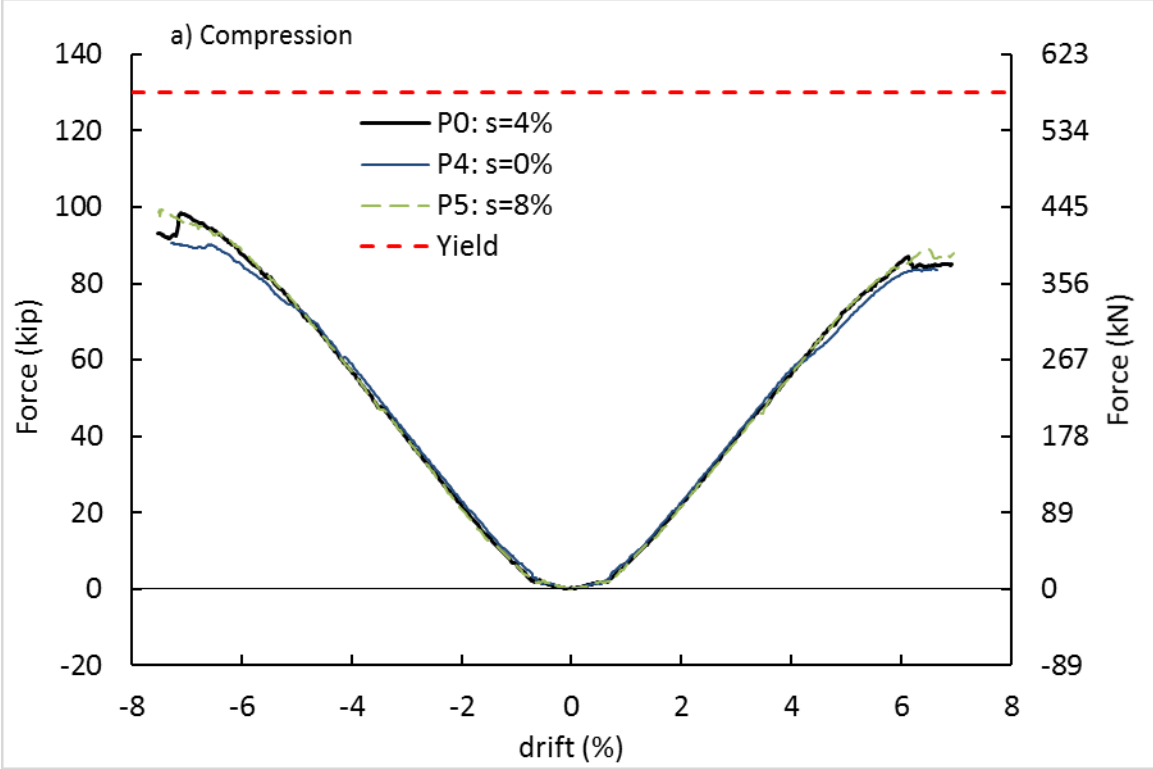

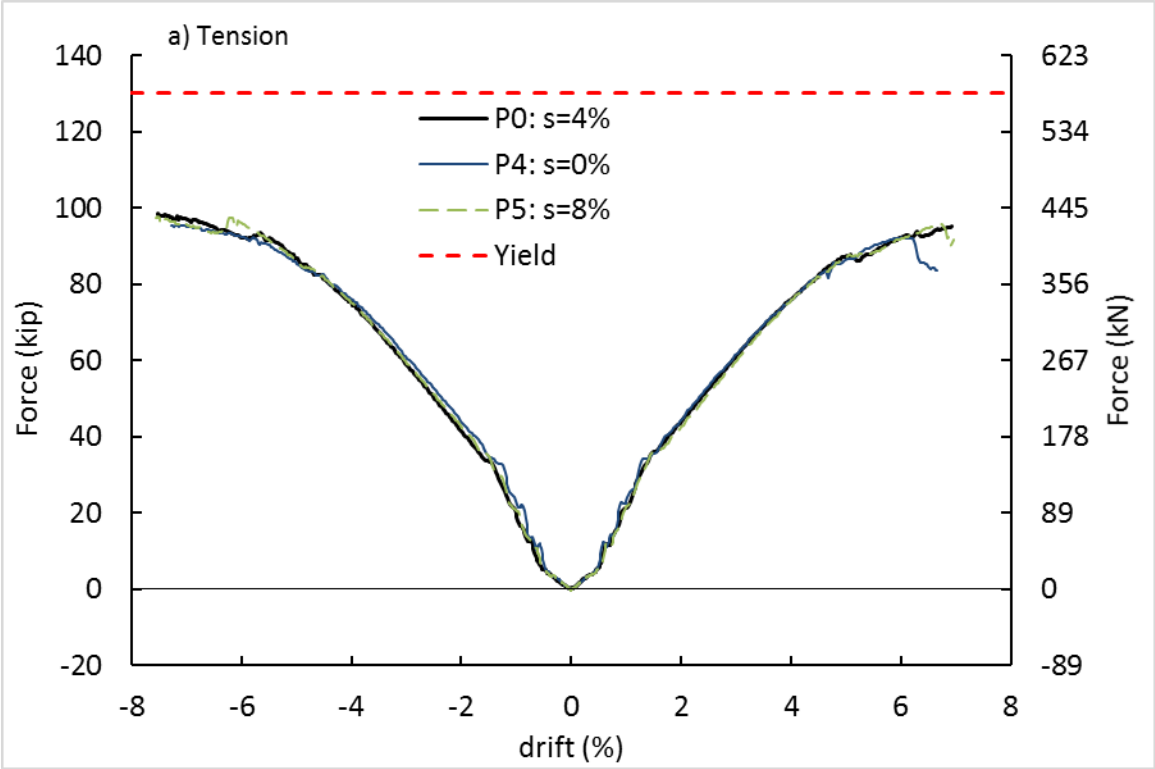

Fig. 5-19. Effect of taper slope on rod force a) compression side due to OM b) tension side due to OM

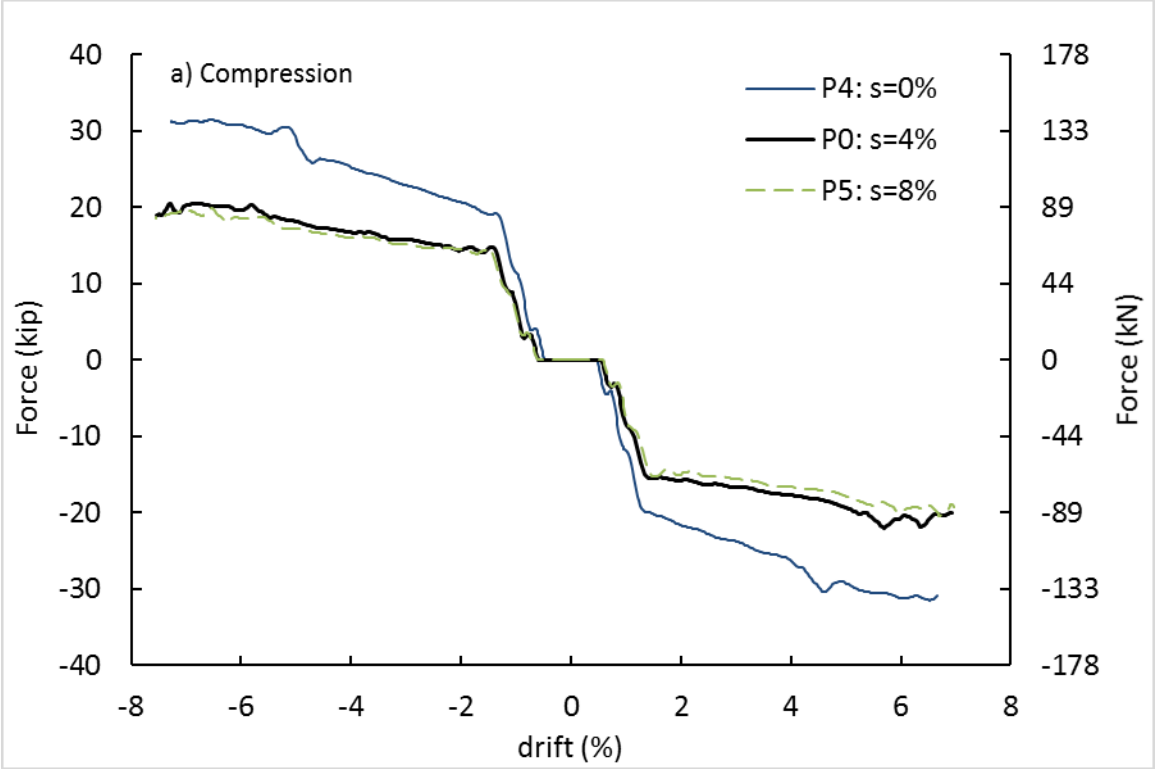

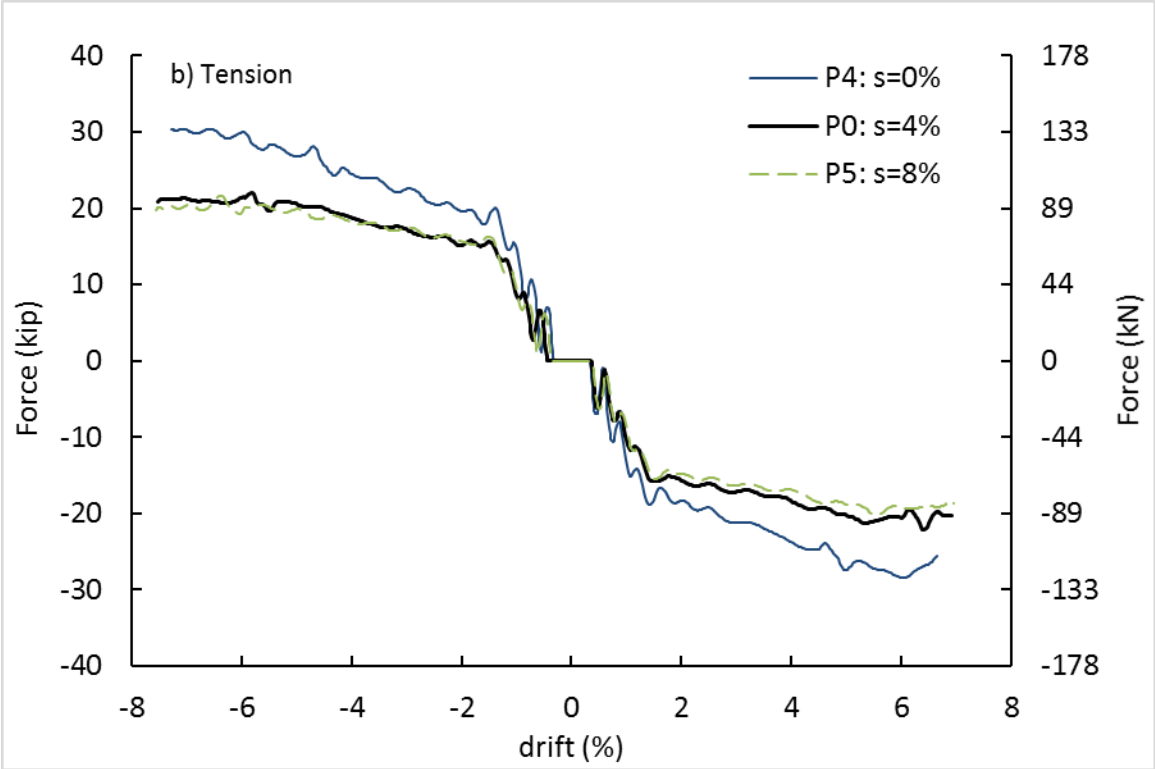

Fig. 5-20. Effect of taper slope on contact force between pipes a) compression side due to OM b) tension side due to OM

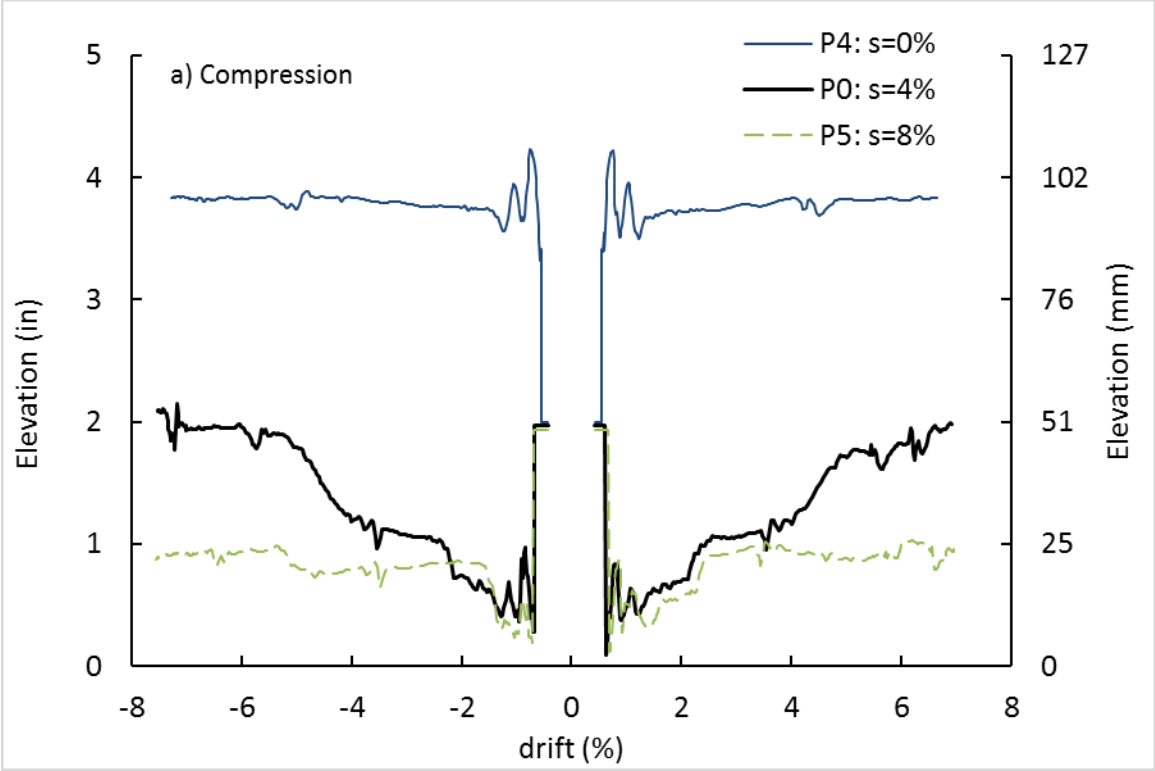

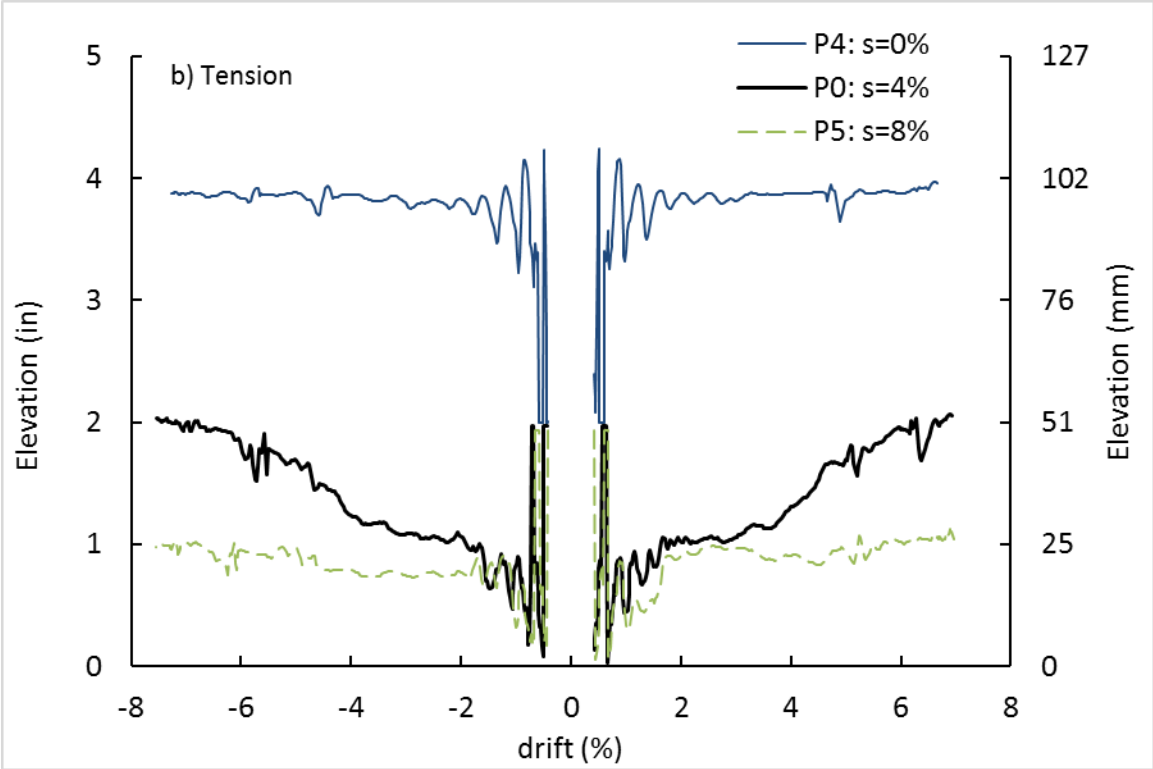

Fig. 5-21. Effect of taper slope on the elevation of contact point between pipes a) compression side due to OM b) tension side due to OM

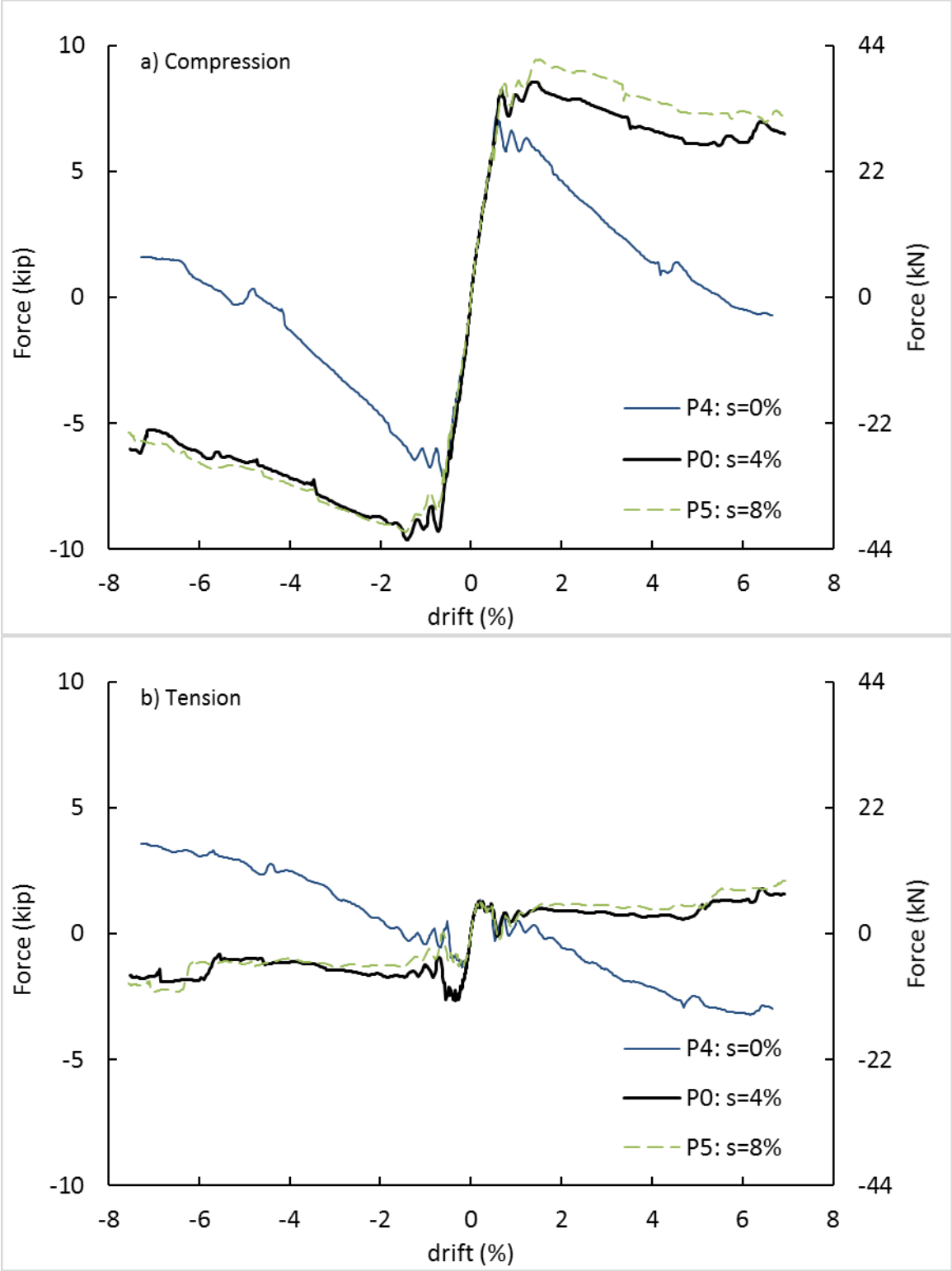

Fig. 5-22. Effect of taper slope on friction in column-pad interface a) compression side due to OM b) tension side due to OM

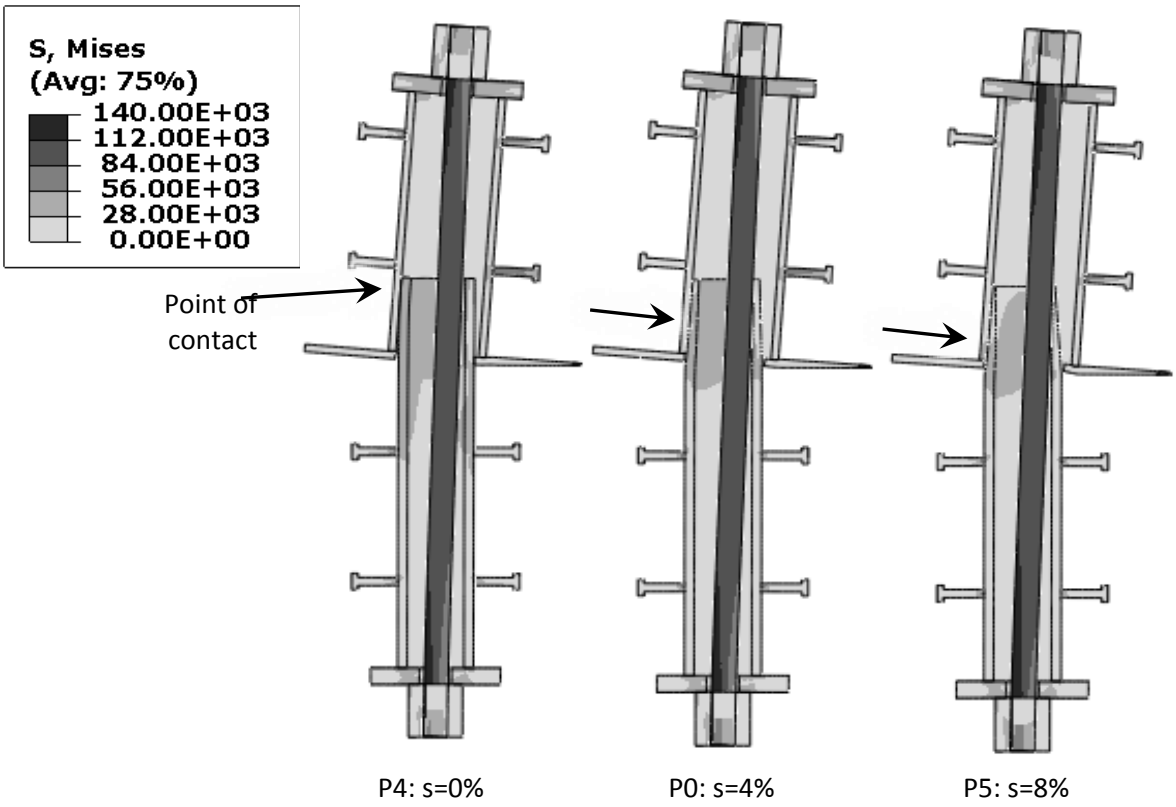

Fig. 5-23. Effect of taper slope of lower pipe on the stress in the pipes and rod

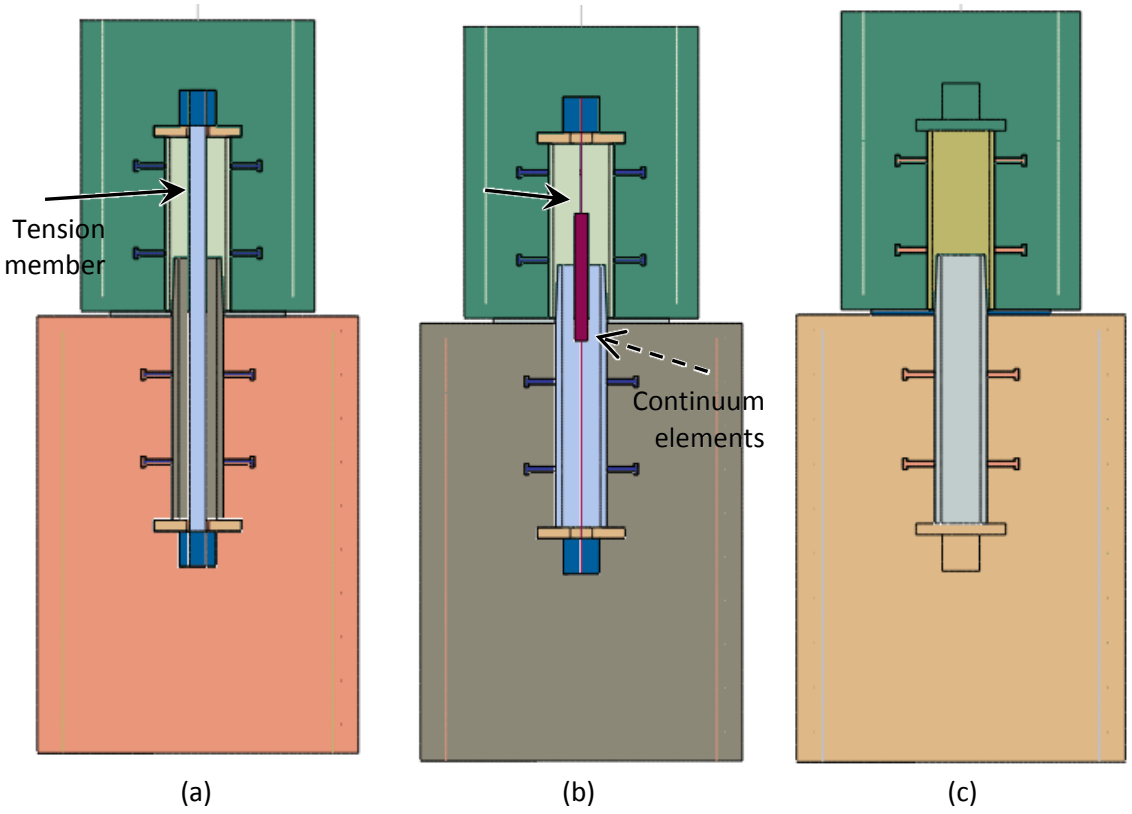

Fig. 5-24. Tension member a) HS-rod b) strand c) no member

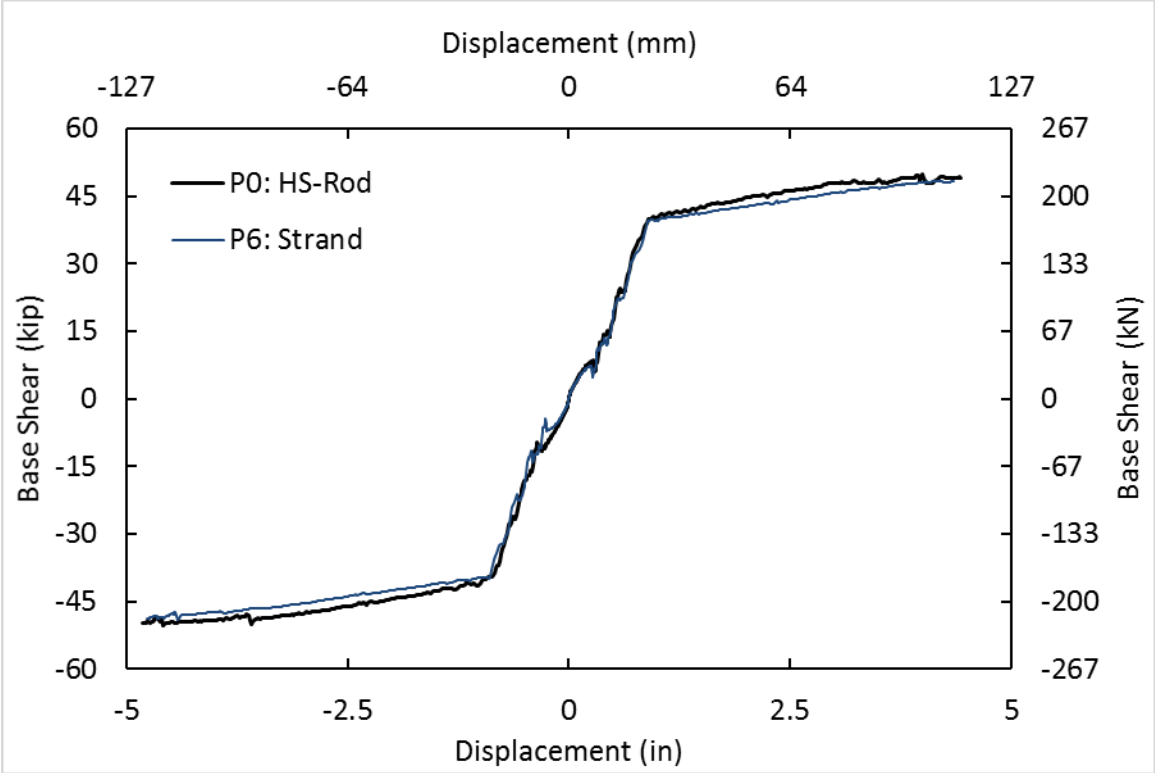

Fig. 5-25. Effect of tension member on the pushover curves in bents with uplift

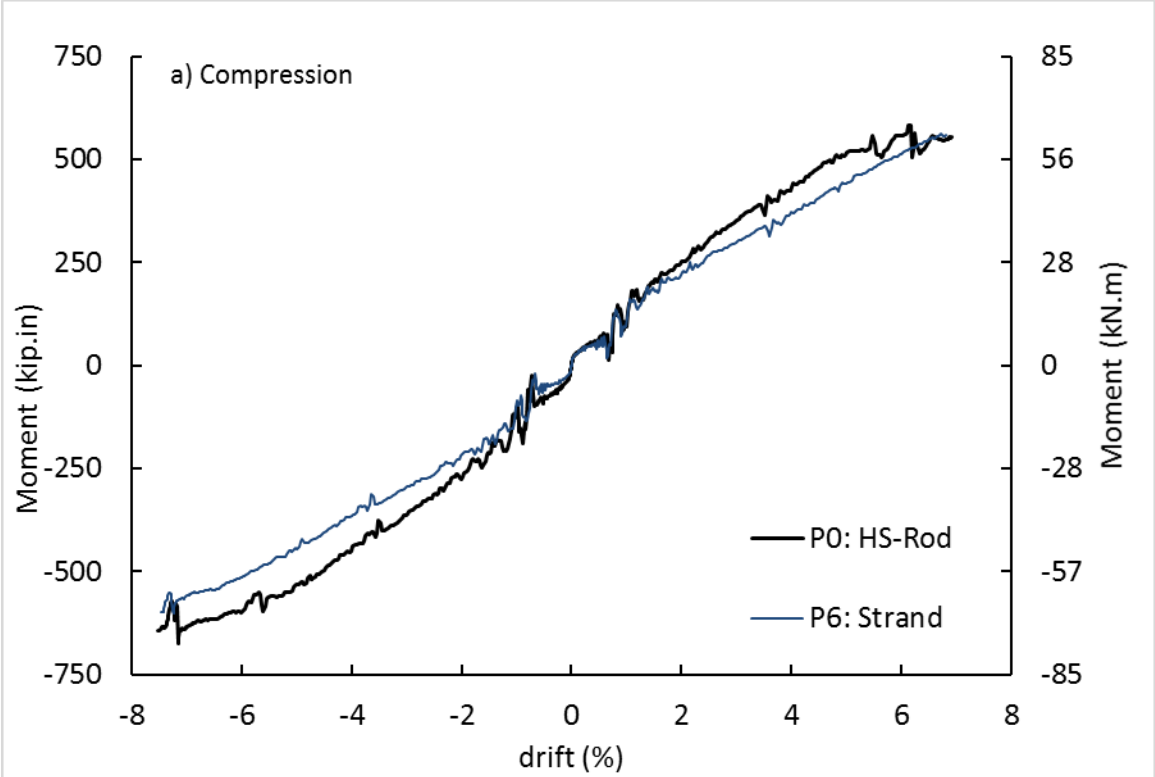

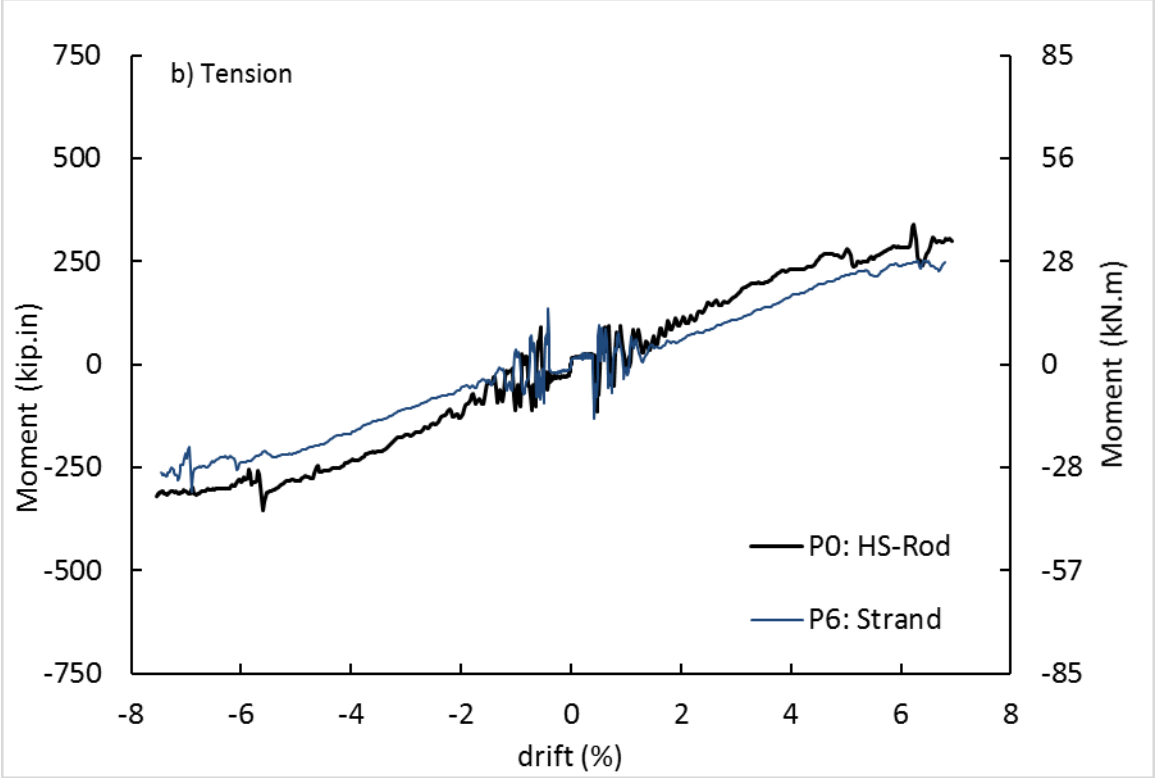

Fig. 5-26. Effect of tension member on pipe-pin moments in bents with uplift a) compression side due to OM b) tension side due to OM

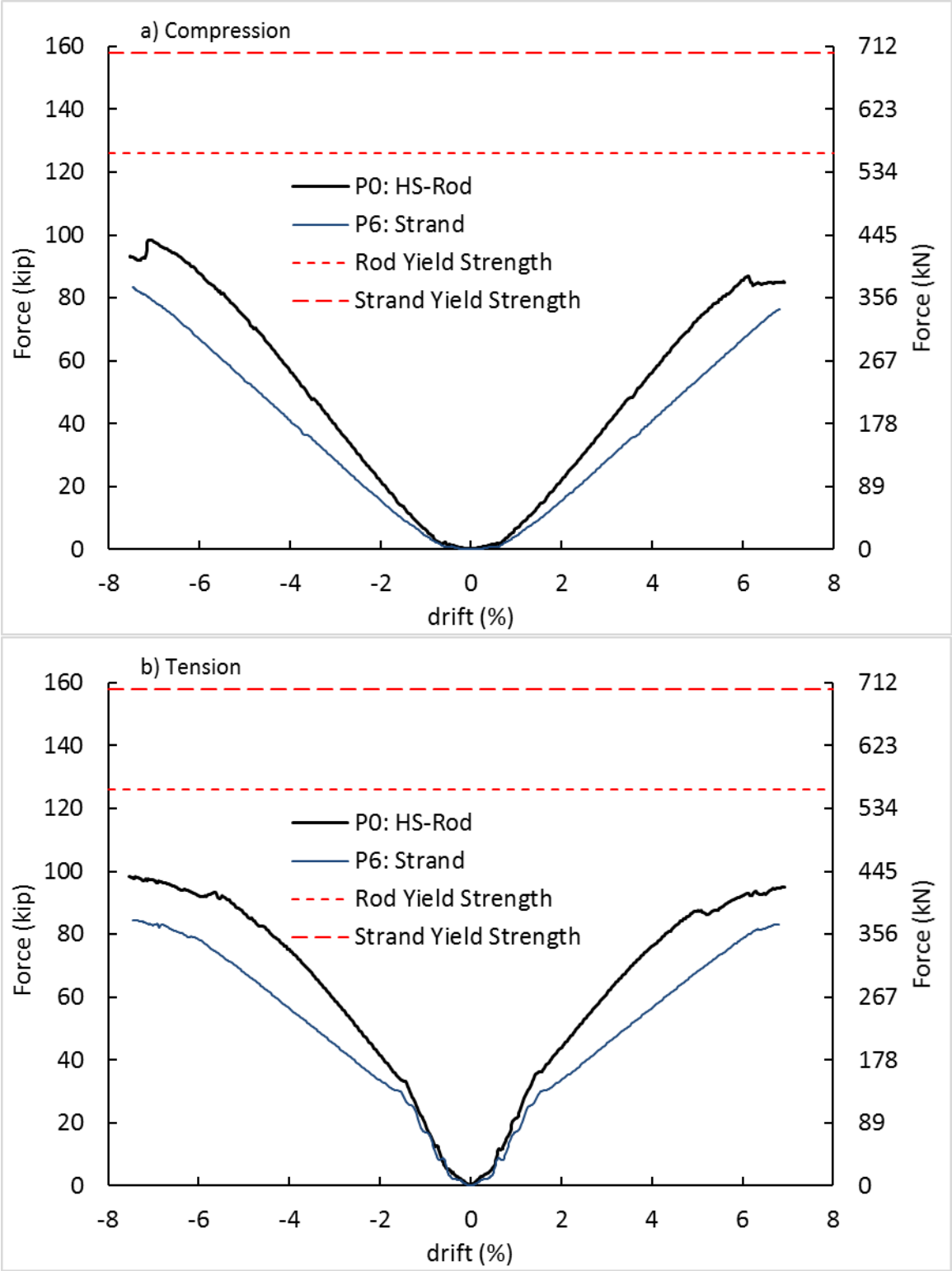

Fig. 5-27. Effect of tension member on tension member force in bents with uplift a) compression side due to OM b) tension side due to OM

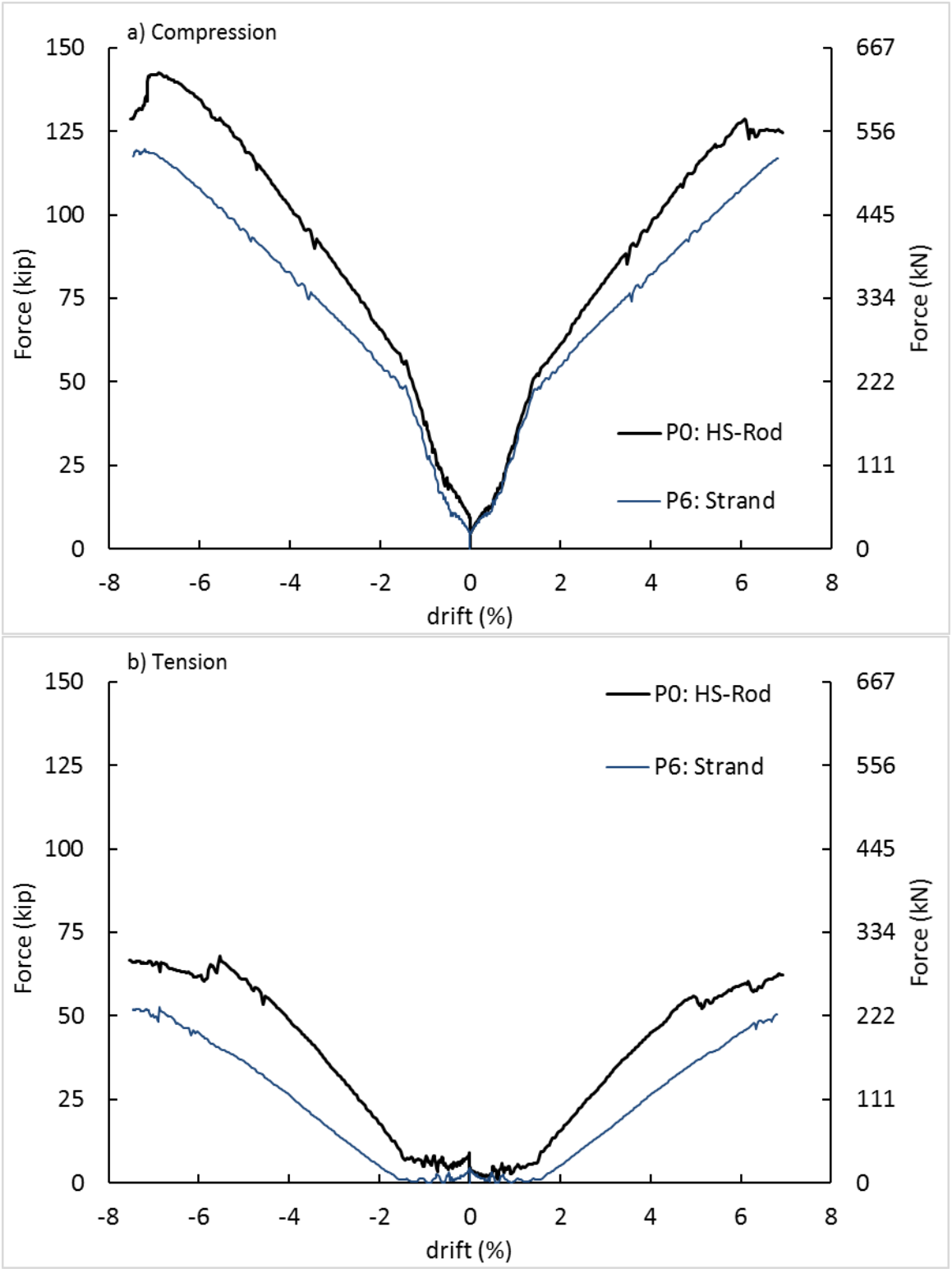

Fig. 5-28. Effect of tension member on normal force in column-pad interface in bents with uplift a) compression side due to OM b) tension side due to OM

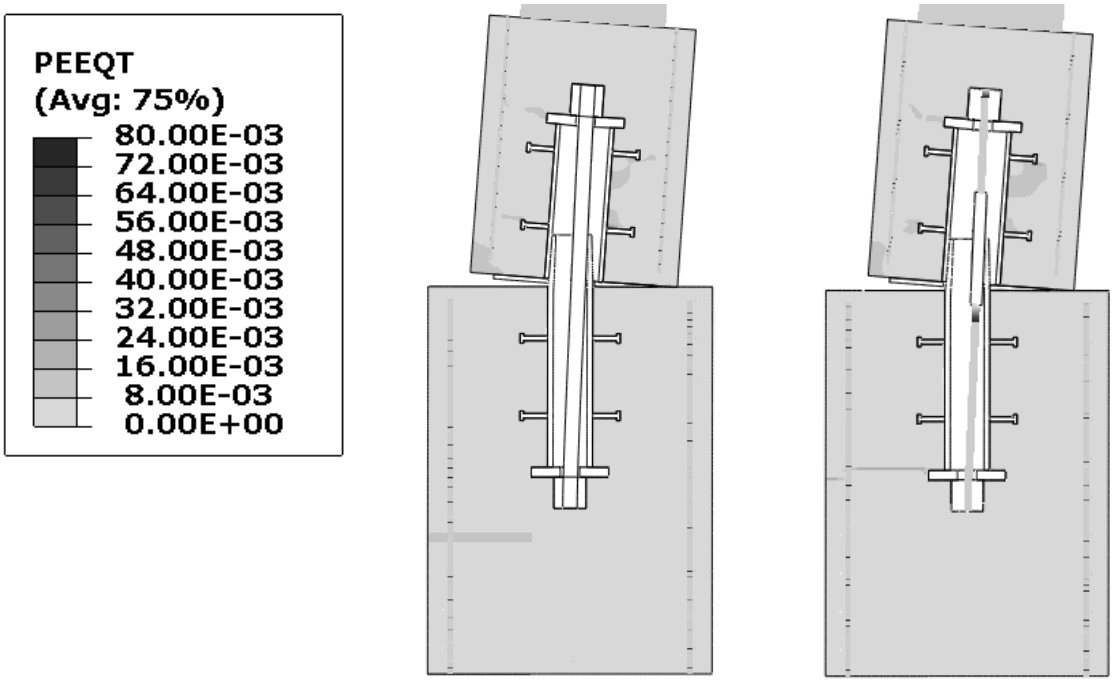

Fig. 5-29. Effect of tension member on cracking pattern of left column in bents with uplift a) HS-rod b) strand

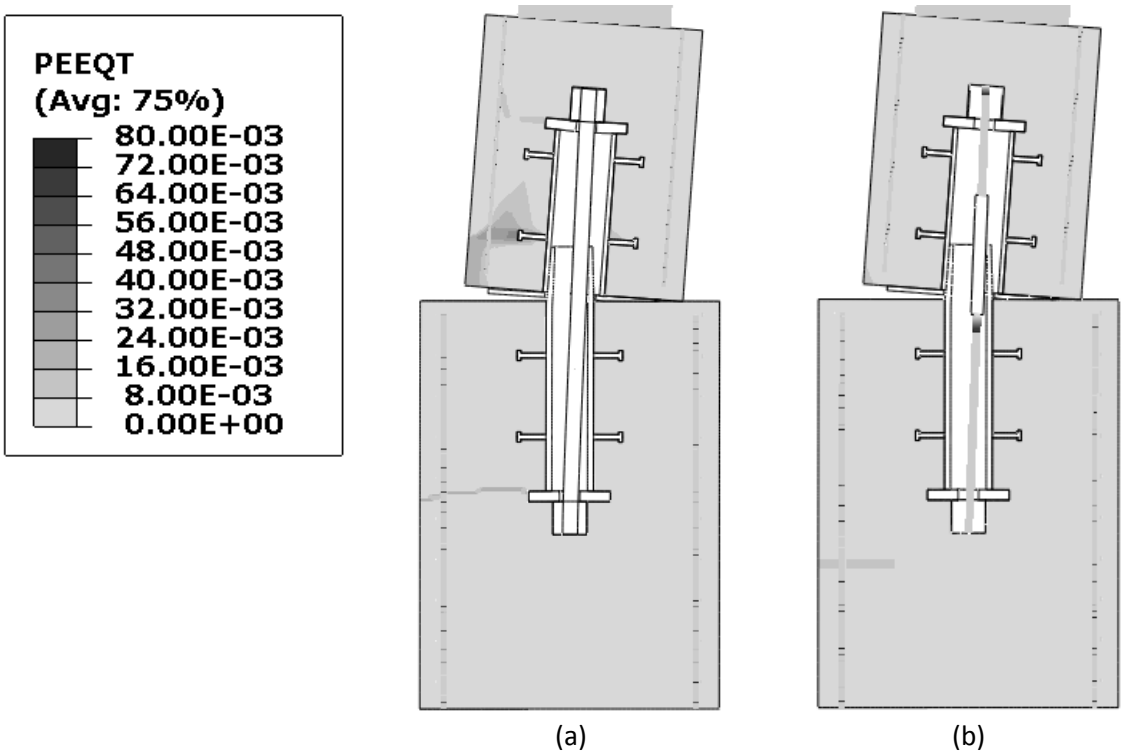

Fig. 5-30. Effect of tension member on cracking pattern of right column in bents with uplift a) HS-rod b) strand

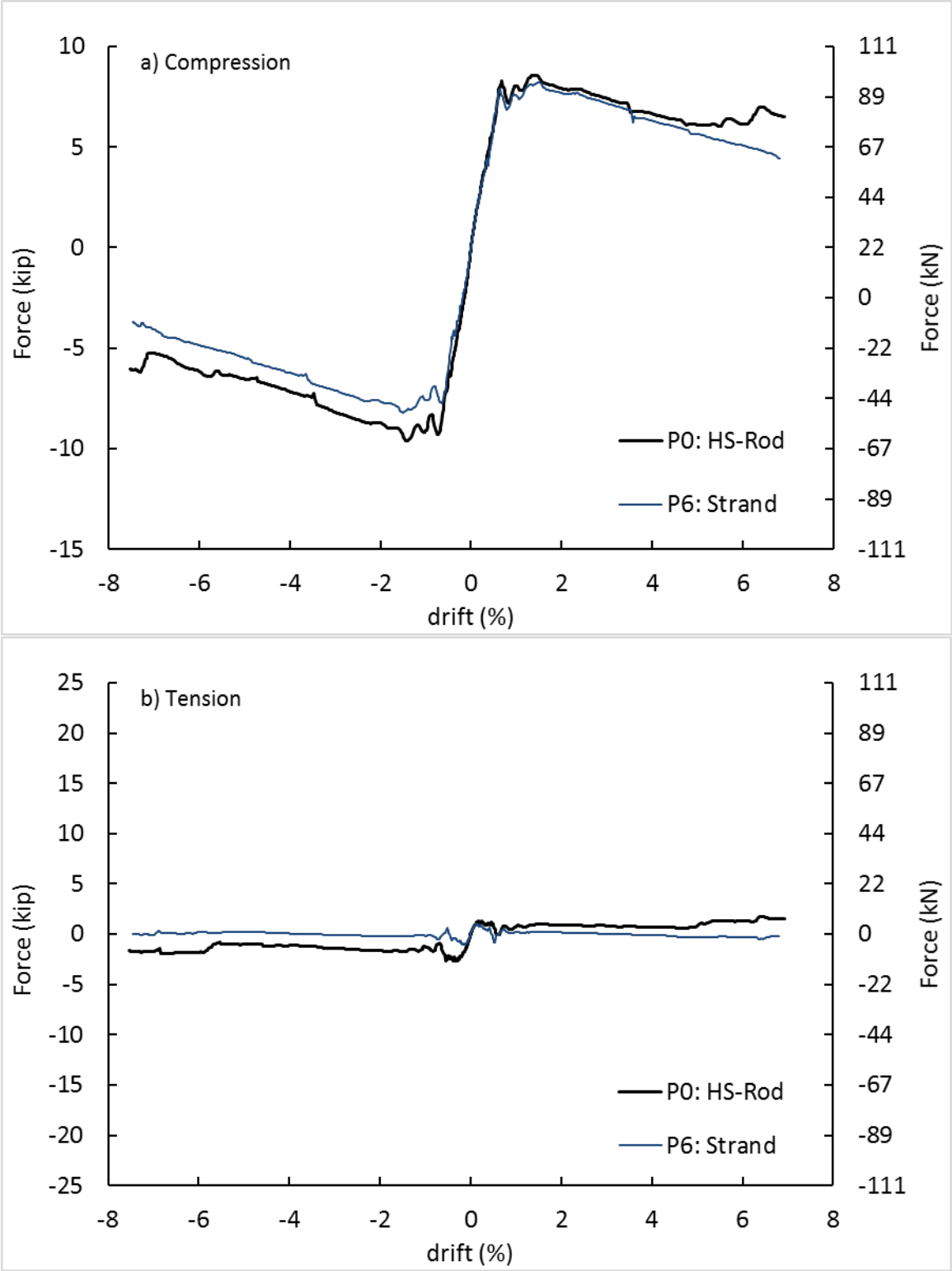

Fig. 5-31. Effect of tension member on friction in column-pad interface in bents with uplift a) compression side due to OM b) tension side due to OM

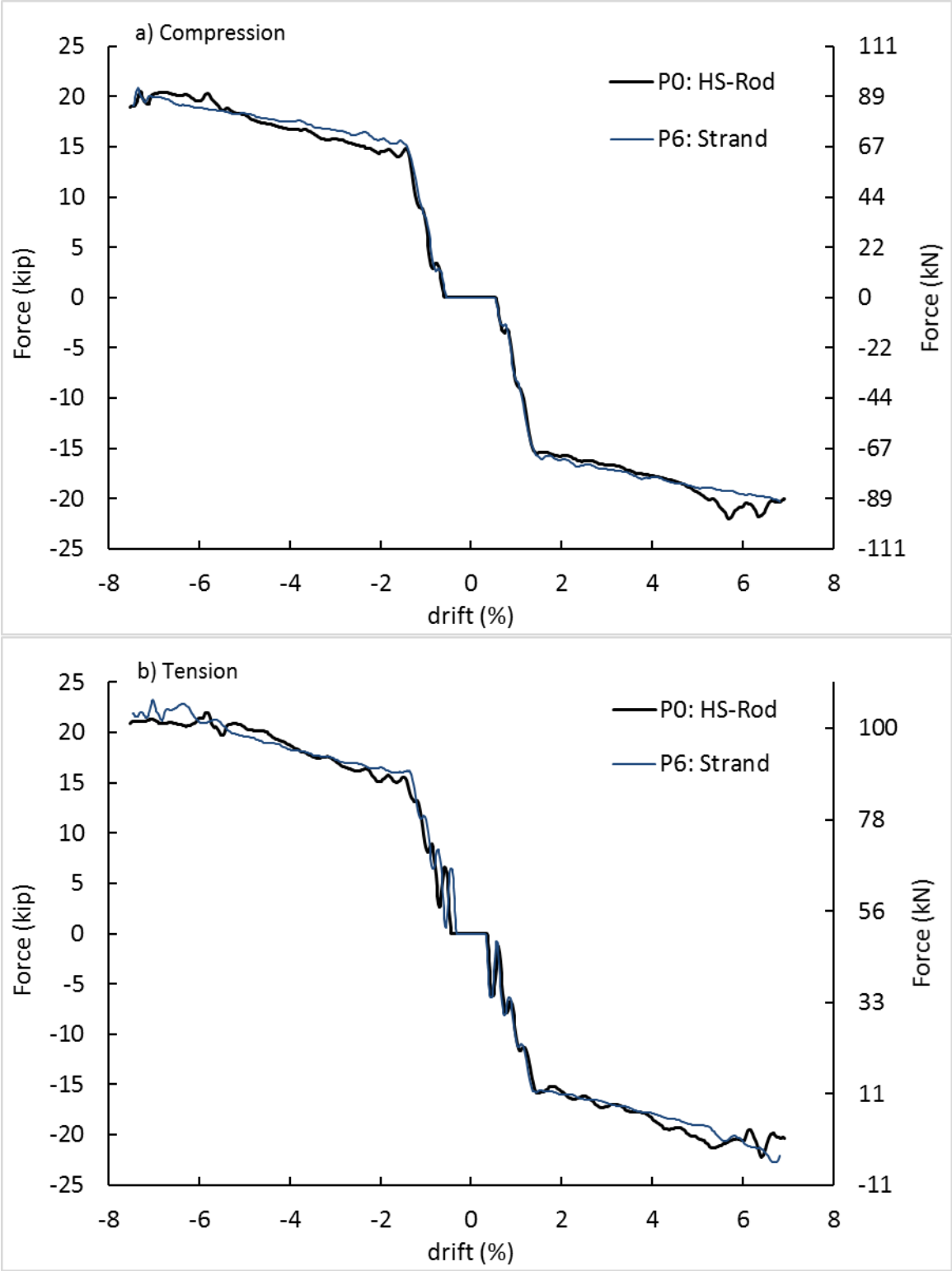

Fig. 5-32. Effect of tension member on pipes contact force in bents with uplift a) compression side due to OM b) tension side due to OM

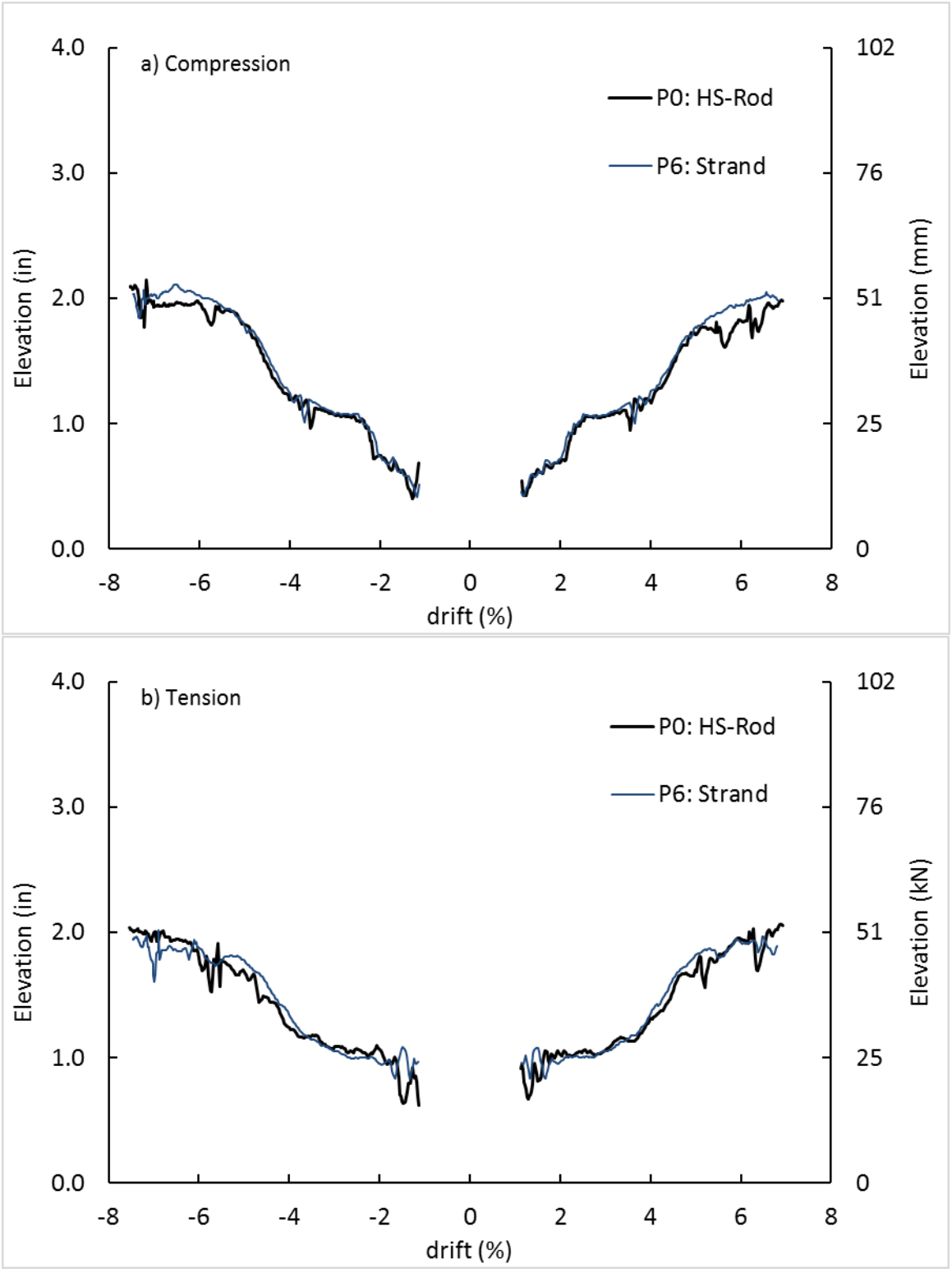

Fig. 5-33. Effect of tension member on pipes contact point in bents with uplift a) compression side due to OM b) tension side due to OM

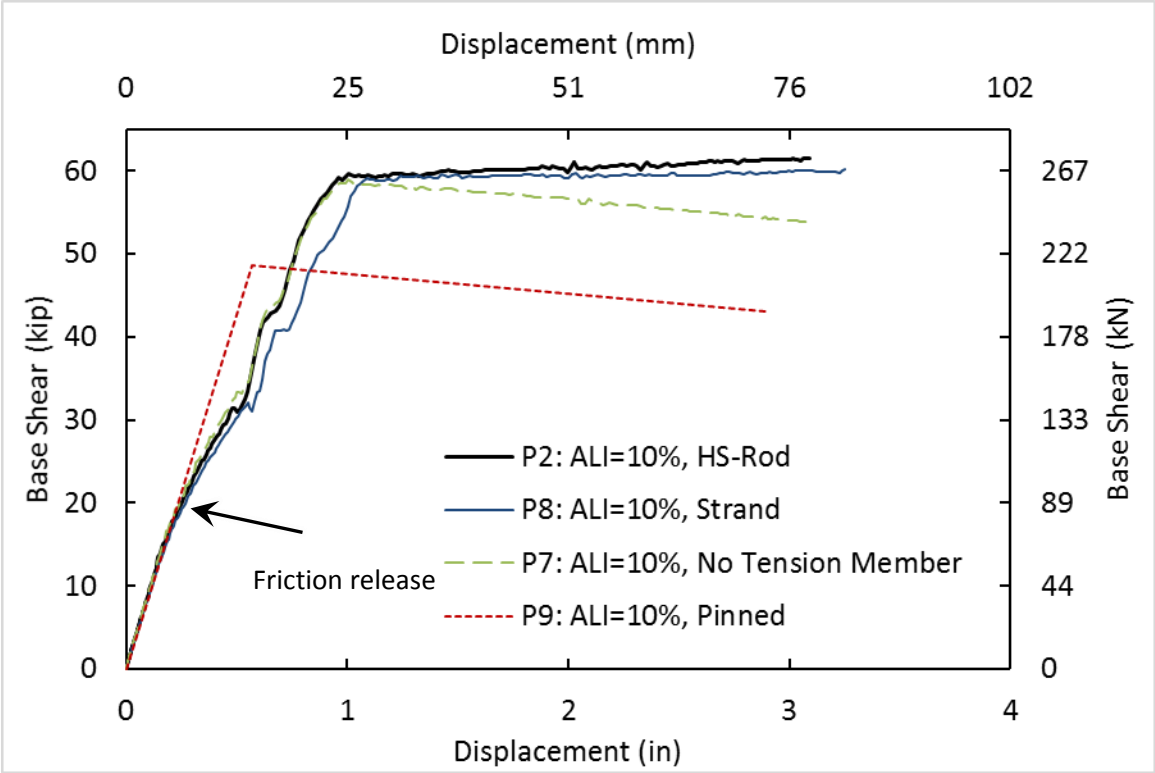

Fig. 5-34. Effect of tension member on pushover curves in bents without uplift

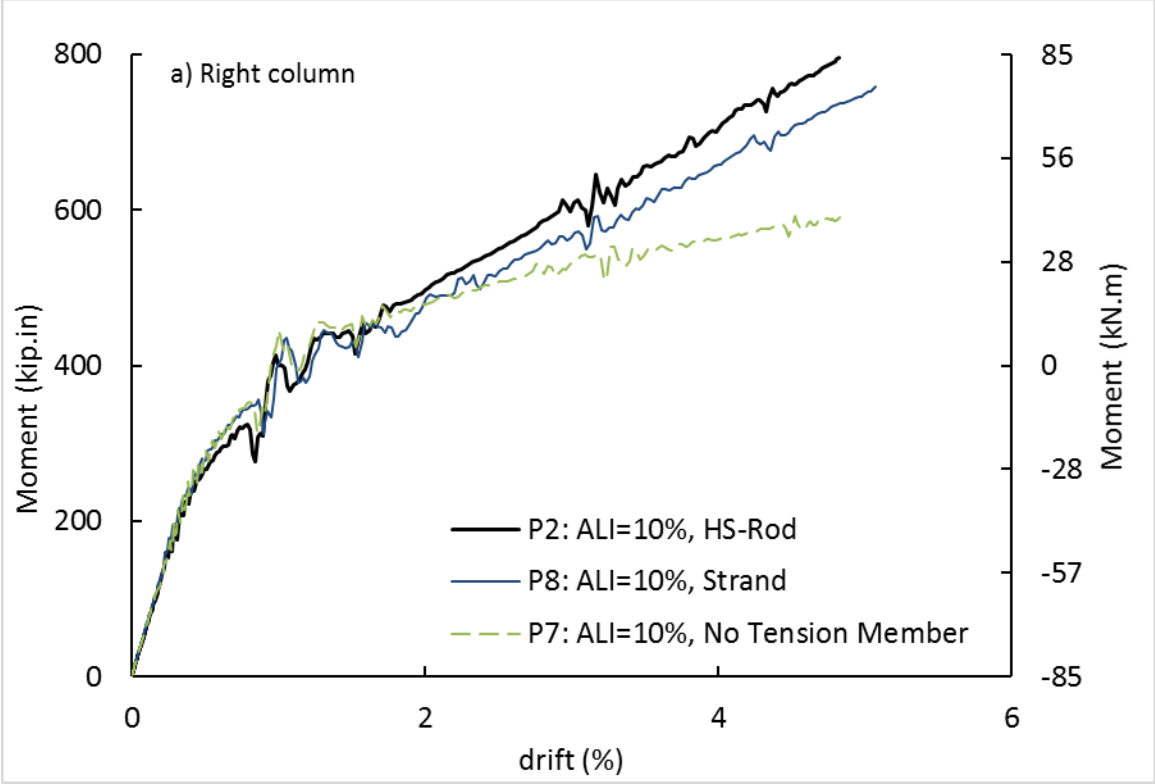

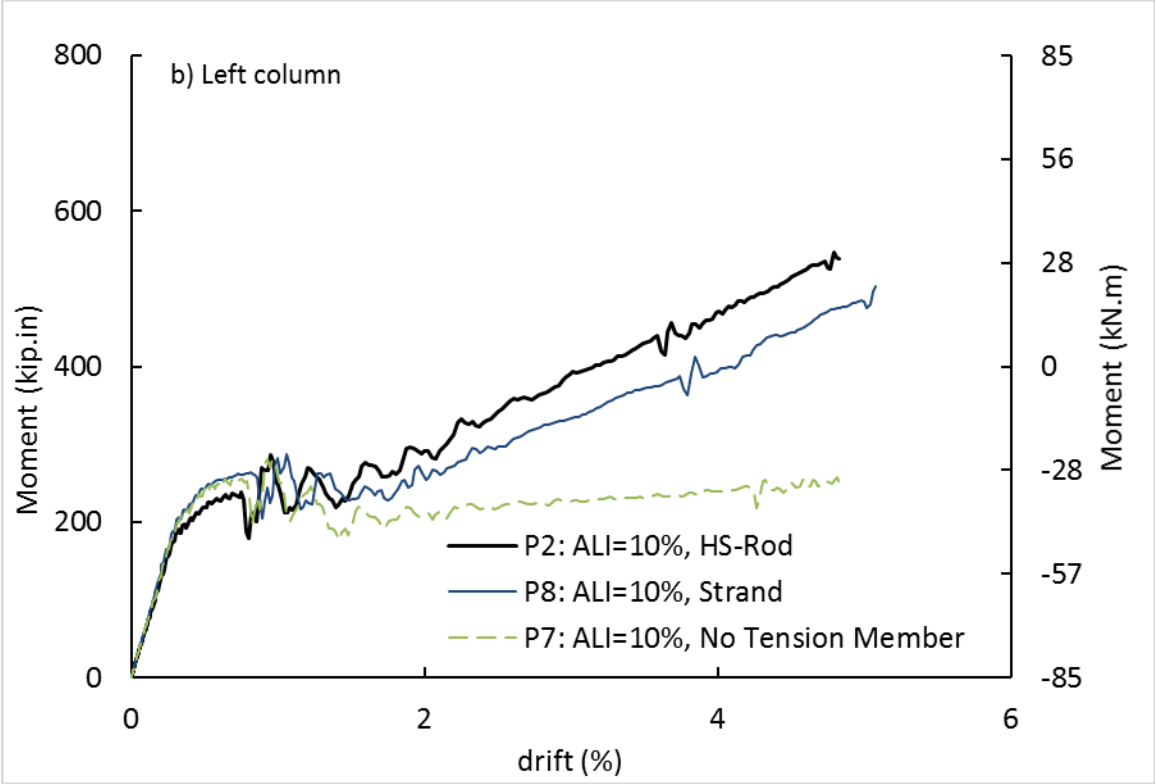

Fig. 5-35. Effect of tension member on pipe-pin moments in bents without uplift a) right column b) left column

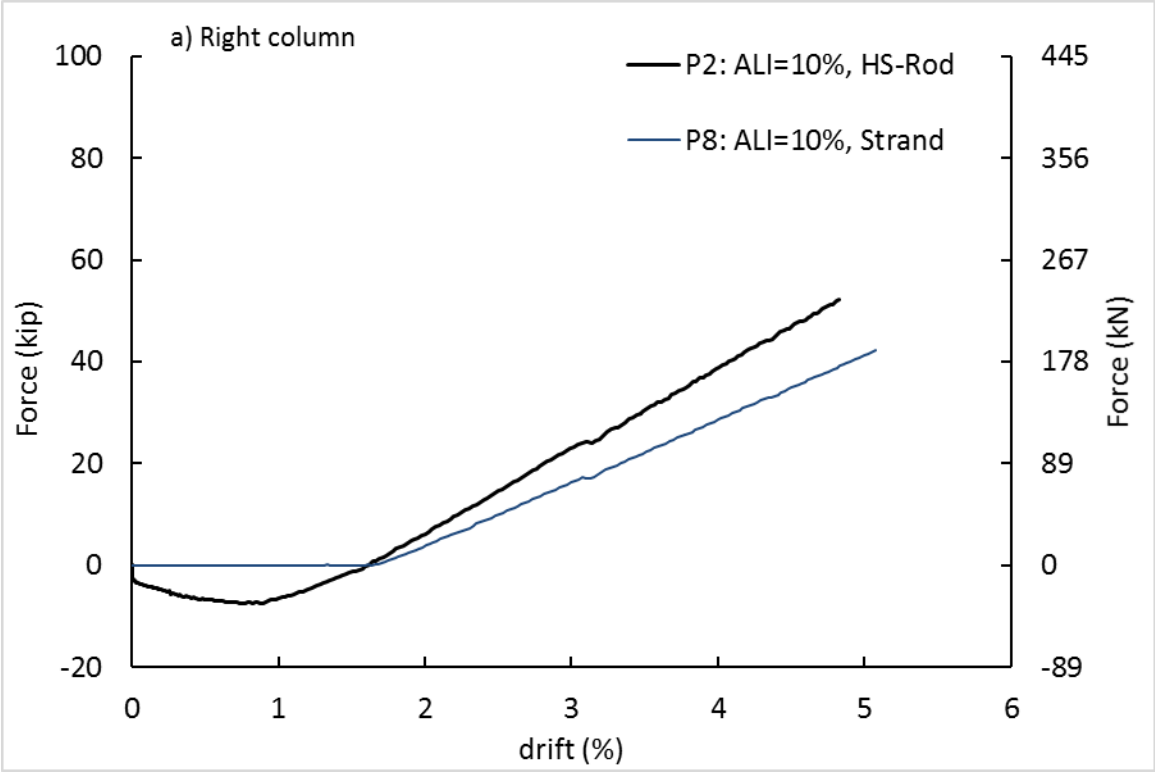

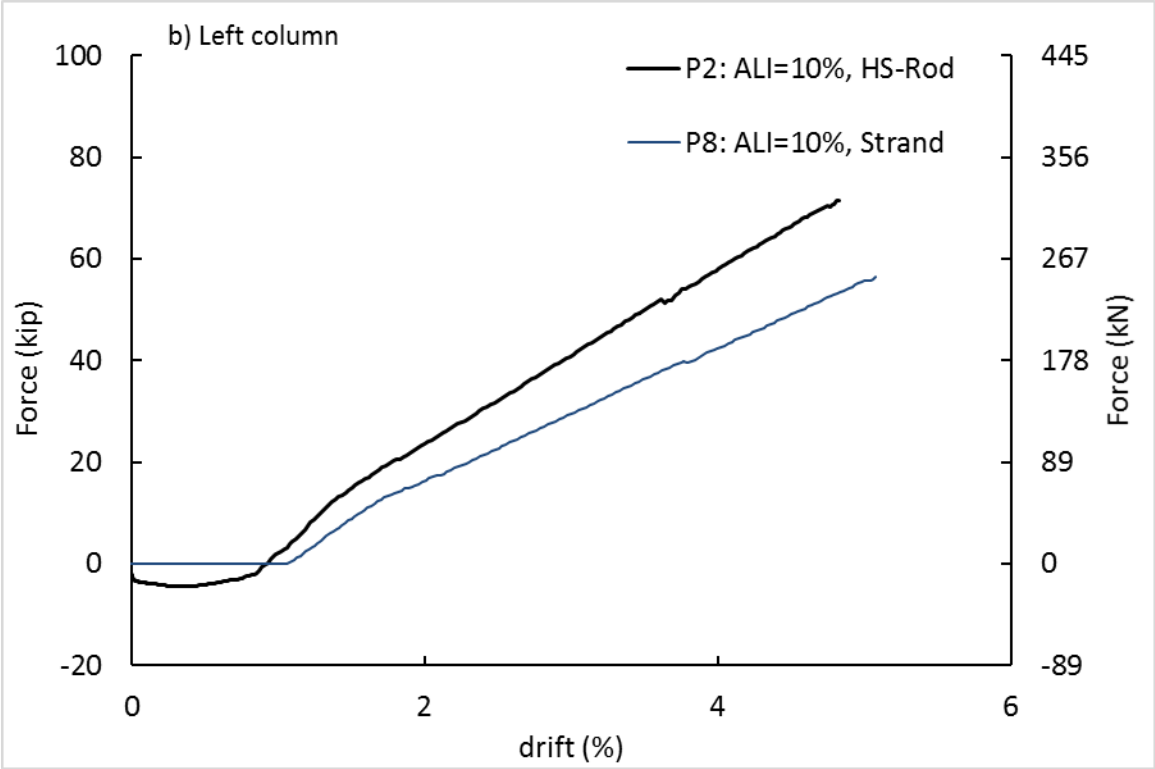

Fig. 5-36. Effect of tension member on tension member force in bents without uplift a) right column b) left column

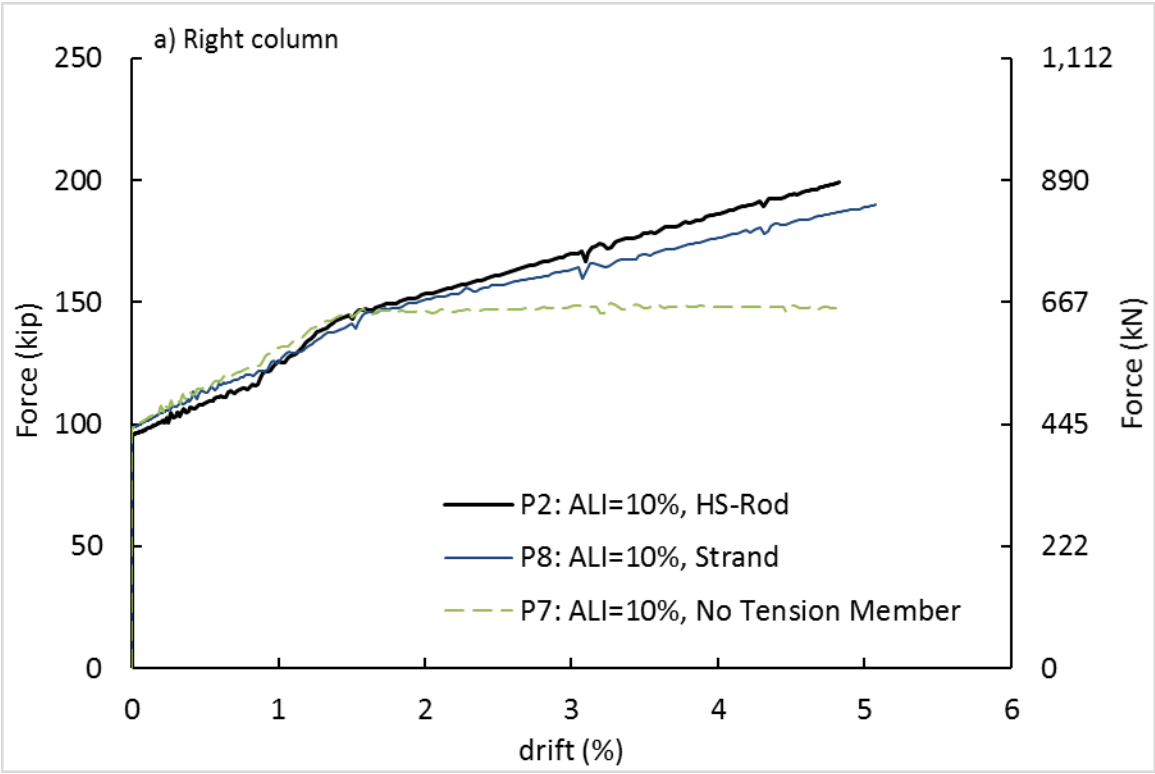

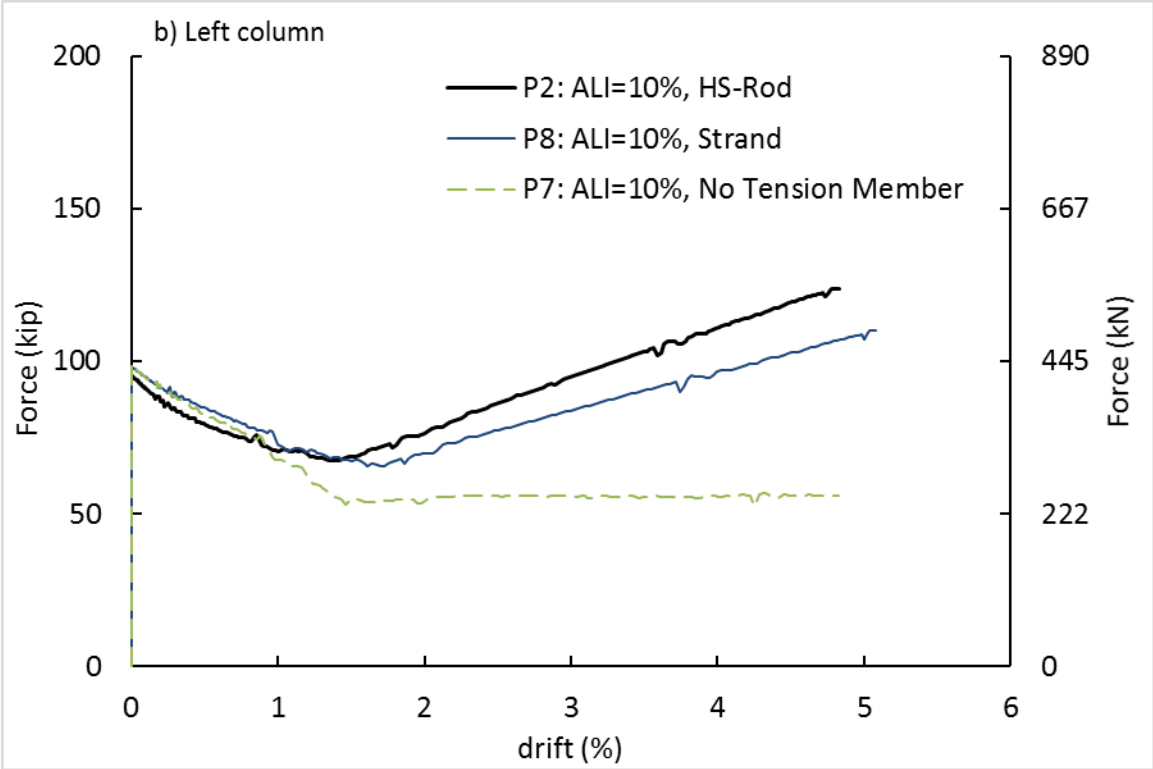

Fig. 5-37. Effect of tension member on normal force in column-pad interface in bents without uplift a) right column b) left column

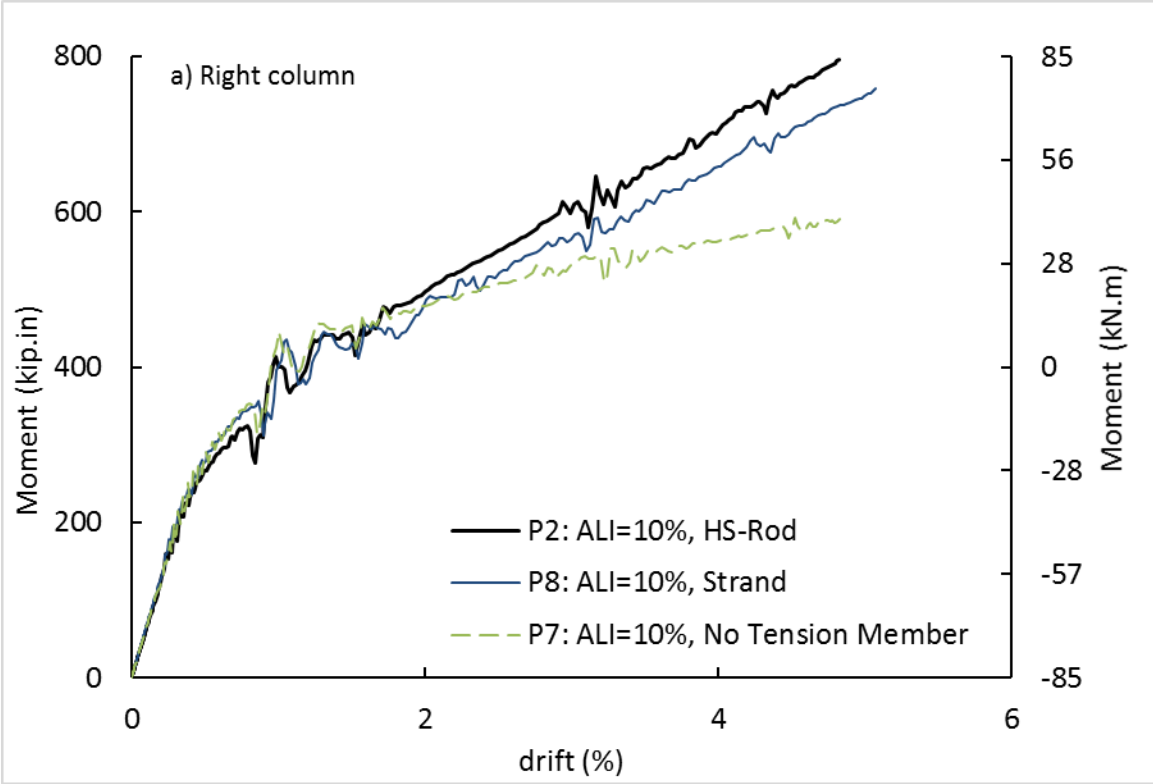

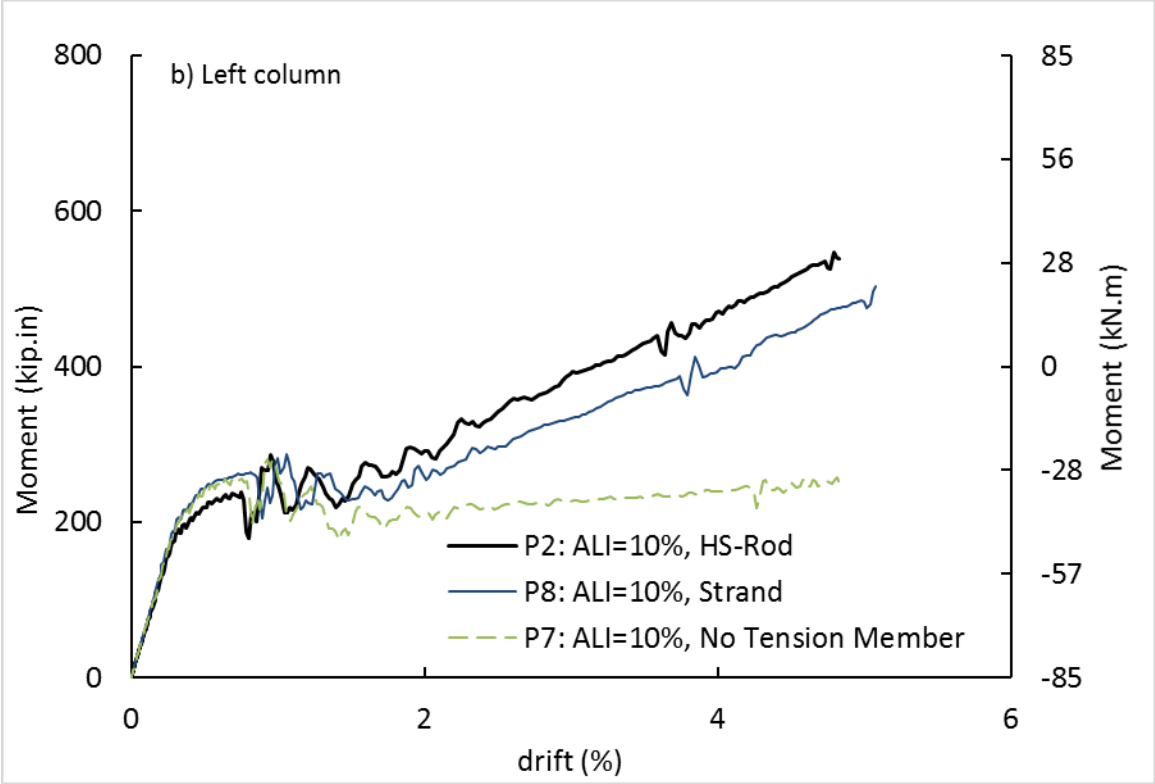

Fig. 5-38. Effect of tension member on column axial load in bents without uplift a) right column b) left column

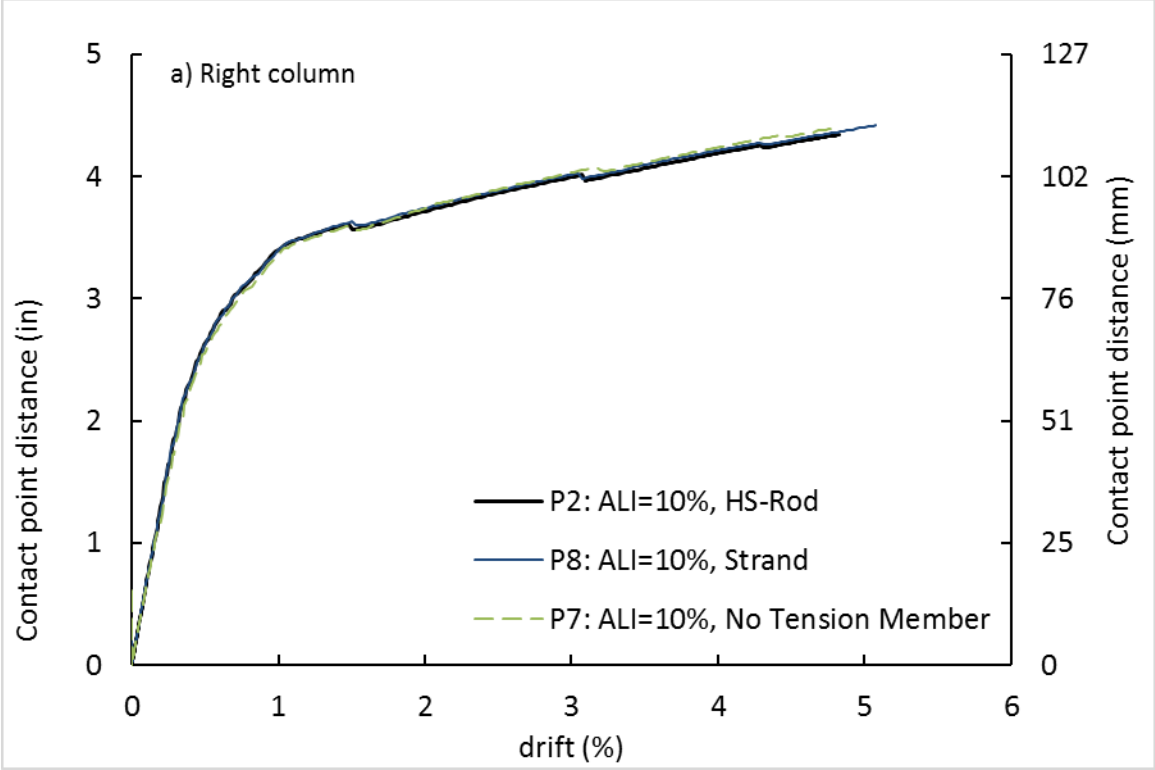

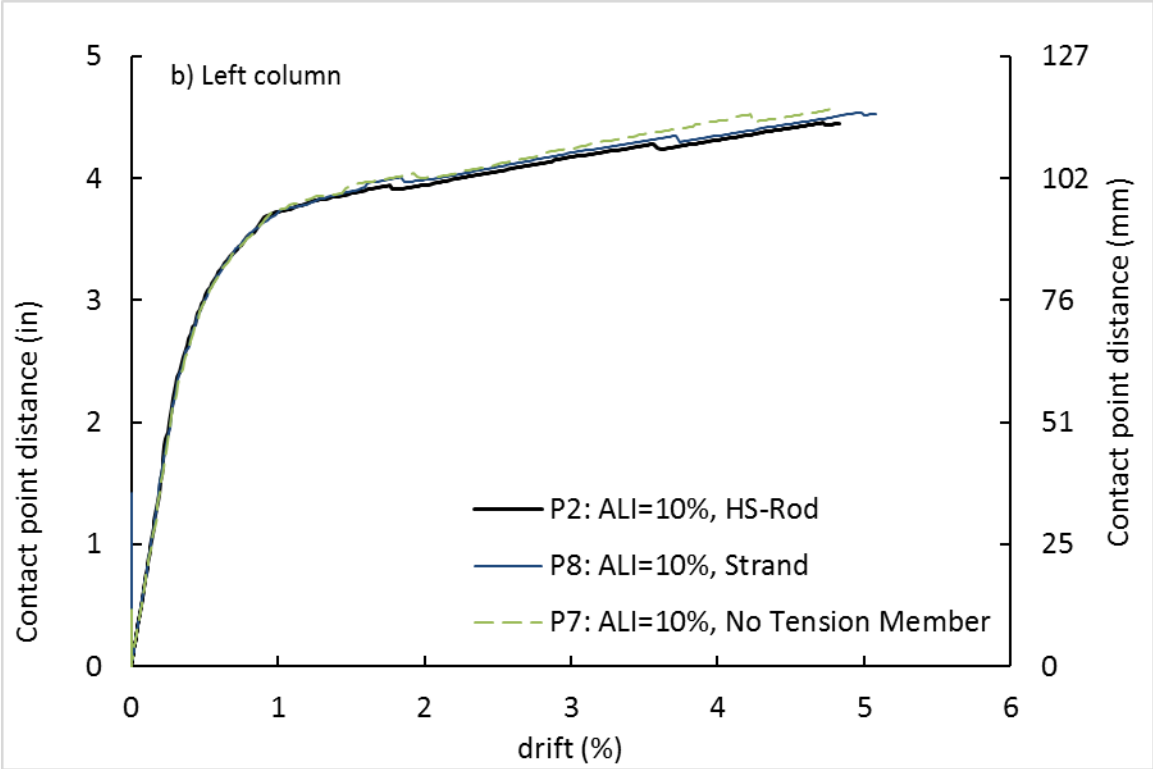

Fig. 5-39. Effect of tension member on eccentricity of column-pad contact in bents without uplift a) right column b) left column

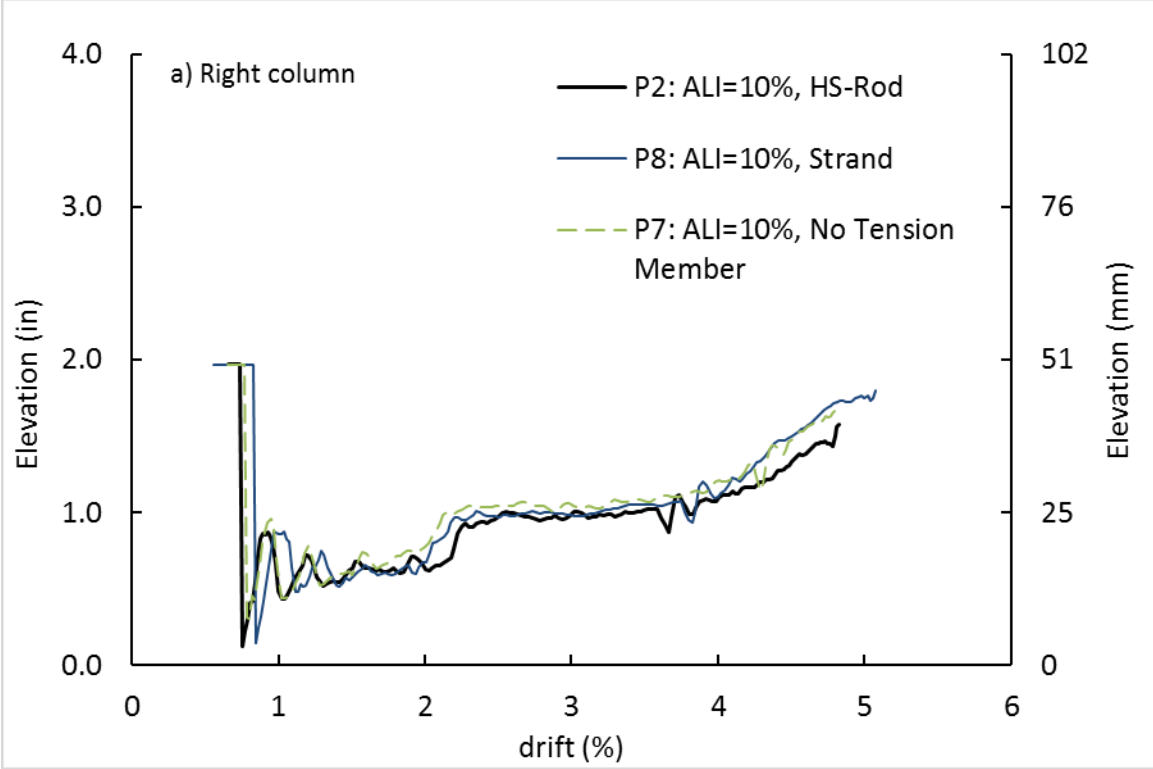

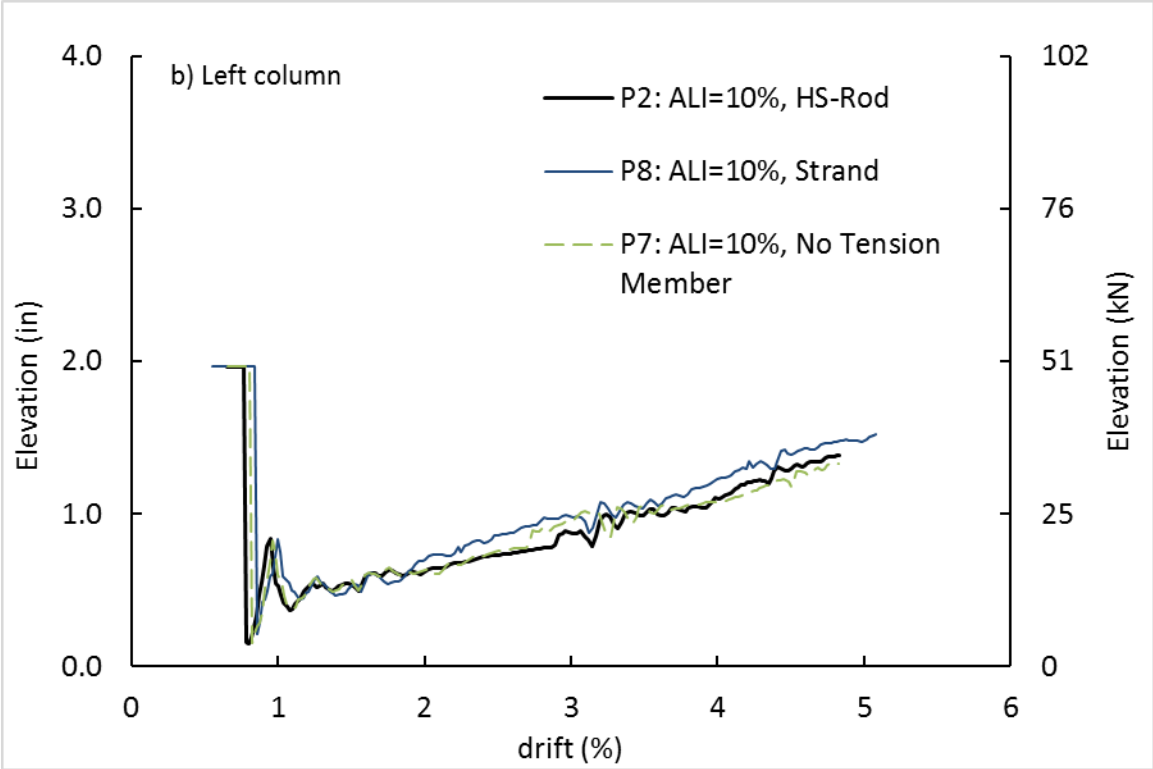

Fig. 5-40. Effect of tension member on height of pipes contact point in bents without uplift a) right column b) left column

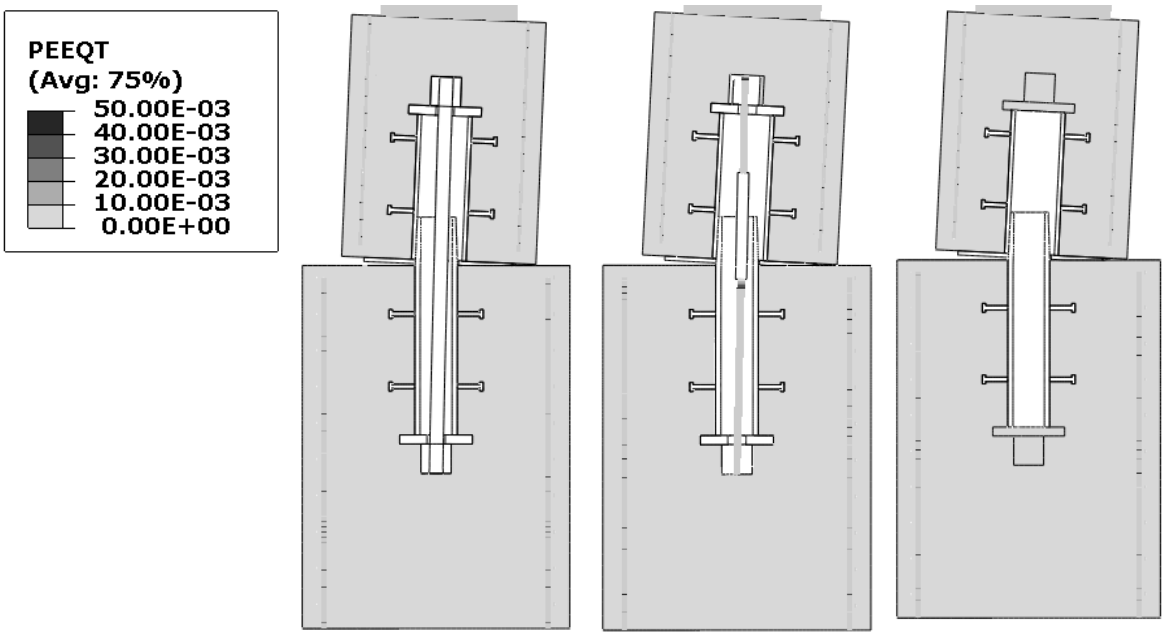

Fig. 5-41. Effect of tension member on cracking pattern in left column in bents without uplift a) HS-rod b) strand c) no tension member

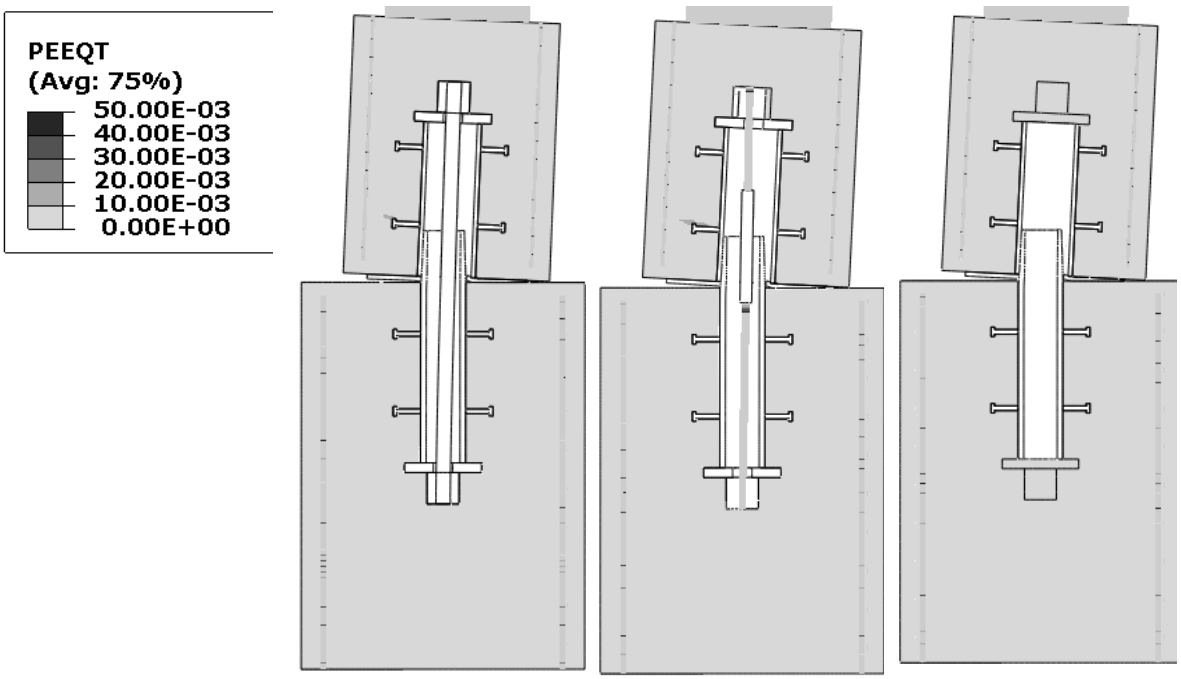

(a) (b) (c)

Fig. 5-42. Effect of tension member on cracking pattern in right column in bents without uplift a) HS-rod b) strand c) no tension member

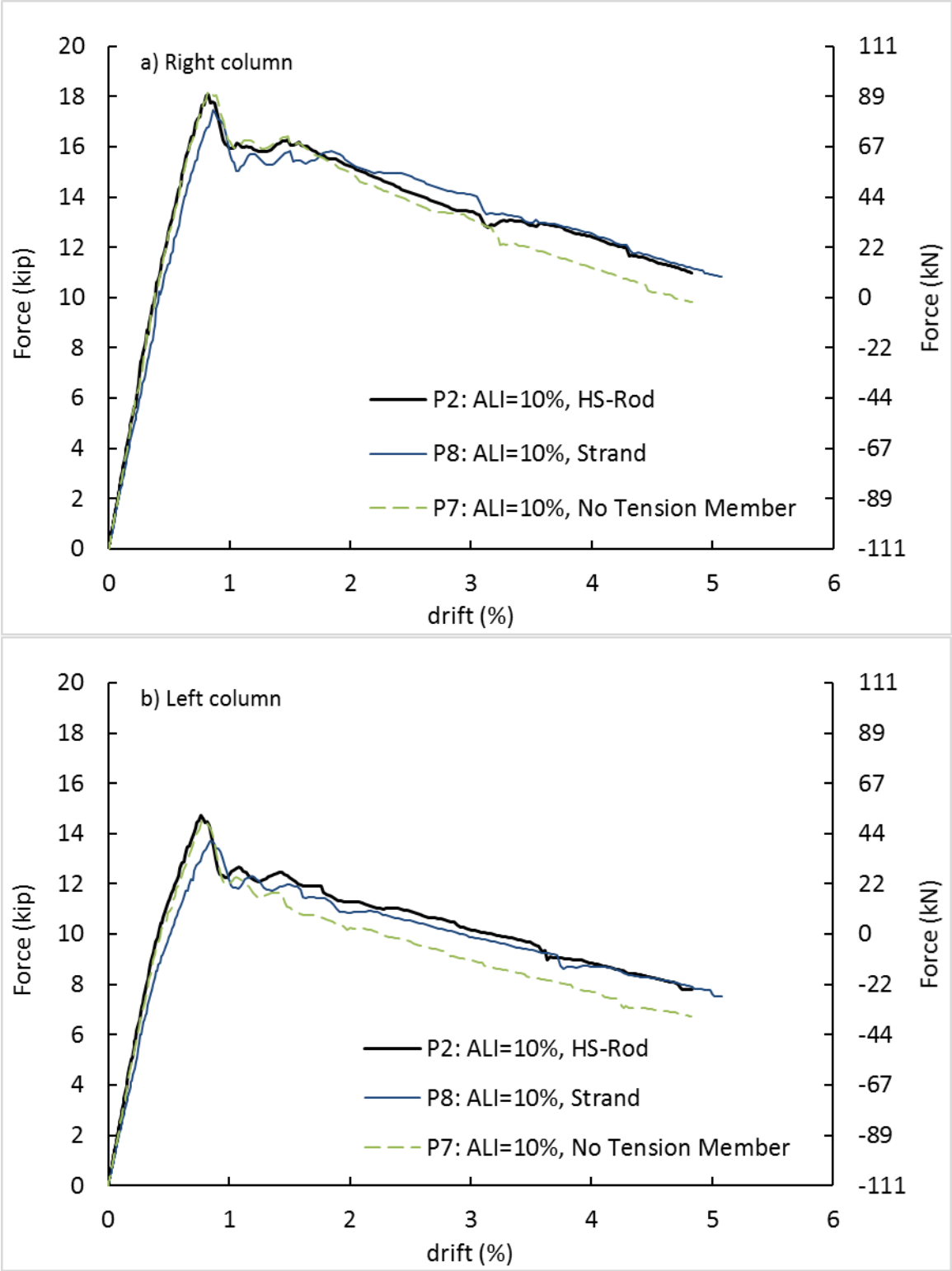

Fig. 5-43. Effect of tension member on friction in column-pad interface normal force in bents without uplift a) right column b) left column

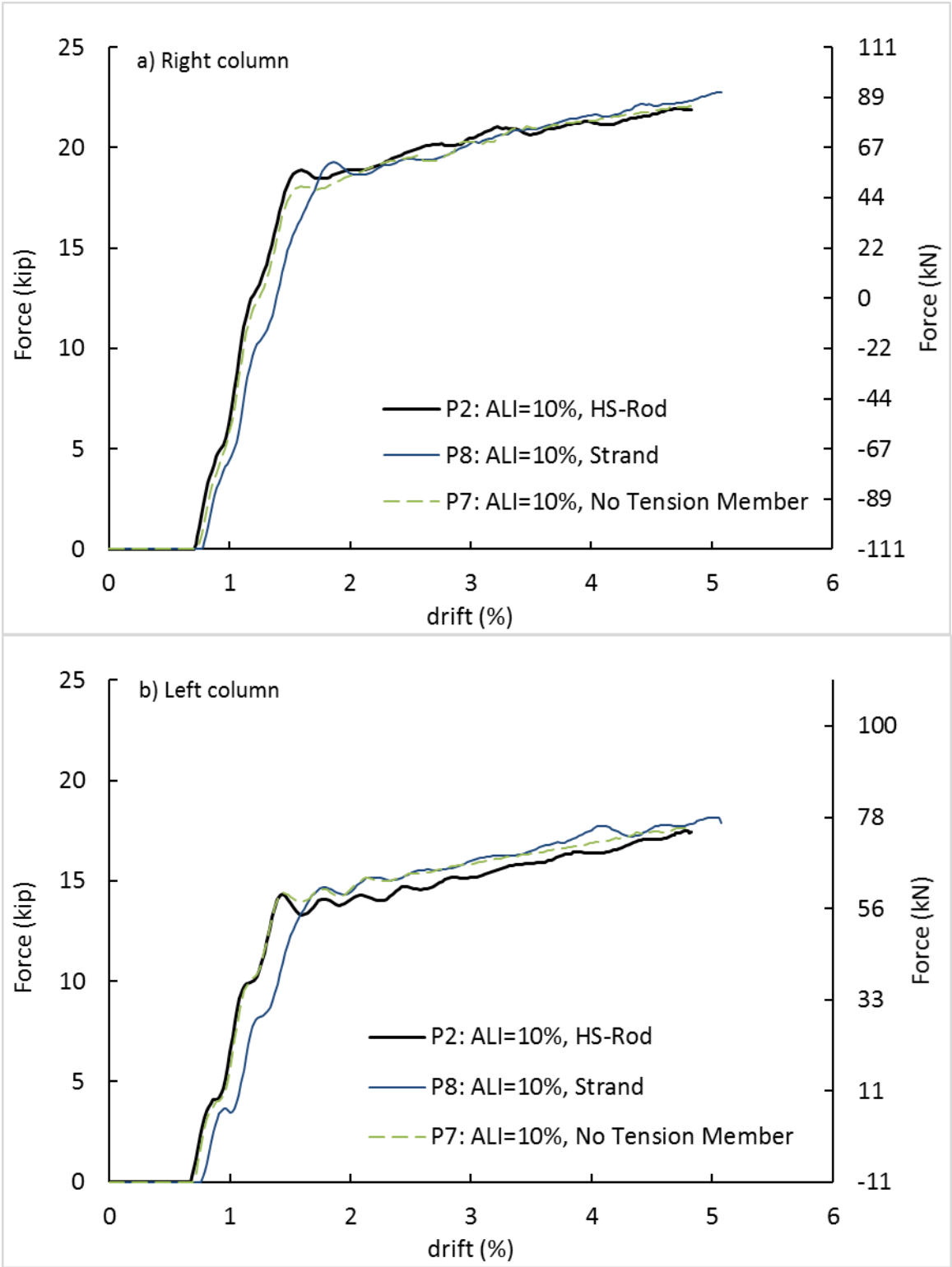

Fig. 5-44. Effect of tension member on contact force between pipes in bents without uplift a) right column b) left column

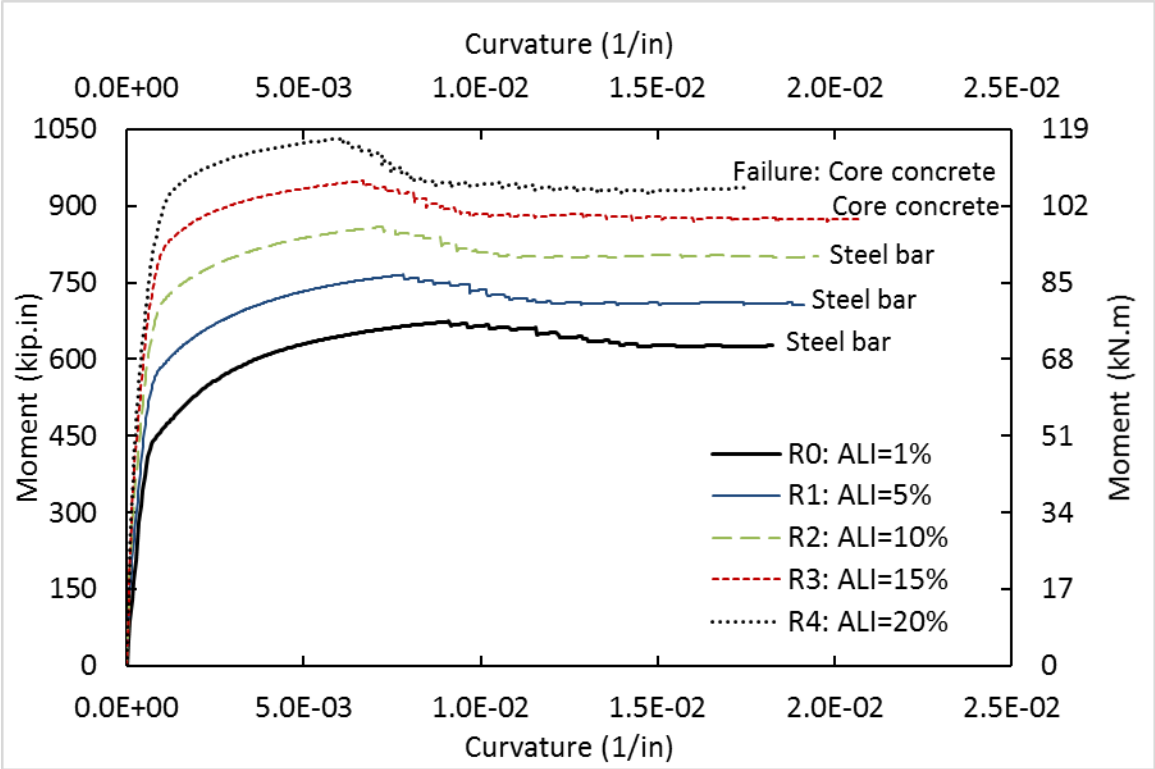

Fig. 5-45. Effect of ALI on moment-curvature relationship of rebar-pins

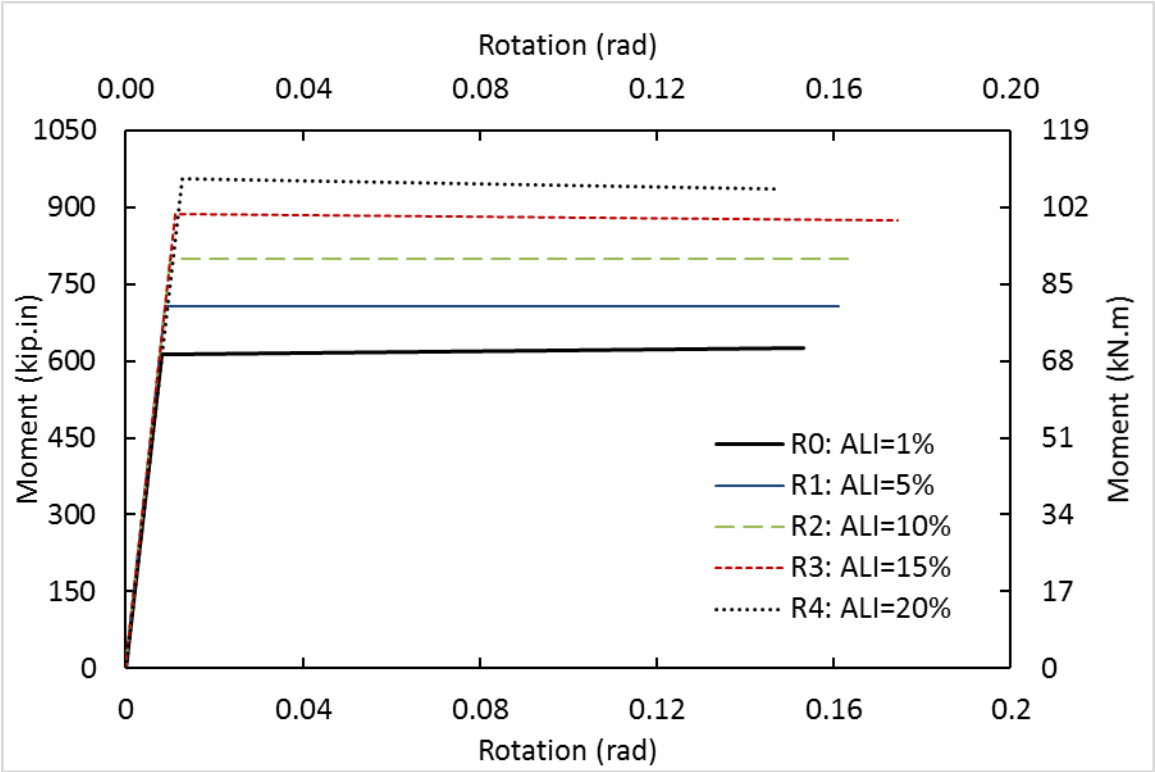

Fig. 5-46. Effect of ALI on moment-rotation relationship of rebar-pin springs

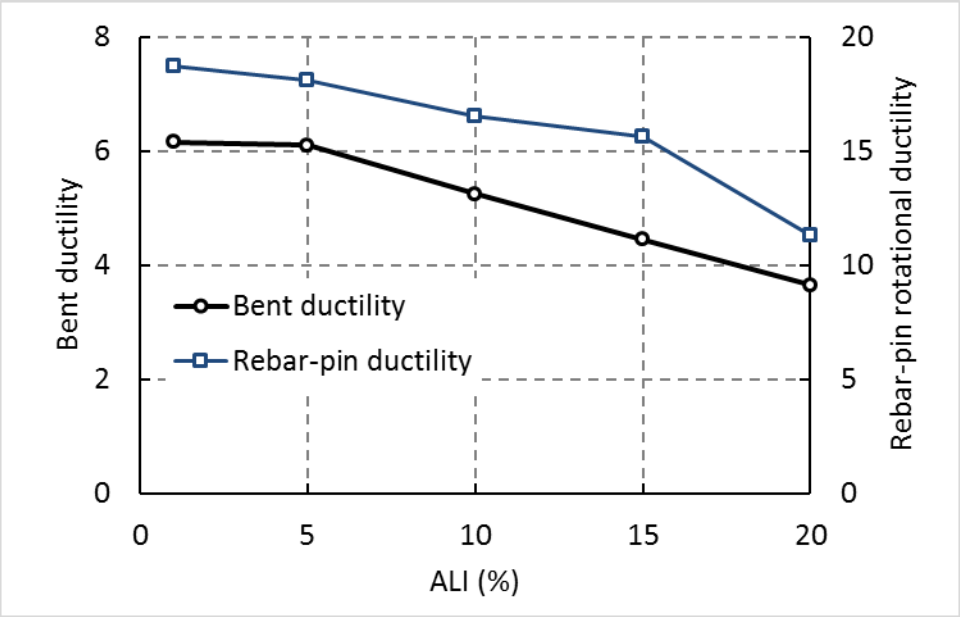

Fig. 5-47. Effect of ALI on bent displacement ductility and rebar-pin rotation al ductility

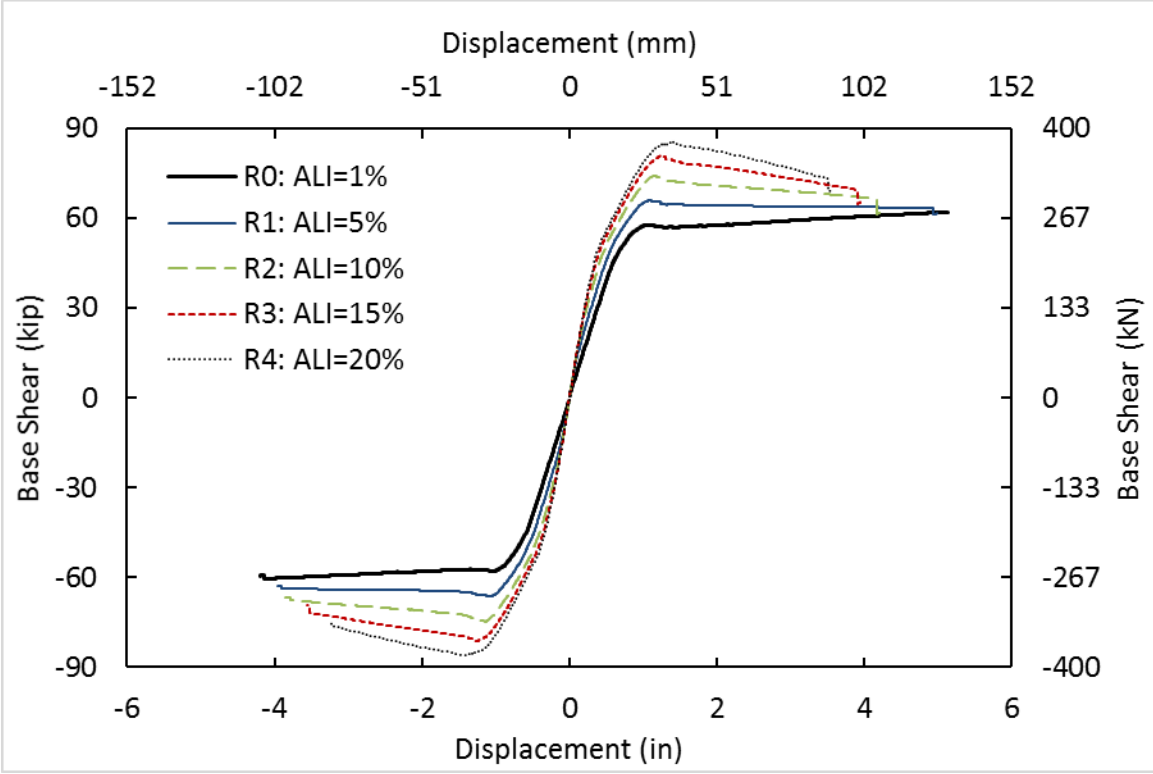

Fig. 5-48. Effect of ALI on pushover curve of bents

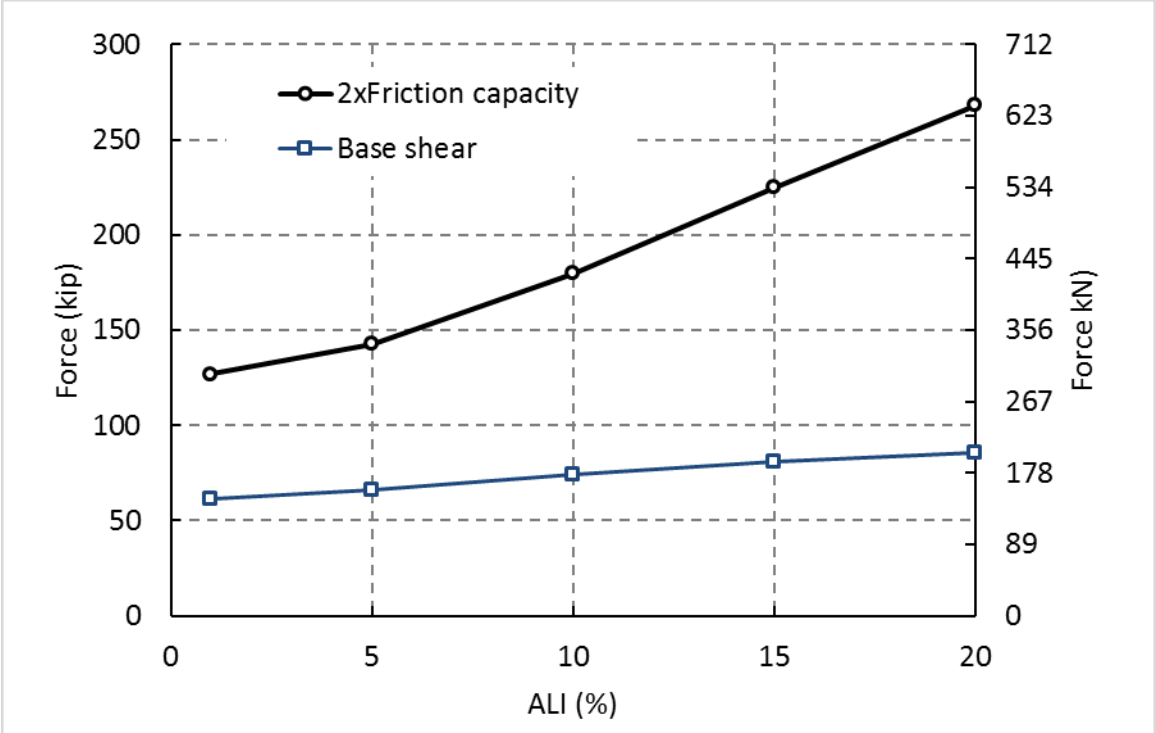

Fig. 5-49. Effect of ALI on base shear and friction capacity

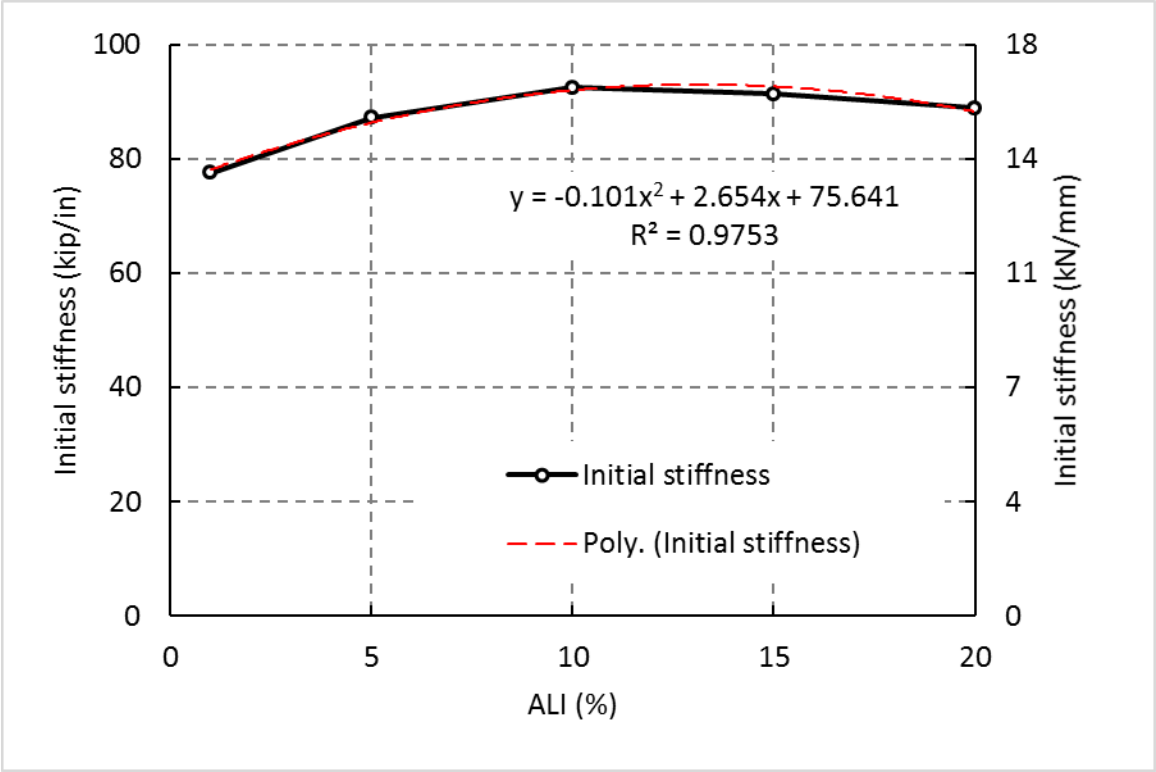

Fig. 5-50. Effect of ALI on initial stiffness of pushover curve

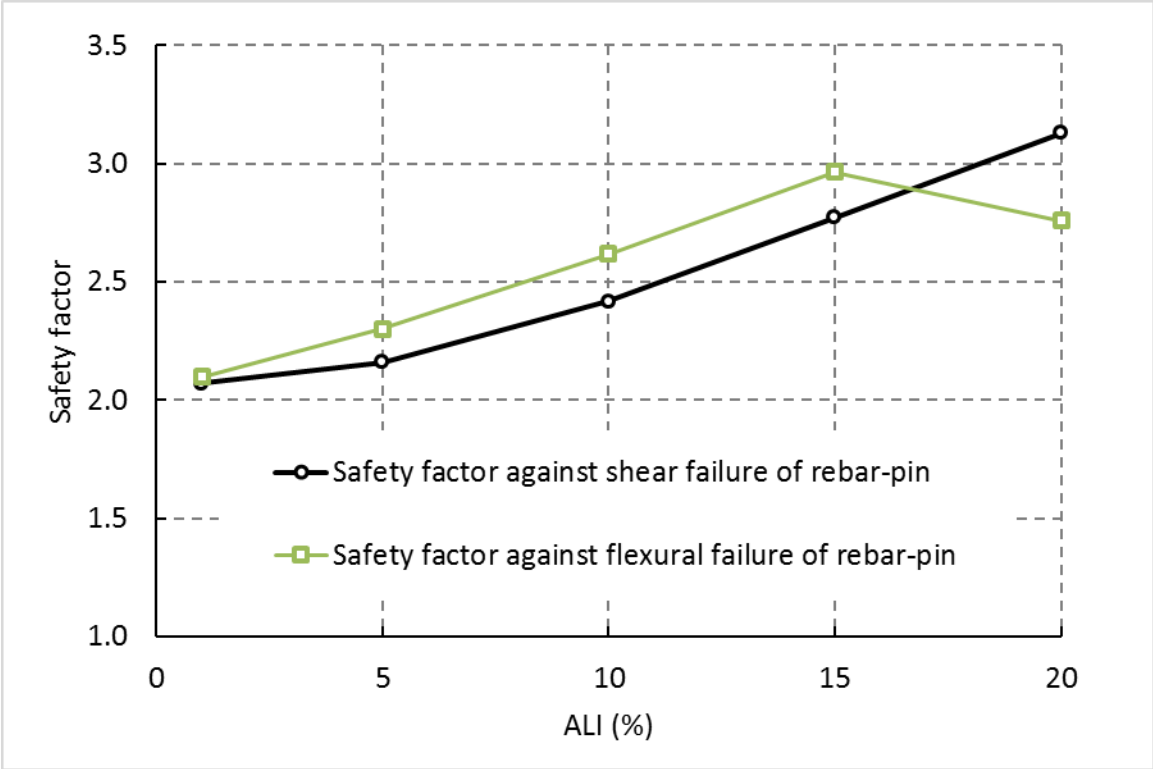

Fig. 5-51. Effect of ALI on the safety factors against shear and flexural failure

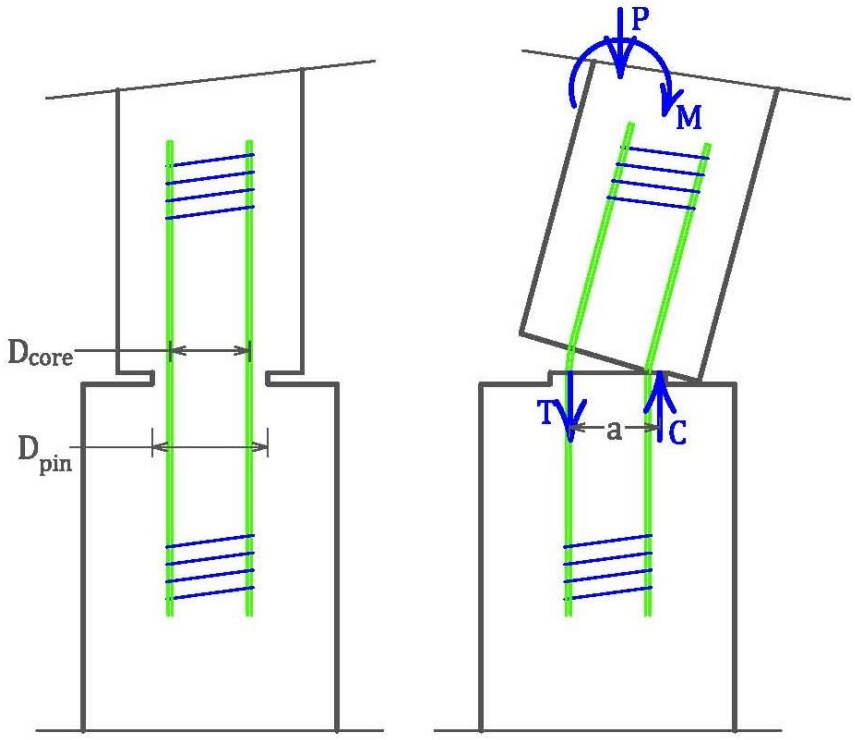

Fig. 5-52. Free-body diagram of rebar-pins

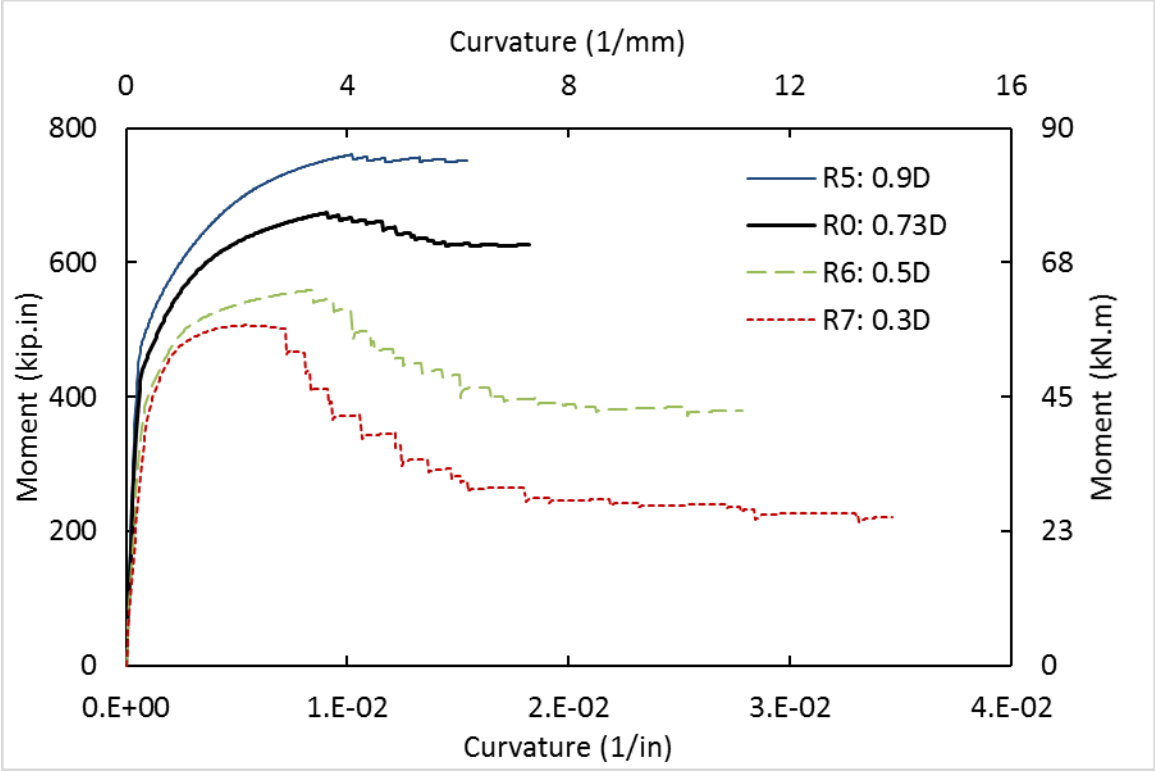

Fig. 5-53. Effect of core diameter on moment-curvature relationship

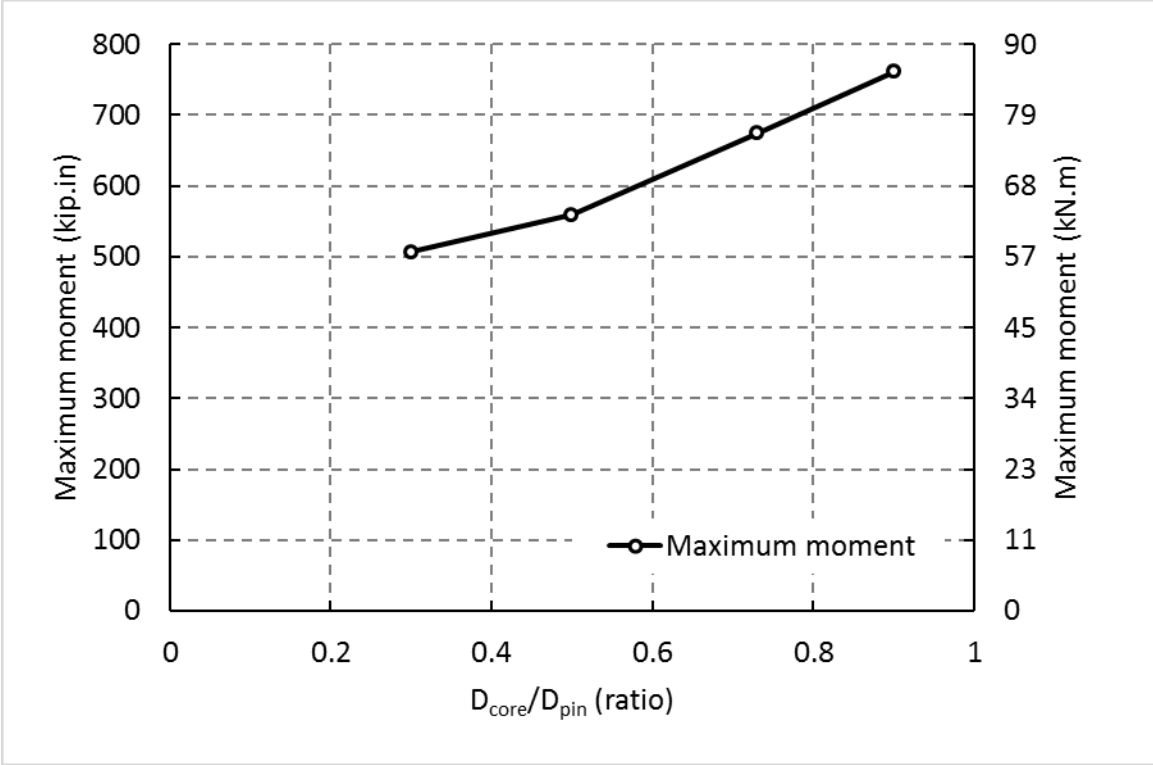

Fig. 5-54. Effect of core diameter on maximum rebar-pin moment

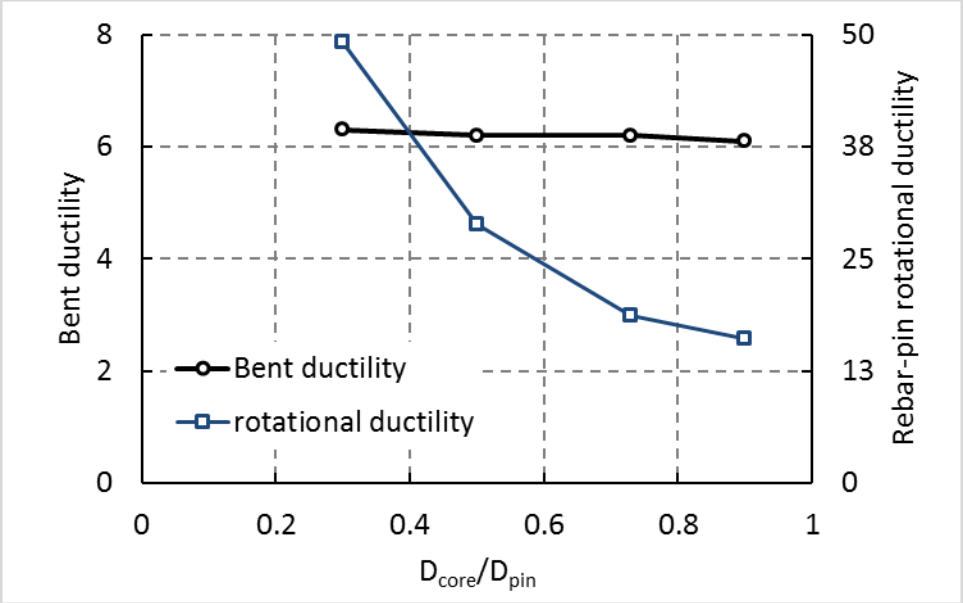

Fig. 5-55. Effect of core diameter on rotation ductility of rebar-pin and displacement ductility of bent

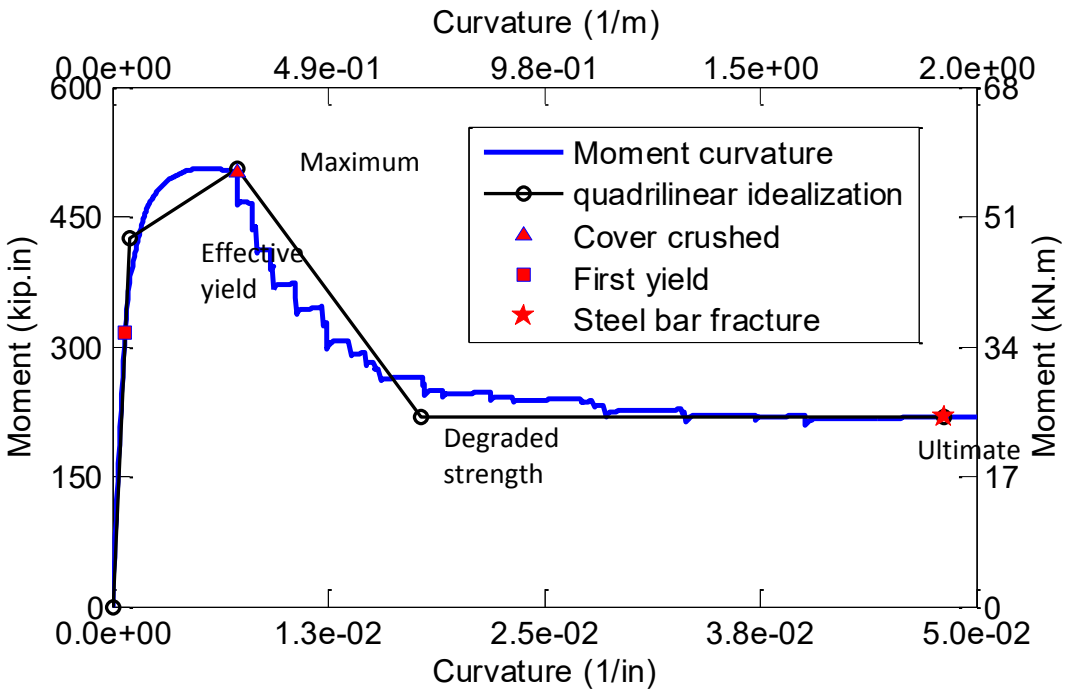

Fig. 5-56. Quadrilinear idealization of R7

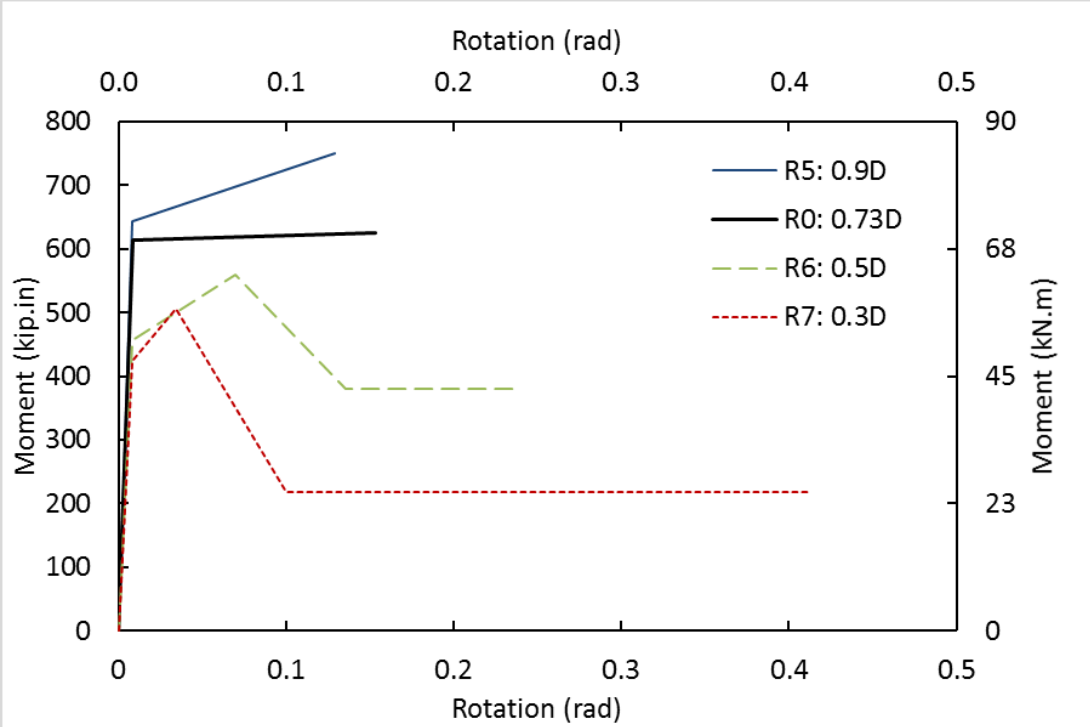

Fig. 5-57. Effect of core diameter on moment-rotation relationships of rebar-pin springs

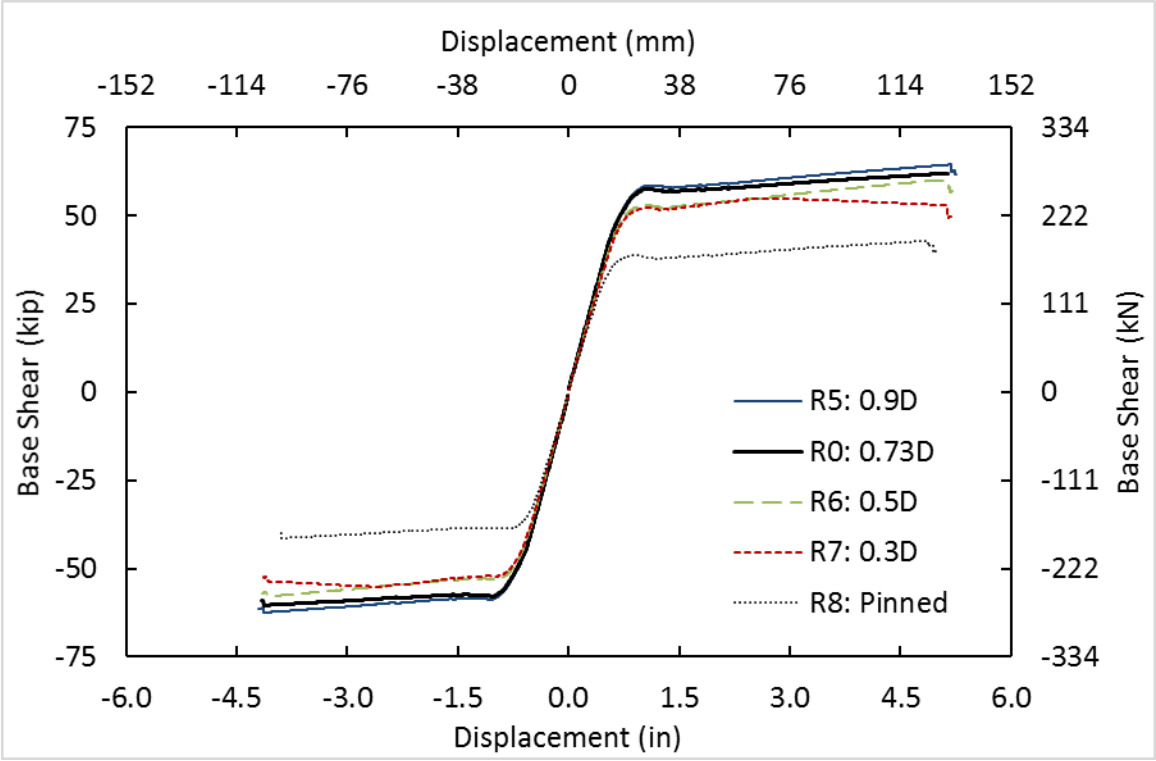

Fig. 5-58. Effect of core diameter on pushover curves of bents

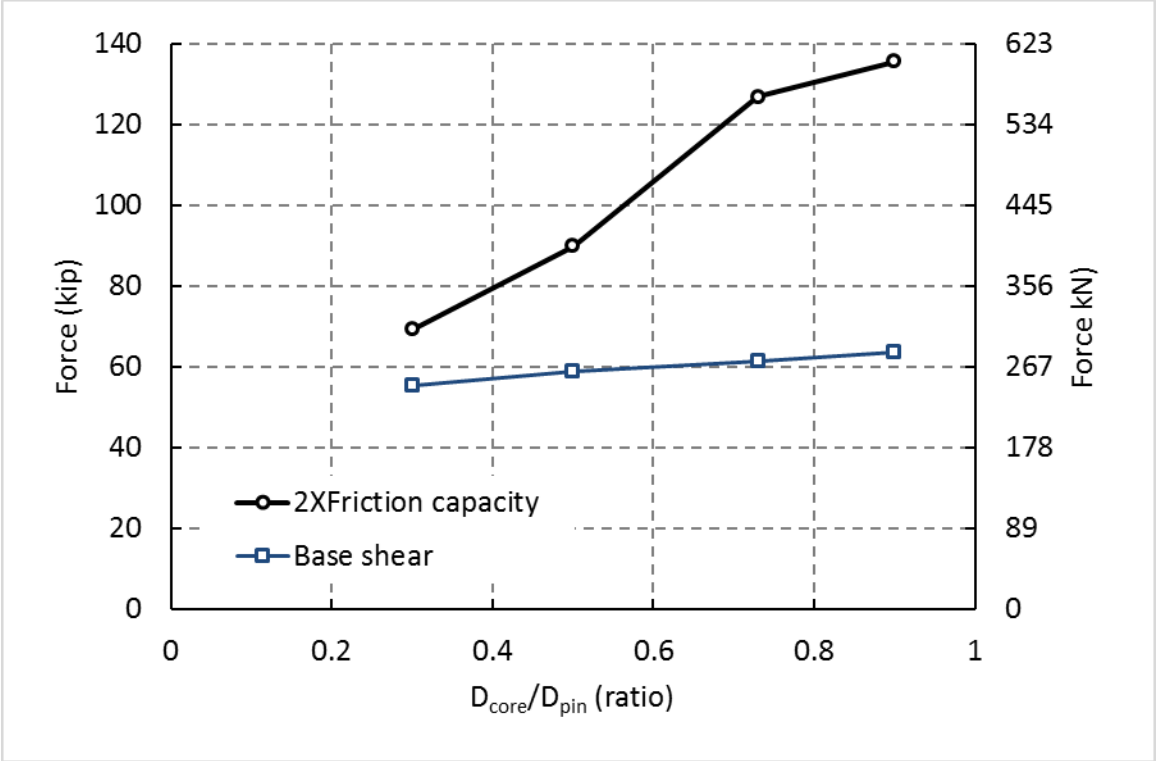

Fig. 5-59. Effect of core diameter on base shear and friction capacity

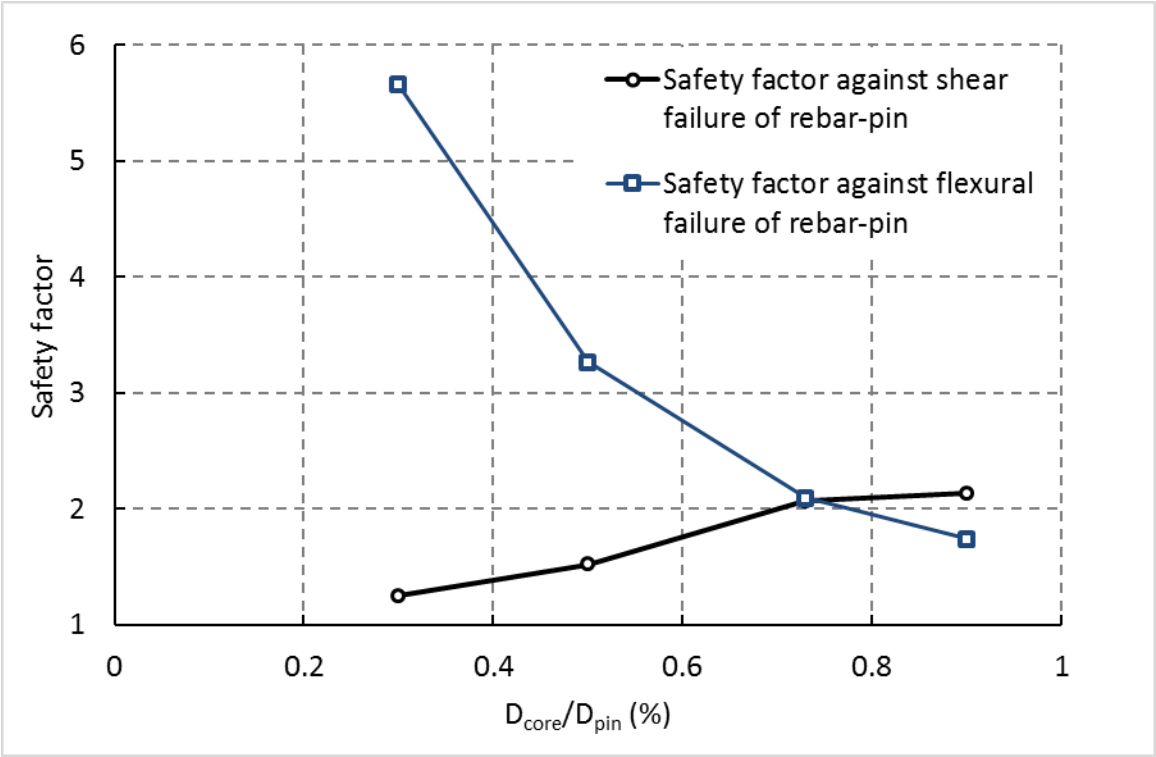

Fig. 5-60. Effect of core diameter on the safety factors against shear and flexural failure

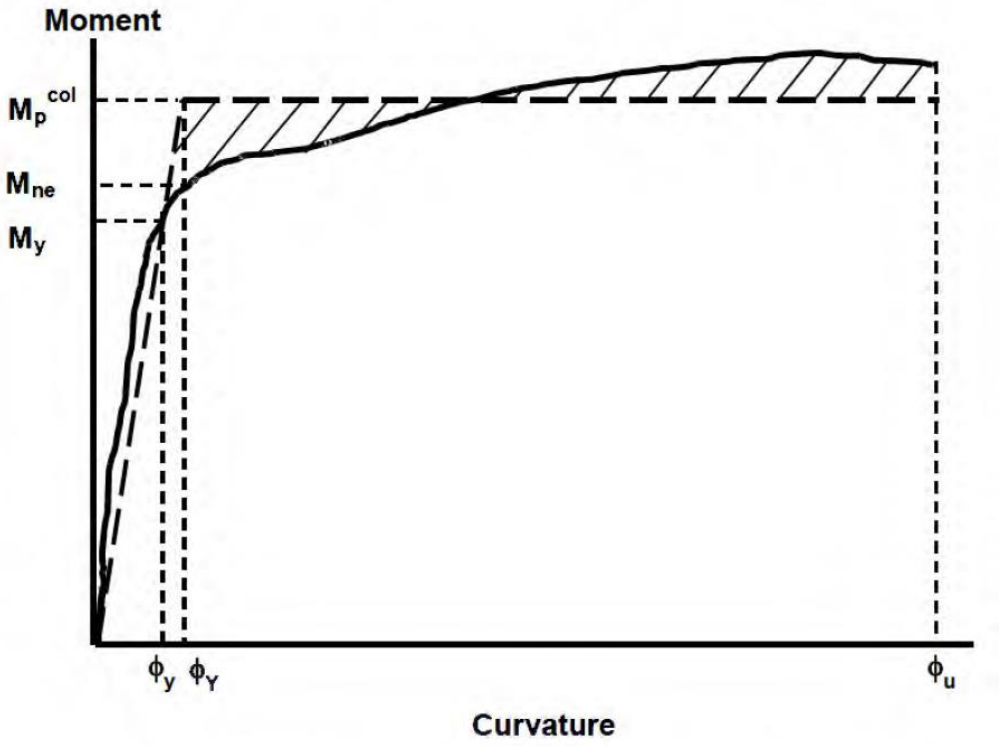

Fig. 6-1. Moment-curvature relationship (Caltrans, 2010)

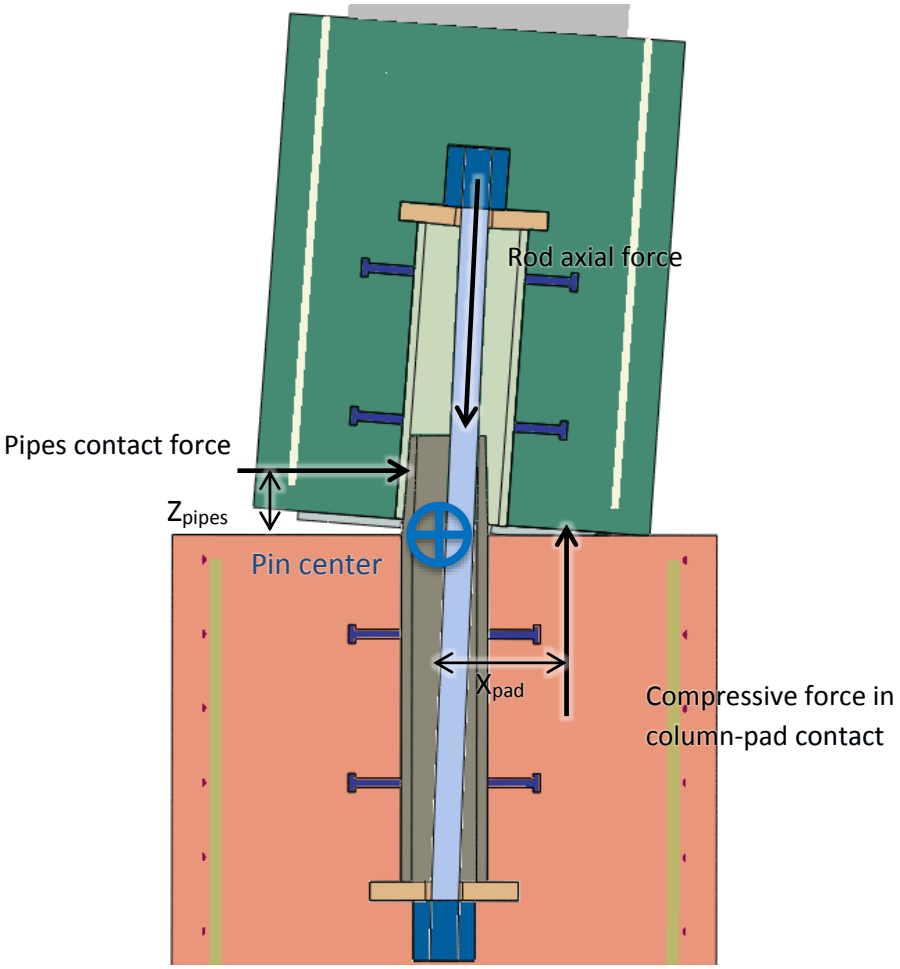

Fig. 6-2. Forces in pipe-pin

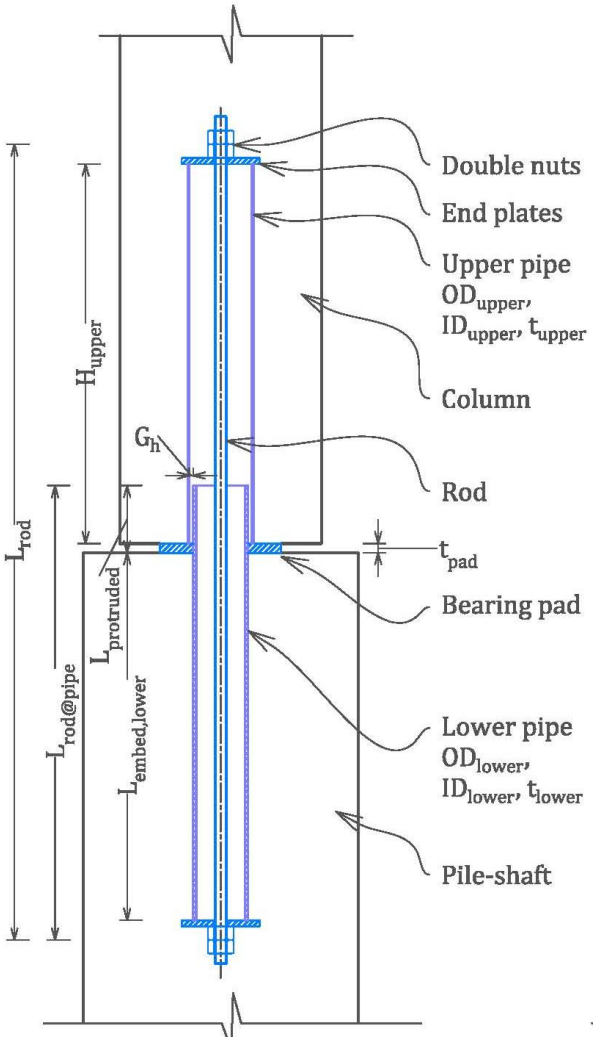

Fig. 6-3. Pipe-pin elements and dimensions

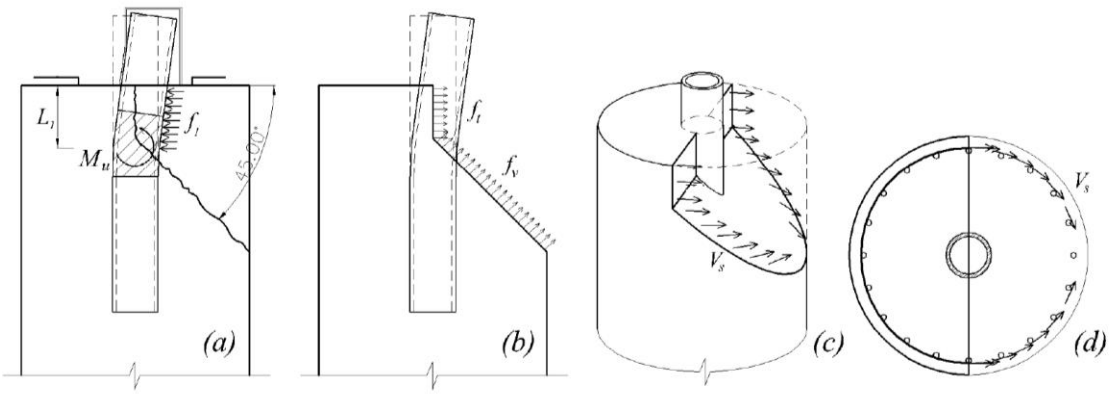

Fig. 6-4. Concrete bearing capacity of lower pipe in pile-shaft for zero axial load (Zaghi and Saiidi, 2010)

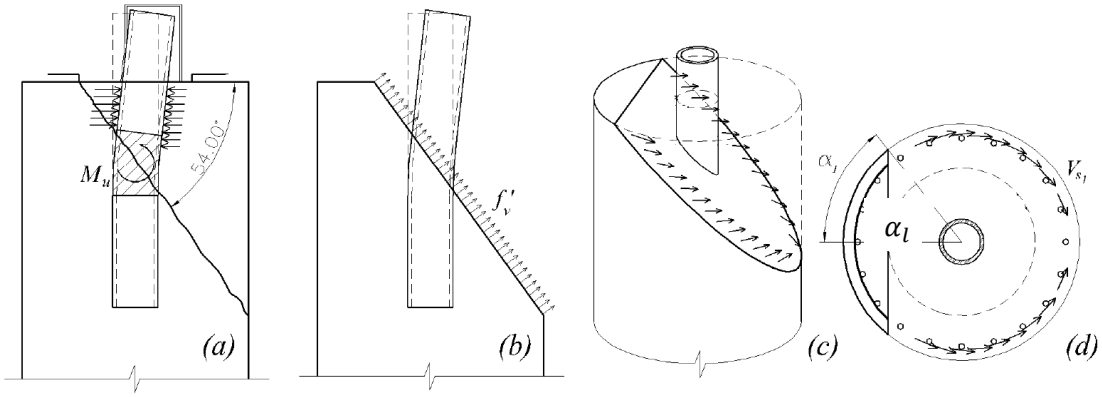

Fig. 6-5. Concrete bearing capacity of lower pipe in pile-shaft for maximum effective axial capacity (Zaghi and Saiidi, 2010)

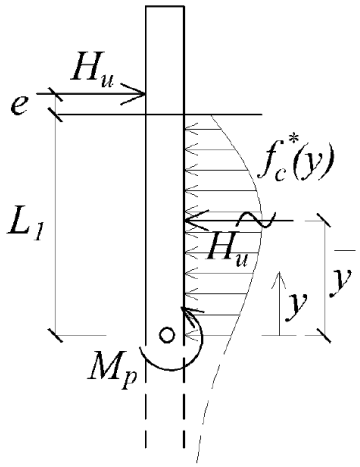

Fig. 6-6. Free- body diagram of lower pipe (Zaghi and Saiidi, 2010)

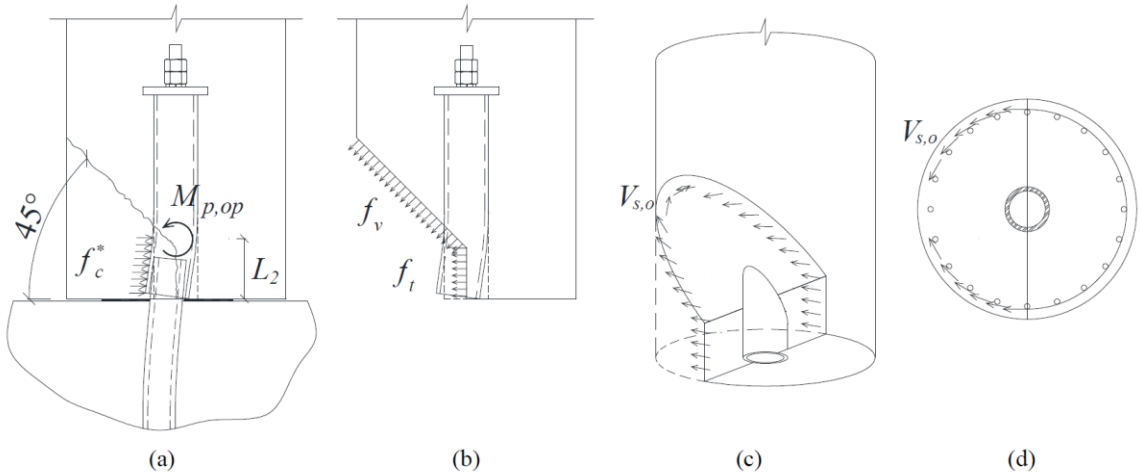

Fig. 6-7. Concrete bearing capacity of upper pipe in column for zero axial load (adopted from Mehrsoroush and Saiidi, 2014)

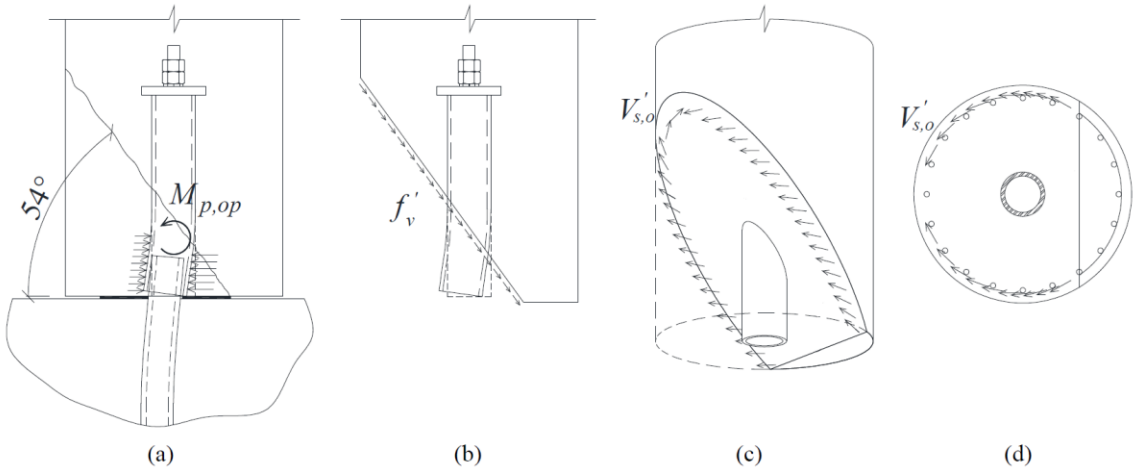

α_u

Fig. 6-8. Concrete bearing capacity of upper pipe in column for maximum effective axial capacity (adopted from Mehrsoroush and Saiidi, 2014)

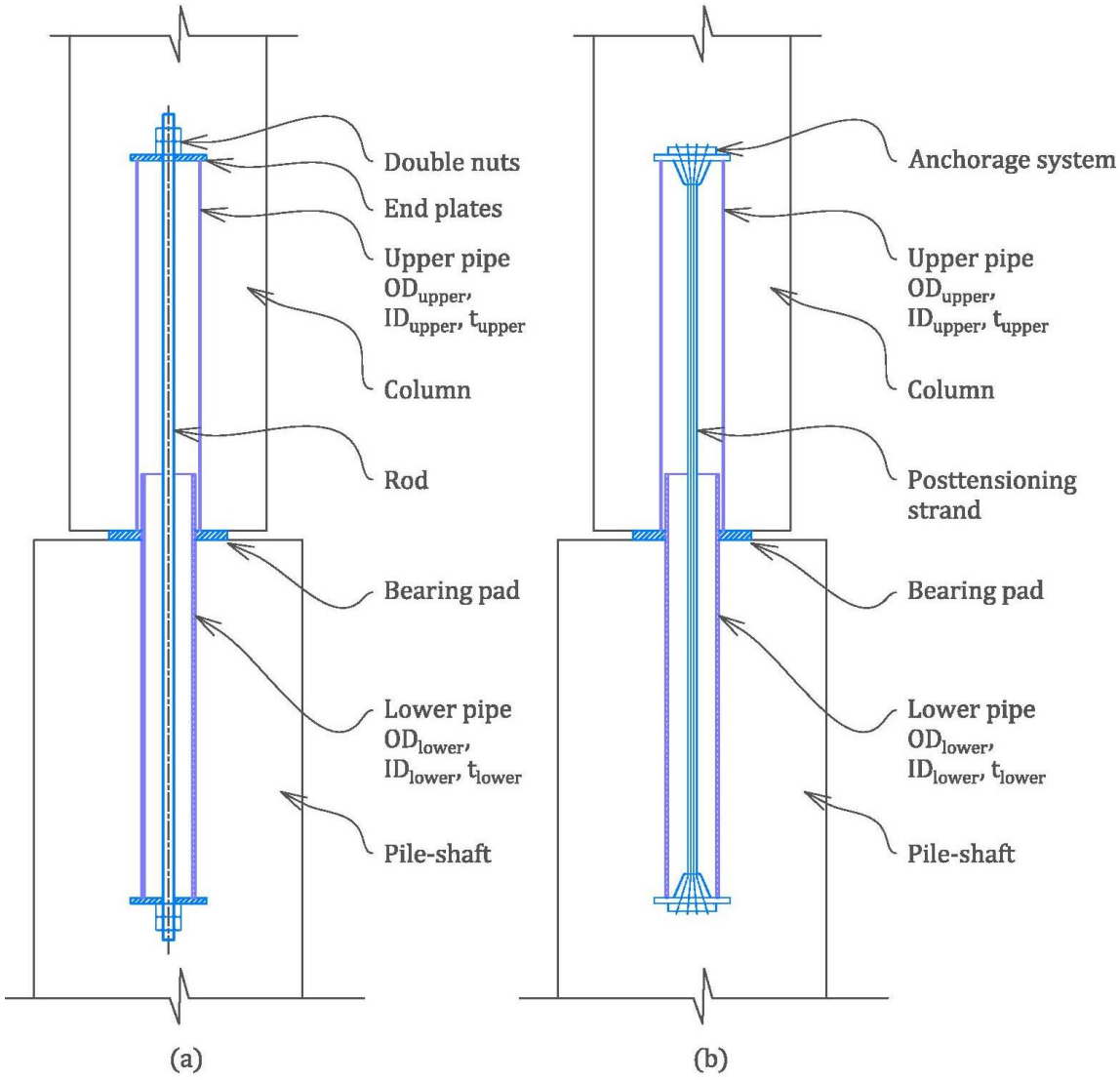

Fig. 6-9. Pipe-pin connection elements with tension member of a) rod b) strand

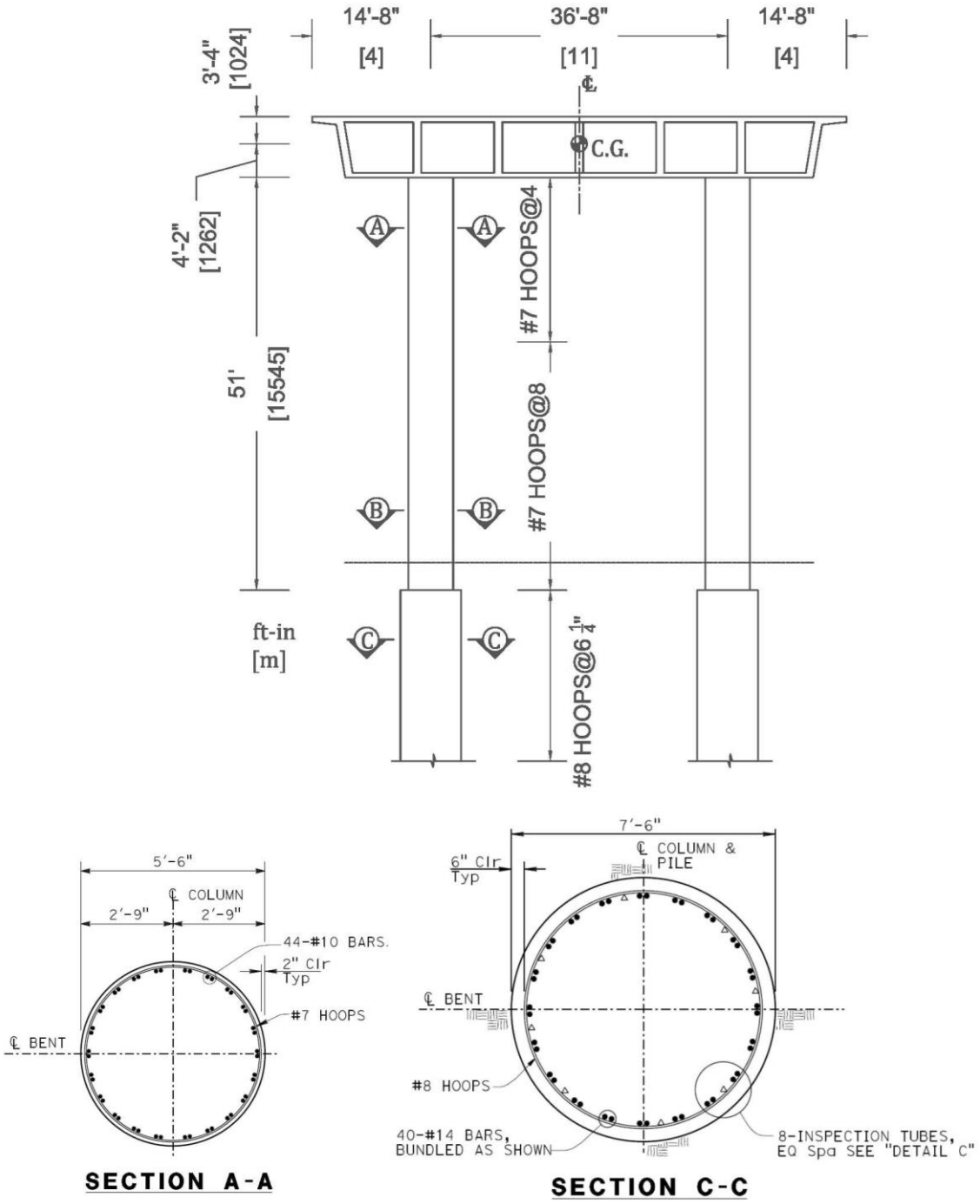

Fig. 6-10. Design example bent on pile-shafts

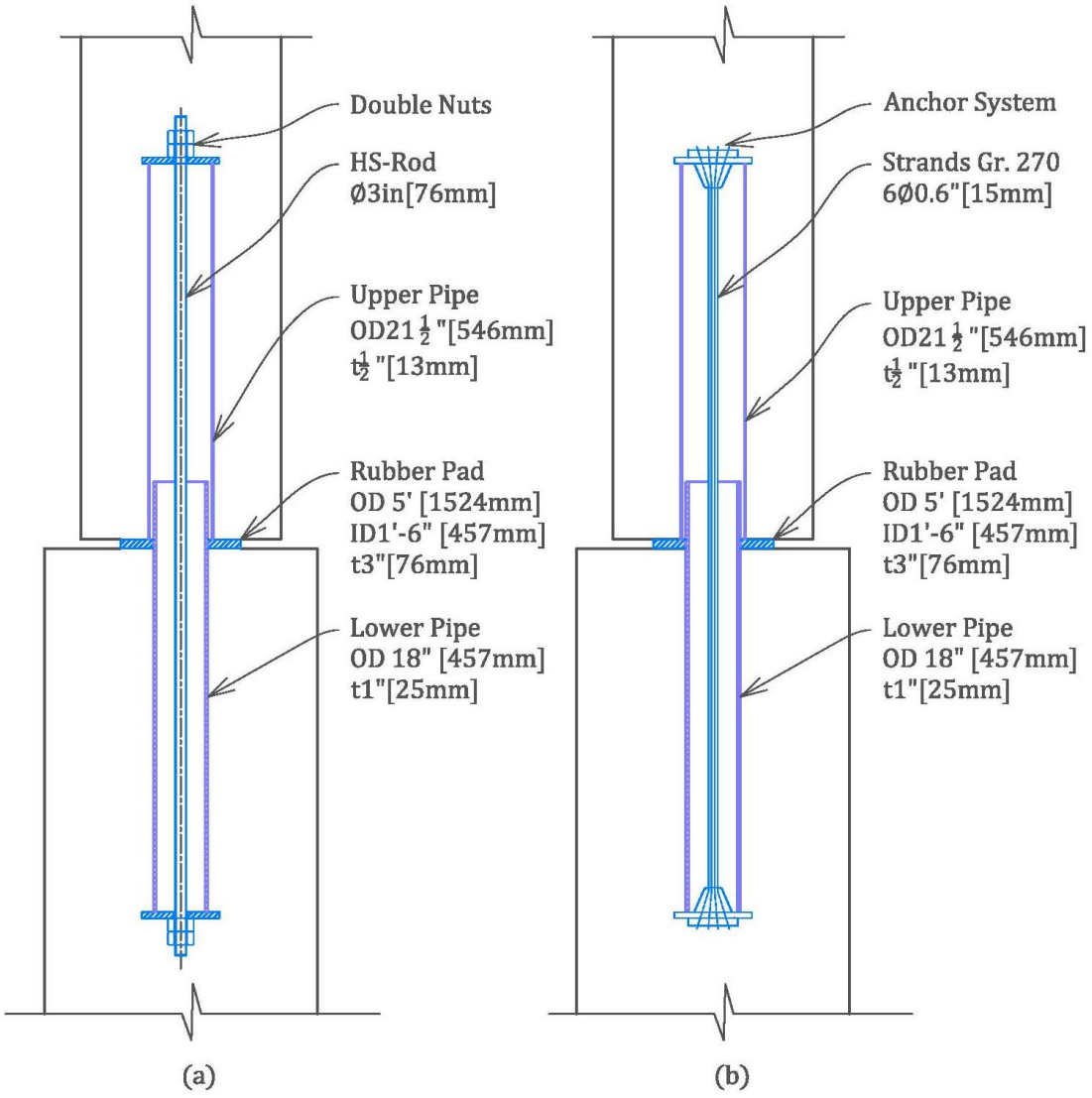

Fig. 6-11. Design example, pipe-pin details with (a) rod (b) strands

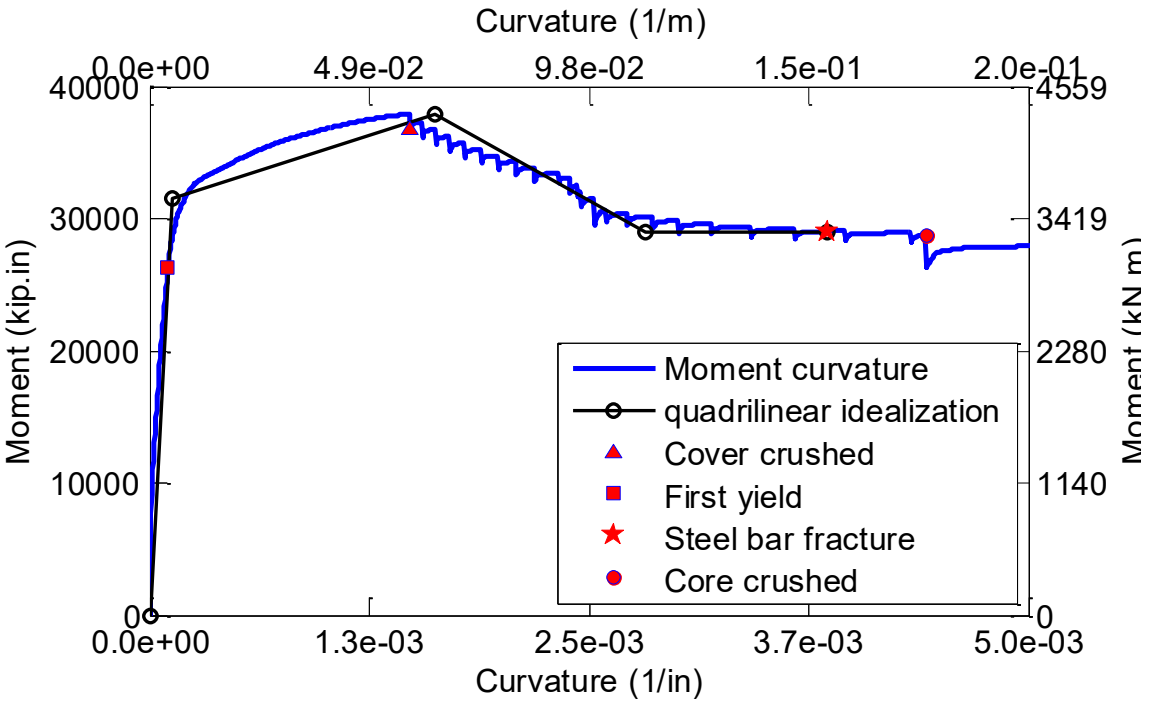

Fig. 6-12. Moment-curvature relationship for rebar-pin in design example

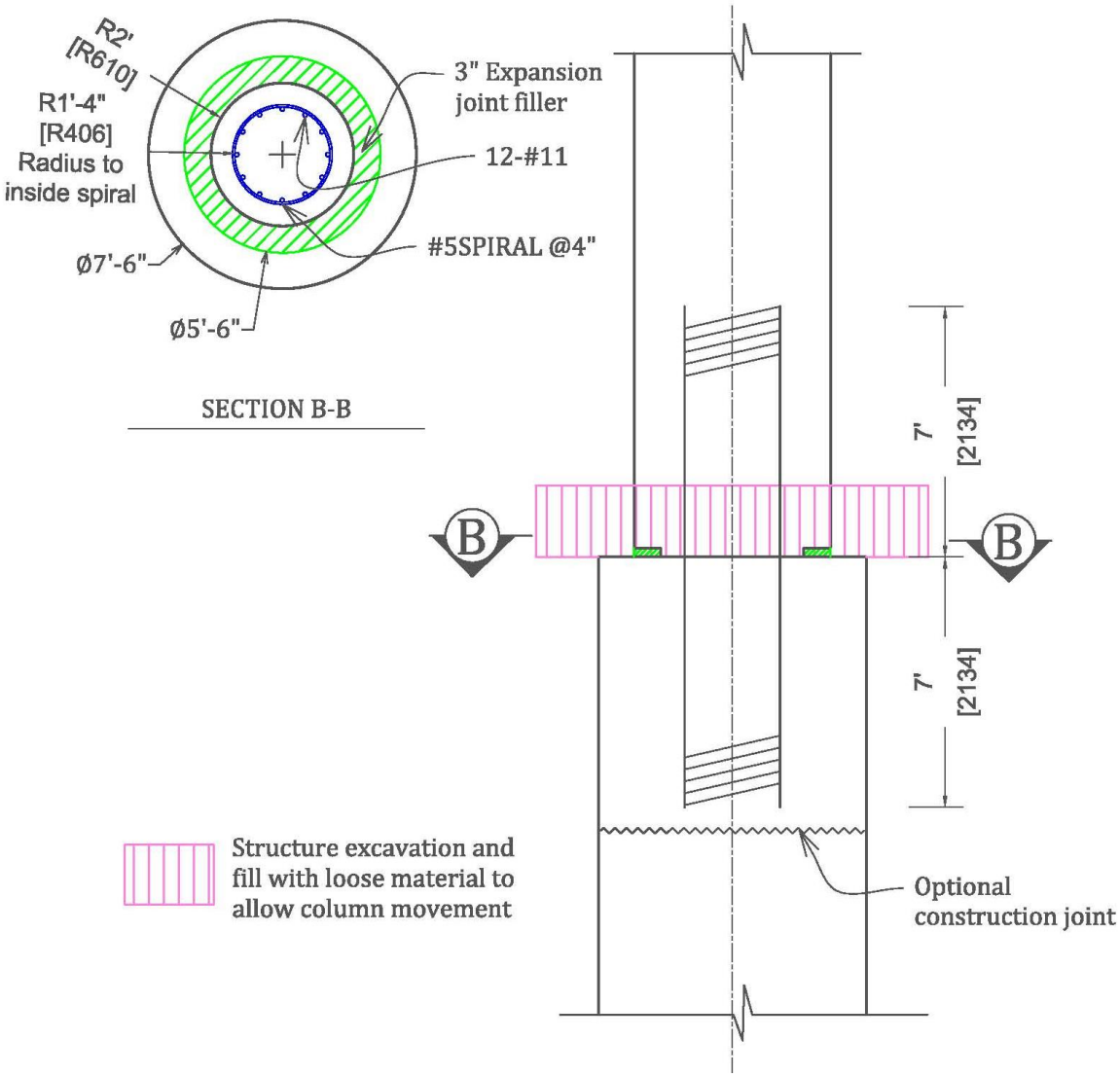

Fig. 6-13. Design example, rebar-pins detail

Appendix A. Determining Dynamic Characteristics from Shake-Table Tests

Dynamic properties of structures are period, damping, number of degree of freedoms (DOFs), and mode shapes. Since the specimen was restricted by the guide structure to move in one direction, the specimens were considered as a single-degree-of-freedom (SDF) problem (section 3.2.4 and 3.3.4). Natural periods and damping of the specimen was calculated from the response to the white noise motions. The fundamental period is associated with the fundamental mode with the first natural period (frequency) of the structure. The method to determine the natural frequency of structure from transfer function is explained in this appendix.

Based on dynamic equilibrium, the equation of motion for a SDF structure subjected to harmonic base motion is as follows (Chopra, 2007).

$$m\ddot{u} + c\dot{u} + ku = -m\ddot{u}_g(t) \tag{A1-1}$$

$$\ddot{u}_g = e^{i\omega t} \tag{A1-2}$$

where,

$i = \sqrt{-1}$

m: mass of structure, kip/in.s^2 [kg]

c: damping of the structure, kip/in.s [N/mm.s]

k: stiffness of structure, kip/in [kN/mm]

u: relative displacement, in [mm]

$\ddot{u}_g$ ground (shake table) acceleration, in/s^2 [mm/s^2]

ω: frequency of harmonic motion, Hz

The steady-state response of Eq. A1-1 is the following.

$$u(t) = H_u(\omega) \cdot e^{i\omega t} \tag{A1-3}$$

where,

$H_u(\omega)$: transfer function

Differentiating and substituting Eq. A1-3 in the equation of motion result in the following equation.

$$H_u(\omega) \cdot e^{i\omega t} \cdot (-m\omega^2 + i\omega c + k) = -m \cdot e^{i\omega t} \tag{A1-4}$$

$$H_u(\omega) = \frac{-m}{-m\omega^2 + i\omega c + k} = \frac{1}{\omega^2 - \omega_n^2 - 2\xi\omega\omega_n i} \tag{A1-5}$$

where ,

$$\frac{k}{m} = \omega_n^2 \tag{A1-5}$$

$$\frac{c}{m} = 2 \cdot \xi \cdot \omega_n \tag{A1-5}$$

The solution of the equation for absolute acceleration is the following (Maddaloni, Ryu, & Reihorn, 2011).

$$\ddot{a}(t) = \ddot{u}(t) + \ddot{u}_g(t) = -\omega^2 H_u e^{i\omega t} + e^{i\omega t} \tag{A1-6}$$

$$\ddot{a}(t) = (1 - \omega^2 \cdot H_u) \cdot \ddot{u}_g(t) \tag{A1-7}$$

where,

$\ddot{a}(\omega)$: absolute acceleration response of SDF

$H(\omega)$: Transfer Function of displacement

The *transfer function*, TF(ω), is defined as the ratio of the response to the base motion of the structure. Transfer function is a function of the structural properties and forcing frequency.

$$TF(\omega) = \frac{\ddot{a}(t)}{\ddot{u}_g(t)} TF(\omega) = 1 + \frac{\omega^2}{\omega^2 - \omega_n^2 - 2\xi\omega\omega_n i} \tag{A1-8}$$

Based on Eq. A1-5, TF has a singularity at the natural frequency of the structure. The natural frequency of structure is found by calculating the transfer function of cap beam acceleration to table acceleration. The natural frequency of the specimen is the frequency corresponding to the peak transfer function.

It is customary in structural engineering to select natural frequency of the structure as the frequency at the peak Fast Fourier Transform (FFT) of response to the white noise motion. The FFT of a perfect white noise is proportion to the transfer function because all the input frequencies have equal amplitudes. However, shake tables could not generate a perfect white noise. That difference was significant in the white noise motion prior to Run-9 for BPSA. The amplitudes of the FFT were not equal near the natural frequency. As a result, FFT of the response carries two peaks, which are marked with solid arrows in Fig. A-1. However, the TF has only one crest near natural period, which is marked with a dashed arrow in Fig. A-1. Therefore, the natural frequencies of the specimens were determined from TF using *tfestimate* function in Matlab.

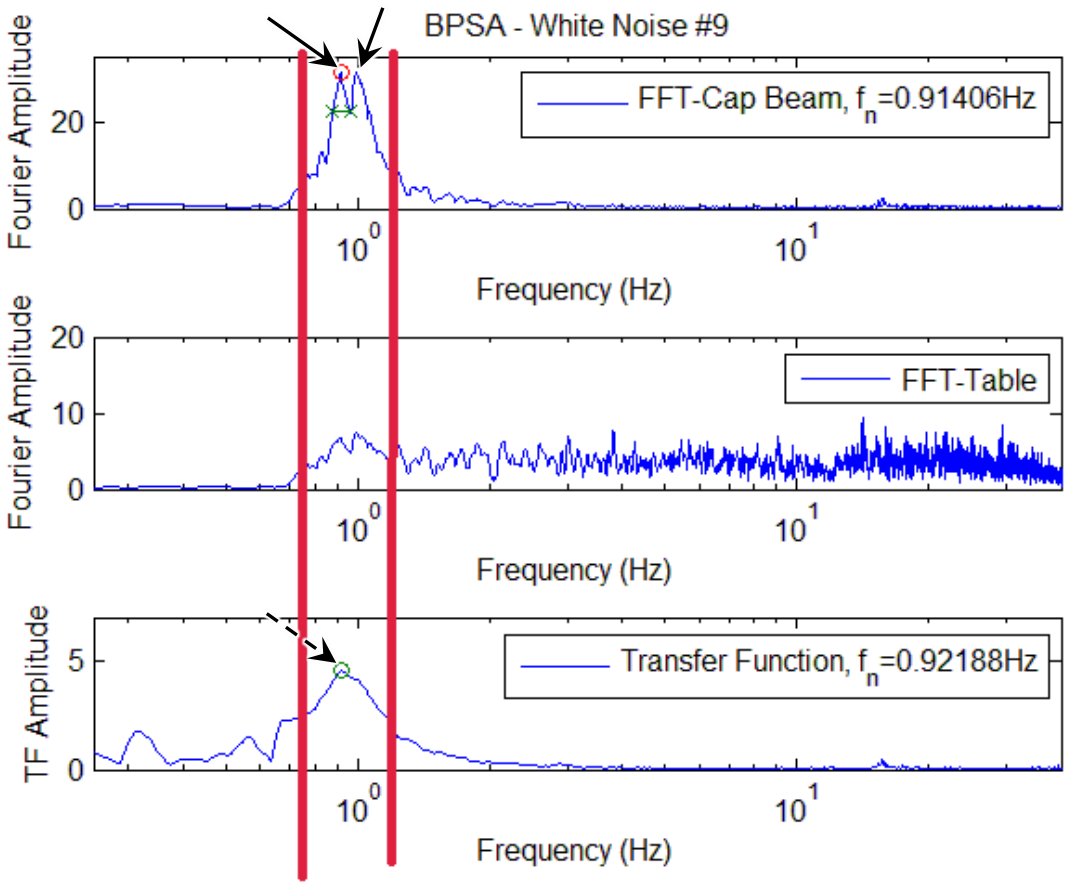

Fig. A-1. Comparison of FFT and TF of white noise prior to Run-9

Appendix B. BPSA Static Numerical Simulation Using Simple Stick Model

Test simulation using sectional Analysis

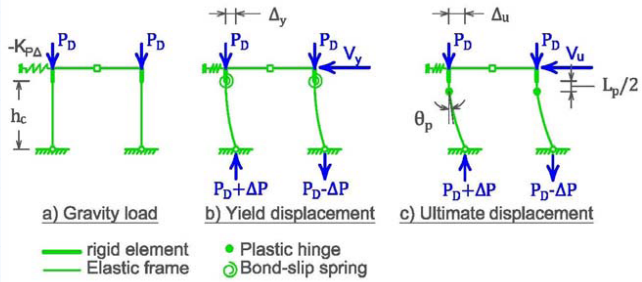

Fig. B-1. BPSA Structural Model

Frame Geometry

Column	$Dc := 16\ in$	$hc := 64\ in$	$gap := 0.25\ in$	
Cap Beam	$hcb := 24\ in$	$bcb := 24\ in$	$bay := 7\ ft$	$overhange := 26.0\ in$
Pedestal	$dp := 22\ in$	$hp := 30\ in$		

Weight

$W_{cap} := 4.5\ kip$ Cap beam + Post-tensioning system

Dead load on the column: $P_{dl} := 4.5\ kip$ $K_{P\Delta} := 546\ \frac{lbf}{in}$

Column Sectional Properties

Reinforcing detail: $\rho = 1.39\%$ $\rho_s = 0.58\%$

Plastic Hinge Length: $f_y := 72.08\ ksi$ $d_{bl} := 0.5\ in$

$$Lp := \max\left(0.08\ hc + 0.15 \cdot \frac{f_y}{ksi} \cdot d_{bl}, 0.3\ \frac{f_y}{ksi} \cdot d_{bl}\right) = 10.81\ in$$ (Paulay & Priestley, 1992)

Confined material Properties for CIP

$f_c = 9.15\ ksi$ $f_{cc} = 10.24\ ksi$ $\varepsilon_{cc} = 3.19 \cdot 10^{-3}$ $\varepsilon_{cu} = 10.77 \cdot 10^{-3}$

Confined material Properties for PC

$f_c = 6.91\ ksi$ $f_{cc} = 7.99\ ksi$ $\varepsilon_{cc} = 3.56 \cdot 10^{-3}$ $\varepsilon_{cu} = 12.68 \cdot 10^{-3}$

****

Pipe-Pin Springs:

****

height of plate+waher+nuts: $h_{end} := (0.75 + 0.5 + 1.25)\ in = 2.50\ in$

height of lower pipe: $h_{lower} := 12\ in + gap + h_{end} = 14.75\ in$

height of upper pipe: $h_{upper} := 14\ in + h_{end}$

effective length rod: $L_{rod} := h_{lower} + h_{upper} = 31.25\ in$

tensile area of HS rod: $A_t := 0.9697\ in^2$

modulus elasticity of rod: $E_{rod} := 29000\ ksi$

horizontal clearance between pipes: $S_g := 0.25\ in$

geometry of pad: $D_{pad} := 12\ in \quad D_{hole} := 3.625\ in \quad t_{pad} := 0.3\ in$

elasticity of pad: $G_{pad} := 670\ psi \quad E_{pad} := 3\ G_{pad} = 2010\ psi$

$$A_{pad} := \frac{\pi}{4} \cdot \left(D_{pad}^{\ 2} - D_{hole}^{\ 2} \right) = 102.78\ in^2$$

$$I_{pad} := \frac{\pi}{64} \left(D_{pad}^{\ 4} - D_{hole}^{\ 4} \right) = 1009.40\ in^4$$

tensile stiffness of rod: $K_{rod} := \frac{E_{rod} \cdot A_t}{L_{rod}} = 899.9\ \frac{kip}{in}$

axial stiffness of pad: $K_{c.pad} := \frac{E_{pad}\ A_{pad}}{t_{pad}} = 689\ \frac{kip}{in}$

Contact rotation: $\theta_g := \frac{2 \cdot gap}{Dc} = 0.031\ rad$

Pipe-Pin Moment at closure: $M_g := \frac{K_{c.pad}}{K_{c.pad} + K_{rod}} \left(\frac{D_{pad}}{2}\ K_{rod} \cdot \theta_g + P_{dl} \right) \cdot \frac{D_{pad}}{2}$

$$K_\theta := \frac{M_g}{\theta_g} = 14418\ kip \cdot in$$

****

Cap Beam Springs:

****

Axial and rotational stiffness:

bolt : $d_{bolt} := 1\ in$ $E_{bolt} := 29000\ ksi$

$L_{shank} := 3.375\ in - 1.75\ in + \frac{1\ in}{2} = 2.13\ in$ $A_{shank} := \frac{\pi}{4} d_{bolt}^{2} = 0.79\ in^{2}$

$L_{thread} := 1.75\ in$ $A_{tensile.Area} := 0.6060\ in^{2}$

$k_{thread} := \frac{A_{tensile.Area} \cdot E_{bolt}}{L_{thread}} = 10042\ \frac{kip}{in}$

$k_{shank} := \frac{A_{shank} \cdot E_{bolt}}{L_{shank}} = \left\langle 1.07 \cdot 10^{4} \right\rangle \frac{kip}{in}$

bolt stiffness: $k_{bolt} := \left(\frac{1}{k_{shank}} + \frac{1}{k_{thread}} \right)^{-1} = \left\langle 5.18 \cdot 10^{3} \right\rangle \frac{kip}{in}$

stiffness of the plate under head:

$d := d_{bolt}$ $D := 1.5 \cdot d_{bolt}$ $t := 1.5\ in$

$$k_1 := \frac{0.577\ \pi \cdot E_{bolt} \cdot d}{\ln\left(\frac{(1.15 \cdot t + D - d)\ (D + d)}{(1.15 \cdot t + D + d)\ (D - d)} \right)} = \left\langle 5.43 \cdot 10^{4} \right\rangle \frac{kip}{in}$$

stiffness of threaded plate:

$d := d_{bolt}$ $D := 1.5 \cdot d_{bolt}$ $t := 3.375\ in - t = 1.88\ in$

$$k_2 := \frac{0.577\ \pi \cdot E_{bolt} \cdot d}{\ln\left(\frac{(1.15 \cdot t + D - d)\ (D + d)}{(1.15 \cdot t + D + d)\ (D - d)} \right)} = \left\langle 5.02 \cdot 10^{4} \right\rangle \frac{kip}{in}$$

stiffness of one bolt connection: $k_{tension} := \left(\frac{1}{k_1} + \frac{1}{k_2} + \frac{1}{k_{bolt}} \right)^{-1} = \left\langle 4.32 \cdot 10^{3} \right\rangle \frac{kip}{in}$

Tensile stiffness of the load cell connection:

$$K_{tension} := \frac{1}{2} \cdot \langle 4 \cdot k_{tension} \rangle = 8649 \ \frac{kip}{in}$$ very stiff

Rotational stiffness of the load cell connection:

$$K_{\theta.CB} := \frac{1}{2} \cdot \left(4 \cdot k_{tension} \cdot (6 \ in)^2 \right) = 311374 \ kip \cdot in$$

Shear stiffness:

The plates acted in friction with the threashold at 30 kips base shear.
The entire sliding occured untill the plated hit the bolt.

Diameters of the holes: $d_{loadcell.plate} := 1.25 \ in$ $d_{bolt} = 1.00 \ in$

$$slide := \frac{d_{loadcell.plate} - d_{bolt}}{2} = 0.13 \ in$$

$$l_{loadcell} := 1 \ ft + 3.675 \ in$$

$$\theta_{slide} := \frac{slide}{\frac{\langle bay - l_{loadcell} \rangle}{2}} = \langle 3.66 \cdot 10^{-3} \rangle \ rad$$

Bent displacement due to the sliding in loadcell prior to post-tensioning

$$\Delta_{y.CB.slide} := \theta_{slide} \cdot \left(hc + \frac{hcb}{2} \right) = 0.28 \ in$$

****

South Direction

****

Columns Sectional Analysis

Try-1: Cap beam dead load for axial load: $P_{dl} = 4.50\ kip$

CIP	PC
$Mu_{CIP} := 1276\ kip \cdot in$	$Mu_{PC} := 1231\ kip \cdot in$
$\phi_{u1} := 6.343 \cdot 10^{-3}\ in^{-1}$	$\phi_{u2} := 6.6 \cdot 10^{-3}\ in^{-1}$
$\phi_{y1} := 0.334 \cdot 10^{-3}\ in^{-1}$	$\phi_{y2} := 0.343 \cdot 10^{-3}\ in^{-1}$
$My_{CIP} := Mu_{CIP}$	$My_{PC} := Mu_{PC}$
$\phi_{p1} := \phi_{u1} - \phi_{y1} = \langle 6.009 \cdot 10^{-3} \rangle\ in^{-1}$	$\phi_{p2} := \phi_{u2} - \phi_{y2} = \langle 6.257 \cdot 10^{-3} \rangle\ in^{-1}$
$\theta_{p1} := Lp \cdot \phi_{p1} = 0.065\ rad$	$\theta_{p2} := Lp \cdot \phi_{p2} = 0.068\ rad$
$\Delta_{p1} := \theta_{p1} \cdot \left(hc - \frac{Lp}{2}\right) = 3.81\ in$	$\Delta_{p2} := \theta_{p2} \cdot \left(hc - \frac{Lp}{2}\right) = 3.96\ in$
$\Delta_{Y1} := \frac{hc^2}{3} \cdot \phi_{y1} = 0.46\ in$	$\Delta_{Y2} := \frac{hc^2}{3} \cdot \phi_{y2} = 0.47\ in$
$\Delta_{c1} := \Delta_{Y1} + \Delta_{p1} = 4.26\ in$	$\Delta_{c2} := \Delta_{Y2} + \Delta_{p2} = 4.43\ in$

$$\Delta_c := min\left(\langle \Delta_{c1}, \Delta_{c2} \rangle\right) = 4.26\ in$$

$$\delta_u := \frac{\Delta_c}{hc} = 6.66\%$$

$$\theta_{u.pin} := \frac{\Delta_c}{hc + 0.5\ hcb} = \langle 5.61 \cdot 10^{-2} \rangle\ rad$$

$$M_{u.pin} := K_\theta \cdot \theta_{u.pin} = 808.70\ kip \cdot in$$

$$V_{CIP} := \frac{Mu_{CIP} + M_{u.pin}}{hc} = 32.57\ kip \qquad V_{PC} := \frac{Mu_{PC} + M_{u.pin}}{hc} = 31.87\ kip$$

$$Vo := V_{CIP} + V_{PC} = 64.44 \ \textbf{kip}$$

updated: $$\Delta P := \frac{\left\langle Vo \cdot \left(hc + \frac{hcb}{2} \right) \right\rangle - 2\, M_{u.pin}}{bay} = 39.1 \ \textbf{kip}$$

Try-2: Adjusting the axial load

CIP (compression)

$P_{CIP} := P_{dl} + \Delta P = 43.6 \ \textbf{kip}$

$Mu_{CIP} := 1418 \ \textbf{kip} \cdot \textbf{in}$

$\phi_{u1} := 5.307 \cdot 10^{-3} \ \textbf{in}^{-1}$

$\phi_{y1} := 0.340 \cdot 10^{-3} \ \textbf{in}^{-1}$

$\phi_{p1} := \phi_{u1} - \phi_{y1} = \left\langle 4.967 \cdot 10^{-3} \right\rangle \ \textbf{in}^{-1}$

$\theta_{p1} := Lp \cdot \phi_{p1} = 0.054 \ \textbf{rad}$

$\Delta_{p1} := \theta_{p1} \cdot \left(hc - \frac{Lp}{2} \right) = 3.15 \ \textbf{in}$

$\Delta_{Y1} := \frac{hc^2}{3} \cdot \phi_{y1} = 0.46 \ \textbf{in}$

$\Delta_{c1} := \Delta_{Y1} + \Delta_{p1} = 3.61 \ \textbf{in}$

PC (tension)

$P_{CIP} := P_{dl} - \Delta P = -34.6 \ \textbf{kip}$

$Mu_{PC} := 1069 \ \textbf{kip} \cdot \textbf{in}$

$\phi_{u2} := 8.196 \cdot 10^{-3} \ \textbf{in}^{-1}$

$\phi_{y2} := 0.374 \cdot 10^{-3} \ \textbf{in}^{-1}$

$\phi_{p2} := \phi_{u2} - \phi_{y2} = \left\langle 7.822 \cdot 10^{-3} \right\rangle \ \textbf{in}^{-1}$

$\theta_{p2} := Lp \cdot \phi_{p2} = 0.085 \ \textbf{rad}$

$\Delta_{p2} := \theta_{p2} \cdot \left(hc - \frac{Lp}{2} \right) = 4.96 \ \textbf{in}$

$\Delta_{Y2} := \frac{hc^2}{3} \cdot \phi_{y2} = 0.51 \ \textbf{in}$

$\Delta_{c2} := \Delta_{Y2} + \Delta_{p2} = 5.47 \ \textbf{in}$

$$\Delta_c := min\left\langle \Delta_{c1}, \Delta_{c2} \right\rangle = 3.61 \ \textbf{in}$$

$$\delta_u := \frac{\Delta_c}{hc} = 5.64\%$$

$$\theta_{u.pin} := \frac{\Delta_c}{hc + 0.5 \cdot hcb} = \left\langle 4.75 \cdot 10^{-2} \right\rangle \ \textbf{rad}$$

$$M_{u.pin} := K_\theta \cdot \theta_{u.pin} = 685.03 \ \textbf{kip} \cdot \textbf{in}$$

$$V_{CIP} := \frac{Mu_{CIP} + M_{u.pin}}{hc} = 32.86 \ \textbf{kip} \qquad V_{PC} := \frac{Mu_{PC} + M_{u.pin}}{hc} = 27.41 \ \textbf{kip}$$

$$Vo := V_{CIP} + V_{PC} = 60.27 \ \textbf{kip}$$

previously: $\Delta P = 39.1 \ \textbf{kip}$ updated: $\Delta P := \frac{\left(Vo \cdot \left(hc + \frac{hcb}{2}\right)\right) - 2 \ M_{u.pin}}{bay} = 38.2 \ \textbf{kip}$

OK

Moment-Curvature Results

a) CIP

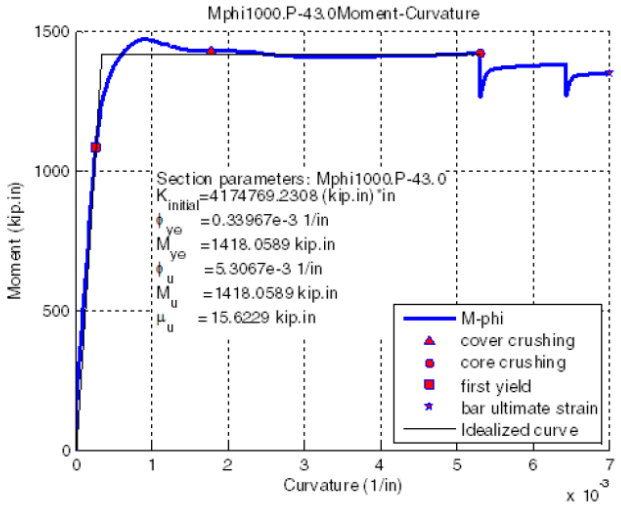

PC:

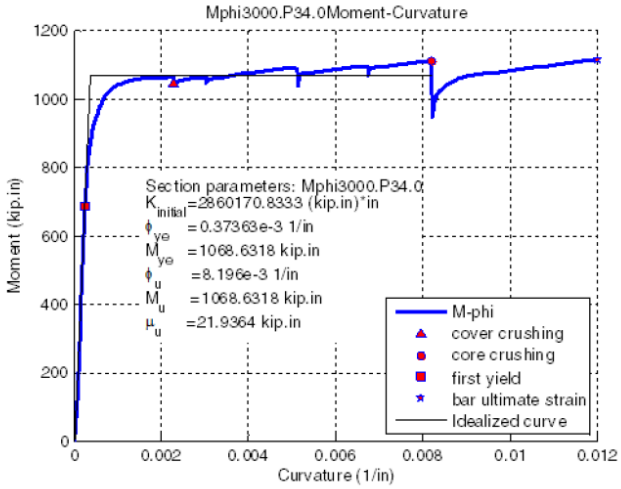

Fig. B-2. Moment-curvature curve of columns section a) CIP b) PC

Ultimate Point

CIP

$\Delta_{u1} := \Delta_{p1} + \Delta_{Y1} + S_g = 3.86$ ***in***

PC

$\Delta_{u2} := \Delta_{p2} + \Delta_{Y2} + S_g = 5.72$ ***in***

$\Delta_u := min\left(\Delta_{u1}, \Delta_{u2}\right) = 3.86$ ***in***

$\delta_u := \frac{\Delta_u}{hc} = 6.03\%$

P-Delta effect: $Vo = 60.27$ ***kip***

$V_{u.base} := Vo - K_{P\Delta} \cdot \Delta_u = 58.16$ ***kip***

Yield Displacement and Force

CIP

PC

Flexural Deformation:

$\Delta_{y1.flex} := \phi_{y1} \cdot \frac{hc^2}{3} = 0.46$ ***in***

$\Delta_{y2.flex} := \phi_{y2} \cdot \frac{hc^2}{3} = 0.51$ ***in***

Bond Deformation,Wehbe's Method: u=800psi

$\theta_{y1.bond} := 1.591 \cdot 10^{-3}$ ***rad***

$\theta_{y2.bond} := 1.449 \cdot 10^{-3}$ ***rad***

$\Delta_{y1.bond} := \theta_{y1.bond} \cdot hc = 0.10$ ***in***

$\Delta_{y2.bond} := \theta_{y2.bond} \cdot hc = 0.09$ ***in***

$\Delta_{y1} := \Delta_{y1.flex} + \Delta_{y1.bond} = 0.57$ ***in***

$\Delta_{y2} := \Delta_{y2.flex} + \Delta_{y2.bond} = 0.60$ ***in***

$\Delta_y := \max\left(\Delta_{y1}, \Delta_{y2}\right) = 0.60$ ***in***

Drift: $\delta_y := \frac{\Delta_y}{hc} = 0.94\%$

$\theta_{y.pin} := \frac{\Delta_y}{hc + 0.5 \cdot hcb} = \left(7.94 \cdot 10^{-3}\right)$ ***rad***

$M_{y.pin} := K_\theta \cdot \theta_{y.pin} = 114.47$ ***kip·in***

$\Delta_y := \max\left(\Delta_{y1}, \Delta_{y2}\right) + S_g = 0.85$ ***in***

$\delta_y := \frac{\Delta_y}{hc} = 1.33\%$

$$Vy_{CIP} := \frac{My_{CIP} + M_{y.pin}}{hc} = 21.73 \ \textbf{kip} \qquad Vy_{PC} := \frac{My_{PC} + M_{y.pin}}{hc} = 21.02 \ \textbf{kip}$$

$$V_y := Vy_{CIP} + Vy_{PC} = 42.75 \ \textbf{kip}$$

P-Delta effect: $V_{y.base} := V_y - K_{P\Delta} \cdot \Delta_y = 42.28 \ \textbf{kip}$

$$drift := \begin{bmatrix} 0 & \delta_y & \delta_u \end{bmatrix}^T = \begin{bmatrix} 0.0000 \\ 1.3334\% \\ 6.0327\% \end{bmatrix} \qquad baseShear := \begin{bmatrix} 0 & V_{y.base} & V_{u.base} \end{bmatrix}^T = \begin{bmatrix} 0.00 \\ 42.28 \\ 58.16 \end{bmatrix} \ \textbf{kip}$$

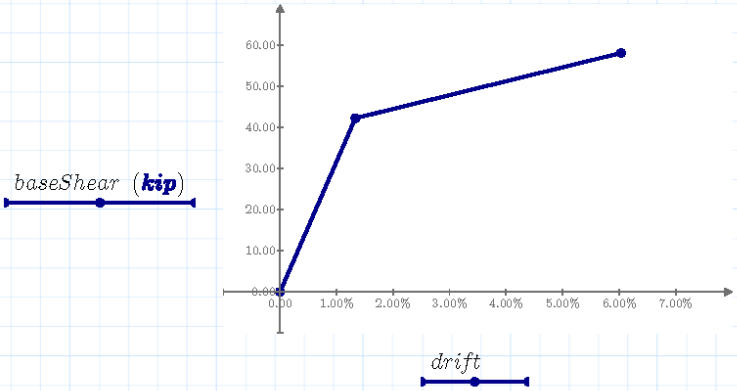

Fig. B-3. Force-drift for south

Effect of cap beam slippage on displacement of the bent

Rotation of loadcell: $M_{cb} := My_{CIP} - My_{PC} = 45.00 \ \textbf{kip} \cdot \textbf{in}$

$$\theta_{cb} := \frac{M_{cb}}{K_{\theta.CB}} = \left(1.45 \cdot 10^{-4}\right) \ \textbf{rad}$$

$$\Delta_{CB.rot} := \theta_{cb} \cdot \left(hc + \frac{hcb}{2}\right) = 0.01 \ \textbf{in}$$

Rotation of loadcell: $\Delta_{y.CB.slide} = 0.28 \ \textbf{in}$

$$\Delta_y := \Delta_y + \Delta_{y.CB.slide} + \Delta_{CB.rot} = 1.14 \ \textbf{in}$$

Drift: $\delta_y := \frac{\Delta_y}{hc} = 1.79\%$

****

North Direction

****

Columns Sectional Analysis

Try-1: Cap beam dead load for axial load: $P_{dl} = 4.50\ kip$

CIP	PC
$Mu_{CIP} := 1276\ kip \cdot in$	$Mu_{PC} := 1231\ kip \cdot in$
$\phi_{u1} := 6.343 \cdot 10^{-3}\ in^{-1}$	$\phi_{u2} := 6.6 \cdot 10^{-3}\ in^{-1}$
$\phi_{y1} := 0.334 \cdot 10^{-3}\ in^{-1}$	$\phi_{y2} := 0.343 \cdot 10^{-3}\ in^{-1}$
$\phi_{p1} := \phi_{u1} - \phi_{y1} = \langle 6.009 \cdot 10^{-3} \rangle\ in^{-1}$	$\phi_{p2} := \phi_{u2} - \phi_{y2} = \langle 6.257 \cdot 10^{-3} \rangle\ in^{-1}$
$\theta_{p1} := Lp \cdot \phi_{p1} = 0.065\ rad$	$\theta_{p2} := Lp \cdot \phi_{p2} = 0.068\ rad$
$\Delta_{p1} := \theta_{p1} \cdot \left(hc - \frac{Lp}{2} \right) = 3.81\ in$	$\Delta_{p2} := \theta_{p2} \cdot \left(hc - \frac{Lp}{2} \right) = 3.96\ in$
$\Delta_{Y1} := \frac{hc^2}{3} \cdot \phi_{y1} = 0.46\ in$	$\Delta_{Y2} := \frac{hc^2}{3} \cdot \phi_{y2} = 0.47\ in$
$\Delta_{c1} := \Delta_{Y1} + \Delta_{p1} = 4.26\ in$	$\Delta_{c2} := \Delta_{Y2} + \Delta_{p2} = 4.43\ in$

$$\Delta_c := min\left\langle \Delta_{c1}, \Delta_{c2} \right\rangle = 4.26\ in$$

$$\delta_u := \frac{\Delta_c}{hc} = 6.66\%$$

$$\theta_{u.pin} := \frac{\Delta_c}{hc + 0.5 \cdot hcb} = \langle 5.61 \cdot 10^{-2} \rangle\ rad$$

$$M_{u.pin} := K_\theta \cdot \theta_{u.pin} = 808.70\ kip \cdot in$$

$$V_{CIP} := \frac{Mu_{CIP} + M_{u.pin}}{hc} = 32.57 \ \textbf{kip} \qquad V_{PC} := \frac{Mu_{PC} + M_{u.pin}}{hc} = 31.87 \ \textbf{kip}$$

$$Vo := V_{CIP} + V_{PC} = 64.44 \ \textbf{kip}$$

updated: $$\Delta P := \frac{\left(Vo \cdot \left(hc + \frac{hcb}{2}\right)\right) - 2 \cdot M_{u.pin}}{bay} = 39.1 \ \textbf{kip}$$

Try-2: Adjusting the axial load

CIP (tension)	PC (compression)
$P_{CIP} := P_{dl} - \Delta P = -34.6 \ \textbf{kip}$	$P_{CIP} := P_{dl} + \Delta P = 43.6 \ \textbf{kip}$
$Mu_{CIP} := 1103 \ \textbf{kip} \cdot \textbf{in}$	$Mu_{PC} := 1397 \ \textbf{kip} \cdot \textbf{in}$
$\phi_{u1} := 8.276 \cdot 10^{-3} \ \textbf{in}^{-1}$	$\phi_{u2} := 6.09 \cdot 10^{-3} \ \textbf{in}^{-1}$
$\phi_{y1} := 0.386 \cdot 10^{-3} \ \textbf{in}^{-1}$	$\phi_{y2} := 0.343 \cdot 10^{-3} \ \textbf{in}^{-1}$
$My_{CIP} := Mu_{CIP}$	$My_{PC} := Mu_{PC}$
$\phi_{p1} := \phi_{u1} - \phi_{y1} = \left(7.89 \cdot 10^{-3}\right) \ \textbf{in}^{-1}$	$\phi_{p2} := \phi_{u2} - \phi_{y2} = \left(5.747 \cdot 10^{-3}\right) \ \textbf{in}^{-1}$
$\theta_{p1} := Lp \cdot \phi_{p1} = 0.085 \ \textbf{rad}$	$\theta_{p2} := Lp \cdot \phi_{p2} = 0.062 \ \textbf{rad}$
$\Delta_{p1} := \theta_{p1} \cdot \left(hc - \frac{Lp}{2}\right) = 5.00 \ \textbf{in}$	$\Delta_{p2} := \theta_{p2} \cdot \left(hc - \frac{Lp}{2}\right) = 3.64 \ \textbf{in}$
$\Delta_{Y1} := \frac{hc^2}{3} \cdot \phi_{y1} = 0.53 \ \textbf{in}$	$\Delta_{Y2} := \frac{hc^2}{3} \cdot \phi_{y2} = 0.47 \ \textbf{in}$
$\Delta_{c1} := \Delta_{Y1} + \Delta_{p1} = 5.53 \ \textbf{in}$	$\Delta_{c2} := \Delta_{Y2} + \Delta_{p2} = 4.11 \ \textbf{in}$

$$\Delta_c := min\left(\Delta_{c1}, \Delta_{c2}\right) = 4.11\ \textbf{in}$$

$$\delta_u := \frac{\Delta_c}{hc} = 6.42\%$$

$$\theta_{u.pin} := \frac{\Delta_c}{hc + 0.5 \cdot hcb} = \left(5.41 \cdot 10^{-2}\right)\ \textbf{rad}$$

$$M_{u.pin} := K_\theta \cdot \theta_{u.pin} = 779.55\ \textbf{kip} \cdot \textbf{in}$$

$$V_{CIP} := \frac{Mu_{CIP} + M_{u.pin}}{hc} = 29.41\ \textbf{kip} \qquad V_{PC} := \frac{Mu_{PC} + M_{u.pin}}{hc} = 34.01\ \textbf{kip}$$

$$Vo := V_{CIP} + V_{PC} = 63.42\ \textbf{kip}$$

previously: $\Delta P = 39.1\ \textbf{kip}$ updated: $\Delta P := \frac{\left(Vo \cdot \left(hc + \frac{hcb}{2}\right)\right) - 2\ M_{u.pin}}{bay} = 38.8\ \textbf{kip}$

good enough

Moment-Curvature Results

CIP:

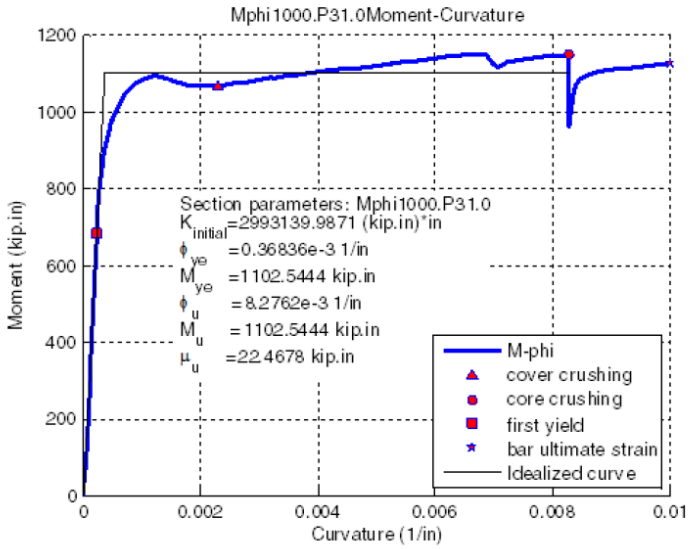

PC:

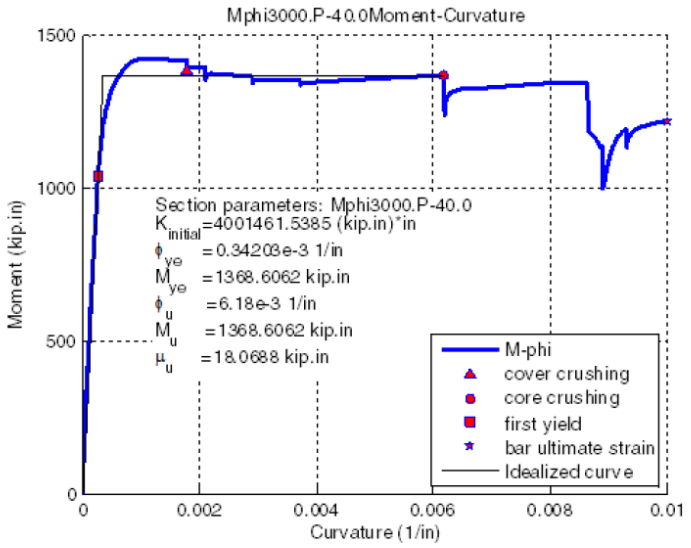

Fig. B-4. Moment-curvature of column

Ultimate Point

CIP

$\Delta_{u1} := \Delta_{p1} + \Delta_{Y1} + S_g = 5.78$ **in**

PC

$\Delta_{u2} := \Delta_{p2} + \Delta_{Y2} + S_g = 4.36$ **in**

$\Delta_u := min\left(\Delta_{u1}, \Delta_{u2}\right) = 4.36$ **in**

$\delta_u := \frac{\Delta_u}{hc} = 6.81\%$

P-Delta effect:

$Vo = 63.42$ **kip**

$V_{u.base} := Vo - K_{P\Delta} \cdot \Delta_u = 61.04$ **kip**

Yield Displacement and Force

CIP

Flexural Deformation:

$\Delta_{y1.flex} := \phi_{y1} \cdot \frac{hc^2}{3} = 0.53$ **in**

Bond Deformation,Wehbe's Method: u=800psi

$\theta_{y1.bond} := 1.4324 \cdot 10^{-3}$ **rad**

$\Delta_{y1.bond} := \theta_{y1.bond} \cdot hc = 0.09$ **in**

$\Delta_{y1} := \Delta_{y1.flex} + \Delta_{y1.bond} = 0.62$ **in**

PC

$\Delta_{y2.flex} := \phi_{y2} \cdot \frac{hc^2}{3} = 0.47$ **in**

$\theta_{y2.bond} := 1.634 \cdot 10^{-3}$ **rad**

$\Delta_{y2.bond} := \theta_{y2.bond} \cdot hc = 0.10$ **in**

$\Delta_{y2} := \Delta_{y2.flex} + \Delta_{y2.bond} = 0.57$ **in**

$\Delta_y := \max\left(\Delta_{y1}, \Delta_{y2}\right) = 0.62$ **in**

Drift: $\delta_y := \frac{\Delta_y}{hc} = 0.97\%$

$\theta_{y.pin} := \frac{\Delta_y}{hc + 0.5 \cdot hcb} = \left(8.14 \cdot 10^{-3}\right)$ **rad**

$M_{y.pin} := K_\theta \cdot \theta_{y.pin} = 117.37$ **kip** $\cdot$ **in**

$\Delta_y := \max\left(\Delta_{y1}, \Delta_{y2}\right) + S_g = 0.87$ **in**

$\delta_y := \frac{\Delta_y}{hc} = 1.36\%$

$$Vy_{CIP} := \frac{My_{CIP} + M_{y.pin}}{hc} = 19.07\ \textbf{kip} \qquad Vy_{PC} := \frac{My_{PC} + M_{y.pin}}{hc} = 23.66\ \textbf{kip}$$

$$V_y := Vy_{CIP} + Vy_{PC} = 42.73\ \textbf{kip}$$

P-Delta effect: $$V_{y.base} := V_y - K_{P\Delta} \cdot \Delta_y = 42.26\ \textbf{kip}$$

$$drift := \begin{bmatrix} 0 & \delta_y & \delta_u \end{bmatrix}^T = \begin{bmatrix} 0.000 \\ 1.357\% \\ 6.811\% \end{bmatrix} \qquad baseShear := \begin{bmatrix} 0 & V_{y.base} & V_{u.base} \end{bmatrix}^T = \begin{bmatrix} 0.00 \\ 42.26 \\ 61.04 \end{bmatrix} \textbf{kip}$$

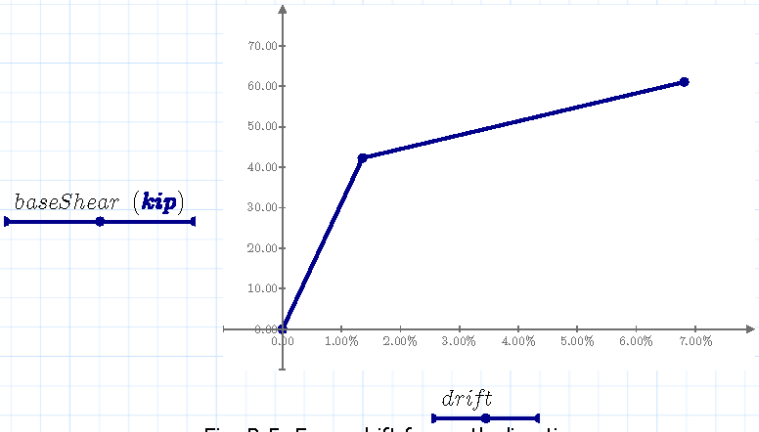

Fig. B-5. Force-drift for north direction

Effect of cap beam slippage on displacement of the bent

Rotation of loadcell: $$M_{cb} := My_{PC} - My_{CIP} = 294.00\ \textbf{kip} \cdot \textbf{in}$$

$$\theta_{cb} := \frac{M_{cb}}{K_{\theta.CB}} = \left(9.44 \cdot 10^{-4}\right)\ \textbf{rad}$$

$$\Delta_{CB.rot} := \theta_{cb} \cdot \left(hc + \frac{hcb}{2}\right) = 0.07\ \textbf{in}$$

Rotation of loadcell: $$\Delta_{y.CB.slide} = 0.28\ \textbf{in}$$

$$\Delta_y := \Delta_y + \Delta_{y.CB.slide} + \Delta_{CB.rot} = 1.22\ \textbf{in}$$

Drift: $$\delta_y := \frac{\Delta_y}{hc} = 1.90\%$$

Appendix C. BRSA Static Numerical Simulation Using Simple Stick Model

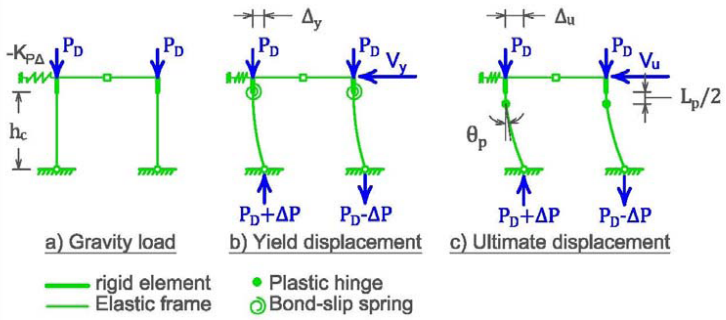

Fig. C-1. Structural Model

Frame Geometry

Column	$Dc := 16\ in$	$hc := 64\ in$	$gap := 1.0\ in$	
Cap Beam	$hcb := 24\ in$	$bcb := 24\ in$	$bay := 7\ ft$	$overhange := 26.0\ in$
Pedestal	$dp := 22\ in$	$hp := 30\ in$		

Loading

Dead load on the column: $P_{dl} := 4.5\ kip$

P-delta stiffness (section 4.2) $K_{P\Delta} := 546\ \frac{lbf}{in}$

Column Sectional Properties

Reinforcing detail:

$\rho = 1.39\%$ $\rho_s = 1.62\%$

Confined material Properties for CIP

$f_c = 6.26\ ksi$ $f_{cc} = 9.33\ ksi$ $\varepsilon_{cc} = 6.90 \cdot 10^{-3}$ $\varepsilon_{cu} = 26.2 \cdot 10^{-3}$

Confined material Properties for PC

$f_c = 9.02\ ksi$ $f_{cc} = 12.24\ ksi$ $\varepsilon_{cc} = 5.57 \cdot 10^{-3}$ $\varepsilon_{cu} = 20.92 \cdot 10^{-3}$

****

Push to South

****

Columns Sectional Analysis

Try-1: Dead load for axial load:

Column: $P_{dl} = 4.50\ kip$ Rebar-Pin: $P_{dl} + 1.3\ kip = 5.80\ kip$

CIP

$Mcol_{CIP} := 1428\ kip \cdot in$

$Mpin_{CIP} := 480\ kip \cdot in$

$V_{CIP} := \frac{Mcol_{CIP} + Mpin_{CIP}}{hc} = 29.81\ kip$

PC

$Mcol_{PC} := 1406\ kip \cdot in$

$Mpin_{PC} := 492\ kip \cdot in$

$V_{PC} := \frac{Mcol_{PC} + Mpin_{PC}}{hc} = 29.66\ kip$

$Vo := V_{CIP} + V_{PC} = 59.47\ kip$

$\Delta P := \frac{\left(Vo \cdot \left(hc + \frac{hcb}{2}\right)\right) - Mpin_{CIP} - Mpin_{PC}}{bay} = 42.23\ kip$

Try-2: Adjusting the axial load

CIP (compression)

$P_{CIP} := P_{dl} + \Delta P = 46.7\ kip$

$P_{CIP} + 1.3\ kip = 48.03\ kip$

$Mcol_{CIP} := 1568\ kip \cdot in$

$Mpin_{CIP} := 571\ kip \cdot in$

$V_{CIP} := \frac{Mcol_{CIP} + Mpin_{CIP}}{hc} = 33.42\ kip$

PC (tension)

$P_{PC} := P_{dl} - \Delta P = -37.7\ kip$

$P_{PC} + 1.3\ kip = -36.43\ kip$

$Mcol_{PC} := 1213\ kip \cdot in$

$Mpin_{PC} := 478\ kip \cdot in$

$V_{PC} := \frac{Mcol_{PC} + Mpin_{PC}}{hc} = 26.42\ kip$

$Vo := V_{CIP} + V_{PC} = 59.84\ kip$

$\Delta P = 42.23\ kip$ $\Delta P := \frac{\left(Vo \cdot \left(hc + \frac{hcb}{2}\right)\right) - Mpin_{CIP} - Mpin_{PC}}{bay} = 41.66\ kip$ Good Enough.

a)

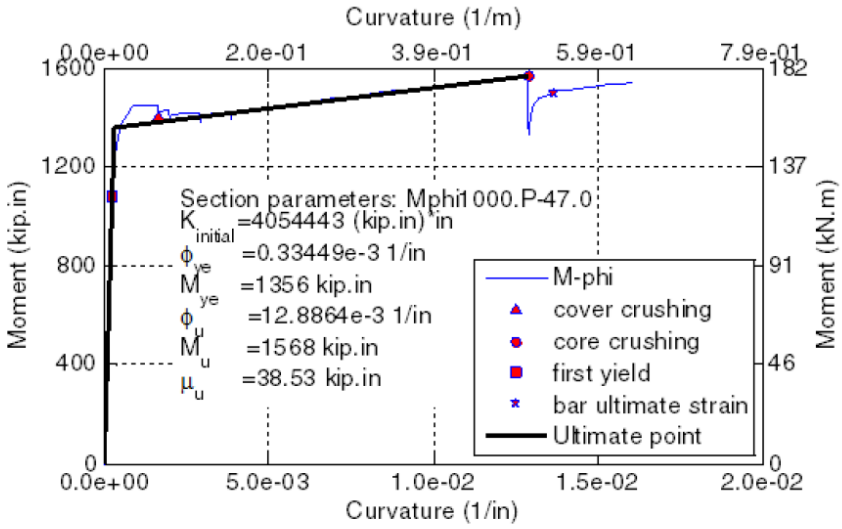

b)

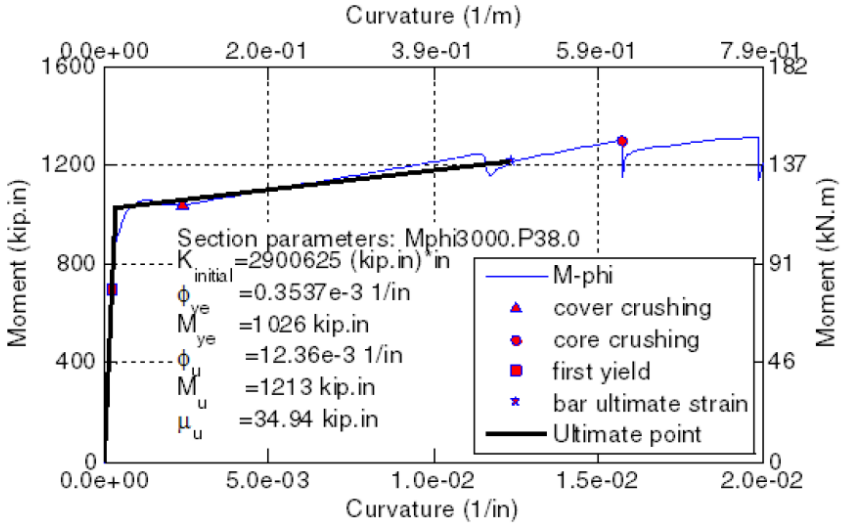

Fig. C-2. Moment-curvature curve of columns section a) CIP b) PC

a)

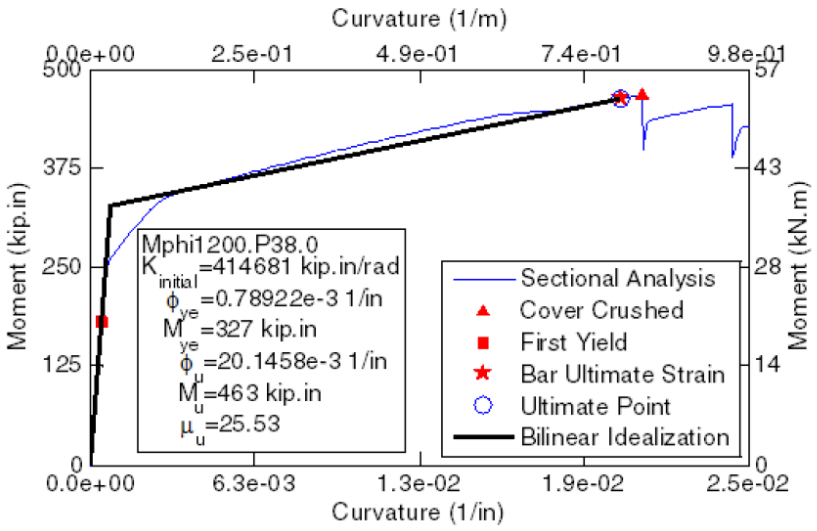

b)

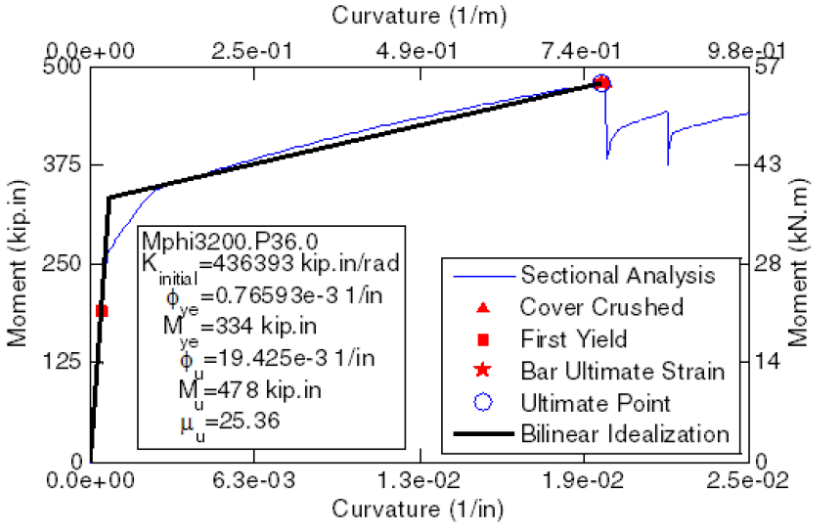

Fig. C-3. Moment-curvature curve of rebar-pins section a) CIP b) PC

Determining Rebar-Pin Springs

Cheng et al. (2006)

$fy := 71.788\ ksi$ $\quad d_b := 0.625\ in$

$$Lp := gap + 0.15 \cdot \frac{fy}{ksi} \cdot d_b = 7.73\ in$$

CIP	PC
$\phi_{y.pin1} := 0.743 \cdot 10^{-3}\ \frac{1}{in}$	$\phi_{y.pin2} := 0.766 \cdot 10^{-3}\ \frac{1}{in}$
$M_{y.pin1} := 545\ kip \cdot in$	$M_{y.pin2} := 334\ kip \cdot in$
$\phi_{u.pin1} := \langle 23.675 \cdot 10^{-3} \rangle\ \frac{1}{in}$	$\phi_{u.pin2} := \langle 19.425 \cdot 10^{-3} \rangle\ \frac{1}{in}$
$M_{u.pin1} := 571\ kip \cdot in$	$M_{u.pin2} := 478\ kip \cdot in$

- Yield Rotation

$\theta_{y.flex1} := \phi_{y.pin1} \cdot gap = \langle 7.43 \cdot 10^{-4} \rangle\ rad$ $\quad \theta_{y.flex2} := \phi_{y.pin2} \cdot gap = \langle 7.66 \cdot 10^{-4} \rangle\ rad$

Bond rotation: Double side bond, Wehbe's Method

$\theta_{y.bond1} := 6.279 \cdot 10^{-3}\ rad$ $\quad \theta_{y.bond2} := 4.948 \cdot 10^{-3}\ rad$

$\theta_{y.pin1} := \theta_{y.flex1} + \theta_{y.bond1} = \langle 7.02 \cdot 10^{-3} \rangle\ rad$ $\quad \theta_{y.pin2} := \theta_{y.flex2} + \theta_{y.bond2} = \langle 5.71 \cdot 10^{-3} \rangle\ rad$

- Ultimate point

$\theta_{p1} := Lp \cdot \langle \phi_{u.pin1} - \phi_{y.pin1} \rangle = 0.177\ rad$ $\quad \theta_{p2} := Lp \cdot \langle \phi_{u.pin2} - \phi_{y.pin2} \rangle = 0.144\ rad$

$\theta_{u.pin1} := \theta_{p1} + \theta_{y.flex1} = 0.178\ rad$ $\quad \theta_{u.pin2} := \theta_{p2} + \theta_{y.flex2} = 0.145\ rad$

$$Mcip.pin := \begin{bmatrix} 0 \\ M_{y.pin1} \\ M_{u.pin1} \end{bmatrix} = \begin{bmatrix} 0.00 \\ 545.00 \\ 571.00 \end{bmatrix} \ kip \cdot in \qquad \theta cip.pin := \begin{bmatrix} 0 \\ \theta_{y.pin1} \\ \theta_{u.pin1} \end{bmatrix} = \begin{bmatrix} 0.00 \\ 7.02 \cdot 10^{-3} \\ 178.01 \cdot 10^{-3} \end{bmatrix} \ rad$$

$$Mpc.pin := \begin{bmatrix} 0 \\ M_{y.pin2} \\ M_{u.pin2} \end{bmatrix} = \begin{bmatrix} 0.00 \\ 334.00 \\ 478.00 \end{bmatrix} \ kip \cdot in \qquad \theta pc.pin := \begin{bmatrix} 0 \\ \theta_{y.pin2} \\ \theta_{u.pin2} \end{bmatrix} = \begin{bmatrix} 0.00 \\ 5.71 \cdot 10^{-3} \\ 145.00 \cdot 10^{-3} \end{bmatrix} \ rad$$

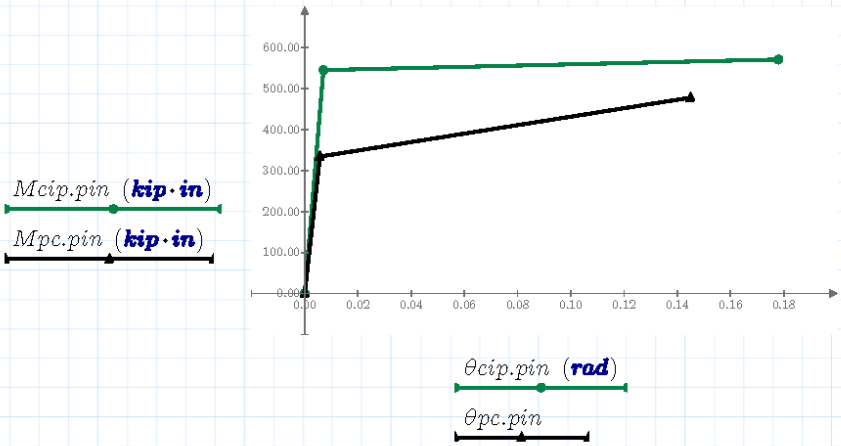

Fig. C-4. Rebar-pins springs

Column Column Plastic Hinge Springs

Paulay & Priestley (1992)

$f_y := 72.08\ \textbf{ksi}$ $d_{bl} := 0.5\ \textbf{in}$ $hc = 64.00\ \textbf{in}$

$$Lp := \max\left(0.08\ hc + 0.15 \cdot \frac{f_y}{\textbf{ksi}} \cdot d_{bl},\ 0.3\ \frac{f_y}{\textbf{ksi}} \cdot d_{bl}\right) = 10.81\ \textbf{in}$$

CIP	PC
$\phi_{y.col1} := 0.346 \cdot 10^{-3}\ \frac{1}{\textbf{in}}$	$\phi_{y.col2} := 0.330 \cdot 10^{-3}\ \frac{1}{\textbf{in}}$
$M_{y.col1} := 977\ \textbf{kip} \cdot \textbf{in}$	$M_{y.col2} := 1409\ \textbf{kip} \cdot \textbf{in}$
$\phi_{u.col1} := 12.621\ 10^{-3}\ \frac{1}{\textbf{in}}$	$\phi_{u.col2} := 9.800\ 10^{-3}\ \frac{1}{\textbf{in}}$
$M_{u.col1} := 1223\ \textbf{kip} \cdot \textbf{in}$	$M_{u.col2} := 1535\ \textbf{kip} \cdot \textbf{in}$

- Yield Rotation

$$\Delta_{y.flex1} := \phi_{y.col1} \cdot \frac{hc^2}{3} = 0.47\ \textbf{in} \qquad \Delta_{y.flex2} := \phi_{y.col2} \cdot \frac{hc^2}{3} = 0.45\ \textbf{in}$$

Bond rotation: Double side bond, Wehbe's Method

$\theta_{y.bond1} := 1.695 \cdot 10^{-3}\ \textbf{rad}$ $\theta_{y.bond2} := 1.438 \cdot 10^{-3}\ \textbf{rad}$

$\Delta_{y.bond1} := \theta_{y.bond1} \cdot hc = 0.11\ \textbf{in}$ $\Delta_{y.bond2} := \theta_{y.bond2} \cdot hc = 0.09\ \textbf{in}$

$$\theta_{y.col1} := \frac{\Delta_{y.flex1} + \Delta_{y.bond1}}{hc} = \left\langle 9.08 \cdot 10^{-3} \right\rangle\ \textbf{rad} \qquad \theta_{y.col2} := \frac{\Delta_{y.flex2} + \Delta_{y.bond2}}{hc} = \left\langle 8.48 \cdot 10^{-3} \right\rangle\ \textbf{rad}$$

- Ultimate point

$\theta_{p1} := Lp \cdot \langle \phi_{u.col1} - \phi_{y.col1} \rangle = 0.133\ \textbf{rad}$ $\theta_{p2} := Lp \cdot \langle \phi_{u.col2} - \phi_{y.col2} \rangle = 0.102\ \textbf{rad}$

$$\Delta_{y.flex1} := \frac{hc^2}{3} \cdot \phi_{y.col1} = 0.47 \ \textbf{in} \qquad \Delta_{y.flex2} := \frac{hc^2}{3} \cdot \phi_{y.col2} = 0.45 \ \textbf{in}$$

$$\theta_{u.col1} := \frac{\theta_{p1} \cdot \left(hc - \frac{Lp}{2}\right) + \Delta_{y.flex1}}{hc} = 0.129 \ \textbf{rad} \qquad \theta_{u.col2} := \frac{\theta_{p2} \cdot \left(hc - \frac{Lp}{2}\right) + \Delta_{y.flex2}}{hc} = 0.101 \ \textbf{rad}$$

$$Mcip.col := \begin{bmatrix} 0 \\ M_{y.col1} \\ M_{u.col1} \end{bmatrix} = \begin{bmatrix} 0.00 \\ 977.00 \\ 1223.00 \end{bmatrix} \ \textbf{kip} \cdot \textbf{in} \qquad \theta cip.col := \begin{bmatrix} 0 \\ \theta_{y.col1} \\ \theta_{u.col1} \end{bmatrix} = \begin{bmatrix} 0.00 \\ 9.08 \cdot 10^{-3} \\ 128.89 \cdot 10^{-3} \end{bmatrix}$$

$$Mpc.col := \begin{bmatrix} 0 \\ M_{y.col2} \\ M_{u.col2} \end{bmatrix} = \begin{bmatrix} 0.00 \\ 1409.00 \\ 1535.00 \end{bmatrix} \ \textbf{kip} \cdot \textbf{in} \qquad \theta pc.col := \begin{bmatrix} 0 \\ \theta_{y.col2} \\ \theta_{u.col2} \end{bmatrix} = \begin{bmatrix} 0.00 \\ 8.48 \cdot 10^{-3} \\ 100.78 \cdot 10^{-3} \end{bmatrix}$$

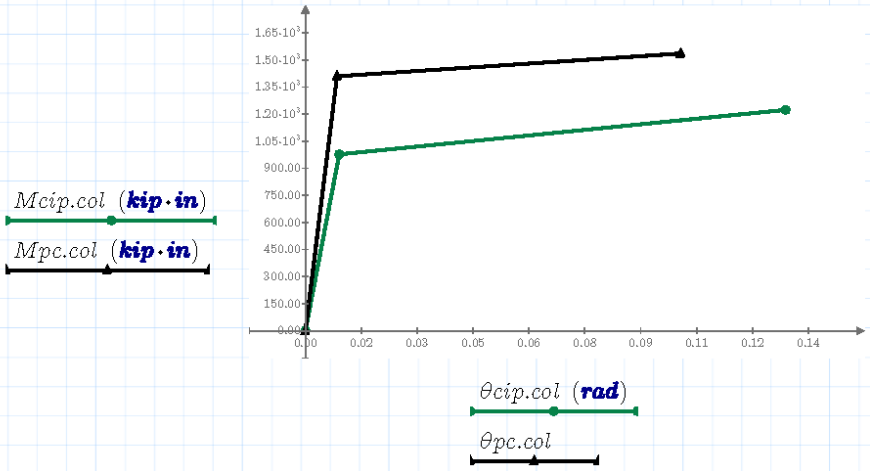

Fig. C-5. Columns plastic hinge springs

First Yield Displacement and Force

Smallest yield rotation was in PC pin:

$$\theta_y := \theta_{y.pin2} = \left(5.71 \cdot 10^{-3}\right)\ \textit{rad}$$

$$\Delta_1 := \theta_y \cdot hc = 0.37\ \textit{in}$$

drift: $$\delta_1 := \frac{\Delta_1}{hc} = 0.57\%$$

CIP

$$M_{col.cip} := \frac{M_{y.col1}}{\theta_{y.col1}} \cdot \theta_y = 615.07\ \textit{kip} \cdot \textit{in}$$

$$M_{pin.cip} := \frac{M_{y.pin1}}{\theta_{y.pin1}} \cdot \theta_y = 443.48\ \textit{kip} \cdot \textit{in}$$

$$V_{CIP} := \frac{M_{col.cip} + M_{pin.cip}}{hc} = 16.54\ \textit{kip}$$

PC

$$M_{col.pc} := \frac{M_{y.col2}}{\theta_{y.col2}} \cdot \theta_y = 949.64\ \textit{kip} \cdot \textit{in}$$

$$M_{pin.pc} := \frac{M_{y.pin2}}{\theta_{y.pin2}} \cdot \theta_y = 334.00\ \textit{kip} \cdot \textit{in}$$

$$V_{PC} := \frac{M_{col.pc} + M_{pin.pc}}{hc} = 20.06\ \textit{kip}$$

$$V_{base_1} := V_{CIP} + V_{PC} = 36.60\ \textit{kip}$$

Second Yield Displacement and Force

Second yield rotation is in CIP pin:

$$\theta_y := \theta_{y.pin2} = \left(5.71 \cdot 10^{-3}\right)\ \textit{rad}$$

$$\Delta_2 := \theta_y \cdot hc = 0.37\ \textit{in}$$

drift: $$\delta_2 := \frac{\Delta_2}{hc} = 0.57\%$$

$$M_{col.cip} := \frac{M_{y.col1}}{\theta_{y.col1}} \cdot \theta_y = 615 \ \textbf{kip} \cdot \textbf{in} \qquad M_{col.pc} := \frac{M_{y.col2}}{\theta_{y.col2}} \cdot \theta_y = 949.64 \ \textbf{kip} \cdot \textbf{in}$$

$$M_{pin.cip} := \frac{M_{u.pin1} - M_{y.pin1}}{\theta_{u.pin1} - \theta_{y.pin1}} \cdot \langle \theta_y - \theta_{y.pin1} \rangle + M_{y.pin1} = 544.80 \ \textbf{kip} \cdot \textbf{in}$$

$$M_{pin.pc} := M_{y.pin2} = 334.00 \ \textbf{kip} \cdot \textbf{in}$$

$$V_{CIP} := \frac{M_{col.cip} + M_{pin.cip}}{hc} = 18.12 \ \textbf{kip} \qquad V_{PC} := \frac{M_{col.pc} + M_{pin.pc}}{hc} = 20.06 \ \textbf{kip}$$

$$V_{base_2} := V_{CIP} + V_{PC} = 38.18 \ \textbf{kip}$$

Third Yield Displacement and Force

Third yield rotation is in PC Column:

$$\theta_y := \theta_{y.col2} = \langle 8.48 \cdot 10^{-3} \rangle \ \textbf{rad}$$

$$\Delta_3 := \theta_y \cdot hc = 0.54 \ \textbf{in}$$

drift: $$\delta_3 := \frac{\Delta_3}{hc} = 0.85\%$$

$$M_{col.cip} := \frac{M_{y.col1}}{\theta_{y.col1}} \cdot \theta_y = 913 \ \textbf{kip} \cdot \textbf{in} \qquad M_{col.pc} := \frac{M_{y.col2}}{\theta_{y.col2}} \cdot \theta_y = \langle 1.41 \cdot 10^3 \rangle \ \textbf{kip} \cdot \textbf{in}$$

$$M_{pin.cip} := \frac{M_{u.pin1} - M_{y.pin1}}{\theta_{u.pin1} - \theta_{y.pin1}} \cdot \langle \theta_y - \theta_{y.pin1} \rangle + M_{y.pin1} = 545.22 \ \textbf{kip} \cdot \textbf{in}$$

$$M_{pin.pc} := \frac{M_{u.pin2} - M_{y.pin2}}{\theta_{u.pin2} - \theta_{y.pin2}} \cdot \langle \theta_y - \theta_{y.pin2} \rangle + M_{y.pin2} = 336.86 \ \textbf{kip} \cdot \textbf{in}$$

$$V_{CIP} := \frac{M_{col.cip} + M_{pin.cip}}{hc} = 22.78 \ \textbf{kip} \qquad V_{PC} := \frac{M_{col.pc} + M_{pin.pc}}{hc} = 27.28 \ \textbf{kip}$$

$$V_{base_3} := V_{CIP} + V_{PC} = 50.06 \ \textbf{kip}$$

Fourth Yield Displacement and Force

Fourth yield rotation is in CIP column:

$$\theta_y := \theta_{y.col1} = \left(9.08 \cdot 10^{-3}\right) \ \textbf{rad}$$

$$\Delta_4 := \theta_y \cdot hc = 0.58 \ \textbf{in}$$

drift: $$\delta_4 := \frac{\Delta_4}{hc} = 0.91\%$$

$$M_{col.cip} := \frac{M_{u.col1} - M_{y.col1}}{\theta_{u.col1} - \theta_{y.col1}} \cdot \langle \theta_y - \theta_{y.col1} \rangle + M_{y.col1} = 977 \ \textbf{kip} \cdot \textbf{in}$$

$$M_{col.pc} := \frac{M_{u.col2} - M_{y.col2}}{\theta_{u.col2} - \theta_{y.col2}} \cdot \langle \theta_y - \theta_{y.col2} \rangle + M_{y.col2} = \left(1.41 \cdot 10^3\right) \ \textbf{kip} \cdot \textbf{in}$$

$$M_{pin.cip} := \frac{M_{u.pin1} - M_{y.pin1}}{\theta_{u.pin1} - \theta_{y.pin1}} \cdot \langle \theta_y - \theta_{y.pin1} \rangle + M_{y.pin1} = 545.31 \ \textbf{kip} \cdot \textbf{in}$$

$$M_{pin.pc} := \frac{M_{u.pin2} - M_{y.pin2}}{\theta_{u.pin2} - \theta_{y.pin2}} \cdot \langle \theta_y - \theta_{y.pin2} \rangle + M_{y.pin2} = 337.48 \ \textbf{kip} \cdot \textbf{in}$$

$$V_{CIP} := \frac{M_{col.cip} + M_{pin.cip}}{hc} = 23.79 \ \textbf{kip} \qquad V_{PC} := \frac{M_{col.pc} + M_{pin.pc}}{hc} = 27.30 \ \textbf{kip}$$

$$V_{base_4} := V_{CIP} + V_{PC} = 51.09 \ \textbf{kip}$$

Ultimate Point

$M_{col.cip} := M_{u.col1} = 1223$ **kip·in**

$M_{pin.cip} := M_{u.pin1} = 571$ **kip·in**

Zero moment point: $h_1 := \frac{M_{col.cip}}{M_{col.cip} + M_{pin.cip}} \cdot hc = 43.63$ **in**

$M_{pin.cip} < M_{y.col1} = 1$ Elastic deformation under zero moment point.

$$\phi_{1.bot} := \frac{M_{pin.cip}}{M_{y.col1}} \cdot \phi_{y.col1} = \left\langle 2.02 \cdot 10^{-4} \right\rangle \frac{1}{\text{in}}$$

$M_{col.pc} := M_{u.col2} = 1535$ **kip·in**

$M_{pin.pc} := M_{u.pin2} = 478$ **kip·in**

Zero moment point: $h_2 := \frac{M_{col.pc}}{M_{col.pc} + M_{pin.pc}} \cdot hc = 48.80$ **in**

$M_{pin.pc} < M_{y.col2} = 1$ Elastic deformation under zero moment point.

$$\phi_{2.bot} := \frac{M_{pin.pc}}{M_{y.col2}} \cdot \phi_{y.col2} = \left\langle 1.12 \cdot 10^{-4} \right\rangle \frac{1}{\text{in}}$$

CIP	PC
$\theta_{p1} := Lp \cdot \langle \phi_{u.col1} - \phi_{y.col1} \rangle = 0.133$ **rad**	$\theta_{p2} := Lp \cdot \langle \phi_{u.col2} - \phi_{y.col2} \rangle = 0.102$ **rad**
$\Delta_{p.col1} := \theta_{p1} \cdot \left(h_1 - \frac{Lp}{2} \right) = 5.073$ **in**	$\Delta_{p.col2} := \theta_{p2} \cdot \left(h_2 - \frac{Lp}{2} \right) = 4.443$ **in**
$\Delta_{y.flex1.top} := \frac{h_1^{\,2}}{3} \cdot \phi_{y.col1} = 0.22$ **in**	$\Delta_{y.flex2.top} := \frac{h_2^{\,2}}{3} \cdot \phi_{y.col2} = 0.26$ **in**
$\Delta_{y.flex1.bot} := \frac{\langle hc - h_1 \rangle^2}{3} \cdot \phi_{1.bot} = 0.03$ **in**	$\Delta_{y.flex2.bot} := \frac{\langle hc - h_2 \rangle^2}{3} \cdot \phi_{2.bot} = \left\langle 8.62 \cdot 10^{-3} \right\rangle$ **in**

$\Delta_{u1} := \Delta_{p.col1} + \Delta_{y.flex1.top} + \Delta_{y.flex1.bot} = 5.32$ **in**

$\Delta_{u2} := \Delta_{p.col2} + \Delta_{y.flex2.top} + \Delta_{y.flex2.bot} = 4.71$ **in**

$\Delta_5 := min(\Delta_{u1}, \Delta_{u2}) = 4.71$ **in**

$\delta_5 := \frac{\Delta_5}{hc} = 7.37\%$

$V_{CIP} := \frac{M_{col.cip} + M_{pin.cip}}{hc} = 28.03$ **kip**

$V_{PC} := \frac{M_{col.pc} + M_{pin.pc}}{hc} = 31.45$ **kip**

$V_{base_5} := V_{CIP} + V_{PC} = 59.48$ **kip**

P-Delta effect: $V_{base} := V_{base} - K_{P\Delta} \cdot \Delta$

Adding Shear Deformation:

$C_{total} := 92.9\ kip$ $Vn := 0.45 \cdot C_{total} = 41.81\ kip$

$V_{CIP} = 28.03\ kip$ $V_{PC} = 31.45\ kip$ In the first segment.

Rebar-Pin Section properties:

$A_{sp} = 0.11\ in^2$ $s := 1.5\ in$ $Es := 29000\ ksi$

$D := 10\ in$ $Dcore := D - 2 \cdot 1\ in - 0.375\ in = 7.63\ in$

$Ag := \frac{\pi}{4} D^2 = 78.54\ in^2$

$fc := 6.26\ ksi$

$Ec := 57\ ksi \cdot \sqrt{\frac{fc}{psi}} = \langle 4.51 \cdot 10^3 \rangle\ ksi$ $n := \frac{Es}{Ec} = 6.43$

$\rho_v := \frac{4 \cdot A_{sp}}{Dcore \cdot s} = 3.86\%$

Cracked section Shear stiffness:

$K_{v45} := \frac{\rho_v}{1 + 4 \cdot n \cdot \rho_v} Es \cdot (0.8 \cdot Ag) = 35305\ \frac{kip}{in} \cdot in$

$Kcr := \frac{K_{v45}}{gap} = 35305.16\ \frac{kip}{in}$

$\Delta s := \frac{0.5 \cdot V_{base}}{Kcr} = \begin{bmatrix} 0.00 \\ 5.15 \cdot 10^{-4} \\ 5.38 \cdot 10^{-4} \\ 7.05 \cdot 10^{-4} \\ 7.19 \cdot 10^{-4} \\ 8.06 \cdot 10^{-4} \end{bmatrix} in$ Negligible.

Walraven & Reinhardt (1981)

$Dcore = 7.63\ in$ $\quad Acore := \frac{\pi}{4} Dcore^2 = 45.66\ in^2$

Concrete cylinder strength: $\quad fc := 6.26\ ksi$

Concrete cube strength: $\quad fcc := 1.25 \cdot fc$

$$vco := \frac{fcc}{30} = 260.83\ psi$$

$$\Delta s_{Walraven}(vci, w) := \frac{\frac{(vci + vco)}{MPa}}{1.8 \cdot \left(\frac{w}{mm}\right)^{-0.8} + \left(0.23 \cdot \left(\frac{w}{mm}\right)^{-0.707} - 0.20\right) \cdot \frac{fcc}{MPa}}\ mm$$

Okamura-Maekawa Model:

$$a := \frac{3}{8}\ in$$

$$fc = \left(6.26 \cdot 10^3\right)\ psi$$

$$vcmax(w) := \frac{\sqrt{\frac{fc}{MPa}}}{0.31 + \frac{24 \cdot \frac{w}{mm}}{\frac{a}{mm} + 16}}\ MPa$$

$i := 1 \quad \theta_{pin} := \delta_i \quad v := \frac{V_{base_i}}{2 \cdot Acore} \quad w := \frac{\theta_{pin} \cdot Dcore}{2} = 0.02\ in \quad \Psi := \frac{v}{vcmax(w)}$

$$\Delta s1_i := \Delta s_{Walraven}(v, w) = 0.02\ in$$

$$\Delta s2_i := w \cdot \sqrt{\frac{\Psi}{1 - \Psi}} = 0.02\ in \qquad \Delta s_i := \frac{\Delta s1_i + \Delta s2_i}{2} = 0.02\ in$$

$i := 2 \quad \theta_{pin} := \delta_i \quad v := \frac{V_{base_i}}{2 \cdot Acore} \quad w := \frac{\theta_{pin} \cdot Dcore}{2} = 0.02 \ in \quad \Psi := \frac{v}{vcmax(w)}$

$\Delta s1_i := \Delta s_{Walraven}(v, w) = 0.02 \ in$

$\Delta s2_i := w \cdot \sqrt{\frac{\Psi}{1 - \Psi}} = 0.02 \ in \quad \Delta s_i := \frac{\Delta s1_i + \Delta s2_i}{2} = 0.02 \ in$

$i := 3 \quad \theta_{pin} := \delta_i \quad v := \frac{V_{base_i}}{2 \cdot Acore} \quad w := \frac{\theta_{pin} \cdot Dcore}{2} = 0.03 \ in \quad \Psi := \frac{v}{vcmax(w)}$

$\Delta s1_i := \Delta s_{Walraven}(v, w) = 0.04 \ in$

$\Delta s2_i := w \cdot \sqrt{\frac{\Psi}{1 - \Psi}} = 0.04 \ in \quad \Delta s_i := \frac{\Delta s1_i + \Delta s2_i}{2} = 0.04 \ in$

$i := 4 \quad \theta_{pin} := \delta_i \quad v := \frac{V_{base_i}}{2 \cdot Acore} \quad w := \frac{\theta_{pin} \cdot Dcore}{2} = 0.03 \ in \quad \Psi := \frac{v}{vcmax(w)}$

$\Delta s1_i := \Delta s_{Walraven}(v, w) = 0.05 \ in$

$\Delta s2_i := w \cdot \sqrt{\frac{\Psi}{1 - \Psi}} = 0.05 \ in \quad \Delta s_i := \frac{\Delta s1_i + \Delta s2_i}{2} = 0.05 \ in$

$i := 5 \quad \theta_{pin} := \delta_i \quad v := \frac{V_{base_i}}{2 \cdot Acore} \quad w := \frac{\theta_{pin} \cdot Dcore}{2} = 0.28 \ in \quad \Psi := \frac{v}{vcmax(w)}$

$\Delta s1_i := \Delta s_{Walraven}(v, w) = -0.03 \ in$

$\Delta s2_i := w \cdot \sqrt{\frac{\Psi}{1 - \Psi}} = 0.32i \ in \quad \Delta s_5 := \Delta s_4 = 0.05 \ in$

$$\Delta := \Delta + \Delta s = \begin{bmatrix} 0.00 \\ 0.38 \\ 0.38 \\ 0.58 \\ 0.63 \\ 4.76 \end{bmatrix} \textit{in} \qquad \delta := \frac{\Delta}{hc} = \begin{bmatrix} 0.00 \\ 0.60\% \\ 0.60\% \\ 0.91\% \\ 0.98\% \\ 7.44\% \end{bmatrix}$$

$$\delta = \begin{bmatrix} 0.0000 \\ 0.5966\% \\ 0.5973\% \\ 0.9106\% \\ 0.9816\% \\ 7.4396\% \end{bmatrix} \qquad V_{base} = \begin{bmatrix} 0.0 \\ 36.4 \\ 38.0 \\ 49.8 \\ 50.8 \\ 56.9 \end{bmatrix} \textit{kip}$$

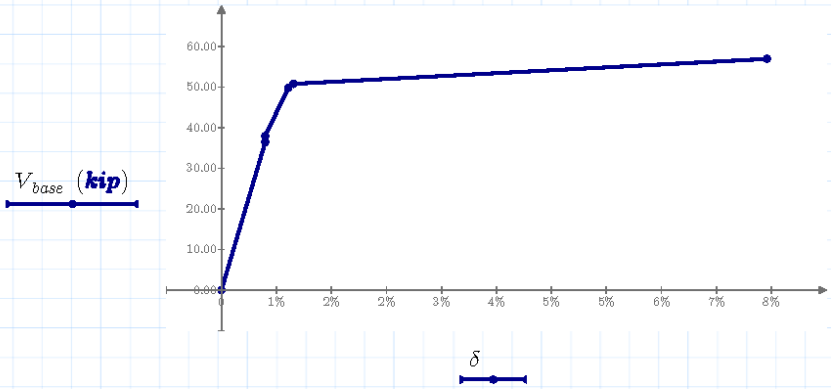

Fig. C-6. Force-displacemnt envelop push to South

****

Push to North

****

Columns Sectional Analysis

Try-1: Dead load for axial load:

Column: $P_{dl} = 4.50\ \textbf{kip}$ Rebar-Pin: $P_{dl} + 1.3\ \textbf{kip} = 5.80\ \textbf{kip}$

CIP

$Mcol_{CIP} := 1428\ \textbf{kip}\cdot\textbf{in}$

$Mpin_{CIP} := 480\ \textbf{kip}\cdot\textbf{in}$

$V_{CIP} := \frac{Mcol_{CIP} + Mpin_{CIP}}{hc} = 29.81\ \textbf{kip}$

PC

$Mcol_{PC} := 1406\ \textbf{kip}\cdot\textbf{in}$

$Mpin_{PC} := 492\ \textbf{kip}\cdot\textbf{in}$

$V_{PC} := \frac{Mcol_{PC} + Mpin_{PC}}{hc} = 29.66\ \textbf{kip}$

$Vo := V_{CIP} + V_{PC} = 59.47\ \textbf{kip}$

$\Delta P := \frac{\left\langle Vo \cdot \left\langle hc + \frac{hcb}{2} \right\rangle \right\rangle - Mpin_{CIP} - Mpin_{PC}}{bay} = 42.23\ \textbf{kip}$

Try-2: Adjusting the axial load

CIP (tension)

$P_{CIP} := P_{dl} - \Delta P = -37.7\ \textbf{kip}$

$P_{CIP} + 1.3\ \textbf{kip} = -36.43\ \textbf{kip}$

$Mcol_{CIP} := 1223\ \textbf{kip}\cdot\textbf{in}$

$Mpin_{CIP} := 478\ \textbf{kip}\cdot\textbf{in}$

$V_{CIP} := \frac{Mcol_{CIP} + Mpin_{CIP}}{hc} = 26.58\ \textbf{kip}$

PC (compression)

$P_{PC} := P_{dl} + \Delta P = 46.7\ \textbf{kip}$

$P_{PC} + 1.3\ \textbf{kip} = 48.03\ \textbf{kip}$

$Mcol_{PC} := 1535\ \textbf{kip}\cdot\textbf{in}$

$Mpin_{PC} := 571\ \textbf{kip}\cdot\textbf{in}$

$V_{PC} := \frac{Mcol_{PC} + Mpin_{PC}}{hc} = 32.91\ \textbf{kip}$

$Vo := V_{CIP} + V_{PC} = 59.48\ \textbf{kip}$ $\Delta P := \frac{\left\langle Vo \cdot \left\langle hc + \frac{hcb}{2} \right\rangle \right\rangle - Mpin_{CIP} - Mpin_{PC}}{bay} = 41.33\ \textbf{kip}$ Good Enough.

a)

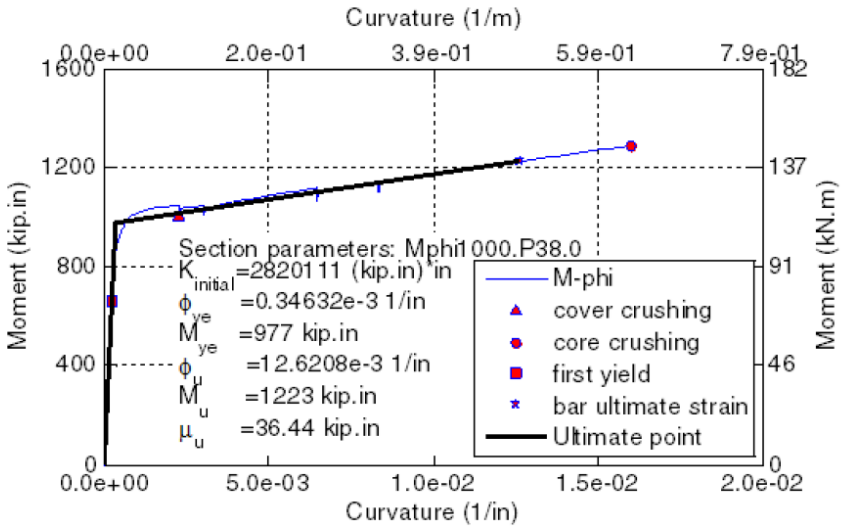

b)

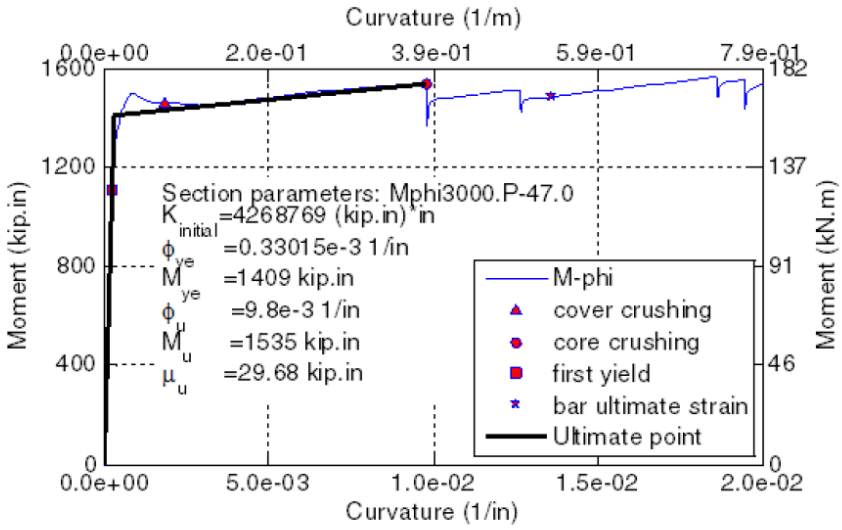

Fig. C-7. moment-curvature analysis of columns a) CIP b) PC

a)

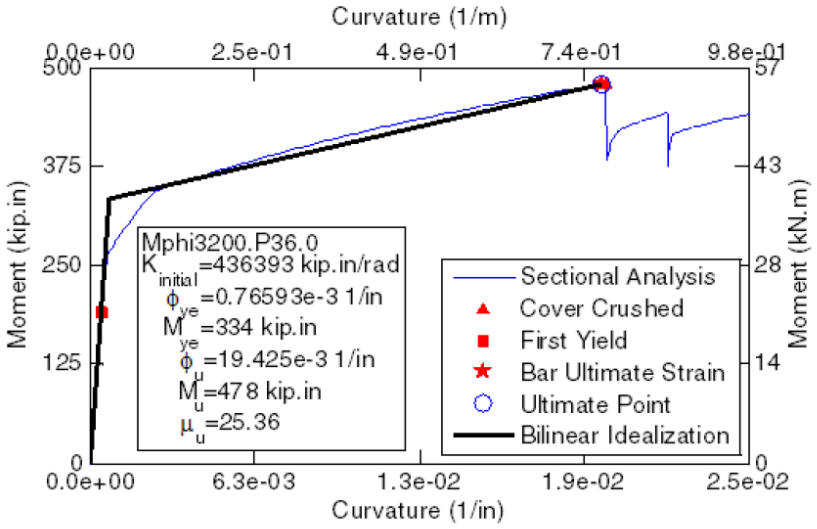

b)

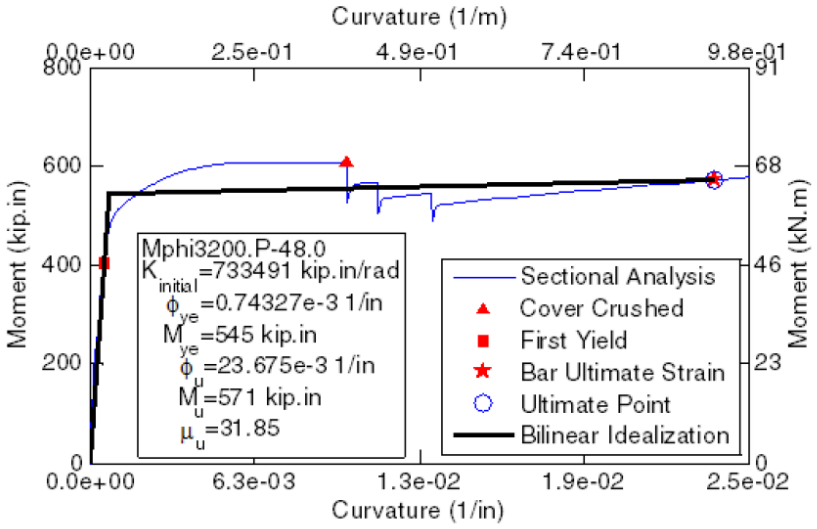

Fig. C-8. moment-curvature analysis of rebar-pins a) CIP b) PC

Determining Rebar-Pin Springs

Cheng et al.(2006)

$fy := 71.788\ ksi$ $d_b := 0.625\ in$

$Lp := gap + 0.15\ \frac{fy}{ksi} \cdot d_b = 7.73\ in$

CIP	PC
$\phi_{y.pin1} := 0.765 \cdot 10^{-3}\ \frac{1}{in}$	$\phi_{y.pin2} := 0.743 \cdot 10^{-3}\ \frac{1}{in}$
$M_{y.pin1} := 334\ kip \cdot in$	$M_{y.pin2} := 545\ kip \cdot in$
$\phi_{u.pin1} := \langle 19.425 \cdot 10^{-3} \rangle\ \frac{1}{in}$	$\phi_{u.pin2} := \langle 23.675 \cdot 10^{-3} \rangle\ \frac{1}{in}$
$M_{u.pin1} := 478\ kip \cdot in$	$M_{u.pin2} := 571\ kip \cdot in$

- Yield Rotation

$\theta_{y.flex1} := \phi_{y.pin1} \cdot gap = \langle 7.65 \cdot 10^{-4} \rangle\ rad$ $\theta_{y.flex2} := \phi_{y.pin2} \cdot gap = \langle 7.43 \cdot 10^{-4} \rangle\ rad$

Bond rotation: Double side bond, Wehbe's Method

$\theta_{y.bond1} := 5.748 \cdot 10^{-3}\ rad$ $\theta_{y.bond2} := 6.449 \cdot 10^{-3}\ rad$

$\theta_{y.pin1} := \theta_{y.flex1} + \theta_{y.bond1} = \langle 6.51 \cdot 10^{-3} \rangle\ rad$ $\theta_{y.pin2} := \theta_{y.flex2} + \theta_{y.bond2} = \langle 7.19 \cdot 10^{-3} \rangle\ rad$

- Ultimate point

$\theta_{p1} := Lp \cdot \langle \phi_{u.pin1} - \phi_{y.pin1} \rangle = 0.144\ rad$ $\theta_{p2} := Lp \cdot \langle \phi_{u.pin2} - \phi_{y.pin2} \rangle = 0.177\ rad$

$\theta_{u.pin1} := \theta_{p1} + \theta_{y.flex1} = 0.145\ rad$ $\theta_{u.pin2} := \theta_{p2} + \theta_{y.flex2} = 0.178\ rad$

$$Mcip.pin := \begin{bmatrix} 0 \\ M_{y.pin1} \\ M_{u.pin1} \end{bmatrix} = \begin{bmatrix} 0.00 \\ 334.00 \\ 478.00 \end{bmatrix} \ kip \cdot in \qquad \theta cip.pin := \begin{bmatrix} 0 \\ \theta_{y.pin1} \\ \theta_{u.pin1} \end{bmatrix} = \begin{bmatrix} 0.00 \\ 6.51 \cdot 10^{-3} \\ 145.01 \cdot 10^{-3} \end{bmatrix} \ rad$$

$$Mpc.pin := \begin{bmatrix} 0 \\ M_{y.pin2} \\ M_{u.pin2} \end{bmatrix} = \begin{bmatrix} 0.00 \\ 545.00 \\ 571.00 \end{bmatrix} \ kip \cdot in \qquad \theta pc.pin := \begin{bmatrix} 0 \\ \theta_{y.pin2} \\ \theta_{u.pin2} \end{bmatrix} = \begin{bmatrix} 0.00 \\ 7.19 \cdot 10^{-3} \\ 178.01 \cdot 10^{-3} \end{bmatrix} \ rad$$

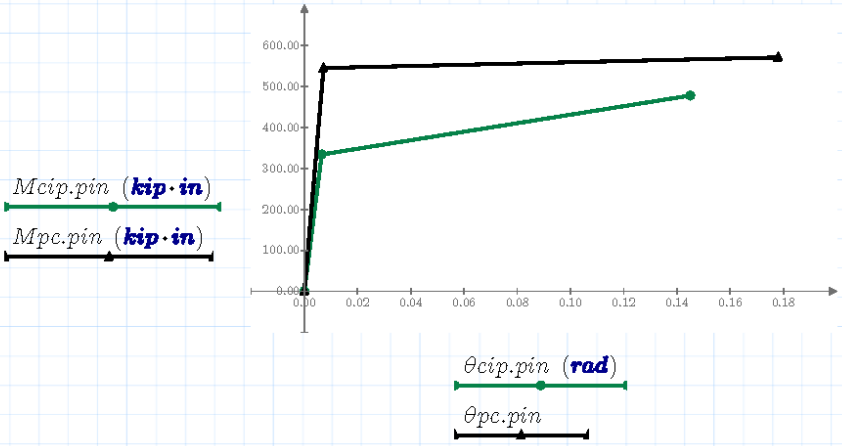

Fig. C-9. Rebar-pin springs

Column Plastic Hinge Springs

Paulay & Priestley (1992)

$f_y := 72.08\ ksi$ $d_{bl} := 0.5\ in$ $hc = 64.00\ in$

$$Lp := \max\left(0.08\ hc + 0.15 \cdot \frac{f_y}{ksi} \cdot d_{bl},\ 0.3\ \frac{f_y}{ksi} \cdot d_{bl}\right) = 10.81\ in$$

CIP	PC
$\phi_{y.col1} := 0.351 \cdot 10^{-3}\ \frac{1}{in}$	$\phi_{y.col2} := 0.328 \cdot 10^{-3}\ \frac{1}{in}$
$M_{y.col1} := 924\ kip \cdot in$	$M_{y.col2} := 1456\ kip \cdot in$
$\phi_{u.col1} := 12.538\ 10^{-3}\ \frac{1}{in}$	$\phi_{u.col2} := 9.56\ 10^{-3}\ \frac{1}{in}$
$M_{u.col1} := 1171\ kip \cdot in$	$M_{u.col2} := 1573\ kip \cdot in$

- Yield Rotation

$\Delta_{y.flex1} := \phi_{y.col1} \cdot \frac{hc^2}{3} = 0.48\ in$ $\Delta_{y.flex2} := \phi_{y.col2} \cdot \frac{hc^2}{3} = 0.45\ in$

Bond rotation: Double side bond, Wehbe's Method

$\theta_{y.bond1} := 1.439 \cdot 10^{-3}\ rad$ $\theta_{y.bond2} := 1.652 \cdot 10^{-3}\ rad$

$\Delta_{y.bond1} := \theta_{y.bond1} \cdot hc = 0.09\ in$ $\Delta_{y.bond2} := \theta_{y.bond2} \cdot hc = 0.11\ in$

$\theta_{y.col1} := \frac{\Delta_{y.flex1} + \Delta_{y.bond1}}{hc} = \left\langle 8.93 \cdot 10^{-3} \right\rangle\ rad$ $\theta_{y.col2} := \frac{\Delta_{y.flex2} + \Delta_{y.bond2}}{hc} = \left\langle 8.65 \cdot 10^{-3} \right\rangle\ rad$

- Ultimate point

$\theta_{p1} := Lp \cdot \langle \phi_{u.col1} - \phi_{y.col1} \rangle = 0.132$ **rad**

$\theta_{p2} := Lp \cdot \langle \phi_{u.col2} - \phi_{y.col2} \rangle = 0.100$ **rad**

$\Delta_{y.flex1} := \frac{hc^2}{3} \cdot \phi_{y.col1} = 0.48$ **in**

$\Delta_{y.flex2} := \frac{hc^2}{3} \cdot \phi_{y.col2} = 0.45$ **in**

$\theta_{u.col1} := \frac{\theta_{p1} \cdot \left(hc - \frac{Lp}{2}\right) + \Delta_{y.flex1}}{hc} = 0.128$ **rad**

$\theta_{u.col2} := \frac{\theta_{p2} \cdot \left(hc - \frac{Lp}{2}\right) + \Delta_{y.flex2}}{hc} = 0.098$ **rad**

$Mcip.col := \begin{bmatrix} 0 \\ M_{y.col1} \\ M_{u.col1} \end{bmatrix} = \begin{bmatrix} 0 \\ 924 \\ 1171 \end{bmatrix}$ **kip·in**

$\theta cip.col := \begin{bmatrix} 0 \\ \theta_{y.col1} \\ \theta_{u.col1} \end{bmatrix} = \begin{bmatrix} 0.00 \\ 8.93 \cdot 10^{-3} \\ 128.12 \cdot 10^{-3} \end{bmatrix}$

$Mpc.col := \begin{bmatrix} 0 \\ M_{y.col2} \\ M_{u.col2} \end{bmatrix} = \begin{bmatrix} 0 \\ 1456 \\ 1573 \end{bmatrix}$ **kip·in**

$\theta pc.col := \begin{bmatrix} 0 \\ \theta_{y.col2} \\ \theta_{u.col2} \end{bmatrix} = \begin{bmatrix} 0.00 \\ 8.65 \cdot 10^{-3} \\ 98.38 \cdot 10^{-3} \end{bmatrix}$

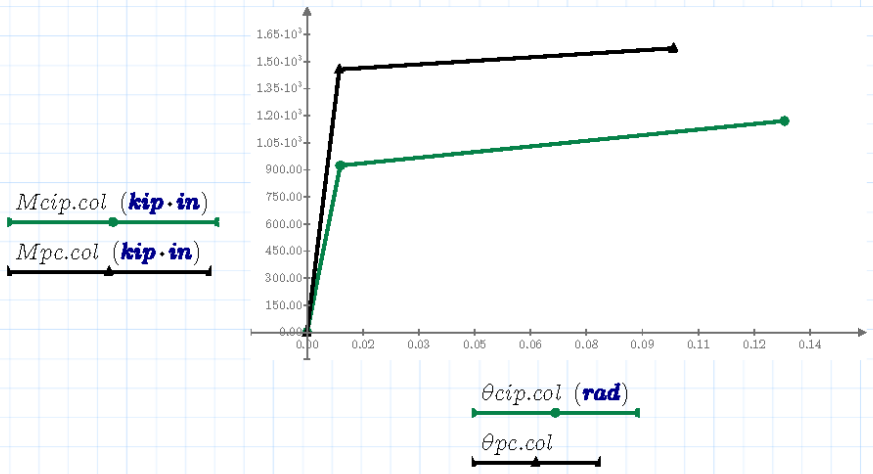

Fig. C-10. Column springs

First Yield Displacement and Force

Smallest yield rotation was in CIP pin:

$$\theta_y := \theta_{y.pin1} = \left(6.51 \cdot 10^{-3}\right)\ \textit{rad}$$

$$\Delta_1 := \theta_y \cdot hc = 0.42\ \textit{in}$$

drift: $$\delta_1 := \frac{\Delta_1}{hc} = 0.65\%$$

CIP

$$M_{col.cip} := \frac{M_{y.col1}}{\theta_{y.col1}} \cdot \theta_y = 674.14\ \textit{kip} \cdot \textit{in}$$

$$M_{pin.cip} := \frac{M_{y.pin1}}{\theta_{y.pin1}} \cdot \theta_y = 334.00\ \textit{kip} \cdot \textit{in}$$

$$V_{CIP} := \frac{M_{col.cip} + M_{pin.cip}}{hc} = 15.75\ \textit{kip}$$

PC

$$M_{col.pc} := \frac{M_{y.col2}}{\theta_{y.col2}} \cdot \theta_y = 1096\ \textit{kip} \cdot \textit{in}$$

$$M_{pin.pc} := \frac{M_{y.pin2}}{\theta_{y.pin2}} \cdot \theta_y = 493.55\ \textit{kip} \cdot \textit{in}$$

$$V_{PC} := \frac{M_{col.pc} + M_{pin.pc}}{hc} = 24.84\ \textit{kip}$$

$$V_{base_1} := V_{CIP} + V_{PC} = 40.59\ \textit{kip}$$

Second Yield Displacement and Force

Second yield rotation is in PC pin:

$$\theta_y := \theta_{y.pin2} = \left(7.19 \cdot 10^{-3}\right)\ \textit{rad}$$

$$\Delta_2 := \theta_y \cdot hc = 0.46\ \textit{in}$$

drift: $$\delta_2 := \frac{\Delta_2}{hc} = 0.72\%$$

$$M_{col.cip} := \frac{M_{y.col1}}{\theta_{y.col1}} \cdot \theta_y = 744 \ \textbf{kip} \cdot \textbf{in} \qquad M_{col.pc} := \frac{M_{y.col2}}{\theta_{y.col2}} \cdot \theta_y = 1211 \ \textbf{kip} \cdot \textbf{in}$$

$$M_{pin.cip} := \frac{M_{u.pin1} - M_{y.pin1}}{\theta_{u.pin1} - \theta_{y.pin1}} \cdot \langle \theta_y - \theta_{y.pin1} \rangle + M_{y.pin1} = 334.71 \ \textbf{kip} \cdot \textbf{in}$$

$$M_{pin.pc} := \frac{M_{u.pin2} - M_{y.pin2}}{\theta_{u.pin2} - \theta_{y.pin2}} \cdot \langle \theta_y - \theta_{y.pin2} \rangle + M_{y.pin2} = 545.00 \ \textbf{kip} \cdot \textbf{in}$$

$$V_{CIP} := \frac{M_{col.cip} + M_{pin.cip}}{hc} = 16.86 \ \textbf{kip} \qquad V_{PC} := \frac{M_{col.pc} + M_{pin.pc}}{hc} = 27.43 \ \textbf{kip}$$

$$V_{base_2} := V_{CIP} + V_{PC} = 44.29 \ \textbf{kip}$$

Third Yield Displacement and Force

Third yield rotation is in PC Column:

$$\theta_y := \theta_{y.col2} = \langle 8.65 \cdot 10^{-3} \rangle \ \textbf{rad}$$

$$\Delta_3 := \theta_y \cdot hc = 0.55 \ \textbf{in}$$

drift: $$\delta_3 := \frac{\Delta_3}{hc} = 0.86\%$$

$$M_{col.cip} := \frac{M_{y.col1}}{\theta_{y.col1}} \cdot \theta_y = 895 \ \textbf{kip} \cdot \textbf{in}$$

$$M_{col.pc} := \frac{M_{u.col2} - M_{y.col2}}{\theta_{u.col2} - \theta_{y.col2}} \cdot \langle \theta_y - \theta_{y.col2} \rangle + M_{y.col2} = 1456 \ \textbf{kip} \cdot \textbf{in}$$

$$M_{pin.cip} := \frac{M_{u.pin1} - M_{y.pin1}}{\theta_{u.pin1} - \theta_{y.pin1}} \cdot \langle \theta_y - \theta_{y.pin1} \rangle + M_{y.pin1} = 336.22 \ \textbf{kip} \cdot \textbf{in}$$

$$M_{pin.pc} := \frac{M_{u.pin2} - M_{y.pin2}}{\theta_{u.pin2} - \theta_{y.pin2}} \cdot \langle \theta_y - \theta_{y.pin2} \rangle + M_{y.pin2} = 545.22 \ \textbf{kip} \cdot \textbf{in}$$

$$V_{CIP} := \frac{M_{col.cip} + M_{pin.cip}}{hc} = 19.24 \ \textit{kip} \qquad V_{PC} := \frac{M_{col.pc} + M_{pin.pc}}{hc} = 31.27 \ \textit{kip}$$

$$V_{base_3} := V_{CIP} + V_{PC} = 50.51 \ \textit{kip}$$

Fourth Yield Displacement and Force

Fourth yield rotation is in CIP Column:

$$\theta_y := \theta_{y.col1} = \left(8.93 \cdot 10^{-3}\right) \ \textit{rad}$$

$$\Delta_4 := \theta_y \cdot hc = 0.57 \ \textit{in}$$

drift: $$\delta_4 := \frac{\Delta_4}{hc} = 0.89\%$$

$$M_{col.cip} := \frac{M_{u.col1} - M_{y.col1}}{\theta_{u.col1} - \theta_{y.col1}} \cdot \left\langle \theta_y - \theta_{y.col1} \right\rangle + M_{y.col1} = 924 \ \textit{kip} \cdot \textit{in}$$

$$M_{col.pc} := \frac{M_{u.col2} - M_{y.col2}}{\theta_{u.col2} - \theta_{y.col2}} \cdot \left\langle \theta_y - \theta_{y.col2} \right\rangle + M_{y.col2} = 1456 \ \textit{kip} \cdot \textit{in}$$

$$M_{pin.cip} := \frac{M_{y.pin1}}{\theta_{y.pin1}} \cdot \theta_y = 457.79 \ \textit{kip} \cdot \textit{in}$$

$$M_{pin.pc} := \frac{M_{u.pin2} - M_{y.pin2}}{\theta_{u.pin2} - \theta_{y.pin2}} \cdot \left\langle \theta_y - \theta_{y.pin2} \right\rangle + M_{y.pin2} = 545.26 \ \textit{kip} \cdot \textit{in}$$

$$V_{CIP} := \frac{M_{col.cip} + M_{pin.cip}}{hc} = 21.59 \ \textit{kip} \qquad V_{PC} := \frac{M_{col.pc} + M_{pin.pc}}{hc} = 31.28 \ \textit{kip}$$

$$V_{base_4} := V_{CIP} + V_{PC} = 52.87 \ \textit{kip}$$

Ultimate Point

$M_{col.cip} := M_{u.col1} = 1171\ \textit{kip}\cdot\textit{in}$

$M_{pin.cip} := M_{u.pin1} = 478\ \textit{kip}\cdot\textit{in}$

Zero moment point: $h_1 := \frac{M_{col.cip}}{M_{col.cip} + M_{pin.cip}} \cdot hc = 45.45\ \textit{in}$

$M_{pin.cip} < M_{y.col1} = 1$ Elastic deformation under zero moment point.

$$\phi_{1.bot} := \frac{M_{pin.cip}}{M_{y.col1}} \cdot \phi_{y.col1} = \left\langle 1.82 \cdot 10^{-4} \right\rangle \frac{1}{\textit{in}}$$

$M_{col.pc} := M_{u.col2} = 1573\ \textit{kip}\cdot\textit{in}$

$M_{pin.pc} := M_{u.pin2} = 571\ \textit{kip}\cdot\textit{in}$

Zero moment point: $h_2 := \frac{M_{col.pc}}{M_{col.pc} + M_{pin.pc}} \cdot hc = 46.96\ \textit{in}$

$M_{pin.pc} < M_{y.col2} = 1$ Elastic deformation under zero moment point.

$$\phi_{2.bot} := \frac{M_{pin.pc}}{M_{y.col2}} \cdot \phi_{y.col2} = \left\langle 1.29 \cdot 10^{-4} \right\rangle \frac{1}{\textit{in}}$$

CIP	PC
$\theta_{p1} := Lp \cdot \langle \phi_{u.col1} - \phi_{y.col1} \rangle = 0.132\ \textit{rad}$	$\theta_{p2} := Lp \cdot \langle \phi_{u.col2} - \phi_{y.col2} \rangle = 0.100\ \textit{rad}$
$\Delta_{p.col1} := \theta_{p1} \cdot \left(h_1 - \frac{Lp}{2} \right) = 5.276\ \textit{in}$	$\Delta_{p.col2} := \theta_{p2} \cdot \left(h_2 - \frac{Lp}{2} \right) = 4.147\ \textit{in}$
$E_{eff1} := \frac{M_{y.col1}}{\phi_{y.col1}} = \left\langle 2.63 \cdot 10^{6} \right\rangle\ \textit{kip}\cdot\textit{in}^2$	$E_{eff1} := \frac{M_{y.col1}}{\phi_{y.col1}} = \left\langle 2.63 \cdot 10^{6} \right\rangle\ \textit{kip}\cdot\textit{in}^2$
$\Delta_{y.flex1.bot} := \frac{\langle hc - h_1 \rangle^2}{3} \cdot \phi_{1.bot} = 0.02\ \textit{in}$	$\Delta_{y.flex2.bot} := \frac{\langle hc - h_2 \rangle^2}{3} \cdot \phi_{2.bot} = 0.01\ \textit{in}$

$\Delta_{u1} := \Delta_{p.col1} + \Delta_{y.flex1.top} + \Delta_{y.flex1.bot} = 5.52\ \textit{in}$

$$\Delta_{u2} := \Delta_{p.col2} + \Delta_{y.flex2.top} + \Delta_{y.flex2.bot} = 4.42\ \textbf{in}$$

$$\Delta_5 := min\left(\Delta_{u1}, \Delta_{u2}\right) = 4.42\ \textbf{in}$$

$$\delta_5 := \frac{\Delta_5}{hc} = 6.91\%$$

$$V_{CIP} := \frac{M_{col.cip} + M_{pin.cip}}{hc} = 25.77\ \textbf{kip} \qquad V_{PC} := \frac{M_{col.pc} + M_{pin.pc}}{hc} = 33.50\ \textbf{kip}$$

$$V_{base_5} := V_{CIP} + V_{PC} = 59.27\ \textbf{kip}$$

P-Delta effect: $V_{base} := V_{base} - K_{P\Delta} \cdot \Delta$

Adding Shear Deformation:

$C_{total} := 91.2\ kip$ $Vn := 0.45 \cdot C_{total} = 41.04\ kip$

$V_{CIP} = 25.77\ kip$ $V_{PC} = 33.50\ kip$ In the first segment.

Rebar-Pin Section properties:

$A_{sp} = 0.11\ in^2$ $s := 1.5\ in$ $Es := 29000\ ksi$

$D := 10\ in$ $Dcore := D - 2 \cdot 1\ in - 0.375\ in = 7.63\ in$

$Ag := \frac{\pi}{4} D^2 = 78.54\ in^2$

$fc := 6.26\ ksi$

$Ec := 57\ ksi \cdot \sqrt{\frac{fc}{psi}} = \langle 4.51 \cdot 10^3 \rangle\ ksi$ $n := \frac{Es}{Ec} = 6.43$

$\rho_v := \frac{4 \cdot A_{sp}}{Dcore \cdot s} = 3.86\%$

Cracked section Shear stiffness:

$K_{v45} := \frac{\rho_v}{1 + 4 \cdot n \cdot \rho_v} Es \cdot (0.8 \cdot Ag) = 35305\ \frac{kip}{in} \cdot in$

$Kcr := \frac{K_{v45}}{gap} = 35305.16\ \frac{kip}{in}$

$\Delta s := \frac{0.5 \cdot V_{base}}{Kcr} = \begin{bmatrix} 0.00 \\ 5.72 \cdot 10^{-4} \\ 6.24 \cdot 10^{-4} \\ 7.11 \cdot 10^{-4} \\ 7.44 \cdot 10^{-4} \\ 8.05 \cdot 10^{-4} \end{bmatrix} in$ Negligible.

Walraven & Reinhardt (1981)

$Dcore = 7.63\ in$ $\quad Acore := \frac{\pi}{4} Dcore^2 = 45.66\ in^2$

Concrete cylinder strength: $\quad fc := 6.26\ ksi$

Concrete cube strength: $\quad fcc := 1.25 \cdot fc$

$$vco := \frac{fcc}{30} = 260.83\ psi$$

$$\Delta s_{Walraven}(vci, w) := \frac{\frac{(vci + vco)}{MPa}}{1.8 \cdot \left(\frac{w}{mm}\right)^{-0.8} + \left(0.23 \cdot \left(\frac{w}{mm}\right)^{-0.707} - 0.20\right) \cdot \frac{fcc}{MPa}}\ mm$$

Okamura-Maekawa Model:

$$a := \frac{3}{8}\ in$$

$$fc = \left(6.26 \cdot 10^3\right)\ psi$$

$$vcmax(w) := \frac{\sqrt{\frac{fc}{MPa}}}{0.31 + \frac{24 \cdot \frac{w}{mm}}{\frac{a}{mm} + 16}}\ MPa$$

$i := 1 \quad \theta_{pin} := \delta_i \quad v := \frac{V_{base_i}}{2 \cdot Acore} \quad w := \frac{\theta_{pin} \cdot Dcore}{2} = 0.02\ in \quad \Psi := \frac{v}{vcmax(w)}$

$$\Delta s1_i := \Delta s_{Walraven}(v, w) = 0.02\ in$$

$$\Delta s2_i := w \cdot \sqrt{\frac{\Psi}{1 - \Psi}} = 0.02\ in \qquad \Delta s_i := \frac{\Delta s1_i + \Delta s2_i}{2} = 0.02\ in$$

$i := 2 \quad \theta_{pin} := \delta_i \quad v := \frac{V_{base_i}}{2 \cdot Acore} \quad w := \frac{\theta_{pin} \cdot Dcore}{2} = 0.03 \text{ in}$

$\Delta s1_i := \Delta s_{Walraven}(v, w) = 0.03 \text{ in} \qquad \Psi := \frac{v}{vcmax(w)}$

$\Delta s2_i := w \cdot \sqrt{\frac{\Psi}{1-\Psi}} = 0.03 \text{ in} \qquad \Delta s_i := \frac{\Delta s1_i + \Delta s2_i}{2} = 0.03 \text{ in}$

$i := 3 \quad \theta_{pin} := \delta_i \quad v := \frac{V_{base_i}}{2 \cdot Acore} \quad w := \frac{\theta_{pin} \cdot Dcore}{2} = 0.03 \text{ in} \quad \Psi := \frac{v}{vcmax(w)}$

$\Delta s1_i := \Delta s_{Walraven}(v, w) = 0.04 \text{ in}$

$\Delta s2_i := w \cdot \sqrt{\frac{\Psi}{1-\Psi}} = 0.04 \text{ in} \qquad \Delta s_i := \frac{\Delta s1_i + \Delta s2_i}{2} = 0.04 \text{ in}$

$i := 4 \quad \theta_{pin} := \delta_i \quad v := \frac{V_{base_i}}{2 \cdot Acore} \quad w := \frac{\theta_{pin} \cdot Dcore}{2} = 0.03 \text{ in} \quad \Psi := \frac{v}{vcmax(w)}$

$\Delta s1_i := \Delta s_{Walraven}(v, w) = 0.05 \text{ in}$

$\Delta s2_i := w \cdot \sqrt{\frac{\Psi}{1-\Psi}} = 0.05 \text{ in} \qquad \Delta s_i := \frac{\Delta s1_i + \Delta s2_i}{2} = 0.05 \text{ in}$

$i := 5 \quad \theta_{pin} := \delta_i \quad v := \frac{V_{base_i}}{2 \cdot Acore} \quad w := \frac{\theta_{pin} \cdot Dcore}{2} = 0.26 \text{ in} \quad \Psi := \frac{v}{vcmax(w)}$

$\Delta s1_i := \Delta s_{Walraven}(v, w) = -0.03 \text{ in}$

$\Delta s2_i := w \cdot \sqrt{\frac{\Psi}{1-\Psi}} = 0.30i \text{ in} \qquad \Delta s_5 := \Delta s_4 = 0.05 \text{ in}$

$$\Delta := \Delta + \Delta s = \begin{bmatrix} 0.00 \\ 0.44 \\ 0.49 \\ 0.60 \\ 0.62 \\ 4.47 \end{bmatrix} \textit{in} \qquad \delta := \frac{\Delta}{hc} = \begin{bmatrix} 0.00 \\ 0.68\% \\ 0.76\% \\ 0.93\% \\ 0.97\% \\ 6.98\% \end{bmatrix}$$

$$\delta = \begin{bmatrix} 0.000 \\ 0.684\% \\ 0.761\% \\ 0.931\% \\ 0.967\% \\ 6.983\% \end{bmatrix} \qquad V_{base} = \begin{bmatrix} 0.0 \\ 40.4 \\ 44.0 \\ 50.2 \\ 52.6 \\ 56.9 \end{bmatrix} \textit{kip}$$

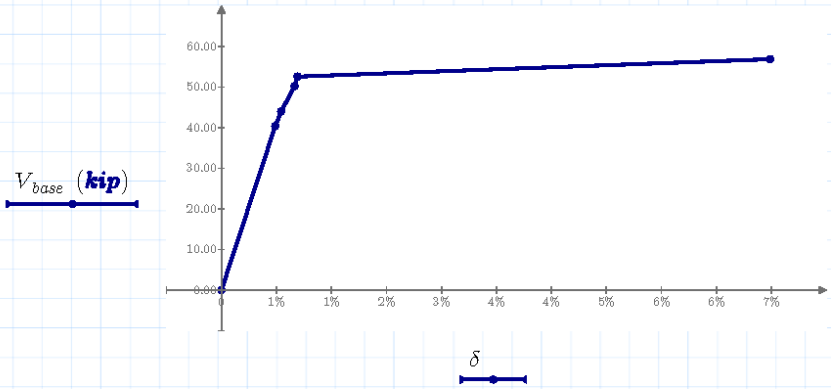

Fig. C-11. Force-displacemnt envelop push to north

Appendix D. OpenSEES Scripts for Numerical Simulation of BPSA

It was explained in the main body of this document that the effects of many analysis options and materials were investigated to determine the options that led to reasonable estimates of the measured response. Due to the large numbers of analyses, the scripts were prepared in modules rather than a single code in OpenSEES. The following scripts were used to model BPSA.

```
# BPSA_test Verification.tcl*****************************************************************
# The main file to model and Analyze the
# "Two-Column Bent with Pipe-pin Column-Pile Shaft Connection for ABC (BPSA)"
# The modules should be copy in two folders: "Modules" and "Model"
# April 16, 2016
# Units: kip, in, sec

# Sign Convention: South +X, Up +Y, Clockwise rotation is positive
#               Y ^
#                 |  _
#                 |   \
#        X  <-------- |
#                  <_ /
#

set log "BPSA_TestVerification.txt";
set temp [open $log w]
puts $temp "\# [clock format [clock seconds]]"
close $temp
logFile $log -append

# Constants
set PI [expr 2.0*asin(1.0)];# define constants
set g [expr 32.2*12.0];     # gravitational acceleration
set largeNum 1.0e9
```

```
source Model_BPSA.tcl
source Modules/Gravity.tcl
set    numModes 2;
source Modules/Modal.tcl
source Modules/damping.tcl
#source Modules/Display_Bent.tcl

# Dynamic Loading----------------------
set DtGround [expr 1.0/256.];
set GMdirection 1
set statVelTol  0.01; #in/s
set statAccTol  0.01; #in/s2

# Parametric #73
set dt(6)  [expr $DtGround*2.0]; set dt(7)  [expr $DtGround*2.0]; set dt(8)  [expr $DtGround*2.0];
set dt(9)  [expr $DtGround*2.0]; set dt(10) [expr $DtGround]; set dt(11) [expr $DtGround*4.0];

set TmaxAnalysis 0.0;
foreach run [list 6 7 8 9 10 11] {
puts "\n\n Starting run: $run _____________________________________"
set outFolder  "Response_TestVerification/RUN-$run"

set tsTag $run
set MotionFile "Input Motions/tableA-RUN-$run.txt";
setTime 0.0
timeSeries Path $tsTag -dt $DtGround -filePath "Input Motions/tableA-RUN-$run.txt" -factor 386.4
pattern UniformExcitation  $run  $GMdirection  -accel $tsTag;
```

```
source Modules/Recorder_Dynamic.tcl

set DtAnalysis      $dt($run);  # time-step Dt for lateral analysis
set TmaxAnalysis     40.0;      # maximum duration of ground-motion analysis -- should be 50*$sec
source Modules/DynamicAnalysis.tcl

# Free-Vibration
set DtAnalysis      [expr 0.05];
while { [expr abs([nodeVel $monitor 1])] > $statVelTol || [expr abs([nodeAccel $monitor 1])] >
$statAccTol   } {
    set TmaxAnalysis    [expr $TmaxAnalysis+20.0];
    source Modules/DynamicAnalysis.tcl
}
remove recorders
remove loadPattern $run
puts "Velocity= [nodeVel $monitor 1] in/s, Acc= [expr ([nodeAccel $monitor 1])/386.4 ] g, ";
source Modules/Modal.tcl
puts "finished BPSA RUN-$run "
puts "_____________________________________________________"
}
wipe

set temp [open $log a]
puts $temp "\# End of log BPSA"
puts $temp "\# [clock format [clock seconds]]"
close $temp
puts "End of BPSA.tcl"
```

#**********
*****

```
# Model_BPSA.tcl
# Sign Convention: South +X, Up +Y, Clockwise rotation is positive
#                Y ^
#                  |  _
#                  |   \
#        X  <--------- |
#                  <_ /
#

puts "\n_____________________________________________________________________________________________";
puts "** ([clock format [clock seconds]]) Starting Model_BPSA.tcl (2D model)..."

wipe;                                # clear memory of all past model definitions
model basic -ndm 2 -ndf 3;           # Define the model builder, ndm=#dimension, ndf=#dofs
# nodal coordinates-------------------------------------------------------------------------
set hp  30.0;
#set gap 0.25;
set gap 0.0;
set hc  63.75;
set hcb 24.0;    # Cap beam height
set bcb 24.0;    # Cap beam height
set bay [expr 7.0*12./2.0]; #half of the bay between columns

# Nodes Tags
set base   10;
set pedTop 20;
```

```
set colBot 30;
set colTop 40;
set cb     50;
# Small mass for numerical solution
set M 1.e-6;

#Node   Label                 X      Y
node    [expr 100+$base]     $bay    [expr 0.0]                    ;
node    [expr 100+$pedTop]   $bay    [expr $hp+$gap]               -mass $M $M 0.0;
node    [expr 100+$colBot]   $bay    [expr $hp+$gap]               -mass $M $M 0.0;
node    [expr 100+$colTop]   $bay    [expr $hp+$gap+$hc]           -mass $M $M 0.0;
node    [expr 100+$cb]       $bay    [expr $hp+$gap+$hc+$hcb/2.0] -mass $M $M 0.0;

node    [expr 200+$cb]       0.0     [expr $hp+$gap+$hc+$hcb/2.0] -mass $M $M 0.0;

node    [expr 300+$base]     -$bay   [expr 0.0]                    ;
node    [expr 300+$pedTop]   -$bay   [expr $hp+$gap]               -mass $M $M 0.0;
node    [expr 300+$colBot]   -$bay   [expr $hp+$gap]               -mass $M $M 0.0;
node    [expr 300+$colTop]   -$bay   [expr $hp+$gap+$hc]           -mass $M $M 0.0;
node    [expr 300+$cb]       -$bay   [expr $hp+$gap+$hc+$hcb/2.0] -mass $M $M 0.0;

set monitor [expr 200+$cb];

# Boundary conditions
fix [expr 100+$base] 1 1 1;     # Fixed at the base
fix [expr 300+$base] 1 1 1;
```

```
# Default materials/springs
set rigidMat 1
set softMat  2
uniaxialMaterial Elastic $rigidMat 1.0e12
uniaxialMaterial Elastic $softMat  1.0e-6
set tol 1.0e-9;
set iter  50;

# Element
GeomTranf
# Columns,Z is in to the plane. Hence; localY: toward -X
# Beams,Z is in to the plane. Hence; localY: toward +Y(Up)
set ColTransfTag  1;
set BeamTransfTag 2;

#geomTransf PDelta $transfTag <-jntOffset $dXi $dYi $dXj $dYj>
geomTransf PDelta $ColTransfTag
geomTransf PDelta $BeamTransfTag

# Modeling Masses and
Pdelta
      source Model/Model_PDelta_Spring.tcl

# Cap Beam-----------------------------------------------------------------------------
------
set CIPcb  130;
```

```
set ABCcb  330;
source "Model/CapBeam_Elastic.tcl"
#COLUMNS
set CIPcolECCsec        1000;   # Tag for ECC concrete sections
set CIPcolBondSec       1010;   # tag for ECC w/ Bond Slip
set CIPcolRegSec        1050;   # Tag for out of plastic hinge(ECC) concrete sections
set CIPCol  100;
source "Model/Model_CIP_Col_MostafaBond.tcl"

set ABCcolSec           3000;   # Tag for ECC concrete sections
set ABCcolBondSec       3010;
set ABCCol  300;
source "Model/Model_PC_Col_MostafaBond.tcl"

# PIPE-
PIN
set CIPpin 120;
set ABCpin 320;

source "Model/PipePin_Spring2.tcl"

#
PEDESTAL
set pedSec      1100;
set pedBondSec  1110;
set CIPPed      110; #Element Tag for the pedestal under CIP column
```

```
set ABCPed      310; #Element Tag for the pedestal under ABC column

source "Model/Model_Pedestals_MostafaBond.tcl"

# Printing the model
connectivity_____________________________________________________________________
puts "\n***NODES:";
set allTags [getNodeTags];
foreach tag  $allTags {
    puts [format "%i: %5.2f %5.2f" $tag [nodeCoord $tag 1] [nodeCoord $tag 2]];
}
puts "\n***Element Connectivity:";
puts "Ele: i-node j-node"
foreach ele [getEleTags] {
    puts "$ele: [eleNodes $ele]"
}
puts "_____________________________________________________________________________________";
#*********************************************************************************
```

```
# Model_PDelta_Spring.tcl*****************************************************************
# Models gravity load and P-Delta spring
# WmassRig=100 kip
# hMassRig=98 in
# K=W/h = 1.0204, Negative because of the nature of Pdelta

set M [expr 104.5/$g]
mass [expr 100+$cb]  $M $M 0.0   ;
set M [expr 4.5/$g]
mass [expr 300+$cb]  $M $M 0.0   ;

set KpDelta  [expr -100.0/183.3];

#uniaxialMaterial Elastic $matTag $E <$eta> <$Eneg>
 uniaxialMaterial Elastic  10      $KpDelta

 node [expr $base] $bay     [expr $hp+$gap+$hc+$hcb/2.0];
 fix  [expr $base] 1 1 1
 element zeroLength 1000  $base [expr 100+$cb]  -mat 10 -dir   1

# Gravity load ============================================================================
  pattern Plain 100 Constant {
       load         [expr 100+$cb]  0.0 -4.50 0.0 ;
       load         [expr 300+$cb]  0.0 -4.50 0.0 ;
 }
#*****************************************************************************************
```

```
# CapBeam_Elastic.tcl*****************************************************************

set fc      6.31;
set Keff    1.0;                                    # Effective stiffness for the beam due to
cracking
set A       [expr 24.0*24.0];                       # Gross sectional area
set E       [expr 57.0*sqrt(1000.0*$fc)];           # Young's Modulus elasticity same as concrete
set Iz      [expr $Keff*$bcb*pow($hcb,3.0)/12.0];   # Moment of Inertia around major axis (horizontal
one)

#element elasticBeamColumn $eleTag $iNode         $jNode         $A $E $Iz $transfTag <-mass
$massDens> <-cMass>
 element elasticBeamColumn $CIPcb  [expr 200+$cb] [expr 100+$cb] $A $E $Iz $BeamTransfTag;
 element elasticBeamColumn $ABCcb  [expr 300+$cb] [expr 200+$cb] $A $E $Iz $BeamTransfTag;
#*************************************************************************************************
***
```

```
#Model_CIP_Col.tcl*************************************************************************
***

# Materials for the full circular section 1000
# Top plastic hinge section
# uniaxialMaterial Concrete02 $matTag $fpc    $epsc0  $fpcu  $epsU    $lambda $ft $Ets
# uniaxialMaterial Concrete02 1010    -10.07  -0.0025 0.00   -0.006    0.10   0.0 0.0;# Cover,
Motaref (2011) Model
# uniaxialMaterial Concrete02 1020    -10.07  -0.0025 -4.028 -0.01011  0.10   0.0 0.0;# Core, Motaref
(2011) Model,

# uniaxialMaterial Concrete02 1010    -9.15   -0.00200   0.00 -0.00500  0.10   0.0 0.0;   # Cover,
Mander Model
# uniaxialMaterial Concrete02 1020    -10.278 -0.00404  -7.481 -0.01075 0.10   0.0 0.0;   # Core,
Mander Model,

#uniaxialMaterial Concrete01WithSITC $matTag $fpc   $epsc0     $fpcu  $epsU <$endStrainSITC>
#uniaxialMaterial Concrete01WithSITC 1010   -9.15   -0.002     0.0   -0.005    0.02;
#uniaxialMaterial Concrete01WithSITC 1020   -10.278 -0.00404   -7.481 -0.01075  0.02;

#uniaxialMaterial Concrete04 $matTag $fc        $ec    $ecu    $Ec <$fct $et> <$beta>
 uniaxialMaterial Concrete04  1010   -9.15   -0.002   -0.005   5452.0
 uniaxialMaterial Concrete04  1020   -10.278 -0.00404 -0.01075 5452.0

# Out-of-plastic hinge section
#uniaxialMaterial Concrete02        $matTag $fpc    $epsc0      $fpcu   $epsU     $lambda $ft $Ets
 #uniaxialMaterial Concrete02       1015    -6.31  -0.0020      0.000   -0.006    0.10   0.0 0.0;   #
Cover, reg. out of plastic hinge
```

```
 #uniaxialMaterial Concrete02       1025    -7.41  -0.00374    -4.764   -0.01231  0.10   0.0 0.0;   #
Core,  reg. out of plastic hinge


#uniaxialMaterial Concrete01WithSITC $matTag $fpc   $epsc0     $fpcu     $epsU <$endStrainSITC>
#uniaxialMaterial Concrete01WithSITC 1015    -6.31  -0.0020     0.000    -0.005   0.02;     # Cover,
reg. out of plastic hinge
#uniaxialMaterial Concrete01WithSITC 1025    -7.41  -0.00374    -4.764   -0.01231 0.02;     # Core,
reg. out of plastic hinge


#uniaxialMaterial Concrete04 $matTag $fc        $ec    $ecu    $Ec <$fct $et> <$beta>
 uniaxialMaterial Concrete04  1015   -6.31   -0.0020   -0.005   4528.
 uniaxialMaterial Concrete04  1025   -7.41   -0.00374  -0.01231 4528.


# Reinforcements
#uniaxialMaterial ReinforcingSteel $matTag $fy  $fu      $Es     $Esh    $esh    $eult -MPCurveParams
$R1 $R2 $R3< -GABuck $lsr $beta $r $gama > < -DMBuck $lsr < $alpha >> < -CMFatigue $Cf $alpha $Cd > <
-IsoHard <$a1 <$limit> > >
uniaxialMaterial ReinforcingSteel 1050      72.08   96.63    29000.0 800.0   0.014   0.14 ;#
Reinforcing bars Modified for strain rate
uniaxialMaterial ReinforcingSteel 1060      72.08   96.63    22705.0 800.0   0.014689    0.140843 ;#
Reinforcing bars



#uniaxialMaterial Steel02 $matTag $Fy   $E     $b       $R0 $cR1 $cR2 <$a1 $a2 $a3 $a4 $sigInit>
#uniaxialMaterial Steel02  1050   68.0  29000. 0.0062   10 0.925  0.15; #NO SRE
# uniaxialMaterial Steel02  1050   72.08 29000. 6.156e-3 10 0.925  0.1; #SRE
# uniaxialMaterial Steel02  1060   72.08 22705. 7.854e-3 10 0.925  0.1; #SRE


set numBar  14;
```

```
set Ab      0.20;               # #4 bars
set R       8.0;                # section outer Radius
set Rcore   6.8125;             # Center of spiral
set Rreinf  6.375;              # bars radius
set circdiv [expr $numBar*1];   # Divides the circular patch in 5 segments between each reinf.

section Fiber [expr $CIPcolRegSec] {;    # section W/ Reg concrete out of plastic hinge
#                   $mattag     $circdiv    $Rdiv       $y0 $z0 $intR       $extrR  $start  $end
        patch circ  1025        $circdiv    5           0.  0.  0.          $Rcore   0.0    360.0   ;
# Define core concrete
        patch circ  1015        $circdiv    2           0.  0.  $Rcore      $R     0.0      360.0   ;
# Define cover concrete

        #           $matTag     $numFiber   $Afiber     $y0 $z0 $radius  $startAng  $endAng
        layer circ  1050        $numBar     $Ab         0.  0.  $Rreinf ;                       #
Radial distribution of bars
};



section Fiber [expr $CIPcolECCsec] {;
#                   $mattag     $circdiv    $Rdiv       $y0 $z0 $intR       $extrR  $start  $end
        patch circ  1020        $circdiv    5           0.  0.  0.          $Rcore  0.0     360.0;
# Define core concrete fibers
        patch circ  1010        $circdiv    2           0.  0.  $Rcore      $R      0.0     360.0;
# Define cover concrete fibers
#                   $matTag     $numFiber   $Afiber     $y0 $z0 $radius     $startAng   $endAng
        layer circ  1050        $numBar     $Ab         0.  0.  $Rreinf;                # Radial
distribution of bars
};
```

```
section Fiber [expr $CIPcolBondSec] {;    # section w/ modified steel for bond-slip action
#                    $mattag     $circdiv    $Rdiv       $y0 $z0 $intR       $extrR  $start  $end
        patch circ  1020        $circdiv    5           0.  0.  0.          $Rcore  0.0     360.0   ;
# Define core concrete
        patch circ  1010        $circdiv    2           0.  0.  $Rcore      $R      0.0     360.0   ;
# Define cover concrete

        #           $matTag     $numFiber   $Afiber     $y0 $z0 $radius  $startAng  $endAng
         layer circ     1060        $numBar     $Ab         0.  0.  $Rreinf ;                       #
Radial distribution of bars
};


# section Aggregator $CIPcolRegSec   1070 Vy 1070 Vz -section 1051; # Adding torsion to the fiber
section
# section Aggregator $CIPcolECCsec  1070 Vy 1070 Vz -section 1001;  # Adding torsion to the fiber
section
# section Aggregator $CIPcolBondSec 1070 Vy -section 1011;  # Adding torsion to the fiber section


# ELEMENT ---------------------------------------------------------------
# FBE_____________________________________________________________________
set nipCip 4; #                    1               2               3               4           5
set CIPsections " -sections $CIPcolRegSec $CIPcolRegSec  $CIPcolECCsec $CIPcolBondSec "
#set CIPsections " -sections $CIPcolRegSec $CIPcolRegSec $CIPcolRegSec $CIPcolECCsec $CIPcolBondSec "
# set CIPsections " -sections $CIPcolECCsec   $CIPcolECCsec $CIPcolECCsec  $CIPcolECCsec
$CIPcolECCsec "
# element forceBeamColumn $eleTag $iNode              $jNode          $numIntgrPts $secTag
$transfTag <-mass $massDens> <-iter $maxIters $tol> <-integration $intType>
```

```
 element forceBeamColumn $CIPCol [expr 100+$colBot] [expr 100+$colTop] $nipCip  $CIPsections
$ColTransfTag -iter 50 $tol;


# Rigid link to the center of cap beam, rigid with 10XE

#element elasticBeamColumn $eleTag $iNode            $jNode             $A     $E    $Iz
$transfTag <-mass $massDens> <-cMass>

 element elasticBeamColumn 106     [expr 100+$colTop] [expr 100+$cb]     201.1 45280. 3217.0
$ColTransfTag


#*********************************************************************************************
*****
```

```
#
Model_PC_Col.tcl*****************************************************************************
***
# PC Column ------------------------------------------------------------------------------
------
# Materials for the full circular section 3000:
# PLASTIC HINGE W Bond Modification & SRE
#uniaxialMaterial Concrete02        $matTag $fpc    $epsc0      $fpcu   $epsU    $lambda $ft $Ets
# uniaxialMaterial  Concrete02       3010    -6.91  -0.002    0.00  -0.0050   0.10  0.0 0.0;    #
Unconfined regular concrete Cover in shell
# uniaxialMaterial  Concrete02       3020    -8.014 -0.0036  -4.578 -0.01265  0.10  0.0 0.0;    #
Confined regular concrete Core in Shell
# uniaxialMaterial  Concrete02       3030    -11.00 -0.00315 -4.386 -0.00959  0.10  0.0 0.0;    #
confined SCC in-fill W/O SRE


#uniaxialMaterial   Concrete04 $matTag $fc        $ec      $ecu     $Ec <$fct $et> <$beta>
 uniaxialMaterial   Concrete04  3010    -6.910   -0.002   -0.00500  4738.0;     # Unconfined regular
concrete Cover in shell
 uniaxialMaterial   Concrete04  3020    -8.014   -0.0036  -0.01265  4738.0;     # Confined regular
concrete Core in Shell
 uniaxialMaterial   Concrete04  3030    -11.00   -0.00315 -0.00959  5663.0;     # confined SCC in-
fill W/O SRE


#uniaxialMaterial Concrete01WithSITC $matTag $fpc    $epsc0    $fpcu     $epsU <$endStrainSITC> W/o
SRE
#uniaxialMaterial Concrete01WithSITC 3010    -6.91   -0.002    0.00     -0.0050   0.02;     #
Unconfined regular concrete Cover in shell
#uniaxialMaterial Concrete01WithSITC 3020    -8.014  -0.0036   -4.578   -0.01265  0.02;     #
Confined regular concrete Core in Shell
#uniaxialMaterial Concrete01WithSITC 3030    -11.0   -0.00315  -4.386   -0.00959  0.02;     #
confined SCC in-fill W/O SRE
```

```
#uniaxialMaterial Concrete02        $matTag $fpc    $epsc0      $fpcu   $epsU    $lambda $ft $Ets
#uniaxialMaterial Concrete02        3031     -11.0   -0.00315  -8.80   -0.00528   0.10   0.0 0.0 ;
# confined SCC in-fill W/O SRE for bond section


#In-fills are the same
#uniaxialMaterial ReinforcingSteel $matTag $fy  $fu      $Es     $Esh    $esh    $eult < -GABuck $lsr
$beta $r $gama > < -DMBuck $lsr < $alpha >> < -CMFatigue $Cf $alpha $Cd > < -IsoHard <$a1 <$limit> >
>
uniaxialMaterial ReinforcingSteel 3050      72.08    96.63   29000.0 800.0   0.014   0.14 ;     #
Reinforcing bars
uniaxialMaterial ReinforcingSteel 3060      72.08   96.63    22705.0 800.0   0.014689    0.140843 ;
# Reinforcing bars


#uniaxialMaterial Steel02 $matTag $Fy   $E     $b    $R0 $cR1 $cR2 <$a1 $a2 $a3 $a4 $sigInit>
http://opensees.berkeley.edu/wiki/index.php/OpenSees uniaxialMaterial Arguments -- Steel02
#uniaxialMaterial Steel02  3050   68.0  29000. 0.0062 10 0.925  0.15
#uniaxialMaterial Steel02  3050   72.08 29000. 6.156e-3 10 0.925  0.1;
#uniaxialMaterial Steel02  3060   72.08 22705. 7.854e-3 10 0.925  0.1;



set numBar  14;
set Ab      0.20;               # #4 bars
set R       8.0;                # section outer Radius
set Rcore   6.8125;             # Center of spiral
set Rreinf  6.375;              # bars radius
set Rfill   5.0;
set circdiv [expr $numBar];     # Divides the circular patch in 5 segments between each reinf.

# Rest of Column
```

```
section Fiber [expr $ABCcolSec] {;
#                   $mattag     $circdiv    $Rdiv       $y0 $z0 $intR       $extrR  $start  $end
        patch circ  3030        $circdiv    2           0.  0.  0.          $Rfill  0.0     360.0;
# Define core concrete fibers
        patch circ  3020        $circdiv    2           0.  0.  $Rfill      $Rcore  0.0     360.0;
# Define core concrete fibers
        patch circ  3010        $circdiv    2           0.  0.  $Rcore      $R      0.0     360.0;
# Define cover concrete fibers
#                   $matTag     $numFiber   $Afiber     $y0 $z0 $radius     $startAng   $endAng
        layer circ  3050        $numBar     $Ab         0.  0.  $Rreinf;                # Radial
distribution of bars
};


# Plastic Hinge section
section Fiber [expr $ABCcolBondSec] {;
#                   $mattag     $circdiv    $Rdiv       $y0 $z0 $intR       $extrR  $start  $end
        patch circ  3030        $circdiv    2           0.  0.  0.          $Rfill  0.0     360.0;
# Define core concrete fibers
        patch circ  3020        $circdiv    2           0.  0.  $Rfill      $Rcore  0.0     360.0;
# Define core concrete fibers
        patch circ  3010        $circdiv    2           0.  0.  $Rcore      $R      0.0     360.0;
# Define cover concrete fibers
#                   $matTag     $numFiber   $Afiber     $y0 $z0 $radius     $startAng   $endAng
        layer circ  3060        $numBar     $Ab         0.  0.  $Rreinf;                # Radial
distribution of bars
};
```

```
# section Aggregator $ABCcolSec     3070 Vy 3070 Vz -section 3001;  # Adding torsion to the fiber
section
# section Aggregator $ABCcolBondSec 3070 Vy -section 3011;  # Adding torsion to the fiber section


# ELEMENT ---------------------------------------------------------------


# FBE
set nipAbc 4; #                1              2      3           4           5        6           7
set ABCsections " -sections  $ABCcolSec $ABCcolSec $ABCcolSec $ABCcolBondSec "
#set ABCsections " -sections $ABCcolSec $ABCcolSec $ABCcolSec $ABCcolSec $ABCcolBondSec "
#element forceBeamColumn $eleTag $iNode              $jNode            $numIntgrPts $secTag
$transfTag <-mass $massDens> <-iter $maxIters $tol> <-integration $intType>
 element forceBeamColumn $ABCCol [expr 300+$colBot] [expr 300+$colTop] $nipAbc      $ABCsections
$ColTransfTag -iter 50 $tol;


#Rigid link to the center of cap beam, rigid with 10XE
#element elasticBeamColumn $eleTag $iNode            $jNode          $A    $E    $Iz    $transfTag
 element elasticBeamColumn 306    [expr 300+$colTop] [expr 300+$cb] 201.1 47380. 3217.0 $ColTransfTag
# ********************************************************************************************
```

```
# PipePin_Spring2.tcl*************************************************************************
# Modeling Pipe-Pin with 3 springs and gaps for horizontal movements**************************

#uniaxialMaterial ElasticBilin $matTag  $EP1    $EP2      $epsP2 <$EN1 $EN2       $epsN2>
 uniaxialMaterial ElasticBilin  111     2.0 500. 0.25

# Vertical Spring-----------------------------------------------------------------
# Stiff in Compression and rod tensile stiffness in tension
set Krod  899.; #kip/in in tension reduced section
set Kpad  689.;
set Kcontact 6890.;

#uniaxialMaterial Elastic $matTag $E    $eta $Eneg
 uniaxialMaterial Elastic 120     $Krod 0.0  $Kpad



# Rotational Spring---------------------------------------------------------------
#uniaxialMaterial Elastic $matTag $E      <$eta> <$Eneg>
 uniaxialMaterial Elastic 130     14436.0

# Connectivity-------------------------------------------------------------------------
#element zeroLength $eleTag  $iNode            $jNode             -mat $matTag1 $matTag2 ... -dir
$dir1 $dir2 ...<-doRayleigh $rFlag> <-orient $x1 $x2 $x3 $yp1 $yp2 $yp3>
 element zeroLength 120 [expr 100+$pedTop] [expr 100+$colBot] -mat 111 120 130 -dir 1  2  3
  element zeroLength 320 [expr 300+$pedTop] [expr 300+$colBot] -mat 111 120 130 -dir 1  2  3
#*************************************************************************************
```

```
#
Model_Pedestals.tcl*************************************************************************
****


# PEDESTALs-----------------------------------------------------------------------------------
------
# Materials for the full circular section 1100:
#uniaxialMaterial  Concrete02      $matTag $fpc    $epsc0      $fpcu   $epsU       $lambda $ft $Ets
 uniaxialMaterial Concrete02        1110    -6.91   -0.002       0.000  -0.0060     0.10    0.0 0.0
 uniaxialMaterial Concrete02        1120    -8.502  -0.0043     -5.809  -0.01367    0.10    0.0 0.0


# uniaxialMaterial ReinforcingSteel $matTag $fy     $fu     $Es     $Esh    $esh     $eult  < -GABuck
$lsr $beta $r $gama > < -DMBuck $lsr < $alpha >> < -CMFatigue $Cf $alpha $Cd > < -IsoHard <$a1
<$limit> > >
# uniaxialMaterial ReinforcingSteel 1150    66.3    93.5    29000.0 850.0   0.009    0.18;
# uniaxialMaterial ReinforcingSteel 1160    66.3    93.5    20384.0 850.0   0.009966 0.180995


#uniaxialMaterial Steel02 $matTag $Fy  $E     $b      $R0 $cR1 $cR2 <$a1 $a2 $a3 $a4 $sigInit>
 uniaxialMaterial Steel02 1150    66.3 29000. 0.006    20 0.925  0.10
 uniaxialMaterial Steel02 1160    66.3 20611. 0.00742  20 0.925  0.10



set numBar  8;
set Ab      0.44;               # #6 bars
set R       11.0;               # section outer Radius
set Rcore   9.8125;             # Center of spiral
set Rreinf  9.25;               # bars radius
set circdiv [expr $numBar];     # Divides the circular patch in 5 segments between each reinf.
```

```
section Fiber [expr $pedSec] {;
#                   $mattag     $circdiv    $Rdiv       $y0 $z0 $intR       $extrR  $start  $end
        patch circ  1120        $circdiv    8           0.  0.  0.          $Rcore    0.0   360.0;
# Define core concrete fibers
        patch circ  1110        $circdiv    2           0.  0.  $Rcore      $R        0.0   360.0;
# Define cover concrete fibers
#                   $matTag     $numFiber   $Afiber     $y0 $z0 $radius     $startAng   $endAng
        layer circ  1150        $numBar     $Ab         0.  0.  $Rreinf     ;                   #
Radial distribution of bars
};


section Fiber [expr $pedBondSec] {;      # section w/ modified steel for bond-slip action
#                   $mattag     $circdiv    $Rdiv       $y0 $z0 $intR       $extrR  $start  $end
        patch circ  1120        $circdiv    8           0.  0.  0.          $Rcore    0.0   360.0;
# Define core concrete
        patch circ  1110        $circdiv    2           0.  0.  $Rcore      $R        0.0   360.0;
# Define cover concrete
        #           $matTag     $numFiber   $Afiber     $y0 $z0 $radius  $startAng  $endAng
        layer circ  1160        $numBar     $Ab         0.  0.  $Rreinf ;                   #
Radial distribution of bars
};


# Connectivity-------------------------------------------------------------------------------
------
set nipPed 3; #                     1       2       3       4       5
set pedSections "-sections      $pedBondSec $pedSec $pedSec "
```

```
#set PedSections "-sections     $pedSec $pedSec $pedSec"


# CIP
#       forceBeamColumn  $eleTag    $iNode           $jNode     $numIntgrPts $secTag  $transfTag
#element forceBeamColumn  $CIPPed    111        [expr 100+$pedTop]  $nipPed      $pedSec
$ColTransfTag -iter 20 $tol;
element forceBeamColumn  $CIPPed  [expr 100+$base]      [expr 100+$pedTop]  $nipPed  $pedSections
$ColTransfTag -iter 20 $tol;


# PC
#       forceBeamColumn  $eleTag    $iNode          $jNode     $numIntgrPts $secTag $transfTag
 #element forceBeamColumn  $ABCPed   311    [expr 300+$pedTop] $nipPed       $pedSec $ColTransfTag -
iter 20 $tol;
 element forceBeamColumn  $ABCPed  [expr 300+$base] [expr 300+$pedTop] $nipPed       $pedSections
$ColTransfTag -iter 20 $tol;


#*********************************************************************************************
******
```

```
#
Gravity.tcl*****************************************************************************
****
#Performs the Gravity load analysis.  The load pattern should be defined before.
#load-controlled static analysis
set dispCode 0; # Print Flag for test
set NstepGravity 10;            # apply gravity in $NstepGravity

set DGravity [expr 1.0/$NstepGravity];  # first load increment;
integrator LoadControl $DGravity 1 ;    # determine the next time step for an analysis

# Convergence test
#                     tolerance maxIter displayCode
#test NormDispIncr      1.0e-10    100        $dispCode
test EnergyIncr        1.0e-12   100        $dispCode

# Solution algorithm
algorithm Newton

# DOF numberer
#numberer RCM
numberer Plain;     # renumber dof's to minimize band-width (optimization), if you want to


# Constraint handler
constraints Penalty 1.0e18 1.0e18
#constraints Plain; # It cannot be used. Due to the rigid links, the boundary conditions are not
homogeneous.
```

```
#constraints Lagrange

# System of equations solver
#system UmfPack
#system SparseGeneral -piv
system BandGeneral
#system ProfileSPD

# Analysis for gravity load
analysis Static

# Perform the gravity load analysis

set numSteps 0
set useInitialTangent 0

while { $numSteps < $NstepGravity } {
   if { $useInitialTangent == 1 } {
      #algorithm Newton -initial
      algorithm ModifiedNewton
      # Convergence test
      #                     tolerance maxIter displayCode
      test NormDispIncr      1.0e-8    1500      $dispCode
      #test EnergyIncr       1.0e-12   2500      $dispCode
   } else {
      algorithm KrylovNewton
      #test NormDispIncr      5.0e-8    100       $dispCode
```

```
        test EnergyIncr        1.0e-12    100      $dispCode
    }
    set res [analyze 1]

    if { $res >= 0 } {
       incr numSteps
       set useInitialTangent 0
     #puts -nonewline "step $numSteps done.\n"
    } else {
       if { $useInitialTangent == 1 } {
          puts "Gravity: gravity load analysis failed (at step $numSteps) !!!!!!!!!!!!!!!!"
          set temp [open $log "a"]
          puts $temp "\n Gravity: gravity load analysis failed (at step $numSteps) !!!"
          puts $temp "\n PROGRAN TERMINATED"
          close $temp
          set numSteps 10
       } else {
          set useInitialTangent 1
       }
    }
}

loadConst -time 0.0
wipeAnalysis

 puts "Gravity is done. res=$res (0=ok)"
#*********************************************************************************************
```

```
# Modal
Analysis*************************************************************************************************
set lambda [eigen $numModes];
set temp [open $log a]
puts $temp
"\n_____________________________________________________________________________________________";
puts $temp "\# Eigen Values: "
puts $temp "$lambda"
puts $temp  "\n# Periods:\n "
puts "\n# Periods:\n "
foreach lam $lambda {
    puts $temp  "[expr 2.0*$PI/sqrt($lam)], "
    puts        "[expr 2.0*$PI/sqrt($lam)], "
}
puts $temp
"\n_____________________________________________________________________________________________";
close $temp
#*************************************************************************************************
*****
```

```
#
Damping.tcl*****************************************************************************
****
# Stiffness proportionate damping
set xi          0.02;                       # 2% damping ratio
set lambda      [eigen 1];                  # eigenvalue mode 1
set omega       [expr pow($lambda,0.5)];
set alphaM      0.0;                        # M-prop. damping; D = alphaM*M
set betaKcurr   0.0;                        # K-proportional damping;      +beatKcurr*KCurrent
set betaKcomm   [expr 2.*$xi/($omega)];     # K-prop. damping parameter;   +betaKcomm*KlastCommitt
set betaKinit   0.0;                        # initial-stiffness proportional damping
+beatKinit*Kini
# D=$alphaM*M + $betaKcurr*Kcurrent + $betaKcomm*KlastCommit + $beatKinit*$Kinitial
rayleigh $alphaM $betaKcurr $betaKinit $betaKcomm;              # RAYLEIGH damping


#region $regTag <-ele ($ele1 $ele2 ...)> <-eleRange $startEle $endEle> <-rayleigh $alphaM $betaK
$betaKinit $betaKcomm>
#region 1       -eleRange  100 999 -rayleigh $alphaM $betaKcurr $betaKinit $betaKcomm;              #
RAYLEIGH damping
#*****************************************************************************************
******
```

```
#
recorder_Dynamic.tcl*************************************************************************
****
# Creating the output folders
file delete -force $outFolder
file mkdir  $outFolder;
file mkdir  $outFolder/Fibers;


# DISPLACEMENTs-----------------------------------------
recorder Node -file $outFolder/Monitor.out     -time    -node $monitor                          -
dof 1 2 3 disp;
recorder Node -file $outFolder/ColTopDisplacement.out   -node [expr 100+$colTop] [expr 300+$colTop] -
dof 1 2 3 disp;
recorder Node -file $outFolder/CapBeamSpringDeform.out  -node [expr 200+$cb]     [expr 210+$cb]     -
dof 1 2 3 disp;
recorder Node -file $outFolder/PedTopDisplacement.out   -node [expr 100+$pedTop] [expr 300+$pedTop] -
dof 1 2 3 disp;
recorder Node -file $outFolder/colBotDisplacement.out   -node [expr 100+$colBot] [expr 300+$colBot] -
dof 1 2 3 disp;
recorder Node -file $outFolder/CapBeamDisplacement.out  -node [expr 100+$cb]     [expr 300+$cb]     -
dof 1 2 3 disp;
recorder Node -file $outFolder/MassRigDisplacement.out  -node [expr $cb]                           -
dof 1 2 3 disp;


recorder Node -file $outFolder/BaseDisplacement.out     -node [expr 100+$base]   [expr 300+$base]   -
dof 1 2 3 disp;
recorder Node -file $outFolder/BaseAcceleration.out     -node [expr 100+$base]   [expr 300+$base]   -
dof 1 2 3 accel;
recorder Node -file $outFolder/BaseVelocity.out         -node [expr 100+$base]   [expr 300+$base]   -
dof 1 2 3 vel;
```

```
recorder Node -file $outFolder/BaseAccelerationAbs.out  -time -timeSeries $tsTag -node [expr
100+$base]     [expr 300+$base]    -dof 1 accel;


# Element Force----------------------------------------
recorder Element -file $outFolder/ColumnsForces.out     -ele $CIPCol $ABCCol  globalForce
recorder Element -file $outFolder/PedestalsForces.out   -ele $CIPPed $ABCPed  globalForce
recorder Element -file $outFolder/massRig_Column.out    -ele 1000  force
recorder Element -file $outFolder/massRig_link.out      -ele 1300  axialForce
recorder Element -file $outFolder/CapBeam_Spring.out    -ele 2300  force


# Reactions-----------------------------------------------
recorder Node -file $outFolder/Reactions.out            -node [expr 100+$base]   [expr 300+$base]   -
dof 1 2 3 reaction; #Records the base Forces on the shake table
recorder Node -file $outFolder/MassRigReaction.out      -node [expr $base]                          -
dof 1 2 3 reaction;
# Fibers-----------------------------------------------------------------------------------------------
------
set address "$outFolder";


# CIP
COLUMN_____________________________________________________________________________________________
set eleMonitor  $CIPCol
set numBar    14;
set R         8.0;              # section outer Radius
set Rcore     6.8125;           # Center of spiral
set Rreinf    6.375;            # bars radius
set matCore   1020; set matCover 1010; set matReinf 1050;
for {set sec 1} { $sec <  $nipCip} {incr sec} {;
```

```
    recorder Element -file [format "%s/ele%s.Forces_sec%s.out"         $address $eleMonitor $sec]  -
ele $eleMonitor section $sec force; # Column sections forces
    recorder Element -file [format "%s/Fibers/ele%s.sec%s_core1.out"   $address $eleMonitor $sec]  -
ele $eleMonitor section $sec fiber  $Rcore  0.0 $matCore  stressStrain
    recorder Element -file [format "%s/Fibers/ele%s.sec%s_core2.out"   $address $eleMonitor $sec]  -
ele $eleMonitor section $sec fiber -$Rcore  0.0 $matCore  stressStrain
    recorder Element -file [format "%s/Fibers/ele%s.sec%s_cover1.out"  $address $eleMonitor $sec]  -
ele $eleMonitor section $sec fiber  $R      0.0 $matCover stressStrain
    recorder Element -file [format "%s/Fibers/ele%s.sec%s_cover2.out"  $address $eleMonitor $sec]  -
ele $eleMonitor section $sec fiber -$R      0.0 $matCover stressStrain
    for {set bar 1} {$bar <= $numBar} {incr bar} {
        set y [expr $Rreinf*cos(($bar-1.0)/$numBar*2.0*$PI)]
        set z [expr $Rreinf*sin(($bar-1.0)/$numBar*2.0*$PI)]
        recorder Element -file [format "%s/Fibers/ele%s.sec%s_Bar%i.out"  $address $eleMonitor $sec
$bar] -ele $eleMonitor section $sec fiber $y $z $matReinf stressStrain
    }
}

# Recorders for the fibers, ECC section W/ bond
set matReinf 1050;
set sec      $nipCip;
    recorder Element -file [format "%s/ele%s.Forces_sec%s.out"         $address $eleMonitor $sec]  -
ele $eleMonitor section $sec force; # Column sections forces
    recorder Element -file [format "%s/Fibers/ele%s.sec%s_core1.out"   $address $eleMonitor $sec]  -
ele $eleMonitor section $sec fiber  $Rcore  0.0 $matCore  stressStrain
    recorder Element -file [format "%s/Fibers/ele%s.sec%s_core2.out"   $address $eleMonitor $sec]  -
ele $eleMonitor section $sec fiber -$Rcore  0.0 $matCore  stressStrain
    recorder Element -file [format "%s/Fibers/ele%s.sec%s_cover1.out"  $address $eleMonitor $sec]  -
ele $eleMonitor section $sec fiber  $R      0.0 $matCover stressStrain
```

```
    recorder Element -file [format "%s/Fibers/ele%s.sec%s_cover2.out"  $address $eleMonitor $sec]  -
ele $eleMonitor section $sec fiber -$R      0.0 $matCover stressStrain
    for {set bar 1} {$bar <= $numBar} {incr bar} {
        set y [expr $Rreinf*cos(($bar-1.0)/$numBar*2.0*$PI)]
        set z [expr $Rreinf*sin(($bar-1.0)/$numBar*2.0*$PI)]
        recorder Element -file [format "%s/Fibers/ele%s.sec%s_Bar%i.out"  $address $eleMonitor $sec
$bar] -ele $eleMonitor section $sec fiber $y $z $matReinf stressStrain
    }


# ABC
COLUMN
set eleMonitor  $ABCCol
set numBar    14;
set R         8.0;              # section outer Radius
set Rcore     6.8125;           # Center of spiral
set Rreinf    6.375;            # bars radius
set matCore   3020; set matCover 3010; set matReinf 3050;
for {set sec 1} { $sec <  $nipAbc} {incr sec} {;
    recorder Element -file [format "%s/ele%s.Forces_sec%s.out"         $address $eleMonitor $sec]  -
ele $eleMonitor section $sec force; # Column sections forces
    recorder Element -file [format "%s/Fibers/ele%s.sec%s_core1.out"   $address $eleMonitor $sec]  -
ele $eleMonitor section $sec fiber  $Rcore  0.0 $matCore  stressStrain
    recorder Element -file [format "%s/Fibers/ele%s.sec%s_core2.out"   $address $eleMonitor $sec]  -
ele $eleMonitor section $sec fiber -$Rcore  0.0 $matCore  stressStrain
    recorder Element -file [format "%s/Fibers/ele%s.sec%s_cover1.out"  $address $eleMonitor $sec]  -
ele $eleMonitor section $sec fiber  $R      0.0 $matCover stressStrain
    recorder Element -file [format "%s/Fibers/ele%s.sec%s_cover2.out"  $address $eleMonitor $sec]  -
ele $eleMonitor section $sec fiber -$R      0.0 $matCover stressStrain
    for {set bar 1} {$bar <= $numBar} {incr bar} {
```

```
        set y [expr $Rreinf*cos(($bar-1.0)/$numBar*2.0*$PI)]
        set z [expr $Rreinf*sin(($bar-1.0)/$numBar*2.0*$PI)]
        recorder Element -file [format "%s/Fibers/ele%s.sec%s_Bar%i.out"  $address $eleMonitor $sec
$bar] -ele $eleMonitor section $sec fiber $y $z $matReinf stressStrain
    }
}

# Recorders for the bond
set matReinf 1060;
set sec      $nipAbc;
    recorder Element -file [format "%s/ele%s.Forces_sec%s.out"         $address $eleMonitor $sec]  -
ele $eleMonitor section $sec force; # Column sections forces
    recorder Element -file [format "%s/Fibers/ele%s.sec%s_core1.out"   $address $eleMonitor $sec]  -
ele $eleMonitor section $sec fiber  $Rcore  0.0 $matCore  stressStrain
    recorder Element -file [format "%s/Fibers/ele%s.sec%s_core2.out"   $address $eleMonitor $sec]  -
ele $eleMonitor section $sec fiber -$Rcore  0.0 $matCore  stressStrain
    recorder Element -file [format "%s/Fibers/ele%s.sec%s_cover1.out"  $address $eleMonitor $sec]  -
ele $eleMonitor section $sec fiber  $R      0.0 $matCover stressStrain
    recorder Element -file [format "%s/Fibers/ele%s.sec%s_cover2.out"  $address $eleMonitor $sec]  -
ele $eleMonitor section $sec fiber -$R      0.0 $matCover stressStrain
    for {set bar 1} {$bar <= $numBar} {incr bar} {
        set y [expr $Rreinf*cos(($bar-1.0)/$numBar*2.0*$PI)]
        set z [expr $Rreinf*sin(($bar-1.0)/$numBar*2.0*$PI)]
        recorder Element -file [format "%s/Fibers/ele%s.sec%s_Bar%i.out"  $address $eleMonitor $sec
$bar] -ele $eleMonitor section $sec fiber $y $z $matReinf stressStrain
    }

#CIP
pedestal
```

```
set eleMonitor $CIPPed
set numBar  8;
set Ab      0.44;               # #6 bars
set R       11.0;               # section outer Radius
set Rcore   9.8125;             # Center of spiral
set Rreinf  9.25;               # bars radius
set matCore  1120; set matCover 1110;   set matReinf 1150;
for {set sec 2} { $sec <=  $nipPed} {incr sec} {;
    recorder Element -file [format "%s/ele%s.Forces_sec%s.out"         $address $eleMonitor $sec]  -
ele  $eleMonitor section $sec force; # Column sections forces
    recorder Element -file [format "%s/Fibers/ele%s.sec%s_core1.out"   $address $eleMonitor $sec]  -
ele $eleMonitor section $sec fiber  $Rcore  0.0 $matCore  stressStrain
    recorder Element -file [format "%s/Fibers/ele%s.sec%s_core2.out"   $address $eleMonitor $sec]  -
ele $eleMonitor section $sec fiber -$Rcore  0.0 $matCore  stressStrain
    recorder Element -file [format "%s/Fibers/ele%s.sec%s_cover1.out"  $address $eleMonitor $sec]  -
ele $eleMonitor section $sec fiber  $R      0.0 $matCover stressStrain
    recorder Element -file [format "%s/Fibers/ele%s.sec%s_cover2.out"  $address $eleMonitor $sec]  -
ele $eleMonitor section $sec fiber -$R      0.0 $matCover stressStrain
    for {set bar 1} {$bar <= $numBar} {incr bar} {
        set y [expr $Rreinf*cos(($bar-1.0)/$numBar*2.0*$PI)]
        set z [expr $Rreinf*sin(($bar-1.0)/$numBar*2.0*$PI)]
        recorder Element -file [format "%s/Fibers/ele%s.sec%s_Bar%i.out"  $address $eleMonitor $sec
$bar] -ele $eleMonitor section $sec fiber $y $z $matReinf stressStrain
    }
}


set matReinf 1160;
set sec 1;
```

```
    recorder Element -file [format "%s/ele%s.Forces_sec%s.out"          $address $eleMonitor $sec]  -
ele  $eleMonitor section $sec force; # Column sections forces

    recorder Element -file [format "%s/Fibers/ele%s.sec%s_core1.out"   $address $eleMonitor $sec]  -
ele $eleMonitor section $sec fiber  $Rcore  0.0 $matCore  stressStrain

    recorder Element -file [format "%s/Fibers/ele%s.sec%s_core2.out"   $address $eleMonitor $sec]  -
ele $eleMonitor section $sec fiber -$Rcore  0.0 $matCore  stressStrain

    recorder Element -file [format "%s/Fibers/ele%s.sec%s_cover1.out"  $address $eleMonitor $sec]  -
ele $eleMonitor section $sec fiber  $R      0.0 $matCover stressStrain

    recorder Element -file [format "%s/Fibers/ele%s.sec%s_cover2.out"  $address $eleMonitor $sec]  -
ele $eleMonitor section $sec fiber -$R      0.0 $matCover stressStrain

    for {set bar 1} {$bar <= $numBar} {incr bar} {

        set y [expr $Rreinf*cos(($bar-1.0)/$numBar*2.0*$PI)]

        set z [expr $Rreinf*sin(($bar-1.0)/$numBar*2.0*$PI)]

        recorder Element -file [format "%s/Fibers/ele%s.sec%s_Bar%i.out"  $address $eleMonitor $sec
$bar] -ele $eleMonitor section $sec fiber $y $z $matReinf stressStrain

    }



# ABC
pedestal_____________________________________________________________________________________

set eleMonitor $ABCPed

set numBar  8;

set Ab      0.44;               # #6 bars

set R       11.0;               # section outer Radius

set Rcore   9.8125;             # Center of spiral

set Rreinf  9.25;               # bars radius

set matCore  1120; set matCover 1110;   set matReinf 1150;

for {set sec 2} { $sec <=  $nipPed} {incr sec} {;
```

```
    recorder Element -file [format "%s/ele%s.Forces_sec%s.out"         $address $eleMonitor $sec]  -
ele  $eleMonitor section $sec force; # Column sections forces

    recorder Element -file [format "%s/Fibers/ele%s.sec%s_core1.out"   $address $eleMonitor $sec]  -
ele $eleMonitor section $sec fiber  $Rcore  0.0 $matCore  stressStrain

    recorder Element -file [format "%s/Fibers/ele%s.sec%s_core2.out"   $address $eleMonitor $sec]  -
ele $eleMonitor section $sec fiber -$Rcore  0.0 $matCore  stressStrain

    recorder Element -file [format "%s/Fibers/ele%s.sec%s_cover1.out"  $address $eleMonitor $sec]  -
ele $eleMonitor section $sec fiber  $R      0.0 $matCover stressStrain

    recorder Element -file [format "%s/Fibers/ele%s.sec%s_cover2.out"  $address $eleMonitor $sec]  -
ele $eleMonitor section $sec fiber -$R      0.0 $matCover stressStrain

    for {set bar 1} {$bar <= $numBar} {incr bar} {

        set y [expr $Rreinf*cos(($bar-1.0)/$numBar*2.0*$PI)]

        set z [expr $Rreinf*sin(($bar-1.0)/$numBar*2.0*$PI)]

        recorder Element -file [format "%s/Fibers/ele%s.sec%s_Bar%i.out"  $address $eleMonitor $sec
$bar] -ele $eleMonitor section $sec fiber $y $z $matReinf stressStrain

    }

}


set matReinf 1160;

set sec 1;

    recorder Element -file [format "%s/ele%s.Forces_sec%s.out"         $address $eleMonitor $sec]  -
ele  $eleMonitor section $sec force; # Column sections forces

    recorder Element -file [format "%s/Fibers/ele%s.sec%s_core1.out"   $address $eleMonitor $sec]  -
ele $eleMonitor section $sec fiber  $Rcore  0.0 $matCore  stressStrain

    recorder Element -file [format "%s/Fibers/ele%s.sec%s_core2.out"   $address $eleMonitor $sec]  -
ele $eleMonitor section $sec fiber -$Rcore  0.0 $matCore  stressStrain

    recorder Element -file [format "%s/Fibers/ele%s.sec%s_cover1.out"  $address $eleMonitor $sec]  -
ele $eleMonitor section $sec fiber  $R      0.0 $matCover stressStrain

    recorder Element -file [format "%s/Fibers/ele%s.sec%s_cover2.out"  $address $eleMonitor $sec]  -
ele $eleMonitor section $sec fiber -$R      0.0 $matCover stressStrain
```

```
    for {set bar 1} {$bar <= $numBar} {incr bar} {
        set y [expr $Rreinf*cos(($bar-1.0)/$numBar*2.0*$PI)]
        set z [expr $Rreinf*sin(($bar-1.0)/$numBar*2.0*$PI)]
        recorder Element -file [format "%s/Fibers/ele%s.sec%s_Bar%i.out"  $address $eleMonitor $sec
$bar] -ele $eleMonitor section $sec fiber $y $z $matReinf stressStrain
    }

puts "\n RECORDERS DEFINED."
#*********************************************************************************************
******
```

```
#
DynamicAnalysis.tcl********************************************************************************
****
puts
"\n_____
___"
puts  "** ([clock format [clock seconds]]) Starting Dynamic analysis..."
puts  "Motion:$MotionFile; Initial Dt=$DtAnalysis; TmaxAnalysis=$TmaxAnalysis";


set (Time0) 0.;
set Time 0.;
set q 0;        # q is a counter for step of analysis
set ok 0;

while { $(Time$q) < $TmaxAnalysis && $ok == 0 } {

    incr q;                 # q is a counter for step of analysis

# Setting the default analysis option

constraints Transformation
numberer RCM
system BandGeneral

set TolDynamic 1.e-10;          # Convergence Test: tolerance
set maxNumIterDynamic 50;       # Convergence Test: maximum number of iterations that will be
performed before "failure to converge" is returned
set printFlagDynamic 5;         # Convergence Test: flag used to print information on convergence
(optional) # 1: print information on each step; 5 if it fails to converge at end
```

```
#test NormDispIncr $TolDynamic $maxNumIterDynamic $printFlagDynamic;
test EnergyIncr $TolDynamic $maxNumIterDynamic $printFlagDynamic
#test RelativeEnergyIncr $TolDynamic $maxNumIterDynamic
#test NormUnbalance $TolDynamic $maxNumIterDynamic

algorithm Broyden 8
#algorithm Newton ; #-initialThenCurrent
#algorithm ModifiedNewton

integrator Newmark 0.50 0.25
#integrator HHT 0.9

analysis VariableTransient
#       analysis Transient                  # define type of analysis: time-dependent

set ok 0;
set (Time$q) [getTime];
set ok [analyze 1 $DtAnalysis];# actually perform one dt analysis; returns ok=0 if analysis was
successful
#       set ok [analyze 1 $DtAnalysis [expr $DtAnalysis/10.] [expr $DtAnalysis*2.] 10]
set numberIteration [testIter];

puts "*Time: [getTime], ok=$ok, iteration= $numberIteration";#, last Norm= [format "%1.3e" $norm]   "

        # if {$ok == 0} {
                # puts  "solved By Broyden "
```

```
# }

if {$ok != 0} {
    puts -nonewline  [format "\n!T=%6g,D=%2.3f" $(Time$q) [nodeDisp $monitor 1]];
    algorithm Broyden 8
          set ok [analyze 1 [expr $DtAnalysis/2.]];
    if {$ok == 0} {
            puts  "solved By Broyden Algorithm & dt/2"
    } else {
        set ok [analyze 1 [expr $DtAnalysis/4.]];
        if {$ok == 0} {
                puts  "solved By Broyden Algorithm & dt/4"
        } else {
            set ok [analyze 1 [expr $DtAnalysis/8.]];
            if {$ok == 0} {
                puts  "solved By Broyden Algorithm & dt/8"
            }
        }
    }
}

if {$ok != 0} {
    algorithm Newton
          set ok [analyze 1 [expr $DtAnalysis/2.]];
    if {$ok == 0} {
            puts  "solved By Newton Algorithm & dt/2"
    } else {
```

```
        set ok [analyze 1 [expr $DtAnalysis/4.]];
        if {$ok == 0} {
                puts  "solved By Newton Algorithm & dt/4"
        } else {
            set ok [analyze 1 [expr $DtAnalysis/6.]];
            if {$ok == 0} {
                puts  "solved By Newton Algorithm & dt/6"
            } else {
                set ok [analyze 1 [expr $DtAnalysis/8.]];
                if {$ok == 0} {
                        puts  "solved By Newton Algorithm & dt/8"
                } else {
                    set ok [analyze 1 [expr $DtAnalysis/10.]];
                    if {$ok == 0} {
                            puts  "solved By Newton Algorithm & dt/10"
                    }
                }
            }
        }
    }
}

if {$ok != 0} {
    algorithm Newton -initial
          set ok [analyze 1 [expr $DtAnalysis/2.]];
    if {$ok == 0} {
            puts  "solved By Newton-initial Algorithm & dt/2"
```

```
    } else {
        set ok [analyze 1 [expr $DtAnalysis/4.]];
        if {$ok == 0} {
                puts  "solved By Newton-initial Algorithm & dt/4"
        } else {
            set ok [analyze 1 [expr $DtAnalysis/6.]];
            if {$ok == 0} {
                puts  "solved By Newton-initial Algorithm & dt/6"
            } else {
                set ok [analyze 1 [expr $DtAnalysis/8.]];
                if {$ok == 0} {
                        puts  "solved By Newton-initial Algorithm & dt/8"
                } else {
                    set ok [analyze 1 [expr $DtAnalysis/10.]];
                    if {$ok == 0} {
                            puts  "solved By Newton-initial Algorithm & dt/10"
                    }
                }
            }
        }
    }
}

if {$ok != 0} {
    algorithm Newton -initialThenCurrent
          set ok [analyze 1 [expr $DtAnalysis/2.]];
    if {$ok == 0} {
```

```
            puts  "solved By Newton-initialThenCurrent Algorithm & dt/2"
    } else {
        set ok [analyze 1 [expr $DtAnalysis/4.]];
        if {$ok == 0} {
                puts  "solved By Newton-initialThenCurrent Algorithm & dt/4"
        } else {
            set ok [analyze 1 [expr $DtAnalysis/6.]];
            if {$ok == 0} {
                puts  "solved By Newton-initialThenCurrent Algorithm & dt/6"
            } else {
                set ok [analyze 1 [expr $DtAnalysis/8.]];
                if {$ok == 0} {
                        puts  "solved By Newton-initialThenCurrent Algorithm & dt/8"
                } else {
                    set ok [analyze 1 [expr $DtAnalysis/10.]];
                    if {$ok == 0} {
                            puts  "solved By Newton-initialThenCurrent Algorithm & dt/10"
                    }
                }
            }
        }
    }
}

 if {$ok != 0} {
     algorithm Newton ModifiedNewton
           set ok [analyze 1 [expr $DtAnalysis/2.]];
```

```
    if {$ok == 0} {
            puts  "solved By ModifiedNewton Algorithm & dt/2"
    } else {
        set ok [analyze 1 [expr $DtAnalysis/4.]];
        if {$ok == 0} {
                puts  "solved By ModifiedNewton Algorithm & dt/4"
        } else {
            set ok [analyze 1 [expr $DtAnalysis/6.]];
            if {$ok == 0} {
                puts  "solved By ModifiedNewton Algorithm & dt/6"
            } else {
                set ok [analyze 1 [expr $DtAnalysis/8.]];
                if {$ok == 0} {
                        puts  "solved By ModifiedNewton Algorithm & dt/8"
                } else {
                    set ok [analyze 1 [expr $DtAnalysis/10.]];
                   if {$ok == 0} {
                            puts  "solved By ModifiedNewton Algorithm & dt/10"
                    }
                }
            }
        }
    }

if {$ok != 0} {
    algorithm BFGS
```

```
                set ok [analyze 1 [expr $DtAnalysis/2.]];# perform analysis; returns ok=0 if
analysis was successful
            if {$ok == 0} {
                    puts  "solved By BFGS Algorithm & dt/2"
            }
        }

        if {$ok != 0} {
            algorithm ModifiedNewton -initial
                    set ok [analyze 1 [expr $DtAnalysis/2.]];         # actually perform analysis;
returns ok=0 if analysis was successful
            if {$ok == 0} {
                    puts  "solved By ModifiedNewton -initial Algorithm & dt/2"
            }
        }

        if {$ok != 0} {
            algorithm KrylovNewton
                    set ok [analyze 1 [expr $DtAnalysis/2.]];         # actually perform analysis;
returns ok=0 if analysis was successful
            if {$ok == 0} {
                    puts  "solved By KrylovNewton Algorithm & dt/2"
            }
        }

        if {$ok != 0} {
            algorithm BFGS
```

```
                set ok [analyze 1 [expr $DtAnalysis/2.]];          # actually perform analysis;
returns ok=0 if analysis was successful
            if {$ok == 0} {
                    puts  "solved By BFGS Algorithm"
            }
        }

        if {$ok != 0} {
            algorithm Broyden 8
                set ok [analyze 1 [expr $DtAnalysis/2.]];          # actually perform analysis;
returns ok=0 if analysis was successful
            if {$ok == 0} {
                    puts  "solved By Broyden Algorithm"
            }
        }

        if {$ok != 0} {
            numberer RCM
                set ok [analyze 1 [expr $DtAnalysis/2.]];          # actually perform analysis;
returns ok=0 if analysis was successful
            if {$ok == 0} {
                    puts  "solved By RCM Numberer & dt/2"
            }
        }

        if {$ok != 0} {
            numberer AMD
```

```
                set ok [analyze 1 [expr $DtAnalysis/4.]];          # actually perform analysis;
returns ok=0 if analysis was successful
            if {$ok == 0} {
                    puts  "solved By AMD Numberer"
            }
        }

        if {$ok != 0} {
            system UmfPack
                set ok [analyze 1 [expr $DtAnalysis/4.]];          # actually perform analysis;
returns ok=0 if analysis was successful
            if {$ok == 0} {
                    puts  "solved By UmfPack System & dt/4"
            }
        }

        if {$ok != 0} {
            system BandGeneral
                set ok [analyze 1 [expr $DtAnalysis/4.]];          # actually perform analysis;
returns ok=0 if analysis was successful
            if {$ok == 0} {
                    puts  "solved By BandGeneral System & dt/4"
            }
        }

        if {$ok != 0} {
            system SparseSPD
```

```
                set ok [analyze 1 [expr $DtAnalysis/4.]];          # actually perform analysis;
returns ok=0 if analysis was successful
            if {$ok == 0} {
                    puts  "solved By SparseSPD System & dt/4"
            }
        }

        if {$ok != 0} {
            system SparseSYM
                set ok [analyze 1 [expr $DtAnalysis/4.]];          # actually perform analysis;
returns ok=0 if analysis was successful
            if {$ok == 0} {
                    puts  "solved By SparseSYM System & dt/4"
            }
        }

        if {$ok != 0} {
            test EnergyIncr 1.0e-4 50
                set ok [analyze 1 [expr $DtAnalysis/2.]];          # actually perform analysis;
returns ok=0 if analysis was successful
            if {$ok == 0} {
                    puts  "solved By EnergyIncr Test & dt/2"
            }
        }

        if {$ok != 0} {
            test NormUnbalance 1.0e-3 50
```

```
                set ok [analyze 1 [expr $DtAnalysis/2.]];          # actually perform analysis;
returns ok=0 if analysis was successful
            if {$ok == 0} {
                    puts  "solved By NormUnbalance Test & dt/2"
            }
        }

        if {$ok != 0} {
            test RelativeNormDispIncr 1.0e-3 50
                set ok [analyze 1 [expr $DtAnalysis/2.]];          # actual ly perform analysis;
returns ok=0 if analysis was successful
            if {$ok == 0} {
                    puts  "solved By NormUnbalance Test & dt/2"
            }
        }




}

puts "\n\n#** ([clock format [clock seconds]]) Analysis ends...End Time: [getTime] of $TmaxAnalysis"
#*******************************************************************************************
*****
```

Appendix E. OpenSEES Scripts for Numerical Simulation of BRSA

It was explained in the main body of this document that the effects of many analysis options and materials were investigated to determine the options that led to reasonable estimates of the measured response. Due to the large numbers of analyses, the scripts were prepared in modules rather than a single code in OpenSEES. The following scripts were used to model BRSA.

```
# BRSA_test
Verification.tcl*************************************************************************
# The main file to run the dynamic simulations of
# Bent with Rebar-pin Column-Pile Shaft Connection for ABC (BRSA)
# The modules should be copy in two folders: "Modules" and "Model"
# April 16, 2016
# Units: kip, in, sec
# Sign Convention: South +X, Up +Y, Clockwise rotation is positive
#               Y ^
#                 |  _
#                 |   \
#        X  <-------- |
#                  <_ /
#

set log "BPSA_TestVerification.txt";
set temp [open $log w]
puts $temp "\# [clock format [clock seconds]]"
close $temp
logFile $log -append
set AnalysisType "Testverification";

# Constants
set PI [expr 2.0*asin(1.0)];# define constants
set g [expr 32.2*12.0];     # gravitational acceleration
set largeNum 1.0e9
```

```
source Model_BRSA.tcl
source Modules/Gravity.tcl
set    numModes 2;
source Modules/Modal.tcl
source Modules/damping.tcl

# Dynamic Loading----------------------
set DtGround [expr 1.0/256.];
set GMdirection 1
set statVelTol  0.01; #in/s
set statAccTol  0.05; #in2/s

#Column=FBE-conc02 + Pin=DBE3 ,
# set dt(1)  [expr $DtGround*2.0]; set dt(2) [expr $DtGround]; set dt(3) [expr $DtGround/1.0];
# set dt(4)  [expr $DtGround/2.0]; set dt(5) [expr $DtGround/1.0]; set dt(6) [expr $DtGround/1.0];

# 3spring,
set dt(1)  [expr $DtGround]; set dt(2) [expr $DtGround]; set dt(3) [expr $DtGround*2.0];
set dt(4)  [expr $DtGround*1.0]; set dt(5) [expr $DtGround*1.0]; set dt(6) [expr $DtGround];



foreach run [list 1 2 3 4 5 6] {
puts "\n\n Starting run: $run _____________________________________________"
set outFolder  "Response_TestVerification/RUN-$run"
source Modules/Modal.tcl
set tsTag $run
```

```
set MotionFile "Input Motions/tableA-RUN-$run.txt";
setTime 0.0
timeSeries Path $tsTag -dt $DtGround -filePath "Input Motions/tableA-RUN-$run.txt" -factor $g
pattern UniformExcitation  $run  $GMdirection  -accel $tsTag;
source Modules/Recorder_Dynamic.tcl

# Strong part of Motion
set DtAnalysis      [expr $dt($run)];    # time-step Dt for lateral analysis
set TmaxAnalysis     25.0;               # maximum duration of ground-motion analysis -- should be
50*$sec
source Modules/DynamicAnalysis.tcl

# Weak part of Motion
set DtAnalysis      [expr 2.*$DtAnalysis];  # time-step Dt for lateral analysis
set TmaxAnalysis     40.0;                  # maximum duration of ground-motion analysis -- should be
50*$sec
source Modules/DynamicAnalysis.tcl

# Free-Vibration
set DtAnalysis      [expr 0.05];
rayleigh 0.05 $betaKcurr 0.05 $betaKcomm;
while { [expr abs([nodeVel $monitor 1]) ] > $statVelTol || [expr abs([nodeAccel $monitor 1])] >
$statAccTol } {
    set TmaxAnalysis    [expr $TmaxAnalysis+20.0];  # maximum duration of ground-motion analysis --
should be 50*$sec
    source Modules/DynamicAnalysis.tcl
}
rayleigh $alphaM $betaKcurr $betaKinit $betaKcomm;
```

```
remove recorders
remove loadPattern $run
puts "Velocity= [nodeVel $monitor 1] in/s, Acc= [expr [nodeAccel $monitor 1]/$g] g, ";
#source Modules/Modal.tcl
puts "Finished run-$run"
puts "_____________________________________________________________"
}
wipe


set temp [open $log a]
puts $temp "\# End of log BPSA"
puts $temp "\# [clock format [clock seconds]]"
close $temp
puts "End of BPSA.tcl"
#*********************************************************************************************
******
```

```
#
Model_BRSA.tcl*********************************************************************************
****
# Sign Convention: South +X, Up +Y, Clockwise rotation is positive
#                Y ^
#                  |  _
#                  |    \
#        X  <--------- |
#                  <_ /
#


puts "\n_____________________________________________________________________________________";
puts "** ([clock format [clock seconds]]) Starting Model_BRSA.tcl (2D model)..."

wipe;                                 # clear memory of all past model definitions
model basic -ndm 2 -ndf 3;            # Define the model builder, ndm=#dimension, ndf=#dofs
# nodal coordinates-----------------------------------------------------------------------
set hp  30.0;
set gap 1.0;
set hc  64.0;
set hcb 24.0;    # Cap beam height
set bcb 24.0;    # Cap beam height
set bay [expr 7.0*12./2.0]; #half of the bay between columns

#set Lpin 0.0; # for Rebar-Pin=pin, 3spring
set Lpin $gap; # Gap Length
```

```
# Nodes Tags
set base   10;
set pedTop 20;
set colBot 30;
set colTop 40;
set cb     50;

#Node   Label                X       Y
node    [expr 100+$base]     $bay    [expr 0.0]                    -mass 1.e-6 1.e-6 1.e-8;
node    [expr 100+$pedTop]   $bay    [expr $hp]                    -mass 1.e-6 1.e-6 1.e-8;
node    [expr 100+$colBot]   $bay    [expr $hp+$Lpin]              -mass 1.e-6 1.e-6 1.e-8;
node    [expr 100+$colTop]   $bay    [expr $hp+$gap+$hc]           -mass 1.e-6 1.e-6 1.e-8;
node    [expr 100+$cb]       $bay    [expr $hp+$gap+$hc+$hcb/2.0]  -mass 1.e-6 1.e-6 1.e-8;

node    [expr 200+$cb]       0.0     [expr $hp+$gap+$hc+$hcb/2.0]  -mass 1.e-6 1.e-6 1.e-8;

node    [expr 300+$base]     -$bay   [expr 0.0]                    -mass 1.e-6 1.e-6 1.e-8;
node    [expr 300+$pedTop]   -$bay   [expr $hp]                    -mass 1.e-6 1.e-6 1.e-8;
node    [expr 300+$colBot]   -$bay   [expr $hp+$Lpin]              -mass 1.e-6 1.e-6 1.e-8;
node    [expr 300+$colTop]   -$bay   [expr $hp+$gap+$hc]           -mass 1.e-6 1.e-6 1.e-8;
node    [expr 300+$cb]       -$bay   [expr $hp+$gap+$hc+$hcb/2.0]  -mass 1.e-6 1.e-6 1.e-8;

set monitor [expr 200+$cb];

# Boundary conditions
fix [expr 100+$base] 1 1 1;     # Fixed at the base
```

```
fix [expr 300+$base] 1 1 1;

# Default materials/springs
set rigidMat 1
set softMat  2
uniaxialMaterial Elastic $rigidMat 1.0e12
uniaxialMaterial Elastic $softMat  1.0e-6

set tol 1.0e-10;
set iter  50;
# Element
GeomTranf
# Columns,Z is in to the plane. Hence; localY: toward -X
# Beams,Z is in to the plane. Hence; localY: toward +Y(Up)
set ColTransfTag  1;
set BeamTransfTag 2;

#geomTransf PDelta $transfTag <-jntOffset $dXi $dYi $dXj $dYj>
 geomTransf PDelta $ColTransfTag
 geomTransf PDelta $BeamTransfTag

# Modeling Masses and
Pdelta
source "Model/Model_PDelta_Spring.tcl"

# Cap
Beam
set CIPcb  130;
```

```
set ABCcb  330;
source "Model/CapBeam_Elastic.tcl"

# REBAR-
PIN_____________________________________________________________________________________
set CIPpin 120;
set ABCpin 320;
set nipPin 4;

#source "Model/Model_RebarPin_CIP_3Spring.tcl"
#source "Model/Model_RebarPin_PC_3spring.tcl"
source "Model/Model_RebarPin_CIP_BondMostafa.tcl"
source "Model/Model_RebarPin_PC_BondMostafa.tcl"

#
COLUMNS_____________________________________________________________________________________
___
set CIPcolSec           1000;   # Tag for ECC concrete sections
set CIPcolBondSec       1010;   # tag for ECC w/ Bond Slip
set CIPCol  100;
source "Model/Model_CIP_Col_Mostafa.tcl"

set ABCcolSec           3000;   # Tag for ECC concrete sections
set ABCcolBondSec       3010;
set ABCCol  300;
source "Model/Model_PC_Col_Mostafa.tcl"
```

```
#
PEDESTAL_____________________________________________________________________________
__
set pedSec      1100;
set pedBondSec  1110;
set CIPPed      110; #Element Tag for the pedestal under CIP column
set ABCPed      310; #Element Tag for the pedestal under ABC column
source "Model/Model_Pedestals_Mostafa.tcl"


# Printing the model
connectivity_____________________________________________________________
puts "\n***NODES:";
set allTags [getNodeTags];
foreach tag  $allTags {
    puts [format "%i: %5.2f %5.2f" $tag [nodeCoord $tag 1] [nodeCoord $tag 2]];
}
puts "\n***Element Connectivity:";
puts "Ele: i-node j-node"
foreach ele [getEleTags] {
    puts "$ele: [eleNodes $ele]"
}
puts "_____________________________________________________________________________";
#*********************************************************************************************
```

```
# Model_PDelta_Spring.tcl*********************************************************************
# WmassRig=100 kip
# hMassRig=98 in
# K=W/h = 1.0204, Negative because of the nature of Pdelta

set M [expr 104.5/$g]
mass [expr 100+$cb]  $M $M 0.0   ;
set M [expr 4.5/$g]
mass [expr 300+$cb]  $M $M 0.0   ;

set KpDelta  [expr -100.0/183.3];

#uniaxialMaterial Elastic $matTag $E <$eta> <$Eneg>
 uniaxialMaterial Elastic  10      $KpDelta

 node [expr $base] $bay     [expr $hp+$gap+$hc+$hcb/2.0];
 fix  [expr $base] 1 1 1
 element zeroLength 1000  $base [expr 100+$cb]  -mat 10 -dir   1

# Gravity load
=============================================================================================
  pattern Plain 100 Constant {
       load         [expr 100+$cb]  0.0 -4.50 0.0 ;
       load         [expr 300+$cb]  0.0 -4.50 0.0 ;
  }
#*************************************************************************************
```

```
#
CapBeam_Elastic.tcl*************************************************************************
***


set fc      6.31;
set Keff    1.0;                                    # Effective stiffness for the beam due to
cracking
set A       [expr 24.0*24.0];                       # Gross sectional area
set E       [expr 57.0*sqrt(1000.0*$fc)];           # Young's Modulus elasticity same as concrete
set Iz      [expr $Keff*$bcb*pow($hcb,3.0)/12.0];   # Moment of Inertia around major axis (vertical
one)



#element elasticBeamColumn $eleTag $iNode         $jNode         $A $E $Iz $transfTag <-mass
$massDens> <-cMass>
 element elasticBeamColumn $CIPcb  [expr 200+$cb] [expr 100+$cb] $A $E $Iz $BeamTransfTag;
 element elasticBeamColumn $ABCcb  [expr 300+$cb] [expr 200+$cb] $A $E $Iz $BeamTransfTag;
#*************************************************************************************
*****
```

```
#
Model_Rebar_Pin_CIP_Spring.tcl**************************************************************************

# Rotational Spring_____________________________________________
# With SRE and deadload axial load
set thetaY  6.887e-3;
set thetaU  0.1771;
set My      495.;
set Mu      495.;

set Ki      [expr $My/$thetaY];
set Kh      [expr ($Mu-$My)/($thetaU-$thetaY)];
set b       [expr  $Kh/$Ki]

set pinchX      1.0; # Pinching factor for strain (or deformation) during reloading
set pinchY      0.6; # pinching factor for stress (or force) during reloading
#set pinchY     1.0; # pinching factor for stress (or force) during reloading
set damage1     0.0; # damage due to ductility: D1(mu-1)
set damage2     0.0; # damage due to energy: D2(Eii/Eult)
set beta        0.0; # power used to determine the degraded unloading stiffness based on ductility,
mu-beta (optional, default=0.0)

#uniaxialMaterial Hysteretic $matTag $s1p $e1p     $s2p $e2p  <$s3p $e3p> $s1n  $e1n      $s2n  $e2n
<$s3n $e3n> $pinchX $pinchY $damage1 $damage2 <$beta>
 uniaxialMaterial Hysteretic 1230    $My  $thetaY  $Mu  $thetaU          -$My -$thetaY  -$Mu  -
$thetaU          $pinchX $pinchY $damage1 $damage2 $beta

# Axial Spring_____________________________________________
```

```
set Kcompression        466916;
set Ktension            441.4;

#uniaxialMaterial Elastic $matTag $E <$eta> <$Eneg>
 uniaxialMaterial Elastic 1220    $Ktension

# ELEMENT ---------------------------------------------------------------------
#element zeroLength $eleTag $iNode                        $jNode              -mat $matTag1 $matTag2
... -dir $dir1 $dir2 ...<-doRayleigh $rFlag> <-orient $x1 $x2 $x3 $yp1 $yp2 $yp3>
 element zeroLength   120   [expr 100+$pedTop]  [expr 100+$colBot]  -mat $rigidMat   1220  1230  -dir
1 2 3
#*****************************************************************************************
```

```
#
Model_Rebar_Pin_PC_Spring.tcl**************************************************************************
****


# Rotational Spring_____________________________________________
# With SRE
set thetaY  5.555e-3;
set thetaU  0.1729;
set My      482.;
set Mu      492.;

set Ki      [expr $My/$thetaY];
set Kh      [expr ($Mu-$My)/($thetaU-$thetaY)];
set b       [expr  $Kh/$Ki]

set pinchX      1.0; # Pinching factor for strain (or deformation) during reloading
#set pinchY     1.0; # Pinching factor for strain (or deformation) during reloading
set pinchY      0.6; # pinching factor for stress (or force) during reloading
set damage1     0.0; # damage due to ductility: D1(mu-1)
set damage2     0.0; # damage due to energy: D2(Eii/Eult)
set beta        0.0; # power used to determine the degraded unloading stiffness based on ductility,
mu-beta (optional, default=0.0)


#uniaxialMaterial Hysteretic $matTag $s1p $e1p     $s2p $e2p  <$s3p $e3p> $s1n  $e1n      $s2n  $e2n
<$s3n $e3n> $pinchX $pinchY $damage1 $damage2 <$beta>
 uniaxialMaterial Hysteretic 3230    $My  $thetaY  $Mu  $thetaU          -$My -$thetaY  -$Mu  -
$thetaU          $pinchX $pinchY $damage1 $damage2 $beta
```

```
# Axial Spring_____________________________________________________
set Kcompression        466916;
set Ktension            441.4;

#uniaxialMaterial Elastic $matTag $E <$eta> <$Eneg>
 uniaxialMaterial Elastic 3220    $Ktension



# ELEMENT ---------------------------------------------------------------
#element zeroLength $eleTag $iNode            $jNode                -mat $matTag1 $matTag2 ... -dir
$dir1 $dir2 ...<-doRayleigh $rFlag> <-orient $x1 $x2 $x3 $yp1 $yp2 $yp3>
 element zeroLength   320   [expr 300+$pedTop] [expr 300+$colBot]   -mat 1210     3220  3230    -dir
1 2 3
#*************************************************************************************************
*****
```

```
#
Model_RebarPin_BondMostafa.tcl**********************************************************************
****
# CIP Rebar-Pin ------------------------------------------------------------------------------------
-----
#uniaxialMaterial Concrete01WithSITC $matTag $fpc   $epsc0     $fpcu  $epsU <$endStrainSITC>
#uniaxialMaterial Concrete01WithSITC 1210   -9.176  -0.0055   -6.248  -0.0204  0.02;
#uniaxialMaterial Concrete01WithSITC 1220   -14.409 -0.0131   -12.309 -0.0425  0.02;

#uniaxialMaterial Concrete02        $matTag $fpc    $epsc0     $fpcu    $epsU   $lambda $ft $Ets
# uniaxialMaterial Concrete02       1210    -9.176  -0.0055     -6.248  -0.0522 0.10   0.0 0.0 ;
# uniaxialMaterial Concrete02       1220    -14.41  -0.0131     -12.31  -0.2143 0.10    0.0 0.0;

#uniaxialMaterial Concrete04 $matTag $fc     $ec        $ecu    $Ec <$fct $et> <$beta>
 uniaxialMaterial Concrete04 1210    -9.176  -0.0055    -0.0204 4510.
 uniaxialMaterial Concrete04 1220    -14.41  -0.0131    -0.0425 4510.



#uniaxialMaterial ReinforcingSteel $matTag $fy  $fu       $Es      $Esh    $esh     $eult < -GABuck
$lsr $beta $r $gama > < -DMBuck $lsr < $alpha >> < -CMFatigue $Cf $alpha $Cd > < -IsoHard <$a1
<$limit> > >
#uniaxialMaterial ReinforcingSteel 1250     71.983  108.465   29000.  1200.0  0.004    0.11000;     #
Reinforcing bars modify for bond slip with modification for strain-rate
#uniaxialMaterial ReinforcingSteel 1260     71.788  103.763   22763.  1199.0  0.004678 0.11078;     #
Reinforcing bars modify for single bond slip with modification for strain-rate


#uniaxialMaterial Steel02 $matTag $Fy      $E     $b     $R0 $cR1  $cR2 <$a1 $a2 $a3 $a4 $sigInit>
 uniaxialMaterial Steel02 1250    71.788  29000.  0.0103 10  0.925 0.15; # SRE
 uniaxialMaterial Steel02 1260    71.788  17730.  0.0138 10  0.925 0.15; # SRE
```

```
set numBar  6;
set Ab      0.31;               # #5 bars
set R       5.0;                # section outer Radius
set Rcore   3.813;              # Center of spiral
set Rreinf  3.313;              # bars radius
set circdiv [expr 3*$numBar];   # Divides the circular patch in 5 segments between each reinf.

section Fiber 1200 {;
#                   $mattag     $circdiv    $Rdiv       $y0 $z0 $intR       $extrR  $start  $end
        patch circ  1220        $circdiv    8           0.  0.  0.          $Rcore  0.0     360.0;
# Define core concrete fibers
        patch circ  1210        $circdiv    4           0.  0.  $Rcore      $R      0.0     360.0;
# Define cover concrete fibers
#                   $matTag     $numFiber   $Afiber     $y0 $z0 $radius     $startAng   $endAng
        layer circ  1250        $numBar     $Ab         0.  0.  $Rreinf;                # Radial
distribution of bars
};

section Fiber 1210 {;
#                   $mattag     $circdiv    $Rdiv       $y0 $z0 $intR       $extrR  $start  $end
        patch circ  1220        $circdiv    8           0.  0.  0.          $Rcore  0.0     360.0;
# Define core concrete fibers
        patch circ  1210        $circdiv    4           0.  0.  $Rcore      $R      0.0     360.0;
# Define cover concrete fibers
#                   $matTag     $numFiber   $Afiber     $y0 $z0 $radius     $startAng   $endAng
        layer circ  1260        $numBar     $Ab         0.  0.  $Rreinf;                # Radial
distribution of bars
};
```

```
# ELEMENT ---------------------------------------------------------------------

# FBE_____________________________________________________________________

#element forceBeamColumn $eleTag $iNode              $jNode               $numIntgrPts $secTag
$transfTag <-mass $massDens> <-iter $maxIters $tol> <-integration $intType>

#element forceBeamColumn $CIPpin [expr 100+$pedTop] [expr 100+$colBot]   $nipPin     1210
$ColTransfTag -iter 50 $tol;


# DBE_____________________________________________________________________

#element dispBeamColumn $eleTag $iNode              $jNode               $numIntgrPts $secTag
$transfTag <-mass $massDens> <-cMass> <-integration $intType>

element dispBeamColumn $CIPpin [expr 100+$pedTop] [expr 100+$colBot]    $nipPin         1210
$ColTransfTag -iter 50 $tol;


#*********************************************************************************************
*****
```

```
#
Model_Rebar_Pin_PC_BondMostafa.tcl**********************************************************************
****
# PC Rebar-Pin ------------------------------------------------------------------------------------
------
#uniaxialMaterial Concrete01WithSITC $matTag $fpc    $epsc0     $fpcu   $epsU <$endStrainSITC>
# uniaxialMaterial Concrete01WithSITC 3210   -11.708  -0.00454   -7.157  -0.01471  0.02;
# uniaxialMaterial Concrete01WithSITC 3220   -17.528  -0.01092   -14.054 -0.03562  0.02;

#uniaxialMaterial Concrete02        $matTag $fpc    $epsc0     $fpcu   $epsU    $lambda $ft $Ets
# uniaxialMaterial Concrete02       3210    -11.71  -0.00454    -7.157  -0.01471    0.10 0.0 0.0 ;
# uniaxialMaterial Concrete02       3220    -17.53  -0.01092    -14.05  -0.03562    0.10 0.0 0.0;

#uniaxialMaterial Concrete04 $matTag $fc        $ec      $ecu    $Ec <$fct $et> <$beta>
 uniaxialMaterial Concrete04  3210   -11.708  -0.00454  -0.01471 5491.
 uniaxialMaterial Concrete04  3220   -17.528  -0.01092  -0.03562 5491.

#uniaxialMaterial ReinforcingSteel $matTag $fy  $fu       $Es      $Esh    $esh     $eult < -GABuck
$lsr $beta $r $gama > < -DMBuck $lsr < $alpha >> < -CMFatigue $Cf $alpha $Cd > < -IsoHard <$a1
<$limit> > >
#uniaxialMaterial ReinforcingSteel 1250     71.983  103.763   29000.  1200.0  0.004    0.11000;     #
Reinforcing bars modify for bond slip with modification for strain-rate
#uniaxialMaterial ReinforcingSteel 1260     71.788  103.763   22763.  1199.0  0.004678 0.11078;     #
Reinforcing bars modify for single bond slip with modification for strain-rate

#uniaxialMaterial Steel02 $matTag $Fy      $E     $b     $R0 $cR1  $cR2 <$a1 $a2 $a3 $a4 $sigInit>
 uniaxialMaterial Steel02 3250    71.788  29000.  0.0103 10  0.925 0.15; # SRE
 uniaxialMaterial Steel02 3260    71.788  17730.  0.0138 10  0.925 0.15; # SRE
```

```
set numBar  6;
set Ab      0.31;               # #5 bars
set R       5.0;                # section outer Radius
set Rcore   3.813;              # Center of spiral
set Rreinf  3.313;              # bars radius
set circdiv [expr 3*$numBar];   # Divides the circular patch in 5 segments between each reinf.

section Fiber 3200 {;
#                   $mattag     $circdiv    $Rdiv       $y0 $z0 $intR       $extrR  $start  $end
        patch circ  3220        $circdiv    8           0.  0.  0.          $Rcore  0.0     360.0;
# Define core concrete fibers
        patch circ  3210        $circdiv    4           0.  0.  $Rcore      $R      0.0     360.0;
# Define cover concrete fibers
#                   $matTag     $numFiber   $Afiber     $y0 $z0 $radius     $startAng   $endAng
        layer circ  3250        $numBar     $Ab         0.  0.  $Rreinf;                # Radial
distribution of bars
};

section Fiber 3210 {;
#                   $mattag     $circdiv    $Rdiv       $y0 $z0 $intR       $extrR  $start  $end
        patch circ  3220        $circdiv    8           0.  0.  0.          $Rcore  0.0     360.0;
# Define core concrete fibers
        patch circ  3210        $circdiv    4           0.  0.  $Rcore      $R      0.0     360.0;
# Define cover concrete fibers
#                   $matTag     $numFiber   $Afiber     $y0 $z0 $radius     $startAng   $endAng
        layer circ  3260        $numBar     $Ab         0.  0.  $Rreinf;                # Radial
distribution of bars
};
```

```
# ELEMENT ---------------------------------------------------------------------
# FBE_____________________________________________________________________
#element forceBeamColumn $eleTag $iNode             $jNode              $numIntgrPts $secTag
$transfTag <-mass $massDens> <-iter $maxIters $tol> <-integration $intType>
#element forceBeamColumn $ABCpin  [expr 300+$pedTop] [expr 300+$colBot]  $nipPin     3210
$ColTransfTag -iter 50 $tol;


# DBE_____________________________________________________________________
#element dispBeamColumn $eleTag  $iNode                 $jNode         $numIntgrPts  $secTag
$transfTag <-mass $massDens> <-cMass> <-integration $intType>
element dispBeamColumn $ABCpin  [expr 300+$pedTop] [expr 300+$colBot] $nipPin        3210
$ColTransfTag -iter 50 $tol;


#*********************************************************************************************
*****
```

```
#
Model_CIP_Col.tcl*****************************************************************************
****
# Full section w/o any ECC
# fc=6.26ksi and w SRE fc=6.46ksi
# 14#4, #3@2",

# CIP Materials
# Materials for the full circular section 1000
# Top plastic hinge section
#uniaxialMaterial Concrete02        $matTag $fpc    $epsc0      $fpcu   $epsU    $lambda $ft $Ets
# uniaxialMaterial Concrete02       1010    -6.26   -0.002      0.00    -0.005      0.10 0.0 0.0;   #
Cover, Mander Model
# uniaxialMaterial Concrete02       1020    -9.354  -0.00694    -7.123  -0.02615    0.10 0.0 0.0;   #
Core, Mander Model,

#uniaxialMaterial Concrete04 $matTag $fc    $ec      $ecu       $Ec <$fct $et> <$beta>
 uniaxialMaterial Concrete04 1010    -6.26  -0.00200 -0.00500  4510.
 uniaxialMaterial Concrete04 1020    -9.354 -0.00694 -0.02615  4510.

#uniaxialMaterial Concrete01WithSITC $matTag $fpc   $epsc0     $fpcu  $epsU <$endStrainSITC>
# uniaxialMaterial Concrete01WithSITC 1010   -6.26  -0.002     0.0    -0.005    0.02;
# uniaxialMaterial Concrete01WithSITC 1020   -9.354 -0.00694   -7.123 -0.02615  0.02;

#uniaxialMaterial ConcreteCM $mattag $fpcc   $epcc      $Ec     $rc     $xcrn   $ft $et $rt $xcrp <-
GapClose $gap>
#uniaxialMaterial ConcreteCM 1010    -6.26  -0.002      4510.   6.4     2.0     0.0 0.0 11. 1000
#uniaxialMaterial ConcreteCM 1020    -9.354 -0.00694    4510.   11.     3.8     0.0 0.0 11. 1000
```

```
#uniaxialMaterial Steel02 $matTag $Fy  $E       $b      $R0 $cR1 $cR2 <$a1 $a2 $a3 $a4 $sigInit>
uniaxialMaterial Steel02  1050   72.352 29000. 6.134e-3 10 0.925  0.15; #SRE
 uniaxialMaterial Steel02  1060   72.352 22852. 7.776e-3 10 0.925  0.15; #SRE


#uniaxialMaterial ReinforcingSteel $matTag  $fy     $fu      $Es     $Esh    $esh    $eult < -GABuck
$lsr $beta $r $gama > < -DMBuck $lsr < $alpha >> < -CMFatigue $Cf $alpha $Cd > < -IsoHard <$a1
<$limit> > >
# uniaxialMaterial ReinforcingSteel 1050    72.352  96.814   29000.0 800.0   0.01400 0.14000; # -
MPCurveParams  0.38 20 4;      # Reinforcing bars Modified for strain rate
# uniaxialMaterial ReinforcingSteel 1060    72.352  96.814   22851.6 799.0   0.01467 0.14082; #
Reinforcing bars modify for bond slip with modification for strain-rate


set numBar  14;
set Ab      0.20;               # #4 bars
set R       8.0;                # section outer Radius
set Rcore   6.8125;             # Center of spiral
set Rreinf  6.375;              # bars radius
set circdiv [expr $numBar];     # Divides the circular patch in 5 segments between each reinf.


section Fiber [expr $CIPcolBondSec] {;   # section w/ modified steel for bond-slip action
#                   $mattag     $circdiv    $Rdiv       $y0 $z0 $intR       $extrR  $start  $end
        patch circ  1020        $circdiv    6           0.  0.  0.          $Rcore  0.0     360.0   ;
# Define core concrete
        patch circ  1010        $circdiv    2           0.  0.  $Rcore      $R      0.0     360.0   ;
# Define cover concrete

        #           $matTag     $numFiber   $Afiber     $y0 $z0 $radius  $startAng  $endAng
```

```
        #layer circ     1050        $numBar     $Ab         0.  0.  $Rreinf ;                   #
Radial distribution of bars
         layer circ     1060        $numBar     $Ab         0.  0.  $Rreinf ;                   #
Radial distribution of bars
};

section Fiber [expr $CIPcolSec] {;   # section W/ Reg concrete out of plastic hinge
#                   $mattag     $circdiv    $Rdiv       $y0 $z0 $intR       $extrR  $start  $end
        patch circ  1020        $circdiv    5           0.  0.  0.          $Rcore   0.0    360.0   ;
# Define core concrete
        patch circ  1010        $circdiv    2           0.  0.  $Rcore      $R     0.0      360.0   ;
# Define cover concrete

        #           $matTag     $numFiber   $Afiber     $y0 $z0 $radius  $startAng  $endAng
        layer circ  1050        $numBar     $Ab         0.  0.  $Rreinf ;                       #
Radial distribution of bars
};


section Fiber [expr $CIPcolSec+2] {;     # section W/ Reg concrete out of plastic hinge
#                   $mattag     $circdiv    $Rdiv       $y0 $z0 $intR       $extrR  $start  $end
        patch circ  1020        $circdiv    5           0.  0.  0.          $Rcore   0.0    360.0   ;
# Define core concrete
        patch circ  1010        $circdiv    2           0.  0.  $Rcore      $R     0.0      360.0   ;
# Define cover concrete

        #           $matTag     $numFiber   $Afiber     $y0 $z0 $radius  $startAng  $endAng
        layer circ  1050        $numBar     $Ab         0.  0.  $Rreinf ;                       #
Radial distribution of bars
```

```
        layer circ  1050        6           0.31        0.  0.  3.313;                  # Radial
distribution of bars
};



# ELEMENT ------------------------------------------------------------------
# FBE_____________________________________________________________________
# set nipCip 3;  set CIPsections " -sections  $CIPcolSec $CIPcolSec  $CIPcolBondSec "
set nipCip 4;  set CIPsections " -sections  $CIPcolSec $CIPcolSec $CIPcolSec $CIPcolBondSec "
# set nipCip 5;  set CIPsections " -sections  $CIPcolSec $CIPcolSec $CIPcolSec $CIPcolSec
$CIPcolBondSec "
 #set nipCip 6;  set CIPsections " -sections  $CIPcolSec $CIPcolSec $CIPcolSec $CIPcolSec $CIPcolSec
$CIPcolBondSec "
# set nipCip 7;  set CIPsections " -sections  $CIPcolSec    $CIPcolSec $CIPcolSec $CIPcolSec
$CIPcolSec     $CIPcolSec $CIPcolBondSec "
#set nipCip 8;  set CIPsections " -sections  $CIPcolSec $CIPcolSec $CIPcolSec $CIPcolSec $CIPcolSec
$CIPcolSec $CIPcolSec $CIPcolBondSec "
#set nipCip 9;  set CIPsections " -sections  $CIPcolSec $CIPcolSec $CIPcolSec $CIPcolSec $CIPcolSec
$CIPcolSec $CIPcolSec $CIPcolSec $CIPcolBondSec "


#element forceBeamColumn $eleTag $iNode              $jNode            $numIntgrPts $secTag
$transfTag <-mass $massDens> <-iter $maxIters $tol> <-integration $intType>
 element forceBeamColumn $CIPCol [expr 100+$colBot] [expr 100+$colTop] $nipCip      $CIPsections
$ColTransfTag -iter 50 $tol;



# Rigid link to the center of cap beam, rigid with 10XE
#element elasticBeamColumn $eleTag $iNode            $jNode             $A     $E    $Iz
$transfTag <-mass $massDens> <-cMass>
```

```
 element elasticBeamColumn 106     [expr 100+$colTop] [expr 100+$cb]     201.1 45100. 3217.0
$ColTransfTag


#*********************************************************************************************
******
```

```
#
Model_PC_Col.tcl*****************************************************************************
****
# fc,ECC= 9.02ksi, l=24in
# fc,SCC= 10.40ksi
# fc,shell=7.45ksi



# PC Column ------------------------------------------------------------------------------
------
# PLASTIC HINGE W Bond Modification & SRE
#uniaxialMaterial Concrete01WithSITC $matTag $fpc    $epsc0    $fpcu     $epsU  <$endStrainSITC> W/o
SRE
# uniaxialMaterial Concrete01WithSITC 3010   -9.02   -0.0020    0.00    -0.0060   0.02;     #
Unconfined ECC concrete Cover in shell
# uniaxialMaterial Concrete01WithSITC 3020   -12.278 -0.00561  -7.865   -0.02087  0.02;     #
Confined ECC concrete Core in Shell
# uniaxialMaterial Concrete01WithSITC 3030   -13.714 -0.00519  -7.873   -0.0191   0.02;     #
confined SCC in-fill W/O SRE


#uniaxialMaterial Concrete02 $matTag    $fpc    $epsc0   $fpcu      $epsU    $lambda $ft $Ets
# uniaxialMaterial Concrete02 3010      -9.02   -0.0020    0.00     -0.00600  0.10   0.0  0.0;      #
Unconfined ECC concrete Cover in shell
# uniaxialMaterial Concrete02 3020      -12.278 -0.00561  -7.865    -0.02087  0.10   0.0  0.0;      #
Confined ECC concrete Core in Shell
# uniaxialMaterial Concrete02 3030      -13.714 -0.00519  -7.873    -0.01910  0.10   0.0  0.0;      #
confined SCC in-fill W/O SRE


# uniaxialMaterial Concrete02 3010      -9.02   -0.00250   0.000    -0.00600  0.10   0.0  0.0;      #
Motaref et al., Unconfined ECC concrete Cover in shell
```

```
# uniaxialMaterial Concrete02 3020      -10.595 -0.00368  -4.238    -0.00767  0.10   0.0  0.0;      #
Motaref et al.,Confined ECC concrete Core in Shell


#uniaxialMaterial ConcreteCM $mattag $fpcc   $epcc      $Ec     $rc     $xcrn   $ft $et $rt $xcrp <-
GapClose $gap>
# uniaxialMaterial ConcreteCM 3010   -9.020  -0.002     5414.   10.1    2.0     0.0 0.0 11. 1000
# uniaxialMaterial ConcreteCM 3020   -12.28  -0.00694   5414.   14.5    3.7     0.0 0.0 11. 1000


#uniaxialMaterial Concrete04 $matTag $fc     $ec        $ecu        $Ec <$fct $et> <$beta>
 uniaxialMaterial Concrete04 3010    -9.02   -0.0020    -0.0060     5414.
 uniaxialMaterial Concrete04 3020    -12.28  -0.00561   -0.02087    5414.
 uniaxialMaterial Concrete04 3030    -13.71  -0.00519   -0.01910    5813.
 uniaxialMaterial Concrete04 3015    -7.450  -0.002     -0.0050     4920.
 uniaxialMaterial Concrete04 3025    -10.63  -0.00626   -0.02071    5414.

#uniaxialMaterial Steel02 $matTag $Fy   $E     $b        $R0 $cR1   $cR2 <$a1 $a2 $a3 $a4 $sigInit>
#uniaxialMaterial Steel02  3050   68.0  29000. 0.0062    10 0.925  0.15
 uniaxialMaterial Steel02  3050   72.352 29000. 6.134e-3 10 0.925  0.15; #SRE
 uniaxialMaterial Steel02  3060   72.352 22852. 7.776e-3 10 0.925  0.15; #SRE


#uniaxialMaterial ReinforcingSteel $matTag  $fy     $fu      $Es     $Esh    $esh    $eult < -GABuck
$lsr $beta $r $gama > < -DMBuck $lsr < $alpha >> < -CMFatigue $Cf $alpha $Cd > < -IsoHard <$a1
<$limit> > >
# uniaxialMaterial ReinforcingSteel 3050    72.352  96.814   29000.0 800.0   0.01400 0.14000;# -
MPCurveParams  0.38 20 4;   # Reinforcing bars Modified for strain rate
```

```
# uniaxialMaterial ReinforcingSteel 3060    72.352  96.814   22852.0 799.0   0.01467 0.14082;   #
Reinforcing bars modify for bond slip with modification for strain-rate



set numBar  14;
set Ab      0.20;               # #4 bars
set R       8.0;                # section outer Radius
set Rcore   6.8125;             # Center of spiral
set Rreinf  6.375;              # bars radius
set Rfill   5.0;
set circdiv [expr $numBar];     # Divides the circular patch in 5 segments between each reinf.


section Fiber [expr $ABCcolBondSec] {;  #ECC w/ Bond
#                   $mattag     $circdiv    $Rdiv       $y0 $z0 $intR       $extrR  $start  $end
        patch circ  3030        $circdiv    3           0.  0.  0.          $Rfill  0.0     360.0;
# Define core concrete fibers
        patch circ  3020        $circdiv    4           0.  0.  $Rfill      $Rcore  0.0     360.0;
# Define core concrete fibers
        patch circ  3010        $circdiv    2           0.  0.  $Rcore      $R      0.0     360.0;
# Define cover concrete fibers
#                   $matTag     $numFiber   $Afiber     $y0 $z0 $radius     $startAng   $endAng
        layer circ  3060        $numBar     $Ab         0.  0.  $Rreinf;                # Radial
distribution of bars
};


section Fiber [expr $ABCcolSec] {; # ECC w/o Bond
```

```
#                   $mattag     $circdiv    $Rdiv       $y0 $z0 $intR       $extrR  $start  $end
        patch circ  3030        $circdiv    2           0.  0.  0.          $Rfill  0.0     360.0;
# Define core concrete fibers
        patch circ  3020        $circdiv    4           0.  0.  $Rfill      $Rcore  0.0     360.0;
# Define core concrete fibers
        patch circ  3010        $circdiv    2           0.  0.  $Rcore      $R      0.0     360.0;
# Define cover concrete fibers
#                   $matTag     $numFiber   $Afiber     $y0 $z0 $radius     $startAng   $endAng
        layer circ  3050        $numBar     $Ab         0.  0.  $Rreinf;                # Radial
distribution of bars


};

section Fiber [expr $ABCcolSec+2] {; # Regular conc. shell
#                   $mattag     $circdiv    $Rdiv       $y0 $z0 $intR       $extrR  $start  $end
        patch circ  3030        $circdiv    2           0.  0.  0.          $Rfill  0.0     360.0;
# Define core concrete fibers
        patch circ  3025        $circdiv    4           0.  0.  $Rfill      $Rcore  0.0     360.0;
# Define core concrete fibers
        patch circ  3015        $circdiv    2           0.  0.  $Rcore      $R      0.0     360.0;
# Define cover concrete fibers
#                   $matTag     $numFiber   $Afiber     $y0 $z0 $radius     $startAng   $endAng
        layer circ  3050        $numBar     $Ab         0.  0.  $Rreinf;                # Radial
distribution of bars
}


section Fiber [expr $ABCcolSec+3] {;    #bottom section reg. conc. shel + rebar reinf.
#                   $mattag     $circdiv    $Rdiv       $y0 $z0 $intR       $extrR  $start  $end
```

```
        patch circ  3030        $circdiv    2           0.  0.  0.          $Rfill  0.0     360.0;
# Define core concrete fibers
        patch circ  3025        $circdiv    3           0.  0.  $Rfill      $Rcore  0.0     360.0;
# Define core concrete fibers
        patch circ  3015        $circdiv    2           0.  0.  $Rcore      $R      0.0     360.0;
# Define cover concrete fibers
#                   $matTag     $numFiber   $Afiber     $y0 $z0 $radius     $startAng   $endAng
        layer circ  3050        $numBar     $Ab         0.  0.  $Rreinf;                # Radial
distribution of bars
        layer circ  3050        6           0.31        0.  0.  3.313;                  # Radial
distribution of bars
};



#ELEMENT ---------------------------------------------------------------------
# FBE
# set nipAbc 3; set ABCsections " -sections $ABCcolSec $ABCcolSec  $ABCcolBondSec "
 set nipAbc 4; set ABCsections " -sections $ABCcolSec $ABCcolSec $ABCcolSec $ABCcolBondSec "
#set nipAbc 5; set ABCsections " -sections $ABCcolSec $ABCcolSec $ABCcolSec $ABCcolSec $ABCcolBondSec
"
#set nipAbc 6; set ABCsections " -sections 3002         3002      3002       $ABCcolSec $ABCcolSec
$ABCcolBondSec "
#set nipAbc 7; set ABCsections " -sections 3002         3002        3002      3002       $ABCcolSec
$ABCcolSec $ABCcolBondSec "
#set nipAbc 8;  set ABCsections " -sections $ABCcolSec $ABCcolSec $ABCcolSec $ABCcolSec $ABCcolSec
$ABCcolSec $ABCcolSec $ABCcolBondSec "
#set nipAbc 9;  set ABCsections " -sections $ABCcolSec $ABCcolSec $ABCcolSec $ABCcolSec $ABCcolSec
$ABCcolSec $ABCcolSec $ABCcolSec $ABCcolBondSec "
```

```
#element forceBeamColumn $eleTag $iNode              $jNode            $numIntgrPts $secTag
$transfTag <-mass $massDens> <-iter $maxIters $tol> <-integration $intType>

 element forceBeamColumn $ABCCol [expr 300+$colBot] [expr 300+$colTop] $nipAbc      $ABCsections
$ColTransfTag -iter 50 $tol;


#Rigid link to the center of cap beam, rigid with 10XE

#element elasticBeamColumn $eleTag $iNode            $jNode          $A    $E    $Iz    $transfTag

 element elasticBeamColumn 306    [expr 300+$colTop] [expr 300+$cb] 201.1 49200. 3217.0 $ColTransfTag


#*************************************************************************************
******
```

```
#
Model_Pedestals_Mostafa.tcl**************************************************************************
****
# PEDESTALs-------------------------------------------------------------------------------------
------
# Materials for the full circular section 1100:
# uniaxialMaterial  Concrete02      $matTag $fpc    $epsc0      $fpcu   $epsU       $lambda $ft $Ets
#  uniaxialMaterial Concrete02      1110    -6.91   -0.002      -0.000  -0.0060     0.10    0.0 0.0
#  uniaxialMaterial Concrete02      1120    -8.502  -0.0043     -5.809  -0.01367    0.10    0.0 0.0

#uniaxialMaterial Concrete04 $matTag $fc     $ec        $ecu        $Ec <$fct $et> <$beta>
 uniaxialMaterial Concrete04  1110   -7.450  -0.00200   -0.00500    4920.
 uniaxialMaterial Concrete04  1120   -9.053  -0.00415   -0.01459    4920.

# uniaxialMaterial ReinforcingSteel $matTag $fy     $fu     $Es     $Esh    $esh     $eult  < -GABuck
$lsr $beta $r $gama > < -DMBuck $lsr < $alpha >> < -CMFatigue $Cf $alpha $Cd > < -IsoHard <$a1
<$limit> > >
#  uniaxialMaterial ReinforcingSteel 1150   66.3    93.5    29000.0 850.0   0.009    0.18;
#  uniaxialMaterial ReinforcingSteel 1160   66.3    93.5    20384.0 850.0   0.009966 0.180995

#uniaxialMaterial Steel02 $matTag $Fy   $E      $b      $R0 $cR1   $cR2 <$a1 $a2 $a3 $a4 $sigInit>
 uniaxialMaterial Steel02 1150    66.3  29000.  5.278e-3 15  0.925  0.15
 uniaxialMaterial Steel02 1160    66.3  20611.  7.424e-3 15  0.925  0.15

set numBar  8;
set Ab      0.44;               # #6 bars
set R       11.0;               # section outer Radius
set Rcore   9.8125;             # Center of spiral
```

```
set Rreinf  9.25;                # bars radius
set circdiv [expr $numBar];      # Divides the circular patch in 5 segments between each reinf.

section Fiber [expr $pedSec] {;
#                   $mattag     $circdiv    $Rdiv       $y0 $z0 $intR       $extrR  $start  $end
        patch circ  1120        $circdiv    6           0.  0.  0.          $Rcore    0.0   360.0;
# Define core concrete fibers
        patch circ  1110        $circdiv    2           0.  0.  $Rcore      $R        0.0   360.0;
# Define cover concrete fibers
#                   $matTag     $numFiber   $Afiber     $y0 $z0 $radius     $startAng   $endAng
        layer circ  1150        $numBar     $Ab         0.  0.  $Rreinf     ;                   #
Radial distribution of bars
};

section Fiber [expr $pedSec+2] {;
#                   $mattag     $circdiv    $Rdiv       $y0 $z0 $intR       $extrR  $start  $end
        patch circ  1120        $circdiv    6           0.  0.  0.          $Rcore    0.0   360.0;
# Define core concrete fibers
        patch circ  1110        $circdiv    2           0.  0.  $Rcore      $R        0.0   360.0;
# Define cover concrete fibers
#                   $matTag     $numFiber   $Afiber     $y0 $z0 $radius     $startAng   $endAng
        layer circ  1150        $numBar     $Ab         0.  0.  $Rreinf     ;                   #
Radial distribution of bars
        layer circ  1150        6           0.31        0.  0.  3.313;                  # Radial
distribution of bars
};

section Fiber [expr $pedBondSec] {;      # section w/ modified steel for bond-slip action
#                   $mattag     $circdiv    $Rdiv       $y0 $z0 $intR       $extrR  $start  $end
```

```
        patch circ  1120        $circdiv    6           0.  0.  0.          $Rcore    0.0   360.0;
# Define core concrete
        patch circ  1110        $circdiv    2           0.  0.  $Rcore      $R        0.0   360.0;
# Define cover concrete
        #           $matTag     $numFiber   $Afiber     $y0 $z0 $radius  $startAng  $endAng
        layer circ  1160        $numBar     $Ab         0.  0.  $Rreinf ;                       #
Radial distribution of bars
};


# Pedestal  Elements-----------------------------------------------------------------------------
------
set nipPed 5; #                   1       2       3       4       5       6       7
#set PedSections "-sections    $pedBondSec $pedSec $pedSec $pedSec $pedSec  "
#set PedSections "-sections    $pedBondSec $pedSec $pedSec 1102 "
set PedSections "-sections    $pedBondSec $pedSec $pedSec $pedSec 1102 "
#set PedSections "-sections    $pedBondSec $pedSec $pedSec $pedSec $pedSec 1102 "
#set PedSections "-sections    $pedBondSec $pedSec $pedSec "


#       forceBeamColumn  $eleTag    $iNode          $jNode          $numIntgrPts $secTag
$transfTag
element forceBeamColumn  $CIPPed [expr 100+$base] [expr 100+$pedTop] $nipPed    $PedSections
$ColTransfTag -iter 50 $tol;
element forceBeamColumn  $ABCPed [expr 300+$base] [expr 300+$pedTop] $nipPed    $PedSections
$ColTransfTag -iter 50 $tol;
#*****************************************************************************************
******
```

```
# Gravity.tcl*********************************************************************************
# Performs the Gravity load analysis
# the load pattern should be defined before

#load-controlled static analysis
set dispCode 0; # Print Flag for test
set NstepGravity 10;            # apply gravity in $NstepGravity

set DGravity [expr 1.0/$NstepGravity];  # first load increment;
integrator LoadControl $DGravity 1 ;    # determine the next time step for an analysis

# Convergence test
#                     tolerance maxIter displayCode
#test NormDispIncr      1.0e-10    100        $dispCode
test EnergyIncr        1.0e-12   100        $dispCode

# Solution algorithm
algorithm Newton

# DOF numberer
#numberer RCM
numberer Plain;     # renumber dof's to minimize band-width (optimization), if you want to

# Constraint handler
constraints Penalty 1.0e18 1.0e18
#constraints Plain; #It cannot be used.  Due to the rigid links, the boundary conditions are not
homogeneous.
```

```
#constraints Lagrange

# System of equations solver
#system UmfPack
#system SparseGeneral -piv
system BandGeneral
#system ProfileSPD

# Analysis for gravity load
analysis Static

# Perform the gravity load analysis
set numSteps 0
set useInitialTangent 0

while { $numSteps < $NstepGravity } {
   if { $useInitialTangent == 1 } {
      #algorithm Newton -initial
      algorithm ModifiedNewton
      # Convergence test
      #                    tolerance maxIter displayCode
      test NormDispIncr      1.0e-8    1500      $dispCode
      #test EnergyIncr       1.0e-12   2500      $dispCode
   } else {
      algorithm KrylovNewton
      #test NormDispIncr      5.0e-8    100       $dispCode
       test EnergyIncr        1.0e-12    100      $dispCode
```

```
    }
    set res [analyze 1]

    if { $res >= 0 } {
        incr numSteps
        set useInitialTangent 0
     #puts -nonewline "step $numSteps done.\n"
    } else {
        if { $useInitialTangent == 1 } {
            puts "Gravity: gravity load analysis failed (at step $numSteps) !!!!!!!!!!!!!!!!"
            set temp [open $log "a"]
            puts $temp "\n Gravity: gravity load analysis failed (at step $numSteps) !!!"
            puts $temp "\n PROGRAN TERMINATED"
            close $temp
            set numSteps 10
        } else {
            set useInitialTangent 1
        }
    }
}

loadConst -time 0.0
wipeAnalysis
 puts "Gravity is done. res=$res (0=ok)"
#*********************************************************************************************
```

```
# Modal
Analysis*************************************************************************************************
set lambda [eigen $numModes];
set temp [open $log a]
puts $temp
"\n_____________________________________________________________________________________________";
puts $temp "\# Eigen Values: "
puts $temp "$lambda"
puts $temp  "\n# Periods:\n "
puts "\n# Periods:\n "
foreach lam $lambda {
    puts $temp  "[expr 2.0*$PI/sqrt($lam)], "
    puts        "[expr 2.0*$PI/sqrt($lam)], "
}
puts $temp
"\n_____________________________________________________________________________________________";
close $temp
#*************************************************************************************************
******
```

```
# Damping.tcl*****************************************************************************
# Stiffness proportionate damping
set xi          0.02;                       # 2% damping ratio
set lambda      [eigen 1];                  # eigenvalue mode 1
set omega       [expr pow($lambda,0.5)];
#set omega      [expr 2.*$PI/0.9014];       # mode-1 from experiment. because of the numerical
modeling at initial is not realistic the period is not correct
set alphaM      0.0;                        # M-prop. damping; D = alphaM*M
set betaKcurr   0.0;                        # K-proportional damping;      +beatKcurr*KCurrent
set betaKcomm   [expr 2.*$xi/($omega)];     # K-prop. damping parameter;   +betaKcomm*KlastCommitt
set betaKinit   0.0;                        # initial-stiffness proportional damping
+beatKinit*Kini
# D=$alphaM*M + $betaKcurr*Kcurrent + $betaKcomm*KlastCommit + $beatKinit*$Kinitial
rayleigh $alphaM $betaKcurr $betaKinit $betaKcomm;              # RAYLEIGH damping

#*****************************************************************************
```

```
#
recorder_Dynamic.tcl*************************************************************************
****
# Creating the output folders
file delete -force $outFolder
file mkdir  $outFolder;
file mkdir  $outFolder/Fibers;


# DISPLACEMENTs-----------------------------------------
recorder Node -file $outFolder/Monitor.out     -time        -node $monitor
-dof 1 2 3 disp;
recorder Node -file $outFolder/ColTopDisplacement.out       -node [expr 100+$colTop]  [expr
300+$colTop]    -dof 1 2 3 disp;
recorder Node -file $outFolder/ColBondDisplacement.out      -node       139                339
-dof 1 2 3 disp;
recorder Node -file $outFolder/PedTopDisplacement.out       -node [expr 100+$pedTop]  [expr
300+$pedTop]    -dof 1 2 3 disp;
recorder Node -file $outFolder/pinBondDisplacement.out      -node       121                321
-dof 1 2 3 disp;
recorder Node -file $outFolder/colBotDisplacement.out       -node [expr 100+$colBot]  [expr
300+$colBot]    -dof 1 2 3 disp;
recorder Node -file $outFolder/CapBeamDisplacement.out      -node [expr 100+$cb]      [expr 300+$cb]
-dof 1 2 3 disp;
recorder Node -file $outFolder/CapBeamMidDisplacement.out   -node [expr 200+$cb]      [expr 210+$cb]
-dof 1 2 3 disp;
recorder Node -file $outFolder/MassRigDisplacement.out      -node [expr $cb]
-dof 1 2 3 disp;


recorder Node -file $outFolder/BaseDisplacement.out         -node [expr 100+$base]    [expr
300+$base]      -dof 1 2 3 disp;
```

```
recorder Node -file $outFolder/BaseAcceleration.out         -node [expr 100+$base]     [expr
300+$base]      -dof 1 2 3 accel;

recorder Node -file $outFolder/BaseVelocity.out             -node [expr 100+$base]     [expr
300+$base]      -dof 1 2 3 vel;

recorder Node -file $outFolder/BaseAccelerationAbs.out      -time -timeSeries $tsTag -node [expr
100+$base]     [expr 300+$base]     -dof 1 accel;


# Element Force----------------------------------------

recorder Element -file $outFolder/ColumnsForces.out     -ele $CIPCol $ABCCol  globalForce

recorder Element -file $outFolder/PedestalsForces.out   -ele $CIPPed $ABCPed  globalForce

recorder Element -file $outFolder/massRig_Column.out    -ele 1000  force

recorder Element -file $outFolder/massRig_link.out      -ele 1300  axialForce


# Reactions-------------------------------------------------

recorder Node -file $outFolder/Reactions.out            -node [expr 100+$base]   [expr 300+$base]   -
dof 1 2 3 reaction; #Records the base Forces on the shake table

recorder Node -file $outFolder/MassRigReaction.out      -node [expr $base]                          -
dof 1 2 3 reaction;


# Fibers-----------------------------------------------------------------------------------------
------

set address "$outFolder";


# CIP
COLUMN_____________________________________________________________________________________________

 set eleMonitor  $CIPCol

 set numBar  14;

 set Ab      0.20;              # #4 bars

 set R       8.0;               # section outer Radius
```

```
 set Rcore    6.8125;             # Center of spiral
 set Rreinf      6.375;              # bars radius
 #set matCore  1025;set matCover 1015;set matReinf 1050;
 set matCore  1020;set matCover 1010;set matReinf 1050;
 for {set sec 1} { $sec <=  $nipCip} {incr sec} {;
     recorder Element -file [format "%s/ele%s.Forces_sec%s.out"            $address $eleMonitor $sec]
-ele  $eleMonitor section $sec force; # Column sections forces
     recorder Element -file [format "%s/Fibers/ele%s.sec%s_core1.out"   $address $eleMonitor $sec]  -
ele $eleMonitor section $sec fiber  $Rcore  0.0 $matCore  stressStrain
     recorder Element -file [format "%s/Fibers/ele%s.sec%s_core2.out"   $address $eleMonitor $sec]  -
ele $eleMonitor section $sec fiber -$Rcore  0.0 $matCore  stressStrain
     recorder Element -file [format "%s/Fibers/ele%s.sec%s_cover1.out"  $address $eleMonitor $sec]  -
ele $eleMonitor section $sec fiber  $R     0.0 $matCover stressStrain
     recorder Element -file [format "%s/Fibers/ele%s.sec%s_cover2.out"  $address $eleMonitor $sec]  -
ele $eleMonitor section $sec fiber -$R     0.0 $matCover stressStrain
     for {set bar 1} {$bar <= $numBar} {incr bar} {
         set y [expr $Rreinf*cos(($bar-1.0)/$numBar*2.0*$PI)]
         set z [expr $Rreinf*sin(($bar-1.0)/$numBar*2.0*$PI)]
         recorder Element -file [format "%s/Fibers/ele%s.sec%s_Bar%i.out"  $address $eleMonitor $sec
$bar] -ele $eleMonitor section $sec fiber $y $z $matReinf stressStrain
     }
 }


 # Recorders for bond
  set eleMonitor 101;
  set matCore   1021;
  set matCover  1010;
  set matReinf  1060;
```

```
     recorder Element -file [format "%s/ele%s.Forces.out" $address $eleMonitor]                -ele
$eleMonitor  force;
     recorder Element -file [format "%s/ele%s.Deformation.out" $address $eleMonitor]           -ele
$eleMonitor  deformation;
     recorder Element -file [format "%s/Fibers/ele%s.Bond_core1.out"   $address $eleMonitor]    -ele
$eleMonitor  section  fiber  $Rcore  0.0 $matCore  stressStrain
     recorder Element -file [format "%s/Fibers/ele%s.Bond_core2.out"   $address $eleMonitor]    -ele
$eleMonitor  section  fiber -$Rcore  0.0 $matCore  stressStrain
     recorder Element -file [format "%s/Fibers/ele%s.Bond_cover1.out"  $address $eleMonitor]    -ele
$eleMonitor  section  fiber  $R      0.0 $matCover stressStrain
     recorder Element -file [format "%s/Fibers/ele%s.Bond_cover2.out"  $address $eleMonitor]    -ele
$eleMonitor  section  fiber -$R      0.0 $matCover stressStrain
     for {set bar 1} {$bar <= $numBar} {incr bar} {
         set y [expr $Rreinf*cos(($bar-1.0)/$numBar*2.0*$PI)]
         set z [expr $Rreinf*sin(($bar-1.0)/$numBar*2.0*$PI)]
         recorder Element -file [format "%s/Fibers/ele%s.Bond_Bar%i.out"  $address $eleMonitor $bar]
-ele $eleMonitor section  fiber $y $z $matReinf stressStrain
     }
```

```
 # ABC
COLUMN
 set eleMonitor $ABCCol
 set numBar  14;
 set Ab      0.20;              # #4 bars
 set R       8.0;               # section outer Radius
 set Rcore   6.8125;            # Center of spiral
 set Rreinf      6.375;             # bars radius
 set matCore  3020;set matCover 3010;set matReinf 3050;
```

```
  for {set sec 1} { $sec <=  $nipAbc} {incr sec} {;
      recorder Element -file [format "%s/ele%s.Forces_sec%s.out"        $address $eleMonitor $sec]  -
ele  $eleMonitor section $sec force; # Column sections forces


      recorder Element -file [format "%s/Fibers/ele%s.sec%s_core1.out"   $address $eleMonitor $sec]
-ele $eleMonitor section $sec fiber  $Rcore  0.0 $matCore  stressStrain
      recorder Element -file [format "%s/Fibers/ele%s.sec%s_core2.out"   $address $eleMonitor $sec]
-ele $eleMonitor section $sec fiber -$Rcore  0.0 $matCore  stressStrain
      recorder Element -file [format "%s/Fibers/ele%s.sec%s_cover1.out"  $address $eleMonitor $sec]
-ele $eleMonitor section $sec fiber  $R    0.0 $matCover stressStrain
      recorder Element -file [format "%s/Fibers/ele%s.sec%s_cover2.out"  $address $eleMonitor $sec]
-ele $eleMonitor section $sec fiber -$R    0.0 $matCover stressStrain
      for {set bar 1} {$bar <= $numBar} {incr bar} {
          set y [expr $Rreinf*cos(($bar-1.0)/$numBar*2.0*$PI)]
          set z [expr $Rreinf*sin(($bar-1.0)/$numBar*2.0*$PI)]
          recorder Element -file [format "%s/Fibers/ele%s.sec%s_Bar%i.out"  $address $eleMonitor $sec
$bar] -ele $eleMonitor section $sec fiber $y $z $matReinf stressStrain
      }
  }


 # Recorders for the fibers, Bond section
  set eleMonitor 301;
  set matCore   3031;
  set matCover  3010;
  set matReinf  3060;
     recorder Element -file [format "%s/ele%s.Forces.out" $address $eleMonitor]                -ele
$eleMonitor  force;
```

```
     recorder Element -file [format "%s/ele%s.Deformation.out" $address $eleMonitor]           -ele
$eleMonitor  deformation;
     recorder Element -file [format "%s/Fibers/ele%s.Bond_core1.out"   $address $eleMonitor]    -ele
$eleMonitor  section  fiber  $Rcore  0.0 $matCore  stressStrain
     recorder Element -file [format "%s/Fibers/ele%s.Bond_core2.out"   $address $eleMonitor]    -ele
$eleMonitor  section  fiber -$Rcore  0.0 $matCore  stressStrain
     recorder Element -file [format "%s/Fibers/ele%s.Bond_cover1.out"  $address $eleMonitor]    -ele
$eleMonitor  section  fiber  $R      0.0 $matCover stressStrain
     recorder Element -file [format "%s/Fibers/ele%s.Bond_cover2.out"  $address $eleMonitor]    -ele
$eleMonitor  section  fiber -$R      0.0 $matCover stressStrain
     for {set bar 1} {$bar <= $numBar} {incr bar} {
         set y [expr $Rreinf*cos(($bar-1.0)/$numBar*2.0*$PI)]
         set z [expr $Rreinf*sin(($bar-1.0)/$numBar*2.0*$PI)]
         recorder Element -file [format "%s/Fibers/ele%s.Bond_Bar%i.out"  $address $eleMonitor $bar]
-ele $eleMonitor section  fiber $y $z $matReinf stressStrain
     }


 # CIP RebarPin
```

```
 set eleMonitor $CIPpin
 set numBar  6;
 set R       5.0;              # section outer Radius
 set Rcore   3.813;         # Center of spiral
 set Rreinf      3.313;             # bars radius
 set matCore  1220;set matCover 1210;set matReinf 1250;
  for {set sec 1} { $sec <=  $nipPin} {incr sec} {;
      recorder Element -file [format "%s/ele%s.Forces_sec%s.out"        $address $eleMonitor $sec]  -
ele  $eleMonitor section $sec force;
```

```
      recorder Element -file [format "%s/Fibers/ele%s.sec%s_core1.out"   $address $eleMonitor $sec]
-ele $eleMonitor section $sec fiber  $Rcore  0.0 $matCore  stressStrain

      recorder Element -file [format "%s/Fibers/ele%s.sec%s_core2.out"   $address $eleMonitor $sec]
-ele $eleMonitor section $sec fiber -$Rcore  0.0 $matCore  stressStrain

      recorder Element -file [format "%s/Fibers/ele%s.sec%s_cover1.out"  $address $eleMonitor $sec]
-ele $eleMonitor section $sec fiber  $R    0.0 $matCover stressStrain

      recorder Element -file [format "%s/Fibers/ele%s.sec%s_cover2.out"  $address $eleMonitor $sec]
-ele $eleMonitor section $sec fiber -$R    0.0 $matCover stressStrain

      for {set bar 1} {$bar <= $numBar} {incr bar} {

          set y [expr $Rreinf*cos(($bar-1.0)/$numBar*2.0*$PI)]

          set z [expr $Rreinf*sin(($bar-1.0)/$numBar*2.0*$PI)]

          recorder Element -file [format "%s/Fibers/ele%s.sec%s_Bar%i.out"  $address $eleMonitor $sec
$bar] -ele $eleMonitor section $sec fiber $y $z $matReinf stressStrain

      }

  }



 # PC RebarPin

 set eleMonitor $ABCpin

 set numBar   6;

 set R        5.0;                # section outer Radius

 set Rcore    3.813;          # Center of spiral

 set Rreinf       3.313;              # bars radius

 set matCore  3220;set matCover 3210;set matReinf 3250;

  for {set sec 1} { $sec <=  $nipPin} {incr sec} {;

      recorder Element -file [format "%s/ele%s.Forces_sec%s.out"        $address $eleMonitor $sec]  -
ele  $eleMonitor section $sec force;
```

```
      recorder Element -file [format "%s/Fibers/ele%s.sec%s_core1.out"   $address $eleMonitor $sec]
-ele $eleMonitor section $sec fiber  $Rcore  0.0 $matCore  stressStrain

      recorder Element -file [format "%s/Fibers/ele%s.sec%s_core2.out"   $address $eleMonitor $sec]
-ele $eleMonitor section $sec fiber -$Rcore  0.0 $matCore  stressStrain

      recorder Element -file [format "%s/Fibers/ele%s.sec%s_cover1.out"  $address $eleMonitor $sec]
-ele $eleMonitor section $sec fiber  $R    0.0 $matCover stressStrain

      recorder Element -file [format "%s/Fibers/ele%s.sec%s_cover2.out"  $address $eleMonitor $sec]
-ele $eleMonitor section $sec fiber -$R    0.0 $matCover stressStrain

      for {set bar 1} {$bar <= $numBar} {incr bar} {

          set y [expr $Rreinf*cos(($bar-1.0)/$numBar*2.0*$PI)]

          set z [expr $Rreinf*sin(($bar-1.0)/$numBar*2.0*$PI)]

          recorder Element -file [format "%s/Fibers/ele%s.sec%s_Bar%i.out"  $address $eleMonitor $sec
$bar] -ele $eleMonitor section $sec fiber $y $z $matReinf stressStrain

      }

  }
```

```
# #CIP
pedestal
# set eleMonitor $CIPPed
# set numBar    8;
# set R         11.0;               # section outer Radius
# set Rcore     9.8125;             # Center of spiral
# set Rreinf    9.25;               # bars radius
# set matCore  1120; set matCover 1110;   set matReinf 1150;
# for {set sec 1} { $sec <  $nipAbc} {incr sec} {;
```

```
    # recorder Element -file [format "%s/ColForces_sec%s.out" $address $sec]  -ele  $eleMonitor
section $sec force; # Column sections forces


    # recorder Element -file [format "%s/Fibers/ele%s.sec%s_core1.out"   $address $eleMonitor $sec]
-ele $eleMonitor section $sec fiber  $Rcore  0.0 $matCore  stressStrain

    # recorder Element -file [format "%s/Fibers/ele%s.sec%s_core2.out"   $address $eleMonitor $sec]
-ele $eleMonitor section $sec fiber -$Rcore  0.0 $matCore  stressStrain

    # recorder Element -file [format "%s/Fibers/ele%s.sec%s_cover1.out"  $address $eleMonitor $sec]
-ele $eleMonitor section $sec fiber  $R    0.0 $matCover stressStrain

    # recorder Element -file [format "%s/Fibers/ele%s.sec%s_cover2.out"  $address $eleMonitor $sec]
-ele $eleMonitor section $sec fiber -$R    0.0 $matCover stressStrain

    # for {set bar 1} {$bar <= $numBar} {incr bar} {

        # set y [expr $Rreinf*cos(($bar-1.0)/$numBar*2.0*$PI)]

        # set z [expr $Rreinf*sin(($bar-1.0)/$numBar*2.0*$PI)]

        # recorder Element -file [format "%s/Fibers/ele%s.sec%s_Bar%i.out"  $address $eleMonitor $sec
$bar] -ele $eleMonitor section $sec fiber $y $z $matReinf stressStrain

    # }

# }

# # Bond section

# set eleMonitor $CIPPed;

# set matCore  1120; set matCover 1110;   set matReinf 1160;

    # recorder Element -file [format "%s/ele%s.Force.Bond.out"        $address $eleMonitor $sec]  -
ele  $eleMonitor section $sec force; # Column sections forces


    # recorder Element -file [format "%s/Fibers/ele%s.Bond_core1.out"   $address $eleMonitor $sec]  -
ele $eleMonitor section $sec fiber  $Rcore  0.0 $matCore  stressStrain

    # recorder Element -file [format "%s/Fibers/ele%s.Bond_core2.out"   $address $eleMonitor $sec]  -
ele $eleMonitor section $sec fiber -$Rcore  0.0 $matCore  stressStrain

    # recorder Element -file [format "%s/Fibers/ele%s.Bond_cover1.out"  $address $eleMonitor $sec]  -
ele $eleMonitor section $sec fiber  $R     0.0 $matCover stressStrain
```

```
    # recorder Element -file [format "%s/Fibers/ele%s.Bond_cover2.out"  $address $eleMonitor $sec]  -
ele $eleMonitor section $sec fiber -$R     0.0 $matCover stressStrain
    # for {set bar 1} {$bar <= $numBar} {incr bar} {
        # set y [expr $Rreinf*cos(($bar-1.0)/$numBar*2.0*$PI)]
        # set z [expr $Rreinf*sin(($bar-1.0)/$numBar*2.0*$PI)]
        # recorder Element -file [format "%s/Fibers/ele%s.Bond_Bar%i.out"  $address $eleMonitor $sec
$bar] -ele $eleMonitor section $sec fiber $y $z $matReinf stressStrain
    # }


# ABC
pedestal_____________________________________________________________________________________
# set eleMonitor $ABCPed
# set numBar    8;
# set R         11.0;              # section outer Radius
# set Rcore     9.8125;            # Center of spiral
# set Rreinf    9.25;              # bars radius
# set matCore  1120; set matCover 1110;   set matReinf 1150;
# for {set sec 1} { $sec <  $nipAbc} {incr sec} {;
    # recorder Element -file [format "%s/ColForces_sec%s.out" $address $sec]  -ele  $eleMonitor
section $sec force; # Column sections forces


    # recorder Element -file [format "%s/Fibers/ele%s.sec%s_core1.out"   $address $eleMonitor $sec]
-ele $eleMonitor section $sec fiber  $Rcore  0.0 $matCore  stressStrain
    # recorder Element -file [format "%s/Fibers/ele%s.sec%s_core2.out"   $address $eleMonitor $sec]
-ele $eleMonitor section $sec fiber -$Rcore  0.0 $matCore  stressStrain
    # recorder Element -file [format "%s/Fibers/ele%s.sec%s_cover1.out"  $address $eleMonitor $sec]
-ele $eleMonitor section $sec fiber  $R    0.0 $matCover stressStrain
    # recorder Element -file [format "%s/Fibers/ele%s.sec%s cover2.out"  $address $eleMonitor $sec]
-ele $eleMonitor section $sec fiber -$R    0.0 $matCover stressStrain
```

```
    # for {set bar 1} {$bar <= $numBar} {incr bar} {
        # set y [expr $Rreinf*cos(($bar-1.0)/$numBar*2.0*$PI)]
        # set z [expr $Rreinf*sin(($bar-1.0)/$numBar*2.0*$PI)]
        # recorder Element -file [format "%s/Fibers/ele%s.sec%s_Bar%i.out"  $address $eleMonitor $sec
$bar] -ele $eleMonitor section $sec fiber $y $z $matReinf stressStrain
    # }
# }
# # Bond section
# set eleMonitor $CIPPed;
# set matCore  1120; set matCover 1110;   set matReinf 1160;
    # recorder Element -file [format "%s/ele%s.Force.Bond.out"        $address $eleMonitor $sec]  -
ele  $eleMonitor section $sec force; # Column sections forces


    # recorder Element -file [format "%s/Fibers/ele%s.Bond_core1.out"   $address $eleMonitor $sec]  -
ele $eleMonitor section $sec fiber  $Rcore  0.0 $matCore  stressStrain
    # recorder Element -file [format "%s/Fibers/ele%s.Bond_core2.out"   $address $eleMonitor $sec]  -
ele $eleMonitor section $sec fiber -$Rcore  0.0 $matCore  stressStrain
    # recorder Element -file [format "%s/Fibers/ele%s.Bond_cover1.out"  $address $eleMonitor $sec]  -
ele $eleMonitor section $sec fiber  $R     0.0 $matCover stressStrain
    # recorder Element -file [format "%s/Fibers/ele%s.Bond_cover2.out"  $address $eleMonitor $sec]  -
ele $eleMonitor section $sec fiber -$R     0.0 $matCover stressStrain
    # for {set bar 1} {$bar <= $numBar} {incr bar} {
        # set y [expr $Rreinf*cos(($bar-1.0)/$numBar*2.0*$PI)]
        # set z [expr $Rreinf*sin(($bar-1.0)/$numBar*2.0*$PI)]
        # recorder Element -file [format "%s/Fibers/ele%s.Bond_Bar%i.out"  $address $eleMonitor $sec
$bar] -ele $eleMonitor section $sec fiber $y $z $matReinf stressStrain
    # }
```

```
puts "\n RECORDERS DEFINED."
#*************************************************************************************************
******
```

```
#
DynamicAnalysis.tcl********************************************************************************
****
puts
"\n_____________________________________________________________________________________________"
puts  "** ([clock format [clock seconds]]) Starting Dynamic analysis..."
puts  "Motion:$MotionFile; Initial Dt=$DtAnalysis;current Time= [getTime],
TmaxAnalysis=$TmaxAnalysis\n";


set (Time0) 0.;
set Time 0.;
set q 0;        # q is a counter for step of analysis
set ok 0;

while { $(Time$q) < $TmaxAnalysis && $ok == 0 } {

    incr q;                 # q is a counter for step of analysis

# Setting the default analysis option

constraints Transformation
#constraints Penalty 10e15 10e15;

numberer RCM
# system UmfPack
system BandGeneral
#system SparseGeneral ; #-piv
```

```
set TolDynamic 1.e-8;           # Convergence Test: tolerance
set maxNumIterDynamic 50;       # Convergence Test: maximum number of iterations that will be performed before "failure to converge" is returned
set printFlagDynamic 0;         # Convergence Test: flag used to print information on convergence (optional) # 1: print information on each step; 5 if it fails to converge at end

test NormDispIncr 1.e-5 $maxNumIterDynamic $printFlagDynamic;
#test EnergyIncr $TolDynamic $maxNumIterDynamic $printFlagDynamic
#test RelativeEnergyIncr $TolDynamic $maxNumIterDynamic
#test NormUnbalance $TolDynamic $maxNumIterDynamic

algorithm Broyden 8
#algorithm Newton ; #-initialThenCurrent
#algorithm ModifiedNewton

integrator Newmark 0.50 0.25

analysis VariableTransient

        set ok 0;
        set (Time$q) [getTime];
        set ok [analyze 1 $DtAnalysis];# actually perform one dt analysis; returns ok=0 if analysis was successful
#       set ok [analyze 1 $DtAnalysis [expr $DtAnalysis/10.] [expr $DtAnalysis*2.] 10]
        puts [format "*Time:%9.5f, OK=%i, D=%6.3f, V=%7.3f, A=%7.3f"  [getTime] $ok [nodeDisp $monitor 1] [nodeVel $monitor 1] [nodeAccel $monitor 1] ]

        # if {$ok == 0} {
```

```
        # puts  "solved By Broyden "
# }

if {$ok != 0} {
    puts -nonewline  [format "\n!T=%6g,D=%2.3f" $(Time$q) [nodeDisp $monitor 1]];
    algorithm Broyden 8
          set ok [analyze 1 [expr $DtAnalysis/2.]];
    if {$ok == 0} {
            puts  "solved By Broyden Algorithm & dt/2"
    } else {
        set ok [analyze 1 [expr $DtAnalysis/4.]];
        if {$ok == 0} {
                puts  "solved By Broyden Algorithm & dt/4"
        } else {
            set ok [analyze 1 [expr $DtAnalysis/8.]];
            if {$ok == 0} {
                puts  "solved By Broyden Algorithm & dt/8"
            } else {
                set ok [analyze 1 [expr $DtAnalysis/8.]];
                if {$ok == 0} {
                        puts  "solved By Broyden Algorithm & dt/8"
                } else {
                    set ok [analyze 1 [expr $DtAnalysis/10.]];
                    if {$ok == 0} {
                            puts  "solved By Broyden Algorithm & dt/10"
                    }
                }
```

```
            }
        }
    }
}

if {$ok != 0} {
    algorithm Newton
          set ok [analyze 1 [expr $DtAnalysis/2.]];
    if {$ok == 0} {
            puts  "solved By Newton Algorithm & dt/2"
    } else {
        set ok [analyze 1 [expr $DtAnalysis/4.]];
        if {$ok == 0} {
                puts  "solved By Newton Algorithm & dt/4"
        } else {
            set ok [analyze 1 [expr $DtAnalysis/6.]];
            if {$ok == 0} {
                puts  "solved By Newton Algorithm & dt/6"
            } else {
                set ok [analyze 1 [expr $DtAnalysis/8.]];
                if {$ok == 0} {
                        puts  "solved By Newton Algorithm & dt/8"
                } else {
                    set ok [analyze 1 [expr $DtAnalysis/10.]];
                    if {$ok == 0} {
                            puts  "solved By Newton Algorithm & dt/10"
                    }
```

```
                }
            }
        }
    }
}

if {$ok != 0} {
    algorithm Newton -initial
          set ok [analyze 1 [expr $DtAnalysis/2.]];
    if {$ok == 0} {
            puts  "solved By Newton-initial Algorithm & dt/2"
    } else {
        set ok [analyze 1 [expr $DtAnalysis/4.]];
        if {$ok == 0} {
                puts  "solved By Newton-initial Algorithm & dt/4"
        } else {
            set ok [analyze 1 [expr $DtAnalysis/6.]];
            if {$ok == 0} {
                puts  "solved By Newton-initial Algorithm & dt/6"
            } else {
                set ok [analyze 1 [expr $DtAnalysis/8.]];
                if {$ok == 0} {
                        puts  "solved By Newton-initial Algorithm & dt/8"
                } else {
                    set ok [analyze 1 [expr $DtAnalysis/10.]];
                    if {$ok == 0} {
                            puts  "solved By Newton-initial Algorithm & dt/10"
```

```
                    }
                }
            }
        }
    }
}

if {$ok != 0} {
    algorithm Newton -initialThenCurrent
          set ok [analyze 1 [expr $DtAnalysis/2.]];
    if {$ok == 0} {
            puts  "solved By Newton-initialThenCurrent Algorithm & dt/2"
    } else {
        set ok [analyze 1 [expr $DtAnalysis/4.]];
        if {$ok == 0} {
                puts  "solved By Newton-initialThenCurrent Algorithm & dt/4"
        } else {
            set ok [analyze 1 [expr $DtAnalysis/6.]];
            if {$ok == 0} {
                puts  "solved By Newton-initialThenCurrent Algorithm & dt/6"
            } else {
                set ok [analyze 1 [expr $DtAnalysis/8.]];
                if {$ok == 0} {
                        puts  "solved By Newton-initialThenCurrent Algorithm & dt/8"
                } else {
                    set ok [analyze 1 [expr $DtAnalysis/10.]];
                    if {$ok == 0} {
```

```
                        puts  "solved By Newton-initialThenCurrent Algorithm & dt/10"
                    }
                }
            }
        }
    }
}

 if {$ok != 0} {
     algorithm Newton ModifiedNewton
           set ok [analyze 1 [expr $DtAnalysis/2.]];
     if {$ok == 0} {
            puts  "solved By ModifiedNewton Algorithm & dt/2"
     } else {
         set ok [analyze 1 [expr $DtAnalysis/4.]];
         if {$ok == 0} {
                puts  "solved By ModifiedNewton Algorithm & dt/4"
         } else {
             set ok [analyze 1 [expr $DtAnalysis/6.]];
             if {$ok == 0} {
                 puts  "solved By ModifiedNewton Algorithm & dt/6"
             } else {
                 set ok [analyze 1 [expr $DtAnalysis/8.]];
                 if {$ok == 0} {
                        puts  "solved By ModifiedNewton Algorithm & dt/8"
                 } else {
                     set ok [analyze 1 [expr $DtAnalysis/10.]];
```

```
                        if {$ok == 0} {
                                puts  "solved By ModifiedNewton Algorithm & dt/10"
                        }
                    }
                }
            }
        }
    }

    if {$ok != 0} {
        algorithm BFGS
              set ok [analyze 1 [expr $DtAnalysis/2.]];          # actually perform analysis;
returns ok=0 if analysis was successful
        if {$ok == 0} {
              puts  "solved By BFGS Algorithm & dt/2"
        }
    }

    if {$ok != 0} {
        algorithm ModifiedNewton -initial
              set ok [analyze 1 [expr $DtAnalysis/2.]];          # actually perform analysis;
returns ok=0 if analysis was successful
        if {$ok == 0} {
              puts  "solved By ModifiedNewton -initial Algorithm & dt/2"
        }
    }
```

```
        if {$ok != 0} {
            algorithm KrylovNewton
                  set ok [analyze 1 [expr $DtAnalysis/2.]];          # actually perform analysis;
returns ok=0 if analysis was successful
            if {$ok == 0} {
                   puts  "solved By KrylovNewton Algorithm & dt/2"
            }
        }

        if {$ok != 0} {
            algorithm BFGS
                  set ok [analyze 1 [expr $DtAnalysis/2.]];          # actually perform analysis;
returns ok=0 if analysis was successful
            if {$ok == 0} {
                   puts  "solved By BFGS Algorithm"
            }
        }
#
#       if {$ok != 0} {
#           algorithm Broyden 8
#                 set ok [analyze 1 [expr $DtAnalysis/2.]];            # actually perform analysis;
returns ok=0 if analysis was successful
#           if {$ok == 0} {
#                  puts  "solved By Broyden Algorithm"
#           }
#       }
#
#       if {$ok != 0} {
```

```
#           numberer RCM
#                   set ok [analyze 1 [expr $DtAnalysis/2.]];            # actually perform analysis;
returns ok=0 if analysis was successful
#           if {$ok == 0} {
#                   puts  "solved By RCM Numberer & dt/2"
#           }
#       }

        if {$ok != 0} {
            numberer AMD
                  set ok [analyze 1 [expr $DtAnalysis/4.]];          # actually perform analysis;
returns ok=0 if analysis was successful
            if {$ok == 0} {
                    puts  "solved By AMD Numberer"
            }
        }

        if {$ok != 0} {
            system UmfPack
                  set ok [analyze 1 [expr $DtAnalysis/4.]];          # actually perform analysis;
returns ok=0 if analysis was successful
            if {$ok == 0} {
                    puts  "solved By UmfPack System & dt/4"
            }
        }

        if {$ok != 0} {
            system BandGeneral
```

```
                set ok [analyze 1 [expr $DtAnalysis/4.]];          # actually perform analysis;
returns ok=0 if analysis was successful
            if {$ok == 0} {
                    puts  "solved By BandGeneral System & dt/4"
            }
        }

        if {$ok != 0} {
            system SparseSPD
                set ok [analyze 1 [expr $DtAnalysis/4.]];          # actually perform analysis;
returns ok=0 if analysis was successful
            if {$ok == 0} {
                    puts  "solved By SparseSPD System & dt/4"
            }
        }

        if {$ok != 0} {
            system SparseSYM
                set ok [analyze 1 [expr $DtAnalysis/4.]];          # actually perform analysis;
returns ok=0 if analysis was successful
            if {$ok == 0} {
                    puts  "solved By SparseSYM System & dt/4"
            }
        }

        if {$ok != 0} {
            test EnergyIncr 1.0e-4 50
```

```
                set ok [analyze 1 [expr $DtAnalysis/2.]];          # actually perform analysis;
returns ok=0 if analysis was successful
            if {$ok == 0} {
                    puts  "solved By EnergyIncr Test & dt/2"
            }
        }

        if {$ok != 0} {
            test NormUnbalance 1.0e-3 50
                set ok [analyze 1 [expr $DtAnalysis/2.]];          # actually perform analysis;
returns ok=0 if analysis was successful
            if {$ok == 0} {
                    puts  "solved By NormUnbalance Test & dt/2"
            }
        }

        if {$ok != 0} {
            test RelativeNormDispIncr 1.0e-3 50
                set ok [analyze 1 [expr $DtAnalysis/2.]];          # actual ly perform analysis;
returns ok=0 if analysis was successful
            if {$ok == 0} {
                    puts  "solved By NormUnbalance Test & dt/2"
            }
        }


}
```

```
puts "\n\n#** ([clock format [clock seconds]]) Analysis ends...End Time: [getTime] of $TmaxAnalysis"
#*****************************************************************************************
```

LIST OF CCEER PUBLICATIONS

Report No.	Publication
CCEER-84-1	Saiidi, M., and R. Lawver, "User's Manual for LZAK-C64, A Computer Program to Implement the Q-Model on Commodore 64," Civil Engineering Department, Report No. CCEER-84-1, University of Nevada, Reno, January 1984.
CCEER-84-1 Reprint	Douglas, B., Norris, G., Saiidi, M., Dodd, L., Richardson, J. and Reid, W., "Simple Bridge Models for Earthquakes and Test Data," Civil Engineering Department, Report No. CCEER-84-1 Reprint, University of Nevada, Reno, January 1984.
CCEER-84-2	Douglas, B. and T. Iwasaki, "Proceedings of the First USA-Japan Bridge Engineering Workshop," held at the Public Works Research Institute, Tsukuba, Japan, Civil Engineering Department, Report No. CCEER-84-2, University of Nevada, Reno, April 1984.
CCEER-84-3	Saiidi, M., J. Hart, and B. Douglas, "Inelastic Static and Dynamic Analysis of Short R/C Bridges Subjected to Lateral Loads," Civil Engineering Department, Report No. CCEER-84-3, University of Nevada, Reno, July 1984.
CCEER-84-4	Douglas, B., "A Proposed Plan for a National Bridge Engineering Laboratory," Civil Engineering Department, Report No. CCEER-84-4, University of Nevada, Reno, December 1984.
CCEER-85-1	Norris, G. and P. Abdollaholiaee, "Laterally Loaded Pile Response: Studies with the Strain Wedge Model," Civil Engineering Department, Report No. CCEER-85-1, University of Nevada, Reno, April 1985.
CCEER-86-1	Ghusn, G. and M. Saiidi, "A Simple Hysteretic Element for Biaxial Bending of R/C in NEABS-86," Civil Engineering Department, Report No. CCEER-86-1, University of Nevada, Reno, July 1986.
CCEER-86-2	Saiidi, M., R. Lawver, and J. Hart, "User's Manual of ISADAB and SIBA, Computer Programs for Nonlinear Transverse Analysis of Highway Bridges Subjected to Static and Dynamic Lateral Loads," Civil Engineering Department, Report No. CCEER-86-2, University of Nevada, Reno, September 1986.
CCEER-87-1	Siddharthan, R., "Dynamic Effective Stress Response of Surface and Embedded Footings in Sand," Civil Engineering Department, Report No. CCEER-86-2, University of Nevada, Reno, June 1987.
CCEER-87-2	Norris, G. and R. Sack, "Lateral and Rotational Stiffness of Pile Groups for Seismic Analysis of Highway Bridges," Civil Engineering Department, Report No. CCEER-87-2, University of Nevada, Reno, June 1987.
CCEER-88-1	Orie, J. and M. Saiidi, "A Preliminary Study of One-Way Reinforced Concrete Pier Hinges Subjected to Shear and Flexure," Civil Engineering Department, Report No. CCEER-88-1, University of Nevada, Reno, January 1988.
CCEER-88-2	Orie, D., M. Saiidi, and B. Douglas, "A Micro-CAD System for Seismic Design of Regular Highway Bridges," Civil Engineering Department, Report No. CCEER-88-2, University of Nevada, Reno, June 1988.
CCEER-88-3	Orie, D. and M. Saiidi, "User's Manual for Micro-SARB, a Microcomputer Program for Seismic Analysis of Regular Highway Bridges," Civil Engineering Department, Report No. CCEER-88-3, University of Nevada, Reno, October 1988.

CCEER-89-1 Douglas, B., M. Saiidi, R. Hayes, and G. Holcomb, "A Comprehensive Study of the Loads and Pressures Exerted on Wall Forms by the Placement of Concrete," Civil Engineering Department, Report No. CCEER-89-1, University of Nevada, Reno, February 1989.

CCEER-89-2 Richardson, J. and B. Douglas, "Dynamic Response Analysis of the Dominion Road Bridge Test Data," Civil Engineering Department, Report No. CCEER-89-2, University of Nevada, Reno, March 1989.

CCEER-89-2 Vrontinos, S., M. Saiidi, and B. Douglas, "A Simple Model to Predict the Ultimate Response of R/C Beams with Concrete Overlays," Civil Engineering Department, Report NO. CCEER-89-2, University of Nevada, Reno, June 1989.

CCEER-89-3 Ebrahimpour, A. and P. Jagadish, "Statistical Modeling of Bridge Traffic Loads - A Case Study," Civil Engineering Department, Report No. CCEER-89-3, University of Nevada, Reno, December 1989.

CCEER-89-4 Shields, J. and M. Saiidi, "Direct Field Measurement of Prestress Losses in Box Girder Bridges," Civil Engineering Department, Report No. CCEER-89-4, University of Nevada, Reno, December 1989.

CCEER-90-1 Saiidi, M., E. Maragakis, G. Ghusn, Y. Jiang, and D. Schwartz, "Survey and Evaluation of Nevada's Transportation Infrastructure, Task 7.2 - Highway Bridges, Final Report," Civil Engineering Department, Report No. CCEER 90-1, University of Nevada, Reno, October 1990.

CCEER-90-2 Abdel-Ghaffar, S., E. Maragakis, and M. Saiidi, "Analysis of the Response of Reinforced Concrete Structures During the Whittier Earthquake 1987," Civil Engineering Department, Report No. CCEER 90-2, University of Nevada, Reno, October 1990.

CCEER-91-1 Saiidi, M., E. Hwang, E. Maragakis, and B. Douglas, "Dynamic Testing and the Analysis of the Flamingo Road Interchange," Civil Engineering Department, Report No. CCEER-91-1, University of Nevada, Reno, February 1991.

CCEER-91-2 Norris, G., R. Siddharthan, Z. Zafir, S. Abdel-Ghaffar, and P. Gowda, "Soil-Foundation-Structure Behavior at the Oakland Outer Harbor Wharf," Civil Engineering Department, Report No. CCEER-91-2, University of Nevada, Reno, July 1991.

CCEER-91-3 Norris, G., "Seismic Lateral and Rotational Pile Foundation Stiffnesses at Cypress," Civil Engineering Department, Report No. CCEER-91-3, University of Nevada, Reno, August 1991.

CCEER-91-4 O'Connor, D. and M. Saiidi, "A Study of Protective Overlays for Highway Bridge Decks in Nevada, with Emphasis on Polyester-Styrene Polymer Concrete," Civil Engineering Department, Report No. CCEER-91-4, University of Nevada, Reno, October 1991.

CCEER-91-5 O'Connor, D.N. and M. Saiidi, "Laboratory Studies of Polyester-Styrene Polymer Concrete Engineering Properties," Civil Engineering Department, Report No. CCEER-91-5, University of Nevada, Reno, November 1991.

CCEER-92-1 Straw, D.L. and M. Saiidi, "Scale Model Testing of One-Way Reinforced Concrete Pier Hinges Subject to Combined Axial Force, Shear and Flexure," edited by D.N. O'Connor, Civil Engineering Department, Report No. CCEER-92-1, University of Nevada, Reno, March 1992.

CCEER-92-2 Wehbe, N., M. Saiidi, and F. Gordaninejad, "Basic Behavior of Composite Sections Made of Concrete Slabs and Graphite Epoxy Beams," Civil Engineering Department, Report No. CCEER-92-2, University of Nevada, Reno, August 1992.

CCEER-92-3 Saiidi, M. and E. Hutchens, "A Study of Prestress Changes in A Post-Tensioned Bridge During the First 30 Months," Civil Engineering Department, Report No. CCEER-92-3, University of Nevada, Reno, April 1992.

CCEER-92-4 Saiidi, M., B. Douglas, S. Feng, E. Hwang, and E. Maragakis, "Effects of Axial Force on Frequency of Prestressed Concrete Bridges," Civil Engineering Department, Report No. CCEER-92-4, University of Nevada, Reno, August 1992.

CCEER-92-5 Siddharthan, R., and Z. Zafir, "Response of Layered Deposits to Traveling Surface Pressure Waves," Civil Engineering Department, Report No. CCEER-92-5, University of Nevada, Reno, September 1992.

CCEER-92-6 Norris, G., and Z. Zafir, "Liquefaction and Residual Strength of Loose Sands from Drained Triaxial Tests," Civil Engineering Department, Report No. CCEER-92-6, University of Nevada, Reno, September 1992.

CCEER-92-6-A Norris, G., Siddharthan, R., Zafir, Z. and Madhu, R. "Liquefaction and Residual Strength of Sands from Drained Triaxial Tests," Civil Engineering Department, Report No. CCEER-92-6-A, University of Nevada, Reno, September 1992.

CCEER-92-7 Douglas, B., "Some Thoughts Regarding the Improvement of the University of Nevada, Reno's National Academic Standing," Civil Engineering Department, Report No. CCEER-92-7, University of Nevada, Reno, September 1992.

CCEER-92-8 Saiidi, M., E. Maragakis, and S. Feng, "An Evaluation of the Current Caltrans Seismic Restrainer Design Method," Civil Engineering Department, Report No. CCEER-92-8, University of Nevada, Reno, October 1992.

CCEER-92-9 O'Connor, D., M. Saiidi, and E. Maragakis, "Effect of Hinge Restrainers on the Response of the Madrone Drive Undercrossing During the Loma Prieta Earthquake," Civil Engineering Department, Report No. CCEER-92-9, University of Nevada, Reno, February 1993.

CCEER-92-10 O'Connor, D., and M. Saiidi, "Laboratory Studies of Polyester Concrete: Compressive Strength at Elevated Temperatures and Following Temperature Cycling, Bond Strength to Portland Cement Concrete, and Modulus of Elasticity," Civil Engineering Department, Report No. CCEER-92-10, University of Nevada, Reno, February 1993.

CCEER-92-11 Wehbe, N., M. Saiidi, and D. O'Connor, "Economic Impact of Passage of Spent Fuel Traffic on Two Bridges in Northeast Nevada," Civil Engineering Department, Report No. CCEER-92-11, University of Nevada, Reno, December 1992.

CCEER-93-1 Jiang, Y., and M. Saiidi, "Behavior, Design, and Retrofit of Reinforced Concrete One-way Bridge Column Hinges," edited by D. O'Connor, Civil Engineering Department, Report No. CCEER-93-1, University of Nevada, Reno, March 1993.

CCEER-93-2 Abdel-Ghaffar, S., E. Maragakis, and M. Saiidi, "Evaluation of the Response of the Aptos Creek Bridge During the 1989 Loma Prieta Earthquake," Civil Engineering Department, Report No. CCEER-93-2, University of Nevada, Reno, June 1993.

CCEER-93-3 Sanders, D.H., B.M. Douglas, and T.L. Martin, "Seismic Retrofit Prioritization of Nevada Bridges," Civil Engineering Department, Report No. CCEER-93-3, University of Nevada, Reno, July 1993.

CCEER-93-4 Abdel-Ghaffar, S., E. Maragakis, and M. Saiidi, "Performance of Hinge Restrainers in the Huntington Avenue Overhead During the 1989 Loma Prieta Earthquake," Civil Engineering Department, Report No. CCEER-93-4, University of Nevada, Reno, June 1993 (in final preparation).

CCEER-93-5 Maragakis, E., M. Saiidi, S. Feng, and L. Flournoy, "Effects of Hinge Restrainers on the Response of the San Gregorio Bridge during the Loma Prieta Earthquake," (in final preparation) Civil Engineering Department, Report No. CCEER-93-5, University of Nevada, Reno.

CCEER-93-6 Saiidi, M., E. Maragakis, S. Abdel-Ghaffar, S. Feng, and D. O'Connor, "Response of Bridge Hinge Restrainers during Earthquakes -Field Performance, Analysis, and Design," Civil Engineering Department, Report No. CCEER-93-6, University of Nevada, Reno, May 1993.

CCEER-93-7 Wehbe, N., Saiidi, M., Maragakis, E., and Sanders, D., "Adequacy of Three Highway Structures in Southern Nevada for Spent Fuel Transportation," Civil Engineering Department, Report No. CCEER-93-7, University of Nevada, Reno, August 1993.

CCEER-93-8 Roybal, J., Sanders, D.H., and Maragakis, E., "Vulnerability Assessment of Masonry in the Reno-Carson City Urban Corridor," Civil Engineering Department, Report No. CCEER-93-8, University of Nevada, Reno, May 1993.

CCEER-93-9 Zafir, Z. and Siddharthan, R., "MOVLOAD: A Program to Determine the Behavior of Nonlinear Horizontally Layered Medium Under Moving Load," Civil Engineering Department, Report No. CCEER-93-9, University of Nevada, Reno, August 1993.

CCEER-93-10 O'Connor, D.N., Saiidi, M., and Maragakis, E.A., "A Study of Bridge Column Seismic Damage Susceptibility at the Interstate 80/U.S. 395 Interchange in Reno, Nevada," Civil Engineering Department, Report No. CCEER-93-10, University of Nevada, Reno, October 1993.

CCEER-94-1 Maragakis, E., B. Douglas, and E. Abdelwahed, "Preliminary Dynamic Analysis of a Railroad Bridge," Report CCEER-94-1, January 1994.

CCEER-94-2 Douglas, B.M., Maragakis, E.A., and Feng, S., "Stiffness Evaluation of Pile Foundation of Cazenovia Creek Overpass," Civil Engineering Department, Report No. CCEER-94-2, University of Nevada, Reno, March 1994.

CCEER-94-3 Douglas, B.M., Maragakis, E.A., and Feng, S., "Summary of Pretest Analysis of Cazenovia Creek Bridge," Civil Engineering Department, Report No. CCEER-94-3, University of Nevada, Reno, April 1994.

CCEER-94-4 Norris, G.M., Madhu, R., Valceschini, R., and Ashour, M., "Liquefaction and Residual Strength of Loose Sands from Drained Triaxial Tests," Report 2, Vol. 1&2, Civil Engineering Department, Report No. CCEER-94-4, University of Nevada, Reno, August 1994.

CCEER-94-5 Saiidi, M., Hutchens, E., and Gardella, D., "Prestress Losses in a Post-Tensioned R/C Box Girder Bridge in Southern Nevada," Civil Engineering Department, CCEER-94-5, University of Nevada, Reno, August 1994.

CCEER-95-1 Siddharthan, R., El-Gamal, M., and Maragakis, E.A., "Nonlinear Bridge Abutment , Verification, and Design Curves," Civil Engineering Department, CCEER-95-1, University of Nevada, Reno, January 1995.

CCEER-95-2 Ashour, M. and Norris, G., "Liquefaction and Undrained Response Evaluation of Sands from Drained Formulation," Civil Engineering Department, Report No. CCEER-95-2, University of Nevada, Reno, February 1995.

CCEER-95-3 Wehbe, N., Saiidi, M., Sanders, D. and Douglas, B., "Ductility of Rectangular Reinforced Concrete Bridge Columns with Moderate Confinement," Civil Engineering Department, Report No. CCEER-95-3, University of Nevada, Reno, July 1995.

CCEER-95-4 Martin, T.., Saiidi, M. and Sanders, D., "Seismic Retrofit of Column-Pier Cap Connections in Bridges in Northern Nevada," Civil Engineering Department, Report No. CCEER-95-4, University of Nevada, Reno, August 1995.

CCEER-95-5 Darwish, I., Saiidi, M. and Sanders, D., "Experimental Study of Seismic Susceptibility Column-Footing Connections in Bridges in Northern Nevada," Civil Engineering Department, Report No. CCEER-95-5, University of Nevada, Reno, September 1995.

CCEER-95-6 Griffin, G., Saiidi, M. and Maragakis, E., "Nonlinear Seismic Response of Isolated Bridges and Effects of Pier Ductility Demand," Civil Engineering Department, Report No. CCEER-95-6, University of Nevada, Reno, November 1995.

CCEER-95-7 Acharya, S.., Saiidi, M. and Sanders, D., "Seismic Retrofit of Bridge Footings and Column-Footing Connections," Civil Engineering Department, Report No. CCEER-95-7, University of Nevada, Reno, November 1995.

CCEER-95-8 Maragakis, E., Douglas, B., and Sandirasegaram, U., "Full-Scale Field Resonance Tests of a Railway Bridge," A Report to the Association of American Railroads, Civil Engineering Department, Report No. CCEER-95-8, University of Nevada, Reno, December 1995.

CCEER-95-9 Douglas, B., Maragakis, E. and Feng, S., "System Identification Studies on Cazenovia Creek Overpass," Report for the National Center for Earthquake Engineering Research, Civil Engineering Department, Report No. CCEER-95-9, University of Nevada, Reno, October 1995.

CCEER-96-1 El-Gamal, M.E. and Siddharthan, R.V., "Programs to Computer Translational Stiffness of Seat-Type Bridge Abutment," Civil Engineering Department, Report No. CCEER-96-1, University of Nevada, Reno, March 1996.

CCEER-96-2 Labia, Y., Saiidi, M. and Douglas, B., "Evaluation and Repair of Full-Scale Prestressed Concrete Box Girders," A Report to the National Science Foundation, Research Grant CMS-9201908, Civil Engineering Department, Report No. CCEER-96-2, University of Nevada, Reno, May 1996.

CCEER-96-3 Darwish, I., Saiidi, M. and Sanders, D., "Seismic Retrofit of R/C Oblong Tapered Bridge Columns with Inadequate Bar Anchorage in Columns and Footings," A Report to the Nevada Department of Transportation, Civil Engineering Department, Report No. CCEER-96-3, University of Nevada, Reno, May 1996.

CCEER-96-4 Ashour, M., Pilling, R., Norris, G. and Perez, H., "The Prediction of Lateral Load Behavior of Single Piles and Pile Groups Using the Strain Wedge Model," A Report to the California Department of Transportation, Civil Engineering Department, Report No. CCEER-96-4, University of Nevada, Reno, June 1996.

CCEER-97-1-A Rimal, P. and Itani, A. "Sensitivity Analysis of Fatigue Evaluations of Steel Bridges," Center for Earthquake Research, Department of Civil Engineering, University of Nevada, Reno, Nevada Report No. CCEER-97-1-A, September, 1997.

CCEER-97-1-B Maragakis, E., Douglas, B., and Sandirasegaram, U. "Full-Scale Field Resonance Tests of a Railway Bridge," A Report to the Association of American Railroads, Civil Engineering Department, University of Nevada, Reno, May, 1996.

CCEER-97-2 Wehbe, N., Saiidi, M., and D. Sanders, "Effect of Confinement and Flares on the Seismic Performance of Reinforced Concrete Bridge Columns," Civil Engineering Department, Report No. CCEER-97-2, University of Nevada, Reno, September 1997.

CCEER-97-3 Darwish, I., M. Saiidi, G. Norris, and E. Maragakis, "Determination of In-Situ Footing Stiffness Using Full-Scale Dynamic Field Testing," A Report to the Nevada Department of Transportation, Structural Design Division, Carson City, Nevada, Report No. CCEER-97-3, University of Nevada, Reno, October 1997.

CCEER-97-4-A Itani, A. "Cyclic Behavior of Richmond-San Rafael Tower Links," Center for Civil Engineering Earthquake Research, Department of Civil Engineering, University of Nevada, Reno, Nevada, Report No. CCEER-97-4, August 1997.

CCEER-97-4-B Wehbe, N., and M. Saiidi, "User's Manual for RCMC v. 1.2 : A Computer Program for Moment-Curvature Analysis of Confined and Unconfined Reinforced Concrete Sections," Center for Civil Engineering Earthquake Research, Department of Civil Engineering, University of Nevada, Reno, Nevada, Report No. CCEER-97-4, November, 1997.

CCEER-97-5 Isakovic, T., M. Saiidi, and A. Itani, "Influence of new Bridge Configurations on Seismic Performance," Department of Civil Engineering, University of Nevada, Reno, Report No. CCEER-97-5, September, 1997.

CCEER-98-1 Itani, A., Vesco, T. and Dietrich, A., "Cyclic Behavior of "as Built" Laced Members With End Gusset Plates on the San Francisco Bay Bridge," Center for Civil Engineering Earthquake Research, Department of Civil Engineering, University of Nevada, Reno, Nevada Report No. CCEER-98-1, March, 1998.

CCEER-98-2 G. Norris and M. Ashour, "Liquefaction and Undrained Response Evaluation of Sands from Drained Formulation," Center for Civil Engineering Earthquake Research, Department of Civil Engineering, University of Nevada, Reno, Nevada, Report No. CCEER-98-2, May, 1998.

CCEER-98-3 Qingbin, Chen, B. M. Douglas, E. Maragakis, and I. G. Buckle, "Extraction of Nonlinear Hysteretic Properties of Seismically Isolated Bridges from Quick-Release Field Tests," Center for Civil Engineering Earthquake Research, Department of Civil Engineering, University of Nevada, Reno, Nevada, Report No. CCEER-98-3, June, 1998.

CCEER-98-4 Maragakis, E., B. M. Douglas, and C. Qingbin, "Full-Scale Field Capacity Tests of a Railway Bridge," Center for Civil Engineering Earthquake Research, Department of Civil Engineering, University of Nevada, Reno, Nevada, Report No. CCEER-98-4, June, 1998.

CCEER-98-5 Itani, A., Douglas, B., and Woodgate, J., "Cyclic Behavior of Richmond-San Rafael Retrofitted Tower Leg," Center for Civil Engineering Earthquake Research, Department of Civil Engineering, University of Nevada, Reno. Report No. CCEER-98-5, June 1998

CCEER-98-6 Moore, R., Saiidi, M., and Itani, A., "Seismic Behavior of New Bridges with Skew and Curvature," Center for Civil Engineering Earthquake Research, Department of Civil Engineering, University of Nevada, Reno. Report No. CCEER-98-6, October, 1998.

CCEER-98-7 Itani, A and Dietrich, A, "Cyclic Behavior of Double Gusset Plate Connections," Center for Civil Engineering Earthquake Research, Department of Civil Engineering, University of Nevada, Reno, Nevada, Report No. CCEER-98-5, December, 1998.

CCEER-99-1 Caywood, C., M. Saiidi, and D. Sanders, "Seismic Retrofit of Flared Bridge Columns with Steel Jackets," Civil Engineering Department, University of Nevada, Reno, Report No. CCEER-99-1, February 1999.

CCEER-99-2 Mangoba, N., M. Mayberry, and M. Saiidi, "Prestress Loss in Four Box Girder Bridges in Northern Nevada," Civil Engineering Department, University of Nevada, Reno, Report No. CCEER-99-2, March 1999.

CCEER-99-3 Abo-Shadi, N., M. Saiidi, and D. Sanders, "Seismic Response of Bridge Pier Walls in the Weak Direction," Civil Engineering Department, University of Nevada, Reno, Report No. CCEER-99-3, April 1999.

CCEER-99-4 Buzick, A., and M. Saiidi, "Shear Strength and Shear Fatigue Behavior of Full-Scale Prestressed Concrete Box Girders," Civil Engineering Department, University of Nevada, Reno, Report No. CCEER-99-4, April 1999.

CCEER-99-5 Randall, M., M. Saiidi, E. Maragakis and T. Isakovic, "Restrainer Design Procedures For Multi-Span Simply-Supported Bridges," Civil Engineering Department, University of Nevada, Reno, Report No. CCEER-99-5, April 1999.

CCEER-99-6 Wehbe, N. and M. Saiidi, "User's Manual for RCMC v. 1.2, A Computer Program for Moment-Curvature Analysis of Confined and Unconfined Reinforced Concrete Sections," Civil Engineering Department, University of Nevada, Reno, Report No. CCEER-99-6, May 1999.

CCEER-99-7 Burda, J. and A. Itani, "Studies of Seismic Behavior of Steel Base Plates," Civil Engineering Department, University of Nevada, Reno, Report No. CCEER-99-7, May 1999.

CCEER-99-8 Ashour, M. and G. Norris, "Refinement of the Strain Wedge Model Program," Civil Engineering Department, University of Nevada, Reno, Report No. CCEER-99-8, March 1999.

CCEER-99-9 Dietrich, A., and A. Itani, "Cyclic Behavior of Laced and Perforated Steel Members on the San Francisco-Oakland Bay Bridge," Civil Engineering Department, University, Reno, Report No. CCEER-99-9, December 1999.

CCEER 99-10 Itani, A., A. Dietrich, "Cyclic Behavior of Built Up Steel Members and their Connections," Civil Engineering Department, University of Nevada, Reno, Report No. CCEER-99-10, December 1999.

CCEER 99-10-A Itani, A., E. Maragakis and P. He, "Fatigue Behavior of Riveted Open Deck Railroad Bridge Girders," Civil Engineering Department, University of Nevada, Reno, Report No. CCEER-99-10-A, August 1999.

CCEER 99-11 Itani, A., J. Woodgate, "Axial and Rotational Ductility of Built Up Structural Steel Members," Civil Engineering Department, University of Nevada, Reno, Report No. CCEER-99-11, December 1999.

CCEER-99-12 Sgambelluri, M., Sanders, D.H., and Saiidi, M.S., "Behavior of One-Way Reinforced Concrete Bridge Column Hinges in the Weak Direction," Department of Civil Engineering, University of Nevada, Reno, Report No. CCEER-99-12, December 1999.

CCEER-99-13 Laplace, P., Sanders, D.H., Douglas, B, and Saiidi, M, "Shake Table Testing of Flexure Dominated Reinforced Concrete Bridge Columns", Department of Civil Engineering, University of Nevada, Reno, Report No. CCEER-99-13, December 1999.

CCEER-99-14 Ahmad M. Itani, Jose A. Zepeda, and Elizabeth A. Ware "Cyclic Behavior of Steel Moment Frame Connections for the Moscone Center Expansion," Department of Civil Engineering, University of Nevada, Reno, Report No. CCEER-99-14, December 1999.

CCEER 00-1 Ashour, M., and Norris, G. "Undrained Lateral Pile and Pile Group Response in Saturated Sand," Civil Engineering Department, University of Nevada, Reno, Report No. CCEER-00-1, May 1999. January 2000.

CCEER 00-2 Saiidi, M. and Wehbe, N., "A Comparison of Confinement Requirements in Different Codes for Rectangular, Circular, and Double-Spiral RC Bridge Columns," Civil Engineering Department, University of Nevada, Reno, Report No. CCEER-00-2, January 2000.

CCEER 00-3 McElhaney, B., M. Saiidi, and D. Sanders, "Shake Table Testing of Flared Bridge Columns With Steel Jacket Retrofit," Civil Engineering Department, University of Nevada, Reno, Report No. CCEER-00-3, January 2000.

CCEER 00-4 Martinovic, F., M. Saiidi, D. Sanders, and F. Gordaninejad, "Dynamic Testing of Non-Prismatic Reinforced Concrete Bridge Columns Retrofitted with FRP Jackets," Civil Engineering Department, University of Nevada, Reno, Report No. CCEER-00-4, January 2000.

CCEER 00-5 Itani, A., and M. Saiidi, "Seismic Evaluation of Steel Joints for UCLA Center for Health Science Westwood Replacement Hospital," Civil Engineering Department, University of Nevada, Reno, Report No. CCEER-00-5, February 2000.

CCEER 00-6 Will, J. and D. Sanders, "High Performance Concrete Using Nevada Aggregates," Civil Engineering Department, University of Nevada, Reno, Report No. CCEER-00-6, May 2000.

CCEER 00-7 French, C., and M. Saiidi, "A Comparison of Static and Dynamic Performance of Models of Flared Bridge Columns," Civil Engineering Department, University of Nevada, Reno, Report No. CCEER-00-7, October 2000.

CCEER 00-8 Itani, A., H. Sedarat, "Seismic Analysis of the AISI LRFD Design Example of Steel Highway Bridges," Civil Engineering Department, University of Nevada, Reno, Report No. CCEER 00-08, November 2000.

CCEER 00-9 Moore, J., D. Sanders, and M. Saiidi, "Shake Table Testing of 1960's Two Column Bent with Hinges Bases," Civil Engineering Department, University of Nevada, Reno, Report No. CCEER 00-09, December 2000.

CCEER 00-10 Asthana, M., D. Sanders, and M. Saiidi, "One-Way Reinforced Concrete Bridge Column Hinges in the Weak Direction," Civil Engineering Department, University of Nevada, Reno, Report No. CCEER 00-10, April 2001.

CCEER 01-1 Ah Sha, H., D. Sanders, M. Saiidi, "Early Age Shrinkage and Cracking of Nevada Concrete Bridge Decks," Civil Engineering Department, University of Nevada, Reno, Report No. CCEER 01-01, May 2001.

CCEER 01-2 Ashour, M. and G. Norris, "Pile Group program for Full Material Modeling a Progressive Failure," Civil Engineering Department, University of Nevada, Reno, Report No. CCEER 01-02, July 2001.

CCEER 01-3 Itani, A., C. Lanaud, and P. Dusicka, "Non-Linear Finite Element Analysis of Built-Up Shear Links," Civil Engineering Department, University of Nevada, Reno, Report No. CCEER 01-03, July 2001.

CCEER 01-4 Saiidi, M., J. Mortensen, and F. Martinovic, "Analysis and Retrofit of Fixed Flared Columns with Glass Fiber-Reinforced Plastic Jacketing," Civil Engineering Department, University of Nevada, Reno, Report No. CCEER 01-4, August 2001

CCEER 01-5 Not Published

CCEER 01-6 Laplace, P., D. Sanders, and M. Saiidi, "Experimental Study and Analysis of Retrofitted Flexure and Shear Dominated Circular Reinforced Concrete Bridge Columns Subjected to Shake Table Excitation," Civil Engineering Department, University of Nevada, Reno, Report No. CCEER 01-6, June 2001.

CCEER 01-7 Reppi, F., and D. Sanders, "Removal and Replacement of Cast-in-Place, Post-tensioned, Box Girder Bridge," Civil Engineering Department, University of Nevada, Reno, Report No. CCEER 01-7, December 2001.

CCEER 02-1 Pulido, C., M. Saiidi, D. Sanders, and A. Itani, "Seismic Performance and Retrofitting of Reinforced Concrete Bridge Bents," Civil Engineering Department, University of Nevada, Reno, Report No. CCEER 02-1, January 2002.

CCEER 02-2 Yang, Q., M. Saiidi, H. Wang, and A. Itani, "Influence of Ground Motion Incoherency on Earthquake Response of Multi-Support Structures," Civil Engineering Department, University of Nevada, Reno, Report No. CCEER 02-2, May 2002.

CCEER 02-3 M. Saiidi, B. Gopalakrishnan, E. Reinhardt, and R. Siddharthan, "A Preliminary Study of Shake Table Response of A Two-Column Bridge Bent on Flexible Footings," Civil Engineering Department, University of Nevada, Reno, Report No. CCEER 02-03, June 2002.

CCEER 02-4 Not Published

CCEER 02-5 Banghart, A., Sanders, D., Saiidi, M., "Evaluation of Concrete Mixes for Filling the Steel Arches in the Galena Creek Bridge," Civil Engineering Department, University of Nevada, Reno, Report No. CCEER 02-05, June 2002.

CCEER 02-6 Dusicka, P., Itani, A., Buckle, I. G., "Cyclic Behavior of Shear Links and Tower Shaft Assembly of San Francisco – Oakland Bay Bridge Tower," Civil Engineering Department, University of Nevada, Reno, Report No. CCEER 02-06, July 2002.

CCEER 02-7 Mortensen, J., and M. Saiidi, "A Performance-Based Design Method for Confinement in Circular Columns," Civil Engineering Department, University of Nevada, Reno, Report No. CCEER 02-07, November 2002.

CCEER 03-1 Wehbe, N., and M. Saiidi, "User's manual for SPMC v. 1.0 : A Computer Program for Moment-Curvature Analysis of Reinforced Concrete Sections with Interlocking Spirals," Center for Civil Engineering Earthquake Research, Department of Civil Engineering, University of Nevada, Reno, Nevada, Report No. CCEER-03-1, May, 2003.

CCEER 03-2 Wehbe, N., and M. Saiidi, "User's manual for RCMC v. 2.0 : A Computer Program for Moment-Curvature Analysis of Confined and Unconfined Reinforced Concrete Sections," Center for Civil Engineering Earthquake Research, Department of Civil Engineering, University of Nevada, Reno, Nevada, Report No. CCEER-03-2, June, 2003.

CCEER 03-3 Nada, H., D. Sanders, and M. Saiidi, "Seismic Performance of RC Bridge Frames with Architectural-Flared Columns," Civil Engineering Department, University of Nevada, Reno, Report No. CCEER 03-3, January 2003.

CCEER 03-4 Reinhardt, E., M. Saiidi, and R. Siddharthan, "Seismic Performance of a CFRP/ Concrete Bridge Bent on Flexible Footings," Civil Engineering Department, University of Nevada, Reno, Report No. CCEER 03-4, August 2003.

CCEER 03-5 Johnson, N., M. Saiidi, A. Itani, and S. Ladkany, "Seismic Retrofit of Octagonal Columns with Pedestal and One-Way Hinge at the Base," Center for Civil Engineering Earthquake Research, Department of Civil Engineering, University of Nevada, Reno, Nevada, and Report No. CCEER-03-5, August 2003.

CCEER 03-6 Mortensen, C., M. Saiidi, and S. Ladkany, "Creep and Shrinkage Losses in Highly Variable Climates," Center for Civil Engineering Earthquake Research, Department of Civil Engineering, University of Nevada, Reno, Report No. CCEER-03-6, September 2003.

CCEER 03- 7 Ayoub, C., M. Saiidi, and A. Itani, "A Study of Shape-Memory-Alloy-Reinforced Beams and Cubes," Center for Civil Engineering Earthquake Research, Department of Civil Engineering, University of Nevada, Reno, Nevada, Report No. CCEER-03-7, October 2003.

CCEER 03-8 Chandane, S., D. Sanders, and M. Saiidi, "Static and Dynamic Performance of RC Bridge Bents with Architectural-Flared Columns," Center for Civil Engineering Earthquake Research, Department of Civil Engineering, University of Nevada, Reno, Nevada, Report No. CCEER-03-8, November 2003.

CCEER 04-1 Olaegbe, C., and Saiidi, M., "Effect of Loading History on Shake Table Performance of A Two-Column Bent with Infill Wall," Center for Civil Engineering Earthquake Research, Department of Civil Engineering, University of Nevada, Reno, Nevada, Report No. CCEER-04-1, January 2004.

CCEER 04-2 Johnson, R., Maragakis, E., Saiidi, M., and DesRoches, R., "Experimental Evaluation of Seismic Performance of SMA Bridge Restrainers," Center for Civil Engineering Earthquake Research, Department of Civil Engineering, University of Nevada, Reno, Nevada, Report No. CCEER-04-2, February 2004.

CCEER 04-3 Moustafa, K., Sanders, D., and Saiidi, M., "Impact of Aspect Ratio on Two-Column Bent Seismic Performance," Center for Civil Engineering Earthquake Research, Department of Civil Engineering, University of Nevada, Reno, Nevada, Report No. CCEER-04-3, February 2004.

CCEER 04-4 Maragakis, E., Saiidi, M., Sanchez-Camargo, F., and Elfass, S., "Seismic Performance of Bridge Restrainers At In-Span Hinges," Center for Civil Engineering Earthquake Research, Department of Civil Engineering, University of Nevada, Reno, Nevada, Report No. CCEER-04-4, March 2004.

CCEER 04-5 Ashour, M., Norris, G. and Elfass, S., "Analysis of Laterally Loaded Long or Intermediate Drilled Shafts of Small or Large Diameter in Layered Soil," Center for Civil Engineering Earthquake Research, Department of Civil Engineering, University of Nevada, Reno, Nevada, Report No. CCEER-04-5, June 2004.

CCEER 04-6 Correal, J., Saiidi, M. and Sanders, D., "Seismic Performance of RC Bridge Columns Reinforced with Two Interlocking Spirals," Center for Civil Engineering Earthquake Research, Department of Civil Engineering, University of Nevada, Reno, Nevada, Report No. CCEER-04-6, August 2004.

CCEER 04-7 Dusicka, P., Itani, A. and Buckle, I., "Cyclic Response and Low Cycle Fatigue Characteristics of Plate Steels," Center for Civil Engineering Earthquake Research, Department of Civil Engineering, University of Nevada, Reno, Nevada, Report No. CCEER-04-7, November 2004.

CCEER 04-8 Dusicka, P., Itani, A. and Buckle, I., "Built-up Shear Links as Energy Dissipaters for Seismic Protection of Bridges," Center for Civil Engineering Earthquake Research, Department of Civil Engineering, University of Nevada, Reno, Nevada, Report No. CCEER-04-8, November 2004.

CCEER 04-9 Sureshkumar, K., Saiidi, S., Itani, A. and Ladkany, S., "Seismic Retrofit of Two-Column Bents with Diamond Shape Columns," Center for Civil Engineering Earthquake Research, Department of Civil Engineering, University of Nevada, Reno, Nevada, Report No. CCEER-04-9, November 2004.

CCEER 05-1 Wang, H. and Saiidi, S., "A Study of RC Columns with Shape Memory Alloy and Engineered Cementitious Composites," Center for Civil Engineering Earthquake Research, Department of Civil Engineering, University of Nevada, Reno, Nevada, Report No. CCEER-05-1, January 2005.

CCEER 05-2 Johnson, R., Saiidi, S. and Maragakis, E., "A Study of Fiber Reinforced Plastics for Seismic Bridge Restrainers," Center for Civil Engineering Earthquake Research, Department of Civil Engineering, University of Nevada, Reno, Nevada, Report No. CCEER-05-2, January 2005.

CCEER 05-3 Carden, L.P., Itani, A.M., Buckle, I.G, "Seismic Load Path in Steel Girder Bridge Superstructures," Center for Civil Engineering Earthquake Research, Department of Civil Engineering, University of Nevada, Reno, Nevada, Report No. CCEER-05-3, January 2005.

CCEER 05-4 Carden, L.P., Itani, A.M., Buckle, I.G, "Seismic Performance of Steel Girder Bridge Superstructures with Ductile End Cross Frames and Seismic Isolation," Center for Civil Engineering Earthquake Research, Department of Civil Engineering, University of Nevada, Reno, Nevada, Report No. CCEER-05-4, January 2005.

CCEER 05-5 Goodwin, E., Maragakis, M., Itani, A. and Luo, S., "Experimental Evaluation of the Seismic Performance of Hospital Piping Subassemblies," Center for Civil Engineering Earthquake Research, Department of Civil Engineering, University of Nevada, Reno, Nevada, Report No. CCEER-05-5, February 2005.

CCEER 05-6 Zadeh M. S., Saiidi, S, Itani, A. and Ladkany, S., "Seismic Vulnerability Evaluation and Retrofit Design of Las Vegas Downtown Viaduct," Center for Civil Engineering Earthquake Research, Department of Civil Engineering, University of Nevada, Reno, Nevada, Report No. CCEER-05-6, February 2005.

CCEER 05-7 Phan, V., Saiidi, S. and Anderson, J., "Near Fault (Near Field) Ground Motion Effects on Reinforced Concrete Bridge Columns," Center for Civil Engineering Earthquake Research, Department of Civil Engineering, University of Nevada, Reno, Nevada, Report No. CCEER-05-7, August 2005.

CCEER 05-8 Carden, L., Itani, A. and Laplace, P., "Performance of Steel Props at the UNR Fire Science Academy subjected to Repeated Fire," Center for Civil Engineering Earthquake Research, Department of Civil Engineering, University of Nevada, Reno, Nevada, Report No. CCEER-05-8, August 2005.

CCEER 05-9 Yamashita, R. and Sanders, D., "Shake Table Testing and an Analytical Study of Unbonded Prestressed Hollow Concrete Column Constructed with Precast Segments," Center for Civil Engineering Earthquake Research, Department of Civil Engineering, University of Nevada, Reno, Nevada, Report No. CCEER-05-9, August 2005.

CCEER 05-10 Not Published

CCEER 05-11 Carden, L., Itani., A., and Peckan, G., "Recommendations for the Design of Beams and Posts in Bridge Falsework," Center for Civil Engineering Earthquake Research, Department of Civil Engineering, University of Nevada, Reno, Nevada, Report No. CCEER-05-11, October 2005.

CCEER 06-01 Cheng, Z., Saiidi, M., and Sanders, D., "Development of a Seismic Design Method for Reinforced Concrete Two-Way Bridge Column Hinges," Center for Civil Engineering Earthquake Research, Department of Civil Engineering, University of Nevada, Reno, Nevada, Report No. CCEER-06-01, February 2006.

CCEER 06-02 Johnson, N., Saiidi, M., and Sanders, D., "Large-Scale Experimental and Analytical Studies of a Two-Span Reinforced Concrete Bridge System," Center for Civil Engineering Earthquake Research, Department of Civil Engineering, University of Nevada, Reno, Nevada, Report No. CCEER-06-02, March 2006.

CCEER 06-03 Saiidi, M., Ghasemi, H. and Tiras, A., "Seismic Design and Retrofit of Highway Bridges," Proceedings, Second US-Turkey Workshop, Center for Civil Engineering Earthquake Research, Department of Civil Engineering, University of Nevada, Reno, Nevada, Report No. CCEER-06-03, May 2006.

CCEER 07-01 O'Brien, M., Saiidi, M. and Sadrossadat-Zadeh, M., "A Study of Concrete Bridge Columns Using Innovative Materials Subjected to Cyclic Loading," Center for Civil Engineering Earthquake Research, Department of Civil Engineering, University of Nevada, Reno, Nevada, Report No. CCEER-07-01, January 2007.

CCEER 07-02 Sadrossadat-Zadeh, M. and Saiidi, M., "Effect of Strain rate on Stress-Strain Properties and Yield Propagation in Steel Reinforcing Bars," Center for Civil Engineering Earthquake Research, Department of Civil Engineering, University of Nevada, Reno, Nevada, Report No. CCEER-07-02, January 2007.

CCEER 07-03 Sadrossadat-Zadeh, M. and Saiidi, M., "Analytical Study of NEESR-SG 4-Span Bridge Model Using OpenSees," Center for Civil Engineering Earthquake Research, Department of Civil Engineering, University of Nevada, Reno, Nevada, Report No. CCEER-07-03, January 2007.

CCEER 07-04 Nelson, R., Saiidi, M. and Zadeh, S., "Experimental Evaluation of Performance of Conventional Bridge Systems," Center for Civil Engineering Earthquake Research, Department of Civil Engineering, University of Nevada, Reno, Nevada, Report No. CCEER-07-04, October 2007.

CCEER 07-05 Bahen, N. and Sanders, D., "Strut-and-Tie Modeling for Disturbed Regions in Structural Concrete Members with Emphasis on Deep Beams," Center for Civil Engineering Earthquake Research, Department of Civil Engineering, University of Nevada, Reno, Nevada, Report No. CCEER-07-05, December 2007.

CCEER 07-06 Choi, H., Saiidi, M. and Somerville, P., "Effects of Near-Fault Ground Motion and Fault-Rupture on the Seismic Response of Reinforced Concrete Bridges," Center for Civil Engineering Earthquake Research, Department of Civil Engineering, University of Nevada, Reno, Nevada, Report No. CCEER-07-06, December 2007.

CCEER 07-07 Ashour M. and Norris, G., "Report and User Manual on Strain Wedge Model Computer Program for Files and Large Diameter Shafts with LRFD Procedure," Center for Civil Engineering Earthquake Research, Department of Civil Engineering, University of Nevada, Reno, Nevada, Report No. CCEER-07-07, October 2007.

CCEER 08-01 Doyle, K. and Saiidi, M., "Seismic Response of Telescopic Pipe Pin Connections," Center for Civil Engineering Earthquake Research, Department of Civil Engineering, University of Nevada, Reno, Nevada, Report No. CCEER-08-01, February 2008.

CCEER 08-02 Taylor, M. and Sanders, D., "Seismic Time History Analysis and Instrumentation of the Galena Creek Bridge," Center for Civil Engineering Earthquake Research, Department of Civil Engineering, University of Nevada, Reno, Nevada, Report No. CCEER-08-02, April 2008.

CCEER 08-03 Abdel-Mohti, A. and Pekcan, G., "Seismic Response Assessment and Recommendations for the Design of Skewed Post-Tensioned Concrete Box-Girder Highway Bridges," Center for Civil Engineering Earthquake Research, Department of Civil and Environmental Engineering, University of Nevada, Reno, Nevada, Report No. CCEER-08-03, September 2008.

CCEER 08-04 Saiidi, M., Ghasemi, H. and Hook, J., "Long Term Bridge Performance Monitoring, Assessment & Management," Proceedings, FHWA/NSF Workshop on Future Directions," Center for Civil Engineering Earthquake Research, Department of Civil and Environmental Engineering, University of Nevada, Reno, Nevada, Report No. CCEER 08-04, September 2008.

CCEER 09-01 Brown, A., and Saiidi, M., "Investigation of Near-Fault Ground Motion Effects on Substandard Bridge Columns and Bents," Center for Civil Engineering Earthquake Research, Department of Civil and Environmental Engineering, University of Nevada, Reno, Nevada, Report No. CCEER-09-01, July 2009.

CCEER 09-02 Linke, C., Pekcan, G., and Itani, A., "Detailing of Seismically Resilient Special Truss Moment Frames," Center for Civil Engineering Earthquake Research, Department of Civil and Environmental Engineering, University of Nevada, Reno, Nevada, Report No. CCEER-09-02, August 2009.

CCEER 09-03 Hillis, D., and Saiidi, M., "Design, Construction, and Nonlinear Dynamic Analysis of Three Bridge Bents Used in a Bridge System Test," Center for Civil Engineering Earthquake Research, Department of Civil and Environmental Engineering, University of Nevada, Reno, Nevada, Report No. CCEER-09-03, August 2009.

CCEER 09-04 Bahrami, H., Itani, A., and Buckle, I., "Guidelines for the Seismic Design of Ductile End Cross Frames in Steel Girder Bridge Superstructures," Center for Civil Engineering Earthquake Research, Department of Civil and Environmental Engineering, University of Nevada, Reno, Nevada, Report No. CCEER-09-04, September 2so009.

CCEER 10-01 Zaghi, A. E., and Saiidi, M., "Seismic Design of Pipe-Pin Connections in Concrete Bridges," Center for Civil Engineering Earthquake Research, Department of Civil and Environmental Engineering, University of Nevada, Reno, Nevada, Report No. CCEER-10-01, January 2010.

CCEER 10-02 Pooranampillai, S., Elfass, S., and Norris, G., "Laboratory Study to Assess Load Capacity Increase of Drilled Shafts through Post Grouting," Center for Civil Engineering Earthquake Research, Department of Civil and Environmental Engineering, University of Nevada, Reno, Nevada, Report No. CCEER-10-02, January 2010.

CCEER 10-03 Itani, A., Grubb, M., and Monzon, E, "Proposed Seismic Provisions and Commentary for Steel Plate Girder Superstructures," Center for Civil Engineering Earthquake Research, Department of Civil and Environmental Engineering, University of Nevada, Reno, Nevada, Report No. CCEER-10-03, June 2010.

CCEER 10-04 Cruz-Noguez, C., Saiidi, M., "Experimental and Analytical Seismic Studies of a Four-Span Bridge System with Innovative Materials," Center for Civil Engineering Earthquake Research, Department of Civil and Environmental Engineering, University of Nevada, Reno, Nevada, Report No. CCEER-10-04, September 2010.

CCEER 10-05 Vosooghi, A., Saiidi, M., "Post-Earthquake Evaluation and Emergency Repair of Damaged RC Bridge Columns Using CFRP Materials," Center for Civil Engineering Earthquake Research, Department of Civil and Environmental Engineering, University of Nevada, Reno, Nevada, Report No. CCEER-10-05, September 2010.

CCEER 10-06 Ayoub, M., Sanders, D., "Testing of Pile Extension Connections to Slab Bridges," Center for Civil Engineering Earthquake Research, Department of Civil and Environmental Engineering, University of Nevada, Reno, Nevada, Report No. CCEER-10-06, October 2010.

CCEER 10-07 Builes-Mejia, J. C. and Itani, A., "Stability of Bridge Column Rebar Cages during Construction," Center for Civil Engineering Earthquake Research, Department of Civil and Environmental Engineering, University of Nevada, Reno, Nevada, Report No. CCEER-10-07, November 2010.

CCEER 10-08 Monzon, E.V., "Seismic Performance of Steel Plate Girder Bridges with Integral Abutments," Center for Civil Engineering Earthquake Research, Department of Civil and Environmental Engineering, University of Nevada, Reno, Nevada, Report No. CCEER-10-08, November 2010.

CCEER 11-01 Motaref, S., Saiidi, M., and Sanders, D., "Seismic Response of Precast Bridge Columns with Energy Dissipating Joints," Center for Civil Engineering Earthquake Research, Department of Civil and Environmental Engineering, University of Nevada, Reno, Nevada, Report No. CCEER-11-01, May 2011.

CCEER 11-02 Harrison, N. and Sanders, D., "Preliminary Seismic Analysis and Design of Reinforced Concrete Bridge Columns for Curved Bridge Experiments," Center for Civil Engineering Earthquake Research, Department of Civil and Environmental Engineering, University of Nevada, Reno, Nevada, Report No. CCEER-11-02, May 2011.

CCEER 11-03 Vallejera, J. and Sanders, D., "Instrumentation and Monitoring the Galena Creek Bridge," Center for Civil Engineering Earthquake Research, Department of Civil and Environmental Engineering, University of Nevada, Reno, Nevada, Report No. CCEER-11-03, September 2011.

CCEER 11-04 Levi, M., Sanders, D., and Buckle, I., "Seismic Response of Columns in Horizontally Curved Bridges," Center for Civil Engineering Earthquake Research, Department of Civil and Environmental Engineering, University of Nevada, Reno, Nevada, Report No. CCEER-11-04, December 2011.

CCEER 12-01 Saiidi, M., "NSF International Workshop on Bridges of the Future – Wide Spread Implementation of Innovation," Center for Civil Engineering Earthquake Research, Department of Civil and Environmental Engineering, University of Nevada, Reno, Nevada, Report No. CCEER-12-01, January 2012.

CCEER 12-02 Larkin, A.S., Sanders, D., and Saiidi, M., "Unbonded Prestressed Columns for Earthquake Resistance," Center for Civil Engineering Earthquake Research, Department of Civil and Environmental Engineering, University of Nevada, Reno, Nevada, Report No. CCEER-12-02, January 2012.

CCEER 12-03 Arias-Acosta, J. G., Sanders, D., "Seismic Performance of Circular and Interlocking Spirals RC Bridge Columns under Bidirectional Shake Table Loading Part 1," Center for Civil Engineering Earthquake Research, Department of Civil and Environmental Engineering, University of Nevada, Reno, Nevada, Report No. CCEER-12-03, September 2012.

CCEER 12-04 Cukrov, M.E., Sanders, D., "Seismic Performance of Prestressed Pile-To-Bent Cap Connections," Center for Civil Engineering Earthquake Research, Department of Civil and Environmental Engineering, University of Nevada, Reno, Nevada, Report No. CCEER-12-04, September 2012.

CCEER 13-01 Carr, T. and Sanders, D., "Instrumentation and Dynamic Characterization of the Galena Creek Bridge," Center for Civil Engineering Earthquake Research, Department of Civil and Environmental Engineering, University of Nevada, Reno, Nevada, Report No. CCEER-13-01, January 2013.

CCEER 13-02 Vosooghi, A. and Buckle, I., "Evaluation of the Performance of a Conventional Four-Span Bridge During Shake Table Tests," Center for Civil Engineering Earthquake Research, Department of Civil and Environmental Engineering, University of Nevada, Reno, Nevada, Report No. CCEER-13-02, January 2013.

CCEER 13-03 Amirihormozaki, E. and Pekcan, G., "Analytical Fragility Curves for Horizontally Curved Steel Girder Highway Bridges," Center for Civil Engineering Earthquake Research, Department of Civil and Environmental Engineering, University of Nevada, Reno, Nevada, Report No. CCEER-13-03, February 2013.

CCEER 13-04 Almer, K. and Sanders, D., "Longitudinal Seismic Performance of Precast Bridge Girders Integrally Connected to a Cast-in-Place Bentcap," Center for Civil Engineering Earthquake Research, Department of Civil and Environmental Engineering, University of Nevada, Reno, Nevada, Report No. CCEER-13-04, April 2013.

CCEER 13-05 Monzon, E.V., Itani, A.I., and Buckle, I.G., "Seismic Modeling and Analysis of Curved Steel Plate Girder Bridges," Center for Civil Engineering Earthquake Research, Department of Civil and Environmental Engineering, University of Nevada, Reno, Nevada, Report No. CCEER-13-05, April 2013.

CCEER 13-06 Monzon, E.V., Buckle, I.G., and Itani, A.I., "Seismic Performance of Curved Steel Plate Girder Bridges with Seismic Isolation," Center for Civil Engineering Earthquake Research, Department of Civil and Environmental Engineering, University of Nevada, Reno, Nevada, Report No. CCEER-13-06, April 2013.

CCEER 13-07 Monzon, E.V., Buckle, I.G., and Itani, A.I., "Seismic Response of Isolated Bridge Superstructure to Incoherent Ground Motions," Center for Civil Engineering Earthquake Research, Department of Civil and Environmental Engineering, University of Nevada, Reno, Nevada, Report No. CCEER-13-07, April 2013.

CCEER 13-08 Haber, Z.B., Saiidi, M.S., and Sanders, D.H., "Precast Column-Footing Connections for Accelerated Bridge Construction in Seismic Zones," Center for Civil Engineering Earthquake Research, Department of Civil and Environmental Engineering, University of Nevada, Reno, Nevada, Report No. CCEER-13-08, April 2013.

CCEER 13-09 Ryan, K.L., Coria, C.B., and Dao, N.D., "Large Scale Earthquake Simulation of a Hybrid Lead Rubber Isolation System Designed under Nuclear Seismicity Considerations," Center for Civil Engineering Earthquake Research, Department of Civil and Environmental Engineering, University of Nevada, Reno, Nevada, Report No. CCEER-13-09, April 2013.

CCEER 13-10 Wibowo, H., Sanford, D.M., Buckle, I.G., and Sanders, D.H., "The Effect of Live Load on the Seismic Response of Bridges," Center for Civil Engineering Earthquake Research, Department of Civil and Environmental Engineering, University of Nevada, Reno, Nevada, Report No. CCEER-13-10, May 2013.

CCEER 13-11 Sanford, D.M., Wibowo, H., Buckle, I.G., and Sanders, D.H., "Preliminary Experimental Study on the Effect of Live Load on the Seismic Response of Highway Bridges," Center for Civil Engineering Earthquake Research, Department of Civil and Environmental Engineering, University of Nevada, Reno, Nevada, Report No. CCEER-13-11, May 2013.

CCEER 13-12 Saad, A.S., Sanders, D.H., and Buckle, I.G., "Assessment of Foundation Rocking Behavior in Reducing the Seismic Demand on Horizontally Curved Bridges," Center for Civil Engineering Earthquake Research, Department of Civil and Environmental Engineering, University of Nevada, Reno, Nevada, Report No. CCEER-13-12, June 2013.

CCEER 13-13 Ardakani, S.M.S. and Saiidi, M.S., "Design of Reinforced Concrete Bridge Columns for Near-Fault Earthquakes," Center for Civil Engineering Earthquake Research, Department of Civil and Environmental Engineering, University of Nevada, Reno, Nevada, Report No. CCEER-13-13, July 2013.

CCEER 13-14 Wei, C. and Buckle, I., "Seismic Analysis and Response of Highway Bridges with Hybrid Isolation," Center for Civil Engineering Earthquake Research, Department of Civil and Environmental Engineering, University of Nevada, Reno, Nevada, Report No. CCEER-13-14, August 2013.

CCEER 13-15 Wibowo, H., Buckle, I.G., and Sanders, D.H., "Experimental and Analytical Investigations on the Effects of Live Load on the Seismic Performance of a Highway Bridge," Center for Civil Engineering Earthquake Research, Department of Civil and Environmental Engineering, University of Nevada, Reno, Nevada, Report No. CCEER-13-15, August 2013.

CCEER 13-16 Itani, A.M., Monzon, E.V., Grubb, M., and Amirihormozaki, E. "Seismic Design and Nonlinear Evaluation of Steel I-Girder Bridges with Ductile End Cross-Frames," Center for Civil Engineering Earthquake Research, Department of Civil and Environmental Engineering, University of Nevada, Reno, Nevada, Report No. CCEER-13-16, September 2013.

CCEER 13-17 Kavianipour, F. and Saiidi, M.S., "Experimental and Analytical Seismic Studies of a Four-span Bridge System with Composite Piers," Center for Civil Engineering Earthquake Research, Department of Civil and Environmental Engineering, University of Nevada, Reno, Nevada, Report No. CCEER-13-17, September 2013.

CCEER 13-18 Mohebbi, A., Ryan, K., and Sanders, D., "Seismic Response of a Highway Bridge with Structural Fuses for Seismic Protection of Piers," Center for Civil Engineering Earthquake Research, Department of Civil and Environmental Engineering, University of Nevada, Reno, Nevada, Report No. CCEER-13-18, December 2013.

CCEER 13-19 Guzman Pujols, Jean C., Ryan, K.L., "Development of Generalized Fragility Functions for Seismic Induced Content Disruption," Center for Civil Engineering Earthquake Research, Department of Civil and Environmental Engineering, University of Nevada, Reno, Nevada, Report No. CCEER-13-19, December 2013.

CCEER 14-01 Salem, M. M. A., Pekcan, G., and Itani, A., "Seismic Response Control Of Structures Using Semi-Active and Passive Variable Stiffness Devices," Center for Civil Engineering Earthquake Research, Department of Civil and Environmental Engineering, University of Nevada, Reno, Nevada, Report No. CCEER-14-01, May 2014.

CCEER 14-02 Saini, A. and Saiidi, M., "Performance-Based Probabilistic Damage Control Approach for Seismic Design of Bridge Columns," Center For Civil Engineering Earthquake Research, Department Of Civil and Environmental Engineering, University of Nevada, Reno, Nevada, Report No. CCEER-14-02, May 2014.

CCEER 14-03 Saini, A. and Saiidi, M., "Post Earthquake Damage Repair of Various Reinforced Concrete Bridge Components," Center For Civil Engineering Earthquake Research, Department Of Civil and Environmental Engineering, University of Nevada, Reno, Nevada, Report No. CCEER-14-03, May 2014.

CCEER 14-04 Monzon, E.V., Itani, A.M., and Grubb, M.A., "Nonlinear Evaluation of the Proposed Seismic Design Procedure for Steel Bridges with Ductile End Cross Frames," Center For Civil Engineering Earthquake Research, Department Of Civil and Environmental Engineering, University of Nevada, Reno, Nevada, Report No. CCEER-14-04, July 2014.

CCEER 14-05 Nakashoji, B. and Saiidi, M.S., "Seismic Performance of Square Nickel-Titanium Reinforced ECC Columns with Headed Couplers," Center For Civil Engineering Earthquake Research, Department Of Civil and Environmental Engineering, University of Nevada, Reno, Nevada, Report No. CCEER-14-05, July 2014.

CCEER 14-06 Tazarv, M. and Saiidi, M.S., "Next Generation of Bridge Columns for Accelerated Bridge Construction in High Seismic Zones," Center For Civil Engineering Earthquake Research, Department Of Civil and Environmental Engineering, University of Nevada, Reno, Nevada, Report No. CCEER-14-06, August 2014.

CCEER 14-07 Mehrsoroush, A. and Saiidi, M.S., "Experimental and Analytical Seismic Studies of Bridge Piers with Innovative Pipe Pin Column-Footing Connections and Precast Cap Beams," Center For Civil Engineering Earthquake Research, Department Of Civil and Environmental Engineering, University of Nevada, Reno, Nevada, Report No. CCEER-14-07, December 2014.

CCEER 15-01 Dao, N.D. and Ryan, K.L., "Seismic Response of a Full-scale 5-story Steel Frame Building Isolated by Triple Pendulum Bearings under 3D Excitations," Center For Civil Engineering Earthquake Research, Department Of Civil and Environmental Engineering, University of Nevada, Reno, Nevada, Report No. CCEER-15-01, January 2015.

CCEER 15-02 Allen, B.M. and Sanders, D.H., "Post-Tensioning Duct Air Pressure Testing Effects on Web Cracking," Center For Civil Engineering Earthquake Research, Department Of Civil and Environmental Engineering, University of Nevada, Reno, Nevada, Report No. CCEER-15-02, January 2015.

CCEER 15-03 Akl, A. and Saiidi, M.S., "Time-Dependent Deflection of In-Span Hinges in Prestressed Concrete Box Girder Bridges," Center For Civil Engineering Earthquake Research, Department Of Civil and Environmental Engineering, University of Nevada, Reno, Nevada, Report No. CCEER-15-03, May 2015.

CCEER 15-04 Zargar Shotorbani, H. and Ryan, K., "Analytical and Experimental Study of Gap Damper System to Limit Seismic Isolator Displacements in Extreme Earthquakes," Center For Civil Engineering Earthquake Research, Department Of Civil and Environmental Engineering, University of Nevada, Reno, Nevada, Report No. CCEER-15-04, June 2015.

CCEER 15-05 Wieser, J., Maragakis, E.M., and Buckle, I., "Experimental and Analytical Investigation of Seismic Bridge-Abutment Interaction in a Curved Highway Bridge," Center For Civil Engineering Earthquake Research, Department Of Civil and Environmental Engineering, University of Nevada, Reno, Nevada, Report No. CCEER-15-05, July 2015.

CCEER 15-06 Tazarv, M. and Saiidi, M.S., "Design and Construction of Precast Bent Caps with Pocket Connections for High Seismic Regions," Center For Civil Engineering Earthquake Research, Department Of Civil and Environmental Engineering, University of Nevada, Reno, Nevada, Report No. CCEER-15-06, August 2015.

CCEER 15-07 Tazarv, M. and Saiidi, M.S., "Design and Construction of Bridge Columns Incorporating Mechanical Bar Splices in Plastic Hinge Zones," Center For Civil Engineering Earthquake Research, Department Of Civil and Environmental Engineering, University of Nevada, Reno, Nevada, Report No. CCEER-15-07, August 2015.

CCEER 15-08 Sarraf Shirazi, R., Pekcan, G., and Itani, A.M., "Seismic Response and Analytical Fragility Functions for Curved Concrete Box-Girder Bridges," Center For Civil Engineering Earthquake Research, Department Of Civil and Environmental Engineering, University of Nevada, Reno, Nevada, Report No. CCEER-15-08, December 2015.

CCEER 15-09 Coria, C.B., Ryan, K.L., and Dao, N.D., "Response of Lead Rubber Bearings in a Hybrid Isolation System During a Large Scale Shaking Experiment of an Isolated Building," Center For Civil Engineering Earthquake Research, Department Of Civil and Environmental Engineering, University of Nevada, Reno, Nevada, Report No. CCEER-15-09, December 2015.

CCEER 16-01 Mehraein, M and Saiidi, M.S., "Seismic Performance of Bridge Column-Pile-Shaft Pin Connections for Application in Accelerated Bridge Construction," Center For Civil Engineering Earthquake Research, Department Of Civil and Environmental Engineering, University of Nevada, Reno, Nevada, Report No. CCEER-16-01, May 2016.